ASNR25 ABSTRACT PROCEEDINGS

Scientific Oral Presentations	2-287
Electronic Scientific Posters	288-520
Excerpta Posters	521-686
Educational Exhibits	687-939

Scientific Oral Presentations

93

Fetal MR imaging anatomy of the hippocampal head

Eleonora Piccirilli MD[1], Sante G Troia MD[1], Valentina Panara MD, PhD[1], Emanuele Pravatà MD[1], Luigi Ippoliti Prof.[2], Massimo Caulo Prof.[1]
[1]University of Chieti, Department of Neuroscience, Imaging and Clinical Sciences, Chieti, Abruzzo, Italy. [2]University of Chieti, Department of Economics, Chieti, Abruzzo, Italy

Abstract Category

Pediatrics

Purpose

The head of the adult hippocampus is characterized by the presence of sulci and digitations, not only visible on histological specimens but also in vivo on MR images. The aim of this MR study is to describe the anatomical variants of these hippocampal digitations in fetuses as well.

Materials & Methods

310 fetal MR acquired on a 1.5T Scanner (Philips Ingenia, The Nederlands) were retrospectively assessed (19-39 weeks of gestational age, GA). The standardized protocol in use at our Institution included ssFSE T1 and T2 sequences, and DWI (*b* values: 0, 500, 700 s/mm^2) on the three orthogonal planes. The head of the fetal hippocampus was identified on coronal T2 sequences using the adults anatomical reference, on a plane passing through the uncle recess of the temporal horn of the lateral ventricle. The anatomical variants of the head of the fetal hippocampus were classified according to the adult classification: class 1, no sulci and one digitation; class 2, single sulcus and two digitations; class 3, two sulci and three digitations. MRIs with pathological findings, abnormal sulcal and gyral pattern according to GA, and extreme motion artifacts were excluded.

Variant frequencies for both hemispheres were grouped by gestational age (GA). In addition to descriptive statistics for class frequencies, a Marginal Homogeneity Test was applied to assess potential differences between hemispheres (p<.05).

Results

214 fetal MRIs were finally included, divided in 8 groups by GA (in weeks): 19–21 (34), 22–23 (58), 24–25 (40), 26–27 (38), 28–29 (76), 30–31 (70), 32–33 (62) e >34 (50). The absolute frequency of the individual classes in the study population is 43.5% for class 1, 41.8% for class 2, and 14.7% for class 3. The variants' frequencies change with GA: the frequency of class 1 decreases with increasing GA age, while the frequencies of classes 2 and 3 increase. Moreover, it was noted that starting from the 24th week of GA there is an increase in the detection of hippocampal digitations, rising from 1 out of 14 fetuses at the 23rd week to 7 out of 14 fetuses at the 24th week (50% of the fetuses). No statistically significant differences were observed in the frequency of the classes between the two hemispheres.

Conclusion

The study allowed the description of anatomical variants of the hippocampal head in fetuses, previously studied in vivo in adults only. It was observed that as gestational age progresses, there is a gradual increase in the number of digitations and a rise in the frequency of variants 2 and 3, gradually aligning with the frequencies seen in adults. This classification provides further insight into hippocampal development and serves as an additional MRI marker for fetal brain maturation.

References

Piccirilli E, Gentile L, Mattei PA, et al. MRI-based classification of the anatomical variants of the hippocampal head. Neuroradiology 2020 Sep;62(9):1105-1110

94

Correlation of MRI with Protoporphyrin IX Fluorescence and Stimulated Raman Histology in Glioblastomas

Matthew D Lee, Andrew Smith, Mustafa Nasir-Moin, Daniel Orringer, Rajan Jain
NYU Grossman School of Medicine, New York, NY, USA

Abstract Category

Adult Brain

Purpose

Maximal safe resection of glioblastomas is variably achieved. Fluorescence-guided surgery with 5-aminolevulinic acid (5-ALA) improves extent of resection by facilitating differentiation of tumor-infiltrated and normal tissue via fluorescence when 5-ALA is metabolized to protoporphyrin IX (PpIX), but the cellular mechanisms and MRI manifestations in glioblastomas remain unclear. An emerging intraoperative microscopic imaging technique, stimulated Raman histology (SRH), may help elucidate these mechanisms by simulating hematoxylin and eosin staining to rapidly reveal cellular and architectural differences between normal and diseased tissue. Our study aims to investigate these cellular differences and their MRI phenotypes by correlating the MRI appearance of paired PpIX fluorescence and SRH imaging of stereotactic biopsy samples using a novel intraoperative multimodal two-photon fluorescence microscope (1).

Materials & Methods

In this prospective study, adult treatment-naïve brain tumor patients found to have IDH-wildtype glioblastoma underwent preoperative MRI with diffusion tensor imaging and dynamic susceptibility-contrast perfusion. Regions of interest (ROIs) for potential biopsy sites were prospectively delineated. During 5-ALA-guided surgery, biopsies were taken using frameless stereotactic navigation. Samples were analyzed with the NIO Laser Imaging System to generate paired SRH and PpIX fluorescence images. SRH involved sequential imaging for lipids, proteins, and DNA with a pseudo-color scheme (2). PpIX fluorescence was quantified, adjusting for lipofuscin interference. Pearson correlation coefficients were calculated between PpIX fluorescence or cellular density and MRI-derived apparent diffusion coefficient (ADC), fractional anisotropy (FA), and leakage-corrected relative cerebral blood volume (rCBV) normalized to contralateral normal-appearing white matter within 10 mm^2 ROIs.

Results

Eleven patients (3 female; median age 60 years) yielded 45 biopsy samples. Fluorescence and cellular density were not significantly correlated (p=.83). Table and Figure show correlations of MRI parameters with fluorescence and cell density. ADC showed moderate negative correlation with cell density (r=-0.32, p=.03). FA showed borderline positive correlation with cell density (r=.31, p=.051) and moderate positive correlation with fluorescence (r=0.34, p=.03), indicating areas with more structured fiber tracts may exhibit greater fluorescence. rCBV was not significantly correlated with fluorescence (p=.54) or cell density (p=.15).

Conclusion

This study highlights the complex relationship between MRI characteristics, PpIX fluorescence, and cellular density in GBM. The association of ADC with cell density may help guide biopsy and treatment planning. The lack of significant rCBV correlations warrants further investigation into tumor vascular properties. The correlation between FA and fluorescence suggests structural characteristics influence fluorescence, which may aid optimization of 5-ALA-guided surgery.

References

1. Nasir-Moin M, Wadiura LI, Sacalean V, Juros D, Movahed-Ezazi M, Lock EK, et al. Localization of protoporphyrin IX during glioma-resection surgery via paired stimulated Raman histology and fluorescence microscopy. Nat Biomed Eng. 2024;8(6):672-88.

2. Orringer DA, Pandian B, Niknafs YS, Hollon TC, Boyle J, Lewis S, et al. Rapid intraoperative histology of unprocessed surgical specimens via fibre-laser-based stimulated Raman scattering microscopy. Nat Biomed Eng. 2017;1.

Images/Tables

Table. Pearson correlation coefficients of MRI parameters with PpIX fluorescence and cell density. P-values in parentheses.

Parameter	Fluorescence	Cell Density (cells/mm^2)
ADC	-0.14 (.38)	-0.32 (.03)
FA	0.34 (.03)	0.31 (.051)
rCBV	0.10 (.54)	-0.23 (.15)

Figure. Correlation of MRI parameters with PpIX fluorescence and cell density.

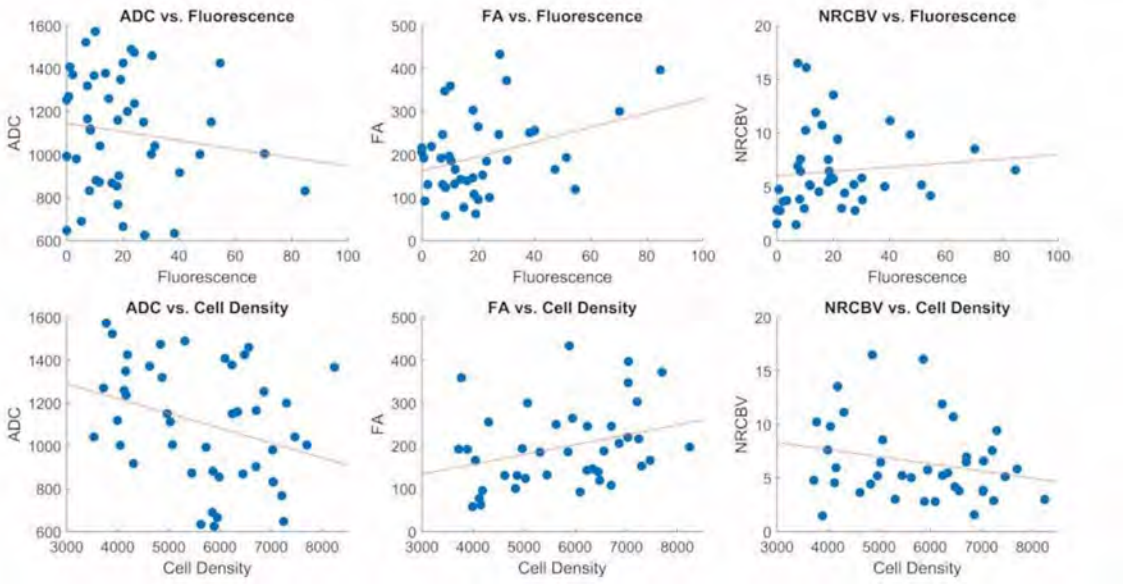

107

The Impact of Diffusion and Perfusion-Weighted Imaging on Glioma Grading

Duy Quang Ngo Medical Doctor
Ha Noi Medical University, Ha Noi, Dong Da, Vietnam

Abstract Category

Adult Brain

Purpose

Determining the grade of a glioma is extremely important for treatment planning and prognosis prediction. The study aimed to evaluate the usefulness of multiparametric perfusion-weighted imaging (PWI) and diffusion-weighted imaging (DWI) in preoperative glioma grading.

Materials & Methods

In this retrospective study, 63 individuals with brain tumors histologically confirmed, of which 23 had low-grade gliomas (LGGs), and 40 had high-grade gliomas (HGGs) were involved. We conducted this paper on apparent diffusion coefficient (ADC) maps using the entire tumor volume method, allowing us to use all ADC values of the tumor. Small-sample regions of interest (ROIs) were drawn to collect parameters of relative cerebral blood flow (rCBF), cerebral blood flow (CBF), and relative cerebral blood volume (rCBV) from both the tumor core and peritumoral edema. The PWI and DWI metrics were compared to identify the most accurate distinguishing HGGs and LGGs, analyze receiver operating characteristics (ROC), and evaluate the diagnostic performance using solitary parameters and combined.

Results

In diffusion MRI, there were significant differences in minimum ADC and mean ADC between LGGs and HGGs ($p<0.05$), with the larger area under the curve (AUC) of 0.898 found for mean ADC at a cut-off value of 1.275, with sensitivity of 82.6 % and specificity of 90 %. The maximum ADC value did not differ significantly ($p>0.05$). All perfusion parameters in both the tumor core and peritumoral edema area were significantly greater values in cases of HGG compared to LGG ($p<0.001$), with the highest AUC of 0.946 found for solid tumor rCBV value (rCBVt), the cut-off is 3.585, sensitivity of

85 % and specificity of 100 %. Combining mean ADC and rCBVt provided an excellent AUC of 0.975, a sensitivity of 92.5 %, and a specificity of 91.3 % for differentiating between HGGs and LGGs.

Conclusion

Perfusion and diffusion MRI are valuable in discriminating between high-grade and low-grade gliomas, with the major criterion in the decision-making process being the combined mean ADC and rCBVt parameters.

References

1. Barnholtz-Sloan, JS, Ostrom, QT, Cote, D. Epidemiology of brain tumors. *Neurol Clin* 2018;36:395–419. https://doi.org/10.1016/j.ncl.2018.04.001.

2. Osborn, AG, Louis, DN, Poussaint, TY, Linscott, LL, Salzman, KL. The 2021 World Health Organization classification of tumors of the central nervous system: what neuroradiologists need to know. *Am J Neuroradiol* 2022;43:928–37. https://doi.org/10.3174/ajnr.a7462.

3. Romanidou, O, Apostolou, P, Kouvelakis, K, Tsangaras, K, Eliades, A, Achilleos, A, et al.. Molecular profile and clinical features of patients with gliomas using a broad targeted next generation-sequencing panel. *Oncol Lett* 2022;25:38. https://doi.org/10.3892/ol.2022.13624.

4. Ostrom, QT, Patil, N, Cioffi, G, Waite, K, Kruchko, C, Barnholtz-Sloan, JS. CBTRUS statistical report: primary brain and other central nervous system tumors diagnosed in the United States in 2013–2017. *Neuro Oncol* 2020;22:iv1–96. https://doi.org/10.1093/neuonc/noaa200.

5. Liang, J, Lv, X, Lu, C, Ye, X, Chen, X, Fu, J, et al.. Prognostic factors of patients with Gliomas – an analysis on 335 patients with Glioblastoma and other forms of Gliomas. *BMC Cancer* 2020;20:35. https://doi.org/10.1186/s12885-019-6511-6.

Images/Tables

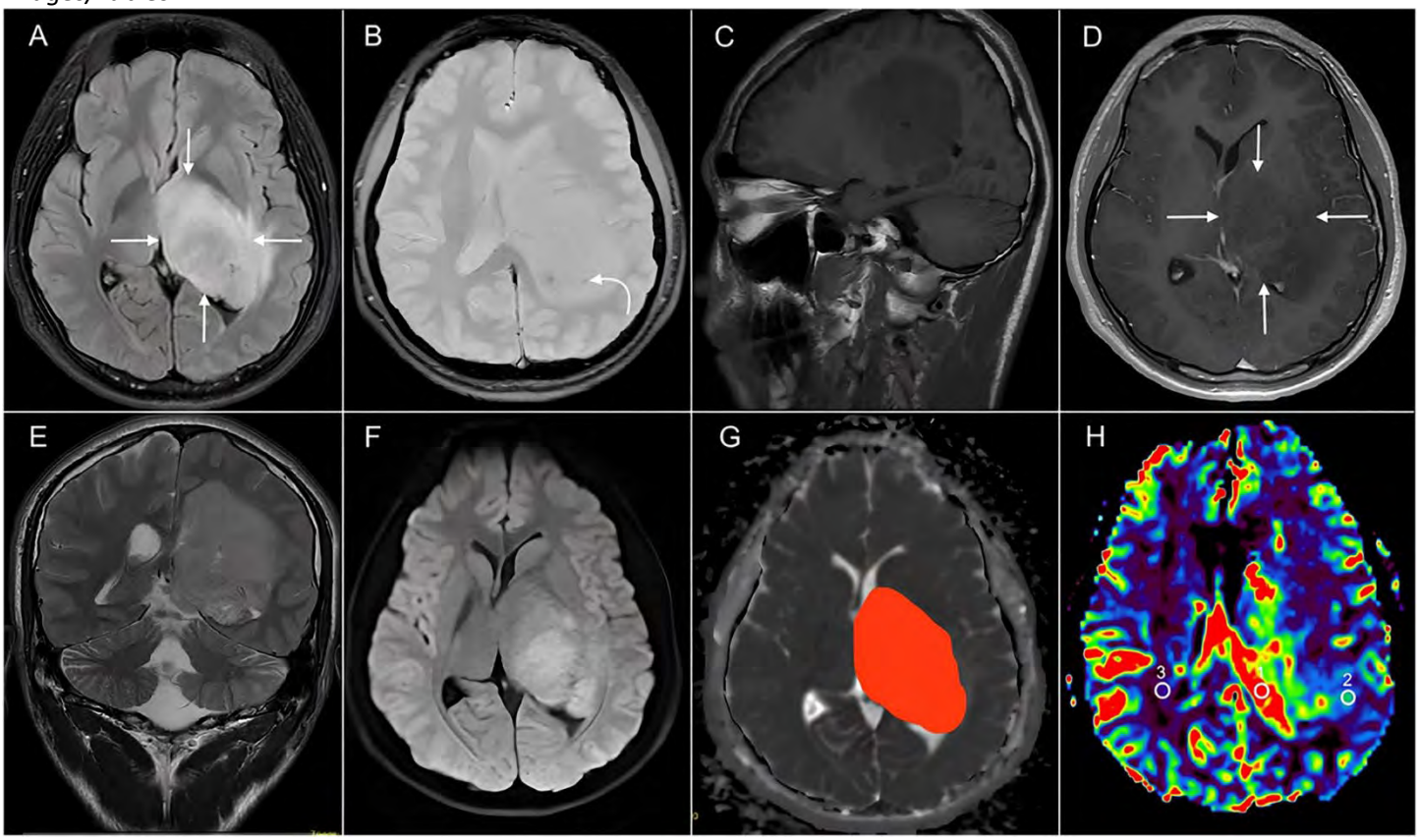

112

CVR as a biomarker of dysregulated blood flow in cerebral tumors

Ece Su Sayin BSc[1], Ruth Lau MD[2], Olivia Sobczyk PhD[2], James Duffin PhD[1], Julien Poublanc MSc[2], Lashmikumar Venkat Raghavan MD[2], Aristotelis Kalyvas MD PhD[2], Gelarah Zadeh MD PhD[2], Joseph A Fisher MD[1], David J Mikulis MD[2]
[1]University of Toronto, Toronto, ON, Canada. [2]Univeristy Health Network, Toronto, ON, Canada

Abstract Category

Adult Brain

Purpose

The proliferation of neoplastic glia is associated with abnormal blood flow in the affected tissue.[1] Measurement of abnormal tumor tissue perfusion has proven useful in tumor typing and in assessing response to treatment. However, an important functional role of tumor vessels, i.e. the ability to augment flow, has not been as thoroughly investigated. Measurement of hemodynamic response to a standard vasoactive stimulus is called cerebrovascular reactivity (CVR). The purpose of this study was to examine the vasodilatory responses of wildtype and mutant and glioblastomas. We hypothesize that CVR may be sensitive to tumor type or grade.

Materials & Methods

14 patients (5 F) with known tumour diagnoses were selected (Table 1). All but 1 patient had their tumour resected and sent for pathological testing. A routine clinical imaging protocol was carried out on a 3T MR system using a 32-channel head coil. A BOLD MRI cerebrovascular reactivity (CVR) study was then performed using a quantitative CO_2 stimulus (RespirAct^{TM}) consisting of a step and ramp protocol (Figure 1). Using AFNI software (Cox, 1996), the whole brain average BOLD signal was shifted to match the onset of $PetCO_2$ and best pixels in the brain. BOLD signal was then separated into two sections: the step and ramp portion. For each of the sections, a linear regression was applied between the BOLD signal and $PETCO_2$. This analysis was conducted on a voxel-by-voxel basis to compute both step CVR values (for higher sensitivity) and ramp CVR values (for greater specificity).. CVR was measured as the percent change in BOLD signal per change in $PetCO_2$ (%/mmHg). The Step-CVR and Ramp-CVR values were compared between IDH-Mutant and IDH-Wildtype in the tumor ROI and the healthy contralateral hemisphere using a paired t-test.

Results

A boxplot distribution (Figure 2) showed that the tumour ROI had lower CVR in comparison to the homologous ROI from the contralateral healthy hemisphere. Figure 3 shows a patient with manually delineated ROI mask and corresponding CVR maps. The tumour exhibited steal physiology (blue indicating that blood flow decreased in the tumor during the vasodilatory stimulus). The distribution of CVR metrics between IDH-Mutant and IDH-Wildtype in the tumour region of interest was a significantly different for Ramp-CVR in the tumour ROI ($p>0.05$), with all other interactions not significantly different (Figure 4).

Conclusion

Limited flow increases, even to the point of steal physiology, are present in gliomas and are more impaired in IDH mutants. Statistical p-values are stronger for the step stimulus indicating its higher sensitivity for detecting the presence of flow dysregulation differences than the ramp stimulus. The findings indicate that measurement of CVR has the potential to add to the armamentarium of radiomic metrics used for tumor assessment.

References

1. Sanchez I, Rahman R. Radiogenomics as an Integrated Approach to Glioblastoma Precision Medicine. Curr Oncol Rep. 2024 Oct;26(10):1213-1222. doi: 10.1007/s11912-024-01580-z. Epub 2024 Jul 16. PMID: 39009914; PMCID: PMC11480134.

Images/Tables

Table 1. Patient demographics and characteristics. The astericks* indicates that the patient has not had their tumour resected.

Patient ID	Age	Sex	Gadolinium Enhancement	Lesion	WHO Grade	IDH Type
1	23	M	no	right frontal	2	Mutant
2	39	M	yes	right frontal	3	Mutant
3	56	M	yes	left frontal	4	Wildtype
4	67	M	yes	left frontal	4	Wildtype
5	60	M	no	right temporoparietal	4	Wildtype
6	50	M	no	right SMA	3	Mutant
7	42	F	no	left preSMA	2	Mutant
8	31	M	yes	left temporal	4	Mutant
9	39	F	yes	left temporomesial	4	Wildtype
10*	65	F	no	left temporal	2	--
11	41	F	yes	right temporal	4	Wildtype
12	36	F	yes	left temporal	4	Wildtype
13	21	M	no	left temporal	3	Mutant
14	23	M	no	left temporal	2	Mutant

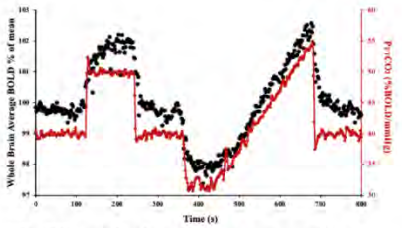

Figure 1. The CVR protocol implemented of a representative participant.

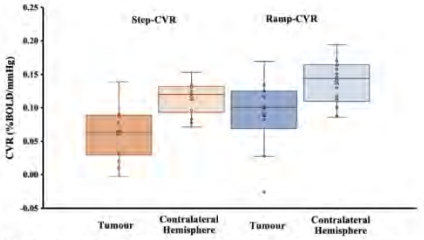

Figure 2. The boxplot distribution of the Step-CVR and Ramp-CVR metrics in the tumour hemisphere and contralateral hemisphere for the 15 patients.

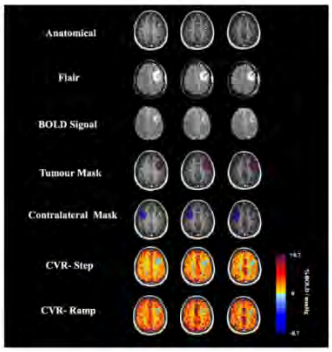

Figure 3. A representative patient with a left frontal high-grade glioblastoma (56 M). An example of the tumour and contralateral mask used to calculate the Step-CVR and Ramp-CVR values within the hand drawn region of interest.

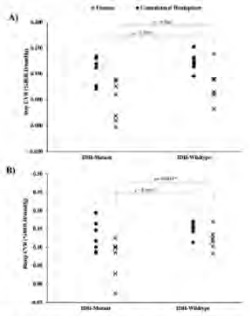

Figure 4. The distribution of CVR metrics between IDH-Mutant and IDH-Wildtype in the tumour region of interest and that in the healthy contralateral hemisphere for A) Step-CVR and B) Ramp-CVR. There was a significant difference in Ramp-CVR in the tumour region of interest between IDH-Mutant and IDH-Wildtype ($p>0.05$), all other interactions were not significantly different.

114

Deep Brain Stimulation Electrode Deviations are Associated with Brain Stiffness Interfaces Measured by Magnetic Resonance Elastography

Chengyuan Wu MD, MSBmE[1], Mahdi Alizadeh PhD[1], Mary K Kramer MS[2], Matthew B Kroen BS[2], Robert Ziechmann MD[1], Feroze Mohamed PhD[1], Qianhong Wu PhD[3], Curtis Johnson PhD[2]

[1]Thomas Jefferson University, Philadelphia, PA, USA. [2]University of Delaware, Newark, DE, USA. [3]Villanova University, Villanova, PA, USA

Abstract Category

Functional/Advanced Imaging

Purpose

Stereotaxy involves planning straight-line trajectories using preoperative imaging and treats the brain as a rigid object. However, 80% of deep brain stimulation (DBS) electrodes bend and deviate from their intended trajectory,[1] even without pneumocephalus and brain shift from introducing intracranial air. With electrode location paramount to optimizing outcomes,[2] target deviation requires consideration of additional brain penetrations to reposition the electrode.

We hypothesized that probe insertion during surgery can deform the brain, with variations in brain tissue mechanical properties between individuals impacting target deviations. Magnetic Resonance Elastography (MRE) provides in vivo quantification of brain stiffness and has shown that stiffness generally increases from cortical gray matter, to white matter, to deep brain structures.[3] The goal of this study was to assess if MRE-defined interfaces are associated with DBS electrode deviation, which may occur at interfaces between tissues of different stiffnesses. Specifically, the electrode may deviate similar to light refraction between different media, with the denser internal capsule (IC) fibers being most influential.[4]

Materials & Methods

Ten patients with Parkinson's disease scheduled for DBS surgery underwent preoperative 3T MRE using synchronized external vibrations (50 Hz) and high-resolution multiband sequences to generate whole-brain maps of shear stiffness. Imaging parameters included: TR=1.92sec; TE=77ms; FOV=240x240mm^2; matrix=192x192; 1.25mm^3 isotropic

voxels. The *IC stiffness interface* (ICSI) was identified as a sharp transition in stiffness between the corona radiata and IC. [Fig1] Descriptive measurements of the ICSI included the *lateral angle* relative to midline and the *anterior-posterior angle* relative to the line connecting the anterior and posterior commissures. [Fig2] The *rate of transition* was calculated as the change in stiffness across the ICSI. Postoperative CTs were used to measure *target deviation*. The *angle of approach* was calculated as the angle between the planned trajectory and the normal vector to the ICSI. [Fig3] Pearson correlations and t-tests were performed to evaluate associations between the angle of approach and target deviation.

Results

Ten patients (7 female, age 61±7.5yo) with 21 trajectories were analyzed. The ICSI was clearly identified in all cases, with anterior-posterior angles of 89.9±39.2° and lateral angles of 90.4±36.2°. The rates of transition were 94.8±64.5$^{Pa}/_{mm}$. Mean electrode deviation was 1.27±0.63mm, with 38% of trajectories >1.5mm. The angle of approach was significantly correlated with electrode deviation ($r=0.57$, $p=0.007$). [Fig4] Deviations >1.5mm were associated with higher angles of approach (mean 50.9° vs. 26.1°; $p<0.001$). [Fig5] Rate of transition did not correlate with deviation ($p=0.947$).

Conclusion

This study demonstrates that brain tissue stiffness along stereotactic trajectories affects DBS electrode deviation; and that that MRE can quantify stiffness profiles in Parkinson's disease. Specifically, the angle of approach to the ICSI correlates with target deviation, supporting the hypothesis that tissue mechanics influence electrode bending. Patient-specific MRE is necessary to measure variability of the ISCI orientation. Future work will further explore the role of other tissue interfaces traversed during DBS implantation and the role of tissue mechanics in electrode deviation. MRE has potential to quantify the likelihood of DBS electrode deviation and influence planned trajectories, which could reduce revision surgeries and enhance clinical outcomes.

References

1. Kim M, Jung NY, Chang JW. Image analysis of the intracranial lead bending phenomenon during deep brain stimulation. *PLoS One*. 2020;15(8):e0237537. doi:10.1371/journal.pone.0237537
2. Ellis TM, Foote KD, Fernandez HH, et al. Reoperation for suboptimal outcomes after deep brain stimulation surgery. *Neurosurgery*. Oct 2008;63(4):754-60; discussion 760-1. doi:10.1227/01.NEU.0000325492.58799.35
3. Hiscox LV, McGarry MDJ, Schwarb H, et al. Standard-space atlas of the viscoelastic properties of the human brain. *Hum Brain Mapp*. Dec 15 2020;41(18):5282-5300. doi:10.1002/hbm.25192
4. Burchiel KJ, McCartney S, Lee A, Raslan AM. Accuracy of deep brain stimulation electrode placement using intraoperative computed tomography without microelectrode recording. *J Neurosurg*. Aug 2013;119(2):301-6. doi:10.3171/2013.4.JNS122324

Images/Tables

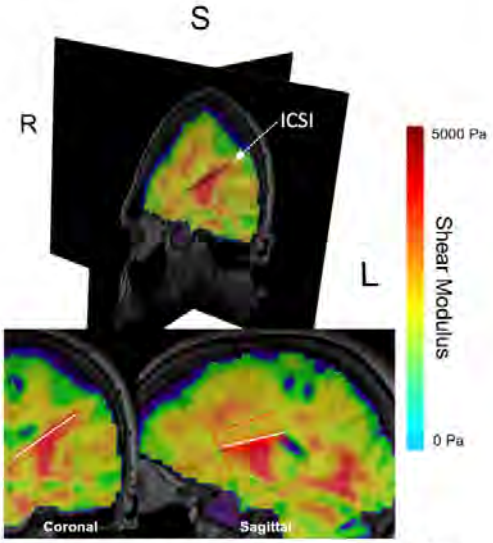

Figure 1 – The *Internal capsule stiffness interface* (ICSI) was defined as a sharp transition in stiffness between the corona radiata and internal capsule. This plane was defined in three dimensions based on the shear modulus measurements obtained from preoperative MRE. A 3-dimensional representation of the ICSI plane (red) is shown relative to cutaway images in the coronal and sagittal planes [top]; and its intersection with coronal and sagittal views is represented by a brighter red line along the plane [bottom]

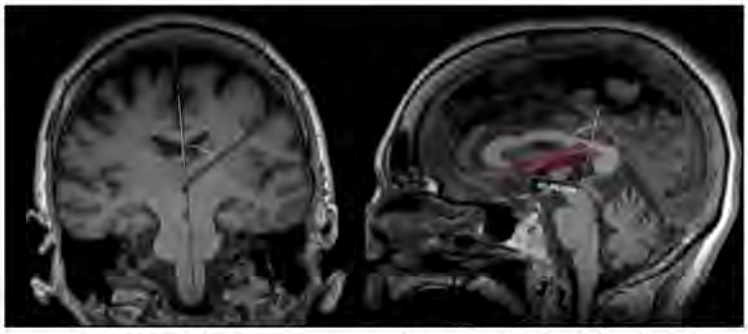

Figure 2 – Descriptive measurements of the internal capsule stiffness interface (ICSI). The *lateral angle* [left] is measured relative to the midline plane on a coronal view. The *anterior-posterior angle* [right] is measured relative to a line perpendicular to a line connecting the anterior commissure to the posterior commissure of the brain (AC-PC line)

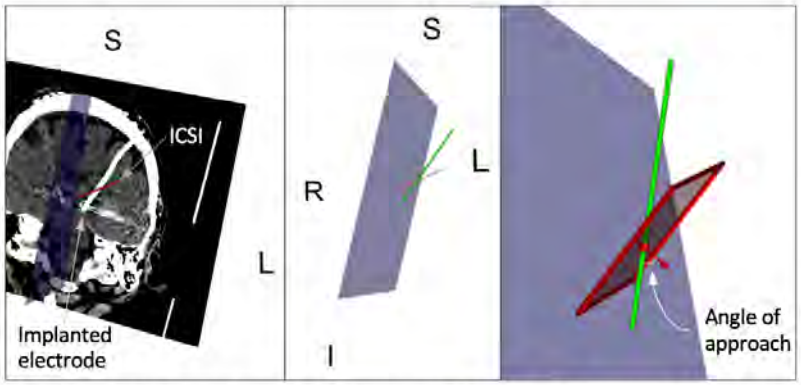

Figure 3 – With the postoperative CT scan coregistered to the preoperative MRI, the relationship between the planned trajectory, implanted electrode, and internal capsule stiffness interface (ICSI) an be observed [left panel]. The blue plane represents the midline plane and serves as a spatial reference. The planned trajectory can be visualized as a path (green) that crosses the ICSI (red) [center panel]. The *angle of approach* (white) can then be measured as the angle between the planned trajectory and the normal vector to the ICSI [right panel].

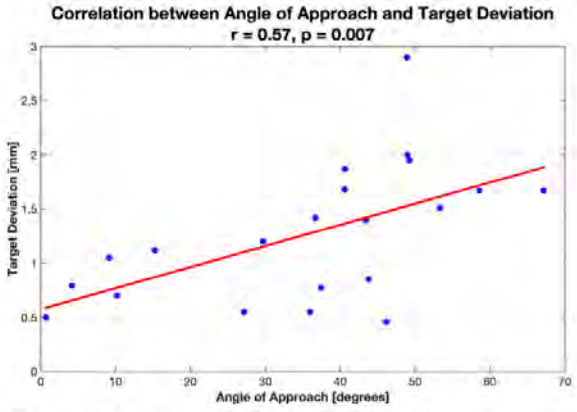

Figure 4 – The *angle of approach* was significantly correlated with the *electrode deviation* (r = 0.57, p = 0.007). As shown in Figure 3, an angle of 0° represents a trajectory that is perfectly orthogonal to the ISCI; while larger values indicate more acute angles of approach. This relationship supports the hypothesis that tissue mechanics – specifically the relationship of the planned trajectory to existing tissue planes – has an influence electrode bending and target deviation.

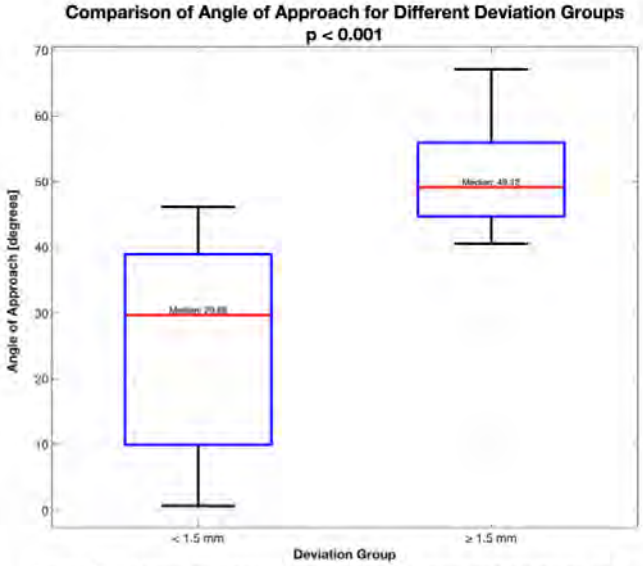

Figure 5 – Larger deviations (≥1.5mm) of the implanted electrode from the intended target were associated with higher angles of approach (mean of 50.9°) than smaller deviations (<1.5mm) (mean of 26.1°) (p = 0.0009). This relationship further supports the hypothesis that the relationship of the planned trajectory to existing tissue planes has an influence electrode bending and target deviation.

124

Acceleration of brain aging after small-volume infarcts

Ying-Ju Peng MD[1], Chen-Yuan Kuo PhD[2], Sheng-Wei Chang MD[1], Ching-Po Lin PhD[3], Yuan-Hsiung Tsai MD, PhD[1]
[1]Department of Diagnostic Radiology, Chang Gung Memorial Hospital, Chiayi, none, Taiwan. [2]Department of Neurology, Neurological Institute, Taipei Veterans General Hospital, Taipei, none, Taiwan. [3]Institute of Neuroscience, National Yang Ming Chiao Tung University, Taipei, none, Taiwan

Abstract Category

Adult Brain

Purpose

Previous studies have shown that stroke patients exhibit greater neuroimaging-derived biological “brain age” than control subjects. This difference, known as the brain age gap (BAG), is calculated by comparing the chronological age with predicted brain age and is used as an indicator of brain health and aging. However, whether stroke accelerates the process of brain aging in patients with small-volume infarcts has not been established. By utilizing longitudinal data, we aimed to investigate whether small-volume infarctions can significantly increase the BAG, indicating accelerated brain aging.

Materials & Methods

A total of 123 stroke patients presenting with small-volume infarcts were included in this retrospective study. The brain age model was trained via established protocols within the field of machine learning and the structural features of the brain from our previous study. We used t-tests and regression analyses to assess longitudinal brain age changes after stroke and the associations between brain age, acute stroke severity, and poststroke outcome factors.

Results

Significant brain aging occurred between the initial and 6-month follow-ups, with a mean increase in brain age of 1.04 years ($t = 3.066$, $p < 0.05$). Patients under 50 years of age experienced less aging after stroke than those over 50 years of age ($p = 0.245$). Additionally, patients with a National Institute of Health Stroke Scale score >3 at admission presented more pronounced adverse effects on brain aging, even after adjusting for confounders such as chronological age, sex, and total intracranial volume ($F1,117 = 7.339$, $p = 0.008$, $\eta2 = 0.059$). There were significant differences in the proportional brain age difference at 6 months among the different functional outcome groups defined by the Barthel Index ($F2,118 = 4.637$, $p = 0.012$, $\eta2 = 0.073$).

Conclusion

Stroke accelerates the brain aging process, even in patients with relatively small-volume infarcts. This phenomenon is particularly accentuated in elderly patients, and both stroke severity and poststroke functional outcomes are closely associated with accelerated brain aging. Further studies are needed to explore the mechanisms underlying the accelerated brain aging observed in stroke patients, with a particular focus on the structural alterations and plasticity of the brain following minor strokes.

References

1. Egorova, N., Liem, F., Hachinski, V., and Brodtmann, A. (2019). Predicted brain age after stroke. Front. Aging Neurosci. 11:348. doi: 10.3389/fnagi.2019.00348
2. Kuo, C.-Y., Lee, P.-L., Peng, L.-N., Lee, W. J., Wang, P. N., Chen, L. K., et al. (2023).Advanced brain age in community-dwelling population with combined physical and cognitive impairments. Neurobiol. Aging 130, 114–123. doi: 10.1016/j. neurobiolaging.2023.06.017
3. Kuo, C.-Y., Tai, T.-M., Lee, P.-L., Tseng, C. W., Chen, C. Y., Chen, L. K., et al. (2021). Improving individual brain age prediction using an ensemble deep learning framework. Front. Psych. 12:626677. doi: 10.3389/fpsyt.2021.626677
4. Lee, P.-L., Chou, K.-H., Lu, C.-H., Chen, H. L., Tsai, N. W., Hsu, A. L., et al. (2018). Extraction of large-scale structural covariance networks from grey matter volume for Parkinson’s disease classification. Eur. Radiol. 28, 3296–3305. doi: 10.1007/s00330-018-5342-1
5. Katan, M., and Luft, A. (2018). Global burden of stroke. Semin. Neurol. 38, 208–211. doi: 10.1055/s-0038-1649503

Images/Tables

TABLE 1 Demographics and sample characteristics of the stroke patients.

	Mean (SD)
Total *N* (% females)	123 (64.2%)
Chronological age (years)	65.53 (11.31)
Hypertension	92 (74.8%)
Smoking	51 (41.5%)
Diabetes mellitus	43 (35%)
Hyperlipidemia	40 (32.5%)
IVTPA	0 (0%)
ICAD on MRA	11 (8.9%)
NIHSS score at ER department (points)	3.41 (2.52)
NIHSS score at admission (points)	3.69 (3.09)
Prestroke mRS score (points)	0 (0–0)*
WMH Vol (V%)	0.39 (0.66)
WMH Vol (cm^3)	5.25 (9.51)
Stroke volume (cm^3)	5.09 (5.71)
Stroke location	
Left	47 (38.2%)
Right	50 (40.7%)
Brain stem/cerebellum	20 (16.3%)
Bilateral	6 (4.9%)
TOAST classification	
Large artery atherosclerosis	0 (0%)
Cardioembolism	2 (1.6%)
Small-vessel occlusion	91 (74%)
Other/undetermined	30 (24.4%)
Length of stay (days)	10.79 (9.43)
Death	0 (0%)
Stroke in evolution	10 (8.1%)
Postacute care (PAC)	12 (9.8%)
Barthel index score (points)	74.79 (24.94)
Poststroke mRS score (points)	2.67 (1.42)

*Presented as the median (IQR).

TABLE 2 Demographics of stroke patients regarding brain age factors ($n = 123$).

	Mean (SD)
Brain age initial (years)	73.71 (9.17)
BAG initial (years)	8.18 (7.12)
Brain age 6 months (years)	75.24 (9.65)
BAG 6 months (years)	9.22 (7.30)
dBAG (years)	1.04 (3.75)
PBAD initial	0.14 (0.14)
PBAD 6 months	0.15 (0.14)
GMV initial (cm^3)	547.62 (63.85)
TIV initial (cm^3)	1366.23 (124.18)
GMV 6 months (cm^3)	543.02 (63.98)
TIV 6 months (cm^3)	1371.86 (121.96)

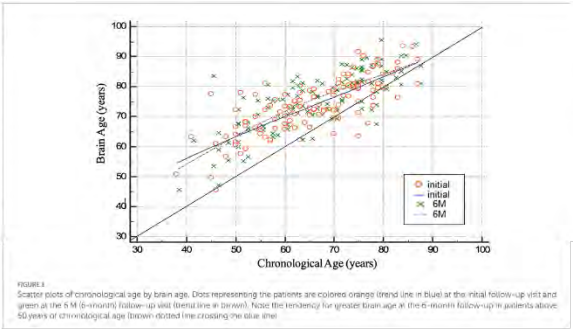

FIGURE 3
Scatter plots of chronological age by brain age. Dots representing the patients are colored orange (trend line in blue) at the initial follow-up visit and green at the 6 M (6-month) follow-up visit (trend line in brown). Note the tendency for greater brain age at the 6-month follow-up in patients above 50 years of chronological age (brown dotted line crossing the blue line).

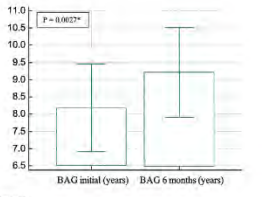

FIGURE 4
Bar graphs showing the results of the paired *t*-test in which we compared BAG by initial and 6-month status. BAG, brain age gap.

125

Assessment of Structural Connectivity in Chronic Blast Postconcussive Vestibular Dysfunction Using Probabilistic Tractography and NODDI

Joseph A Behnke MD, PhD[1], Vishwadeep Ahluwalia Ahluwalia PhD[2], Jeremy L Smith PhD, MSDS, MAMFT[3], Piper Lashley[4], Benjamin B Risk PhD[3], Russell K Gore MD[4], Jason W Allen MD, PhD[5]

[1]University of Pennsylvania, Philadelphia, PA, USA. [2]Georgia Institute of Technology, Atlanta, GA, USA. [3]Emory University, Atlanta, GA, USA. [4]Shepherd Center, Atlanta, GA, USA. [5]Indiana University School of Medicine, Indianapolis, IN, USA

Abstract Category

Functional/Advanced Imaging

Purpose

Postconcussive vestibular dysfunction (PCVD) is a common consequence following blast-mediated concussion that is associated with a protracted recovery from injury [1], yet there is a limited understanding of the structural changes following injury and their corresponding relationship to clinical symptoms. Comorbid affective disorders including post-traumatic stress disorder, depression and anxiety are highly prevalent in PCVD. Diffusion MRI (dMRI) provides a non-invasive technique to investigate underlying white matter integrity within PCVD. Using a combination of advanced dMRI techniques, including probabilistic tractography and neurite orientation dispersion and density imaging (NODDI), together with vestibular and affective clinical testing, the present study sought to characterize structural connectivity within brain regions involved in vestibular function and their relationship to clinical vestibular and affective impairment following blast injury within a military veteran population with chronic PCVD.

Materials & Methods

Chronic blast-mediated PCVD (n=26) and healthy control (n=24) subjects
underwent comprehensive clinical vestibular and affective testing, and multi-shell diffusion-weighted imaging (DWI). DWI was subjected to standard FMRIB Software Library (FSL) preprocessing workflows, including “topup” and “eddy” [2] for susceptibility- and eddy current-induced distortions, respectively. Both conventional diffusion tensor imaging (DTI; using “dtifit”) and multi-compartment modeling (using neurite orientation dispersion and density imaging [NODDI)]) [3] were performed. Multiple fiber orientations were estimated using “bedpostx”.
Automated probabilistic tractography was then performed on “bedpostx” data using “xtract” [4]: 1) “probtrackx”-generated connectivity distributions using apriori seed and target ROIs to generate white matter tract streamlines, then 2) extraction of tract-wise diffusion metric and volumetric summary statistics from DTI and NODDI maps using thresholded tract streamlines. Seed/target ROIs used within "probtrackx” were derived from vestibular cortical ROIs from the collated Eagle-449 vestibular atlas [5].

To assess the relationship between structural connectivity and clinical impairment, robust linear regression was performed using clinical measures as the response variable regressed over the ROI-extracted tract-wise summary statistics adjusted for age and time since injury.

Results

The posterior insular cortex (PIC) and parietal area OP2 (OP2), collectively known as the "core" vestibular cortex were used as seed ROIs for probabilistic tractography. Target ROIs included the inferior parietal/supramarginal area PFcm (IPL-PFcm), inferior parietal area PF/40/anterior supramarginal gyrus (IPL-PF), caudal cingulate area 23 (A23c) and dorsolateral middle temporal area 37/hMST (A37dl).

Robust linear regression revealed significant associations between clinical measures and tract-wise diffusion metrics. Connections with PIC were more prominent than those with OP2. Interestingly, right PIC-based connections appeared to be predominantly associated with vestibular clinical measures whereas those involving the left PIC were mostly associated with affective clinical measures. In particular, lower orientation dispersion index (ODI) within PIC-based connections was associated with higher clinical impairment within chronic PCVD.

Conclusion

The present study highlights novel associations between structural connectivity implicated in vestibular function and their corresponding relationship to vestibular and affective impairment following blast-mediated PCVD. This study is the first to our knowledge to demonstrate structural differences within white matter regions connecting vestibular ROIs that are associated with affective impairment within PCVD. These findings may reflect organizational remodeling in response to injury or anatomical predisposition to the development of chronic symptoms.

References

1. Rosenfeld JV, McFarlane AC, Bragge P, Armonda RA, Grimes JB, Ling GS. Blast-related traumatic brain injury. The Lancet Neurology. 2013;12(9):882-93. doi: https://doi.org/10.1016/S1474-4422(13)70161-3.
2. Smith SM, Jenkinson M, Woolrich MW, Beckmann CF, Behrens TEJ, Johansen-Berg H, Bannister PR, De Luca M, Drobnjak I, Flitney DE, Niazy RK, Saunders J, Vickers J, Zhang Y, De Stefano N, Brady JM, Matthews PM. Advances in functional and structural MR image analysis and implementation as FSL. NeuroImage. 2004;23:S208-S19. doi: https://doi.org/10.1016/j.neuroimage.2004.07.051.
3. Tariq M, Schneider T, Alexander DC, Gandini Wheeler-Kingshott CA, Zhang H. Bingham–NODDI: Mapping anisotropic orientation dispersion of neurites using diffusion MRI. NeuroImage. 2016;133:207-23. doi: https://doi.org/10.1016/j.neuroimage.2016.01.046.
4. Warrington S, Bryant KL, Khrapitchev AA, Sallet J, Charquero-Ballester M, Douaud G, Jbabdi S, Mars RB, Sotiropoulos SN. XTRACT-Standardised protocols for automated tractography in the human and macaque brain. Neuroimage. 2020;217:116923.
5. Smith JL, Ahluwalia V, Gore RK, Allen JW. Eagle-449: A volumetric, whole-brain compilation of brain atlases for vestibular functional MRI research. Scientific Data. 2023;10(1):29.

Images/Tables

Table 1 Demographics and Clinical Measure Summary

	Chronic Blast PCVD (CT)	Healthy Controls (HC)	n CT	n HC	P value* CT vs HC
Demographic					
N	26	24			
Age, years	38.0 (7.5)	31.5 (12.0)	26	24	p=0.022
Days since concussion	3696.0 (2972.0)				
Affective Measures					
BAI	34.0 (18.5)	0.0 (2.0)	22	22	p<.00001
BDI	32.0 (10.0)	1.0 (4.8)	21	22	p<.00001
PTSD - PCL 5	47.0 (23.5)	0.0 (2.0)	15	22	p<.00001
Subjective Clinical Measures					
PCSS	70.0 (33.0)	0.0 (0.0)	7	19	p<.00001
DHI	56.0 (43.0)	0.0 (0.0)	23	22	p<.00001
VVAS	39.0 (30.6)	0.0 (0.0)	23	22	p<.00001
SOT					
Composite SOT	63.0 (23.5)	77.0 (7.0)	24	23	p<.01
SOT Condition #1	90.7 (8.8)	92.3 (2.3)	24	23	n.s.
SOT Condition #2	87.5 (7.6)	91.3 (3.7)	24	23	p<.01
SOT Condition #3	87.0 (11.4)	92.7 (3.3)	24	23	p<.01
SOT Condition #4	61.2 (23.6)	77.0 (10.2)	24	23	p<.01
SOT Condition #5	43.5 (35.5)	65.3 (14.5)	24	23	p<.01
SOT Condition #6	51.7 (37.8)	70.3 (8.7)	24	23	p<.01
Sensory Analysis Ratios					
SOM	0.97 (0.05)	0.98 (0.03)	24	23	n.s.
VIS	0.68 (0.16)	0.84 (0.11)	24	23	p<.01
VEST	0.51 (0.43)	0.71 (0.14)	24	23	p<.01
PREF	1.03 (0.20)	1.03 (0.09)	24	23	n.s.
VOMS (minus baseline)					
Composite VOMS	10.5 (21.2)	0.0 (1.0)	24	23	p<.0001
Smooth Pursuits	0.0 (1.0)	0.0 (0.0)	25	24	p<.01
Horizontal Saccades	1.0 (1.0)	0.0 (0.0)	25	24	p<.0001
Vertical Saccades	1.0 (4.0)	0.0 (0.0)	25	24	p<.0001
NPC	1.0 (4.0)	0.0 (0.0)	25	24	p<.0001
NPC Avg (cm)	9.0 (12.7)	3.5 (2.2)	25	24	p<.0001
Horizontal VOR	3.0 (4.0)	0.0 (0.0)	25	24	p<.0001
Vertical VOR	2.5 (4.0)	0.0 (0.0)	24	23	p<.0001
VMS	3.0 (5.0)	0.0 (0.0)	25	24	p<.00001

Note, unless otherwise indicated, values correspond to median with interquartile range (IQR) within parentheses. Abbreviations: BAI, Beck anxiety inventory; BDI, Beck depression inventory; PCVD, post-concussive vestibular dysfunction; PCSS, post-concussion symptom scale; DHI, dizziness handicap scale; VVAS, visual vertigo analog scale; SOT, sensory organization test; SOM, somatosensory; VIS, visual; VEST, vestibular; PREF, visual preference; VOMS, vestibular/ocular motor screening; NPC, near-point convergence; VOR, vestibular-ocular reflex; VMS, visual motion sensitivity. *Mann-Whitney U test w/ BH correction

Table 2 Results of Robust Regression between Clinical Measures (Vestibular and Affective) and Tract-Wise Diffusion Metric Summary Statistics

	Clinical Measure	Tract (ROI:ROI)	Diffusion Metric (or volume)	Robust Regression β	std. error	Adj. R^2	P $value_{unadj.}$	P value FDR adj.	Spearman Correlation Coefficient (ρ) PCVD	Ctrl
1	BDI	OP2(L):A23c(L)	DA_R	0.55	0.14	0.18	3.3e-04	2.0e-03	0.55	0.19
2	BAI	OP2(R):PIC_PFcm(L)	DA_R	0.47	0.16	0.16	5.3e-03	3.1e-02	0.49	0.29
3	BDI	PIC(L):A23c(R)	ODI_T	-0.68	0.16	0.23	7.9e-06	4.7e-03	-0.32	0.31
4	BAI	PIC(L):A23c(R)	ODI_T	-0.31	0.11	0.06	8.4e-03	4.9e-02	-0.36	0.4
5	BDI	PIC(L):A23c(R)	ODI_D	-0.6	0.17	0.24	1.2e-03	7.2e-03	-0.47	0.36
6	BAI	PIC(L):A23c(R)	ODI_D	-0.33	0.11	0.07	5.9e-03	3.5e-02	-0.33	0.46
7	BDI	PIC(L):IPL PF(R)	ODI_T	-0.57	0.18	0.23	3.6e-03	2.1e-02	-0.44	0.33
8	BAI	PIC(L):IPL PF(R)	ODI_T	-0.52	0.17	0.21	4.1e-03	2.4e-02	-0.63	0.12
9	BAI	PIC(L):IPL PF(R)	ODI_D	-0.49	0.16	0.19	5.3e-03	3.1e-02	-0.64	0.07
10	BDI	PIC(R):A23c(L)	Volume	-0.39	0.11	0.13	7.6e-06	4.5e-03	-0.48	0.09
11	BAI	PIC(R):A37d(L)	ODI_T	-0.47	0.15	0.16	4.3e-03	2.5e-02	-0.55	0.15
12	BAI	PIC(R):A37d(R)	ODI_T	-0.48	0.16	0.14	4.9e-03	2.9e-02	-0.49	0.23
13	BAI	PIC(R):A37d(R)	ODI_D	-0.47	0.17	0.12	8.3e-03	4.8e-02	-0.43	0.18
14	V VOR	PIC(R):IPL PF(R)	RD	0.49	0.13	0.05	5.3e-04	3.1e-02	0.55	0.09
15	DHI	PIC(R):PL PF(R)	Volume	-0.61	0.1	0.26	6.9e-07	5.0e-04	-0.55	-0.12
16	SOT 3	PIC(R):IPL PFcm(L)	ODI_T	-0.65	0.18	0.13	6.5e-04	3.7e-02	-0.41	0.03
17	VVAS	PIC(R):IPL PFcm(R)	FA	-0.54	0.14	0.16	3.5e-04	2.1e-02	-0.53	-0.4

Abbreviations:PIC, posterior insular cortex; IPL PFcm, inferior parietal/supramarginal area PFcm; IPL PF, inferior parietal area PF/40/anterior supramarginal gyrus; OP2, parietal area OP2 (parieto-insular vestibular cortex, PIVC); A37dl, dorsolateral middle temporal area 37/hMST; A23c, caudal cingulate area 23 (vestibular cingulate, CSv); '(R)' and '(L)' designate right and left, respectively. PCVD, post-concussive vestibular dysfunction; BDI, Beck's depression index; BAI, Beck's anxiety index; SOT, sensory organization test; DHI, dizziness handicap scale; VVAS, visual vertigo analog scale; VOMS, vestibular/ocular motor screening; NPC, near-point convergence; VOR, vestibular-ocular reflex; VMS, visual motion sensitivity; H, horizontal; V, vertical; FA, fractional anisotropy; RD, radial diffusivity; DA_R, dispersion anisotropy; ODI_T orientation dispersion index (primary); "Volume" corresponds to tract volume. For each plot, a straight-line linear model trendline with 95% confidence interval band is included.

Multiple comparisons of robust regressions adjusted for using the false-discovery rate (FDR). Spearman correlation coefficients between standardized tract-wise diffusion and clinical measures for the control and PCVD groups are included for descriptive purposes.

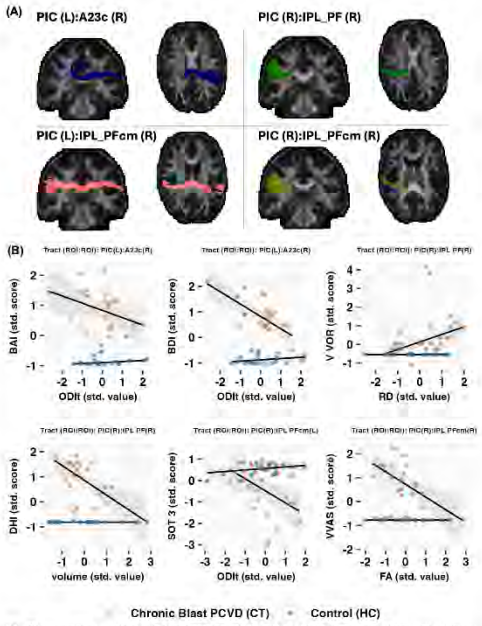

(A) Representative probabilistic tractography white matter tracts generated from pre-selected vestibular ROI seed regions from the Eagle 449 vestibular atlas (ROI:ROI denoted within parentheses) **(B)** Representative scatter plots of standardized clinical vestibular and affective measures, and tract-extracted and averaged diffusion metrics for both healthy controls (HC) and Chronic Blast PCVD (CT). Representative clinical measures include: BAI, Beck's anxiety index; BDI, Beck's depression index; V VOR, VOMS vertical vestibular-ocular reflex; DHI, dizziness handicap index; VVAS, visual vertigo analog scale; SOT 3, sensory organization test 3. Representative tracts correspond to ROIs from the following regions: PIC, posterior insular cortex; IPL PFcm, inferior parietal/supramarginal area PFcm; IPL PF, inferior parietal area PF/40/anterior supramarginal gyrus; A23c, caudal cingulate area 23 (vestibular cingulate, CSv); '(R)' and '(L)' designate right and left, respectively. Of note, with the exception of SOT conditions, higher clinical scores correspond to greater clinical severity i.e, worse symptoms. Representative diffusion metrics include: FA, fractional anisotropy; RD, radial diffusivity; ODI_T, orientation dispersion index (primary; "Volume" corresponds to tract volume. For each plot, a straight-line linear model trendline with 95% confidence interval band is included.

136

Comparison between Contrast-Enhanced Fat-Suppressed 3D FLAIR Brain MR images and T2-weighted Orbital MR images at 3 Tesla for the Diagnosis of Acute Optic Neuritis

Sharmiladevi Manasse MD, Patricia Koskas, Julien Savatovsky, Romain Deschamps, Catherine Vignal-Clermont MD, Marine Boudot de la Motte, Caroline Papeix, Stephanie Trunet, Augustin Lecler MD PhD
Fondation Adolphe de Rothschild Hospital, Paris, France, France

Abstract Category

Adult Brain

Purpose

The purpose of this study was to compare the capabilities of contrast-enhanced fat-suppressed (CE FS) three-dimensional fluid-attenuated inversion recovery (3D FLAIR) brain magnetic resonance imaging (MRI) with those of coronal T2-weighted orbital MRI obtained at 3 Tesla for the diagnosis of optic neuritis (ON).

Materials & Methods

Patients who presented to our center with acute visual loss and underwent MRI examination of the orbits and the brain between November 2014 and February 2020 were retrospectively included. Three radiologists independently and blindly analyzed CE FS 3D FLAIR and coronal T2-weighted images. Disagreements in image interpretation were resolved by consensus with an independent neuroradiologist who was not involved in the initial reading sessions. The primary adjudication criterion for the diag- nosis of ON was the presence of an optic nerve hypersignal. Sensitivity, specificity, and accuracy of CE 3D FLAIR brain images were compared with those of coronal T2-weighted orbital images using McNemar test. Artifacts were classified into three categories and compared between the two image sets.

Results

A total of 1023 patients were included. There were 638 women and 385 men with a mean age of 42 § 18.3 (standard deviation) years (age range: 6–92 years). Optic nerve hyperintensities were identified in 375/400 (94%) patients with ON using both 3D FLAIR and coronal T2-weighted images. Sensitivity, specificity, and accuracy of both sequences were 94% (95% CI: 91.3–96.1), 79% (95% CI: 75.5–82.2), and 89% (95% CI: 86.8 –90.7), respectively. Optic disc hypersignal was detected in 120/400 patients (30%) using 3D FLAIR compared to 3/400 (0.75%) using coronal T2-weighted images (P <

0.001). Optic radiation hypersignal was observed in 2/400 (0.5%) patients using 3D FLAIR images. Significantly more artifacts (moderate or severe) were observed on coronal T2-weighted images (801/1023; 78%) by comparison with 3D FLAIR images (448/1023; 44%) (P < 0.001).

Conclusion

The performance of 3D FLAIR brain MRI for the diagnosis of ON is not different from that of coronal T2-weighted orbital MRI and its use for optic nerve analysis may be beneficial.

References

1. Petzold A, Fraser CL, Abegg M, et al. Diagnosis and classification of optic neuritis. Lancet Neurol 2022;21:1120–34.
2. Wattjes MP, Ciccarelli O, Reich DS, et al. 2021 MAGNIMS-CMSC-NAIMS consensus recommendations on the use of MRI in patients with multiple sclerosis. Lancet Neurol 2021;20:653–70.
3. Brisset J-C, Kremer S, Hannoun S, et al. New OFSEP recommendations for MRI assessment of multiple sclerosis patients: Special consideration for gadolinium deposition and frequent acquisitions. J Neuroradiol 2020;47:250–8.
4. Panyaping T, Tunlayadechanont P, Jindahra P, et al. Diagnostic value of contrast-enhanced 3D FLAIR sequence in acute optic neuritis. Neuroradiol J 2023;36:674–9.
5. Riederer I, Sollmann N, Mühlau M, et al. Gadolinium-Enhanced 3D T1-Weighted Black-Blood MR Imaging for the Detection of Acute Optic Neuritis. AJNR Am J Neuroradiol 2020;41:2333–8.

Images/Tables

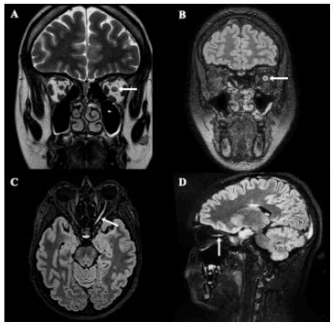

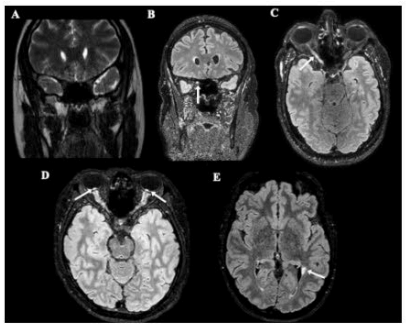

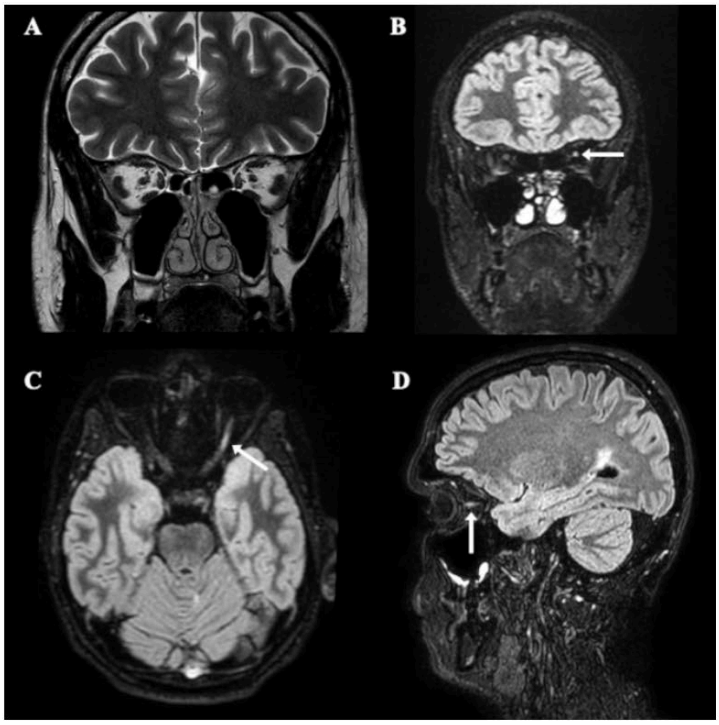

177

Machine Learning Predicts Hemorrhagic Transformation after Stroke Using Diffusion and Perfusion Weighted MR Imaging

Jing Wang MD, PhD[1], Yike Guo[2]
[1]Shanghai Fourth People's Hospital, School of Medicine, Tongji University, Shanghai, SH, China. [2]Zu Chongzhi Center for Mathematics and Computational Sciences, Duke Kunshan University, Kunshan, Suzhou, China

Abstract Category

AI/Informatics

Purpose

Hemorrhagic transformation (HT) following acute ischemic stroke (AIS) critically affects patient prognosis. This study aims to develop reliable machine learning (ML) models for predicting HT in AIS patients using magnetic resonance imaging (MRI).

Materials & Methods

379 AIS patients were enrolled (HT: 131; non-HT: 248) and randomly split into the training and testing set with a ratio of 70% to 30%. All underwent MRI, including diffusion- (DWI) and perfusion-weighted imaging (PWI), within 24 hours of symptom onset, and had follow-up CT or MRI within 14 days. Clinical baseline features and MRI parameters (volumes of ADC < 620 × 10^{-6} mm^2/s, various Tmax thresholds, PWI-DWI mismatch area, and hypoperfusion intensity ratio [HIR]) were collected. Six ML algorithms—Logistic Regression, Support Vector Machine, Decision Tree, XGBoost, LightGBM, and Random Forest—were trained and optimized using 5-fold cross-validation with 1,000 times' shuffling. Various fusion models were created, including soft voting, stacking, and integrating key patient characteristics into robust baseline models. The best-performing model was selected based on testing set performance.

Results

The Logistic Regression-based model was chosen as the practical model with a relatively high area under the curve (AUC) of 0.907 for its simplicity and efficiency by utilizing only three characteristics: the volume of Tmax > 6 s, the National Institutes of Health Stroke Scale score at admission, and HIR with feature importance scores of 0.7507, 0.2269, and 0.0996, respectively. The refined fusion model, by utilizing HIR as a prior stratification parameter with cutoff value set as 0.5 and two robust baseline models (XGBoost and LightGBM), achieved the highest AUC of 0.9161 with an accuracy of 0.8947 among all fusion models and exceeded all baseline models. Both the practical and refined models are accessible at https://yike-wood.github.io/HT-Predict/.

Conclusion

Both the practical and refined ML models, leveraging MRI-DWI and PWI, reliably predict HT in AIS patients, potentially aiding radiologists and clinicians in timely HT risk assessment post-MRI.

References

Li M, Lv Y, Wang M, et al. Magnetic resonance perfusion-weighted imaging in predicting hemorrhagic transformation of acute ischemic stroke: a retrospective study. *Diagnostics* 2023;13:3404. DOI: 10.3390/diagnostics13223404

Images/Tables

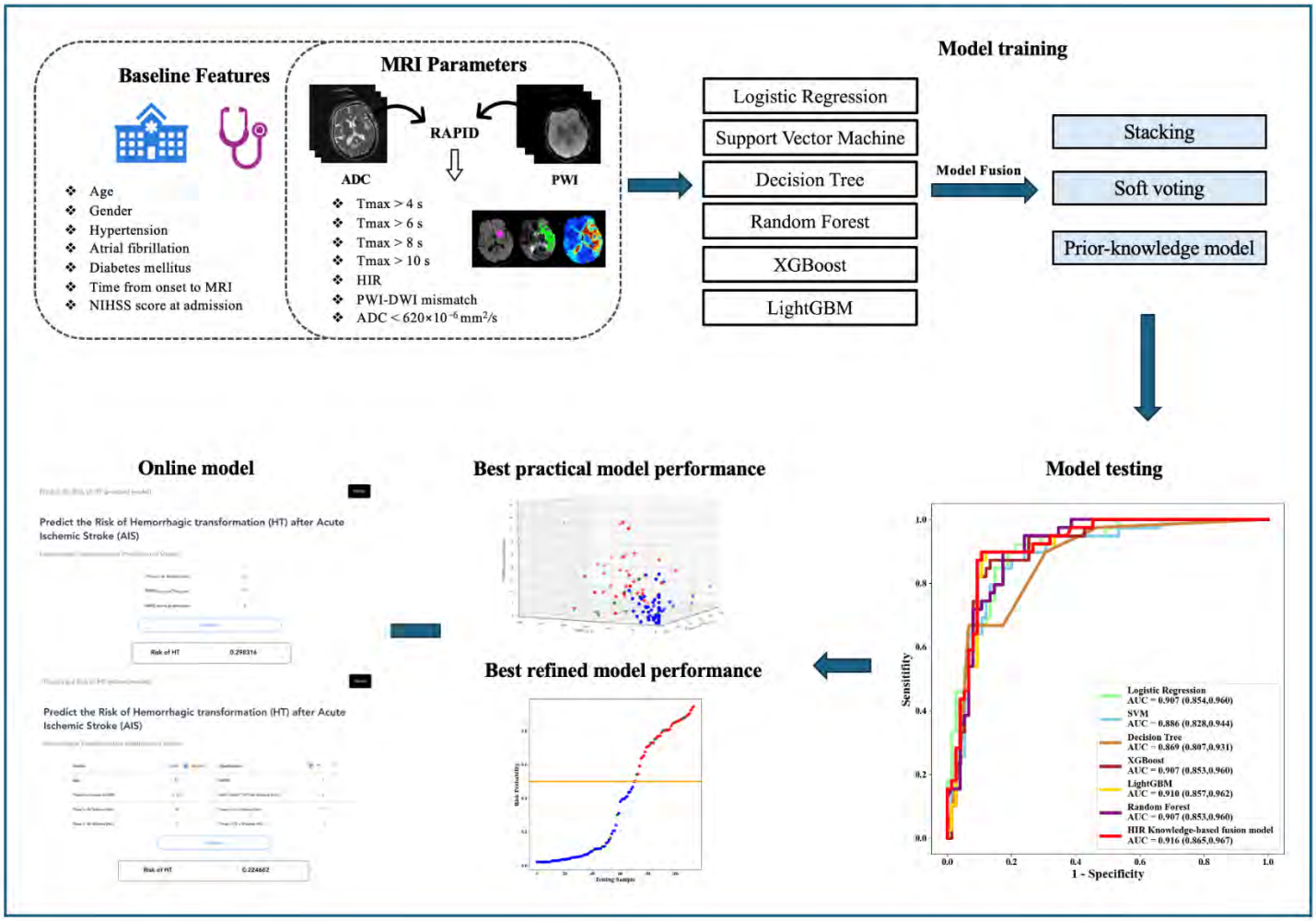

178

Tumor habitat derived from quantitative MRI to characterize spatial-temporal heterogeneity of glioblastoma microenvironment during antiangiogenic therapy

Junfeng Zhang Ph.D.
Department of Radiology, General Hopital of Western Theater Command of PLA, Chengdu, Sichuan, China

Abstract Category

Adult Brain

Purpose

To investigate whether quantitative MRI-based tumor habitat is a novel potential imaging biomarker to characterize the spatial-temporal heterogeneity of tumor microenvironment and evaluate antiangiogenic therapy response in glioblastoma (GBM).

Materials & Methods

Patient-derived orthotopic GBM xenografts in mice were established and quantitative MRI (DCE-MRI and IVIM) to characterize vasculature, cellularity, and hypoxia in tumor microenvironment were conducted sequentially during bevacizumab or saline treatment (baseline, day2, day5, day8, day14, day25). The tumor habitats were generated by the Gaussian mixture model. MRI-histology coregistration and spatial-paired analysis of multiregional single-cell RNA sequencing were performed to validate the biological meaning of tumor habitats.

Results

Eight habitats, including four structural and four physiologic habitats, were generated to quantify the spatial-temporal heterogeneity of tumor microenvironment. Compared with the saline control group, bevacizumab group reduced tumor microvascular density, alleviated hypoxia, and inhibited tumor cell proliferation. These phenotypes were more homogenous spatiotemporally measured by distribution and fraction volumes of tumor habitats based on quantitative MRI. Furthermore, physiologic habitats positively correlated with angiogenesis and hypoxia-associated pathological features and gene expression at the *in situ* level.

Conclusion

Quantitative MRI-based tumor habitat has much potential as a novel imaging biomarker to quantify the spatial-temporal heterogeneity of tumor microenvironment and evaluate antiangiogenic therapy response in GBM. In particular, physiologic habitats may provide insights into the relationship between imaging phenotype and molecular cell characterization.

References

1. van den Bent MJ, Geurts M, French PJ, et al. Primary brain tumours in adults. Lancet. 2023; 402(10412):1564-1579.
2. Cao Y, Langer R, Ferrara N. Targeting angiogenesis in oncology, ophthalmology and beyond. Nature Reviews Drug Discovery. 2023; 22(6): 476-495.
3. Huinen ZR, Huijbers EJM, van Beijnum JR, et al. Anti-angiogenic agents-overcoming tumour endothelial cell anergy and improving immunotherapy outcomes. Nature Reviews Clinical Oncology. 2021; 18(8): 527-540.
4. Jayaram MA, Phillips JJ. Role of the Microenvironment in Glioma Pathogenesis. Annual Review of Pathology. 2024; 19: 181-201.
5. Li B, Xu D, Zhou J, et al. Monitoring Bevacizumab-Induced Tumor Vascular Normalization by Intravoxel Incoherent Motion Diffusion-Weighted MRI. Journal of Magnetic Resonance Imaging. 2022; 56(2): 427-439.
6. Park JE, Kim HS, Kim N, et al. Spatiotemporal Heterogeneity in Multiparametric Physiologic MRI Is Associated with Patient Outcomes in IDH-Wildtype Glioblastoma. Clinical Cancer Research. 2021; 27(1): 237-245.
7. Wu H, Tong H, Du X, et al. Vascular habitat analysis based on dynamic susceptibility contrast perfusion MRI predicts IDH mutation status and prognosis in high-grade gliomas. European Radiology. 2020; 30(6): 3254-3265.
8. Tomaszewski MR, Gillies RJ. The Biological Meaning of Radiomic Features. Radiology. 2021; 298(3): 505-516.
9. Huang EP, O'Connor JPB, McShane LM, et al. Criteria for the translation of radiomics into clinically useful tests. Nature Reviews Clinical Oncology. 2023; 20(2):69-82.
10. Lohmann P, Franceschi E, Vollmuth P, et al. Radiomics in neuro-oncological clinical trials. Lancet Digital Health. 2022; 4(11):e841-e849.

181

What Are We forgetting? A Three-Year Single Institution Retrospective Review of Reporting Neuroimaging Studies for Cognitive Impairment.

Samantha L. Watts[1], Chad W. Farris M.D.[2]

[1]Boston University School of Medicine, Boston, Massachusetts, USA. [2]Boston Medical Center, Boston, Massachusetts, USA

Abstract Category

Adult Brain

Purpose

The primary role of neuroimaging in evaluating cognitive impairment (CI) has traditionally been to exclude potentially treatable structural intracranial abnormalities as possible etiologies. Subtler imaging findings, however, can aid in differentiating dementia subtypes and guiding treatment decisions. With new anti-amyloid therapies, such as Lecanemab, certain findings must also be reported to assess treatment eligibility. This study examines the completeness of neuroimaging reports at a single institution in describing traditional structural abnormalities, features relevant for differentiating dementia subtypes, and findings essential for determining eligibility for anti-amyloid therapies.

Materials & Methods

A retrospective, IRB exempt study reviewed 814 contiguous de-identified neuroimaging reports from outpatient MRI Brain and CT Head scans performed for CI at an urban safety-net medical center over a 32-month period (Nov 2017 - Jun 2020). Seventeen patients were excluded due to limited or absent reports resulting from artifacts, anxiety, claustrophobia, or missing data, leaving 797 reports for analysis. Reports were reviewed by a medical student (SW) trained for review of the reports by an attending neuroradiologist (CF). Reports were reviewed for descriptions in three areas: (1) traditional treatable structural abnormalities (e.g., masses, hydrocephalus, acute/subacute hemorrhage); (2) diagnostic markers for dementia subtypes (e.g., general and hippocampal atrophy, white matter (WM) disease, chronic infarcts, encephalomalacia/gliosis); and (3) findings required for assessing anti-amyloid therapy eligibility (acute and chronic hemorrhage, encephalomalacia/gliosis, acute and chronic infarcts, WM disease severity). For each area, analysis examined (a) whether specific findings were documented in the neuroimaging reports, and (b) how often positive findings appeared when documented.

Results

The presence or absence of traditionally treatable structural abnormalities was described in 79.8% of the reviewed reports, though these findings were rare (mass 3.5%, acute/subacute hemorrhage 1.4%, and hydrocephalus 1.1%). All features relevant for CI differential diagnosis were described in only 0.5% of the reviewed reports. When reported, these markers were more prevalent than traditional abnormalities (general atrophy 61.2%, hippocampal atrophy 5.6%, WM hyperintensities/hypodensities 75.3%, chronic infarcts 15.2%, encephalomalacia/gliosis 13%). All features necessary to determine eligibility for anti-amyloid therapy were described in 1.6% of MRI Brain examination reports. Based on the reports, none of the participants would have been eligible for Lecanemab, either due to exclusionary findings or missing required information.

Conclusion

This single-institution study found that reports for CI exams consistently address the presence or absence of traditional, treatable structural abnormalities, though these findings are rare. In contrast, imaging features that could help identify dementia subtypes and guide treatment decisions are reported inconsistently, despite their more common occurrence. Improvements in the documentation of these imaging findings can add significant clinical value and diagnostic precision to these reports. Notably, nearly all reports lack comprehensive information needed to assess eligibility for the anti-amyloid therapy, Lecanemab. Since these reports predate the approval of anti-amyloid therapies, updating current reporting practices is essential to align with evolving treatment options, improve documentation of historically underreported imaging features, and support patient eligibility for available therapies.

References

1. Moonis, Gul et al. ACR Appropriateness Criteria® Dementia. Journal of the American College of Radiology **2020**, Volume 17, Issue 5, S100 - S112

2. Cummings J, Apostolova L, Rabinovici GD, et al. Lecanemab: Appropriate Use Recommendations. J Prev Alzheimers Dis. **2023**;10(3): 362-377

Images/Tables

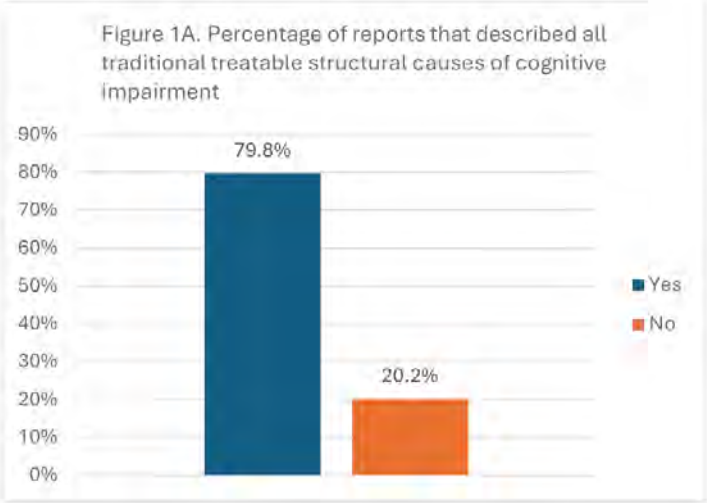

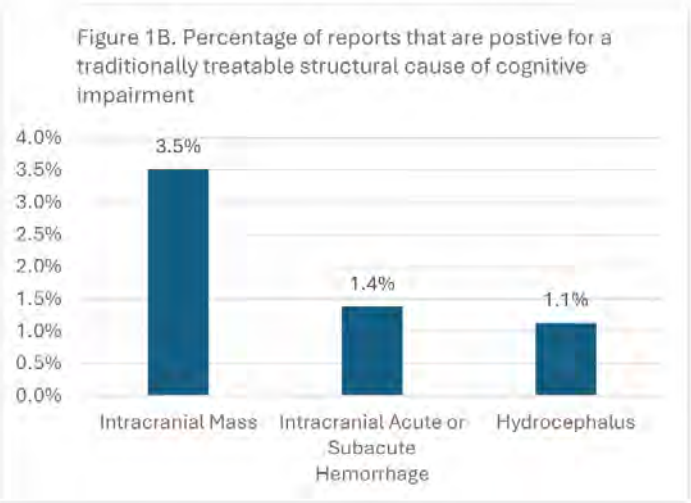

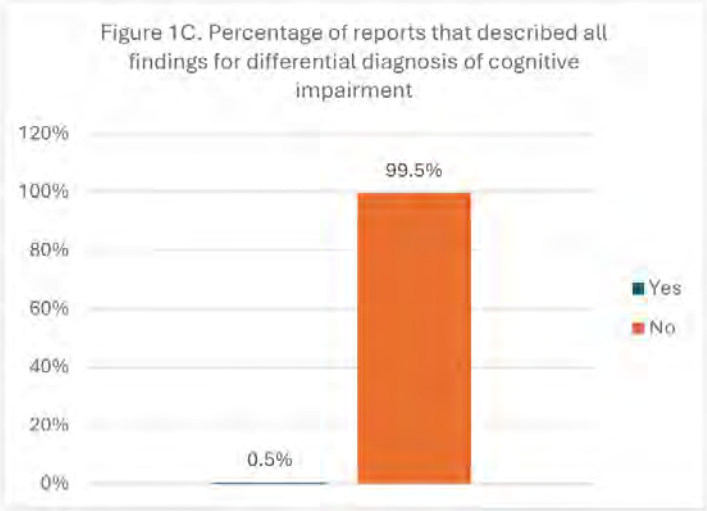

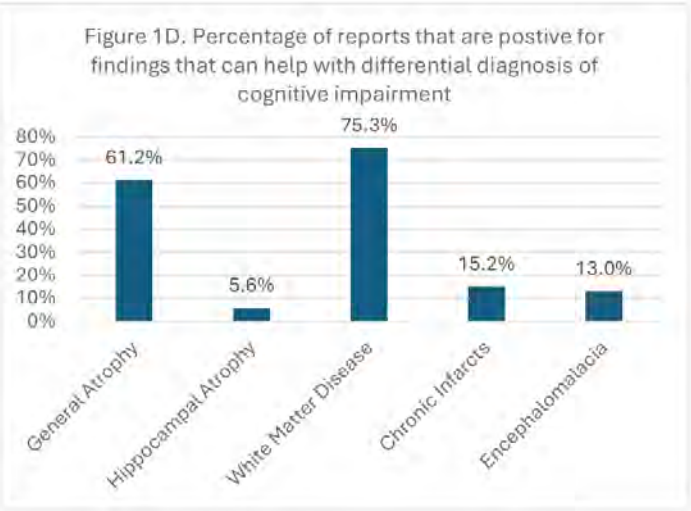

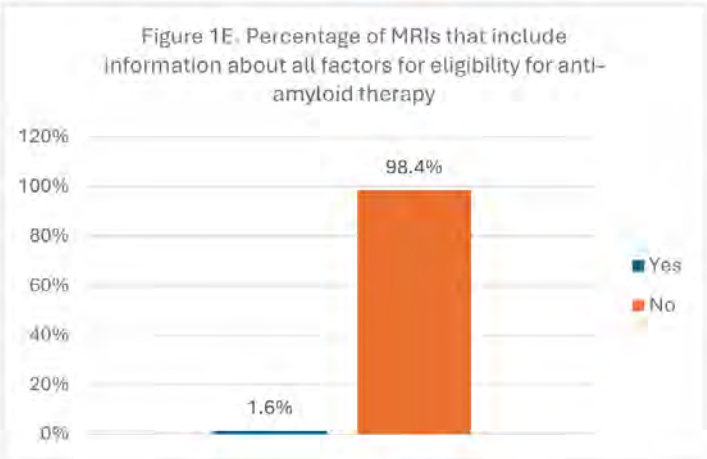

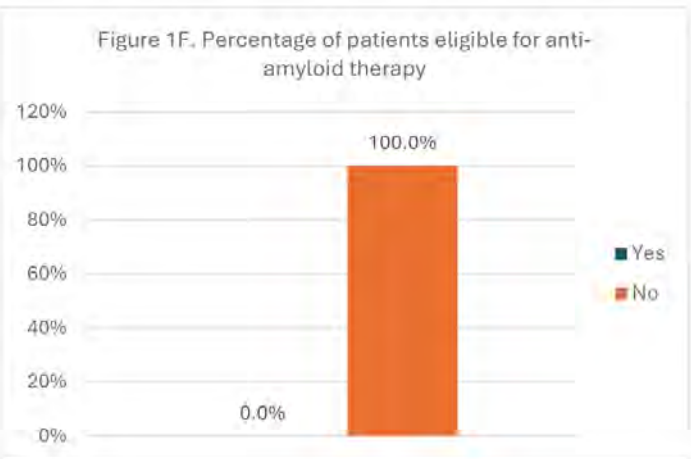

183

High-Resolution Isotropic 3D CISS MR Imaging of the Human Cadaveric Vagus Nerve: Initial Experience from SPARC-REVA

Shruti Kumari MBBS
Case Western Reserve University, Cleveland, Ohio, USA

Abstract Category

Functional/Advanced Imaging

Purpose

The purpose of this research is to study the course of the vagus nerve (CN X) on 3-Tesla (3-T) MR imaging (MRI) and perform anatomic correlation after dissection. CN X, the longest cranial nerve, is the main component of the parasympathetic nervous system reaching as far as the abdomen. Clinical MRI of CN X is currently challenging and it is not well visualized. In this study we used 3D CISS of the human cadaver correlated to dissection to elucidate anatomic details previously not well seen in cross section.

Materials & Methods

We scanned 40 embalmed cadavers with a 3T MRI scanner using 3-D isotropic 0.5-0.6 mm resolution CISS; a total of 80 vagus nerves were examined. Two readers independently evaluated the course of the main trunk of CN X according to a qualitative scale (excellent, good, fair, poor). We then dissected CN X from the brainstem to abdomen, and an anatomic-radiologic correlation using morphometric analysis (nerve main trunk cross sectional dimensions and distance from pre-defined landmarks) was performed to validate the findings on MRI. This research is a part of SPARC-REVA (Stimulating Peripheral Activity to Relieve Conditions-Reconstructing Vagal Anatomy).

Results

High resolution CISS of the cadaver best demonstrates the main trunk of CN X in portions of the neck and upper chest. In this work we provide correlated cross sectional images with anatomic dissection to aid the reader in better understanding the course of the vagus on cross sectional imaging.

Conclusion

According to the preliminary results of our study the use of 3-T CISS MRI allows visualization of the main trunk of CN X into portions of the chest. The inter-individual variability and complexity of branching patterns far surpassed descriptions in textbooks and prior literature. These data provide essential anatomical insights into CN X for advancing anatomic knowledge and may aid in the future understanding of clinical imaging of CN X.

References

1. Blitz AM, Choudhri AF, Chonka ZD, et al. Anatomic considerations, nomenclature, and advanced cross-sectional imaging techniques for visualization of the cranial nerve segments by MR imaging. Neuroimaging Clin N Am. 2014 Feb;24(1):1-15. DOI: 10.1016/j.nic.2013.03.020

Images/Tables

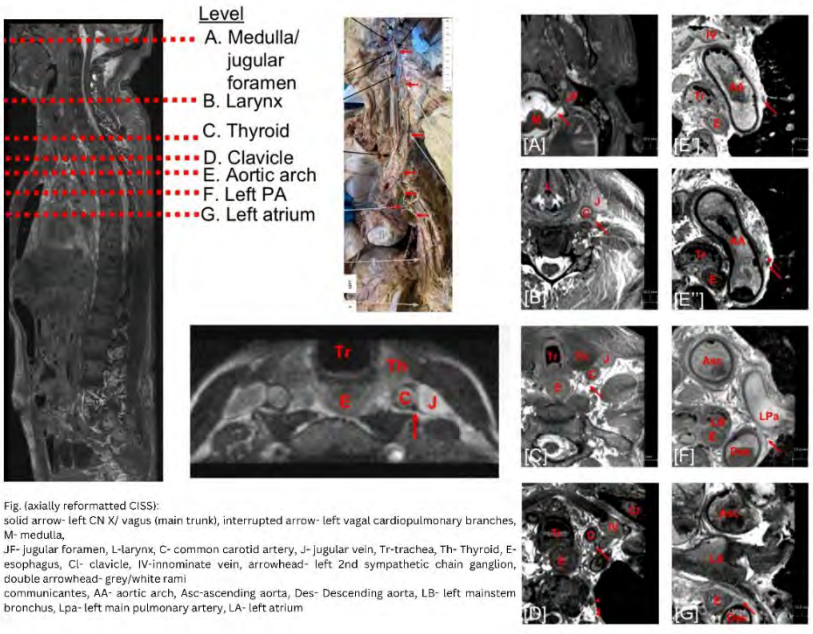

Fig. (axially reformatted CISS):
solid arrow- left CN X/ vagus (main trunk), interrupted arrow- left vagal cardiopulmonary branches, M- medulla,
JF- jugular foramen, L-larynx, C- common carotid artery, J- jugular vein, Tr-trachea, Th- Thyroid, E- esophagus, Cl- clavicle, IV-innominate vein, arrowhead- left 2nd sympathetic chain ganglion, double arrowhead- grey/white rami communicantes, AA- aortic arch, Asc-ascending aorta, Des- Descending aorta, LB- left mainstem bronchus, Lpa- left main pulmonary artery, LA- left atrium

189

A Proposed Grading System for Endovascular Treatment Success in Dural Arteriovenous Fistulae

Yunji Seo MS[1], Benjamin Pulli MD[2]
[1]Stanford School of Medicine, Stanford, CA, USA. [2]Stanford Department of Interventional Neuroradiology, Stanford, CA, USA

Abstract Category

Interventional

Purpose

Currently used dural arteriovenous fistula (dAVF) grading systems such as Borden[1] and Cognard[2] scores are designed to estimate risk of intracranial hemorrhage and thus are widely used to guide indication for dAVF treatment. Endovascular treatment (EVT) with transarterial and/or transvenous embolization has emerged as the standard of care for most dAVF but is limited by cure rates as low as 50% and need for re-treatment[3,4,5]. With this study, we sought to elucidate clinical and imaging markers that allow for prediction of EVT success/failure.

Materials & Methods

Data from consecutive dAVF patients treated at our institution in 2022 and 2023 (n=45) who underwent EVT were reviewed retrospectively. Complete angiographic cure after initial single stage EVT attempt was defined as treatment success. Clinical and angiographic features that were hypothesized to render EVT more challenging were assessed, including age, gender, history of venous sinus thrombosis (VST), diameter of the most accessible arterial feeder, number of arterial pedicles, length of affected vein or venous sinus, presence of accessible venous compartment/pouch, presence of a transosseous network as the main arterial supply, and angiographic transit time through the fistula. Univariate linear regression and multivariate logistic regression were performed to select the statistically significant factors, which were then used to develop a grading system. The proposed grading system was then compared with the Cognard score (ranked as 6 levels) for its ability to predict EVT success/failure.

Results

Transosseous arterial network (OR 8.31, p <0.05) and number of arterial feeders (OR 1.71, p<0.05) were associated with increased risk for embolization failure whereas artery feeder diameter (OR 0.31, p=0.06) was associated with a trend towards decreased risk (Table 2). Clinical data such as age, gender, and presence of VST did not reach statistical significance, and neither did imaging factors such as length of the affected vein, presence of an accessible venous compartment or angiographic transit time. The proposed scoring system that consists of three imaging markers assessed on digital subtraction angiography (DSA, Table 3) resulted in an area under the curve (AUC) of 0.81 compared to 0.33 for the Cognard grading system (p<0.001). Optimal cut-off score (Youden's Index) for EVT success/failure was 2.5, with higher scores associated with increased risk of failure. Addition of other features did not significantly improve the AUC.

Conclusion

The proposed grading system can provide an estimate of EVT success in dAVF. A more complex angioarchitecture on the arterial side with smaller and more numerous arterial feeders that shunt into a vein/venous sinus via a transosseous network decrease the odds of EVT success. These results may be used to counsel patients and manage expectations with regards to EVT outcome including need for additional stages or microsurgical obliteration. Further investigations are underway to confirm these preliminary results in a larger independent cohort.

References

1. Borden JA, Wu JK, Shucart WA. A proposed classification for spinal and cranial dural arteriovenous fistulous malformations and implications for treatment. *J Neurosurg* 1995;**82**:166–79
2. Cognard C, Gobin YP, Pierot L, et al. Cerebral dural arteriovenous fistulas: clinical and angiographic correlation with a revised classification of venous drainage. *Radiology* 1995;**194**:671–80
3. Gandhi D, Chen J, Pearl M et al. Intracranial Dural Arteriovenous Fistulas: Classification, Imaging Findings, and Treatment. *AJNR Am J Neuroradiol* 2012;**33**:1007-13
4. Hiramatsu M, Sugia K, Hishikawa T *et al.* Results of 1940 embolizations for dural arteriovenous fistulas: Japanese Registry of Neuroendovascular Therapy (JR-NET3). *J Neurosurg.* 2019;**133**:166–173
5. Li Y, Chen SH, Guniganti R, et al. Onyx embolization for dural arteriovenous fistulas: a multi-institutional study. *J Neurointerventional Surg.* 2002;**14**:neurintsurg-2020-017109

Images/Tables

Seo Y, Pulli B.
A Proposed Grading System for Endovascular Treatment Success in Dural Arteriovenous Fistulae
Figures & Tables

Table 1. Univariate analysis of case features as comparison between embolization success and failure cases

Feature	EVT success (n=32)	EVT failure (n=14)	*P* value
Age	61.8 + 11.6	64.3+ 9.2	0.5
Male	25 (80.6%)	10 (71.4%)	0.7
History of VST	4 (12.9%)	3 (21.4%)	0.7
Arterial feeder diameter	1.8 + 0.8	1.5 + 0.9	0.2
Arterial feeder #	2.8 + 1.7	4.4 + 2.1	**0.01**
Accessible venous compartment	4 (12.9%)	2 (14.2%)	1
Length of affected vein	30.9 + 12.2	38.6 + 21.9	0.5
Transosseous network	9 (29.0%)	10 (71.4%)	**0.01**
Angiographic transit time (# of frames)	8.6 + 3.3	8.9 + 4.5	0.9

Table 2. Multivariate analysis of angiographic features as correlates of embolization failure

Variable	Coefficient	Standard error	*P* value	Odds ratio
Intercept	-1.01	1.86	0.9	
Transosseous network [Y]	2.12	0.87	**0.01**	8.33
Arterial feeder #	0.54	0.23	**0.02**	1.71
Arterial feeder diameter	-1.15	0.62	0.06	0.31

Table 3. Proposed Scoring system for dAVF EVT Outcome

dAVF features		Points
Presence of transosseous network	Yes	2
	No	0
Number of arterial feeders	1-2	0
	3-4	1
	5+	2
Arterial feeder diameter (mm)	<1	2
	1-2	1
	>2	0

191

Assessment of GPT-4V(ision) as a Potential Foundation Model in Neuroradiology

Quirin D Strotzer M.D.[1], Gerardo Napodano M.D.[1], Isabel Wiesinger M.D.[2], Andreas Schicho M.D.[1], Christina Wendl M.D.[1]
[1]Institute of Radiology, University of Regensburg Medical Center, Regensburg, Bavaria, Germany. [2]Center of Neuroradiology, medbo District Hospital and University Medical Center Regensburg, Regensburg, Bavaria, Germany

Abstract Category

AI/Informatics

Purpose

Large Language Models have already proven their potential in medical text processing[1]. The recently introduced GPT-4V(ision), a large vision-language model that allows images as input, shows potential for advancement in medical imaging. We aimed to quantitatively evaluate the performance of GPT-4V in interpreting neuroradiological images.

Materials & Methods

This IRB-approved, HIPAA-compliant retrospective study comprised the common neuroradiological pathologies of ischemic stroke, multiple sclerosis, brain tumors, and cerebral hemorrhage, as well as normal controls. A representative image (CT or MRI section) was used for each case to generate reports via the OpenAI Application Programming Interface. The factual correctness of free-text reports and the performance in detecting pathologies in binary classification tasks (25 positive and negative images per pathology) were assessed using accuracy, among others. Binary classification performance was compared to that of four board-certified radiologists and a first-year non-radiological resident.

Results

GPT-4V correctly identified modality and body part in all 256 included images. When tasked to create free-text reports, diagnostic accuracy was mixed with 1.3% for inconspicuous scans, 32.3% for multiple sclerosis, 52.0% for ischemic stroke, 64.0% for brain hemorrhage, and 90.0% for brain tumors. In binary classification tasks, GPT-4V showed poor performance with accuracies between 0.46 [95% confidence interval: 0.32, 0.60] for ischemic stroke and 0.60 [0.46, 0.72] for multiple sclerosis compared to the human readers, who achieved pooled accuracies between 0.97 [0.94, 0.99] for multiple sclerosis and 1.00 [1.00, 1.00] for the other pathologies. The model showed a clear tendency towards overdiagnosis of pathologies, with 98.7% and 73.3% false-positive rates for the free text and binary classification tasks, respectively.

Conclusion

GPT-4V, in its current version, reliably determines modality and anatomical region from single images. It must not be used to detect, classify, or rule out pathologies. Although the model still lacks performance, the technology may serve as a basis for future foundation models in radiology (models that can perform a wide range of different tasks without requiring special training). Currently, possible use cases include detecting out-of-distribution data in upstream analyses, obviating the need to create task-specific data sets and models.

References

1. Chien A, Tang H, Jagessar B, et al. AI-Assisted Summarization of Radiologic Reports: Evaluating GPT3davinci, BARTcnn, LongT5booksum, LEDbooksum, LEDlegal, and LEDclinical. AJNR Am J Neuroradiol 2024;45:244–

48. http://dx.doi.org/10.3174/ajnr.A8102 .

Images/Tables

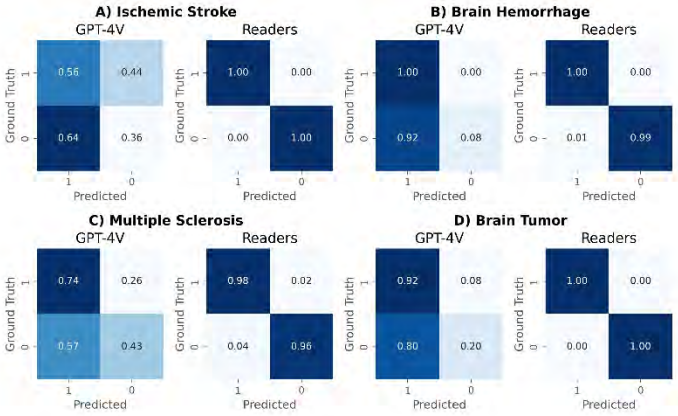

Figure 1 (top): Confusion matrices show the actual vs. predicted classes for each classification task separately (A-D). Results of all human readers were pooled. The true positive rate = sensitivity (top left), the false negative rate (top right), the false positive rate (bottom left), and the true negative rate = specificity (bottom right) are reported.

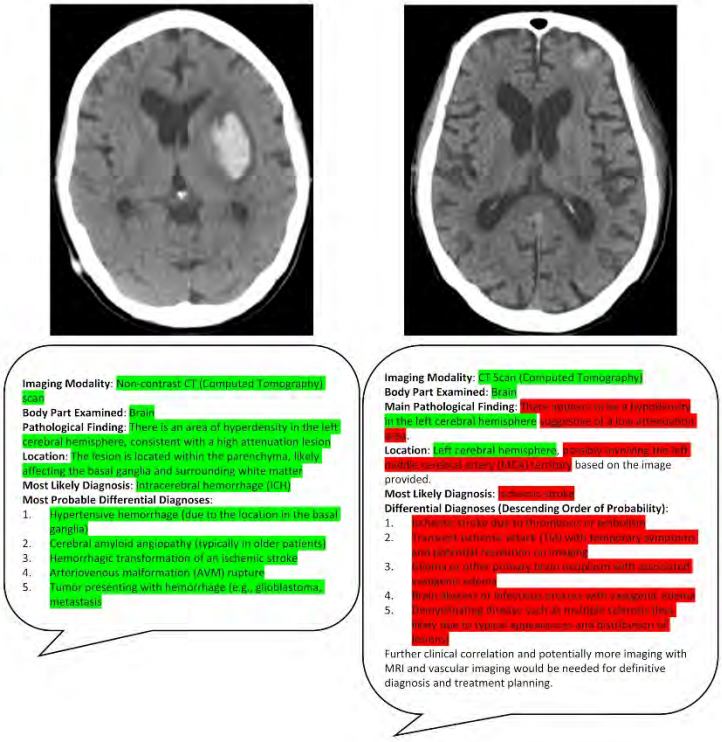

Figure 2 (right): Two example images of brain hemorrhages and their interpretation by GPT-4V with correct (left) and incorrect (right) main findings and diagnosis are shown. Correct items in the response text are highlighted green, and incorrect items are highlighted red.

199

Image Synthesis of Double Inversion Recovery-like Series for Superior Contrast and Multiple Sclerosis Lesion Visibility

Long Wang, Campbell Arnold, Zechen Zhou, Lei Xiang, Ajit Shankaranarayanan, Suzie Bash, Lawrence Tanenbaum
Menlo Park, CA, USA

Abstract Category

AI/Informatics

Purpose

In multiple sclerosis (MS), detection of new lesions is crucial for assessing therapeutic efficacy and driving patient management. Lesions can be challenging to detect, as they are often small and have subtle contrast differences from surrounding healthy tissue. This study examines both the value of synthesized Double Inversion Recovery (DIR)-like images in enhancing lesion-to-white-matter contrast and improving lesion visibility. The method's reliability in longitudinal patient assessment was also evaluated.

Materials & Methods

Our previous work described an algorithm we developed that can synthesize a STIR-like image from T1-weighted (T1w) and T2-weighted (T2w) DICOM spine image inputs [1]. Here, we repurpose the algorithm and apply it to T1w and T2-FLAIR brain images of MS patients to synthesize a DIR-like (Syn-DIR) image with high lesion-to-white matter contrast. The study evaluated two MS cohorts, one with 30 subjects scanned at a single time point and a second longitudinal study with 20 subjects scanned at two time points [2].

The T1w and T2-FLAIR were co-registered using SimpleITK [3] and used as inputs for the image synthesis network. For the first dataset, input and output images were quantitatively assessed for gray-to-white matter contrast and lesion-to-white matter contrast using FSL [4] using lesion masks provided in the dataset. For the longitudinal dataset, the gray-to-white matter contrast of the Syn-DIR images was calculated separately at each time point. A Wilcoxon signed-rank test [5] was performed to evaluate whether the enhancement level was consistent across scans.

Results

A sample case illustrating improved lesion enhancement is available in Figure 1A. For the 30 MS patients, the average gray-to-white matter and lesion-to-white matter contrast for T2-FLAIR was 0.2790 ± 0.0264 and 0.4978 ± 0.0933, while

the synthesized DIR images increased contrast to 0.5967 ± 0.0558 and 0.9119 ± 0.2514, respectively (Figure 1B). A Wilcoxon signed-rank test showed significant increase in both contrast metrics for synthetic DIR images compared to T2-FLAIR ($p < 0.001$). For the longitudinal study, the average gray-to-white matter contrast of the Syn-DIR images at two time points was 0.3179 ± 0.1155 and 0.3170 ± 0.1776, respectively (Figure 1C). A Wilcoxon signed-rank test showed no significant difference between time points ($p = 0.113$), suggesting robust and consistent image synthesis across scans at different time points.

Conclusion

In conclusion, synthesized DIR demonstrates potential in enhancing lesion-to-white-matter contrast, leading to improved lesion visibility and delineation. Furthermore, longitudinal analysis confirms the stability of synthesized images across time points, suggesting that this method is robust and reliable for longitudinal monitoring of brain abnormalities. Further validation of this approach may support integration into the clinical setting.

References

[1] Tanenbaum, L. N., Bash, S. C., Zaharchuk, G., Shankaranarayanan, A., Chamberlain, R., Wintermark, M., ... & Wang, L. (2023). Deep learning–generated synthetic MR imaging STIR spine images are superior in image quality and diagnostically equivalent to conventional STIR: a multicenter, multireader trial. *American Journal of Neuroradiology*, *44*(8), 987-993.

[2] Lesjak, Ž., Galimzianova, A., Koren, A., Lukin, M., Pernuš, F., Likar, B., & Špiclin, Ž. (2018). A novel public MR image dataset of multiple sclerosis patients with lesion segmentations based on multi-rater consensus. *Neuroinformatics*, *16*, 51-63.

[3] Beare, R., Lowekamp, B., & Yaniv, Z. (2018). Image segmentation, registration and characterization in R with SimpleITK. *Journal of statistical software*, *86*.

[4] Woolrich, M. W., Jbabdi, S., Patenaude, B., Chappell, M., Makni, S., Behrens, T., ... & Smith, S. M. (2009). Bayesian analysis of neuroimaging data in FSL. *Neuroimage*, *45*(1), S173-S186.

[5] Conover, W. J. (1999). *Practical nonparametric statistics*. John Wiley & Sons, Inc.

Images/Tables

Figure:

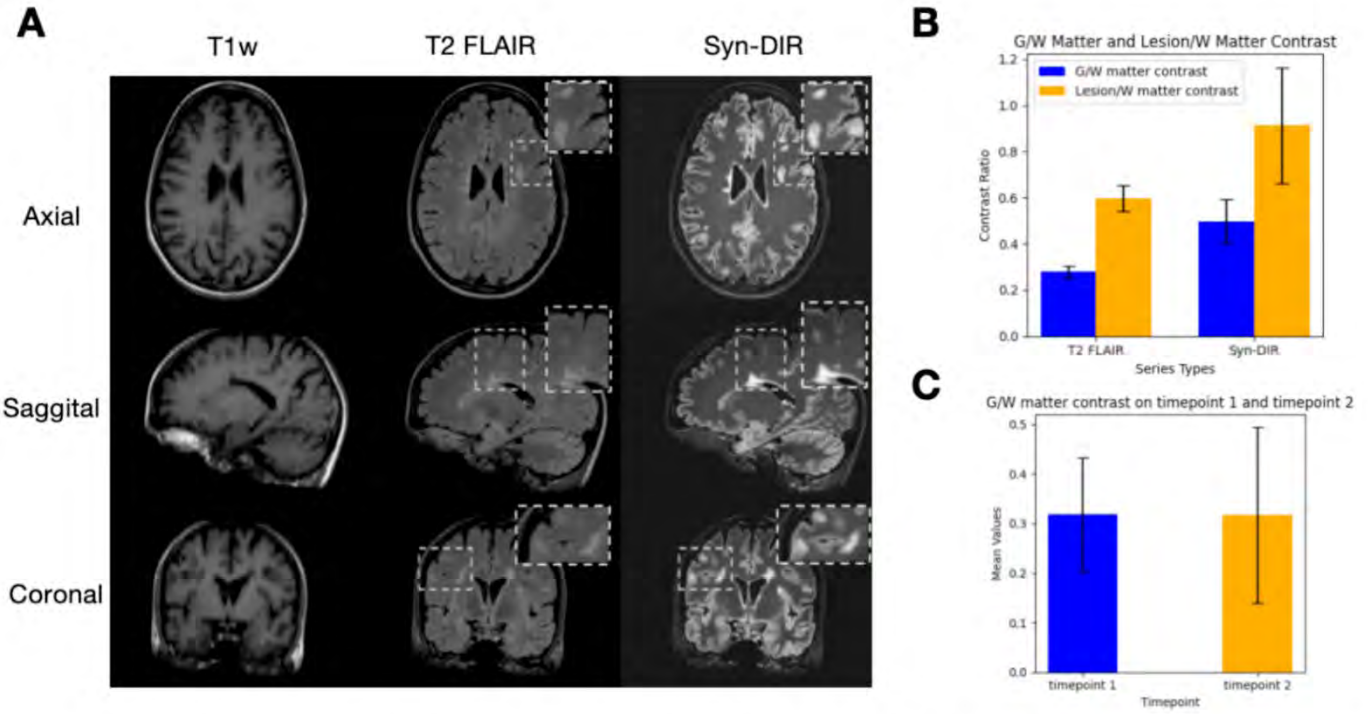

Figure 1.A) Sample case. Three orthogonal orientations (from left to right, the T1-weighted, T2 FLAIR, the Syn-DIR image). B) Comparison of gray/white matter and lesion/white matter contrast on T2 FLAIR and the Syn-DIR image. C). The comparison of the gray/white matter contrast on the longitudinal study.

209

Rates of spinal epidural contrast extravasation at puncture site by needle type during CT myelography

Joshua Loewenstern MD, Pierce McMahon BS, Usama Sattar MBBS, Andrew Schweitzer MD, Sara Strauss MD, Gayle Salama MD
New York Presbyterian-Weill Cornell, New York, NY, USA

Abstract Category

Spine

Purpose

Epidural contrast extravasation (ECE) at the level of puncture site after the lumbar puncture and contrast injection portion of CT myelography (CTM) is a noted phenomenon without determined clinical relevance. While previous randomized studies in obstetrical spinal analgesia have demonstrated clinical benefits of pencil-type spinal needles relative to cutting-type spinal needles during dural puncture procedures, such as fewer post-dural puncture headaches (PDPH) and less frequent need for epidural blood patch (EBP), rates of ECE on imaging have not been closely investigated.

Materials & Methods

All CTM cases performed over an 8-year period for any indication (e.g., spontaneous intracranial hypotension CSF leak evaluation, low back pain or radiculopathy evaluation, pre-procedural planning) were retrospectively reviewed. Those with adequate imaging including the puncture site in the field of view (n=276) were reviewed by two independent neuroradiologists for the presence of puncture site ECE (n=63), ECE at the puncture site extending greater than one vertebral body level (n=15), or no ECE (n=198). Rates of ECE were compared by several technical factors including spinal needle type (pencil-type (Gertie Marx) or cutting-type (Quincke)), needle gauge, and puncture site level.

Results

Pencil-type spinal needles had significantly greater rates of any ECE (32%) versus cutting-type spinal needles (25%, p=0.03) and for mild extension (25% vs. 20%, respectively) and extension greater than one vertebral body level (7% vs. 4%, respectively, p=0.004). The rate of ECE did not differ by spinal needle gauge, needle type/gauge combinations, or spinal level of access (p's>0.05). The need for post-dural puncture targeted EBP did not differ by presence of ECE (p=0.19).

Conclusion

The rate of ECE in CTM was common (28% of cases) and occurred with slightly greater frequency with pencil-type spinal needles relative to cutting-type. The trace amount of epidural contrast is likely resorbed in the surrounding soft tissues and of insignificant clinical relevance. Asymptomatic ECE can be a common expected post-dural puncture finding and should not be confused for the site of leak when evaluating patients for spontaneous spinal CSF leak. Additionally, immediate ECE does not correlate with symptomatic PDPH and the imaging finding alone does not warrant further evaluation or treatment in an asymptomatic patient.

References

Milants WP, Parizel PM, de Moor J, et al. Epidural and subdural contrast in myelography and CT myelography. *European journal of radiology 1993*;*16:*147-150.

Xu H, Liu Y, Song W, et al. Comparison of cutting and pencil-point spinal needle in spinal anesthesia regarding postdural puncture headache: A meta-analysis. *Medicine* 2017;96:e6527.

214

7 Tesla MRI with Parallel Transmission: Coil Comparison and Multivariate Analysis of Image Quality

Quayd Robertson DO[1], Mojgan Golzy PhD[1], James C. Jones RT[1], Caleb Minor RT[1], Britton Odle DO[1], Edvin Isufi MD[1], Xiaoxi Chen MD[2], Erica O'Dell RT[1], Mai-Lan Ho MD[1]
[1]University of Missouri, Columbia, MO, USA. [2]Affiliated Hospital of Zunyi Medical University, Zunyi, Guizhou, China

Abstract Category

Functional/Advanced Imaging

Purpose

Conventional 7T MRI utilizes a single-transmit (sTx) radiofrequency coil, yielding large B0/B1 field inhomogeneities with artifacts and signal dropout near the skull base and field periphery. Parallel-transmit (pTx) coils offer improved image uniformity and power deposition. We compared clinical pTx image quality using two head coils: Nova 8Tx/32Rx (Nova Medical) and decoupled transceiver 8x2 TxRx (Resonance Research).

Materials & Methods

Imaging parameters were optimized for pTx using a reduced specific absorption rate (SAR) protocol for the Magnetom Terra platform (Siemens Healthineers). Prescan B0 and B1 shimming were performed. Routine pulse sequences included 3D T1, 3D FLAIR, and axial 2D T2. Coronal 2D T2 and postcontrast 3D T1 were optionally acquired based on clinical indication.

Patients were scanned using the Nova or transceiver coils during separate enrollment periods, then matched for analysis based on age and body mass index (BMI). Imaging reviewers were four faculty neuroradiologists blinded to imaging technique. Reviewers completed standardized training on anatomic landmarks and reference scores based on conventional sTx images (Nova 1Tx/32Rx). Raters provided ordinal ratings from 0–5 [0–10%, 11–30%, 31–50%, 51–70%, 71–90%, 91–100% visualization] for 10 anatomic structures [high cortex, white matter, inner ear, medulla, cerebellum, gyri recti, inferior temporal gyri, hippocampi, optic pathway, pituitary]. Scores were issued according to sequence [T1/FLAIR/T2], as well as side [R/L] and plane [axial/coronal] where applicable.

Nonparametric univariate comparisons of overall scores were performed for two samples (Wilcoxon rank-sum) and multiple pairwise comparisons (Kruskal-Wallis). Multivariate analysis was conducted by fitting a general linear model with Box-Cox transformation to assess the effect of the main variables (coil, plane, sequence, reviewer) on score outcomes when controlling for sex, age, and BMI.

Results

28 patients were analyzed: 17 female / 11 male, age 43±19 (20–78) years, BMI 25.2±4.5 (17.6–33.5). Exam indications included 17 epilepsy, 3 migraine, 3 dementia, 2 stroke, 1 multiple sclerosis, 1 trauma, and 1 tumor.

Demographic analysis showed significantly higher scores for females than males. For each 1-year increase in age, t-score decreased significantly by 0.0057. For each 1-unit increase in BMI, t-score increased by 0.01288 but was not significant. Rater scores were significantly lower for reviewer #1, higher for #2, and not markedly different for #3 and #4. Axial scores were significantly higher than coronal. 3D FLAIR scores were significantly lower than 3D T1 and 2D T2, which did not markedly differ.

When controlling for other variables, Nova had significantly lower overall scores than the transceiver coil ($p<0.0001$). Subgroup analysis showed that transceiver performed better for inferior temporal gyri, inner ears, and cerebellum; Nova was superior for high cortex and white matter. Coils did not differ significantly for gyri recti, hippocampi, pituitary, optic pathway, and medulla.

Conclusion

Using a low-SAR protocol for 7T pTx MRI, the transceiver coil shows higher overall quality ratings than Nova. Transceiver performs better for structures near the skull base, while Nova performs better in the superior brain. Patient sex, age, structure, and sequence all have significant effects on image quality.

References

1. Deniz CM. Parallel Transmission for Ultrahigh Field MRI. Top Magn Reson Imaging. 2019 Jun;28(3):159-171.
2. Klodowski K, Zhang M, Jen JP, et al. Parallel transmit improves 7T MRI adult epilepsy pre-surgical evaluation. https://doi.org/10.1101/2024.10.28.24316232.
3. Gras V, Boland M, Vignaud A, et al. Homogeneous non-selective and slice-selective parallel-transmit excitations at 7 Tesla with universal pulses: A validation study on two commercial RF coils. PLoS One. 2017 Aug 21;12(8):e0183562.
4. Li X, Gong H, Pan JW, et al. Modelling and B1 Shim Analysis of 16-Element Transceiver Array at 7 T. Int Conf Electromagn Adv Appl. 2019 Sep;2019:1291-1295.
5. Kim J, Sun C, Moon CH, et al. Evaluation of the performance of a 7-T 8 × 2 transceiver array. NMR Biomed. 2024 Aug;37(8):e5146.

Images/Tables

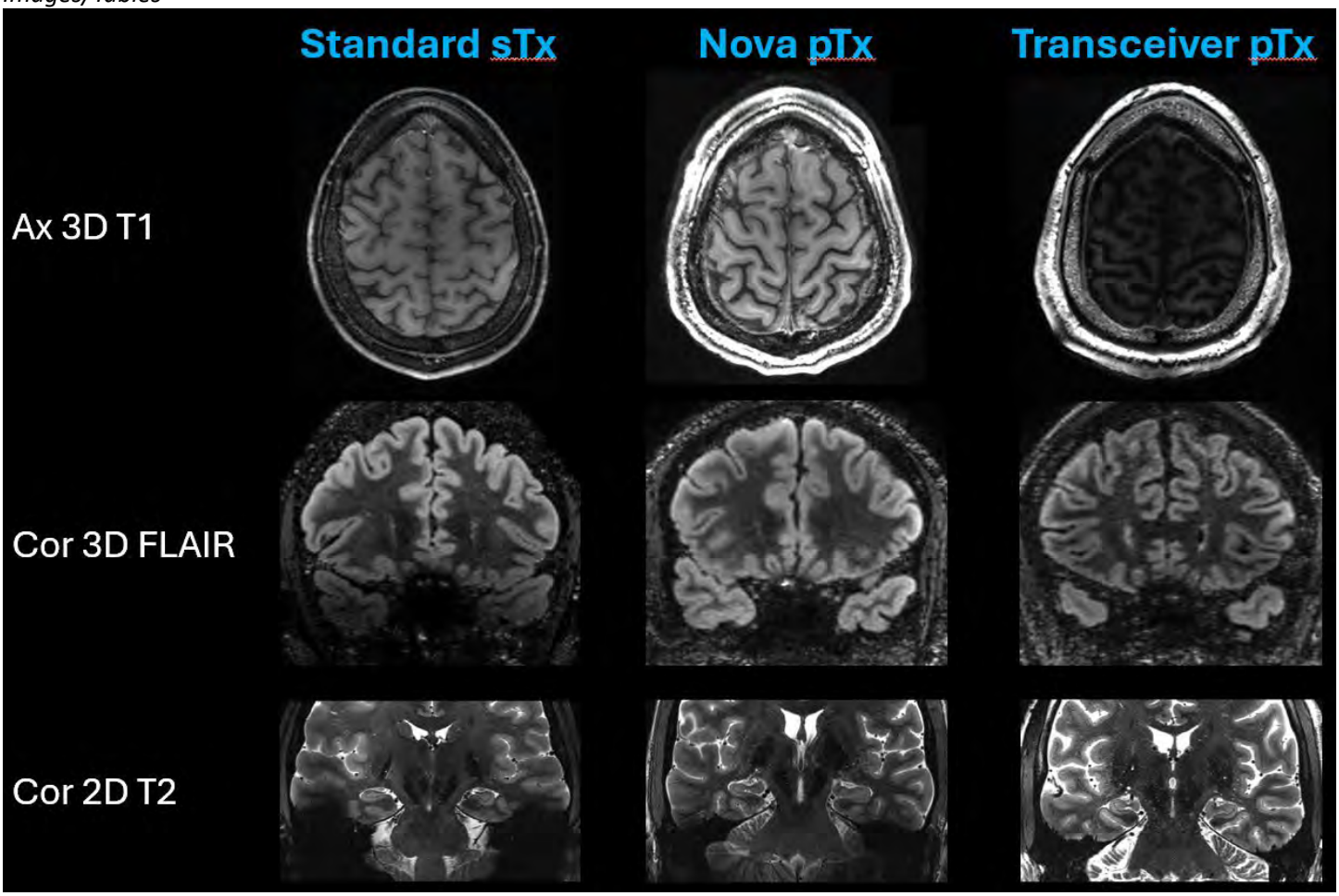

215

Choroid Plexus Uptake on Amyloid PET Predicts Cognitive Decline and Tau Burden Across Alzheimer's Disease Continuum in Amyloid-positive individuals

Yoon Seong Choi MD, PhD[1], Megan Ching M.Sc[1], Wenhao Han M.Sc[1], Pei-Ing Ngam MBBS[2]

[1]National University of Singapore, Singapore, Singapore, Singapore. [2]National University Hospital, Singapore, Singapore, Singapore

Abstract Category

Adult Brain

Purpose

The choroid plexus (CP) is gaining attention for its role in brain waste clearance, including amyloid plaque. Studies have also demonstrated amyloid plaques in the ChP, indicating its role in plaque clearance. Despite this, current literature lacks investigation into clinical significance of ChP amyloid accumulation measured by in vivo amyloid PET. Our study aimed to investigate the prognostic value of choroid plexus (CP) uptake on amyloid PET (CP-SUVR) in 1) the prediction of future cognitive decline, and 2) current tau burden in amyloid-positive (A+) individuals beyond cortical SUVR.

Materials & Methods

We analysed the participants from the Alzheimer's Disease Neuroimaging Initiative (ADNI, n=581) and Standardized Centralized Alzheimer's Neuroimaging (SCAN, n=223) who were A+ on PET. For the aim 1), Kaplan-Meier curves for cognitive decline was plotted in two or three A+ subgroups that were divided based on the tertiles or median values of CP-SUVR. Prognosis was compared between subgroups via log-rank test. In addition, the prognostic value of CP-SUVR for predicting future cognitive decline was assessed using Cox regression analyses in participants with baseline Clinical Dementia Rating-Sum of Boxes (CDR-SB) ≤ 9. Covariates included age, sex, and APOE4 status. Cognitive decline was defined as an an increase in CDR-SB ≥ 0.5 from baseline CDR-SB. For the aim 2), the prognostic value of CP-SUVR for predicting current tau burden measured by meta-temporal SUVR on tau PET was assessed using linear regression in the

participants who underwent a tau PET scan within 180 days from A+ amyloid PET scan. The same covariates of age, sex, APOE4 was included.

Results

Th A+ subgroups based on tertiles or median of CP-SUVR shows significantly different prognosis of cognitive decline on Kaplan-Meier curve, with lower CP-SUVR group showing worse prognosis (P<0.001 by log-rank in both ADNI and SCAN, Figure). In Cox regression analyses, CP-SUVR was independently prognostic for future cognitive decline (<0.001 by log-rank, Figure B) in presence of cortical SUVR and clinical information (HR 0.12 [0.06 – 0.25]. P <0.001 in ADNI, and HR 0.31 [0.13 – 0.74], P=0.008 in SCAN), indicating that lower CP-SUVR at given cortical SUVR was linked to higher risks for cognitive decline. Additionally, CP-SUVR showed a significant negative association with tau meta-temporal-SUVR (b=-0.39, SE=0.07, P<0.001 in ADNI, and b=-0.15, SE=0.04, P<0.001 in SCAN).

Conclusion

Our findings highlight the potential of CP-SUVR as a practical imaging marker, improving the resource utilization of amyloid PET beyond cortical SUVR for prognostication of A+ individuals.

References

1. Chapleau M, Iaccarino L, Soleimani-Meigooni D, et al. The Role of Amyloid PET in Imaging Neurodegenerative Disorders: A Review. *J Nucl Med* 2022;63:13s-19s

2. Crossgrove JS, Li GJ, Wei Z. The Choroid Plexus Removes β-Amyloid from Brain Cerebrospinal Fluid. *Experimental Biology and Medicine* 2005;230:771-776

Images/Tables

Figure. Kaplan-Meier curves for predicting future cognitive decline in the ADNI and SCAN datasets.

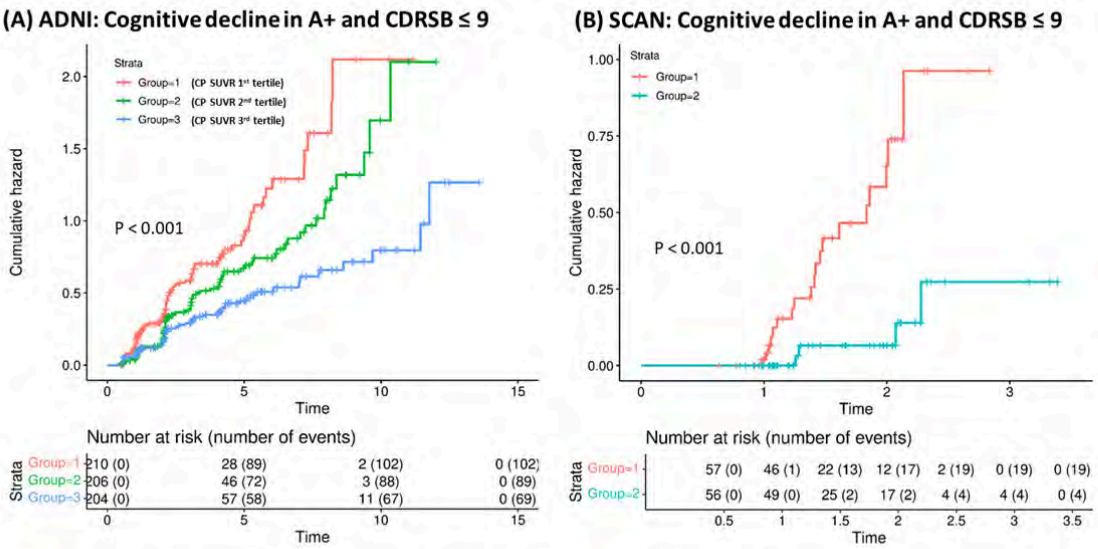

Table. Cox regression analysis for future cognitive decline in the ADNI and SCAN datasets.

Data	Predictors	HR (95% CI)			P value
ADNI	CP SUVR	0.12	0.06	0.25	<0.001
	Cortical SUVR	74.23	29.77	185.10	<0.001
	Age	0.99	0.97	1.01	0.460
	Gender	0.89	0.69	1.15	0.378
	Education	0.97	0.93	1.01	0.151
	APOE4	1.36	1.12	1.64	0.002
SCAN	CP SUVR	0.31	0.13	0.74	0.008
	Cortical SUVR	11.24	1.21	104.62	0.034
	Age	0.96	0.89	1.02	0.199
	Gender	0.71	0.27	1.88	0.489
	Education	1.00	0.83	1.22	0.980
	APOE4	0.52	0.30	0.91	0.021

Table. Linear regression analysis for current meta temporal SUVR on tau PET in the ADNI and SCAN datasets.

Data	Predictors	Beta	SE	P values
ADNI	CP SUVR	-0.39	0.07	<0.001
	Cortical SUVR	0.62	0.09	<0.001
	Age	-0.01	<0.01	<0.001
	Gender	0.02	0.03	0.510
	Education	-0.01	0.01	0.155
	APOE4	0.03	0.02	0.213
SCAN	CP SUVR	-0.15	0.04	<0.001
	Cortical SUVR	0.67	0.08	<0.001
	Age	-0.01	<0.01	<0.001
	Gender	0.03	0.03	0.510
	Education	-0.01	0.01	0.155
	APOE4	0.01	0.02	0.213

225

Diagnostic Accuracy of Cone-Beam CT for Acute Intracranial Hemorrhage in Suspected Ischemic Stroke Patients: A Systematic Review and Meta-analysis

Nicholas G Ferrone Student, Maria X Sanmartin PhD, Joseph O'Hara, Jean Jimenez, Sophia R Ferrone Student, Jason J Wang PhD, Jeffrey M Katz MD, Pina C Sanelli MD, MPH
Northwell Health, New Hyde Park, NY, USA

Abstract Category

Adult Brain

Purpose

Emerging technologies, such as Cone-Beam CT (CBCT), may improve workflows in acute ischemic stroke (AIS). Direct-to-angiography workflow relies on CBCT to exclude intracranial hemorrhage (ICH) to determine treatment eligibility for intravenous thrombolysis (IVT) and/or mechanical thrombectomy (MT). Prior studies evaluated CBCT for ICH detection using small, selected cohorts and variable diagnostic metrics yielding a wide range of sensitivity and specificity values. Our purpose was to synthesize available evidence to determine the diagnostic accuracy of CBCT for ICH detection, with particular focus on specific hemorrhage types: intraparenchymal (IPH), subarachnoid (SAH), and intraventricular (IVH).

Materials & Methods

We performed a systematic review and meta-analysis following the Preferred Reporting Items for Systematic Review and Meta-Analyses (PRISMA) guidelines. Our protocol was registered with the International Prospective Register of Systematic Reviews (PROSPERO). Systematic searches were last performed on April 1, 2024 in EMBASE, PubMed, Web-of-Science, Scopus, and CINAHL databases. Inclusion criteria: (1) Studies reporting diagnostic metrics of CBCT for ICH; (2) Studies using a reference standard to determine ICH. Exclusion criteria: (1) Case reports, abstracts, and reviews; (2) Studies without patient-level data. Pooled estimates and 95% confidence intervals (CI) were calculated for the Log diagnostic Odds ratio (DOR), sensitivity, and specificity for ICH and hemorrhage types using random-effects and common-effects models.

Results

The initial search yielded 5,771 studies. After removing 1,565 duplicates and 4,136 irrelevant studies which did not meet the inclusion criteria, 70 studies advanced to full-text review. An additional 58 studies were excluded for the following reasons: unsuitable study designs (n=43), different imaging exams (n=7), abstracts only (n=7), and retracted from the literature (n=1). During data extraction of the remaining 12 studies, an additional 4 studies were eliminated because the study aim did not include diagnostic outcomes of CBCT for detection of ICH. A total of 8 studies were included in the systematic review. Of these studies, a total of 7 studies had appropriate data for inclusion in the meta-analysis.
The 7 studies included in the meta-analysis yielded 466 patients. Pooled Log DOR, sensitivity, and specificity (95%CI) for ICH were 5.28 (4.11,6.46), 0.88 (0.79,0.97), and 0.99 (0.98,1.0), respectively (Figure 1). Pooled sensitivity (95%CI) for IPH, SAH, and IVH were 0.98 (0.95,1.0), 0.82 (0.57,1.0), and 0.78 (0.55,1.0). Pooled specificity (95%CI) for IPH, SAH, and IVH were 0.99 (0.98,1.0), 0.99 (0.97,1.0), and 1.0 (0.98,1.0).

Conclusion

CBCT had high specificity for ICH and hemorrhage types. However, sensitivity was lower and varied with the highest sensitivity for IPH followed by SAH and IVH. These findings indicate that CBCT may be reliable for exclusion of ICH in determining MT eligibility in AIS patients who are not IVT candidates. However, the high false-negatives of CBCT for SAH and IVH requires caution for IVT decision-making, where missing a small hemorrhage could result in devastating outcomes. Understanding the diagnostic performance of CBCT will enable clinicians to determine its appropriate utilization in the stroke imaging workflow.

References

Requena M, Olivé-Gadea M, Muchada M, et al. Direct to Angiography Suite Without Stopping for Computed Tomography Imaging for Patients With Acute Stroke. JAMA Neurol. 2021;78(9):1099. doi:10.1001/jamaneurol.2021.2385

Images/Tables

Figure 1: Log diagnostic Odds Ratio (DOR), sensitivity, and specificity for the individual datasets in the selected studies included in the meta-analysis. The pooled logDOR was 5.28 (95%CI 4.11,6.46), sensitivity was 0.88 (95%CI 0.79,0.97), and specificity was 0.99 (95%CI 0.98,1.0) for intracranial hemorrhage.

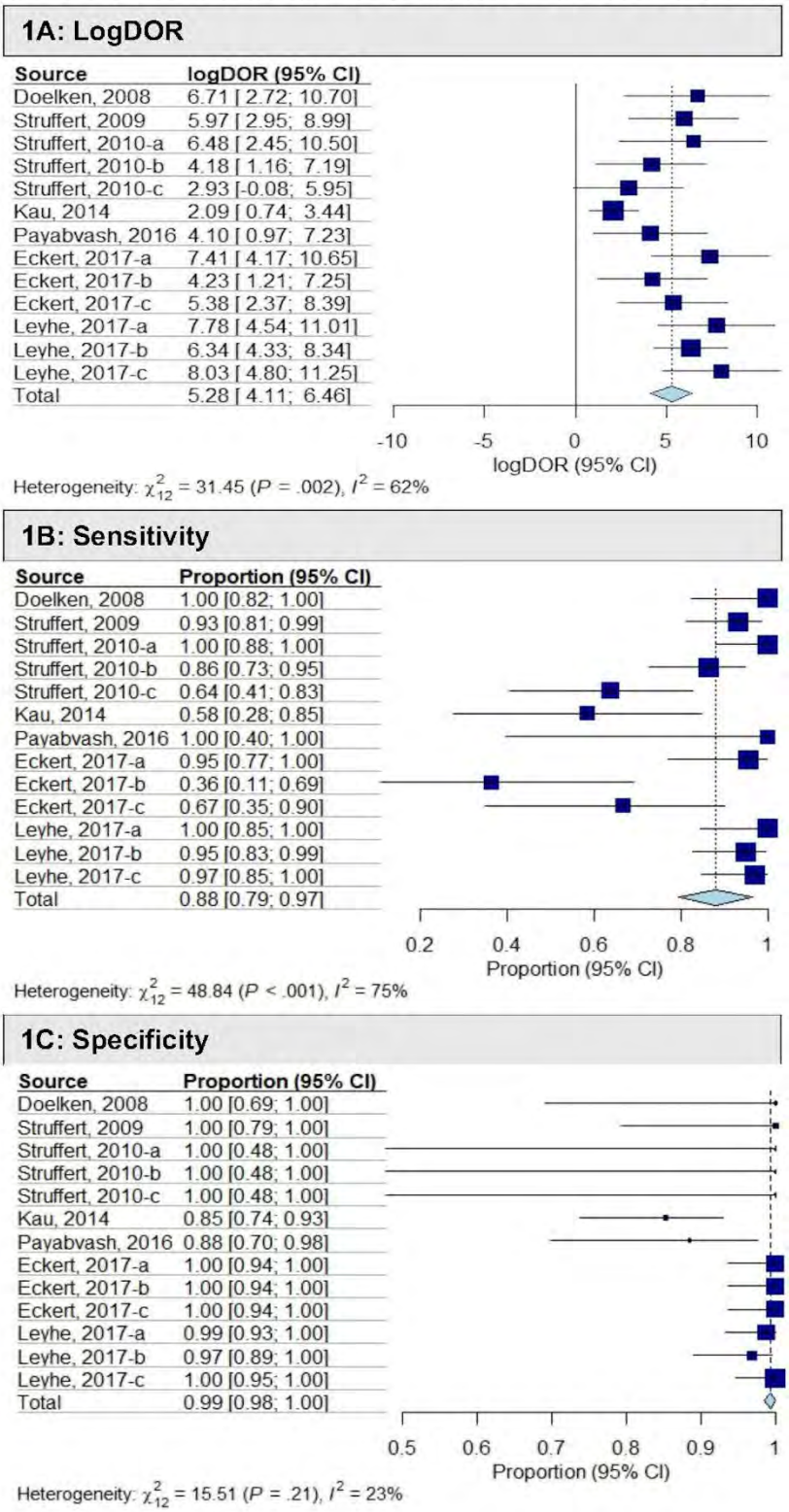

227

10-Year Trends in Last Known Well to Arrival Time in Acute Ischemic Stroke Patients: 2014-2023

Nicholas G Ferrone Student, Maria X Sanmartin PhD, Joseph O'Hara, Sophia R Ferrone Student, Jason J Wang PhD, Jeffrey M Katz MD, Pina C Sanelli MD, MPH
Northwell Health, New Hyde Park, NY, USA

Abstract Category

Interventional

Purpose

Many national initiatives focus on promoting early hospital arrival of acute ischemic stroke (AIS) patients because treatment effectiveness is time-dependent. However, several studies reported time-delays in hospital arrival, especially during the COVID-19 pandemic. Our purpose was to evaluate the 10-year trends in last known well to arrival (LKWA) time and assess disparities in AIS patients.

Materials & Methods

A retrospective study of consecutive AIS patients admitted to a large, socioeconomically diverse healthcare system was performed from 2014-2023. LKWA time groups were categorized according to treatment eligibility: 0-4.5, >4.5-24, and >24 hours. Demographic and clinical characteristics, treatment utilization, and modified Rankin Scale (mRS) at discharge were extracted from electronic health records. Trend analysis was performed by calculating the proportion of AIS patients in each LKWA groups by year and plotting the frequency data over time from 2014-2023. Cochran–Mantel-Haenszel trend test was used to assess significant differences in the LKWA groups by discharge year (2014-2023). Bivariate analyses were conducted using Chi-square tests to determine statistical differences in the study cohort's characteristics among the LKWA groups. Treatment utilization and early clinical outcomes were also compared amongst LKWA groups. Multivariable logistic regression analyses were conducted to evaluate the associations between the dependent variable (late LKWA >4.5 groups) and patient characteristics, compared to the LKWA 0-4.5 group. The independent variables included age, sex, race, health insurance, MHI, arrival mode, NIHSS, stroke risk factors, and discharge year. Odds ratio (OR), 95% confidence intervals (CI), and p-values were estimated.

Results

A total of 11,563 AIS patients were included with 53% (6,163) LKWA0-4.5, 34% (3,988) LKWA>4.5-24, and 12% (1,412) LKWA>24 groups. From 2014-2023, there was a significant downward trend in the early LKWA0-4.5 (61% to 46%) with upward trends in the later LKWA>4.5-24 (31% to 43%) and LKWA>24 (8% to 11%) groups (p<.001) (**Figure 1A**). In the LKWA>4.5 groups, the gap widened between racial categories (p=0.004) during the recent guideline changes (2015-2018) and COVID aftermath (2021-2023) (**Figure 1B**). Compared to LKWA0-4.5, the LKWA>4.5-24 group was less likely to receive EVT (p<.001) and more likely to have worse outcomes (mRS2-5) (p<.001). LKWA>4.5 groups were more likely to be older >80 years (Odds Ratio=1.33 [95% Confidence Intervals:1.11-1.58]), males (1.11 [1.03-1.20]), Black (1.21 [1.09-1.34]), Asian (1.20 [1.03-1.39]), Medicaid insurance (1.18 [1.08-1.29]), and low-income <$80,000 (1.39 [1.20-1.61]).

Conclusion

In the past decade, there was a significant downtrend in AIS patients arriving in the early LKWA0-4.5 group and uptrend in the late LKWA>4.5 groups. During the peak of the COVID pandemic (2020), these trends were further exaggerated and did not return to pre-pandemic levels in 2021-2023. Socioeconomic disparities were observed with a persistent upward trend in Non-White patients in the late LKWA>4.5 groups after the COVID pandemic. The LKWA>4.5 groups were more likely to be older, males, Black or Asian race, Medicaid insurance, lower income, and more comorbidities. Furthermore, the LKWA>4.5-24 group was less likely to receive EVT and more likely to have worse outcomes. These findings highlight the need of implementing targeted efforts towards the late LKWA groups to improve disparities in stroke treatment and outcomes.

References

Powers WJ, Rabinstein AA, Ackerson T, et al. Guidelines for the Early Management of Patients With Acute Ischemic Stroke: 2019 Update to the 2018 Guidelines for the Early Management of Acute Ischemic Stroke: A Guideline for Healthcare Professionals From the American Heart Association/American Stroke Association. Stroke. 2019;50(12).

Images/Tables

Figure 1A: 10-Year Trends in Last Known Well to Arrival (LKWA) Time

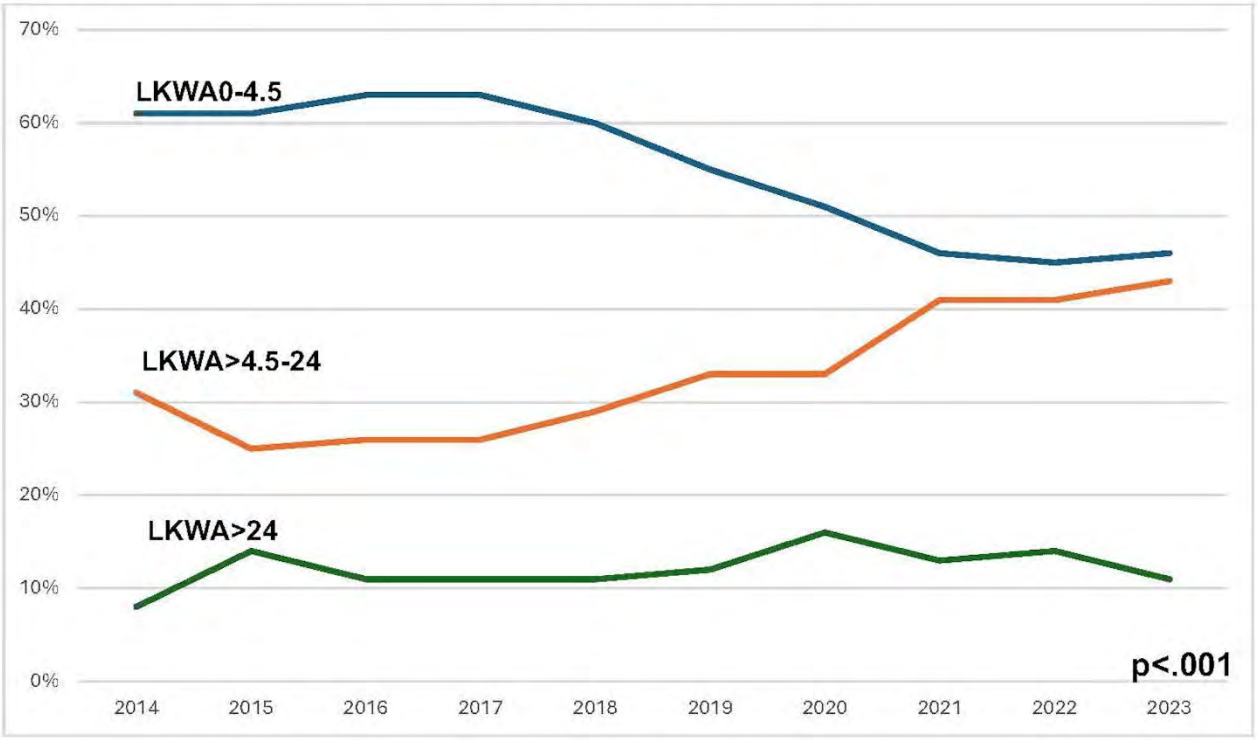

Figure 1B: Trends in Late Last Known Well to Arrival (LKWA) >4.5 Hours by Race

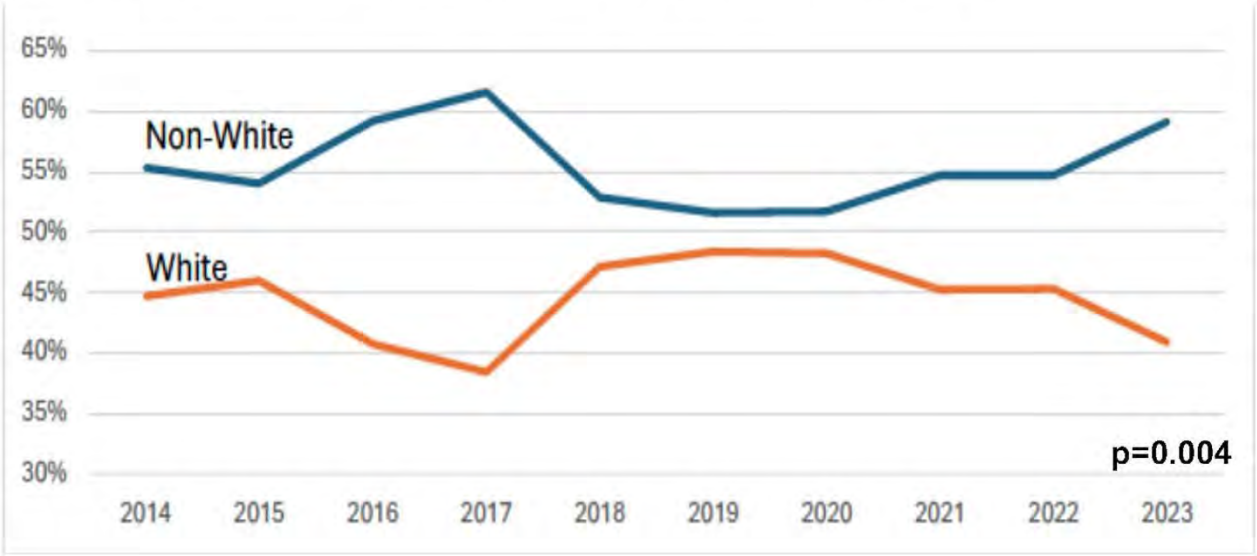

232

Prolonged Venous Transit Is Associated with Higher Odds of Unfavorable Functional Outcomes in Large Core Stroke Patients

Hamza Adel Salim MD[1], Dhairya A. Lakhani MD[2], Janet Mei MD[3], Nathan Z. Hyson MD[3], Vaibhav Vagal MD[4], Gregory W Albers MD[5], Tobias D. Faizy MD[6], Jeremy J. Heit MD PhD[5], Max Wintermark MD[1], Vivek Yedavalli MD[3]
[1]Department of Neuroradiology, MD Anderson Medical Center,, Houston, TX, USA. [2]Department of Radiology, West Virginia University, Morgantown, WV, USA. [3]Department of Radiology, Division of Neuroradiology, Johns Hopkins Medical Center, Baltimore, MD, USA. [4]Renaissance School of Medicine at Stony Brook University, NewYork, NY, USA. [5]Department of Neuroimaging and Neurointervention, Stanford Medical Center, Palo Alto, CA, USA. [6]Department of Radiology, Neuroendovascular Program, University Medical Center Münster, Münster, Münster, Germany

Abstract Category

Head & Neck

Purpose

Large core acute ischemic stroke (AIS) is associated with high rates of disability despite mechanical thrombectomy (MT) treatment. Recent studies suggest that prolonged venous transit (PVT) may indicate impaired venous drainage, influencing functional outcomes. However, its prognostic value in large core stroke patients remains unclear.

Materials & Methods

We conducted a retrospective cohort study using data from consecutive patients with AIS-LVO and large ischemic core volumes (ASPECTS <6 or relative cerebral blood flow < 30% volume ≥50 mL) between September 2017 and September 2022. PVT was assessed based on time-to-maximum (Tmax) ≥10 seconds in the superior sagittal sinus or torcula. The primary outcome was unfavorable functional recovery at 90 days, defined as a modified Rankin Scale (mRS) score of 4-6.

Results

100 patients met inclusion criteria, and 41 (41%) had PVT. Unfavorable functional outcomes were more frequent in the PVT+ group (59% vs. 37%, p=0.036). Multivariable analysis confirmed that PVT was independently associated with unfavorable outcomes (adjusted OR 4.07, 95% CI 1.15-14.4, p=0.03). Other predictors included older age (adjusted OR 1.07, 95% CI 1.02 to 1.11, P=0.003), higher admission NIHSS (adjusted OR 1.16, 95% CI 1.05 to 1.29, P=0.005), and larger rCBF <30% volume (adjusted OR 1.02, 95% CI 1.00 to 1.04, P=0.032).

Conclusion

PVT is independently associated with unfavorable outcomes in patients with large core infarcts. These findings suggest PVT may serve as a prognostic marker, warranting further investigation in larger prospective studies to guide treatment decisions in this high-risk population.

References

Salim HA, Yedavalli V, Musmar B, et al. Endovascular therapy versus best medical management in distal medium middle cerebral artery acute ischaemic stroke: a multinational multicentre propensity score-matched study. *J Neurol Neurosurg Psychiatry*. Published online July 23, 2024. doi:10.1136/jnnp-2024-333669

Images/Tables

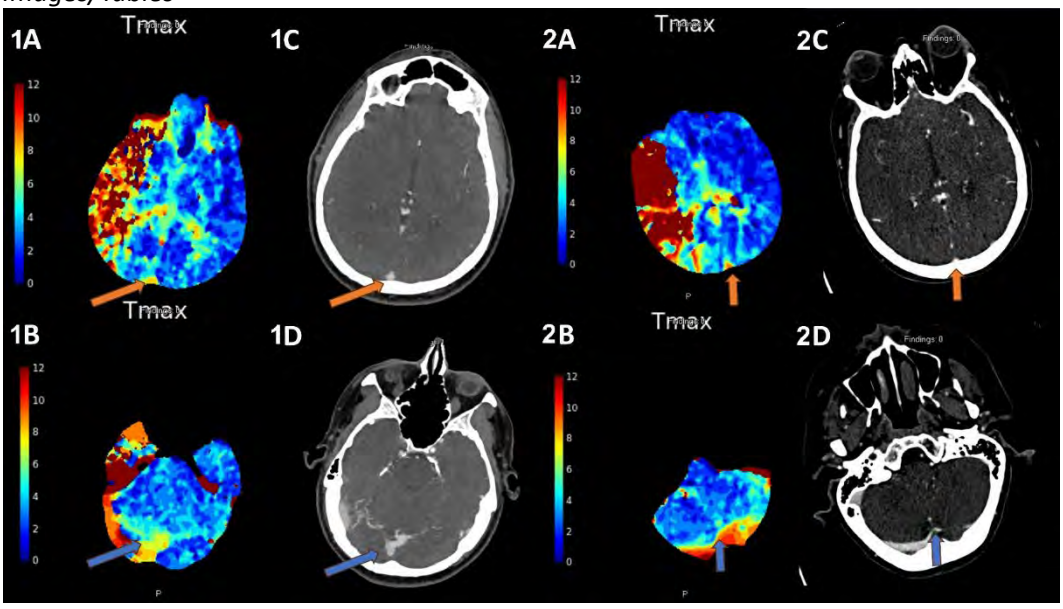

236

Tmax 10 Volume Is Independently Associated With NWU Delta in Large Core Stroke

Vivek Yedavalli MD[1], Hamza Adel Salim MD[2], Dhairya A. Lakhani MD[3], Janet Mei MD[1], Nathan Z. Hyson MD[1], Vaibhav Vagal MD[4], Gregory W Albers MD[5], Max Wintermark MD[2], Jeremy J. Heit MD PHD[5], Tobias D. Faizy MD[6]
[1]Department of Radiology, Division of Neuroradiology, Johns Hopkins Medical Center, Baltimore, MD, USA. [2]Department of Neuroradiology, MD Anderson Medical Center, Houston, TX, USA. [3]Department of Radiology, West Virginia University, Morgantown, WV, USA. [4]Renaissance School of Medicine at Stony Brook University, NY, NY, USA. [5]Department of Neuroimaging and Neurointervention, Stanford Medical Center, Palo Alto, CA, USA. [6]Department of Radiology, Neuroendovascular Program, University Medical Center Münster, Münster, Münster, Germany

Abstract Category

Head & Neck

Purpose

This study investigates the relationship between severe tissue hypoperfusion, indicated by Tmax > 10 seconds volume, and cerebral edema growth, quantified as net water uptake (ΔNWU), in large vessel occlusions acute ischemic (AIS-LVO) patients treated with endovascular thrombectomy (EVT).

Materials & Methods

This multicenter retrospective cohort study involved AIS-LVO patients with ASPECTS ≤5, undergoing EVT at two comprehensive stroke centers between January 2013 and December 2019. We investigated the relationship between Tmax > 10 s volume derived from perfusion imaging and ΔNWU measured on non-contrast head CT images, hypothesizing that larger Tmax > 10 s volumes are indicative of greater edema growth in large core strokes.

Results

A total of 95 patients were analyzed. Both Tmax > 10 s volumes and ASPECTS were independently associated with ΔNWU. Specifically, higher Tmax > 10 s volumes and lower ASPECTS were linked to increased ΔNWU, suggesting worse functional outcomes due to higher edema growth in critically hypoperfused brain areas.

Conclusion

The study highlights the importance of considering severe pretreatment hypoperfusion, as reflected by larger Tmax > 10 seconds volumes, in predicting cerebral edema growth in AIS-LVO patients, which could inform clinical strategies, emphasizing the need for larger prospective studies to validate and explore implications.

References

Faizy TD, Winkelmeier L, Mlynash M, Broocks G, Heitkamp C, Thaler C, et al. Brain edema growth after thrombectomy is associated with comprehensive collateral blood flow. J Neurointerv Surg. 2023. doi:10.1136/jnis-2023-020921

Steffen P, Winkelmeier L, Kniep H, Geest V, Soltanipanah S, Fiehler J, et al. Quantification of ischemic brain edema after mechanical thrombectomy using dual-energy computed tomography in patients with ischemic stroke. Sci Rep. 2024;14: 4148.

Broocks G, Flottmann F, Ernst M, Faizy TD, Minnerup J, Siemonsen S, et al. Computed Tomography–Based Imaging of Voxel-Wise Lesion Water Uptake in Ischemic Brain: Relationship Between Density and Direct Volumetry. Invest Radiol. 2018;53: 207.

Images/Tables

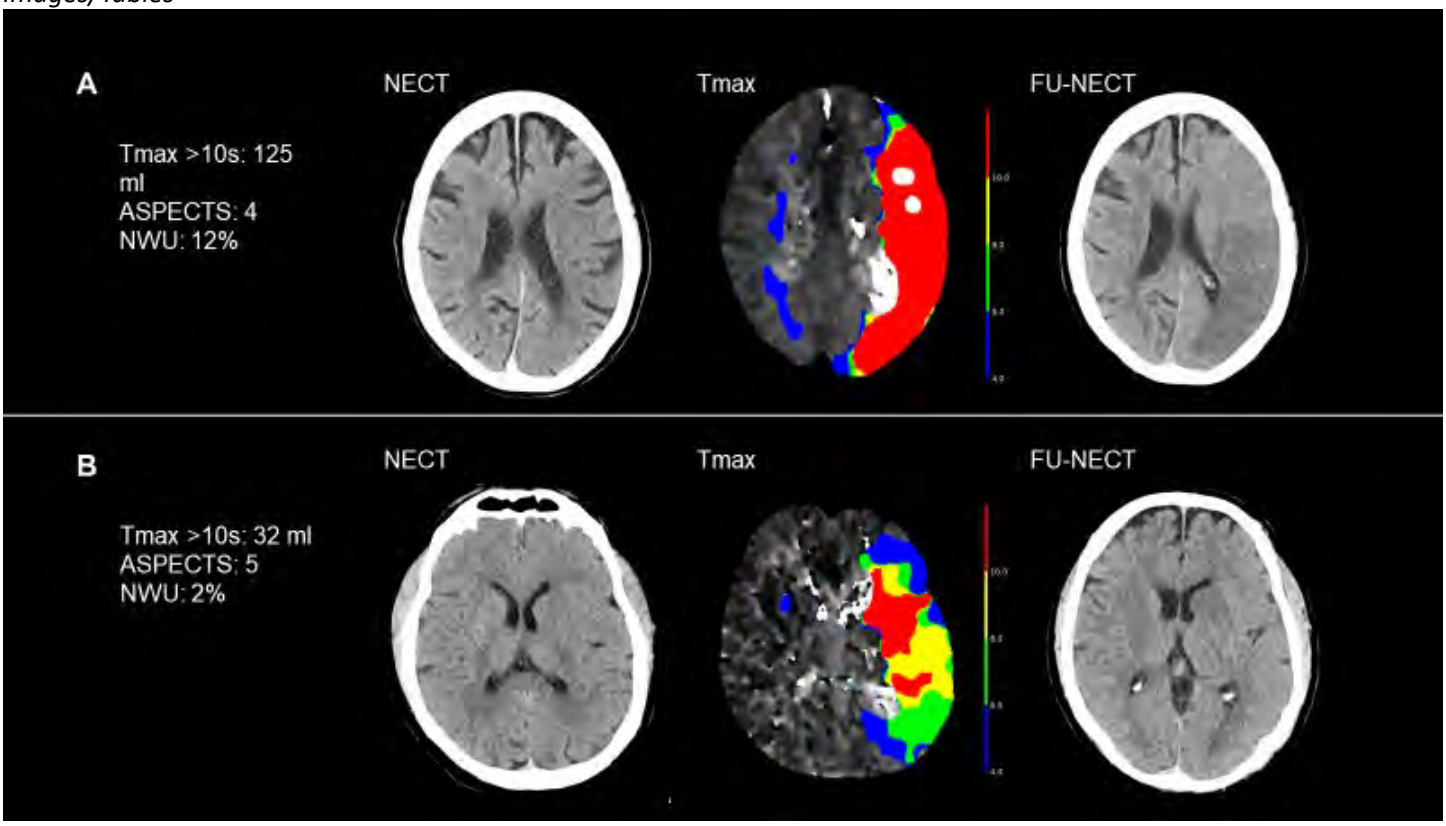

239

Enhancing Diagnostic Accuracy in IDH-Mutant Gliomas: A Three-Step Model for Preoperative Classification and Grade Determination via MRI Imaging Predictors

Klara M. Willms[1], Wondwossen Lerebo PhD[2], Marc von Reppert[1], Niklas Tillmanns[1], Jan Lost[1], Ujjwal Baid PhD[3], Spyridon Bakas MD/PhD[4], Fatima Memon MD[5], Elizabeth Schrickel MD[6], Mariam Aboian MD/PhD[2]

[1]Yale University, New Haven, Connecticut, USA. [2]University of Pennsylvania, Children's Hospital of Philadelphia, Philadelphia, Pennsylvania, USA. [3]Emory University, Atlanta, Georgia, USA. [4]Department of Radiology and Imaging Sciences; Neurological Surgery; Biostatistics and Health Data Sciences, Indiana University School of Medicine, Indianapolis, Indiana, USA. [5]Carolina Radiology Associates LLC, Florence, South Carolina, USA. [6]The Ohio State University, Columbus, Ohio, USA

Abstract Category

Adult Brain

Purpose

Isocitrate dehydrogenase (IDH)-mutant gliomas vary in survival based on molecular subtype.[1,2] Accurate classification of IDH-mutant, 1p/19q non co-deleted astrocytomas and IDH-mutant, 1p/19q co-deleted oligodendrogliomas is essential for optimizing outcomes and treatment.[3,4] Early noninvasive diagnosis can guide treatment decisions and facilitate neoadjuvant trials. This study uses VASARI MRI features and T2-FLAIR mismatch to provide a framework for classifying and grading of IDH-mutant gliomas, improving preoperative diagnosis and planning. This study seeks to identify VASARI features with high predictive value for grading IDH-mutant gliomas to enhance diagnostic confidence and enable tailored patient care.

Materials & Methods

We retrospectively reviewed 1,031 patients treated for glioma between January 2000 and December 2023 of which 167 adult patients had IDH-mutant gliomas, confirmed by histopathology per WHO 2021 CNS5 criteria and pre-treatment MRI. Two board-certified neuroradiologists independently conducted assessments of preoperative imaging on multiple MRI sequences to diagnose glioma subtype and qualitatively assess the T2/FLAIR mismatch sign.

To classify and grade IDH-mutant gliomas, we implemented a three-step logistic regression process: (1) binary logistic regression distinguished astrocytomas from oligodendrogliomas, (2) ordinal logistic regression graded astrocytomas

(grade 2, 3 4), and (3) binary logistic regression differentiated between grade 2 and 3 oligodendrogliomas. Feature selection included high Variance Inflation Factor exclusion (threshold >5) to mitigate multicollinearity. Model performance was assessed via area under the curve (AUC) for binary models and cumulative AUC for ordinal models, alongside odds ratios and relative risk ratios for interpretation.

Results

Diagnostic accuracy of the raters distinguishing between tumor entities was limited, with fair overall agreement for glioma subtype diagnosis (κ = 0.27). When employing the step-by-step approach, models achieved an AUC of 0.83 in distinguishing astrocytomas from oligodendrogliomas. For astrocytoma grading, the AUCs were 0.82, 0.71, and 0.81 for grades 2, 3, and 4, respectively, while oligodendroglioma grading achieved an AUC of 0.85. Specific imaging features proved to be significant predictors.

In Step 1, a partial T2/FLAIR mismatch (OR = 8.84, 95% CI 2.99–26.12, p<0.001) and edema crossing the midline (OR = 7.07, 95% CI 1.77–28.21, p=0.006) were highly predictive of astrocytoma, with a proportion enhancing >5% also being significant (OR = 4.27, 95% CI 1.60–11.37, p=0.004). Additionally, a proportion of enhancing tumor >5% was a significant predictor (OR = 4.27, 95% CI 1.60–11.37, p=0.004). Step 2 showed lesion size of 6–8 cm (RRR = 6.22, 95% CI 1.26–30.54, p=0.024) and proportion enhancing >5% (RRR = 3.67, 95% CI 1.26–10.70, p=0.017) as significant for astrocytoma grading. In Step 3, hemorrhage strongly predicted oligodendroglioma grade 3 (OR = 127.35, 95% CI 3.96–4094.81, p=0.006), with additional predictors including proportion enhancing >5% (OR = 5.17, 95% CI 1.01–26.36, p=0.048) and proportion of edema <5%, inversely predicting grade 3 status (OR = 0.24, 95% CI 0.07–0.85, p=0.027).

Conclusion

The imaging characteristics of IDH-mutant gliomas are highly heterogeneous, complicating clinical diagnosis. Analyzing the predictive value of specific qualitative imaging features in a stepwise manner contributes to a precise understanding of IDH-mutant subtype radiology appearances.

References

1. Claus EB, Walsh KM, Wiencke JK, et al. Survival and low-grade glioma: the emergence of genetic information. *Neurosurg Focus.* 2015;38(1). doi:10.3171/2014.10.FOCUS12367.
2. Jenkins RB, Blair H, Ballman KV, et al. A t(1;19)(q10;p10) mediates the combined deletions of 1p and 19q and predicts a better prognosis of patients with oligodendroglioma. *Cancer Res.* 2006;66(20):9852-9861. doi:10.1158/0008-5472.CAN-06-1796.
3. Alshiekh Nasany R, de la Fuente MI. Therapies for IDH-Mutant Gliomas. *Curr Neurol Neurosci Rep.* 2023;23(5):225-233. doi:10.1007/s11910-023-01265-3.
4. Oberheim Bush NA, Chang S. Treatment strategies for low-grade glioma in adults. *J Oncol Pract.* 2016;12(12):1235-1241. doi:10.1200/JOP.2016.018622.

Images/Tables

VASARI Feature Assessment in IDH-mutant Gliomas

Step Analysis	Feature	Crude RRR/OR (95% CI)
Step 1	Lesion Size_6-8cm	OR 2.79 (1.09, 7.16)*
	Proportion of Edema_<5%	OR 2.09 (1.02, 4.29)*
	Proportion of Edema_>68%	OR 6.89 (1.77, 26.82)**
	Edema Crosses Midline_Yes	OR 7.07 (1.77, 28.21)**
	Proportion Enhancing_>5%	OR 4.27 (1.60, 11.37)**
	Proportion nCET_<5%	OR 0.13 (0.03, 0.68)*
	Diffusion_Neither/Equivocal	OR 0.48 (0.24, 0.93)*
	Hemorrhage_Yes	OR 0.17 (0.05, 0.62)**
	T2/FLAIR Mismatch_partial mismatch	OR 8.84 (2.99, 26.12)***
	T2/FLAIR Mismatch_positive mismatch	OR 6.24 (2.79, 13.97)***
Step 2	Lesion Size_6-8cm	RRR 6.22 (1.26, 30.54)*
	Proportion Enhancing_>5%	RRR 3.67 (1.26, 10.70)*
Step 3	Proportion of Edema_<5%	OR 0.24 (0.07, 0.85)*
	Proportion Enhancing_>5%	OR 5.17 (1.01, 26.36)*
	Hemorrhage_Yes	OR 127.35 (3.96, 4094.81)**

Binary and Ordinal Logistic Regression Analysis Results for VASARI Features in IDH-Mutant Gliomas.
Significance levels are indicated by asterisks: * $p < 0.05$, ** $p < 0.01$, *** $p < 0.001$.
Step Descriptions:
Step 1: Binary Logistic Regression (astrocytoma (AS) vs. oligodendroglioma (OD))
Step 2: Ordinal Logistic Regression (astrocytoma grading: grade 2 astrocytoma (AS2), grade 3 astrocytoma (AS3), grade 4 astrocytoma (AS4))
Step 3: Binary Logistic Regression (oligodendroglioma grading: grade 2 oligodendroglioma (OD2), grade 3 oligodendroglioma (OD3))

241

Association Between Venous Transit and Excellent Neurological Outcomes Post Thrombectomy in Acute Basilar Artery Occlusion

Maya Schwartz BA[1], Vivek Yedavalli MD, MS[2], Nicole Yuen MS[3], Michael Mlynash MD[3], Pierre Seners MD[4], Maarten G Lansberg MD, PhD[3], Gregory W Albers MD[3], Jeremy J Heit MD, PhD[1]

[1]Department of Radiology, Stanford University School of Medicine, Palo Alto, CA, USA. [2]Department of Radiology and Radiological Sciences, Johns Hopkins School of Medicine, Baltimore, MD, USA. [3]Department of Neurology and Neurological Sciences, Stanford University School of Medicine, Palo Alto, CA, USA. [4]Department of Neurology, Rothschild Institute, Paris, Paris, France

Abstract Category

Interventional

Purpose

Endovascular thrombectomy (ET) has emerged as an effective therapy for patients with acute ischemic strokes caused by basilar artery occlusions (BAO). However, even in cases where successful reperfusion is achieved, many patients still experience significant morbidity or mortality. There is a need to develop accurate pre-treatment prognostication tools to identify favorable BAO candidates for ET. A novel perfusion imaging marker, prolonged venous transit (PVT), reflects impaired tissue perfusion and is associated with increased mortality in patients with large vessel occlusions in the anterior circulation. We hypothesized that PVT absence (PVT-) correlates with better outcomes in acute ischemic stroke patients with BAO.

Materials & Methods

We performed a multi-center retrospective analysis of BAO patients who had pre-treatment CT or MR bolus perfusion imaging. PVT presence (PVT+) was defined as Tmax≥10s timing delay in either the regions of the torcula, left or right transverse sinus, or a combination of these areas (Figure 1). PVT+ or PVT- was independently scored by a research associate and experienced diagnostic and interventional neuroradiologists. Disagreements were adjudicated by consensus. Favorable outcome was defined as mRS 0-3 at 90-days, and an excellent outcome as an mRS of 0-1. Baseline and clinical characteristics were compared between PVT groups using Mann-Whitney U test and $\chi 2$ tests. Agreement between raters was assessed by Cohen's kappa.

Results

99 patients with BAO were assessed for PVT status, and baseline characteristics were available for 79 patients. 40 patients (40%) were PVT- and 59 patients (60%) were PVT+. Raters had substantial agreement on PVT ratings with a kappa of 0.71 (95% CI 0.56-0.86). PVT- patients were younger (median age 62 years [IQR 50-70] versus 67 years [IQR 62-78] in PVT+; P=0.014) and were more likely to present with a wake-up stroke (42% versus 15% in PVT+; P=0.047). There were no other differences in patient characteristics, treatment, or thrombectomy success. After ET, PVT- was associated with more favorable mRS scores on an ordinal shift analysis (Figure 2), but this finding did not reach statistical significance (P=0.061). Excellent outcomes (mRS 0-1) were observed in 44% of patients with PVT- versus 22% with PVT+ (P=0.027).

Conclusion

In this subset of BAO patients, those with PVT- were younger and more likely to present with wake-up strokes. PVT- also was associated with excellent outcomes (mRS 0-1) compared to PVT+, however, larger studies are needed to better assess the strength of these findings.

References

Yedavalli VS, Koneru M, Hoseinyazdi M, et al. Prolonged venous transit on perfusion imaging is associated with higher odds of mortality in successfully reperfused patients with large vessel occlusion stroke. J Neurointerv Surg. 2024. DOI: 10.1136/jnis-2024-021488

Images/Tables

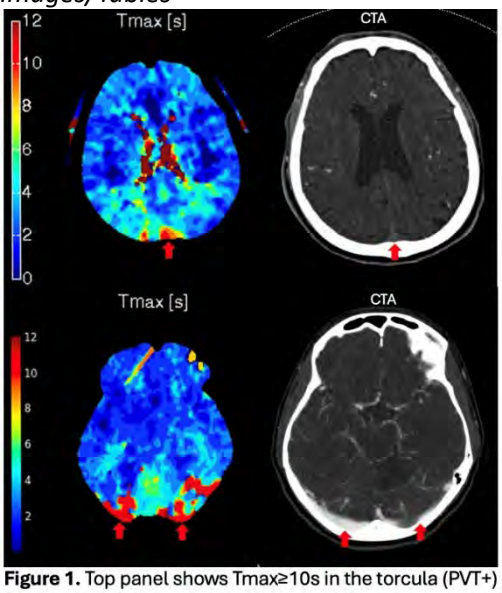

Figure 1. Top panel shows Tmax≥10s in the torcula (PVT+) colocalized with CTA imaging. Bottom panel shows Tmax≥10s in the left transverse and right transverse (PVT+) colocalized with CTA imaging.

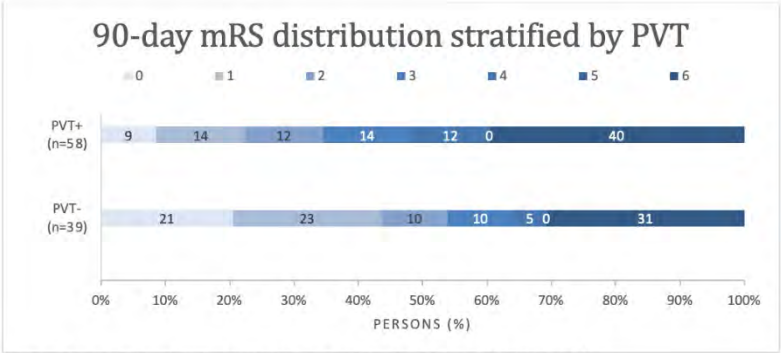

Figure 2. mRS distribution in patients with and without PVT (P=0.061)

249

Post Treatment Surveillance of NIRADS 1 Human Papillomavirus Oropharyngeal Squamous Cell Carcinoma (HPV OPSCC): The Emory Experience.

Mark Greenhill DO, James Mitchell MD, Patrick Arraj MD, Jacqueline Junn MD, Kristen Baugnon MD, Elizabeth Krupinski PhD, Ashley Aiken MD, Jennifer Becker MD
Emory, Atlanta, GA, USA

Abstract Category

Head & Neck

Purpose

HPV-associated Oropharyngeal squamous cell carcinoma (HPV OPSCC) incidence is increasing, now accounting for up to 90% of new diagnoses[1,2]. HPV OPSCC is generally associated with improved prognosis and survival compared to the HPV-negative OPSCC[3]. As a result, these patients are receiving an increasing number of surveillance imaging studies during their lifetime. Newly available novel serum biomarker circulating DNA detection techniques are showing promise in detecting disease recurrence, and, combined with the ACR Neck Imaging and Reporting Database (NI-RADS), may allow for less frequent imaging surveillance for select patients.

The purpose of this retrospective study is to evaluate HPV OPSCC treatment outcomes in those without disease on their baseline 3-month posttreatment imaging (NI-RADS 1) to optimize the frequency and timing of imaging surveillance of these patients.

Materials & Methods

Retrospective analysis of HPV OPSCC NI-RADS 1 patients without prior head and neck cancer treated at Emory from January 2016 through December 2023. Initial TNM stage, risk factors for aggressive disease (including but not limited to

positive margins and extranodal extension on surgical pathology and drinking/smoking history), treatment type, and outcome data obtained from the EMR will be presented, including HPV circulating DNA trends when available.

Results

To date, 65 patients with NI-RADS 1 have been analyzed. Only 1/65 (1.5%) had recurrent disease at the primary site at 66 weeks, with NPV of NI-RADS 1 of 98.5% (64/65).

Conclusion

The rate of malignancy recurrence in our initial HPV OPSCC patient cohort with NI-RADS 1 is very low at 1.5%, with NI-RADS 1 conveying a high NPV. The results of our full analysis may allow for reduced imaging surveillance of such patients in the future.

References

1. Stein AP, Saha S, Kraninger JL, Swick AD, Yu M, Lambert PF, Kimple RJ. Prevalence of Human Papillomavirus in Oropharyngeal Cancer: A Systematic Review. Cancer J. 2015 May-Jun;21(3):138-46.
2. Gillison ML, Chaturvedi AK, Anderson WF, Fakhry C: Epidemiology of Human Papillomavirus–Positive Head and Neck Squamous Cell Carcinoma. Journal of Clinical Oncology 2015, 33:3235-42.
3. Guo T, Kang SY, Cohen EEW. Current perspectives on recurrent HPV-mediated oropharyngeal cancer. Front Oncol. 2022;12:966899.

266

Reporting the Degree of Certainty of CSF-Venous Fistulas in Patients with Spontaneous Intracranial Hypotension: The Duke CSF-Venous Fistula Confidence Score

Daphne Zhu BS[1], Peter G Kranz MD[2], Michael D Malinzak MD[2], Kayla W Kilpatrick PhD[3], Al Erkanli PhD[3], Jay Willhite MD[2], Linda G Leithe MD[2], Timothy J Amrhein MD[2]

[1]Duke University School of Medicine, Durham, NC, USA. [2]Duke University Medical Center, Durham, NC, USA. [3]Department of Biostatistics and Bioinformatics, Duke University, Durham, NC, USA

Abstract Category

Spine

Purpose

CSF-venous fistulas (CVFs) are an increasingly recognized cause of spontaneous intracranial hypotension (SIH). While imaging features of CVFs are well established, there is currently no standardized method for reporting the degree of confidence about the presence or absence of a CVF on CT myelography (CTM).[1] Reliably reporting certainty of the presence of a CVF has critical implications for patient care and treatment decision-making. For example, referral for surgical ligation or transvenous embolization (TVE) of a CVF is appropriate when imaging is definitive but may not be optimal when there is uncertainty.

The purpose of this study was to develop a standardized reporting system to describe the degree of certainty for the presence of a CVF at a particular nerve root level on CTM. This was accomplished by comparing a proposed imaging feature-based scoring system, the Duke CVF Confidence Score (DCCS), to the performance of subjective interpretation by expert readers.

Materials & Methods

This retrospective reader agreement study was derived from a cohort that included ICHD-3 confirmed SIH patients who underwent CTM to detect a CSF leak from 10/02/2017-03/15/2024 at Duke University.[2] Exclusion criteria were incomplete or nondiagnostic CTMs, CSF leak subtype other than CVF, and prior Onyx embolization. A balanced set of cases representative of varying degrees of CVF certainty was established via a review of radiology reports and imaging by a board-certified neuroradiologist with 11 years of experience interpreting myelography in SIH patients (25 each: definitive, high probability, low probability, negative).

Five board-certified radiologists with 6-18 years of experience interpreting myelograms in SIH patients independently reviewed cases and determined their subjective confidence regarding the presence of a CVF, then applied the DCCS (Figure). Readers were blinded to clinical data and patient information. Inter-reader agreement for each scoring method was calculated using model-based Nelson and Edwards' kappa statistics, adjusting for reader and scan variability. Fleiss' kappas were calculated for each scoring method as a sensitivity analysis. Since distinguishing between definitive and non-definitive CVFs is critical for consideration of therapeutic interventions including surgery and TVE, a separate analysis comparing the frequencies of definitive CVFs using both scoring methods was performed.

Results

In total, 100 individual nerve root levels were assessed for the presence of a CVF in 59 patients (mean age 57.7 +- 12.5 years, 59.3% female). Inter-reader agreement was (κ=0.431; 95% CI: [0.354, 0.507]) for subjective scoring and (κ=0.406; 95% CI: [0.348, 0.463]) for the DCCS, both moderate and with overlapping confidence intervals.

For the overall dataset comprising 25 definitive CVFs based on expert assessment, the frequency of a definitive score using subjective scoring ranged from 25-46% compared to 19-28% using the DCCS.

Conclusion

This study reports a novel scoring system, the DCCS, to describe reader confidence in CVF presence on CTM at a nerve root level. The DCCS resulted in agreement similar to subjective interpretation by expert readers and more closely approximated the frequency of definitive CVFs, as established by an expert radiologist interpretation. The DCCS will standardize CVF categorization and facilitate clearer communication with patients and physicians, aiding treatment decision-making.

References

1. Kranz PG, Gray L, Malinzak MD, et al. CSF-Venous Fistulas: Anatomy and Diagnostic Imaging. *AJR Am J Roentgenol* 2021;217(6):1418-1429. doi:10.2214/AJR.21.26182

2. Headache Classification Committee of the International Headache S. The International Classification of Headache Disorders, 3rd edition (beta version). *Cephalalgia* 2013;33:629-808

Images/Tables

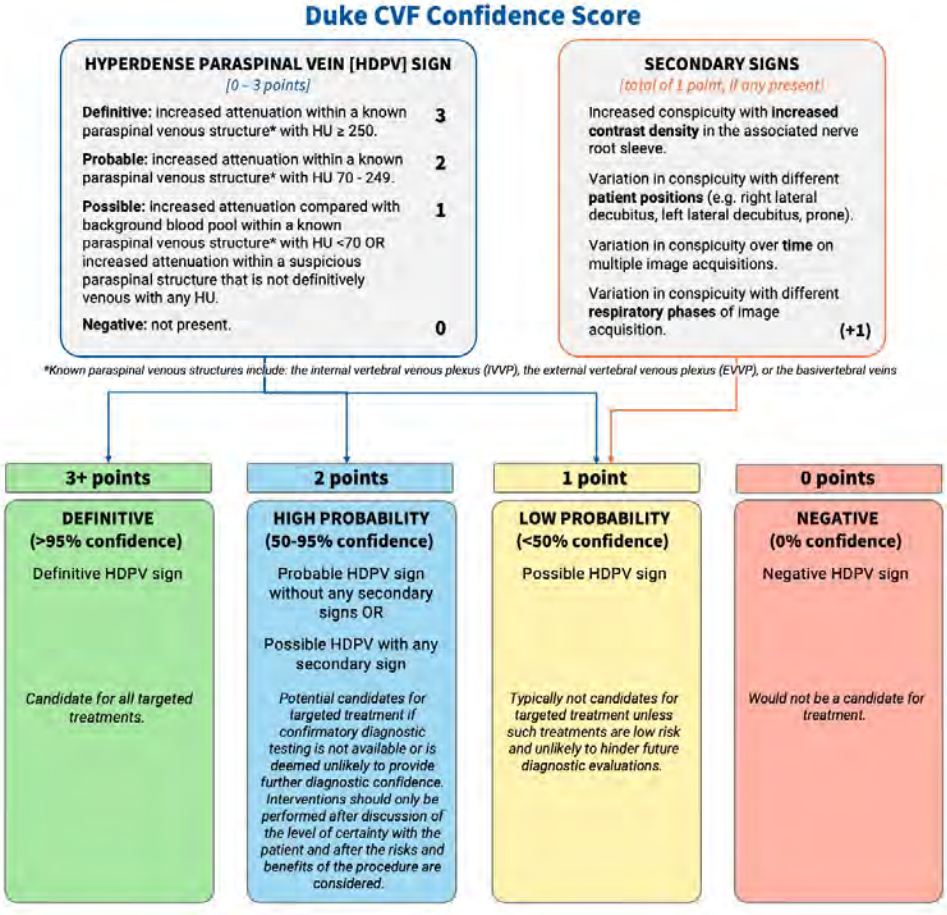

270

Contrast Adds Little Diagnostic Value to Brain MRI for Evaluation of Headaches

Emil J Barkovich MD, William A Mehan Jr. MD, MBA, Karen Buch MD

Massachusetts General Hospital, Boston, MA, USA

Abstract Category

Adult Brain

Purpose

To evaluate the yield of contrast-enhanced brain MRI relative to non-contrast imaging for the outpatient evaluation of headache in adults.

Materials & Methods

In this IRB-approved retrospective study, we reviewed 1448 consecutive brain MRIs performed with and without contrast for headache between 2018 and 2024. Emergency department, inpatient and pediatric cases were excluded. Exams were also excluded if history indicated a specific need for contrast: malignancy, immunocompromise or concern for intracranial infection, neurovascular follow-up, trigeminal symptomatology, vessel wall imaging or simultaneous follow-up of non-headache pathology. As well, studies were removed if a prior report recommended follow-up with contrast for any reason. The reports of the 874 remaining exams were reviewed for any impression points potentially related to headache and ultimately placed into eighteen categories (see Table 1). Incidental findings unrelated to headache were also tracked: pituitary lesions <10 mm, extra-axial masses ≤10 mm and extracranial lesions. Subsequently, a subset of 100 high-yield cases were selected for blinded review. Two attending neuroradiologists independently reviewed these images without contrast and, following a three week washout period, with and without contrast.

Results

Of the 874 cases, 17.5% had findings related to headache included in the original report's impression. However, 33% of these were extracranial (mainly sinus and temporomandibular joint disease) and 25% were atypical white matter changes. Only 7.0% of all cases had treatable intracranial findings; more than half of these were idiopathic intracranial hypertension (IIH) spectrum. Only 1.9% of all cases were deemed contrast relevant: intracranial lesions, spontaneous intracranial hypotension (SIH) and cerebral venous sinus thrombosis (CVST). The rate of incidental findings was 3.7%, mostly pituitary incidentalomas and small meningiomas.

Blinded double review showed the number of positive cases (as subjectively determined by the reviewers) was essentially unchanged with contrast, decreasing from 26% to 24.5%. All intra-axial masses and extra-axial lesions causing parenchymal edema were detected without contrast. Equivocal cases of CVST and SIH were questioned more frequently on post-contrast images, but no new consensus diagnoses were reached. Detection-rate of small meningiomas more than doubled, while small pituitary lesions were noted slightly more often. Reporting of IIH spectrum cases was similar without and post contrast.

Conclusion

Post-contrast headache imaging in the absence of specific clinical red-flags has low overall yield with < 2% of our cases demonstrating findings for which contrast adds theoretical value. Blinded non-contrast subset review did not show substantially decreased sensitivity for actionable intracranial pathology, although the low incidence of SIH and CVST limits our ability to comment definitively on these important diagnoses. Furthermore, post-contrast imaging doubles the detection rate of small (≤10 mm) meningiomas. Meanwhile, the time, resource, financial and patient discomfort costs as well as the tiny but nonzero safety risks associated with intravenous access and gadolinium administration are nontrivial. Therefore, we believe that the vast majority of brain MRI for initial headache work-up should be performed without contrast EXCEPT when there is high-concern for CVST, SIH, trigeminal symptomatology, infection/inflammation or malignancy.

References

Expert Panel on Neurological, I., et al., *ACR Appropriateness Criteria(R) Headache: 2022 Update.* J Am Coll Radiol, 2023. 20(5S): p. S70-S93.

Images/Tables

Table 1: Positive Headache Related Findings (ordered by frequency)
Sinus disease with secretions
Nonspecific white matter changes (patient <50 years old)
Nonspecific for idiopathic intracranial hypertension (some findings)
Suggestive of idiopathic intracranial hypertension (many findings)
Temporomandibular joint disease
Extra-axial lesion > 10 mm
Intra-axial lesion (any size)
Old traumatic injury (post concussive/traumatic brain injury)
Intracranial hypotension
Chiari I deformity
Ventriculomegaly without periventricular signal abnormality (possible communicating hydrocephalus)
Dural venous sinus filling defect (thrombus vs other etiologies)
Large arachnoid cyst (causing midline shift)
Hemiplegic migraine (asymmetric venous signal on susceptibility-weighted imaging)
Marked dental disease
Advanced craniocervical degenerative changes
Ventriculomegaly with periventricular signal abnormality (obstructive hydrocephalus)
Subarachnoid hemorrhage

284

Association of Pretreatment Perfusion Imaging Parameters With 90-Day Excellent Functional Outcomes in Anterior Circulation Distal Medium Vessel Occlusion Stroke

Hamza Adel Salim MD[1], Dhairya A. Lakhani MD[2], Janet Mei MD[3], Nathan Z. Hyson MD[3], Vaibhav Vagal MD[3], Gregory W Albers MD[4], Tobias D. Faizy MD[5], Jeremy J. Heit MD PhD[4], Max Wintermark MD[1], Vivek Yedavalli MD[3]
[1]Department of Neuroradiology, MD Anderson Medical Center, Houston, TX, USA. [2]Department of Radiology, West Virginia University, Morgantown, WV, USA. [3]Department of Radiology, Division of Neuroradiology, Johns Hopkins Medical Center, Baltimore, MD, USA. [4]Department of Neuroimaging and Neurointervention, Stanford Medical Center, Palo Alto, CA, USA. [5]Department of Radiology, Neuroendovascular Program, University Medical Center Münster, Münster, Münster, Germany

Abstract Category

Head & Neck

Purpose

Acute ischemic strokes caused by distal medium vessel occlusions (DMVO) represent a significant proportion of all stroke cases, yet the predictors of excellent functional outcomes in these patients remain poorly understood. This study aims to identify pretreatment computed tomography perfusion (CTP) parameters associated with excellent functional outcomes, defined as a modified Rankin Scale (mRS) score of 0-1 at 90 days, in patients with anterior circulation DMVO.

Materials & Methods

We conducted a retrospective multicenter study involving patients with anterior DMVO, from three stroke centers within the Johns Hopkins Medical Enterprise. Baseline demographic, clinical, and imaging data were collected, with CTP parameters analyzed using RAPIDAI software. Univariable and multivariable logistic regression models were used to identify predictors of excellent outcomes. Receiver operating characteristic (ROC) curves were constructed to assess the predictive accuracy of CTP parameters.

Results

Among the 82 patients (median age, 71 years; 57% female), occlusions were located in the M2 segment in 89%, M3 in 8.5%, and A2 in 2.4%. IVT was administered to 37% of patients, and EVT was attempted in 60%. Excellent outcomes at 90 days were achieved in 45% of patients. In univariate analysis, white race (OR, 4.14; 95% CI, 1.66–10.9; P=0.003), higher CBV index (OR per 0.1-unit change, 1.45; 95% CI, 1.08–2.05; P=0.022), and lower relative cerebral blood flow (rCBF < 20%) volumes (OR, 0.91; 95% CI, 0.81–0.98; P=0.038) were significantly associated with excellent outcomes. In multivariate analysis adjusting for age, sex, race, IVT administration, EVT attempted, dyslipidemia, and premorbid mRS, higher CBV index remained a significant independent predictor (OR per 0.1-unit change, 1.72; 95% CI, 1.14–2.81;

P=0.017), and lower rCBF < 20% volume was associated with better outcomes (OR, 0.91; 95% CI, 0.80–0.98; P=0.05). The multivariate model demonstrated good predictive performance (area under the ROC curve, 80%; 95% CI, 70%–90%; P < 0.001).

Conclusion

In patients with anterior circulation DMVO, a higher CBV index on pretreatment CTP is an independent predictor of excellent functional outcomes at 90 days. These findings suggest that CTP parameters, particularly the CBV index, may be useful in prognostic assessment for this stroke population. Further studies are needed to validate these results and optimize therapeutic approaches.

References

Aslan A, Abuzahra S, Adeeb N, et al. The feasibility of mechanical thrombectomy versus medical management for acute stroke with a large ischemic territory. J NeuroInterventional Surg. Published online March 12, 2024. doi:10.1136/jnis-2023-021368

Salim HA, Yedavalli V, Musmar B, et al. Endovascular therapy versus best medical management in distal medium middle cerebral artery acute ischaemic stroke: a multinational multicentre propensity score-matched study. J Neurol Neurosurg Psychiatry. Published online July 23, 2024. doi:10.1136/jnnp-2024-333669

Images/Tables

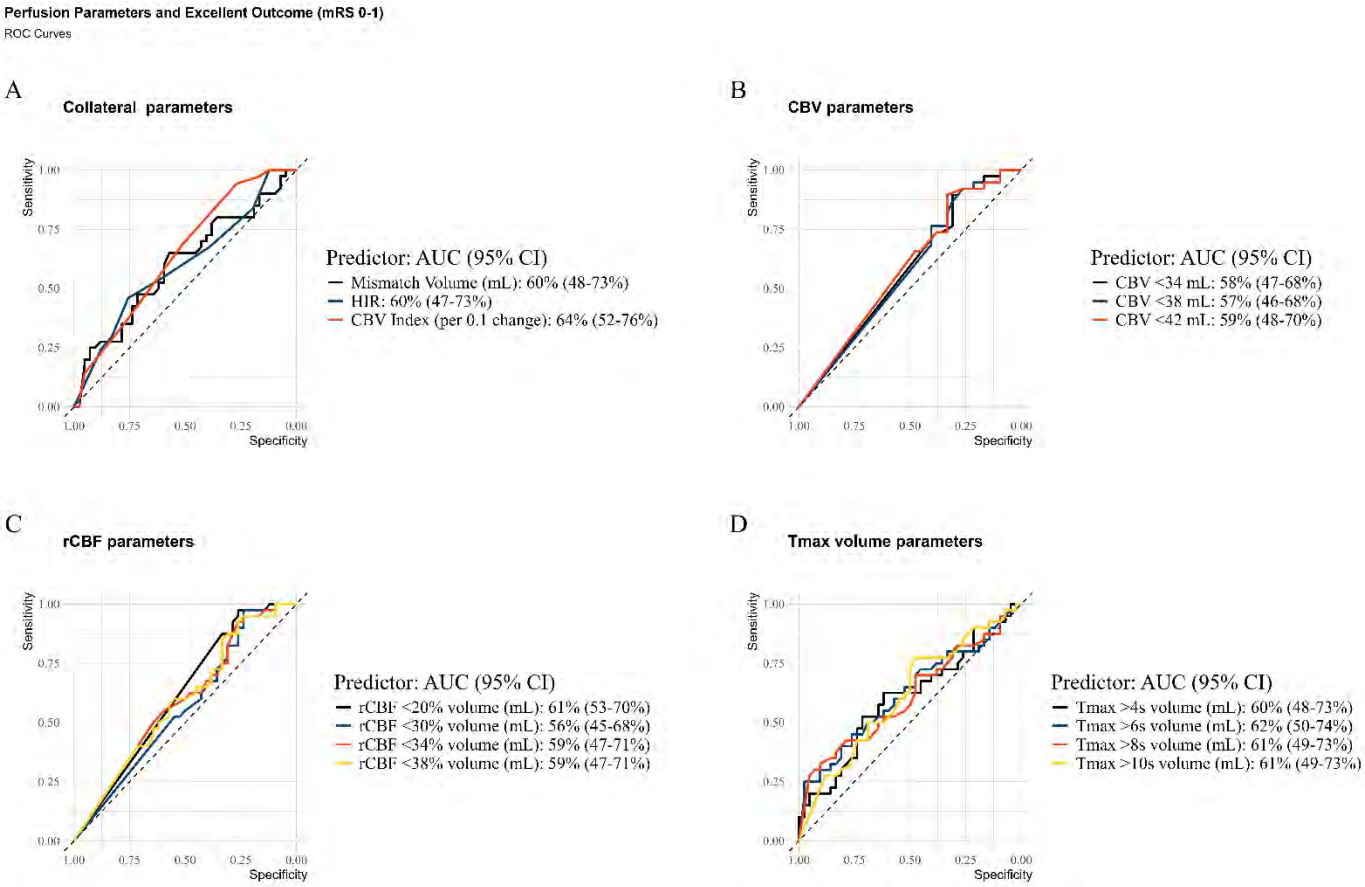

299

Systematic Review of the Adverse Events in Patients with Cochlear Implants Following MRI

Lauren E Mak MD, PhD, Pejman J Maralani MD, FRCPC
University of Toronto, Toronto, Ontario, Canada

Abstract Category

Head & Neck

Purpose

The use of cochlear implants (CIs) has increased on an exponential scale and is estimated to grow at a compounded annual rate of 8.62% between 2022 and 2027. Further, the use of concomitant MRIs in these patients has also increased. It is the imaging modality of choice in many conditions associated with the need for CIs and there is a rise in the utility of MRIs in general. There have been safety implications that have been realized over the years due to the interaction of the main magnetic field and the CI's magnet. The purpose of this review is to assess the safety of MRIs in patients with CIs.

Materials & Methods

Relevant studies were searched systematically up to March 2024. Studies were identified through EMBASE, MEDLINE, Ovid Healthstar, AMED and the grey literature. Reference lists from the identified articles and relevant reviews were searched for articles that did not appear in the above databases and two studies were subsequently added. Search terms were cochlear implant, MRI, safety, adverse, malfunction, discomfort, compatibility, heat and stimulation. Limits were set to include human subjects, the English language and full text availability. After duplicated were removed, a total of 642 titles were identified. Two reviewers (L.E.M. and P.J.M.) used predetermined inclusion and exclusion criteria and determined that 14 studies were eligible to be included in the final analysis

Results

657 separate ears with CIs underwent 808 separate MRI scans. 1.5T scanners were exclusively used in 6/14 studies, the remainder included magnets from 1T to 3T. A total of 163 adverse events were reported, which equates to a prevalence of 20%. The most common adverse event reported was pain, with this accounting for 52% of the adverse events (85/163). Displacement or dislodgement accounted for 21% of the adverse events (35/163). Polarity reversal accounted for 2% of the adverse events (3/163). The remainder of the adverse events were more difficult to delineate a true correlation between the CI and MRI, for example anxiety, the sensation of vertigo and sweating. Only one study separated their adverse outcomes between the traditional axial magnet versus the newer diametric magnet, which showed that adverse effects only impacted the traditional axial magnets.

Conclusion

The use of CIs and the number of patients receiving this technology is increasing. Furthermore, more patients are aging with their CIs. Both populations are increasingly receiving MRIs. It has been well documented through multiple case reports and studies that show patients with CIs who undergo MRIs are at risk for adverse effects. However, the definition and severity of adverse event is broad. From our work, the most common adverse event experienced was pain. Promising evidence is emerging that since the advent of the diametric magnets, studies are showing that they are not associated with adverse events. It is even more promising since many of the studies did not employ measures such as head wrapping. However, future studies should aim to explicitly investigate if there is an association between adverse events and the type of magnet.

References

1. Young NM, Hoff SR, Ryan M. Impact of Cochlear Implant With Diametric Magnet on Imaging Access, Safety, and Clinical Care. *Laryngoscope* 2021;131.
2. Orgeta V, Mukadam N, Sommerlad A, et al. The Lancet Commission on Dementia Prevention, Intervention, and Care: A call for action. *Ir J Psychol Med* 2019;36.
3. Srinivasan R, So CW, Amin N, et al. A review of the safety of MRI in cochlear implant patients with retained magnets. *Clin Radiol* 2019;74.
4. Svirsky MA, Teoh SW, Neuburger H. Development of language and speech perception in congenitally, profoundly deaf children as a function of age at cochlear implantation. In: *Audiology and Neuro-Otology*.Vol 9.; 2004.
5. Carlson ML, Neff BA, Link MJ, et al. Magnetic Resonance Imaging With Cochlear Implant Magnet in Place: Safety and Imaging Quality. *Otology and Neurotology* 2015;36.

Images/Tables

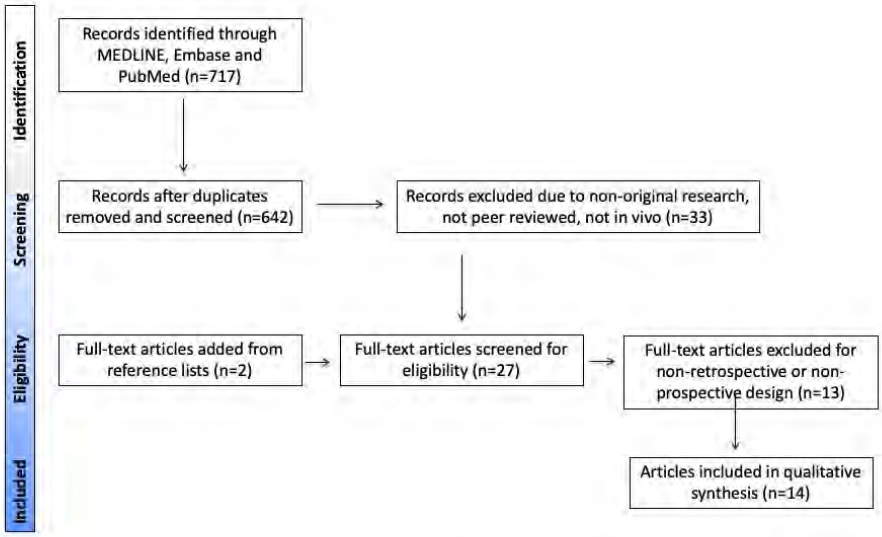

Figure 1 PRISMA flowchart depicting selection of included studies in final analysis

302

Multimodal Approach for Descending Trigeminal Nerve Tractography

Maria Burritt St. Angelo BS, Andrew Ghannad BS, Dayna Sloane BS, Rachyl Shanker MD, Kerry Steed MD, Luke Rosenblum BS, Mohammad Alhusseini PhD, Anand Germanwala MD, Douglas Anderson MD, Atul Mallik MD PhD
Loyola University Medical Center, Chicago, IL, USA

Abstract Category

Functional/Advanced Imaging

Purpose

Type 1 trigeminal neuralgia (TN) is characterized by severe, lancinating facial pain associated with the trigeminal nerve. Our institution has implemented a novel procedure, the microsurgical descending pontine tractotomy, in which nociceptive fibers of the descending trigeminal spinal tract can be lesioned for a subset of patients who are not responsive to current TN treatment options. Due to the dense nature of the brainstem, confident localization of the descending tract of the trigeminal nerve is essential for successful and extensive implementation of this procedure across care facilities.

Although standard magnetic resonance imaging (MRI) sequences allow clear and detailed monitoring of anatomical structures, they fall short in describing functional pathways throughout the cortex. Diffusion tensor imaging (DTI) can be useful for creating enhanced visualizations of neural networks through tractography, providing neurosurgeons the ability to trace patient-specific pathways and explore long-range connections across white matter regions. The potential for DTI tractography to reinforce neurosurgical preoperative planning is strengthened by the application of constrained spherical deconvolution (CSD). CSD enhances DTI by modeling fiber orientation probabilities in each voxel, which are then integrated into cross cortical pathways.

Additional white matter nulling can be performed with Fast Gray Matter Acquisition T1 Inversion Recovery (FGATIR) sequencing. The current clinical use of FGATIR is unable to identify the descending tract of the trigeminal nerve alone, but FGATIR's structural focus resolves distortion commonly found in DTI and provides additional information to accurately localize tracts in conjunction with MR and DT imaging. A multimodal approach has potential to provide neurosurgeons with a powerful, patient-specific map for preoperative planning. This review aims to analyze advancements in white matter modeling and explore the use of tracts as a preoperative tool, particularly for microsurgical descending pontine tractotomy.

Materials & Methods

High resolution 3D heavily T2-weighted, DTI, and FGATIR sequences were acquired for patients presenting with severe trigeminal neuralgia. These images were imported to the Medtronic StealthStation™ Surgical Navigation System where the descending tract of trigeminal nerve was localized and visualized using standard DTI-based and enhanced CSD tractography. The tracts were then reviewed by an experienced radiologist and neurosurgeon for resolution quality and confidence in proper tract localization.

Results

This investigation found that probalistic CSD tractography compared to deterministic DTI tractography improves resolution of crossing fibers and provides a more complete anatomical context. Our findings additionally highlight that enhanced CSD prevails over standard DTI in preparation of tracts comprised of limited individual fibers, specifically the trigeminal nerve.

Attempting to delineate the descending tract of the trigeminal nerve for surgical planning, we found a multimodal, FGATIR assisted approach to prepare superior CSD-based tracts when accurately co-registered across MR and DT imaging. Off-target co-registration substantially reduced confidence in tract localization due to improperly identified regions of interest (ROIs). Accurate superimposing of functional and anatomical imaging is imperative for assured descending tract localization.

Conclusion

Modeling white matter with spherical deconvolution provides potential for a new gold standard. Our utilization of multimodal CSD-based tractography for presurgical planning strongly suggests promise for increased surgical confidence in localization of the descending trigeminal spinal tract.

References

1. Basser PJ, Mattiello J, LeBihan D. MR diffusion tensor spectroscopy and imaging. Biophys J. Jan 1994;66(1):259-67. doi:10.1016/S0006-3495(94)80775-1

2. Behrens TE, Berg HJ, Jbabdi S, Rushworth MF, Woolrich MW. Probabilistic diffusion tractography with multiple fibre orientations: What can we gain? Neuroimage. Jan 01 2007;34(1):144-55. doi:10.1016/j.neuroimage.2006.09.018

3. Delettre C, Messé A, Dell LA, et al. Comparison between diffusion MRI tractography and histological tract-tracing of cortico-cortical structural connectivity in the ferret brain. Netw Neurosci. 2019;3(4):1038-1050. doi:10.1162/netn_a_00098

4. Dell'Acqua F, Tournier JD. Modelling white matter with spherical deconvolution: How and why? NMR in Biomedicine. 2019;32(4):e3945. doi:10.1002/nbm.3945

Images/Tables

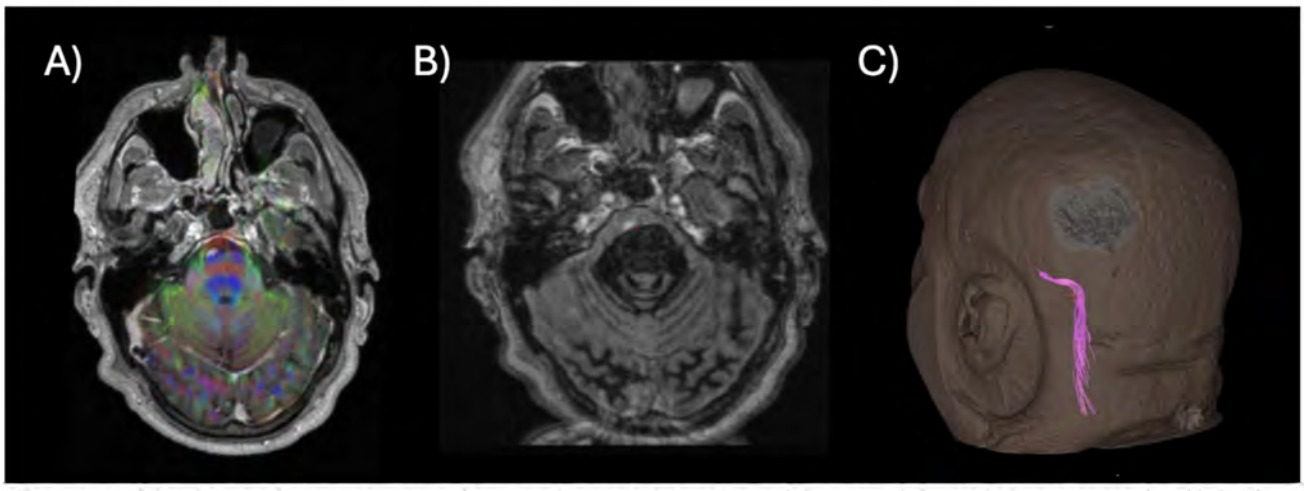

Figure 1. Single patient sequencing and tractography with a multimodal approach. A) DTI superimposed on high resolution 3D heavily T2-weighted MRI. B) Axial FGATIR sequence. C) Tract of the trigeminal nerve with enhanced CSD tractography. Tract shows accurate discrimination of the descending nerve through the brainstem, highlighting a valuable feature of CSD tractography.

309

Evaluate Effectiveness and Accuracy of Deep Learning for Detecting ICH in a Pediatric Population

Hadiseh Kavandi MD, Kyle Costenbader MD, Peter Kamel MD, Sandrine Yazbek MD, Noushin Yahyavi MD
University of Maryland Medical Center, Baltimore, MD, USA

Abstract Category

Pediatrics

Purpose

Detection of intracranial hemorrhage (ICH) in patients is a critical task in medical imaging, as timely diagnosis can significantly impact patient outcomes. This task increases in complexity and critical need for timely diagnosis in pediatric patients. While deep learning has shown promise in assisting radiologists and clinicians in diagnosis, there is a notable lack of research in regards to pediatric populations. The purpose of this study is to explore the performance of a commercially available ICH AI solution (Aidoc, Tel Aviv), that was trained on adult patient populations, in a pediatric population.

Materials & Methods

This is a single center, retrospective pediatric study. Patients between 6 and 17 years of age that underwent a non-contrast head CT between January 2017 and November 2022 were included. Both the radiological reports (unaided by AI) and CT images were collected and were analyzed by a natural language processing (NLP) algorithm and an image based algorithm (AI) to classify for the presence or absence of ICH. Ground truth was assumed for all concordant cases. An independent review by 3 radiologists was employed to adjudicate discrepant cases using majority voting.

Results

A total of 2,502 pediatric patients that underwent non-contrast head CT were included. The ICH prevalence was 6% (150/2,502). The AI algorithm flagged 292 cases as suspected positive for ICH. A total of 174 discordant cases between the NLP and AI were independently reviewed to create the reference standard. A total of 144 true positives, 6 false negatives, 148 false positives and 2,204 true negatives were observed. This resulted in a sensitivity of 96.0% (91.5%-98.5%) and a specificity of 93.7% (92.6%-94.7%). The overall algorithm accuracy was 93.8% (92.8%-94.8%).

Conclusion

This study demonstrates that a deep learning AI algorithm, initially trained on adults, is also effective in detecting intracranial hemorrhage in children. With a sensitivity of 96.0% and specificity of 93.7%, the algorithm shows robust diagnostic capabilities, suggesting its usefulness in supporting pediatric radiology. The low rates of false positives and negatives underscore its clinical reliability. These results support further development and testing of AI in pediatric imaging to improve diagnostic accuracy and patient outcomes.

Pediatric populations are notably underserved in the application of AI, often due to the scarcity of tools and specific training datasets. This study addresses a critical gap by evaluating the generalizability of an AI algorithm, trained on adult data, in pediatric settings.

References

Zia A, Fletcher C, Bigwood S, Ratnakanthan P, Seah J, Lee R, Kavnoudias H, Law M. Retrospective analysis and prospective validation of an AI-based software for intracranial hemorrhage detection at a high-volume trauma center. *Sci Rep* 2022;12:19885.

322

Analyzing Trends in Neuroradiology Trainee Discrepancies using Large Language Models

Shawn Lyo MD, Satvik Tripathi, Colbey Freeman MD, Alvand Hassankhani MD, Suyash Mohan MD, Yu Sakai MD, James E Schmitt MD PhD, Mary Scanlon MD, Robert Kurtz MD, Tessa Cook MD PhD
University of Pennsylvania, Philadelphia, PA, USA

Abstract Category

AI/Informatics

Purpose

To identify trends in neuroradiology trainee performance by analyzing discrepancies between trainees' preliminary and attendings' finalized reports using large language models (LLMs). To assess whether systematic analysis of these

discrepancies with LLMs can enable the identification of patterns across training levels over time, facilitating future development of data-driven, targeted curriculum development to address specific knowledge gaps and ultimately enhance clinical performance and patient care.

Materials & Methods

We conducted a retrospective analysis of 36,421 pairs of preliminary and finalized on-call neuroradiology reports by trainees from 07/01/2023-07/01/2024. The dataset included only reports dictated by residents and neuroradiology fellows, finalized by neuroradiology attendings. Each finalized report contained attending feedback on discrepancy level (agree, agree with additions, minor change, or major change).

A multi-stage analysis pipeline was developed using the Azure OpenAI GPT-4-32K API, selected for its extensive context window and institutional availability. The pipeline identified and classified discrepancies between preliminary and final reports, using prompting strategies adapted from prior studies[1]. After preprocessing, validation, and anonymization, discrepancies were analyzed with an ensemble prompting approach incorporating in-context learning, chain of thought, tree of thought, and universal self-consistency methods.

Using the LLM, discrepancies were systematically classified by
severity, with additional with classifications ongoing Additional analyses examining trends across training levels, examination types, report timing, and other factors are concurrently performed.

Results

Of the 36,421 reports, the largest proportion was dictated by neuroradiology fellows (n=16,692, 45.8%) followed by R2 residents (n=5,867, 16.1%). A total of 199 on-call reports were identified by institutional macros as containing major changes. Fellows had the lowest major change rate (0.41%), while R2 residents had the highest (1.09%). Neuroradiology fellows interpreted 5,498 MRIs on call (32.94%), with a higher major change rate for MRI (0.56%) than for CT (0.26%). LLM analysis of the 199 major-change reports showed complete concordance between the LLM's maximal discrepancy severity classification and that of attending neuroradiologists (Figure 2 demonstrates an example of the severity analysis). Additional analyses of other report characteristics and expansion to other report types are ongoing.

Conclusion

Our study demonstrates the feasibility of using LLMs to identify and assess discrepancies in neuroradiology reports dictated on call. We developed a pipeline to apply LLM-based analysis to data transactions from our reporting software and achieved high concordance between the LLM's classification of discrepancy severity and that of attending neuroradiologists within our preliminary results. Pairing LLM-generated insights with report metadata offers a deeper understanding of factors influencing trainee performance and enables future targeted educational interventions. The deployment of these interventions is currently underway.

The LLM's consistent classification of discrepancies by severity and topic provides a scalable, automated method for monitoring trainee progress. The LLM-driven analysis offers insights into specific educational needs and facilitates the development of dynamically adaptive, data-driven curricula. We are currently expanding the analysis to include a greater breadth of reports and assessing the potential impact of interventions based on these insights.

References

Lyo S, Mohan S, Hassankhani A, et al. From Revisions to Insights: Converting Radiology Report Revisions into Actionable Educational Feedback Using Generative AI Models. Journal of Imaging Informatics in Medicine 2024. [Epub ahead of print].

Bala W, Li H, Moon J, et al. Enhancing Radiology Training with GPT-4: Pilot Analysis of Automated Feedback in Trainee Preliminary Reports. Current Problems in Diagnostic Radiology 2024. [Epub ahead of print].

Masur J, Schmitt J, Lalevic D, et al. Am I Ready to Be an Independent Neuroradiologist? Objective Trends in Neuroradiology Fellows' Performance during the Fellowship Year. American Journal of Neuroradiology 2021;42:815–23.

Wildenberg JC, Chen P-H, Scanlon MH, et al. Attending radiologist variability and its effect on radiology resident discrepancy rates. Academic Radiology 2017;24:694–9.

Images/Tables

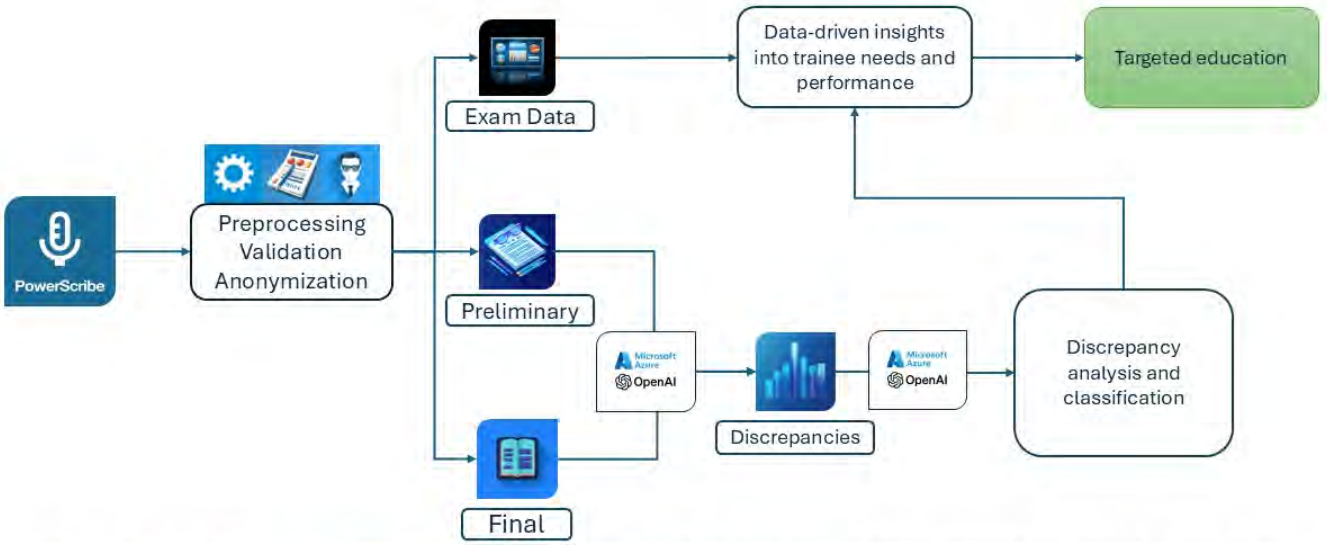

Figure 1. Diagram for Discrepancy Analysis Pipeline. Transaction data from the dictation software is preprocessed, validated and anonymized to extract exam data, trainee preliminary and attending finalized reports. An LLM then identifies discrepancies between the preliminary and finalized report. The discrepancies are used for further analysis and classification (severity, pathology, anatomy, etc.). The geerated analyses can then be used for multiple purposes including targeted education.

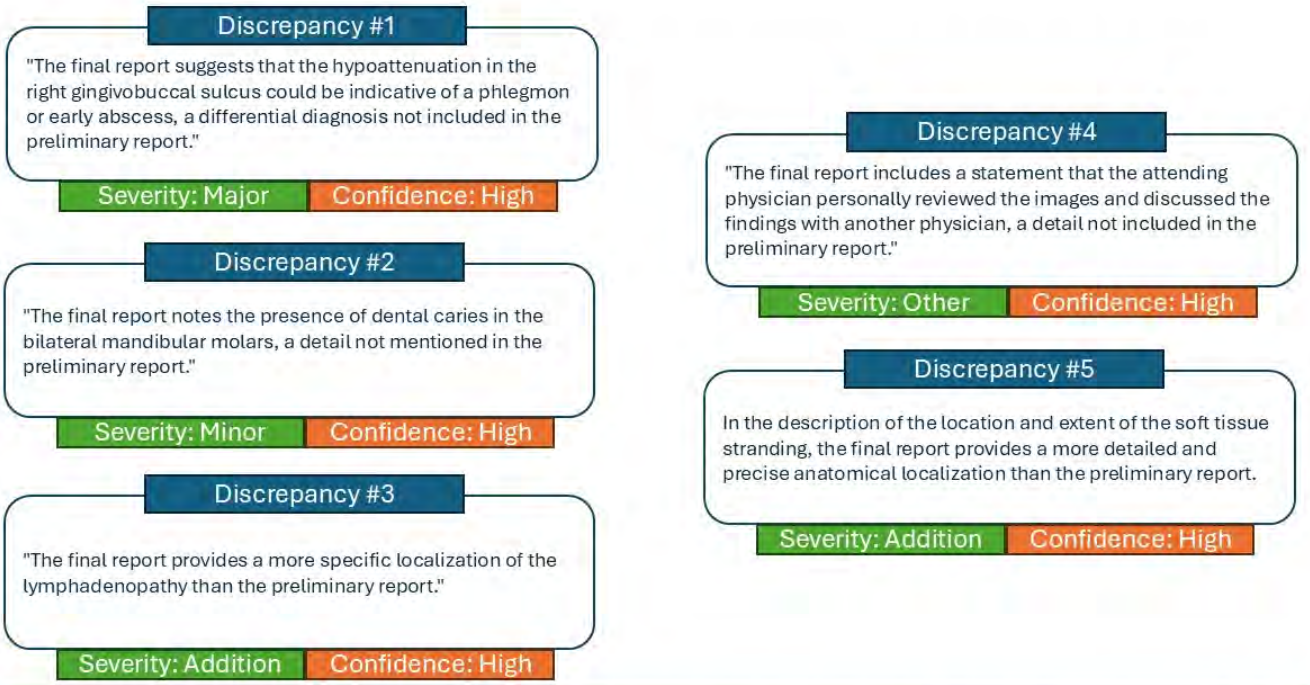

Figure 2. Example of Discrepancy Severity Assessment from One Report. The LLM analyzes discrepancies identified between the preliminary and final report and performs an ensemble consensus analysis to determine the severity of each discrepancy. The LLM identifies the discrepancy, severity and the confidence of its assessment.

348

Photon-counting CT assessment of carotid plaques: Preliminary observations from a prospective case series

Yu Sakai MD[1], Martin Rybertt[1], Courteney Wiredu[1], Pargol Balali MD[1], Marisa Sanchez[1], Taylor Panczner[1], Michael Colfer[1], Jean M White[1], John H Woo MD[1], Brett Cucchiara MD[1], Scott E Kasner MD[1], Luca Saba MD[2], Peter B Noël PhD[1], Jae W Song MD MS[1]

[1]University of Pennsylvania, Philadelphia, PA, USA. [2]Università di Cagliari, Cagliari, Sardinia, Italy

Abstract Category

Adult Brain

Purpose

Photon-counting CT (PCCT) offers improved spatial resolution over conventional CT. Intraplaque hemorrhage (IPH) is a high-risk noncalcified plaque component. The primary aim of this proof-of-concept study is to evaluate IPH in carotid plaques using PCCT; literature suggests plaques with <25 HU contain IPH [1]. From initial cases, we also examine PCCT's potential in evaluating carotid stenosis and plaque calcification morphology.

Materials & Methods

This is an ongoing single-center prospective study using multi-phase PCCT to analyze carotid plaques. Included patients were adults admitted with stroke/TIA who had conventional CTA neck showing non-calcified carotid bifurcation plaque > 3mm.

Conventional CTA was performed as per institutional standards (0.75 mm and 5 mm slices, soft tissue kernel). PCCTA images were acquired with a research protocol on the NAEOTOM Alpha scanner (Siemens Healthineers) and reconstructed in 0.2 mm slices with soft tissue and bone kernels. Radiologists performed quantitative assessments, including noncalcified plaque attenuation in Hounsfield units (HU) and carotid stenosis grading by NASCET criteria. Windowing impact was evaluated using preset vascular (center: 108, width: 877) and bone (center: 570, width: 3077) window settings in PACS. Qualitative assessments included conspicuity of calcifications and visualization of plaque morphology and ulcerations.

Results

Four patients (two female, mean age 78) underwent prospective research PCCTA.

Patient 1: The patient had right carotid artery complex plaque. There was hypoattenuating area measuring >25 HU on conventional CTA and PCCT soft tissue kernel but <25 HU on PCCT bone kernel, suggesting the presence of IPH (**Figure 1A**). A semi-automated segmentation software (Elucid) confirmed IPH in this plaque. Calcifications and ulcerations were more conspicuous on PCCTA (**Figure 1B**, bottom row).

Patient 2: Conventional CTA showed 55% right carotid stenosis, while PCCTA (bone kernel, bone window) showed 35%. Area of noncalcified plaque measured 106 HU on conventional CTA and 43 HU on PCCTA. Calcification morphology was most conspicuous on PCCT bone kernel (**Figure 1B,** top row).

Patient 3: Conventional CTA indicated 74% right carotid stenosis, suggesting endarterectomy candidacy, but PCTTA (bone kernel, bone window) showed 48% stenosis. Difference in stenosis measurement due to imaging settings for the same patient are shown on **Figure 1C**. Digital subtraction angiography (DSA) confirmed <50% stenosis. Patient had left non-stenotic noncalcified plaque measuring 80 HU on conventional CTA and 43 HU on PCCTA. Calcification morphology was most conspicuous on PCCT bone kernel.

Patient 4: The patient had thick concentric calcified left plaque resulting in severe blooming artifacts. On conventional CTA, the lumen was not visible with vascular window (100% stenosis), and bone window showed 55% stenosis. However, PCCTA at 0.2 mm, in both soft tissue and bone kernels with bone window, showed 43% stenosis. Noncalcified area measured 148 HU on conventional CTA and 99 HU on PCCTA. Calcification morphology was most conspicuous on PCCT bone kernel.

Conclusion

Initial observations from an ongoing prospective PCCT study to evaluate carotid plaques suggests PCCT's potential in improving the evaluation of IPH, carotid plaque stenosis, and calcifications.

References

1. Saba, L., et al., *CT Attenuation Analysis of Carotid Intraplaque Hemorrhage.* AJNR Am J Neuroradiol, 2018. 39(1): p. 131-137.

Images/Tables

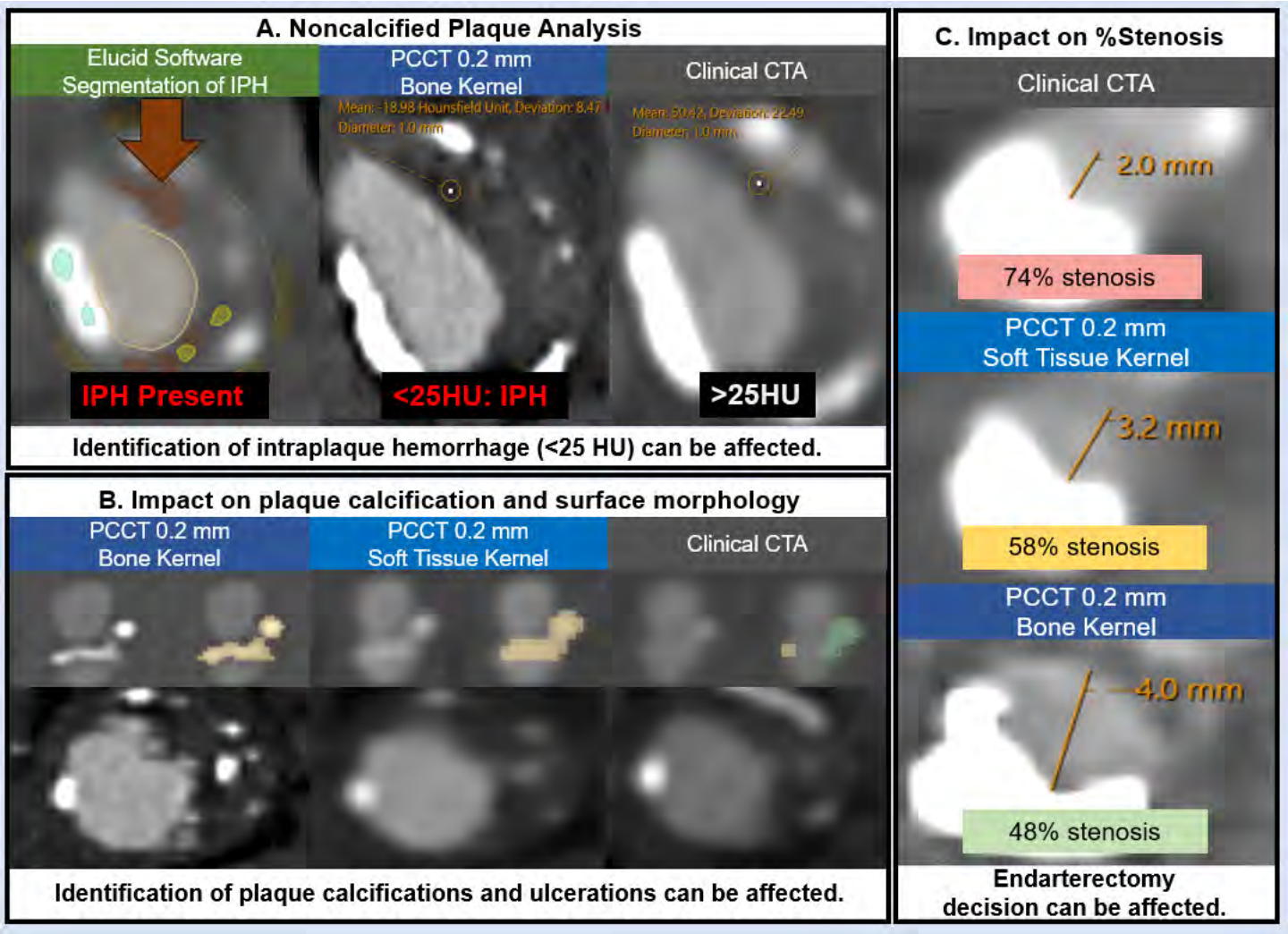

350

Innovative Educational Program to Aid Clinical Vessel Wall MR Imaging Interpretation Among Neuroradiologists at An Academic Medical Center

Jae W Song MD, MS, Sriharsha Voleti MD, Lori Huang BS, Ronald L Wolf MD, PhD, Alvand Hassankhani MD, John H Woo MD, Robert M Kurtz MD, Jeffrey B Ware MD, Colbey Freeman MD, Suehyb G Alkhatib MD, Laurie A Loevner MD
University of Pennsylvania, Philadelphia, PA, USA

Abstract Category

Adult Brain

Purpose

Barriers to the clinical implementation of vessel wall MR imaging (VWI) identified by the ASNR Vessel Wall MR Imaging Study Group included insufficient knowledge among radiologists regarding its applications and limited image interpretation expertise. To address these challenges, we implemented a multifaceted program aimed at educating a large sub-specialized Neuroradiology Division by creating a focused VWI-expert super-user group to support the Division and measured the impact through a structured survey.

Materials & Methods

\Implementation tools included interactive case-based lectures and the development of an accessible online resource featuring guides on the application/indications and image interpretation of VWI. Additionally, 7 neuroradiology faculty (Super-users) with interest and expertise in advanced cerebrovascular imaging were identified. The Super-users' roles included facilitating case discussions and providing daily needs, coverage and support for the Division. To measure the effectiveness of the intervention, a survey on the self-perceived confidence for (a) evaluating VWI exam appropriateness/indications, (b) checking image quality for MR technologists, and (c) image interpretations for VWI

Brain, Neck, and Scalp (giant cell arteritis) exams was distributed at the start of the implementation in July 2023 and August 2024. The survey instrument measured scores on a sliding scale [0% (not confident) to 100% (confident)]. Student's t-test was used to compare scores.

Results

Survey response rates were 61% (2023-Divison), 52% (2024-Division), and 100% (2024, Super-users). Mean scores for evaluating appropriateness/indications, image quality, and diagnostic interpretations for all VWI exam types increased over 12-months (**Figure**). Mean scores among the Super-users increased significantly for all VWI exam types in all domains (VWI Brain: appropriateness, 36.4 vs 77.1, p=0.0005), image quality, 49.5 vs 86.0, p=0.007; interpretation, 54.6 vs 80.7, p=0.005), VWI Neck: appropriateness, 37.7 vs 75.7, p=0.002; image quality, 52.6 vs 81.3, p=0.0.01; interpretation, 50.6 vs 79.3, p=0.006; VWI Scalp: appropriateness, 46.7 vs 84.3, p=0.006; image quality, 44.5 vs 83.6, p=0.004; interpretation, 46.7 vs 86.4, p=0.0004). Within the entire Division, mean scores trended upwards after 12-months with a significant increase for assessing appropriateness/indications for VWI Brain exams (36.4 vs 56.4, p=0.04).

Conclusion

The implementation strategy yielded increases in mean scores across all evaluated domains, suggesting an overall enhancement in neuroradiologists' confidence levels when assessing case appropriateness, evaluating image quality, and formulating diagnostic interpretations. The observed upward trends underscore the benefits of a dedicated Super-user group for Divisional support, as well as a positive impact of our targeted educational initiatives within a large subspecialized academic neuroradiology setting.

References

Mossa-Basha M, Zhu C, Yuan C, et al. Survey of the American Society of Neuroradiology Membership on the Use and Value of Intracranial Vessel Wall MRI. *AJNR Am J Neuroradiol.* 2022;43(6). doi:10.3174/ajnr.A7541

Song JW, Frame MY, Sellers RT, et al. Implementation of a Clinical Vessel Wall MR Imaging Program at an Academic Medical Center. *AJNR Am J Neuroradiol.* 2024;45(5):554-561. doi:10.3174/ajnr.A8191

Images/Tables

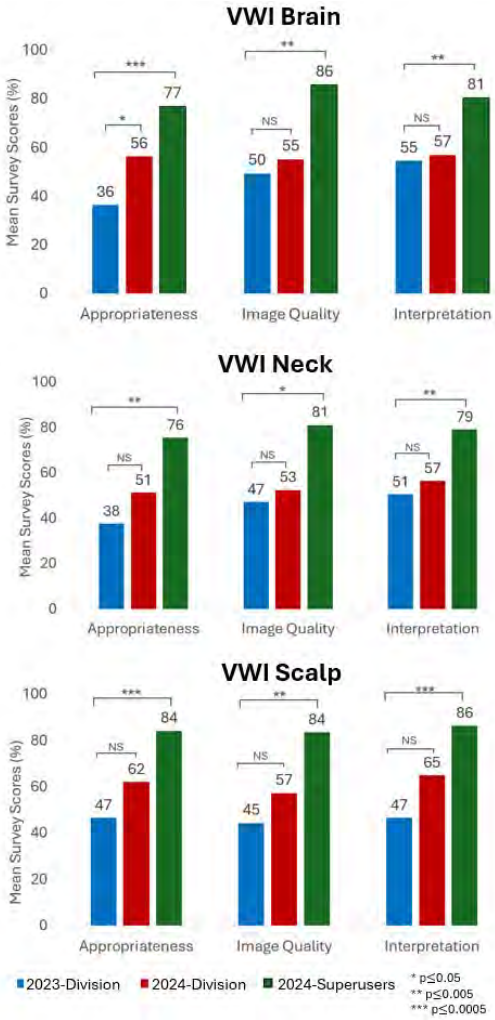

352

FeTS 2.0 Initiative: Federated Learning for Postoperative Segmentation of Treated Glioblastoma

Dominic LaBella[1], Alejandro Aristizabal[2], Raymond Huang[3], Hasan Kassem[2], Brandon Edwards[4], Sarthak Pati[5], Ujjwal Baid[6], Micah Sheller[4], Alexandros Karargyris[2], Spyridon Bakas[5], Evan Calabrese[1]

[1]Duke University Medical Center, Durham, NC, USA. [2]MLCommons, Beaverton, OR, USA. [3]Brigham and Women's Hospital, Boston, MA, USA. [4]Intel Corporation, Santa Clara, CA, USA. [5]Indiana University, Indianapolis, IN, USA. [6]Emory University, Atlanta, GA, USA

Abstract Category

Adult Brain

Purpose

The Federated Tumor Segmentation 2.0 (FeTS) initiative, also known as Federated Learning for Postoperative Segmentation of Treated Glioblastoma (FL-PoST), aims to develop an AI-driven platform for assessing postoperative glioblastoma treatment outcomes, and extends the pioneering efforts of the FeTS 1.0 initiative on preoperative Glioblastoma automated segmentation. In partnership with the Response Assessment in Neuro-Oncology (RANO) group, the study leverages federated learning to enable secure, decentralized AI model training across institutions, thereby improving postoperative glioblastoma segmentation without compromising patient privacy. This work addresses the critical need for standardized, volumetric tumor assessments to improve clinical response evaluations in postoperative glioblastoma.

Materials & Methods

FeTS 2.0 leverages a federated learning infrastructure that allows collaborating institutions to process data locally while sharing only model weight updates, thus preserving patient privacy. Data preparation follows a standardized protocol using the FeTS tools, GaNDLF, and MedPerf. MedPerf is used as a federated orchestrator, and it ensures data consistency and quality across institutions and enables smooth execution of the training and evaluation steps. Participating institutions collect private brain MRI data from postoperative glioblastoma cases, temporally ranging from the immediate postoperative setting to long term longitudinal follow-ups. The FeTS software preprocesses brain MRI by performing skull-stripping and coregistration of T1, T1Gd, T2, and FLAIR MRI to the SRI24 atlas space, presegments tumor regions using a nnUnet based presegmentation model, and incorporates manual annotation review and correction through a 4-compartment labeling system: necrotic core, edema, enhancing tumor core, and resection cavity. The federated learning training sessions run on MedPerf and OpenFL tools, using a server-based model that integrates updates from each institution to progressively refine a global consensus model to optimize a multi-compartment dice similarity coefficient (DSC).

Results

As of November 2024, 53 institutions have joined the FeTS 2.0 initiative, with 43 institutions completing data annotations and the others in various stages of data preparation. Results from preliminary federated training of 6033 cases from 26 contributing sites indicate that the FeTS 2.0 model provides improved segmentation accuracy compared to historical benchmarks, with a validation set global aggregated mean DSC of 0.849 after 220 epochs. Historically, Bianconi et al. demonstrated a mean global aggregated DSC of 0.7231 for postoperative glioma. The FeTS 2.0 federated learning model performance is expected to continue to improve as more institutions finalize their data contributions and larger federated training sessions are performed.

Conclusion

The FeTS 2.0 initiative represents a significant advancement in the application of federated learning for postoperative glioblastoma segmentation, establishing a reproducible, privacy-respecting model that integrates diverse institutional expertise. This work demonstrates the feasibility and potential impact of decentralized learning on clinical neuro-oncology, allowing real-world variability to enhance model generalizability. Preliminary federated learning automated segmentation results are the best to date for postoperative glioblastoma. The resulting AI tool supports the radiological assessment process, fostering standardized evaluations across global sites. Future iterations of FeTS 2.0 federated learning aims to incorporate additional data sites to further the generalizability of model deployment.

References

1. Pati, S., Baid, U., Edwards, B., Sheller, M., Wang, S. H., Reina, G. A., ... & Poisson, L. (2022). Federated learning enables big data for rare cancer boundary detection. *Nature communications*, *13*(1), 7346.

2. Wen, P. Y., van den Bent, M., Youssef, G., Cloughesy, T. F., Ellingson, B. M., Weller, M., ... & Chang, S. M. (2023). RANO 2.0: update to the response assessment in neuro-oncology criteria for high-and low-grade gliomas in adults. *Journal of Clinical Oncology*, 41(33), 5187-5199.
3. Pati S, Thakur SP, Hamamcı İE, et al. GaNDLF: the generally nuanced deep learning framework for scalable end-to-end clinical workflows. Commun Eng. 2023;2:23. Published 2023 May 16. doi:10.1038/s44172-023-00066-3
4. Karargyris, A., Umeton, R., Sheller, M. J., Aristizabal, A., George, J., Wuest, A., ... & Mattson, P. (2023). Federated benchmarking of medical artificial intelligence with MedPerf. *Nature machine intelligence*, *5*(7), 799-810.
5. Bianconi, A., Rossi, L. F., Bonada, M., Zeppa, P., Nico, E., De Marco, R., ... & Morra, L. (2023). Deep learning-based algorithm for postoperative glioblastoma MRI segmentation: a promising new tool for tumor burden assessment. *Brain Informatics*, 10(1), 26.

Images/Tables

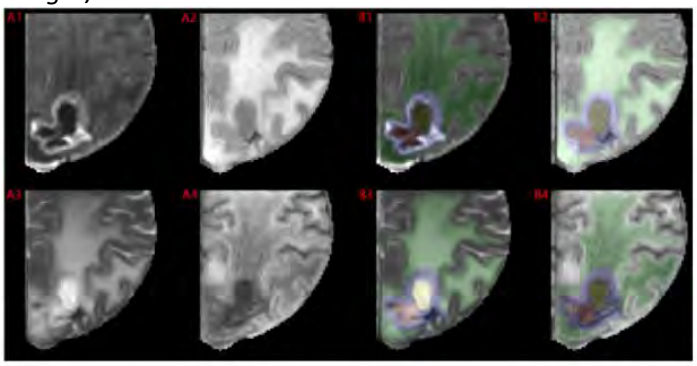

Figure 1:

This is a case from the FeTS 2.0 Example Segmentation Labels reference guide showing T1Gd axial images (A1, B1), FLAIR axial images (A2, B2), T2 axial images (A3, B3), and T1 axial images (A4, B4) showing enhancing tumor (blue), non-enhancing tumor necrosis (red), surrounding non-enhancing FLAIR hyperintensity (green), and post-resection cavity (yellow).

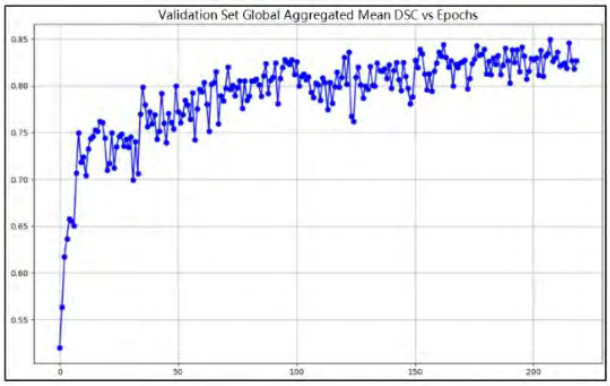

Figure 3:

Line plot of the validation set global aggregated mean DSC over training epochs from FeTS 2.0 preliminary federated training of 6033 cases from 26 contributing sites

Figure 2:

World map with institutions participating in the clinical study that have completed dataset registration on MedPerf. As of August 2024, fifty-one (51) institutions have joined. Map generated using Plotly Express and Google's Places API.

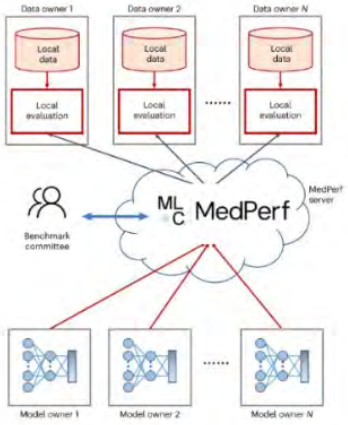

Figure 4:

Federated evaluation on MedPerf. Machine learning models are distributed to data owners for local evaluation on their premises without the need or requirement to move their data to a central location. MedPerf relies on the benchmark committee to define the requirements and assets of federated evaluation for a particular use case

355

Gestational PBDE Serum Concentrations from Flame Retardants and Adolescent Functional Connectivity

KIM M Cecil PhD, Jonathan Dudley PhD, Yingying Xu PhD, Kimberly Yolton PhD
Cincinnati Children's Hospital Medical Center, Cincinnati, OH, USA

Abstract Category

Pediatrics

Purpose

Despite being phased out of production, polybrominated diphenyl ethers (PBDEs) are synthetic flame retardants used in commercial and consumer products that are found in our homes, workplaces and community environments and accumulate in the human body. Childhood cognitive deficits have been linked with prenatal and childhood exposure to PBDEs (1). However, the mechanisms underlying these associations are unknown. We estimated the association of gestational PBDE serum concentrations and adolescent intrinsic functional connectivity from participants in a prospective pregnancy and birth cohort longitudinally followed throughout development.

Materials & Methods

We measured maternal serum concentrations of five individual PBDE congeners and created a summary variable (Σ_5BDE) during pregnancy (2). At age 12 years, we acquired high resolution anatomical and resting state functional magnetic resonance neuroimaging at 3 Tesla. Image processing was performed using CONN and Statistical Parameter Mapping software (3, 4). We examined the relationships between gestational PBDE serum concentrations and voxelwise connectivity metrics for local (LCOR) and global (GCOR) correlation, respectively, adjusting for covariates (age, sex, maternal education) in the cohort for 143 typically developing adolescents (mean age (SD) 12.2 (0.7) years, 59% female). Post hoc analyses examined network-level associations.

Results

Higher gestational BDE-153 serum concentration was associated with increased local correlation in the left inferior lateral occipital cortex (Figure 1, A-red, B-bottom left). On average, a doubling of the gestational PBDE-153 serum concentration corresponded to a 5.3% increase in LCOR. Higher gestational PBDE serum concentrations (BDE-28, 47, 99, 100, and Σ_5BDE) were associated with reduced global correlation in the primary visual cortex (Figure 1, A-blue, B-bottom right). On average, a doubling of the gestational sum of BDE concentration corresponded to a 21.9% reduction in GCOR. Network analyses revealed the increased gestational sum of BDE concentration was associated with lower connectivity between the visual network and salience/ventral attention network ($F(3,136) = 4.45$, $p = 0.0051$), surviving corrections for multiple comparisons.

Conclusion

Increased gestational BDE serum concentrations may influence childhood neurodevelopment by altering how salience and ventral attention networks in the brain receive visual information.

References

1. Cecil, K. M., et al., 2024. Gestational PBDE concentrations, persistent externalizing, and emerging internalizing behaviors in adolescents: The HOME study. Environ Res. 252**,** 118981.
2. Vuong, A. M., et al., 2017. Prenatal and postnatal polybrominated diphenyl ether exposure and visual spatial abilities in children. Environ Res. 153**,** 83-92.
3. Whitfield-Gabrieli, S., Nieto-Castanon, A., 2012. Conn: a functional connectivity toolbox for correlated and anticorrelated brain networks. Brain Connect. 2**,** 125-41.
4. Penny, W. D., et al., 2007. Statistical parametric mapping : the analysis of functional brain images. Academic Press, London.

Images/Tables

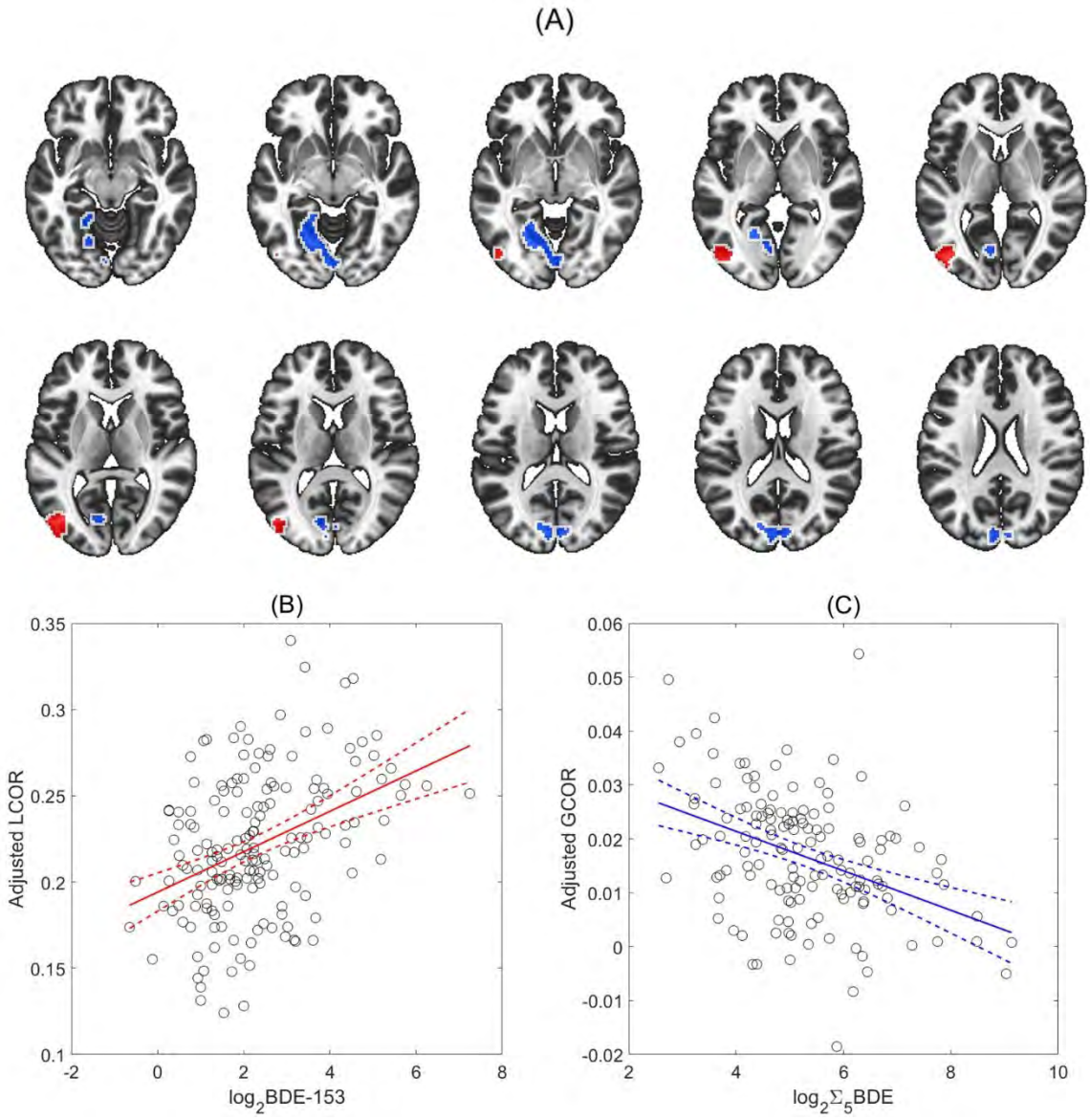

365

Radiomics in Medulloblastoma: Advancing Non-Invasive Diagnosis, Molecular Subtyping, and Prognostication

Maryam Fotouhi MD[1], Ataollah Shahbandi MD[2], Fardin Samadi Khoshe Mehr MSc[3], Mahdi Mohammadzadeh Shahla MD[4], Seyed Mobin Nouredini MD[5]

[1]Advanced Diagnostic and Interventional Radiology Research Center, Tehran, Tehran, Iran, Islamic Republic of. [2]School of Medicine, Tehran University of Medical Sciences, Tehran, Tehran, Iran, Islamic Republic of. [3]Medical Physics and Engineering Department, Tehran University of Medical Sciences, Tehran, Tehran, Iran, Islamic Republic of. [4]School of Medicine, Ardabil University of Medical Sciences, Ardabil, Ardabil, Iran, Islamic Republic of. [5]Faculty of Medicine, Lorestan University of Medical Sciences, Khorramabad, Khorramabad, Iran, Islamic Republic of

Abstract Category

Pediatrics

Purpose

As radiomics continues to develop in the treatment of medulloblastomas (MBs), it offers a valuable and useful tool for diagnosis, subtyping, and prognosis that does not require any invasive techniques. As part of this systematic review, we aim to consolidate and evaluate the current role of radiomics in these areas, assessing its diagnostic accuracy, ability to differentiate subtypes, and prognostic importance.

Materials & Methods
The database was searched following PRISMA guidelines from its inception to November 2022. A specific search phrase was employed to identify research focusing on radiomic applications in the diagnosis, classification, or prognosis of medulloblastoma (MB). Two reviewers independently evaluated titles and abstracts to verify full-text eligibility according to predefined criteria. Despite the variability of the studies, no systematic analysis was conducted.
Results
We analyzed 21 papers out of a pool of 249 that met the inclusion criteria, demonstrating the potential of radiomics to treat MB non-invasively. Multiple models were evaluated for their ability to effectively distinguish medulloblastomas from other posterior fossa tumors, including ependymomas and pilocytic astrocytomas, with classification accuracy rates ranging from 70% to 95%. For diagnosis, CE-T1 and T2W sequences were particularly beneficial. CE-T1 was characterized by contrast-enhanced features highlighting vascular and structural heterogeneity, while T2W measured significant shape and intensity parameters. In addition to identifying molecular subtypes (WNT+, SHH+, group 3, and group 4), radiomics proved effective in identifying multi-class classifications with a 71% to 92% accuracy rate. CE-T1 characteristics, including energy and gray-level co-occurrence matrix (GLCM), are associated with survival outcomes, particularly 2-year overall survival rates. Texture characteristics derived from apparent diffusion coefficient (ADC) improve prognostic accuracy by defining intratumor heterogeneity, integrating clinical variables with radiomic data, and enhancing model accuracy for diagnostic and prognostic applications. CE-T1 and ADC have demonstrated significant potential as radiomics strategies for managing MB, highlighting the need for further clinical validation.
Conclusion
This review emphasizes the potential of radiomics to enhance the clinical management of medulloblastomas through a non-invasive method for early diagnosis, precise subtyping, and survival predictions, thereby facilitating timely and personalized treatment. The chosen radiomic features, including CE-T1 energy, GLCM texture, and ADC-based heterogeneity metrics, reflect underlying biological characteristics in medulloblastomas, highlighting variations in tumor vascularity, cellular density, and structural complexity that are associated with distinct subtypes and prognostic outcomes. The findings are favorable; however, most studies were retrospective with limited sample sizes. This highlights the necessity for larger, multi-center prospective research and external validation to enhance the reliability of radiomics-based models. Radiomics presents considerable potential for incorporation into the management of MB; however, additional research is necessary to comprehensively determine its clinical utility.
References
1. Zhou L, Ji Q, Peng H, et al. Automatic image segmentation and online survival prediction model of medulloblastoma based on machine learning. *European Radiology* 2024;34:3644-3655
2. Yimit Y, Yasin P, Tuersun A, et al. Multiparametric MRI-Based Interpretable Radiomics Machine Learning Model Differentiates Medulloblastoma and Ependymoma in Children: A Two-Center Study. *Academic Radiology* 2024;31:3384-3396

374

Bern Score as a Predictive Tool to Monitor Treatment Success for Spinal CSF Leaks

Karen Buch MD, Aaron B Paul MD, William A Mehan, Jr MD, MBA
Massachusetts General Hospital, Boston, MA, USA
Abstract Category
Spine
Purpose
The Bern score is a widely used scoring system to determine the probability of having a spinal CSF leak based on brain MRI findings[1]. The purpose of this study was to assess changes in the Bern score in patients with myelographically proven and surgically treated spinal CSF leaks (types I-III) before and after treatment.
Materials & Methods
This was a retrospective, IRB-approved study on adult patients with clinical features and imaging features of spontaneous intracranial hypotension (SIH) who underwent myelography and surgical repair. All patients had pre-surgery and post-surgery brain MRIs performed with contrast on a 1.5/3T scanner which included a conventional FLAIR and 3D T1 post-contrast (e.g. BRAVO, MPRAGE, etc). The Bern score was calculated for each patient on pre- and post-treatment MRI exams. Basic demographic data, type of CSF leak, as well as the dates of myelography, surgical repair, and pre- and post-treatment brain MRIs were recorded. Basic two-tailed t-tests were used to compare Bern scores between the pre- and post-treatment groups.

Results

Forty SIH patients with myelographically identified spinal CSF leak were included. Twenty-two patients (55%) had a type I spinal CSF leak and 18 patients (45%) had a type III spinal CSF leak. The mean age was 52 years (standard deviation 14 years). Mean pre-treatment Bern score was 7 (standard deviation 1.8) compared to post-treatment Bern score of 1.3 (standard deviation 1.6) (p-value < 0.0001).

Conclusion

For patients with spinal CSF leaks including CSF-venous fistula (type III leaks), the Bern score is a reliable indicator for assessing treatment success and monitoring patients post procedure.

References

1. Dobrocky T, Grunder L, Breiding PS, et al. Assessing Spinal Cerebrospinal Fluid Leaks in Spontaneous Intracranial Hypotension With a Scoring System Based on Brain Magnetic Resonance Imaging Findings. JAMA Neurol. 2019 May 1;76(5):580-587. doi: 10.1001/jamaneurol.2018.4921. PMID: 30776059; PMCID: PMC6515981.

Images/Tables

Table 1: Demographic Data and Bern Scores for Patients Pre and Post Spinal CSF Leak Repair

	Parameters	P-value
Age (years)	Mean 52, Range: 27-80, STD= 14	
Gender F:M	26:15	
Spinal CSF Leak Type	I: 22 (55%) III: 18 (45%)	
Pre-treatment Bern	7 (range 1-9), STD: 1.8	P<0.0001
Post-treatment Bern	1.3 (range 0-7), STD 1.6	

STD = standard deviation, F = female, M = male

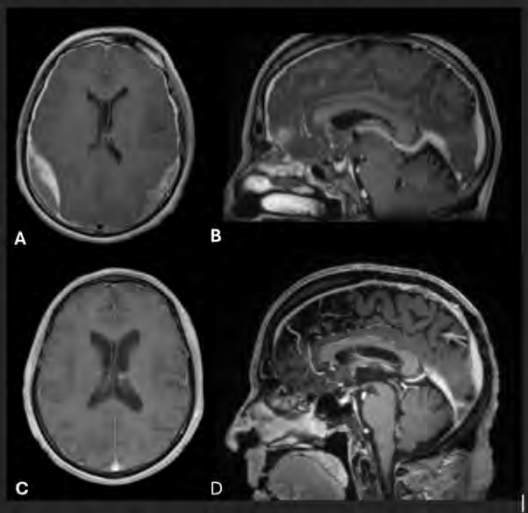

Figure 1: 59 year old male with a type III CSF leak. Post-contrast axial and sagittal pre-treatment MRI images A and B demonstrate pachymeningeal thickening and venous distention. In the axial postcontrast image A from the pretreatment MRI also demonstrates bilateral subdural hematomas. Sagittal postcontrast image B demonstrates narrowing of the mamillopontine distance, prepontine cistern, and suprasellar cistern for a Bern score of 9. Post-contrast T1 weighted images from the post-treatment MRI are shown in the axial image C and sagittal image D. Image C demonstrates resolution of subdural hematomas and pachymeningeal thickening/enhancement. Sagittal image D demonstrates improvement in the suprasellar cistern, mamillopontine distance, and prepontine cistern. The post-treatment Bern score was 2.

376

Choroid Plexus Volumes Are a Marker of Successful Spinal CSF Leak Repair

William A Mehan, Jr. MD, MBA, Neo C. Poyiadji MD, Aaron B Paul MD, Karen Buch MD
Massachusetts General Hospital, Boston, MA, USA

Abstract Category

Spine

Purpose

Patients with intracranial hypotension from spinal CSF leaks have increased choroid plexus volumes in response to CSF leakage[1]. The purpose of this study was to assess changes in choroid plexus volumes in patients before and after spinal CSF leaks repair.

Materials & Methods

This was a retrospective, IRB-approved on patients with spinal CSF leak who had pre- and post-CSF leak repair MRI exams. Brain MRIs with contrast were performed on a 1.5/3T scanner with acquisition of 3D T1 post-contrast (e.g. BRAVO, MPRAGE, etc). Choroid plexus volumes at the level of the trigonum ventriculi were calculated for the left and right sides on all pre- and post-treatment MRIs using Visage-7 segmentation tools. Basic demographic data, type of CSF leak, and choroid plexus volumes were recorded for all patients. Basic two-tailed t-tests were used to compare choroid plexus volumes between the pre- and post-treatment groups.

Results

Twenty SIH patients from spinal CSF leak were included. 11 patients (55%) had a type Ia (ventral tear) spinal CSF leak, 5 patients (25%) had type 1b (lateral tear) and 4 patients (20%) had a type III spinal CSF leak (Table 1). The mean age was 47.6 years (standard deviation 13.8 years). Mean choroid plexus volumes pre-treatment were 0.82 cm^3 (standard deviation 0.29) compared to 0.38 cm^3 (standard deviation 0.19) post-treatment (p-value < 0.0001) (Figures 1 and 2).

Conclusion

Significantly decreased choroid plexus volumes were seen in SIH patients following spinal CSF leak repair. This highlights the modulation and dynamic role of the choroid plexus in states of low CSF volumes.

References

Mehan WA, Poyiadji N, Paul AB, Buch K. Volumetric Changes in the Choroid Plexus Associated with Spontaneous Intracranial Hypotension in Patients with Spinal CSF Leak. AJNR Am J Neuroradiol. 2024 Jul 18. doi: 10.3174/ajnr.A8291. Epub ahead of print. PMID: 39025635.

Images/Tables

Table 1: Basic demographic, clinical and imaging features for SIH patients. Pre-treatment spinal CSF choroid plexus volumes were compared to post-treatment spinal CSF choroid plexus volumes for a cohort of 20 patients. SIH = spontaneous intracranial hypotension, std = standard deviation, CSF = cerebrospinal fluid, CP = choroid plexus.

	Pre-Treatment SIH Pts (n=20)	Post-Treatment SIH Pts (n=20)	p-value
Age (mean, std) (years)	47.6, 13.8		
Sex (M:F)	8:12		
Bern score (mean, std)	7.1, 1.6	0,0	<0.0001
Type of spinal CSF leak			
type 1	16		
type 3	4		
CP volume (mean, std)(cm3)	0.82, 0.29	0.38, 0.22	<0.0001

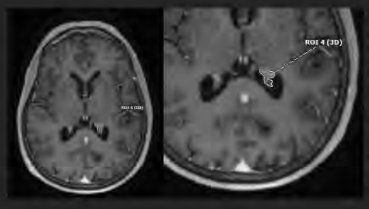

Figure 1: 65-year old female with a type III CSF leak, status post surgical repair presenting for routine followup brain MRI. Axial T1 post-contrast MPRAGE sequences are shown demonstrating a manual segmentation of the left choroid plexus. A magnified view of the same patient, same slice is shown on the right-hand panel.

Figure 2: Axial T1 postcontrast MPRAGE sequences at the level of the atria in the same 65-year old female with a type III spinal CSF leak shown in Figure 1. The top image demonstrates the pre-treatment brain MRI. The bottom image shows the post-treatment brain MRI. By visual inspection of the volume of the choroid plexus on the pre-treatment exam compared to the post-treatment MRI has markedly decreased.

383

Characteristics and Risk Factors for Enlargement of Intracranial Subdural Hematomas

Mahla Radmard MD, Armin Tafazolimoghadam MD, Caline Azzi MD, Tej D Azad MD, Ali Bydon MD, David M Yousem MD, Arjun Chanmugam MD
Johns Hopkins, Baltimore, MD, USA

Abstract Category

Head & Neck

Purpose

Subdural hematomas (SDHs) are common non-contrast CT (NCCT) findings in patients with closed head trauma, often necessitating serial CT imaging under inpatient observation to monitor for potential growth. We sought to determine the patient characteristics and risk factors for SDH growth in order to suggest parameters for possible discharge of patients without follow-up imaging from the Emergency Department (ED).

Materials & Methods

We reviewed non-contrast head and cervical spine CT reports for all patients scanned in our health system's EDs from July 1, 2018, to June 30, 2024. Patient demographics, comorbidities (e.g., hypertension, chronic kidney disease, diabetes), other NCCT findings, and SDH growth status were extracted from the electronic medical record (EMR). Gender and racial demographics included 151 males (Mean age: 56.15, SD: 17.29) and 82 females (Mean age: 61.63, SD: 14.76); racial breakdown consisted of 141 White patients (92 males, 49 females), 77 Black patients (48 males, 29 females), and 15 patients of other races (11 males, 4 females).

Results

There were 171 SDH cases which remained stable in size or got smaller and 62 SDH cases that grew. Using a bivariate analysis, we found that SDH enlargement was significantly associated with age over 65 ($p = 0.03$), non-White race ($p = 0.02$), and hypertension ($p = 0.02$). Other imaging findings associated with SDH enlargement included subarachnoid hemorrhage ($p = 0.04$), the initial size greater than 5 mm ($p = 0.01$) and initial midline shift ($p = 0.01$). The patients with SDH growth over time had more frequent complications ($p = 0.001$), longer hospital stays ($p = 0.003$) with more surgeries ($p = 0.001$), and they were less likely to be discharged home ($p = 0.003$). The multivariate analysis odds ratio for SDH growth was 2.010 (95% CI: 1.105–3.658, $p = 0.022$) for those with an initial SDH size of > 5mm. Age greater than 65 showed an odds ratio of 1.812 (95% CI: 0.960–3.419, $p = 0.066$).

Conclusion

Subdural hematomas enlarge around ¼ of the time (62/233). While a number of variables may be associated with SDH growth (age, hypertension, non-White race), initial SDH size greater than 5 mm and older age survive multivariate analysis and are considered risk factors for growth. Outcomes are worse in those patients who have SDH growth

References

Vande Vyvere T, Pisică D, Wilms G, Claes L, Van Dyck P, Snoeckx A, van den Hauwe L, Pullens P, Verheyden J, Wintermark M, Dekeyzer S, Mac Donald CL, Maas AIR, Parizel PM. Imaging Findings in Acute Traumatic Brain Injury: a National Institute of Neurological Disorders and Stroke Common Data Element-Based Pictorial Review and Analysis of Over 4000 Admission Brain Computed Tomography Scans from the Collaborative European NeuroTrauma Effectiveness Research in Traumatic Brain Injury (CENTER-TBI) Study. J Neurotrauma. 2024 Oct;41(19-20):2248-2297. doi: 10.1089/neu.2023.0553. Epub 2024 Apr 18. PMID: 38482818.

Chen H, Colasurdo M, Malhotra A, Gandhi D, Bodanapally UK. Advances in chronic subdural hematoma and membrane imaging. Front Neurol. 2024;15:1366238. Published 2024 Apr 25. doi:10.3389/fneur.2024.1366238

Images/Tables

Table: Assessing the relation between study variables and the SDH growth in size

		SDH (ENLARGE= NO) N=171	SDH (ENLARGE= YES) N=62	P-value
Age group (65+)		95 (55.6%)	44 (71.0%)	0.03
Gender (F)		58 (33.9%)	24 (38.7%)	0.50
Race	White	111 (64.9%)	30 (48.4%)	0.02
	Black	53 (31.0%)	24 (38.7%)	
	others	7 (4.1%)	8 (12.9%)	
History of medication (Antiplatelet/Anticoagulant)		53 (31.0%)	27 (43.5%)	0.08
Alcohol abuse		44 (25.7%)	13 (21.0%)	0.46
Mechanism	Fall	102 (59.6%)	40 (64.5%)	0.41
	MVA	35 (20.5%)	12 (19.4%)	
	Assault	26 (15.2%)	5 (8.1%)	
	Others	8 (4.7%)	5 (8.1%)	
Recurrent Trauma		43 (25.1%)	18 (29.0%)	0.55
GCS	13-15	131 (81.9%)	47 (78.3%)	0.84
	9-12	7 (4.4%0	3 (5.0%)	
	3-8	22 (13.8%)	10 (16.7%)	
Elevated INR/PTT		39 (23.4%)	16 (25.8%)	0.70
Thrombocytopenia		24 (14.2%)	11 (17.7%)	0.51
HTN		70 (40.95)	36 (58.1%)	0.02
DM		41 (24.0%)	10 (16.1%)	0.20
CKD		10 (5.8%)	7 (11.3%)	0.16
Bleeding Diathesis		8 (4.7%)	6 (9.7%)	0.16
Prior ICH		20 (11.7%)	5 (8.1%)	0.43
Time from injury <24hrs		151 (91.5%)	58(95.1%)	0.37
Location	Frontal	45 (26.3%)	15 (24.2%)	0.11
	Temporal	10 (5.8%)	0	
	Parietal	12 (7.0%)	3 (4.8%)	
	Occipital	6 (3.5%)	0	
	Multiple	91 (53.2%)	43 (69.4%)	
	Others	7 (4.1%)	1 (1.6%)	
SAH		68 (39.8%)	34 (54.8%)	0.04
EDH		2 (1.2%)	2 (3.2%)	0.29
Midline shift		37 (21.6%)	24 (38.7%)	0.01
Brain atrophy		26 (15.2%)	8 (12.9%)	0.66
Surgical Tx (surgical)		14 (8.2%)	8 (12.9%)	0.28
Specific surgical TX	None	154 (90.1%)	54 (87.1%)	0.45
	Craniotomy	12 (7.0%)	6 (9.7%)	
	Burr hole	3 (1.8%)	0	
	others	2 (1.2%)	2(3.2%)	
Medical Management (Prophylaxis for ICP/Hematoma/Seizures)		160 (93.6 %)	62 (100%)	0.04
Complication (at least one)		40 (23.4%)	29 (46.8%)	0.001
Mortality (NO)		148 (86.5%)	48 (77.4%)	0.09
Rehospitalization		20 (11.9%)	7 (11.7%)	0.96
Discharge	Home	110 (64.3%)	31 (50.0%)	0.003
	Rehabilitation	52 (30.4%)	19 (30.6%)	
	Death	9 (5.3%)	12 (19.4%)	
SDH initial size (>5)		70 (40.9%)	37 (59.7%)	0.01
Observation (ICU)		80 (46.8%)	13 (21.0%)	<0.001
Total number of follow-up		2.00 (1.00, 4.00)	4.00 (3.00, 7.00)	<0.001
Length of hospitalization		3.00 (1.00, 9.00)	5.00 (2.00, 14.25)	0.003
Follow-up surgical(yes)		2 (1.2%)	8 (12.9%)	<0.001

- Categorical data are presented as numbers (percentages) and analyzed using the Chi-square test.
- Quantitative data are presented as the median (first quartile [Q1], third quartile [Q3]) and analyzed using the Mann-Whitney test.

392

Feasibility and Toxicity of Ferumoxytol Contrast Use in Relative Cerebral Blood Volume Calculations

Jared Stoller M.S.[1], Daniel L Schwartz B.S[1], Doonyaporn Wongsawaeng M.D.[2], Leslie L Muldoon PhD[1], Rochelle Fu PhD[1], Ramon F Barajas MD[1], Prakash Ambady MD[3]

[1]Oregon Health and Science University, Portland, Oregon, USA. [2]Siriraj Hospital, Mahidol University, Bangkok, THAILAND, Thailand. [3]Providence Portland Medical Center, Portland, Oregon, USA

Abstract Category

Functional/Advanced Imaging

Purpose

Intravenous Feraheme (ferumoxytol, [Fe]) is FDA-approved to treat anemia and was granted orphan drug status as a MRI contrast agent for brain tumor imaging. At early imaging sessions (vascular phase 1-2 hrs), Fe is a blood pool contrast agent that allows high resolution steady state (ss-MRI) , a measure of tumor vascularity. At delayed imaging sessions (parenchymal phase , >24 hrs) Fe accumulates in brain regions rich in phagocytic *tumor-associated macrophage (CD 68+)* and activated astrocytes (GFAP+) and can be quantified using Segregation and Extravascular Localization of Ferumoxytol Imaging (SELFI). *Neither* ss-MRI nor SELFI can be performed with Gd-MRI. We report the feasibility and safety of serial Fe-MRI in a prospective open label single arm phase 2 clinical trial (NCT03347617).

Materials & Methods

Fifty-two consenting patients with newly diagnosed WHO 2007 grade 4 glioma were prospectively enrolled to receive pembrolizumab (200mg intravenous every 3 weeks) in addition to standard of care (SOC) chemoradiotherapy (CRT) until a dose limiting toxicity or progression. Study imaging sessions consisted of Fe-MRI in the same session as the SOC Gd-MRI when feasible. Patients underwent two-day Fe-MRI (early phase and 24-hour delayed phase) at four predetermined imaging sessions: 1. pre-radiation, 2. post-radiation, 3. suspected progression (SP), and 4. one-month post-SP. Patients who received at least 1 follow up Fe-MRI after CRT were eligible for this imaging study. Safety and toxicity were measured using NCI CTCAE Version 4.0 and attributed as i) unrelated, ii) possibly related or iii) definitely related to Fe, pembrolizumab or SOC.

Results

Fifty-two patients were enrolled to achieve a predetermined forty-three eligible patients (15 female, median age = 58 years, age range = 22-77 years) with at least one post CRT response assessment Fe-MRI. A total of 143 Fe imaging sessions were available. Fifteen patients received all 4 categories of imaging session.

One-hundred-seventeen imaging sessions had Gd and Fe given in same session and twenty-six imaging sessions were standalone Fe scans, primarily at the SP imaging session. One-hundred twenty-seven imaging sessions had both days of Fe-MRI, with ten imaging sessions having insufficient second day data, and six having insufficient data for both days. Proportions of evaluable scans were 96.5% in early phase and 86.5% in delayed phase.

Among the 52 enrolled patients, 51 patients had at least one AE (adverse event), and 36 patients had at least one AE with grade ≥ 3. Additionally, 45 patients experienced at least one AE possibly related to Fe. Of these, 19 patients had an AE grade ≥ 3, and no patients had any AE that were definitively related to Fe.

Conclusion

Fe allows early vascular phase and delayed parenchymal phase that may noninvasively monitor tumor vascularity and tumor immune microenvironment. Our data suggests that it is feasible to conduct serial Fe-MRIs in a separate session independent of Gd-MRIs in the same setting with minimal interference with SOC imaging in a brain tumor immunotherapy clinical trial. Use of Fe as an imaging agent was safe. This data may help develop similar Fe-MRI protocols for future clinical trials.

References

Barajas RF Jr, Schwartz D, McConnell HL, Kersch CN, Li X, Hamilton BE, Starkey J, Pettersson DR, Nickerson JP, Pollock JM, Fu RF, Horvath A, Szidonya L, Varallyay CG, Jaboin JJ, Raslan AM, Dogan A, Cetas JS, Ciporen J, Han SJ, Ambady P, Muldoon LL, Woltjer R, Rooney WD, Neuwelt EA. Distinguishing Extravascular from Intravascular Ferumoxytol Pools within the Brain: Proof of Concept in Patients with Treated Glioblastoma. AJNR Am J Neuroradiol. 2020 Jul;41(7):1193-1200. doi: 10.3174/ajnr.A6600. Epub 2020 Jun 11. PMID: 32527840; PMCID: PMC7357650.

Images/Tables

Feasibility				
Total # of Sessions	Early Phase	Evaluable scans (%)	Delayed phase	Evaluable scans# (%)
42	Pre Radiation	95.2%	Pre Radiation	81%
41	Post Radiation	97.6%	Post Radiation	90.2%
21	Suspected	95.2%	Suspected	95.2%
37	Confirmatory	97.3%	Confirmatory	83.8%
141	Total	96.5%	Total	86.5%

407

Optimizing Photon-Counting CT Angiography for Enhanced Visualization of Intracranial Stents

Riccardo Ludovichetti[1], Dunja Gorup[1], Miklos Krepuska[1], Sebastian Winklhofer[2], Patrick Thurner[1], Jawid Madjidyar[1], Thomas Flohr[1], Lars Michels[1], Victor Mergen[1], Zsolt Kulcsar[1], Tilman Schubert[1]
[1]University Hospital Zurich, Zurich, Zurich, Switzerland. [2]Zurich, Zurich, Switzerland

Abstract Category

Adult Brain

Purpose

Patients with intracranial flow diverters and non-flow diverting stents require regular imaging follow-up to assess stent patency and to rule out in-stent stenosis. CT angiography or MR angiography may not reliably evaluate stent patency due to imaging artifacts. To address this limitation, we optimized reconstruction and scanning parameters to evaluate the potential of CT angiography using a photon-counting detector (PCD) CT.

Materials & Methods

A phantom study was conducted using a vascular phantom with two implanted flow-diverters to optimize CT imaging parameters for evaluating intracranial stents. The phantom was scanned with both conventional EID (energy integrating detector) CT and high-resolution PCD-CT, testing various dose levels and reconstruction kernels to assess subjective image quality. Following these optimizations, 14 patients with intracranial flow diverters and non-flow diverting stents were imaged with PCD-CT. Image reconstructions were performed using three kernels identified in the phantom study (Hv56, Hv64, and Hv72) and an additional standard-resolution kernel (Hv40) for comparison. Signal-to-noise ratio (SNR) and contrast-to-noise ratio (CNR) were measured in patient scans, while diagnostic confidence (in patient scans) and subjective image quality (in both phantom and patient scans) were rated by two independent neuroradiologists. A three-point scale (1 = best, 3 = worst) was used for diagnostic confidence, and a five-point scale (5 = best, 1 = worst) was used for image quality.

Results

Phantom images indicated that 0.2 mm reconstructions using kernels Hv56 (4.5), Hv64 (5), and Hv72 (5) delivered the highest image quality across all dose levels.

In patient imaging, both the signal-to-noise ratio (SNR) and the contrast-to-noise ratio (CNR) showed significant reductions ($P < 0.001$) with the use of sharper kernels compared to the control settings that employed the Hv40 kernel. Despite this decrease, these sharper kernels provided substantially improved image quality and diagnostic confidence relative to the control reconstruction, enhancing the definition of the areas surrounding the metallic structures and effectively reducing blur.

The highest ratings for image quality and diagnostic confidence were achieved with the Hv64 (0.2 mm) kernel for non-flow-diverting stents and the Hv72 (0.2 mm) kernel for flow diverters. The differences between these two kernels were minimal and did not affect overall diagnostic confidence.

Conclusion

In summary, our research established that CT angiography using a photon-counting detector (PCD) CT serves as an effective imaging modality for assessing both intracranial non-flow diverting stents and flow diverters. The best image quality was attained with the high sharpness kernels, Hv64 and Hv72, utilizing a slice thickness of 0.2 mm.

References

1. Ludovichetti R, Gorup D, Krepuska M, Winklhofer S, Thurner P, Madjidyar J, Flohr T, Piccirelli M, Michels L, Alkadhi H, Mergen V, Kulcsar Z, Schubert T. Ultra-high resolution CT angiography for the assessment of intracranial stents and flow diverters using photon counting detector CT. J Neurointerv Surg. 2024 Oct 22:jnis-2024-022041. doi: 10.1136/jnis-2024-022041. Epub ahead of print. PMID: 39438133.
2. Abel F, Schubert T, Winklhofer S. Advanced Neuroimaging With Photon-Counting Detector CT. *Investigative Radiology* 2023;58:472.

Images/Tables

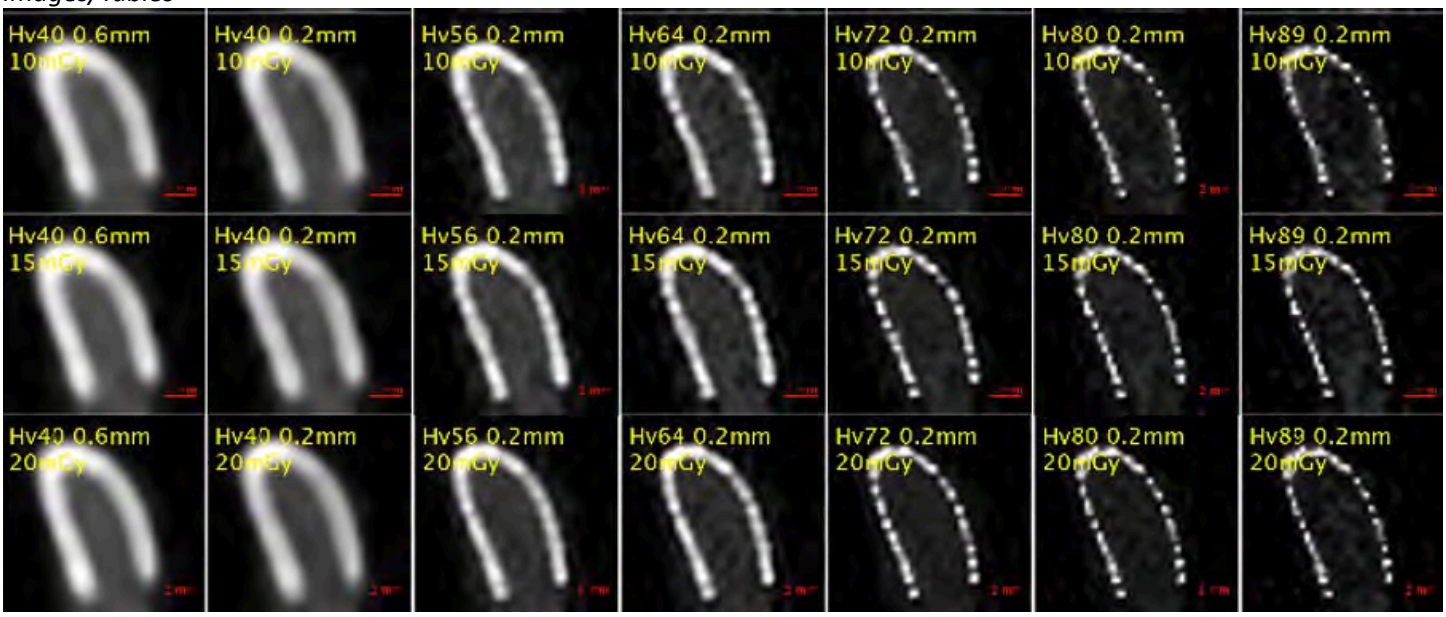

411

Concordance between Centiloid quantification and visual interpretation of amyloid PET scans across the Alzheimer's disease continuum

Mohammad Khalafi, Seyed Hani Hojjati, Xiuyuan Hugh Wang, Yi Li, Lidia Glodzik, Liangdong Zhou, Qolamreza R Razlighi, Emily B Tanzi, Tracy A Butler, Nancy S Foldi, Silky Pahlajani, Mony J de Leon, Gloria C Chiang

Weill Cornell Medicine, New York, NY, USA

Abstract Category

Adult Brain

Purpose

To evaluate amyloid beta (Aβ) accumulation among individuals with cognitively impaired and unimpaired, visual interpretation of PET images is approved as the routine method for image interpretation. We aimed to evaluate the visual interpretation results compared to quantitative centiloid-assessed (CL) to understand the concordance between these two methods of interpreting amyloid PET images.

Materials & Methods

Two hundred forty-seven amyloid PET images were enrolled in a monocentric [11C]-Pittsburgh Compound B (PiB) and [18F]-Florbetaben (FBB) Aβ-PET study. SUVR values were converted to the CL using the GAAIN guidelines. In this study, two radiologists investigated the images blindly, and in the case of uncertain discrepancies were presented at a second, joint round of VR and multidisciplinary consensus diagnostic meetings.

Results

The highest concordance rate for the whole cohort was 93% using CL cutoffs of 18, 20, and 24. Using FBB, the concordance rate was highest using a CL cutoff of 24 (97%), whereas the concordance rate for PiB peaked at 94% at a CL cutoff of 18. Concordance was higher in negative rather than positive amyloid PET cases, 98% versus 90%. Concordance was slightly higher in cognitively impaired participants, compared to unimpaired (96% versus 93%). Visual interpretation and CL assessments of amyloid PET positivity including PiB and FBB showed the highest overall concordance at CL18 (κ = 0.825), followed by CL16 and CL20. PiB tracer demonstrated its highest concordance with VR at CL18, while FBB showed the best concordance at CL24. Among cognitively impaired subjects, PiB demonstrated superior performance compared

to FBB. Conversely, in cognitively unimpaired subjects, FBB exhibited higher concordance at higher CL thresholds, though its concordance diminished at lower threshold levels.

Conclusion

Global CL quantification of amyloid PET scans is highly concordant with visual interpretation. Disagreement frequently arose when focal amyloid-positive regions were identified on visual interpretation but fell below the global threshold on CL quantification. Combining both methods can provide a more complete assessment of the extent of amyloid deposition in the brain.

References

Klunk WE, Koeppe RA, Price JC, et al. The Centiloid Project: standardizing quantitative amyloid plaque estimation by PET. Alzheimers Dement 2015;11:1-15.e11-14

Collij L, Salvadó G, Alves IL, et al. Examining centiloid quantification against visual assessment using [18F]flutemetamol PET. Alzheimer's & Dementia 2020;16:e042653

Collij LE, Salvadó G, Shekari M, et al. Visual assessment of [18F]flutemetamol PET images can detect early amyloid pathology and grade its extent. European Journal of Nuclear Medicine and Molecular Imaging 2021;48:2169-2182

Images/Tables

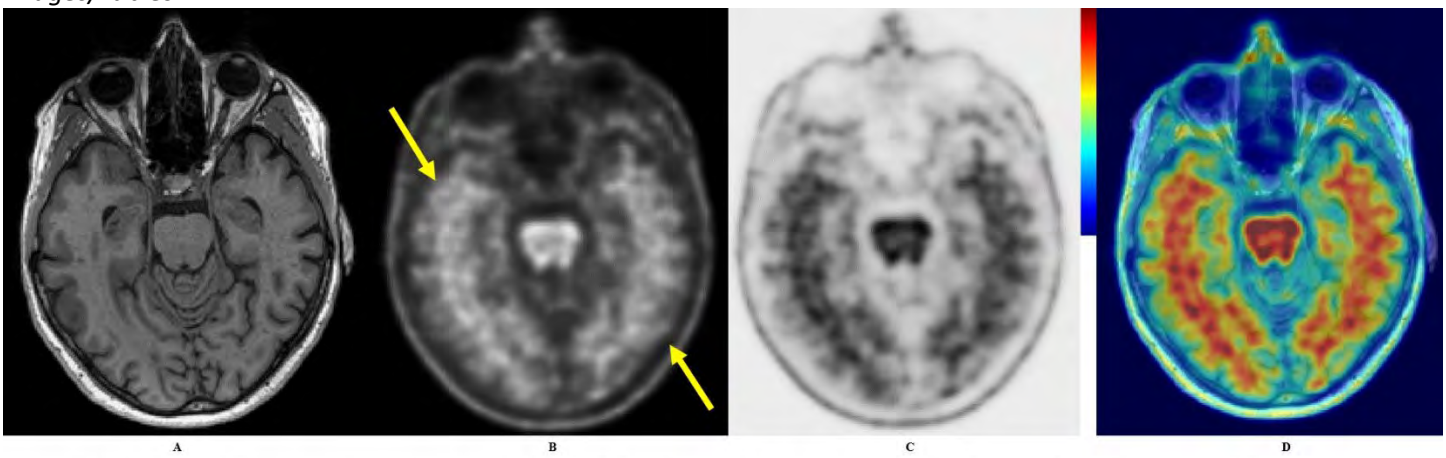

Figure 1. Discordant case of [11C]-Pittsburgh compound-B PET, interpreted as a negative amyloid PET scan visually, but positive by quantification (42 centiloid). Axial 3D T1 MPRAGE image through the temporal lobes (A) and [11C]-Pittsburgh compound-B PET, shown in grayscale (B), inverse grayscale (C), and rainbow fused with the coregistered T1 (D). This study was visually interpreted as negative. However, there are areas of confluent cortical tracer uptake primarily in the temporal lobes (yellow arrows). The study also showed an atypical area of tracer uptake in the left basal ganglia (double arrows).

413

Temporal Bone CT for Conductive Hearing Loss: Does the Audiogram Facilitate Radiologist Identification of Potential Causes?

Louis M Leon MD, William T Malouf MD, Meagan P Bachmann AuD, Pedrom C Sioshansi MD, Kevin D Hiatt MD, Paul M Bunch MD

Wake Forest University School of Medicine, Winston Salem, NC, USA

Abstract Category

Head & Neck

Purpose

Traditional teaching states that in patients with conductive hearing loss (CHL), a cause should be evident on temporal bone CT. A recent article asserts that incorporating audiologic test results into temporal bone CT evaluation of CHL allows radiologists to 1) perform a more informed and intentional search for causative lesions(s) and 2) provide more confident and more accurate interpretations (1).

However, data to support these positions is lacking, and radiologists at our institution have not traditionally reviewed audiologic results when interpreting temporal bone CT.

Our purposes are to 1) determine the proportion of temporal bone CTs performed for CHL with no candidate cause(s) initially identified and 2) assess the audiogram's potential value to facilitate identification of candidate CHL causes not initially reported.

Materials & Methods

For this retrospective, IRB-approved, HIPAA-compliant study, we searched our radiology report database for patients meeting the following inclusion criteria: 1) temporal bone CT without contrast performed January 2021-December 2023 and 2) CT indication of "conductive hearing loss."

A radiology resident reviewed all CT reports to determine whether potential cause(s) of CHL were described by the interpreting radiologist. CTs were excluded if the report indicated nondiagnostic imaging.

For each patient with no potential CHL cause reported, the most recent audiogram acquired before the CT was extracted from the electronic health record. Patients without an available audiogram predating the CT were excluded.

A neuroradiology attending reviewed the audiogram for the presence or absence of CHL – defined as a ≥15 dB air-bone gap at 2 or more frequencies (2, 3) – corresponding to the reportedly "normal" temporal bone CT side(s). Patients without audiogram-confirmed CHL were excluded.

Finally, the neuroradiology attending reviewed the CT images and audiograms for the presence or absence of candidate CHL causes by applying recently described principles of incorporating audiologic results into temporal bone CT interpretation (1).

Results

A total of 502 patients met initial inclusion criteria (Figure 1A). In 413 (82.3%), at least one potential CHL cause was described by the interpreting radiologist. In 89 (17.7%), no potential cause of CHL was reported, of whom 33 were excluded from further evaluation – 7 (7.9%) for no available audiogram and 26 (29.2%) for no CHL.

In the remaining 56, the neuroradiologist incorporating information from the audiogram into CT interpretation identified at least 1 candidate CHL cause in 46 (82.1%), most commonly possible ossicular fixation (n=17; Figure 1B), otospongiosis (n=14; Figure 1C), and third window lesion (n=5; Figure 1D).

Conclusion

Among patients for whom "CHL" was the indication for temporal bone CT, at least 1 possible cause was initially reported in over 80%. Among the remainder, audiogram review showed no CHL to be present in nearly one-third.

In the subset of patients with audiogram-confirmed CHL and no potential cause initially identified, further review of the CT images in conjunction with the audiogram enabled identification of at least 1 candidate cause in over 80%.

Incorporating audiogram results into temporal bone CT interpretation may facilitate identification of CHL causes, particularly when no cause is apparent after initial image review.

References

1. Malouf WT, Bachmann MP, Meegalla NT, et al. Evaluation of Hearing Loss: Understanding Audiologic Testing to Refine Image Interpretation. Radiographics 2024;44(10):e240018.

2. Rosenhall U, Hederstierna C, Idrizbegovic E. Otological diagnoses and probable age-related auditory neuropathy in "younger" and "older" elderly persons. Int J Audiol 2011;50(9):578–581.

3. Göthberg H, Skoog I, Tengstrand T, et al. Pathophysiological and Clinical Aspects of Hearing Loss Among 85-Year-Olds. Am J Audiol 2023;32(2):440–452.

Images/Tables

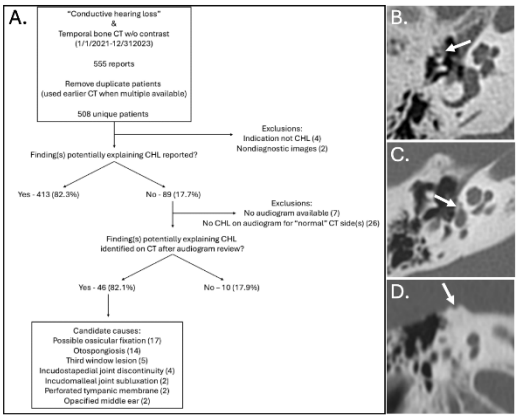

Figure 1. (a) Flow of participant selection and key results. (b) Axial CT image demonstrates abnormal thickening and mineralization of the right anterior malleal ligament (arrow, A), representing a candidate site of ossicular fixation. (c) Axial CT image demonstrates abnormal osseous lucency and thickening (arrow, B) associated with the stapes footplate and extending anterior to the oval window, compatible with otospongiosis. (d) Coronal CT image demonstrates dehiscence (arrow, D) of the superior semicircular canal, the most common third window lesion.

426

The Los Angeles Motor Scale (LAMS) is Independently Associated with CT Perfusion Collateral Status Markers

Andrew Cho[1], Kevin Chen[1], Minsoo Kim[1], Ishan Mazumdar[1], Janet Mei[1], Nathan Hyson[1], Francis Deng[2], Mona Shahriari[1], Jee Moon[1], Licia Luna[1], Vaibhav Vagal[3], Tobias Faizy[4], Jeremy Heit[5], Greg Albers[5], Max Wintermark[6], Kambiz Nael[7], Aneri Balar[8], Dhairya Lakhani[9], Vivek Yedavalli[1]

[1]Department of Radiology and Radiology Sciences, Johns Hopkins University, Baltimore, MD, USA. [2]Department of Radiology, Division of Neuroradiology, Johns Hopkins Medical Center, Baltimore, MD, USA. [3]Department of Neurology, University of Cincinnati, Cincinnati, OH, USA. [4]Department of Radiology, Neuroendovascular Division, University Medical Center, Münster, ., Germany. [5]Department of Neurology, Stanford University, Stanford, CA, USA. [6]Department of Neuroradiology, MD Anderson Medical Center, Houston, TX, USA. [7]David Geffen SChool of Medicine, University of California, Los Angeles, Los Angeles, CA, USA. [8]Neuroendovascular Program, Massachusetts General Hospital, Harvard University, Boston, MA, USA. [9]Department of Neuroradiology, Rockefeller Neuroscience Institute, West Virginia University, Morgantown, WV, USA

Abstract Category

Functional/Advanced Imaging

Purpose

The Los Angeles Motor Scale (LAMS) is an objective tool that has been used to rapidly assess and predict the presence of large vessel occlusion (LVO) in the pre-hospital setting successfully in several studies. However, studies assessing the relationship between LAMS score and CT perfusion collateral status (CS) markers such as cerebral blood volume (CBV) index, and hypoperfusion intensity ratio (HIR) are sparse. Our study therefore aims to assess the association of admission LAMS score with established CTP CS markers CBV Index and HIR in AIS-LVO cases.

Materials & Methods

In this prospectively collected, retrospectively reviewed analysis, inclusion criteria were as follows: a) CT angiography (CTA) confirmed anterior circulation LVO from 9/1/2017 to 10/01/2023, and b) diagnostic CT perfusion (CTP). Logistic regression analysis was performed to assess the relationship between admission LAMS with CTP CS markers HIR and CBV Index. $p \leq 0.05$ was considered significant.

Results

In total, 285 consecutive patients (median age = 69 years; 56% female) met our inclusion criteria. Multivariable logistic regression analysis adjusting for sex, age, ASPECTS, tPA, premorbid mRS, admission NIH stroke scale, prior history of TIA, stroke, atrial fibrillation, diabetes mellitus, hyperlipidemia, coronary artery disease and hypertension, admission LAMS was found to be independently associated with CBV Index (adjusted OR: 0.82, $p < 0.01$), and HIR (adjusted OR:0.59, $p < 0.05$).

Conclusion

LAMS is independently associated with CTP CS markers, CBV index, and HIR. This finding suggests that LAMS may also provide an indirect estimate of CS.

References

Lakhani DA, Mehta TR, Balar AB et al. The Los Angeles motor scale (LAMS) is independently associated with CT perfusion collateral status markers. *J Clin Neurosci*. 2024 Jul;125:32-37

Llanes JN, Kidwell CS, Starkman S et al. The Los Angeles Motor Scale (LAMS): a new measure to characterize stroke severity in the field. *Prehosp Emerg Care* 2004;8:46–50.

Nazliel B, Starkman S, Liebeskind DS et al. A brief prehospital stroke severity scale identifies ischemic stroke patients harboring persisting large arterial occlusions. *Stroke* 2008;39:2264–7.

Stead TG, Banerjee P, Ganti L. Real-world field performance of the los angeles motor scale as a large vessel occlusion screen: a prospective muticentre study. *Cerebrovasc Dis* 2021;50(5):543–50.

437

Concordance of Central Vein Sign and McDonald Criteria for the Diagnosis of Multiple Sclerosis

Fang Liu[1], Elaina Gombos[2], Meghan Kilbane[3], Meredith Dever[3], Enrique Alvarez[4], Christina Azevedo[5], Peter Calabresi[6], Jeffrey Cohen[3], Salim Chahin[7], Leorah Freeman[8], Erin Longbrake[9], Ruth A Marrie[10], Aaron Miller[11], Nandita Mitra[1], Ellen M Mowry[6], Jiwon Oh[12], Matthew K Schindler[1], Elias Sotirchos[6], Karlo Toljan[2], Emmanuelle Waubant[13], Gary R Cutter[14], Andrew J Solomon[15], Daniel S Reich[16], Nancy Sicotte[2], Pascal Sati[2], Russell T Shinohara[1], Daniel Ontaneda[3]
[1]University of Pennsylvania, Philadelphia, PA, USA. [2]Cedars Sinai, Los Angeles, CA, USA. [3]Cleveland Clinic, Cleveland, OH, USA. [4]University of Colorado, Aurora, CO, USA. [5]University of Southern California, Los Angeles, CA, USA. [6]Johns Hopkins University, Baltimore, MD, USA. [7]Washington University, St. Louis, MO, USA. [8]University of Texas Austin, Austin, TX, USA. [9]Yale University, New Haven, CT, USA. [10]Dalhousie University, Halifax, Nova Scotia, Canada. [11]Mount Sinai School of Medicine, New York, NY, USA. [12]University of Toronto, Toronto, Ontario, Canada. [13]University of California San Francisco, San Francisco, CA, USA. [14]University of Alabama, Birmingham, AL, USA. [15]University of Vermont, Burlington, VT, USA. [16]NIH, Bethesda, MD, USA

Abstract Category

Functional/Advanced Imaging

Purpose

Previous research has demonstrated that the central vein sign (CVS) is an imaging biomarker that distinguishes multiple sclerosis (MS) lesions from those due to MS mimics. The CVS (as Select6*) was recently recommended for inclusion as an additional diagnostic tool for MS in the updated 2024 McDonald criteria (MC), underscoring its utility in improving diagnostic accuracy. Unlike the MC, which relies on iterative subjective clinical assessments performed by providers with varying expertise, CVS provides an objective imaging marker that could standardize MS diagnosis, especially in asymptomatic individuals and those with an atypical onset. This could lead to earlier diagnosis and improved patient outcomes. The objective is to assess the CVS as a standalone test for the diagnosis of MS compared to the 2017 McDonald criteria.

Materials & Methods

Baseline 3T MRI scans were obtained from 420 participants undergoing evaluation for MS in a 24-month, 11-site multi-center study. MS sub-specialist neurologists at each site determined if participants fulfilled the 2017 MC. Diagnoses were then centrally adjudicated by expert neurologists (international panel members). North American Imaging in MS Cooperative (NAIMS) guidelines were used for abbreviated manual CVS rating. For Select6*, site PIs used post-contrast T2* EPI combined with FLAIR (FLAIR*) images and rated a scan as CVS-positive if six lesions meet CVS criteria (3 lesions for Select3* ratings). Ratings were then adjudicated centrally by neuroradiologists. The concordance between Select3*/Select6* results and the MC was reported, along with the positive predictive value (PPV) of the CVS for the MC.

Results

420 participants were recruited: 210 (50%) with MS-typical onset, 166 (40%) with MS-atypical symptom onset, 25 (6%) with radiologically isolated syndrome (RIS), and 19 (4%) with progressive onset. Of 210 participants with typical presentations, 136 (65%) fulfilled the 2017 McDonald criteria, of whom 76% were CVS-positive using Select3* and 57% using Select6*. The PPV of CVS indicates that 80% of cases identified as CVS+ met the MC. For the typical onset group, concordance between CVS and MC was 71% using Select3* and 63% using Select6*. For reference, the concordance between dissemination in space (DIS) (based on a single study MRI) and MC was 82%. When the typical and progressive onset groups were assessed together (n=229), 148 (65%) fulfilled MC for MS; 110 (74%) of the MS cases were CVS+ using Select3* and 81 (55%) using Select6*. The PPV of CVS is 0.78 and the concordance rate for this combined group was 69% using Select3* and 61% using Select6*.

Conclusion

Using baseline data from a cohort of patients undergoing evaluation for MS, the CVS as a standalone test showed reasonable concordance with the 2017 McDonald criteria (69-71% for Select3*). The CVS is a simple diagnostic test for MS as compared to the MC which in this study was determined by MS sub-specialists with extensive research expertise and centrally adjudicated – something not typically applied in daily clinical practice. In routine settings, MC often relies on subjective clinical assessments that can be prone to error. Agreement between CVS and MC will be further evaluated following a 24-month prospective follow-up.

References

Ontaneda D, Sati P, Raza P, et al. Central vein sign: A diagnostic biomarker in multiple sclerosis (CAVS-MS) study protocol for a prospective multicenter trial. *Neuroimage Clin* 2021;32:102834. DOI: https://doi.org/10.1016/j.nicl.2021.102834

Sati P, Oh J, Constable RT, et al. The central vein sign and its clinical evaluation for the diagnosis of multiple sclerosis: a consensus statement from the North American Imaging in Multiple Sclerosis Cooperative. *Nat Rev Neurol* 2016;12(12):714-722. DOI: https://doi.org/10.1038/nrneurol.2016.166

443

CT Perfusion Based rCBF <38% Volume is Independently and Negatively Associated with Digital Subtraction Angiography Collateral Score in Anterior Circulation Large Vessel Occlusions

Andrew Cho[1], Kevin Chen[1], Minsoo Kim[1], Ishan Mazumdar[1], Janet Mei[1], Nathan Hyson[1], Francis Deng[2], Mona Shahriari[1], Jee Moon[1], Licia Luna[1], Vaibhav Vagal[3], Tobias Faizy[4], Jeremy Heit[5], Greg Albers[5], Max Wintermark[6], Kambiz Nael[7], Aneri Balar[8], Dhairya Lakhani[9], Vivek Yedavalli[1]

[1]Department of Radiology and Radiological Sciences, Johns Hopkins University, Baltimore, MD, USA. [2]Department of Radiology, Division of Neuroradiology, Johns Hopkins Medical Center, Baltimore, MD, USA. [3]Department of Neurology, University of Cincinnati, Baltimore, MD, USA. [4]Department of Radiology, Neuroendovascular Division, University Medical Center, Münster, ., Germany. [5]Department of Neurology, Stanford University, Stanford, CA, USA. [6]Department of Neuroradiology, MD Anderson Medical Center, Houston, TX, USA. [7]David Geffen School of Medicine, University of California, Los Angeles, Los Angeles, CA, USA. [8]Neuroendovascular Program, Massachusetts General Hospital, Harvard University, Boston, MA, USA. [9]Department of Neuroradiology, Rockefeller Neuroscience Institute, West Virginia University, Morgantown, WV, USA

Abstract Category

Functional/Advanced Imaging

Purpose

Collateral status (CS) is an important biomarker of functional outcomes in patients with acute ischemic stroke secondary to large vessel occlusion (AIS-LVO). Pretreatment CT perfusion (CTP) parameters serve as reliable surrogates of collateral status (CS). In this study, we aim to assess the relationship between the relative cerebral blood flow less than 38% (rCBF <38%), with the reference standard American Society of Interventional and Therapeutic Neuroradiology (ASITN) collateral score (CS) on DSA.

Materials & Methods

In this prospectively collected, retrospectively reviewed analysis, inclusion criteria were as follows: (a) CT angiography (CTA) confirmed anterior circulation large vessel occlusion from 9/1/2017 to 10/01/2023; (b) diagnostic CT perfusion; and (c) underwent mechanical thrombectomy with documented ASITN CS. The ratios of the CTP-derived CBF values were calculated by dividing the values of the ischemic lesion by the corresponding values of the contralateral normal region (which were defined as rCBF). Spearman's rank correlation and logistic regression analysis were performed to determine the relationship of rCBF <38% lesion volume with DSA ASITN CS. $p \leq .05$ was considered significant.

Results

In total, 223 patients [mean age: 67.77 ± 15.76 years, 56.1% (n = 125) female] met our inclusion criteria. Significant negative correlation was noted between rCBF <38% volume and DSA CS ($\rho = 0.37$, $p < .001$). On multivariate logistic regression analysis, rCBF <38% volume was found to be independently associated with worse ASITN CS (unadjusted OR: 3.03, 95% CI: 1.60 5.69, $p < .001$, and adjusted OR: 2.73, 95% CI: 1.34–5.50, $p < .01$).

Conclusion

Greater volume of tissue with rCBF <38% is independently associated with better DSA CS. rCBF <38% is a useful adjunct tool in collateralization-based prognostication. Future studies are needed to expand our understanding of the role of rCBF <38% within the decision-making in patients with AIS-LVO.

References

Lakhani DA, Balar AB, Koneru M et al. CT perfusion based rCBF <38% volume is independently and negatively associated with digital subtraction angiography collateral score in anterior circulation large vessel occlusions. *Neuroradiol J*. 2024 Aug;37(4):462-467.

Rosenthal ES, Schwamm LH, Roccatagliata L, et al. Role of recanalization in acute stroke outcome: rationale for a CT angiogram-based "benefit of recanalization" model. *AJNR Am J Neuroradiol* 2008; 29(8): 1471–1475.

Potreck A, Scheidecker E, Weyland CS, et al. RAPID CT perfusion-based relative CBF identifies good collateral status better than hypoperfusion intensity ratio, CBV-index, and time to-maximum in anterior circulation stroke. *AJNR Am J Neuroradiol* 2022; 43(7): 960–965.

444

CT Perfusion Derived rCBV < 42% Lesion Volume is Independently Associated with Followup FLAIR Infarct Volume in Anterior Circulation Large Vessel Occlusion

Andrew Cho[1], Kevin Chen[1], Minsoo Kim[1], Ishan Mazumdar[1], Janet Mei[1], Nathan Hyson[1], Francis Deng[2], Mona Shahriari[1], Jee Moon[1], Licia Luna[1], Vaibhav Vagal[3], Tobias Faizy[4], Jeremy Heit[5], Greg Albers[5], Max Wintermark[6], Kambiz Nael[7], Aneri Balar[8], Dhairya Lakhani[9], Vivek Yedavalli[1]

[1]Department of Radiology and Radiological Sciences, Johns Hopkins University, Baltimore, MD, USA. [2]Department of Radiology, Division of Neuroraadiology, Johns Hopkins Medical Center, Baltimore, MD, USA. [3]Department of Neurology, University of Cincinnati, Cincinnati, OH, USA. [4]Department of Radiology, Neuroendovascular Division, University Medical Center, Münster, ., Germany. [5]Department of Neurology, Stanford University, Stanford, CA, USA. [6]Department of Neuroradiology, MD Anderson Medical Center, Houston, TX, USA. [7]David Geffen School of Medicine, University of California, Los Angeles, Los Angeles, CA, USA. [8]Neuroendovascular Program, Massachusetts General Hospital, Harvard University, Boston, MA, USA. [9]Department of Neuroradiology, Rockefeller Neuroscience Institute, West Virginia University, Morgantown, WV, USA

Abstract Category

Functional/Advanced Imaging

Purpose

Pretreatment CT Perfusion (CTP) parameter rCBV < 42% lesion volume has recently been shown to predict 90-day mRS. In this study, we aim to assess the relationship between rCBV < 42% and a radiographic follow-up infarct volume delineated on FLAIR images.

Materials & Methods

In this retrospective evaluation of our prospectively collected database, we included acute stroke patients triaged by multimodal CT imaging, including CT angiography and perfusion imaging, with confirmed anterior circulation large vessel occlusion between 9 January 2017 and 10 January 2023. Follow-up FLAIR imaging was used to determine the final infarct volume. Student t, Mann-Whitney-U, and Chi-Square tests were used to assess differences. Spearman's rank correlation and linear regression analysis were used to assess associations between rCBV < 42% and follow-up infarct volume on FLAIR.

Results

In total, 158 patients (median age: 68 years, 52.5% female) met our inclusion criteria. rCBV < 42% ($\rho = 0.56$, $p < 0.001$) significantly correlated with follow-up-FLAIR infarct volume. On multivariable linear regression analysis, rCBV < 42% lesion volume (beta = 0.60, $p < 0.001$), ASPECTS (beta = −0.214, $p < 0.01$), mTICI (beta = −0.277, $p < 0.001$), and diabetes (beta = 0.16, $p < 0.05$) were independently associated with follow-up infarct volume.

Conclusion

The rCBV < 42% lesion volume is independently associated with FLAIR follow-up infarct volume

References

Lakhani DA, Balar AB, Salim H et al. CT Perfusion Derived rCBV < 42% Lesion Volume Is Independently Associated with Followup FLAIR Infarct Volume in Anterior Circulation Large Vessel Occlusion. *Diagnostics (Basel)*. 2024 Apr 19;14(8):845.

Arenillas, J.F., Cortijo, E., García-Bermejo, P et al. Relative cerebral blood volume is associated with collateral status and infarct growth in stroke patients in SWIFT PRIME. *J. Cereb. Blood Flow Metab*. 2018, 38, 1839–1847.

Rex, N.B.; McDonough, R.V.; Ospel, J.M.; Kashani, N.; Sehgal, A.; Fladt, J.C.; McTaggart, R.A.; Nogueira, R.; Menon, B.; Demchuk, A.M.; et al.CT Perfusion Does Not Modify the Effect of Reperfusion in Patients with Acute Ischemic Stroke Undergoing Endovascular Treatment in the ESCAPE-NA1 Trial. *AJNR Am. J. Neuroradiol*. 2023, 44, 1045–1049.

451

Comparison of High-Resolution MR Features of Hippocampal Sclerosis Using Subfield Analysis with International League Against Epilepsy (ILAE) Subtypes on Histopathology

Bejoy Thomas MD, DNB, PDCC, Smily Sharma MD,DNB, FRCR, Aditya Ajith MD, Ashalatha Radhakrishnan MD, DM, Rajalakshmi Poyuran MD, George C Vilanilam MS, MCh

Sree Chitra Tirunal Institute for Medical Sciences and Technology, Thiruvananthapuram, Kerala, India

Abstract Category

Adult Brain

Purpose

The purpose of the study was to evaluate the utility of high-resolution MRI in grading of hippocampal sclerosis (HS) using subfield analysis compared to histopathology subtypes based on International League Against Epilepsy (ILAE) classification[1].

Materials & Methods

After institutional ethics committee approval, a retrospective observational study was conducted in a tertiary referral centre. Consecutive histopathology proven cases of HS operated for unilateral mesial temporal sclerosis from January 2018 to June 2023 who had a pre- operative high resolution MR study on a 3 Tesla MR scanner in 'HARNESS' protocol were included. Patients with bilateral, dual/ double pathologies were excluded. Two Neuroradiologists, blinded to the histopathology subtypes of HS, independently performed MR grading of HS using subfield analysis, in accordance with the recently published HS grading by Middlebrooks et al.[2] Any discrepancy in the findings were resolved in consensus with a senior Neuroradiologist. HR 2D coronal T2 sequence with slice orientation orthogonal to the long axis of the hippocampus was used for assessment of the MR grade. Hippocampal subfields were assessed for atrophy as compared contralateral normal hippocampus by visual analysis. In addition, Cornu Ammonis (CA) 1 was also considered atrophic if there was loss of normal smooth tapering as we move from subiculum, CA1 to C2. HS type1 (HS1) was diagnosed on MR when significant atrophy was seen in all the CA1, CA2/3, and hilum; HS2 when atrophy was seen in only CA1; HS3 when atrophy was seen only in the hilum and HS0 when no significant atrophy was seen in any of the subfields, however there was T2 signal alteration in the hippocampus.

Results

A total of 106 patients (males: 57, female: 49) were included in the study with a mean age of 23.8 years (age range: 2 years to 50 years). HS1 was the most common subtype both on MR (n: 72) and histopathology grading (n: 89). On MR, HS2 was found in 13, HS 3 in 12, and HS 0 in 9 patients. A good interobserver agreement (Cohen's kappa:0.770, *P*:<0.01) was found between MR grading by the two Neuroradiologists. However, MR and histopathology grading showed only a fair agreement (Fleiss' kappa: 0.294, p: <0.01). Considering better post- op prognosis of HS1 and its larger proportion in our cohort, we attempted also agreement between MR and histopathology grading in HS1 vs all others, but again showed only a fair agreement (Fleiss' kappa: 0.327, p: <0.01)

Conclusion

This showed that MR grading, despite of having high degree of interobserver agreement, may not predict ILAE HS subtypes with high accuracy pre- operatively with the current clinical 3T MR protocols, probably because MR detects mainly only the gliosis and volume reduction of the hippocampal subfields, but not the neuronal loss detected on histopathology, which is an important determinant for subclassification of HS.

References

1. Blümcke I, Thom M, Aronica E, Armstrong DD, Bartolomei F, Bernasconi A et al. International consensus classification of hippocampal sclerosis in temporal lobe epilepsy: a Task Force report from the ILAE Commission on Diagnostic Methods. *Epilepsia* 2013; 54(7):1315-29.

2. Middlebrooks EH, Gupta V, Agarwal AK, Freund BE, Messina SA, Tatum WO, et al. Radiologic Classification of Hippocampal Sclerosis in Epilepsy. *AJNR AM J Neuroradiol* 2024; 45(9):1185-93. https://doi.org/10.3174/ajnr.A8214

Images/Tables

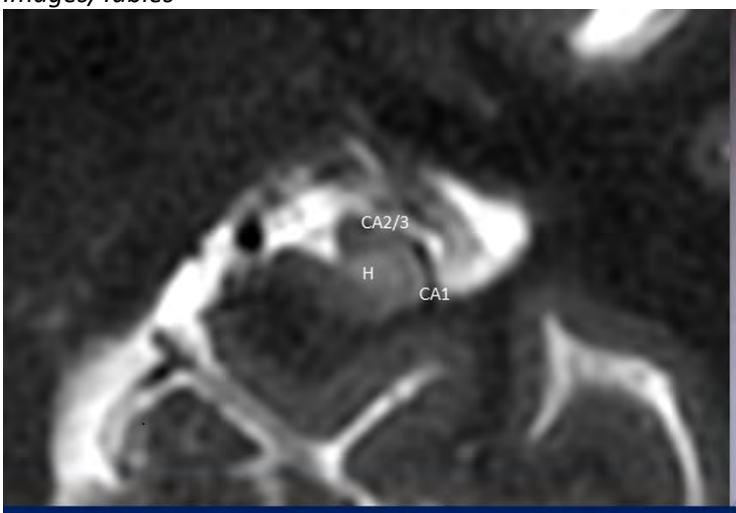

Type 1 Hippocampal Sclerosis [Severe atrophy in Cornu Ammonis(CA)1, CA2/3, and hilum (H) (CA4 +Dentate gyrus)]

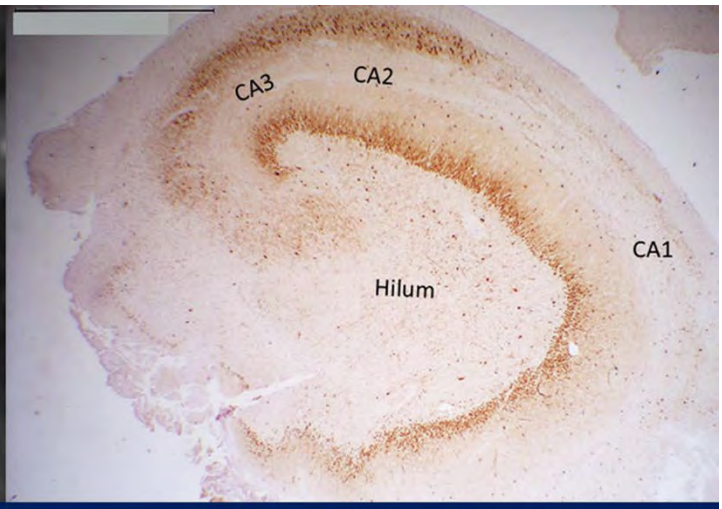

Type 1 Hippocampal Sclerosis (Severe neuronal loss in CA1 and Hilum sectors)

461

The "Outline sign": Presence of a thin hyperenhancing perimeter on MRI can help differentiate meningiomas from other common neoplasms in the temporal bone region.

Anil K Vasireddi MD[1], Katherine L Reinshagen MD[2], Donghoon Shin MD[3], Laura V Romo MD[2], Amy F Juliano MD[2]
[1]Duke University, Durham, NC, USA. [2]Massachusetts Eye and Ear, Boston, MA, USA. [3]Massachusetts General Hospital, Boston, MA, USA

Abstract Category

Head & Neck

Purpose

Meningiomas can occur in various locations within the temporal bone region, including the jugular foramen, internal auditory canal, petroclival region and tegmen. When occurring in these locations, primary differential considerations include other enhancing extra-axial neoplasms commonly occurring around the temporal bone such as schwannomas and jugular/jugulotympanic paragangliomas. Although imaging features such as presence of a dural tail or adjacent bony hyperostosis may be useful in differentiating a meningioma from other etiologies, these signs are not always present and may sometimes be difficult to identify. We propose the “outline sign”, defined as the presence of a thin rim of hyperenhancement around the tumor on contrast enhanced T1 weighted MRI, as a potential imaging feature of meningiomas. In this study we evaluate the utility of the outline sign in identifying meningiomas and differentiating them from other common neoplasms of the temporal bone such as schwannomas and paragangliomas.

Materials & Methods

A total of 39 consecutive clinical MRI of meningiomas (n = 14), schwannomas (n = 22), and paragangliomas (n = 3) with confirmed histopathological data performed at Massachusetts Eye and Ear were studied retrospectively. Two experienced head and neck radiologists independently assessed for the presence or absence of an outline sign and subsequently formed a consensus opinion while blinded to patient information and histopathological data. Inter-reader reliability in identifying the outline sign was assessed by Cohen’s kappa statistics. Simple bivariate comparisons, Fisher’s exact test, were performed on the consensus opinions to assess for statistical differences in presence of the sign in meningiomas vs. schwannomas and paragangliomas. Sensitivity, specificity, and accuracy of the sign with respect to identifying an underlying meningioma were calculated.

Results

Both readers displayed identical opinions in assessing the presence of an outline sign in 34 of 39 cases (87%), including 13 out of 14 meningiomas (93%) and with substantial agreement (Cohen's kappa of 0.74). The outline sign was present in 12 out of 14 meningiomas (86%), which was significantly greater in frequency compared to schwannomas (3 of 22, 14%) and paragangliomas (1 of 3, 33%) ($p<0.001$). The outline sign also demonstrated high sensitivity (86%), specificity (84%) and accuracy (85%) in identifying an underlying meningioma.

Conclusion

The outline sign, characterized by the presence of thin rim of hyperenhancement on contrast enhanced T1 weighted imaging around a mass lesion, can serve as a useful tool in distinguishing meningiomas from other common enhancing neoplasms in the temporal bone region such as schwannomas and paragangliomas. It is thought to reflect the presence of a microvascular-rich tumor capsule, which is more often seen with meningiomas than other common tumors in the temporal bone.

References

1. Juliano AF, Ginat DT, Moonis G. Imaging review of the temporal bone: part I. Anatomy and inflammatory and neoplastic processes. *Radiology*. Oct 2013;269(1):17-33. doi:10.1148/radiol.13120733
2. Oguz KK, Cila A. Rim enhancement of meningiomas on fast FLAIR imaging. *Neuroradiology*. Feb 2003;45(2):78-81. doi:10.1007/s00234-002-0914-8
3. Panyaping T, Punpichet M, Tunlayadechanont P, Tritanon O. Usefulness of a Rim-Enhancing Pattern on the Contrast-Enhanced 3D-FLAIR Sequence and MRI Characteristics for Distinguishing Meningioma and Malignant Dural-Based Tumor. *AJNR Am J Neuroradiol*. Mar 2023;44(3):247-253. doi:10.3174/ajnr.A7780
4. Takeguchi T, Miki H, Shimizu T, et al. Evaluation of the tumor-brain interface of intracranial meningiomas on MR imaging including FLAIR images. *Magn Reson Med Sci*. Dec 31 2003;2(4):165-9. doi:10.2463/mrms.2.165
5. Uchida H, Hirano H, Moinuddin FM, et al. Radiologic and histologic features of the T2 hyperintensity rim of meningiomas on magnetic resonance images. *Neuroradiol J*. Feb 2017;30(1):48-56. doi:10.1177/1971400916678228

Images/Tables

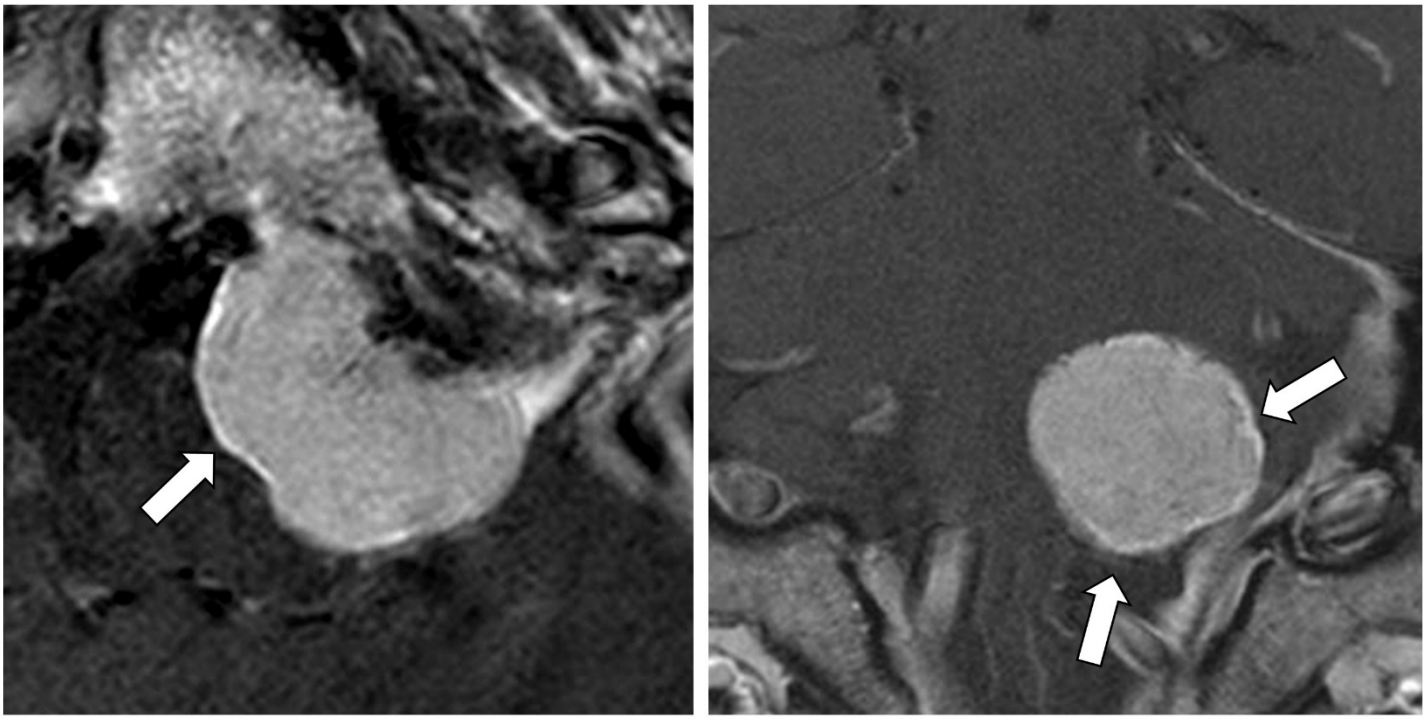

Figure 1. Axial and coronal contrast-enhanced T1-weighted images in a 47-year-old with pathologically-proven meningioma shows an outline sign around the periphery of the lesion (white arrows).

468

Pretreatment MR Oxygen Extraction Fraction as an Imaging Biomarker of Infarct Progression in Successfully Reperfused Stroke Patients

Mona Asghariahmadabad MD[1], Pouya Metanat MD[1], Elham Tavakol MD[2], Ameera F Ismail MD[2], Mersedeh Bahr Hosseini MD[2], Viktor Szeder MD, PhD[2], Geoffrey P Colby MD, PhD[2], Jeffrey L Saver MD[2], David S Liebeskind MD[2], Vivek Yedavalli MD[3], Wade S Smith MD[1], Kim Anthony MD[1], Cathra Halabi MD[1], Nerissa Ko MD[1], Anirudh Sreekrishnan[1], S. Andrew

Josephson MD[1], Kazim Narsinh MD[1], Luis E Savastano MD, PhD[1], Steven Hetts MD[1], Christopher P Hess MD, PhD[1], Kambiz Nael MD[1]
[1]University of California San Francisco, San Francisco, CA, USA. [2]UCLA, Los Angeles, CA, USA. [3]Jonhs Hopkins University, Baltimore, MD, USA
Abstract Category
Adult Brain
Purpose
Despite recent advancements in endovascular therapies for acute ischemic stroke (AIS), 20-50% of patients experience continued infarct growth and poor functional outcomes even after successful reperfusion [1,2]. Oxygen extraction fraction (OEF) has shown promise in evaluating ischemic tissue viability and can now be quantified using routinely performed dynamic-susceptibility-contrast (DSC) perfusion MRI [3]. This study aimed to determine the association between quantitative values of OEF on pretreatment MRI and infarct growth in AIS patients who underwent successful reperfusion.
Materials & Methods
In this retrospective study, patients were included if they had an anterior circulation large vessel occlusion (LVO), achieved successful reperfusion (TICI ≥2b), and had undergone pretreatment DSC perfusion and follow-up MRI within 48 hours of reperfusion. DSC perfusion was analyzed using Cercare Medical Neurosuite 15.1 (Cercare Medical, Denmark) to generate OEF maps. DWI, ADC, Tmax, OEF series were imported into 3D Slicer 5.6.2 and registered using linear transformation. Volumes of interest (VOI) were created for the ischemic core (ADC ≤ 620×10^{-6} mm^2/s) and penumbra tissue (Tmax > 6 sec) on pretreatment MRI, and masks were applied to coregistered OEF maps to extract OEF voxel values associated with ischemic core and penumbra. The OEF values were then divided by the mean OEF value of a VOI, which was created on the contralateral (non-infracted) MCA distribution to calculate relative-OEF values (rOEF). Infarct growth was determined if the final infarct volume was ≥ 10 mL larger than baseline ischemic core volume. Associations between rOEF and infarct growth, along with demographic, clinical, and imaging variables, were evaluated using univariate and multivariate analyses.
Results
Among 89 patients who achieved successful reperfusion, 30 (33%) demonstrated infarct growth ≥ 10 mL. A total of 238,782 ischemic core voxels and 827,442 penumbra voxels were extracted for analysis. The rOEF values were significantly lower ($p<0.001$) in ischemic core in comparison to penumbral tissue. While univariate analysis showed increased rOEF values in both ischemic core and penumbra were significantly ($p<0.001$) associated with a lower probability of infarct growth, only penumbra-rOEF remained as an independent predictor of infarct growth ($p = 0.002$) following multivariate regression analysis.
Conclusion
Conclusion:
This study showed that pretreatment rOEF derived from DSC perfusion MRI can predict infarct growth in AIS patients following successful reperfusion. Lower rOEF values in the ischemic core and penumbra were associated with increased infarct growth, with penumbra-rOEF emerging as an independent predictor. These findings suggest that rOEF could serve as a valuable imaging biomarker to assess tissue viability and in prediction of infarction growth despite successful reperfusion.
References
1. Bala F, Ospel J, Mulpur B, et al. Infarct Growth despite Successful Endovascular Reperfusion in Acute Ischemic Stroke: A Meta-analysis. *AJNR Am J Neuroradiol*. Aug 2021;42(8):1472-1478. doi:10.3174/ajnr.A7177
2. Nie X, Leng X, Miao Z, Fisher M, Liu L. Clinically Ineffective Reperfusion After Endovascular Therapy in Acute Ischemic Stroke. *Stroke*. 2023/03/01 2023;54(3):873-881. doi:10.1161/STROKEAHA.122.038466
3. Bani-Sadr A, Hermier M, de Bourguignon C, et al. Oxygen Extraction Fraction Mapping on Admission Magnetic Resonance Imaging May Predict Recovery of Hyperacute Ischemic Brain Lesions After Successful Thrombectomy: A Retrospective Observational Study. *Stroke*. 2024/11/01 2024;55(11):2685-2693. doi:10.1161/STROKEAHA.124.047311

Images/Tables

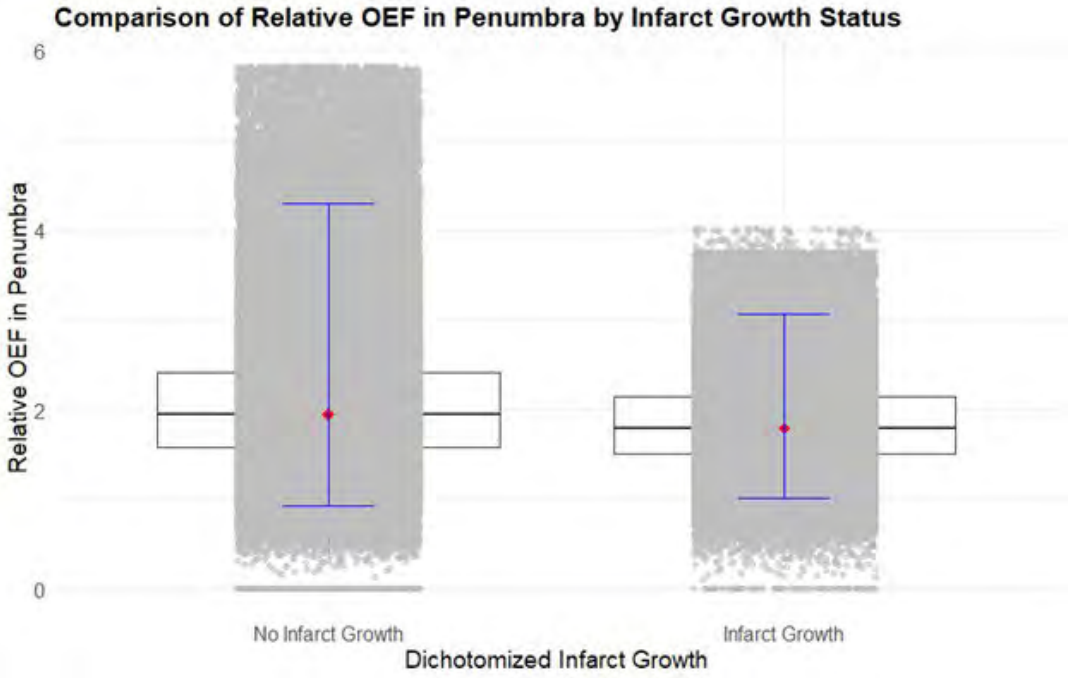

476

Application of Machine Learning Algorithms on Whole Brain Connectivity Resting-State fMRI to Phenotype Superagers

Laiz Laura de Godoy MD, PhD[1], Wenqi Min[2], Demetrius Ribeiro de Paula MBA, MSc[3], Adalberto Studart-Neto MD, PhD[4], Nathan Green PhD[5], Paula Arantes MD, PhD[4], Khallil Taverna Chaim MSc[4], Natália Cristina Moraes MSc[4], Mônica Sanches Yassuda PhD[4], Ricardo Nitrini MD, PhD[4], Claudia da Costa Leite MD, PhD[4], Andrea Soddu PhD[6], Sotirios Bisdas MD, PhD[7], Jasmina Panovska-Griffiths DPhil[8]

[1]Perelman School of Medicine at the University of Pennsylvania, Philadelphia, PA, USA. [2]Mathematical Institute, University of Oxford, Oxford, -, United Kingdom. [3]Radboud University Medical Centre, Nijmegen, -, Netherlands. [4]University of Sao Paulo, Sao Paulo, SP, Brazil. [5]University College London, London, -, United Kingdom. [6]Western Institute for Neuroscience, London, ON, Canada. [7]University College Lon, London, -, United Kingdom. [8]University of Oxford, Oxford, -, United Kingdom

Abstract Category

Functional/Advanced Imaging

Purpose

Superagers are older adults with episodic memory performance similar or superior to middle-aged individuals.[1,2] We used machine learning to identify the key neural networks and nodes responsible for superagers brain function connectivity abilities employing resting state fMRI (rs-fMRI) at 3 Tesla (T) and 7T scanners.

Materials & Methods

A cohort of 31 older adults, 80 or older, were grouped as superagers (n=14) or age-matched healthy older adults (n=17). The MRI DICOM files were entered into an automatic pipeline in GraphICA.[3] Anatomic and functional images were preprocessed using FSL 6.03.[4] We employed random forest machine-learning algorithm (RF-MLA) to phenotype the functional activity of superagers and identify the key networks and nodes within the networks to differentiate superagers from controls. The most important nodes were defined as the nodes with Mean Decrease Gini (MDA) and Mean Decrease Accuracy (MDG) 1 standard deviation above the average. We characterized the most discriminative networks by the number of most important nodes. Our RF analysis was two-folded: *i) Preselected Network analysis:* we phenotyped superagers in the preselected cognitive networks [default mode network (DMN), executive control network right (ECN-R), executive control network left (ECN-L), hippocampal, language, and salience network] to compare findings to our previous work,[5] where we used the Elastic Net regression model on the same networks and cohort. Given this area remains underexplored, this was important to ensure replicability and generalizability using different methods. *ii) Whole-Brain Network analysis*: we expanded the superagers phenotyping in a novel way to explore the whole-brain

connectivity across 11 distinct networks, including the six networks used in the *Preselected Network analysis,* plus the auditory, sensorimotor, visual lateral, visual medial, and visual occipital networks.

Results

Our findings showed that in both *preselected* and *whole-brain network analyses*, the key networks and nodes that differentiate superagers and controls were similar to our previous work,[5] where we used Elastic Net regression. Specifically, we identified the SN, DMN, and ECN as pivotal networks for superager classification, with particular importance for the SN in the present study. We also replicated the most discriminative nodes to predict superagers, including the precuneus, posterior cingulate cortex, prefrontal cortex, inferior parietal lobule, temporo-occipital junction, and extrastriate superior cortex, strengthening the importance of the prefrontal cortex group when utilizing RF-MLA. Exploring whole-brain connectivity, the RF-MLA determined additional nodes in the auditory, visual-lateral, and visual-medial networks pertinent to superagers and highlighted the discriminative value of the visual-lateral network. Our results showed that 7T rs-fMRI had better prediction accuracy than 3T (83.9% for 3T and 85.7% for 7T) in the whole-brain network analyses. Therefore, the most accurate results should rely on the 7T dataset. The results are demonstrated in lollipop plots and brain maps for the 7T dataset (Figure 1), reflecting the nodes within each network with the highest superagers prediction.

Conclusion

Our study utilized machine-learning to shed light on the significance of key networks and nodes in characterizing superagers. Our advanced analytical techniques and whole-brain approaches validated existing findings and provided new insights into sensory cortices that may be important for comprehending cognitive resilience.

References

1. Rogalski EJ, Gefen T, Shi J, Samimi M, Bigio E, Weintraub S, et al. Youthful memory capacity in old brains: anatomic and genetic clues from the Northwestern SuperAging Project. J Cogn Neurosci. 2013;25: 29–36.
2. de Godoy, L. L. *et al.* Understanding brain resilience in superagers: a systematic review. *Neuroradiology* (2020) doi:10.1007/s00234-020-02562-1.
3. Ribeiro de Paula, D. *et al.* A method for independent component graph analysis of resting-state fMRI. *Brain Behav.* **7**, e00626 (2017).
4. Nickerson, L. D., Smith, S. M., Öngür, D. & Beckmann, C. F. Using Dual Regression to Investigate Network Shape and Amplitude in Functional Connectivity Analyses. *Front. Neurosci.* **11**, 115 (2017).
5. de Godoy, L. L. *et al.* Phenotyping Superagers Using Resting-State fMRI. *AJNR Am. J. Neuroradiol.* **44**, 424–433 (2023)

Images/Tables

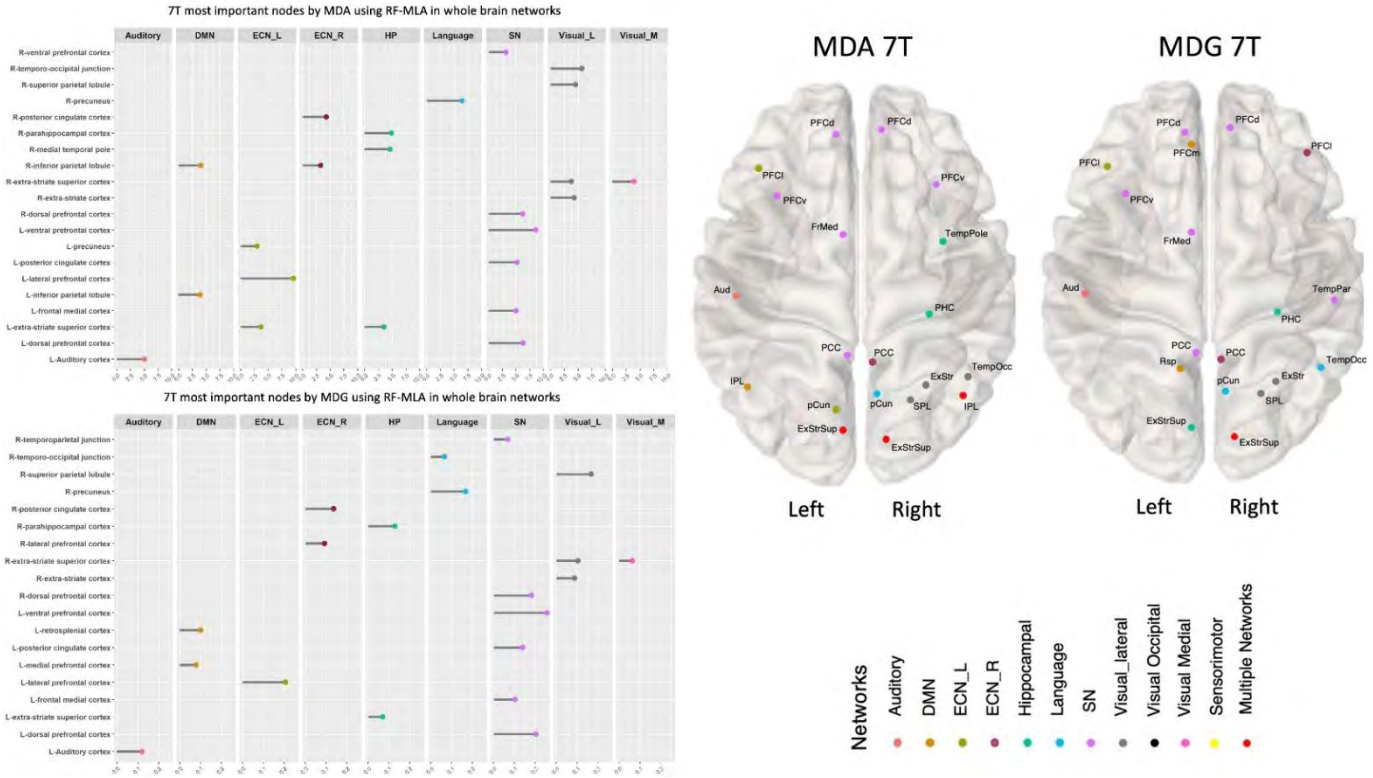

478

Hybrid ^{18}F-Fluoroestradiol (FES) PET/MRI for Enhanced Detection of ER-Positive Brain and Calvarial Metastases

Faizullah Mashriqi MD[1], Michelle Chen MD[1], Graham Keir MD[2], Christopher Caravella LNMT, MHA[1], Sean A. P. Clouston PhD[3], Josephine Rini MD[1], Ana M. Franceschi MD, PhD[1]

[1]Donald and Barbara Zucker School of Medicine at Hofstra/Northwell, Manhasset, NY, USA. [2]Piedmont South Imaging, Newnan, GA, USA. [3]Stony Brook University, Stony Brook, NY, USA

Abstract Category

Functional/Advanced Imaging

Purpose

In certain breast cancer subtypes that exhibit specific metastatic patterns, such as estrogen receptor (ER)-positive breast cancer with its predilection for the central nervous system, MRI remains the gold standard for detecting structural brain abnormalities. However, conventional MRI lacks the ability to provide information on the receptor status of metastases, which is particularly relevant for patient management of ER-positive breast cancer. [^{18}F]-fluoroestradiol (^{18}F -FES) is a novel molecular imaging radiopharmaceutical which binds specifically to ER, and enables direct visualization of ER-positive metastases. Our purpose was to determine if hybrid ^{18}F-FES PET/MRI is superior to conventional MRI alone for detecting ER-positive brain and calvarial metastases.

Materials & Methods

Following IRB approval, a retrospective analysis was conducted of patients that underwent ^{18}F –FES brain PET/CT and contrast-enhanced MRI brain at our institution. The ^{18}F-FES brain PET and MRI were fused using MIMNeuro software (version 7.3.2). All intracranial lesions, including parenchymal, dural based, calvarial, and extracranial soft tissue/scalp, were analyzed by a board-certified fellowship trained neuroradiologist with 10 years of clinical and research experience in brain PET/MRI, and lesion size, location and SUVmax were recorded. Two radiology residents reviewed separately acquired contrast-enhanced MRI brain reports, and documented the number and location of intracranial lesions listed.

Results

Eleven female patients with ER-positive breast cancer with 92 metastatic brain and calvarial lesions were included. The mean age was 64.3 years (SD +/- 7.5). 55/92 (59.8%) lesions were positive on ^{18}F –FES, while 37/92 (40.2%) were negative on ^{18}F –FES. SUVmax values for ^{18}F –FES positive lesions ranged from 0.77-14.47 with an average value of 3.27 (SD +/- 2.6). Of the 92 lesions, 16 (17.4%) were occult by contrast-enhanced MRI brain, and detected only by ^{18}F-FES PET/MRI. Two additional ^{18}F –FES PET positive lesions in the head and neck were not included in the field of view on MRI brain.

Conclusion

By integrating [^{18}F]-fluoroestradiol (^{18}F -FES) PET/MRI into our clinical workflow, we improved detection of ER-positive lesions that may otherwise remain occult on structural imaging alone. Hybrid ^{18}F –FES PET/MRI leverages the high-resolution anatomical information provided by MRI with the specific receptor-based molecular data conferred by ^{18}F-FES PET to optimize detection and identification of ER-positive metastases. The increased sensitivity and specificity of hybrid ^{18}F –FES PET/MRI for ER-positive lesions contributes to a comprehensive assessment of the anatomic and molecular tumor profile, thereby addressing the limitations of structural imaging. In addition to its diagnostic advantages, the theranostic impact of hybrid ^{18}F –FES PET/MRI will be elucidated by further research, as it carries significant implications for personalized and precise therapeutic interventions.

References

1. Ivanidze J, Sharbatdaran A, McCalla A, et al. [^{18}F]-Fluoroestradiol (FES) brain PET in the evaluation of patients with estrogen receptor positive breast cancer and known or suspected brain metastases. *Eur J Radiol*. Published online October 15, 2024. doi:10.1016/j.ejrad.2024.111791.
2. Ivanidze J, Subramanian K, Youn T, et al. Utility of [^{18}F]-fluoroestradiol (FES) PET/CT with dedicated brain acquisition in differentiating brain metastases from posttreatment change in estrogen receptor-positive breast cancer. *Neurooncol Adv*. 2021;3(1):vdab178. Published 2021 Nov 30. doi:10.1093/noajnl/vdab178.
3. Ulaner GA, Mankoff DA, Clark AS, et al. Summary: Appropriate Use Criteria for Estrogen Receptor-Targeted PET Imaging with 16α-18F-Fluoro-17β-Fluoroestradiol. *J Nucl Med*. 2023;64(3):351-354. doi:10.2967/jnumed.123.265420.

4. Urso L, Bonatto E, Nieri A, et al. The Role of Molecular Imaging in Patients with Brain Metastases: A Literature Review. *Cancers (Basel)*. 2023;15(7):2184. Published 2023 Apr 6. doi:10.3390/cancers15072184.

Images/Tables

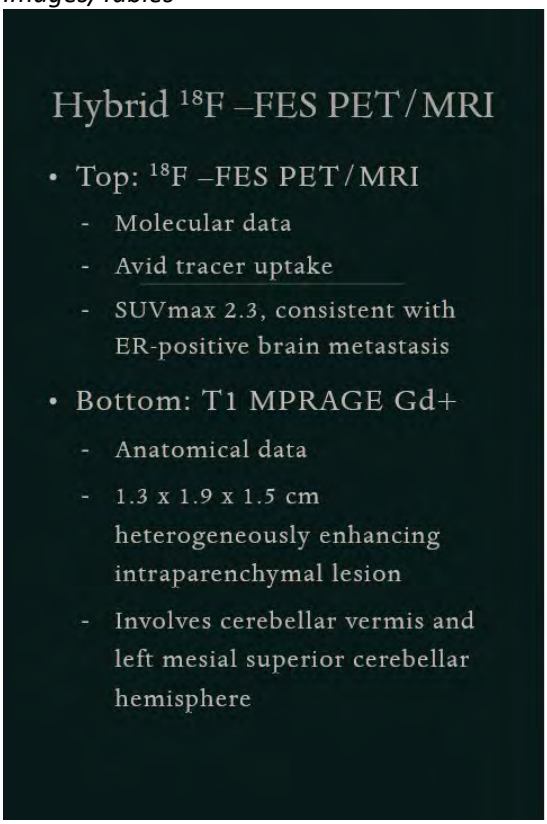

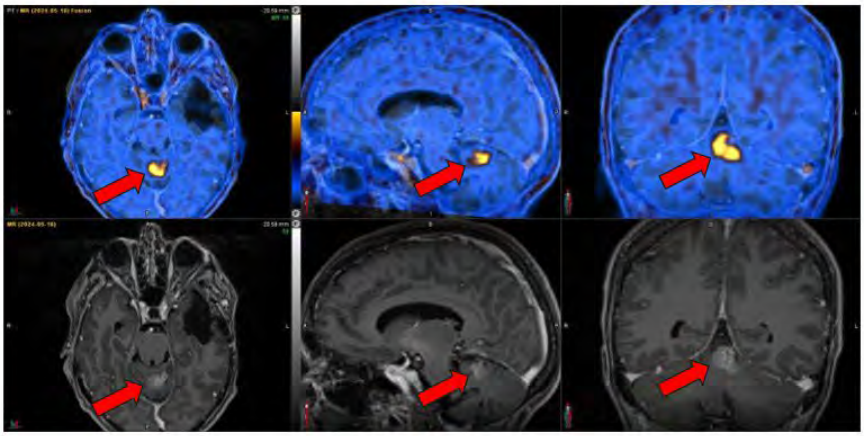

485

GRASP MRI of Low-flow Vascular Malformations and Infantile Hemangiomas in the Head and Neck

Angela Kanna MD[1], Matthew Lee MD[1], Mari Hagiwara MD[1], Nabeeha Khan[1], Joanne Rispoli MD[2], Gopi Nayak MD[1], Girish Fatterpekar MD[1], Gul Moonis MD[1]

[1]NYU Grossman School of Medicine, New York, New York, USA. [2]Boston Children's Hospital, Boston, MA, USA

Abstract Category

Head & Neck

Purpose

Golden-angle Radial Sparse Parallel (GRASP) MRI is a 3D dynamic contrast-enhanced sequence with high spatial and temporal resolution, and decreased vulnerability to motion artifacts. Previous research has demonstrated the utility of contrast-enhanced MRI in distinguishing high-flow lesions such as infantile hemangiomas (1) from low-flow vascular malformations throughout the body, thus impacting clinical management (2,3). The purpose of this study was to use GRASP imaging to evaluate perfusion characteristics and differentiate between low-flow vascular malformations and infantile hemangiomas in the head and neck.

Materials & Methods

This retrospective study is institutional review board-approved and Health Insurance Portability and Accountability Act compliant. We performed a radiology report search for the terms “venous malformation, venolymphatic malformation, lymphatic malformation, and hemangioma” and MRI of the head and neck using GRASP imaging between 2015 and 2020. This yielded a total of 23 patients (aged 1 to 78 years, 14 female and 9 male) with clinically diagnosed and untreated neck and skull base vascular lesions, of which 17 patients had venous, lymphatic, or venolymphatic malformations, and 6 patients had infantile hemangiomas.

GRASP technique has been previously described. Imaging was performed using MRI systems with a field strength of 1.5T or 3T (Siemens Healthcare). Acquisition parameters included the following: repetition time = 3.44 to 5.17 ms, echo time = 1.70 to 2.28 ms, flip angle = 9 to 12 degrees, field of view = 180x180 to 256x256, and 1 mm isotropic spatial resolution.

After a delay of 20 seconds from sequence start, a single 0.1 mL/kg gadobutrol bolus (Gadavist, Bayer Schering Pharma) was administered intravenously at the rate of 4 mL/second. Time of acquisition for the GRASP sequence ranged from 2 to 4 minutes, and images were reconstructed with a median temporal resolution of 11.4 seconds/frame (range, 7.7 to 12.3 seconds/frame).

Data collection and analysis was performed under the supervision of a board-certified neuroradiologist. Using the software Olea Sphere 3.0 (Olea Medical), an elliptical region of interest (ROI) with an area of approximately 1 to 5 mm^2 was drawn in the maximally enhancing portion of the lesion. An additional ROI was drawn in the superior sagittal sinus (SSS) on each scan as an internal control. Signal-time data were obtained from each ROI, and the slopes of the curves during wash-in were derived, defined as the period of maximal rate of increasing signal in the SSS. Wash-in slope ratios were calculated, normalized to the SSS. Comparison was made between the mean normalized wash-in slope ratios of low-flow vascular malformations and infantile hemangiomas. Unpaired one-tail unequal variance T-test was performed using Microsoft Excel with significance level < 0.05.

Results

Mean wash-in ratios of venous, lymphatic, and mixed venolymphatic malformations were significantly lower when compared to infantile hemangiomas (Table 1, p value = 0.005).

Conclusion

GRASP MRI provides high-resolution perfusion data that can reliably differentiate between infantile hemangiomas and low-flow vascular malformations in the head and neck and can be a useful adjunct to conventional imaging.

References

1. Behr GG, Johnson C. Vascular anomalies: hemangiomas and beyond—part 1, fast-flow lesions. Am J Roentgenol 2013; 200(2): 414-422. DOI: https://www.ajronline.org/doi/10.2214/AJR.11.7852
2. van Rijswijk CSP, van der Linden E, van der Woude HJ, et al. Value of dynamic contrast-enhanced MR imaging in diagnosing and classifying peripheral vascular malformations. Am J Roentgenol 2002;178(5): 1181-1187. DOI: https://doi.org/10.2214/ajr.178.5.178118
3. Lee MD, Young MG, Fatterpekar GM. The pituitary within GRASP – Golden-angle radial sparse parallel dynamic MRI technique and applications to the pituitary gland. Semin Ultrasound CT MRI 2021;42:307-315. DOI: https://doi.org/10.1053/j.sult.2021.04.007
4. Khan N, Lee M, Ismail N, et al. GRASP dynamic contrast enhanced MRI can be used to monitor response to radiation in head and neck paragangliomas. Eastern Neuroradiological Society, 2024 annual meeting, Washington, D.C.
5. Ohgiya Y, Hashimoto T, Gokan T, et al. Dynamic MRI for distinguishing high-flow from low-flow peripheral vascular malformations. Am J Roentgenol 2005; 185(5): 1131-1137. DOI: https://doi.org/10.2214/AJR.04.1508

Images/Tables

Table 1: Mean wash-in ratios of low-flow (venous, lymphatic, and mixed venolymphatic) malformations as compared to infantile hemangiomas. Values reported are mean ± standard deviation.

Low-flow Vascular Malformations	Infantile Hemangiomas	P Value
0.190 ± 0.196	0.722 ± 0.341	0.005

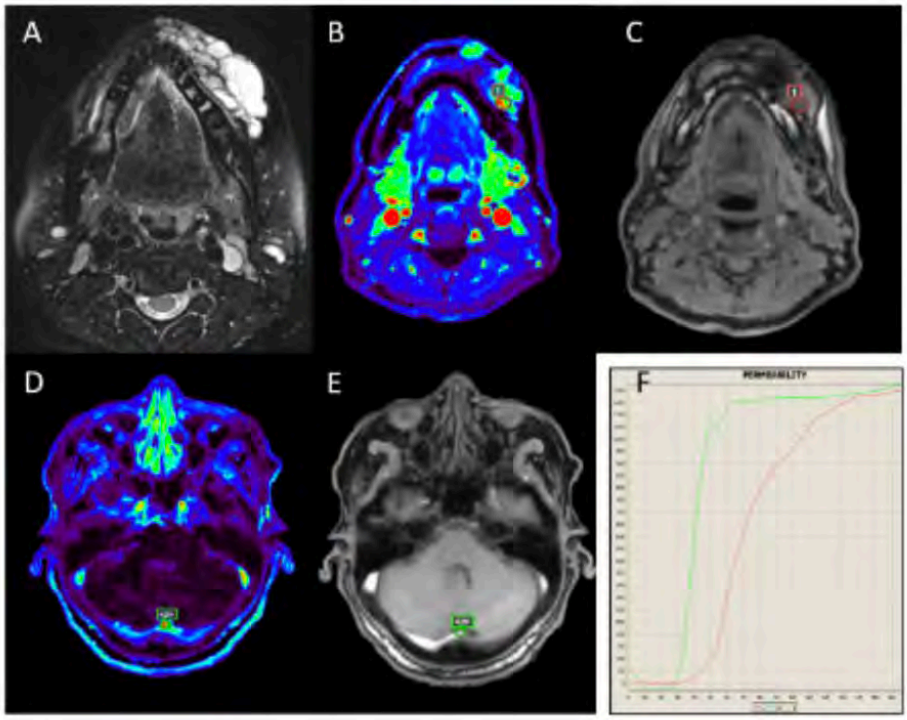

Figure 1: Axial STIR image (A) shows a lobulated, hyperintense lesion in the left premandibular buccal space. A region of interest (ROI) was drawn in the area of greatest enhancement within the lesion using color maps (B) derived from GRASP images (C), and a control ROI was drawn in the superior sagittal sinus (D and E). The lesion demonstrates slow but progressive enhancement relative to the superior sagittal sinus (F) and proved to be a venous malformation.

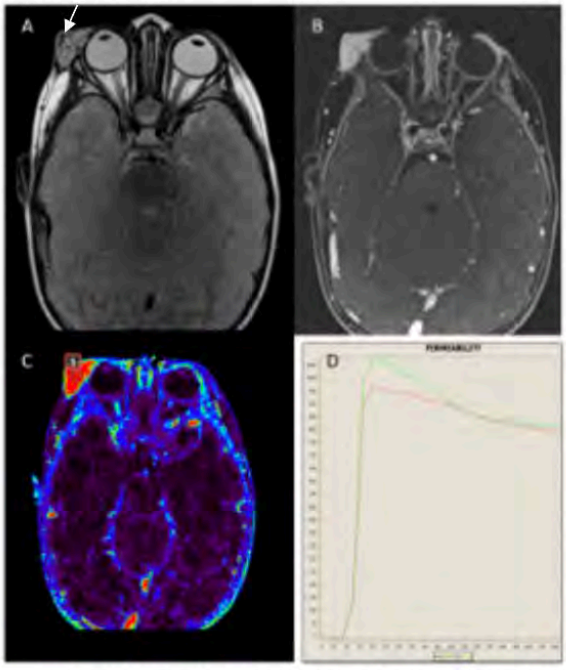

Figure 2: Axial T2-weighted image (A) shows a hyperintense lesion with flow voids (white arrow) in the right periorbital soft tissues, with avid enhancement on post-contrast GRASP images (B). An ROI was drawn within the lesion on peak enhancement color maps (C), as well as within the superior sagittal sinus (not shown). The permeability curve of the lesion closely follows that of the superior sagittal sinus. This was a capillary hemangioma in a two-year old child.

489

Web-like Arachnoid Membranes are Common in Intracranial Hemorrhage and "Benign" Enlargement of Subarachnoid Spaces in Infancy

Onur Simsek MD[1], Amirreza Manteghinejad MD[2], Carmen Cerron Vela MD[1], Sara Reis Teixeira MD, PhD[2], Matthew T Whitehead MD[2]

[1]Children's Hospital of Philadelphia, Philadlephia, PA, USA. [2]Children's Hospital of Philadelphia, Philadelphia, PA, USA

Abstract Category

Pediatrics

Purpose

Enlargement of subarachnoid spaces in infancy (ESSI) is an idiopathic condition characterized by macrocephaly and subarachnoid space expansion. ESSI is generally considered a benign entity due to its typical self-resolving nature and is usually diagnosed incidentally. Posthemorrhagic and postinflammatory arachnoid membranes in the subarachnoid cisterns can be a barrier to normal CSF flow dynamics. We aim to compare arachnoid membrane visibility among healthy children, children with ESSI, and children with hemorrhage using balanced steady-state free procession (b-SSFP) sequences.

Materials & Methods

In this IRB-approved cross-sectional study from a single pediatric hospital, brain MRI examinations with balanced steady-state free procession sequences were evaluated from three groups of subjects: (1) infants with intracranial hemorrhage, (2) infants with ESSI, and (3) infants with no intracranial pathology. Subjects with a history of prior intracranial intervention and subjects with pathologies other than hemorrhage were excluded. In each case, b-SSFP sequences were assessed for (1) web-like arachnoid membranes in the cisternal/subarachnoid spaces of the posterior fossa and suprasellar region (categorically as present or absent), (2) Liliequist membrane visibility [ordinally as absent (0), likely present (1), or present (2) for each of its three subsections summing to a maximum score of 6], and (3) Liliequist membrane thickening[ordinally as compared to 3rd ventricular floor thickness: <½ thickness (1), ½ to full thickness (2), or > full thickness (3). Fifty-one randomly selected cases were evaluated by a second pediatric radiologist to assess interobserver variability. Pearson's chi-square test, Fisher-Freeman-Halton exact test, Fisher's exact test, Kruskal-Wallis test, and Dunn's test were used to compare the groups and the pair-wise comparisons. The Benjamini-Hochberg method was used to correct the p-values for pairwise comparisons. Cohen's kappa and two-way random effects model, absolute agreement intraclass correlation coefficient (ICC) were used to assess the agreements between the readers.

Results

A total of 76 patients were included: 44 males (57.9%) and 32 females (42.1%). Of these, 34 (44.7%) had hemorrhage, 13 (17.1%) were diagnosed with ESSI, and 29 (38.2%) were healthy. Web-like subarachnoid membrane visibility differed significantly among the three groups ($p<0.001$). Pair-wise comparisons showed the differences were between the hemorrhage and healthy groups (94.1% vs. 41.4%, $p<0.003$) and the ESSI and healthy groups (92.3% vs. 41.4%, $p=0.003$). Liliequist membrane visibility also differed significantly among groups (hemorrhage group: 5[IQR:4-6]; ESSI group: 5[IQR: 4-5.5]; healthy group: 4 [IQR: 3-5], $p=0.011$). Pair-wise comparisons showed the differences were between the hemorrhage and healthy groups ($p=0.026$) and the ESSI and healthy groups ($p=0.026$). Liliequist membrane thickness varied significantly among and between groups, being thicker in subjects with ESSI and hemorrhage ($p=0.005$); however, pair-wise comparisons showed the difference was only between the ESSI and healthy groups ($p=0.009$). The inter-rater reliability analysis for diagnosing web-like membranes resulted in a kappa coefficient of 0.748, indicating substantial agreement.

Conclusion

Web-like arachnoid membranes and Liliequist membrane prominence are shared common features in children with intracranial hemorrhage and ESSI. Our findings suggest that ESSI may be associated with prior intracranial hemorrhage, especially since both ESSI and intracranial hemorrhage have a higher prevalence in premature patients.

References

1. Fushimi Y, Miki Y, Ueba T, et al. Liliequist membrane: three-dimensional constructive interference in steady state MR imaging. Radiology 2003;229:360–5; discussion 365. DOI: https://10.1148/radiol.2292021507

2. Lu S, Brusic A, Gaillard F. Arachnoid Membranes: Crawling Back into Radiologic Consciousness. AJNR Am J Neuroradiol 2022;43:167–75. DOI: https://10.3174/ajnr.A7309

3. Dinçer A, Kohan S, Ozek MM. Is all “communicating” hydrocephalus really communicating? Prospective study on the value of 3D-constructive interference in steady state sequence at 3T. AJNR Am J Neuroradiol 2009;30:1898–906. DOI: https://10.3174/ajnr.A1726
4. Raissaki M, Adamsbaum C, Argyropoulou MI, et al. Benign enlargement of the subarachnoid spaces and subdural collections-when to evaluate for abuse. Pediatr Radiol 2023;53:752–67. DOI: https://10.1007/s00247-023-05611-y
5. Fossmark MO, Bakøy H, Songstad NT, et al. The prevalence of subdural blood products in extremely premature infants with no history of abusive head trauma, studied by magnetic resonance imaging around term-equivalent age. Pediatr Radiol https://doi.org/10.1007/s00247-024-06060-x. DOI: https://10.1007/s00247-024-06060-x

Images/Tables

Web-like Arachnoid Membranes are Common in Intracranial Hemorrhage and “Benign” Enlargement of Subarachnoid Spaces in Infancy

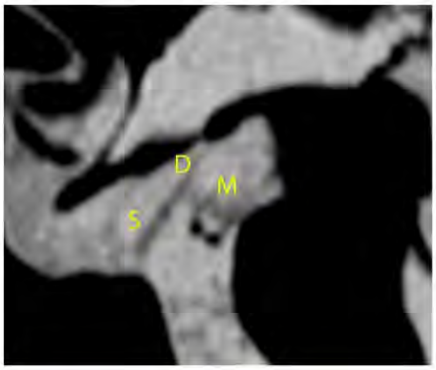

Sagittal brain CISS MRI of an infant with ESSI shows sellar (S), diencephalic (D), and mesencephalic (M) components of the Liliequist membrane. We scored each component of the Liliequist membrane as no identification = 0, probable identification= 1, and positive identification= 2. Higher visibility of the Liliequist membrane was a common feature of both the ESSI group and the hemorrhage group.

Plot shows the prevalence of web-like membranes within the subarachnoid space on balanced steady-state free precession (b-SSFP) sequences. Visibility of the web-like membranes was significantly different among the three groups but was a common feature between infants with ESSI and infants with hemorrhage.

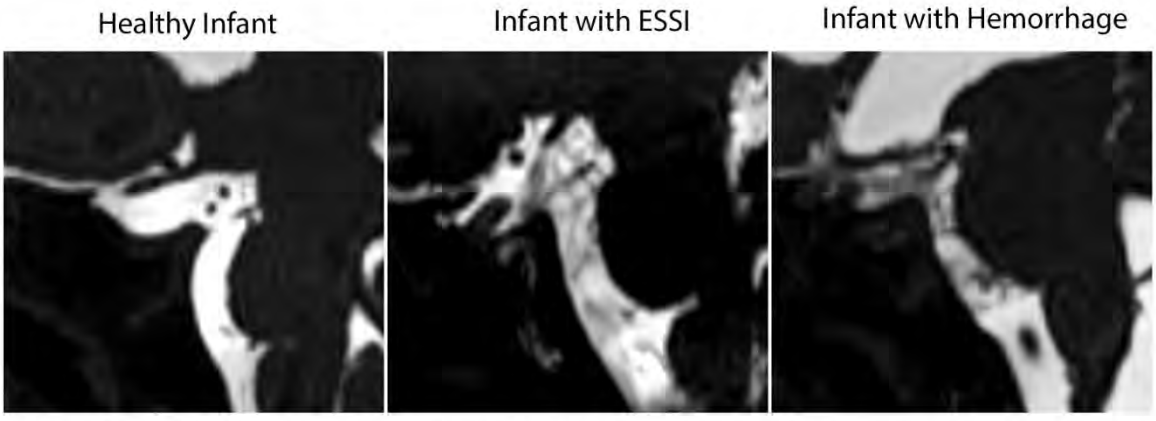

Sagittal brain CISS MRI of three different infants. MRI of the healthy infant shows normal subarachnoid cisterns without any web-like membranes. MRI of the infant with ESSI demonstrates web-like arachnoid membranes within the interpeduncular and prepontine cisterns. MRI of the infant with intraventricular hemorrhage again shows webbed arachnoid membranes within the chiasmatic, interpeduncular, and prepontine cisterns.

508

Endovascular Therapy vs. Medical Management in Isolated Anterior Cerebral Artery Acute Ischemic Stroke: A Multinational Multicenter Propensity Score-Weighted Study

Hamza Adel Salim MD[1], Benjamin Pulli MD[2], Dhairya A. Lakhani MD[3], Tobias D. Faizy MD[4], Jeremy J. Heit MD PhD[2], Basel Musmar MD[5], Adam A. Dmytriw MD[6], Adrien Guenego MD[7], Max Wintermark MD[1], Vivek Yedavalli MD[8]
[1]MD Anderson Cancer Center, Houston, TX, USA. [2]Stanford Medical Center, Palo Alto, CA, USA. [3]West Virginia University, Morgantown, WV, USA. [4]University Medical Center Münster, Münster, Germany, Germany. [5]Louisiana State University, Louisiana, LA, USA. [6]Massachusetts General Hospital, Boston, MA, USA. [7]Erasme University Hospital, Brussels, Brussels, Belgium. [8]Johns Hopkins Medical Center, Baltimore, MD, USA

Abstract Category

Pediatrics

Purpose

Isolated anterior cerebral artery occlusions (ACAo) in acute ischemic stroke patients present significant challenges due to their rarity. The efficacy and safety of endovascular therapy (EVT) in comparison with best medical therapy (BMT) for ACAo remains unclear. We aimed to assess the outcomes of these treatments.

Materials & Methods

This multinational, multicenter study analyzed data from the MAD-MT registry. Data were collected retrospectively from 37 sites across North America, Asia, and Europe. Inverse Probability of Treatment Weighting (IPTW) was applied to balance confounding variables. The primary outcome was functional independence (modified Rankin Scale (mRS) scores of 0-2) at 90 days. Secondary outcomes included excellent outcomes (mRS 0-1), mortality at 90 days, and NIH Stroke Scale (NIHSS) score on day one post treatment.

Results

Of the 108 patients, 36 received BMT and 72 underwent EVT. The median age was 75 years, and 56% were male. At 90 days, 40% of patients achieved mRS 0-2, with no significant difference between EVT and BMT (38% vs. 45%, p=0.46). Procedural success (mTICI 2b-3) was 91% in EVT patients, with a sICH rate of 2.9%. IPTW-adjusted analysis showed no significant difference between EVT and BMT for functional independence (OR 1.17, 95% CI 0.23-6.02, p=0.85), mortality (25% vs. 21%, p=0.71) or day-one NIHSS scores (Beta 2.2, 95% CI -0.51 to 4.8, p=0.11).

Conclusion

EVT showed high procedural success but did not significantly improve functional outcomes or mortality compared to BMT in ACAo patients. Further randomized trials are needed to clarify EVT's role in ACAo.

References

Salim HA, Yedavalli V, Musmar B, Adeeb N, E L Naamani K, Henninger N, Sundararajan SH, Kühn AL, Khalife J, Ghozy S, Scarcia L, Tan BYQ, Heit JJ, Regenhardt RW, Cancelliere NM, Bernstock JD, Rouchaud A, Fiehler J, Essibayi MA, Sheth SA, Puri AS, Barreau X, Colasurdo M, Renieri L, Dyzmann C, Marotta T, Spears J, Mowla A, Jabbour P, Filipe JP, Biswas A, Harker P, Clarençon F, Radu RA, Siegler JE, Nguyen TN, Varela R, Ota T, Gonzalez N, Moehlenbruch MA, Altschul D, Gory B, Costalat V, Stracke CP, Aziz-Sultan MA, Hecker C, Shaikh H, Liebeskind DS, Baker A, Pedicelli A, Alexandre A, Faizy TD, Tancredi I, Kalsoum E, Lubicz B, Patel AB, Mendes Pereira V, Guenego A, Dmytriw AA; MAD MT Investigators. Endovascular therapy versus best medical management in distal medium middle cerebral artery acute ischaemic stroke: a multinational multicentre propensity score-matched study. J Neurol Neurosurg Psychiatry. 2024 Jul 23:jnnp-2024-333669. doi: 10.1136/jnnp-2024-333669. Epub ahead of print. PMID: 39043567.

Images/Tables

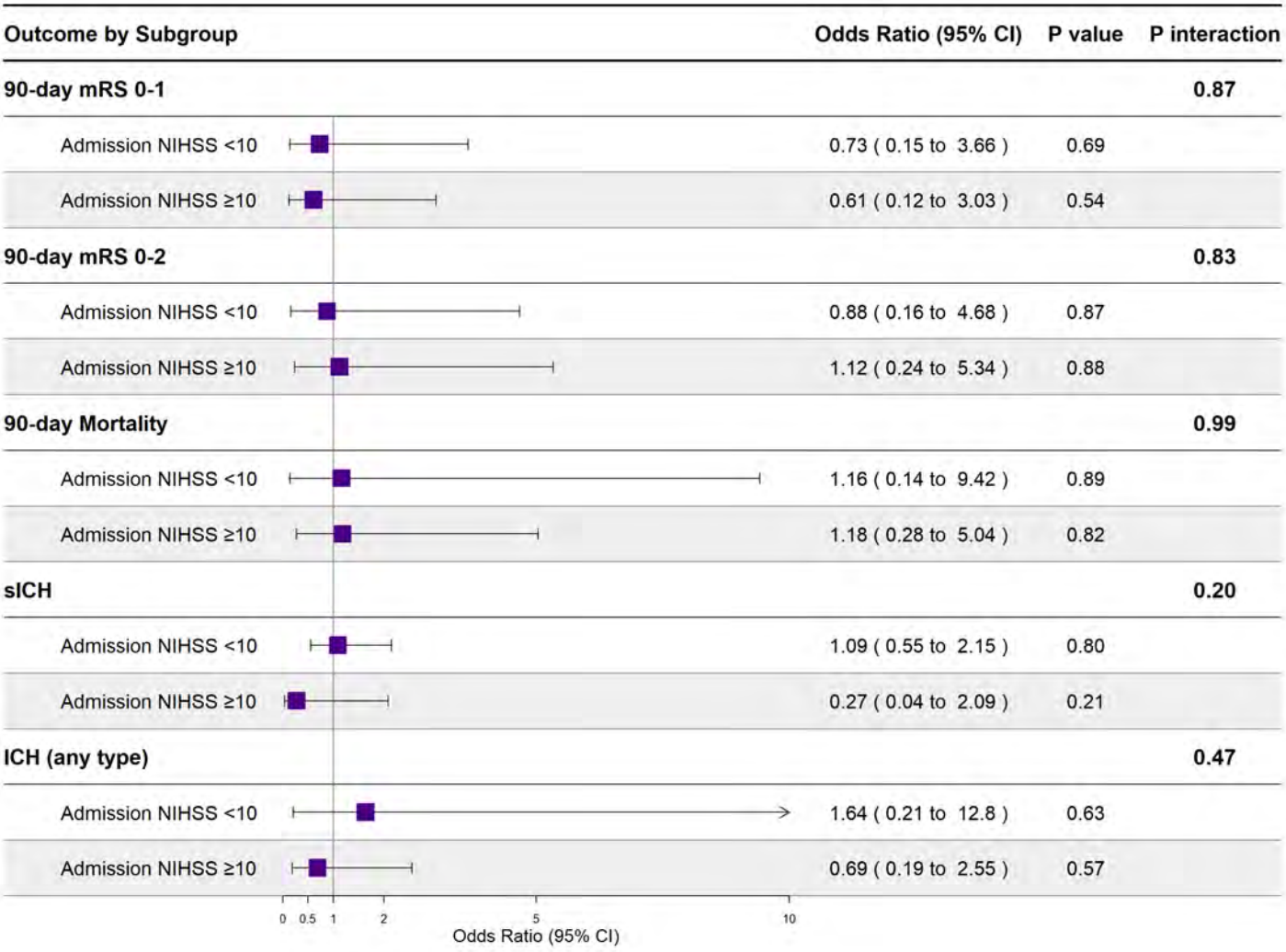

510

Prolonged Venous Transit Associated with Reduced Likelihood of Excellent Functional Outcome After Successful Reperfusion in Anterior Circulation Large-Vessel Occlusion Stroke

Hamza Adel Salim MD[1], Dhairya A. Lakhani MD[2], Janet Mei MD[3], Nathan Z. Hyson MD[3], Vaibhav Vagal MD[4], Kambiz Nael MD[5], Gregory W Albers MD[6], Tobias D. Faizy MD[7], Jeremy J. Heit MD PhD[6], Max Wintermark MD[1], Vivek Yedavalli MD[3]
[1]MD Anderson Cancer Center, Houston, TX, USA. [2]West Virginia University, Morgantown, WV, USA. [3]Johns Hopkins Medical Center, Baltimore, MD, USA. [4]Renaissance School of Medicine at Stony Brook University, New York, NY, USA. [5]University of California San Francisco, San Francisco, CA, USA. [6]Stanford Medical Center, Palo Alto, CA, USA. [7]University Medical Center Münster, Münster, Münster, Germany

Abstract Category

Head & Neck

Purpose

Acute ischemic stroke due to anterior circulation large-vessel occlusion (AIS-LVO) remains a leading cause of disability despite successful reperfusion therapies. Prolonged venous transit (PVT) has emerged as a potential prognostic imaging biomarker in AIS-LVO. We investigated whether PVT is associated with a decreased likelihood of excellent functional outcome (modified Rankin Scale [mRS] score of 0–1 at 90 days) after successful reperfusion.

Materials & Methods

In our prospectively collected, retrospectively reviewed database, we analyzed data from 104 patients with AIS-LVO who achieved successful reperfusion (modified Thrombolysis in Cerebral Infarction [mTICI] score of 2b/2c/3) between September 2017 and September 2022. PVT was defined as a time to maximum (Tmax) of ≥10 seconds in the superior

sagittal sinus and/or torcula on computed tomography perfusion imaging. Patients were categorized into PVT-positive and PVT-negative groups. The primary outcome was excellent functional recovery at 90 days.

Results

Of the 104 patients, 30 (29%) were PVT+. Excellent functional outcome was achieved in 38 patients (37%). PVT+ patients had a significantly lower rate of excellent recovery compared to PVT- patients (11% vs. 39%; P<0.001). After adjusting for possible confounders, PVT+ was independently associated with lower odds of excellent recovery (adjusted OR, 0.11; 95% CI, 0.02 to 0.48; P=0.006).

Conclusion

Among patients with AIS-LVO who achieved successful reperfusion, PVT+ was independently associated with a decreased likelihood of excellent functional outcome at 90 days. Assessment of PVT on CT perfusion may provide valuable prognostic information and aid in clinical decision-making for patients with AIS-LVO.

References

Salim HA, Yedavalli V, Musmar B, Adeeb N, E L Naamani K, Henninger N, Sundararajan SH, Kühn AL, Khalife J, Ghozy S, Scarcia L, Tan BYQ, Heit JJ, Regenhardt RW, Cancelliere NM, Bernstock JD, Rouchaud A, Fiehler J, Essibayi MA, Sheth SA, Puri AS, Barreau X, Colasurdo M, Renieri L, Dyzmann C, Marotta T, Spears J, Mowla A, Jabbour P, Filipe JP, Biswas A, Harker P, Clarençon F, Radu RA, Siegler JE, Nguyen TN, Varela R, Ota T, Gonzalez N, Moehlenbruch MA, Altschul D, Gory B, Costalat V, Stracke CP, Aziz-Sultan MA, Hecker C, Shaikh H, Liebeskind DS, Baker A, Pedicelli A, Alexandre A, Faizy TD, Tancredi I, Kalsoum E, Lubicz B, Patel AB, Mendes Pereira V, Guenego A, Dmytriw AA; MAD MT Investigators. Endovascular therapy versus best medical management in distal medium middle cerebral artery acute ischaemic stroke: a multinational multicentre propensity score-matched study. J Neurol Neurosurg Psychiatry. 2024 Jul 23:jnnp-2024-333669. doi: 10.1136/jnnp-2024-333669. Epub ahead of print. PMID: 39043567.

537

Reevaluating Occipital Condyle Fractures: Key Findings from Trauma Data

Mahla Radmard MD, Armin Tafazolimoghadam MD, Akua Afrah Amoah MD, Dhairya A Lakhani MD, Tej D Azad MD, Ali Bydon MD, David M Yousem MD

Johns Hopkins University School of Medicine, Baltimore, MD, USA

Abstract Category

Head & Neck

Purpose

Occipital condyle fractures (OCFs) are classified by the Anderson and Montesano system into Type I (comminuted, minimally displaced), Type II (stable, associated with basilar skull fractures), and Type III (unstable avulsion fractures) and are often associated with cervical and intracranial injuries.

We sought to determine the incidence and characteristics of the different types of OCFs, their respective mechanisms of injury, and rate of associated intracerebral and cervical spine injuries.

Materials & Methods

We retrospectively reviewed the CT brain and CT cervical spine reports performed from July 2018 to August 2023 for OCFs. Variables collected included age, sex, clinical presentation, mechanism of injury, coincident brain and cervical spine injuries, treatments, and Anderson and Montesano classification.

Results

Sixty-three of 24,986 patients (0.25%) had OCFs, predominantly male (41 males, 22 females), with an average age of 51.1 years; 22/63 (34.9%) occurred in asymptomatic patients. Concurrent injuries included cervical spine fractures (33.3%) at C1 and C2 and intracranial injuries (47.6%), mostly subarachnoid and subdural hemorrhages. OCFs were categorized into Type I (9 cases), Type II (24 cases), and Type III (30 cases), with unstable Type III fractures more common in MVC victims; stable fractures had higher rates of intracranial injuries. There were no significant differences in morbidity, mortality, or concurrent cervical spine or chest/abdominal/pelvic findings between stable and unstable OCFs.

Conclusion

The study highlights the importance of comprehensive imaging and evaluation in trauma cases to identify OCFs, even in asymptomatic patients, with a high rate of concurrent C1-2 and intracranial injuries.

References
Anderson PA, Montesano PX. Morphology and treatment of occipital condyle fractures. *Spine (Phila Pa 1976).* 1988;13(7):731-736.

539

Characterizing Axonal Damage in Ischemic Stroke Using AxCaliber MRI in High-Gradient Diffusion Imaging

Aneri Bhatt[1], Qiuyun Fan[1], Liqi Shu[2], David Lin[3], Susie Y Huang[1]
[1]Athinoula A. Martinos Center for Biomedical Imaging, Department of Radiology, Massachusetts General Hospital, Boston, MA, USA. [2]Warren Alpert Medical School of Brown University, Providence, RI, USA. [3]Massachusetts General Hospital, Boston, MA, USA, Boston, MA, USA

Abstract Category
Adult Brain

Purpose
Stroke is a leading cause of death and neurological disability. The axon plays a central role in both injury and repair phases, such that the efficacy of axonal repair directly determines functional recovery. A non-invasive biomarker of axonal integrity would be invaluable for tracking and predicting motor outcomes and determining rehabilitation strategies[1].

AxCaliber MRI enables the extraction of axon diameter and density in white matter tracts in patients, independent of fiber orientation and distribution[2]. This could expand our understanding of white matter damage and recovery in the living human brain beyond diffusion tensor imaging. In this study, the AxCaliber-SMT method was used to evaluate these alterations in patients following acute ischemic stroke using high-gradient diffusion MRI on the 3T Connectome scanner. We also investigated the relationship between axonal injury and recovery of motor function.

Materials & Methods
We prospectively recruited adult patients who had experienced first-ever middle cerebral artery territory ischemic stroke occurring ≥6 months and ≤ 1 year prior to enrollment, with stroke affecting the motor cortex within one hemisphere and NIHSS arm score at presentation of 3-4.

Five patients (38-74 years, 5M) and five healthy age-matched controls (34-69 years, 2M)were included (Fig. 1). The Fugl-Meyer Assessment (FMA) was administered at patient visits. Diffusion MRI was acquired on the 3T Connectome scanner with maximum gradient strength of 300 mT/m using a custom-built 64 channel coil[3]. A 2D-diffusion-weighted EPI protocol with two diffusion times (D=19,49 ms) and 8 gradient strengths (25-293 mT/m per diffusion time) was used. DTI fitting was performed on b=950 s/mm^2 data to obtain fractional anisotropy (FA) maps. The AxCaliber-SMT framework was used on corrected dMRI data to estimate axon diameter index (a) and restricted signal fraction (f_r) as a measure of axon density. The JHU-ICBM-DTI-81 white matter atlas[4] was used to identify the posterior limb of the internal capsule (PLIC) and corona radiata, and labels were transformed to native subject space. ROI averages were extracted from each hemisphere.

The Wilcoxon rank sum test compared the ipsilesional hemisphere against contralateral hemisphere in stroke patients. The Mann-Whitney U test assessed differences between stroke patients and healthy controls.

Results
Figure 2 shows axial FA, a, and f_r maps in a representative stroke patient and age-matched control. f_r showed a significant decrease in the PLIC and corona radiata of the affected hemisphere compared to the contralateral (Fig. 3). A trend toward decreased f_r in the bilateral PLIC and corona radiata was seen in stroke patients compared to controls.

Conclusion
We observed significant reductions in restricted signal fraction in white matter tracts (PLIC + corona radiata) emanating from lesioned cortex compared to the contralateral hemisphere in stroke patients. Of note, FA may be reduced in normal crossing fiber-regions and injured white matter but was not consistently reduced in the stroke patients, suggesting that high-gradient diffusion MRI measures were more specific for axonal injury and loss[5]. The AxCaliber-SMT method provides new insight into axonal degeneration following ischemic injury and will be validated in larger, longitudinal studies examining the association between these metrics and stroke recovery.

References
1. Maraka, S., et al. Degree of corticospinal tract damage correlates with motor function after stroke. Ann Clin Transl Neurol 1, 891-899. 2014. doi: 10.1002/acn3.132.

2. Fan Q, Nummenmaa A, Witzel T, et al., 2020. Axon diameter index estimation independent of fiber orientation distribution using high-gradient diffusion MRI. Neuroimage 222, 117197. https://doi.org/10.1016/j.neuroimage.2020.117197.
3. Keil B, Blau JN, Biber S, et al., 2013. A 64-channel 3T array coil for accelerated brain MRI. Magn. Reson. Med 70, 248–258. DOI: 10.1002/mrm.24427.
4. JHU-ICBM-DTI-81 white matter atlas. https://fsl.fmrib.ox.ac.uk/fsl/fslwiki/Atlases. Accessed October 2024.
5. Alexander DC, Hubbard PL, Hall MG, et al., 2010. Orientationally invariant indices of axon diameter and density from diffusion MRI. Neuroimage 52, 1374–1389. DOI: 10.1016/j.neuroimage.2010.05.043.

Images/Tables

Figure 1: Demographics, time from initial presentation to imaging, and clinical characteristics of the stroke patients. NIHSS=NIH stroke scale. FMA=Fugl-Meyer Assessment. FMA-UE=Fugl-Meyer Upper Extremity. MCA=Middle Cerebral Artery.

	Age	Sex	Stroke Subtype	NIHSS Score	Time from Stroke	FMA-UE Score	FMA Score
Patient #1	60	M	R striatocapsular	7	13 months	3	23
Patient #2	74	M	R MCA	6	12 months	55	79
Patient #3	68	M	L MCA	11	9 months	59	82
Patient #4	61	M	R MCA	5	12 months	57	78
Patient #5	38	M	L MCA	2	5 months	65	89

Figure 2: Representative maps for FA, axon diameter, and restricted signal fraction in a 38-year-old man with left-sided middle cerebral artery (MCA) stroke (Patient #5) and an age- and sex-matched healthy control.

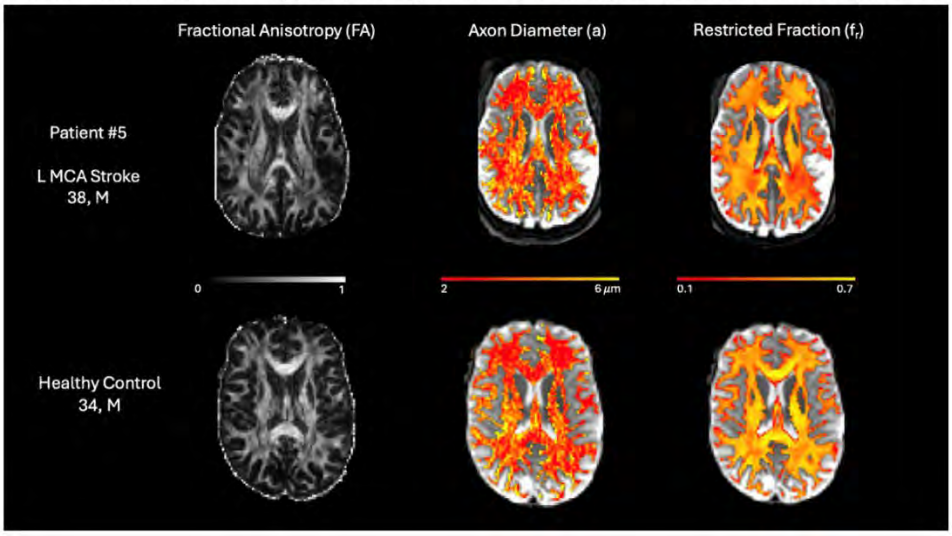

Figure 3: Boxplots comparing mean FA, axon diameter & restricted fraction between affected & contralateral normal-appearing PLIC & corona radiata within stroke patients.

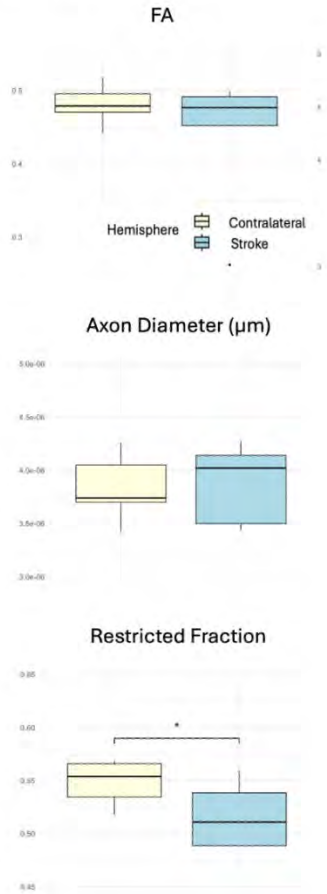

540

Towards Improved Diagnostic Accuracy of Amyloid-Targeted PET: Correlation of Z-scores derived from Normative Database Comparison with Clinical Standard-of-Care Visual Analysis.

Ashley Knight-Greenfield MD, Divya Yadav MD, Samantha Keil PhD, Arindam RoyChoudhury PhD, Michelle Roytman MD, Joseph R Osborne MD, PhD, Anna Nordvig MD, Gloria Chiang MD, Jana Ivanidze MD, PhD
New York Presbyterian Hospital - Weill Cornell Medical College, New York, NY, USA

Abstract Category

Adult Brain

Purpose

Amyloid-targeted PET (AβPET) is critical in the clinical diagnosis and management of Alzheimer disease. Clinical AβPET interpretation is based on visual assessment, assigning regional cortical tracer uptake (RCTU)-scores based on grey-white matter differentiation. Statistical Parametric Mapping (SPM) quantifies single-subject PET data by comparing to a

reference database, generating region-specific z-score maps. Here, we compared SPM-generated z-scores with corresponding visually determined RCTU-scores in a real-world cohort of patients undergoing AβPET as part of their clinical evaluation for cognitive impairment and consideration for Aβ-targeted therapy.

Materials & Methods

An IRB-approved retrospective analysis was performed on consecutive patients undergoing AβPET/CT or PET/MRI with [F18]Florbetaben. Researchers were blinded to clinical diagnosis. RCTU-scores were recorded for the frontal, parietal, temporal, and posterior cingulate gyrus (PCG)/precuneus regions per clinical standard-of-care. PET data were subsequently analyzed using SPM (Syngo.Via, Siemens Healthineers), generating region-specific z-scores. Spearman's correlation analyses and Mann-Whitney tests were performed to assess region-specific RCTU-z-score correlations, and to compare median z-scores between RCTU groups, respectively.

Results

42 patients met inclusion criteria. Mean age was 76 years; 43% were female. 26% of patients had brain amyloid plaque load (BAPL) 1, 12% BAPL 2, and 62% BAPL 3. There was a significant, strong correlation between RCTU- and z-scores in all regions with correlation coefficient of 0.88 in the frontal ($p<0.0001$, CI 0.78-0.93), 0.78 in the parietal ($p<0.0001$, CI 0.61-0.88), 0.84 in the temporal ($p<0.0001$, CI 0.72-0.91), and 0.86 in the PCG/precuneus regions ($p<0.0001$, CI 0.74-0.92). There were a total of 54, 18, and 96 RCTU1, 2, and 3 across all 42 subjects, respectively. A composite comparison pooling all regional RCTUs and corresponding z-scores demonstrated a significant difference between RCTU1 and RCTU2, RCTU2 and RCTU3, and RCTU1 and RCTU3 ($p<0.0001$ for all comparisons, figure). Region-specific subanalyses demonstrated median frontal z-score of 6.7 (range 2.8-11.5) corresponding to frontal RCTU3, and median z-score of –1.2 (range –3.5-1.9) corresponding to frontal RCTU1. A median parietal z-score of 3.1 (range 1.2-7.7) corresponded to parietal RCTU3, and median z-score of –1.1 (range –3-1.5) corresponded to parietal RCTU1. A median temporal z-score of 7.5 (range 2.4-17) corresponded to temporal RCTU3, and a median temporal z-score of –0.95 (range –4.8-2) corresponded to temporal RCTU1. A median PCG/precuneus z-score of 6.5 (range 2.8-9.9) corresponded to PCG/precuneus RCTU3, and a median PCG/precuneus z-score of –0.2 (range –2-1.9) corresponded to PCG/precuneus RCTU1. There was a significant difference between median z-scores comparing RCTU1 and RCTU3 in all regions ($p<0.0001$). Comparison between RCTU1 vs. RCTU2 and RCTU2 vs. RCTU3 was not analyzed for each individual region due to the small sample size of RCTU2.

Conclusion

This study establishes a baseline of region-specific z-score ranges generated from SPM, and respective RCTU-scores in a clinical cohort, and demonstrates a strong correlation between AβPET quantitative and visual assessment. Limitations include retrospective nature of the study and cohort heterogeneity. This work lays the foundation for integration of AβPET quantification into the clinical setting, and has the potential of improving diagnostic accuracy as well as enabling imaging-based treatment response assessment.

References

1. Rabinovici GD, Gatsonis C, Apgar C, et al. Association of Amyloid Positron Emission Tomography With Subsequent Change in Clinical Management Among Medicare Beneficiaries With Mild Cognitive Impairment or Dementia. JAMA. 2019 Apr 2;321(13):1286-1294. doi: 10.1001/jama.2019.2000. PMID: 30938796; PMCID: PMC6450276.

2. Smith NM, Ford JN, Haghdel A, et al. Statistical Parametric Mapping in Amyloid Positron Emission Tomography. Front Aging Neurosci. 2022 Apr 25;14:849932. doi: 10.3389/fnagi.2022.849932. PMID: 35547630; PMCID: PMC9083453.

Images/Tables

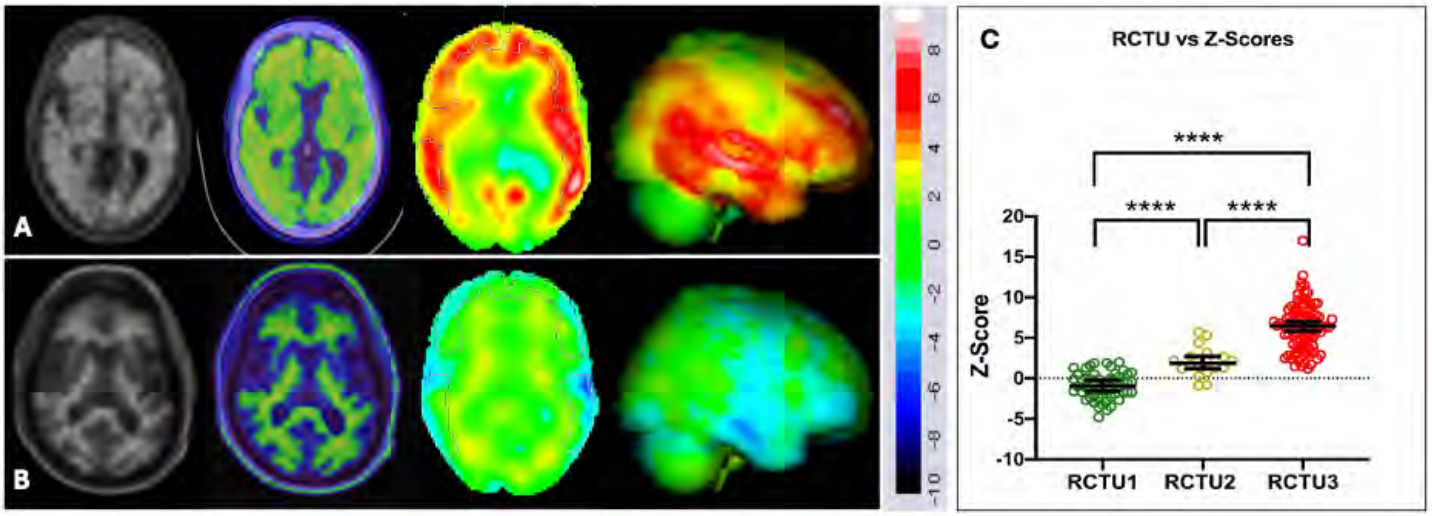

Figure: A, B. From left to right, representative axial slice [F18]Florbetaben AβPET images at the level of the frontal and temporal lobes, fused PET and PET CT (A) / PET MR (B) images, statistical parametric mapping (SPM, colors indicating Z-scores) with regions for Z-score calculations outlined, and right lateral 3D renderings of SPM. Rainbow color bar along the right of the figure demonstrates color scale with corresponding Z-scores/number of standard deviations from the mean in comparison to the normative control database (Syngo.Via, Siemens Healthineers). **A.** RCTU 3 in the frontal and temporal lobes, corresponding to Z-scores of 6.7 and 9.3, respectively. **B.** RCTU 1 in the frontal and temporal lobes, corresponding to Z-scores of -2.4 and -4.8, respectively. **C.** Scatter plot of composite data from all regions demonstrating difference in median Z-scores between RCTU 1, 2, and 3, with significant difference between all RCTU scores (**** denotes p<0.0001).

555

Characterization of the Internal Anatomy of the Human Dorsal Root Ganglion

Mridhula Muthukumar Masters in Anatomy
University Hospitals Cleveland, Cleveland, OH, USA

Abstract Category

Spine

Purpose

The dorsal root ganglion (DRG) is the collection of first-order pseudounipolar neuronal cell bodies that relay afferent information from the PNS to the CNS. The DRG is frequently evaluated by neuroradiologists, but its anatomic organization is not widely understood. Due to its significance in understanding pain sensation and its implications in chronic pain management and treatment, the microarchitecture of DRG has been the focus of numerous studies in recent years. Studies have shown that the DRG is divided into 2 distinct regions, the Cell-Body Rich Area (CBRA) and the Nerve Fiber Rich Area (NFRA), but these findings primarily depend on two-dimensional imaging methods which are inefficient in accurately visualizing the internal anatomy of a 3D neural structure. Microscopic-Computed Topography (microCT or µCT) is a 3D imaging technique that produces a complete three-dimensional visualization of neural structures at higher resolutions without disrupting tissue integrity. Therefore, using microCT, our team aims to better characterize the microarchitecture of the human DRG.

Materials & Methods

Laminectomies were conducted on four cadavers to extract the bilateral C4,T4 and L4 levels. These samples were either unstained or stained with radio-opaque stains such as phosphotungstic acid (PTA), osmium tetroxide and imaged via microCT (n=24) at isotropic voxel sizes of 25 µm, 20 µm, and 11.4 µm. 3D Slicer Image Computing Platform was used to segment and create 3D reconstructions of human DRGs.

Results

We report the first three-dimensional reconstruction of the human DRG at an isotropic voxel size of 11.4 µm. MicroCT and histology of human DRGs showed nerve fibers traveling centrally in the NFRA and cell bodies located in the periphery in the CBRA.

Conclusion

Our findings reveal that the internal anatomy of the human DRG is largely consistent with observations made in animal studies. There are distinct regions of the DRG that primarily consist of cell bodies vs nerve fibers. These findings help to better understand DRG fascicular organization and microarchitecture, which may aid neuroradiologists in accurately identifying abnormalities within the DRG on cross-sectional imaging. This, in turn, may aid in selecting targets for treatment of neuropathic or chronic low back pain.

References

Graham, R. D., Bruns, T. M., Duan, B., & Lempka, S. F. (2019). Dorsal root ganglion stimulation for chronic pain modulates Aβ-fiber activity but not C-fiber activity: A computational modeling study. *Clinical neurophysiology : official journal of the International Federation of Clinical Neurophysiology*, *130*(6), 941–951. https://doi.org/10.1016/j.clinph.2019.02.016

Images/Tables

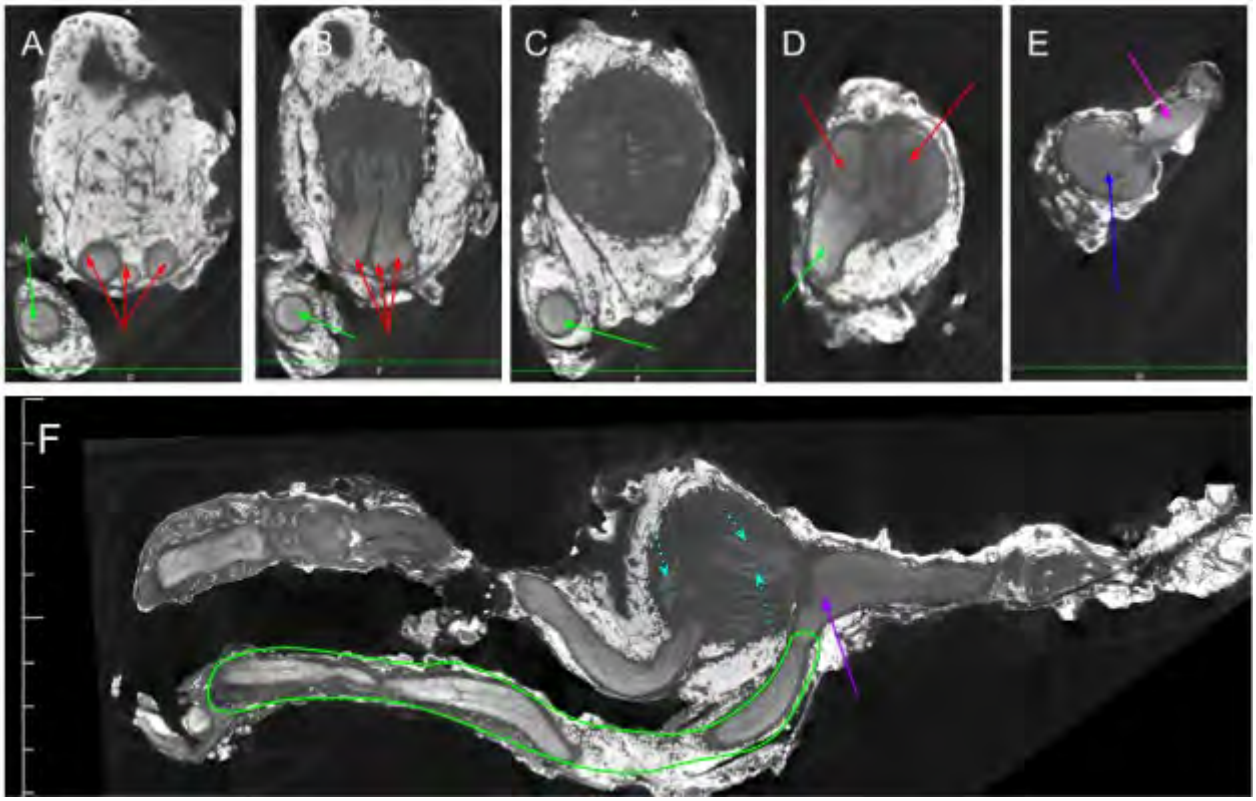

571

Prolonged venous transit as a superior predictor of functional outcomes in successfully reperfused large vessel occlusions: comparative analysis with cerebral blood volume index and hypoperfusion intensity ratio

Janet Mei[1], Hamza Salim[1], Dhairya Lakhani[2], Cynthia Greene[1], Francis Deng[1], Nathan Hyson[1], Licia Luna[1], Mona Shahriari[1], Jee Moon[1], Gregory Albers[3], Jeremy Heit[3], Tobias Faizy[4], Vivek Yedavalli[1]

[1]Johns Hopkins Hospital, Baltimore, MD, USA. [2]West Virginia University, Morgantown, West Virginia, USA. [3]Stanford University, Stanford, CA, USA. [4]University Medical Center Münster, Münster, N/A, Germany

Abstract Category

Head & Neck

Purpose

Collateral status is critical in the prognosis of acute ischemic stroke due to large vessel occlusion (AIS-LVO). Key components of a comprehensive collateral status evaluation include tissue-level collaterals (TLC) and venous outflow

(VO) following successful mechanical thrombectomy (MT) where arterial inflow has been restored. CT perfusion imaging-derived parameters, cerebral blood volume (CBV) index and hypoperfusion intensity ratio (HIR), serve as indicators of TLC, while prolonged venous transit (PVT) reflects VO. This study aims to assess the predictive power of these parameters for 90-day functional outcomes individually and in combination.

Materials & Methods

We conducted a retrospective analysis of prospectively collected data from consecutive adult AIS-LVO patients who underwent MT with successful reperfusion (modified Thrombolysis in Cerebral Infarction scores of 2b, 2c, or 3). PVT+ was defined by Tmax ≥10 seconds in the superior sagittal sinus (SSS), torcula, or both. Favorable HIR was categorized as < 0.4, while a favorable CBV index was defined as ≥ 0.8. We evaluated the sensitivity and specificity of PVT-, HIR < 0.4, and CBV index ≥ 0.8, and performed ROC analysis of PVT, HIR, CBV index, and their combinations generated by logistic regression models to compare the diagnostic and predictive performance of these parameters for favorable 90-day mRS outcomes (≤ 2).

Results

The study included 119 patients with a median age of 71 years (IQR 63-81), of whom 71 (59.7%) were female. Among these patients, 37 (30.3%) were classified as PVT+. Favorable HIR was observed in 57 (47.9%) patients, and 78 (65.5%) had a favorable CBV index. At the 90-day follow-up, 53.8% of patients achieved a favorable mRS score.

PVT- demonstrated a sensitivity of 84.4% for predicting favorable 90-day mRS outcomes, outperforming the CBV index (75.0%) and HIR (54.7%). The diagnostic performance of PVT- was significantly superior to HIR < 0.4 ($p<0.001$). PVT had a higher area under the curve (AUC) than continuous CBV index or HIR (AUC: 0.658, 0.60, 0.573, respectively), although there was no significant difference. Adding PVT to the CBV index significantly improved the prediction performance (PVT + continuous CBV index vs. continuous CBV index AUC: 0.716 vs 0.601, p=0.020; PVT + dichotomized CBV index vs. dichotomized CBV index AUC: 0.716 vs 0.602, p=0.013). Similarly, combining PVT with HIR improved prediction than HIR alone (PVT + continuous HIR vs. continuous HIR AUC: 0.702 vs 0.593, p=0.010; PVT + dichotomized HIR vs. dichotomized HIR AUC: 0.694 vs 0.573, p=0.007). Combinations of PVT and HIR, PVT and CBV index, and all three parameters yielded AUCs close to or exceeding 0.7, with the highest AUC of 0.727 achieved by combining PVT with dichotomized CBV index and dichotomized HIR.

Conclusion

The findings suggest that PVT is a relatively superior predictor of 90-day mRS outcomes compared to CBV index and HIR, highlighting the critical role of venous outflow in the overall assessment of collateral status in successfully reperfused AIS-LVO patients.

References

1. Faizy TD, Heit JJ. Rethinking the Collateral Vasculature Assessment in Acute Ischemic Stroke: The Comprehensive Collateral Cascade. *Top Magn Reson Imaging* 2021;30.

Images/Tables

Table. Areas under the curve for PVT, CBV index, HIR, and their combinations for predicting favorable functional outcomes at 90-day follow-up (mRS ≤ 2).

	AUC (95%CI)
Individual parameter	
PVT-	0.658 (0.566-0.743)
CBV index	0.601 (0.507-0.690)
CBV index ≥ 0.8	0.602 (0.508-0.691)
HIR	0.593 (0.499-0.682)
HIR < 0.4	0.573 (0.479-0.664)
Combination[a], using continuous CBV index and/or HIR	
CBV index + HIR	0.616 (0.522-0.703)
PVT + HIR	0.702 (0.611-0.782)
PVT + CBV index	0.716 (0.626-0.795)
PVT + HIR + CBV index	0.721 (0.631-0.799)
Combination[a], using dichotomized CBV index and/or HIR	
CBV index ≥ 0.8 + HIR < 0.4	0.630 (0.536-0.716)
PVT + HIR < 0.4	0.694 (0.603-0.775)
PVT + CBV index ≥ 0.8	0.716 (0.626-0.795)
PVT + HIR < 0.4 + CBV index ≥ 0.8	0.727 (0.638-0.805)

[a] The parameters were combined using binary logistic regression models.

AUC: area under the curve; CBV index: cerebral blood volume index; CI: confidence interval; HIR: hypoperfusion intensity ratio; PVT: prolonged venous transit.

581

High-Specificity EfficientNet-B0 U-Net Model for Cerebral Microbleed Detection on QSM MRI

Pin-Yu Lin[1], Sabina Iqbal[2], Yan Wen[3], Rafeeque Bhadelia[1], Katherine Tucker[4], Salil Soman[1]
[1]Radiology, Beth Israel Deaconess Medical Center, Harvard Medical School, Boston, MA, USA. [2]Beth Israel Deaconess Medical Center, Harvard Medical School, Boston, MA, USA. [3]General Electric, New York, NY, USA. [4]Biomedical & Nutritional Sciences, Health Assessment Laboratory (HAL), Center for Population Health (CPH), University of Massachusetts Lowell, Lowell, MA, USA

Abstract Category

AI/Informatics

Purpose

Cerebral microbleeds (CMBs) are MRI markers of neurovascular health commonly associated with neurodegenerative and cerebrovascular diseases such as stroke, dementia, and cerebral amyloid angiopathy. Due to their small size and low contrast, many automated CMB segmentation methods[1] exhibit high sensitivity but often produce numerous false positives, limiting clinical usefulness. This study introduces a lightweight, high-precision deep learning model tailored for CMB segmentation in Quantitative Susceptibility Mapping (QSM) MRI, explicitly aiming to reduce false positives and provide radiologists with reliable diagnostic support.

Materials & Methods

The study included 207 Boston Puerto Rican Health Study (BPRHS)[2] participants who underwent multi-echo GRE MRI on a 3.0T MR system (Discovery MR750; GE Healthcare). The mcTFI QSM[3] MRI images were generated and reviewed by an experienced neuroradiologist and a trained research assistant to annotate the presence of CMBs. Of the participants, 49 subjects were found to have CMBs, which were hand-segmented by this same staff using ITK Snap 4[4]. Using this dataset, we developed a U-Net model[5] using segmentation-models-pytorch (qubvel-org, n.d.) with EfficientNet-B0 as the encoder backbone, chosen for its balance of computational efficiency and feature extraction capabilities. Preprocessing steps included reframing to exclude non-brain regions and patching images into 64x64 sections with a 32x32 stride to emphasize small structures. Patches were adjusted for contrast, and a pseudo-3D stacking approach (2-1-2 configuration), where five QSM slices were merged into RGB channels to enhance CMB visibility. Focal and Dice Loss were applied to handle class imbalance, focusing on high sensitivity and precision. The model was trained on a dataset with a 50% positive rate, divided into 65% training, 15% validation, and 20% testing, using the Adam optimizer over 15 epochs.

Results

Our model demonstrated strong performance, achieving an average Dice score of 0.7290, sensitivity of 0.8171, and specificity of 0.9506. Notably, the high precision (0.9470) effectively reduced false positives, addressing a key limitation in other CMB detection methods. The model maintained a balanced performance with an F1 Score of 0.8773 and an overall accuracy of 0.8813, showcasing its ability to reliably differentiate true CMBs from non-CMB regions, which reduces the false-positive burden on radiologists.

Conclusion

This EfficientNet-B0-based U-Net model provides a clinically viable, high-precision solution for CMB segmentation in QSM MRI. It is optimized to support radiologist workflows by minimizing false positives and enhancing diagnostic reliability. Its efficient design allows seamless integration into clinical MRI workflows, making it suitable for large-scale studies and multi-center applications. The model's low false-positive rate is particularly valuable for radiologists, streamlining clinical review and advancing neurovascular diagnostics. Future validation across diverse patient populations will further establish its robustness and generalizability.

References

1. Sundaresan V, Arthofer C, Zamboni G, et al. Automated detection of cerebral microbleeds on MR images using knowledge distillation framework. *Front Neuroinform*. 2023;17:1204186. doi:10.3389/fninf.2023.1204186
2. Tucker KL, Mattei J, Noel SE, et al. The Boston Puerto Rican Health Study, a longitudinal cohort study on health disparities in Puerto Rican adults: challenges and opportunities. *BMC Public Health*. Mar 1 2010;10:107. doi:10.1186/1471-2458-10-107
3. Wen Y, Spincemaille P, Nguyen T, et al. Multiecho complex total field inversion method (mcTFI) for improved signal modeling in quantitative susceptibility mapping. *Magn Reson Med*. May 24 2021;doi:10.1002/mrm.28814

4. Yushkevich PA, Piven J, Hazlett C, et al. User-Guided 3D Active Contour Segmentation of Anatomical Structures: Significantly Improved Efficiency and Reliability. *Neuroimage*. 2006;31(3):1116–1128.
5. Ronneberger O, Fischer P, Brox T. U-Net: Convolutional Networks for Biomedical Image Segmentation. 2015:arXiv:1505.04597. doi:10.48550/arXiv.1505.04597 Accessed May 01, 2015. https://ui.adsabs.harvard.edu/abs/2015arXiv150504597R

Images/Tables

ASNR25

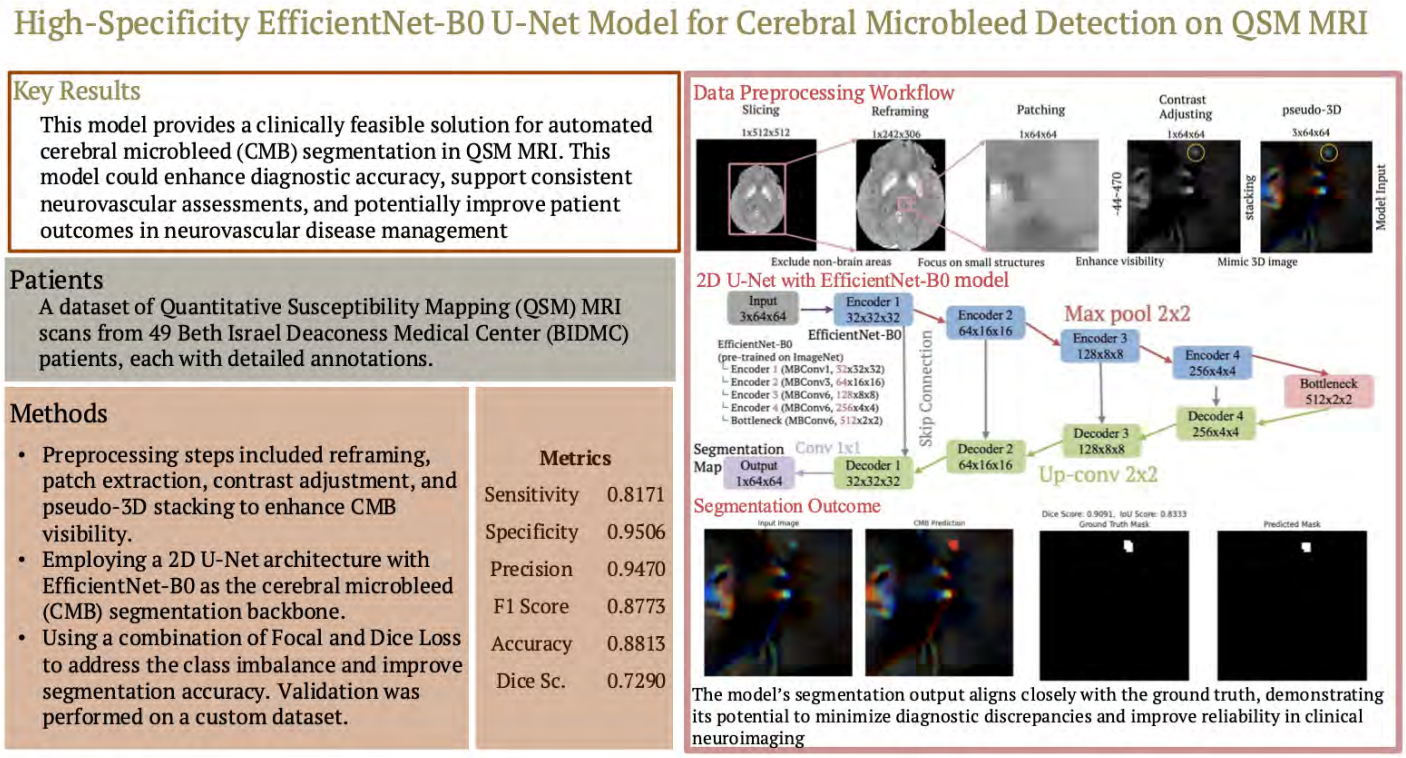

591

Longitudinal patterns in volumetric and diffusion MR measurements of brain metastases after laser interstitial thermal therapy

Francesco Sanvito[1], Jingwen Yao[1], Gianluca Nocera[2], Guowen Shao[1], Zexi Wang[1], Nicholas S Cho[1], Ashley Teraishi[1], Catalina Raymond[1], Kunal Patel[1], Nader Pouratian[3], Richard Everson[1], Isaac Yang[1], Noriko Salamon[1], Won Kim[1], Benjamin M Ellingson[1]

[1]University of California, Los Angeles, CA, USA. [2]Università Vita-Salute San Raffaele, Milan, Italy, Italy. [3]University of Texas Southwestern, Dallas, TX, USA

Abstract Category

Adult Brain

Purpose

Laser interstitial thermal therapy (LITT) is a novel local treatment option for brain metastases (BM)[1,2]. LITT consists in positioning the tip of a laser fiber in a targeted lesion and achieve a heat-induced ablation while monitoring thermal changes with MR thermometry[3]. Post-LITT radiographic changes have been systematically described only in few studies[4,5]. This study aims to characterize and model volumetric and diffusion post-LITT changes in BM, while evaluating group differences between responders and progressors.

Materials & Methods

Longitudinal scans from patients with LITT-treated BM were retrospectively analyzed. Treatment response was categorized as durable response, long-term disease control (i.e., stable at one year), stable disease within one year, or progression within one year. Volumetric and diffusion MRI changes after LITT were analyzed for each subregion (enhancing, central non-enhancing, whole lesion). Volumetric changes were modeled with lesion-specific bi-exponential fits in responding lesions and progressors. Diffusion changes were modeled with cubic polynomial fits at the group level.

Results

295 follow-up MRI scans from 47 lesions across 42 patients (57.8±14.3 years old, males:females 21:21) were analyzed. Overall, the post-LITT scan showed a lesion enlargement (p<0.0001 for all subregions, **Figure 1A**), more pronounced in the contrast-enhancing (CE) component (median=+77%, p<0.0001, **Figure 1B–C**), and a reduction in the apparent diffusion coefficient (ADC) (p<0.001, **Figure 1D**), especially in the central non-CE component (median=–224×10^{-6} mm^2/s, p<0.0001, **Figure 1E**), with no significant differences between responders and progressors. Based on mathematical modeling, the responding lesions shrank to half of the post-LITT size after 79.83 days (median "pseudo-half-life", **Figure 1F**), and the progressing lesions shrank for a median of 27 days (median time-to-growth, **Figure 1G**) before regrowing. The spider plots and mathematical modeling of diffusion changes over time showed a similar behavior between lesions achieving response or long-term disease control and progressing lesions, with an initial ADC reduction followed by an ADC increase (**Figure 1H**). **Figure 1I** depicts a representative case of BM responding to LITT with the typical post-LITT volumetric and diffusion pattern.

Conclusion

BM responding to LITT typically exhibit an early volume increase with diffusion restriction, followed by a bi-exponential shrinkage with gradual diffusion increase. Progressing lesions overall show a similar pattern, therefore early radiographic findings may not be reliable markers to predict treatment efficacy, and progression can usually be detected only after 3-4 months.

References

1. Sanvito F, Telesca D, Cho NS, et al. Small pretreatment lesion size and high sphericity as favorable prognostic factors after laser interstitial thermal therapy in brain metastases. *J Neurosurg* 2024;140:338–49.
2. Bastos DC de A, Rao G, Oliva ICG, et al. Predictors of Local Control of Brain Metastasis Treated With Laser Interstitial Thermal Therapy. *Neurosurgery* 2020;87:112–22.
3. Salem U, Kumar VA, Madewell JE, et al. Neurosurgical applications of MRI guided laser interstitial thermal therapy (LITT). *Cancer imaging Off Publ Int Cancer Imaging Soc* 2019;19:65.
4. Schwabe B, Kahn T, Harth T, et al. Laser-induced thermal lesions in the human brain: short- and long-term appearance on MRI. *J Comput Assist Tomogr* 1997;21:818–25.
5. Xue Z, Guan X, Yuan L, et al. Laser interstitial thermal therapy in the treatment of brain metastases: the relationship between changes in postoperative magnetic resonance imaging characteristics and tumor recurrence. *Acta Neurochir (Wien)* 2023;165:1379–87.

Images/Tables

Observed radiographic changes between pre-LITT, immediate post-LITT, and first follow-up (FU1) scan:

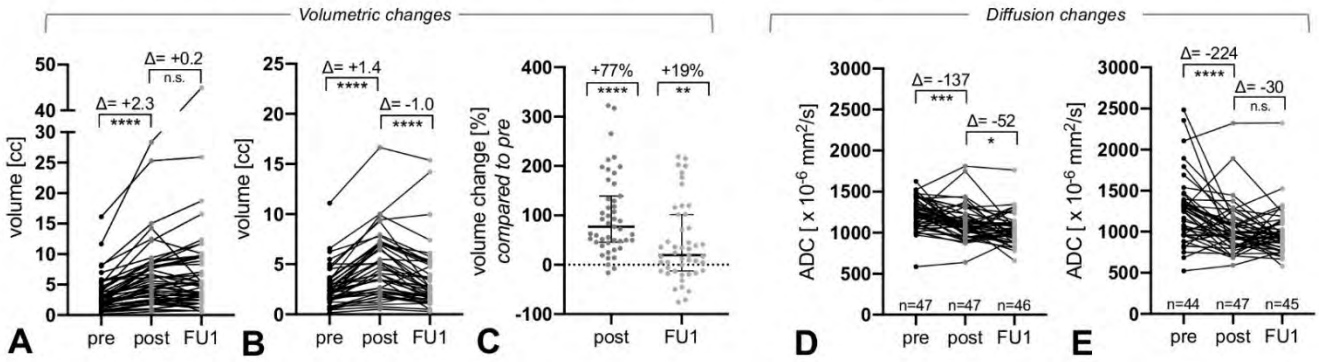

Modeled radiographic changes after LITT:

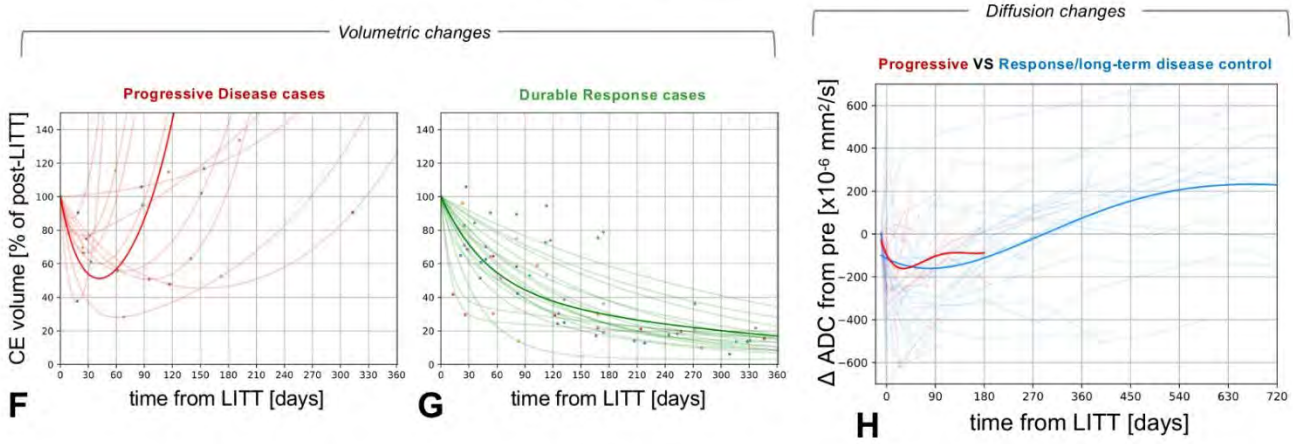

Typical post-LITT radiographic pattern in a responding case:

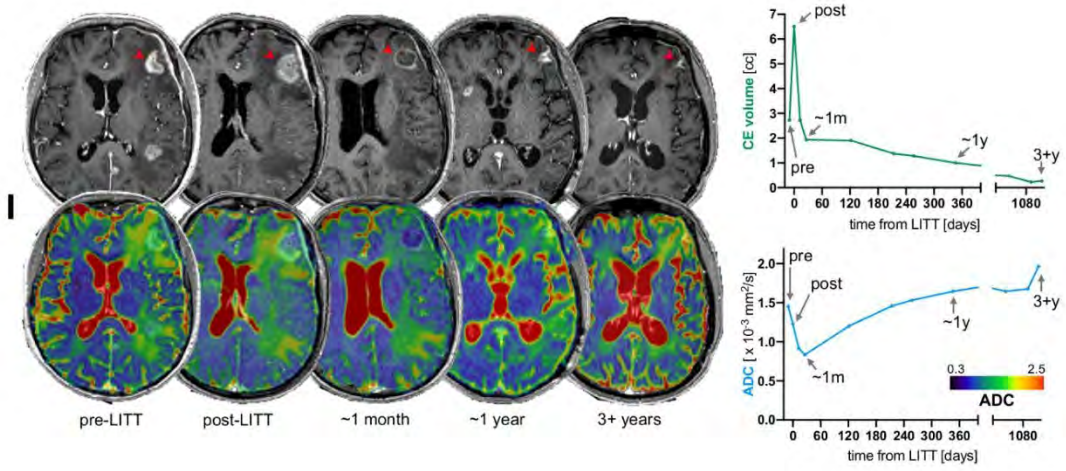

594

Contrast-enhancement and diffusion MRI phenotypes associated with immune checkpoint inhibitors and immune infiltration in brain metastases

Francesco Sanvito[1], Gianluca Nocera[2], Zexi Wang[1], Sonoko Oshima[1], Eileen Shiuan[1], Lu Sun[1], Guowen Shao[1], Nicholas S Cho[1], Asher Kim[1], Noriko Salamon[1], Benjamin M Ellingson[1], Robert Prins[1], Won Kim[1], Jingwen Yao[1]
[1]University of California Los Angeles, Los Angeles, CA, USA. [2]Università Vita-Salute San Raffaele, Milan, Italy, Italy

Abstract Category

Adult Brain

Purpose

Immune checkpoint inhibitors (ICIs) promote immune cell infiltration in brain metastases (BM)[1], which potentially enhances immune response against tumor cells. The apparent diffusion coefficient (ADC) from diffusion MRI (dMRI) has been shown to detect ICI-induced microstructural changes in brain tumors[2], and anecdotal findings suggest that pronounced immune cell infiltration can correspond to high ADC and prominent contrast-enhancement (CE) in BM. This study aims at investigating how diffusion MRI and contrast-enhancement are associated with exposure to ICIs and with histopathological immune infiltration.

Materials & Methods

Images of 125 lesions across 93 patients were analyzed (**Fig.1A**). T_1-subtraction maps were generated by normalizing, registering, and subtracting post- and pre-contrast T_1-weighted images. Segmentations of the CE tumor (CET) were obtained, and used to extract bivariate histogram distributions of ADC values and T_1-subtraction values, which allowed to calculate the voxel frequency in the highADC-highCE and in the lowADC-lowCE quadrants ("ADC-CE quadrants") (**Fig.1B**). Voxel frequency in ADC-CE quadrants was compared between ICI-naïve and ICI-exposed lesions. Linear mixed models (LMM) were implemented to evaluate the association between ICI exposure and voxel frequency in ADC-CE quadrants, while accounting for the interplay between ICI and corticosteroid exposure, and adjusting for primary tumor, prior radiation, and for multiple lesions belonging to the same patient (random effect). Finally, in a subset of patients (n=20), immune cell count (CD45+ cell density) from tissue samples were available, and their correlation with voxel frequency in ADC-CE quadrants was assessed.

Results

ICI and corticosteroid exposure was associated with distinct ADC-CE phenotypes on bivariate histograms (**Fig.1C**). Lesions previously treated with ICI showed significantly higher voxel frequency in the highADC-highCE quadrant (p<0.001) and lower voxel frequency in the lowADC-lowCE quadrant (p<0.01) compared to ICI-naïve lesions (**Fig.1D**). This result was confirmed by LMM, which revealed that ICI exposure determined higher voxel frequency in the highADC-highCE quadrant (p=0.001) and lower voxel frequency in the lowADC-lowCE quadrant (p=0.01) in absence of corticosteroid treatment after adjusting for the other variables and after accounting for random effects (**Fig.1E**). Both the visual assessment of bivariate histograms (**Fig.1C**) and the results of the interaction variable in the LMM (**Fig.1E**) demonstrated that corticosteroid usage influences the relationship between voxel frequency in ADC-CE quadrants and ICI exposure. Finally, voxel frequency in the highADC-highCE was directly correlated with CD45+ cell density in histopathology (partial ρ=0.64, p<0.01), while voxel frequency in the lowADC-lowCE was inversely correlated (partial ρ=–0.63, p<0.01) (**Fig.1F**).

Conclusion

ICI exposure determines a characteristic MRI phenotype in BM, that can be identified with quantitative diffusion imaging and contrast-enhancement analyses. This MRI phenotype is associated with a more pronounced immune cell infiltration on histopathology. Overall, our results suggest that immune cell infiltration, which is known to be promoted by ICI, yields higher diffusivity and more prominent contrast-enhancement, possibly due to a more marked vascular permeability. Notably, the use of corticosteroids influences ADC and CE values, as expected[3,4]. Imaging phenotypes predicting immune cell infiltration would be valuable to non-invasively monitor tissue changes related to immune response following ICIs.

References

1. Sun L, Kienzler JC, Reynoso JG, et al. Immune checkpoint blockade induces distinct alterations in the microenvironments of primary and metastatic brain tumors. *J Clin Invest* 2023;133.
2. Hagiwara A, Oughourlian TC, Cho NS, et al. Diffusion MRI is an early biomarker of overall survival benefit in IDH wild-type recurrent glioblastoma treated with immune checkpoint inhibitors. *Neuro Oncol* 2022;24:1020–8.

3. Cairncross JG, Macdonald DR, Pexman JH, et al. Steroid-induced CT changes in patients with recurrent malignant glioma. *Neurology* 1988;38:724–6.
4. Minamikawa S, Kono K, Nakayama K, et al. Glucocorticoid treatment of brain tumor patients: changes of apparent diffusion coefficient values measured by MR diffusion imaging. *Neuroradiology* 2004;46:805–11.

Images/Tables

A

Characteristics	All lesions	Lesions with histology
Number of subjects (lesions)	93 (125)	20 (20)
Age (mean ± SD years)	60.3 ± 13.0	54.2 ± 13.3
Sex (M/F)	40/53	4/16
Primary cancer histology	Melanoma N = 28 Lung cancer N = 40 Other types N = 57	Melanoma N = 6 Lung cancer N = 6 Other types N = 8
Brain radiation treatment within 6 months (yes/no)	24/101	3/17
Immune checkpoint inhibitor treatment within 6 months (yes/no)	All: 22/103 Melanoma: 8/20 Lung cancer: 10/30 Other types: 4/53	All: 5/15 Melanoma: 0/6 Lung cancer: 1/5 Other types: 4/4
Extended steroid (> 2 month) within 6 months (yes/no)	48/77	3/17
Biopsy sample CD45+ cell density (mean ± SD count/mm²)	/	514.8 ± 624.8

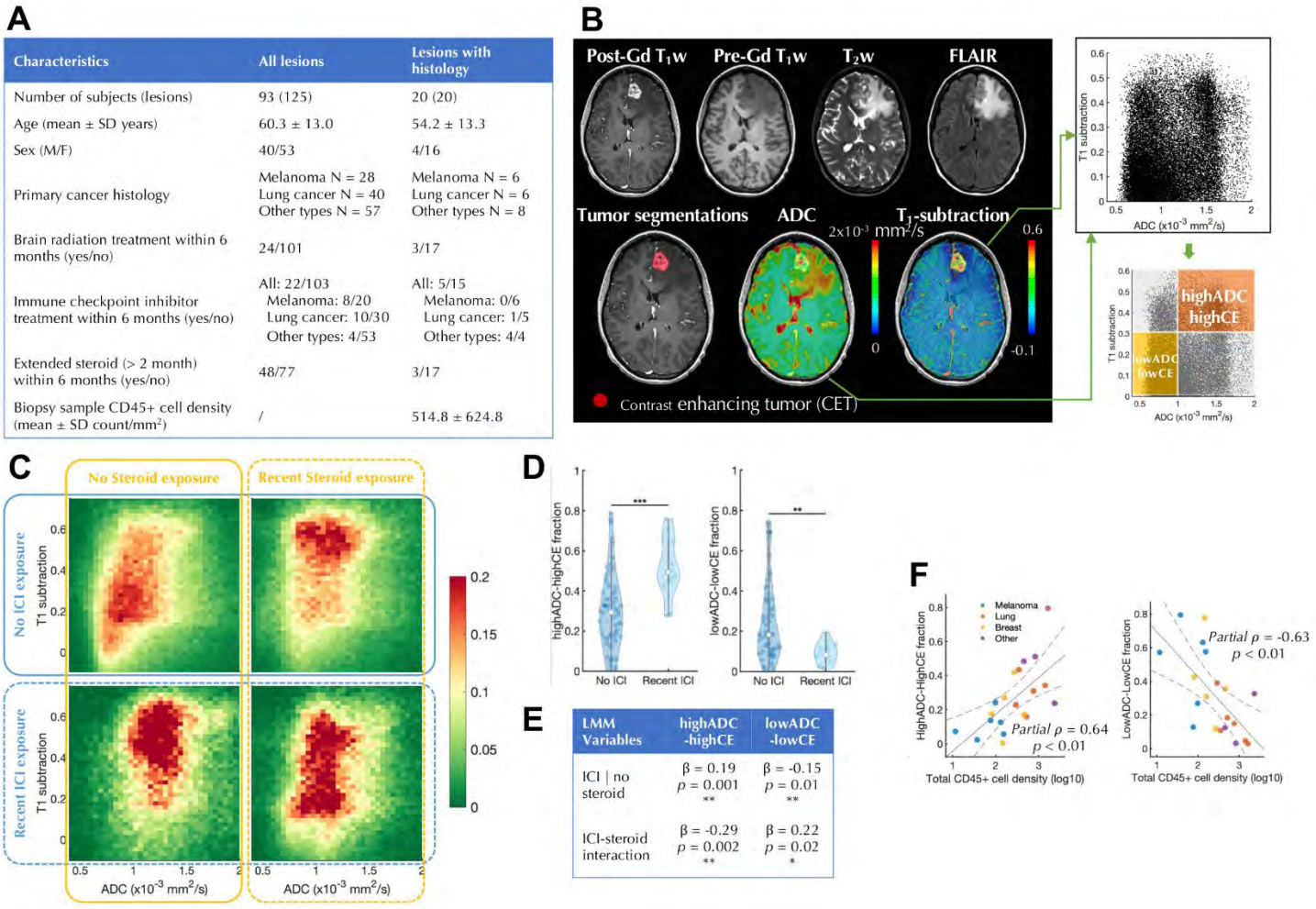

E

LMM Variables	highADC -highCE	lowADC -lowCE
ICI | no steroid	β = 0.19 *p* = 0.001 **	β = -0.15 *p* = 0.01 **
ICI-steroid interaction	β = -0.29 *p* = 0.002 **	β = 0.22 *p* = 0.02 *

597

Accelerating MRI Protocols Through Combined Image Enhancement and Image Synthesis

Thomas C Arnold PhD[1], Zechen Zhou PhD[1], Long Wang MS[1], Lanhong Yao MS[1], Ajit Shankaranarayanan PhD[1], Suzie Bash MD[2], Lawrence Tanenbaum MD[3]
[1]Subtle Medical, Menlo Park, CA, USA. [2]RadNet Inc., Los Angeles, CA, USA. [3]drt consulting, Riverside, CT, USA

Abstract Category

Spine

Purpose

Restoring accelerated MR sequences to standard-of-care image quality using image enhancement algorithms has proven an effective approach to improving imaging efficiency and sustainability. Recently, the FDA cleared the first STIR image synthesis algorithm[1], which can further accelerate protocols by reducing the total number of sequences acquired on the scanner. Here, we present an examination of the image synthesis algorithm's performance and associated scan time savings when combined with accelerated MR sequences in spine protocols.

Materials & Methods

We analyzed data from 22 participants who underwent spinal MRI (cervical: 3, thoracic: 5, lumbar: 14) across 6 different scanners (3 GE, 2 Siemens, 1 Hitachi: range 1.16-3T). Each protocol included 2D sagittal T1w, T2w, and STIR sequences and 2D Axial T1w and T2w sequences. Images were grouped into 3 datasets: 1) Acquired 2) Enhanced 3) Enhanced + Synth. Enhanced images were accelerated sequences with image quality restored through a deep-learning-based

denoising algorithm[2]. Synthetic sagittal STIR images were generated from enhanced sagittal T1w and T2w inputs[3]. Regions of interest were drawn in vertebrae, discs, spinal cord, and cerebral spinal fluid (CSF) for signal-to-noise ratio (SNR) and contrast-to-noise ratio (CNR) evaluation.

Results

Participants were 62 ± 15 years old (11 female, 11 male). Across all sequences, the enhancement algorithm resulted in a significant SNR increase (**Figure 1A**) in the vertebrae (T1w: $p < 0.05$, T2w and STIR: $p < 0.001$), discs (T1w and T2w: $p < 0.05$, STIR: $p < 0.001$), and spinal cord (T1w: $p < 0.001$, T2w and STIR: $p < 0.05$). In CSF, T1w SNR increased ($p<0.05$) while T2w and STIR showed no change ($p > 0.85$). Synthesized STIR sequences further increased SNR over acquired and enhanced sequences in all regions: vertebrae ($p < 0.001$), discs (acquired: $p < 0.001$, enhanced: $p < 0.05$), spinal cord ($p < 0.001$), and CSF ($p < 0.05$). After enhancement, T1w CNR significantly improved for all ROIs ($p < 0.001$) and T2w CNR improved for vertebrae-to-CSF and cord-to-CSF ($p < 0.05$) (**Figure 1B**). Image enhancement showed no change in STIR CNR ($p > 0.05$). However, synthesized STIR had improved CNR for vertebrae-to-CSF and cord-to-CSF ($p < 0.001$). **Figure 1C** illustrates an example case, demonstrating improved image quality and 59% scan time savings (7:07 minutes versus 17:31 minutes).

Conclusion

MRI protocols can be further accelerated by combining image enhancement and synthesis algorithms. Furthermore, synthesized STIR sequences had higher SNR and contrast than acquired and enhanced images. This approach can both increase imaging efficiency and promote sustainable imaging by allowing scanners to service larger populations.

References

1. FDA 510(k) Premarket Notification for SubtleSYNTH. https://www.accessdata.fda.gov/cdrh_docs/pdf24/K241329.pdf Accessed November 1, 2024.
2. Bash S, Johnson B, Gibbs W, et al. Deep learning image processing enables 40% faster spinal MR scans which match or exceed quality of standard of care: a prospective multicenter multireader study. Clinical Neuroradiology. 2022 Mar;32(1):197-203.
3. Tanenbaum LN, Bash SC, Zaharchuk G, et al. Deep learning–generated synthetic MR imaging STIR spine images are superior in image quality and diagnostically equivalent to conventional STIR: a multicenter, multireader trial. American Journal of Neuroradiology. 2023 Aug 1;44(8):987-93.

Images/Tables

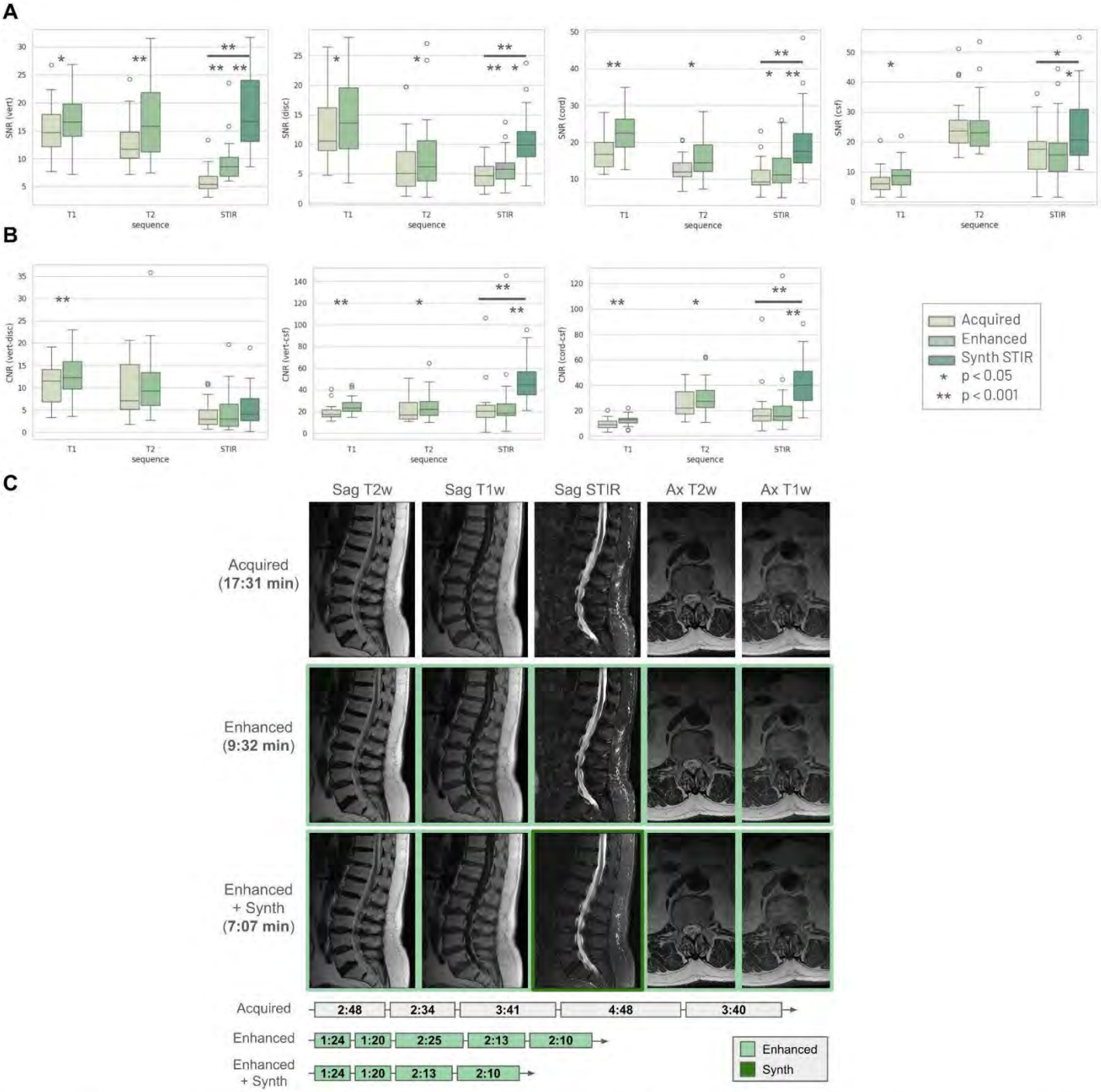

Figure 1. Improved SNR, CNR, and 59% scan time savings with combined image enhancement and synthesis algorithms. A) SNR improvements for enhanced and synthesized images across 4 regions of interest (vertebral body, vertebral disc, spinal cord, cerebral spinal fluid). B) Image enhancement improved CNR for T1 and T2 sequences. Image synthesis improved CNR for STIR sequences. C) Illustrates Acquired, Enhanced, and Enhanced + Synth images from an example case with the associate scan times and total protocol time savings. When combining image enhancement and synthesis, total protocol time savings is 59% (from 17:31 minutes to 7:07 minutes).

598

Influence of Stroke Onset Location on the Efficacy of Endovascular Thrombectomy:Comparison of Outcomes Between In-hospital vs. Community-Onset Strokes

Paulo Puac-Polanco MD, MSc, Nima Omid-Fard MD, Eduardo Portela de Oliveira MD, Vered Tsehmaister-Abitbul MD, Santanu Chakraborty MD, Carlos Torres MD
University of Ottawa, Ottawa, ON, Canada

Abstract Category

Interventional

Purpose

Previous studies have suggested that patients suffering an in-hospital stroke (IHS) may face delays in treatment and worse outcomes compared to patients with community-onset strokes (COS). However, most studies occurred when intravenous thrombolysis was the primary treatment. This study aimed to examine the outcomes of patients experiencing an IHS in the endovascular thrombectomy (EVT) era.

Materials & Methods

Single-center retrospective cohort study of patients older than 18 years with acute ischemic stroke (AIS) treated with EVT within 12 hours of stroke onset from January 1, 2015, to April 30, 2021. Patients were classified into two groups: in-hospital strokes (IHS) and community-onset strokes (COS). We compared time metrics of stroke care delivery, rate of successful reperfusion, and functional outcome as scored using the modified Rankin Scale (mRS) score at 90 days (favorable outcome was defined as mRS 0-2). Differences in proportions were assessed using Fisher's exact and Chi-Square tests as appropriate. For continuous variables, differences in medians between groups were evaluated using Mann-Whitney U tests.

Results

A total of 676 consecutive patients were included, with 69 (10%) comprising the IHS group. IHS patients were more likely to have diabetes (36% vs. 18%, p=0.02) and less likely to receive thrombolysis (25% vs 68%, p<0.001) than the COS group but were otherwise similar. IHS patients had significantly faster overall time metrics, most notably from stroke recognition to imaging (median [IQR], 70 [38-141] min vs 121 [74-228] min, p<0.001). Successful recanalization was achieved in > 75% in both groups (p=0.39), with a median NIHSS at discharge <4 (p=0.18). The 90-day mRS was similar in both groups, with a trend of higher in-hospital mortality in the IHS group (p=0.06).

Conclusion

IHS patients had shorter workflow delays to initiation of EVT compared to their community counterparts but with a similar rate of successful recanalization and clinical outcomes. Importantly, 90 day mortality and mRS scores were equivalent between IHS and COS.

References

1. Blacker DJ. In-hospital stroke. Vol. 2, Lancet Neurology. Lancet Neurol; 2003. p. 741–6.
2. Farooq MU, Reeves MJ, Gargano J, Wehner S, Hickenbottom S, Majid A. In-hospital stroke in a statewide stroke registry. Cerebrovascular Diseases. 2008 Feb;25(1–2):12–20.
3. Saltman AP, Silver FL, Fang J, Stamplecoski M, Kapral MK. Care and outcomes of patients with in-hospital stroke. JAMA Neurology. 2015 Jul;72(7):749–55.
4. Cumbler E. In-Hospital Ischemic Stroke. Vol. 5, The Neurohospitalist. SAGE Publications; 2015. p. 173–81.
5. Azzimondi G, Nonino F, Fiorani L, Vignatelli L, Stracciari A, Pazzaglia P, et al. Incidence of stroke among inpatients in a large italian hospital. Stroke. 1994;25(9):1752–4.

600

From Data Sharing to Synthetic Generation: Diffusion Models as an Alternative to Federated Learning for IDH Mutation Classification

Nghi C.D. Truong PhD[1], Chandan Ganesh Bangalore Yogananda PhD[1], Benjamin C Wagner BM[1], Niloufar Saadat MD[1], James M Holcomb BS[1], Divya Reddy MS[1], Jason Bowerman BS[1], Sadeem Lohdi MD[1], Kimmo J Hatanpaa MD, PhD[1], Toral R Patel MD[1], Baowei Fei PhD[2], Matthew D. Lee MD[3], Rajan Jain MD[3], Richard J Bruce MD[4], Marco C Pinho MD[1], Joseph A Maldjian MD[1]
[1]University of Texas Southwestern Medical Center, Dallas, TX, USA. [2]University of Texas at Dallas, Richardson, TX, USA. [3]NYU Grossman School of Medicine, New York, NY, USA. [4]University of Wisconsin-Madison, Madison, WI, USA

Abstract Category

AI/Informatics

Purpose

Datasets from multiple clinical centers provide invaluable diversity, capturing variations in imaging protocols and patient populations that enhance the robustness of medical imaging deep-learning models. However, privacy constraints often prevent direct data sharing. Federated learning (FL) (1) is a common solution to address privacy concerns by allowing decentralized model training without sharing raw data. Still, its practical implementation is often limited by significant communication overhead and complex coordination among centers. This study introduces a novel alternative to FL using latent diffusion models (LDM) (2, 3), which can generate synthetic, site-specific samples without sharing sensitive data, thereby potentially reducing communication demands and simplifying multi-center collaborations.

Materials & Methods

To simulate a multi-center study, we used retrospective MRI scans from three "sites," including 1) The Cancer Genome Atlas (TCGA, n=198) (4), 2) the Erasmus Glioma Database (EGD, n=456) (5), and 3) an internal dataset from UT Southwestern Medical Center (UTSW, n=360) to train isocitrate dehydrogenase (IDH) classification models using standard centralized training, standard FL, and a model based on site-specific LDMs. The LDMs to generate synthetic IDH-mutation and site-specific MRI samples were built upon our previous work (3) with notable improvements, including enhancing IDH-specific conditioning mechanisms and incorporating the whole tumor mask as part of the output. Site-specific LDMs were created based on local MRI data from each site, resulting in three separately trained LDMs for TCGA, UTSW, and EGD datasets. The trained LDMs were then transferred to a central server, where synthetic IDH mutation-specific MRI images were generated, emulating the characteristics of each center's data. These synthetic images were combined to form a comprehensive dataset, which was subsequently used to train a centralized synthetic IDH classification model. The performance of this model was evaluated using an independent real data test set comprised of MRI scans from the University of California San Francisco Preoperative Diffuse Glioma MRI dataset (UCSF, n=495) (6), the University of Pennsylvania Glioblastoma dataset (UPENN, n=419) (7), and internal datasets from New York University (NYU, n=181) and the University of Wisconsin-Madison (UWM, n=218), totaling 1,313 patients. Finally, we compared the IDH classification model trained on synthetic samples with models trained on real data from TCGA, UTSW, and EGD, using both centralized and FL approaches.

Results

The IDH classification model, trained solely on synthetic site-specific data and tested on 1,313 real patients, achieved an overall accuracy of 95.5%. In comparison, centralized training with real datasets yielded an accuracy of 96.4%, while FL with the same datasets achieved 96%. Details of the models' performance on testing datasets are presented in Table 2. Statistical analysis using McNemar's test revealed no significant differences in model performance across the three models ($p > 0.05$).

Conclusion

Our diffusion-based approach demonstrated comparable performance to traditional centralized and FL methods for IDH mutation classification in gliomas. By mitigating privacy concerns and reducing the communication burden compared to FL, this method offers a novel, effective, and efficient alternative to FL for multi-center collaborations in medical imaging research and applications.

References

1. Silva S, Gutman BA, Romero E, Thompson PM, Altmann A, Lorenzi M, et al. Federated Learning in Distributed Medical Databases: Meta-Analysis of Large-Scale Subcortical Brain Data. I S Biomed Imaging. 2019:270-4. doi: 10.1109/isbi.2019.8759317. PubMed PMID: WOS:000485040000058.

2. Rombach R, Blattmann A, Lorenz D, Esser P, Ommer B. High-Resolution Image Synthesis with Latent Diffusion Models. Proc Cvpr Ieee. 2022:10674-85. doi: 10.1109/Cvpr52688.2022.01042. PubMed PMID: WOS:000870759103073.

3. Truong NCD, Yogananda CGB, Wagner BC, Holcomb JM, Reddy D, Saadat N, et al. Synthesizing 3D Multi-Contrast Brain Tumor MRIs Using Tumor Mask Conditioning. Proc SPIE Int Soc Opt Eng. 2024;12931. Epub 20240402. doi: 10.1117/12.3009331. PubMed PMID: 38715792; PubMed Central PMCID: PMC11075745.

4. Ceccarelli M, Barthel FP, Malta TM, Sabedot TS, Salama SR, Murray BA, et al. Molecular Profiling Reveals Biologically Discrete Subsets and Pathways of Progression in Diffuse Glioma. Cell. 2016;164(3):550–63-–63.

5. van der Voort SR, Incekara F, Wijnenga MMJ, Kapsas G, Gahrmann R, Schouten JW, et al. The Erasmus Glioma Database (EGD): Structural MRI Scans, WHO 2016 Subtypes, and Segmentations of 774 Patients with Glioma. Data in Brief. 2021;37:107191-.

6. Calabrese E, Villanueva-Meyer JE, Rudie JD, Rauschecker AM, Baid U, Bakas S, et al. The University of California San Francisco Preoperative Diffuse Glioma MRI Dataset. Radiology: Artificial Intelligence. 2022;4(6):e220058-e.
7. Bakas S, Sako C, Akbari H, Bilello M, Sotiras A, Shukla G, et al. The University of Pennsylvania glioblastoma (UPenn-GBM) cohort: advanced MRI, clinical, genomics, & radiomics. Sci Data. 2022;9(1):453. Epub 20220729. doi: 10.1038/s41597-022-01560-7. PubMed PMID: 35906241; PubMed Central PMCID: PMC9338035.

Images/Tables

Table 1: Training and testing data for the LDMs and IDH classification models.

	Training data			Total training	Testing data				Total testing
	TCGA (n=198)	UTSW (n=360)	EGD (n=456)	(n=1,014)	NYU (n=181)	UWM (n=218)	UCSF (n=495)	UPENN (n=419)	(n=1,313)
Mutated	91	104	150	345	48	18	103	11	180
Wildtype	107	256	306	669	133	200	392	408	1,133

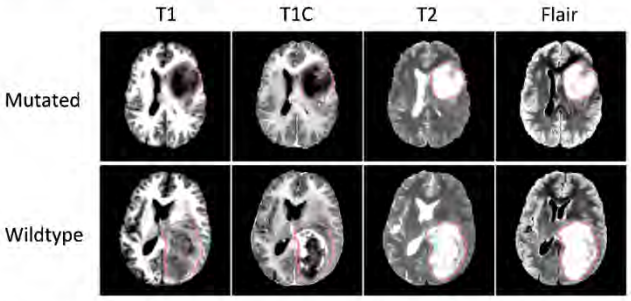

Figure 1: Multi-contrast MRI samples generated by the LDM with the conditional IDH mutation status for the UTSW site. The whole tumor masks (red contour) are also part of the generated output.

Table 2: Performance of IDH classification models using three different training approaches: centralized training using real data; FL training with 100 rounds and using FedAvg for aggregating the model weights; and the proposed site-specific synthetic data approach using diffusion models as an alternative to FL.

		Centralized training using real data	FL with 100 rounds using real data	Centralized training using site-specific synthetic samples
UCSF	ACC	96.2	95.6	95.2
	SEN (MT)	88.4	89.3	83.5
	SPE (WT)	98.2	97.2	98.2
	AUC	0.980	0.983	0.960
NYU	ACC	94.5	92.8	92.8
	SEN (MT)	87.5	85.4	89.6
	SPE (WT)	97.0	95.5	94.0
	AUC	0.966	0.968	0.954
UWM	ACC	95.9	95.4	94.5
	SEN (MT)	77.8	77.8	88.9
	SPE (WT)	97.5	97.0	95.0
	AUC	0.969	0.961	0.955
UPENN	ACC	97.9	97.9	97.6
	SEN (MT)	72.7	63.6	72.7
	SPE (WT)	98.5	98.8	98.3
	AUC	0.978	0.975	0.961
Overall	ACC	96.4	95.9	95.5
	SEN (MT)	86.1	85.6	85.0
	SPE (WT)	98.1	97.5	97.2
	AUC (95% CI)	0.976 [0.960, 0.992]	0.978 [0.963, 0.993]	0.965 [0.946, 0.984]
	McNemar p-value	-	0.3320 (ns)	0.5596 (ns)

601

Associations of Brain Structural Imaging with Midlife Obesity and Insulin Resistance: Implications for Alzheimer's disease

Soheil Mohammadi[1], Mahsa Dolatshahi[1], Paul K. Commean[1], Farzaneh Rahmani[1], Caitlyn Nguyen[1], LaKisha Lloyd[1], Sara Hosseinzadeh Kasani[1], Mahshid Naghashzadeh[1], Bettina Mittendorfer[2], Claude Sirlin[3], Tammie L.S. Benzinger[1], Joseph E. Ippolito[1], John C. Morris[1], Cyrus A. Raji[1]

[1]Mallinckrodt Institute of Radiology, Washington University in St. Louis, St. Louis, MO, USA. [2]Departments of Medicine and Nutrition & Exercise Physiology, School of Medicine, University of Missouri, Columbia, MO, USA. [3]Liver Imaging Group, Department of Radiology, University of California, San Diego, CA, USA

Abstract Category

Adult Brain

Purpose

Midlife obesity and insulin resistance increase the risk of Alzheimer's disease. However, it remains unclear whether the interplay between obesity and insulin resistance is associated with alterations in brain structure. In this study, we aimed to investigate the associations of obesity, defined as a body mass index (BMI) of 30 kg/m² or higher, and insulin resistance, calculated using the homeostatic model of insulin resistance (HOMA-IR), with MRI-derived brain cortical thickness and cortical volume in regions of interest (ROI) related to Alzheimer's disease.

Materials & Methods

A total of 80 cognitively normal middle-aged subjects (48.87 ± 6.25 years, male: 26 (32.5%), obesity: 39 (48.75 %), BMI: 31.52 ± 7.72 kg/m²) underwent 3T MRI, along with metabolic assessments. Insulin resistance was measured using HOMA-IR, with values ≥ 1.9 classified as insulin resistant. Automatic segmentation of cortical and subcortical brain regions was performed using FreeSurfer 7.1.1, accompanied by visual inspection, quality control, and manual adjustments as needed. Based on HOMA-IR and obesity status, participants were divided into four groups: metabolically normal non-obese (MNNO), metabolically abnormal non-obese (MANO), metabolically normal obese (MNO), and metabolically abnormal obese (MAO). One-way ANOVA was conducted to investigate between-group differences in brain cortical thickness and volumes in regions of interest (ROI) related to Alzheimer's disease, with age and sex as covariates. Post-hoc analyses were performed, with p-values adjusted for multiple comparisons using the Bonferroni method.

Results

The one-way ANOVA revealed significant between-group differences in the right posterior cingulate volume, right superior temporal volume, and total temporal lobe volume. ANCOVA post-hoc analysis indicated a significantly lower right posterior cingulate volume in the MAO compared to the MNNO. Cortical thickness analysis in ROIs showed significant differences in the left superior temporal and left temporal pole regions, with post-hoc results revealing significantly lower left temporal pole thickness in the MAO compared to the MNNO.

Conclusion

Our findings provide evidence of the association between midlife obesity and decreased volume of the posterior cingulate, as well as decreased thickness in the left temporal pole. Given the compelling evidence supporting the involvement of these regions in Alzheimer's pathology1, our results suggest a mediating role of midlife obesity and insulin resistance in the risk of developing Alzheimer's disease.

References

1. Choo IH, Lee DY, Oh JS, et al. Posterior cingulate cortex atrophy and regional cingulum disruption in mild cognitive impairment and Alzheimer's disease. *Neurobiology of aging* 2010; **31**(5): 772-9.

Images/Tables

Table 1. demographic and clinical characteristics by group

		Metabolically normal non-obese	Metabolically abnormal non-obese	Metabolically normal obese	Metabolically abnormal obese	P-value
N		25	17	13	29	
Age (mean (SD))		47.00 (5.78)	49.35 (6.15)	50.08 (6.32)	50.00 (6.68)	0.3
Education (mean (SD))		15.72 (1.84)	15.94 (2.41)	14.85 (2.12)	15.14 (2.36)	0.427
Obesity (%)	0	25 (100.0)	17 (100.0)	0 (0.0)	0 (0.0)	**<0.001**
	1	0 (0.0)	0 (0.0)	13 (100.0)	29 (100.0)	
Cholesterol (mean (SD))		179.56 (33.74)	182.06 (33.98)	175.31 (46.97)	183.24 (28.15)	0.911
Triglyceride (mean (SD))		66.76 (23.94)	120.12 (69.35)	76.85 (33.34)	106.52 (36.32)	**<0.001**
HDL (mean (SD))		70.48 (14.16)	50.00 (8.37)	57.08 (12.92)	49.38 (12.13)	**<0.001**
LDL (mean (SD))		95.72 (26.15)	108.06 (33.58)	102.77 (40.60)	112.59 (25.39)	0.223
NON-HDL Cholesterol (mean (SD))		108.48 (29.02)	132.06 (34.62)	118.23 (40.91)	133.86 (28.85)	**0.023**
Chol/HDL ratio (mean (SD))		2.60 (0.71)	3.88 (1.11)	3.15 (0.80)	3.86 (1.13)	**<0.001**
Hb A1C (mean (SD))		5.29 (0.40)	5.65 (0.45)	5.39 (0.44)	5.84 (0.58)	**<0.001**
HOMA.IR (mean (SD))		1.04 (0.48)	3.82 (2.77)	1.42 (0.40)	6.37 (3.74)	**<0.001**
MMSE (mean (SD))		29.45 (0.69)	29.50 (1.09)	29.33 (1.00)	29.09 (1.24)	0.594
Amyloid status (%)		1 (4.0)	0 (0.0)	0 (0.0)	2 (6.9)	0.831
	Neg	21 (84.0)	13 (76.5)	10 (76.9)	23 (79.3)	
	Pos	0 (0.0)	1 (5.9)	1 (7.7)	2 (6.9)	
	NA	3 (12.0)	3 (17.6)	2 (15.4)	2 (6.9)	
Race (%)	White	17 (68.0)	14 (82.4)	7 (53.8)	18 (62.1)	0.583
	African/American	5 (20.0)	1 (5.9)	5 (38.5)	9 (31.0)	
	Asian	1 (4.0)	1 (5.9)	0 (0.0)	0 (0.0)	
	Other	2 (8.0)	1 (5.9)	1 (7.7)	2 (6.9)	
SAT (mean (SD))		1557.27 (662.09)	2198.35 (591.59)	3492.96 (908.53)	3874.47 (1409.80)	**<0.001**
VAT (mean (SD))		486.94 (197.85)	871.00 (403.25)	937.13 (352.77)	1433.44 (565.75)	**<0.001**

BMI: Body Mass Index, MMSE: Mini-mental state examination, HDL: High Density Lipoprotein, LDL: Low Density Lipoprotein, HbA1C: Hemoglobin A1C, HOMA-IR: Homeostatic Model Assessment for Insulin Resistance, SAT: subcutaneous adipose tissue, VAT: visceral adipose tissue. Significant p-values are emboldened.

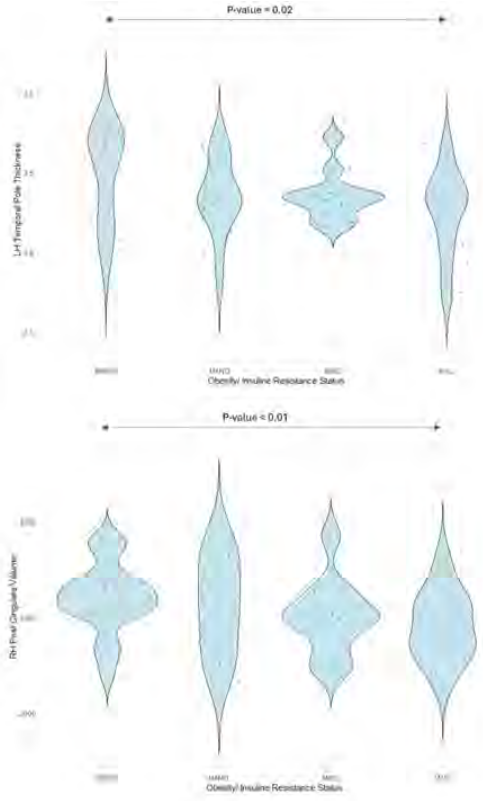

605

Early PET Biomarker for detecting Post-Radiation Changes in Central Nervous System

Behnaz Khazai M.D[1], Nazanin Maleki M.D[2], Marta Baro PhD[3], Takuya Toyonaga M.D, PhD[4], Matthew Sala M.D(c)[5], Divya Ramakrishnan M.D[6], Anasthasia Janas M.D, PhD[7], Borna Roohani M.D(c)[8], David Weiss M.D(c)[9], Alaaddin Ibrahimy PhD(c)[6], Evan Morris PhD[6], Jason Cai PhD[6], Veronica Chiang M.D[10], Anita Huttner M.D[11], Michael Hollander M.D[12], Joseph Contessa M.D, PhD[13], Richard Carson PhD[14], Mariam Aboian MD, PhD[15]

[1]Radiology department, Massachusetts General Hospital, Boston, Ma, USA. [2]Children's Hospital of Philadelphia, Philadelphia, PA, USA. [3]Department of Therapeutic Radiology, Yale School of Medicine, New Haven, CT, USA. [4]Department of Radiology and Biomedical Imaging, Yale School of Medicine, New Haven, CT, USA. [5]Tulane University School of Medicine, New Orleans, LA, USA. [6]Yale School of Medicine, New Haven, CT, USA. [7]Charité Universitatsmedizin Berlin, Berlin, Berlin, Germany. [8]University Medical Center Hamburg-Eppendorf, Hamburg, Hamburg, Germany. [9]Department of Diagnostic and Interventional Radiology and Neuroradiology, University Hospital Essen, Essen, Essen, Germany. [10]Yale School of Medicine,Department of Neurosurgery, New Haven, CT, USA. [11]Yale School of Medicine, Department of Pathology, New Haven, CT, USA. [12]Nuvance Health - Norwalk Hospital, Norwalk, CT, USA. [13]Yale School of Medicine, Department of Therapeutic Radiology, New Haven, CT, USA. [14]Yale School of Medicine, Department of Radiology and Biomedical Imaging, New Haven, CT, USA. [15]Radiology department, The Children's hospital of Philadelphia, Philadelphia, PA, USA

Abstract Category

Functional/Advanced Imaging

Purpose

Radiation therapy is an essential treatment in majority of brain tumor cases, but can also cause significant cognitive decline in up to 90% of patients receiving whole brain radiation therapy (WBRT). Currently, there are no definitive methods for prevention of radiation induced cognitive decline. Hippocampal-sparing radiation and targeted radiation has fewer cognitive sequelae and is increasingly used, but cognitive decline is still found in up to 65% of patients. Characterization of when the pathogenic changes occur during and after radiation treatment is limited in humans, because current methods require post-mortem analysis of the brain. This is a translational study of a novel radiotracer ^{18}F-SynVesT-1 that binds to SV2A, a transmembrane protein on pre-synaptic vesicles, as a potential early *in vivo* biomarker of radiation neuronal injury in the rodent model.

Materials & Methods

Seventy two Sprague Dawley rats were studied in 3 groups of 24. After a baseline brain PET each group was further divided into 4 subgroups of 6 to receive either whole brain, left hemisphere, right hemisphere or sham radiation. Follow up PET were then obtained at 1,3 and 6 months. Rats received 30 Gy total devided into 10 fractions of 3Gy on alternating days. 18F-SynVesT-1 PET was performed over 60 min in list-mode, reconstructed, post-processed, co-registered to the Waxholm Space Atlas of the Rat Brain template and auto-segmented. Simplified reference tissue model was used to obtain SUVR, DVR and R1 for 11 bilateral ROIs(reference: brainstem).

Results

There was no significant difference in the baseline hippocampal DVR between groups. At 1 month post radiation, the left brain irradiated subgroup showed significantly higher DVR in the left hippocampi compared to the sham irradiated subgroup (mean DVR of 1.46± 0.029 vs. 1.37± 0.04, adjusted p value: 0.01). Similarly, the right brain irradiated subgroup showed significantly higher DVR in the right hippocampi compared to the sham (mean DVR of 1.44± 0.05 vs. 1.35±0.036, adjusted p value: 0.04). Similar trend of higher DVR was seen in bilateral hippocampi of the whole brain irradiation subgroup though it was not significant (Whole brain Rx, Right side 1.42±0.13, Left side 1.43±0.13, Sham right side 1.35±0.036, Left side 1.37±0.04; P value:) . DVR asymmetry indices showed congruent changes. There was no significant difference when all ROIs were compared but a similar trend of higher DVR ipsilateral to the radiation side was seen for most ROIs. These findings of 1m were not seen at 3 and 6m post radiation. The uptakes were erratic without significant difference or observable trend.

Conclusion

The consistent pattern of increased SynVesT-1 uptake in irradiated brain regions at 1 month post-radiation appears to be a robust indicator of post-radiation changes to neurons. Notably, this increase in uptake was not observed at 3 and 6 months, suggesting a potential time window for its effectiveness as a biomarker. Our study suggests that 18F-SynVesT-1 PET could be a valuable tool for early detection of radiation-induced neuronal injury, which could potentially improve patient outcomes through timely radiotherapy plan adjustments and the application of preventive measures.

References

- Cai Z, Li S, Zhang W, et al. Synthesis and preclinical evaluation of an 18F-labeled synaptic vesicle glycoprotein 2A PET imaging probe: [18F]SynVesT-2. ACS Chem Neurosci 2020;11:592-603. DOI: https://doi.org/10.1021/acschemneuro.9b00618
- Connor M, Karunamuni R, McDonald CR, et al. Dose-dependent white matter damage after brain radiotherapy. Radiother Oncol 2016;121:209-16. DOI: https://doi.org/10.1016/j.radonc.2016.10.003
- Greene-Schloesser D, Moore E, Robbins ME. Molecular pathways: radiation-induced cognitive impairment. Clin Cancer Res 2013;19:2294-300. DOI: https://doi.org/10.1158/1078-0432.CCR-11-2903
- Greene-Schloesser D, Robbins ME, Peiffer AM, et al. Radiation-induced brain injury: a review. Front Oncol 2012;2:73. DOI: https://doi.org/10.3389/fonc.2012.00073
- Naganawa M, Li S, Nabulsi N, et al. First-in-human evaluation of 18F-SynVesT-1, a novel radioligand for PET imaging of synaptic vesicle protein 2A. J Nucl Med. DOI: https://doi.org/10.2967/jnumed.120.249144

Images/Tables

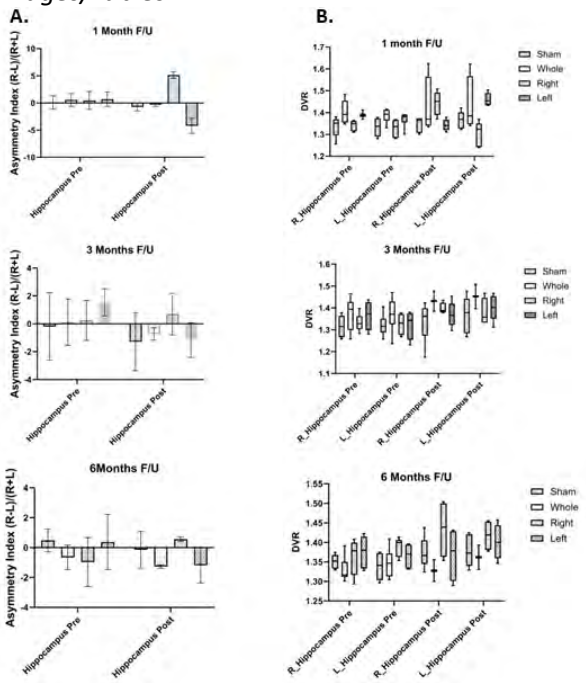

Fig1.
A. Asymmetry Index in Hippocampus SV2A measurements between groups at different time point after radiation
B. Hippocampus SV2A changes at 1, 3, 6 month after radiation.

Table 1: Hippocampal DVR across Four Irradiation Groups, Pre- and Post-Irradiation

Irradiation group	Sham Rx		Whole Brain Rx		Right sided Rx		Left sided Rx	
	Right side	Left side	Right side	Left side	Right side	Left side	Right side	Left side
Pre Rx	1.34±0.048	1.33±0.04	1.4±0.05	1.39±0.03	1.34±0.024	1.32±0.04	1.38±0.01	1.37±0.03
Post Rx 1 M	1.35±0.036	1.37±0.04	1.43±0.13	1.43±0.13	1.44±0.05	1.3±0.057	1.34±0.025	1.46±0.029
Post Rx 3 M	1.34±0.09	1.37±0.08	1.4±0.066	1.45±0.08	1.4±0.026	1.38±0.06	1.37±0.057	1.4±0.059
Post Rx 6 M	1.35±0.02	1.34±0.036	1.33±0.03	1.35±0.04	1.36±0.046	1.39±0.024	1.38±0.04	1.37±0.03

Rx: Irradiated

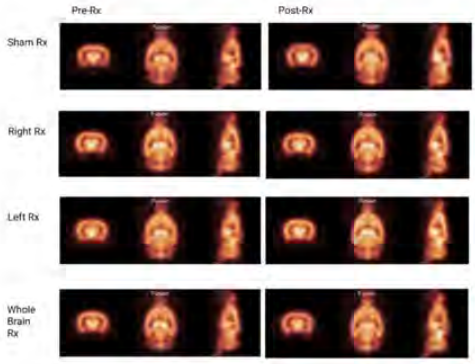

Fig2. 18F-SynVest-1 (SV2A) PET Imaging and Quantification in rat brains that underwent either whole brain, right, left, or sham irradiation. Image of SV2A uptake within the brain at different time points (Axial, coronal, sagittal).

613

Quantitative Intracranial Vessel Wall Imaging Features Differentiate Vasculitis from Atherosclerosis

Mona Kharaji MD[1], Yin Guo[1], Gador Canton PhD[1], Mohamad Hosaam Mosi MD[1], Xin Wang[1], Seyyed Kazem HashemizadehKolowri[2], Chun Yuan PhD[2], Niranjan Balu PhD[1], Mahmud Mossa-Basha MD[1]
[1]University of Washington, Seattle, Washington, USA. [2]University of Utah, Salt Lake City, Utah, USA

Abstract Category

Adult Brain

Purpose

Intracranial vasculopathy differentiation is one of the most frequent clinical indications for intracranial vessel wall MRI (IVW)[1]. Qualitative criteria using multi-contrast IVW have been established to aid in diagnosing conditions such as atherosclerosis, vasculitis and Reversible Cerebral Vasoconstriction Syndrome[2], however qualitative markers have varying definitions in the literature and may have limited reproducibility. This study describes a newly developed semi-automated quantitative IVW tool used to determine whether IVW features can effectively distinguish between atherosclerosis and vasculitis.

Materials & Methods

Seven patients with established intracranial vasculopathies based on clinical evaluation underwent multi-contrast IVW with and without contrast. Each imaging dataset was processed using the MOCHA pipeline[3]: multi-contrast IVW were registered, each arterial segment was independently traced on TOF-MRA and then displayed in a multi-planar view. A deep-learning algorithm automatically segmented the vessel lumen and outer wall boundaries. A radiologist reviewed each arterial segment, adjudicated the presence of atherosclerotic and vasculitis lesions, and corrected any segmentation errors. A contrast-enhancement color map was generated by pixel-wise subtraction of pre- and post-contrast IVW images with automated normalization of the vessel wall signal intensity on post-contrast IVW using the intensity measured in the genu of the corpus callosum[4].

For each lesion, maximum wall thickness, lesion length, and percent wall volume (wall volume / total vessel volume × 100%) features were extracted. The eccentricity index was computed as (maximum wall thickness–minimum wall thickness)/maximum wall thickness. The mean enhancement ratio was the mean signal intensity on the normalized

post-contrast IVW. Enhancing volume was defined as the volume of the vessel wall with an enhancement ratio>1, and percent enhancing volume was calculated as (enhancement volume/wall volume)×100.
Quantitative IVW features from atherosclerotic and vasculitis lesions were compared using generalized estimating equation-based univariate regression to account for multiple lesions identified within the same patient.

Results

Among the seven patients, six were clinically diagnosed with vasculitis. Vasculitis lesions were identified in 30 arterial segments. One patient was diagnosed with intracranial atherosclerosis, with 15 plaques detected. Additionally, six plaques were identified in three of the vasculitis patients, based on lesion morphology and vascular risk factors present. Comparing the 30 vasculitis lesions to the 21 atherosclerotic plaques, significant differences were observed in lesion length (14.2±7.6 mm vs. 4.7±2.1 mm, p<0.001), maximum wall thickness (1.52±0.29 mm vs. 1.82±0.29 mm, p<0.001), and eccentricity (0.58±0.05 vs. 0.61±0.09, p<0.001). No significant difference was found in percent wall volume (68.1±5.26 vs. 67.6±6.82, p=0.73).
Contrast enhancement was observed in 76.2% (16/21) of plaques compared to 93.3% (28/30) of vasculitis lesions. Vasculitis lesions demonstrated a significantly higher mean enhancement ratio (1.26 ± 0.47 vs. 0.71 ± 0.38, p < 0.001) and higher percent enhancing volume (59.7±32.0 vs. 17.4±27.3, p<0.001).

Conclusion

Quantitative IVW features revealed that compared to atherosclerotic plaque, vasculitis is characterized by longer lesions, lower wall thickness, lower wall eccentricity, and more intense and diffuse contrast enhancement. Future large-scale studies should focus on developing predictive models to improve the differentiation of atherosclerosis, vasculitis, and other intracranial vasculopathies using quantitative IVW features.

References

1. Mossa-Basha M, Zhu C, Yuan C, et al. Survey of the American Society of Neuroradiology Membership on the Use and Value of Intracranial Vessel Wall MRI. *American Journal of Neuroradiology* 2022;43:951–7.
2. Mossa-Basha M, Hwang WD, De Havenon A, et al. Multicontrast High-Resolution Vessel Wall Magnetic Resonance Imaging and Its Value in Differentiating Intracranial Vasculopathic Processes. *Stroke*2015;46:1567–73.
3. Guo Y, Canton G, Chen L, et al. Multi-Planar, Multi-Contrast and Multi-Time Point Analysis Tool (MOCHA) for Intracranial Vessel Wall Characterization. *Journal of Magnetic Resonance Imaging* 2022;56:944–55.
4. Sanchez S, Raghuram A, Fakih R, et al. 3D Enhancement Color Maps in the Characterization of Intracranial Atherosclerotic Plaques. *American Journal of Neuroradiology* https://doi.org/10.3174/ajnr.A7605.

Images/Tables

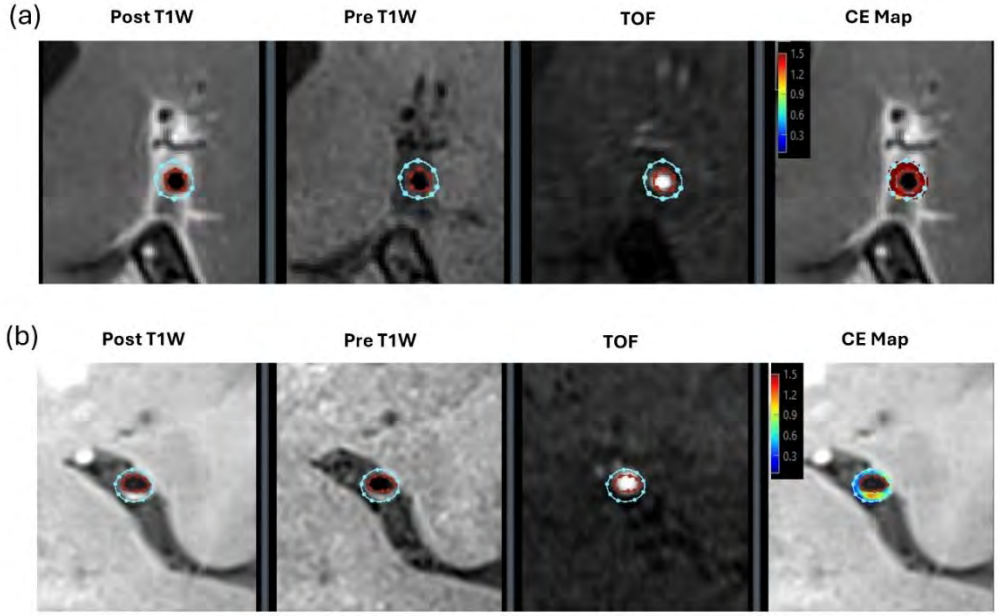

Figure *.Examples of M1 MCA analyzed using MOCHA, showing multi-contrast IVW in cross sections with lumen (red) and outer wall (blue) contours, along with a contrast enhancement (CE) color map. (a) Vasculitis lesion showing diffuse concentric enhancement, and (b) atherosclerotic plaque showing eccentric wall thickening and less enhancing volume.*

618

MRI OEF and $CMRO_2$ in Predicting Ischemic Lesion Survival in Acute Stroke: New insight on Diffusion Reversibility

Mona Asghariahmadabad MD[1], Pouya Metanat MD[1], Elham Tavakol MD[2], Ameera F Ismail MD[2], Mersedeh Bahr-Hosseini MD[2], Viktor Szeder MD, PhD[2], Geoffrey P Colby MD, PhD[2], Jeffrey L Saver MD[2], David S Liebeskind MD[2], Vivek Yedavalli MD[3], Wade S Smith MD[1], Anthony Kim MD[1], Cathra Halabi MD[1], Nerissa Ko MD[1], Anirudh Sreekrishnan MD[1], S Andrew Josephson MD[1], Kazim Narsinh MD[1], Luis E Savastano MD, PhD[1], Steven Hetts MD[1], Christopher P Hess MD, PhD[1], Kambiz Nael MD[1]

[1]University of California San Francisco, San Francisco, CA, USA. [2]UCLA, Los Angeles, CA, USA. [3]Johns Hopkins, Baltimore, MD, USA

Abstract Category

Adult Brain

Purpose

In patients with acute ischemic stroke (AIS), overestimation of ischemic core also known as “ghost core” is rare on pretreatment MRI, although has been reported when initial tissue with reduced diffusion reverses following successful reperfusion [1]. Oxygen extraction fraction (OEF) and cerebral metabolic rate of oxygen ($CMRO_2$) have emerged as important metabolic indicators of tissue viability in brain ischemia, where elevation of OEF has been associated with tissue survival after reperfusion[2], suggesting that such metabolic markers can predict the reversibility of DWI lesions. In this study we aimed to perform a quantitative voxel-based analysis to determine the association of OEF and $CMRO_2$ alterations on pretreatment MRI and diffusion reversibility in patients with AIS who underwent successful reperfusion.

Materials & Methods

In this retrospective study, patients were included if they had an anterior circulation large vessel occlusion (LVO), achieved successful reperfusion (TICI ≥ 2b), and had pre-treatment DSC perfusion and post-treatment MRI within 48 hours post-reperfusion. The segmentation of ischemic core and final infarct volume was performed using Olea Sphere (SP.23, Olea Medical). The ischemic core volume on pretreatment MRI was calculated using ADC ≤ 620×10^{-6} mm^2/s. Final infraction volume was segmented using posttreatment MRIs (obtained within 48-hour after reperfusion) by applying a volume of interest on b1000 images, using a voxel-based signal intensity method subsuming the entire region of DWI hyperintensity. The pre and posttreatment DWI images were imported to 3D Slicer (Version 5.6.2) for image coregistration using a linear transform approach and subsequently subtraction was performed to generate masks for common (persistent) infarct and survived (revered diffusion) tissue. DSC perfusion was processed by Cercare Medical Neurosuite (Cercare Medical) to generate OEF and $CMRO_2$ maps. These maps were then imported to 3D Slicer and coregistered with DWI masks. The voxel values of OEF and $CMRO_2$ from the infarcted and survived masks were extracted for voxel-based analysis. In each patient, a VOI was created on the contralateral (non-infracted) MCA distribution for normalization and to obtain relative OEF and $CMRO_2$ values. The differences between rOEF and $rCMRO_2$ in both survived and infarcted voxels was evaluated.

Results

Among 94 patients who achieved successful reperfusion, 5 (5.3%) had ghost core with overestimation of ischemic core volume by >10 mL which was reversed on the subsequent posttreatment MRI. The rOEF values (Figure 1) measured in the survived voxels were significantly higher than those in infarcted tissue (median 1.627 [IQR 1.264-2.415] vs. 1.486 [IQR 1.034-2.392] $p < 0.001$). Similarly, the $rCMRO_2$ values in survived voxels were significantly higher than in infarcted voxels (median 0.29 [IQR 0.118-0.59] vs. 0.093 [IQR 0.04-0.231], $p < 0.001$).

Conclusion

Increased rOEF and $rCMRO_2$ within the overestimated hyperacute ischemic lesion on admission DWI is associated with tissue survival and reversibility of reduced diffusion. These findings suggest that the higher OEF and $CMRO_2$ values in pretreatment ischemic core may predict diffusion reversibility, indicating the presence of metabolically active and potentially recoverable tissue despite reduction in diffusion values.

References

1. McArthur MA, Tavakkol E, Bahr-Hosseini M, et al. Overestimation of ischemic core on baseline MRI in acute stroke. *Interventional Neuroradiology*. 2024:15910199231224500. doi:10.1177/15910199231224500

2. Bani-Sadr A, Hermier M, de Bourguignon C, et al. Oxygen Extraction Fraction Mapping on Admission Magnetic Resonance Imaging May Predict Recovery of Hyperacute Ischemic Brain Lesions After Successful Thrombectomy: A Retrospective Observational Study. *Stroke*. 2024/11/01 2024;55(11):2685-2693. doi:10.1161/STROKEAHA.124.047311

Images/Tables

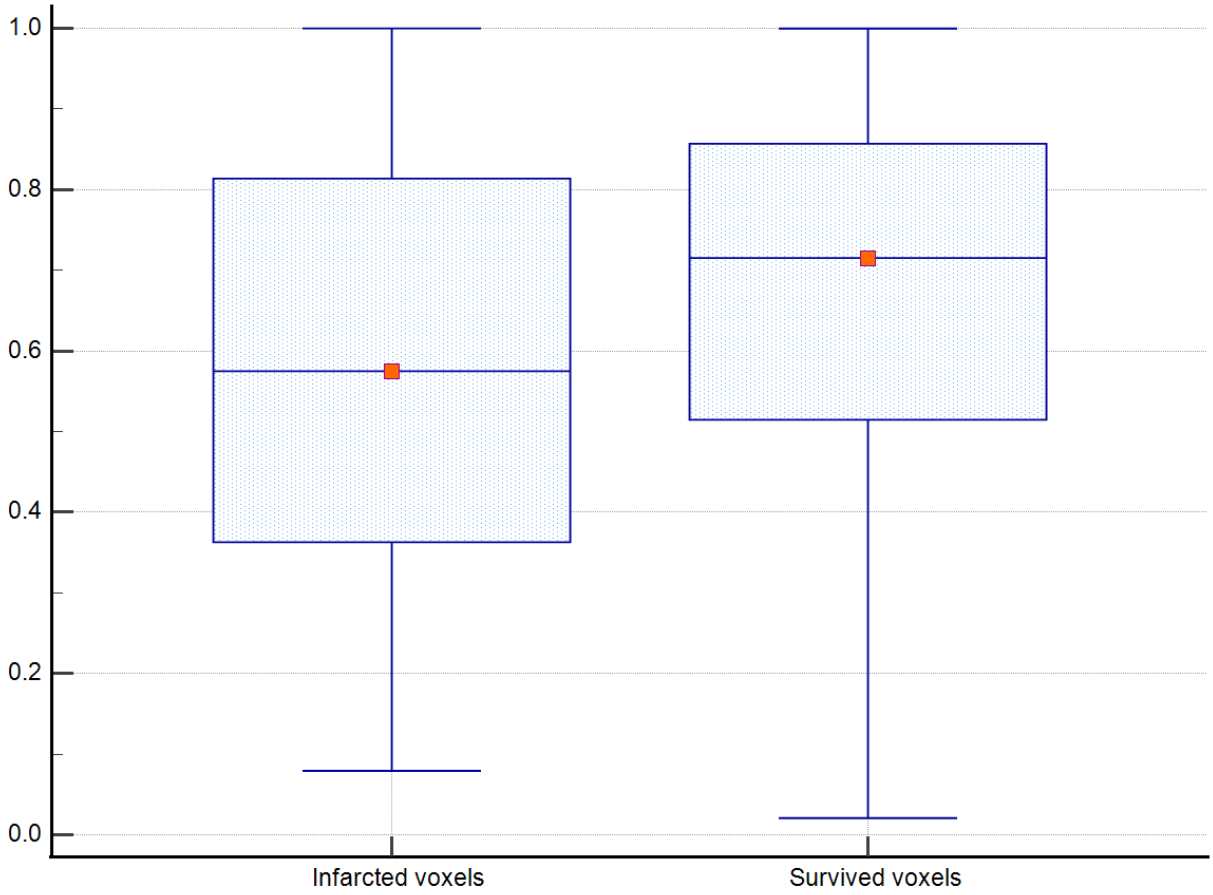

630

CSF Opening Pressures in Spontaneous Intracranial Hypotension Due To CSF-Venous Fistula: A Retrospective Analysis

Bala McRae-Posani MSc, Sara Strauss MD, Matthew S Robbins MD, Gayle Salama MD
Weill Cornell Medicine, New York, NY, USA

Abstract Category

Spine

Purpose

Low CSF pressure has classically been considered a defining feature in the pathogenesis of spontaneous intracranial hypotension (SIH) and is part of the International Headache Society (IHS) diagnostic criteria for SIH (IHS 2018). However, normal or elevated CSF pressures are commonly measured in SIH during myelography (Callen et al 2023, Duvall et al 2019, Kranz et al 2016). We report on CSF pressures in patients with SIH due to CSF-venous fistula (CVF).

Materials & Methods

Following IRB approval, consecutive SIH patients with spinal CSF leak undergoing myelography between 2021 and 2024 at a single quaternary care center were retrospectively analyzed. Leak type classification was done following Schievink et al (2016): Type 1 = dural tear; Type 2 = meningeal diverticulum; Type 3 = CSF venous fistula (CVF). The CSF pressure was defined as the opening pressure (OP) with patient in decubitus positioning with mild hip elevation during the CT/MR myelogram procedure. Low OP was defined as < 6 cm H2O. Elevated OP was defined as > 20 cm H2O.

Results

Of the 70 SIH patients analyzed, 26 (37%) had a Type-3 leak (CVF) [average age 58±13; 8/26 (31%) male; 18/26 (69%) female]. Of the 26, OP was reported for 24 patients. The mean ± SD OP was 14.88 ± 4.79 cm H2O (range of 6-25 cm

H2O). None (0%) of the patients had a low OP (<6 cm H2O). 20/24 (83%) had OP in the normal range (6-20 cm H2O) and 4/24 (17%) had elevated OP (>20 cm H2O).

Conclusion

All of the patients with SIH due to CVF in our study had either normal or elevated CSF pressures. This finding has clinical implications. An absence of low CSF pressure or the presence of mildly elevated CSF pressure should not be used to rule out SIH. As such, the current IHS criteria for SIH may need to be updated. Additionally, high normal or elevated OP readings obtained during myelography in patients with active CVF suggest that underlying intracranial hypertension may be associated with the development of CVF and with post-treatment rebound intracranial hypertension.

References

Callen AL, Pattee J, Thaker AA, et al.. Relationship of Bern Score, Spinal Elastance, and Opening Pressure in Patients With Spontaneous Intracranial Hypotension. Neurology. 2023 May 30;100(22):e2237-e2246. DOI: https://doi.org/10.1212/WNL.0000000000207267

Duvall JR, Robertson CE, Cutsforth-Gregory JK, et al. Headache due to spontaneous spinal cerebrospinal fluid leak secondary to cerebrospinal fluid-venous fistula: Case series. Cephalalgia. 2019 Dec;39(14):1847-1854. DOI: https://doi.org/10.1177/0333102419881673

Headache Classification Committee of the International Headache Society (IHS) The International Classification of Headache Disorders, 3rd edition. Cephalalgia. 2018 Jan;38(1):1-211. DOI: https://doi.org/10.1177/0333102417738202.

Kranz PG, Tanpitukpongse TP, Choudhury KR, et al. How common is normal cerebrospinal fluid pressure in spontaneous intracranial hypotension? Cephalalgia. 2016 Nov;36(13):1209-1217. DOI: https://doi.org/10.1177/0333102415623071

Schievink WI, Maya MM, Jean-Pierre S, et al. A Classification System of Spontaneous Spinal CSF Leaks. Neurology 2016; 87(7):673-679. DOI: https://doi.org/10.1212/wnl.0000000000002986

633

Whole Brain Spectroscopic Imaging Guided Planning of Tumor Treating Fields in Glioblastomas: Our Initial Experience

Sanjeev Chawla PhD, Archith Rajan PhD, Laiz Laura de Godoy MD, PhD, Kristina Vineis BS, Demetrius Lee, Lisa Desiderio, Stephen Bagley MD, Suyash Mohan MD

Perelman School of Medicine at the University of Pennsylvania, Philadelphia, PA, USA

Abstract Category

Functional/Advanced Imaging

Purpose

Glioblastomas (GBMs) infiltrate extensively into adjacent normal brain regions, beyond enhancing margins where inevitable recurrence occurs.[1] An optimal treatment for GBM requires precise targeting of all viable tumor cells, many of which are not visible on conventional neuroimaging. Tumor treating fields (TTFields) are a loco-regional and noninvasive therapy delivered by means of transducer arrays on patient's shaved scalp close to the tumor.[2] Despite promising clinical outcomes, significant inter-individual variability in treatment response to TTFields has been observed.[3] This is because only solid/contrast enhancing regions of GBMs are targeted for TTFields delivery in the current clinical practice. In this study, our aim was to utilize whole brain spectroscopic imaging (WBSI) derived choline/N-acetylaspartate (NAA) maps to identify infiltrating tumor cells in patients with GBM for selecting a precise target volume (solid contrast-enhancing + infiltrative regions) for personalized mapping of transducer arrays for enhanced delivery of TTFields to the entire 'viable' tumor bed.

Materials & Methods

Forty-two GBM patients underwent anatomical imaging, and WBSI on 3T-MRI. Processing steps for WBSI data included field inhomogeneity and eddy current correction, k-space regridding, spatial and Fourier transformation.[4] In each case, quality assurance was evaluated by considering Cramer-Rao lower bounds, line-shape, line-width, CSF contamination, and degree of residual water/lipid signals. Choline/NAA maps, and anatomical images were co-registered. One 3D-composite mask was drawn manually on post-contrast-T1 and T2-FLAIR hyperintense tumor abnormalities and labeled as 'anatomical target volume (ATV)' for TTFields delivery using a conventional transducer array layout. Another mask was drawn on contralateral normal-appearing brain parenchyma by selecting a volume comparable to tumor size and at same slice level and was labeled as 'normal mask'. A mean value of choline/NAA was computed from normal mask, and all those voxels exceeding a two-fold threshold value of choline/NAA as measured from normal mask were included into

a 3D-composite mask from tumor region and labeled as “metabolic target volume (MTV)” for TTFields delivery using an experimental transducer array layout.[5]

Results

The total number of good quality voxels covering the brain was in range of 16448 -19428 (~72%). The number of voxels encompassing MTV on choline/NAA maps were found to be 1 to 3.6 folds higher (mean±SD=43953.1±28548.7 vs. 36555.4±28549.2) than those drawn on ATV. While estimating dosimetry profile, MTVs received more TTFields dose compared to ATVs. **Figure 1.** from a GBM patient shows selections of target volumes using PC-T1 and WBSI derived choline/NAA map. As evident, approximately 2.3 times more viable tumor cells were detected using metabolic map than PC-T1 image. Also, MTV guided delivery of TTFields dose is higher at tumor bed than that of ATV [average power density (3.5mW/cm^3 vs. 2.5 mW/cm^3) and average field intensity (2.4V/cm vs. 1.6 V/cm)]. Moreover, WBSI derived Cho/NAA maps at baseline identified regions at high risk for tumor recurrence (confirmed by histopathology) at followup in 4 cases.

Conclusion

WBSI derived metabolite maps project a more comprehensive representation of tumor’s true spatial extent and provide more accurate assessment of margins of viable tumor for delivering TTFields in GBMs.

References

1. Chawla S, Zhang Y, Wang S, et al. Proton magnetic resonance spectroscopy in differentiating glioblastomas from primary cerebral lymphomas and brain metastases. J Comput Assist Tomogr. 2010;34(6):836-41.
2. Wong ET, Lok E, Swanson KD. Alternating Electric Fields Therapy for Malignant Gliomas: From Bench Observation to Clinical Reality.
   Prog Neurol Surg. 2018;32:180-95.
3. Stupp R, Taillibert S, Kanner AA, et al. Maintenance Therapy With Tumor-Treating Fields Plus Temozolomide vs Temozolomide Alone for Glioblastoma: A Randomized Clinical Trial. JAMA. 2015;314(23):2535-43.
4. Verma G, Chawla S, Mohan S, Wang S, Nasrallah M, Sheriff S, Desai A, Brem S, O'Rourke DM, Wolf RL, Maudsley AA, Poptani H. Three-dimensional echo planar spectroscopic imaging for differentiation of true progression from pseudoprogression in patients with glioblastoma. NMR Biomed. 2019;32(2):e4042.
5. Guo J, Yao C, Chen H, et al. The relationship between Cho/NAA and glioma metabolism: implementation for margin delineation of cerebral gliomas. Acta Neurochir. 2012:154; 1361-70.

Images/Tables

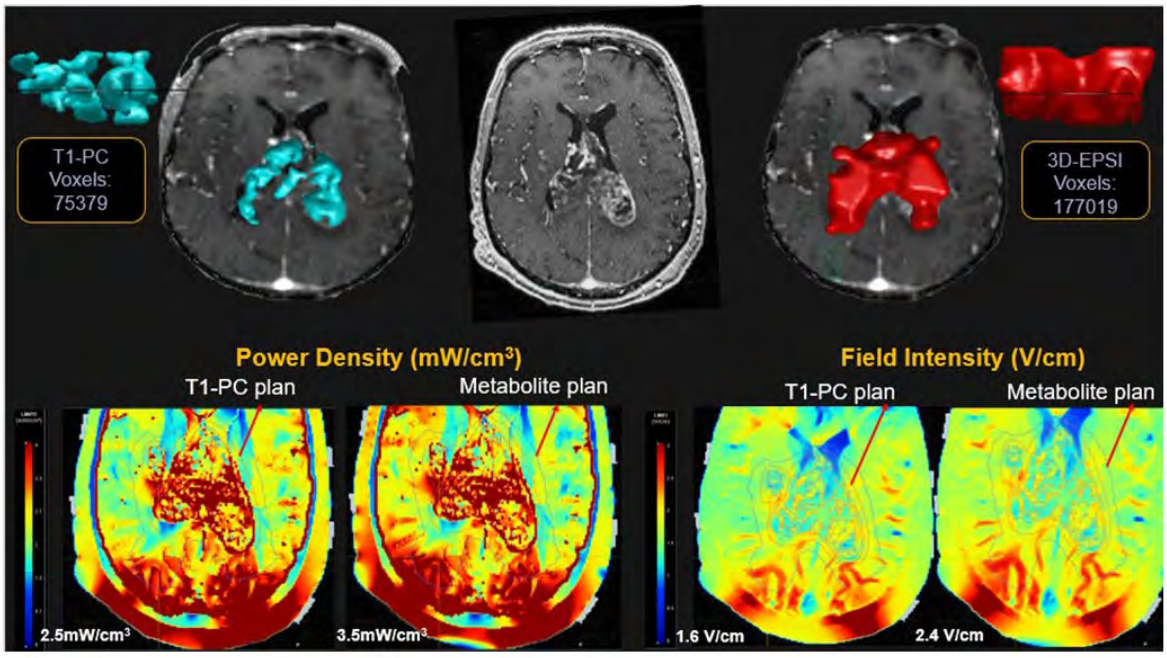

636

Point-Of-Care Portable MR Imaging as part of Neurocritical Care: Initial UC Davis experiences and current Barriers

Neha Antil MD, Kader Karli Oguz MD, Maryam Shahrzad MD, Lotfi Hacein-Bey MD, Matthew Bobinski MD
UC Davis, Sacramento, CA, USA

Abstract Category

Functional/Advanced Imaging

Purpose

We aim to share our experience and evaluate the clinical utility of Point-of-Care (POC) MRI in neurocritical care. Additionally, seeks to identify potential obstacles that may limit the broader implementation and use of POC MRI within our institution.

Materials & Methods

The study was performed in two portions. For the first portion, a retrospective study was conducted on patients who underwent POC MRI as part of their neurocritical care management between February 2022 and July 2024. The POC findings were compared with the follow-up fixed MRI.

For the second portion, a cross-sectional survey was conducted among physicians and technicians involved in neurocritical care. The survey aimed to identify barriers related to the POC MRI use: (1) equipment limitations (e.g., maintenance and reliability), (2) clinical practice factors (e.g., time constraints, workflow integration), and (3) institutional factors (e.g., cost, training, and availability). Responses were analyzed qualitatively to identify common themes.

Results

A total of 27 patients were identified who underwent Point-of-Care (POC) MRI, out of which 17 had acute findings (such as infarct; shown in figure below, and anoxic brain injury) and 10 had no acute abnormality. POC MRI correctly identified acute findings in 16 out of 17 positive cases (94.11%) and were later confirmed on the fixed MRI. However, POC MRI missed sub centimeter infarcts in a few cases; 1 out of 17 (5.88%) positive cases and 3 out 10 (30%) negative cases, which were subsequently detected on the fixed MRI.

A total of 21 physicians in neurocritical care and 12 technologists completed the survey. The findings reveal key differences in perspectives between the two groups.

Neurocritical care physicians' Responses:

The major factors affecting the decision of neuro physicians (13/21; 61.9%) to order a POC scan was identified as Low Image Quality and low diagnostic yield. On the other hand, Lack of Familiarity and Availability of POC scanners were found to be less of an issue for neuro physicians.

Technologists' Responses:

For technologists, the primary challenges in utilizing POC scanners were: 1. Patient Positioning: 10 out 13 (76.92%) technologists stated that proper positioning of the patient during POC scans was a significant challenge, particularly given the mobile nature of the scanners and the need for accurate positioning to obtain high-quality images and 2. Time Required to Transport the Scanner: 5 out 13 (38.46%) technologists cited the time-consuming process of moving both the scanner and the patient as a key barrier to efficient use.

Conclusion

The POC MRI offers a valuable, rapid imaging for certain acute conditions, its sensitivity for small lesions may not be sufficient for comprehensive evaluation, highlighting the importance of confirmatory imaging with fixed MRI or CT for a complete diagnosis.

The survey findings suggest that while neurophysicians are more concerned with the diagnostic effectiveness of POC scanners—specifically image quality and yield—technologists are primarily concerned with the logistical and operational challenges, such as the time required for transport and the complexity of patient positioning. These insights could guide improvements in both the technology itself and the operational protocols surrounding POC scanner usage.

References

1. Arnold TC, Freeman CW, Litt B, Stein JM. Low-field MRI: Clinical promise and challenges. J Magn Reson Imaging. 2023 Jan;57(1):25-44. doi: 10.1002/jmri.28408. Epub 2022 Sep 19. PMID: 36120962; PMCID: PMC9771987.
2. Deoni SCL, Medeiros P, Deoni AT, Burton P, Beauchemin J, D'Sa V, Boskamp E, By S, McNulty C, Mileski W, Welch BE, Huentelman M. Development of a mobile low-field MRI scanner. Sci Rep. 2022 Apr 5;12(1):5690. doi: 10.1038/s41598-022-09760-2. PMID: 35383255; PMCID: PMC8982311.

3. Sheth KN, Mazurek MH, Yuen MM, Cahn BA, Shah JT, Ward A, Kim JA, Gilmore EJ, Falcone GJ, Petersen N, Gobeske KT, Kaddouh F, Hwang DY, Schindler J, Sansing L, Matouk C, Rothberg J, Sze G, Siner J, Rosen MS, Spudich S, Kimberly WT. Assessment of Brain Injury Using Portable, Low-Field Magnetic Resonance Imaging at the Bedside of Critically Ill Patients. JAMA Neurol. 2020 Sep 8;78(1):41–7. doi: 10.1001/jamaneurol.2020.3263. Epub ahead of print. PMID: 32897296; PMCID: PMC7489395.
4. Kimberly WT, Sorby-Adams AJ, Webb AG, Wu EX, Beekman R, Bowry R, Schiff SJ, de Havenon A, Shen FX, Sze G, Schaefer P, Iglesias JE, Rosen MS, Sheth KN. Brain imaging with portable low-field MRI. Nat Rev Bioeng. 2023 Sep;1(9):617-630. doi: 10.1038/s44222-023-00086-w. Epub 2023 Jul 17. PMID: 37705717; PMCID: PMC10497072.
5. Kuoy E, Glavis-Bloom J, Hovis G, Yep B, Biswas A, Masudathaya LA, Norrick LA, Limfueco J, Soun JE, Chang PD, Chu E, Akbari Y, Yaghmai V, Fox JC, Yu W, Chow DS. Point-of-Care Brain MRI: Preliminary Results from a Single-Center Retrospective Study. Radiology. 2022 Dec;305(3):666-671. doi: 10.1148/radiol.211721. Epub 2022 Aug 2. PMID: 35916678; PMCID: PMC9713449.

Images/Tables

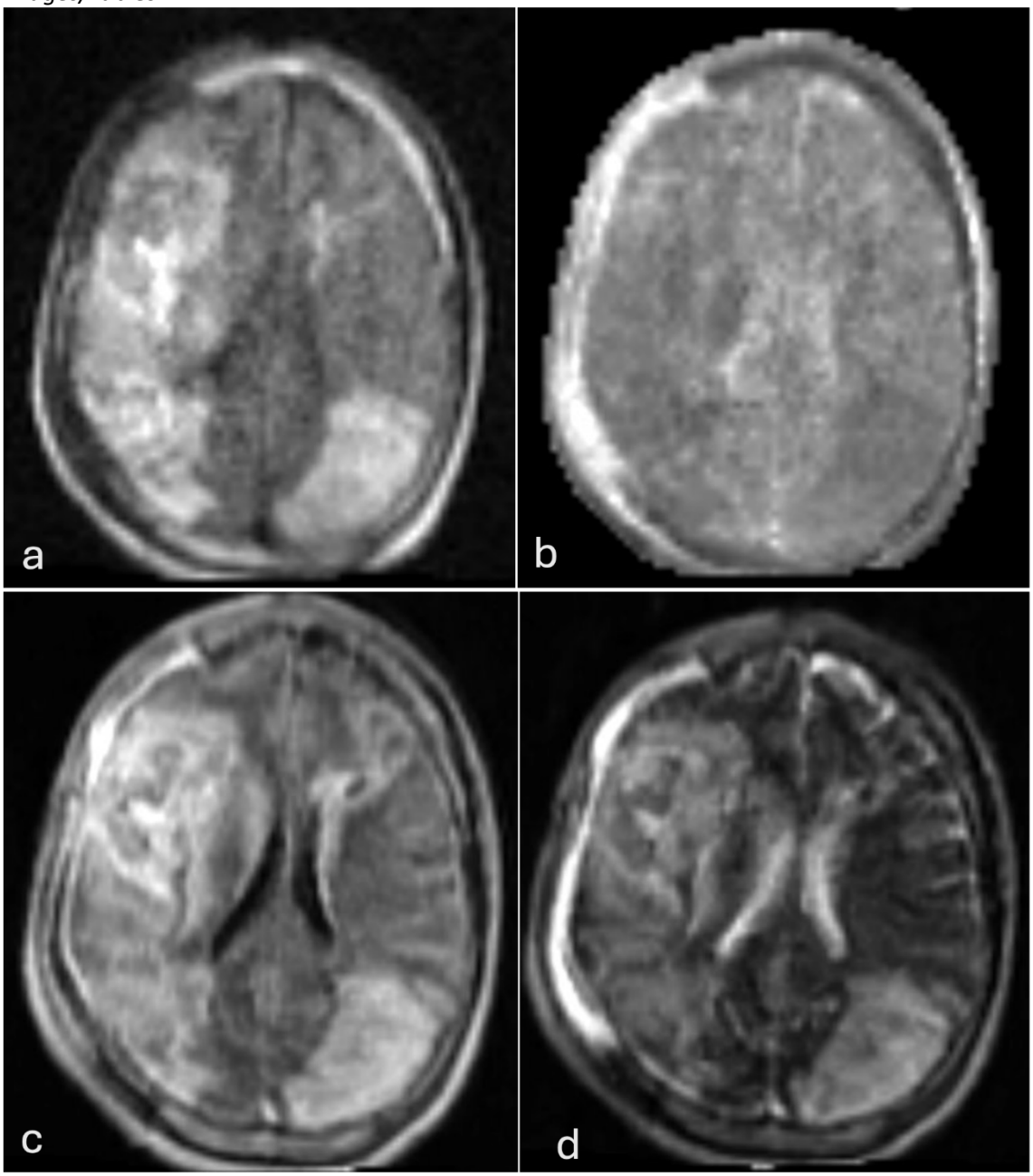

640

Are Mesial Temporal Sclerosis- Hippocampal Sclerosis (MTLE-HS) and MTLE-HS with Temporal Neocortical Changes (MTLE-HS-N), Two Distinct Entities?

Bejoy Thomas MD, DNB, PDCC, Viswanadh Kalaparti Sri Venkata Ganesh MD, DM, Ashalatha Radhakrishnan MD, DM, Deepti A Narasimhaiah MD, PhD, George C Vilanilam MS, MCh
Sree Chitra Tirunal Institute for Medical Sciences and Technology, Thiruvananthapuram, Kerala, India

Abstract Category

Adult Brain

Purpose

High- field strength MRI has shown that Mesial Temporal Sclerosis (MTS) can be divided into two entities, depending on presence or absence of abnormality beyond the mesial temporal lobe. The objective of the study was to identify any possible differences in clinical, electrophysiological, histopathological features, post-surgical outcomes between these entities and to evaluate the potential role of Arterial Spin Labeling perfusion imaging (ASL) in their differentiation.

Materials & Methods

Institutional Ethics Committee approved, this prospective study included consecutive cases recruited in a tertiary referral centre for comprehensive epilepsy care from Jan2017-Dec 2022. MTS-patients who underwent epilepsy protocol-MRI including 3D ASL followed by anterior temporal lobectomy+ amygdalohippocampectomy (ATL+AH), after complete pre- surgical evaluation were included. The patients were divided into two groups based on the findings on T2, 3D-FLAIR MRI. MTLE-HS with mesial temporal lobe sclerosis (1) and MTLE-HS-N with involvement of the temporal neocortex in addition to the mesial temporal structures (2). Pathological evaluation of the resected labelled specimens was done after staining with NeuN, Luxol Fast Blue and Immunohistochemistry with Glial Fibrillary Acid Protein (GFAP). The clinical, VEEG, pathological characteristics and postoperative outcomes were compared. A P-value<0.05 was taken as statistically significant.

Results

During the study period, 6000 patients underwent VEEG of which 251 patients underwent ATL+AH after pre- surgical evaluation. Finally, 107 patients met the inclusion criteria. Sixty-three patients were included in the MTLE-HS-N group and, 37 in the MTLE-HS group based on T2' FLAIR MR imaging. Age of epilepsy onset was earlier in the MTLE-HS-N compared to MTLE-HS group (7.82 ± 6.19 versus 11.12 ± 8.16, P-value=0.04). There was a higher incidence of neocortical epileptogenesis in the MTLE-HS-N group (66.67% vs 13.51%, P-value<0.0001). Histopathological analysis revealed diffuse astrogliosis in the temporal neocortex in all patients, myelin loss in many patients from both groups and neocortical temporal lobe dysplasia in only 6 patients. No significant difference was seen in individual histopathological characteristics or post-operative outcomes. Within the MTLE-HS -N group, more number of patients with neocortical temporal seizures had ASL abnormality (P<0.05). Qualitative ASL abnormality was also seen in most (5/6, 83.33%) patients with neocortical dysplasia.

Conclusion

Although MTLE-HS and MTLE-HS-N show differences in certain clinical and electrophysiological features, they do not show a significant difference in the postoperative outcome. MRI cannot predict the exact histopathological substrate responsible for temporal neocortical changes. ASL may be useful to predict neocortical epileptogenesis in these patients. It could also help to postulate the presence of dysplasia, although this needs further evaluation for confirmation.

References

1. Rémi J, Vollmar C, de Marinis A, at al. Congruence and discrepancy of interictal and ictal EEG with MRI lesions in focal epilepsies. *Neurology.* 2011; 77(14):1383-90. doi: 10.1212/WNL.0b013e31823152c3
2. Barba C, Barbati G, Minotti L, Hoffmann D, Kahane P. Ictal clinical and scalp-EEG findings differentiating temporal lobe epilepsies from temporal "plus" epilepsies. *Brain.* 2007;130(7):1957–67. doi: 10.1093/brain/awm108.
3. Mittal A, Singh Dhanota D, Saggar K, Singh G, Ahluwalia A. Role of interictal arterial spin labeling magnetic resonance perfusion in mesial temporal lobe epilepsy. *Ann Indian Acad Neurol.* 2021;24(4):495. doi:1 0.4103/aian.AIAN_1274_20

Images/Tables

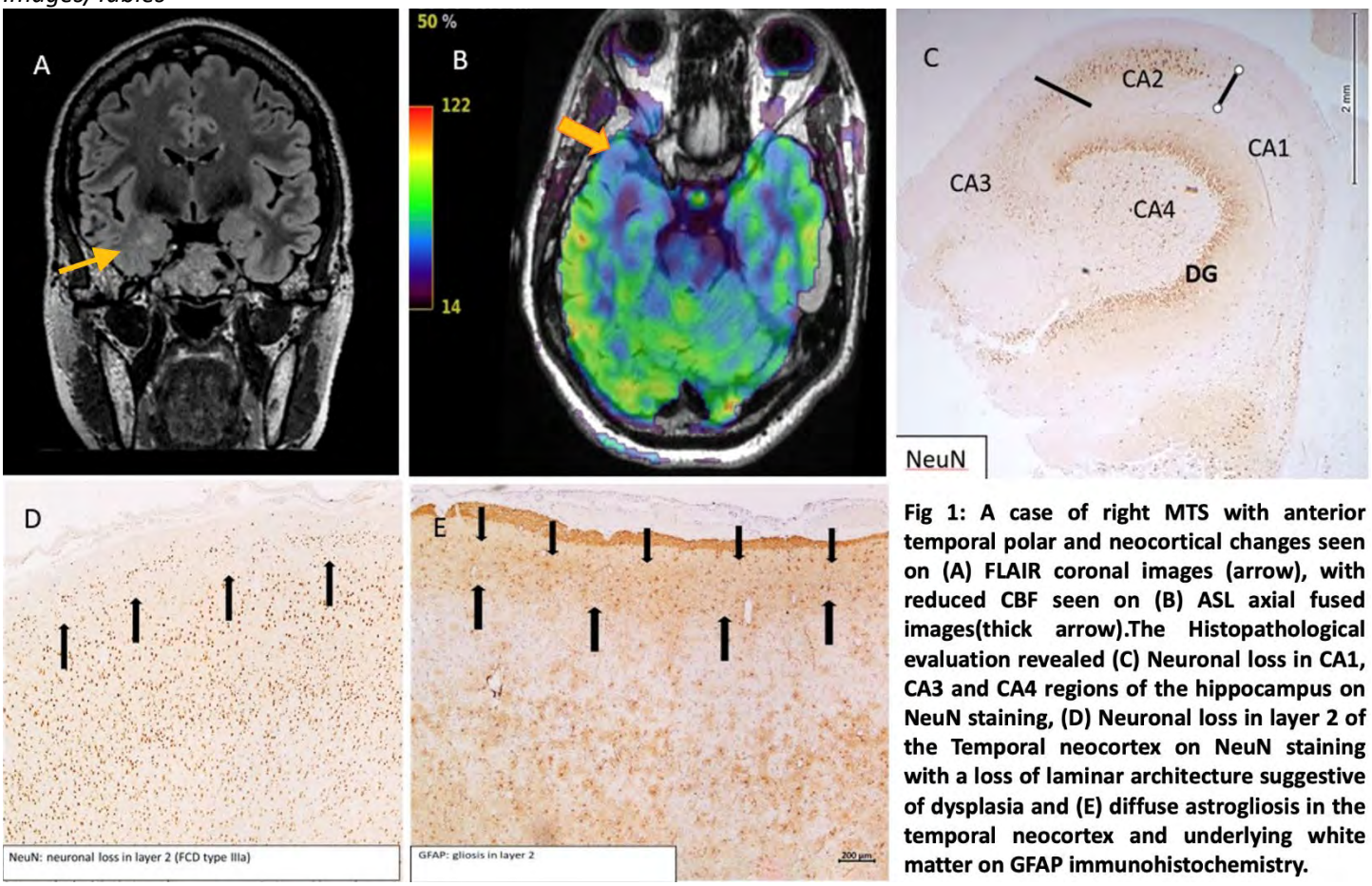

Fig 1: A case of right MTS with anterior temporal polar and neocortical changes seen on (A) FLAIR coronal images (arrow), with reduced CBF seen on (B) ASL axial fused images(thick arrow).The Histopathological evaluation revealed (C) Neuronal loss in CA1, CA3 and CA4 regions of the hippocampus on NeuN staining, (D) Neuronal loss in layer 2 of the Temporal neocortex on NeuN staining with a loss of laminar architecture suggestive of dysplasia and (E) diffuse astrogliosis in the temporal neocortex and underlying white matter on GFAP immunohistochemistry.

648

Association of Glymphatic Flow at Diffusion-Tensor MRI with Motor Symptoms and Dopaminergic Degeneration in Parkinson's Disease

Chae Jung Park MD, PhD[1], Jun Hwee Kim MD, PhD[1], Sang-Young Kim PhD[2]
[1]Yongin Severance hospital, Yongin-si, Gyeonggi-do, Korea, Republic of. [2]Philips Healthcare Korea, Seoul, Seoul, Korea, Republic of

Abstract Category

Adult Brain

Purpose

The Diffusion Tensor Image-Analysis aLong the Perivascular Space (DTI-ALPS) is a non-invasive tool which indirectly assess glymphatic function. This study aimed to investigate the association between DTI-ALPS, nigrostriatal dopaminergic degeneration and motor symptoms in patients with Parkinson's disease (PD).

Materials & Methods

This retrospective study included consecutive participants diagnosed with drug-naïve PD (n = 270). All study subjects underwent brain MRI including DTI and dopamine transporter (DAT) scanning using using N-(3-fluoropropyl)-2β-carbonethoxy-3β-(4-iodophenyl) nortropane positron emission tomography. The ALPS index reflecting glymphatic activity was calculated by a ratio of the diffusivities along the x-axis in the projection and association neural fibers to the diffusivities perpendicular to them. The relationship between ALPS index, DAT availability and Unified PD Rating Scale Part III (UPDRS-III) scores was assessed using multivariate linear regression. Mediation analyses were performed to identify causal link between ALPS index, DAT availability in the posterior putamen, and UPDRS-III.

Results

A total of 270 participants diagnosed with PD (152 females; mean age 71.8 years ± 10.0 years]) were included. The UPDRS-III score was 21.9 ± 10.5 (mean ± standard deviation). The multivariate linear regression analysis revealed that DAT availability in the posterior putamen (β=-5.263, P<0.001), and ALPS index (β=-8.023, P=0.005) were independently

associated with UPDRS-III score even after adjusting for age and disease duration. At mediation analysis, ALPS index significantly affected UPDRS-III (Direct effect: β=-8.216, P=0.006), however, the mediation effect of DAT availability in the posterior putamen was not significant (Indirect effect: β=1.160, P=0.364). On the contrary, DAT availability in the posterior putamen also significantly affected UPDRS-III (Direct effect: β =-5.436, P<0.001) without significant mediating effect of ALPS index (Indirect effect: β=0.128, P=0.370).

Conclusion

Nigrostriatal dopaminergic degeneration in the posterior putamen and ALPS index both had significant impact on UPDRS score independently, without significant mediation effect between each other. Decreased ALPS index, indicating dysfunction of glymphatic system, was associated with worse UPDRS score which may involve extra-nigrostriatal neurodegeneration.

References

1. Li Y, Zhou Y, Zhong W, et al. **Choroid Plexus Enlargement Exacerbates White Matter Hyperintensity Growth through Glymphatic Impairment.** *Ann Neurol* 2023;94:182-95
2. Li H, Jacob MA, Cai M, et al. **Perivascular Spaces, Diffusivity Along Perivascular Spaces, and Free Water in Cerebral Small Vessel Disease.** *Neurology* 2024;102:e209306
3. Linortner P, McDaniel C, Shahid M, et al. **White Matter Hyperintensities Related to Parkinson's Disease Executive Function.** *Movement Disorders Clinical Practice* 2020;7:629-38
4. Zhang W, Zhou Y, Wang J, et al. **Glymphatic clearance function in patients with cerebral small vessel disease.** *Neuroimage* 2021;238:118257

Images/Tables

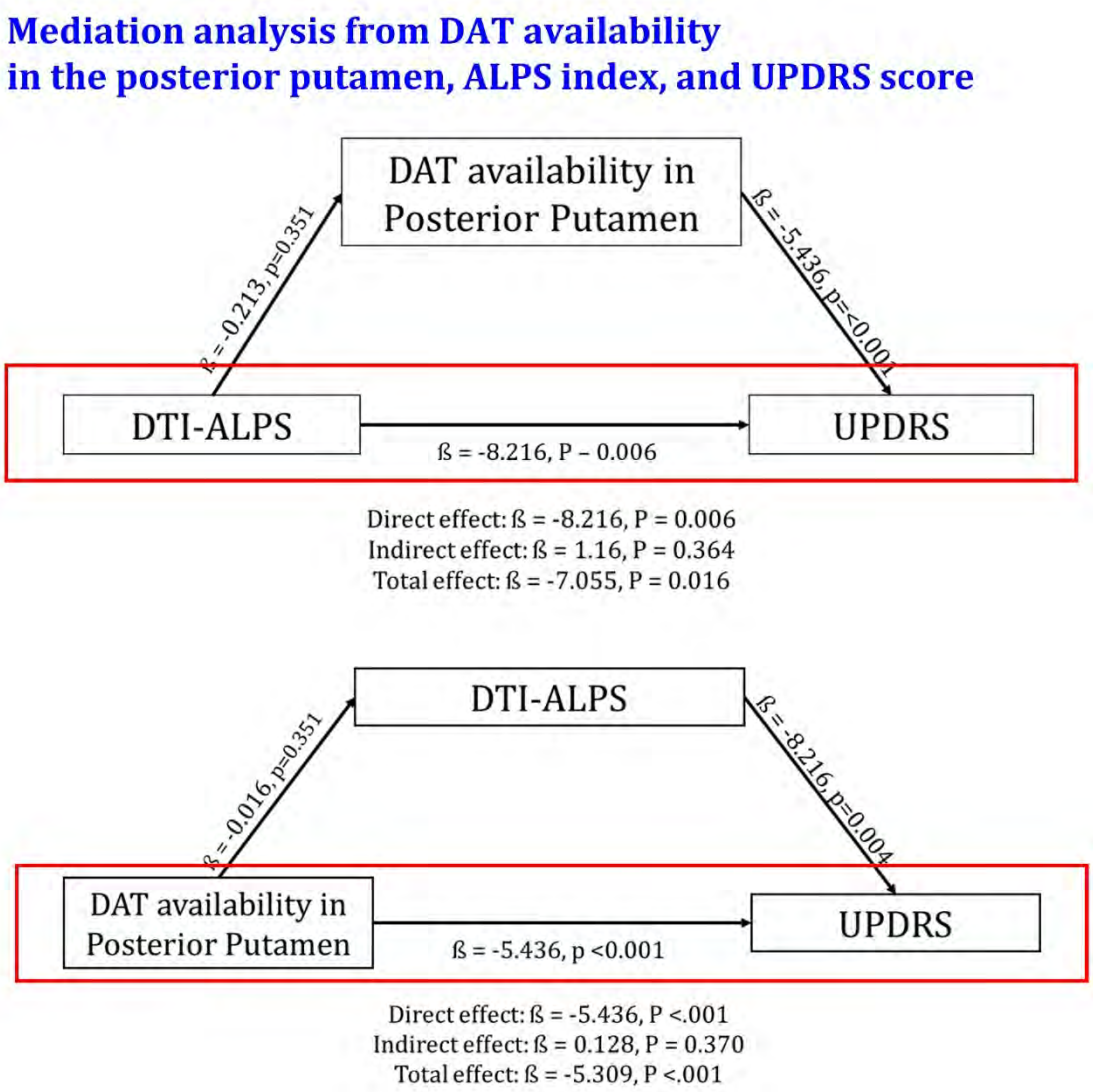

653

Subiculum/CA1 Thickness as a Potential Simple Imaging Biomarker for Hippocampal Sclerosis

Anna Cui BA, Chad Farris MD, PhD
Boston University Chobanian & Avedisian School of Medicine, Boston, MA, USA

Abstract Category

Adult Brain

Purpose

Hippocampal sclerosis (HS) is commonly seen with Limbic-predominant age-related TDP-43 encephalopathy (LATE), which causes an amnestic dementia syndrome like Alzheimer's disease (AD). Volumetric analysis of MRIs with hippocampal sclerosis has demonstrated volume loss in the subiculum/CA1, but volumetric analysis of these regions is not practical in routine clinical practice. We investigate if simple thickness measurements of the subiculum/CA1 can serve as a biomarker for hippocampal sclerosis and discriminate HS from AD.

Materials & Methods

This retrospective study used the National Alzheimer's Coordinating Center (NACC) database to identify MRIs with 3D-T1 sequences of participants with pathologically confirmed HS and/or AD and controls without HS and AD that had an MRI Brain performed within 2 years before death. Four groups were created based on the present or absence of HS and AD: HS present AD absent (HS+AD-, n=8), HS absent AD present (HS-AD+, n=7), HS present AD present (HS+AD+, n=7), or HS absent AD absent (HS-AD-, n=8). MRIs for the selected cases in the NACC database were analyzed in 3D Slicer to obtain measurements of the bilateral anterior, middle, and posterior hippocampal CA1/subiculum thickness measured perpendicular to the long access of the hippocampus. The smaller of the two measurements at each level of the hippocampus was used. One-way ANOVA followed by Tukey HSD were used to evaluate for significant differences.

Results

Anterior hippocampal CA1/subiculum thickness was significantly smaller in the HS+AD- 0.85 mm (0.63-1.06 mm), HS+AD+ 0.89 mm (0.66-1.12 mm), and HS-AD+ 1.25 mm (1.02-1.48 mm) groups versus the HS-AD- group 1.89 mm (1.67-2.10) (mean (95% CI)) ($p<0.002$ for all comparisons). Additionally, there was a trend towards a smaller thickness in the anterior hippocampus in the HS+AD- and HS+AD+ groups relative to the HS-AD+ group ($p=0.06$ and $p=0.13$, respectively). There was no significant difference in thickness in the anterior hippocampus between the HS+AD- and HS+AD+ groups ($p=0.99$). Middle hippocampal CA1/subiculum thickness was significantly smaller in the HS+AD- group 1.26 mm (0.84-1.67 mm) relative to the HS-AD- 2.19 mm (1.77-2.60 mm) and HS-AD+ 2.23 mm (1.78-2.67 mm) groups ($p<0.02$ for both comparisons). No additional significant differences were found in middle hippocampus thickness, HS+AD+ 1.60 mm (1.15-2.04 mm). No significant differences were observed in the posterior hippocampal CA1/subiculum thickness among the groups with HS+AD- 2.01 mm (1.55-2.46 mm), HS+AD+ 1.86 mm (1.37-2.34 mm), HS-AD- 2.7 mm (2.25-3.15 mm), and HS-AD+ 1.94 mm (1.46-2.42 mm).

Conclusion

Overall, both HS and/or AD result in a significant reduction in CA1/subiculum thickness relative to controls without HS and AD in the anterior hippocampus with less pronounced or no differences found in the middle and posterior hippocampus. Anterior hippocampal CA1/subiculum thickness is a potential biomarker for the presence of HS and/or AD. Additionally, anterior hippocampal CA1/subiculum thickness maybe more reduced in HS with or without AD and could possibly serve as a biomarker to help discriminate the presence or absence of HS with or without AD, but further evaluation is needed in a larger study to examine this possibility.

References

1. Smirnov DS, Galasko D, Hansen LA, Edland SD, Brewer JB, Salmon DP. Trajectories of cognitive decline differ in hippocampal sclerosis and Alzheimer's disease. Neurobiology of Aging 2019;75:169-177. doi: https://doi.org/10.1016/j.neurobiolaging.2018.11.015
2. Zarow C, Wang L, Chui HC, Weiner MW, Csernansky JG. MRI Shows More Severe Hippocampal Atrophy and Shape Deformation in Hippocampal Sclerosis Than in Alzheimer's Disease. International Journal of Alzheimer's Disease 2011;2011(1):483972. doi: https://doi.org/10.4061/2011/483972

Images/Tables

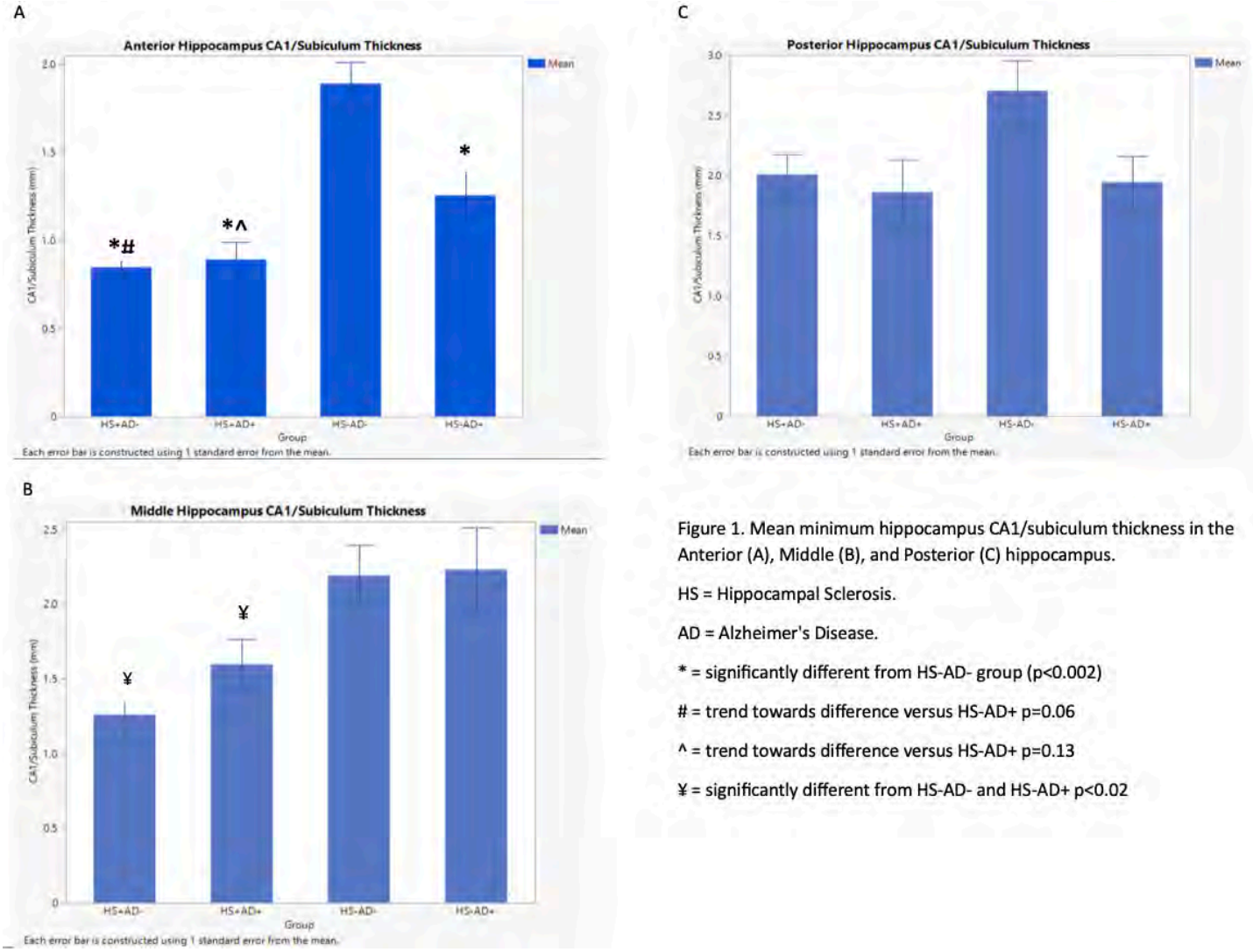

Figure 1. Mean minimum hippocampus CA1/subiculum thickness in the Anterior (A), Middle (B), and Posterior (C) hippocampus.

HS = Hippocampal Sclerosis.

AD = Alzheimer's Disease.

* = significantly different from HS-AD- group (p<0.002)

= trend towards difference versus HS-AD+ p=0.06

^ = trend towards difference versus HS-AD+ p=0.13

¥ = significantly different from HS-AD- and HS-AD+ p<0.02

654

Increased Relative Risk of Delayed Hemorrhage in Patients on Anticoagulant/Antiplatelet Medications: 8 Year Experience and Evidence Based Practice Changes in a Large Health System

Warren Chang MD, MBA[1], Charles Li MD[1], Laura Eisenmenger MD[2], Michael Goldberg MD, MPH[1]

[1]Allegheny Health Network, Pittsburgh, PA, USA. [2]University of Wisconsin, Madison, WI, USA

Abstract Category

Adult Brain

Purpose

The risk of delayed posttraumatic intracranial hemorrhage (DH) in patients on anticoagulant (AC) and antiplatelet (AP) medications, especially in patients taking direct oral anticoagulant medications (DOACs), ACs with concurrent aspirin, and dual antiplatelet therapy is not well established, with studies reporting between 1-10% risk of DH and 0-3% mortality. Management of these patients is difficult due to the risk of potentially catastrophic DH after discharge, balanced with increased time in the emergency department (ED) or observation units. We report our eight-year results and our network-wide changes in patient management based on these results for patients on AP/AC medications with and without concurrent aspirin therapy.

Materials & Methods

2101 patients (1034 male, 1067 female, average age 77.4 years) taking AP/AC medication as documented in the electronic medical record (EMR) presenting to network EDs with head trauma were included in the study. Repeat examinations were typically performed within 24 hours (average follow-up time was 21 hours and 99% were within 3 days). Average time to DH was 20 hours. Patients who had repeat examinations within the same encounter were

included in the study if their initial examination was interpreted as negative and there were no additional instances of trauma between the examinations. All positive studies were reviewed by two board certified neuroradiologists. Patients were excluded from the study if hemorrhage was retrospectively identified on the initial examination. Cases were reclassified as negative if hemorrhage on the follow-up examination was thought to be not present or thought to be artifactual. Cases were considered positive if the initial examination was considered negative and the follow-up examination demonstrated new hemorrhage.

Results

Overall, there was 2.1% incidence (44 patients) of DH and 0.4% overall mortality (9 patients). The group of patients taking AP/AC medications with aspirin had significantly higher risk of DH (34/44, 4.1% vs 0.8%, RR 5.4) and mortality (8/9, 2.0% vs 0.2%) when compared to those taking AP/AC medications alone. The patients taking warfarin or AP medications without aspirin had higher risk of DH when compared to those taking DOAC medications (1.4% vs 0.3%, RR 4.7). Patients taking DOACs with aspirin had significantly higher risk of DH than those not taking aspirin (2.0% vs 0.3%, RR 6.7).

Conclusion

Patients taking AP/AC medications with concurrent aspirin had significantly higher risk of DH and mortality than those taking AP/AC medications without aspirin. Based on these results, we updated our EMR to automatically display the AC/AP medications including aspirin that patients are taking. repeat head CTs on patients taking AP/AC medications with aspirin and administer reversal agents if hemorrhage is detected.

Patients taking warfarin or AP medications without aspirin had significantly higher risk of DH compared to those taking DOACs alone. We now repeat head CTs on patients taking warfarin or AP agents without aspirin, and reverse the medications when hemorrhage is detected.

Patients taking DOACs alone have relatively low risk of DH (1/333 exams) and repeat examinations are deferred unless there is a dangerous mechanism of injury or CT evidence of traumatic injury.

References

Chang W, Yin JD, Li CQ,et al. Increased Relative Risk of Delayed Hemorrhage in Patients Taking Anticoagulant/Antiplatelet Medications with Concurrent Aspirin Therapy: Implications for Clinical Practice Based on Three year Retrospective Analysis in a Large Health System. Emergency Radiology. November, 2021

Nishijima DK, Offerman SR, Ballard DW, et al. Risk of traumatic intracranial hemorrhage in patients with head injury and preinjury warfarin or clopidogrel use. Acad Emerg Med. 2013;20(2):140-145.

Swap C, Sidell M, Ogaz R, Sharp A. Risk of Delayed Intracerebral Hemorrhage in Anticoagulated Patients after Minor Head Trauma: The Role of Repeat Cranial Computed Tomography. Perm J. 2016;20(2):14-16. doi:10.7812/TPP/15-095

Bauman ZM, Ruggero JM, Squindo S, et al. Repeat Head CT? Not Necessary for Patients with a Negative Initial Head CT on Anticoagulation or Antiplatelet Therapy Suffering Low-Altitude Falls. Am Surg. 2017;83(5):429-435.

Huang JL, Woehrle TA, Conway P, McCarty CA, Eyer MM, Eyer SD. Evaluation of a protocol for early detection of delayed brain hemorrhage in head injured patients on warfarin. Eur J Trauma Emerg Surg. 2019;45(3):481-487.

Images/Tables

Medication	Total Patients	Negative	Positive	% Positive	Deaths	% Death	Aspirin	Positive w/ aspirin
Apixiban (Eliquis)	715	712	3	0.04%	0	0	305	3
Warfarin (Coumadin)	572	552	20	3.49%	6	1.2%	206	14
Rivaroxaban (Xarelto)	321	313	8	2.49%	0	0	100	6
Clopidogrel (Plavix)	344	331	13	3.77%	3	0.9%	150	11
Other	149	149	0	0	0	0	63	0
Total	2101	2057	44	2.09%	9	0.4%	824	34

All Patients

	DH	No DH
Aspirin	34 (4.1%)	790
No Aspirin	10 (0.8%)	1267

$p < 0.0001$, RR = 5.4

DOACs

	DH	No DH
Aspirin	9 (2.0%)	431
No Aspirin	2 (0.3%)	673

$p < 0.01$, RR = 6.7

Warfarin + AP

	DH	No DH
Aspirin	25 (7.0%)	356
No Aspirin	8 (1.4%)	552

$p < 0.001$, RR = 5.0

Figure 1: **a)** Patients taking AP/AC medications, and number of patients taking aspirin. **b)** Number of patients with DH taking AP/AC medications with and without aspirin therapy.

659

The Mediolateral Diameter of the Falcine Sinus as a Predictor of Clinical Outcomes in Fetal Vein of Galen Malformations

Patrisha C Lazatin MD, MMSc (2025), Emma N Puglisi BA, Julie Meadows BA, Alfred P See MD, Darren B Orbach MD, PhD
Boston Children's Hospital, Boston, Massachusetts, USA

Abstract Category

Pediatrics

Purpose

The mediolateral diameter of the falcine sinus (FS), measured on fetal magnetic resonance imaging (MRI) is a robust predictor of clinical evolution to aggressive postnatal clinical presentation patients with vein of Galen malformations (VOGM) (1). Patients with a wide FS have increased likelihood of neonatal cardiopulmonary failure requiring intubation and high-risk neonatal embolization (1–3). Given the usefulness of FS to predict which cohort of newborns require early intervention, we aimed to see if FS could provide a more sophisticated prediction of cardiac, cerebrovascular and developmental outcomes.

Materials & Methods

The FS was measured by 2 independent experienced pediatric neurointerventionalists on fetal MR imaging. Inter-rater reliability was measured via the inter-cluster coefficient. The FS was systematically correlated using logistic regression modelling with mortality, cardiac dysfunction, brain parenchymal defects and neurodevelopmental outcomes obtained through retrospective review of patients' records. A marginal analysis of the logistic regression model was conducted to calculate the predicted risk of the outcome at a specific FS measurement.

Results

A total of 59 patients were identified. The median average FS is 6 mm (2 mm,8 mm), ICC 0.95. FS was predictive of mortality ($p = 0.000$), right ventricular (RV) dysfunction ($p = 0.02$), brain parenchymal defect at birth ($p = 0.02$) and discharge ($p = 0.02$), ventriculomegaly at birth ($p = 0.03$) and developmental delay at 1-month ($p = 0.001$), 6-months ($p = 0.001$) and 12-months ($p = 0.002$).

Mortality amongst patients with FS >6mm is 72.0%. Marginal analysis revealed that the risk of mortality increased from 16.2% at 5mm FS to 78.4% at 9mm FS. RV systolic dysfunction follows a similar trend with prevalence at 66.7% amongst patients with FS >6mm and increased risk from 26.9% to 67.1% from 5mm FS to 9mm FS.

68.8% of patients with FS >6mm had brain parenchymal defect. This increased to 75.0% upon discharge. The risk for brain parenchymal defect for FS at birth increased from 37.6% at 5mm FS to 75.8% at 9mm FS. A similar trend is seen at discharge with a risk of 40.7% at 5mm FS to 79.4% at 9mm FS.

Only 21.7% of patients with FS > 6mm met developmental milestones at 1-month. This further decreased to 18.2% at 6-months and 14.3% at 12-months. The probability of meeting milestones decreased from 70.0% at 5mm FS to 20.5% at 9mm FS at birth. This further decreased at 6-months (68.5% at 5mm FS to 17.0% at 9mm FS) and 12-months (60.8% at 5mm FS to 9.6% at 9mm FS).

Conclusion

Fetal MRI measurement of the mediolateral falcine sinus diameter in patients with vein of Galen malformations can be used as a highly robust prognosticator for clinical outcomes. These results suggest that the FS is a potentially useful tool for identifying vulnerable cohorts that may benefit from fetal intervention. Most importantly, it is evident that a wide mediolateral falcine sinus diameter on fetal MR imaging is associated with high risk for mortality, cardiac dysfunction, brain parenchymal injury, and short and intermediate-term developmental delay. These findings can greatly facilitate informed discussions between clinicians and families.

References

1. Arko L, Lambrych M, Montaser A, Zurakowski D, Orbach DB. Fetal and Neonatal MRI Predictors of Aggressive Early Clinical Course in Vein of Galen Malformation. AJNR Am J Neuroradiol. 2020 Jun;41(6):1105.

2. Alvarez H, Garcia Monaco R, Rodesch G, Sachet M, Krings T, Lasjaunias P. Vein of Galen Aneurysmal Malformations. Neuroimaging Clin N Am. 2007 May 1;17(2):189–206.

3. Paladini D, Deloison B, Rossi A, Chalouhi GE, Gandolfo C, Sonigo P, et al. Vein of Galen aneurysmal malformation (VGAM) in the fetus: retrospective analysis of perinatal prognostic indicators in a two-center series of 49 cases. Ultrasound Obstet Gynecol Off J Int Soc Ultrasound Obstet Gynecol. 2017 Aug;50(2):192–9.

Images/Tables

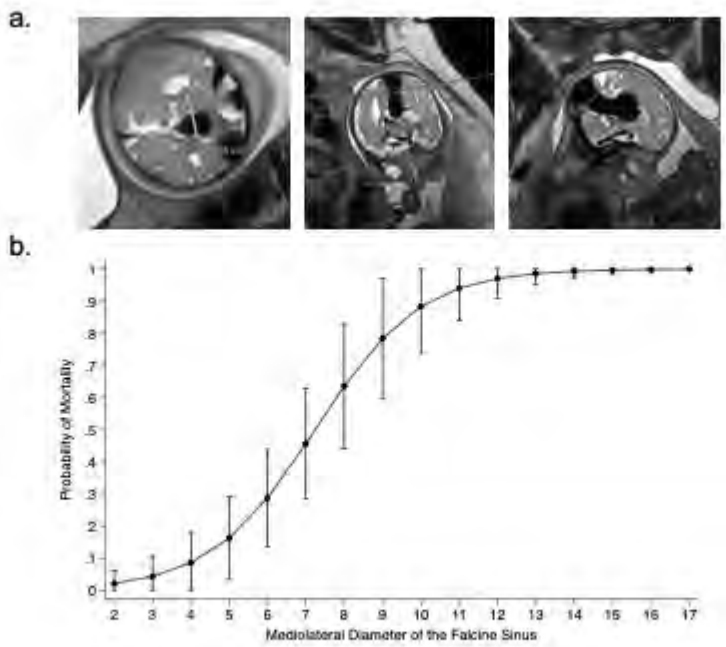

Figure 1. Mediolateral diameter of the falcine sinus (FS) as a predictor of mortality. (a) Measurement of the mediolateral diameter of the falcine sinus via the narrowest point on the fetal MR imaging. (b) Probability of mortality as a function of the FS. Patients with 12mm FS has a predicted mortality of 97.0%

673

Photon Counting Detector CT for the Identification of Pituitary Microadenomas in Cushing Disease

Ian Mark, Jamie Van Gompel, Lifeng Yu
Mayo Clinic, Rochester, MN, USA

Abstract Category

Head & Neck

Purpose

MRI fails to localize up to 40–60% of corticotroph microadenomas in Cushing Disease (CD), impacting cure rates and forcing surgeons to explore the whole gland. Photon-counting detector CT (PCD-CT) is a newly introduced CT technique that can potentially increase spatial and contrast resolution. The purpose of our study was to evaluate PCD-CT for the identification of pituitary microadenomas in CD.

Materials & Methods

We reviewed consecutive patients with CD who underwent a contrast enhanced PCD-CT and MRI of the pituitary prior to undergoing surgical resection from Sept 2023 to June 2024. Images were reviewed for pituitary lesion identification, enhancement relative to the normal pituitary, and maximum lesion dimension. Basic demographic information, patient symptoms, surgical records, and pathology results were recorded.

Results

Fifteen patients with CD were included. The median age was 54 years old (interquartile rage: 44 – 63), and 87% of the patients were female. At diagnosis, 93% had central obesity, 73% had hypertension, 53% had type II diabetes mellitus, and 27% had osteoporosis. A potential lesion was identified on MRI in 12 patients and on PCD-CT in all 15. True adenoma location was defined by intraoperative visualization and pathologic confirmation in 12 cases, and by intraoperative visualization and biochemical remission in 3 cases. MRI failed to accurately identify the tumor in 33% of cases – including 3 cases where it was unable to localize a lesion and 2 cases where it was misleading; PCD-CT identified the lesion accurately in all 15 cases (67% vs. 100%, p = 0.04).

Conclusion
PCD-CT achieves high rates of adenoma localization in CD, even among MR-negative cases. Its role in the clinical workflow of preoperative evaluation for CD remains to be determined, but current evidence supports its value in lesion localization, especially in MR-negative disease.
References
Mark IT, Van Gompel J, Bancos I, et al. Back to the Future: Dynamic Contrast-Enhanced Photon-Counting Detector CT for the Detection of Pituitary Adenoma in Cushing Disease. *AJNR Am J Neuroradiol*. Jun 7 2024;45(6):743-746. doi:10.3174/ajnr.A8171
Images/Tables
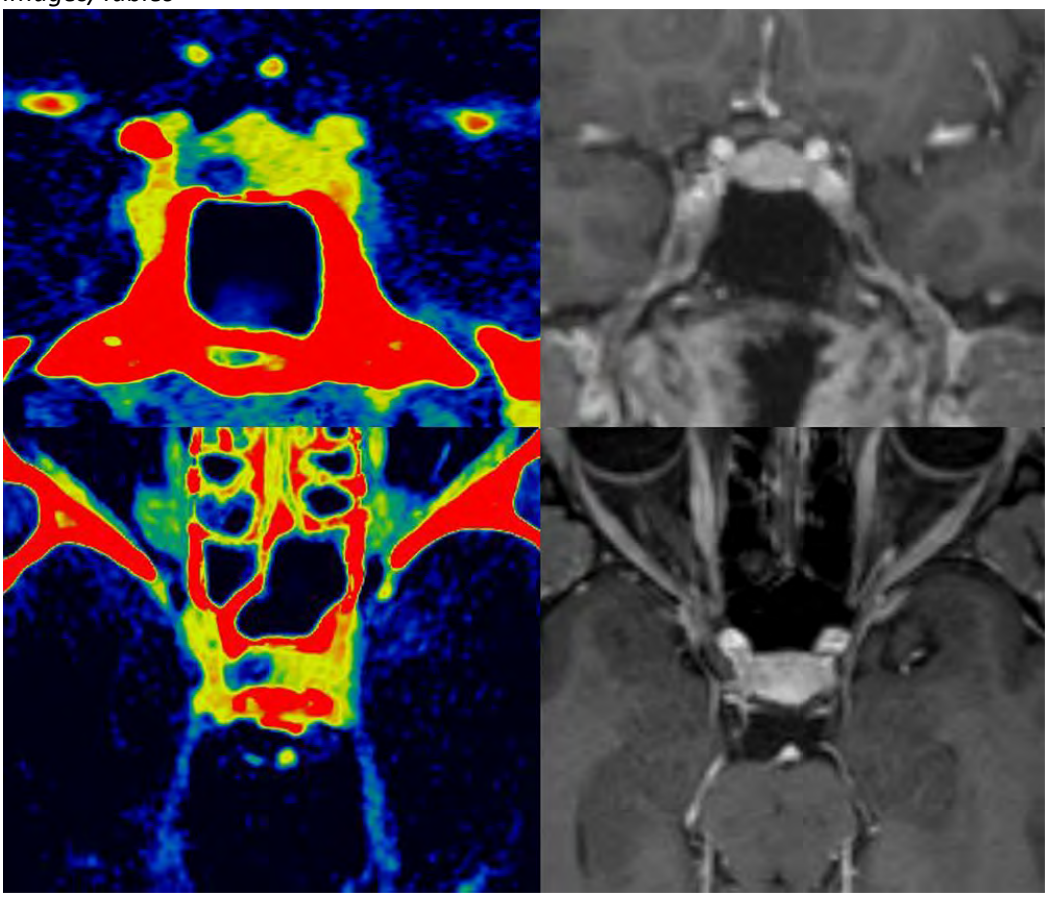

674

Association Between Noncontiguous Injuries of Cervical Spine with Spinal Cord Injury and Admission Glasgow Scale in Patients with Upper Cervical Spine Trauma

Rocco Hlis MD, Kamand Khalaj MD, Elham Tavakkol MD, Andres Rodriguez MD, Arash Kamali MD, David Timaran MD, Roy Riascos MD
The University of Texas Health Science Center at Houston, Houston, TX, USA
Abstract Category
Spine
Purpose
Noncontiguous injuries of the cervical spine typically result from complex or successive high-energy traumatic injuries.1 Ligamentous injury, which causes instability of multiple segments, may create hypermobile intervening segments that, in theory, put the spinal cord at greater risk.2,3 The aim of the study is to investigate the association between noncontiguous injuries of the cervical spine with spinal cord injury and admission Glasgow scale of patients with upper cervical spine trauma.
Materials & Methods
The cervical spine MRIs performed at a level one trauma center (7/14/2012 to 5/22/2015) of one hundred sixty-five patients with craniocervical junction (CCJ) injuries were reviewed; 154 had comparison cervical spine CTs available. Two

readers independently reviewed images, with injury characterization decided upon by consensus. The patient population consisted of 62 females and 102 males, with an average age of 41. A multiple linear regression analysis was performed using IBM SPSS statistics 30.0.0 to explore outcomes (Glasgow coma scale, spinal cord injury) concerning sub-axial cervical spine fractures and disco-ligamentous injury while controlling pre-existing degenerative stenosis.

Results

Spinal cord injury was identified in 23 patients (13.9%). In 12 patients (52.1%), SCI compromised the upper and subaxial cervical spine; in 11 patients (47.8%), only the subaxial cord was compromised. The average Glasgow scale was 10.6. The presence of an additional sub-axial cervical spine fracture was significantly associated with spinal cord injury (β=0.252, $p<0.001$) and Glasgow coma scale (β= -0.217, $p=0.006$) while controlling for the covariate, degenerative stenosis. The presence of additional sub-axial cervical spine disco-ligamentous injury was significantly associated with spinal cord injury (β=0.221, $p<0.001$) but not significantly related to the Glasgow coma scale.

Conclusion

Sub-axial cervical spine fractures and disco-ligamentous injuries in a cohort with confirmed CCJ injuries were significantly related to the presence of spinal cord injury. Results support a biomechanical model of segmental instability after noncontiguous trauma with a compounded effect on the likelihood of spinal cord injury.

References

1. Choi S-J, Shin MJ, Kim SM, et al. Non-contiguous spinal injury in cervical spinal trauma: evaluation with cervical spine MRI. Korean J Radiol. 2004;5:219-224.

2. Chen Z-D, Tu C-Q, Jiang Y-J, Zeng Y-Z, Huang Z-Z, Cai T-Y. Management of non-contiguous upper and lower cervical spine fractures. Int Orthop. 2024;48:2941-2952. doi:10.1007/s00264-024-06308-z.

3. Pirillo V, Berti PP, Prontera A, Rizzo P, Broger M. Biomechanics considerations in the treatment of double traumatic non-contiguous subaxial cervical lesions. Br J Neurosurg. 2023;37(6):1781-1785. doi:10.1080/02688697.2021.1907309.

Images/Tables

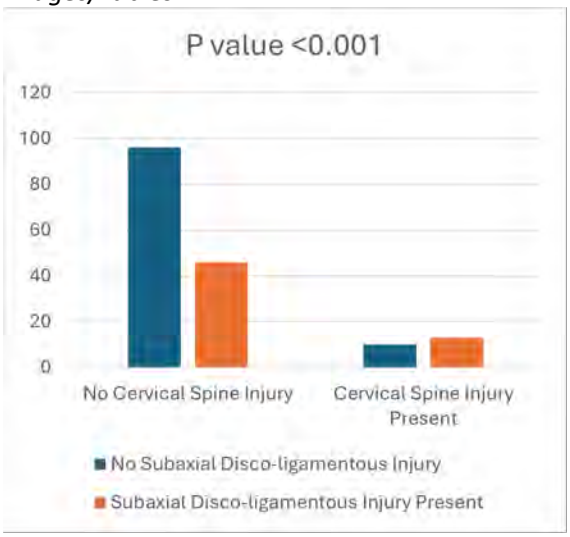

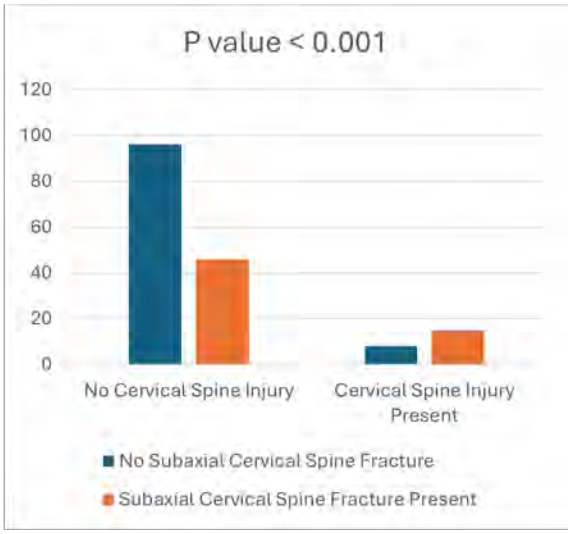

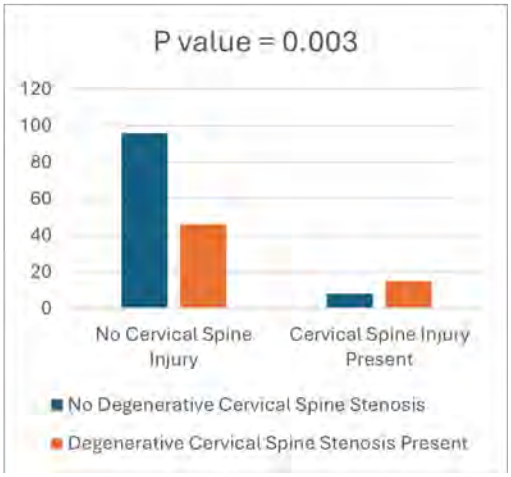

691

Ferumoxytol MRI for the Detection of Brain Arteriovenous Malformations Lesions in Patients with Hereditary Hemorrhagic Telangiectasia

Alex Gill, Emma Benech, Yoo Jin Lee, Michael Ohliger, Jing Liu, Miles Conrad, Daniel Langston, Lindsay Park, Torianna Lomax Truong, Janine Lupo, David Saloner, Steven Hetts
University of California, San Francisco, San Francisco, CA, USA

Abstract Category

Adult Brain

Purpose

Patients with hereditary hemorrhagic telangiectasia (HHT) have a high likelihood (10-20%) of developing one or more brain AVMs. For patients with brain AVMs, there is a risk of intracranial hemorrhage. Current guidelines recommend screening MRI/MRA in childhood and adulthood to determine if HHT patients have brain AVMs, and therefore guide counseling regarding observation or treatment. As part of a head-through-abdomen ferumoxytol-enhanced 3T MRI/MRA (FeMR) protocol that allows evaluation of multiple organs in a single examination, we have begun to evaluate the sensitivity of this novel scan for brain AVMs.

Materials & Methods

32 subjects have undergone high resolution FeMR. Of these subjects, 26 had HHT of whom 8 had known brain AVMs, based on gold-standard digital subtraction angiograms (DSA). Following informed consent, 3mg/kg ferumoxytol was administered by intravenous infusion over 15 minutes. After subsequent monitoring, VIBE imaging was acquired at 3 resolutions for all subjects, in order to establish the most favorable image quality: (1) 1.0 mm isotropic (TE 1.3 ms, TR 2.9 ms, acquisition time 1 minute), (2) 0.8 mm isotropic (TE 1.6 ms, TR 3.3 ms, acquisition time 2 minutes), and (3) 0.5 mm isotropic (TE 1.9 ms, TR 4.3 ms, acquisition time 4 minutes). The MRI data was reformatted on multiple planes and with multiple maximal intensity projection (MIP) slab thicknesses. FeMR was compared to DSA images by an experienced neurointerventional radiologist.

Results

All known brain AVMs were detected by 3T ferumoxytol-enhanced VIBE MRA. While as expected, 0.5mm isotropic provides the sharpest image appearance, preliminary analysis indicates that it might result in variable intraluminal signal. Edge-enhanced high-resolution (0.5 mm) images accentuated angioarchitecture within the AVM nidus, but were more challenging to interpret in terms of nidus size given overall pixelated image appearance. Higher resolution images with increased echo times may also have had signal dropout due to T2* effects. AVMs were most easily detected at low spatial resolution (1.0 mm) imaging, as the halo of small nidus vessels were more clearly delineated compared to low signal brain parenchymal background. Compared to DSA, FeMR accentuated the principal draining veins of AVMs as opposed to the halo of associated AVM nidus vessels. HHT lesions appeared to have an enhancing “blush” on catheter angiography that was not apparent on MR. The MRI data was reformatted to simulate catheter angiography in terms of views and summation of signal in projection view. This approach provides a better match between the modalities and reveals that FeMR is able to capture the underlying physiology of HHT, namely the dilated capillary bed.

Conclusion

3T FeMR appears to identify all AVMs previously seen on DSA. The results likely indicate that 0.8mm isotropic is the most favorable resolution. Quantitative MR techniques may also be less subject to inter-operator-dependency, thus providing a more objective means for tracking over time. These imaging approaches may be generalized to any patients needing high-resolution vascular imaging. Further studies are needed to determine if high-risk features (e.g., feeding artery aneurysms, nidus aneurysms, venous outflow stenoses) of such AVMs can be reliably identified as compared to DSA.

References

Hetts SW, Shieh JT, Ohliger MA, Conrad MB. Hereditary Hemorrhagic Telangiectasia: The Convergence of Genotype, Phenotype, and Imaging in Modern Diagnosis and Management of a Multisystem Disease. Radiology. 2021 May 11; 203487.

Nguyen KL, Yoshida T, Kathuria-Prakash N, Zaki IH, Varallyay CG, Semple SI, Saouaf R, Rigsby CK, Stoumpos S, Whitehead KK, Griffin LM, Saloner D, Hope MD, Prince MR, Fogel MA, Schiebler ML, Roditi GH, Radjenovic A, Newby DE, Neuwelt EA, Bashir MR, Hu P, Finn JP. Multicenter Safety and Practice for Off-Label Diagnostic Use of Ferumoxytol in MRI. Radiology. 2019 Dec;293(3):554-564. doi: 10.1148/radiol.2019190477. Epub 2019 Oct 22. PMID: 31638489; PMCID: PMC6884068.

Vella M, Alexander MD, Mabray MC, Cooke DL, Amans MR, Glastonbury CM, Kim H, Wilson MW, Langston DE, Conrad MB, Hetts SW. Comparison of MRI, MRA, and DSA for Detection of Cerebral Arteriovenous Malformations in Hereditary Hemorrhagic Telangiectasia. AJNR Am J Neuroradiol. 2020 May 07.
Alyafaie A, Han W, Li Y, Vydro SA, Vella M, Truong TL, Park L, Langston D, Him H, Conrad MB, Hetts SW. Arterial Spin-Labeling MR Imaging in the Detection of Intracranial Arteriovenous Malformations in Patients with Hereditary Hemorrhagic Telangiectasia. AJNR 2024 45(8):1019-1024.
Images/Tables

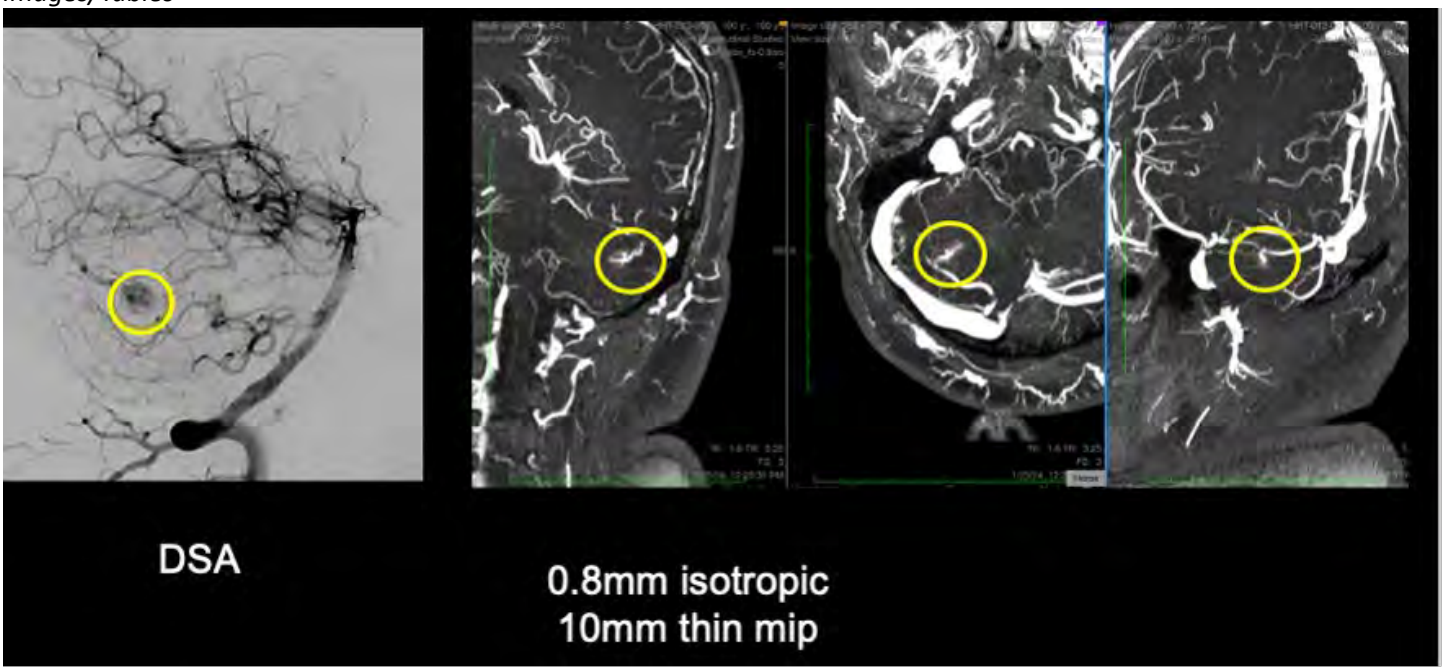

694

Pre- and Postoperative Cross-Sectional and Diffusion Measurements Distal from Spinal Cord Injury Site

Sriyaa Suresh BA[1], Devon M Middleton PhD[2], Pushpa B Thippeswamy MBBS[3], Karthik Ramachandran MBBS[3], Kiran Talekar MD[2], Zahra S Adl MS[2], Laura Krisa PhD[2], Rajasekaran Shanmuganathan MBBS, PhD[3], Feroze Mohamed PhD[2]
[1]University of Virginia School of Medicine, Charlottesville, VA, USA. [2]Thomas Jefferson University, Philadelphia, PA, USA. [3]Ganga Spine Injury and Rehabilitation Center, Coimbatore, Tamil Nadu, India
Abstract Category
Spine
Purpose
This study analyzes structural and diffusion spinal cord data away from the injury epicenter (at C2-level), demonstrating correlations with clinical data in acute spinal cord injury (SCI) patients who were followed for 6 months postoperatively.
Materials & Methods
Structural and diffusion MRI imaging and clinical data of 19 subjects (mean age = 36.2) with acute SCI at baseline prior to intervention were obtained from the Ganga Spine Injury and Rehabilitation Center (GSIRC) in India. Two 0.8 mm^3 isotropic 3D SPACE T2-weighted volumes were obtained using a 3.0T Siemens Lumina MRI scanner system and 24-channel spine array coil for each subject, one covering the cervical to upper thoracic and another covering the lower thoracic cord. The cervical cord diffusion images were acquired using the reduced FOV Zoomit sequence with 20 diffusion directions, 3 averages, b=800s/mm^2. We focused our analysis on 7 patients (mean age = 28.3) for which follow-up imaging and clinical ISNCSCI scores have been collected up to 6 months postoperatively. Using Spinal Cord Toolbox (SCT), quantitative spinal cord cross sectional area (CSA) measurements and diffusion metrics that indicate axonal density and white matter integrity (Fractional Anisotropy (FA), Mean Diffusivity (MD), Axial Diffusivity (AD), Radial Diffusivity (RD)) were extracted for each case and correlated with lower extremity motor scores (LEMS).
Results
Figure 1a illustrates the distribution of CSA, FA, AD, MD, and RD data at C2 preoperatively and postoperatively. Majority of cases indicate that CSA and FA changes occur in the opposite direction. Discarding negligible changes, CSA and AD

trends are unidirectional except for Patient 6, who uniquely sustained a mid-thoracic (T5-T6) injury. Limiting to the three patients that exhibited LEMS conversion, Spearman's plots are shown in Figure 1b with corresponding correlation coefficients. CSA, MD, and RD show a strong positive correlation with LEMS at 1-month follow-up (rho=0.87, p=0.33) and a moderate positive correlation with LEMS at 3 and 6 months (rho=0.50, p=0.67). A strong negative correlation with LEMS at 1 month (rho=-0.87, p=0.33) and moderate negative correlation at 3 and 6 months (rho=-0.50, p=0.67) are found with FA values. AD displays a strong positive correlation with 1 month LEMS (rho=0.87, p=0.33) but moderate negative correlations with 3 and 6 month LEMS scores (rho=-0.50, p=0.67).

Conclusion

Observable changes are present in the cervical spinal cord irrespective of injury location, etiology, and severity for subjects who all sustained thoracic/lumbar injuries except one. This is highly suggestive that metrics superior to the injury site may serve as sensitive biomarkers for prediction of recovery. While patterns are to be noted in CSA and diffusion metric changes, many confounds remain unexplored including age, timeline of injury, and intervention. Encouragingly, observable changes and correlations between imaging metrics and clinical data are already apparent, especially at 1 month follow-up. Additional data collection may identify key feature combinations that can reliably predict prognosis.

References

Krisa L, Middleton DM, Saksena S, Faro SH, Leiby BE, Mohamed FB, Mulcahey MJ.Top Spinal Cord Inj Rehabil. 2022 Spring;28(2):1-12. doi: 10.46292/sci21-00048. Epub 2022 Apr 12

Images/Tables

Figure 1

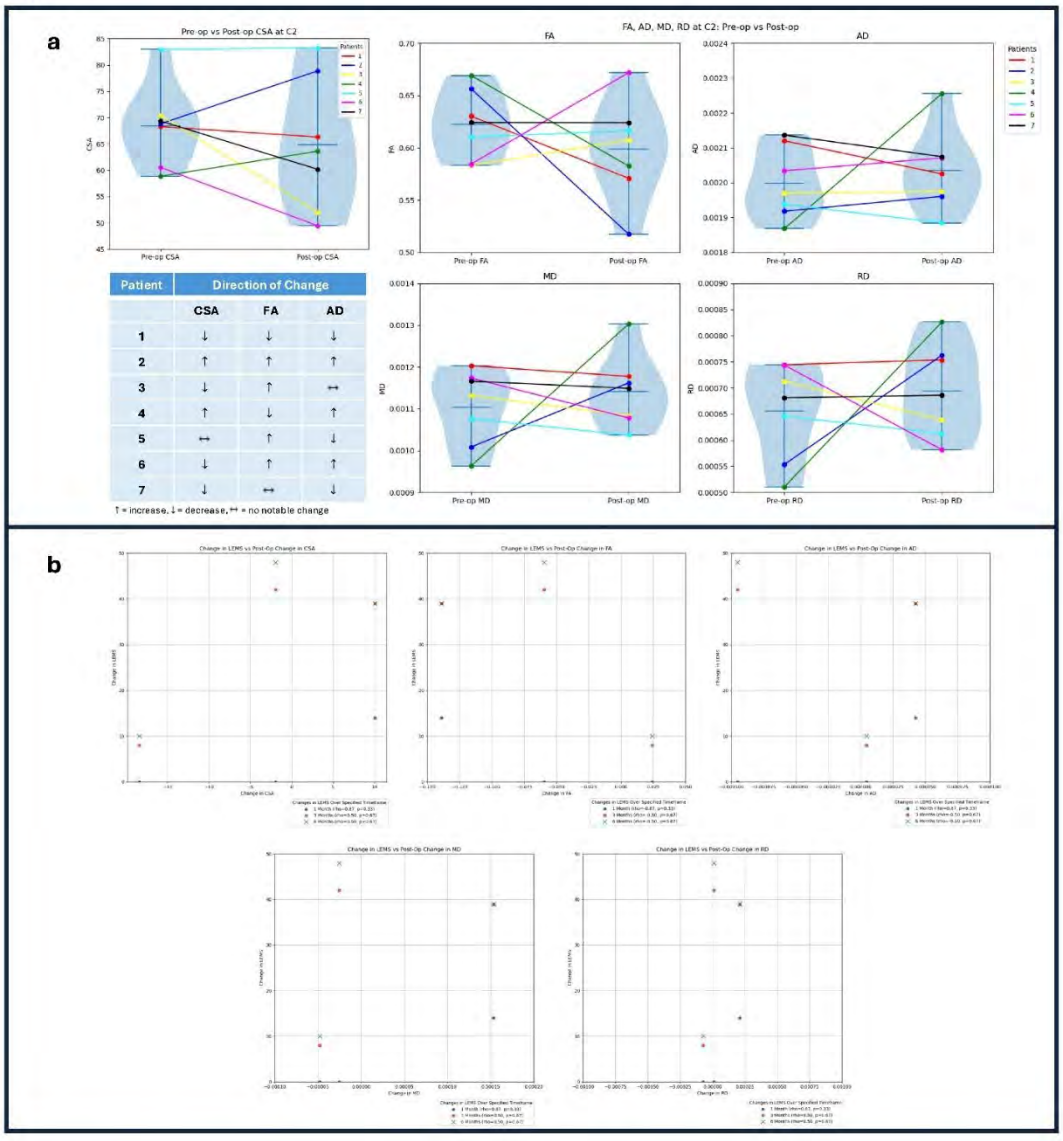

Patient	Direction of Change		
	CSA	FA	AD
1	↓	↓	↓
2	↑	↑	↑
3	↓	↑	↔
4	↑	↓	↑
5	↔	↑	↓
6	↓	↑	↑
7	↓	↔	↓

↑ = increase, ↓ = decrease, ↔ = no notable change

696

Automated Reformat Algorithm Improves Brain Alignment To Enhance Radiologist & Radiographer Workflow Efficiency

Thomas C Arnold PhD[1], Praveen K Gulaka PhD[1], Ronny Elor[1], Joel M Stein MD, PhD[2], Ajit hankaranarayanan PhD[1], Lawrence Tanenbaum MD FACR[3]

[1]Subtle Medical, Menlo Park, CA, USA. [2]University of Pennsylvania, Philadelphia, PA, USA. [3]drt consulting, Riverside, CT, USA

Abstract Category

Adult Brain

Purpose

Growing demand for radiology services combined with workforce shortages has resulted in increased pressure on radiologists and radiographers for efficiency. Consistent, symmetric image orientation facilitates disease diagnosis and tracking. Poor image alignment necessitates manual realignment, causing workflow disruptions and frustration. Here, we present an evaluation of a recently FDA cleared machine-learning-based brain alignment algorithm[1].

Materials & Methods

The algorithm we developed leverages two methods to achieve realignment: bilateral symmetry optimization and morphological feature based alignment[2-4]. Using this algorithm, we processed 373 3D brain MRI scans, encompassing T1, T1+Gad, T2, and T2-FLAIR sequences from over 20 centers. Demographic details are presented in **Figure 1A**. Two neuroimaging experts (TCA and PG: 10 & 17 years experience, respectively) independently labeled four anatomical points (**Figure 1B**: anterior/posterior commissures, left/right eye centers). A third-party neuroradiologist (JMS: 12 years experience) adjudicated cases where labels differed beyond a predetermined threshold (pitch<5°, roll<3°, or yaw<3°). We applied the image reformatting algorithm and compared its output with ground truth alignment to assess pitch, roll, and yaw error (**Figure 1C**).

Results

Raters exhibited high consistency, with pitch differing by < 2° and both roll and yaw by < 0.5°. Input image absolute errors averaged 10.46° ± 7.22° for pitch (-35° to 24°), 2.44° ± 2.10° for roll (-9° to 9°), and 2.95° ± 2.64° for yaw (-17° to 14°). The algorithm reduced absolute error by 77.9% for pitch (to 2.31°), 64.4% for roll (to 0.87°), and 78.1% for yaw (to 0.65°). Summed absolute error improved in 96.8% of subjects by an average of 8.2° (**Figure 1D**). We assessed the impact of large anatomical anomalies on algorithm performance for 3 pathology subgroups: brain tumors (N=24, avg. 34cc, max 129cc), tumor resections (N=24, avg. 37cc, max 81cc), and neurodegenerative disorders (N=90). Pathology groups demonstrated stable performance (pitch: 2.28°, 2.49°, & 2.01°, roll: 1.10°, 0.88°, & 1.07°, yaw: 0.91°, 0.54°, & 0.70°, respectively). Two pediatric subgroups (age 5-11: N=30, age 12-21: N=30) also showed similar performance (pitch: 2.11° & 2.83°, roll: 0.73° & 0.83°, yaw: 0.73° & 0.64°).

Conclusion

Poor image alignment can disrupt radiographer and radiologist workflows and impair assessments of bilateral symmetry. We presented an algorithm that improved alignment in 96.8% of subjects with an average improvement of 8.2°. The algorithm can preprocess images prior to PACS display, thus eliminating manual reorientation and streamlining radiology workflows.

References

1. FDA 510(k) Premarket Notification for SubtleALIGN. https://www.accessdata.fda.gov/cdrh_docs/pdf23/K233699.pdf Accessed November 1, 2024.
2. Prabhu P, Karunakar AK, Sinha S, Mariyappa N, Bhargava GK, Velmurugan J, Anitha H. Content-based estimation of brain mri tilt in three orthogonal directions. Journal of Digital Imaging. 2021 Jun;34:760-71.
3. Wu H, Wang D, Shi L, Wen Z, Ming Z. Midsagittal plane extraction from brain images based on 3D SIFT. Physics in Medicine & Biology. 2014 Feb 28;59(6):1367.
4. Lowe DG. Distinctive image features from scale-invariant keypoints. International journal of computer vision. 2004 Nov;60:91-110.

Images/Tables

A

Age	Sample Size
Adult (22+)	313
Adolescents (age 12-21)	30
Children (age 5-11)	30
Sex	Sample Size
Male	175
Female	163
Other or unspecified	35
Pathology	Sample Size
Alzheimer's	90
Brain tumor	24
Tumor Resection	24
Sequence	Sample Size
T1	225
T1 + Gad	61
T2	30
T2-FLAIR	57
Orientation	Sample Size
Sagittal	243
Axial	105
Coronal	25
Manufacturer	Sample Size
GE	144
Siemen	138
Philips	82
Hitachi	9
Field Strength	Sample Size
1.5T	107
3T	266
Grand Total	373

B

C

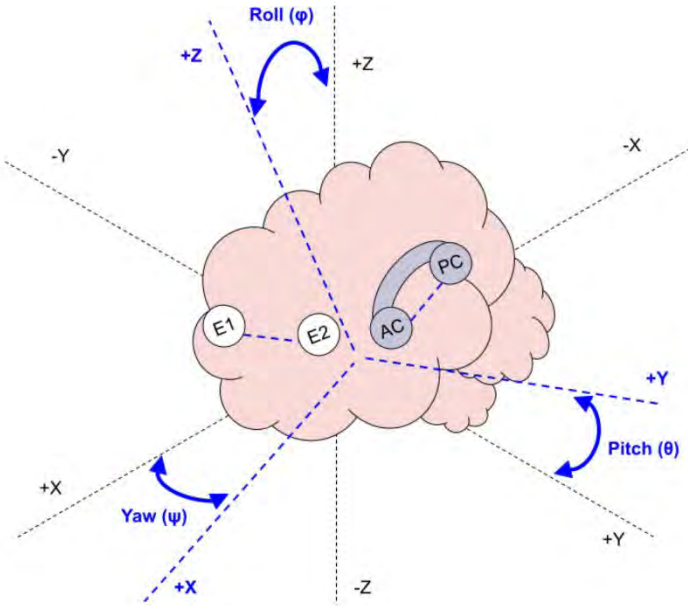

D

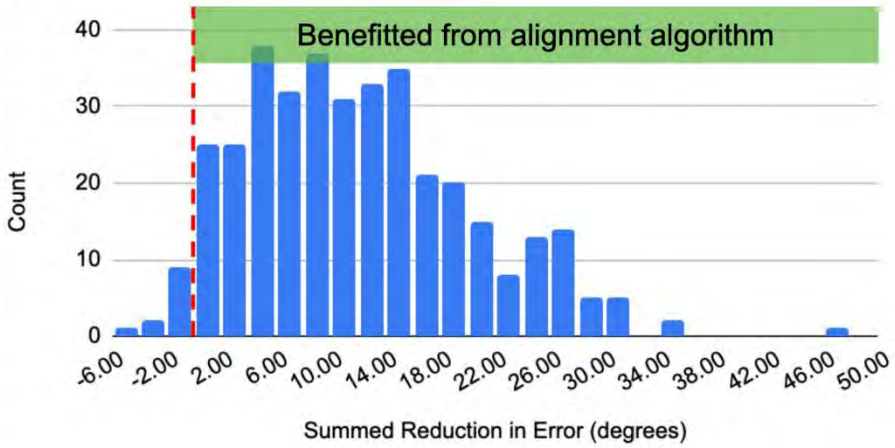

Figure 1: A) Table of demographic information. **B)** Four anatomical landmarks (anterior commissure, posterior commissure, left eye center, and right eye center) were labeled by two experts. **C)** Illustration of how ground truth error in pitch, roll, and yaw are calculated relative to the AC-PC and E1-E2 lines. **D)** The algorithm improved alignment for 96.8% (361/373) of subjects, as measured by the summed reduction in error across pitch, roll, and yaw.

700

Three-Dimensional Voxel-Based Wall Enhancement Quantification Improve Symptomatic Stratification in Fusiform Aneurysms

Carlos Dier MD[1], Elena Sagues MD[1], Andres Gudino MD[1], Navami Shenoy BA[1], Martin Cabarique MD[1], Gustavo Chiriboga MD[1], Shubhangi Setia MD[1], Sebastian Sanchez MD[2], Connor Aamot BS[1], Edgar A Samaniego MD, MS[1]
[1]University of Iowa, Iowa, IA, USA. [2]Yale University, New Haven, CT, USA

Abstract Category

Adult Brain

Purpose

Aneurysm wall enhancement (AWE) has been widely studied in saccular aneurysms. However, fusiform intracranial aneurysms (FIAs) display different AWE patterns, and its potential for risk stratification remains underexplored.

Materials & Methods

Patients with unruptured FIAs were prospectively recruited, and 3T high resolution-magnetic resonance imaging was performed. Aneurysm size was defined as the maximum luminal diameter, and FIAs were classified as symptomatic if they caused cranial nerve palsy, hydrocephalus, or dizziness due to brain parenchyma compression. 3D Slicer was utilized to generate 3D models of the FIAs, and the signal intensity (SI) distribution within the aneurysm wall was quantified using a validated in-house MATLAB 2020a code, with SI normalized to the corpus callosum (CC). This method generates 3D-AWE maps that correlate with enhancement curves and detect regions of enhancement. A FIA was classified as enhancing if the mean SI on post-contrast (3D-CAWE = SI of the aneurysm body/SI of the CC) exceeded one.[1] Regions of enhancement on 3D-AWE maps and areas causing brain parenchyma compression were then displayed simultaneously. The previous 3D method was modified to allow voxel-level SI quantification in these areas (Regional AWE = SI of the vessel wall region/SI of the CC). The Mann-Whitney test was used to compare AWE-related metrics: (1) 3D-CAWE between symptomatic and asymptomatic FIAs, and (2) regional AWE between these groups. Univariate logistic regression was performed to identify predictors of symptomatic status, including sex, aneurysm size, 3D-CAWE, and regional AWE. Subsequently, two multivariate models based on clinical judgment were developed, incorporating either 3D-CAWE or regional AWE with FIA size, to assess their accuracy in detecting symptomatic FIAs.

Results

Forty-eight patients with FIAs were analyzed, of whom 16 (33%) were symptomatic. The mean size of symptomatic aneurysms was 16.34 ± 7.89 mm. Symptomatic aneurysms exhibited significantly higher 3D-CAWE values than asymptomatic ones (1.18 ± 0.34 vs 0.82 ± 0.23, $p < 0.001$). Similarly, symptomatic aneurysms exhibited higher regional AWE compared to those in asymptomatic aneurysms (1.37 ± 0.32 vs 0.92 ± 0.27, *p 0.009*). Factors associated with symptomatic presentation included female sex (OR 4.58, 95% CI 1.26 – 19.7, *p 0.027*), larger aneurysm size (OR 1.38, 95% CI 1.15 – 1.75, *p 0.002*), 3D-CAWE (OR 8.17, 95% CI 2.31 – 33.1, *p 0.002*) and regional AWE (OR 24.8, 95% CI 2.53 – 402, *p 0.011*). The combination of AWE-related metrics and aneurysm size effectively identified symptomatic status, with AUCs of 0.87 for size and 3D-CAWE, and 0.909 for size and regional AWE.

Conclusion

Three-dimensional voxel-based AWE quantification are valuable tools for assessing enhancement patterns in fusiform aneurysms and aiding in risk stratification.

References

Raghuram A, Varon A, Roa JA, et al. Semiautomated 3D mapping of aneurysmal wall enhancement with 7T-MRI. *Sci Rep*. 2021;11:18344. doi: 10.1038/s41598-021-97727-0

Images/Tables

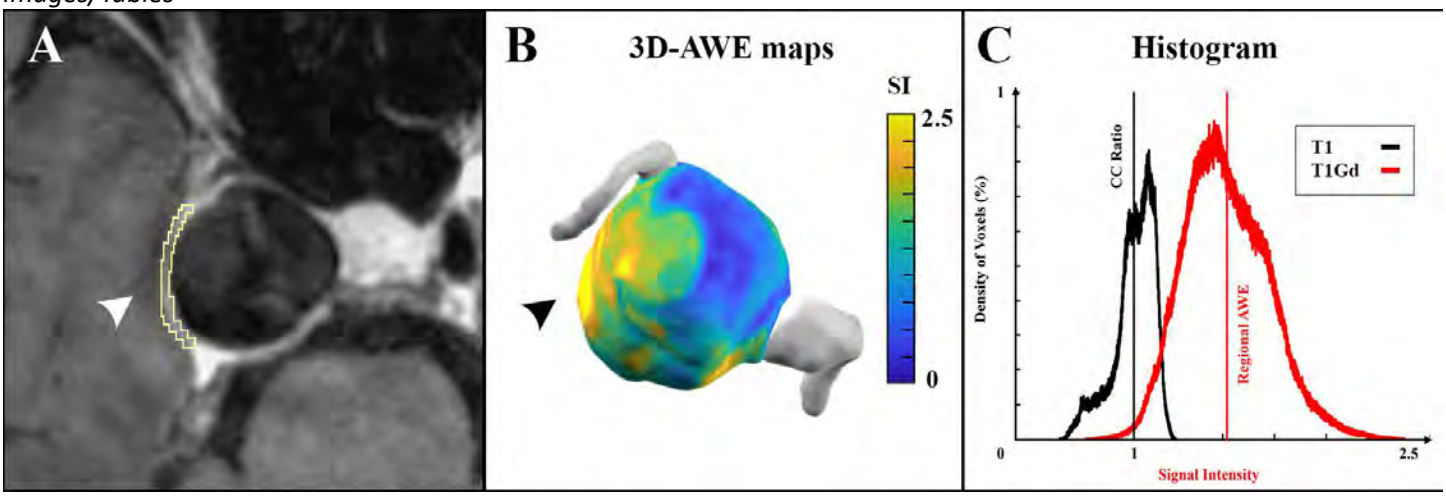

709

Carotid Plaque RADS Related to Stroke Risk with Mild/Moderate Stenosis: a CARE II study

Maoxue Wang MD[1], Yin Guo PhD[1], Xihai Zhao MD[2], Chun Yuan PhD[3], Luca Saba MD[4], Mahmud Mossa-Basha MD[1]
[1]University of Washington, Seattle, Washington, USA. [2]Department of Biomedical Engineering, Center for Biomedical Imaging Research, Tsinghua University School of Medicine, Beijing, Beijing, China. [3]Department of Radiology and Imaging Sciences, University of Utah, Salt Lake City, Utah, USA. [4]5. Department of Radiology, University of Cagliari, Cagliari, Cagliari, Italy

Abstract Category

Adult Brain

Purpose

Stroke is a major cause of death and the leading cause of permanent disability worldwide. There has been a lot of research focused on carotid plaque composition to determine vulnerability, including evaluation of thinned or ruptured fibrous cap, presence of intraplaque hemorrhage (IPH), and presence of a large lipid-rich necrotic core (LRNC) in determining their associations with stroke and predictive value for recurrent events. However, there is a lack of consensus in reporting and interpreting carotid plaque features. Carotid plaque-Reporting And Data System (Plaque-RADS) is a novel stroke risk classification system[1], which provides a standardized approach for evaluating carotid plaque composition and morphology across multiple imaging modalities like ultrasound, CT, and MRI.

The aim of this study was to evaluate carotid Plaque RADS and ancillary features, and its relationship with ischemic stroke and transient ischemic attack events in a multi-center data set.

Materials & Methods

The patients were recruited from the CARE II (Chinese Atherosclerosis Risk Evaluation, NCT 02017756) database, which was a Chinese cross-sectional, multicenter prospective study of ischemic stroke patients who had undergone carotid vessel wall imaging (VWI). Carotid plaque calcification (Ca), LRNC, ulceration, IPH, thick or thin fibrous cap, fibrous cap rupture, intraluminal thrombi, maximum normalized wall index (max_nwi), and stenosis degree were identified using the published criteria. Based on the MR imaging features, carotid Plaque-RADS from 1 to 4c were classified. The ancillary features including calcification and plaque burden (max_nwi) were collected. Generalized Estimating Equation (GEE) - based logistic regression was performed to assess the relationship between Plaque RADS score and cerebrovascular events.

Results

A total of 434 patients (62 years old ± 9.97, 302 males) were included in this study. Symptomatic carotid arteries had higher stenosis degree (11.82% ± 24.68 vs 8.55% ± 18.78, p=0.012), Plaque RADS score (2.14±1.0 vs 2.04±0.96, p=0.021) and Max_nwi (0.53±0.14 vs 0.51±0.13, p=0.002) compared to asymptomatic side. Plaque RADS score was significantly related to stenosis degree (r=0.490, p<0.001), Max_nwi (r=0.689, p<0.001), and presence of calcification (r=0.572, p<0.001). Univariable regression analysis showed that Plaque RADS was significantly associated with cerebrovascular events (OR 1.11, 95%CI: 1.01,1.24; p=0.04), especially with Plaque RADS > 2 (OR 1.30, 95%CI: 1.03,1.64; p=0.029) (table 1). In patients with mild/moderate bilateral carotid artery stenosis, Plaque RADS > 2 was significantly associated with

stroke (OR 1.30, 95%CI: 1.01,1.68; p=0.044) (figure 1). However, in the multivariable regression analysis, there was no significant relationship between stroke and Plaque RADS combined with either stenosis, max_nwi, or calcification.

Conclusion

Symptomatic carotid atherosclerosis had a significantly higher Plaque RADS score compared to the asymptomatic side. Carotid Plaque RADS correlates with recent cerebrovascular events, and for mild/moderate carotid stenosis, a score >2 increased the likelihood of events.

References

Reference

1. Saba L, Cau R, Murgia A, et al. Carotid Plaque-RADS: A Novel Stroke Risk Classification System. *JACC Cardiovasc Imaging*. 2024; **17**: 62-75.

Images/Tables

Table 1. Regression results in Plaque RADS and stroke.

	P	OR	95%CI
Univariable regression			
Stenosis	0.011	1.01	(1.00, 1.01)
RADS	0.040	1.11	(1.01, 1.24)
RADS (> 2 vs ≤ 2)	0.029	1.30	(1.03, 1.64)
RADS (Mild/moderate stenosis)	0.044	1.30	(1.01, 1.68)
Ca	0.161	1.16	(0.94, 1.44)
Max_nwi	0.01	1.0	(1.0, 1.02)
Multivariable regression			
Stenosis	0.067	1.01	(1.0,1.01)
RADS	0.433	1.05	(0.93,1.19)
Multivariable regression			
RADS	0.169	1.10	(0.96, 1.27)
Ca	0.789	1.04	(0.78, 1.38)
Multivariable regression			
RADS	0.695	1.03	(0.87, 1.22)
Max_nwi	0.193	1.01	(1.00, 1.02)

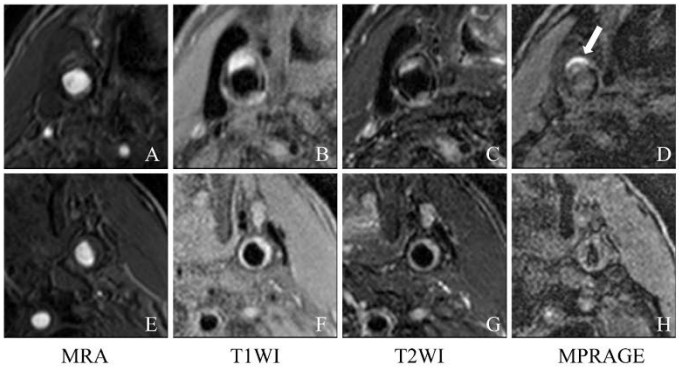

Figure 1. MR images of bilateral carotid arteries with mild/moderate stenosis. The symptomatic side (A-D) had a Plaque RADS score of 4a, which intraplaque hemorrhage was found on MPRAGE (White arrow). The asymptomatic side (E-H) had a Plaque RADS score of 2.

716

Low Incidence of Acute Actionable Imaging Findings in Emergency Department Patients with Provided Diagnosis of Vertigo: 14 Year Retrospective Analysis in a Large Health System

Warren Chang MD, MBA[1], Charles Li MD[1], Laura Eisenmenger MD[2], Raven Spencer MD[1], Michael Goldberg MD, MPH[1]

[1]Allegheny Health Network, Pittsburgh, PA, USA. [2]University of Wisconsin, Madison, WI, USA

Abstract Category

Adult Brain

Purpose

Vertigo is a common indication for examinations performed both in the emergency department (ED) setting. However, benign etiologies without acute relevant imaging findings are common in patients with vertigo, with studies finding that approximately 27% of patients presenting to the ED with symptoms of vertigo are diagnosed with BPPV (benign paroxysmal positional vertigo), 25% with vestibular migraines, 5% with Meniere's Disease, and an additional 20% with vertigo (not otherwise specified). The risk of stroke appears variable but most studies have found it to be less than 5% of patients. However, patients are commonly imaged in the ED with CT, MRI, CTA and MRA examinations because of concern for posterior fossa/brainstem stroke or hemorrhage, often revealing no evidence of acute relevant imaging findings. In this study, we examine the incidence of acute actionable imaging findings in ED patients with the provided diagnosis of vertigo in a large health system over a 14 year period.

Materials & Methods

5774 examinations were performed on 3811 patients between 2010 and 2024 in network EDs on patients with the provided diagnosis of vertigo. Patients had an average age of 61 years. 1960 patients were female and 1851 were male. Studies included 2806 head CTs, 543 brain MRIs, 2199 CT angiograms, 156 MR angiograms, and 70 other exams. Each examination with positive acute actionable findings which were communicated with a clinician and reported in the radiology report was reviewed by a board certified neuroradiologist, and studies without relevant acute findings were considered negative.

Results

68 examinations (1.1%) had acute relevant imaging findings. Of positive exams, 20 had acute infarcts (16 involving the cerebellum and two involving brainstem, including one lateral medullary infarct), 15 had new vascular occlusion (12 involving the vertebral or basilar arteries, 3 involving the carotid or middle cerebral arteries), 16 had new or worsening high grade arterial stenosis (10 involving the vertebral or basilar arteries, 3 likely related to dissection), 8 had acute hemorrhage (4 of which involved the posterior fossa), 5 had a new diagnosis of a brain tumor, mostly vestibular schwannomas or posterior fossa metastases, 2 had increasing mass effect or from known tumors or hemorrhage, 1 had venous sinus thrombosis, and one had a pulmonary embolism.

Conclusion

Patients with the provided diagnosis of vertigo had a low incidence of acute actionable findings, with ~99% of examinations demonstrating no acute pathology. The risk of stroke was extremely low (<0.5%) in our study. Given high prevalence of BPPV, thorough physical exam (Epley Maneuver) may help prevent unnecessary imaging. With the relatively low percentage of patients (<0.5%) that had acute strokes having mostly having posterior fossa infarcts, mostly involving the cerebellum, higher imaging priority could be considered for those patients with cerebellar signs on neurologic exam. More thorough evaluation prior to imaging in patients with relatively low risk of acute findings may prevent unnecessary exams, lower healthcare costs, and improve patient care.

References

Ghosh, A., Dorasala, S. Epidemiology of benign paroxysomal positional vertigo (BPPV) and risk factors for secondary BPPV: a population-based study. Egypt J Otolaryngol 39, 93 (2023).

Formeister EJ, Rizk HG, Kohn MA, Sharon JD. The Epidemiology of Vestibular Migraine: A Population-based Survey Study. Otol Neurotol. 2018;39(8):1037-1044. doi:10.1097/MAO.0000000000001900

Saber Tehrani AS, Kattah JC, Mantokoudis G, Pula JH, Nair D, Blitz A, Ying S, Hanley DF, Zee DS, Newman-Toker DE. Small strokes causing severe vertigo: frequency of false-negative MRIs and nonlacunar mechanisms. Neurology. 2014 Jul 8;83(2):169-73. doi: 10.1212/WNL.0000000000000573. Epub 2014 Jun 11. PMID: 24920847; PMCID: PMC4117176.

Neuhauser HK. The epidemiology of dizziness and vertigo. Handb Clin Neurol. 2016;137:67-82. doi:10.1016/B978-0-444-63437-5.00005-4

Leker RR, Hur TB, Gomori JM, Paniri R, Eichel R, Cohen JE. Incidence of DWI-positive stroke in patients with vertigo of unclear etiology, preliminary results. Neurol Res. 2013;35(2):123-126. doi:10.1179/1743132812Y.0000000114

Images/Tables

Figure 1: a) Restricted diffusion in the right lateral medulla (Wallenberg's Syndrome) in a patient presenting with vertigo. **b)** Right lateral cerebellar infarct in a patient presenting with vertigo. **c)** Left vestibular schwannoma in a patient presenting with vertigo. **d)** Cerebellar hemorrhage in a patient presenting with vertigo.

721

Impact of Corticosteroid Dose on Radiographic Changes in Glioblastoma

Asher J Kim[1], Francesco Sanvito M.D.[1], Ashley M Teraishi B.S.[2], Catalina Raymond MSc[2], Richard G Everson M.D.[3], Noriko Salamon M.D., Ph.D.[4], Timothy F Cloughesy M.D.[5], Jingwen Yao Ph.D.[2], Benjamin M. Ellingson Ph.D.[2]
[1]UCLA Brain Tumor Imaging Laboratory (BTIL), Center for Computer Vision and Imaging Biomarkers, University of California, Los Angeles, California, USA. [2]UCLA Brain Tumor Imaging Laboratory (BTIL), Center for Computer Vision and Imaging Biomarkers, University of California, Los Angeles, Los Angeles, California, USA. [3]Department of Neurosurgery, David Geffen School of Medicine at UCLA, Los Angeles, CA, USA. [4]Department of Radiological Sciences, David Geffen School of Medicine, University of California, Los Angeles, Los Angeles, CA, USA. [5]Department of Neurology, David Geffen School of Medicine, University of California Los Angeles, Los Angeles, CA, USA

Abstract Category

Adult Brain

Purpose

Historical data shows that enhancing tumor volume is the best radiologic surrogate of tumor burden in glioblastoma[1]. However, the radiographic evaluation of treatment response through changes in volume of contrast-enhancing (CE) tumor tissue are clouded by the effects of corticosteroids, which are commonly prescribed to mitigate edema and mass effect. As data quantifying the impact of corticosteroids on the radiographic features of brain tumors are still sparse[2–4], this study aims at quantifying the impact of corticosteroids on CE tumor size and diffusion MRI.

Materials & Methods

We retrospectively studied patients with treatment-naïve glioblastoma for which at least 2 pre-surgical MRI scans were available, as well as information on corticosteroid administration. Radiographic findings within each pair of pre-surgical scans were analyzed according to corticosteroid changes, which were categorized as “increased” (>2mg/day increase in dexamethasone), “stable” (<2mg/day change), or “decreased” (>2mg/day decrease) dose groups as proposed in RANO 2.0 criteria[5]. CE tumor volumes were quantified with 3D segmentations. RANO-compliant bidirectional measurements were performed by a neuroradiologist. In a sub-cohort with available diffusion MRI, apparent diffusion coefficient (ADC) maps were registered to CE-T1w images and median ADC values were extracted from the CE tumor segmentation. Changes in CE tumor size and ADC were compared across groups.

Results

61 pairs of MRI scans across 58 patients were analyzed. For 25 pairs, the corticosteroid doses were “increased” between the timepoints, 33 “stable”, and 3 “decreased”. Tumors with “stable” corticosteroid dose showed a growth in CE tumor volume (median +1.227 cc, p=0.0011, Figure 1A) as well as in bidirectional measurements (median +1.530 cm^2 cc, p<0.0001, Figure 1A). Conversely, tumors with “increased” corticosteroid dose showed a shrinkage of the CE tumor volume (median –3.884 cc, p=0.0337, Figure 1A) and a non-significant change in bidirectional measurements (p=0.6528, Figure 1A). Tumors with “stable” corticosteroid dose showed a percentual growth of CE volume (median +21.68%), while tumors with “increased” corticosteroids showed a shrinkage (median –22.51%), and this difference between groups was statistically significant (p=0.0007, Figure 1A). The group differences in the percent change of bidirectional measurements exhibited a trend in the same direction (median +19.40% “stable” vs +3.540% “increased” dose, p=0.0524, Figure 1A). Similar group differences were also seen when accounting for the time interval between scans (Figure 1A).
39 pairs of scans had diffusion datasets. While tumors with “stable” corticosteroid doses exhibited a stable ADC between timepoints (median change $–24.44\times10^{-6}$ mm^2/s, p=0.2643, Figure 1B), tumors receiving an “increased” dose showed a significant ADC reduction ($–186.0\times10^{-6}$ mm^2/s, p=0.0013). The ADC changes were significantly different between these two groups (p=0.0123, Figure 1B).
Representative cases are displayed in Figure 1C.

Conclusion

Increased corticosteroid doses can determine a reduction of enhancing tumor size and cloud the observation of tumor growth. A precise quantification of the interplay between corticosteroid dose and tumor growth is warranted to inform the interpretation of tumor progression in the clinical practice and in clinical trials. Additionally, quantifying the effects of corticosteroids on diffusion metrics can improve the interpretation of ADC as a tumor biomarker.

References

1. Sanvito F, Kaufmann TJ, Cloughesy TF, et al. Standardized brain tumor imaging protocols for clinical trials: current recommendations and tips for integration. Frontiers in Radiology 2023;3.
2. Kural C, Atac GK, Tehli O, et al. The evaluation of the effects of steroid treatment on the tumor and peritumoral edema by DWI and MR spectroscopy in brain tumors. Neurol Neurochir Pol 2018;52.

3. Minamikawa S, Kono K, Nakayama K, et al. Glucocorticoid treatment of brain tumor patients: Changes of apparent diffusion coefficient values measured by MR diffusion imaging. Neuroradiology 2004;46.
4. Cairncross JG, Macdonald DR, Pexman JHW, et al. Steroid-induced CT changes in patients with recurrent malignant glioma. Neurology 1988;38.
5. Wen PY, Van Den Bent M, Youssef G, et al. RANO 2.0: Update to the Response Assessment in Neuro-Oncology Criteria for High- and Low-Grade Gliomas in Adults. Journal of Clinical Oncology 2023;41.

Images/Tables

Figure 1

A) Tumor Size Plots Changes for "Stable" and "Increased" Corticosteroid Dose Groups

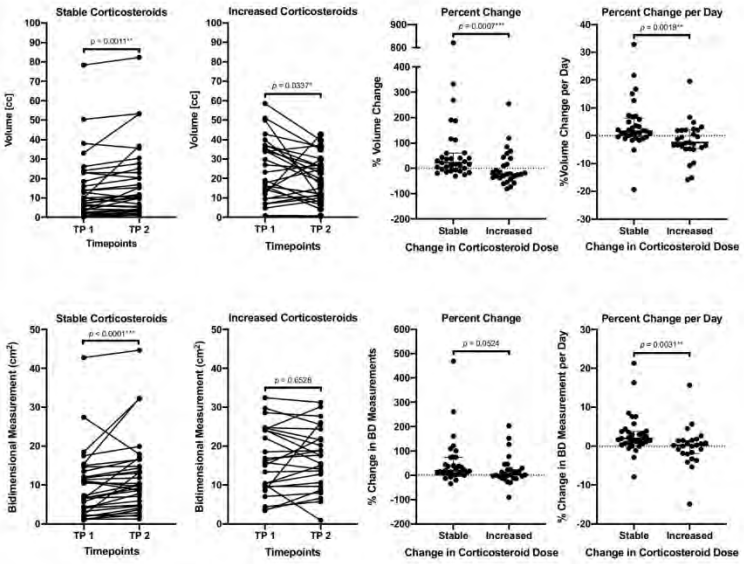

B) ADC Changes for "Stable" and "Increased" Corticosteroid Dose Groups

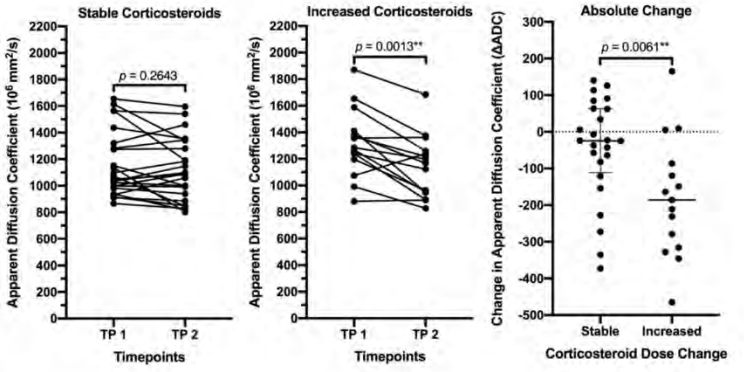

$\Delta ADC = ADC_{timepoint\ 2} - ADC_{timepoint\ 1}$

C) Representative Cases of "Stable," "Increased," and "Decreased" Corticosteroid Dose Groups

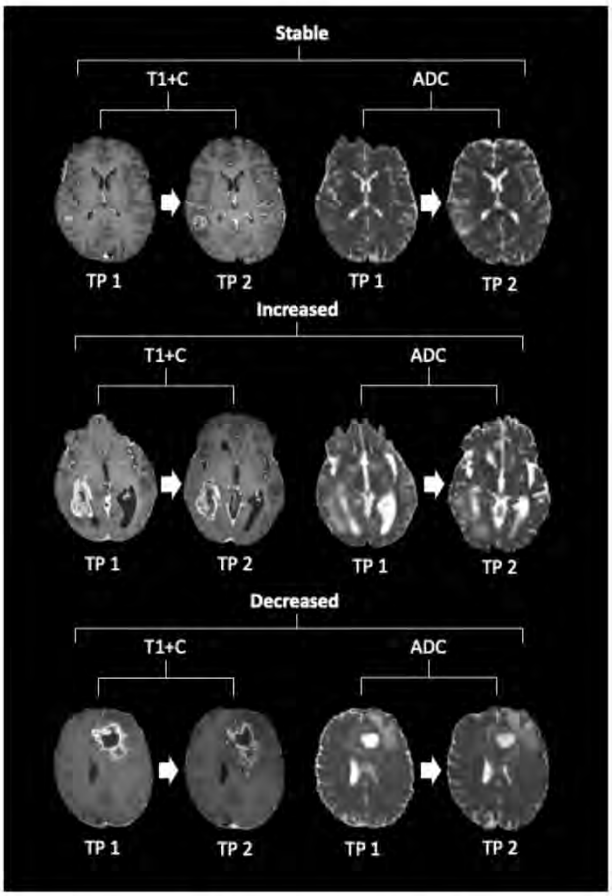

"TP"="timepoint"; T1+C=post-contrast T1w images; "stable"/"increased"/"decreased" refers to the corticosteroid dose change between timepoints; ADC = apparent diffusion coefficient.

722

A PDL1 targeted PET scan in patients with head and neck Squamous Cell Carcinoma

Nazanin Maleki M.D[1], Faryal Shareef MD[2], Takuya Toyonaga MD, PhD[3], David Weiss MD(c)[4], Eliot Funai[5], Saral Mehra M.D[6], Ansley Roche M.D[6], Aarti Bhatia M.D[6], Melissa Rasar Young M.D[7], Anita Huttner M.D[8], Barbara Burtness M.D[9], Richard Carson PhD[3], Julius Chapiro MD,PhD[3], Mariam Aboian MD, PhD[1]

[1]Children's Hospital of Philadelphia, Radiology Department, Philadelphia, PA, USA. [2]Naugatuck Valley Radiology, Waterbury, CT, USA. [3]Department of Raiology and Biomedical Imaging, Yale School of Medicine, New Haven, CT, USA. [4]Department of Diagnostic and Interventional Radiology and Neuroradiology, University Hospital Essen, Essen, Essen, Germany. [5]Department of Raiology and Biomedical Imaging,Division of Interventional Radiology, Yale School of Medicine, New Haven, CT, USA. [6]Department of Surgery, Division of Otolaryngology, Yale school of Medicine, New Haven, CT, USA. [7]Department of Therapeutic Radiology, Yale School of Medicine, New Haven, CT, USA. [8]Department of Pathology, Yale School of Medicine, New Haven, CT, USA. [9]Yale School of Medicine, New Haven, CT, USA

Abstract Category

Functional/Advanced Imaging

Purpose

Metastatic cancer is a leading cause of early death in patients with a variety of cancers including melanoma, lung cancer, breast cancer, and head and neck cancer. Immune checkpoint inhibitors are a promising treatment for end-stage metastatic cancers and Program death ligand-1(PDL1) expression is a potential biomarker for predicting response to the therapy. The current measurement of PDL1 is immunohistochemistry(IHC) based which requires invasive biopsies and has limitations caused by sampling error and difficulty in obtaining the tissue. In this study, we evaluated the newly developed positron emission tomography (PET) tracer [18F]PDL192 (aka [18F]BMS-986192) for quantitative assessment of PD-L1 in patients with head and neck cancer.

Materials & Methods

We enrolled patients with histologically confirmed squamous cell carcinoma visible on cross-sectional imaging (tumor/lymph node). Patients underwent dynamic [^{18}F]PDL1 PET/CT. Each received an intravenous tracer injection followed by a 120-minute PET scan. Primary tumors and metastatic/non-metastatic lymph nodes were segmented by a neuroradiologist. SUV (mean, max, voxel-based) and VT were measured for each ROI with the available arterial input function. The correlation between SUVmean and pathology PDL1 was assessed.

Results

Seven patients with a median age of 60[IQR 60-72] were included in this study. Median follow-up time was calculated at 5.4 months (IQR 3.5- 8.9). Five patients were evaluated to have stage 4, two patients had stage 3. Three (42.8%) of patients had PDL1 CPS>1 and 4 (57.14%) had CPS<1.

SUVmean in 8 primary tumors (1 patient with multifocal primary) was 1.73 ±0.81 with 0.25 skewness. Lesions in PD-L1 positive subjects SUVmean was 2.02±0.73 with 0.44 skewness, in negative was 1.62±0.82 with skewness 0.29. SUVmean in normal lymph nodes (LN) across the subjects was 1.88±0.82 with skewness 1.11. SUVMax in primary tumors, normal LN, and Metastatic LN were 4.3± 1.62, 3.87± 1.3, and 3.36± 1.55 respectively.

Conclusion

We present a prospective clinical trial for the evaluation of PD-L1 measurement using quantitative PET/CT in head and neck cancer. We demonstrate heterogeneity in PD-L1 signal within primary tumor and metastatic lesions which suggests that biopsy location may not capture the full picture of PDL1 expression. PDL1 PET could provide valuable additional information for clinicians to optimize patient selection for immune checkpoint inhibitor therapy.

References

1.Niemeijer AN, Leung D, Huisman MC, et al. Whole-body PD-1 and PD-L1 positron emission tomography in patients with non-small-cell lung cancer. Nat Commun 2018;9:4664. DOI: https://doi.org/10.1038/s41467-018-07131-y

Images/Tables

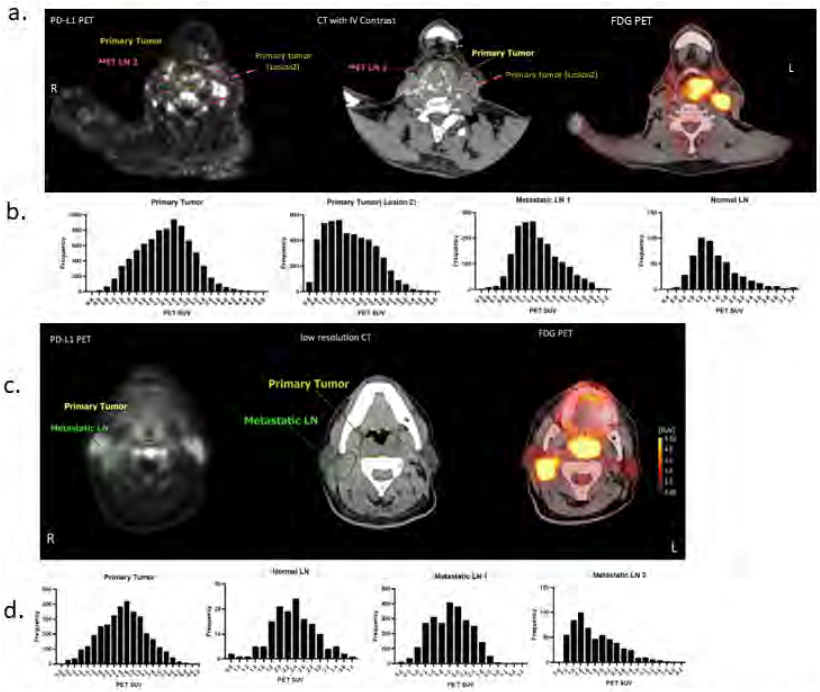

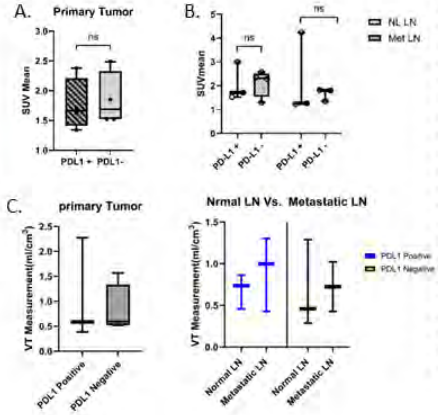

Fig2. **A**. Demonstrates comparable mean uptake in primary tumors with or without PD-L1 expression. **B**. Demonstrates higher mean uptake in both normal lymph and metastatic lymph node but this difference is not significant. (P value =0.6 , P value=0.8 as tested by Mann-Whitney U-test)
VT measurements in **C**. primary tumor, and **D**. Normal Lymph nodes and metastatic Lymph nodes across the patients with PDL1 positive and negative.

Fig1.a.Representative image of [18F]PDL192 PET scan (One-hour post-injection imaging) diagnosed with laryngeal SCC (PDL1 CPS>1) demonstrates tracer uptake heterogeneity within tumor and lymph nodes, IV contrast CT scan and FDG PET from archived imaging. FDG PET demonstrates intense FDG avidity in both primary tumor and metastatic lymph nodes.
b. Shows SUV distribution histogram in PDL1 PET in the same patient in the primary tumor (Lesion1 and Lesion2), metastatic and normal lymph nodes.
c. [18F]PDL192 PET scan in a patient diagnosed with Oropharyngeal SCC(PDL1 CPS<1), depicts a moderate uptake in both primary and metastatic lymph nodes. FDG PET image within 3 weeks of PDL1 PET shows hypermetabolic posterior oropharyngeal mass and bilateral FDG avid level II cervical lymph nodes.

725

Investigating the interplay between tumor location, prognostic variables, and experimental treatment in glioblastoma, using voxel-wise multivariate Cox proportional hazard statistical parameter mapping

Francesco Sanvito[1], Catalina Raymond[1], Donatello Telesca[1], Jingwen Yao[1], Lauren E Abrey[2], Josep Garcia[3], Brian Simmons[3], Olivier Chinot[4], Frank Saran[5], Ryo Nishikawa[6], Roger Henriksson[7], Warren P Mason[8], Wolfgang Wick[9], Timothy F Cloughesy[1], Benjamin M Ellingson[1]

[1]University of California Los Angeles, Los Angeles, CA, USA. [2]F.Hoffman - La Roche, Ltd, Basel, Switzerland, Switzerland. [3]Genentech Inc, South San Francisco, CA, USA. [4]Aix-Marseille University, Marseille, France, France. [5]The Royal Marsden NHS Foundation Trust, Sutton, UK, United Kingdom. [6]Saitama Medical University, Saitama, Japan, Japan. [7]University of Umea, Umea, Umea, Sweden. [8]Princess Margaret Hospital, Toronto, Ontario, Canada. [9]Heidelberg University, Heidelberg, Germany, Germany

Abstract Category

Adult Brain

Purpose

Tumor location is known to impact overall survival (OS) in glioblastoma[1,2], due to its relation to brain functions, surgical resectability[3], and tumor biology[4]. However, there is a lack of quantitative tools for studying the interplay between tumor location, prognostic variables, and treatments. Such tools would be valuable in clinical trials to disentangle the differential efficacy of treatment protocols on glioblastomas arising in different brain areas. In the current study we develop a voxel-wise statistical parameter mapping technique using a multivariable Cox regression model to describe the influence of tumor location on treatment effects in newly diagnosed glioblastoma.

Materials & Methods

598 newly diagnosed glioblastoma patients from the phase 3 AVAglio trial[5] were studied. Areas of T_2/FLAIR hyperintensity and resection cavities on post-surgical MRI scans were segmented and aligned to MNI atlas space. A voxel-wise Cox proportional hazards model for OS was run voxel-wise (e.g., for each image voxel) and included tumor presence in a specific voxel, age, MGMT promoter methylation, baseline tumor volume, and treatment (chemoradiation with or without bevacizumab). Additional models were run with interaction variables between baseline tumor volume

and tumor presence, and between treatment and tumor presence, to establish whether these variables had a different impact on OS in different brain regions.

Results

After adjusting for other variables, tumor location was an independent predictor of favorable OS for tumors with involvement in the right prefrontal cortex (p<0.05, HR ranging ~0.48–0.65) and a predictor of shorter OS for tumors in the left mesial/basal temporo-occipital areas (p<0.05, HR ~3–6.2) and in the left hemisplenium of the corpus callosum (p<0.05, HR ~2.5–3) (**Figure 1A**). Using a dedicated interaction model, baseline tumor volume was a predictor of shorter OS when tumors were located in most brain regions (p<0.05, HR ~1.005–1.025), except for bilateral prefrontal areas (p>0.05), where baseline volume in presence of tumor was not a significant prognostic factor (**Figure 1B**). With a similar interaction approach, a treatment regimen that included bevacizumab was associated with a significantly longer OS in specific brain regions such as left Rolandic subcortical locations (p<0.05, HR ~0.3–0.5), and with a shorter OS in other regions such as the right thalamus and corticospinal tract (p<0.05, HR ~1.5–5) (**Figure 1C**).

Conclusion

Statistical parametric mapping with voxel-wise Cox models that include interaction variables represent a novel tool to study the interplay between tumor location and treatment regimens in influencing prognosis, while accounting for other prognostic factors such as molecular status, tumor size, and age. Their application to clinical trial datasets may reveal that subsets of patients with specific tumor locations may benefit more from specific experimental treatments.

References

1. Yuile P, Dent O, Cook R, et al. Survival of glioblastoma patients related to presenting symptoms, brain site and treatment variables. *J Clin Neurosci Off J Neurosurg Soc Australas* 2006;13:747–51.
2. Fekete B, Werlenius K, Tisell M, et al. What predicts survival in glioblastoma? A population-based study of changes in clinical management and outcome. *Front Surg* 2023;10:1249366.
3. Mineo J-F, Bordron A, Baroncini M, et al. Prognosis factors of survival time in patients with glioblastoma multiforme: a multivariate analysis of 340 patients. *Acta Neurochir (Wien)* 2007;149:243–5.
4. Ellingson BM, Lai A, Harris RJ, et al. Probabilistic radiographic atlas of glioblastoma phenotypes. *AJNR Am J Neuroradiol* 2013;34:533–40.
5. Chinot OL, Wick W, Mason W, et al. Bevacizumab plus radiotherapy-temozolomide for newly diagnosed glioblastoma. *N Engl J Med* 2014;370:709–22.

Images/Tables

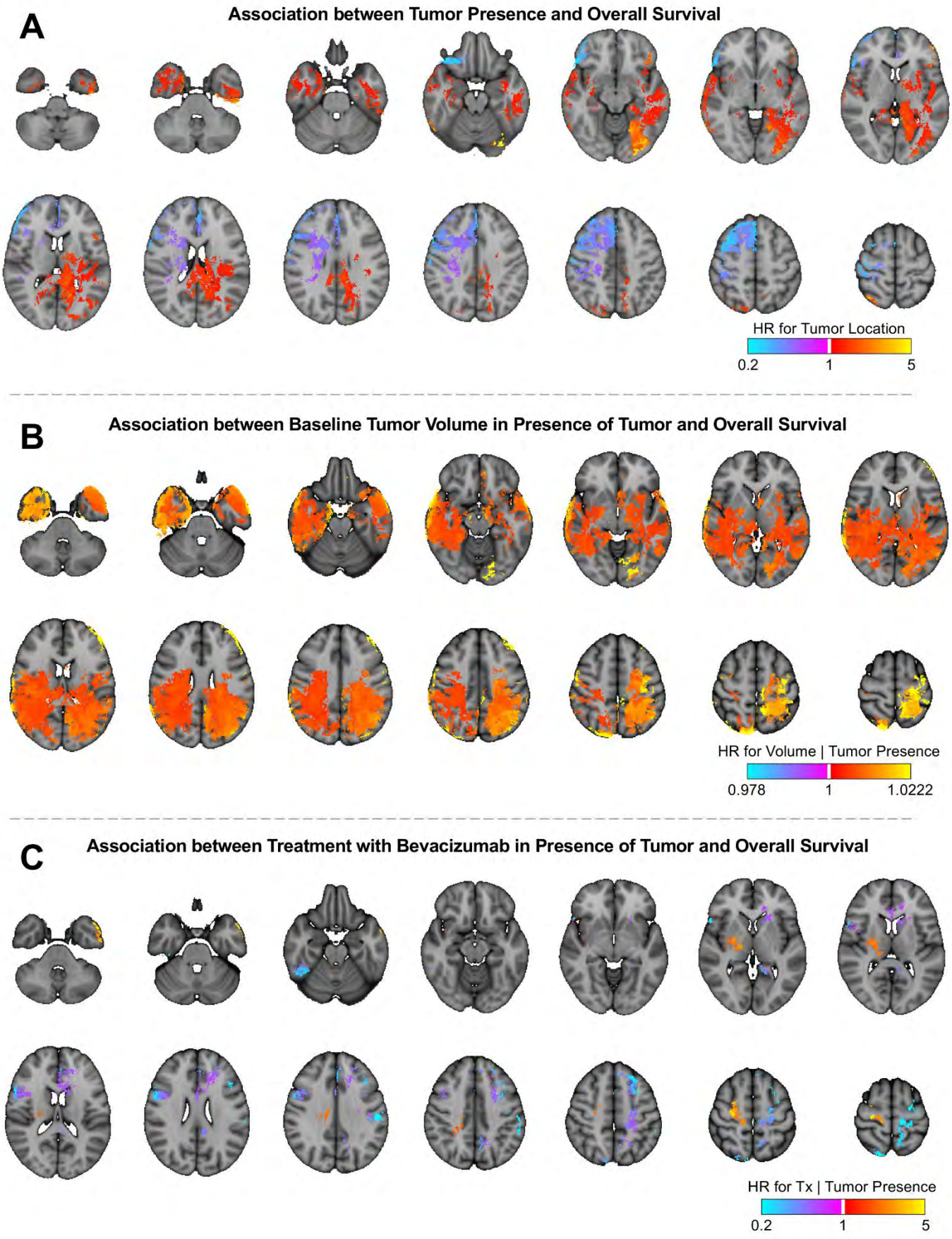

726

Resting-State Co-Activation Patterns of Language Reorganization in Brain Tumors

Luca Pasquini MD, PhD[1], Antonio Napolitano PhD[2], Leonardo Spitoni[2], Mehrnaz Jenabi[3], Kyung Peck[3], Andrei Holodny[3]
[1]Yale University, New Haven, CT, USA. [2]OPBG, Rome, Lazio, Italy. [3]MSKCC, New York, NY, USA

Abstract Category

Functional/Advanced Imaging

Purpose

Language reorganization has been described in brain tumors as a possible compensatory mechanism against speech deficits(1,2). Despite extensive research, the modifications of brain function and cognitive processing in patients who reorganize language are unknown. Co-Activation Pattern (CAP) analysis can monitor cognitive processing by quantifying brain transitions across networks, thereby identifying which cognitive functions ('mental states' such as attention, awareness, sensory/motor processing) are active and for how long(3). Our objective was to study CAP of resting-state fMRI in patients with and without language reorganization and brain tumors, compared to healthy controls (HC). We hypothesized that patients would display an alteration of mental states reflective of neuroplasticity.

Materials & Methods

Right-handed patients with left hemispheric tumors, language task-based fMRI and resting-state fMRI were retrospectively rectuited. Resting-state fMRI data was pre-processed for motion correction, spatial smoothing and MNI coregistration. Language dominance was assessed on phonemic fluency task-based fMRI through multiple laterality indexes (left dominant if LI>0.2). CAPs were extracted using TbCAPs toolbox (4). Bold data was concatenated across subjects and k-means clustering was used to classify data into k states. Labelling of each CAP into a brain network was performed using Component Labeler by GIFT toolbox. We obtained the following metrics: 1) persistence = total state-to-state maintenance of a specific brain state; 2) transitions = total frequency of state-to-state transitions from one volume to the next; 3) in-degree kin = how likely a CAP is visited from any other; 4) out-degree kout = how likely a CAP is exited towards any other. Differences in CAP metrics between the groups were studied with t-test. P-values were corrected using Benjamini Hochman correction (significance at p<.05).

Results

64 patients were recruited (31 HGG, 22 LGG, 11 metastases, age 51+/- 8, 36 F) and 100 age-matched healthy controls. Six CAPs were characterized. Significant differences were found in the dorsal component of the default mode network (DMN) in patients with language reorganization: lower persistence (p=0.003), higher transitions (p=0.006), higher kin and kout (p=0.003 and 0.004 respectively). Both reorganized and left dominant patients showed significant differences compared to HC in the DMN and executive network.

Conclusion

The mental state of patients with language reorganization transits more often through the DMN. This behavior is characterized by more frequent access in and out of the network with lower persistence. The DMN is a bi-hemispheric, symmetric network that connects the frontal, temporal and parietal lobes(5). Due to widespread distribution across both hemispheres, the DMN can coordinate the transfer of information from distant regions. Based on these features, one may speculate the DMN being involved in the inter-hemispheric communication underlying reorganization of language in response to tumor growth.

References

1. Pasquini L, Jenabi M, Yildirim O, et al. Brain Functional Connectivity in Low- and High-Grade Gliomas : Differences in Network Dynamics Associated with Tumor Grade and Location. *Cancers (Basel)* 2022;14:3327.
2. Quinones A, Jenabi M, Pasquini L, et al. Longitudinal Functional MRI Demonstrates Translocation of Language Function in Patients with Brain Tumors. *J Neurosurg* 2022; 139:29-37.
3. Matsui T, Pham TQ, Jimura K, et al. On co-activation pattern analysis and non-stationarity of resting brain activity. *Neuroimage* 2022;249:118904.
4. Bolton TAW, Tuleasca C, Wotruba D, et al. TbCAPs: A toolbox for co-activation pattern analysis. *Neuroimage* 2020;211:116621.
5. Marcotte K, Perlbarg V, Marrelec G, et al. Default-mode network functional connectivity in aphasia: Therapy-induced neuroplasticity. *Brain Lang* 2013;124:45–55.

Images/Tables

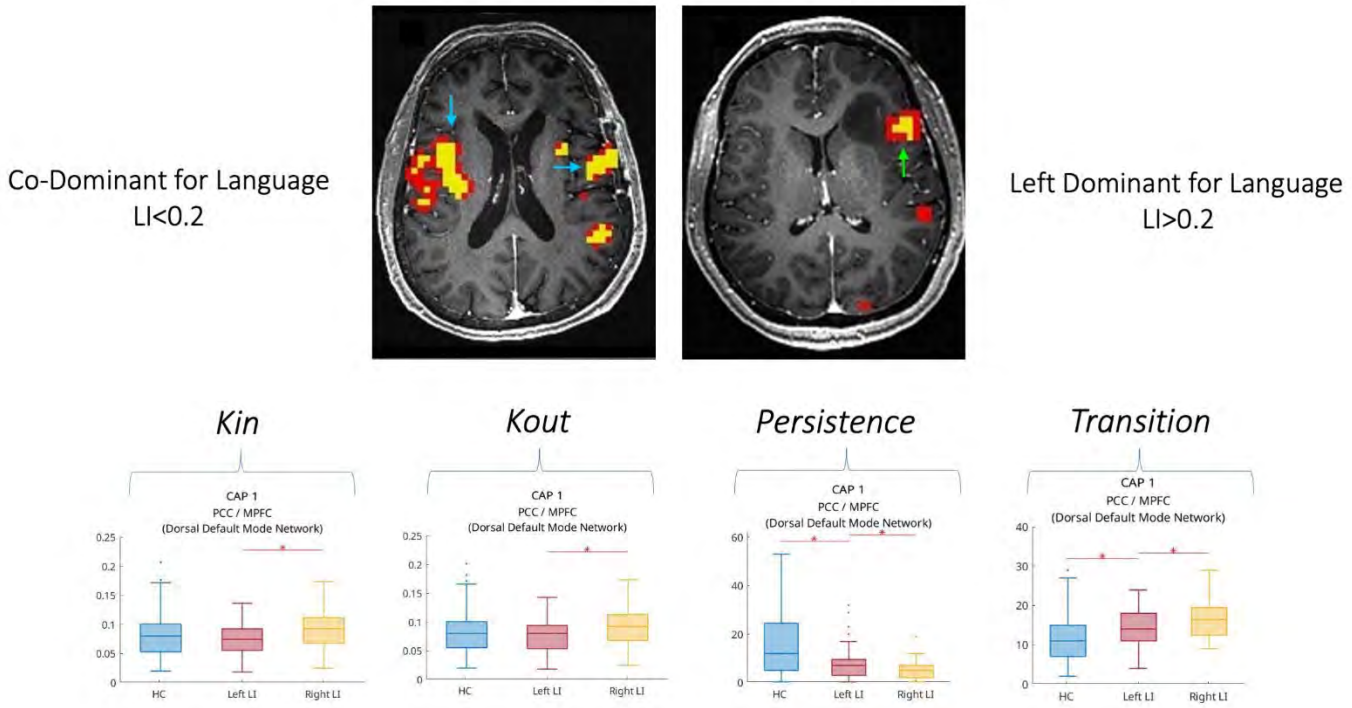

727

Preliminary Findings from a Longitudinal Study on Intracranial Atherosclerotic Disease and Stroke Risk in Brain Tumor Patients

Beibei Sun MD, PHD, Mohamed H D Hassan MD, Mohamad H Mosi MD, Ahmed A Safwat MD, Chengcheng Zhu, Mahmud Mossa-Basha MD
University of Washington, Seattle, WA, USA

Abstract Category

Adult Brain

Purpose

Cancer patients have twice the stroke risk of the general population, with brain tumor patients at particularly high risk [1]. As cancer survival rates have improved in recent years [2], it is crucial to identify survivors at elevated stroke risk. Since intracranial atherosclerotic disease (ICAD) is a leading cause of stroke globally [3], we developed a unique longitudinal vessel wall MRI (IVW) database to assess ICAD and track acute ischemic stroke (AIS) incidence in brain tumor patients, offering valuable insights into the vascular health of this high-risk group.

Materials & Methods

We prospectively and consecutively enrolled brain tumor patients (diagnosed from 1984 to 2024) at our oncology center from 2018 to 2024. Demographic and clinical data, including cardiovascular risk factors and brain tumor (primary or metastasis, WHO grade and IDH mutation) and therapy details (surgery, radiation, and chemotherapy), were recorded. All patients underwent brain MRI with IVW surveillance during follow-up. Three neuroradiologists reviewed each IVW for ICAD features, evaluating plaque prevalence, multiple plaque prevalence (total plaque number≥2), total plaque number and degree of ICAD lumen stenosis. Additionally, AIS occurrence was assessed as an endpoint event.

Results

To date, we have enrolled 1,400 patients, with enrollment still ongoing. For preliminary analysis, we examined a subset of the dataset consisting of 242 participants (46.7% male) with a mean age of 50.5±15.2 years (Table 1). Among them, 199 (82.2%) were diagnosed with primary brain tumors and 169 (69.8%) underwent surgical intervention. Of the tumors, 165 (65.8%) were classified by WHO grade I to IV (Grade I: 6.2%, Grade II: 16.9%, Grade III: 18.2%, Grade IV: 26.9%).

Table 1 also presents detailed demographic information and risk factors for these patients. The median follow-up duration was 3 years [interquartile range: 1.45–5 years], with 93 patients (38.4%) dying during follow-up.
Table 2 demonstrates the IVW findings. Patients underwent between 2 and 24 IVW and MRI brain scans throughout follow-up. At baseline, no cases of vasculitis, moyamoya disease, or arterial dissection were observed. However, 4 patients (2.4%) were found to have an aneurysm. Atherosclerosis was present in 41.3% of patients, with a total plaque count of 248, and 26.9% had multiple plaques. At the final MRI assessment of the follow-up period, the total plaque count had risen to 268, with 44.2% of patients showing plaque presence and 29.3% having multiple plaques. Additionally, 12 patients (4.9%) experienced an acute ischemic stroke during the follow-up period, 8 of them have intracranial plaque.

Conclusion

In this prospective study, we observed a significant prevalence of intracranial atherosclerotic plaques among brain tumor patients, with an increase in plaque burden over time. The presence of ICAD in this population suggests an elevated risk of cerebrovascular complications, possibly exacerbated by cancer and treatment-associated factors. Additionally, the incidence of acute ischemic stroke in brain tumor patients, albeit low, underscores the need for vigilant cardiovascular monitoring in this high-risk group. These findings highlight the importance of early detection and management of ICAD to mitigate stroke risk and improve patient outcomes.

References

[1] Zaorsky NG, Zhang Y, Tchelebi LT, et al. Stroke among cancer patients. Nat Commun. 2019;10:5172. DOI: 10.1038/s41467-019-13120-6
[2] Siegel RL, Miller KD, Fuchs HE, et al. Cancer Statistics, 2021. CA Cancer J Clin. 2021;71:7-33. DOI: 10.3322/caac.21654
[3] Gutierrez J, Turan TN, Hoh BL, Chimowitz MI. Intracranial atherosclerotic stenosis: risk factors, diagnosis, and treatment. Lancet Neurol. 2022;21:355-368. DOI: 10.1016/S1474-4422(21)00376-8

Images/Tables

Table1. Basic information of our patients.

Demographic information	
Age, years	50.5±15.2
Age group(<40ys;40-60;>60ys)	
<40yrs, n, %	70(28.9%)
40-60yrs, n, %	95(39.3%)
>60yrs, n, %	77(31.8%)
Gender (male, n, %)	113(46.7%)
BMI, kg/m^2	27.8±5.9
Risk factors	
Hypertension, n, %	79(32.6%)
Diabetes, n, %	20(8.3%)
HbA1c (%)	6.65±1.32
Dyslipidemia, n, %	64(26.4%)
LDL-C (mg/dL)	120.4±43.4
Coronary artery disease, n, %	9(3.7%)
A-fib, n, %	6(2.5%)
History of stroke, n, %	17(7.0%)
Family history of CVD, n, %	73(30.2%)
Smoke, n, %	51(21.1%)
Brian tumor information	
Time of diagnosis	1984-2024
Primary, n, %	199(82.2%)
Surgery, n, %	169(69.8%)
WHO grade of primary tumor, n, %	165(65.8%)
WHO1/2/3/4 grade, n, %	6.2%/16.9%/18.2%/26.8%
IDH mutation (1/2/3), n, %	29%/0%/26.4%
Radiation therapy, n, %	201(83.1%)
Chemotherapy, n, %	167(69.0%)
Concurrent therapy, n, %	158(65.3%)
Other therapy	
Immunol or hormonal therapy, n, %	78(32.2%)

Values are mean± SD, or n (%). BMI indicates body mass index; HbA1c, hemoglobin A1c; LDL, low-density-lipoprotein; A-fib, Atrial Fibrillation; IDH, Isocitrate Dehydrogenase.

Table 2. Vessel wall imaging findings during follow-up

Vessel wall images findings	
Baseline	
Vasculitis	0(0%)
Moyamoya	0(0%)
Aneurysm	4(2.4%)
Dissection	0(0%)
Atherosclerosis plaques (%)	100(41.3%)
Multiple plaques (%)	65(26.9%)
Total Plaque numbers (n)	248
Plaque stenosis (>50%)	0(0%)
Follow up (median [IQR], years)	3 [1.3-5]
Atherosclerosis plaques (%)	109(44.2%)
Multiple plaques (%)	71(29.3%)
Total Plaque numbers (n)	265
Plaque stenosis (>50%)	0(0%)
Stroke prevalence (%)	12 (4.9%)

Values are median (IQR), or n (%). IQR, interquartile range

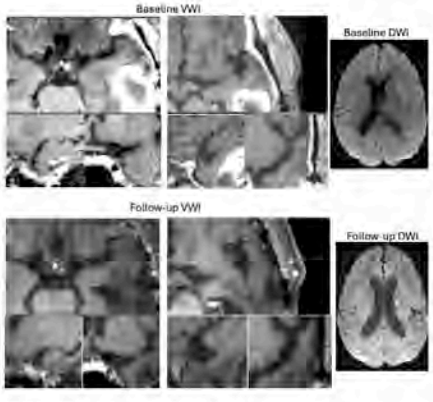

Figure. This 51-year-old male was diagnosed with a WHO Grade IV glioblastoma in the left temporal region in 2018. He underwent tumor resection followed by radiotherapy and chemotherapy. His first baseline vessel wall imaging (VWI) was conducted on September 4, 2018, with a subsequent follow-up VWI performed later. At baseline, no intracranial plaques were observed in the LC7 and distal LMCA. However, the follow-up VWI revealed new plaques in these areas, along with evidence of an acute infarction located in the left corona radiata.

733

Differentiating LITT-Related Necrosis from Avastin-Related Cytotoxicity, Radiation Necrosis, and Recurrent Glioblastoma Using Apparent Diffusion Coefficient Values

Kamand Khalaj MD-MPH, Elham Tavakkol MD, Andres Rodriguez MD, David Timaran-Montenegro MD, Shrey Derasari, Arash Kamali
UTHealth Houston, Houston, Texas, USA

Abstract Category

Adult Brain

Purpose

Laser interstitial thermal therapy (LITT) has become a valuable salvage treatment for glioblastoma (GBM), particularly for tumors that are difficult to access through conventional surgery. However, interpreting post-LITT imaging findings is complex and remains an active area of research. Previous studies have described early laser-tissue interactions in LITT as central coagulation necrosis surrounded by peripheral edema, with delayed resorptive changes and granulation tissue formation. Diffusion Weighted Imaging (DWI) typically shows an initial increase in diffusion restriction within the center of the lesion due to necrosis, which then diminishes over time. This study aimed to evaluate whether Apparent Diffusion Coefficient (ADC) values, derived from DWI, could serve as a reliable, non-invasive biomarker to distinguish LITT-induced necrosis from other post-treatment effects, such as Avastin-related cytotoxicity, radiation necrosis, and true tumor progression in GBM patients.

Materials & Methods

Extending our prior work on smaller GBM cohorts, this IRB-approved, retrospective study included 157 patients with histologically confirmed IDH-wild type glioblastoma, divided into four groups: 21 patients with Avastin-related cytotoxicity, 49 with recurrent glioblastoma, 58 with radiation necrosis, and 29 treated with LITT. MRI scans were evaluated, and ADC values were measured in areas of diffusion restriction within the lesion and normal-appearing white matter (NAWM) from the contralateral hemisphere. Relative ADC (rADC) values were calculated by dividing the ADC values of the lesion by the contralateral NAWM for normalization of the data across different scanners. ADC values are expressed in units of 1 x 10^-6 mm^2/s.

Results

Significant differences in ADC and rADC values were observed across groups. The mean ADC values in different lesions were as follows: 248.1 ± 67.2 mm^2/s for Avastin-related cytotoxicity, 752.8 ± 132.5 mm^2/s for recurrent glioblastoma, 479.0 ± 105.2 mm^2/s for radiation necrosis, and 555.7 ± 116.6 mm^2/s for LITT-induced necrosis. Relative ADC values were 0.39 ± 0.10 for Avastin, 1.07 ± 0.22 for glioblastoma, 0.66 ± 0.14 for radiation necrosis, and 0.67 ± 0.16 for LITT. All pairwise comparisons were statistically significant ($p < 0.001$), except between radiation necrosis and LITT ($p = 0.97$), indicating that ADC values could distinguish LITT from Avastin-related cytotoxicity and recurrent glioblastoma but not from radiation necrosis.

Conclusion

ADC and rADC values are promising markers for non-invasive differentiation of LITT-related necrosis from Avastin-induced cytotoxicity and glioblastoma recurrence. However, distinguishing LITT from radiation necrosis remains a challenge, suggesting the need for additional imaging markers to improve the differentiation of these treatment effects.

References

- Khalaj K, Jacobs MA, Zhu JJ, Esquenazi Y, Hsu S, Tandon N, Akhbardeh A, Zhang X, Riascos R, Kamali A. The Use of Apparent Diffusion Coefficient Values for Differentiating Bevacizumab-Related Cytotoxicity from Tumor Recurrence and Radiation Necrosis in Glioblastoma. Cancers (Basel). 2024 Jul 2;16(13):2440. doi: 10.3390/cancers16132440. PMID: 39001500; PMCID: PMC11240552.
- Schwarzmaier H, Eickmeyer F, Tempelhoff W, Fiedler V, Niehoff H, et al. (2006) Ulrich S, Yang Q, and Ulrich F, MR-guided laser-induced interstitial thermotherapy of recurrent glioblastoma multiforme: Preliminary results in 16 patients, European Journal of Radiology, vol. 59, pp.208–215.
- Swartz LK, Holste KG, Kim MM, Morikawa A, Heth J. Outcomes in Patients Treated with Laser Interstitial Thermal Therapy for Primary Brain Cancer and Brain Metastases. Oncologist. 2019 Dec;24(12):e1467-e1470. doi: 10.1634/theoncologist.2019-0213. Epub 2019 Aug 22. PMID: 31439811; PMCID: PMC6975949.

Images/Tables

Table 1. Descriptive statistics of ADC values

Group	N	Lesion	Normal	P value
		Mean ± SD	Mean ± SD	
Avastin	21	248.1 ± 67.2	647.2 ± 94.6	<0.001
Progressive glioblastoma	49	752.8 ± 132.5	709.2 ± 63.5	0.08
Radiation necrosis	58	479.0 ± 105.2	723.3 ± 64.0	<0.001
LITT	29	555.7 ± 116.6	839.0 ± 110.4	<0.001

Table 2. Descriptive statistics of rADC values (*P=0.97* for comparison between radiation necrosis and LITT groups, all other pairwise comparisons had *P<0.001*)

Group	N	Mean ± SD
Avastin	21	0.39 ± 0.10
Progressive glioblastoma	49	1.07 ± 0.22
Radiation necrosis	58	0.66 ± 0.14
LITT	29	0.67 ± 0.16

740

Quantifying the Impact of FAST MRIs and a Dedicated Emergency Department MRI System on Patient Wait Times

Sheena Y Chu MS, Ali Pirasteh MD, Elizabeth A Briel BSRT, Kristi B Klein MBA, RTR (M), Tabassum A Kennedy MD, Gregory D Avey MD, Kelly W Capel MD, John W Garrett PhD, Scott B Reeder MD, PhD, Laura B Eisenmenger MD
University of Wisconsin-Madison, Madison, WI, USA

Abstract Category

AI/Informatics

Purpose

MRI order volumes from the emergency department (ED) increased by more than 60% in the last five years. This has not been accompanied by additional MRI resources, leading to increased imaging wait times, and worsened delays in patient care **(Figure 1)**.

Dedicated MRI availability in the ED has been proven to expedite patient care[1–3]. Focused Acquisition for reduced Scan Time (FAST) MRI protocols are designed to answer focused clinical questions. They include fewer and/or shorter sequences when compared to a conventional MRI protocol and improve overall exam efficiency[4]. **The purpose of this study was to determine the impact of dedicated ED MRI hours (weekdays 3-11pm) and the use of FAST protocols on workflow and wait times.**

Materials & Methods

The FAST workflow is only available during ED Hours. This timeframe was selected due to peak ED volumes and low outpatient volumes. Patients under 18 or requiring conscious sedation or general anesthesia are not eligible. Of the available FAST protocols, seven of them are neuro-specific (**Table 1**). The FAST workflow also includes a dedicated transporter to pre-screen for MRI safety and move FAST MRI patients **(Figure 2)**.

Data were retrospectively collected from August and September 2024, and August and September 2023 as a historical control. The time between order placement and first image acquisition is defined as order-to-image time. Order time and first image time are recorded in the electronic health record (EHR) and the DICOM header, respectively.

Studies were extracted from the local Picture Archiving and Communication System (PACS; Change Healthcare) and the EHR (Epic). Patients with multiple orders at a time were consolidated as one exam. The Wilcoxon rank-sum test and Mood's median test compared the averages and medians of order-to-image times. P<0.05 was considered statistically significant.

Results

In August and September 2023, 226 MRI orders were placed during ED hours. In August and September 2024, 226 were ordered during ED hours. 101 (44.6%) of them were FAST protocols and 85 (37.6%) were FAST neuro protocols **(Table 2).** The average order-to-image time during ED hours decreased from 2.84 hours in 2023 to 2.42 hours in 2024 ($P<0.005$), and the median decreased from 2.31 hours to 1.60 hours ($P<0.005$). For the FAST neuro exams, the order-to-image was 1.58 hours, and the median time was 1.21 hours. In comparison, the average conventional exam order-to-image time was 3.02 hours, and the median time was 1.87 hours **(Table 3)**.

Conclusion

In this work, we successfully implemented a FAST ED MRI workflow. Patients who received a prioritized FAST exam during ED hours were imaged significantly faster than before prioritization. Additionally, all patients who received an MRI during ED hours were imaged significantly quicker than before. We conclude that the implementation of dedicated ED MRI availability and prioritized FAST protocols significantly decreased order-to-image time.

Limitations include that it was a single institution study. Additionally, we are unable to definitively determine what factors potentially contribute to delays in order-to-image. Future studies could examine mitigation of causes for delays, to identify solutions for accelerating workflow even further.

References

1. Buller M, Karis JP. Introduction of a Dedicated Emergency Department MR Imaging Scanner at the Barrow Neurological Institute. *Am J Neuroradiol*. 2017;38(8):1480-1485. doi:10.3174/ajnr.A5210
2. Gil H, Tuttle AA, Dean LA, et al. Dedicated MRI in the emergency department to expedite diagnostic management of hip fracture. *Emerg Radiol*. 2020;27(1):41-44. doi:10.1007/s10140-019-01729-5
3. Kepka S, Zarca K, Lersy F, et al. MRI dedicated to the emergency department for diplopia or dizziness: a cost-effectiveness analysis. *Eur Radiol*. 2022;32(11):7344-7353. doi:10.1007/s00330-022-08791-7
4. Vietti Violi N, Taouli B. Abbreviated MRI for HCC surveillance: is it ready for clinical use? *Eur Radiol*. 2020;30(8):4147-4149. doi:10.1007/s00330-020-06904-8

Images/Tables

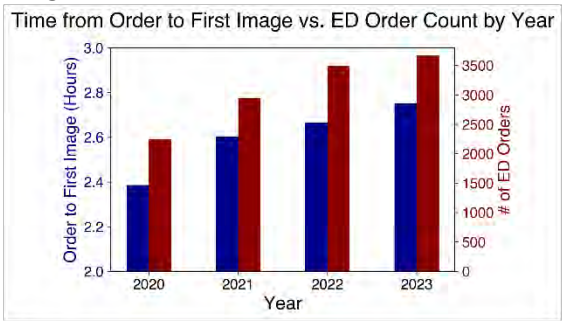

Figure 1: The number of orders placed annually in the ED has increased in the last 4 years at our institution. Similarly, there has been a slight increase in the time from order to first image acquisition for those ED orders. This indicates a need for order prioritization as the number of annual orders continues to increase.

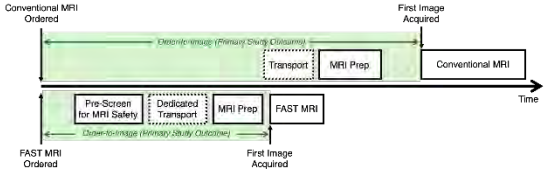

Figure 2: Workflow diagram of conventional vs. FAST MRI Exam ED workflow. In addition to a FAST protocol, FAST orders also have a dedicated ED to MRI transporter and patients are pre-screening for MRI safety by trained ED triage or transport staff. The time between order placement and acquisition of the first image in the MRI exam is defined as the order-to-image which is the primary study outcome. Note that if the number of MRI requests exceeds the ED MRI system capacity, some exams may need to be completed on other MRI systems, and delays may occur.

FAST Protocol	Protocol Details	Clinical Indications
FAST Stroke W/WO	Ax DWI, Sag T1, FAST COW, PWI, Sag e3DCPA, Ax SSFSE, Ax PseudoSwan, Ax T2 FLAIR, Cor T1 CUBE	Stroke Large vessel Stenosis or Occlusion Masses/parenchymal abnormalities over ~5 mm Mass effect abnormalities Fluid collections
FAST Stroke WO	Ax DWI, Sag T1, FAST COW, Ax PseudoSwan, Ax SSFSE, Ax T2 FLAIR, Sag e3DPCA	
FAST Brain W/WO	Ax DWI, Sag T1, SSFSE (Ax, Sag, Cor), Ax PseudoSwan, PWI, Sag T2 CUBE FLAIR, Ax T1 FSPGR, Cor T1 CUBE	Same as FAST Stroke + Completed CTA
FAST Brain WO	Ax DWI, Sag T1, Ax PseudoSwan, Ax SSFSE, Ax T2 FLAIR	
FAST Cauda Equina	Sag T1 CUBE, Sag STIR, axial reformats, Axial T2	Cauda Equina Syndrome
FAST Total Spine W/WO	(C, T, L spine): Sag T1 CUBE, Sag STIR, Post Sag T1 CUBE FAT	Fracture, overt trauma evaluation Screening for larger spine abnormalities
FAST Total Spine WO	(C, T, L spine): Sag T1 CUBE, Sag STIR	
FAST MRA Chest	MRA Cor (Pre, Dur, Post, Low Flip), Ax T1, Ax SSFP	Pulmonary embolism
FAST MRV Lower Extremity	Ax T1 (Iliac Crest to Ankle)	Deep venous thrombosis
FAST Hip MRI	Cor T1, Cor STIR, Ax T2 FAT	Occult hip fracture
FAST Scaphoid MRI	Ax T2 FAT, Cor T2 FAT, Cor T1	Occult scaphoid fracture

Table 1: Available FAST MRIs that can be ordered from the Emergency Department, protocol, and associated clinical indications. FAST neuro protocols are italicized and bolded.

Time from Order to First Image Statistical Analysis: Weekdays 3 – 11pm		
	Before (Aug/Sept 2023)	**After (Aug/Sept 2024)**
# of Orders	226	226
Average	2:50:29	2:25:49*
Median	2:18:43	1:36:14*
90th Percentile	4:37:39	3:56:23

Table 2: The overall average and median times from order to first image regardless of conventional or FAST protocol were significantly less than prior to implementation. This table summarizes study results during ED hours, which are 3pm-11pm on weekdays. * = statistical significance

Conventional vs. FAST Protocol Statistical Analysis: **Weekdays 3 – 11pm**			
	Conventional	**FAST**	**FAST (Neuro Only)**
# of Orders	125	101	85
Average	3:01:32	1:41:37*	1:35:12*
Median	1:51:59	1:17:54*	1:12:34*
90th Percentile	5:19:38	2:58:20	2:41:21

Table 3: After implementation of FAST protocols on a dedicated MRI system the median time from order to image was 1 hour, 17 minutes, 54 seconds. For FAST neuro protocols, the average was even lower at 1 hour, 12 minutes, and 34 seconds. This table summarizes study results split into conventional, FAST, and FAST neuro protocols during ED hours which are from 3pm-11pm on weekdays. * = statistical significance

742

The Ability of Modern Screening Whole Body Trauma CTA to Accurately Detect Blunt Cerebrovascular Injury in a Large Polytrauma Cohort

AbdulAziz Shakfa MD, Lei Wu MD, Monique A. Mogensen MD, Daniel S. Hippe MS, Ahmed A. Safwat MD, Mahmud Mossa-Basha MD

Department of Radiology, University of Washington, Seattle, WA, USA

Abstract Category

Adult Brain

Purpose

Blunt cerebrovascular injury (BCVI) represents a significant clinical concern due to its potential to cause ischemic strokes. These injuries, involving the carotid and vertebral arteries, occur in patients with blunt force trauma. The purpose of this study is to assess the effectiveness of whole-body trauma CTA in comparison to neck CTA for the detection of BCVI, aiming to determine the most efficient diagnostic approach to support early intervention and reduce the incidence of BCVI-related strokes.

Materials & Methods

Retrospectively identified trauma patients with blunt cerebrovascular injury (BCVI) and control trauma patients without BCVI who received WBT-CTA with neck CTA reconstructions on a 128-channel multidetector CT between January 1, 2013, and December 31, 2016, were de-identified and randomized together. Two neuroradiologists independently evaluated all WBT-CTAs, identifying any BCVIs and assigning the appropriate injury grade. The number and grade of BCVIs were compared between WBT-CTAs and reference thin-slice standard neck CTAs reconstructed from the WBT-CTAs. WBT-CTA sensitivity, specificity, and inter-rater agreement for the detection of BCVI were determined.

Results

Moderate agreement was found between WBT-CTA and neck CTA (Table 1) for detecting and grading injuries (weighted κ=0.51), with no significant difference in injury grade detection (p=0.30). WBT-CTA sensitivity and specificity for any injury were 60% and 89% at the artery level and 71% and 75% at the patient level, respectively. Sensitivity was higher for high-grade injuries (71% at the artery level, 80% at the patient level), with a good inter-rater agreement for severe cases (κ=0.72) (Table 2).

Conclusion

Screening whole-body trauma (WBT) CTA effectively detects BCVI in acute trauma patients. There was overall moderate agreement on the grade of injury using WBT-CTA, with no statistically significant differences between WBT-CTA and CTA neck, with improved sensitivity for WBT-CTA for severe injuries.

References

1. Wu L, Christensen D, Call L, Vranic J, Colip C, Hippe DS, Witt C, Bonow RH, Mossa-Basha M. Natural history of blunt cerebrovascular injury: experience over a 10-year period at a Level I trauma center. Radiology. 2020;297(2):428–35.

Images/Tables

TABLE 1: Grading of injury on screening whole body trauma (WBT) CTA and neck CTA evaluations at the artery-level.

	Series*		
BCVI grade	WBT-CTA	Neck CTA	P-value†
0 (no injury)	1381 (80.3)	1422 (82.7)	0.30
1	187 (10.9)	144 (8.4)	
2	97 (5.6)	86 (5.0)	
3	18 (1.0)	36 (2.1)	
4	35 (2.0)	32 (1.9)	
5	2 (0.1)	0 (0.0)	

*Values are no. (%) out of 1720 ratings of 860 cervical arteries (2 raters);
†Wilcoxon signed-rank test for bias between screening WBT and neck CTA ratings, clustered by patient to account for multiple readers and vessels per patient.

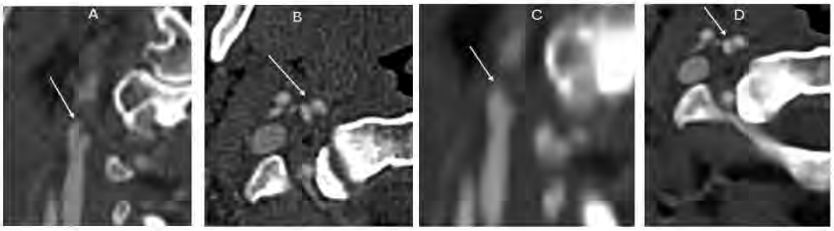

FIGURE 1: A 25-year-old male who was in a motor vehicle accident presents with multiple cervical fractures, sagittal (A) and axial (B) CTA neck reconstructions and sagittal (C) and axial (D) whole-body trauma CTA showing right cervical internal carotid artery blunt cerebrovascular injury with pseudoaneurysm (white arrows), representing high-grade, Biffl grade III injury.

TABLE 2: Diagnostic performance of screening whole body trauma (WBT) CTA for BCVI detection.

	Any Injury on Neck CTA						High Grade Injury (grade ≥ 3) on Neck CTA					
	Sensitivity			Specificity			Sensitivity			Specificity		
Variable	No.	%	(95% CI)	No.	%	(95% CI)	No.	%	(95% CI)	No.	%	(95% CI)
Any injury on WBT-CTA, artery level	180/298	60.4	(53.4-67.4)	1263/1422	88.8	(86.3-91.2)	48/68	70.6	(56.8-84.5)	1361/1652	82.4	(79.5-85.1)
Any injury on WBT-CTA, patient level	154/216	71.3	(64.4-77.8)	162/216	75.0	(68.1-81.5)	45/56	80.4	(69.6-89.3)	213/376	56.6	(50.8-62.5)

751

Machine Learning-Based Molecular Subtype Identification of Pediatric Low-Grade Gliomas Using T2-Weighted MRI: A Bi-Institutional Study

Anat Yahav Dovrat MD[1], Khashayar Namdar MSc, MEng[2], Matthias W Wagner MD[1], Kristen K Yeom MD[3], Cynthia Hawkins MD[4], Uri Tabori MD[5], Farzad Khalvati PhD, MSc[2], Birgit B Ertl-Wagner MD[6]

[1]Department of Diagnostic Imaging & Image-Guided Therapy, The Hospital for Sick Children, Toronto, Ontario, Canada. [2]Neurosciences & Mental Health Research Program, Research Institute, The Hospital for Sick Children, Toronto, Ontario, Canada. [3]Department of Radiology, Stanford University School of Medicine, Lucile Packard Children's Hospital, Paulo Alto, California, USA. [4]Paediatric Laboratory Medicine, Division of Pathology, The Hospital for Sick Children, Toronto, Ontario, Canada. [5]Department of Neuro-oncology, The Hospital for Sick Children, Toronto, Ontario, Canada. [6]Department of Medical Imaging, University of Toronto, Toronto, Ontario, Canada

Abstract Category

AI/Informatics

Purpose

Pediatric low-grade gliomas are the most common pediatric brain tumors[1]. These tumors exhibit diverse clinical outcomes and molecular characteristics, often driven by an activating B-Raf proto-oncogene, serine/threonine kinase (BRAF) mutation, either the BRAF-V600E point mutation or fusion events, with BRAF status showing important implications for prognosis and therapy. Tissue sampling allows mutational assessment but is not always feasible[2]. Non-invasive, imaging-based tumor molecular subtyping offers a promising solution[3]. Radiomics-based machine learning models have demonstrated the ability to distinguish between BRAF fusion and BRAF V600E mutation[4]. In this study, we conduct a multiclass and bi-institutional classification using T2-weighted MRI scans. Our aim was to train and validate a radiomics approach to predict *BRAF* fusion versus *BRAF* V600E mutation versus non-*BRAF* status.

Materials & Methods

This bi-institutional retrospective study included T2-weighted imaging datasets of children diagnosed with pediatric low-grade glioma acquired between January 2000 and April 2023. The local hospital dataset comprised brain T2-weighted MRIs from patients with BRAF fusion (n=179), BRAF V600E mutation (n=84), and non-BRAF mutation (n=160), while the external dataset included patients with BRAF fusion (n=23) and BRAF V600E mutation (n=7) only. Tumor segmentations were provided by a pediatric neuroradiology fellow and verified by a senior pediatric neuroradiologist. PyRadiomics was used for extracting the radiomics features. We followed open-radiomics, which offers a protocol for radiomics-based research, provides open-source radiomics datasets, and establishes a robust pipeline to improve the reproducibility of radiomics-based results in medical image analysis[5].

We conducted a 3-class classification; BRAF Fusion vs BRAF V600E Mutation vs non-BRAF. We created 18 radiomics datasets using 3 sets of radiomics extraction hyperparameters (binWidth of 15, 25, 35), and nine image normalization methods (No normalization, Min Max, Z-Score, Image Histogram Equalization, Gamma normalization with 0.5 and 1.5 as gamma coefficient, ROI-based Z Score normalization, Min Max normalization and histogram equalization). We used Random Forests as the classifiers. For each dataset, we repeated the experiment with different data splits and model random states 100 times and calculated the Area Under Receiver Operating Characteristic Curve (AUC). We trained and evaluated our models with and without clinical variables including age, sex, and tumor location.

Results

The study included 454 patients with an average age of 8.5 years (SD = 4.99), of whom 244 (53.7%) were male. Analyses were conducted comparing BRAF fusion versus non-BRAF fusion, BRAF V600E versus non-BRAF V600E, and BRAF versus non-BRAF cases. Overall, using the combination of radiomics and clinical variables, the average one-vs-the-rest AUC was 0.793 95% CI [0.790, 0.796]. Best results were achieved for binwidth=15 with Gamma normalization (gamma=0.5). The best set for radiomics and clinical variables demonstrated AUC of 0.804, per-class [0.869 0.809 0.733]. For radiomics features alone, AUC was 0.731, per-class [0.784 0.791 0.619]. For non-radiomics only, AUC was 0.712, per-class [0.796 0.677 0.663]. The most predictive feature was tumor location.

Conclusion

Our bi-institutional study shows radiomics-based machine-learning models trained on T2-extracted features differentiate BRAF fusion, V600E mutation, and other molecular subtypes of pLGG with good diagnostic accuracy. Integrating clinical variables with radiomics enhances these models.

References

1. Moreira DC, Lam CG, Bhakta N, et al. *Tackling Pediatric Low-Grade Gliomas: A Global Perspective*.; 2024.
2. Sturm D, Pfister SM, Jones DTW. JOURNAL OF CLINICAL ONCOLOGY Pediatric Gliomas: Current Concepts on Diagnosis, Biology, and Clinical Management. *J Clin Oncol* 2017;35:2370–7.
3. Trasolini A, Erker C, Cheng S, et al. MR Imaging of Pediatric Low-Grade Gliomas: Pretherapeutic Differentiation of BRAF V600E Mutation, BRAF Fusion, and Wild-Type Tumors in Patients without Neurofibromatosis-1. *American Journal of Neuroradiology* 2022;43:1196–201.
4. Kudus K, Wagner MW, Namdar K, et al. Increased confidence of radiomics facilitating pretherapeutic differentiation of BRAF-altered pediatric low-grade glioma. *Eur Radiol* 2024;34:2772–81.
5. Namdar K, Wagner MW, Ertl-Wagner BB, et al. *Open-radiomics: A Collection of Standardized Datasets and a Technical Protocol for Reproducible Radiomics Machine Learning Pipelines*.

754

Exploring the Link: Atrial Fibrillation and Atherosclerotic Intraplaque Hemorrhage in the setting of Cerebral Acute Infarct

Ahmed A Safwat, Maoxue Wang, Mona Kharaji, Cristina Sanchez-Vizcaino, Mohammed Kanani, Mahmud M Basha
University of Wahington, seattle, WA, USA

Abstract Category

Adult Brain

Purpose

Stroke is a significant global health concern, with over 12.2 million new cases reported annually according to the World Stroke Organization. Several risk factors contribute to the likelihood of experiencing a stroke, with atrial fibrillation (A-Fib) and Intraplaque hemorrhage (IPH) being significant factors, accounting for approximately 45-50% of all stroke cases (1). The occurrence of IPH at extracranial ICA in patients with concurrent A-Fib, along with other vascular risk factors such as hypertension & hyperlipidemia, raises various concerns about the relationship between these conditions and the underlying stroke etiology. Understanding these correlations is crucial for developing targeted prevention and treatment strategies.

Materials & Methods

At the University of Washington, all acute stroke patients undergo vessel wall MRI (VWI) covering the intracranial and carotid vasculature on their post-stroke MRI. We reviewed 550 stroke patients with VWI and collected cases with acute infarct or TIA and carotid IPH or A-Fib. Clinical information and risk factors were collected from the medical system. Carotid IPH was identified based on VWI, acute infarct on diffusion-weighted imaging, and A-Fib based on clinical reports. The patients were divided into three groups: 1) A-Fib+IPH, 2) only A-Fib, and 3) only IPH. Multiple logistic regression was used to assess the relationship between high-risk factors and patients with IPH and A-Fib.

Results

A total of 103 patients were included in the study, 26 patients with A-Fib + IPH, 28 patients with only A-Fib, and 49 patients with only IPH. Hypertension was significantly higher in group 1 (1: 100% vs 2: 82.63% vs 3: 75%, $p<0.03$). Additionally, LDL absolute level was the lowest in group 1 (1: 69.92 ±32.75 vs 2: 83.86 ±32.07 vs 3: 102.5 ±34.78, $p<0.002$) (Table 1).Sex was significantly related to patients with both of IPH and A-Fib ($p=0.048$, OR 0.288, 95%CI 0.084, 0.989).

Conclusion

The study consistently identified hypertension in A-Fib+IPH group. In addition, A-Fib+IPH group had lower dyslipidemia compared to the other two groups. Finally, there was a male predilection among the three groups, suggesting males are at higher risk for A-Fib and/or IPH. Further investigation determining the relationship and contribution to stroke is necessary.

References

(1) Kamtchum-Tatuene J, Wilman A, Saqqur M, Shuaib A, Jickling GC. Carotid Plaque With High-Risk Features in Embolic Stroke of Undetermined Source. Stroke. 2020;51(1):311-4.

Images/Tables

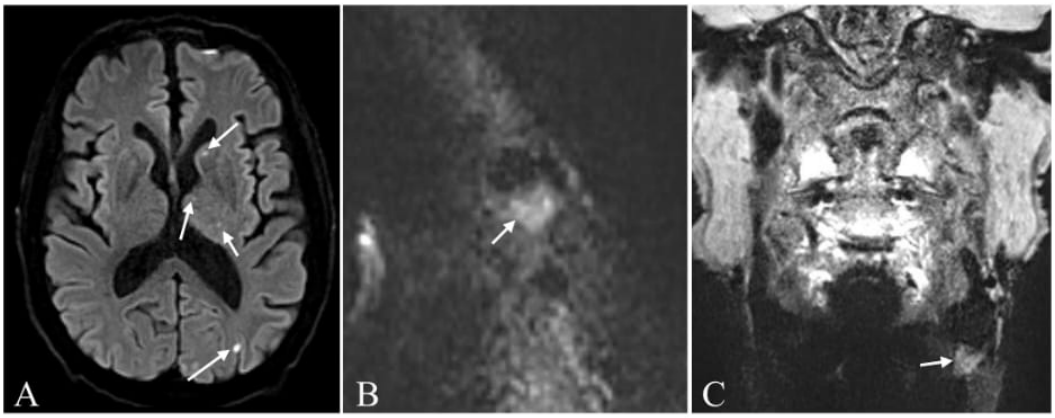

Figure 1. An 80 years old male with atrial fibrillation. Diffusion restriction at the left head of caudate, thalamus, and occipital lobe on the diffusion weighted image (A), Intraplaque hemorrhage of the left carotid bifurcation on the pre-contrast vessel wall imaging (B,C: Axial, Coronal planes)

Table 1: Clinical information and vascular risk factors among the three groups

	Only A-Fib n=49	Only IPH n=28	IPH and A-Fib n=26	p
Age (years old)	71±13.89	71±10.64	77±9.98	0.114
Sex (male)	26/49	19/28	21/26	0.052
Dyslipidemia	36/49	23/28	22/26	0.464
Hypertension	40/49	21/28	100%	0.03
Diabetes	15/49	6/28	9/26	0.539
Smoking	18/49	12/28	17/26	0.057
BNP (pg/ml)	367.18±437.42	157.5±271.53	270.73±328.04	0.076
Hgb A1c (mmol/mol)	6.13±1.79	6.54±1.87	6.08±1.14	0.525
LDL (mg/dl)	83.86±32.07	102.5±34.78	69.92±32.75	0.002
Acute infarct	34/49	23/28	19/26	0.471

756

Improved Detection of Central Vein Sign in Multiple Sclerosis Using Optimized Susceptibility Weighted Imaging at 3 Tesla

Yin-Chen Hsu MD[1], Sreekanth Madhusoodhanan Nair PhD[2], Elaina Luskin MS[2], Diana Ayrapetyan BA[3], Angel Liu BS[2], Nader Binesh PhD[4], Marcel Maya MD[4], Yibin Xie PhD[1], Debiao Li PhD[1], Marwa Kaisey MD[3], Omar Al-Louzi MD[3], Daniel Ontaneda MD, PhD[5], Nancy Sicotte MD[3], Pascal Sati PhD[2]

[1]Biomedical Imaging Research Institute, Cedars-Sinai Medical Center, Los Angeles, CA, USA. [2]Neuroimaging Program, Department of Neurology, Cedars-Sinai Medical Center, Los Angeles, CA, USA. [3]Department of Neurology, Cedars-Sinai Medical Center, Los Angeles, CA, USA. [4]Department of Imaging, Cedars-Sinai Medical Center, Los Angeles, CA, USA. [5]The Mellen Center for Multiple Sclerosis and Research, Department of Neurology, Neurological Institute, Cleveland Clinic Foundation, Cleveland, OH, USA

Abstract Category

Adult Brain

Purpose

The newly revised McDonald criteria for multiple sclerosis (MS) includes the central vein sign (CVS) as a key diagnostic feature.[1] Among the different brain MRI sequences proposed for detecting CVS, susceptibility weighted imaging (SWI) using gradient echo (GRE) acquisition offers the advantage of broad clinical availability across MRI vendors. However, standard SWI protocols used in routine clinical practice are not optimized for standalone CVS detection. Instead, simultaneous evaluation of SWI images and T2-weighted fluid attenuated inversion recovery (T2-FLAIR) images is required for colocalizing hypointense veins and T2-hyperintense lesions, thus complicating the radiological evaluation

and reducing the accuracy of CVS detection.[2] These shortcomings also result in lower diagnostic performance using SWI as compared to optimized sequences,[3] such as T2*-weighted 3D echo-planar-imaging[4] and FLAIR* imaging.[5] In this study, we aim to address this issue with an optimized SWI protocol specifically tailored for improving CVS detection in brain lesions.

Materials & Methods

Ten participants with MS were scanned on a 3T MRI scanner under an IRB-approved protocol. Two different SWI protocols were compared: i) standard SWI using vendor-provided parameters; flip angle (FA) =15°, resolution = mm, scan time = 4 minutes; ii) optimized SWI using a lower FA=5° to maximize lesion-to-white matter and lesion-to-vein contrasts based on Bloch equations, all other parameters were kept the same including scan time (4 min). Both sets of standard and optimized SWI images along with 3D T2-FLAIR images were randomly mixed for independent review by a neuroradiologist. When the lesions were undetectable on SWI alone, T2-FLAIR aided lesion identification and the presence of central vein was evaluated using a crosshair for guidance. For each CVS+ lesion, the reviewer recorded confidence level (high or low) with high confidence corresponding to a typical CVS+ lesion identified as a hyperintense focal lesion traversed centrally by a hypointense linear structure or dot depending on the vein orientation; and low confidence corresponding to those lesions where the central vein was less distinctly visible, resulting in uncertainty regarding its association with the lesion. Up to 6 CVS+ lesions were counted for each subject and these subjects were subsequently classified as either being CVS+ or CVS- using the select-6 criterion.

Results

Across the 10 subjects, 39 CVS+ lesions were detected with standard SWI against 48 CVS+ lesions with optimized SWI (e.g., 23% increase). Twenty (51%) of the 39 CVS+ lesions detected on standard SWI were rated as low confidence, whereas only 5 (10%) of the 48 CVS+ lesions detected on optimized SWI were rated as low confidence. The number of MS subjects meeting select-6 increased from 3 with standard SWI to 7 optimized SWI. Among the remaining 3 MS participants who were classified as CVS- with optimized SWI, two participants had only 1 CVS+ lesion (20%) out of 5 brain lesions and one participant had 4 CVS+ lesions (44%) out of 9 brain lesions.

Conclusion

Our study indicates that an optimized SWI sequence can increase the detection rate and confidence level when evaluating CVS, showcasing a feasible solution for CVS assessment on standard clinical scanners.

References

1. Sati P, Oh J, Constable RT, et al. The central vein sign and its clinical evaluation for the diagnosis of multiple sclerosis: a consensus statement from the North American Imaging in Multiple Sclerosis Cooperative. Nature Reviews Neurology 2016;12:714–22.
2. Sinnecker T, Clarke MA, Meier D, et al. Evaluation of the Central Vein Sign as a Diagnostic Imaging Biomarker in Multiple Sclerosis. JAMA Neurology 2019;76:1446–56.
3. Castellaro M, Tamanti A, Pisani AI, et al. The Use of the Central Vein Sign in the Diagnosis of Multiple Sclerosis: A Systematic Review and Meta-analysis. Diagnostics 2020;10.
4. Sati P, Thomasson D, Li N, et al. Rapid, high-resolution, whole-brain, susceptibility-based MRI of multiple sclerosis. Multiple Sclerosis Journal. 2014;20(11):1464-70.
5. Sati P, George IC, Shea CD, et al. FLAIR*: a combined MR contrast technique for visualizing white matter lesions and parenchymal veins. Radiology. 2012;265(3):926-32.

Images/Tables

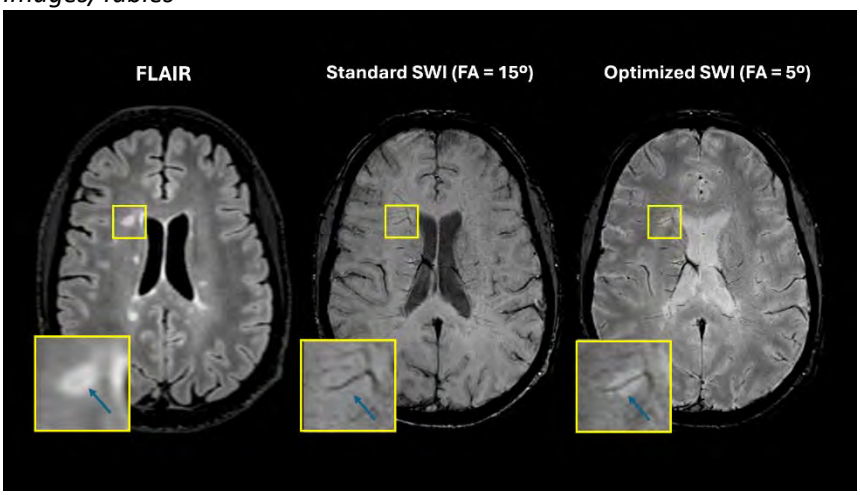

758

Alterations in Functional Connectivity following Surgical Resection in Glioblastoma Measured using Pseudo-Resting State fMRI Derived from DSC Perfusion MRI

Chencai Wang PhD, Jingwen Yao PhD, Francesco Sanvito MD, Noriko Salamon MD, Richard G Everson MD, Linda M Liau MD, PhD, MBA, Kunal S Patel MD, Albert Lai MD, Phioanh L Nghiemphu MD, Timothy F Cloughesy MD, Benjamin M Ellingson PhD

UCLA, Los Angeles, CA, USA

Abstract Category

Functional/Advanced Imaging

Purpose

Surgical resection plays an important role in the management of glioblastoma (GBM), allowing for improved survival and accurate molecular diagnoses. However, surgical resection can also result in cognitive impairment or altered neurological function.[1] Previous studies have shown that resting-state functional MRI (rsfMRI) can provide an unbiased estimate of neurological or cognitive impairment in patients with brain tumors based on patterns in brain activity, or functional connectivity (FC).[2] However, traditional rsfMRI is not routinely performed due to long scan times and added exam costs. In the current study, we explored the use of "pseudo"-rsfMRI signal (Ps-rsfMRI) derived from DSC perfusion MRI[3] to investigate the impact of surgical resection on cortical functional connectivity (FC) in patients with newly diagnosed or recurrent GBM.

Materials & Methods

25 GBM patients (10 newly diagnosed and 15 recurrent) underwent DSC perfusion MRI before (within 1 month), after (within 72 hours), and 3-6 months following tumor resection. Ps-rsfMRI data were generated by correcting DSC perfusion data for motion and contrast leakage,[4] then performing voxel-wise subtraction between the resulting time-series data and a gamma-variate model of the contrast bolus. Ps-rsfMRI time series data were then pre-processed using the CONN toolbox[5] using default fMRI pre-processing parameters. FC was then computed between all cortically-based ROIs after exclusion of the resection cavity and residual tumor. Graph theory was applied to FC data to extract network characteristics including integration (global efficiency), segregation (local efficiency), and transitivity. Wilcoxon signed-rank tests, with the significance set at $p<0.05$, were applied to identify network changes before, after, and 3-6 months after surgical resection (***Figure. A***).

Results

Generally, GBM patients showed altered FCs after surgery. By seeding ROIs in the default mode network (DMN), we observed weakened FC between medial prefrontal cortex and multiple temporal and parietal regions immediately after and 3-6 months following resection (***Figures. B*** and ***C***). Network global efficiency did not show significant changes after and 3-6 months following surgery. Decreased network local efficiency ($p=0.0065$) and transitivity ($p=0.0065$) were observed immediately after surgery but appeared to stabilize or recover 3-6 months following surgery (***Figures. D***).

Conclusion

GBM patients exhibit an immediate alteration in FC following surgical resection that appears to improve 3-6 months after surgery as measured using Ps-rsfMRI derived from routine clinical DSC perfusion MRI. Future studies aimed at relating these changes to direct measures of neurological function and patient outcomes will be important to demonstrate clinical impact of these observations.

References

1. Noll KR, Chen HS, Wefel JS, et al. Alterations in Functional Connectomics Associated With Neurocognitive Changes Following Glioma Resection. *Neurosurgery* 2021;88:544-551

2. Wang C, Van Dyk K, Cho N, et al. Characterization of cognitive function in survivors of diffuse gliomas using resting-state functional MRI (rs-fMRI). *Brain Imaging Behav* 2022;16:239-251

3. Cho NS, Wang C, Van Dyk K, et al. Pseudo-Resting-State Functional MRI Derived from Dynamic Susceptibility Contrast Perfusion MRI Can Predict Cognitive Impairment in Glioma. *AJNR Am J Neuroradiol* 2024;45:1552-1561

4. Leu K, Boxerman JL, Cloughesy TF, et al. Improved Leakage Correction for Single-Echo Dynamic Susceptibility Contrast Perfusion MRI Estimates of Relative Cerebral Blood Volume in High-Grade Gliomas by Accounting for Bidirectional Contrast Agent Exchange. *AJNR Am J Neuroradiol* 2016;37:1440-1446

5. Whitfield-Gabrieli S, Nieto-Castanon A. Conn: a functional connectivity toolbox for correlated and anticorrelated brain networks. *Brain Connect* 2012;2:125-141

Images/Tables

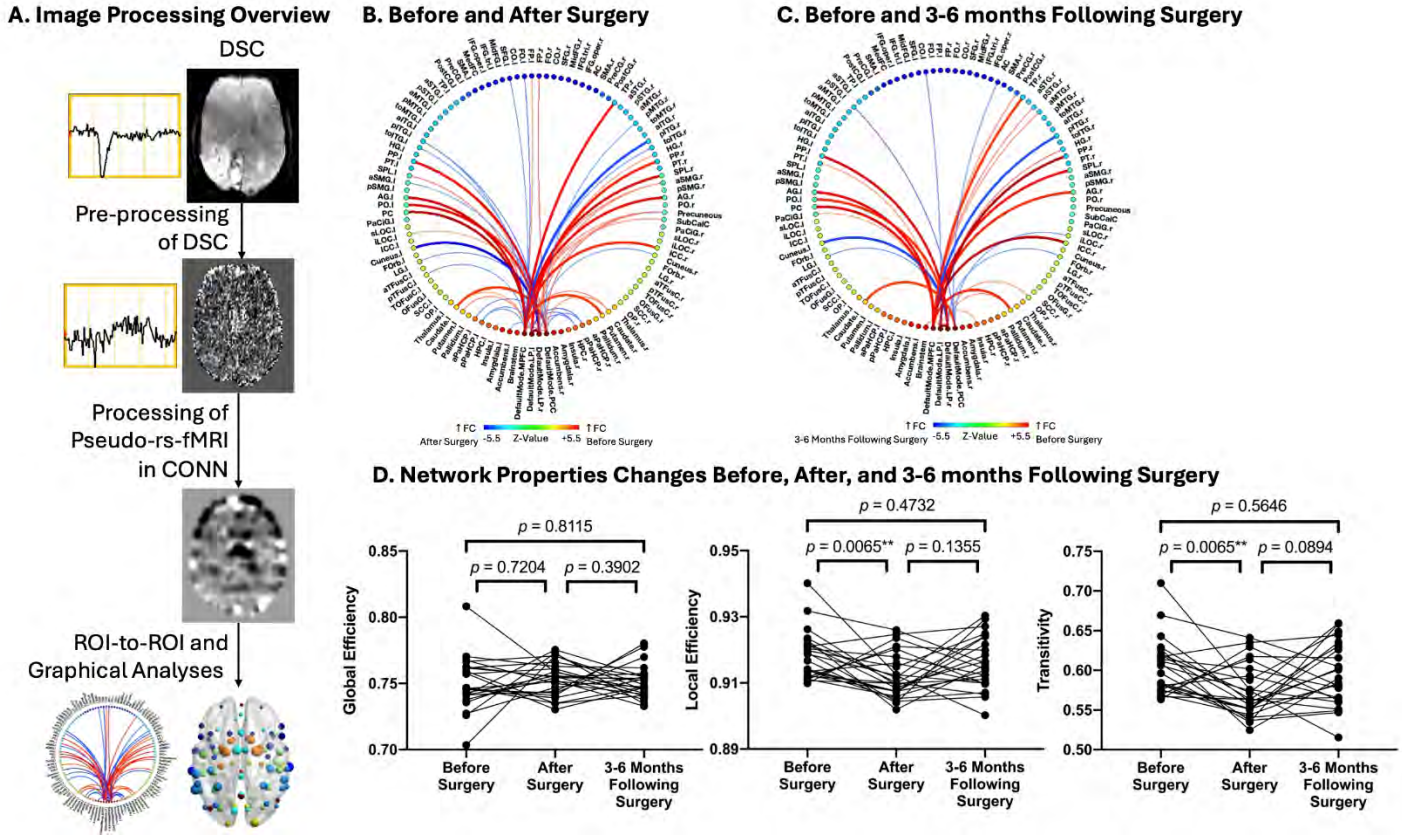

762

Characterizing the longitudinal white matter integrity with multi-modal MRI measurements

Faezeh Vedaei[1], Dhivya Srinivasan[1], Drew Parker[1], Guray Erus[1], Sudipto Dolui[1], Farzaneh A. Sorond[2], David R. Jacobs[3], Lenore J. Launer[4], Daniel T. Lackland[5], Christos Davatzikos[1], R. Nick Bryan[1], Ilya M. Nasrallah[1]

[1]University of Pennsylvania, Philadelphia, Pennsylvania, USA. [2]Northwestern University, Chicago, illinois, USA. [3]University of Minnesota, minneapolis, Minnesota, USA. [4]National Institute on Aging, Bethesda, Maryland, USA. [5]Medical University of South Carolina, Charleston, South Carolina, USA

Abstract Category

Functional/Advanced Imaging

Purpose

White matter hyperintensities (WMHs) are age-related indicators of cerebrovascular diseases. Normal appearing WM (NAWM) adjacent to WMH, termed “penumbra,” in known to be vulnerable to WMH pathology. Characteristics of WM integrity can be measured using magnetic resonance imaging (MRI) modalities.[1,2] We investigated the progression of WMHs within penumbra versus more distant normal appearing WM (NAWM) over 5-year interval to identify predictive features of WMH growth using baseline multimodal MRI. We hypothesized that imaging features of at-risk WM tissues at baseline may provide predictive patterns of new WMHs and the risk of vascular disorders.

Materials & Methods

Four hundred eighty-five participants from the Coronary Artery Risk Development in Young Adults (CARDIA) cohort were included in the analysis. These participants had baseline scans and 5-year follow-up scans which included T1, T2, FLAIR, diffusion tensor imaging (DTI), and cerebral blood flow (CBF). Baseline multimodal MRI signal was measured within WM regions of interest (ROIs) including baseline WMH, penumbra, WM tissue proximal to baseline WMH (contiguous WMH) and separated from baseline WMH (noncontiguous WMH) that progressed to new WMHs at follow up, and distant NAWM (dNAWM). Penumbra was delineated as 0-4 mm rims around baseline WMHs masks (Figure 1). Statistical analysis of variance (ANOVA) and pair-wise t-test were employed for group comparisons.

Results

Volumetric analysis demonstrated that about 80% of new WMHs appear within 4-mm of baseline WMH; the remaining 20% are defined as noncontiguous WMHs. ANOVA of standardized MRI signal intensities comparing between the multiple WM ROIs showed significant differences for each MRI measurement ($p < 0.001$). Subsequent pair-wise t-test comparison showed significant differences between all ROIs for FLAIR, and most pairs of ROIs for fractional anisotropy (FA) and median diffusivity (MD). Particularly, DTI detected WM abnormalities in several ROIs where FLAIR did not differ. FLAIR intensity was lower in contiguous and noncontiguous WMHs compared to baseline WMH, while FA was lower in contiguous WMH compared to baseline WMH and MD was higher in noncontiguous WMH versus baseline WMH. CBF showed significant differences for only a few ROIs, largely between those regions near baseline WMH and dNAWM ($p < 0.05$) (Table1, Figure 2).

Conclusion

This study provides evidence of spatial and signal features of WMH development using longitudinal MRI. Tissue immediately surrounding baseline WMH, a penumbra, is most at risk of future WMH progression.[3] Higher FLAIR and MD and lower FA and CBF are indicators of WM abnormalities in tissue that develops to WMH within 5 years relative to longitudinally stable normal WM.[1,4] However, DTI metrics are the most robust predictors of new WMHs. These findings may contribute to monitoring the conversion of NAWM into WMH and intervention procedures in clinical trials aimed at preserving WM integrity.

References

1. Nasrallah, I. M., Hsieh, M. K., Erus, G., Battapady, H., Dolui, S., Detre, J. A., Launer, L. J., Jacobs, D. R., Davatzikos, C., & Bryan, R. N. (2019). White Matter Lesion Penumbra Shows Abnormalities on Structural and Physiologic MRIs in the Coronary Artery Risk Development in Young Adults Cohort. *AJNR Am J Neuroradiol*, *40*(8), 1291-1298. https://doi.org/10.3174/ajnr.A6119.
2. Maillard, P., Fletcher, E., Harvey, D., Carmichael, O., Reed, B., Mungas, D., & DeCarli, C. (2011). White matter hyperintensity penumbra. *Stroke*, *42*(7), 1917-1922. https://doi.org/10.1161/strokeaha.110.609768.
3. Khan, W., Khlif, M. S., Mito, R., Dhollander, T., & Brodtmann, A. (2021). Investigating the microstructural properties of normal-appearing white matter (NAWM) preceding conversion to white matter hyperintensities (WMHs) in stroke survivors. *Neuroimage*, *232*, 117839. https://doi.org/10.1016/j.neuroimage.2021.117839.
4. Maillard, P., Carmichael, O., Harvey, D., Fletcher, E., Reed, B., Mungas, D., & DeCarli, C. (2013). FLAIR and diffusion MRI signals are independent predictors of white matter hyperintensities. *AJNR Am J Neuroradiol*, *34*(1), 54-61. https://doi.org/10.3174/ajnr.A3146.

Images/Tables

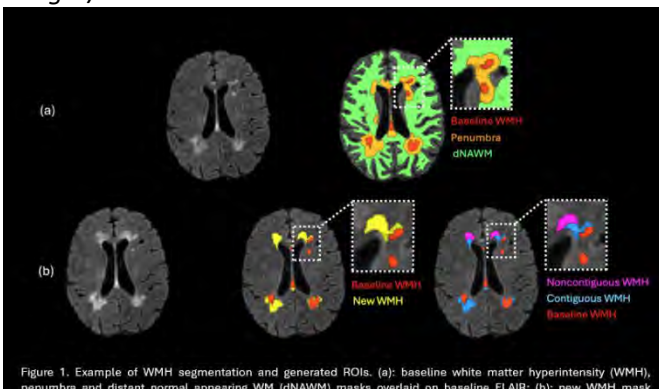

Figure 1. Example of WMH segmentation and generated ROIs. (a): baseline white matter hyperintensity (WMH), penumbra and distant normal appearing WM (dNAWM) masks overlaid on baseline FLAIR; (b): new WMH mask dividing in contiguous and noncontiguous WMH ROI masks overlaid on follow-up FLAIR data.

Table 1. T-test group comparison in normalized MRI parameters between each pair of WM ROIs.

ROIs	FA		MD		FLAIR		CBF	
	T-value	p-value	T-value	p-value	T-value	p-value	T-value	p-value
Baseline WMH vs. Penumbra	-5.96	**< 0.001**	1.67	0.01	44.82	**< 0.001**	-0.44	0.65
Baseline WMH vs. Contiguous WMH	2.38	**0.017**	-1.34	0.18	14.97	**< 0.001**	1.22	0.22
Baseline WMH vs. Noncontiguous WMH	1.12	0.26	-2.01	**0.04**	18.80	**< 0.001**	-1.43	0.15
Baseline WMH vs. dNAWM	-16.15	**< 0.001**	4.12	**< 0.001**	56.56	**< 0.001**	-7.78	**< 0.001**
Penumbra vs. Contiguous WMH	9.00	**< 0.001**	-4.02	**< 0.001**	-41.11	**< 0.001**	1.77	0.08
Penumbra vs. Noncontiguous WMH	5.97	**< 0.001**	-4.48	**< 0.001**	-30.76	**< 0.001**	-1.25	0.21
Penumbra vs. dNAWM	-14.91	**< 0.001**	4.43	**< 0.001**	26.05	**< 0.001**	-8.43	**< 0.001**
Contiguous WMH vs. Noncontiguous WMH	-0.82	0.41	-0.84	0.40	5.84	**< 0.001**	-2.10	**0.03**
Contiguous WMH vs. dNAWM	-19.86	**< 0.001**	7.45	**< 0.001**	60.11	**< 0.001**	-8.21	**< 0.001**
Noncontiguous WMH vs. dNAWM	-13.88	**< 0.001**	7.23	**< 0.001**	47.23	**< 0.001**	-3.95	**< 0.001**

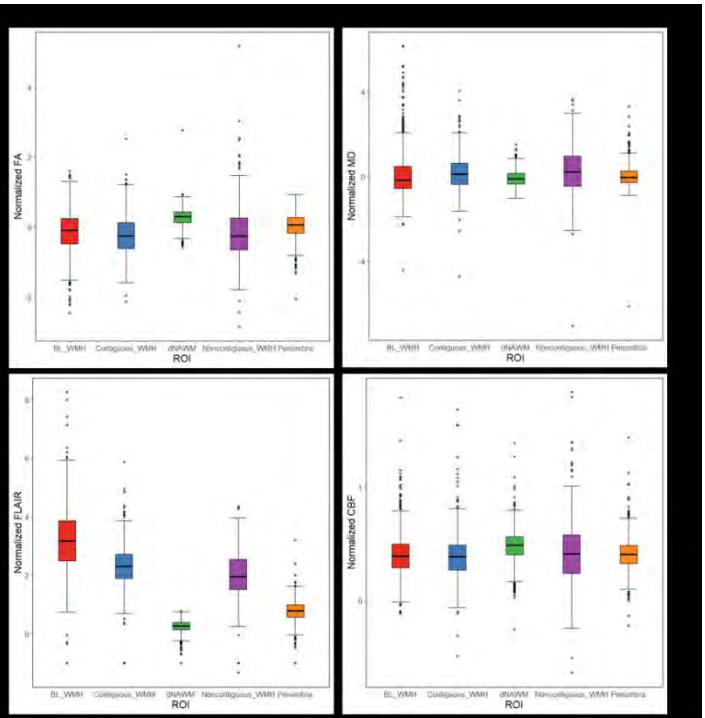

Figure 2. Box plots of mean normalized MRI intensity values across WM ROIs. FA, fractional anisotropy; MD, mean diffusivity; FLAIR, fluid attenuated inversion recovery; CBF, cerebral blood flow; BL, baseline; WMH, white matter hyperintensity; contiguous WMH are new lesions that are proximal to baseline WMH while noncontiguous WMH are separated; dNAWM, distant normal appearing white matter.

780

Assessing AI Accuracy for Intracranial Aneurysms Detection in a Clinical Setting compared to Neuroradiologists

Mohamed H.D. Hassan MD, Babatunde J. Akinpelu MD, MS, Negar Firoozeh MD, Eardi Lila PhD, Chengcheng Zhu PhD, Pattana Wangaryattawanich MD, Michael R. Levitt MD, Mahmud Mossa-Basha MD
University of Washington, Seattle, Washington, USA

Abstract Category

Adult Brain

Purpose

Intracranial aneurysms detected in 2-5% of the population represent a major healthcare issue, as ruptured aneurysms with resultant hemorrhage may be associated with substantial risk of severe morbidity or mortality. With the increasing role of artificial intelligence (AI) in diagnostic radiology, we assessed the accuracy of a commercial AI tool (AIDOC) to detect intracranial aneurysms on head or head/neck CTA relative to fellowship-trained neuroradiologists.

Materials & Methods

We retrospectively extracted CTA head or head/neck studies from three University of Washington Medicine hospital system's clinical databases between 11/1/2018 and 11/2/2021; they were then analyzed through the AI tool for evaluation of presence of aneurysms. A Natural Language Processing (NLP) algorithm reviewed the radiology reports looking for the term "aneurysm", "infundibulum", and "infundibulum or aneurysm". Concordance or discrepancies between AI and NLP were further adjudicated by 3 neuroradiologist for consensus, which served as the reference standard. Aneurysm features including size, morphology, and site of origin were extracted for each positive case and correlations with AI and radiologist performance were assessed based on these features. A vascular neurosurgeon independently reviewed the aneurysms to determine management of the aneurysms based on imaging features and patient-specific characteristics.

Results

A total of 2,647 CTA scans were reviewed for intracranial aneurysms with 190 positives CTAs and 249 aneurysms i.e. 1.31 aneurysm per positive CTA case. AI achieved a sensitivity of 91.6% (95% CI=87.4-94.7%), specificity of 98.7% (95% CI=98.1-99.1%), and accuracy of 98.0% (95% CI=97.4%-98.5%). In comparison, radiologists achieved a sensitivity of 93.6% (95% CI=89.8-96.3%), specificity of 99.8% (95% CI=99.6-100%) and accuracy of 99.3% (95% CI=98.9-99.5%). Radiologists had a higher positive predictive value of 98.3% (95% CI=95.6-99.4%) than AI with 87.4% (95% CI=831-90.7%), primarily due to AI's higher false positives. While the AI tool was not designed to detect ruptured IAs, it detected 93% (55/59) of such aneurysms, compared to 100% (59/59) detected by radiologists.

Conclusion

Our multi-site study showed that radiologists and a commercial AI tool for intracranial aneurysm detection performed comparably in terms of accuracy, sensitivity and specificity, although AI had a lower positive predictive value due to its higher false positives. Given their comparable sensitivities for aneurysm detection, AI could serve as a complementary triage tool for automated and rapid detection prior to radiologist evaluation.

References

1-Hosny A, Parmar C, Quackenbush J, et al. Artificial intelligence in radiology. *Nat Rev Cancer.* 2018 Aug;18(8):500-510. DOI: https://doi.org/10.1038/s41568-018-0016-5

2- Ebrahimian S, Digumarthy SR, Homayounieh F, et al. Predictive values of AI-based triage model in suboptimal CT pulmonary angiography. *Clin Imaging.* 2022 Jun;86:25-30. DOI: https://doi.org/10.1016/j.clinimag.2022.03.011

Images/Tables

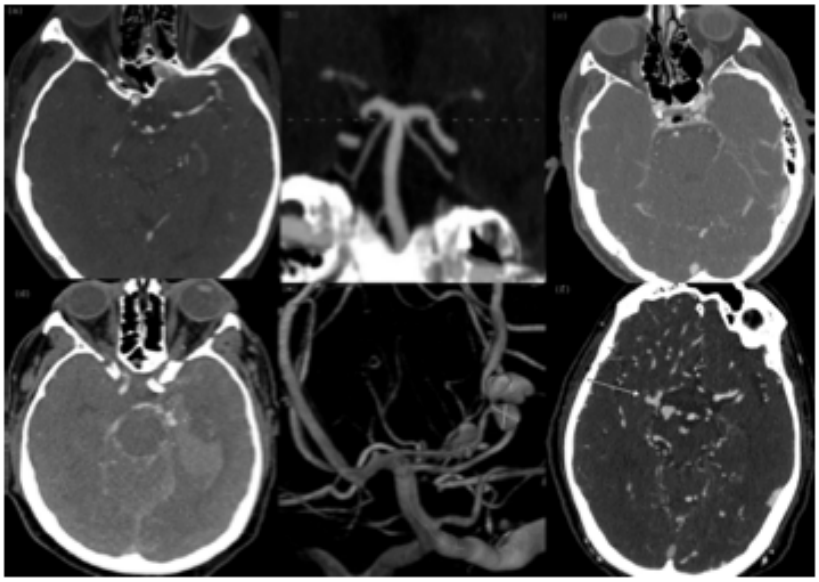

Figure 4. (a, b) Basilar arterial tortuosity resulting in a hairpin turn mimicking an aneurysm on axial x1CTA (FP). (c) Right cavernous ICA calcifications mimic an IA due to bright attenuation and its focality (FP). (d, e) Left PCA ruptured mycotic IA missed by AI likely due to surrounding hemorrhage (FN). (f) Venous varix in a patient with an arteriovenous malformation mimicking an IA (FP).

792

DSC Perfusion Imaging with Gadopiclenol: Reduced Signal at Standard Dosing

Mohamed Shaif S Yusufishaq MD, Alexey Samsonov PhD, Aaron S Field MD PhD
University of Wisconsin, Madison, WI, USA

Abstract Category

Functional/Advanced Imaging

Purpose

Gadopiclenol (Vueway, VW) is a novel gadolinium-based contrast agent (GBCA) approved by the FDA in 2022, notable for its high T1 relaxivity. It has been proven noninferior at a dose of 0.05 mmol/kg compared to gadobenate dimeglumine (MultiHance, MH) at a dose 0.10 mmol/kg for CNS lesion assessment in contrast-enhanced MRI (1). Our institution has adopted this agent as it allows for a lower (half) dose of gadolinium without losing contrast-to-noise ratio or lesion detectability. However, using a lower dose of GBCA might be detrimental to cerebral perfusion imaging, an important component of many common neuroimaging protocols, typically acquired using a dynamic susceptibility contrast (DSC) technique (2). We compared the efficacy of VW to that of MH for generating first-pass susceptibility contrast at the recommended dosing for both agents.

Materials & Methods

This was a retrospective analysis of 17 adult patients (age 24-86 years) who underwent DSC perfusion imaging at 1.5T using the recommended dosing of both VW (0.05 mmol/kg) and MH (0.10 mmol/kg) on separate occasions between January 2023 and September 2024. The mean time between exams was 172 days. Instances of dissimilar acquisition protocols were excluded. Mean signal intensity vs. time curves were generated for a single axial slice matched in location between VW and MH scans, remote from any visible pathology or susceptibility-related artifacts. After normalization for baseline signal intensity and conversion to concentration-time curves using 'concentration $=\log(S/S_0)/TE$,' the area under the concentration-time curve (AUC) and maximum %signal change were compared between VW and MH using Bland-Altman analysis.

Results

Both AUC and maximum %signal change were non-equivalent between VW and MH at recommended dosing ($p < 0.0001$). Specifically, AUC and %signal change for VW relative to MH were biased by -54% and -44%, respectively (Figure). The degree of bias is roughly equivalent to gadolinium dose; notably, if the analysis is repeated with AUC normalized for contrast dose, VW and MH become statistically equivalent ($p=0.09$).

Figure (A) Normalized concentration-time curve AUC for VW versus MH. (B) Bland-Altman plot of the same data.

Conclusion

The high T1 relaxivity benefits of VW that allow for a lower (one-half) dose in routine contrast-enhanced neuroimaging do not extend to the most used technique for perfusion imaging, which is susceptibility-based. With VW, we observed significantly weaker susceptibility effects commensurate with its lower dose, as theory would predict. DSC perfusion imaging plays an important role in stroke and tumor imaging; institutions using or considering this novel GBCA should be aware of its potential limitations in this application. The impact of weaker signal transients on derived perfusion parameters remains to be determined.

References

1. Loevner LA, Kolumban B, Hutóczki G, Dziadziuszko K, Bereczki D, Bago A, Pichiecchio A. Efficacy and Safety of Gadopiclenol for Contrast-Enhanced MRI of the Central Nervous System: The PICTURE Randomized Clinical Trial. *Invest Radiol.* 2023;58:307-313. DOI: 10.1097/RLI.0000000000000944.
2. Essig M, Shiroishi MS, Nguyen TB, Saake M, Provenzale JM, Enterline D, Anzalone N, Dörfler A, Rovira A, Wintermark M, Law M. Perfusion MRI: the five most frequently asked technical questions. *AJR Am J Roentgenol*. 2013;200:24-34. DOI: 10.2214/AJR.12.9543.

Images/Tables

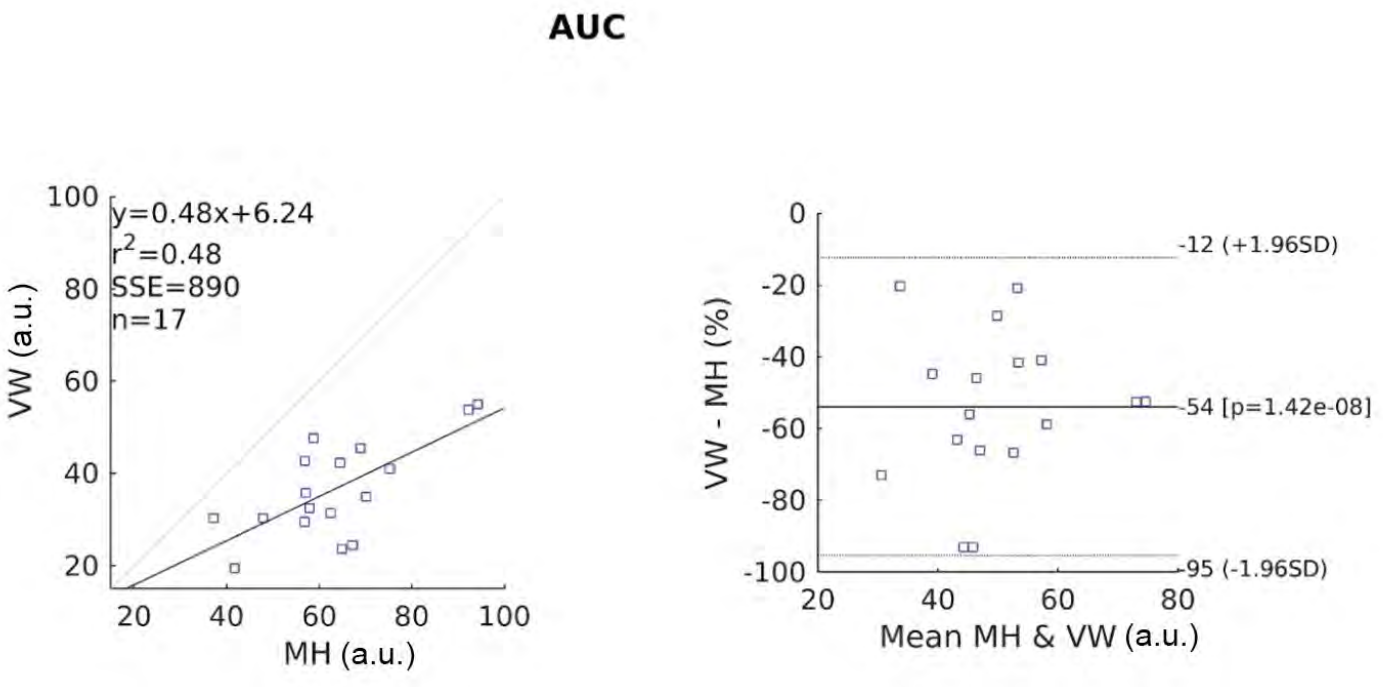

821

Association of Double Lumen Appearance on High-Resolution Magnetic Resonance Vessel Wall Imaging with Acute Ischemic Infarcts and Recurrent Neurological Event Free Survival in Patients with Intracranial Arterial Dissections.

Andrew Ngo MD[1], Elham Tavakkol MD[1], Kamand Khalaj MD[1], Konstanze Guggenberger MD[2], Andres Rodriguez MD[1], Arash Kamali MD[1], David Timaran Montenegro MD[1], Roy Riascos MD[1]

[1]UTHealth Houston, Houston, Texas, USA. [2]UTHealth Houston, Houston, TX, USA

Abstract Category

Adult Brain

Purpose

High-resolution magnetic resonance vessel wall imaging (HRMR-VWI) has helped characterize the different etiologies of intracranial vascular diseases, including intracranial arterial dissection. However, the associations between HRMR-VWI characteristics of intracranial dissections, diffusion-weighted imaging (DWI) infarction, and recurrent neurological event-free survival have not been well studied. We aim to investigate the association between HRMR-VWI characteristics in patients with intracranial dissection, ischemic infarcts, and recurrent neurological event-free survival.

Materials & Methods

This was a retrospective observational study. Of the 180 patients studied with HRMR-VWI for various indications, 23 patients determined to have arterial dissection by CTA and confirmed with angiogram were included in the study. Various HRMR-VWI characteristics were analyzed. The patients were followed for a median time of 10 months (interquartile range [IQR], 1-13 months), and recurrent neurological event-free survival was determined.

Results

Of the 23 patients with arterial dissection, the most frequently involved vessel was the right vertebral artery, with 10/23 (43.38%). Single artery involvement was seen in most of the cases (60.87%). The most frequently involved vascular territory with positive DWI abnormality was the left MCA territory (43.38%). Multifocal ischemia was seen in 3/17 patients (17.65%), with 6 patients not included. Occlusions were seen in 4/23 patients (17.39%) with severe stenosis seen in 22/23 patients (95.65%). Of the 23 arterial dissections, HRMR-VWI showed that 10 had wall enhancement (43.48%), 21 had intramural T1 signal (91.30%), 15 had intimal flaps (65.22%), 5 had double lumen appearance (21.74%), 12 had proximal (A1/M1/P1) locations (52.17%), and 16 had distal locations (69.57%). In patients with double lumen appearance, 2 (40%) presented acute ischemia on DWI (p=0.08). Additionally, there were statistically significant associations between double-lumen appearance on HRMR-VWI and recurrent neurological event-free survival, with patients not having double-lumen appearance showing 90% free survival at 7 months and 72% free survival at 13 months. Of the five patients with double lumen appearance, 1 had a recurrent neurological event within 1 month (p-value 0.0263).

Conclusion

The incidence of acute ischemia in patients with double lumen appearance on HRMR-VWI reached 40%. Similarly, shorter recurrent neurologic event-free survival rates were identified in patients with double-lumen appearance HRMR-VWI.

References

Kano Y, Inui S, Oguri T, et al. Utility of T2-weighted high-resolution vessel wall imaging for the diagnosis of isolated posterior inferior cerebellar artery dissection at acute and early subacute stages. *J Neurol Sci*. 2020;411:116693. doi:10.1016/j.jns.2020.116693

Images/Tables

Figure 1: Dissection of the left M1 segment, subintimal high T1 signal corresponds to intramural hematoma (A, B, arrows). The fine linear high T2 signal indicates the intimal flap (C, arrow).

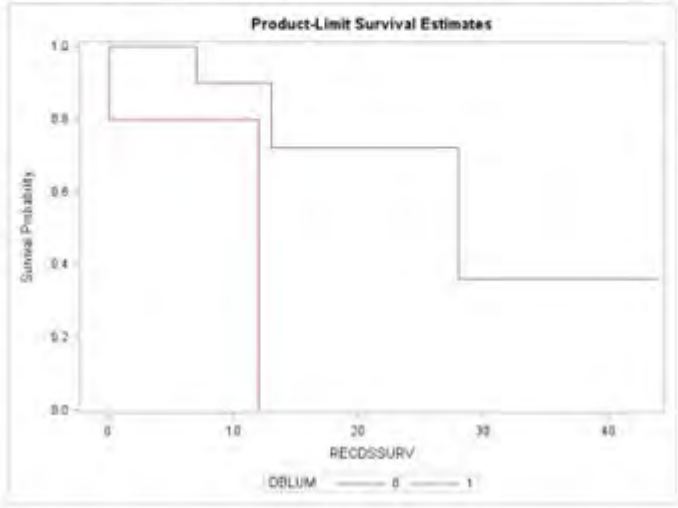

Table 1: Kaplan-Meier free survival curve. Association between double lumen appearance (DBLUM) and recurrent neurological event free. X-axis: months.

823

BraTS 2025 Lighthouse Challenge: Establishing Protocols for Dataset Reference Standards by Neuroradiologists

Nazanin Maleki MD[1], Raisa Amiruddin[1], Nikolay Yordanov[2], Pascal Fehringer[3], Athanasios Gkampenis[4], Ahmed Moawad[5], Amirreza Manteghinejad[6], Anastasia Janas[7], Mohanad Ghonim[8], Mohamed Ghonim[8], Melisa S Guelen[9], Nathan Page[3], Sedra Abou Ali Mhana[8], Albara Alotaibi[10], Prisha Bhatia[11], Yasaman Sharifi[12], Salma Abosabie[13], Sara Abosabie[14], Marko Jakovljevic[6], Fabian Umeh[15], Dominic La Bella[16], Rachit Saluja[17], Maria Correia de Verdier[18], Ujjwal Baid[19], Jeffrey D Rudie[20], Evan Calabrese[21], Florian Kofler[22], Devon James Godfrey[16], Scott Richard Floyd[16], Basimah Albalooshy[1], Tiffany So[23], Lorenna Moreira Vidal[6], Virginia Hill[24], Vilma Kosovic[25], Adam Goldman-Yassen[26], Fatima Memon[27], Michael Veronesi[28], Bojan Petrovic[29], Brooke Schrickel[30], Justin Cramer[31], Ichiro Ikuta[31], Gerard Thampson[32], Mark Krycia[27], Sanjay Aneja[33], Mariam Aboian[1], Spyridon Bakas[34]

[1]Department of Radiology, Children's Hospital of Philadelphia, Philadelphia, PA, USA. [2]Faculty of Medicine, Medical University, Sofia, Sofia, Bulgaria. [3]Faculty of Medicine, Jena University Hospital, Friedrich Schiller University, Jena, Jena, Germany. [4]School of Medicine, University of Ioannina, Ioannina, Epirus, Greece. [5]Trinity Health Mid Atlantic Hospitals, Darby, PA, USA. [6]Children's Hospital of Philadelphia, Philadelphia, PA, USA. [7]Charité – Universitätsmedizin Berlin, Berlin, Berlin, Germany. [8]Department of Radiology, Hospital of the University of Pennsylvania, Philadelphia, PA, USA. [9]Massachusetts General Hospital, Harvard Medical School, Charlestown, MA, USA. [10]Jordan University of Science and Technology, Jordan, Amman, Jordan. [11]Mohammed Bin Rashid University of Medicine and Health Sciences, Dubai, Dubai, UAE. [12]Department of Radiology, Iran University School of Medicine,, Tehran, Tehran, Iran, Islamic Republic of. [13]Faculty of Medicine, Julius Maximilians University of Wuerzburg, Wuerzburg, Wuerzburg, Bavaria, Germany. [14]Charité – Universitätsmedizin, Berlin, Berlin, Germany. [15]School of Computing, Engineering and Digital Technologies, Teesside University, Middlesbrough, North Yorkshire, United Kingdom. [16]Duke department of Radiation Oncology, Durham, NC, USA. [17]Cornell University, New York, NY, USA. [18]Uppsala University, Uppsala, Uppsala, Sweden. [19]Division of Computational Pathology, Department of Pathology and Laboratory Medicine, Indiana University School of Medicine, Indianapolis, IN, USA. [20]University of California San Diego, San Diego, CA, USA. [21]Duke department of Radiology, Durham, NC, USA. [22]Department of Informatics, Technical University Munich, Munich, Munich, Germany. [23]Department of Imaging and Interventional Radiology, The Chinese University of Hong Kong, Hong Kong, Hong Kong, China. [24]Department of Radiology, Northwestern Medicine,University Feinberg School of Medicine, Chicago, IL, USA. [25]Department of Radiology , General Hospital of Dubrovnik, Dubrovnik, Dubrovnik, Croatia. [26]Department of Pediatrics at Emory University School of Medicine, Atlanta, Georgia, USA. [27]Carolina Radiology, Myrtle Beach, SC, USA. [28]Department of Radiology, University of Wisconsin-school of Medicine and Public health, Madison, WI, USA. [29]NorthShore Endeavor Health, Evanston, IL, USA. [30]Ohio State College of Medicine, Columbus, OH, USA. [31]Mayo Clinic, Phoenix, Arizona, USA. [32]The University of Edinburgh, Edinburgh, Edinburgh, United Kingdom. [33]Department of Therapeutic Radiology, Yale School of Medicine, New Haven, CT, USA. [34]32Departments of Radiology and Imaging Sciences; Neurological Surgery; Biostatistics and Health Data Science, Indiana University School of Medicine, Indianapolis, IN, USA

Abstract Category

AI/Informatics

Purpose

Brain tumor segmentation is crucial in clinical decision-making for diagnosis, treatment planning, and monitoring disease progression. Despite the significant algorithmic advancements in AI-based segmentation algorithms, their output variability paired with limited data standardization and annotators' experience hamper their incorporation into clinical routine. Manually generated ground truth segmentations form the foundational basis of development and benchmarking of all AI-based segmentation algorithms. However, un-avoided inter- and intra-observer variability caused by factors like human fatigue and interpretation biases, has not been systematically assessed. The BraTS Lighthouse Challenge 2025 aims to evaluate inter- and intra-rater variability in brain tumor segmentation, towards establishing the reference standard for annotation and curation of high-quality databases for translation of AI algorithms into practice.

Materials & Methods

Data from the open access BraTS 2024 challenge were used, including MRI scans of brain metastases, gliomas, and meningiomas (pre- and post-treatment). 14 board-certified neuroradiologists were recruited from ASNR2023 to annotate 25 tumor cases in 4 separate instances to assess intra- and inter-observer variability, as well as bias to pre-

segmentations, using the Dice Similarity Coefficient. Annotations were structured into four blocks per neuroradiologist. In the first two blocks, manual annotations of 25 cases from scratch are performed, with a one-week interval between each block. The third and fourth blocks involve modifying nnUNet-derived pre-segmented masks, again with a one-week break between blocks. Each neuroradiologist was paired with a trainee (medical students, radiology residents) while annotating, with the complete annotation process being recorded for further analysis. Annotators use ITK-SNAP or 3DSlicer, and each case has at least 2 neuroradiologists for segmentation.

Results

The segmentation masks for brain metastases, gliomas, meningiomas pre- and post-treatment are depicted in Figure 1. A total of 18.75 hours was spent on faculty training in segmentation, averaging 1.25 ± 0.7 hours per faculty member. The cumulative time for segmentations was 14.88±10.03 hours per faculty and 223.19 hours overall. The segmentation masks for metastases include "Tumor core", "SNFH (Surrounding Non-enhancing FLAIR Hyperintensity), "Necrotic core", and "Resection Cavity". The number of brain metastases cases segmented is 265, gliomas is 45, meningioma pre is 58, and meningioma post is 174. Mean segmentation times per case for manual annotation were 28.76 ± 23.92, 24.01 ± 17.6, and 12.97 ± 18.08, and 40.7±26.1 minutes for metastases, pre-treatment meningiomas, post-treatment meningiomas, and gliomas respectively. The total number of screen recordings from segmentations is 353. The Dice coefficients for annotators who completed the first round are shown in Table 1.

Conclusion

We present the first reported supervised process for dataset annotation of a heterogeneous group intra-axial and extra-axial brain tumors that evaluates the inter- and intra-rater variability among neuroradiology faculty annotators, as well as their bias to automated segmentations. This process will be critical for establishment of normative values and protocols for dataset annotation by human experts and for future development of AI algorithms where variability in the output of segmentation algorithms is minimized.

References

1. Mohammed YA, El Garouani S, Jellouli I. A survey of methods for brain tumor segmentation-based MRI images. J Comput Des Eng 2023;10:266–93. https://doi.org/10.1093/jcde/qwac141

2. Moawad AW, Janas A, Baid U, et al. The Brain Tumor Segmentation (BraTS-METS) Challenge 2023: Brain Metastasis Segmentation on Pre-treatment MRI. arXiv 2023;2306.00838. https://doi.org/10.48550/arXiv.2306.00838

3. Hamamci A, Kucuk N, Karaman K, Engin K, Unal G. Tumor-Cut: Segmentation of brain tumors on contrast-enhanced MR images for radiosurgery applications. IEEE Trans Med Imaging 2012;31:790–804. doi:10.1109/TMI.2011.2181857

4. Lampert TA, Stumpf A, Gançarski P. An empirical study into annotator agreement, ground truth estimation, and algorithm evaluation. IEEE Trans Image Process 2016;25:2557–72. doi:10.1109/TIP.2016.2544703

5. Kofler F, Ezhov I, Isensee F, et al. Are we using appropriate segmentation metrics? Identifying correlates of human expert perception for CNN training beyond rolling the DICE coefficient. MELBA 2023 May 3. DOI: 10.59275/j.melba.2023-dg1f.

Images/Tables

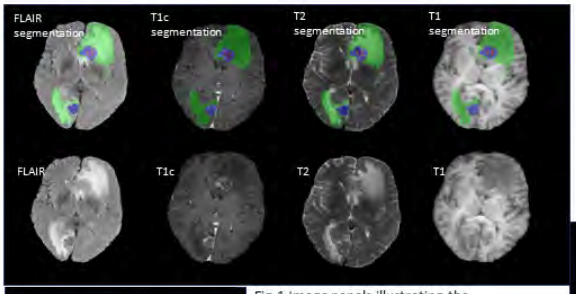

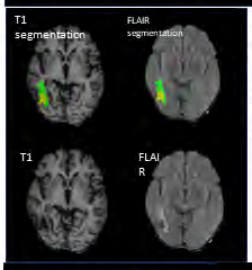

Fig.1 Image panels illustrating the annotated brain metastasis sub-regions across various MRI scans with segmentations of Tumor core(Blue), SNFH (green), and Necrotic core (red) and Resection cavity (Yellow) done on ITK-SNAP.

Table 1: Inter-rater variability among neuroradiologists in brain tumor segmentation.

Dataset	Dice Similarity Coefficient	Mean segmentation times/case	Cumulative hours/dataset
Mets1	0.63	28.27±17.33	24.07
Mets2	0.73	39.28±39.09	66.79
Mets3	0.67	18.71±16.36	24.1
Meningioma-RT1	0.76	12.97 ± 10.08*	40.7*
Meningioma-RT2	0.76		
Meningioma-RT3	0.75		
Meningioma-Pre	TBC	24.01 ± 17.6	26.89
Glioma	TBC	40.7±26.1	39.55

*Cumulative for 3 annotators; TBC: To be calculated
Mets1,2,3: There are two annotators in three separate group of brain metastases
Meningioma-RT1,2,3: There are three annotators in this group

Table 2: Intra-rater variability in brain tumor segmentation

Annotator	Dataset	Dice Similarity Coefficient
Annotator1	Mets	0.8
Annotator2	Mets	0.8
Annotator3	Mets	0.77
Annotator4	Mets	0.83
Annotator5	Meningioma-RT	0.82
Annotator6	Meningioma-RT	0.89
Annotator7	Meningioma-RT	0.83

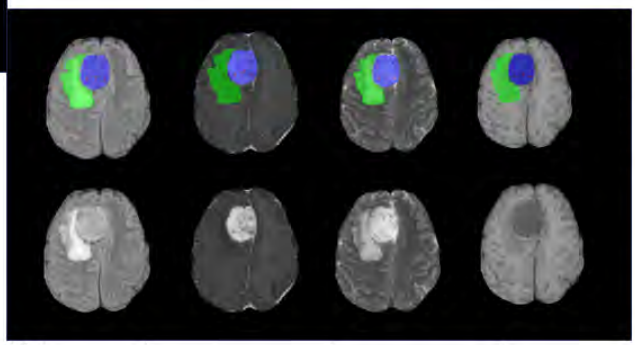

Intracranial Meningioma sub-regions labels seen in mpMRI as described by ET(Enhancing Tumor, in blue), NETC(Non-Enhancing Tumor Core, in red), SNFH(Surrounding non-enhancing FLAIR Hyperintensity, in green).

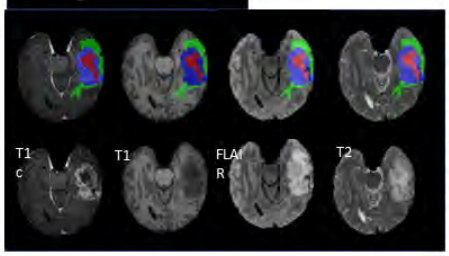

Glioma sub-regions labels seen in mpMRI as described by ET(Enhancing Tumor, in blue), NETC(Non-Enhancing Tumor Core, in red), SNFH(Surrounding non-enhancing FLAIR Hyperintensity, in green), and Resection Cavity(not depicted in this case)

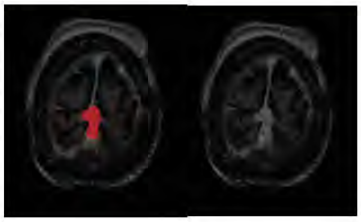

Example of a Gross Tumor Volume (GTV)segmentation for a postoperative/post-treatment meningioma

840

Comparison of balloon guide catheters versus standard guide sheaths for mechanical thrombectomy at a single large-volume stroke center

Gnaneswari Karayi B.A.[1], Elias Shaaya M.D.[2], Radmehr A. Tohrabi M.D.[3], Krisztina Moldovan M.D.[2], Vivek Yedavalli M.D., M.S.[4], Mahesh Jayaraman M.D.[2], Dylan Wolman M.D.[2]

[1]Warren Alpert Medical School, Providence, RI, USA. [2]Brown University Health Department of Neurosurgery, Providence, RI, USA. [3]Brown University Health Department of Brown University Health DepartmeBrown University Health Department of Neurosurgerynt of Neurosurgery, Providence, RI, USA. [4]Johns Hopkins Medicine, Baltimore, MD, USA

Abstract Category

Interventional

Purpose

Efficacy of balloon-guide catheters (BGC) for mechanical thrombectomy (MT) in acute ischemic stroke (AIS) remains contentious, with literature reports spanning both improved [1,2]and worsened[3] thrombectomy efficacy and clinical outcomes with BGC use. We present a retrospective analysis of a single high-volume comprehensive stroke center comparing the use BGCs versus standard guide sheaths (GS) to further clarify if the use of BGCs improves the efficacy of AIS.

Materials & Methods

We performed a retrospective review of patients who underwent MT for AIS due to anterior circulation large-vessel occlusion (LVO) from 2005 to 2023 at our comprehensive stroke center. Inclusion criteria were age >18 with an occlusion of the ICA terminus, M1, or M2 segment of the middle cerebral artery. Thrombectomy candidacy, procedural approach, and equipment were decided by the attending neurointerventionalist, with 6 separate operators included. Patients with missing procedural data were excluded. Patient demographics, clinical details, 90-day clinical outcomes, and equipment were derived from the chart. Primary outcome measures were first pass effect (FPE; mTICI ≥2c on the first pass), excellent final reperfusion (mTICI ≥2c), and 90-day mRS. Secondary outcomes included time from access-to-reperfusion, access-to-first device deployment, NIHSS shift (change in NIHSS from presentation to discharge), number of passes, and rates of adequate reperfusion (mTICI ≥2b). Subgroup analyses between proximal (ICA/M1) and distal (M2) LVOs were performed. Chi-squared, unpaired t-tests, and Mann-Whitney U tests were used for statistical analysis.

Results

A total of 3587 patients were screened with 3348 included. 786 (23%) patients underwent BGC-MT and 2562 (77%) patients underwent GS-MT. Baseline patient demographics, stroke characteristics, and thrombectomy approaches are summarized in Table 1. FPE was achieved in 49% of BGC-MT patients, as compared to the 35% of GS-MT patients (p<0.001). Subgroup analyses comparing proximal (ICA/M1) versus distal (M2) occlusions with and without BGC demonstrated persistent improved FPE with BGC-MT (49% vs 36% proximal; 47% vs 34% distal; p<0.001). Median number of passes was 1 with BGC-MT (IQR: 2-1) as well as for GS-MT (IQR: 1-1)[DW1] . Overall rate of mTICI≥2c and ≥2b was 94% for BGC-MT versus 82% for GS-MT (p<0.00001). Mean time from access-to-reperfusion was significantly faster with BGC-MT (25.6±18.8 vs. 36.4±30.4 min; p<0.001), as was time from access-to-deployment (15.8±11.8 vs. 19.6±15 min; p<0.001). Clinical outcomes with BGC-MT were superior, with overall median NIHSS shift of -10 (IQR: -4- (-15)) for BGC-MT and -7 (IQR -1- (-13)) for GS-MT (p<0.001). This effect was seen in proximal occlusions for BGC-MT (-10, IQR: -4.25-(-15)) versus GS-MT (-7, IQR: -7-(-13), p<0.001) but not for distal occlusions. However, the baseline median NIHSS was significantly different between patients treated by BGC-MT (17, IQR: 21.5-12) versus GS-MT (16, IQR 21-10, p<0.0001). 90-day mRS 0-2 for patients treated with BGC-MT was 35% versus 33% for GS-MT (NS; p=0.326), however there was significant loss to follow-up (only 20% with adequate clinical follow-up data).

Conclusion

BGC-MT is associated with improved FPE, overall reperfusion, fewer passes, faster procedure time, and possibly superior clinical outcomes relative to GS-MT. A randomized controlled trial of BGC-MT is warranted.

References

[1] Zaidat, Osama O., et al. "Impact of balloon guide catheter use on clinical and angiographic outcomes in the STRATIS stroke thrombectomy registry." *Stroke* 50.3 (2019): 697-704.

[2] Pederson, John M., et al. "Comparison of Balloon Guide Catheters and Standard Guide Catheters for Acute Ischemic Stroke: An updated systematic review and meta-analysis." *World neurosurgery* (2024).

[3] Zhou, Yu, et al. "PROximal TEmporary oCclusion using balloon guide caTheter for Mechanical Thrombectomy (PROTECT-MT)." *medRxiv* (2024): 2024-07.

Images/Tables

Variables	BGC-MT (n=786)	GS-MT (n= 2562)
Mean Age	72 ± 14.7 (n=786)	71 ± 15.3 (n=2562)
Sex (% female)	52% (408/786)	49% (1255/2562)
Initial NIHSS (median) (IQR)	17 (IQR 21.5-12), n=759	16 (IQR 21-10), n=1572
tPA/TNK Administration (%)	34% (262/774)	62% (658/1061)
% of Patients on 1 or More Antiplatelet/Anticoagulant	50% (386/765)	59% (693/1179)
% ICA-T Occlusion	23% (177/776)	17% (278/1603)
% M1 Occlusion	65% (503/776)	59% (942/1603)
% M2 Occlusion	12% (96/776)	24% (383/1603)
Mean Access to Reperfusion time (min)	25.6 ± 18.8, n=750	36.4 ± 30.4, n=1248
Mean Access to First Deployment time (min)	15.8 ± 11.8, n=780	19.6 ± 15, n=1178
% FPE	49% (380/776)	35% (694/1417)
% ADAPT	14% (106/776)	50% (571/1148)
%CAPTIVE	86% (664/776)	49% (562/1148)
% Stent Retriever Traditional	1% (8/776)	1% (15/1148)
Median 90-day mRS	3 (IQR 6-2), n=459	4 (IQR: 6-2), n=971

843

Human versus Machine - External Validation of Fully Automated FET PET Evaluation in Brain Tumor Patients

Keith George Ciantar[1], Matthew E Larson[2], Nathaniel J Smith[3], Shaun D Grega[3], Mark Tann[3], Wendy Territo[3], Brian D Graner[3], Sharon S Sidenbender[3], Mark A Green[3], Karl-Josef Langen[1], Norbert Galldiks[1], Michael C Veronesi[2], Philipp Lohmann[1]

[1]Inst. of Neuroscience and Medicine (INM-3/INM-4), Research Center Juelich (FZJ), Juelich, NRW, Germany. [2]Dept. of Radiology, University of Wisconsin School of Medicine and Public Health, Madison, Wisconsin, USA. [3]Dept. of Radiology and Imaging Sciences, Indiana University School of Medicine, Indianapolis, Indiana, USA

Abstract Category

Functional/Advanced Imaging

Purpose

The amino acid PET tracer O-(2-[^{18}F]fluoroethyl)-L-tyrosine (FET) has gained increasing importance in the USA as a companion to structural MRI in patients with brain tumors and is nearing FDA approval. Despite existing guidelines for the evaluation of FET PET scans, there are discrepancies in the manual evaluation, especially for the assessment of tumor volume and among inexperienced readers[1]. Consequently, we investigated the value of a fully automated workflow in comparison to human readers for the assessment of the metabolic tumor volume (MTV).

Materials & Methods

Sixty-one patients with gliomas (mainly glioblastoma, 74%; median age 52y; range 17–77y; 41 male) underwent FET PET/MRI on a Siemens Biography mMR following an equivocal MRI with the clinical question of recurrent disease versus treatment-induced changes. FET was prepared in accordance with FDA IND 150833[2]: FET was administered as a bolus via IV catheter (median dose 702.3MBq; range 284.9–751.1MBq). High injected doses (>5.0mCi) were given to enhance detection of small (<10mm) lesions, with an estimated critical organ dose commensurate with clinical nuclear medicine procedures. Dynamic list-mode PET imaging was initiated over 40 min and reconstructed using an ordinary Poisson OSEM algorithm supplied by the manufacturer and included MR-based attenuation correction (DIXON-VIBE sequence), as well as corrections for decay, scatter, random coincidence events, and system deadtime. MTVs were manually evaluated by readers of varying experience levels (including medical student, staff image analyst, and board-certified neuroradiologist) using different tumor-to-brain ratios for segmentation ranging from 1.6 to 5.0 (Figure 1). The same patients were analyzed using a fully automated workflow based on a previously developed artificial neural network JuST_BrainPET[3,4]. To automatically determine the mean uptake in the healthy tissue, brain masking was performed, followed by dilation and removal of the detected lesion. Undesired regions like vessels, ventricles, and resection cavities were excluded by percentile-based masking. The Pearson correlation coefficient for different tumor-to-brain ratios was computed to compare the performance between the mean of the experts and the automated workflow for the assessment of the MTV.

Results

The Pearson correlation coefficient showed a strong correlation between manual and fully automated evaluation of FET PET ranging from 0.92 for a tumor-to-brain ratio of 1.6 up to 0.98 for a tumor-to-brain ratio of 4.0 or more. *Despite good statistical correlations between segmented volumes, the network segmentations appear to show a bias towards underestimating the metabolic tumor volume (Figure 1).* Comparison of volume values at a tumor-to-brain ratio of 1.6 revealed that the automated script obtained only one false positive and three false negatives. Further visual inspection comparing segmented lesions from the workflow and one of the readers highlighted that lesion overlap decreases with smaller lesions.

Conclusion

The presented fully automated workflow has proven its potential for an improved and more uniform evaluation of FET PET scans in brain tumor patients and offers great potential for a successful implementation into the clinical workflow. In addition to increased consistency, such a system could be utilized for triaging patients, to ensure more difficult cases are assessed first.

References

1. Barry N, Francis RJ, Ebert MA, et al. Delineation and agreement of FET PET biological volumes in glioblastoma: results of the nuclear medicine credentialing program from the prospective, multi-centre trial evaluating FET PET In Glioblastoma (FIG) study-TROG 18.06. *Eur J Nucl Med Mol Imaging* 2023;50:3970-3981

2. Smith NJ, Deaton TK, Territo W, et al. Hybrid (18)F-Fluoroethyltyrosine PET and MRI with Perfusion to Distinguish Disease Progression from Treatment-Related Change in Malignant Brain Tumors: The Quest to Beat the Toughest Cases. *J Nucl Med* 2023;64:1087-1092
3. Gutsche R, Lowis C, Ziemons K, et al. Automated Brain Tumor Detection and Segmentation for Treatment Response Assessment Using Amino Acid PET. *J Nucl Med* 2023;64:1594-1602
4. Lohmann P, Gutsche R, Werner JM, et al. Example of Artificial Intelligence-Based Decision Support for Amino Acid PET: Early Prediction of Suspected Brain Tumor Foci for Patient Management. *J Nucl Med* 2024

Images/Tables

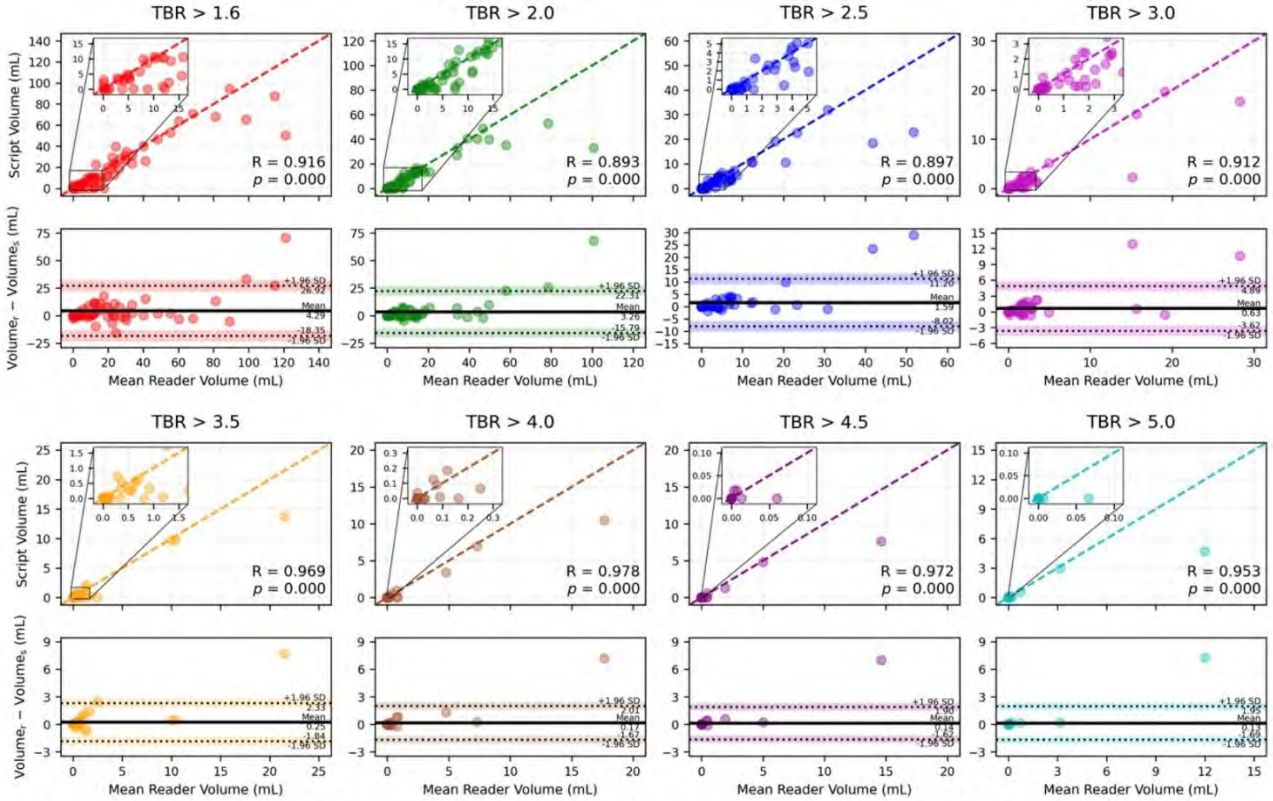

Figure 1: Pearson correlation coefficients and Bland-Altman analysis for the assessment of the metabolic tumor volume in FET PET scans of brain tumor patients for different tumor-to-brain ratios between the experts (Reader, r) and the fully automated workflow (Script, s).

847

Evaluating the Diagnostic Value of Head MRI in Hospitalized Pregnant Women with Acute Headache: A Retrospective Analysis of Clinical and Imaging Correlations

Adva Livne MD, Shai Shrot MD
Sheba Medical Center, Ramat Gan, Israel, Israel

Abstract Category

Adult Brain

Purpose

To assess the utilization of head MRI in hospitalized pregnant patients presenting with acute headache, with an emphasis on examining their clinical characteristics, imaging findings, and subsequent imaging-related decisions.

Materials & Methods

This retrospective, single-center study analysed pregnant women admitted to our hospital with acute headache who underwent MRI following neurological consultation between 2011 and 2024. Clinical data, including presenting symptoms, vital signs, neurological assessment, and MRI findings, were systematically extracted from each patient's medical records. The study further assessed the clinical utility of head MRI and examined the concordance between clinical and radiological evaluations.

Results

In this study of 348 women, MRI findings were unremarkable in 257 cases. Of the remaining 91 cases, 46 presented with incidental findings, primarily characterized by nonspecific white-matter signal abnormalities or small benign cysts, which were unrelated to the etiology of headache. In the remaining 45 cases, sinusitis was suggested in 25 patients, imaging findings consistent with elevated intracranial pressure disorders (e.g., idiopathic intracranial hypertension) were observed in eight patients, and possible vascular pathologies (e.g., vessel irregularities on TOF-MRA) were identified in five patients. Venous thrombosis was diagnosed in three cases, intracranial hemorrhage was found in two cases (one due to apoplexy and another associated with a brainstem cavernous malformation), and space-occupying lesions were detected in two cases. Among patients with abnormal brain MRI findings, clinical diagnoses at discharge aligned with imaging diagnoses in 30 out of 45 cases. The most significant discrepancies were observed in patients with potential vascular pathologies (60% non-matching) and those with suspected increased intracranial pressure (37.5% non-matching).

Conclusion

Most MRIs performed on hospitalized pregnant women with acute headache showed normal results, with only a few cases displaying clinically significant abnormalities. Among the abnormal findings, most were mild diagnoses, such as sinusitis or suspected idiopathic intracranial hypertension, which could likely be diagnosed clinically rather than through brain imaging. Due to the limited number of positive intracranial findings, no predictive model could be developed to guide more selective MRI use for acute headache evaluation. Refining criteria for MRI selection could improve diagnostic efficiency and reduce unnecessary imaging in pregnant women with acute headache.

References

1. Robbins MS, Farmakidis C, Dayal AK, Lipton RB. Acute headache diagnosis in pregnant women. Neurology. 2015;85(12):1024-1030. doi:10.1212/WNL.0000000000001954
2. Raffaelli B, Neeb L, Israel-Willner H, et al. Brain imaging in pregnant women with acute headache. J Neurol. 2018;265(8):1836-1843. doi:10.1007/s00415-018-8924-6
3. Jordan JE, Flanders AE. Headache and Neuroimaging: Why We Continue to Do It. Am J Neuroradiol. 2020;41(7):1149-1155. doi:10.3174/ajnr.A6591
4. Gadde JA, Cantrell S, Patel SS, Mullins ME. Neuroimaging of Adults with Headache: Appropriateness, Utilization, and an Economical Overview. Neuroimaging Clin N Am. 2019;29(2):203-211. doi:10.1016/j.nic.2019.01.001
5. Sandoe CH, Lay C. Secondary Headaches During Pregnancy: When to Worry. Curr Neurol Neurosci Rep. 2019;19(6):27. doi:10.1007/s11910-019-0944-9

849

A Novel Approach at Demyelinating Lesion Detection in Patients with Multiple Sclerosis at 3T Using Deep Learning Reconstruction

Lela Okromelidze MD, John Murray MD, Richard D. Beegle MD, Erik H. Middlebrooks MD
Mayo Clinic, Jacksonville, FL, USA

Abstract Category

Functional/Advanced Imaging

Purpose

The limitations of detection of infratentorial demyelinating lesions on brain MRI in patients with multiple sclerosis (MS) is a well-described phenomenon, the so-called clinicoradiologic paradox. Recently, the lesion-attenuated magnetization prepared gradient echo acquisition(LAMA), was developed on 7T MRI to improve detection of these lesions compared to traditional sequences. However, its translatability to 3T MRI has been limited due to long exam time and lower signal-to-noise ratio(SNR). The aim of this study was to develop a LAMA-MP2RAGE sequence at 3T using deep learning(DL) reconstruction to simultaneously reduce imaging time and improve image quality.

Materials & Methods

DL reconstruction of k-space data was performed on 3T Siemens MRI in 50 consecutive MS patients. The DL algorithm was trained on fully sampled k-space data and highly accelerated data using GRAPPA to identify signatures of acceleration-related noise for purposes of reducing g-factor penalty. In a subset of patients, images were reconstructed using both standard reconstruction pipeline and DL pipeline for direct image comparison. Quantitative measures included assessment of image contrast-to-noise ratio (CNR) and lesion CNR. Diagnostic performance was compared

between LAMA versus T2-weighted and 3D-FLAIR sequences. Image quality was also compared in 17 patients with both 7T LAMA-MP2RAGE and 3T DL LAMA-MP2RAGE.

Results

The 3T LAMA-MP2RAGE sequence was 40% shorter than on 7T with an imaging time of 4:53 min on 3T versus 8:10 min on 7T. Acquired image resolution was 1mm isotropic on 3T in comparison to 0.8mm at 7T. Compared to 3T standard reconstruction, the 3T DL LAMA image CNR was increased by the DL reconstruction from 5.7 ± 1.5 to 14.2 ± 4.3 ($p = 0.002$). Despite the significant reduction in scan time versus 7T LAMA-MP2RAGE, the 3T DL LAMA image CNR was not significantly different (11.9 ± 2.9 versus 13.2 ± 3.1; $p = 0.07$); however, lesion CNR was improved in 3T LAMA DL compared to 7T (4.9 ± 1.7 versus 3.5 ± 1.5; $p = 0.009$).

LAMA revealed significantly more infratentorial lesions than T2/FLAIR (mean 7.58 +/- 7.63 for LAMA, versus 3.30 +/- 5.54 for T2/FLAIR, $p < 0.001$) on 3T imaging. There were 11 patients with a consensus of no infratentorial lesions on T2/FLAIR; all 11 of these (100%) had at least one lesion visible on the LAMA image.

Conclusion

Using DL reconstruction, we have demonstrated the feasibility of a highly accelerated, high SNR LAMA-MP2RAGE sequence for 3T MRI. Despite a 40% reduction in scan time versus 7T, the 3T DL LAMA had improved image and lesion CNR, likely reflecting challenges with B1+ transmit homogeneity at 7T. Our approach allows the simultaneous acquisition of LAMA, while also providing a high-quality 3D T1-weighted image and T1 map. Similar to 7T MRI, the 3T DL LAMA significantly improved detection of posterior fossa demyelinating lesions in MS.

References

Middlebrooks EH, Patel V, Zhou X, et al. 7 T Lesion-Attenuated Magnetization-Prepared Gradient Echo Acquisition for Detection of Posterior Fossa Demyelinating Lesions in Multiple Sclerosis. Invest Radiol. 2024;59(7):513-518. DOI: 10.1097/RLI.0000000000001050. PMID: 38193790.

Images/Tables

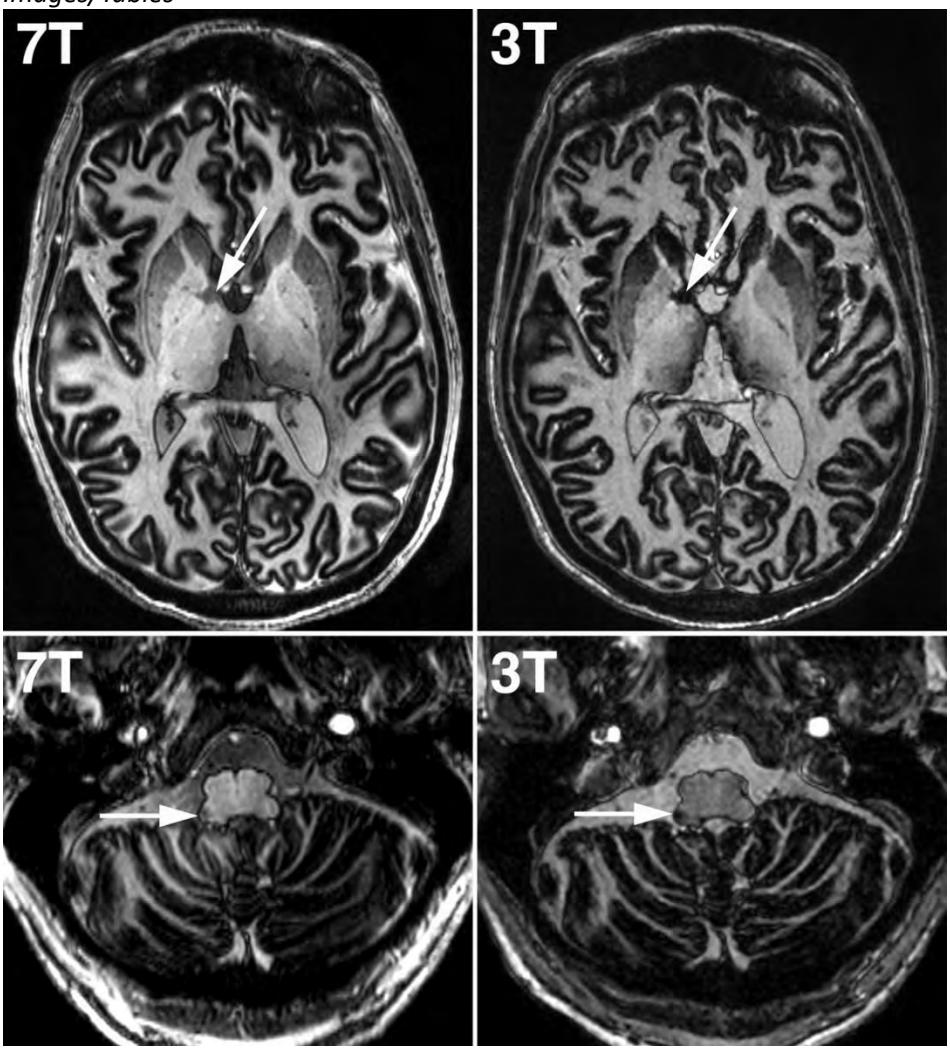

856

Image-Based Search in Radiology: Identification of Brain Tumor Subtypes within Databases using MRI-Based Radiomic Features

Saahil Chadha BA[1], Marc von Reppert[1], Klara Willms[1], Nazanin Maleki MD[2], Tal Zeevi MSc[1], Jan Lost[1], Niklas Tillmanns[1], Leon Jekel[1], Sarah M Jacobs MD[1], Francesca Conti[1], Gabriel Cassinelli Petersen[3], Ujjwal Baid PhD[4], Ichiro Ikuta MD, MMSc[1], Claudia Kirsch MD[1], Spyridon Bakas PhD[4], MingDe Lin PhD[1], Karl-Titus Hoffmann MD[5], Sanjay Aneja MD[1], Mariam Aboian MD, PhD[2]

[1]Yale School of Medicine, New Haven, CT, USA. [2]Children's Hospital of Philadelphia, Philadelphia, PA, USA. [3]University of Göttingen, Göttingen, NI, Germany. [4]Indiana University School of Medicine, Indianapolis, IN, Germany. [5]University of Leipzig, Leipzig, SN, Germany

Abstract Category

AI/Informatics

Purpose

Current neuroradiology references mainly provide classic disease images, requiring users to know specific search terms, which limits their utility for trainees. Institutional imaging databases offer a broader spectrum of disease phenotypes verified during clinical care, but they remain underutilized for educational purposes. Text-based search engines offer some diversity but depend on precise terms[1], while machine learning models, though promising, struggle with generalizability and interpretability[2]. This study introduces an image-based search algorithm using a convolutional neural networks (CNN) for automatic tumor segmentation and clustering. It retrieves similar cases by visual similarity, validated on primary brain tumors and distinguishing glioma subtypes.

Materials & Methods

This retrospective study included 295 patients (mean age and SD, 51 ± 20 years) with histopathologically confirmed glioblastoma, astrocytoma, oligodendroglioma, meningioma, and pilocytic astrocytoma based on CNS WHO 2021 classification. Those patients who underwent surgical and/or radiotherapeutic treatment between 2000 and 2021 were included in this retrospective study. The study applied a convolutional neural network-based algorithm[3] for semi-automatic tumor segmentation and extracted 2,364 radiomic features from pre-treatment MRIs. The dataset was split into reference and query subsets, and four dimensionality reduction methods (Principal Component Analysis [PCA], t-Distributed Stochastic Neighbor Embedding [t-SNE], Uniform Manifold Approximation and Projection [UMAP], and Potential of Heat-diffusion for Affinity-based Trajectory Embedding [PHATE]) were evaluated for clustering reference cases, and the best-performing dimensionality reduction technique was identified. Mean average precision at 5 (mAP@5) was used to assess retrieval accuracy. Expert readers independently rated visual similarity using a validated five-point Likert scale[4].

Results

In a study of 295 brain tumor patients, t-Distributed Stochastic Neighbor Embedding (t-SNE) was identified as the optimal dimensionality reduction method for clustering MRI-based reference cases, achieving a high mean average precision (mAP@5). Among tumor types, glioblastoma/astrocytoma, oligodendroglioma, meningioma, and pilocytic astrocytoma achieved high clustering performance, with t-SNE notably outperforming PHATE. Mean average precision at 5 for the best-performing dimensionality reduction method, t-SNE with six components, ranged from 78% to 100% by tumor type. Visual similarity assessments by four neuroradiologists showed strong inter-rater reliability (ICC 0.78), with 83% of top-ranked cases rated "similar" or "very similar" to the query lesions. Agreement was highest for glioblastoma/astrocytoma and pilocytic astrocytoma (ICC > 0.9), supporting the model's relevance for educational MRI retrieval applications.

Conclusion

This study introduces an image-based search algorithm to help neuroradiologists and trainees quickly retrieve reference cases of brain tumors based on MRI appearance, supporting differential diagnosis, research, and education. Using dimensionality reduction and radiomic feature clustering, the algorithm—optimized by t-Distributed Stochastic Neighbor Embedding—achieved high retrieval accuracy. Unlike previous models, it incorporates convolutional neural network-based automatic segmentation, eliminating the need for manual input and enhancing clinical practicality. Expert assessments validated the algorithm's performance, showing a high mean visual similarity score. Though limitations include difficulty in distinguishing similar subtypes, the method shows promise for broader educational application.

References
1. Demner-Fushman D, Kohli MD, Rosenman MB, et al. Preparing a collection of radiology examinations for distribution and retrieval. *Journal of the American Medical Informatics Association* 2016;23:304–10.
2. Eche T, Schwartz LH, Mokrane F-Z, et al. Toward Generalizability in the Deployment of Artificial Intelligence in Radiology: Role of Computation Stress Testing to Overcome Underspecification. *Radiology: Artificial Intelligence* 2021;3:e210097.
3. Aboian M, Bousabarah K, Kazarian E, et al. Development of a workflow efficient PACS based automated brain tumor segmentation and radiomic feature extraction for clinical implementation (N2.003). *Neurology* 2022;98.
4. Hwang HJ, Seo JB, Lee SM, et al. Content-Based Image Retrieval of Chest CT with Convolutional Neural Network for Diffuse Interstitial Lung Disease: Performance Assessment in Three Major Idiopathic Interstitial Pneumonias. *Korean Journal of Radiology* 2021;22:281.
Images/Tables

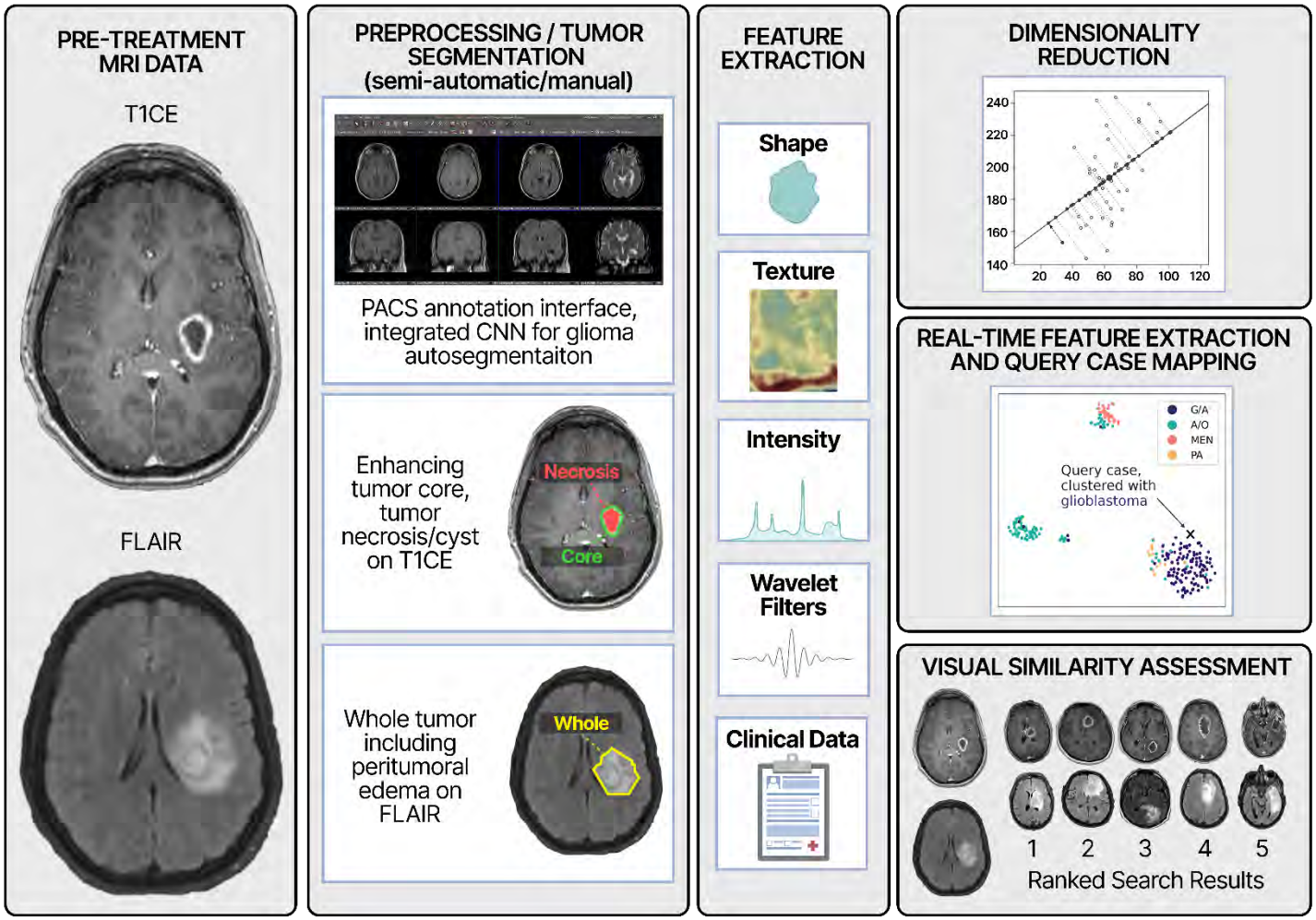

857

Safety and Efficacy of the Neuroform Atlas Stent in Treating Intracranial Aneurysms: A Systematic Review, Meta-Analysis, and Meta-Regression

Umar Akram[1], Arsalan Nadeem MBBS[1], Shahzaib Ahmed[2], Zain A Nadeem[1], Hamza Ashraf[1], Haider Ashfaq[1], Eeshal Fatima[3], Muhammad Ahmed Raza[1], Aimen Nadeem[4], Zuha Majid[4], Tayyab Ahmad[1], Ammara Akram MBBS[5], Sana Rehman MD[6], Abeer Sarwar MBBS[2], Janet Mei MD[6], Francis Deng MD[6], Licia Pacheco-Luna MD[6], Nathan Hyson MD[6], Vivek S Yedavalli MD, MS[6]

[1]Allama Iqbal Medical College, Lahore, Punjab, Pakistan. [2]Fatima Memorial Hospital College of Medicine and Dentistry, Lahore, Punjab, Pakistan. [3]Services Institute of Medical Sciences, Lahore, Punjab, Pakistan. [4]King Edward Medical University, Lahore, Punjab, Pakistan. [5]Sir Ganga Ram Hospital, Lahore, Punjab, Pakistan. [6]Russell H. Morgan Department of Radiology and Radiological Science, Johns Hopkins School of Medicine, Baltimore, Maryland, USA

Abstract Category

Interventional

Purpose

Intracranial aneurysms (IAs) are the major cause of subarachnoid hemorrhage.[1] Stent-assisted coiling, especially with the Neuroform Atlas stent (NAS), has proven more effective than coiling alone for treating these aneurysms.[2] We aimed to perform a systematic review and meta-analysis to investigate the efficacy and safety of NAS in treating IAs.

Materials & Methods

A comprehensive literature search was conducted on PubMed, Embase, Cochrane CENTRAL library, and clinicaltrials.gov from inception till June 2024. We included studies on ruptured and unruptured IAs treated with the NAS, covering experimental, observational, and case series across all age groups. The aneurysm occlusion rate was assessed using the Raymond-Roy classification (RROC).[3] The modified Rankin Scale (mRS) and adverse events related to stent use were recorded. The statistical analysis was conducted on R version 4.3.2 using the packages “meta” and “metasens”.[4] We reported our results as proportions with their corresponding 95% confidence intervals (CIs). Leave-one-out and sensitivity analyses were conducted to confirm the robustness of our results. Meta-regression was conducted using the following co-variates: Age, aneurysm size, neck size, and dome-to-neck ratio. This systematic review and meta-analysis was conducted in line with the guidelines provided by the Cochrane Handbook for Systematic Reviews of Interventions and PRISMA statement.[5] This review is registered with the PROSPERO under the identifier CRD42024521033.

Results

A total of 42 studies including 2434 participants with a mean age of 51 to 73 years were included. Among angiographic outcomes, Initial RROC 1/RROC 2 was achieved in 93% of the patients, initial RROC 1 in 69%, RROC 2 in 19%, and RROC 3 in 7% of the patients. At the end of the follow-up period, the final RROC 1/RROC 2 was achieved in 95% of the patients, final RROC 1 in 82%, RROC 2 in 12%, and RROC 3 in 5% of the patients. Additionally, 93% of the patients showed mRS grade 0, 5% showed mRS grade 1, 3% achieved showed mRS grade 2, 2% showed mRS grade 3, 0% showed mRS grade 4, 0% showed mRS grade 5, and 1% showed mRS grade 6. Within 30 days - rupture, ischaemic complications, hemorrhage, symptomatic morbidity, stent displacement, and stroke were all observed in 1% of the patients, while stent thrombosis was observed in 2% of the patients. Our analysis revealed a 1% mortality rate, delayed complications in 1% of the patients, overall complications in 5% of the patients, rupture in 0% of the patients after 30 days, and permanent neurological deficit in 0% of the patients.

Conclusion

Although the generalizability of our findings is limited, this meta-analysis demonstrates that NAS is highly effective for treating IAs, with high occlusion rates and a low incidence of adverse events. The stent's performance, supported by robust evidence and comprehensive analysis, highlights its safety and efficacy in managing both ruptured and unruptured aneurysms. Due to limited cause-specific data, we were unable to analyse mortality specific to the stent placement and complications. Further research is needed through well-designed comparative studies to assess long-term outcomes and refine treatment protocols for different aneurysm types.

References

[1] Brown RD, Broderick JP. Unruptured intracranial aneurysms: epidemiology, natural history, management options, and familial screening. *The Lancet Neurology*. 2014 Apr 1;13(4):393-404. DOI: https://doi.org/10.1016/s1474-4422(14)70015-8

[2] Pranata R, Yonas E, Deka H, et al. Stent-assisted coiling of intracranial aneurysms using a nitinol-based stent (Neuroform Atlas): a systematic review and meta-analysis. *CardioVascular and Interventional Radiology*. 2020 Jul;43:1049-61. DOI: https://doi.org/10.1007/s00270-020-02502-9

[3] Mascitelli JR, Moyle H, Oermann EK, et al. An update to the Raymond-Roy Occlusion Classification of intracranial aneurysms treated with coil embolization. *J Neurointerv Surg*. 2015 Jul;7(7):496-502. DOI: https://doi.org/10.1016/S1474-4422(14)70015-8

[4] Balduzzi S, Rücker G, Schwarzer G. How to perform a meta-analysis with R: a practical tutorial. *Evid Based Ment Health*. 2019 Nov;22(4):153-160. DOI: https://doi.org/10.1136/ebmental-2019-300117

[5] Moher D, Liberati A, Tetzlaff J, et al.; PRISMA Group. Preferred reporting items for systematic reviews and meta-analyses: the PRISMA statement. *BMJ*. 2009 Jul 21;339:b2535. DOI: https://doi.org/10.1136/bmj.b2535

Images/Tables

Figure: PRISMA Diagram

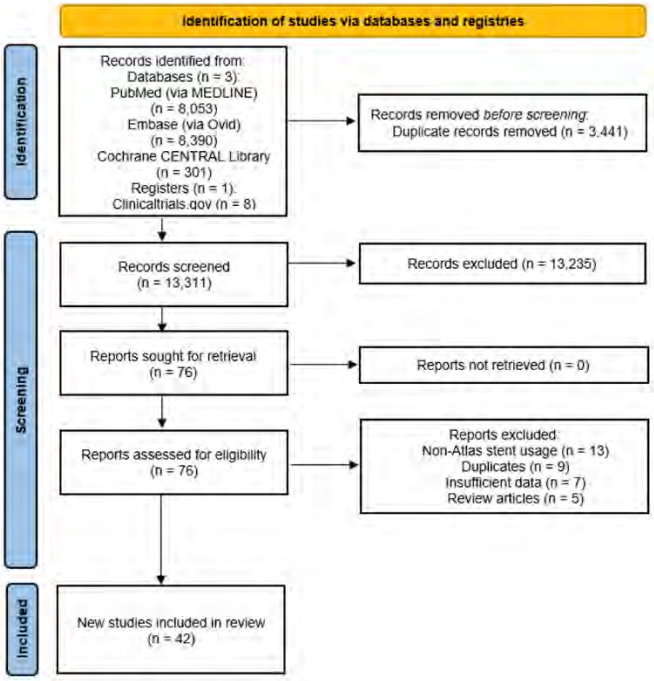

Table: Detailed Results of Clinical Outcomes and Adverse Events

Outcome	No. of Studies (n)	Events/Total	Pooled Proportion	95% CI	I^2	Publication Bias (P-values)	Meta-Regression Covariates (P-values)			
							Age	Aneurysm Size	Neck Size	Dome-to-Neck Ratio
Clinical Outcomes										
Initial RROC ½	37	1917/2138	0.93	0.88 to 0.95	75%	0.0207*	0.81	0.1591	0.242	0.6286
Initial RROC 1	37	1461/2138	0.69	0.61 to 0.76	88%	0.3384	0.2023	0.1206	0.2237	0.256
Initial RROC 2	37	456/2138	0.19	0.15 to 0.24	82%	0.9672	0.0022*	0.4443	0.8191	0.1412
Initial RROC 3	38	224/2193	0.07	0.05 to 0.12	75%	0.0198*	0.9015	0.1803	0.23	0.6286
Final RROC 1/2	38	1712/1833	0.95	0.93 to 0.97	54%	0.3255	0.8864	0.0561	0.012*	0.5574
Final RROC 1	36	1382/1690	0.82	0.78 to 0.86	63%	0.1555	0.0724	0.0691	0.0664	0.6652
Final RROC 2	34	199/1571	0.12	0.10 to 0.15	51%	0.4448	0.0159*	0.928	0.4304	0.9329
Final RROC 3	37	97/1762	0.05	0.03 to 0.07	22%	0.046*	0.8295	0.0567	0.0302	0.4014
mRS grade 0	32	1641/1847	0.93	0.88 to 0.96	77%	0.5353	0.6043	0.5175	0.3074	0.458
mRS grade 1	23	262/1289	0.05	0.02 to 0.13	89%	0.5525	0.6682	0.6939	0.6086	0.937
mRS grade 2	20	37/1208	0.03	0.01 to 0.05	0%	0.5065	0.9357	0.4713	0.3291	0.9239
mRS grade 3	20	23/1012	0.02	0.01 to 0.04	0%	0.172	0.0481*	0.4631	0.3822	0.1663
mRS grade 4	16	11/763	0	0.00 to 0.03	0%	0.6697	0.9333	0.436	0.8957	0.6255
mRS grade 5 [4]	17	7/825	0	0.00 to 0.01	13%	1.954391e-06**	0.3987	0.2225	0.9877	0.2688
mRS grade 6	18	17/953	0.01	0.00 to 0.03	0%	0.1653	0.3982	0.0648	0.1352	0.6956
Adverse Events < 30 Days										
Rupture	40	35/2578	0.01	0.01 to 0.02	0%	0.0001*	0.4494	0.4566	0.1233	0.4157
Ischaemic complications	36	58/2212	0.01	0.01 to 0.02	33%	0.4648	0.711	0.1993	0.5286	0.5034
Stent thrombosis	39	81/2272	0.02	0.01 to 0.03	55%	0.6009	0.4971	0.4206	0.7532	0.4832
Haemorrhage	38	35/2337	0.01	0.01 to 0.02	0%	0.0358*	0.3258	0.0755	0.4053	0.7271
Symptomatic morbidity	36	38/2084	0.01	0.00 to 0.02	0%	0.1381	0.8139	0.3607	0.8904	0.611
Stent displacement	37	26/2282	0.01	0.00 to 0.01	0%	0.0276*	0.8122	0.3985	0.7906	0.2892
Stroke	37	50/2423	0.01	0.00 to 0.02	0%	0.5815	0.6577	0.4005	0.1511	0.1543
Adverse Events > 30 Days										
Delayed complications	39	52/2227	0.01	0.00 to 0.02	0%	0.2584	0.7413	0.1429	0.5952	0.9663
Mortality	40	31/2326	0.01	0.00 to 0.02	0%	0.0603	0.9969	0.2619	0.554	0.5504
Overall complications	40	156/2275	0.05	0.03 to 0.07	50%	0.3975	0.8281	0.0402*	0.35	0.1421
Rupture	40	10/2284	0	0.00 to 0.01	0%	0.6776	0.3306	0.7338	0.5963	0.759
Permanent neurological deficit	39	39/2227	0	0.00 to 0.02	0%	0.0078*	0.7194	0.0275*	0.1097	0.5614

CI = Confidence interval, I^2 = Heterogeneity, * = Significant values, ** = Egger's test, ^ = Freeman Tukey double arcsine transformed data used for analysis

872

Inter-Rater Reliability of RANO2 Criteria in Assessing Tumor Response in Low-Grade Gliomas Treated With and Without Radiation

Parisa Arjmand MD[1], Grayson Warren Hooper DO[1], Wassim Malak MD[1], Yilun Sun PHD[2], Robin Ghotra[1], Sree Gongala MS[1], Herbert Newton MD[3], Prashant Vempati MD[3], Haley Perlow MD[3], Tiffany Hodges MD[4], Chaitra Badve MD[1]
[1]Department of Radiology, University Hospitals Cleveland Medical Center, Cleveland, Ohio, USA. [2]Case Western Reserve University School of Medicine, Cleveland, Ohio, USA. [3]Department of Radiation Oncology, University Hospitals Cleveland Medical Center Cleveland, Cleveland, Ohio, USA. [4]Department of Neurological Surgery, University Hospitals Cleveland Medical Center, Cleveland, Ohio, USA

Abstract Category

Adult Brain

Purpose

Our study aims to evaluate the Inter-Rater Reliability (IRR) of the RANO2 criteria in assessing tumor response among Low-Grade Glioma (LGG) patients with and without radiation.

Materials & Methods

In this ongoing study, we have completed a retrospective review of 26 LGG patients treated at our institution (see Figure 1 for patient flowchart). Ground truth assessments were based on tumor board consensus at the time of the latest (outcome) MRI scans.

Inclusion criteria were pathologically confirmed Grade II gliomas in the supratentorial brain with at least four MRI scans. In accordance to RANO2, the baseline MRI for post-RT patients was conducted approximately four weeks after RT

completion, whereas the post-surgery MRI served as the baseline for non-RT patients. Exclusion criteria included high-grade glioma cases, patients without adequate imaging (per RANO2), and the presence of enhancing lesions at baseline or subsequent scans.

Three radiologists— two fellowship-trained neuroradiologists with 3 (Radiologist 1) and 8 years (Radiologist 2) of experience, respectively, and one neuroradiology fellow (Radiologist 3)—independently evaluated the scans using RANO2 criteria, with no access to clinical history. Measurements were conducted on FLAIR axial slices, by multiplying the two longest diameters of the target lesion. Tumor responses were categorized into four groups: Progressive Disease (PD), Partial Response (PR), Stable Disease (SD), and Non-Measurable Disease (NMD), based on RANO2 criteria for non-enhancing tumors.[1] For statistical analyses, SPSS Statistics (v29.0.1.1) and MATLAB (vR2024a) were used.

IRR was assessed using the Intraclass Correlation Coefficient (ICC), Bland-Altman plots, and Cohen's kappa. ROC analysis was used to evaluate the accuracy of RANO2 against ground truth in both post-RT and non-RT groups.

Results

The IRR for tumor size measurements when assessed on the final outcome scans was excellent for without-RT cases (ICC = 0.986) and moderate for post-RT cases (ICC = 0.516). Bland-Altman plots revealed increased variability and bias in post-RT measurements, especially between Radiologists 1 and 2 (SD = 102.1) and Radiologists 1 and 3. Agreement in categorizing tumor response was also reduced in post-RT cases, dropping from moderate agreement (κ = 0.43-0.52, $p<0.05$) in without-RT cases to slight-to-moderate agreement (κ = 0.12-0.52, $p<0.05$) in post-RT.

Accuracy analysis indicated that RANO2 measurements in without-RT cases had an acceptable AUC of 0.71. In post-RT cases, accuracy was higher when using baseline scans rather than prior scans (AUC = 0.9 vs. 0.6).

Conclusion

Our study highlights significant challenges in implementing RANO2 criteria for monitoring LGGs following RT due to increased variability in radiologists' interpretations (see Figure 2). Post-RT gliosis often resembles tumor progression on FLAIR imaging, complicating accurate assessments.[2,3] We found that using post-RT baseline scans improves diagnostic accuracy, possibly because of large interval change. However, the availability of baseline scans is often limited in LGG patients with long-term follow-up. Our findings suggest the need for novel imaging techniques to enhance diagnostic precision and consistency in post-RT LGG cases. Given the limitations of current advanced imaging methods, future research should prioritize developing new tissue characterization techniques to improve LGG monitoring.

References

1. Wen PY, Huang RY, Bent MVD, Youssef G, et al. RANO 2.0: Update to the Response Assessment in Neuro-Oncology Criteria for High- and Low-Grade Gliomas in Adults; Journal of Clinical Oncology, vol. 41, no. 33, pp. 5187–5199, Nov. 2023, doi: 10.1200/JCO.23.01059.

2. Qin D, Yang G, Jing H, Tan Y, Zhao B, Zhang H. Tumor Progression and Treatment-Related Changes: Radiological Diagnosis Challenges for the Evaluation of Post Treated Glioma. Cancers 2022, 14, 3771. https://doi.org/10.3390/cancers14153771

3. 3. Walker AJ, Ruzevick J, Malayeri AA, et al. Postradiation Imaging Changes in the CNS: How Can We Differentiate Between Treatment Effect and Disease Progression? Future Oncol. 2014;10(7):1277-1297. doi:10.2217/fon.13.271.

Images/Tables

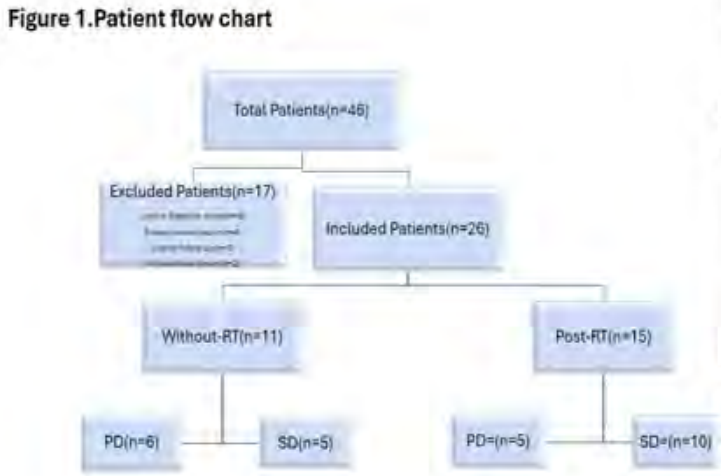

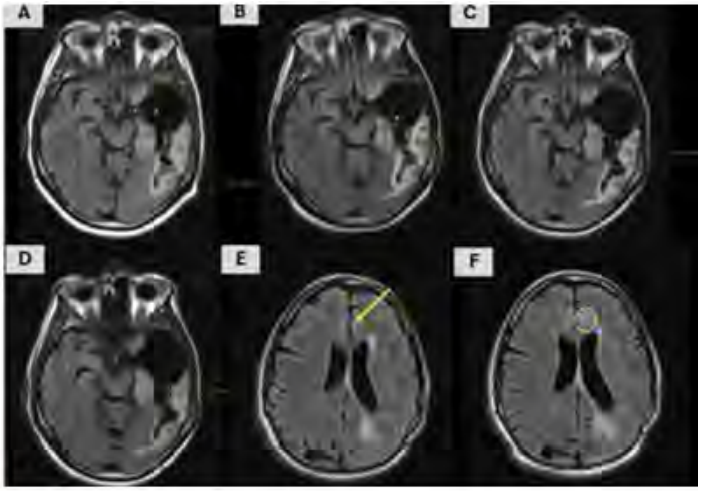

Figure 2. Axial FLAIR MRI scans of a post-RT patient include a baseline scan (A) and three follow-up scans over two years (B–D). Although two radiologists classified the case as Stable Disease (SD) based on RANO2 measurements, a new lesion appeared in a different location, indicating Progressive Disease (PD). In the baseline scan (E), no lesion is present in the corresponding area (yellow arrow), whereas the latest MRI (F) reveals a new lesion (yellow circle) that was missed.

873

Automated Intracranial Hemorrhage Detection: Real-World Experience in a Large Comprehensive Stroke Center

Michael Oswald MD[1], Aakanksha Sriwastwa MD[1], Bin Zhang PhD[2], Yasmin Aziz MD[3], Achala Vagal MD[1]
[1]University of Cincinnati Dept. of Radiology, Cincinnati, OH, USA. [2]Cincinnati Children's Hospital, Cincinnati, OH, USA. [3]University of Cincinnati Dept. of Neurology, Cincinnati, OH, USA

Abstract Category

AI/Informatics

Purpose

Timely and accurate detection of intracranial hemorrhage (ICH) is critical for appropriate triage and treatment of patients.[1] Automated ICH detection tools are widespread, yet data are limited regarding their performance in real-world practice. Our primary objective was to assess a commercially available automated ICH detection tool at a large comprehensive stroke center for its performance in accurately detecting ICH.[2] Our secondary objective was to determine the accuracy of the software in specific anatomical locations, including subdural, subarachnoid, intraventricular, and intraparenchymal compartments. Lastly, we analyzed the trends associated with false negative and false positive cases of ICH.

Materials & Methods

We retrospectively analyzed non-contrast CT head (CTH) images of consecutive code stroke patients from January 2022 to February 2023 in a comprehensive stroke center. Cases were included if their indication was stroke, and images were assessed by an automated platform. Radiology reports were considered ground truth. The primary outcome was the performance of the automated software tool compared to board-certified radiologists for ICH detection. The sensitivity, specificity, positive predictive value, negative predictive value, and accuracy were calculated using SAS software.

Results

Of 1,430 code stroke CTs, 1,402 were analyzed by the automated detection tool (mean age 67.3±16 years, 51% female, 65% White). The software accurately identified 105/129 (81%) ICH cases and 1,255/1,273 (99%) non-ICH cases. The sensitivity, specificity, positive predictive value, and negative predictive value with 95% confidence intervals were 0.83 (0.77-0.89), 0.99 (0.98-0.99), 0.87 (0.81-0.99), and 0.98 (0.97-0.99), respectfully (Table 1). Detection was highest for intraparenchymal hemorrhage with concomitant intraventricular hemorrhage (96%), intraventricular hemorrhage with

or without multicompartment involvement (93%), and isolated intraparenchymal hemorrhage (93%). The lowest detection rates were noted for isolated subdural and subarachnoid hemorrhages (62% and 33%, respectively). Comprehensive detection percentages based on subtypes are provided in Figure 1.

There were 24 false negative cases confirmed following independent adjudication of primary images: isolated IPH (3), IPH with extra-axial extension (4), isolated SAH (8), isolated SDH (5), SAH with SDH (3), and IVH with SAH (1). Of the isolated IPH cases (n=3), all were less than 5cc (Figure 2A). Of the eight cases of isolated SAH not detected by the software, five had diffuse and bilateral hemispheric sulcal involvement (Figure 2B), and three had trace SAH limited to a few sulci (Figure 2C).4 All of the five isolated SDH cases not detected by the software were crescentic collections less than 5mm thick along the cerebral convexity, closely paralleling the hyperdense calvaria (Figure 2D).

All 18 false positive cases were negative for ICH upon study adjudication, with potential causes identified as follows: co-existing acute/subacute infarction (n=3) (Figure 3A), presence of arterial thrombus (n=2), retained contrast (n=2) (Figure 3B), encephalomalacia (n=2) (Figure 3C), parenchymal calcification (n=1) (Figure 3D), atherosclerotic vascular calcification (n=1), beam hardening artifact5 (n=2), and significant atrophy (n=5).

Conclusion

Automated ICH detection software demonstrates high accuracy in detecting ICH in real-world practice. Sensitivity for intra-axial hemorrhage is particularly high, with detection of extra-axial hemorrhage reaching acceptable parameters when co-presenting with intraparenchymal or intraventricular hemorrhage.

References

1. Greenberg SM, Ziai WC, Cordonnier C, et al. 2022 Guideline for the Management of Patients With Spontaneous Intracerebral Hemorrhage: A Guideline From the American Heart Association/American Stroke Association. Stroke. 2022;53(7):e282-e361. doi:10.1161/STR.0000000000000407
2. 510(k) Premarket Notification. Accessed September 3, 2024. https://www.accessdata.fda.gov/scripts/cdrh/cfdocs/cfpmn/pmn.cfm?ID=K210209

Images/Tables

Metric	Estimate	Lower 95% CI	Upper 95% CI
Sensitivity	0.83	0.77	0.89
Specificity	0.99	0.98	0.99
Positive Predictive Value	0.87	0.81	0.99
Negative Predictive Value	0.98	0.97	0.99
Accuracy	0.96	0.97	0.98

TABLE 1: Performance of Automated ICH Detection Platform for "Code Stroke" Patients. All metrics were compared to radiology reads as ground truth.

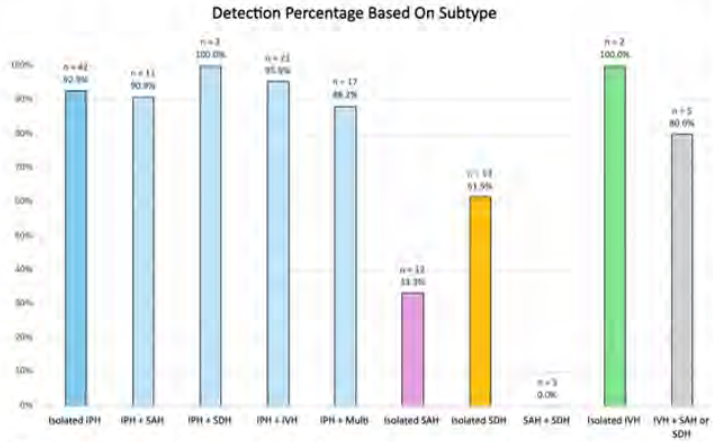

Figure 1: Automated Detection Rate by Intracranial Hemorrhage Subtype. Individual cases were adjudicated to determine a dominant subtype if more than one subtype was present in the study, which is reflected as the first named subtype in the figure's classifications.

Figure 2. Study examples demonstrating false negative cases by the AI software for automated ICH detection. Small right basal ganglia intraparenchymal hemorrhage (less than 5cc in volume) (arrow in A) and extensive bilateral subarachnoid hemorrhage (arrows in B), trace subarachnoid hemorrhage isolated to left high frontoparietal sulcus (arrow in C) and small right temporal convexity subdural hematoma (arrow in D) not alerted by the AI software.

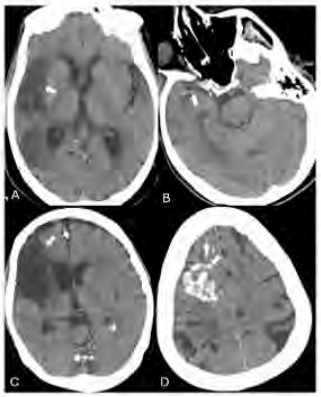

Figure 3: Study examples demonstrating false positive cases by the AI software for automated ICH detection. Late acute/ early subacute infarct right MCA vascular territory (arrow in A), retained contrast in right MCA trunk (arrow in B), encephalomalacia right frontal lobe (arrow in C), and parenchymal calcification in right frontal lobe secondary to oligodendroglioma (arrow in D) alerted by the AI software for suspected ICH. No intracerebral hemorrhage was detected on review by the radiologists.

877

Differences in CA1/Subiculum Atrophy in Hippocampal Sclerosis of Aging and Alzheimer's Disease Assessed with a Novel Visual Rating Scale and Compared with Existing Visual Rating Scales for Entorhinal Cortex and Medial Temporal Lobe Atrophy

Ali Siddiqui M.D., Chad W Farris M.D., Ph.D.
Boston Medical Center/Boston University, Boston, MA, USA

Abstract Category

Adult Brain

Purpose

Previous volumetric analysis of Brain MRIs demonstrated CA1 and subiculum volume loss in hippocampal sclerosis of aging (HS), a pathology associated with an amnestic dementia syndrome commonly mistaken for Alzheimer's disease (AD). Imaging biomarkers for HS have the potential to help differentiate the amnesic syndrome associated with HS from AD. We investigate differences in CA1/Subiculum atrophy in HS and/or AD relative to controls without HS and AD using a simple novel visual rating scale for atrophy of the CA1/Subiculum (CA1/Subiculum Score).

Materials & Methods

This retrospective study used the National Alzheimer's Coordinating Center database to identify participants with pathologically confirmed HS and/or AD and controls without HS and AD with an MRI Brain with 3DT1 performed within 2 years of death. Four groups were evaluated: HS+AD-(n=8), HS-AD+(n=7), HS+AD+(n=7), or HS-AD-(n=8). MRIs were visually rated with a CA1/Subiculum Score from 0 (no atrophy) to 3 (severe atrophy) for both hippocampi and scores from each side summed. Scores were obtained at the levels of the anterior, middle, and posterior hippocampus by a rater blinded to the pathologic data. MRIs were also rated for entorhinal cortex atrophy (ERICA Score) and Medial Temporal Lobe Atrophy (MTA Score) with scores from each hemisphere summed. One-way ANOVA followed by Tukey HSD were used to evaluate for significant differences.

Results

There was a significant overall difference among groups for MTA Score, HS+AD- 5.0(3.8-6.2), HS+AD+ 5.3(4.0-6.6), HS-AD- 2.5(1.3-3.7), and HS-AD+ 4.2(3.0-5.6) (mean(95% CI)) (F-ratio=4.34, p=0.01). HS+AD+ and HS+AD- groups both had significantly higher MTA Scores than HS-AD- (p=0.02 and p=0.03, respectively). There was a significant overall difference among groups for ERICA Score, HS+AD- 3.6(2.5-4.8), HS+AD+ 4.0(2.75-5.25), HS-AD- 1.5(0.3-2.7), and HS-AD+ 2.3(1.0-3.5) (F-ratio=3.97, p=0.02). HS+AD+ group had a significantly higher ERICA score than HS-AD- (p=0.03). There was an overall difference among the groups for Anterior CA1/Subiculum Score, HS+AD- 3.8(2.9-4.9), HS+AD+ 4.0(2.9-5.1), HS-AD- 1.4(0.4-2.4), and HS+AD- 1.9(0.8-3.0) (F-ratio=7.01, p=0.001). HS+AD+ and HS+AD- groups had significantly higher CA1/Subiculum Score than HS-AD- (p=0.007 and p=0.008, respectively). HS+AD- and HS+AD+ groups had significantly higher CA1/Subiculum Score than the HS-AD+ group (p=0.04 and p=0.48, respectively). There was no overall difference among the groups for Middle CA1/Subiculum Score, HS+AD- 3.8(2.6-4.9), HS+AD+ 4.0(2.8-5.2), HS-AD- 2.1(0.1-3.3), and HS-AD+ 2.3(1.1-3.5). There was an overall difference among the groups for Posterior CA1/Subiculum Score, HS+AD- 3.5(2.7-4.3), HS+AD+ 4.4(3.6-5.3), HS-AD- 2.0(1.2-2.8), and HS-AD+ 3.4(2.6-4.3) (F-ratio=6.73,p=0.002). HS+AD- and HS+AD+ groups had significantly higher Posterior CA1/Subiculum Score than HS-AD- (p=0.0009 and p=0.04, respectively).

Conclusion

HS results in greater CA1/Subiculum atrophy than controls and those with AD without HS, as measured by the novel visual rating scale utilized in this study. The novel visual rating scale could potentially be a clinically useful metric to differentiate HS from AD and may better differentiate HS from AD over MTA and ERICA scores.

References

1. Enkirch SJ, Traschütz A, Müller A, Widmann CN, Gielen GH, Heneka MT, Jurcoane A, Schild HH, Hattingen E. The ERICA Score: An MR Imaging–based Visual Scoring System for the Assessment of Entorhinal Cortex Atrophy in Alzheimer Disease. Radiology 2018;288(1):226-333. doi: 10.1148/radiol.2018171888Scheltens P, Leys D, Barkhof F, Huglo D, Weinstein HC, Vermersch P, Kuiper M, Steinling M, Wolters EC, Valk J. Atrophy of medial temporal lobes on MRI in "probable" Alzheimer's disease and normal ageing: diagnostic value and neuropsychological correlates. Journal of Neurology, Neurosurgery & Psychiatry 1992;55(10):967-972. doi: 10.1136/jnnp.55.10.967
2. Scheltens P, Leys D, Barkhof F, Huglo D, Weinstein HC, Vermersch P, Kuiper M, Steinling M, Wolters EC, Valk J. Atrophy of medial temporal lobes on MRI in "probable" Alzheimer's disease and normal ageing: diagnostic value

and neuropsychological correlates. Journal of Neurology, Neurosurgery & Psychiatry 1992;55(10):967-972. doi: 10.1136/jnnp.55.10.967
3. Smirnov DS, Galasko D, Hansen LA, Edland SD, Brewer JB, Salmon DP. Trajectories of cognitive decline differ in hippocampal sclerosis and Alzheimer's disease. Neurobiology of Aging 2019;75:169-177. doi: https://doi.org/10.1016/j.neurobiolaging.2018.11.015
4. Woodworth DC, Nguyen HL, Khan Z, Kawas CH, Corrada MM, Sajjadi SA. Utility of MRI in the identification of hippocampal sclerosis of aging. Alzheimer's & Dementia 2021;17(5):847-855. doi: https://doi.org/10.1002/alz.12241
5. Zarow C, Wang L, Chui HC, Weiner MW, Csernansky JG. MRI Shows More Severe Hippocampal Atrophy and Shape Deformation in Hippocampal Sclerosis Than in Alzheimer's Disease. International Journal of Alzheimer's Disease 2011;2011(1):483972. doi: https://doi.org/10.4061/2011/483972

Images/Tables

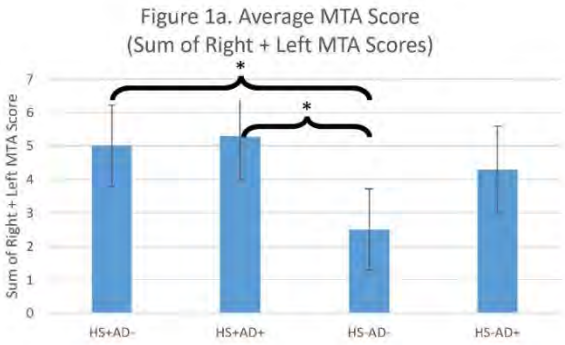

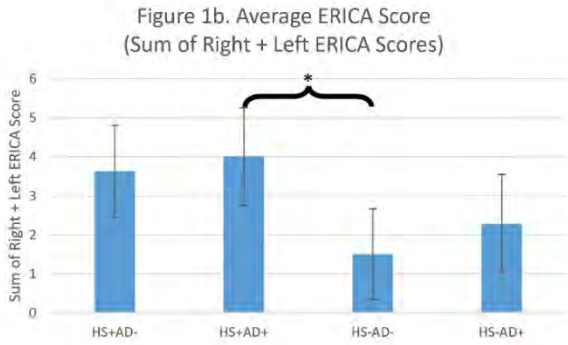

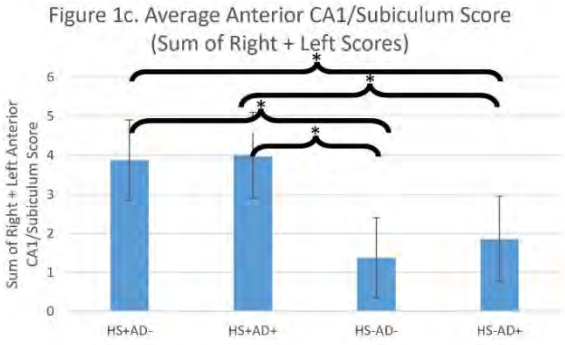

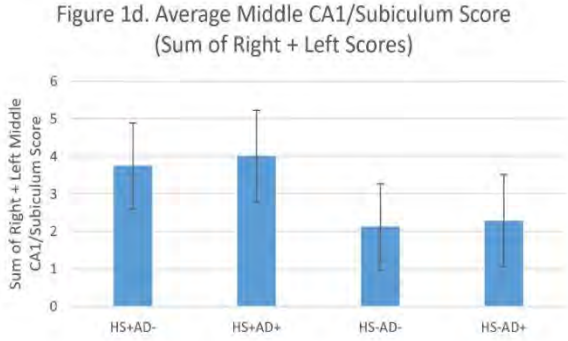

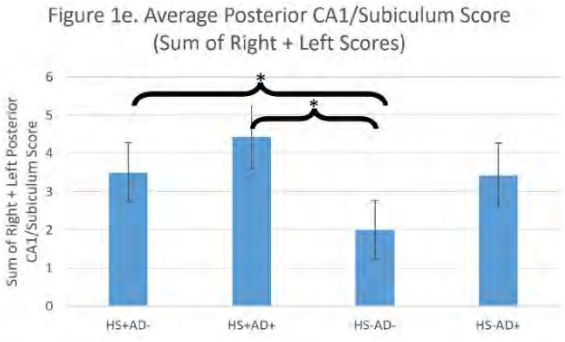

Figure 1. Comparison of different atrophy scores.

HS+AD- = Hippocampal Sclerosis Present and Alzheimer's Disease Absent

HS+AD+ = Hippocampal Sclerosis Present and Alzheimer's Disease Present

HS-AD- = Hippocampal Sclerosis Absent and Alzheimer's Disease Absent

HS-AD+ = Hippocampal Sclerosis Absent and Alzheimer's Disease Present

*Significant difference with $p<0.05$ (corrected for multiple comparisons)

Error Bars = 95% Confidence Intervals

880

Enhanced ARIA Detection with icobrain aria v1.1: A Validation Study

Ricardo Magalhaes PhD, Simon Van Eyndhoven PhD, Thanh Van Phan PhD, Arno Liseune PhD, Rafay A Khan PhD, Arne Brys, Diana M Sima PhD, Dirk Smeets PhD
icometrix, Leuven, BE, Belgium

Abstract Category

Adult Brain

Purpose

ico**brain aria**, an automated quantification and detection tool designed to aid radiologists in assessing amyloid-related imaging abnormalities (ARIA), a side effect of anti-amyloid therapies for Alzheimer's Disease (AD), has been previously shown to be robust and reliable (Sima et al., 2024). Crucially, use of icobrain aria is seen to help radiologists in more accurately detecting and quantifying ARIA (Sima et al., 2024). With additional training data available, the present study aimed to improve the standalone performance of ico**brain aria**, and to assess the impact on sensitivity and specificity of ARIA detection of the new version of the software.

Materials & Methods

The deep-learning models underlying the previous version of ico**brain aria** (v1.0), trained and tuned with 475 image pairs for ARIA-E and 326 for ARIA-H, were retrained with an additional 253 and 250 image pairs respectively, leading to a total of 728 and 576 image pairs in the training and tuning dataset for the new version of icobrain aria (v1.1). Using the baseline and follow-up MRI scans, ARIA-E (edema) were measured on T2 FLAIR images, while ARIA-H (new microhemorrhages and/or superficial siderosis relative to the previous scan) were measured on T2* GRE images.
The testing dataset included 199 test cases with 123 ARIA-E positive cases, and 120 ARIA-H positive cases for (82 with microhemorrhages and 78 with superficial siderosis). ARIA detection results of both versions of ico**brain aria** were compared with ground truth, which was determined by the consensus read of three expert ARIA readers. Differences in sensitivity and specificity across the two versions of ico**brain aria** relative to the ground truth were evaluated. For ARIA-H, microhemorrhage and superficial siderosis detection were assessed independently.

Results

ico**brain aria** showed an ARIA-E detection sensitivity of 0.95 and 0.94, and specificity of 0.74 and 0.67, for v1.1 and v1.0, respectively.
The ARIA-H microhemorrhage detection sensitivity was 0.84 and 0.86, and specificity was 0.72 and 0.67, for ico**brain aria** v1.1 and ico**brain aria** v1.0, respectively.
The ARIA-H superficial siderosis detection sensitivity was 0.72 and 0.67, and specificity was 0.94 and 0.95, for ico**brain aria** v1.1 and icobrain aria v1.0, respectively.

Conclusion

ico**brain aria** v1.1 improves upon icobrain aria v1.0 in terms of both sensitivity and specificity for ARIA-E detection. Relative to the previous version, ico**brain aria** v1.1 trades off a decrease in sensitivity (7%) of ARIA-H microhemorrhage detection for an increased specificity (11%), while there is trade off of a small decrease in specificity (1%) for ARIA-H superficial siderosis for an increased sensitivity (5%). This study demonstrates that the expansion of the training data set led to an overall improvement for icobrain aria over the previous version.

References

- Sima, D. M., Vân Phan, T., Van Eyndhoven, S., Vercruyssen, S., Magalhães, R., Liseune, A., ... & Smeets, D. (2024). Artificial Intelligence Assistive Software Tool for Automated Detection and Quantification of Amyloid-Related Imaging Abnormalities. JAMA Network Open, 7(2), e2355800-e2355800.

881

Differentiation between non-enhancing tumor in glioblastoma and vasogenic edema using diffusion-weighted and dynamic susceptibility contrast MR imaging

Sahar Alizada[1], Yasmin Aly[2], Hongbo Bao[2], Ahmed Msherghi[1], Ceylan Altintas Taslicay[1], Samir A Dagher[1], Richard Dagher[1], Dhairya Lakhani[2], Vivek Yedavalli[2], Haris Sair[2], Janet Mei[2]
[1]MD Anderson Cancer Center, Houston, TX, USA. [2]The Johns Hopkins Hospital, Baltimore, MD, USA

Abstract Category

Adult Brain

Purpose

Glioblastoma (GBM) typically exhibits post-contrast enhancement, but non-enhancing lesions can be present and carry clinical significance[1,2]. These non-enhancing tumors may progress rapidly and are associated with poor prognosis, but aggressive treatment, including surgery or radiation, can improve survival[3,4]. Differentiating non-enhancing GBM from vasogenic edema, both of which appear as T2 hyperintensity, is crucial for accurate diagnosis and optimal treatment planning. This study aimed to evaluate the diagnostic value of diffusion-weighted imaging (DWI) and dynamic susceptibility contrast (DSC) MR imaging in distinguishing non-enhancing GBM from vasogenic edema.

Materials & Methods

This retrospective study examined patients with GBM using MRI data from January 1, 2022, to December 31, 2023. Non-enhancing lesions were identified as a solitary non-enhancing lesion confirmed as GBM by biopsy or as distant non-enhancing lesion without visible communication with pathologically confirmed enhancing lesion of GBM. Patients with IDH mutations or other brain conditions were excluded. Imaging analysis assessed non-enhancing GBM features, including location, size, and T2 FLAIR (relative to ventricles), ADC, rCBV (relative to normal-appearing contralateral white matter) measurements, comparing them to 30 matched brain metastasis cases.

Results

110 GBM patients identified and 13 non-enhancing lesions in 15 patients identified. Our results showed that non-enhancing GBMs exhibited significantly lower apparent diffusion coefficient (ADC) values and higher relative cerebral blood volume (rCBV) compared to vasogenic edema (ADC: (1.075 ± 0.222) x ´ 10^{-3} mm^2/s vs. (1.737 ± 0.171) ´10^{-3} mm^2/s, p=<0.0001; rCBV: 2.399 ± 0.864 vs. 0.3 ± 0.125, p=<0.0001). The diagnostic cutoff values were established as follows: for FLAIR intensity, a threshold of 15.56 yielded a sensitivity of 0.9 and a specificity of 0.53; for ADC, a value of 1.36 × 10^-3 mm^2/s provided a sensitivity of 1 and a specificity of 0.75; and for rCBV, a cutoff of 1.04 achieved both a sensitivity and specificity of 1. Additionally, non-enhancing GBMs exhibited subsequent enhancement in 80%.

Conclusion

Our study underscores the utility of DWI and DSC MRI in differentiating non-enhancing GBM from vasogenic edema, enhancing diagnostic accuracy and aiding in clinical decision-making. Future research with larger cohorts is recommended to validate these results and explore their broader clinical applicability.

References

1. Eichberg DG, Di L, Morell AA, et al. Incidence of high grade gliomas presenting as radiographically non-enhancing lesions: experience in 111 surgically treated non-enhancing gliomas with tissue diagnosis. *J Neurooncol* 2020;147:671–9. DOI: https://doi.org/10.1007/s11060-020-03474-z
2. Upadhyay N, Waldman AD. Conventional MRI evaluation of gliomas. *Br J Radiol* 2011;84:S107–11. DOI: https://doi.org/10.1259/bjr/65711810
3. Jain R, Poisson LM, Gutman D, et al. Outcome Prediction in Patients with Glioblastoma by Using Imaging, Clinical, and Genomic Biomarkers: Focus on the Nonenhancing Component of the Tumor. *Radiology* 2014;272:484–93. DOI: https://doi.org/10.1148/radiol.14131691
4. Pasquini L, Di Napoli A, Napolitano A, et al. Glioblastoma radiomics to predict survival: Diffusion characteristics of surrounding nonenhancing tissue to select patients for extensive resection. *J Neuroimaging* 2021;31:1192–200. DOI: https://doi.org/10.1111/jon.12903

Images/Tables

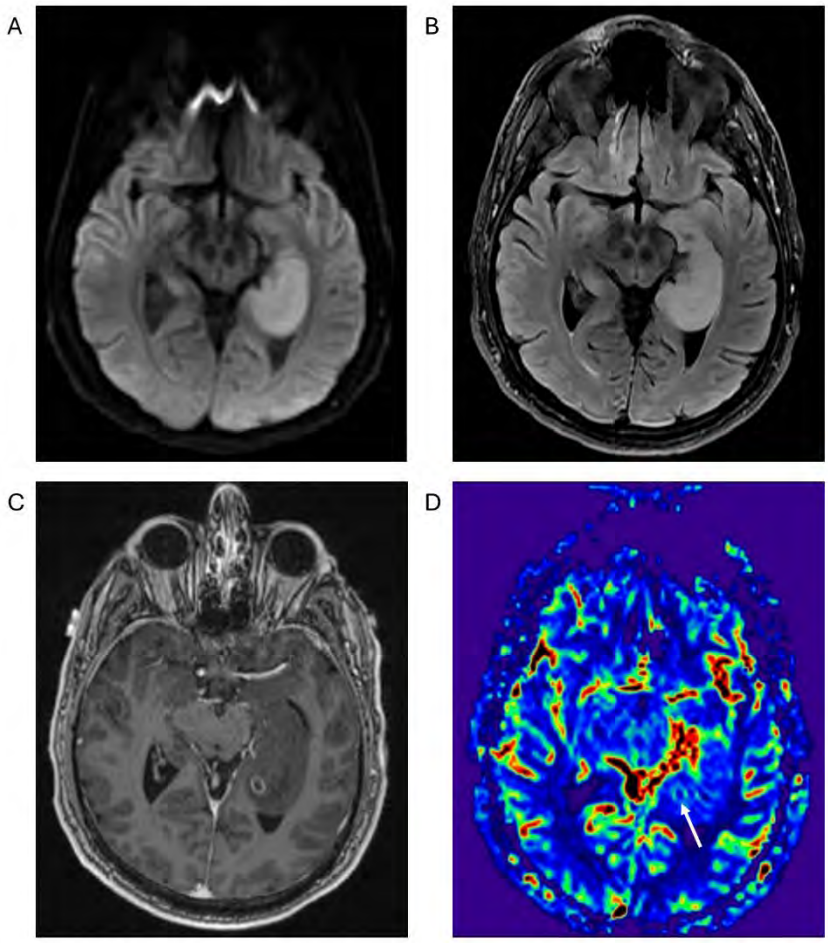

Figure 1: MRI sequences demonstrating non-enhancing lesion with subsequent enhancement on follow-up.
(A) Apparent Diffusion Coefficient (ADC) map from the initial MRI, showing diffusion restriction, (B) Fluid-Attenuated Inversion Recovery (FLAIR) sequence from the initial MRI, highlighting FLAIR hyperintensity, (C) Post-contrast T1-weighted image with gadolinium from the subsequent MRI, illustrating enhancement, (D) Relative Cerebral Blood Volume (rCBV) map from the subsequent MRI, depicting increased vascularity.

885

Enhancing 1p/19q Classification in Brain Gliomas using IDH status: A Deep Learning study

Jason E Bowerman[1], Ashwath S Kapilavai[1], Benjamin C Wagner[1], Nghi C. D. Truong PhD[1], James M Holcomb[1], Divya Reddy[1], Niloufar Saadat MD[1], Kimmo J Hatanpaa MD, PhD[1], Toral R Patel MD[1], Baowei Fei MSc, PhD[1], Matthew D Lee MD[2], Rajan Jain MD[2], Richard J Bruce MD[3], Marco C Pinho MD[1], Chandan Ganesh Bangalore Yogananda PhD[1], Joseph A Maldjian MD[1]

[1]UT Southwestern Medical Center, Dallas, TX, USA. [2]NYU Grossman School of Medicine, New York, NY, USA. [3]University of Wisconsin, Madison, WI, USA

Abstract Category

Adult Brain

Purpose

IDH mutation & 1p/19q-co-deletion are important biomarkers for glioma diagnosis & therapy. IDH-wildtype brain tumors are typically 1p19q-non-co-deleted[1], forming the basis for this study. We developed a non-invasive, MRI-based deep learning method combining IDH & 1p19q-classification-networks to enhance 1p19q-predictions.

Materials & Methods

Multi-contrast brain tumor MRI & genomic information were obtained from six publicly available (TCIA, UCSF, IvyGAP, EGD, UPenn & LGG)[2-5], and three collaborator institutions (UTSW, NYU, UWM). Subjects were screened for the availability of at least T2w MRI, IDH & 1p19q statuses. Missing MR-contrasts for the LGG database were generated using an in-house multi-contrast-simulator. Two separate *U-Nets* were developed for 1p19q-classification including a multi-contrast (*MCon-net)* & a T2w-only (*OT2-net*) network. A separate *U-Net* was developed for IDH-classification (*IDH-net*). The *IDH-net* was trained using TCIA+UTSW+UPenn and the 1p19q-networks were trained using TCIA+UTSW+LGG datasets. The trained networks were tested on true held-out-cases from NYU, UWM, EGD & UCSF. Subjects were initially classified for IDH-status using the *IDH-net.* Predicted IDH-wildtype cases were defaulted as 1p19q-non-codeleted. The 1p19q-status for IDH-mutant cases were determined using the 1p19q-networks (*Fig.1*).

Results

IDH-net achieved a classification accuracy of 93.74%. *MCon-net* & *OT2-net* achieved a classification accuracy of 86.59% & 86.04% respectively. Combining *IDH-net with MCon-net* & *OT2-net separately* achieved accuracies of 91.43% & 91.21% respectively, improving the classification accuracy by 5%.

Conclusion

This study demonstrates the effectiveness of leveraging IDH-status for 1p19q-classification. *IDH-net+MCon-net* & *IDH-net+OT2-net* enhanced the 1p19q-classification accuracy by 5%. The developed method offers a reliable non-invasive method to determine important biomarkers for glioma diagnosis. Training the 1p/19q-networks exclusively on IDH-mutated cases may further improve classification accuracy.

References

- Li YX, Shi Z, Aibaidula A, Chen H, Tang Q, Li KK, Chung NY, Chan DT, Poon WS, Mao Y, Wu J, Zhou L, Chan AK, Ng HK. Not all 1p/19q non-codeleted oligodendroglial tumors are astrocytic. Oncotarget. 2016 Oct 4;7(40):64615-64630. doi: 10.18632/oncotarget.11378. PMID: 27556304; PMCID: PMC5323103.
- Clark K, Vendt B, Smith K, et al. The Cancer Imaging Archive (TCIA): maintaining and operating a public information repository. *Journal of digital imaging* 2013;26:1045-1057
- Calabrese E, Villanueva-Meyer JE, Rudie JD, et al. The university of california san francisco preoperative diffuse glioma mri dataset. *Radiology: Artificial Intelligence* 2022;4:e220058
- van der Voort SR, Incekara F, Wijnenga MMJ, et al. The Erasmus Glioma Database (EGD): Structural MRI scans, WHO 2016 subtypes, and segmentations of 774 patients with glioma. *Data in brief* 2021;37:107191
- S. Bakas, C. Sako, H. Akbari, M. Bilello, A. Sotiras, G. Shukla, J. D. Rudie, N. F. Santamaría, A. F. Kazerooni, and S. Pati, "The University of Pennsylvania glioblastoma (UPenn-GBM) cohort: Advanced MRI, clinical, genomics, & radiomics," Scientific data, vol. 9, no. 1, pp. 453, 2022.

Images/Tables

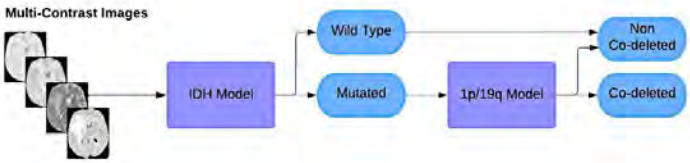

Figure 1. 1p/19q prediction model leveraging the IDH network for initial classification.

IDH-Net and *OT2-Net*/*MCon-Net* Results					
	IDH-Net	*OT2-Net*	*MCon-Net*	*IDH-Net + OT2-Net*	*IDH-Net + MCon-Net*
Accuracy (%)	93.74	86.04	86.59	91.21	91.43
Sensitivity (%)	86.35	80.2	83.17	72.28	74.26
Specificity (%)	97.25	86.7	87.02	93.57	93.57

Figure 2. Standalone and combined results for IDH-Net, OT2-Net and MCon-Net.

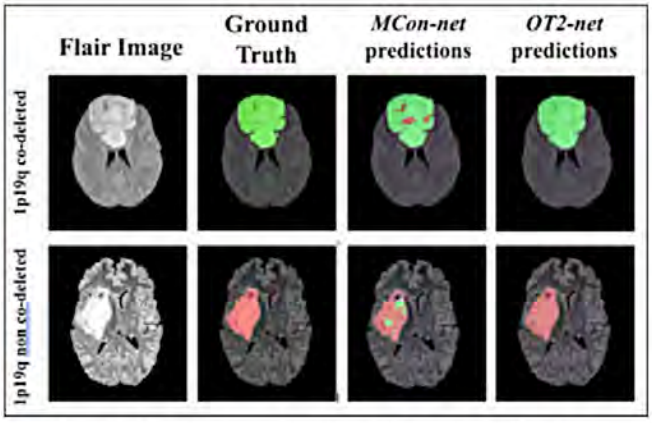

Figure 3. Axial FLAIR images showing MCon-net and OT2-net predictions. Voxel-wise classification is demonstrated with co-deleted voxels appearing in green and non co-deleted voxels in red

887

MRI Imaging Patterns and Perfusion Abnormalities in Subacute Sclerosing Panencephalitis: Correlation with Clinical Stages and Disease Progression

Sabha Ahmed MD DM FRCR[1], Ankit Arora MD DNB[1], Jitender Saini MD DM[1], Viswanathan L G MBBS MD DM[2], Chiraag Mandal[1], Srinivas Meharwade[1], Srinath Reddy Chitti[1]
[1]NIMHANS, BANGALORE, KARNATAKA, India. [2]NIMHANS, Bangalore, Kamataka, India

Abstract Category

Pediatrics

Purpose

To comprehensively study the MR imaging patterns of Subacute Sclerosing Panencephalitis (SSPE) and correlate neuroparenchymal signal changes with perfusion alterations. Additionally, we sought to identify potential imaging biomarkers for clinical outcomes.

Materials & Methods

This retrospective study, conducted at a tertiary Neuroscience institution in India, evaluated MRI scans from 26 confirmed SSPE cases. Conventional sequences (T1, T2, FLAIR, DWI, SWI) and advanced imaging (ASL) were analyzed for neuroparenchymal signal changes and perfusion abnormalities. Clinical data, including presenting symptoms and disease stage, were also recorded.

Imaging was reviewed by two neuroradiologists with 5–7 years of experience, with discrepancies resolved by a senior neuroradiologist. Statistical analysis was used to assess correlations between clinical stage, imaging changes, and perfusion.

Results

Of 26 patients (5 females, 21 males, mean age: [13.67 years]), the clinical stages were: 10 in Stage III, 13 in Stage II, and 3 in Stage I.

- **FLAIR Signal Changes**: Seen in 18 patients, most commonly affecting **bifrontal subcortical white matter (SCWM) and periventricular white matter (PVWM)**, primarily in Stages II and III.
- **DWI Signal Changes**: Observed in 3 patients, predominantly in the **bilateral basal ganglia**, seen in both Stage II and III.
- **SWI Signal Changes**: Noted in 3 patients with **Stage III**, showing **susceptibility rim signs**, but absent in Stage I and II.
- **Perfusion Findings (ASL)**:
    - **Bilateral basal ganglia hyperperfusion** was most common, followed by bilateral occipital hyperperfusion and **bifrontal hypoperfusion**.
    - **Hyperperfusion** was noted in both **Stage II and Stage III**, while **hypoperfusion** was predominantly associated with **Stage III**.

Statistical Analysis:

- **Hypoperfusion on ASL** was significantly associated with **Stage III**, suggesting “burnt-out” demyelination, evidenced by hypointense signals on conventional imaging.
- **Basal ganglia hyperperfusion** was seen in both **Stage II and III**, with **Stage III** patients also showing **SWI rim sign,**
- No clear stage-specific imaging biomarker emerged, though **hyperperfusion** and **hypoperfusion** were observed in both stages, with certain patterns more prominent in advanced disease.

Conclusion

- SWI Rim Sign: A susceptibility rim on SWI is a potential marker of the "burnt-out" phase of SSPE, corresponding with Stage III disease, and signifies advanced demyelination and neuronal damage.
- Perfusion Findings:
    - Hyperperfusion was the most common perfusion alteration in Stages II and III.
    - Hypoperfusion was predominantly seen in Stage III, likely representing more advanced neuronal loss and demyelination.
- Biomarkers and Clinical Correlation: While various imaging abnormalities were noted, no independent imaging biomarker could be conclusively established that correlates perfusion alterations with specific clinical stages or

outcomes. However, these findings suggest that advanced imaging modalities such as ASL and SWI may assist in tracking disease progression and could complement clinical assessment.

References

1. Carra-Dalliere C, Menjot de Champfleur N, Deverdun J, Ayrignac X, Nerrant E, Makinson A, Casanova ML, Labauge P. Use of quantitative susceptibility mapping (QSM) in progressive multifocal leukoencephalopathy. J Neuroradiol. 2016 Feb;43(1):6-10. doi: 10.1016/j.neurad.2015.08.001. Epub 2015 Oct 23. PMID: 26475668.
2. Prasad C, Netravathi M, Kulanthaivelu K, Bhat MD, Pendharkar H. Subacute Sclerosing Panencephalitis: Restricted Diffusion and Clinical Evolution. Neurol India. 2022 Jan-Feb;70(1):275-280. doi: 10.4103/0028-3886.338737. PMID: 35263895.
3. Li R, Jin S, Wang Y, Li JF, Xiao HF, Wang YL, Ma L. Brain Perfusion Alterations on 3D Pseudocontinuous Arterial Spin-Labeling MR Imaging in Patients with Autoimmune Encephalitis: A Case Series and Literature Review. AJNR Am J Neuroradiol. 2022 May;43(5):701-706. doi: 10.3174/ajnr.A7478. Epub 2022 Apr 7. PMID: 35393361; PMCID: PMC9089268.

Images/Tables

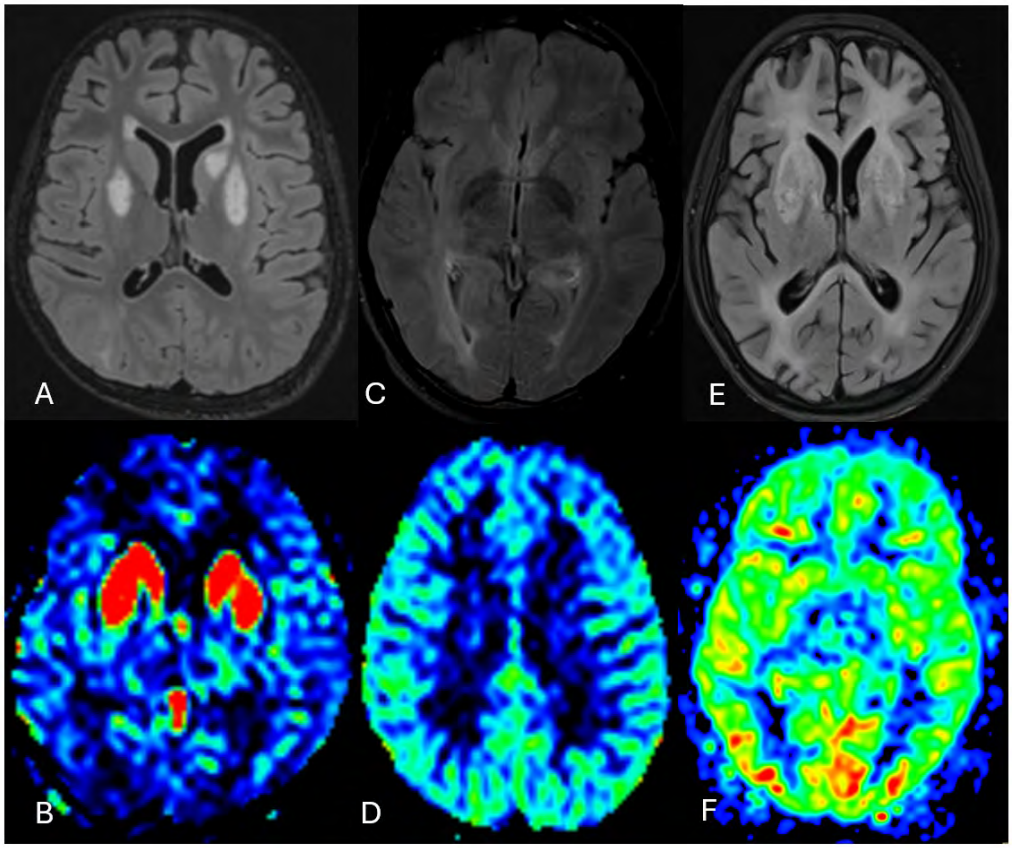

889

Undetected Radiologic Disease Activity on Conventional Side-by-Side Comparison is Associated with Future Radiologic Progression in Multiple Sclerosis: Adopting Semiautomated Coregistration-Fusion into Clinical Practice

Minth - Punpichet MD[1], Timothy Reynold Lim MD[1], Amy Wei Lin MD, FRCPC[1], Shobhit - Mathur MD[1], Yingming Amy Chen MD, FRCPC[1], Aditya - Bharatha MD, FRCPC[1], Jiwon - Oh MD, FRCPC, PhD[2], Suradech - Suthiphosuwan MD, FRCR[1]

[1]Division of Neuroradiology, Department of Medical Imaging, St Michael's Hospital, University of Toronto, Toronto, Ontario, Canada. [2]Division of Neurology, Department of Medicine, St Michael's Hospital, University of Toronto, Toronto, Ontario, Canada

Abstract Category

Adult Brain

Purpose

MRI is an important tool for prognostication, disease monitoring, and assessment of treatment efficacy in people with multiple sclerosis (pwMS).[1] New asymptomatic brain and spinal cord lesions on sequential MRIs are routinely monitored in MS clinical care as their presence is associated with poor clinical outcomes.[1,2] Previous studies have shown that PACS-integrated semi-automated 3D-FLAIR coregistration-fusion method is more sensitive for detecting new/enlarging MS lesions in pwMS than the conventional side-by-side method.[3,4] It is unknown whether undetected radiologic disease activity on an early follow-up scan is related to further radiologic disease progression on subsequent follow-up scans. The aim of this study was to assess whether improved lesion detection using the semi-automated 3D-FLAIR coregistration-fusion method is associated with more accurate predication of future radiologic progression.

Materials & Methods

This retrospective study included relapsing-remitting pwMS who underwent serial brain MRIs at baseline and a follow-up MRI reported as stable on conventional side-by-side method within 12-24 months. These participants also had to have a second follow-up MRI 12-24 months from the first follow-up MRI. The semi-automated coregistration-fusion method was used to compare 3D FLAIR images from the baseline and first follow-up MRIs. Any missed new/enlarging MS lesions were documented. MRI reports of the second follow-up MRI were used to extract information on new radiologic disease activity compared to the first follow-up MRI. Chi-square ($\chi 2$) test was used to compare the presence of radiologic disease activity on the 2nd follow-up MRI between pwMS with and without undetected radiologic disease activity on the 1st follow-up MRI.

Results

250 pwMS (79% females, mean age 45 years) were included. The median time interval of between the 1st follow up and baseline MRIs was 16 months, and undetected new/enlarging MS lesions (median 2 lesions, range 1-17 lesions) based on the side-by-side method were found in 48 pwMSs (19%). The median time interval between 2nd follow-up and 1st follow-up MRIs was 15 months. A significantly higher proportion of pwMS who had undetected radiologic disease activity on the 1st follow-up MRI showed new radiologic activity compared to pwMS who did not have missed radiologic disease activity (82% versus 19.5%, $p<0.001$).

Conclusion

Improved lesion detection using the semi-automated 3D-FLAIR coregistration-fusion method is associated with more accurate predication of future radiologic progression. Incorporating the semi-automated coregistration-fusion method into routine MRI monitoring in pwMS may enable earlier detection of MS disease activity and facilitate treatment optimization, improving long-term outcomes in pwMS.

References

1. Suthiphosuwan S, Kim D, Bharatha A, et al. Imaging Markers for Monitoring Disease Activity in Multiple Sclerosis. Curr Treat Options Neurol. 2017 May;19(5):18.

2. Zecca C, Disanto G, Sormani MP, et al. Relevance of asymptomatic spinal MRI lesions in patients with multiple sclerosis. Mult Scler. 2016 May;22(6):782-91.

3. Galletto Pregliasco A, Collin A, Guéguen A, et al. Improved Detection of New MS Lesions during Follow-Up Using an Automated MR Coregistration-Fusion Method. AJNR Am J Neuroradiol. 2018 Jul;39(7):1226-1232.

4. Dahan A, Pereira R, Malpas CB, et al. PACS Integration of Semiautomated Imaging Software Improves Day-to-Day MS Disease Activity Detection. AJNR Am J Neuroradiol. 2019 Oct;40(10):1624-1629.

Images/Tables

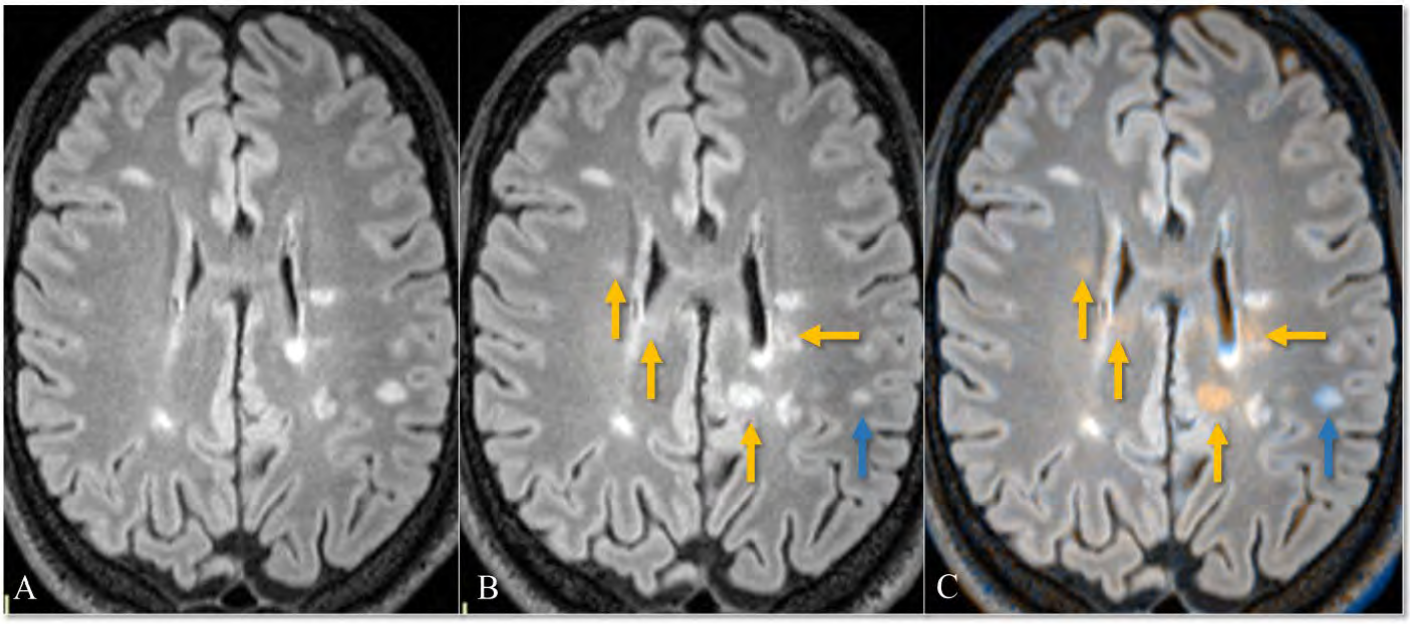

Figure 1: PACS integrated semi-automated co-registration fusion: Axial reformats of 3D FLAIR sequences at baseline (A) and at 1st follow-up (B), and co-registration fusion image (C). New lesions are highlighted in "orange" (orange arrows), and involuting lesions are highlighted in "blue" (blue arrow).

893

Relationship between Apo-E Genotype Status and Amyloid related Imaging Features in Patients with Alzheimer's Disease undergoing Anti-amyloid beta Therapy

Maryam Vejdani-Jahromi MD, PhD, Esteban Calle Cadavid MD, Odette Ganem Chagui, Hana Farzaneh MD, Harry Griffin MD, Shenghua Zhu MD, PhD, Jarrel Seah MBBS, Benjamin Kozak MD, Jeremy Ford MD, Saurabh Rohatgi MD, Javier Romero MD

Harvard Medical School, Massachusetts General Hospital, Boston, MA, USA

Abstract Category

Adult Brain

Purpose

Alzheimer's disease (AD) is a progressive neurodegenerative disorder that primarily affects the aging population. Recent anti-amyloid beta (anti-Aβ) therapies aim to decelerate or halt AD progression, yet identifying individuals at risk for treatment-related side effects—specifically amyloid-related imaging abnormalities (ARIA), including ARIA-E (edema/effusion) and ARIA-H (hemorrhage)—remains a significant clinical challenge. A notable association exists between the ApoE-e4 genotype and microhemorrhages in AD, though the impact of specific ApoE genotypes on amyloid-related imaging changes in patients receiving anti-Aβ therapies requires further investigation. This study aims to examine the association between ApoE genotypes and imaging markers, including microhemorrhages, white matter hyperintensities, perivascular spaces, as well as cognitive function, in patients undergoing Lecanemab treatment.

Materials & Methods

This retrospective study included patients with AD and ApoE genotyping who were considered for Lecanemab therapy. Key measures included microhemorrhage counts, white matter hyperintensity scores, perivascular space assessment, and cognitive function. Microhemorrhages were quantified using susceptibility-weighted imaging (SWI), and cognitive status was assessed via the Montreal Cognitive Assessment (MoCA) on a 30-point scale. White matter hyperintensities were rated on the Fazekas scale (0-3) from FLAIR sequences, and perivascular spaces were scored (1-4) in the Centrum Semiovale and Basal Ganglia regions using T2-weighted images. Imaging assessments were conducted independently by six radiologists blinded to ApoE genotype. Matlab program was used for statistical analysis.

Results

A total of 85 patients (43 male, 42 female; mean age = 71 years) were included. Three patients with rare genotypes (e2/e3, e2/e4) were excluded from the ANOVA analysis due to low frequency. Among the common genotypes, e3/e4 was the most prevalent (45 patients, 55%), followed by e3/e3 (23 patients, 28%) and e4/e4 (14 patients, 17%). Figure 1 shows the prevalence of the common APOE genotypes and relationship between the prevalent Apo-E Genotypes with microhemorrhages, white matter hyperintensities and cognitive scores (MoCa). ANOVA revealed a significant association between ApoE genotype and microhemorrhage count ($p = 0.003$), with an overall mean microbleed count of 1 (e3/e3: mean = 0.7, e3/e4: mean = 0.6, e4/e4: mean = 2.7). However, associations with MoCA scores (mean = 20.0), Fazekas scores for white matter hyperintensities (mean = 1.2), and perivascular spaces (Centrum Semiovale mean = 2.2; Basal Ganglia mean = 1.9) were not statistically significant. Of the 31 patients who received Lecanemab therapy with follow-up imaging, 7 developed ARIA (6 with e3/e4 and 1 with e4/e4). Notably, the single patient with an e2/e4 genotype exhibited a higher-than-average microhemorrhage count (7) compared to e2/e3 carriers (1 and 0 microhemorrhages, respectively).

Conclusion

In this cohort of patients with AD under consideration for Lecanemab, e3/e4 was the most common ApoE genotype. A significant association was observed between the number of microhemorrhages and ApoE genotype status. All the patient who developed ARIA had at least one copy of ApoE-e4 allele. No significant associations were found between ApoE status and white matter hyperintensities, perivascular spaces, or cognitive impairment. Future studies are needed for further characterization of ApoE status and degrees of ARIA-E and ARIA-H developed in patients receiving Lecanemab therapy.

References

1. Ramanan, V. K. & Day, G. S. Anti-amyloid therapies for Alzheimer disease: finally, good news for patients. Mol. Neurodegener. 18, 42 (2023).
2. 2020 Alzheimer's disease facts and figures. Alzheimers Dement. 16, 391–460 (2020).
3. Van Dyck, C., Swanson, C., Aisen, P., et al. Lecanemab in Early Alzheimer's Disease. N. Engl. J. Med. 388, 9–21 (2023).
4. Hampel, H., Elhage, A., Cho, M., et al. Amyloid-related imaging abnormalities (ARIA): radiological, biological and clinical characteristics. Brain 146, 4414–4424 (2023).
5. Kane, M. Lecanemab Therapy and APOE Genotype, Medical Genetics Summary, (August 2024).

Images/Tables

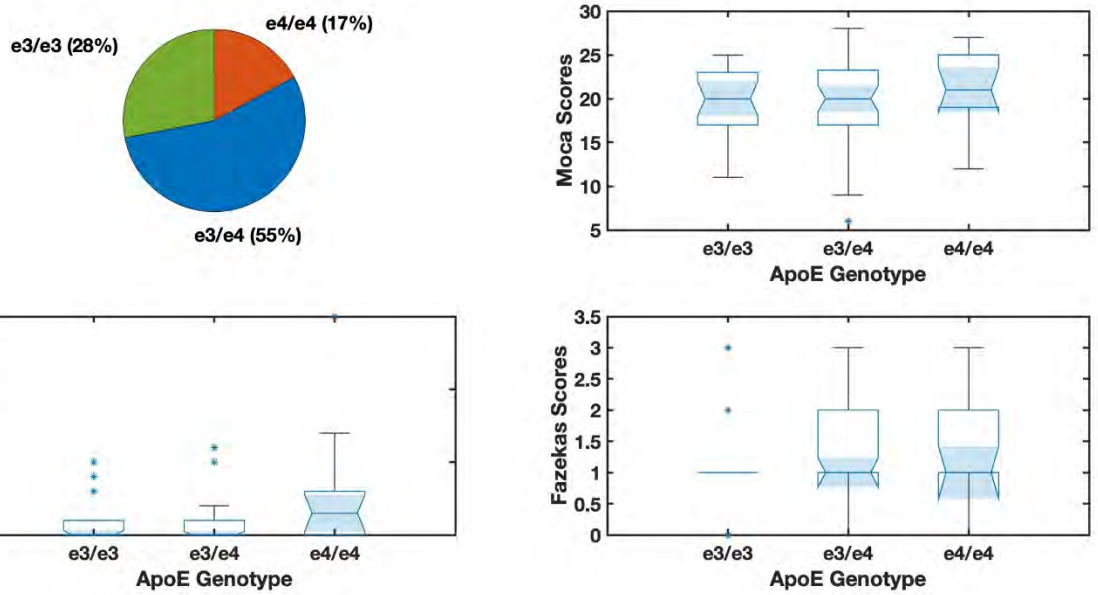

899

Delineating the Link between Cerebral Small Vessel Disease and Alzheimer's Disease with [^{11}C]CS1P1, a Novel PET Tracer of Neuroinflammation

Inema E Orukari MD; PhD, Yujie Wang BEng, Yasheng Chen DSc, Biwen Wang MS, Karl Friedrichsen PhD, Matt Brier MD; PhD, Ying Hwey Nai PhD, Lynne Jones BS, Farzaneh Rahmani MD, Jude-Patrick Okafor MD, Jayashree Rajamanickam BS, Shaney Flores MS, Jin-Moo Lee MD; PhD, Andria Ford MD; MSCI, Zhude Tu PhD, Tammie Benzinger MD; PhD, Hongyu An DSc

Washington University in St Louis, St. Louis, MO, USA

Abstract Category

Adult Brain

Purpose

There are about 7 million Americans diagnosed with Alzheimer's Disease (AD)[1], a type of dementia. Disease modifying therapy (DMT) have been approved with modest benefit, possibly due to DMTs provided late in the disease course[2]. Cerebral small vessel disease (cSVD) is a precursor state that may identify early AD[3]. The diagnosis of cSVD relies on the identification of MRI biomarkers, including white matter hyperintensities (WMHs). Neuroinflammation possibly mediates the development of cSVD[4]. The S1PR1 receptor has been implicated in neuroinflammation through the efficacy of fingolimod – an agonist of the S1PR1 receptor – in treating multiple sclerosis. We have created [^{11}C]CS1P1, a PET probe targeting the S1PR1 receptor in the brain. The goal of this study is to characterize [^{11}C]CS1P1 PET in the setting of cSVD and AD in human subjects.

Materials & Methods

In this study, we enrolled 23 participants who were older than 50 years old (Table 1). Each had an MPRAGE MRI scan for anatomic segmentation of gray matter (GM), white matter, and CSF; a T2 FLAIR MRI scan for segmentation of WMHs (Figure 1) using a deep learning method[5], a [^{11}C]CS1P1 PET scan for quantifying S1PR1 activity (Figure 2), a PiB scan for assessing amyloid burden via Centiloid, and CDR tests for assessing cognition. All the MRI scans were co-registered to the [^{11}C]CS1P1 PET scans and the standard uptake value (SUV) at 45-60 minutes post injection were obtained for the GM, normal appearing white matter (NAWM), and WMH regions of interests (ROIs). Relative WMH volumes that were normalized to the volume of the grey and white matter and log transformed to indicate WMH burden. Ultimately, stepwise multiple linear regression models were performed to evaluate the association between log-transformed relative WMH lesion volume and [^{11}C]CS1P1 PET SUV in WMH, NAWM, and GM ROIs with age, sex, and cSVD vascular risk factors as covariates. Moreover, a correlation analysis was performed between global PiB Centiloid and [^{11}C]CS1P1 PET SUV in WMH, NAWM, or GM.

Results

rV_{WMH} significantly correlated with [^{11}C]CS1P1 PET SUV in the NAWM region (R = 0.4558, p-value = 0.0288). Stepwise multiple linear regression models showed rV_{WMH} was significantly correlated with [^{11}C]CS1P1 PET SUVs from NAWM (adjusted R^2=0.391, beta=1.436, p=0.00978) and GM (adjusted R^2=0.354, beta=0.91972, p=0.0188) (Figure 3), even after controlling for age, sex, and CSVD vascular risk factors. However, [^{11}C]PiB Centiloid values w not significantly correlated with the [^{11}C]CS1P1 SUV due to a bimodal distribution.

Conclusion

Binding of [^{11}C]CS1P1 could potentially identify patient at the early stages of CSVD and AD. These patients may be candidates for disease modifying therapy when the drugs have increased efficacy. Thus, [^{11}C]CS1P1 may play a role in risk stratification in CSVD and AD and may determine novel treatment paradigms. Further studies are needed to evaluate regional amyloid or tau correlations with [^{11}C]CS1P1, [^{11}C]CS1P1 correlation with cognition, and long-term outcomes.

References

1. Alzheimer's Disease Facts and Figures. Alzheimer's Disease and Dementia. Accessed October 28, 2024. https://www.alz.org/alzheimers-dementia/facts-figures

2. Assunção SS, Sperling RA, Ritchie C, et al. Meaningful benefits: a framework to assess disease-modifying therapies in preclinical and early Alzheimer's disease. *Alzheimers Res Ther*. 2022;14(1):54. doi:10.1186/s13195-022-00984-y

3. Cannistraro RJ, Badi M, Eidelman BH, Dickson DW, Middlebrooks EH, Meschia JF. CNS small vessel disease. *Neurology*. 2019;92(24):1146-1156. doi:10.1212/WNL.0000000000007654

4. Evans LE, Taylor JL, Smith CJ, Pritchard HAT, Greenstein AS, Allan SM. Cardiovascular comorbidities, inflammation, and cerebral small vessel disease. *Cardiovasc Res*. 2021;117(13):2575-2588. doi:10.1093/cvr/cvab284
5. Phuah CL, Chen Y, Strain JF, et al. Association of Data-Driven White Matter Hyperintensity Spatial Signatures With Distinct Cerebral Small Vessel Disease Etiologies. *Neurology*. 2022;99(23):e2535-e2547. doi:10.1212/WNL.0000000000201186

Images/Tables

Table 1 – Demographic Characteristics

	mean [percent/range]
Subjects	23 [100%]
Age	66.13 [53 77]
Females	19 [83%]
Race	
Cauc	20 [87%]
AA	3 [13%]
Years of Education	15.70 [13 19]
Cardiac Risk Factors	
Hypertension	11 [48%]
Hypercholesterolemia	9 [39%]
Diabetes	4 [17%]
Stroke	0
Tobacco	9 [39%]
n = 0	5 [22%]
n = 1	6 [26%]
n = 2	5 [22%]
n = 3	4 [17%]
n = 4	1 [5%]
CDR	
n = 0	20 [87%]
n = 0.5	3 [10%]
PiB Centiloid	
Mean CL	15.94 [-15.49 108.91]
CL > 24	6 [26%]
WMH (cm^3)	8.38 [1.005 30.751]

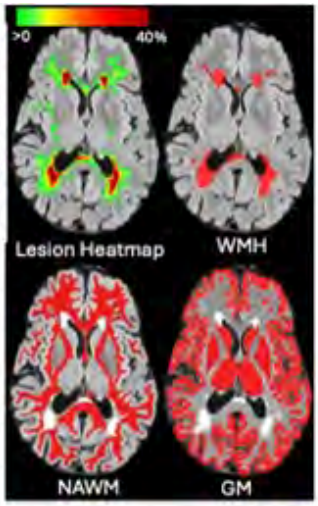

Figure 1 – Brain segmentation. Heatmap of white matter hyperintensities of all 23 subjects in the upper left. In the upper right, the lesion heatmap has a threshold set to above 5% to make a group defined white matter hyperintensity mask. The lower left is a representative normal appearing white matter mask and the lower left is a representative gray matter mask.

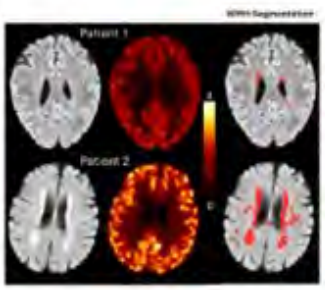

Figure 2. MR FLAIR (left) images, PET 11C-CS1P1 SUV maps (middle), and white matter hyperintensities segmentation for two representative patients with low and high matter hyperintensity (WMH) burden. WMH volumes were 3.3 ml and 20.6 ml from patient 1 and 2, respectively. The mean SUV were 0.85, 1.17, and 1.55 in the WMH, NAWM, and GM, respectively, from patient 1. The mean SUV were 0.91, 1.77, and 2.36 in the WMH, NAWM, and GM, respectively, from patient 2.

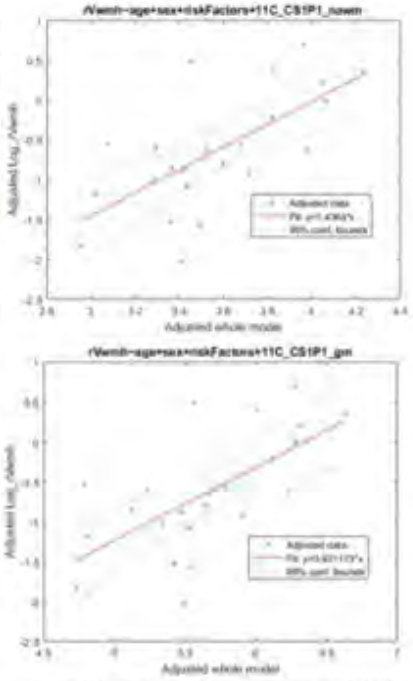

Figure 3. Stepwise multiple linear regression. 11C-CS1P1 SUV values in NAWM (upper, p-value = 0.00978) or GM (lower, p-value = 0.0168) is significantly associated with rV_{Wmh} stepwise multiple linear regression after controlling for age, sex, and cardiac risk factors.

903

Spectrum of Liquid Embolic Distribution on Noncontrast Computed Tomography (NCCT) After Middle Meningeal Artery Embolization (MMAE): Implications for Imaging-Based Prognostication

Arjun Ganga[1], Elias Shaaya MD[2], Santos Santos Fontánez MD[2], Joshua Feler MD, MS[3], Radmehr Torabi MD[2], Krisztina Moldovan MD[2], Mahesh Jayaraman MD[2], Dylan Wolman MD[1]
[1]The Warren Alpert Medical School of Brown University, Providence, Rhode Island, USA. [2]The Warren Alpert Medical School of Brown University, Providence, RI, USA. [3]The Warren Alpert Medical School of Brown University, Pro, RI, USA

Abstract Category

Interventional

Purpose

Liquid embolic agents are increasingly used in middle meningeal artery embolization (MMAE) to treat chronic subdural hematomas (cSDHs), yet the specific patterns of embolic distribution on non-contrast computed tomography (NCCT) following MMAE remain poorly characterized. With the expanding role of MMAE, detailed understanding of post-procedural embolic distribution patterns on imaging is essential. We aim to establish a framework for categorizing the spectrum of visible embolic material on follow-up NCCT after liquid MMAE.

Materials & Methods

A retrospective review was conducted using a prospectively maintained MMAE database for cSDHs >5 mm at a single institution from 2019-2024. Patients with <1 month of follow-up imaging or embolization with coils or particles were excluded. Each cSDH was analyzed as a separate entity. Patterns of embolic distribution were categorized, including membrane penetration during angiography, defined as non-linear embolic material seen outside the vessel course on

roadmap injection images, which then remained visible on un-subtracted images. On post-procedure NCCT, we then classified the anatomic distribution and patterns of visible embolic material as linear or globular in appearance and recorded the anatomic distribution of hyperattenuating embolic material relative to the cSDH collection as either a) inner surface penetration; b) outer surface penetration; or c) penetration within the hematoma. Baseline demographics, including antiplatelet/anticoagulant use and prior cSDH evacuation, were recorded to contextualize imaging findings.

Results

Among 88 patients (73.9% male; mean age 73.5 ± 11.2 years) with 109 unilateral cSDHs, fluoroscopic membrane penetration occurred in 39 cases (35.8%, **Figure 1**). On follow-up NCCT, liquid embolic material was visualized on the outer surface of the cSDH in 85 cases (78.0%), within the hematoma in 16 cases (14.7%), and on the inner surface of the hematoma in 8 cases (7.3%, **Figure 2**). N-butyl-cyanoacrylate (nBCA) was more likely to penetrate the subdural membrane (55.1%) and reach deeper compartments (40.8%) compared to Onyx-18 (17.0% and 7.5%; both $p<0.0001$). Embolic distribution patterns demonstrated that membrane penetration was associated with greater mean absolute cSDH reduction (1.05 cm vs. 0.66 cm, $p<0.001$), mean percent reduction (73.8% vs. 53.5%, $p=0.013$), and resorption rate (0.013 mm/day vs. 0.007 mm/day, $p=0.001$). Deeper compartment penetration of liquid embolic on follow-up NCCT was associated with faster resorption rates (0.014 mm/day vs. 0.008 mm/day, $p=0.010$) without a significant impact on absolute reduction or complete resorption.

Conclusion

We characterize the spectrum of liquid embolic distribution patterns post-MMAE, describing their distinct appearances on NCCT and highlighting the propensity of nBCA for deeper compartment penetration. These findings provide a framework for interpreting post-MMAE embolic patterns on NCCT, with implications for providers to assess procedure efficacy and predict potential resorption outcomes. Further multi-center studies are needed to expand these findings to continue inform imaging-based prognostication in cSDH management.

References

Tudor T, Capone S, Vivanco-Suarez J, et al. Middle Meningeal Artery Embolization for Chronic Subdural Hematoma: A Review of Established and Emerging Embolic Agents. Stroke Vasc Interv Neurol 2023;4(1). DOI: https://doi.org/10.1161/SVIN.123.000906

Images/Tables

Figure 1

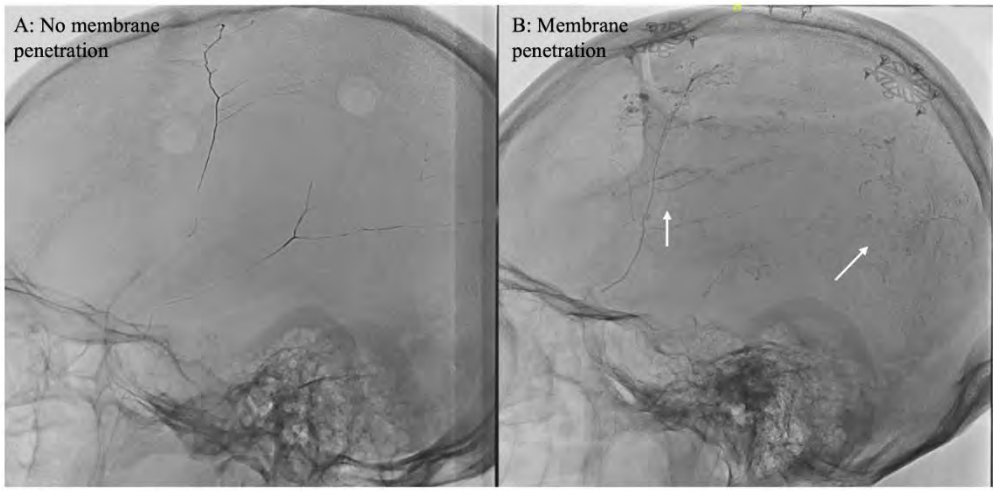

Figure 2

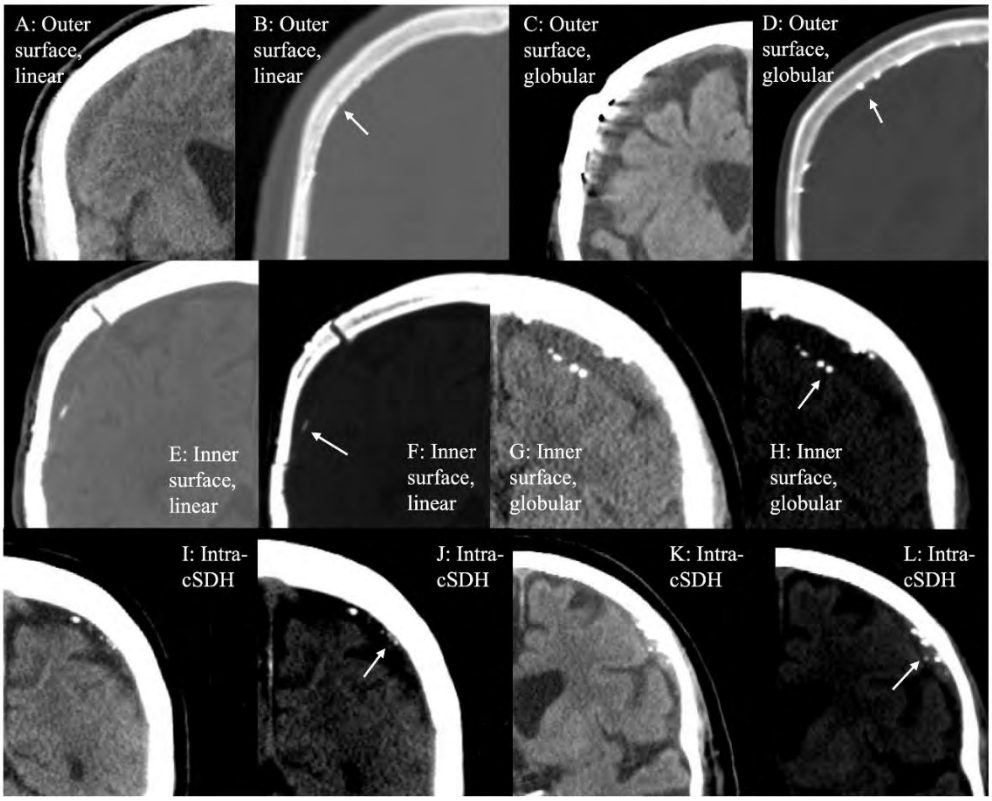

908

Trends and Disparities in Depression Diagnosis Within One-Year of Ischemic Stroke

Maria X Sanmartin PhD[1], Jeffrey K. Katz[1], Mir M Ali[2], Jason J Wang[3], Elizabeth G Cohn[1], Elizabeth Rula[4], Liron D Sinvani[1], Pina Sanelli[1]

[1]Northwell Health, Manhasset, NY, USA. [2]University of Maryland, College Park, Maryland, USA. [3]Northwell Health, Manhasset, NY, USA. [4]Neiman Health Policy, Reston, VA, USA

Abstract Category

Socioeconomics & Health Policy

Purpose

One of the most frequent neuropsychiatric complications after a stroke is post-stroke depression (PSD). However, it is unclear whether disparities exist in the clinical work up of PSD. The main objectives of this study were to estimate the 10-year trend in PSD by socioeconomic characteristics and examine patient characteristics associated with PSD diagnosis.

Materials & Methods

A retrospective cohort study of acute ischemic stroke (AIS) patients admitted to a large, integrated, urban-suburban stroke network comprising 14 hospitals was performed from January 1, 2014, to December 31, 2023. PSD was defined as newly diagnosed major depression by ICD9/10 codes and/or initiation of antidepressant medication up to one-year post-stroke. Data collected from the electronic health records included patient sociodemographic, clinical characteristics, and discharge stroke outcomes (modified Rankin Scale (mRS) and discharge disposition). Trend, bivariate, and multivariable logistic regression analyses were conducted.

Results

Of the 23,514 AIS patients, 15% (3,534) met the study criteria for PSD. The trend analyses showed differences in PSD diagnosis by sociodemographic characteristics. Females and non-Hispanic whites were diagnosed with PSD at higher rates than males and non-white patients, respectively. AIS patients between the ages of 50-79 and median household income (MHI) $80,000-$120,000 had the highest rate of PSD diagnosis. Higher odds of PSD were associated with female sex (OR=1.32 [95% CI:1.22-1.43]), ages 50-79 years (1.26 [1.15-1.38]), Medicare (1.20 [1.09-1.32]) and Medicaid (1.12 [1.02-1.22]) insurance, admission National Institutes of Health Stroke Scale 6-15 (1.23 [1.10-1.37]), discharge mRS 2-3 (1.32 [1.19-1.46]) and 4-5 (1.38 [1.24-1.53]), and discharge to rehabilitation facility (1.40 [1.25-1.56]). Decreased odds of PSD were associated with non-Hispanic Black (0.42 [0.37-0.47]), Hispanic (0.73 [0.64-0.84]), Asian (0.49 [0.42-0.58]), and other races (0.66 [0.58-0.74]); NIHSS 0 (0.83 [0.72-0.94]), MHI < $80,000 (0.74 [0.67-0.82]) and MHI $80,000-$120,000 (0.81 [0.74-0.88]).

Conclusion

PSD diagnosis was more likely in females, non-Hispanic white, middle-aged patients, with moderate stroke severity upon presentation and poor functional outcomes at discharge. Although PSD diagnosis was less likely in Blacks, Hispanics, and Asians, more uniform and rigorous depression screening in these groups may help to identify PSD in minority groups.

References

Medeiros GC, Roy D, Kontos N, Beach SR. Post-stroke depression: A 2020 updated review. *Gen Hosp Psychiatry*. 2020;66:70-80. doi:10.1016/j.genhosppsych.2020.06.011

2. Ayerbe L, Ayis S, Wolfe CDA, Rudd AG. Natural history, predictors and outcomes of depression after stroke: systematic review and meta-analysis. *British Journal of Psychiatry*. 2013;202(1):14-21. doi:10.1192/bjp.bp.111.107664

3. Mitchell AJ, Sheth B, Gill J, et al. Prevalence and predictors of post-stroke mood disorders: A meta-analysis and meta-regression of depression, anxiety and adjustment disorder. *Gen Hosp Psychiatry*. 2017;47:48-60. doi:10.1016/j.genhosppsych.2017.04.001

4. Das J, G.K. R. Post stroke depression: The sequelae of cerebral stroke. *Neurosci Biobehav Rev*. 2018;90:104-114. doi:10.1016/j.neubiorev.2018.04.005

5. Terrill AL. Mental Health Issues Poststroke: Underrecognized and Undertreated. *Stroke*. 2023;54(6):1528-1530. doi:10.1161/STROKEAHA.123.042585

Images/Tables

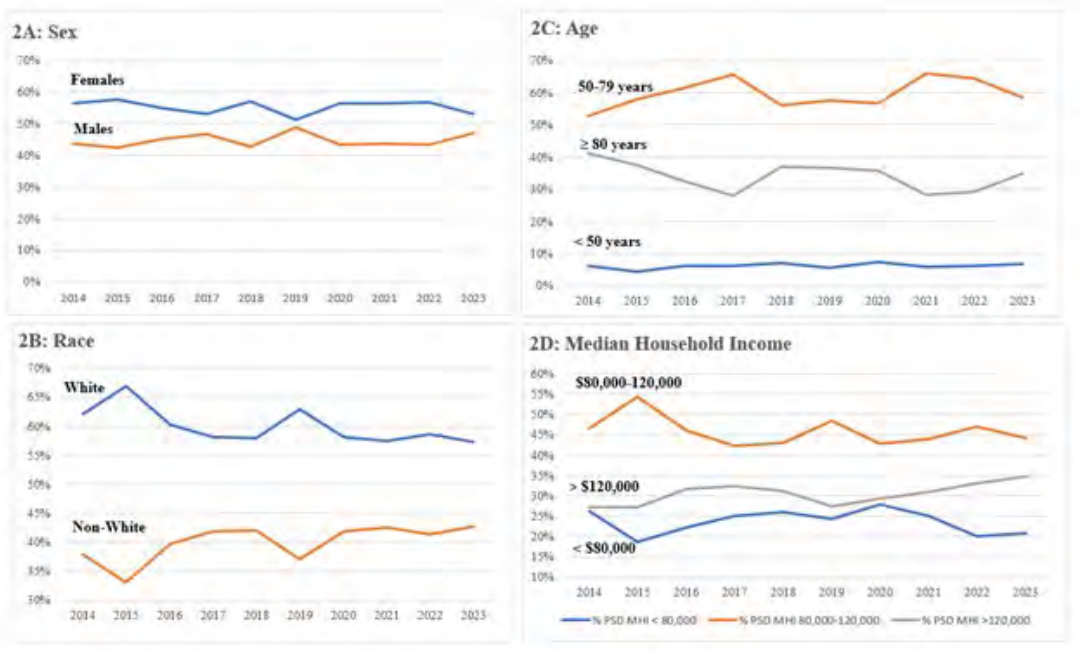

912

^{18}F-Fluoroethyltyrosine (^{18}F-FET) PET Volumes Derived from Maximum Tumor to Brain Ratio (TBRmax) Threshold Cutoffs Contain Prognostic Information in Patients with Diffuse Adult Type Glioma

Shaun D Grega[1], Nathaniel J Smith[1], Keith George Ciantar[2], Matthew E Larson[3], Mark Tann[1], Wendy Territo[1], Brian D Graner[1], Sharon Sidenbender[1], Mark A Green[1], Karl-Josef Langen[2], Norbert Galldiks[2], Philipp Lohmann[2], Michael C Veronesi[3]

[1]Department of Radiology and Imaging Sciences, Indianapolis, Indiana, USA. [2]Institute of Neuroscience and Medicine (INM-3/INM-4), Juelich (FZJ), NRW, Germany. [3]Department of Radiology, Madison, Wisconsin, USA

Abstract Category

Functional/Advanced Imaging

Purpose

O-(2-[^{18}F]fluoroethyl)-L-tyrosine (^{18}F-FET) is an increasingly utilized amino acid radiotracer for positron emission tomography (PET) imaging of patients with malignant brain tumors[1] as recommended by EANO/RANO/SNMMI working groups[2] and is nearing FDA approval in the U.S for glioma imaging. ^{18}F-FET PET targets the L-amino transporter 1 (LAT1) receptor, is upregulated in malignant tumors, and can be quantified based on, e.g., the tumor to brain ratio (TBR, equivalent to SUV of tumor/SUVmean of normal brain). The purpose of this study was to determine whether ^{18}F-FET PET volumes at a given TBR threshold add additional prognostic information combined with non-volumetric TBR thresholds.

Materials & Methods

Patients with adult diffuse type gliomas (WHO Grade 3 and 4 glioma) with a brain MRI equivocal for progressive disease vs treatment-induced changes underwent a hybrid ^{18}F-FET PET/MRI (3T Biograph mMR; Siemens) during routine clinical care at a U.S. institution through Expanded Access use (Indiana University, EA IND# 150833) as previously published1. Sixty-one patients (45/61 grade 4; median age 52 yrs (17 – 77 yrs); 41/61 male from Aug 2022 - Jun 2023) were included in the study. Using the MiM Software®v7.4, 3 independent analysts (neuroradiologist, PET imaging analyst, and medical student) identified the TBRmax which allowed generation of TBR maps (Figure 1). A single VOI was generated and volumes above a TBR threshold of 1.6, 2.0, 2.5, 3.0, 3.5, 4.0, 4.5, and 5.0 were calculated. Intraclass correlation coefficients (ICC 2,1) were calculated according to the method of Shrout[4]. Receiver-operator characteristic (ROC) enabled calculation of thresholds for prediction of tumor progression and treatment-related changes using mean reader volumetric calculations. Kaplan-Meier survival analysis was subsequently performed with patients stratified by tumor volumes exceeding the calculated ROC thresholds.

Results

ICC values showed high concordance (r > 90%) among readers of varying expertise at all TBR volumetric thresholds. ROC analysis identified volumes of 8.4 mL, 2.1 mL, and 0.6 mL as optimal cutoffs for TBR thresholds above 1.6, 2.0, and 2.5, respectively. Kaplan-Meier analysis demonstrated significant survival differences between active tumor volume groups, as well as poor survival with any tumor volume exceeding a TBR of 3.0 (not shown). A TBRmax threshold of 2.5 was also prognostically significant.

Conclusion

^{18}F-FET PET volumetric analysis provides relevant prognostic information in cases where maximal tumor uptake remains low. Active tumor volume may be used in conjunction with TBRmax in assessing prognosis and making timely treatment modifications. The follow-up time for patients in this study remains too short to fully characterize median survival for patients not meeting volumetric uptake thresholds.

References

1. Smith NJ et al., Hybrid ^{18}F-Fluoroethyltyrosine PET and MRI with Perfusion to Distinguish Disease Progression from Treatment-Related Change in Malignant Brain Tumors: The Quest to Beat the Toughest Cases. J Nucl Med. 2023 Jul;64(7):1087-1092.
2. Law et al. Joint EANM/EANO/RANO practice guidelines/SNMMI procedure standards for imaging of gliomas using PET with radiolabelled amino acids and [18F]FDG: v1.0. Eur J Nucl Med Mol Imaging 2019;46:540–57.
3. Shrout PE, Fleiss JL. Intraclass correlations: Uses in assessing rater reliability. Psychological Bulletin 1979;86:420–8. 82 words

Images/Tables

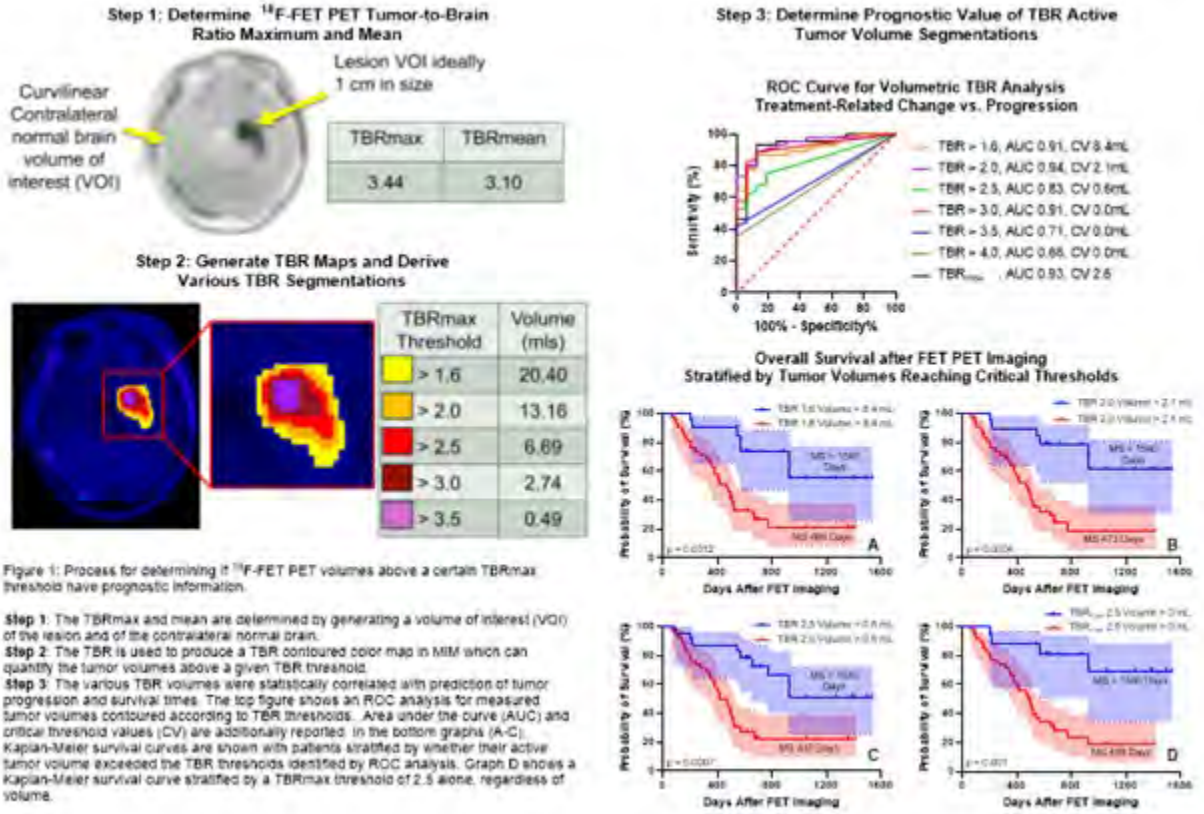

Figure 1: Process for determining if ^{18}F-FET PET volumes above a certain TBRmax threshold have prognostic information.

Step 1: The TBRmax and mean are determined by generating a volume of interest (VOI) of the lesion and of the contralateral normal brain.
Step 2: The TBR is used to produce a TBR contoured color map in MIM which can quantify the tumor volumes above a given TBR threshold.
Step 3: The various TBR volumes were statistically correlated with prediction of tumor progression and survival times. The top figure shows an ROC analysis for measured tumor volumes contoured according to TBR thresholds. Area under the curve (AUC) and critical threshold values (CV) are additionally reported. In the bottom graphs (A-C): Kaplan-Meier survival curves are shown with patients stratified by whether their active tumor volume exceeded the TBR thresholds identified by ROC analysis. Graph D shows a Kaplan-Meier survival curve stratified by a TBRmax threshold of 2.5 alone, regardless of volume.

919

Assessing the Correlation Between Freezing of Gait and Visual Disorders in Parkinson's Disease: A Study of Associated Brain Networks

SARA NAGHIZADEHKASHANI[1], Omid Shoraka[2], Caio Matias[2], Mahdi Alizadeh[2]
[1]Thomas Jefferson University, Philadelphia, PA, USA. [2]Philadelphia, PA, USA

Abstract Category

Functional/Advanced Imaging

Purpose

Gait and visual disorders are recognized as debilitating symptoms in individuals with Parkinson's disease (PD). (1) The primary goal of this study is to assess whether there is a correlation between the emergence of freezing of gait (FOG) and visual disorders (VD) in PD subjects. The secondary goal is to investigate the potential brain regions responsible for the onset of these symptoms.

Materials & Methods

11 PD subjects with FOG and 29 PD subjects with no gait disorder (NGD) were recruited. VD were identified, and each group was divided into two subgroups based on VD presence: FOG+VD, FOG-VD, NGD+VD, and NGD-VD. Resting-state fMRI was performed using a 3T Siemens scanner with 64 channels head and neck coil. Inter-subject hemisphere dominance was uniformed by flipping the MRI to align the disease-dominant hemisphere. ROI-to-ROI analysis was performed using Conn toolbox. Group-based analysis was then performed between each pair of the two groups. The voxel threshold p-value was set at <0.05, with Bonferroni correction applied for multiple comparisons (0.05/170=0.00029). Network analysis was controlled for disease and dopaminergic therapy duration as confounding variables.

Results

Visual disorders, longer disease duration, and extended dopaminergic therapy were correlated with the presence of FOG in subjects with PD (Table 1). After conducting ROI-to-ROI network analysis between subjects with FOG+VD and FOG-VD, the salience network demonstrated increased functional connectivity (FC) with regions from the language network.

When comparing subjects with NGD+VD to NGD-VD, four pairs of networks demonstrated increased FC, and one pair showed decreased FC. Details of these networks are provided in Table 2 and Figures 1-2.

Conclusion

Disrupted FC in the salience and default mode networks is a significant factor in the emergence of visual and gait disorders. Alterations in FC, especially in the salience network, are correlated with both manifestations in PD subjects.

References

Gan L, Yan R, Su D, et al. Alterations of structure and functional connectivity of visual brain network in patients with freezing of gait in Parkinson's disease. Frontiers in Aging Neuroscience. 2022 Sep 7;14:978976.

Images/Tables

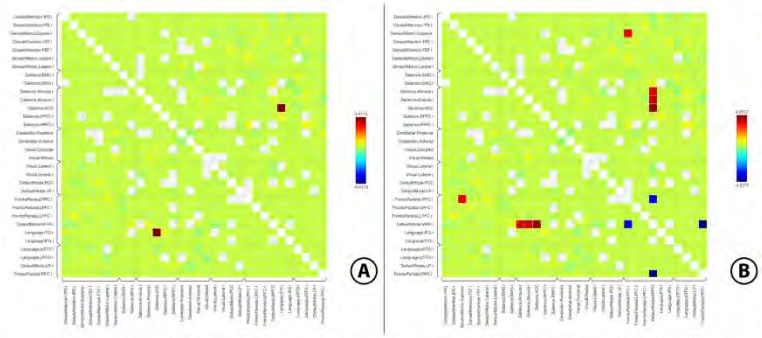

Figure 1. Graph theory diagrams of A. One pair of regions demonstrating increased functional connectivity (red square) in FOG+VD compared to FOG-VD B. Five pairs of regions demonstrating both increased and decreased (blue square) functional connectivity in NGD+VD compared to NGD-VD.

Table 1. Demographics and disease related variables in PD subjects with freezing of gait vs. PD subjects with no gait disorders

	Total, N=40	No Gait Disorder, N=29	Freezing of Gait, N=11	p-value
Age, mean±SD	65.4 ± 8.9	65.9 ± 8.9	64.1 ± 9.2	0.573
Gender, Male n (%)	27 (67.5)	20 (69.0)	7 (63.6)	0.748
UPDRS III, mean±SD	22.6 ± 13.2	21.3 ± 12.1	25.8 ± 15.9	0.401
Tremor Dominant Disease, n (%)	30 (75.0)	22 (75.9)	8 (72.7)	0.838
Symptom Side, Right n (%)	19 (47.5)	12 (41.4)	7 (63.6)	0.208
Handedness, Right n (%)	29 (87.9)	23 (88.5)	6 (85.7)	0.843
Disease Duration, mean±SD	8.8 ± 3.4	8.1 ± 3.1	10.7 ± 3.6	0.029
Dopaminergic Therapy Duration, mean±SD	6.2 ± 3.0	5.1 ± 2.1	8.7 ± 3.5	<0.001
Presence of Any Visual Disorders, n (%)	12 (30.0)	6 (20.7)	6 (54.5)	0.037

Bold value indicates statistical significance. (p-value<0.05)

Table 2. ROI-to-ROI brain connectivity results comparing FOG+VD versus FOG-VD, and NGD+VD versus NGD-VD.

Pairwise Analysis	Networks		T-value	p-unc	p-FDR
FOG+VD vs. FOG-VD	Salience ACC	NDDS Language IFC	3.41	1.3×10^{-3}	6.4×10^{-1}
NGD+VD vs. NGD-VD	Salience ACC	DMN MPFC	4.06	1.7×10^{-4}	4.3×10^{-2}
	Salience AI	DMN MPFC	3.44	1.2×10^{-3}	1.2×10^{-1}
	Sensorimotor Superior	FP DDS PPC	3.36	1.5×10^{-3}	1.2×10^{-1}
	FP PPC	DMN MPFC	-3.38	1.4×10^{-3}	1.2×10^{-1}

The red line connecting each pair of regions indicates increased functional connectivity (FC), while the blue line indicates decreased FC.
Abbreviations: FOG, Freezing of Gait; NGD, No Gait Disorders; VD, Visual disorders; ACC, Anterior Cingulate Cortex; IFC, Inferior Frontal Cortex; IFG, Inferior Frontal Gyrus; MPFC, Middle Prefrontal Cortex; AI, Anterior Insula; PPC, Posterior Parietal Cortex; FP, Frontoparietal Network; DMN, Default Mode Network; DDS, Dominant Disease Side; NDDS, Nondominant Disease Side

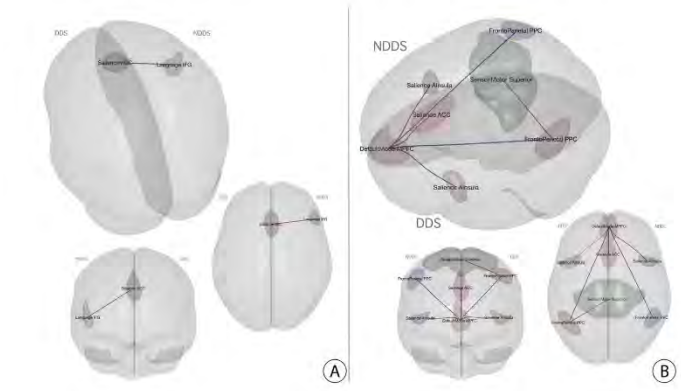

Figure 2. 3D brain maps of A. One pair of regions demonstrating increased functional connectivity (red line) in FOG+VD compared to FOG-VD B. Five pairs of regions demonstrating both increased and decreased (blue line) functional connectivity in NGD+VD compared to NGD-VD.
Abbreviations: FOG, Freezing of Gait; NGD, No Gait Disorders; VD, Visual disorders; ACC, Anterior Cingulate Cortex; IFC, Inferior Frontal Cortex; IFG, Inferior Frontal Gyrus; MPFC, Middle Prefrontal Cortex; AI, Anterior Insula; PPC, Posterior Parietal Cortex; FP, Frontoparietal Network; DMN, Default Mode Network; DDS, Dominant Disease Side; NDDS, Nondominant Disease Side

929

Deep Learning Image Reconstruction for Enhancing Image Quality and Acquisition Speed in 3T EDGE-MP2RAGE

Manasi Arora MBBS, Vishal Patel MD, PhD, Shengzhen Tao Phd, Chen Lin PhD, Erik H Middlebrooks MD
Mayo Clinic, Jacksonville, Florida, USA

Abstract Category

Functional/Advanced Imaging

Purpose

The 3D edge-enhancing gradient echo (EDGE) sequence has been shown to improve visualization and detection of subtle cortical lesions, such as focal cortical dysplasia (FCD). However, the signal-nulling effect results in relatively low contrast-to-noise ratio (CNR) necessitating long scan times. Image quality and scan time are improved with 7T EDGE; however, there is limited access to 7T MRI. Application of deep learning (DL) image reconstruction has recently shown substantial improvements in scan time and image quality versus traditional acceleration techniques. In this study, we assess a novel 3T DL EDGE-MP2RAGE sequence that aims to substantially reduce scan time and simultaneously improve CNR with comparison to a standard 3T EDGE-MP2RAGE and 7T EDGE-MP2RAGE.

Materials & Methods

We conducted a retrospective study of 50 MRI scans (20 DL 3T, 20 standard 3T, and 10 7T MRIs). The standard 3T EDGE-MP2RAGE was acquired in 8:47 mins at 1mm isotropic voxels and 7T EDGE-MP2RAGE was acquired in 9:02 mins at 0.8mm isotropic voxels. The 3T DL EDGE-MP2RAGE was acquired in 4:44 mins at 1mm isotropic voxels. For quantitative

analysis, manual ROIs were placed in the corpus callosum and caudate head. Noise was measured as the standard deviation (SD) of the signal intensity in the homogenous corpus callosum ROI. CNR was calculated as the absolute difference in the mean signal intensity of the two regions divided by the noise. Data were expressed as a median with 95% CI. Quantitative metrics were compared using a two-sided, nonparametric Mann-Whitney test with a Bonferroni-corrected p-value <0.05 considered significant.

Results

The 3T DL EDGE-MP2RAGE image acquisition resulted in a 46.1% time decrease versus standard 3T and 47.6% time decrease versus 7T. There was a significant decrease in noise in the 3T DL sequence versus the standard sequence (median 7.1 [95% CI: 6.5 - 7.9] versus 9.8 [95% CI: 8.0 - 11.5]; p=0.0007), as well as increased CNR in the 3T DL sequence (median 13.6 [95% CI: 12.1 - 16.3] versus 7.1 [95% CI: 6.4 - 8.9]; p<0.0001). The noise decreased by a median of 27.6% and a 91.6% increase in CNR.

Compared to 7T, the 3T DL EDGE had significantly lower noise (median 7.1 [95% CI: 6.5 - 7.9] versus 11.5 [95% CI: 9.0 - 15.9]; p<0.0001) and greater CNR (median 13.6 [95% CI: 12.1 - 16.3] versus 8.0 [95% CI: 7.1 - 10.2]; p<0.0001). The 3T DL had a 38.3% decrease in noise and 70% increase in CNR versus the 7T EDGE.

Conclusion

With a nearly 50% decrease in image time versus standard 3T and 7T EDGE-MP2RAGE, our 3T DL EDGE-MP2RAGE still outperforms in image quality metrics with statistically significant less noise and greater CNR compared to standard 3T and 7T EDGE-MP2RAGE. Our approach increases the feasibility and access to EDGE and may facilitate improved detection of cortical lesions.

References

1. Middlebrooks E.H., et al., *Improved detection of focal cortical dysplasia using a novel 3D imaging sequence: Edge-Enhancing Gradient Echo (3D-EDGE) MRI.* Neuroimage Clin. 2020; **28**:102449.
2. Middlebrooks, E.H., et al., *Edge-Enhancing Gradient Echo MRI at 7T for detection of focal cortical dysplasia in epilepsy.* Neuroimage: Reports, 2023. **3**(4): p. 100187.
3. Suh, P.S., et al., *Improving Diagnostic Performance of MRI for Temporal Lobe Epilepsy With Deep Learning-Based Image Reconstruction in Patients With Suspected Focal Epilepsy.* Korean J Radiol, 2024. **25**(4): p. 374-383.
4. Tao, S., et al., *Edge-Enhancing Gradient-Echo MP2RAGE for Clinical Epilepsy Imaging at 7T.* AJNR Am J Neuroradiol, 2023. **44**(3): p. 268-270.

Images/Tables

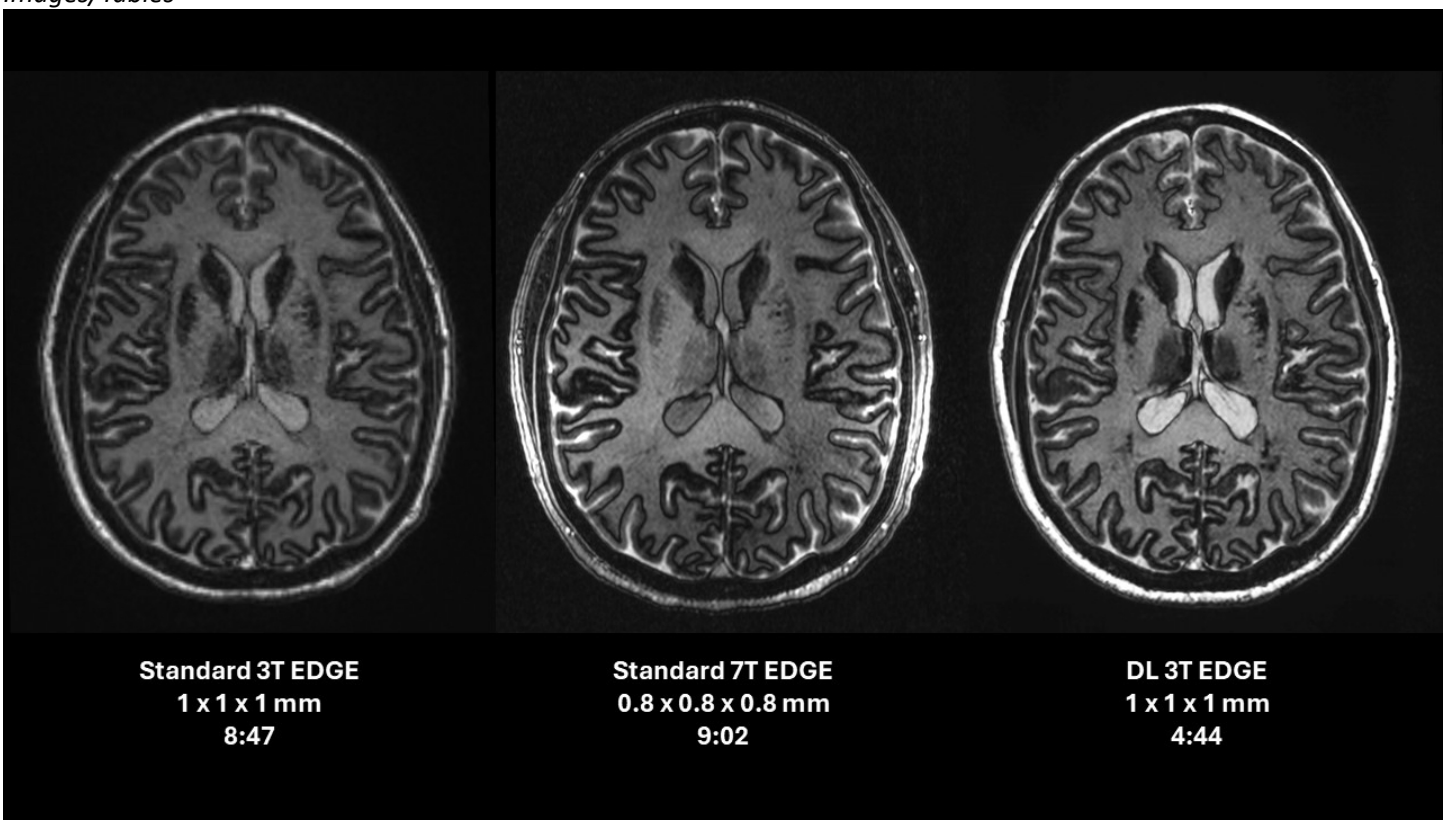

930

Enhancing Brain MRI Synthesis Using Conditional Diffusion Models with Brain and Tumor Mask Guidance

Moinak Bhattacharya[1], Prateek Prasanna[1], Gagandeep Singh[2]
[1]Stony Brook University, Stony Brook, New York, USA. [2]Columbia University, New York, New York, USA

Abstract Category

AI/Informatics

Purpose

Data scarcity is a significant challenge in medical imaging research, particularly in neurooncology. Limited data hampers the ability to train robust machine learning models, restricting advancements in automated diagnostic tools and personalized treatment strategies. Existing methods to augment datasets often fall short due to issues with image quality, diversity, and realism, which can lead to suboptimal model performance. Generative models, such as generative adversarial networks (GANs), have been employed to address these limitations; however, they frequently struggle with stability and producing consistent, high-resolution outputs. This is where diffusion models come into play[1]. This study explores the use of diffusion models for generating synthetic brain MRI images, aiming to enhance the quality and variability of datasets for brain tumor research. By introducing brain and tumor masks as additional conditional inputs, we enable finer control over the image synthesis process, particularly in localizing and visualizing tumor regions within generated images[2]. This approach holds promise for aiding training in machine learning models, data augmentation in clinical studies, and pre-clinical model development, ultimately contributing to improved diagnostic accuracy and individualized patient care.

Materials & Methods

A Stable Diffusion model was initially pre-trained on MRI images from the BRATS dataset using 2D slices extracted from the MRI volumes. Each slice was normalized and resized to resolutions of 64x64 and 128x128 pixels. Training employed a Mean Squared Error (MSE) loss function and the Adam optimizer, with a learning rate of 2.5e-5. Following initial training, the model was fine-tuned with additional conditioning signals from brain and tumor masks. During this retraining phase, most parameters of the pre-trained model were locked to preserve the core MRI image structure, while specific layers were selectively updated to integrate the new conditional information effectively. We use Fréchet Inception Distance (FID) and Structural Similarity Index Measure (SSIM) to evaluate the generated image quality.

Results

The proposed approach resulted in a model capable of generating high-quality brain MRIs with tumor regions accurately represented according to the input conditions. The ControlNet model trained at a resolution of 64x64 achieves a FID score of 76.03±10.47 (FLAIR: 84.65, T1: 77.00, T1CE: 83.82, T2: 58.64) and an SSIM score of 0.34±0.07 (FLAIR: 0.45, T1: 0.34, T1CE: 0.28, T2: 0.30). In comparison, the ControlNet model trained at a resolution of 128x128 achieves a FID score of 76.65±14.71 (FLAIR: 90.23, T1: 74.46, T1CE: 88.44, T2: 53.46) and an SSIM score of 0.26±0.04 (FLAIR: 0.20, T1: 0.31, T1CE: 0.27, T2: 0.25).

Conclusion

Conditional generation with brain and tumor masks in diffusion models enables the creation of clinically plausible and anatomically accurate synthetic brain MRIs. This method offers a valuable tool for augmenting medical imaging datasets, which can significantly enhance the robustness of model training for brain tumor detection, segmentation, and classification tasks. By generating diverse yet realistic images, this approach helps in training deep learning algorithms that are more generalizable, ultimately improving their performance in real clinical scenarios.

References

1. Ho, Jonathan, Ajay Jain, and Pieter Abbeel. "Denoising diffusion probabilistic models." *Advances in neural information processing systems* 33 (2020): 6840-6851.
2. Zhang, Lvmin, Anyi Rao, and Maneesh Agrawala. "Adding conditional control to text-to-image diffusion models." *Proceedings of the IEEE/CVF International Conference on Computer Vision*. 2023.

Images/Tables

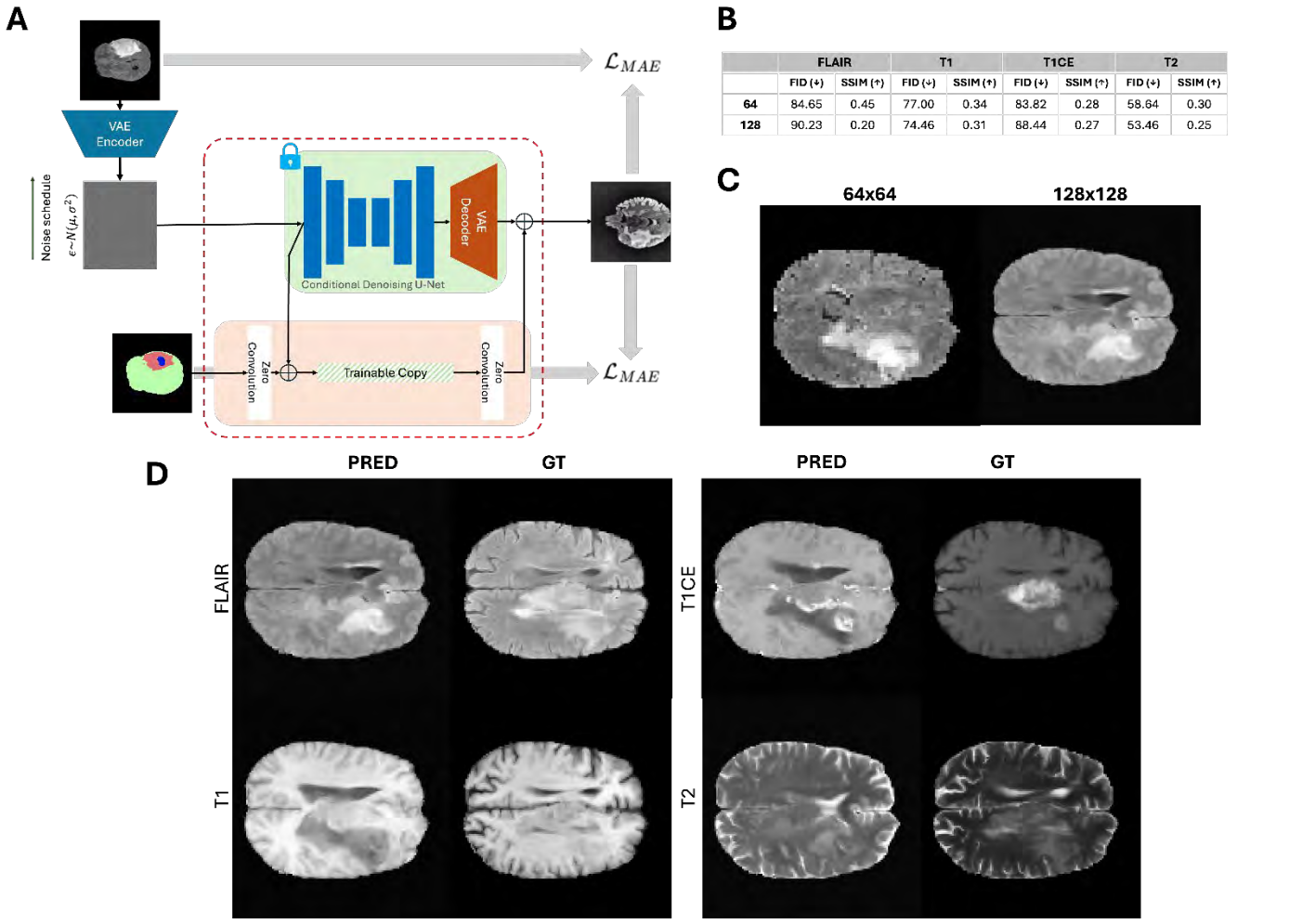

	FLAIR		T1		T1CE		T2	
	FID (↓)	SSIM (↑)	FID (↓)	SSIM (↑)	FID (↓)	SSIM (↑)	FID (↓)	SSIM (↑)
64	84.65	0.45	77.00	0.34	83.82	0.28	58.64	0.30
128	90.23	0.20	74.46	0.31	88.44	0.27	53.46	0.25

Figure: A. The pipeline of a diffusion model incorporating brain and tumor masks as control inputs, B. Image quality assessment metrics, including FID and SSIM, are reported for resolutions of 64x64 and 128x128, C. Examples of images generated by the models at 64x64 and 128x128 resolutions are presented, D. Ground truth (GT) and predicted (PRED) images of various MRI sequences are shown for qualitative comparison.

942

Deep and Machine Learning for Automated Segmentation of Acute Ischemic Stroke: a Systematic Review and Meta-Analysis

Michelle Zhu[1], Yun Jun Jiang[2], Li Ting Ngiam[3], Srijan Bhasin[4], Jin Hean Koh[5], Doreen Goh[2], Derrick Murcia[1], Septian Hartono[2], Ling Ling Chan[2]

[1]University of Texas Southwestern Medical Center, Dallas, Texas, USA. [2]Singapore General Hospital, Singapore, Singapore, Singapore. [3]Singapore, Singapore, Singapore. [4]Duke University School of Medicine, Durham, North Carolina, USA. [5]Duke-NUS Medical School, Singapore, Singapore, Singapore

Abstract Category

AI/Informatics

Purpose

As artificial intelligence (AI) becomes more ubiquitous, clinicians should have a better understanding of the research basis before adopting AI clinical tools. Recent machine learning (ML) and deep learning (DL) approaches for automated localization and contouring of acute ischemic stroke (AIS) hold promise to alleviate clinical burden of this top indication for brain MRI orders [1]. In this systematic review and meta-analysis (SRMA), we evaluate current AI model accuracy of AIS segmentation and the impacts of data curation and annotation decisions on performance.

Materials & Methods

Systematic review was performed of articles published from January 2010 to December 2023 in PubMed, Web of Science, Scopus, Embase, and Cochrane that satisfied inclusion criteria of: 1) diffusion weighted imaging (DWI) dataset, 2) AIS as indication for MRI, and 3) ML/DL methodology for AIS semantic segmentation.

Data was collected according to an adaptation of the Minimum Information about Clinical Artificial Intelligence Modeling (MI-CLAIM) checklist. Study quality and applicability was assessed using Radiological Society of North America's (RSNA) 9 key considerations for evaluating AI research.

Random-effects meta-analysis combined results from all studies with dice similarly coefficient (DSC). Subgroup analyses examined the effects on performance of data curation and AI model decisions. Publication bias was assessed using a funnel plot and Egger's bias test.

Results

There were 1149 initial studies reduced to 25 for systematic review, and 13 for meta-analysis where dice similarity coefficient (DSC) was available. The pooled average DSC on unseen test sets was 0.79 (95% CI 0.73-0.86, n=13) with moderate heterogeneity (Higgins I^2 = 72.50%), with inter-rater DSC within studies of 0.75 (95% CI 0.64-0.86, n=5) and pooled external validation DSC of 0.75 (95% CI 0.53-0.98, n=3). Publication bias was high with funnel plot asymmetry and Egger's bias test ($p<0.01$). There was average of 5 out of 9 points addressed of RSNA's 9 key considerations for evaluating AI research.

On subgroup analysis of model architecture and preprocessing strategies, DL performed better than classical ML ($p<0.01$). Strategies including internal validation methods had superior performance to hold-out, K-fold, and leave-one-out cross validation methods ($p=0.04$). Other factors resulted no difference, including normalization of DWI to standardized anatomical space ($p=0.89$), use of ensemble ($p=0.36$), U-Net as backbone ($p=0.26$), and 2D versus 3D DL architectures ($p=0.72$).

Dataset characteristics such as annotator expertise (neuroradiologist, non-neuroradiologist medical doctor, non-medical doctor) ($p=0.04$) and retrospective data curation ($p=0.04$) also showed effect on AI performance. Magnetic strength by 3-T or 1.5-T of MRI machine used to procure DWI images had no effect on performance ($p=0.06$).

Conclusion

We conclude that most current deep learning models produce adequate performance, comparable to inter-rater DSC scores within studies. Dataset quality by level of annotator expertise and retrospective data curation affect performance. DL and internal validation methods affect performance, though other AI model design decisions do not. 1.5-T MRI scanners may be used without loss in performance. Our findings may guide future model development decisions. However, more testing on additional diverse, real-world and international datasets is required for future directions to generalizable and reliable AI adequate for clinical application.

References

[1] Sheth SA, Giancardo L, Colasurdo M, et. al. Machine learning and acute stroke imaging. *J NeuroIntervent Surg* 2023;15:195–199. doi:10.1136/neurintsurg-2021-018142

Images/Tables

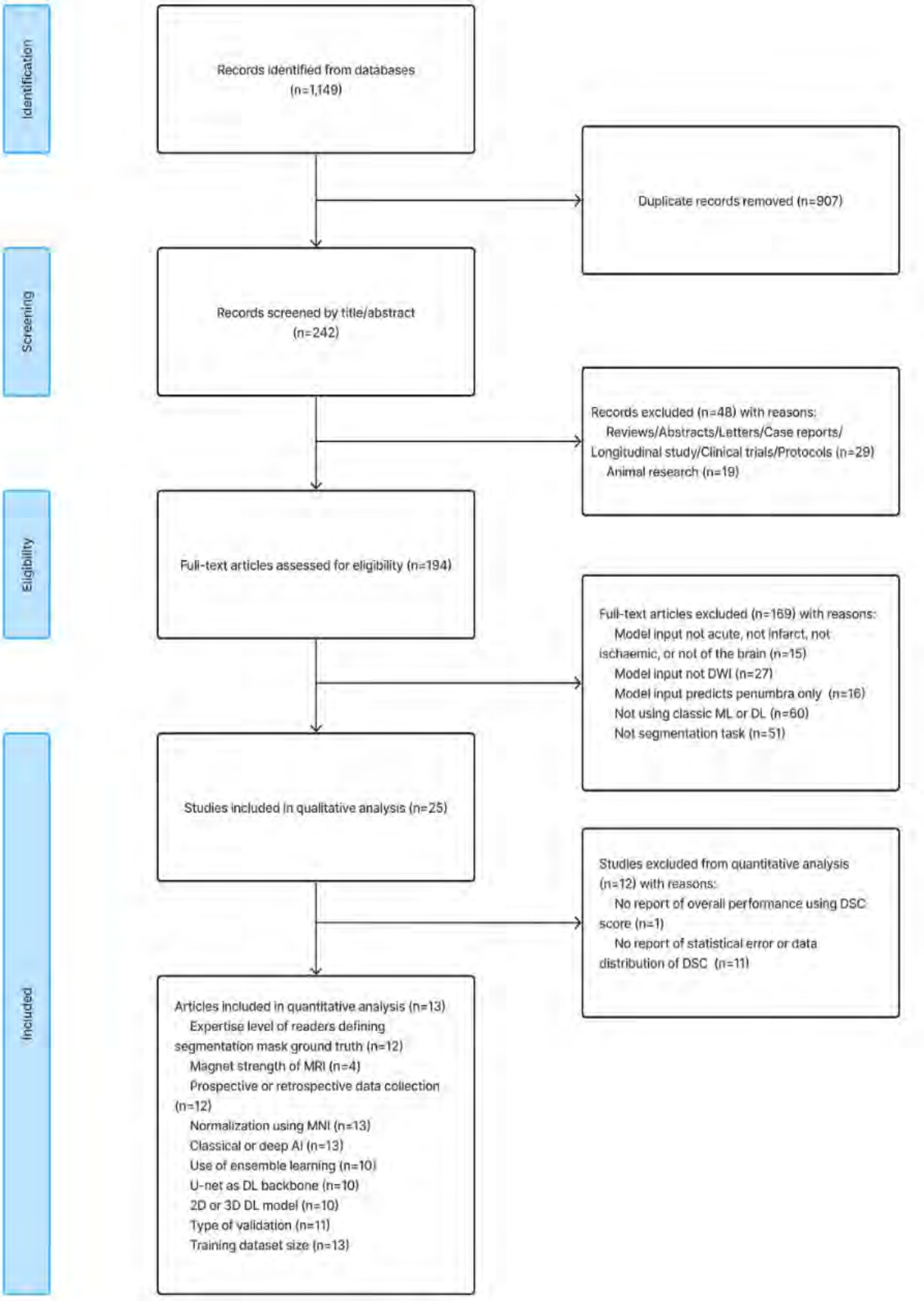

945

The Influence of Calling Sinking Flap Syndrome on the Timing of Cranioplasty

Kyril L. Cole MD, MPH, MBA, Robert C. Rennert MD, Samuel Tenhoeve BS, Timothy J. Wardrop BS, Drew Artrip MD, Paulo Miro MD, Melissa Warstadt MD, Karen Salzman MD, Sarah Menacho MD, MBA, Edward Quigley MD, PhD
University of Utah, Salt Lake City, UT, USA

Abstract Category

Adult Brain

Purpose

Sinking Flap Syndrome (SFS), also known as syndrome of the trephined or paradoxical brain herniation, is a potentially life-threatening complication following craniectomy. Quick recognition and intervention are critical, yet the syndrome may be under-diagnosed.[1] This study evaluates the impact of radiologist-initiated identification of SFS on the timing to cranioplasty and further characterizes SFS incidence and risk factors to improve clinical outcomes.

Materials & Methods

Our hospital dataset was queried for cranioplasties >5cm performed between 2019 and 2024. Radiology reports were searched for the terms "sinking flap" and "paradoxical shift." We compared clinically relevant outcomes between patients aged >18 with radiologist-called SFS and those without this specific identification.

Results

A total of 166 patients who underwent cranioplasty were included in the analysis. Overall, trauma was the leading cause of craniectomy (52.4%), with subdural hematomas being the most common type of bleeding (28.9%). Radiologists identified SFS in 55 cases (33.1%), while 78 cases (47.0%) met radiographic criteria for SFS.[2] Median time from craniectomy to SFS development was 49 [28, 117] days. Patients with radiographically defined SFS were predominantly male (71.8%) and had trauma-based injuries necessitating decompressive craniectomy (67.3%). Larger bone flap sizes correlated with a higher incidence of SFS (16.0 vs. 14.7 cm, p=0.026). Those with radiographically defined SFS were more frequently symptomatic at baseline before cranioplasty (80% vs. 60%, p=0.019) and showed higher maximum midline shifts (8.0 vs. 3.5 mm, p<0.001) and increased concern for ventricle entrapment (35.1% vs. 18.4%, p=0.015) on imaging. Patients with radiologist-called SFS had longer hospital and ICU stays (p=0.009 and 0.002, respectively), required more trips to the OR, and had higher rates of new stroke/hemorrhage post-cranioplasty (p=0.029 and 0.018, respectively). Timing from craniectomy to cranioplasty was significantly shorter when SFS was identified by a radiologist (median 57 vs. 80 days, p=0.045). Calling SFS also shortened the time from symptom onset to cranioplasty (12 vs. 29 days, p=.030), while the time from cranioplasty to stable imaging was similar between groups (p=.460). Timing from imaged SFS to cranioplasty was shorter when explicitly called by radiology vs. meeting the criteria for SFS only (9 vs. 18 days, p=.042). Post-cranioplasty complications, such as implant infection and skin erosion, were similar between groups (p=0.098).

Conclusion

Sinking Flap Syndrome is a frequent but under-recognized complication following craniectomy. Radiologists' early identification of SFS significantly reduces the time to cranioplasty. Earlier identification to allow for earlier surgical intervention may decrease ICU and hospital stay durations and unnecessary complication rates, thereby enhancing patient outcomes. Recognizing risk factors such as larger bone flap size and trauma-related craniectomies can guide early diagnosis and targeted monitoring of at-risk patients.

References

1. Sveikata L, Vasung L, El Rahal A, et al. Syndrome of the trephined: clinical spectrum, risk factors, and impact of cranioplasty on neurologic recovery in a prospective cohort. *Neurosurg Rev*. 2022 Apr;45(2):1431-1443. doi: 10.1007/s10143-021-01655-6.
2. Sarov M, Guichard JP, Chibarro S, et al. Sinking skin flap syndrome and paradoxical herniation after hemicraniectomy for malignant hemispheric infarction. *Stroke*. 2010 Mar;41(3):560-2. doi: 10.1161/STROKEAHA.109.568543.

Images/Tables

Figure 1. Examples of Sinking Flap Syndrome (SFS) – axial (A) and coronal (B) CT images, demonstrating SFS effect on midline structures.

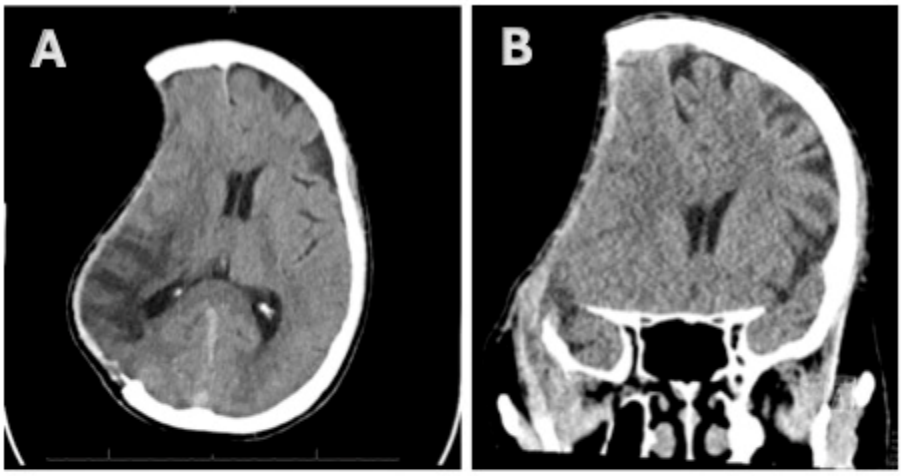

Figure 2. Axial CT images demonstrating a patient's anatomy at the time of SFS called (A) and immediately postoperative after cranioplasty (B).

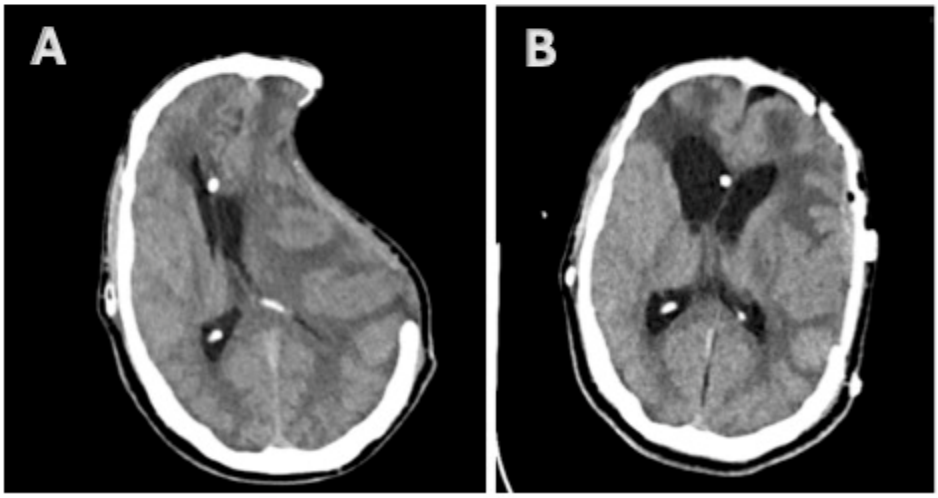

950

Necessity of Preoperative Ultrasound in addition to 4D-CT in patients undergoing Parathyroid Surgery

Soha Mohammadi MD[1], Mary Elizabeth Cunnane MD[1], Amy F. Juliano MD[1], Katherine L Reinshagen MD[1], Yuh-Shin Chang MD, PhD[1], Manuel Patino Galindo MD[1], Hillary R. Kelly MD[2]

[1]Department of Radiology, Massachusetts Eye and Ear, Harvard Medical School, Boston, MA, USA. [2]Department of Radiology, Massachusetts General Hospital, Massachusetts Eye and Ear, Harvard Medical School, Boston, MA, USA

Abstract Category

Head & Neck

Purpose

Primary hyperparathyroidism (PHPT) is an endocrine disorder primarily caused by parathyroid adenomas, leading to excessive secretion of parathyroid hormone (PTH). Surgical resection, guided by precise preoperative localization of adenomas, is the definitive treatment for PHPT. While four-dimensional (4D) CT has become the first-line imaging modality for many of these patients, ultrasound (US) is frequently used as a complementary study to confirm findings as well as to evaluate thyroid pathology that may be encountered at the time of surgery. Given the high accuracy of 4D-CT, we aimed to determine if the preoperative US is necessary for accurate localization.

Materials & Methods
This retrospective study included 40 patients diagnosed with PHPT through clinical and biochemical criteria who underwent preoperative 4D-CT (3 phases: non-contrast, arterial, and venous phases) and US, followed by surgery with histopathological confirmation. Four radiologists independently reviewed imaging cases using either 4D-CT alone or a combination of 4D-CT and US. Each radiologist reviewed 20 cases: 10 with 4D-CT and 10 with 4D-CT and US. Localization accuracy was assessed by counting the number of pathology-proven lesions correctly identified by radiologists. Candidate lesion sizes were compared between true positive and false positive findings in each group (4D-CT alone and 4D-CT + US). Statistical analyses were performed using GraphPad Prism version 10.4.0, including t-tests for comparing mean lesion sizes and variance analysis to assess size variability between True Positives and False Positives. All tests were considered significant at p-values <0.05.
Results
Of the 40 patients initially enrolled, 39 were analyzed after excluding one patient who did not achieve surgical cure (mean age 59.2 ± 12 years; 82% female). 49 histologically confirmed parathyroid lesions were found at surgery. The combined use of 4D-CT and US demonstrated slightly higher localization accuracy at 89.8% (44/49) compared to 87.8% (43/49) with 4D-CT alone. True positives (correctly identified lesions) were marginally higher in group 2 (44 vs. 43), with a small increase in false positives (12 vs. 9). False negatives were reduced in group 2 (5 vs. 6), indicating improved sensitivity in the group using both 4D-CT and US. Lesion sizes differed significantly between true positives and false positives across both imaging groups. True positive lesions were similar in size between groups (16.59 mm for 4D-CT vs. 16.33 mm for 4D-CT + US; p-value = 0.91), while false positives were significantly smaller (7.22 mm and 7.25 mm, respectively; p-value < 0.0001).
Conclusion
Although 4D-CT and Ultrasound are complementary modalities in the detection of diseased parathyroid glands, our results demonstrate a minimal increase in accuracy with the addition of US, suggesting that 4D-CT can serve as a stand-alone exam for the accurate preoperative detection of parathyroid adenomas.

References

1. Kelly HR, Bunch PM. Parathyroid Computed Tomography: Pearls, Pitfalls, and Our Approach. Neuroimaging Clin N Am 2022;32:413-31. DOI: https://doi.org/10.1016/j.nic.2022.01.006

952

Fazekas Score Predicts Amyloid-Related Imaging Abnormalities in Alzheimer's Patients Treated with Lecanemab

Shenghua Zhu MD, PhD, Saurabh Rohatgi MD, Jeremy N Ford MD, Esteban Calle Cadavid MD, Odette Ganem Chagui, Benjamin M Kozak MD, Maryam Vejdani-Jahromi MD, PhD, Harry R Griffin MD, Jarrel C Seah MBBS, Nima Omid-Fard MD, Hana Farzaneh MD, Javier M Romero MD
Massachusetts General Hospital, Boston, MA, USA

Abstract Category
Adult Brain
Purpose
Anti-amyloid immunotherapies (AAIs) like lecanemab are increasingly used to treat Alzheimer's disease (AD) but are often associated with amyloid-related imaging abnormalities (ARIA), raising concerns in clinical trials and patient management. The mechanisms underlying ARIA remain unclear, highlighting the need to identify risk factors to optimize treatment eligibility. White matter hyperintensities (WMH) and enlarged perivascular spaces (PVS) are imaging markers of cerebral small vessel disease linked to vascular dementia. This study aims to investigate the relationship between baseline WMH, PVS, and the risk of developing ARIA in AD patients treated with lecanemab.
Materials & Methods
We retrospectively analyzed baseline clinical, genomic, and radiological data from 54 AD patients treated with lecanemab at Massachusetts General Hospital. ARIA events were identified from surveillance MRI scans. Statistical analyses included t-tests and Mann–Whitney tests to compare cognitive assessments (MoCA, MMSE), Fazekas scores, and PVS grades. Logistic regression assessed the impact of baseline cognitive function, Fazekas scores, and PVS in the basal ganglia and centrum semiovale on ARIA development.

Results

Of the 54 patients analyzed, 27 were ARIA-positive. Baseline characteristics were comparable between ARIA-positive and ARIA-negative groups regarding age (69.2 vs. 70.1 years, p=0.717), sex (51.8% vs. 48.1% female, p=1.0), APOE ε4 carrier status (70.4% vs. 51.8%, p=0.264), comorbidities (hypertension 48.1% vs. 51.8%, diabetes 7.41% vs. 11.1%, dyslipidemia 70.4% vs. 74.1%), and anticoagulant use (22.2% vs. 18.5%). No significant differences were observed in cognitive assessments (MoCA: 20.4 vs. 19.1, p=0.304; MMSE: 24.8 vs. 22.9, p=0.076). ARIA-positive patients had significantly higher Fazekas scores (1.37 vs. 1.0; p=0.0262). PVS grades were higher in ARIA-positive patients in the basal ganglia (1.81 vs. 1.56, p=0.0733) and centrum semiovale (2.33 vs. 2.15, p=0.460), but these differences did not reach statistical significance. Logistic regression identified the Fazekas score as a significant predictor of ARIA (odds ratio 2.812, 95% CI: 1.076–8.438; p=0.0343), with an area under the ROC curve of 0.640.

Conclusion

Higher baseline Fazekas scores are significantly associated with an increased risk of developing ARIA in AD patients treated with lecanemab. The Fazekas score may serve as a candidate imaging biomarker for predicting ARIA risk, potentially enhancing patient selection and monitoring during therapy.

References

1. Hampel H, Elhage A, Cho M, Apostolova LG, Nicoll JAR, Atri A. Amyloid-related imaging abnormalities (ARIA): radiological, biological and clinical characteristics. Brain. 2023;146(11):4414-4424.

2. Agarwal A, Gupta V, Brahmbhatt P, et al. Amyloid-related Imaging Abnormalities in Alzheimer Disease Treated with Anti-Amyloid-β Therapy. Radiographics. 2023;43(9):e230009.

3. Van Dyck, C., Swanson, C., Aisen, P., et al. Lecanemab in Early Alzheimer's Disease. N. Engl. J. Med. 388, 9–21 (2023).

Images/Tables

Table 1

	ARIA Positive	ARIA Negative	*p* values
Total patients included	27	27	
Female	14 (51.8%)	13 (48.1%)	1.0
Age (in years)			
Mean	69.2	70.1	
Median	68	69	0.717
Range	56-84	56-88	
Baseline Cognition			
MoCA	20.4	19.1	0.304
MMSE	24.8	22.9	0.076
Genetic profile			
APOE ε4 carrier status	19 (70.4%)	14 (51.8%)	0.264
Comorbidities			
Hypertension	13 (48.1%)	14 (51.8%)	1.0
Diabetes	2 (7.41%)	3 (11.1%)	1.0
Dyslipidemia	19 (70.4%)	20 (74.1%)	1.0
Anticoagulation			
Aspirin use	6 (22.2%)	5 (18.5%)	1.0

Figure 1

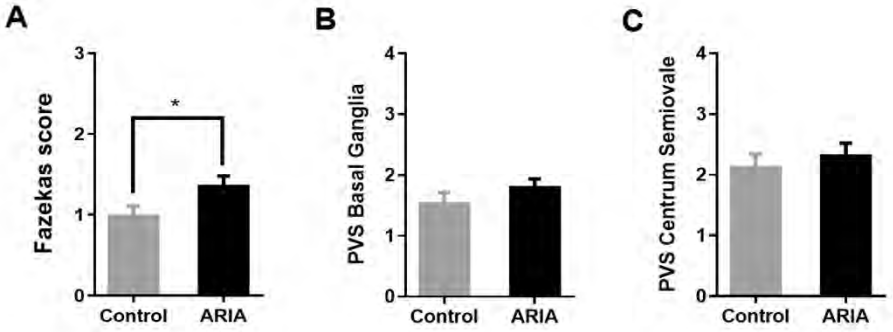

Figure 2

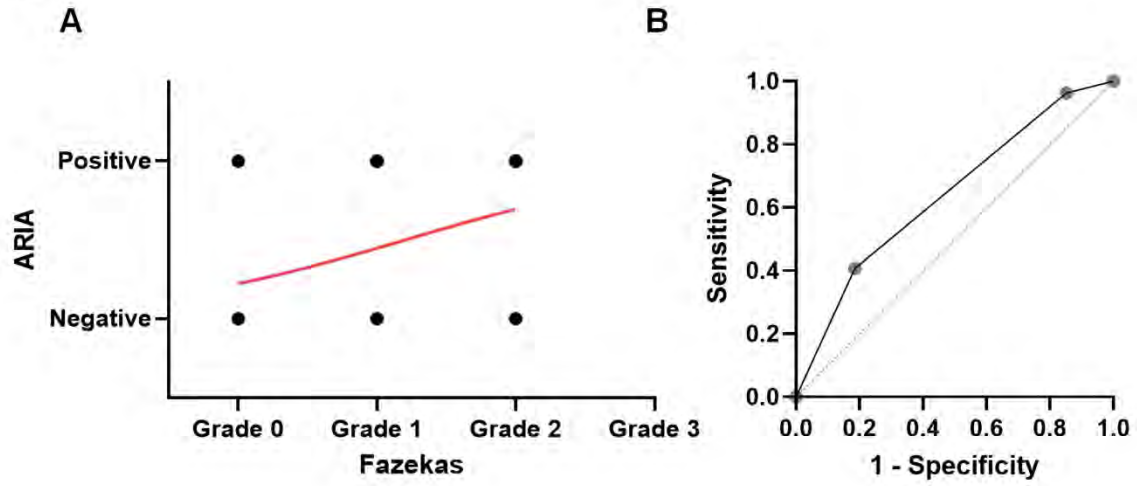

956

Potent *in vivo* efficacy of the novel iron mimetic gallium maltolate for the treatment of primary brain tumors

Mona M Al-Gizawiy PhD, Robert T Wujek, Kyle Johnson PhD, Jason W Sidabras PhD, Melissa A Prah, Jennifer M Connelly MD, Christopher R Chitambar MD, Kathleen M Schmainda PhD
Medical College of Wisconsin, Milwaukee, WI, USA

Abstract Category

Functional/Advanced Imaging

Purpose

We present results demonstrating the potent *in vivo* treatment response to the novel metallocompound, gallium maltolate (GaM), in adult glioblastoma (GBM), pediatric high-grade glioma (HGG) and atypical teratoid rhabdoid tumors (ATRT). Gallium mimics iron and, therefore, interferes with crucial iron-dependent processes within the cancer cell, such as DNA repair, leading to cell death.

Materials & Methods

The study is summarized in **Figure 1A**. ***Animal model:*** Athymic rats were inoculated intracranially with treatment-resistant GBM, pediatric HGG, or ATRT cells, as established in our laboratory.[1] Following tumor confirmation on MRI, treatment (oral GaM 50 mg/kg/day or vehicle) commenced. A subset of GBM animals on GaM underwent radiation treatment (RT) in a small animal radiotherapy unit that allows for full treatment planning. ***Data acquisition:*** Preclinical MRI was performed on a 9.4T Bruker scanner every 7-10 days. Examinations included pre- and post-contrast T1-weighted (T1w) anatomical images, as well as pre-contrast T2-weighted (T2w) imaging. Point resolved spectroscopy (PRESS) with variable pulse power and optimized relaxation delays (VAPOR) water suppression was collected from 2mm^3 voxels. Pre- and post-contrast T2w GRE scans were obtained. Dynamic susceptibility contrast perfusion imaging was acquired using a spin-and-gradient echo (SAGE) MRI sequence. A bolus of 5 mg/kg monocrystalline iron oxide nanoparticles was injected halfway into the perfusion scan at a rate of 10 ml/min using a power-injector. Post-contrast T1w scans were acquired following the additional injection of 0.2 mmol/kg gadobutrol. ***Data analysis:*** MRI data was processed using Imaging Biometrics (IB) analysis software and custom-made MATLAB scripts. Quantitative delta-T1 maps (dT1) of true tumor enhancement were generated from calibrated pre- and post-contrast T1w images using the IB Delta Suite™plugin within the Horos 8.5.1 (Lite) DICOM viewer.[2] Standardized steady-state cerebral blood volume maps were generated from R2* maps created from pre- and post-contrast T2*w images. Tumor volume (mm^3) was extracted from regions of interest (ROIs) drawn manually on dT1 maps. The same ROIs were used to extract mean ssCBV values (a.u.). Additional standardized relative cerebral blood volume maps (rCBV) were generated from SAGE scans.[3, 4] Fractional tumor burden (FTB) maps were created using a combination of enhancing tumor and rCBV.[5] Metabolic spectra collected with PRESS were analyzed with TopSpin in Paravision 6.0.1.

Results

We observed a profound tumor inhibition in GBM (**Figure 1B**), HGG, and ATRT (**Figure 1D**) associated with a significant survival benefit (GBM p<0.001 [**Figure 1 C**], HGG p=0.014, ATRT p=0.011). Preliminary studies investigating the combination of GaM+RT *in vivo* show that pre-treatment with GaM potentiates GBM inhibition (**Figure 1E,F**). Longitudinal MR spectroscopy confirms the formation of apoptosis and quadrupling of median survival compared to GaM monotherapy (**Figure 1C,G**).

Conclusion

We show that GaM has a profound *in vivo* cytotoxic effect on primary brain tumors. This effect is potentiated by RT. Our multimodal imaging approach allows us to characterize more effectively *in vivo* the longitudinal biologic changes in response to GaM treatment. We are well positioned to translate GaM for future clinical studies, which have the potential to change how brain cancer patients with limited therapeutic options are treated.

References

1. Al-Gizawiy MM, Wujek RT, Alhajala HS, et al. Potent in vivo efficacy of oral gallium maltolate in treatment-resistant glioblastoma. *Frontiers in Oncology* 2024;13
2. Schmainda KM, Prah MA, Zhang Z, et al. Quantitative Delta T1 (dT1) as a Replacement for Adjudicated Central Reader Analysis of Contrast-Enhancing Tumor Burden: A Subanalysis of the American College of Radiology Imaging Network 6677/Radiation Therapy Oncology Group 0625 Multicenter Brain Tumor Trial. *AJNR Am J Neuroradiol* 2019;40:1132-1139

3. Boxerman JL, Schmainda KM, Weisskoff RM. Relative cerebral blood volume maps corrected for contrast agent extravasation significantly correlate with glioma tumor grade, whereas uncorrected maps do not. *AJNR Am J Neuroradiol* 2006;27:859-867
4. Stokes AM, Ragunathan S, Robison RK, et al. Development of a spiral spin- and gradient-echo (spiral-SAGE) approach for improved multi-parametric dynamic contrast neuroimaging. *Magn Reson Med* 2021;86:3082-3095
5. Prah MA, Al-Gizawiy MM, Mueller WM, et al. Spatial discrimination of glioblastoma and treatment effect with histologically-validated perfusion and diffusion magnetic resonance imaging metrics. *Journal of neuro-oncology* 2018;136:13-21

Images/Tables

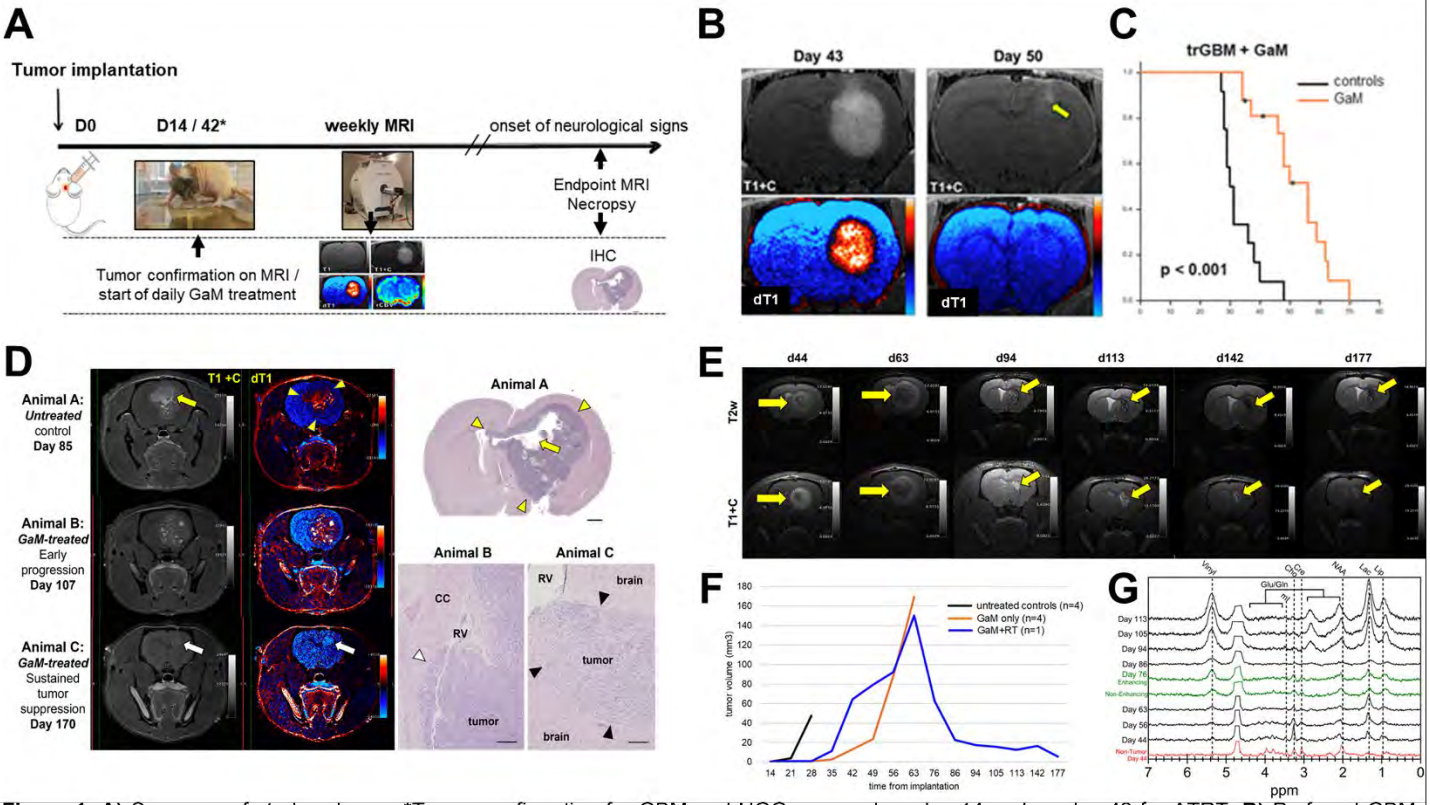

Figure 1. A) Summary of study schema. *Tumor confirmation for GBM and HGG occurred on day 14 and on day 42 for ATRT. **B)** Profound GBM inhibition *in vivo* with a doubling of median survival **(C)**. Data for B) and C) was modified from Ref. #1. **D)** Untreated ATRT tumors were found to invade the adjacent ventricle, as evidenced by leakage of contrast agent (yellow arrow) on post-contrast T1-weighted imaging (T1+C). This was confirmed on histology. Although not easily discernible on T1+C, tumors with sustained response to GaM were readily visible on dT1, a clinical imaging biomarker that outlines true tumor enhancement (white arrows). Early progression in GaM-treated ATRT (Animal B) was associated with considerable mass effect, compressing the right ventricle (RV) and invasion of the corpus callosum (CC, white arrowhead), while a sustained response (Animal C) did not. Black arrowheads show clear demarcation between tumor and surrounding brain tissue without invasive edges on spatially correlated histology. H&E scale bars = 4 mm (Animal A), 200 µm (Animals B and C). **E)** Representative pre-contrast T2-weighted and post-contrast T1w (T1+C) MRI slices, showing the trGBM tumor evolution following RT (3 daily fractions of 7 Gy each), starting on day 44 post tumor implantation (day 28 of GaM treatment). Yellow arrows show the shrinking lesion. **F)** Tumor volumes of untreated control animals (black line), GaM only treated animals (orange), and of the representative animal from panel A (blue line). **G)** Longitudinal MR spectroscopy shows development of necrosis (lactate peak) with apoptosis (vinyl peak), a return to normal tissue brain metabolism (NAA peak), and a loss in the choline to creatine ratio (tumor marker).

958

Exploring Alterations in Brain Functional Connectivity in Parkinson's Disease and Concomitant Visual Disturbances and Hallucinations Using Resting-state fMRI

Sara Naghizadehkashani MD, Omid Shoraka MD, Caio Matias MD, Chengyuan Wu MD, Mahdi Alizadeh MD
Thomas Jefferson University, Philadelphia, PA, USA

Abstract Category

Functional/Advanced Imaging

Purpose

Parkinson's disease (PD) is frequently accompanied by visual disturbances (VD) and its spectrum arises from blurred vision and can get as serious as visual hallucinations (VH). (1,2) This study aimed to analyze the alterations in brain functional connectivity (FC) in subjects with PD and concomitant VD or VH compared to no visual disorder.

Materials & Methods

A total of 67 subjects with PD were included in the study. Among them, 21 exhibited some form of visual disturbances (VD; n=21), with 10 of these 21 experiencing visual hallucinations (VH; n=10). Additionally, we recruited 46 PD subjects who had no visual disturbances (ND). Resting-state fMRI was performed using a 3T Siemens scanner with 64 channels head and neck coil. Inter-subject hemisphere dominance was uniformed by flipping the MRI for the eligible subjects. ROI-to-ROI analysis of the whole brain was performed using Conn toolbox. Group-based analysis was then performed between the three groups. A voxel threshold p-value set of <0.05 was used, with results corrected for multiple comparisons using Bonferroni correction (0.05/170=0.00029). Age, gender, and disease severity based on the Unified Parkinson's Disease Rating Scale (UPDRS III) were used as confounding variables.

Results

Results of the whole brain connectivity alterations are represented in Table 1, and the pairwise analysis brain map for each group is represented in Figure 1. The VD group compared to the ND only showed decreased FC in 4 pairs of brain regions out of 5 alterations reported. The VH group compared to the ND showed decreased FC in 3 pairs of brain regions. The majority of regions demonstrating alterations in FC are situated within the visual pathway (spanning from the retina to the visual cortex and the ventral visual pathway) or within the sensorimotor network.

Conclusion

Alterations in FC were noted in thalamic nuclei associated with visual pathways and the ventral visual pathway, which plays a role in visual and spatial memory. Additional alterations were detected in various sensorimotor regions. Understanding the nature of these alterations can provide valuable insights into how neurodegenerative processes contribute to the development of VD and VH in PD.(3)

References

1. Thomas GE, Zeidman P, Sultana T,et al. Changes in both top-down and bottom-up effective connectivity drive visual hallucinations in Parkinson's disease. Brain Communications. 2023 Feb 1;5(1):fcac329

2. Spinosa V, Brattico E, Campo F, et al. A systematic review on resting state functional connectivity in patients with neurodegenerative disease and hallucinations. NeuroImage: Clinical. 2022 Jan 1;35:103112.

3. Olde Dubbelink KT, Schoonheim MM, Deijen JB, Twisk JW, Barkhof F, Berendse HW. Functional connectivity and cognitive decline over 3 years in Parkinson disease. Neurology. 2014 Nov 25;83(22):2046-53.

Images/Tables

Table 1. Statistically significant ROI-to-ROI brain connectivity results based on AAL3 atlas for subjects with PD and VD compared to ND and PD subjects with VH compared to ND

Pairwise Analysis	Regions		T-value	p-unc	p-FDR
VD compared to ND group	DDS IOG	DDS Red nucleus	4.70	2.3×10^{-5}	3.2×10^{-1}
	DDS Precuneus	NDDS OFCmedial	-4.26	9.6×10^{-5}	6.5×10^{-1}
	NDDS PFCventmed	NDDS IPG	-4.15	1.3×10^{-4}	6.5×10^{-1}
	Cerebellar Vermis X	DDS Red nucleus	-4.06	1.8×10^{-4}	6.5×10^{-1}
	NDDS Amygdala	NDDS PostCG	-3.96	2.5×10^{-4}	7.2×10^{-1}
VH compared to ND group	DDS IPG	NDDS ACCsup	-4.26	9.9×10^{-5}	6.0×10^{-1}
	NDDS tVA	DDS IOG	-4.23	1.1×10^{-4}	6.0×10^{-1}
	NDDS IOG	NDDS Cerebellar Crus I	-4.18	1.3×10^{-4}	6.0×10^{-1}

Regions demonstrating altered connectivity are next to each other with a positive T-value representing increased connectivity and a negative T-value representing decreased connectivity between two regions.
Abbreviations: VD, Any Visual Disturbance; ND, No Visual Disorder; VH, Visual Hallucination; DDS, Dominant Disease Side; NDDS, Nondominant Disease Side; OFC medial, Orbitofrontal cortex medial; PFC vent-med, Prefrontal cortex ventromedial; IPG, Inferior Parietal Gyrus; IOG, Inferior Occipital Gyrus; Post CG, Postcentral Gyrus, ACC sup, Anterior Cingulate Cortex Supra callosal; t VA, Thalamus Ventral Anterior.

Figure 1. 3D brain maps comparing VH with ND are shown on the left, while comparisons of VD to ND are on the right. VH compared to ND revealed 3 pairs of regions with decreased functional connectivity (FC), whereas VD compared to ND revealed 5 pairs of regions, 4 of which exhibited decreased FC. Decreased FC is represented by a blue line, and increased FC is represented by a red line.

960

Functional Connectivity Alterations in Tremor-Dominant Parkinson's Disease vs. Essential Tremor: Insights into Neural Mechanisms

Sara Naghizadehkashani MD, Omid Shoraka MD, Caio Matias MD, Chengyuan Wu MD, Katelyn Mann, Mahdi Alizadeh PhD
Thomas Jefferson University, Philadelphia, PA, USA

Abstract Category

Functional/Advanced Imaging

Purpose

While both tremor-dominant Parkinson's disease (TDPD) and essential tremor (ET) are movement disorders characterized by tremors, their underlying neural mechanisms remain distinct. (1) Understanding the unique patterns of functional connectivity (FC) alterations in these disorders can provide valuable insights into their pathophysiology and aid in targeted treatment strategies. (2,3) Our study aimed to analyze the alterations in brain FC in subjects with tremor-dominant PD compared to ET subjects.

Materials & Methods

58 TDPD subjects and 13 ET subjects were enrolled in this study. Resting-state fMRI was performed using a 3T Siemens scanner with 64 channels head and neck coil. Inter-subject hemisphere dominance was uniformed by flipping the MRI to align the disease-dominant hemisphere. Whole-brain ROI-to-ROI analysis was carried out using the Conn toolbox. A group-based analysis was performed to compare the two groups. The voxel threshold p-value was set at <0.05, with Bonferroni correction applied for multiple comparisons ($0.05/32=0.0015$). ROI-to-ROI analysis was controlled for disease duration as a confounding variable.

Results

Disease duration was the only disease-related variable showing a significant difference between the TDPD and ET groups ($p < 0.001$) (Table 1). Three pairs of regions exhibited increased FC in TDPD subjects compared to ET cases. Increased FC was observed between DDS Putamen with DDS Thalamic ventral lateral and mediodorsal nuclei. Additionally, increased FC was observed between NDDS Heschl's Gyrus and NDDS Cerebellar Lobule 3 (Table 2 & Figure 1).

Conclusion

Increased FC was observed in the basal ganglia, thalamus, and cerebellar regions in TDPD subjects compared to ET cases. This correlation potentially indicates a higher level of dysfunction in these areas in ET disorder compared to PD.

References

1. Louis ED. Diagnosis and management of tremor. CONTINUUM: Lifelong Learning in Neurology. 2016 Aug 1;22(4):1143-58.
2. Prasad S, Saini J, Bharath RD, et al. Differential patterns of functional connectivity in tremor dominant Parkinson's disease and essential tremor plus. Journal of Neural Transmission. 2024 Mar 2:1-9.
3. Angelini L, Paparella G, Bologna M. Distinguishing essential tremor from Parkinson's disease: clinical and experimental tools. Expert Review of Neurotherapeutics. 2024 Aug 2;24(8):799-814.

Images/Tables

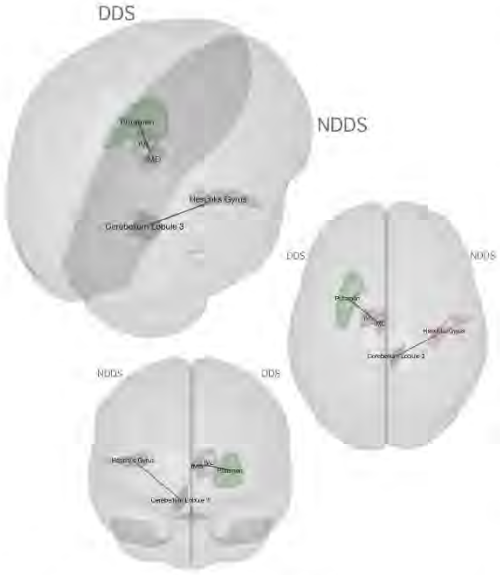

Figure 1. 3D brain maps of 3 pairs of regions, all demonstrating increased functional connectivity (Red line) in the TDPD Subjects compared to ET cases.
Abbreviations: TDPD, Tremor-dominant Parkinson's disease; ET, Essential Tremor; t VL, Thalamus Ventral Lateral; t MD, Thalamus Mediodorsal; DDS, Dominant Disease Side; NDDS, Nondominant Disease Side

Table 1. Demographics and disease related variables in subjects with Tremor Dominant Parkinson's Disease vs. subjects with Essential Tremor

	Total, N=71	TDPD, N=58	ET, N=13	p-value
Age, mean ± SD	63.7 ± 10.1	64.1 ± 9.2	61.6 ± 13.4	0.418
Gender, Male n (%)	48 (67.6)	42 (72.4)	6 (46.2)	0.067
Disease Severity Score, mean± SD	29.7 ± 12.2	29.5 ± 13.0	30.4 ± 7.0	0.771
Symptom Side, Right n (%)	27 (38.0)	23 (39.7)	4 (30.8)	0.551
Handedness, Right n (%)	50 (86.2)	41 (89.1)	9 (75.0)	0.206
Disease Duration, mean ± SD	10.9 ± 7.5	8.4 ± 3.2	22.1 ± 10.4	<0.001

Bold value indicates statistical significance. (p-value<0.05)

Table 2. ROI-to-ROI brain connectivity results based on AAL3 atlas comparing TDPD subjects with ET cases

Pairwise Analysis	Regions	T-value	p-unc	p-FDR
TDPD vs. ET	DDS Putamen — DDS tVL	4.32	4.5×10^{-5}	6.1×10^{-1}
	DDS Putamen — DDS tMD	4.06	1.2×10^{-4}	6.1×10^{-1}
	NDDS Heschl's Gyrus — NDDS Cerebellar Lobule III	4.03	1.2×10^{-4}	6.1×10^{-1}

The red line between each pair of regions demonstrates increased FC.
Abbreviations: TDPD, Tremor-dominant Parkinson's disease; ET, Essential Tremor; t VL, Thalamus Ventral Lateral; t MD, Thalamus Mediodorsal; DDS, Dominant Disease Side; NDDS, Nondominant Disease Side

969

Exploring the Crosstalk between Acrolein and Myeloperoxidase in Neuroinflammation Using a myeloperoxidase-targeting PET probe (18F-MAPP)

Sepideh Parsi PhD, Hongzhi Yang PhD, Cindy Zhu, Justin D Chen, Mariane Le Fur PhD, Cuihua Wang PhD, Nicholas J Rotile, John W Chen MD PhD
Massachusetts General Hospital, CHARLESTOWN, MA, USA

Abstract Category

Functional/Advanced Imaging

Purpose

Multiple sclerosis (MS) is a multifaceted autoimmune disorder that causes progressive neuroinflammation and demyelination, significantly impacting patient quality of life. A crucial factor in MS is the sustained neuroinflammation driven by myeloperoxidase (MPO), an enzyme abundantly produced by inflammatory immune cells. MPO generates reactive species such as acrolein, a toxic aldehyde with protein-modifying effects that may exacerbate disease progression. We aimed to track MPO activity in vivo post-acrolein scavenging treatment in SJL mice induced with experimental autoimmune encephalomyelitis (EAE) by molecular PET imaging targeting MPO activity to study the crosstalk between MPO activity and acrolein.

Materials & Methods

Female SJL mice (6-10 weeks) were induced with EAE using a standard protocol involving PLP 139-151 peptide. We conducted daily weight monitoring and clinical assessments. EAE mice received intraperitoneal dimercaprol 5mg/kg (acrolein scavenger) shortly after symptom onset. We monitored dimercaprol's effect in vivo using the MPO PET probe ^{18}F-MAPP. Histopathology and biochemical studies were performed to compare treated and PBS-treated mice to correlate with markers, including neurofilament light chain (NFL), choline acetyltransferase (CHAT), as well as inflammatory markers CD40, MPO protein, MPO activity, and acrolein protein adducts. Biochemical analysis measured MPO activity in mice brain lysates as previously described.

Results

PET imaging enabled non-invasive, real-time quantification of MPO activity. Our findings revealed a noticeable correlation between in vivo MPO PET signals and acrolein protein adducts in the brain, indicating a reduction in the

inflammatory response post-treatment. Immunofluorescence results from the same brains imaged with ^{18}F-MAPP indicated similar spatial patterns with colocalized MPO and acrolein adducts. Additionally, dimercaprol treatment reduced acrolein adduct presence in motor neurons within the spinal cord. In the spinal cord, PBS-treated mice exhibited higher levels of MPO/acrolein adduct-positive cells and F4/80+ cells compared to the dimercaprol-treated group. Biochemical analysis also confirmed the reduction of MPO enzymatic activity in the drug-treated group, corresponding to decreased clinical scores observed post-onset of disease.

Conclusion

MPO-targeted PET imaging revealed the relationship between MPO and acrolein in neuroinflammatory conditions, providing a tool for visualizing and quantifying neuroinflammation in CNS diseases that can offer unique insight into disease mechanisms and therapeutic responses.

References

- Wang, C., Keliher, E., Zeller, M. W., Wojtkiewicz, G. R., Aguirre, A. D., Buckbinder, L., ... & Chen, J. W. (2019). An activatable PET imaging radioprobe is a dynamic reporter of myeloperoxidase activity in vivo. *Proceedings of the National Academy of Sciences*, *116*(24), 11966-11971.
- John W. Chen, Michael O. Breckwoldt, Elena Aikawa, Gloria Chiang, Ralph Weissleder, Myeloperoxidase-targeted imaging of active inflammatory lesions in murine experimental autoimmune encephalomyelitis, *Brain*, Volume 131, Issue 4, April 2008, Pages 1123–1133
- Forghani, R., Wojtkiewicz, G. R., Zhang, Y., Seeburg, D., Bautz, B. R., Pulli, B., ... & Chen, J. W. (2012). Demyelinating diseases: myeloperoxidase as an imaging biomarker and therapeutic target. *Radiology*, *263*(2), 451-460.
- Pulli B, Ali M, Forghani R, Schob S, Hsieh KL, Wojtkiewicz G, Linnoila JJ, Chen JW. Measuring myeloperoxidase activity in biological samples. PLoS One. 2013 Jul 5;8(7):e67976. doi: 10.1371/journal.pone.0067976. PMID: 23861842; PMCID: PMC3702519.

Images/Tables

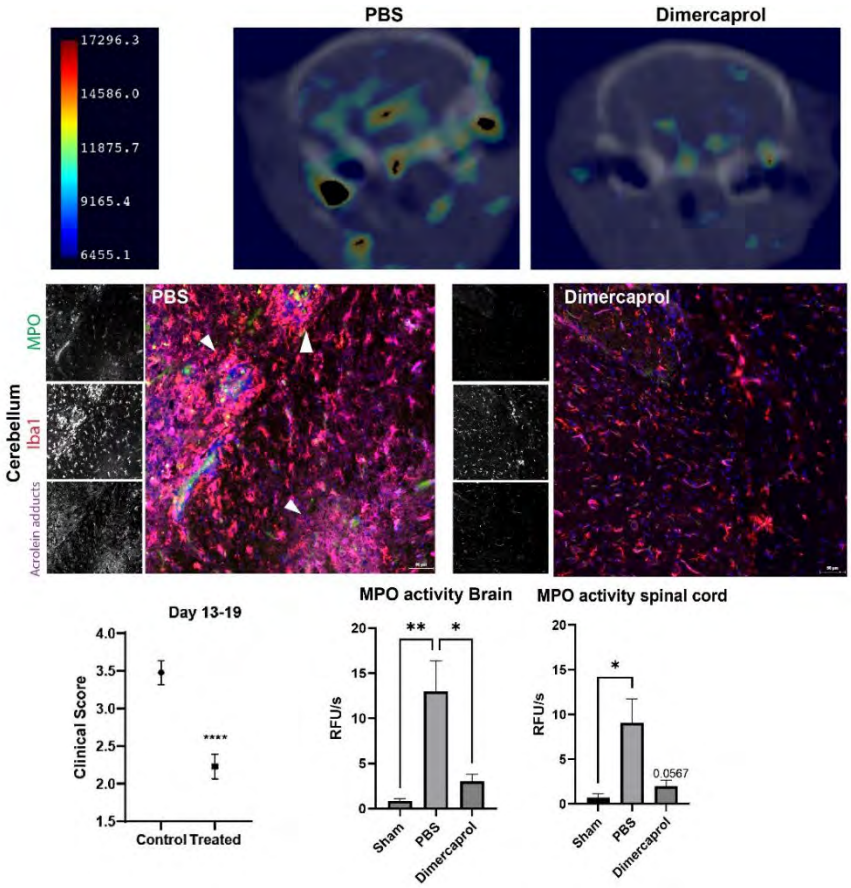

972

Mechanical Stroke Thrombectomy Practice Improvement– a Longitudinal NVQI-QOD Study

Shyam Chandrasekar BS, Dayeong An PhD, Arian Shahidi MD, Anas Al-Smadi MD, Ramez N. Abdalla MD, PhD, Donald R. Cantrell MD, PhD, Ali Shaibani MD, MBA, Sameer A. Ansari MD, PhD
Departments of Radiology, Neurosurgery, and Neurology, Northwestern University Feinberg School of Medicine, Chicago, IL, USA

Abstract Category

Interventional

Purpose

The publication of the DAWN and DEFUSE 3 trials in November 2017 and January 2018 respectively punctuated a shift in endovascular stroke intervention, extending the thrombectomy eligibility window from 6 to 24 hours. This study assesses the interval practice improvement of thrombectomy in the United States using the Neurovascular Quality Initiative-Quality Outcomes Database (NVQI-QOD) AIS Thrombectomy Registry.

Materials & Methods

Patients who underwent mechanical thrombectomy (MT) between 2014 and 2023 for anterior circulation stroke were retrospectively identified from the NVQI-QOD database. Comorbidities, procedural variables, and clinical outcomes were subsequently compared between patients pre- and post-Extension (2018). Favorable functional outcome was defined by a modified Rankin Scale (mRS) of 0 to 2 at 90 days post-thrombectomy. Demographic data was assessed using chi-squared analysis and t-tests as indicated, and odds Ratios (OR) were generated with logistical regression.

Results

Among 9577 patients, 4961 or 51.8% were female, with an average age of 68.5 years ± 15.32 (SD). There was no association between sex or age and Extension (p=0.899, p=0.986 respectively). Patients post-Extension were more likely to present with obesity (OR 1.14, p=0.041), coronary artery disease (OR 1.17, p=0.050), less likely to present with atrial fibrillation (OR 0.852, p=0.014), and equally likely to present with hypertension (OR 1.01, p=0.918), insulin-dependent diabetes (OR 1.01, p=0.942), and symptomatic congestive heart failure (OR 0.77, p=0.264).

There was no difference in presenting NIHSS [mean 15.97 vs. 15.63 post (p=0.131), 24-hour NIHSS [mean 10.95 vs. 10.96 post (p=0.959)], or discharge NIHSS [mean 7.23 vs. 7.35 post; p=0.685]. The post-Extension cohort demonstrated an increase of 88 minutes in last-well-known (LWK) to groin puncture time from a baseline of 394 minutes (p<0.001), but shorter ED arrival to groin puncture time by 31.2 minutes (p<0.001) from a baseline of 112.6 minutes. Post-Extension procedures were completed in less time [38 minutes vs 46 minutes pre-Extension; p<0.001], with fewer passes [mean 1.71 vs 1.82 passes; p=0.003], and with increased first-pass successful reperfusion (OR 1.60, p<0.001).

Univariate analysis showed no association between 24-hour and discharge mortality and Extension (p=0.452 and p=0.314, respectively) but did reveal a significant increase in 90-day post-operative mortality (OR 1.98, p<0.001) and a decreased likelihood of favorable functional improvement (OR 0.76, p=0.004) after Extension. Multivariate logistical regressions controlling for age, comorbidities, and procedural variables LKW to puncture, time from ED to Puncture, and total procedure time robustly redemonstrated these associations, with an increased 90-day mortality (OR 2.42, p<0.001) and a decreased 90-day functional improvement (OR 0.69, p=0.05).

Conclusion

This study reveals a significant evolution in stroke thrombectomy practice following the expanded eligibility window. Post-extension, centers adjusted to the increased time allowance, treating patients later after last-known-well from an average of 6.6 to 8.1 hours. Despite increasing procedural volumes, operational efficiency improved with reduced procedure times and fewer passes required for reperfusion. However, the extended window was independently associated with a decreased likelihood of favorable functional recovery and increased likelihood of mortality 90 days post-operation independently. Further research is needed to better understand these trends in the real-world environment.

References

Nogueira RG, Jadhav AP, Haussen DC, et al. Thrombectomy 6 to 24 Hours after Stroke with a Mismatch between Deficit and Infarct. *N Engl J Med*. 2018;378(1):11-21.

Albers GW, Marks MP, Kemp S, et al. Thrombectomy for Stroke at 6 to 16 Hours with Selection by Perfusion Imaging. *N Engl J Med*. 2018;378(8):708-718.

Images/Tables

Table 1: Favorable Functional Outcome at 90 days Post-Operation – Logistic Regression with Odds Ratio

Variable	Odds Ratio	p-value	95% Conf. Interval
Obesity*	1.3656	0.000	1.1589 - 1.6091
Symptomatic CHF*	0.6538	0.000	0.5164 - 0.8277
Atrial Fibrillation	0.9260	0.408	0.7719 - 1.1109
Hypertension*	0.7544	0.004	0.6236 - 0.9125
Insulin-dependent Diabetes	0.8074	0.070	0.6406 - 1.0176
Coronary Artery Disease	1.0959	0.390	0.8894 - 1.3503
Age (years)*	0.9641	0.000	0.9581 - 0.9702
After Extension (2018+)*	0.6914	0.005	0.5347 - 0.8939
LWK to Groin Puncture (mins)*	0.9996	0.000	0.9994 - 0.9998
Procedure time (mins)*	0.9927	0.000	0.9896 - 0.9957
ED Arrival to Groin Puncture (mins)	0.9994	0.302	0.9982 - 1.0006

Table 2: Mortality at 90 days Post-Operation – Logistic Regression with Odds Ratio

Variable	Odds Ratio	p-value	95% Conf. Interval
Obesity*	0.7067	0.001	0.5767 - 0.8662
Symptomatic CHF*	1.8315	0.000	1.4364 - 2.3354
Atrial Fibrillation	1.1512	0.175	0.9392 - 1.4111
Hypertension	1.1266	0.340	0.8819 - 1.4392
Insulin-dependent Diabetes	1.1025	0.469	0.8466 - 1.4358
Coronary Artery Disease	1.0218	0.856	0.8101 - 1.2888
Age (years)*	1.0628	0.000	1.0533 - 1.0723
After Extension (2018+)*	2.4185	0.000	1.6514 - 3.5421
LWK to Groin Puncture (mins)*	1.0003	0.003	1.0001 - 1.0006
Procedure time (mins)*	1.0065	0.000	1.0035 - 1.0096
ED Arrival to Groin Puncture (mins)	1.0006	0.430	0.9992 - 1.0020

987

Trends in Pediatric Neuroradiology Research: A Bibliometric Analysis of Publications in Neuroradiology Journals.

Amirreza Manteghinejad MD[1], Arastoo Vossough MD, PhD[2]

[1]Children's Hospital of Philadelphia, Philadelphia, PA, USA. [2]Children's Hospital of Philadelphia, Perelman School of Medicine, Philadelphia, PA, USA

Abstract Category

Pediatrics

Purpose

Neuroimaging has improved our understanding of brain function and structure and acts as a powerful diagnostic tool in medicine. However, the unique characteristics of the pediatric brain and distinct disease patterns and progression have, at times, necessitated different neuroimaging approaches and interpretations. As a result, pediatric neuroradiology emerged as a sub-specialized branch of neuroradiology to help in understanding brain development and diagnosing neurological conditions in children.

A bibliometric study involves a quantitative analysis of academic literature within a specific field or topic and aims to identify trends, assess impact, and map knowledge structures. Since no published bibliometric study has been conducted in pediatric neuroradiology to date, this study aims to conduct one to assess publication trends in neuroradiology journals.

Materials & Methods

We conducted a cross-sectional study using retrospective data, evaluated all the Scopus-indexed journal titles on the subject of radiology, and selected the journals specifically in the field of neuroradiology. We extracted titles, authors, affiliations, abstracts, and keywords from all publications in these journals. To identify pediatric neuroradiology articles, we employed the ChatGPT Application Programming Interface (API), version 4o-mini, with a custom prompt to select based on titles, abstracts, and keywords. Descriptive statistics, collaboration network visualizations, and word clouds were used to assess publication trends, geographical origin distribution, institutional contributions, and collaborations.

Results

Eleven journals containing 40207 articles were included in this study, spanning 1970 to 2024. Of those, 5850 (14.5%) were specifically in the field of pediatric neuroradiology. The least number of papers was in 1970, with only 4 papers, and the maximum was in 2019, with 231 papers. The median number of citations was 15 [interquartile range:5-34]. Evaluation of the authors' countries of origin showed that most contributions are from the United States (2341 papers,40%), followed by the United Kingdom (351, 6%) and Japan (345,5.9%). Evaluation of the institutions showed that institutions and hospitals affiliated with Harvard University (226,3.9%), University of Toronto (224,3.8%), and University of Pennsylvania (190,3.2%) had the most contributions in this field. Anthony James Barkovich, Thierry Huisman, and Robert Zimmerman were the most published authors in this field based on just the number of publications.

Conclusion

This study aims to present a preliminary result based on a bibliometric study in the field of pediatric neuroradiology. This study revealed that countries such as the United States, the United Kingdom, and Japan, as well as institutions like Harvard University, University of Toronto, and University of Pennsylvania had the highest number of papers in this field. However, it is important to interpret and generalize these results with caution. This study is solely based on clinical neuroradiology journals and overlooked papers published in general radiology, neurology, and other pediatric journals. Additionally, the use of ChatGPT for paper topic selection creates a level of uncertainty that must be acknowledged. Despite these limitations, we believe our study provides an informative starting point for understanding the current state of pediatric neuroradiology research and serves as a foundation for future, more comprehensive analyses that can offer both a holistic and granular view of research in the field.

References

Kokol P, Blažun Vošner H, Završnik J. Application of bibliometrics in medicine: a historical bibliometrics analysis. Health Information & Libraries Journal. 2021 Jun;38(2):125-38.

Images/Tables

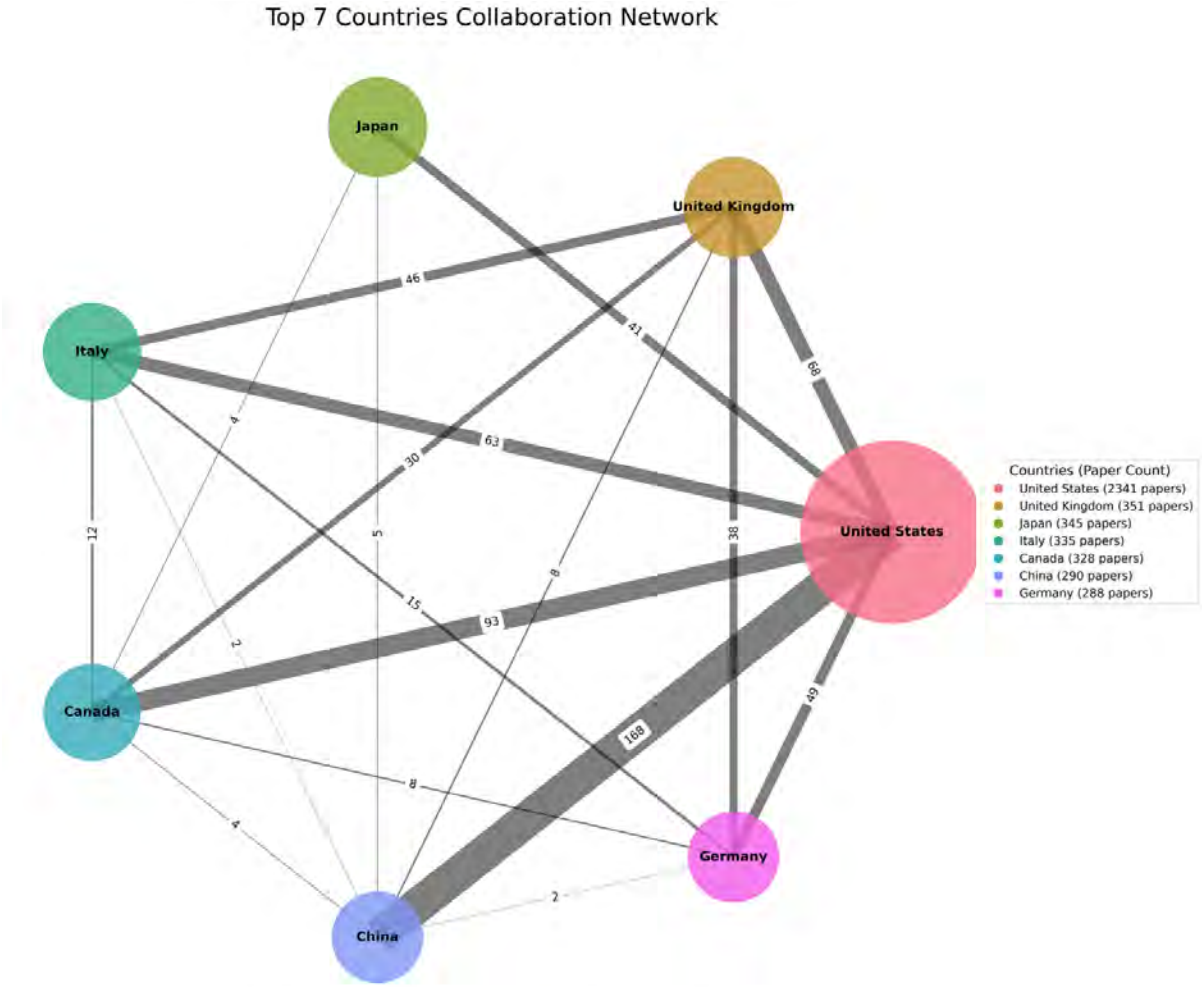

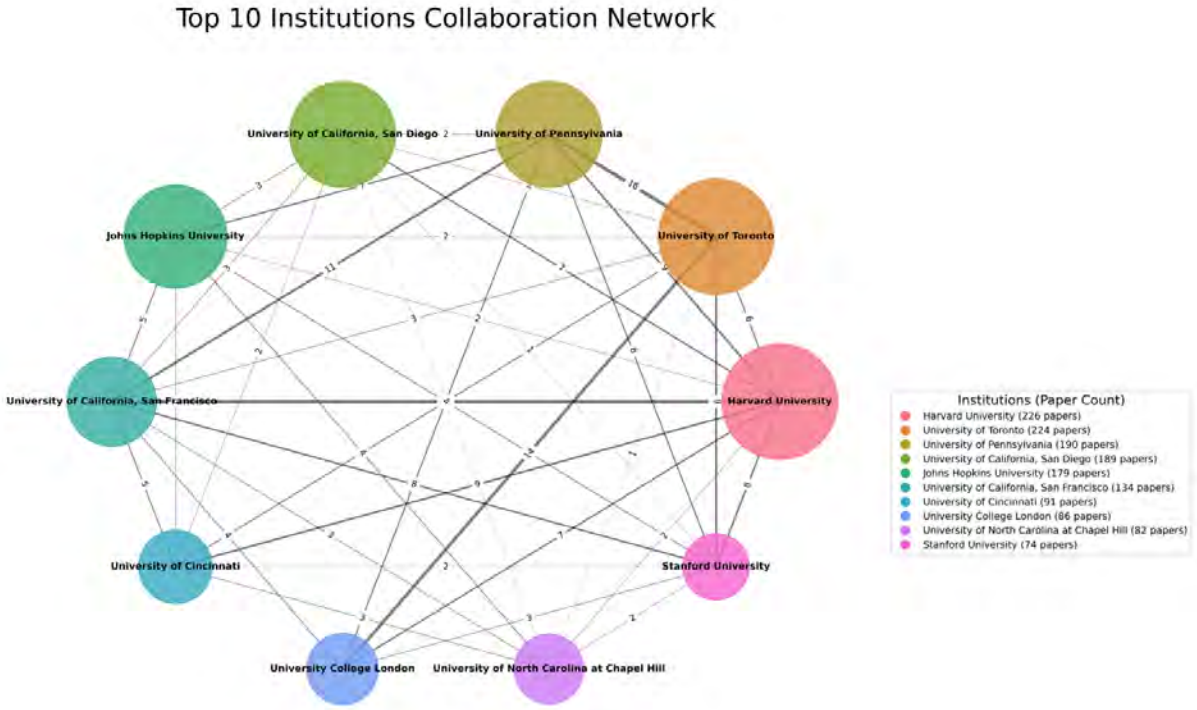

997

Exploring Neural Dynamics: How Visual Disturbances and Hallucinations Impact Dynamic Brain Connectivity in Parkinson's Disease

Sara Naghizadehkashani MD, Omid Shoraka MD, Sahar Darabi Monadi MD, Chengyuan wu MD, Feroze Mohamed PhD, Scott Faro MD
Thomas Jefferson University, Philadelphia, PA, USA

Abstract Category

Functional/Advanced Imaging

Purpose

Parkinson's disease (PD) is frequently accompanied by visual disturbances (VD) and visual hallucinations (VH). (1-2) This study aimed to analyze the alterations of Dynamic Functional Connectivity (dFC) in subjects with PD and concomitant VD and/or VH compared to no visual disorder (ND). We hypothesized that the commonality in the results between VHD vs VD/ND analysis is due to hallucination and the commonality between VHD/VD vs. ND is due to visual disorders.

Materials & Methods

11 PD subjects with VH and/or VD (VHD; n=11), and 11 subjects experiencing solely VD (VD, n=11) were included in this study. Additionally, 47 PD subjects with ND were also enrolled. 12 minutes Resting-state fMRI was performed and group ICA analysis was executed using GIFT toolbox. 40 components were extracted and labeled based on CONN atlas. dFC analysis was performed, using the sliding window method, followed by k-means clustering (window size = 30, TRs=44, sliding in 1 TR=2ms step). A two-sample t-test was performed to compare the dFC between groups ($P<0.05$).

Results

4 reoccurring FC "States" were identified for the whole sample (figure 1). Hallucinations appear to increase dFC between the language network (LN) and visual network (VN) in state 4 and default mode network (DMN) in state 2, as well as decrease dFC between VN and dorsal attention network (DAN) in state 4. Furthermore, visual disturbance decreases connectivity between VN and DMN/LN in state 4 (figure 2). Two sample t-tests of mean dwell time (MDT) in each state between groups VD and ND demonstrated significantly lower MDT for VD in state 2 ($p=0.03$). The changes between states were also significantly higher in VHD vs VD ($p=0.03$). Detailed findings are presented in Tables 1-2.

Conclusion

Network-level dFC analysis in our study suggests dysfunctions in LN, VN, and DMN networks which appear to play a significant role in the emergence of both VH and VD in subjects with PD. Furthermore, decreased connectivity between DAN and VN in the VH group indicates the potential role of DAN in visual hallucination in PD patients.
Understanding the nature of these alterations can lead to a better insight into the pathophysiology of visual hallucinations and disorders. (2)

References

1) Spinosa V, Brattico E, Campo F, et al A systematic review on resting state functional connectivity in patients with neurodegenerative disease and hallucinations. NeuroImage: Clinical. 2022 Jan 1;35:103112.
2) Tan JB, Müller EJ, Orlando IF, et al. Abnormal higher-order network interactions in Parkinson's disease visual hallucinations. Brain. 2024 Feb;147(2):458-71.

Images/Tables

Table 1. Commonalities in DFC analysis results for two pairs of groups

	States	Networks
Visual Hallucination: commonalities between two group-based analyses: VHD vs. ND and VHD vs. VD	State 2	DMN (MPFC) — LN
	State 4	VN — DAN; VN — LN
Visual disturbance: commonalities between two group-based analyses: VHD vs. ND and VD vs. ND	State 4	VN — DMN (LP, PCC)

The red line connecting each pair of regions indicates increased functional connectivity (FC), while the blue line indicates decreased FC.
Abbreviations: DFC, Dynamic functional connectivity; VHD, Visual hallucinations and/or disorders; VD, Visual disorders; ND, No visual disorders; DAN, Dorsal attention network; VN, Visual network; LN, Language network; DMN, Default Mode Network; MPFC, Middle Prefrontal Cortex; LP, Lateral Parietal; PCC, Posterior Cingulate Cortex

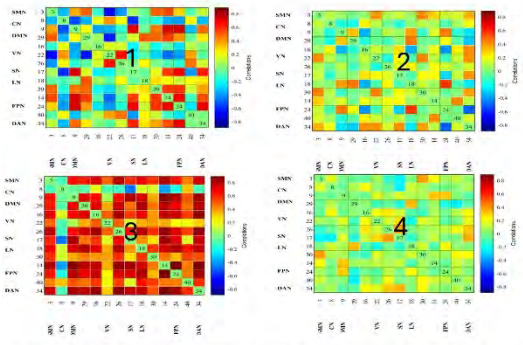

Fig.1. 4 reoccurring functional connectivity states of the whole sample data is shown in connectivity matrices.

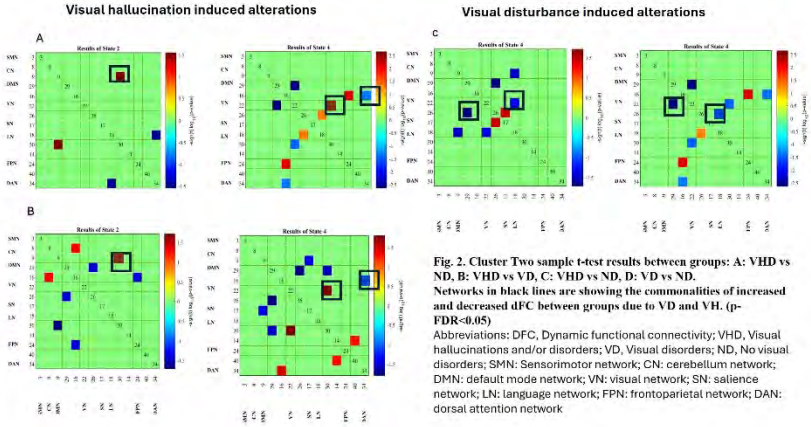

Fig. 2. Cluster Two sample t-test results between groups: A: VHD vs ND, B: VHD vs VD, C: VHD vs ND, D: VD vs ND. Networks in black lines are showing the commonalities of increased and decreased dFC between groups due to VD and VH. (p-FDR<0.05)
Abbreviations: DFC, Dynamic functional connectivity; VHD, Visual hallucinations and/or disorders; VD, Visual disorders; ND, No visual disorders; SMN: Sensorimotor network; CN: cerebellum network; DMN: default mode network; VN: visual network; SN: salience network; LN: language network; FPN: frontoparietal network; DAN: dorsal attention network

Table 2. Two-sample T-test results for mean dwelling time and meta state in each group analysis.

	VHD vs. VD		VHD vs. ND		VD vs. ND	
	T-value	p-value	T-value	p-value	T-value	p-value
MDT in State 1	0.389	0.702	0.997	0.323	0.0406	0.686
MDT in State 2	2.091	0.052	0.701	0.487	-20117	**0.039**
MDT in State 3	-1.392	0.183	-0.604	0.548	1.705	0.094
MDT in State 4	-1.194	0.250	-0.165	0.870	1.521	0.134
Number of States	1.925	0.072	0.782	0.438	-0.998	0.323
Changes between States	2.354	**0.032**	1.187	0.241	-1.176	0.245
State Span	0.934	0.364	0.669	0.506	-0.310	0.758
Total Distance	2.501	**0.024**	1.358	0.181	-1.176	0.245

Bold value indicates statistical significance. (p-value<0.05)

998

Fractional Tumor Burden Accurately Predicts Histological Diagnosis

Melissa A Prah, Max O Krucoff MD, Kathleen M Schmainda PhD
Medical College of Wisconsin, Milwaukee, WI, USA

Abstract Category

Adult Brain

Purpose

Contrast-enhancement on MRI is the target for neurosurgical biopsy despite both tumor and non-tumor/necrosis appearing the same on post-contrast MRI. This lack of distinction on MRI increases the possibility of inaccurate or incomplete sampling that could lead to an underdiagnosis.[1,2] The purpose of this work is to evaluate the diagnostic accuracy of Fractional Tumor Burden (FTB) as a target for surgical biopsy.[3]

Materials & Methods

All patients provided written, informed consent for this prospective HIPAA compliant and IRB-approved study. Patients with advanced imaging who were scheduled for surgical biopsy were included. Prior to surgery, FTB maps were created using OsiriX MD (Bernex, Switzerland) and Imaging Biometrics LLC (Elm Grove, WI) suite of plugins. FTB maps distinguish regions of tumor (red + yellow) from non-tumor (blue) based on a class map of standardized relative cerebral blood volume within calibrated dT1-defined regions of enhancement.[3,4,5] FTB maps were subsequently uploaded to the Brainlab (Munich, Germany) surgical navigation system. Surgical trajectory placement was performed by the neurosurgeon and recorded. Following surgery, FTB trajectories were visually assessed in the axial, coronal, and sagittal planes and categorized as either tumor or non-tumor. Tissue was classed as tumor when the majority of the sampled FTB trajectory was red or yellow, and non-tumor when the majority of the sampled FTB trajectory was blue. The FTB predicted class was compared to the pathologic diagnosis for each biopsy sample, and accuracy was assessed along with Fisher's exact test (P<.05), positive and negative predictive values, and sensitivity and specificity.

Results

Figure 1 shows the use of FTB as a surgical biopsy target. A total of 22 unique biopsy samples were prospectively targeted using FTB from 15 patients (7 male/8 female) between February and October of 2024. Advanced MR imaging was performed a median of 6 (range = 1-10) days prior to surgical biopsy. Histologic diagnosis of the biopsy samples

included WHO grade 4 astrocytoma (N=1), GBM WHO grade 4 with (N=3) and without (N=8) radiation effect, reactive changes with no evidence of tumor (N=8), and metastatic disease (N=2). This resulted in 14 tumor and 8 non-tumor histologic samples. FTB predicted tumor for 16 samples and non-tumor for 6 samples. Fisher's exact p-value was .0004, confirming that FTB class is significantly associated with histologic outcome. The accuracy of surgically targeting tissue based on FTB class was 0.909 with sensitivity/specificity = 1.00/0.75. The positive and negative predictive values were 0.875 and 1.00, respectively.

Conclusion

These initial results demonstrate the utility of FTB maps to guide surgical biopsy. Of 22 samples, only 2 were incorrectly classified as tumor using FTB for biopsy guidance. For these misclassed samples, a significant extent of the sampled tissue was in non-enhancing regions, which are not included on FTB maps. Future work will include quantitative assessment of FTB class relative to histologic diagnosis in a larger population.

References

1. McGirt MJ, Villavicencio AT, Bulsara KR, and Friedman AH. MRI-guided stereotactic biopsy in the diagnosis of glioma: comparison of biopsy and surgical resection specimen. Surgical Neurology 2003;59(4):279-28
2. Mikkelsen VE, Solheim O, Salvesen Ø and Tor SH. The histological representativeness of glioblastoma tissue samples. Acta Neurochirurgica 2021;163:1911–1920.
3. Prah MA, Al-Gizawiy MM, Mueller WM, Cochran EJ, Hoffmann RG, Connelly JM, Schmainda KM. Spatial discrimination of glioblastoma and treatment effect with histologically-validated perfusion and diffusion magnetic resonance imaging metrics. J Neurooncol. 2018 Jan;136(1):13-21.
4. Bedekar D, Jensen T, Schmainda KM. Standardization of relative cerebral blood volume (rCBV) image maps for ease of both inter- and intrapatient comparisons. Magn Reson Med 2010;64(3):907-913.
5. Schmainda KM, Prah MA, Zhang Z, Snyder BS, Rand SD, Jensen TR, Barboriak DP, Boxerman JL. Quantitative Delta T1 (dT1) as a Replacement for Adjudicated Central Reader Analysis of Contrast-Enhancing Tumor Burden: A Subanalysis of the American College of Radiology Imaging Network 6677/Radiation Therapy Oncology Group 0625 Multicenter Brain Tumor Trial. Am J Neuroradiol. 2019 Jul;40(7):1132-1139.

Images/Tables

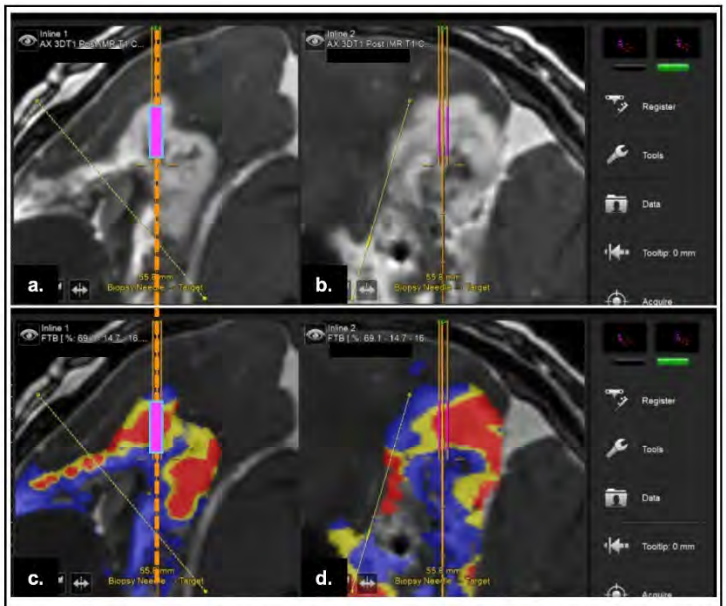

Figure 1. Biopsy trajectories superimposed on T1+C and FTB maps *for a 67y female with MGMT-unmethylated, IDH-wildtype recurrent GBM. The biopsy trajectory and 2 mm sampling extent are indicated by the orange line and pink box (with color emphasis added to a,c). Note the possibility of sampling tumor or non-tumor tissue along the trajectory, which is difficult to distinguish using T1+C alone (a,b). The FTB (c,d) directs sampling to the location with the greatest likelihood of tumor, confirmed here to be GBM.*

1003

Subarachnoid Space Measurements in Second Trimester Using MR Imaging

Onur Simsek MD, Amirreza Manteghinejad MD, Mix Wannasarnmetha MD, Apoorva Kotha MD, Sara Reis Teixeira MD, PhD, Deborah Zarnow MD, Erin Simon Schwartz MD, Matthew T Whitehead MD
Children's Hospital of Philadelphia, Philadelphia, PA, USA

Abstract Category

Pediatrics

Purpose

The subarachnoid space is an important component of the developing intracranial compartment. As fetal brain MRI is becoming more commonplace for early central nervous system (CNS) disease diagnosis, it is imperative to determine age-based standards for normal subarachnoid space depth. We aim to provide 2D reference measurements of the supratentorial subarachnoid spaces in apparently healthy mid- and later second trimester fetuses.

Materials & Methods

In this cross-sectional study, we included all singleton fetal brain MRIs between gestational weeks 19 and 27 without visible CNS pathology. The frontal, insular, and inferior temporal subarachnoid space widths were measured from the inner calvarium to the brain surface bilaterally. Intra-class coefficients (ICC) and Bland-Altman plots were utilized to evaluate agreement between two raters. Left and right-side measurements were compared using Wilcoxon tests. Quade tests were used to compare measurements between male and female fetuses. Generalized additive modeling for location, scale, and shape (GAMLSS) was used to create centile curves.

Results

A total of 177 cases were included. ICC was highest (0.95) for the coronal plane insula width and lowest (0.68) for the coronal plane frontal width. Neither left-right nor male-female comparisons were significantly different when considering age as a confounder; therefore, a single chart was created for each measurement.

Conclusion

As fetal MRI utilization in the second trimester becomes increasingly utilized, a normal reference range for the supratentorial subarachnoid spaces is valuable. Subarachnoid space alterations can be a sign of maldevelopment. This study provides a normal reference range of fetal subarachnoid space widths on fetal MRI from 19-27 weeks of gestation. While the insular subarachnoid space generally increases with advancing gestational age, the frontal and inferior temporal subarachnoid space distances show a more linear or near-linear adaptation to the growing calvarium.

References

1. Watanabe Y, Abe S, Takagi K, Yamamoto T, Kato T. Evolution of subarachnoid space in normal fetuses using magnetic resonance imaging. Prenat Diagn. 2005 Dec;25(13):1217-22. doi: 10.1002/pd.1315. PMID: 16353268.
2. Wandel A, Weissbach T, Katorza E, Ziv-Baran T. Subarachnoid Space Measurements in Apparently Healthy Fetuses Using MR Imaging. AJNR Am J Neuroradiol. 2023 Jun;44(6):716-721. doi: 10.3174/ajnr.A7864. Epub 2023 May 18. PMID: 37202119; PMCID: PMC10249698.
3. Corbacioglu Esmer A, Yuksel A, Aksu Uzunhan T, Demir O, Sarac Sivrikoz T, Aydinli N. Evaluation of fetal subarachnoid space using transabdominal ultrasonography and normal values during pregnancy. Springerplus. 2016 Aug 30;5(1):1439. doi: 10.1186/s40064-016-3121-5. PMID: 27652015; PMCID: PMC5005224.

Images/Tables

Subarachnoid Space Measurements in Second Trimester Using MR Imaging

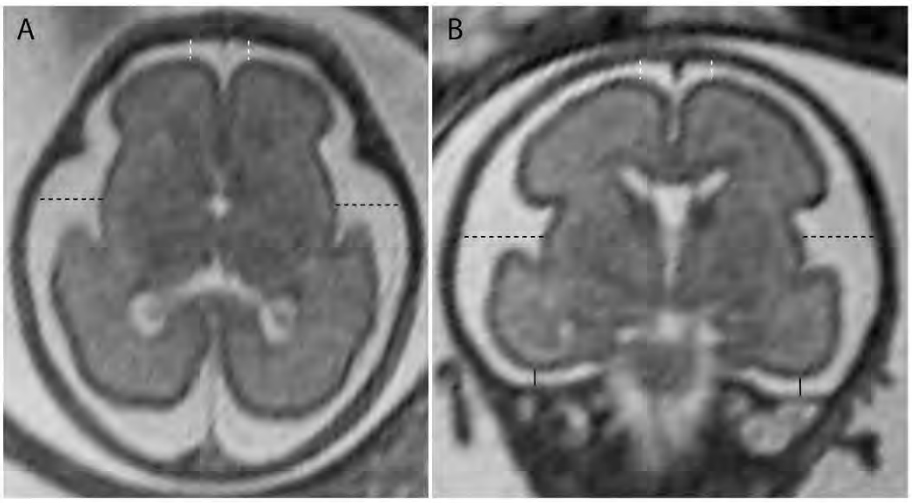

Measurement methodology. A, Ultrafast axial T2-weighted MRI of a 22-week GA fetus shows frontal (dotted white line) and insular (dotted black line) measurements. B, coronal T2-weighted image of the same patient shows frontal (dotted white line), insular (dotted black line), and inferior temporal (black line) measurements.

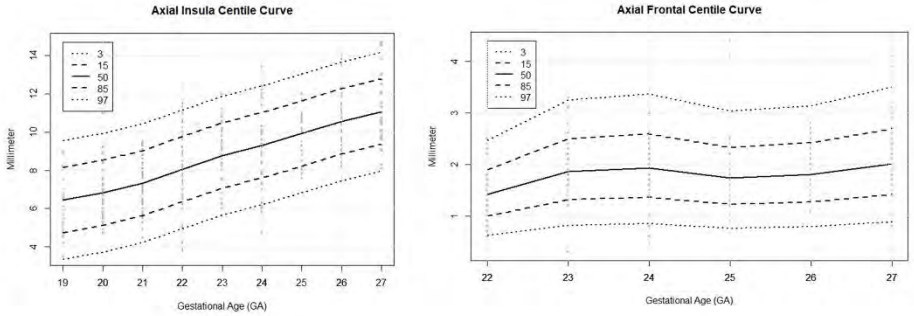

Axial measurement centile curves

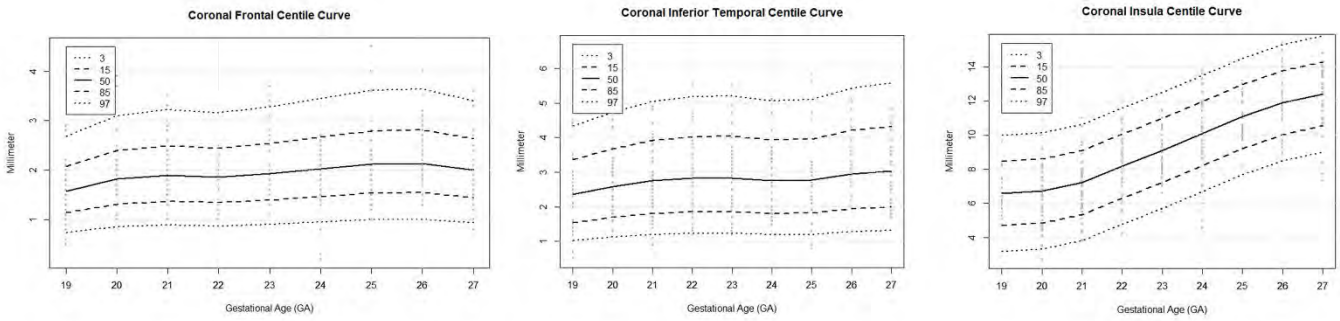

Coronal Measurement Centile Curves

1004

Exploring neural alterations in patients with tumor-related language deficits using graph theory measures; a resting-state fMRI study

Sara Naghizadehkashani MD[1], Mahdi Alizadeh MD[1], Devon Middleton PhD[1], Feroze Mohamed PhD[1], Spandana Tammiraju MD[1], Omid Shoraka MD[1], Zahra Sadeghi Adl[1], Sahar Darabi Monadi MD[2], scott Faro[1], Kiran Talekar MD[1]
[1]Thomas Jefferson University, Philadelphia, PA, USA. [2]London, London, United Kingdom

Abstract Category

Functional/Advanced Imaging

Purpose

Temporal lobe tumors can produce debilitating results when involving language eloquent areas. However, brain neural plasticity can develop wider connections amidst dysfunctions. [1,2] Recent studies have mapped resting-state(rs) fMRI network patterns in healthy adults and children using Graph theory measures, but their application to brain tumors' impact on network topology is limited. [3,4] Our study applies graph theory analysis to rs- fMRI to assess connectivity in patients with language deficits caused by temporal lobe tumors.

Materials & Methods

Twenty-two patients with left temporal tumors underwent resting-state fMRI (rs-fMRI) on a Siemens 3T scanner. The group included 8 males (mean age 52 ± 4) and 9 females (mean age 56 ± 5.5) with normal language (NL) function, as well as 2 males (mean age 57 ± 2.3) and 3 females (mean age 61 ± 2.4) with language deficits (LD). During the 7.5-minute scan, patients were instructed to look at a crosshair and remain awake. After manually segmenting the tumor area, we excluded the tumor mask and conducted ROI-to-ROI analyses using CONN toolbox. Graph metrics were calculated from correlation signals across 164 regions in the CONN atlas and compared between LD and NL groups. (Adjacency matrix threshold = 0.08, p-FDR corrected < 0.05).

Results

At the global level, LD patients showed significantly lower global efficiency in various cerebellar regions ($p<0.0001$), while also showing higher cost and degree values in the contra lesional supramarginal gyrus ($p=0.001$). At the local level, LD patients demonstrated significantly lower local efficiency and clustering coefficient values in the left cerebellum ($p<0.0001$) and left middle temporal gyrus ($p=0.002$). Furthermore, in LD patients, the higher closeness and betweenness centrality in the left cerebellum ($p=0.0001$) and right supramarginal gyrus ($p=0.002$), respectively. Results are shown in detail in Table and Figure 1.

Conclusion

In conclusion, the lower global efficiency and local metrics indicate compromised integration and specialized processing within the brain network of LD patients. Additionally, the increased resource demands in the contra lesional supramarginal gyrus further highlight the challenges in maintaining connectivity in this group. Furthermore, significantly higher closeness and betweenness centrality in the left cerebellum and right supramarginal gyrus in LD patients may indicate that these regions enhance communication within the network.[1,2,5] Finally, our results highlight the potential role of the cerebellum as a hub to preserve language-related connections in the brain and compensate for any tumor-related language function disabilities.[5]

References

1. Semmel ES, Quadri TR, King TZ. Graph theoretical analysis of brain network characteristics in brain tumor patients: A systematic review. Neuropsychology Review. 2022 Sep;32(3):651-75.

2. Cho NS, Peck KK, Gene MN,et al. Resting-state functional MRI language network connectivity differences in patients with brain tumors: exploration of the cerebellum and contralesional hemisphere. Brain Imaging and Behavior. 2022 Feb 1:1-1.

3. Youssofzadeh V, Williamson BJ, Kadis DS. Mapping Critical Language Sites in Children Performing Verb Generation: Whole-Brain Connectivity and Graph Theoretical Analysis in MEG. Front Hum Neurosci. 2017 Apr 5;11:173. doi: 10.3389/fnhum.2017.00173. PMID: 28424604; PMCID: PMC5380724.

4. Li Q, Del Ferraro G, Pasquini L, et al. Core language brain network for fMRI language task used in clinical applications. Netw Neurosci. 2020 Feb 1;4(1):134-154. doi: 10.1162/netn_a_00112. PMID: 32043047; PMCID: PMC7006870.

5. Zhang N, Xia M, Qiu T, et al. Reorganization of cerebro-cerebellar circuit in patients with left hemispheric gliomas involving language network: A combined structural and resting-state functional MRI study. Hum Brain Mapp. 2018 Dec;39(12):4802-4819. doi: 10.1002/hbm.24324. Epub 2018 Jul 27. PMID: 30052314; PMCID: PMC6866325.

Images/Tables

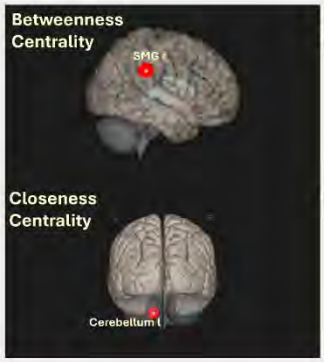

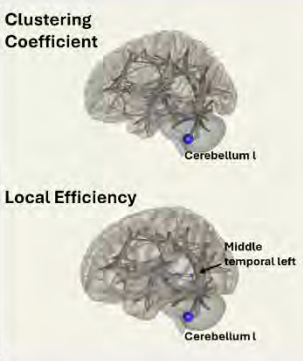

ROI	Rank
Cerebellum	4
SMG	2
Middle Temporal	1

Fig.1. Three regions of interest (ROI) showed significant differences between language deficit and normal language groups across seven graph theory measures. ROIs were ranked based on the number of measures in which they showed significance. SMGr: Supramarginal gyrus right.

Analysis measure	ROI	T-value	p- unc	p-FDR
Global Efficiency	Cerebellum left	-7.13	<0.0001	<0.0001
	Cerebellum right	-6.46	<0.0001	<0.0001
Local Efficiency	Cerebellum left	-13.11	<0.0001	<0.0001
	Middle temporal gyrus left	-4.53	<0.0001	0.002
Betweenness Centrality	Supramarginal gyrus right	+3.91	0.0008	0.002
Closeness Centrality	Cerebellum left	+6.20	<0.0001	0.0001
Cost	Supramarginal gyrus right	+4.21	0.0004	0.001
Clustering Coefficient	Cerebellum left	-11.41	<0.0001	<0.0001
Degree	Supramarginal gyrus right	+4.21	0.0004	0.001

Table 1. Graph theory analysis results in different ROIs compared between the Language deficit and Normal language groups.

1013

Imaging Differentiation of Pediatric Thalamic Tumors: Modified VASARI Features Distinguish Diffuse Midline Glioma and Pilocytic Astrocytoma

Nakul Sheth MD[1], Fabricio G Goncalves MD, EDiNR, EDiPNR[2], Amirreza Manteghinejad MD[1], Carmen R Cerron-Vela MD[1], Mix Wannasarnmetha MD[1], Dmitry Khrichenko PhD[1], Angela N Viaene MD[3], Aashim Bhatia MD, MS[1]
[1]Department of Radiology, Children's Hospital of Philadelphia, University of Pennsylvania, Philadelphia, Pennsylvania, USA. [2]Department of Pediatric Radiology, Children's of Alabama, University of Alabama, Birmingham, Alabama, USA. [3]Department of Pathology and Laboratory Medicine, Children's Hospital of Philadelphia, University of Pennsylvania, Philadelphia, Pennsylvania, USA

Abstract Category

Pediatrics

Purpose

This study evaluated whether a modified VASARI (Visually AcceSAble Rembrandt Images) MRI feature set can distinguish among different histologically and molecularly defined pediatric thalamic tumors. The original VASARI features have been validated in adult gliomas for reproducible qualitative MRI interpretation and for predicting grading, molecular markers, and survival. However, no evidence-based standardized imaging features for pediatric thalamic tumors have been validated to date. Thalamic tumors account for 1% to 5% of pediatric brain tumors. Historically, these tumors were considered inoperable due to their deep location and proximity to critical structures, but advances in neuroimaging and microsurgical techniques have made more extensive resections possible. Studies have shown that aggressive resection improves survival in low-grade thalamic gliomas. In contrast, the role of surgery in high-grade thalamic gliomas lacks consensus, with chemoradiation considered with or without partial debulking. Differentiating various thalamic tumors on imaging is challenging due to overlapping qualitative morphologic features; however, an accurate preoperative diagnosis can change the treatment approach. We hypothesize that modified VASARI features can reliably distinguish low-grade gliomas from H3K27-altered diffuse midline gliomas (DMG) and other high-grade gliomas (HGG) within the thalamus.

Materials & Methods

This retrospective study identified 65 pediatric thalamic tumors at our quaternary hospital. Two blinded neuroradiologists independently reviewed pre-treatment MRI examinations using modified VASARI features. Discrepancies were resolved by a third neuroradiologist. The following 17 imaging features were rated: tumor unilaterality, brainstem extension, basal ganglia involvement, internal capsule involvement, cerebral parenchyma involvement, metastasis, hydrocephalus, intraventricular extension, predominantly solid morphology, hemorrhage, calcification, necrosis, circumscribed margins, peritumoral edema, cystic degeneration, diffusion restriction, and solid enhancement. Chi-square and Fisher exact tests were used to evaluate differences among tumor types.

Results

Thirty tumors were excluded from the final analysis due to lack of molecular testing, precise histologic grading, or adequate diffusion-weighted imaging. A total of 35 tumors were included for analysis: 19 DMG (grade 4), 8 pilocytic astrocytomas (PA, grade 1), 3 ependymomas (grade 3), 1 diffuse pediatric-type HGG (H3-wildtype and IDH-wildtype, grade 4), 1 atypical teratoid/rhabdoid tumor (grade 4), 1 pleomorphic xanthoastrocytoma (grade 2), 1 rosette-forming glioneuronal tumor (grade 1), and 1 ganglioglioma (grade 1). Four of the 17 imaging features demonstrated significant differences between PA and DMG. PA showed a higher prevalence of cystic degeneration ($p=0.033$) and basal ganglia involvement ($p=0.033$). DMG demonstrated a higher prevalence of diffusion restriction ($p<0.001$; infinite odds ratio) and necrosis ($p=0.033$). Low case numbers of other tumor types limited their statistical analysis, rendering them non-contributory to the overall results.

Conclusion

Modified VASARI features can be applied to differentiate thalamic DMG from PA in children, thereby improving neuroradiologists confidence in guiding treatment decisions. Diffusion restriction is the strongest indicator of DMG, with necrosis as an additional reliable feature. Cystic degeneration and basal ganglia involvement are reliable features of PA. Future studies with larger case numbers and inclusion of other thalamic tumor types are needed to further validate the diagnostic and prognostic value of modified VASARI features.

References

1. Biswas A, Amirabadi A, Wagner MW, Ertl-Wagner BB. Features of Visually AcceSAble Rembrandt Images: Interrater Reliability in Pediatric Brain Tumors. AJNR Am J Neuroradiol. 2022 Feb;43(2):304-308. doi: 10.3174/ajnr.A7399. Epub 2022 Jan 20. PMID: 35058297; PMCID: PMC8985665.
2. Chaturvedi A, Sadashiva N, Shukla D, Konar S, Krishna U, Beniwal M, Rao S, Santosh V, Saini J, Vazhayil V, Prabhuraj AR, Pruthi N, Arimappamagan A. Thalamic H3K27M altered diffuse midline gliomas: Clinicopathological and outcome analysis. Clin Neurol Neurosurg. 2024 Sep;244:108449. doi: 10.1016/j.clineuro.2024.108449. Epub 2024 Jul 14. PMID: 39053322
3. Cinalli G, Aguirre DT, Mirone G, Ruggiero C, Cascone D, Quaglietta L, Aliberti F, Santi SD, Buonocore MC, Nastro A, Spennato P. Surgical treatment of thalamic tumors in children. J Neurosurg Pediatr. 2018 Mar;21(3):247-257. doi: 10.3171/2017.7.PEDS16463. Epub 2017 Dec 22. PMID: 29271729.
4. Rodriguez D, Calmon R, Aliaga ES, Warren D, Warmuth-Metz M, Jones C, Mackay A, Varlet P, Le Deley MC, Hargrave D, Cañete A, Massimino M, Azizi AA, Saran F, Zahlmann G, Garcia J, Vassal G, Grill J, Peet A, Dineen RA, Morgan PS, Jaspan T. MRI and Molecular Characterization of Pediatric High-Grade Midline Thalamic Gliomas: The HERBY Phase II Trial. Radiology. 2022 Jul;304(1):174-182. doi: 10.1148/radiol.211464. Epub 2022 Apr 12. PMID: 35412366.
5. Wegscheid ML, Jennings JW. VASARI Glioma Features: Insights into Their Impact and Performance. Radiol Imaging Cancer. 2024 Sep;6(5):e249018. doi: 10.1148/rycan.249018. PMID: 39269896; PMCID: PMC11443470.

Images/Tables

Variable	Pilocytic Astrocytoma (n=8)	H3K27- altered Glioma (n=19)	P-value	Odds Ratio
Tumor Unilaterality	8 (100%)	16 (84.2%)	0.532	
Extension Into Brainstem	7 (87.5%)	15 (78.9%)	1.000	
Involvement of Basal Ganglia	**7 (87.5%)**	**7 (36.8%)**	**0.033**	**12.000 [1.211-118.889]**
Involvement of Internal Capsule	7 (87.5%)	10 (52.6%)	0.190	
Involvement of Cerebral Hemisphere Parenchyma	7 (87.5%)	15 (78.9%)	1.000	
Metastasis at Diagnosis	0 (0%)	2 (10.5%)	1.000	
Hydrocephalus	7 (87.5%)	19 (100%)	0.296	
Intraventricular Extension	1 (12.5%)	7 (36.8%)	0.364	
Solid Morphology	4 (50%)	12 (63.2%)	0.675	
Hemorrhage	2 (25%)	12 (63.2%)	0.103	
Calcification	0 (0%)	2 (10.5%)	1.000	
Necrosis	**1 (12.5%)**	**12 (63.2%)**	**0.033**	**0.083 [0.008-0.826]**
Circumscribed Margins	6 (75%)	10 (52.6%)	0.405	
Edema	7 (87.5%)	16 (84.2%)	1.000	
Cysts	**5 (62.5%)**	**3 (15.8%)**	**0.027**	**8.889 [1.344-58.796]**
Diffusion Restriction	**0 (0%)**	**14 (73.7%)**	**<0.001**	**indefinite**
Enhancement	8 (100%)	18 (94.7%)	1.000	

1019

Histopathology of CSF-Venous Fistulas: Analysis of Three Patients with Spontaneous Intracranial Hypotension After Surgical Nerve Root Ligation and Resection

Andrew Mecum BA[1], BK Kleinschmidt-DeMasters MD[2], Debayan Bhaumik MD[3], Samantha Pisani Petrucci MD PhD[3], Peter Lennarson MD[4], Andrew L. Callen MD[3]

[1]University of Colorado School of Medicine, Aurora, CO, USA. [2]Department of Pathology, University of Colorado Anschutz Medical Campus, Aurora, CO, USA. [3]Department of Radiology, Neuroradiology Section, University of Colorado Anschutz Medical Campus, Aurora, CO, USA. [4]Department of Neurosurgery, University of Colorado Anschutz Medical Campus, Aurora, CO, USA

Abstract Category

Spine

Purpose

To elucidate the histopathological characteristics and potential pathophysiology of cerebrospinal fluid-venous fistulas (CVF) in patients with spontaneous intracranial hypotension (SIH).

Materials & Methods

Three patients with SIH who underwent CVF ligation and nerve root resection after confirmation of CVF on dynamic CT myelography (dCTM) were retrospectively analyzed. Histopathological examination of the resected tissues, including nerve roots and associated cysts, was performed.

Results

Histopathological examination across the three cases revealed several consistent and notable findings:

- Juxtaposition of Leptomeninges and Large Veins: In each case, there was a close anatomical relationship between leptomeninges and large-caliber veins, suggestive of a structural predisposition for CVF formation, although no definitive fistulous connection was visualized on immunohistochemistry (IHC).
- Vascular and Fibrous Changes: Specimens consistently showed dilated, congested veins, alongside fibrosis within surrounding fibroadipose tissues. This chronic vascular congestion and fibrosis could reflect a longstanding pathophysiological process, potentially related to degenerative or inflammatory changes.
- Hemorrhage and Osseous Metaplasia: In two of the cases, dilated subarachnoid spaces demonstrated hemorrhage and osseous metaplasia, indicating chronic tissue response to persistent changes in CSF dynamics. This finding may highlight the role of mechanical stress or repeated microtrauma in CVF development.
- Epineurial Thickening: Thickened muscularis in epineurial vessels was noted in one case, with equivocal thrombosis in a small epineurial vessel, suggesting localized vascular remodeling, possibly influenced by chronic pressure or vascular anomalies.

Conclusion

The histopathological findings across these cases reveal a pattern of venous dilation, vascular congestion, and fibrosis, underscoring the complexity of CVF anatomy and hinting at a potential link to chronic mechanical or vascular stress. While IHC supported CVF diagnosis, definitive CSF-venous connections were not observed, highlighting the elusive nature of this pathology. These observations align with hypotheses of age-related or degenerative changes contributing to CVF formation[1] and emphasize the need for a multidisciplinary approach in managing SIH related to CVFs.

References

1. Kranz PG, Gray L, Malinzak MD, et al. CSF-Venous Fistulas: Anatomy and Diagnostic Imaging. AJR Am J Roentgenol. 2021 Dec;217(6):1418-1429. DOI: 10.2214/AJR.21.26182.

Images/Tables

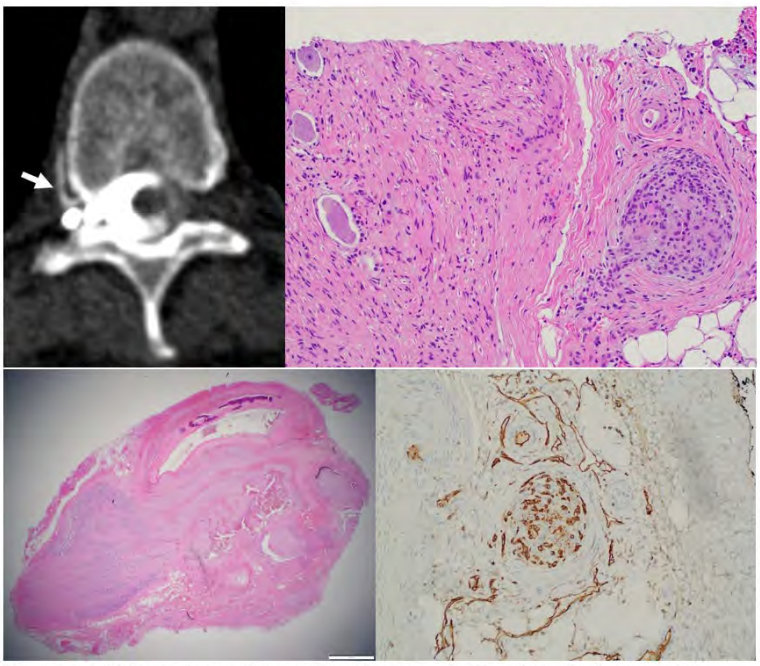

Figure 1. Axial CT image from right lateral decubitus dynamic CT myelography demonstrates a hyperdense paraspinal segmental vein adjacent to the right T10 nerve root, consistent with a CSF venous fistula (upper left). Intimal proliferation (upper right) and dystrophic mineralization (bottom left) are observed on hematoxylin and eosin stain. Immunohistochemistry (bottom right) labeling with essentially all cystic lining cells present, which also shows patchy labeling with epithelial membrane markers. Cell adhesion and endothelial markers label endothelial cells in various surrounding vessels, as well as those in small capillaries surrounding the cystic areas. Across all stains, close juxtaposition of the vascular and leptomeningeal elements is seen, though no definitive CSF-venous connection is identified, with Van Gieson's stain labeling the elastic lamina of larger vessels away from the cystic subarachnoid structures.

1022

Functional Connectivity Alterations in patients with left temporal and frontal lobe tumors expressing language deficits: Impact of Tumor Location on Network Reorganization

Sara Naghizadehkashani MD[1], Kiran Talekar MD[1], Devon Middleton PhD[1], Feroze Mohamed PhD[1], Mahdi Alizadeh PhD[1], Zahra Sadeghi Adl[1], Sahar Darabi monadi[2], Omid Shoraka MD[3], Scott Faro MD[1]

[1]Thomas Jefferson University, Philadelphia, PA, USA. [2]London, London, United Kingdom. [3]Philadelphia, PA, USA

Abstract Category

Functional/Advanced Imaging

Purpose

Brain tumors can lead to network reorganization and neurological deficits depending on their location.[1] Functional connectivity (FC) analysis offers insights into these tumor-related neural disruptions. [2,3,4] In this study, we examined FC alterations in patients with left temporal and frontal lesions, both with and without language deficits, to identify potential brain regions that may help compensate for tumor-related damage in language areas and support functional preservation.

Materials & Methods

7.5 minutes Resting-state (rs) fMRI was performed on 39 right-handed patients with left frontal or temporal brain tumors. Of the 22 patients with left temporal tumors, 17 had normal language (NL) function (mean age 62.5 years; 8 males, 9 females), while 5 had language deficits (LD) (mean age 59.4 years; 2 males, 3 females). Among the 17 patients with left frontal tumors, 13 had NL function (mean age 59.5 years; 7 males, 6 females), while 4 had LD (mean age 60 years; 2 males, 2 females).

After manually segmenting the tumor area, we preprocessed the rs-fMRI data and performed ROI-to-ROI FC analyses using the CONN toolbox, excluding the tumor mask. Functional connectivity comparisons between the LD and NL groups were conducted across 133 regions of interest (ROIs) with Bonferroni correction applied ($p < 0.0003$) and within 32 rs-fMRI networks defined by the CONN network ROIs. (p-FDR corrected < 0.05).

Results

Decreased FC was shown in the LD group for both tumor locations in various ROIs. In the temporal tumor group, the network-based analysis showed significantly lower FC in left and right pSTG with various ROIs in DMN, Salience, SMN, and visual networks in addition to decreased FC within the language network. (Table and Figure 1) In the frontal tumor group, the network-based analysis (32 ROIs) showed no significant differences between LD/NL groups, however, using the CONN-ALL3 atlas (133 ROIs), cerebellum showed significantly decreased FC to various brain areas. (Table and Figure 2)

Conclusion

Our results highlight the areas of the brain which potentially might play a role in preserving language function in patients with tumor in different language eloquent areas. Understanding these neural reorganizations of different tumor locations could aid improvement in treatment strategies and outcomes for these patients.

References

1. IJzerman-Korevaar M, Snijders TJ, de Graeff A, Teunissen SC, de Vos FY. Prevalence of symptoms in glioma patients throughout the disease trajectory: a systematic review. Journal of neuro-oncology. 2018 Dec 15;140:485-96.
2. Lakhani DA, Sabsevitz DS, Chaichana KL, Quiñones-Hinojosa A, Middlebrooks EH. Current state of functional MRI in the presurgical planning of brain tumors. Radiology: Imaging Cancer. 2023 Oct 20;5(6):e230078.
3. Liouta E, Katsaros VK, Stranjalis G, Leks E, Klose U, Bisdas S. Motor and language deficits correlate with resting state functional magnetic resonance imaging networks in patients with brain tumors. Journal of Neuroradiology. 2019 May 1;46(3):199-206.
4. Cho NS, Peck KK, Gene MN, Jenabi M, Holodny AI. Resting-state functional MRI language network connectivity differences in patients with brain tumors: exploration of the cerebellum and contralesional hemisphere. Brain Imaging and Behavior. 2022 Feb 1:1-1.

Images/Tables

ROI	T-value	P-UNC	P-FDR Cor
Default mode MPFC[1]– Language pSTG[2] left	-4.51	0.000211	0.0065
Default mode LP[3] left – Language pSTG left	-2.79	0.011	0.037
Visual right- Language IFG[4] left	-4.09	0.00056	0.017
Language pSTG left – Default mode PCC[5]	-3.71	0.0013	0.029
Language pSTG left – Default mode LP right	-3.58	0.0018	0.019
Language pSTG left – Salience Ainsula right	-3.28	0.0037	0.027
Language pSTG left – language IFG right	-3.13	0.0055	0.027
Language pSTG left – visual lateral right	-3.07	0.0061	0.027
Language pSTG left – sensorimotor right	-3.05	0.0063	0.027
Language pSTG left – Visual medial	-2.98	0.0074	0.028
Language pSTG left – Salience SMG[6] right	-2.72	0.013	0.037
Language pSTG left – Salience RPFC[7] right	-2.63	0.015	0.037
Language pSTG left – Language pSTG right	-2.61	0.016	0.037
Language pSTG left – visual lateral left	-2.61	0.016	0.037
Language pSTG left- Salience ACC[8]	-2.61	0.016	0.031
Language pSTG left – visual occipital	-2.56	0.018	0.038

Table 1. Network based ROI-to-ROI FC measures comparison between LD and NL groups of temporal tumor patients. 1.Medial Prefrontal Cortex, 2. Posterior Superior Temporal Gyrus, 3. Left Parietal, 4. Inferior Frontal Gyrus, 5. Posterior Cingulate Cortex, 6. Supramarginal Gyrus, 7. Right Prefrontal Cortex, 8. Anterior Cingulate Cortex

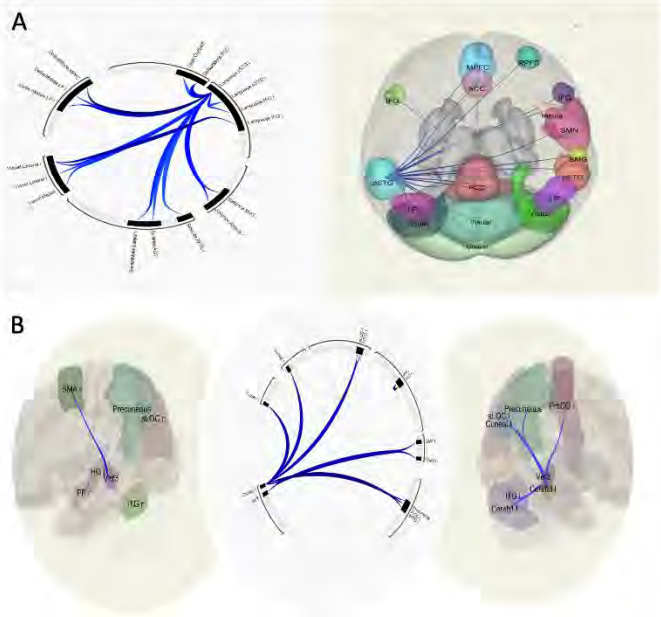

Fig. 1. A: The left panel shows a connectogram illustrating the results of ROI-to-ROI network-based functional connectivity (FC) analysis, comparing Language Deficit and Normal Language groups in temporal tumor patients. The right panel presents a 3D brain map highlighting the regions with reduced FC. Blue lines indicate regions with significantly decreased FC in the Language Deficit group. Abbreviations: MPC: Medial Prefrontal Cortex, pSTG: Posterior Superior Temporal Gyrus, LP: Left Parietal, IFG: Inferior Frontal Gyrus, PCC: Posterior Cingulate Cortex, SMG: Supramarginal Gyrus, PFC: Prefrontal Cortex, ACC: Anterior Cingulate Cortex

B: 3D brain maps on the right and the left are showing areas with significantly decreased functional connectivity (FC) in language deficit (LD) group versus normal language (NL), in patients with frontal tumor. In the center, a connectogram is highlighting the significantly hypo-connected areas among 133 regions of interest (ROI) using CONN atlas, in LD group vs NL group of frontal tumor patients. Abbreviations: ITG: Inferior Temporal Gyrus, sLOC: Lateral Occipital Cortex, superior division, HG: Heschl's Gyrus, SMA: Juxtapositional Lobule Cortex -formerly Supplementary Motor Cortex, Pre CGI: Pre-Central Gyrus.

ROI	T-Value	P-UNC
Left Cerebellum – tolTG L[1]	-5.53	<0.0001
Left Cerebellum – sLOC L[2]	-5.50	<0.0001
Left cerebellums – Left cerebellum Crus	-5.06	0.000142
Left cerebellums – Left Precentral Gyrus	-4.95	0.000175
Left cerebellums – Left Cuneal Cortex	-4.91	0.000188
Left cerebellums - Praecuneus Cortex	-4.83	0.000219
Left cerebellums - tolTG R[3]	-4.77	0.000246
Left cerebellums - sLOC R[4]	-4.69	0.000290
HG R[5] – Right Planum Polare	-5.04	0.000146
Vermis - SMA R[6]	-4.90	0.000192

Table 2. ROI-to-ROI FC measures comparison between LD and NL groups of frontal tumor patients 1. Left Inferior Temporal Gyrus, temporooccipital part, 2. Left Lateral Occipital Cortex, superior division, 3. Right Inferior Temporal Gyrus, temporooccipital part, 4. Right Lateral Occipital Cortex, superior division, 5. Right Heschl's Gyrus, 6. Right Juxtapositional Lobule Cortex -formerly Supplementary Motor Cortex

1034

Representation of International Medical Graduates among Diagnostic Radiology Chairs, Neuroradiology Chiefs, and Program Directors

Fatemeh Dehghani Firouzabadi[1], Mina Hesami[2], Ali Sheikhy[3], Mahla Radmard[4], Mona Dabiri[4], Sara Ramezanpour[5], David M. Yousem[4]

[1]San Francisco, California, USA. [2]New Haven, Connecticut, USA. [3]NAtional Institutes of Health, Bethesda, Maryland, USA. [4]Russell H. Morgan Department of Radiology and Radiological Science, Johns Hopkins Medical Institution, Baltimore, Maryland, USA. [5]South Miami, Florida, USA

Abstract Category

Socioeconomics & Health Policy

Purpose

The number of international medical graduates (IMGs) entering radiology residencies and neuroradiology fellowships averaged 9.7% and 20.9% from 2021-2023 respectively. We aimed to determine whether IMG graduates are populating leadership roles at a proportionate rate in diagnostic radiology (DR) and neuroradiology (NR).

Materials & Methods

We surveyed 191 DR program directors (PDs), 94 NR PDs, 192 chairs of DR and 91 directors of NR inquiring about their original citizenship and medical school [American Medical Graduates (AMG) vs IMG]. We reviewed institutional web sites to obtain missing data and recorded H indices for each person using Scopus.

Results

We confirmed the original citizenship and medical school location in 61 75% and 93-98% of each leadership group. We found that 19/119 (16.2%) DR PDs, 31/71 (43.7%) NR PDs, 33/116 (28.5%) DR Chairs and 28/69 (40.6%) NR Chiefs were not originally US citizens. The IMG rate was 18/188 (9.6%), 20/90 (22.2%), 26/186 (14.0%), and 19/85 (22.4%) for DR PDs, NR PDs, Chairs and NR Chiefs respectively. The most common country of origin and medical school cited was India for all leadership groups. IMGs had a median H index of 14 while AMGs 10, significantly different (p=0.021)

Conclusion

Compared to the rate of DR/NR trainees entering from 2021-2023, IMGs are proportionately represented at the NR PD), NR chief, DR Chairs, and DR PDs positions. The H index of the IMGs was higher than AMGs. We conclude that IMGs have made substantial and proportionate inroads in radiology and neuroradiology leadership. The proportional presence of IMGs in critical leadership roles within DR and NR, alongside their notably higher academic productivity, signifies a promising trend towards a more inclusive and dynamic leadership paradigm. This advancement not only enriches the diversity of perspectives but also enhances a culture of excellence and innovation within these pivotal medical specialties.

References

Ritika Manik, Gelareh Sadigh, Diversity and inclusion in radiology: a necessity for improving the field, *British Journal of Radiology*, Volume 94, Issue 1126, 1 October 2021, 20210407, https://doi.org/10.1259/bjr.20210407

Images/Tables

TABLE 1. Data Regarding Citizenship and Medical School Site

Numbers/ (%)	Citizenship	First Citizenship	Medical School Location
DR PD (191)	Available data (115)	Available data (117)	Available data (188)
US	114 (99.1%)	98 (83.8%)	170 (90.4%)
Non-US	1 (0.9%)	19 (16.2%)	18 (9.6%)
NR PD (94)	Available data (68)	Available data (71)	Available data (90)
US	61 (89.7%)	40 (56.3%)	70 (77.8%)
Non-US	7 (10.3%)	31 (43.7%)	20 (22.2%)
Chair of DR (192)	Available data (121)	Available data (116)	Available data (186)
US	120 (99.2%)	83 (71.5%)	160 (86.0%)
Non-US	1 (0.8%)	33 (28.5%)	26 (14.0%)
NR Chief (91)	Available data (67)	Available data (69)	Available data (85)
US	63 (94.0%)	41 (59.4%)	66 (77.6%)
Non-US	4 (6.0%)	28 (40.6%)	19 (22.4%)
TOTAL (568)*	371 (65.3%)	373 (65.7%)	549 (96.6%)

There were 46 people who had multiple roles in their departments, including six IMGs and 40 AMGs

TABLE 2. Median H indices of AMGs and IMGs

H index differences		
AMGs	10 [7,12]	p-value = 0.021
IMGs	14 [11,20]	

TABLE 3. Median H Index Differences Between IMG and AMG for Each Leadership Group Separately

H Index	AMG	IMG	p-value
DR PD	5 [4,7]	7 [5,16]	0.387
NR PD	8 [7,12]	11.5 [8,14]	0.160
DR Chair	15 [12,20]	19 [16,50]	0.243
NR Chief	20 [16,28]	21 [20,29]	0.818

1042

Exploring Longitudinal CSF Changes Using Rapid Hybrid-state qMT MRI in Mild Traumatic Brain Injury

Sohae Chung PhD, Sebastian Flassbeck PhD, Alaleh Alivar PhD, Elisa Marchetto PhD, Andrew Mao PhD, Joseph F. Rath PhD, Steven R. Flanagan MD, Jakob Assländer PhD, Yvonne W. Lui MD
NYU Grossman School of Medicine, New York, NY, USA

Abstract Category

Functional/Advanced Imaging

Purpose

Mild traumatic brain injury (MTBI) is a common but potentially serious condition often resulting in significant clinical outcomes. However, our understanding of the underlying mechanisms and pathophysiology of MTBI remains limited. Cerebrospinal fluid (CSF) is crucial to the central nervous system, reflecting biochemical changes in the brain post-injury. After MTBI, the CSF-brain barrier may be compromised, allowing larger molecules - such as microbial metabolites, cytoskeletal proteins, and neuronal and glial components – to enter the CSF [1]. These changes in CSF composition may serve as potential biomarkers for MTBI, though they are not easily detectable with conventional MRI. Quantitative magnetization transfer (qMT) imaging offers enhanced sensitivity for subtle tissue changes by analyzing the interactions between free and bound hydrogen nuclei [2]. This study aims to investigate CSF changes and their relationship to symptoms in MTBI patients by employing a 12-minute hybrid-state qMT protocol [3] paired with an unconstrained 2-pool model [4]. We hypothesize that qMT imaging reveals early CSF changes that could serve as non-invasive biomarkers for MTBI.

Materials & Methods

We studied 44 MTBI subjects at three timepoints (< 1 month, 1-3 months, and 3-6 months post-injury) and 16 controls (Table 1). Symptoms were assessed using the Rivermead post-concussion symptoms questionnaire (RPQ). Hybrid-state qMT imaging was performed on a 3T scanner (Prisma, Siemens) with an unconstrained qMT model [4] to extract the semi-solid spin pool size and entropy of (Fig. 1). Four CSF regions (lateral ventricles, CSF, 3rd ventricle, and 4th ventricle) were segmented using Freesurfer (Fig. 2a). An ROI analysis compared MTBI and NC groups with age and sex as covariates. Correlation analysis examined the relationship between qMT parameters and RPQ scores in MTBI patients.

Results

Significant increases in all ROIs were observed between MTBI and NC groups in both m_0^s and m_0^s entropy across timepoints (Fig. 2). Correlation analysis revealed a significant increase in m_0^s and a trend of increased m_0^s entropy with higher RPQ total scores in MTBI patients only at 3–6 months post-injury (Fig. 3).

Conclusion

This study uses qMT imaging to demonstrate longitudinal CSF composition changes and their association with persistent symptoms following MTBI using qMT imaging. Findings support that CSF composition is altered post-MTBI [1], suggesting qMT imaging's promise as a biomarker for detecting subtle, progressive CSF changes. Increased m_0^s entropy indicates greater variability in the macromolecular fraction, suggesting microstructural disorder following injury. Future research will focus on CSF recovery patterns post-MTBI, potentially enhancing diagnostic accuracy and guiding targeted treatment strategies.

References

[1] Bohnert S. et al, Neuroforensomics: metabolites as valuable biomarkers in cerebrospinal fluid of lethal traumatic brain injuries. Scientific Reports 2024; 14:13651.
[2] Filippi et al. Magnetization transfer magnetic resonance imaging in the assessment of neurological disease. J Neuroimaging 2004; 14(4):303-313.
[3] Assländer et al. Rapid quantitative magnetization transfer imaging: Utilizing the hybrid state and the generalized Bloch model. MRM 2024; 91(4):1478-1497.
[4] Assländer et al. Unconstrained quantitative magnetization transfer imaging: disentangling T1 of the free and semi-solid spin pools. Imaging Neuroscience 2024; 2:1-16.

Images/Tables

Table 1: Study Population

	Normal Control (NC)	< 1 month of MTBI	1-3 months of MTBI	3-6 months of MTBI
# of subjects	16	14	28	32
AGE (years)	39 ± 15	39 ± 14	42 ± 12	46 ± 17
Sex (male: female)	7:9	5:9	10:18	10:22
RPQ total score (mean ± SD)	3 ± 4	29 ± 13	27 ± 13	26 ± 13

Table 2: ROI analysis results showing significant differences (red, $p < 0.05$) in the semi-solid spin pool size, m_0^s, and its entropy between MTBI and NC groups across three timepoints, with corresponding p-values.

	ROI	< 1 month of MTBI	1-3 months of MTBI	3-6 months of MTBI
m_0^s	Lateral ventricle	0.705	0.001	< 0.001
	3rd ventricle	0.855	0.061	0.002
	4th ventricle	0.549	0.025	0.008
	CSF	0.322	0.066	0.006
Entropy of m_0^s	Lateral ventricle	0.564	0.002	0.003
	3rd ventricle	0.679	0.027	0.001
	4th ventricle	0.602	0.006	0.002
	CSF	0.175	0.040	0.001

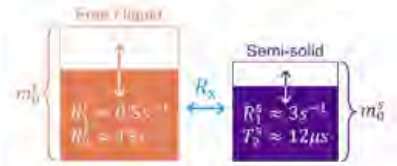

Figure 1. The sketch of 2-pool qMT model [4] describes all magnetization arising from protons bound in liquids by the spin pool m_0^f and protons bound in macromolecules by the pool m_0^s. R_x: exchange rate between the pools. $R_1^{s,f}$ and $R_2^{s,f}$: longitudinal and transverse relation rate in free/semi-solid pools.

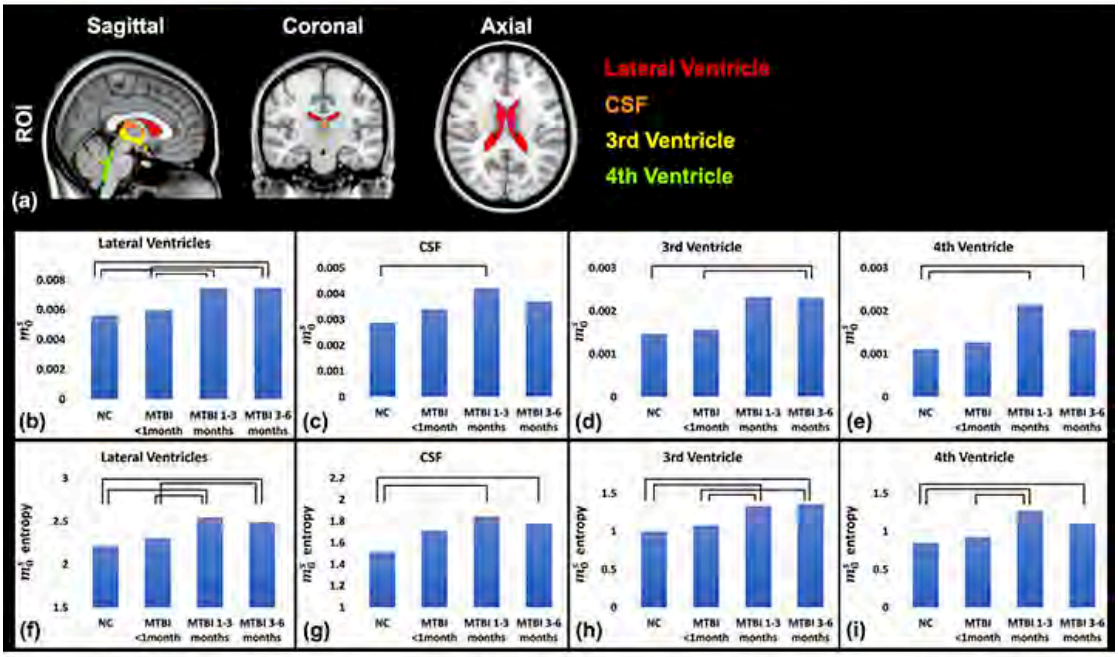

Figure 2. (a) Regions of interest (ROIs): lateral ventricles, CSF, 3rd ventricle and 4th ventricle. Bar graphs show significant increases of m_0^s (b-e) and m_0^s entropy (f-i) in MTBI patients compared to normal controls (NC) across timepoints in the lateral ventricles, CSF, 3rd ventricle and 4th ventricle, respectively. See Table 2 for p-values.

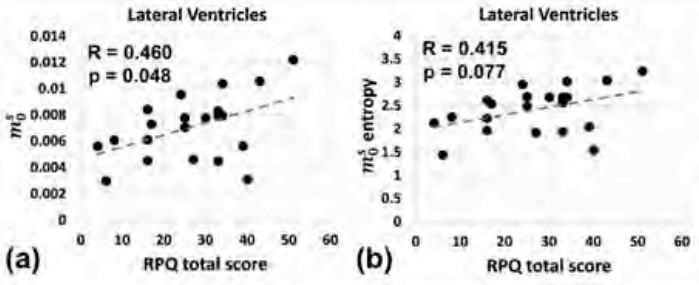

Figure 3. Scatter plots show (a) significantly increased m_0^s and (b) a trend of increased m_0^s entropy with higher RPQ total scores in MTBI patients at 3 – 6 months post-injury.

Acknowledgements:

This work was supported in part by grant funding from the NIH/NINDS: R01 NS119767-01A1, R01 NS131458-01, and R01 NS131948. This work was also performed under the rubric of the Center for Advanced Imaging Innovation and Research (CAI2R), a NIBIB Biomedical Technology Resource Center (NIH P41 EB017183). AM acknowledges support from the NIH/NIA (T32 GM136573 and F30 AG077794).

1043

Poor R-wave Progression on EKG Associates with Brain Amyloid Deposition on PET: A Potential Link Between Cardiac and Cerebral Proteinopathies

Stephen J Sozio DO, MBS[1], Mony J de Leon EdD[1], Adi Sayahi MD[2], Jiwon Kim MD[2], Parag Goyal MD[2], Silvia Fossati PhD[3], Tracy Butler MD[1], Lidia Glodzik MD, PhD[1], Yi Li MD, PhD[1], Hani Hojjati PhD[1], Liangdong Zhou PhD[1], Silky Pahlajani MD[1], Hugh Wang MS[1], Emily Tanzi MS[1], Patrick Harvey MS[1], Gloria Chia-Yi Chiang MD[1]

[1]Weill Cornell Medicine, Department of Radiology, Brain Health Imaging Institute, New York, NY, USA. [2]Weill Cornell Medicine, Department of Cardiology, New York, NY, USA. [3]Temple University, Lewis Katz School of Medicine, Alzheimer's Center at Temple, Philadelphia, PA, USA

Abstract Category

Adult Brain

Purpose

Brain amyloidosis is a pathological hallmark of Alzheimer's disease (AD), in which accumulation of $A\beta_{40}$ and $A\beta_{42}$ plaques and tau neurofibrillary tangles leads to neuronal dysfunction and ultimately neuronal death. Amyloid deposition in the heart leads to cardiac amyloidosis (CA) and raises the question of whether presence of amyloid in one organ system may increase the risk of developing amyloid in another. Despite the possibility of parallel pathogenesis of these proteinopathies, little has been documented regarding the risk profile and incidence of co-existence of AD and CA. Thus, this study sought to examine the relationship between AD and CA by evaluating electrocardiograms for evidence of CA in individuals with brain amyloidosis on PET.

Materials & Methods

191 individuals (mean age 66 +/- 13 years, 66% cognitively normal) were prospectively enrolled into an IRB-approved AD research study and retrospectively analyzed. Inclusion criteria included having undergone an amyloid PET scan and EKG within 1 year. EKGs analyzed for common findings associated with CA, including low QRS voltage, poor R wave progression, and bundle branch block. Amyloid PET studies were quantified using the Centiloid scale. Ordinary least squares regression analyses were used to evaluate associations among EKG findings, amyloid PET centiloid values, and degree of cognitive impairment, based on the Clinical Dementia Rating (CDR) scale. In a subgroup that underwent tau PET, logistic regression analysis was performed to test the relationship between EKG findings and presence of cortical tau deposition.

Results

Poor R-wave progression was associated with a greater degree of brain amyloid deposition on PET (coefficient = 44.7 +/- 11.96, $p<0.001$), which remained significant even after adjusting for age ($p=0.001$) and APOE ε2 or ε4 carrier status ($p=0.001$). Poor R-wave progression was also associated with higher CDR sum of boxes (coefficient = 1.04 +/- 0.49, $p=0.035$) and CDR global scores (coefficient = 0.29 +/- 0.101, $p=0.005$), compatible with greater cognitive impairment. In subgroup analysis, poor R-wave progression was also associated with a higher likelihood of having cortical tau deposition (odds ratio = 1.3 +/- 0.66, $p = 0.049$), but only a trend after adjusting for age ($p=0.066$) and APOE ε2 or ε4 carrier status ($p=0.089$). There was no association between low QRS complex voltage or bundle branch block and brain amyloid deposition ($p>0.05$).

Conclusion

Our findings demonstrate an association among poor R-wave progression, suggestive of underlying cardiac amyloidosis, cerebral amyloid deposition, and cognitive impairment, which supports a relationship between CA and AD. Poor R-wave progression has been described as one of the earliest arrhythmias to emerge due to an underlying conduction anomaly, such as that caused by the pathological deposition of amyloid within the heart. Further prospective clinically-based and pathologically-based analyses to further explore the relationship between CA and AD are warranted.

References

1. Gouras GK, Tampellini D, Takahashi RH, et al. Intraneuronal β-amyloid accumulation and synapse pathology in Alzheimer's disease. *Acta Neuropathol* 2010, 119: 523-541.
2. Bloom GS. Amyloid-β and tau: the trigger and bullet in Alzheimer disease pathogenesis. *JAMA Neurol* 2014, 71: 505-508.
3. Troncone L, Luciani M, Coggins M, et al. Aβ Amyloid Pathology Affects the Hearts of Patients with Alzheimer's Disease. *J Am Coll Cardiol* 2017, 68: 2395-2407.
4. Elia A, Parodi-Rullan R, Vazquez-Torres R, et al. Amyloid β induces cardiac dysfunction and neuro-signaling impairment in the heart of an Alzheimer's disease model. BioRxiv 2023. 1.

5. Hartnett J, Jaber W, Maurer M, et al. Electrophysiological Manifestations of Cardiac Amyloidosis: *JACC: CardioOncology* State-of-the-Art Review. *JACC Cardiooncol* 2021, 3: 506-515.

1052

CLIPS (Clinoidal, Lateral, Inferior, Posterior, Superior): Development of a Magnetic Resonance Grading System to Predict Invasion of Cavernous Sinus Compartments in Pituitary Adenoma.

Felipe Constanzo MD[1], Johannes H Decker MD, PhD[2], Jonathan Rychen MD[3], Nancy Fischbein MD[2], Juan Carlos Fernandez-Miranda MD[2]
[1]Hospital Clinico Regional de Concepcion, Concepcion, NA, Chile. [2]Stanford, Palo Alto, California, USA. [3]Lenox Hill Hospital, New York, NY, USA

Abstract Category

Head & Neck

Purpose

Preoperative assessment of cavernous sinus (CS) invasion is of paramount importance in the surgical planning of pituitary adenomas. The most widely used classification - the Knosp grading system - has several limitations, such as its evaluation of only superior and inferior compartments, and variability in the positioning of the lines, leading to widely variable incidences of true CS invasion and low interobserver agreement. Therefore, we set out to develop a new classification to address these shortcomings.

Materials & Methods

A new classification was developed based on the evaluation of each CS compartment (superior, inferior, lateral, posterior) and clinoidal space. For each compartment, a single line bisecting the carotid artery, following anatomical planes, was used to grade the lateral extension of the adenoma. Tumors medial to these lines were graded as 0, and those lateral to it were graded as 1. The classification was used to evaluate 255 patients (510 CS) that underwent endoscopic endonasal approach (EEA), either with transcavernous surgical extension (TC-EEA group = 139 CS) or without (EEA group = 258 CS). Invasion of each compartment was evaluated by intraoperative assessment in the TC-EEA group, and by postoperative MRI in the EEA group. Results were compared with the Knosp classification, stratified by the presence of apoplexy, hormonal status, and previous surgery, and then, inter-observer agreement (IOA) was calculated.

Results

Cavernous sinus invasion was present in 19.4% of CS. Our new classification yielded an overall sensitivity of 90.8% (95% CI 86.6-94%), specificity of 98.4% (95% CI 97.8-98.9%), PPV of 86.5% (95% CI 82.3-89.8%), NPV of 99% (95% CI 98.5-99.3%), +LR of 56.2 (95% CI 40.7-77.5), -LR of 0.09 (95% CI 0.06-0.14), and accuracy of 97.6% (95% CI 96.9-98.2%), with comparable results in all compartments. Previous surgery increased the rate of CS invasion of grade 0 in the superior and posterior compartments (false negatives), as well as in Knosp grade 2 cases. IOA was almost perfect for superior and inferior compartments; and substantial for lateral, posterior, and clinoidal space. Knosp classification only achieved moderate agreement.

Conclusion

Our new classification provides a reliable and accurate tool to evaluate CS compartment invasion by pituitary adenoma, outperforming the Knosp classification.

References

1, 25, 33,

"CLIPS" (clinoidal, lateral, inferior, posterior, and superior)
1. Knosp E, Steiner E, Kitz K, Matula C. Pituitary Adenomas with Invasion of the Cavernous Sinus Space: A Magnetic Resonance Imaging Classification Compared with Surgical Findings. Neurosurgery 1993;33(4):610-618.
25. Mooney MA, Hardesty DA, Sherry JP, Bird R, Chapple K, White WL, Little AS. Interrater and Intrarater Reliability of the Knosp Scale for Pituitary Adenoma Grading. J Neurosurg 2017;126:1714-1719.
33. Fernandez-Miranda, JC, Zwagerman NT, Abhinav K, Lieber S, Wang EW, Snyderman CH, Gardner PA. Cavernous Sinus Compartments from the Endoscopic Endonasal Approach: Anatomical Considerations and Surgical Relevance to Adenoma Surgery. J Neurosurg 2018;129:430-441.

Images/Tables

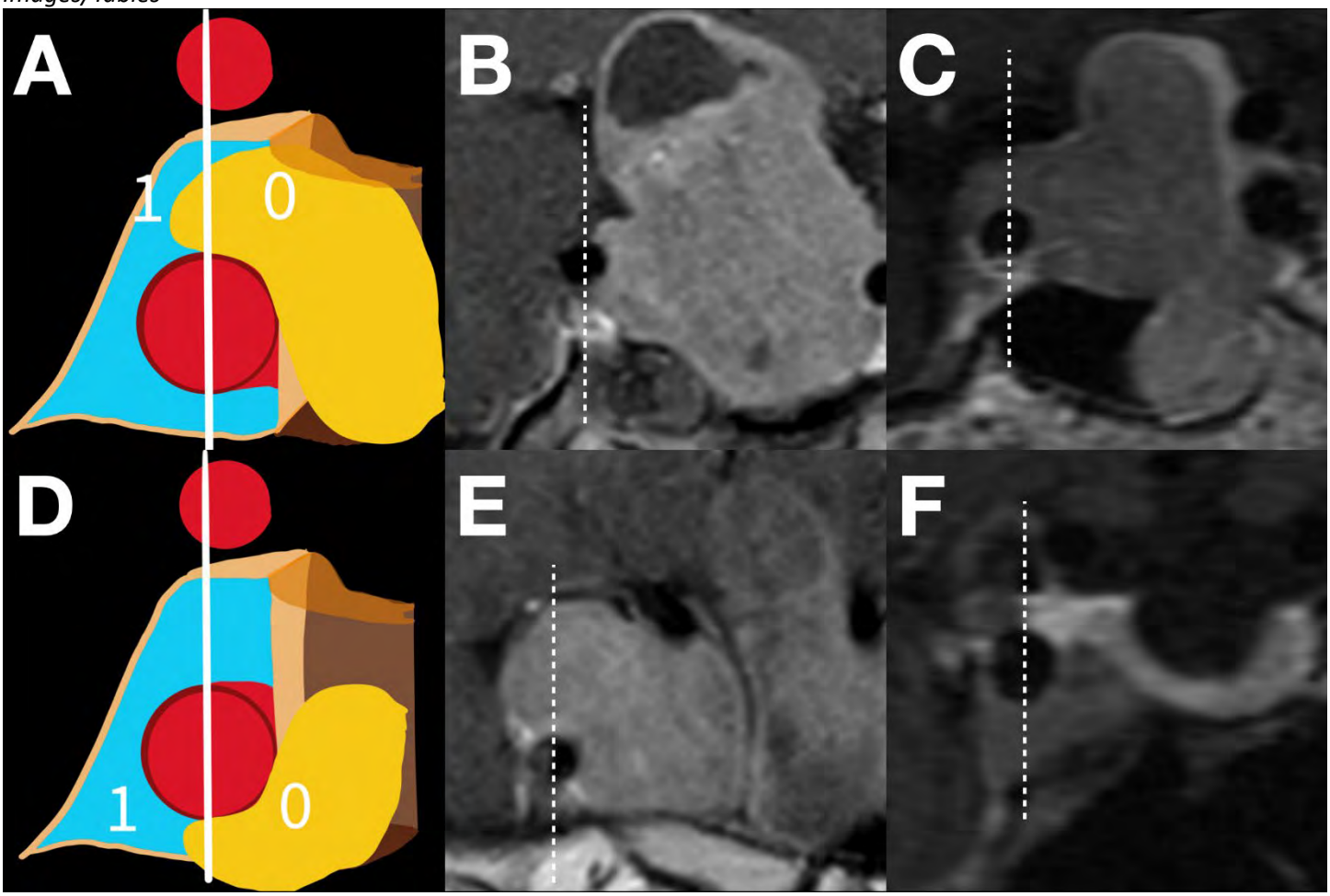

1058

Vessel wall imaging-dedicated deep learning (VWI-DL): Toward a 5-min clinically robust whole-brain VWI protocol

Pengcheng Wang[1], Junzhou Chen[1], Jiayu Xiao[1], Zhenjia Wang[2], Qi Yang[3], Steven Yong Cen[1], Sophia Cui[4], William Mack[1], Nasim Sheikh-Bahaei[1], Zhaoyang Fan[1]

[1]University of Southern California, Los Angeles, CA, USA. [2]Anzhen Hospital, Beijing, Beijing, China. [3]Chaoyang Hospital, Beijing, Beijing, China. [4]Siemens Healthineers, Los Angeles, CA, USA

Abstract Category

Head & Neck

Purpose

Long scan times (8–12 minutes) in whole-brain MR vessel wall imaging (VWI)[1] cause patient discomfort and motion artifacts, limiting clinical utilization. Faster VWI with preserved image quality is highly desirable. Recently, deep learning (DL) was attempted to accelerate VWI [2, 3], but these models were not specifically trained for VWI and only tested on data acquired with 64-channel head coils. This work aims to develop and validate a VWI-dedicated DL (VWI-DL) model specifically designed to accelerate 3D MR VWI with a standard 20-channel head-neck coil. Our overarching goal is to enable a 5-min clinically robust whole-brain MR VWI protocol.

Materials & Methods

A dataset of 68 whole-brain VWI scans (45 pre-contrast, 23 post-contrast) was acquired on a 3T system using a 12min10sec protocol with a 20-channel head-neck coil. The k-space data (denoted as GRAPPA2) of each scan underwent retrospective undersampling in the k_y-k_z plane with a mask of 4-fold CAIPIRINHA (CAIPI4) [Figure 1]. LORAKS[4], an advanced reconstruction method, was applied to CAIPI4 data to generate images. Illustrated in Figure 2, we decomposed the paired 3D CAIPI4 and GRAPPA2 images into corresponding 2D slices to serve as inputs and ground truths, respectively. For each input slice, four adjacent slices from both above and below are included for context,

totaling five slices. We utilized SwinIR[5], a 2D denoising network, as our model backbone. Separate models were trained for axial, sagittal, and coronal views, and their predictions were combined using a voting mechanism.
The dataset was split into training and testing sets in a 54:14 ratio. The model was trained using a combination of L1, Mean Squared Error (MSE), and Structural Similarity Index Measure (SSIM) losses with the Adam optimizer. Additional prospective testing was conducted on two volunteers using various protocols, including CAIPI4 and GRAPPA2 with different scan times and field-of-view (FOV) settings [Table 1]. Performance was evaluated using SSIM, Peak Signal-to-Noise Ratio (PSNR), and a 5-point image quality score rated by a blinded radiologist.

Results

Our VWI-DL model effectively reduced noise and enhanced image contrast in both pre- and post-contrast images [Figure 3A]. It successfully recovered the delineation of atherosclerotic plaques, comparable to the 12min10sec scans [Figure 3B]. Compared to input CAIPI4 images obtained in 5min50sec, the model increased PSNR by 9.69, SSIM by 0.28, and image quality score by 2 points [Table 2]. While the voting DL model had slightly lower PSNR and SSIM than the sagittal DL model, it offered better overall image consistency and compatible diagnostic quality with a mean difference in quality score of -0.18 95% CI (-0.82, 0), within the non-inferiority boundary of -1 when compared to CAIPI4. Prospective testing demonstrated that the model could restore anatomical details effectively, even with shorter scan times and smaller FOV, achieving acceptable image quality in scans as short as 4min44sec.

Conclusion

Our VWI-DL model allows for accelerated acquisitions while preserving diagnostic image quality and holds the potential to help achieve a 5-min clinically robust imaging protocol. Large-scale prospective testing along with more VWI-focused image analyses are warranted to further benchmark its performance.

References

1. Fan Z, Yang Q, Deng Z, et al. Whole-brain intracranial vessel wall imaging at 3 T esla using cerebrospinal fluid–attenuated T1-weighted 3 D turbo spin echo. *Magnetic resonance in medicine* 2017;77:1142-1150
2. Bathla G, Messina SA, Black DF, et al. Deep Learning–Based Reconstruction of 3D T1 SPACE Vessel Wall Imaging Provides Improved Image Quality with Reduced Scan Times: A Preliminary Study. *American Journal of Neuroradiology* 2024
3. Kharaji M, Canton G, Guo Y, et al. DANTE-CAIPI Accelerated Contrast-Enhanced 3D T1: Deep learning-based image quality improvement for Vessel Wall MR. *American Journal of Neuroradiology* 2024
4. Haldar JP. Low-rank modeling of local k-space neighborhoods (LORAKS) for constrained MRI. *IEEE transactions on medical imaging* 2013;33:668-681
5. Liang J, Cao J, Sun G, et al. Swinir: Image restoration using swin transformer. *Proceedings of the IEEE/CVF international conference on computer vision*; 2021:1833-1844

Images/Tables

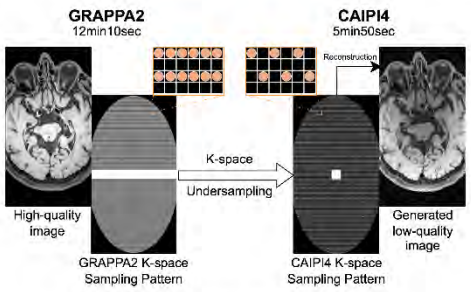

Figure 1 Internal dataset development

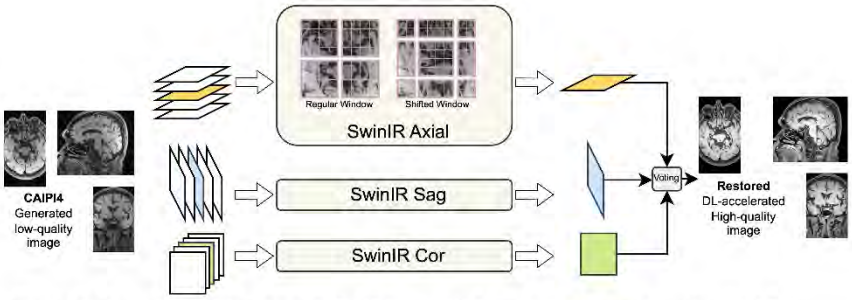

Figure 2 The pipeline of Accelerated 3D MR Vessel Wall Imaging with Deep Learning (VWI-DL)

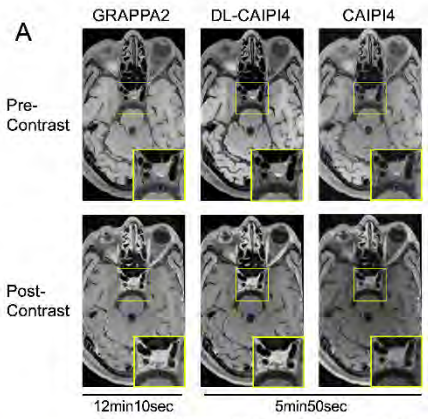

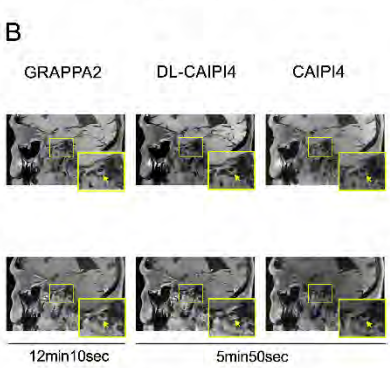

Figure 3 Retrospective testing on a 70-year-old male patient

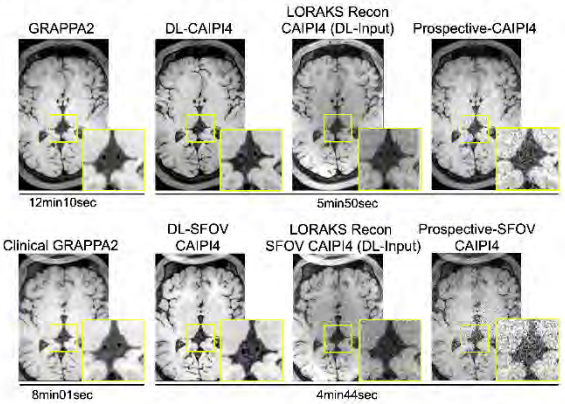

Figure 4 Prospective testing on a 26-year-old healthy volunteer. Prospective-CAIPI4s are from Siemens online reconstruction.

	GRAPPA 2	Clinical GRAPPA 2	CAIPI 4	Smaller FOV CAIPI 4
TR (ms)	900	900	900	900
TE (ms)	15	15	15	15
Resolution (mm²)	0.55	0.55	0.55	0.55
Slice thickness (mm)	0.55	0.55	0.55	0.55
FOV (mm²)	248 × 230 × 124	210 × 174 × 124	248 × 230 × 124	210 × 174 × 124
Matrix	448 × 414 × 224	384 × 318 × 224	448 × 414 × 224	384 × 318 × 224
Autocalibration region	24 × 224	24 × 224	24 × 24	24 × 24
Acquisition plane	Sagittal	Sagittal	Sagittal	Sagittal
Acceleration (PE × 3D)	2 × 1	2 × 1, 6/8 Slice Partial Fourier	2 × 2	2 × 2
Scan Time	12min10sec	8min01sec	5min50sec	4min44sec

Table 1 The protocol parameters for four vessel wall imaging sequences

	PSNR (Mean ± Std)	SSIM (Mean ± Std)	Image quality score (Mean ± Std)
CAIPI4	20.7782 ± 1.9267	0.6144 ± 0.0815	1.7857 ± 0.5789
Axial DL-CAIPI4	28.5686 ± 0.9553	0.8790 ± 0.0145	3.2143 ±0.4258
Sagittal DL-CAIPI4	31.1181 ± 0.8871	0.9068 ± 0.0189	3.2857 ± 0.4688
Coronal DL-CAIPI4	27.8076 ± 0.7249	0.8617 ± 0.0185	3.1429 ± 0.3631
Voting DL-CAIPI4	30.4695 ± 0.7579	0.8997 ± 0.0165	3.7857 ± 0.4258
GRAPPA2	-	-	4.0000 ± 0.0000

Table 2 PSNR, SSIM, and diagnostic image quality score comparisons. Diagnostic image quality score: (0: Nondiagnostic, 1: Poor, 2. Acceptable, 3: Good, 4: Optimal). All p-values, calculated using Wilcoxon signed-rank test between the CAIPI4 and DL-CAIPI4, are below 0.001.

1059

Systematic Review of Uncertainty Quantification in Deep Learning Applications for Neuroradiology

Mahsa Heidari-Foroozan[1], Ali Abdolizadeh[2], Mastoore Sagharichi[1], Mohammad Amin Aalipour[1], Hosein Jafary[1], Amir Mohahammad Vahdani MD[3], Shahriar Faghani MD[4]

[1]Shahid Beheshti University of Medical Sciences, Tehran, Tehran, Iran, Islamic Republic of. [2]University of Toronto, Toronto, ON, Canada. [3]Tehran University of Medical Sciences, Tehran, Tehran, Iran, Islamic Republic of. [4]Mayo Clinic, Rochester, Minnesota, USA

Abstract Category

AI/Informatics

Purpose

Deep learning (DL) has facilitated neuroradiology practice by improving diagnostic accuracy and enabling automated image analysis. However, the uncertainty inherent in DL models presents significant challenges in clinical settings, specially in high-stakes fields. Uncertainty quantification (UQ) is vital for evaluating the reliability of DL outputs, enhancing decision-making processes, and ensuring patient safety. It is important to note that prediction's uncertainty differs from the model'snumerical output which is supposed to be the likelihood. UQ provides an uncertainty measure

per individual prediction. Despite its critical role, the integration of UQ into DL models for neuroradiology remains largely unexamined.

Materials & Methods

We conducted a systematic review across PubMed, Scopus, Web of Science, and Google Scholar from inception to July 4, 2024, focusing on studies that bridge neuroradiology, DL, and UQ. From an initial pool of 782 studies, 195 were selected based on title and abstract relevance. Following full-text screening, 87 studies were included in our final analysis.

Results

Among the 87 studies reviewed, 21 focused on Alzheimer's disease, 17 examined brain tumors, 10 investigated strokes and hemorrhages, and 39 addressed other conditions or healthy brains. The analysis revealed that 28 studies employed DL for classification, 18 for segmentation, eight for reconstruction, four for registration, and 29 for other applications. UQ was primarily used to enhance data reliability and identify outliers, but only 15 studies established specific thresholds for uncertainty to enhance the trustworthiness of the workflow.

Conclusion

Our findings underscore the inconsistent application of UQ in DL for neuroradiology, with a notable lack of clearly defined uncertainty thresholds. Moreover,although there are some UQ methods that provide statistical guarantee in predictions most of the used UQ methods do not have a statistical guarantee. There is a need for standardized UQ frameworks to improve the reliability and clinical applicability of DL models. Future research should prioritize the development of robust, task-specific UQ methodologies that can be effectively integrated into clinical practice, ultimately improving patient outcomes and decision-making in neuroradiology.

References

Faghani S, Moassefi M, Rouzrokh P, Khosravi B, Baffour FI, Ringler MD, Erickson BJ. Quantifying Uncertainty in Deep Learning of Radiologic Images. Radiology 2023;308(2)

Images/Tables

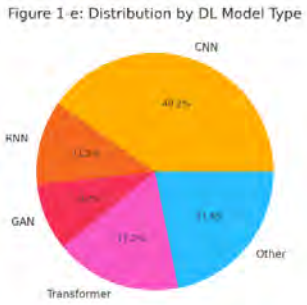

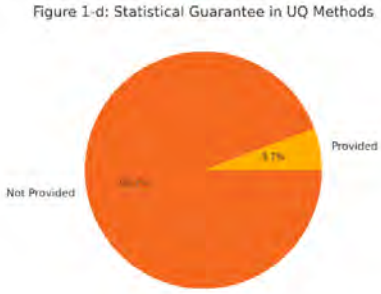

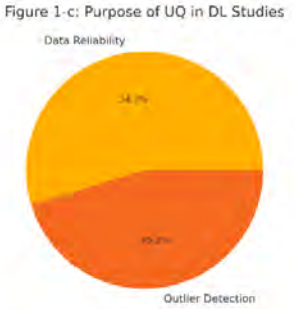

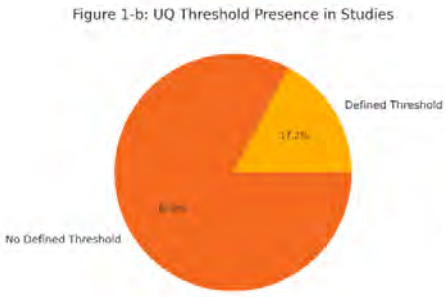

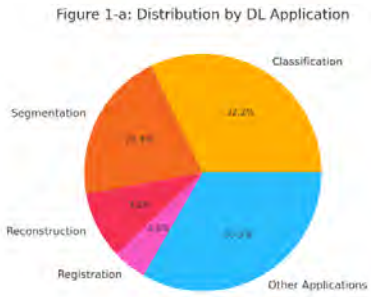

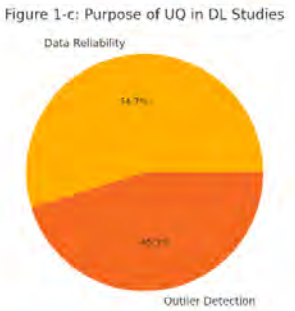

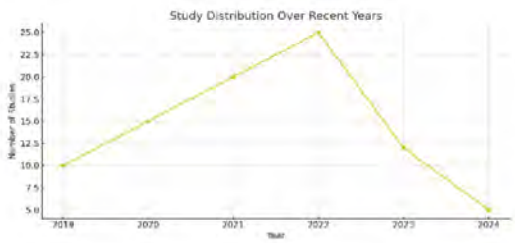

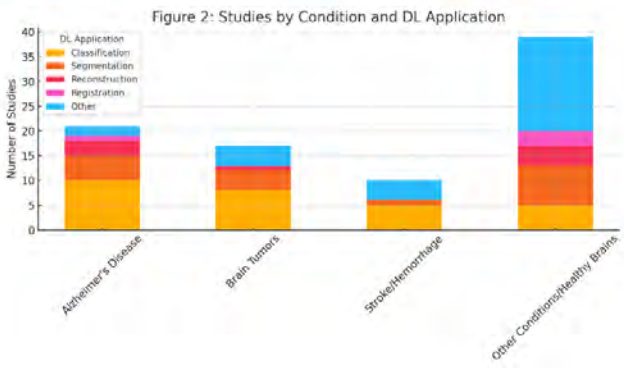

1060

Systematic review: the Role of DCE-MRI in Radiogenomics for Glioblastoma

Sina Goodarzi[1], Parna GhannadiKhosh[2], Aida Mehrani[3], Sina Porkawosh[4], Shaghayegh Karami[5], Mohammad Amin Karimi[6], Sara Salehi[7], Sadaf Salehi[8], Shahrair Faghani[7]

[1]Lorestan University of Medical Sciences, Khoramabad, Lorestan, Iran, Islamic Republic of. [2]Tabriz University of Medical Sciences, Tabriz, Tabriz, Iran, Islamic Republic of. [3]Isfahan University of Medical Sciences, Isfahan, Isfahan, Iran, Islamic Republic of. [4]Urmia University of Medical Sciences, Urmia, Urmia, Iran, Islamic Republic of. [5]Tehran University of Medical Sciences, Tehran, Tehran, Iran, Islamic Republic of. [6]Shahid Beheshti University of Medical Sciences, Tehran, Tehran, Iran, Islamic Republic of. [7]Mayo Clinic, Rochester, Minnesota, USA. [8]Iran University of Medical Sciences, Tehran, Tehran, Iran, Islamic Republic of

Abstract Category

Adult Brain

Purpose

Glioblastoma (GBM) remains one of the most aggressive and common primary brain tumors with significant challenges in diagnosis and treatment because of tumor heterogeneity. Radiogenomics, which integrates imaging features and tumor genetic profile, offers a better understanding of GBM characteristics. Recent advances in machine learning and deep learning have expanded radiogenomics research, enabling imaging techniques to predict genetic markers. Several imaging sequences have been used for GBM work up. Among these, Dynamic Contrast Enhanced MRI (DCE- MRI) stands out for its ability to study changes in tumor hemodynamics, vascularity, perfusion, and permeability, which are critical in GBM evaluation. In this systematic review, we aim to examine the role of DCE-MRI in radiogenomics for glioblastoma, with a focus on machine learning-based predictive models.

Materials & Methods

Our study was conducted based on the PRISMA guideline. We systematically searched PubMed, Scopus, Web of Science, Embase, and ProQuest databases with related keywords such as "DCE-MRI", "Machine learning", "Deep learning", "Glioblastoma" and "Radiogenomics" and included prospective/retrospective cohort, randomized/non-randomized clinical trial, case-control, and cross-sectional study. Duplicate studies were excluded, then a two-step screening (Title/Abstract and Fulltext screening) according to inclusion and exclusion criteria were performed. Finally, Reviewers assessed the risk of bias and quality of evidence for each article based on the National Institute of Health (NIH) tool. Data such as dataset description, tumor classification, MRI sequences, predicted genes, machine learning approach, performance metrics and results, absence or presence of external validation, and interpretability method were extracted.

Results

Our search results indicated 815 articles, we excluded the 214 duplicates and screened 601 records. A total of 5 studies met the eligibility criteria and were included in the study. Included studies were conducted from 2016 to 2023 in the USA, Italy, Germany, and South Korea. The data of 621 patients diagnosed with glioblastoma was extracted and analyzed. These studies used different MRI sequences including T1-weighted, T2-weighted, FLAIR, diffusion-weighted images (DWI), apparent diffusion coefficient (ADC), and perfusion-weighted images (PWI) in addition to dynamic susceptibility contrast (DSC) or dynamic contrast-enhanced (DCE). One study focused on IDH1 mutation, one study predicted EGFR mutation, one study investigated MGMT methylation, and two studies determined other genes and pathways. 40% of studies used deep learning and the rest of the studies used the classic machine learning approach to predict the status of a specific gene. Studies measured different metrics such as the area under receiver operating curve (AUROC), sensitivity, and specificity. Just one study performed external validation.

Conclusion

Our systematic review results show that we need more research on radiogenomics based on DCE-MRI images. Our study highlights the growing potential of DCE-MRI in the radiogenomics of GBM, particularly when combined with ML. The key finding from our review is the lack of external validation in many studies. Although internal validation provides good insight, validating these models in independent, multi-center datasets is essential to assess their generalizability.
The overall number of radiogenomics studies is still limited. This suggests that researchers should pay greater attention to this area.

References

Page MJ, McKenzie JE, Bossuyt PM, Boutron I, Hoffmann TC, Mulrow CD, et al. The PRISMA 2020 statement: An updated guideline for reporting systematic reviews. Int J Surg. 2021;88:105906

Images/Tables

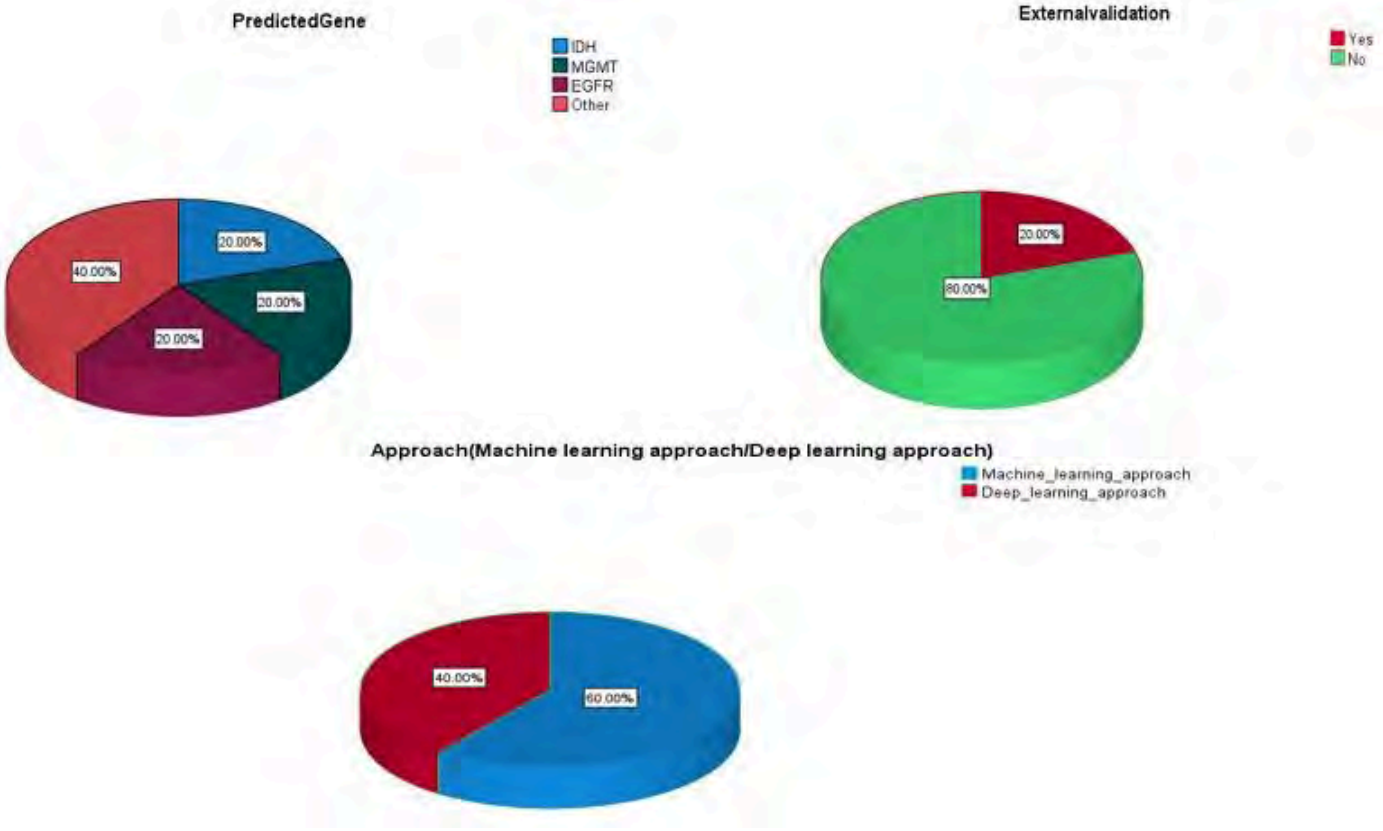

1062

Validation of Deep Learning-Reconstructed Volume Interpolated Breath-hold Exam (VIBE) Compared with Standard VIBE for Detection of Internal Auditory Canal Lesions

Chen Hua Chiang[1], Sittaya Buathong[1], Azadeh Hajati[1], Azadeh Tabari[1], Wei-Ching Lo[2], Dominik Nickel[3], Bryan Clifford[2], Robert Sellers[4], Stephen F. Cauley[2], John Conklin[1], Susie Y. Huang[1]

[1]Department of Radiology, Athinoula A. Martinos Center for Biomedical Imaging, Massachusetts General Hospital, Boston, Massachusetts, USA. [2]Siemens Medical Solutions USA, Boston, Massachusetts, USA. [3]Siemens Healthineers AG, Forchheim, Bavaria, Germany. [4]Siemens Medical Solutions USA, Philadelphia, Pennsylvania, USA

Abstract Category

AI/Informatics

Purpose

To evaluate the diagnostic performance of deep learning (DL)-reconstructed VIBE (DL-VIBE) compared to standard VIBE (ST-VIBE) in assessing the internal auditory canal (IAC) and associated pathologies.

Materials & Methods

In this IRB-approved, HIPAA-compliant prospective study, from June-September 2024, 64 consecutive adult patients undergoing clinical evaluation for hearing loss and/or vestibular pathology with an IAC brain MRI protocol on 3T MRI scanners (MAGNETOM Vida, Siemens Healthineers, Forchheim, Germany) were recruited. Each underwent a ST-VIBE (TA=3:02 min) sequence and DL-VIBE (TA=2:35 min) research sequence. A two-step deep learning-based reconstruction process was employed. First, an unrolled variational network architecture reconstructed images from undersampled k-space data through six iterations of data consistency updates and regularization.[1] This was followed by a super-resolution algorithm that upscaled spatial resolution by a factor of 2 across all dimensions, optimizing data consistency for partial Fourier acquisitions.[2] Standard and DL-VIBE sequences were obtained using comparable parameters. Two board-certified radiologists independently assessed image quality, motion artifacts, noise, sharpness, and visualization of key anatomical structures and pathologies using a 5-point scale.[3] A third board-certified neuroradiologist

adjudicated cases with discrepant ratings. Interrater agreement was evaluated with weighted Cohen's κ. Quantitative analysis was performed involving segmentation of all identified enhancing lesions with signal-to-noise ratio (SNR), contrast-to-noise ratio (CNR), and lesion volume measurements in the lesions and adjacent normal-appearing white matter (NAWM). A 15% noninferiority margin was used to test whether post-contrast DL-VIBE was noninferior to ST-VIBE with Z statistics.

Results

62 patients were included (mean age: 52.5 ± 16.6 years; 35 females). Two patients were excluded due to incomplete scanning. There was about 15% of time saved compared DL-VIBE to standard VIBE.

Substantial to almost perfect interrater agreement was observed for abnormal cranial nerve enhancement ($\kappa = 1.00$, $p < 0.001$), leptomeningeal enhancement ($\kappa = 0.98$, $p < 0.001$), parenchymal enhancement ($\kappa = 0.93$, $p = 0.001$), and IAC/CPA mass ($\kappa = 0.65$, $p = 0.002$).

DL-VIBE was considered non-inferior to standard VIBE in several categories, including overall diagnostic quality (upper-bound 95% CI: pcrit = 9%; p = 0.002), motion artifact (upper-bound 95% CI: pcrit = 11%; p = 0.005), noise (upper-bound 95% CI: pcrit = 11%; p = 0.005), and sharpness (upper-bound 95% CI: pcrit = 11%; p = 0.005). Additionally, DL-VIBE demonstrated non-inferiority for many intracranial structures, including inner ear, cerebellopontine angle (CPA), $7^{th}/8^{th}$ cranial nerve and IAC/CPA mass.

Quantitative analysis demonstrated that DL VIBE and ST-VIBE had comparable SNR and CNR (mean SNR 21.97 vs. 19.79, FDR-adjusted p = 0.33; mean CNR 3.37 vs. 2.65, FDR-adjusted p = 0.13 respectively). Tumor volumes were also comparable between sequences (median: 0.03 mm^3, range: 0.0008–1.7548).

Conclusion

DL-VIBE is a strong alternative to standard ST-VIBE for intracranial MRI, providing non-inferior image quality across multiple diagnostic categories, high interrater reliability for evaluating enhancing lesions, and notable workflow efficiency due to reduced scan time. These strengths, combined with consistent quantitative performance in SNR, CNR, and tumor volume measurement, affirm that DL-VIBE can be effectively integrated into clinical protocols, enhancing patient care without compromising diagnostic accuracy.

References

1. Hammernik K, Klatzer T, Kobler E, et al. Learning a variational network for reconstruction of accelerated MRI data. *Magn Reson Med* 2018;79:3055-3071

2. Afat S, Wessling D, Afat C, et al. Analysis of a Deep Learning-Based Superresolution Algorithm Tailored to Partial Fourier Gradient Echo Sequences of the Abdomen at 1.5 T: Reduction of Breath-Hold Time and Improvement of Image Quality. *Invest Radiol* 2022;57:157-162

3. Goncalves Filho ALM, Awan KM, Conklin J, et al. Validation of a highly accelerated post-contrast wave-controlled aliasing in parallel imaging (CAIPI) 3D-T1 MPRAGE compared to standard 3D-T1 MPRAGE for detection of intracranial enhancing lesions on 3-T MRI. *Eur Radiol* 2023;33:2905-2915

Images/Tables

	Standard VIBE	DL VIBE
TE/TR (ms)	1.44/3.8	1.47/3.59
Slice thickness (mm)	0.8	0.7
Field of view (mm)	256 x 192	220 x 220
Acquisition matrix	320 x 216	320 x 288
Acceleration	??	3
Voxel size (mm^3)	0.8 x 0.8 x0.8	0.7 x 0.7 x 0.7
Number of excitations	1	2
Flip angle (degree)	9	9
Acquisition time (min:s)	3:02	2:35

Acquisition parameters for post-contrast T1-weighted Volume Interpolated Breath-hold Examination (VIBE) sequences. DL: deep learning.

Patient Characteristics	
Number of participants	62
Mean age (years ± SD)	52.5 ± 16.6
Sex	Female: 35 (56.5%) Male: 27 (43.5%)
Number of participants with enhancing lesions	25 (40.3%)
Lesion Frequency	0 lesions: 37 (59.7%) 1 lesion: 18 (29.0%) 2 lesions: 2 (3.2%) >3 lesions: 5 (8.1%)
Clinical indication for IAC MRI	Vertigo: 9 (14.5%) Mass: 23 (37.1%) Hearing loss: 14 (22.6%) NF2: 8 (12.9%) Tinnitus: 3 (4.8%) Cranial neuropathy: 5 (8.1%) Other (e.g., post-operative): 1 (1.6%)

Demographics and clinical characteristics of the recruited patients

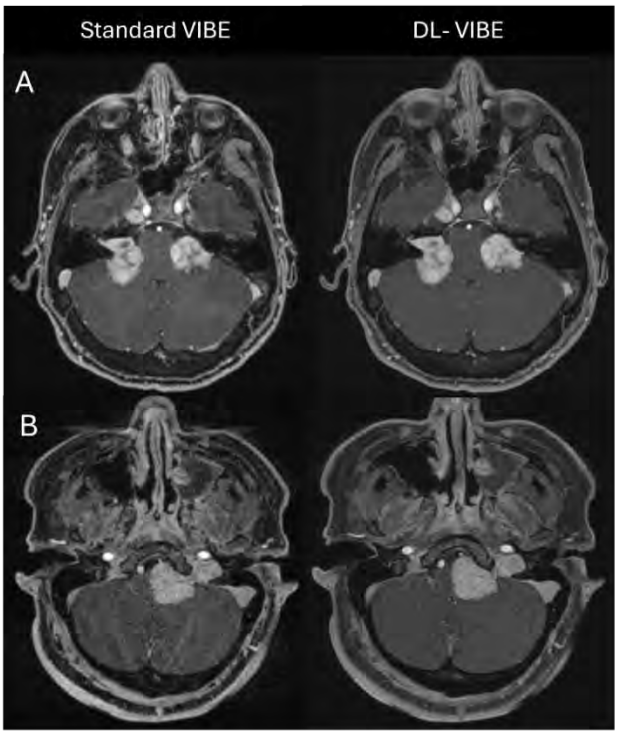

Two examples of head-to-head comparison of post-contrast standard and DL-VIBE

Category	Kappa Score	P-Value	Z-Score	P-Value
Overall diagnostic quality	0.20	0.03	-2.95	0.0016
Motion Artifact	0.35	0.002	-2.60	0.0047
Noise	0.21	0.03	-2.60	0.0047
Sharpness	0.49	< 0.001	-2.60	0.0047
Inner ear visibility	0.01	0.51	-3.31	< 0.001
Cerebellopontine angle visibility	0.37	0.003	-3.31	< 0.001
7th/8th CN visibility	0.08	0.27	-3.31	< 0.001
Normal vascular enhancement	-0.17	1.00	-3.31	< 0.001
IAC/CPA Mass	0.65	0.002	-1.88	0.03
Abnormal cranial nerve enhancement	1.00	< 0.001	-0.94	0.17
Leptomeningeal enhancement	0.98	< 0.001	-0.42	0.34
Parenchymal enhancement	0.93	0.001	-0.59	0.28
Dural enhancement	0.67	0.005	-1.39	0.08
Ependymal enhancement	1.00	0.15	-0.73	0.2

Weighted Cohen kappa scores and non-inferiority scores for all categories

1064

MRI-Based Decision Tree to Distinguish “Hippocampal Sclerosis (HS) ILAE Type 1” and “No HS Gliosis Only” in Medial Temporal Lobe Epilepsy

Ivan Y Luu BS[1], Abhi Jain DO[1], Paul E Kim MD[1], Alexander Lerner MD[1], Reza Assadsangabi MD[1], Steven Cen PhD[1], Ryan McGinn MD[1], Hosung Kim PhD[1], Misque Boswell MS[1], Dominique Duncan PhD[1], Christianne N Heck MD[1], Charles Liu MD[1], Samuel Guzman MD[2], Saman Hazany MD[1]

[1]Keck School of Medicine of USC, Los Angeles, CA, USA. [2]University of Colorado, Anschutz, Aurora, Colorado, USA

Abstract Category

Adult Brain

Purpose

Despite recent advances in preoperative work-up of drug resistant MTLE, predicting post-surgical seizure and memory outcomes remains challenging. “No HS Gliosis Only” (GO) and “HS International League Against Epilepsy (ILAE) Type 1” (HSILAE1) are distinct histopathological entities in MTLE with different clinical characteristics. Notably, patients with MTLE and GO demonstrate later onset of epilepsy, less pronounced pre-operative memory impairments, and more significant memory decline post-surgery. HSILAE1 is typically associated with longer duration of postoperative seizure freedom compared to HS ILAE types 2 and 3 and GO. In this study, we developed a classification and regression tree (CART®) using our previously introduced qualitative and clinical MRI-based HS grading system to differentiate between GO and HSILAE1.

Materials & Methods

61 patients with drug resistant MTLE (mean age 39.5 ±12.6 years; 36 [59.0%] females) underwent our routine institutional epilepsy protocol MRI on either a 1.5T (36 patients) or 3T (25 patients) scanner prior to temporal lobectomy or amygdala-hippocampectomy. Histopathologic diagnoses of the resected hippocampi were assigned by a neuropathologist and divided into 3 categories: 1. GO, 2. HSILAE1 Total Sclerosis (TS), and 3. HSILAE1 Classic Sclerosis (CS).

Brain MRI protocol included 3D (1 mm isometric voxel) T1, and coronal T2, and T2-FLAIR (3 mm slice thickness) sequences. Four experienced academic neuroradiologists arrived at consensus in grading the hippocampi of the 61 patients after independent grading of the first 20 cases.

The radiologic grading system visually assessed three features of HS: 1. Hippocampal head digitations, 2. Internal architecture with assessment of the Stratum Radiatum Lacunosum and Moleculare (SRLM) layer, and 3. Qualitative total hippocampal volume loss. Each feature was given a score on a scale of 0 – 2 based on severity. The Hippocampal Total Score (“HC Total Score”) was summed for a final score of “0” - “6”. CART® with 10-fold cross-validation identified the optimal prediction model with appropriate clinical cut points. The associated sensitivity and specificity were calculated with Copper Pearson 95% confidence interval.

Results

The HC total score reached the great agreement between raters with ICC (3,1) of 1 [95% CI of 1- 1] and 0.98 [0.94-0.99] for left and right hippocampus respectively. When using the HC total score with a cutoff point of ≤2 versus >2, we achieved a sensitivity of 80% and specificity of 86.3% for detecting GO. Restricting the analysis to 3T MRI data improved our outcomes to sensitivity and specificity of 88% and 88%, respectively. HC total score 6 has higher rate of HSILAE1 CS (85.7% CS, 14.3% TS, and 0% GO) leading to a sensitivity of 34.3% and specificity of 92% for HSILAE1 CS.

Conclusion

The distinction between GO and HSILAE1 can be achieved by visual evaluation of clinical epilepsy protocol brain MRI. Further distinguishing HSILAE1 subtypes remains challenging on visual MRI evaluation with segmentation of hippocampal subfields techniques as a potential solution. Distinguishing GO and HSILAE1 using clinical brain MRI provides a novel means of establishing likely pathological subtyping, which can guide clinicians in determining prognosis and therapeutic modalities, ultimately improving patient outcomes in MTLE patients.

*First two authors are co-first authors.

References

Middlebrooks EH, Gupta V, Agarwal AK, et al. Radiologic Classification of Hippocampal Sclerosis in Epilepsy. *AJNR Am J Neuroradiol*. 2024 Sep 9;45(9):1185-1193. doi: 10.3174/ajnr.A8214.,

Saghafi S, Ferguson L, Hogue O, et al. Histopathologic subtype of hippocampal sclerosis and episodic memory performance before and after temporal lobectomy for epilepsy. *Epilepsia*. 2018 Apr;59(4):825-833. doi: 10.1111/epi.14036.

Na M, Ge H, Shi C, et al. Long-term seizure outcome for international consensus classification of hippocampal sclerosis: a survival analysis. *Seizure*. 2015 Feb;25:141-6. doi: 10.1016/j.seizure.2014.10.006.
Taube J, Witt JA, Grote A, et al. Preoperative and postoperative memory in epilepsy patients with 'gliosis only' versus hippocampal sclerosis: a matched case-control study. *J Neurol Neurosurg Psychiatry*. 2022 Aug 25:jnnp-2022-329224. doi: 10.1136/jnnp-2022-329224.
Images/Tables

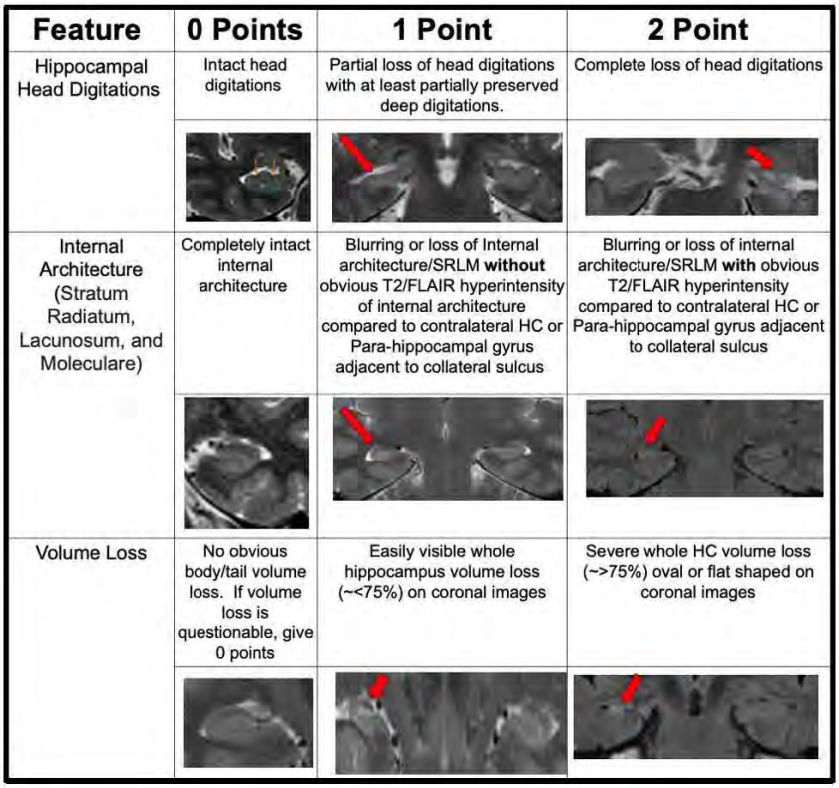

Feature	0 Points	1 Point	2 Point
Hippocampal Head Digitations	Intact head digitations	Partial loss of head digitations with at least partially preserved deep digitations.	Complete loss of head digitations
Internal Architecture (Stratum Radiatum, Lacunosum, and Moleculare)	Completely intact internal architecture	Blurring or loss of Internal architecture/SRLM **without** obvious T2/FLAIR hyperintensity of internal architecture compared to contralateral HC or Para-hippocampal gyrus adjacent to collateral sulcus	Blurring or loss of internal architecture/SRLM **with** obvious T2/FLAIR hyperintensity compared to contralateral HC or Para-hippocampal gyrus adjacent to collateral sulcus
Volume Loss	No obvious body/tail volume loss. If volume loss is questionable, give 0 points	Easily visible whole hippocampus volume loss (~<75%) on coronal images	Severe whole HC volume loss (~>75%) oval or flat shaped on coronal images

1065

Safety and Efficacy of Vertebral Augmentation for Painful Vertebral Compression Fractures in Patients Aged 90 and Older.

Saif M Ibrahim[1], Joanna Pilipczuk MD[2], Saad M Ibrahim MD, MS[1]
[1]Indiana University School of Medicine, Fort Wayne, IN, USA. [2]Chicago Medical School at Rosalind Franklin University of Medicine and Science, Chicago, IL, USA
Abstract Category
Interventional
Purpose
This study evaluates the safety and efficacy of balloon kyphoplasty (BKP) and vertebroplasty (VP) for treating painful osteoporotic vertebral compression fractures (VCF) in patients aged 90 years and older.
Materials & Methods
We retrospectively reviewed patients aged 90+ years who were treated with BKP or VP for painful osteoporotic VCF from four institutions over a 7 year period (2015-2022). Data reviewed included time from diagnosis to treatment, number of vertebral compression fractures treated, anatomic location of fracture (thoracic, lumbar, both thoracic and lumbar), improvement in pain using the visual analog pain score (VAS), and 30-day mortality.
Results
A total of 235 patients (49 males, 186 females) were included, with a median age of 91 years (range 90-106). There were 174 patients between the ages of 90-94, 47 patients between the ages of 95-99, and 14 patients between the ages of 100-106. The median follow-up was 943 days. Of the 235 patients, 170 had one level treated, 41 had two levels treated, and 24 had three or more levels treated in a single session. The average time from diagnosis to treatment was 10.7 days.

There were 127 thoracic vertebral compression fractures, 80 lumbar vertebral compression fractures, and 28 combined thoracic /lumbar vertebral compression fractures.
Treatment consisted of vertebroplasty in 61 patients, kyphoplasty in 159 patients, and both vertebroplasty and kyphoplasty in 15 patients. Average moderate sedation time was 43.9 minutes for the treatment of one level, 55.0 minutes for the treatment of two levels, and 69.0 minutes for the treatment of three or more levels. Post-procedure, 165 patients reported improvement in pain and 21 patients reported no improvement (*p <0.005)*. Pain scores were not available for 49 patients. There were no reported 30 day mortalities.
Conclusion
Vertebral augmentation with BKP and VP is a safe and effective treatment for elderly patients aged 90 years and older with painful VCF, providing significant pain relief with minimal complications.
References
Yang B, Zhao Y, Zhao Y, et al. Is percutaneous kyphoplasty safe and beneficial for patients aged 90 and over? *Medicine* 2022 Aug 19;101(33):e30138. doi: 10.1097/MD.0000000000030138. PMID: 35984140; PMCID: PMC9387994.

1072

Meso-scale CISS Imaging for the Detection of Dural Defects in Spinal CSF Leaks

Michelle L. Wegscheid MD, PhD, Manu S. Goyal MD, MSc, Arash Nazeri MD
Mallinckrodt Institute of Radiology, Washington University School of Medicine, St. Louis, MO, USA
Abstract Category
Spine
Purpose
Spontaneous intracranial hypotension (SIH) results from spinal cerebrospinal fluid (CSF) leaks. Spinal CSF leaks consist of three major categories, with two associated with spinal longitudinal extradural CSF collections (SLECs): Type 1, caused by dural tears often due to herniated discs or osteophytes, and Type 2, resulting from ruptured meningeal diverticula[1]. Although fat-saturated heavily T2-weighted (FS-HT2) MRI demonstrates high accuracy for SLEC detection, precise localization of the leak site often requires contrast myelography[2]. Here we propose a two-stage spine MRI protocol to localize CSF leak sites for patients with suspected SIH. First, 3D FS-HT2 imaging is performed to identify the presence of SLEC. If SLEC is detected, meso-scale resolution imaging with constructive interference in steady state (meso-CISS) is employed for direct localization of the CSF leak site (Figure 1A). Unlike turbo-spin echo sequences, CISS is not limited by T2-dependent blurring, yielding high-resolution images with sharp tissue boundaries and superior contrast between CSF and dura.
Materials & Methods
All patients with suspected SIH evaluated between April 2024 and September 2024 underwent total spine MRI with the CSF leak protocol. This protocol included an FS-HT2 sequence optimized for uniform shimming and high-resolution imaging, utilizing a compressed-sensing accelerated 3D SPACE sequence with a constant flip angle. FS-HT2 images were reviewed in real time by a neuroradiologist. For patients with a positive SLEC finding on FS-HT2 scans, targeted imaging was performed using a limited field-of-view meso-CISS sequence (0.5 x 0.5 x 0.5 mm^3). Multiplanar reconstruction was employed to locate dural defects.
Results
Of the 12 patients referred for the dedicated CSF leak total spine MRI protocol, three were SLEC-positive on FS-HT2 imaging. In all three cases, a dural defect was successfully localized in the thoracic spine using the meso-CISS sequence. One patient had a Type 1 CSF leak, presenting with a ventral dural tear at T8-T9 (defect size: 2 x 8 mm), later confirmed by dynamic subtraction myelography (Figure 1B). Another patient exhibited a defect at the tip of a right-sided perineural cyst with surrounding SLEC at T8-T9 (Type 2 leak; defect size: 2.5 x 1 mm; Figure 1C). The third patient had a dural defect along the dorsal axilla of a right-sided perineural cyst, which communicated with a dorsal SLEC at T3-T4 (Type 2 leak; defect size: 1.5 x 1 mm; Figure 1D).
Conclusion
Results from this small-scale study of a two-stage spine MRI protocol, which integrates FS-HT2 for detecting SLECs and targeted meso-CISS for precise CSF leak localization, demonstrate promising accuracy in identifying dural defects in patients with SLEC. Notably, dural defects were smaller than 2 mm in at least one dimension, highlighting the value of the sharpness and isotropic high-resolution of meso-CISS images. This approach may enable targeted narrowing of the

region of interest during subsequent myelography, potentially reducing radiation exposure and improving detection accuracy. Larger-scale studies are needed to comprehensively assess the diagnostic accuracy of this strategy.

References

1. Dillon WP. Spinal Cerebrospinal Fluid Leak Localization with Dynamic Computed Tomography Myelography: Tips, Tricks, and Pitfalls. Radiol Clin North Am 2024;62:311–9.
2. Dobrocky T, Nicholson P, Häni L, et al. Spontaneous intracranial hypotension: searching for the CSF leak. Lancet Neurol 2022;21:369–80.

Images/Tables

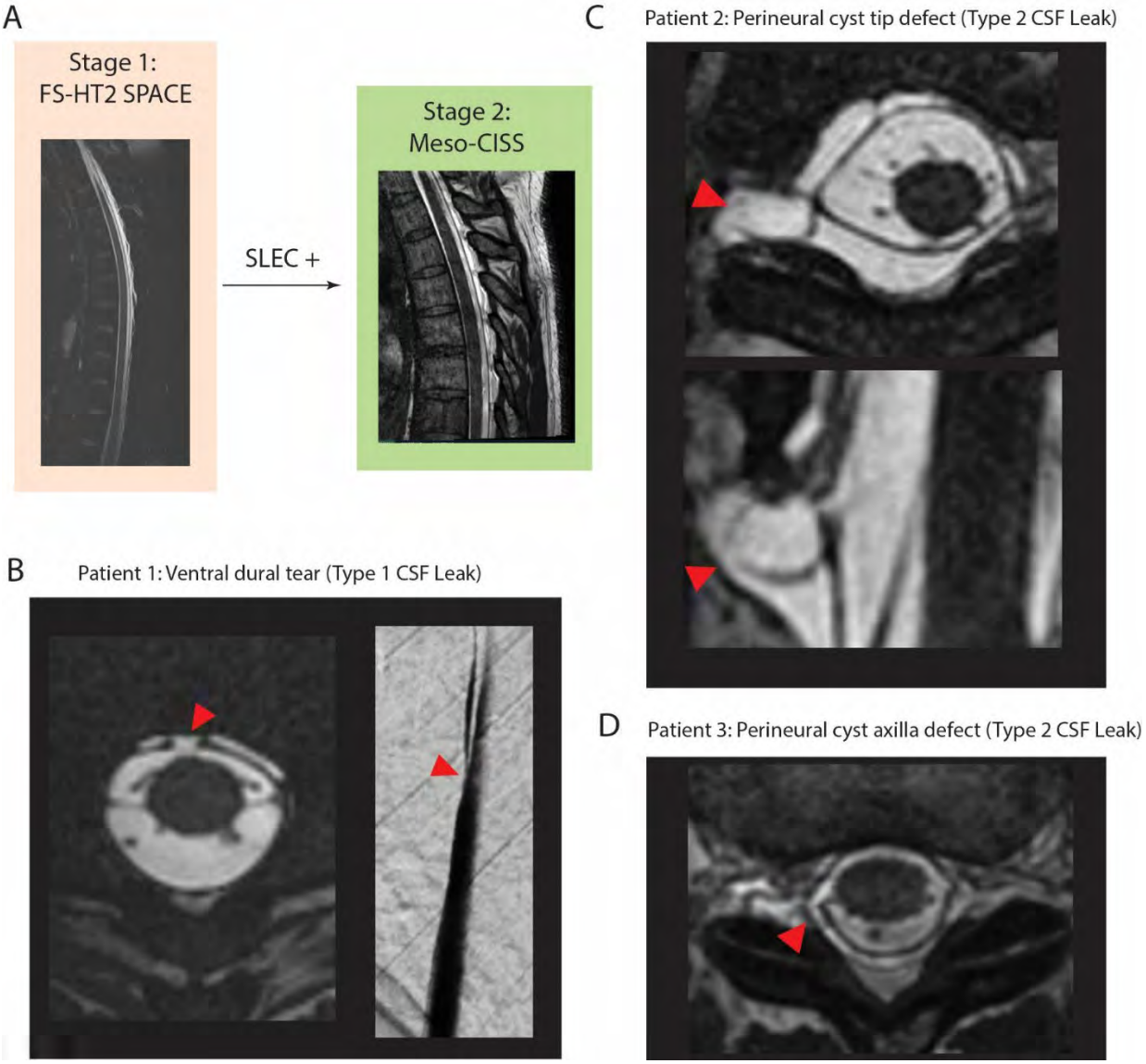

1073

Medicare Reimbursement Reductions in Neuroimaging: Trends and Implications for MR and CT Services

Dheeman Futela MBBS[1], Nagaraj S Moily MD, PhD, MBA, MAM[1], Dheeraj Gandhi[2], Sam Payabvash MD[1], Ajay Malhotra MD MMM[1]

[1]Department of Radiology, Yale School of Medicine, New Haven, CT, USA. [2]Department of Radiology, University of Maryland School of Medicine, Baltimore, MD, USA

Abstract Category

Socioeconomics & Health Policy

Purpose

Despite technological advancements and a growing demand for imaging services, reimbursement rates have not kept pace with the rising costs required to maintain high standards in neuroimaging. Due to budget neutrality, Medicare reimbursement adjustments often lead to reductions, impacting specialized fields like neuroradiology more significantly. This study investigates trends in reimbursements for neuroimaging, a field heavily reliant on high-cost MRI and CT technologies and specialized expertise.

Materials & Methods

We analyzed Physician Fee Schedule (PFS) reimbursement rates for select CPT codes from 2007 to 2024, sourced from CMS. Selected CPT codes included routine CT and MR neuroimaging studies, alongside comparable chest and abdominal imaging studies. All values were adjusted for inflation to 2024 USD using the Consumer Price Index. For each imaging study, yearly and total percent changes and the compound annual growth rate (CAGR) were calculated for inflation-adjusted reimbursements. Trends were analyzed for statistical significance by simple linear regression using Python libraries, SciPy and Matplotlib.

Results

Our analysis reveals a consistent downward trend in inflation-adjusted reimbursements for neuroimaging from 2007 to 2024. The mean reimbursements for CT and MR neuroimaging studies declined by 74% between 2007-2024. MRI studies experienced more substantial reimbursement reductions than CT, with CPT code 70553 (MR brain with and without contrast) showing the steepest annual decrease, averaging -8.7% (-$66.7) per year.

Notably, the steepest cuts occurred from 2007 to 2015 (CAGR -11.0%), coinciding with the Medicare Sustainable Growth Rate policy aimed at curbing spending. From 2015 to 2020, declines moderated (CAGR ~-2.3%), reflecting a period of relative stabilization post-policy revision. However, recent Medicare adjustments, including revaluation of Evaluation and Management (E/M) services, have renewed reimbursement declines, with a CAGR drop of 7.2% from 2021 onward. Overall, the greatest annual percent reimbursement cut was observed between 2013-14 (-28.5%) and 2014-15 (-13.9%). Neuroimaging, especially MRI, has faced disproportionately higher cuts than chest and abdominal imaging. According to reimbursements for CT with and without contrast, the abdomen CPT code (74170) had a lower decline (CAGR -5.0%) compared to the head (70470, CAGR -6.1%) and spine (72133 CAGR -6.4%) studies. Similarly, for CT angiography and MR studies, the reimbursement declines for neuroradiology (CAGR -8.7%) surpassed that of abdominal (-8.3%) and chest imaging (-6.7%), highlighting the increased financial burden on neuroradiology practices.

Conclusion

Our study shows significant reductions in Medicare reimbursements, particularly for MRI procedures, which threaten the financial viability of high-quality neuroimaging services. Recent policy changes redistributing reimbursements from procedural to E/M services have exacerbated financial pressures for neuroradiology. While these changes aim to balance reimbursement equity between procedural and cognitive services, they risk intensifying provider shortages, increasing workloads, and potentially contributing to burnout among neuroradiologists. Future policies should strive to balance budget neutrality with the unique requirements of specialized fields such as neuroradiology. Additionally, further investigation is necessary to examine the effects of current reimbursement trends on patient access, provider distribution, and the integration of novel imaging technologies that enhance diagnostic precision.

References

1. Wang KY, Hirsch JA, Nicola GN, Golding LP, Lee RK, Chen MM. Implications of the Revisions and Revaluation of Office/Outpatient Evaluation and Management Codes for Neuroradiology Reimbursement. *AJNR Am J Neuroradiol*. 2020;41(7):1160-1164

2. Bureau of Labor Statistics. Consumer Price Index. Latest Numbers. https://www.bls.gov/cpi/latest-numbers.htm.

3. Neprash HT, Golberstein E, Ganguli I, Chernew ME. Association of Evaluation and Management Payment Policy Changes With Medicare Payment to Physicians by Specialty. *JAMA*. 2023;329(8):662-669.

Images/Tables

Fig. Trends in average inflation-adjusted reimbursements for CT and MR neuroimaging studies.
(CPT codes: 70450, 70496, 70551, 70553, 72131, 72148)

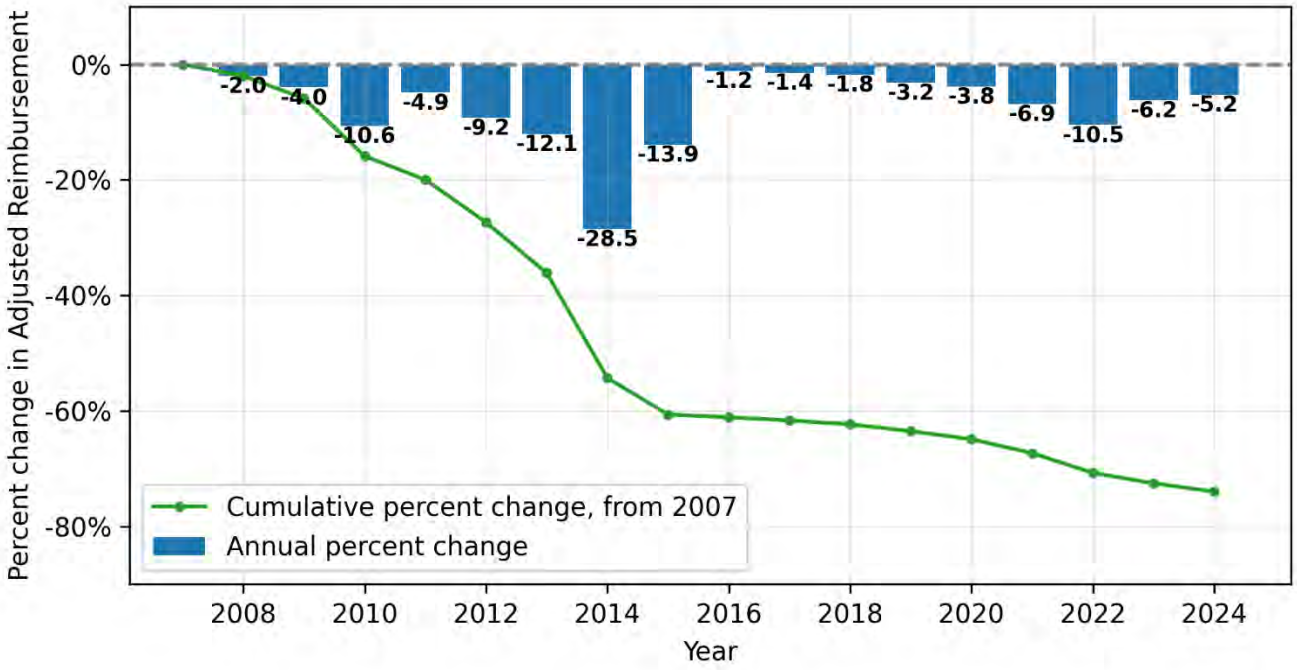

1076

Role of Diffusion along the perivascular space as a potential biomarker for glioma grading

Joga R Chaganti MD, PhD, David Posocco MD, Kiran Talekar MD, Weelic Chong MD, Scott Faro MD
Thomas Jefferson Hospital, Philadelphia, PA, USA

Abstract Category

Adult Brain

Purpose

The diffusion tensor image analysis along the perivascular space (DTI-ALPS) may have the potential to reflect glymphatic dysfunction in patients with glioma. The study aimed to determine the correlation of DTI-ALPS with glioma grade and to then compare the ALPS index with other diffusion metrics.

Materials & Methods

In this retrospective study, 38 patients with Grade-3 and Grade-4 were evaluated for the ALPS-index, fractional anisotropy (FA), mean diffusivity (MD), Radial diffusivity (RD)from 64 directional diffusion data. Wilcoxon rank sum test was used to test the significance of the values between the tumour grades in normal and tumor side hemispheres for both the grade 3 and 4 tumour groups as well as between the ALPS values and other DTI-metrics. Statistically significant threshold was set at $p < .05$.

Results

In patients with glioma, the ALPS-index of the hemisphere ipsilateral to glioma was significantly lower than that of the hemisphere contralateral to glioma (1.417±0.177 vs. 1.478±0.165; P=0.002). The ALPS-index was significantly higher in lower-grade gliomas (grade-3) than that in glioblastomas (GBMs) (1.495±0.151 vs. 1.320±0.159; P<0.001). FA, MD, also showed significant differences between grade-3 and Grade-4 (P<0.05).

Furthermore, the combination of the ALPS-index with FA, MD have shown superior discrimination ability compared to each metric used alone. The ALPS-index combined with FA had the highest area under the curve (AUC) of 0.854 as compared to that of 0.614–0.807 for a single metric in glioma grading.

Conclusion

The reduced ALPS-index may reflect tumor-induced glymphatic system impairment, and the ALPS-index may be able to complement conventional diffusion metrics in glioma grading.

References

Zhu H, Xie Y, Li L, Liu Y, Li S, Shen N, Zhang J, Yan S, Liu D, Li Y, Zhu W. Diffusion along the perivascular space as a potential biomarker for glioma grading and isocitrate dehydrogenase 1 mutation status prediction. Quant Imaging Med Surg. 2023 Dec 1;13(12):8259-8273. doi: 10.21037/qims-23-541. Epub 2023 Oct 21. PMID: 38106240; PMCID: PMC10721998.

Images/Tables

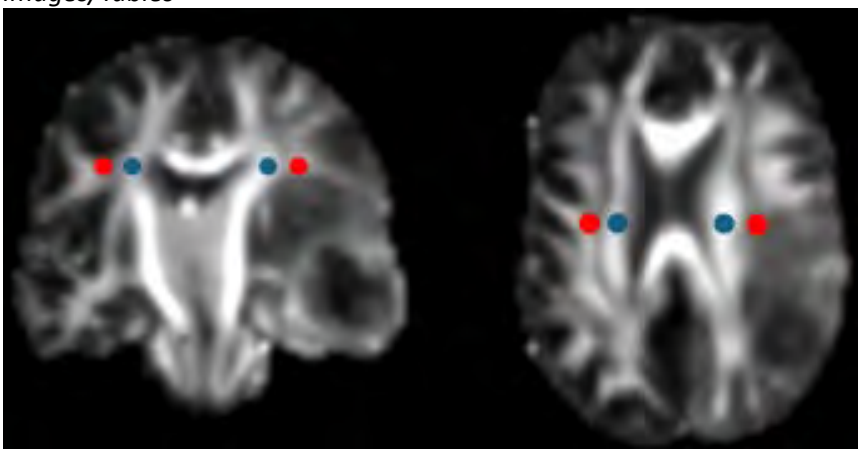

1087

Amide proton transfer weighted (APTw) imaging can predict outcome and identify true progression in IDH wildtype glioblastoma

Thomas Zeyen MD[1], Inga Krause[2], Andreas Decker PhD[3], Daniel Paech MD PhD[4], Jochen Keupp[5], Matthias Schneider MD[6], Ulrich Herrlinger Professor, MD[7], Alexander Radbruch Professor, MD[8], Christoph Katemann[5]

[1]Department of Neurooncology, center for neurology and integrated oncology (CIO), University hospital Bonn, Bonn, North Rhine Westphalia, Germany. [2]clinic for Neuroradiology, University hospital Bonn, Bonn, North Rhine Westphalia, Germany. [3]German Center for neurodegenerative disease (DZNE), Bonn, North Rhine Westphalia, Germany. [4]Department of Radiology, Brigham and Women´s Hospital, Harvard Medical School, Boston, Massachusetts, USA. [5]Philips Research, Hamburg, Hamburg, Germany. [6]Clinic for Neurosurgery, University hospital Bonn, Bonn, North Rhine Westphalia, Germany. [7]Department of Neurooncology, center for neurology and Integrated Oncology (CIO), University hospital Bonn, Bonn, North Rhine Westphalia, Germany. [8]Clinic for Neuroradiology, University hospital Bonn, Bonn, North Rhine Westphalia, Germany

Abstract Category

Functional/Advanced Imaging

Purpose

Treatment-induced MRI changes are common in glioblastoma patients, yet they remain challenging to differentiate from true tumor progression. [1] Their influence on outcome is controversially discussed. While advanced imaging (e.g. DWI, MRI perfusion imaging) are available, their sensitivity and specificity are limited, especially when used individually. Smaller studies already suggest that amide proton transfer weighted (APTw) imaging can help to differentiate between therapy-related and progression-related MRI changes. [2]

Materials & Methods

In this study, we analyzed 145 glioblastoma (IDH wildtype, CNS WHO grade 4) patients with available APTw imaging. For 61 cases with suspected progression, as defined by the latest Response Assessment in Neuro-Oncology (RANO) criteria, a “Region of Interest” (ROI) of contrast-enhancing tissue was segmented on gadolinium enhanced T1w images using the automated segmentation tool “HD-GLIO” [3, 4] and, if necessary, corrected manually. The mean APTw signal intensity of each ROI was measured and compared between confirmed progression (biopsy or clinical follow-up) and treatment-induced MRI changes using unpaired t-test. For assessing the influence of treatment-induced MRI changes on outcome Cox regression analysis was performed.

Results

After a median follow-up of 15 months, median overall survival in the respective cohort was 28 months (95% CI: 15.0–50.0). Mean APTw signal intensity was 2.36 in true progression cases versus 1.56 in treatment-induced changes ($p < 0.0003$). Excluding cases affected by treatments impacting vascular permeability (primarily Bevacizumab), the mean

APTw signal intensity was 2.48 in true progression versus 1.54 in treatment-related changes (p < 0.0001). Cox regression analysis revealed a trend for correlation of the Mean APT signal (%) with survival from the time point of suspected progression (Hazard ratio 1.81, 95% CI 0.97-3.37, p=0.06).

Conclusion

APT signal intensity of contrast-enhancing volume is significantly higher in cases of confirmed progression vs treatment-induced MRI changes. Low APT signal (%) at the time point of suspected progression is associated with longer overall survival. Future studies should investigate the combination of APTw imaging with other advanced techniques (e.g., DWI) and confirm its potential through prospective analyses in brain tumor assessment.

References

1. Wen PY, et al J Clin Oncol. 2023;41(33):5187-5199.
2. Ma B, et al. J Magn Reson Imaging 2016;44(2):456-462.
3. Kickingereder P, et al. Lancet Oncol 2019;20(5):728-740.
4. Isensee F, et al. Nat Methods 2021;18:203–211.

Images/Tables

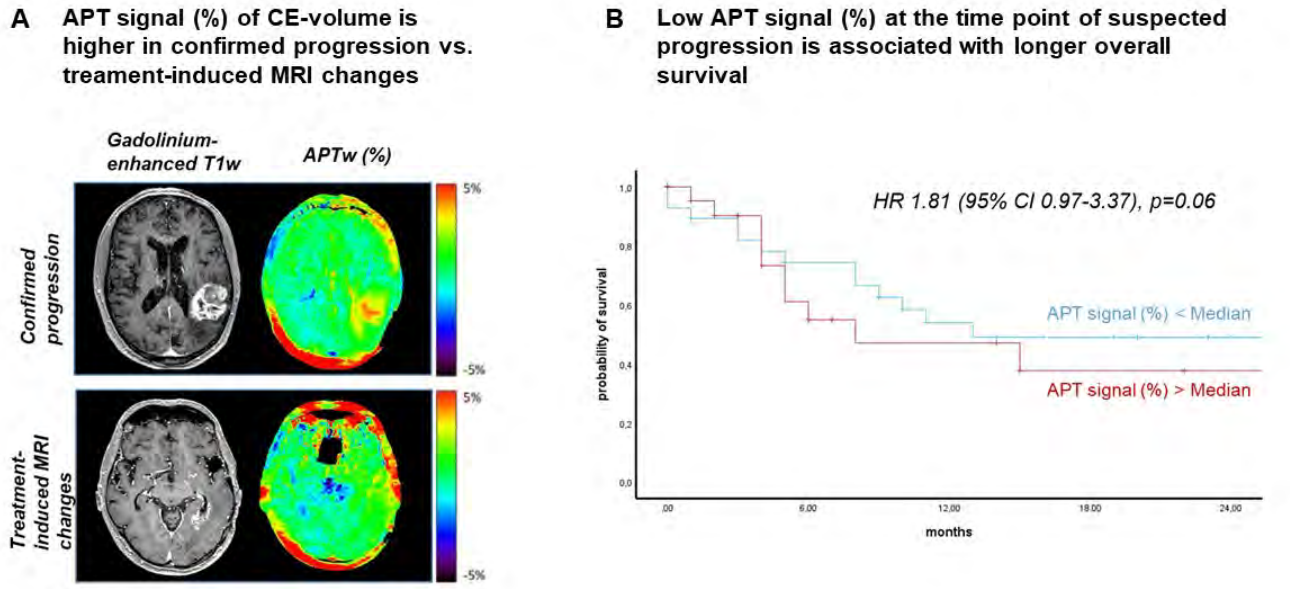

1107

Accuracy of Financial Disclosures by Scientific Presenters/Authors at the ASNR 2024 Annual Meeting

Dheeman Futela MBBS[1], Chris Lee[1], Sam Payabavash MD[1], Dheeraj Gandhi MD FACR[2], Ajay Malhotra MD MMM[1]
[1]Department of Radioilogy, Yale School of Medicine, New Haven, CT, USA. [2]Department of Radiology, University of Maryland School of Medicine, Baltimore, MD, USA

Abstract Category

Socioeconomics & Health Policy

Purpose

Physician-industry financial relationships can drive research and innovation, but potentially raise ethical concerns if not disclosed appropriately. Recent studies have shown high rates of non-disclosures by authors in radiology journals despite the financial relationships being common. National society meetings like the American Society of Neuroradiology (ASNR) annual meeting are avenues for dissemination of knowledge, including medical breakthroughs, and are widely attended. The aim of this study is to assess the disclosure rates of industry financial relationships by presenters at the ASNR 2024 national meeting.

Materials & Methods

The online archive of 21 scientific sessions at ASNR 2024, Las Vegas, in May 2024 was accessed via the virtual attendee platform. Full names, affiliations, and self-reported financial disclosures of presenters and co-authors of scientific presentations in each session were collected using an HTML scraping script. Industry payments made within the previous 24 months (as per ASNR disclosure policy) were recorded for each author found in the Open Payments database (OPD).

Each payment was classified as 'disclosed' or 'undisclosed' based on the authors' self-reported disclosure statement, and the authors were classified based on the completeness of disclosed industry relationships.

The OPD data was analyzed using Python v3.10 libraries, Pandas and NumPy, and the ASNR24 online meeting archive was scraped using Beautiful Soup v4.4.

Results

A total of 1222 authorships, including 886 unique authors, were included from 190 scientific presentations at ASNR24. From the OPD, 162 authors/ presenters were found by name and affiliation, and 68% (110/162) presenters received industry payments within the previous 24 months.

The total sum of payments to the 110 unique authors amounted to $2.9 million, and the median payment per author was $1420 (IQR = $171–$13 291). Research payments amounted to $1.2 mil to 22 authors (median = $35,517; IQR = $16,004 -$99,018), and "General" category payments amounted to $1.2 mil to 107 authors (median = $744; IQR = $164 - $4657). Ownership interest to 3 authors amounted to $528,647.

Out of the 110 authors that received industry payments, 2 authors self-reported all industry payments and 13 authors self-reported some of the industry payments. The remaining 95 (86.4%) authors failed to disclose any financial relationship.

The total amount of undisclosed payments was $2.7 mil (89.9% of the total), and the median undisclosed amount per author was $772 (IQR = $157-$8,139).

Conclusion

This study shows high rates of non-disclosures by authors/presenters at the ASNR 2024 annual meeting despite strict requirements. A commonly cited reason for non-disclosure is that physicians may deem the financial relationship as not relevant to the subject matter of the presentation. However, the ASNR policy on disclosures is non-ambiguous: "*Individuals in a position to control the content must disclose all relationships, regardless of their view of the relevance of the relationship(s) to the education.*"

In conclusion, greater awareness and transparency on disclosures of financial conflicts of interest are needed. It would reduce the risk of bias and increase the public's trust in the science being presented.

References

1. What is the Open Payments™ Program?: Centers for Medicare & Medicaid Services https://www.cms.gov/priorities/key-initiatives/open-payments.

2. Lee C, Khunte M, Tegtmeyer K, et al. Distribution and Disparities of Industry Payments to Neuroradiologists. *AJNR Am J Neuroradiol* 2024.

3. Futela D, Khunte M, Bajaj S, et al. Accuracy of Financial Disclosures in Radiology Journals. J Am Coll Radiol 2024;21:1527-1533

Images/Tables

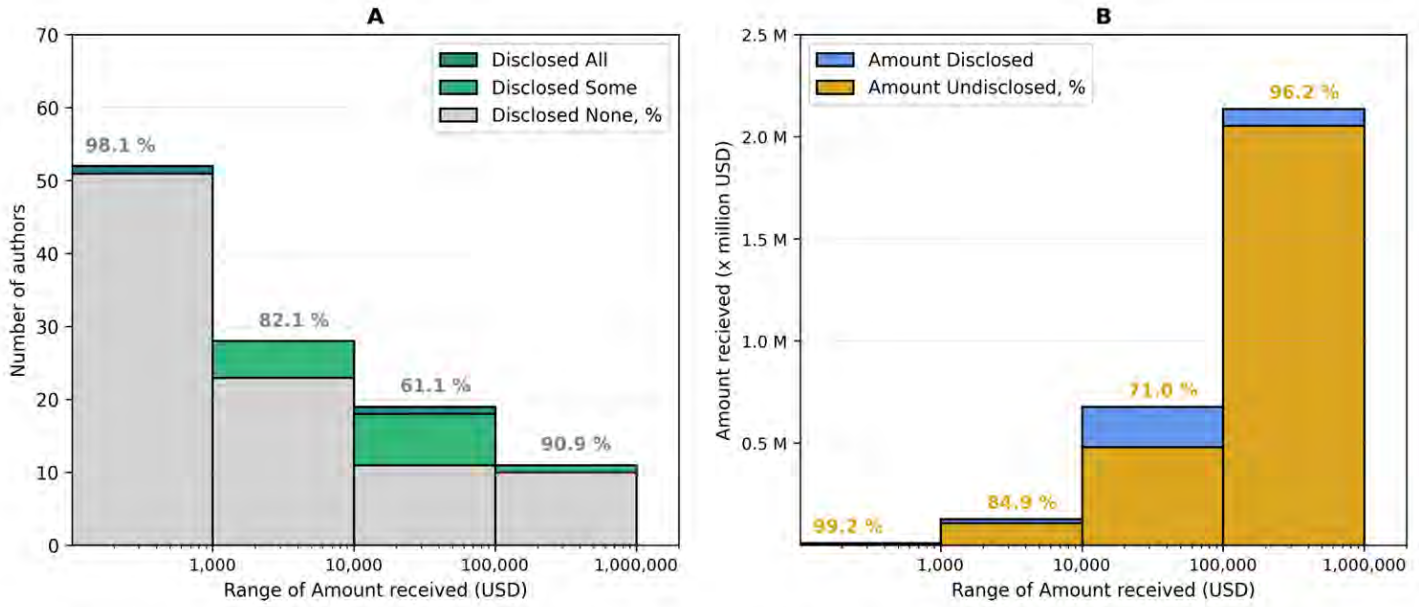

FIGURE. Disclosure rate by industry relationships (A) and by amount (B). X axis represents the range of total amount received, stratified on a logarithmic scale (<1000, 1000 - 10 000, 10 000 - 100 000, and >100 000).

1109

Clinical Outcomes of Staged Bilateral MR-guided High Intensity Focused Ultrasound Thalamotomy Utilizing Four-tract Tractography Targeting for Treatment of Essential Tremor

Parker Lawson M.D., Nil Saez Calveras M.D., Padraig O'Suilleabhain M.D., Bhavya Shah M.D.
UT Southwestern Medical Center, Dallas, TX, USA

Abstract Category

Adult Brain

Purpose

MR- guided high-intensity focused ultrasound thalamotomy is an incision-less procedure for medically refractory essential tremor (ET). Staged MRgHIFU is FDA-approved to treat bilateral ET but has an increased risk for adverse effects. Kaplitt, et al. have recently reported the rate of adverse effects persisting for greater than 3 months after bilateral MRgHIFU: 10% for imbalance, 22% for paresthesia, 20% for dysarthria, 14% for dysgeusia, 2% for weakness, and 8% for dysphagia. However, the use of our multi-parametric, advanced imaging targeting approach, four tract tractography, could reduce adverse effects and improve treatment response. This study aims to evaluate the outcomes of essential tremor patients treated with staged bilateral MR-guided high-intensity focused ultrasound thalamotomy.

Materials & Methods

We performed a retrospective analysis of 24 patients treated with staged bilateral MRgHIFU thalamotomy between March 2021 and August 2024. All 24 patients obtained clinical follow-up within the first month after treatment. Of these, 17 obtained 3-month follow-up, 8 obtained 6-month follow-up, and 6 obtained follow-up at or greater than 1 year. A board-certified movement disorder neurologist with 25+ years of experience employed a standardized tremor rating scale to evaluate postural and kinetic tremor response and Archimedes spirals before and after treatment. Side effects and their duration were also documented in this clinical assessment. Post-treatment tremor improvement was calculated with the formula: (pre-treatment score – post-treatment score) / (post-treatment score).

Results

There was a statistically significant reduction of kinetic and postural tremor on each side after staged bilateral MRgHIFU. Combined bilateral tremor improvement for the extension tremor was 93 %, near-nose tremor was 91% , finger-to-nose tremor was 85% , and Archimedes spiral test was 85% . 14 patients were observed to have a head tremor at the time of the second treatment, with additional head tremor improvement of 43% after the first side. 12 patients (50%) reported subjective imbalance within the first month after completion bilateral MRgHIFU, with 4 of those patients (17%) persisting for greater than 3 months, and only 1 (4%) for greater than 12 months. 10 patients (42%) reported

perioral or fingertip paresthesia that developed a few days after treatment, with 7 of those (29%) persisting for greater than 3 months, and 2 (8%) for greater than 12 months. 5 (20%) patients reported dysgeusia starting a few days after treatment but only 1 (4%) patient reported dysgeusia at 1 year. There was 1 case (4%) of transient dysphagia that resolved by 3 months. No patients reported dysarthria or weakness. All cases of paresthesia and imbalance were subjectively reported as “mild” by both the patient and the movement disorder neurologist.

Conclusion

This study supports the use of bilateral MRgHIFU thalamotomy with bilateral four tract tractography as a viable treatment for patients with treatment refractory bilateral essential tremor. This technique allows for significant symptom reduction with mild, often transient, adverse effects as well as significantly reduced rates of dysphagia, dysarthria, and weakness compared to other techniques.

References

1. Iorio-Morin C, Yamamoto K, Sarica C, et al. Bilateral Focused Ultrasound Thalamotomy for Essential Tremor (BEST-FUS Phase 2 Trial). Mov Disord. 2021 Nov;36(11):2653-2662. doi: 10.1002/mds.28716. Epub 2021 Jul 20. PMID: 34288097.
2. Shah BR, Lehman VT, Kaufmann TJ, et al. Advanced MRI techniques for transcranial high intensity focused ultrasound targeting. Brain. 2020 Sep 1;143(9):2664-2672. doi: 10.1093/brain/awaa107. PMID: 32537631.
3. Feltrin FS, Chopra R, Pouratian N, et al. Focused ultrasound using a novel targeting method four-tract tractography for magnetic resonance-guided high-intensity focused ultrasound targeting. Brain Commun. 2022 Oct 25;4(6):fcac273. doi: 10.1093/braincomms/fcac273. PMID: 36751499; PMCID: PMC9897190.
4. Kaplitt MG, Krishna V, Eisenberg HM, et al. Safety and Efficacy of Staged, Bilateral Focused Ultrasound Thalamotomy in Essential Tremor: An Open-Label Clinical Trial. JAMA Neurol. 2024 Sep 1;81(9):939-946. doi: 10.1001/jamaneurol.2024.2295. PMID: 39073822; PMCID: PMC11287440.

1118

Predicting 90-Day Outcomes in Acute Ischemic Stroke from Baseline Non-Contrast CT: A Deep Learning Approach vs. ASPECTS

Yongkai Liu PhD[1], Bin Jiang MD[1], Henk van Voorst MD, PhD[1], Yannan Yu MD[2], Greg Zaharchuk MD, PhD[1]
[1]Stanford University, Palo Alto, California, USA. [2]University of California, San Francisco, San Francisco, California, USA

Abstract Category

AI/Informatics

Purpose

Predicting long-term clinical outcomes based on immediate hospital admission data is invaluable for treatment decisions, prognostication, resource management, clinical trials, and setting patient expectations. Non-Contrast CT (NCCT) scans are fast, widely available, and can detect early stroke signs. However, the current interpretation method, the Alberta Stroke Program Early CT Score (ASPECTS), is subjective and may have limited ability to detect subtle changes or complex presentations (1). This study aimed to predict functional outcomes in acute ischemic stroke (AIS) patients using deep learning (DL) from the initial NCCT and compare its performance with the ASPECTS.

Materials & Methods

A total of 1,365 AIS patients from Lausanne University Hospital, who had baseline non-contrast CT scans and 90-day mRS data, were randomly divided into three groups: 70% (n=951) for model training, 15% (n=205) for validation, and 15% (n=205) for independent testing. The DL model utilized a tailored 3D Residual neural network structure, with the neuron count in the final fully connected layer reduced to one, enabling the model to generate a continuous prediction of the 90-day modified Rankin Scale (mRS) score. For ASPECTS prediction, a Support Vector Regressor was used to also generate continuous predictions of the 90-day mRS score. Evaluation metrics focused on the determination of unfavorable outcomes, defined as mRS scores greater than 2, comparing the performance of both the ASPECTS and the DL model.

Results

In the testing set, to predict unfavorable outcomes, the DL model demonstrated enhanced performance with an AUC of 0.74 (95% CI: 0.67, 0.81) compared to ASPECTS' AUC of 0.61 (95% CI: 0.53, 0.69; p = .01). This improvement was particularly notable in patients with unknown reperfusion status and those without EVT, where the DL model achieved significantly higher AUCs of 0.77 (95% CI: 0.66, 0.87; p=.03) and 0.75 (95% CI: 0.68, 0.83; p=.008), respectively, compared to ASPECTS' AUCs of 0.59 in both categories.

Conclusion

The proposed DL model outperformed the conventional ASPECTS in predicting unfavorable outcomes from baseline non-contrast CT scans. By providing superior accuracy in predicting 90-day outcomes for acute ischemic stroke patients, the DL model offers potential advantages in personalized treatment planning and reducing the subjectivity of traditional methods. This approach could lead to more reliable assessments and informed clinical decisions, ultimately enhancing patient care.

References

1. Barber, Philip A., et al. "Validity and reliability of a quantitative computed tomography score in predicting outcome of hyperacute stroke before thrombolytic therapy." The Lancet 355.9216 (2000): 1670-1674.

Images/Tables

PATIENT DATA

Male	Age median (IQR)	HTN	Baseline NIHSS median (IQR)	Treatment Status				Reperfusion Status				90-day outcome	
				Only IV tPA	Only EVT	IV tPA &EVT	NO	Minor	Major	Partial	UK	Favorable	Unfavorable
131 (56.2)	72 (60, 79)	118 (67.0)	11 (5,17)	60 (29.3)	27 (13.2)	18 (8.8)	100 (48.8)	34 (16.6)	66 (32.2)	23 (11.2)	82 (40.0)	114 (55.6)	91 (44.4)

Summary of the characteristics of AIS Patients included in Internal Test Set (ITS) Cohort. Unless specified differently, the given data is represented as the count (proportion) of patients. Here are some abbreviations for reference: NIHSS stands for National Institutes of Health Stroke Scale, mRS refers to modified Rankin scale, and LUH denotes Lausanne University Hospital. IV tPA is an abbreviation for intravenous tissue plasminogen activator, while EVT represents endovascular therapy.

METHOD

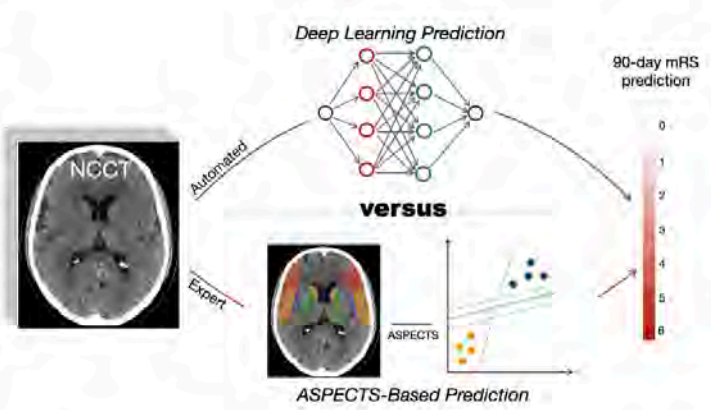

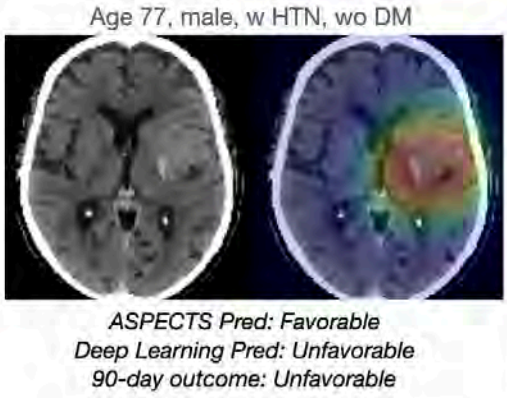

Saliency Map

RESULT

	All patients	Different Reperfusion Status				Different Treatment Type	
		Major	Minor	Partial	Unknown	Non-EVT	EVT
ASPECTS	0.61 (0.53, 0.69)	0.56 (0.38,0.75)	0.61 (0.42, 0.79)	0.75 (0.52, 0.95)	0.59 (0.47, 0.71)	0.59 (0.50-0.68)	0.67 (0.49-0.83)
Deep Learning	0.74 (0.67, 0.81) p=.01	0.73 (0.57,0.87) p=.17	0.70 (0.48, 0.90) p=.57	0.71 (0.46, 0.95) p=.83	0.77 (0.66, 0.87) p=.03	0.75 (0.68-0.83) p=.008	0.69 (0.53-0.84) p=.88

The presented AUC values are accompanied by their 95% confidence intervals. The p-values indicate the difference in AUC values between ASPECTS and the deep learning model.

1124

Clinical Evaluation of Motion-Corrected 2D Axial T2-Weighted Turbo Spin Echo 3T Brain MRI in the Neurological Intensive Care Unit

Azadeh Hajati MD[1], Chen-Hua Chiang MD[1], Azadeh Tabari MD[1], Seonghwan Yee PhD[1], Daniel Polak PHD[2], Daniel Nicolas Splithoff PHD[2], Bryan Clifford PHD[3], Wei-Ching Lo PHD[3], Yantu Huang PHD[4], Stephen F. Cauley PHD[3], John M. Conklin[1], Susie Y. Huang MD, PHD[1]

[1]Department of Radiology, Athinoula A. Martinos Center for Biomedical Imaging, Massachusetts General Hospital, Boston, MA, USA. [2]Siemens Healthcare, Erlangen, Bavaria, Germany. [3]Siemens Medical Solutions USA, Boston, MA, USA. [4]Siemens Shenzhen Magnetic Resonance Ltd, Shenzhen, Guangdong sheng, China

Abstract Category

AI/Informatics

Purpose

Axial T2-weighted brain images using Turbo Spin Echo (TSE) or Fast Spin Echo (FSE) sequences are essential for detecting brain pathologies like stroke, tumors, infections, inflammation, and hydrocephalus. However, patient motion, common in acute and critical settings, causes blurring and ghosting artifacts that can obscure or mimic pathology. Motion correction is therefore crucial for T2-weighted TSE/FSE sequences in brain MRI, especially for inpatient and emergency assessments. (1) While optimized Cartesian sampling can reduce motion sensitivity, patient movement often worsens motion artifacts. The SAMER (scout accelerated motion estimation and reduction) method uses guidance lines for robust data consistency-based retrospective correction, previously validated for 3D T1-weighted MPRAGE acquisitions. (2,3) This study aimed to validate SAMER for axial T2 TSE brain imaging in patients evaluated for acute pathology in emergency and inpatient settings, fully utilizing MRI's diagnostic power. SAMER uses a low-resolution "scout" scan and added phase-encoding lines to estimate rigid motion parameters and create a motion-corrected reconstruction. (4)

Materials & Methods

This IRB-approved, HIPAA-compliant single-center study collected data from 100 patients undergoing brain MRI for acute intracranial pathology in emergency and inpatient settings from March to May 2024 on a 3T scanner (MAGNETOM Vida, Siemens Healthcare, Forchheim, Germany) using a 20-channel head coil. The imaging protocol included an axial T2-weighted TSE research sequence incorporating SAMER. Retrospective reconstructions of the axial T2 TSE data were performed with and without SAMER correction and evaluated in a head-to-head fashion. Two neuroradiologists independently reviewed motion-affected cases using a 5-tier grading scale, with adjudication by a third radiologist as needed. Motion grades before and after SAMER were compared using the Wilcoxon Signed-Rank Test.

Results

Among the 100 patients (mean age 59.3), common indications included brain tumors (26%), postoperative brain tumors (24%), stroke (15%), and altered mental status (13%). Motion was moderate in 19% of cases, mild in 45%, and absent in 36%. Post-SAMER correction showed significant improvement in motion grades ($p=0.00024$). SAMER correction improved scores by at least one point in 21% of cases for reader 1 and 14% for reader 2. (Image 1)

Conclusion

SAMER effectively reduces motion artifacts in T2-weighted imaging, enhancing diagnostic reliability in critical care settings. Future work will explore further optimizations and real-time applications across diverse clinical settings.

References

1. Polak D, Hossbach J, Splitthoff DN, et al. Motion guidance lines for robust data consistency-based retrospective motion correction in 2D and 3D MRI. Magn Reson Med 2023;89(5):1777-1790. doi:10.1002/mrm.29534
2. Lang M, Tabari A, Polak D, et al. Clinical Evaluation of Scout Accelerated Motion Estimation and Reduction Technique for 3D MR Imaging in the Inpatient and Emergency Department Settings. AJNR Am J Neuroradiol. 2023;44(2):125-133. doi:10.3174/ajnr.A7777
3. Gil N, Tabari A, Lo WC, et al. Quantitative evaluation of Scout Accelerated Motion Estimation and Reduction (SAMER) MPRAGE for morphometric analysis of brain tissue in patients undergoing evaluation for memory loss. NeuroImage. 2024; 300:120865. doi:10.1016/j.neuroimage.2024.120865
4. Vecchiato K, Egloff A, Carney O, et al. Evaluation of DISORDER: Retrospective Image Motion Correction for Volumetric Brain MRI in a Pediatric Setting. AJNR Am J Neuroradiol. 2021;42(4):774-781. doi:10.3174/ajnr.A7001

Images/Tables

Patient Characteristics		
Number of participants	100	
Mean age (years ± SD)	59.3 ± 14.8	
Sex	Female: 46(46%) Male: 54 (54%)	
Clinical indication for Brain MRI	Brain tumor	26
	Brain tumor - post-op	24
	Stroke	15
	Altered mental status	13
	Stroke/hemorrhage	8
	Seizure	6
	Infection	5
	Vascular malformation	1
	Headache	1
	Hemorrhage	1

Table1: Demographic information of the patients

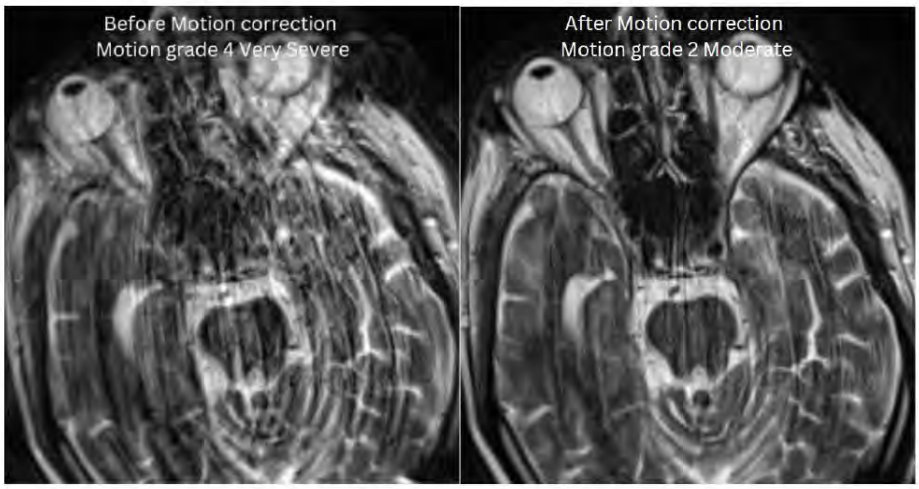

Image 1: A 67-year-old man with a brain tumor showing images before and after SAMER correction

1126

Radio-Pathomic Estimates of Glioma Composition Distinguish Grade Groups and IDH Mutation Status

Samuel A Bobholz PhD[1], Michael Flatley[1], Savannah R Duenweg PhD[2], Aleksandra Winiarz[2], Benjamin Chao[2], Allison K Lowman[1], Biprojit Nath MS[1], Fitzgerald Kyereme[1], Jennifer Connelly MD[1], Kelly Mrachek MD[1], Elaine Tanhehco[1], Max Krucoff MD[1], Peter S LaViolette PhD[1]

[1]Medical College of Wisconsin, Milwaukee, WI, USA. [2]e of Wisconsin, Milwaukee, WI, USA

Abstract Category

Adult Brain

Purpose

Glioblastoma (GBM) is a devastating illness with a median survival time of 18 months and a five-year survival rate of 6%[1,2]. Better clinical outcomes are often seen in lower grade gliomas, as well as patients with protective genetic mutations such as those for isocitrate dehydrogenase (IDH) enzymes. This study assessed the ability for tumor composition analysis via autopsy-based radio-pathomic maps to non-invasively discriminate between glioma tumor grade and IDH mutation status.

Materials & Methods

This study using pre-treatment MR imaging data from the publicly available UCSF-PDGM dataset (n=501). Pre- and post-contrast T1-weighted images, along with T2-weighted FLAIR and apparent diffusion coefficient (ADC) images were used as input to generate radio-pathomic maps of cellularity (in cells/mm^2) and extracellular fluid density (%) using a previously published algorithm[3,4]. The model used autopsy tissue aligned to the last MRI prior to death as input and have shown to reliably detect areas of tumor infiltration beyond the contrast enhancing margin, offering substantial improvement over conventional tumor localization. These maps were then thresholded to identify radio-pathomic tumor composites (RPTC) that distinguish common pathological features in glioma in pathological analyses, including hypercellularity (>1900 cells/mm^2, <25% ECF), necrosis (<1900 cells/mm^2, >25% ECF), and pseudopalisading necrosis (>1900 cells/mm^2, >25% ECF). The proportion of these features within contrast enhancement (CE) and non-enhancing FLAIR hyperintensity (FH) were derived from the datasets included tumor segmentations and compared across tumor grade group (ANOVA) and IDH status (2-sample t-test).

Results

Higher proportions of necrotic presence were observed within CE for Grade 2 patients ($F=3.195$, $p=0.042$), where higher CE proportions of pseudopalisading necrosis were found in Grade 3 patients ($F=7.336$, $p=0.001$). A higher proportion of hypercellularity was observed within FH in Grade 4 patients, likely indicating more infiltrative tumors that extend beyond the traditional imaging margin ($F=6.224$, $p=0.002$). IDH mutant patients saw reduced hypercellularity within CE ($t=3.661$, $p<0.001$), as well as higher proportions of necrosis ($t=-2.774$, $p=0.006$) and pseudopalisading necrosis ($t=-2.702$, $p=0.007$). Within FH, IDH patients saw less hypercellularity compared to IDH wildtype patients ($t=2.006$, $p=0.045$).

Conclusion

These results indicate that the radio-pathomic composition of glial tumors can aid in distinguishing between grade groups and IDH mutation status, two critical factors that impact prognosis. Hypercellularity beyond CE was reliably found in higher grade tumors, highlighting that tumor infiltration beyond the contrast enhancing margin, particularly when seen prior to treatment, may substantially impact prognosis. The appearance of pseudopalisading necrosis in lower grade cases was unexpected as this is often a hallmark of Grade 4 GBM, and future research assessing the pathological and transcriptomic characteristics of these areas of hypercellularity and necrosis colocalization may aid in distinguishing lower grade forms from pathological pseudopalisading necrosis observed in GBM to more precisely denote these regions.

References

References

1. Ostrom QT, Cioffi G, Gittleman H, et al. CBTRUS Statistical Report: Primary Brain and Other Central Nervous System Tumors Diagnosed in the United States in 2012-2016. *Neuro Oncol*. 2019;21(Suppl 5):v1-v100. doi:10.1093/neuonc/noz150

2. Ostrom QT, Cote DJ, Ascha M, Kruchko C, Barnholtz-Sloan JS. Adult Glioma Incidence and Survival by Race or Ethnicity in the United States From 2000 to 2014. *JAMA Oncol*. 2018;4(9):1254-1262. doi:10.1001/jamaoncol.2018.1789

3. Bobholz SA, Lowman AK, Brehler M, et al. Radio-pathomic maps of cell density identify glioma invasion beyond traditional MR imaging defined margins. *American Journal of Neuroradiology*. 2021;(May).

4. Bobholz SA, Lowman AK, Connelly JM, et al. Noninvasive Autopsy-Validated Tumor Probability Maps Identify Glioma Invasion Beyond Contrast Enhancement. *Neurosurgery*. 2024;95(3). https://journals.lww.com/neurosurgery/fulltext/2024/09000/noninvasive_autopsy_validated_tumor_probability.9.aspx

Images/Tables

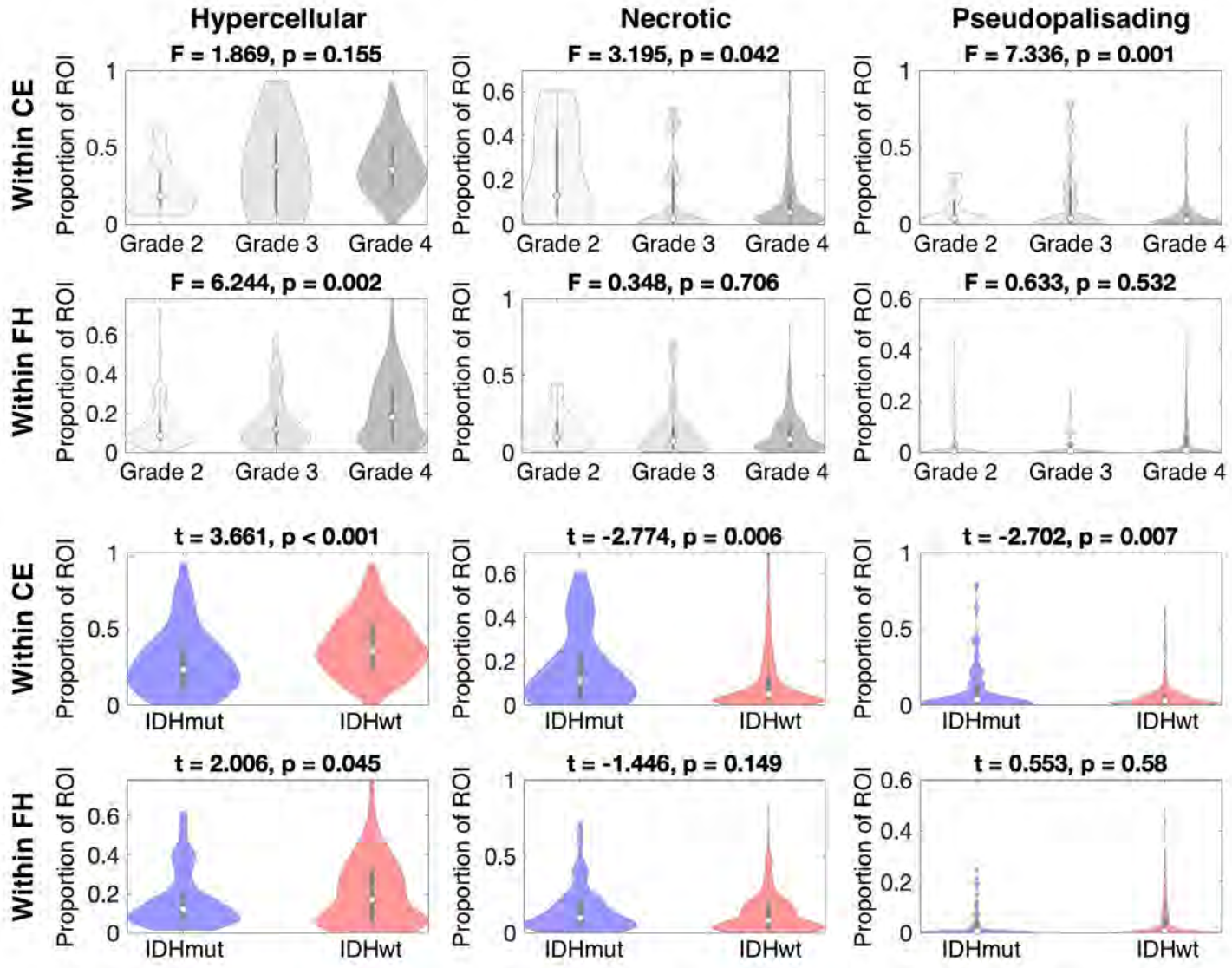

Figure 1: Tumor composition differences in glioma grade and IDH status within contrast enhancement (CE) and non-enhancing FLAIR hyperintensity (FH).

1130

Transfer Learning in Large Language Models for Integration of Pathology-Radiology Reports in Brain Tumor Diagnosis

Lulu Bi[1], Zhuoqi Ma PhD[2], Paige Collins[2], Grayson Baird PhD[2], Shaolei Lu MD[2], Owen P Leary[3], Nikos Tapinos MD, PhD[3], Jerrold L Boxerman MD[2], Zhicheng Jiao PhD[2]

[1]Warren Alpert Medical School, Providence, RI, USA. [2]Rhode Island Hospital, Department of Diagnostic Imaging, Providence, RI, USA. [3]Rhode Island Hospital, Department of Neurosurgery, Providence, RI, USA

Abstract Category

AI/Informatics

Purpose

Biopsy and imaging are crucial variables that can improve outcomes for glioblastoma patients by facilitating early detection and monitoring. Due to its ability to automatically classify features whilst minimizing inter-rater variability and the amount of time spent per case, deep learning (DL) is increasingly being incorporated into impactful discoveries for automated magnetic resonance imaging (MRI) interpretation. Transfer learning can boost the performance of DL models by pre-training one on a related, larger dataset and fine-tuning it on a smaller, specific dataset. This project evaluates

two pre-trained large language models (LLMs) for glioblastoma prediction in brain MRI reports, as well as the change in performance when combined with pathology-radiology fusion data.

Materials & Methods

In this IRB-approved retrospective study at Rhode Island Hospital, we trained a multilayer perceptron (MLP) classifier composed of linear layers and incorporated it into BioBERT and Gatortron, two LLMs pre-trained on public medical datasets that served as text encoders. We first assessed the performance of the two models across two tasks: detecting tumor presence (cancer present or no cancer present) and tumor status (improving/responding, worsening/enlarging, or stable/no change), then evaluated the superior model's performance when combined with pathology-radiology fusion data on the same tasks. For the first step, we included 4726 and 4518 report-pairs (model-generated and radiologist-generated as ground truths), and we included 4684 and 4277 report pairs for the latter step, respectively. Both datasets were split into training, validation, and test sets using a 8:1:1 ratio. Performance metrics were micro F1, precision, and recall.

Results

Figure 1 depicts the performance of each model. For the tumor presence task, the Gatortron model with the MLP classifier had micro F1, precision, and recall scores of 0.78, 0.77, and 0.78, and the BioBERT model with the MLP classifier had scores of 0.73, 0.72, and 0.73, respectively. For the tumor status task, the Gatortron model with the MLP classifier had micro F1, precision, and recall scores of 0.82, 0.77, and 0.82, while the BioBERT model with the MLP classifier had scores of 0.75, 0.72, and 0.75, respectively. The model that combined Gatortron and pathology-radiology fusion data scored the highest across all three metrics in both tasks.

Conclusion

The superior performance of the model that combined Gatortron and pathology-radiology fusion data suggests that transfer learning may be used to improve DL-based models for interpreting brain MRIs. Future work will use the superior trained model to conduct survival analysis for glioblastoma patients. With further training and fine-tuning of the combined pathology-radiology model, such findings may be used as a tool for automating parts of the diagnostic workflow in the clinical setting.

References

Bauer S, Wiest R, Nolte L P, et al. A survey of MRI-based medical image analysis for brain tumor studies. *Physics in Medicine & Biology*, 2013, 58(13): R97. https:/doi.org/10.1088/0031-9155/58/13/R97

Yang R, Tan T F, Lu W, et al. Large language models in health care: Development, applications, and challenges. *Health Care Science*, 2023, 2(4): 255-263. https://doi.org/10.1002/hcs2.61

Images/Tables

Models	Tumor Presence	Tumor Status
Gatortron + MLP classifier	Micro F1: 0.78	Micro F1: 0.82
	Precision: 0.77	Precision: 0.77
	Recall: 0.78	Recall: 0.82
BioBERT + MLP classifier	Micro F1: 0.73	Micro F1: 0.75
	Precision: 0.72	Precision: 0.72
	Recall: 0.73	Recall: 0.75
Gatortron + MLP classifier + pathology-radiology fusion data	Micro F1: 0.83	Micro F1: 0.83
	Precision: 0.82	Precision: 0.82
	Recall: 0.83	Recall: 0.83

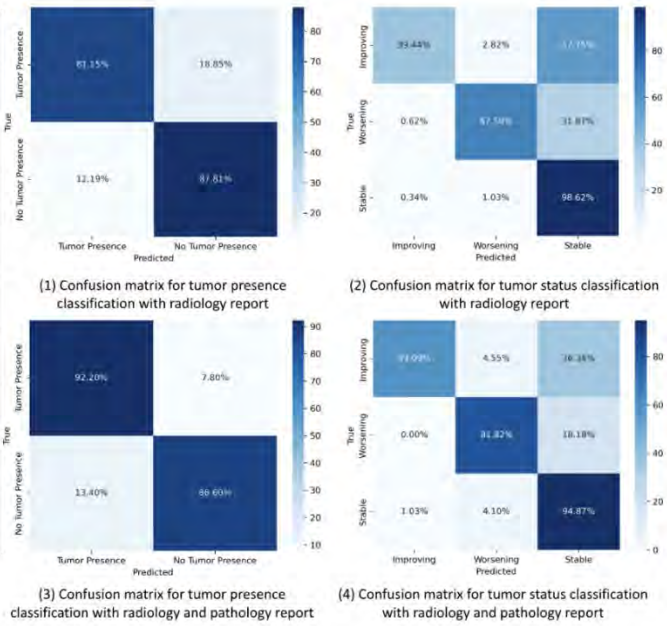

Figure 1. Performance of LLMs with only radiology reports versus with radiology and pathology reports

1133

Association between BRAFV600E Mutation, Disease Severity, and Germ Line Layer Involvement in Erdheim-Chester Disease by Using Radiological Findings from a Unique ECD Population

Fatemeh Dehghani Firouzabadi[1], Ali Sheikhy[2], Safa Samimi[2], Fahimul Huda[3], Aryan Zahergivar[2], Moozhan Nikpanah[4], Mojdeh Mirmomen[5], Faraz Farhadi[6], Mahshid Golagha[2], Fatemeh Homayounieh[2], Evrim Turkbey[2], Jhanavi Rao[2], Mark A. Ahlman[2], Corina Millo[2], Babak Saboury[2], Ashkan A. Malayeri[2]

[1]San Francisco, California, USA. [2]National Institutes of Health, Bethesda, Maryland, USA. [3]Louisville, Kentucky, USA. [4]Department of radiolog, Birmingham, Alabama, USA. [5]Department of radiolog, San Diego, California, USA. [6]Hanover, New Hampshire, USA

Abstract Category

Adult Brain

Purpose

This study evaluates the relationship between $BRAF^{V600E}$ mutation, disease severity, and germ line layer involvement in Erdheim-Chester Disease (ECD) using radiological findings.

Materials & Methods

A prospective analysis of radiological findings from a cohort of 40 biopsy-confirmed ECD patients were conducted. These patients had available imaging data along with $BRAF^{V600E}$ mutation status. Our evaluation of radiological findings comprised 10 organ involvements (including bone, pulmonary, CNS, uropathy, nephropathy, cardiac, vascular, orbit, hepatobiliary, and spleen)(table 1) and germ line layer involvement (Mesoderm, Endoderm, Ectoderm), based on radiological findings. A team of expert radiologists, comprising 5 body, 2 neuro, 1 thoracic, 2 clinical fellows, and 2 nuclear medicine specialists, reviewed MRI/CT/PET-CT/Bone Scan studies. Discrepancies were resolved either by a third reader or by achieving consensus between two radiologists.

Results

A significant association was found between $BRAF^{V600E}$ mutation and disease severity based on organ involvement. Bone and pulmonary regions exhibited the highest frequency of involvement, regardless of the presence of $BRAF^{V600E}$mutation (95% and 92% respectively). Positive associations were found between $BRAF^{V600E}$ mutation and cardiac (OR=4.55, p=0.027) and vascular (OR=5.60, p=0.013) involvement. ECD patients showed full involvement in Mesoderm (100%), 93% in Endoderm, and 75% in Ectoderm using radiological findings. However, no significant correlation existed between germ line layer involvement and $BRAF^{V600E}$ mutation.

Conclusion

BRAF mutation is associated with disease severity in ECD, particularly in cases with more organ involvement. Bone and pulmonary regions are consistently affected, while cardiac and vascular involvement are associated with $BRAF^{V600E}$mutation. ECD patients showed full involvement in Mesoderm while no direct correlation was found with $BRAF^{V600E}$mutation with any specific germ line layer.This study represents the largest single-center investigation of ECD patients, encompassing a comprehensive assessment of radiological findings to elucidate the impact of the $BRAF^{V600E}$ mutation on disease severity, thereby facilitating risk stratification and treatment decision-making in ECD. Furthermore, the identification of $BRAF^{V600E}$ mutation status as a potential prognostic indicator highlights the multifaceted nature of ECD, underscoring the imperative for targeted therapeutic approaches and additional molecular research.

References

1. Goyal G, Heaney ML, Collin M, Cohen-Aubart F, Vaglio A, Durham BH, et al. Erdheim-Chester disease: consensus recommendations for evaluation, diagnosis, and treatment in the molecular era. Bloo
2. d, The Journal of the American Society of Hematology. 2020;135(22):1929-45.

Images/Tables

Association between $BRAF^{V600E}$ mutation and Organ involvement

	OR (95% CI)	P- value
Bone	1.11 (0.06, 19.09)	0.942
Orbital	1.87 (0.45, 7.82)	0.388
CNS	0.5 (0.08, 3.10)	0.456
Uropathy	1.45 (0.40, 5.26)	0.568
Nephropathy	3.5 (0.75, 16.28)	0.110
Pulmonary	2.35 (0.19, 28.26)	0.499
Cardiac	4.55 (1.18, 17.52)	0.027
Vascular	5.60 (1.43, 21.95)	0.013
Hepatobiliary	0.39 (0.06, 2.45)	0.318
Spleen	0.625 (0.12, 3.24)	0.575

* Logistic regression model

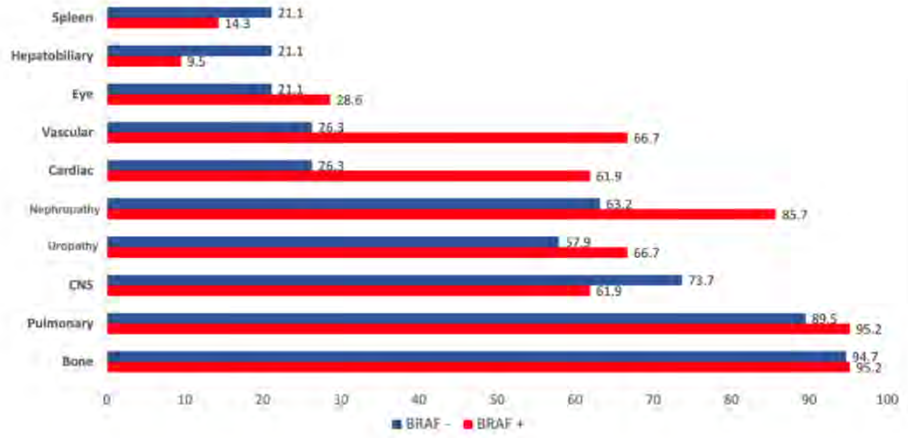

1138

The Role of Apparent diffusion coefficient the diagnosis and Evaluation of Intraspinal pathologies – Can it offer additional insights?

Simran Singh Cheema MD[1], Aditya Duhan MD[2], FNU Vaibhav MBBS[3], Rajiv Mangla MD[2]
[1]University of alabama, Birmingham, AL, USA. [2]State University of New York Upstate Medical University, Syracuse, NY, USA. [3]Pt. B.D. Sharma PGIMS, Rohtak, Haryana, India

Abstract Category

Spine

Purpose

The apparent diffusion coefficient (ADC) has emerged as a valuable imaging biomarker in the diagnosis and evaluation of intraspinal pathologies.[1] Effectiveness of ADC in distinguishing between different tumour types and grades, such as high-grade gliomas and low-grade tumors, thereby enhancing diagnostic precision.[2] The study aims to assess the diagnostic utility of diffusion-weighted imaging (DWI) especially Apparent diffusion coefficient (ADC) values in diagnosing and characterizing different spinal lesions including tumours. It aims to assess the degree of diffusion restriction in various pathologies of spinal cord and to calculate average ADC values for various spinal pathologies.

Materials & Methods

This retrospective study comprised 125 adult patients who underwent magnetic resonance imaging of the spine and were positive for either spinal tumours, infarcts, inflammatory/ infective or vascular pathologies. DWI sequences were performed along with routine sequences on Siemens MRI scanners. ADC values were calculated by placing two regions

of interest. Cases with artifacts were excluded from the study and average ADC values were calculated for 105 cases. Average ADC values were calculated for various pathologies separately. Tumours were further divided into high grade tumours and low grade tumours and average ADC values were deduced for these.

Results

For spinal infarcts (N=18), DWI showed restricted diffusion within the infarct area with decreased ADC values (mean 0.84 $x10^{-3}$ mm^2/s). In cases of drop metastases from medulloblastoma (n = 23), subtle metastases were identified through DWI, providing critical information that were less conspicuous by conventional MRI. In different spinal cord tumours analysis indicated higher ADC values in low grade tumours ($1.2x10^{-3}$) and Low ADC values in high grade tumours ($0.9x10^{-3}$). The ADC value for metastases arising from the primary cancer site (n=26) was 0.83×10^{-3} mm^2/s. It helps to differentiate from post-treatment changes. Mean ADC in demyelinating diseases (n=7) was significantly high with mean of 1.28 x 10 -3. Higher ADC values were obtained in infective/inflammatory pathologies (n=16) and vascular pathologies(n=9).

Conclusion

In conclusion, the potential utility of ADC values and DWI in diagnosing various spinal diseases should be considered. Diffusion restriction with ADC values can help distinguish between benign and malignant lesions. Routine calculation of ADC values in spinal lesions adds valuable information and helps differentiate benign and malignant spinal lesions.

References

1. Allam KE, Abd Elkhalek YI, Hassan HGEMA, et al. Diffusion-weighted magnetic resonance imaging in differentiation between different vertebral lesions using ADC mapping as a quantitative assessment tool. Egyptian Journal of Radiology and Nuclear Medicine 2022;53:155
2. Küker W, Weller M, Klose U, et al. Diffusion-weighted MRI of spinal cord infarction. J Neurol 2004;251:818–24
3. Gitto S, Bologna M, Corino VDA, et al. Diffusion-weighted MRI radiomics of spine bone tumors: feature stability and machine learning-based classification performance. Radiol med 2022;127:518–25
4. Niknejad MT. Apparent diffusion coefficient | Radiology Reference Article | Radiopaedia.org. Radiopaedia https://doi.org/10.53347/rID-21759

Images/Tables

Condition	N	DWI Findings	Mean ADC Value ($\times10^{-3}$ mm^2/s)	Remarks
Spinal Infarcts	18	Restricted diffusion in infarct area	0.84	Indicates decreased ADC values
Drop Metastases (Medulloblastoma)	23	Subtle metastases identified on DWI	-	Less conspicuous on conventional MRI
Low-Grade Tumors (Spinal Cord)	-	Higher ADC values	1.2	Helps in differentiating low-grade tumors
High-Grade Tumors (Spinal Cord)	-	Lower ADC values	0.9	Helps in differentiating high-grade tumors
Metastases (Primary Cancer Site)	26	-	0.83	Helps to differentiate from post-treatment changes
Demyelinating Diseases	7	-	1.28	Significantly high ADC values
Infective/Inflammatory Pathologies	16	-	-	Higher ADC values
Vascular Pathologies	9	-	-	Higher ADC values

1153

Visualizing Microstructural Changes in Aging and Cognitive Decline through SANDI Analysis in Ultra-High Gradient Diffusion Imaging

Aneri Bhatt, Hansol Lee, Kwok-Shing Chan, Yixin Ma, Jeremy N Ford, Susie Y Huang
Athinoula A. Martinos Center for Biomedical Imaging, Department of Radiology, Massachusetts General Hospital, Boston, MA, USA

Abstract Category

Functional/Advanced Imaging

Purpose

The biological process of aging, as well as neurodegenerative conditions, are associated with structural changes in the human cortex. Structural MRI can provide insight into cortical thinning and atrophy, but only at the macroscopic level when cellular damage is already evident[1]. The Connectome 2.0 scanner allows for advanced diffusion imaging through ultra-high gradient strengths up to 500 mT/m, providing higher sensitivity and resolution from the macroscopic to microscopic levels[2]. Coupled with state-of-the-art microstructure imaging methods like Soma and Neurite Density Imaging (SANDI) model[3], this study investigates age-related alterations in grey matter microstructure, and associations with cognition in older adults.

Materials & Methods

Thirty-six participants were recruited (19-83 years, 27F9M), from which 10 participants (51-83 years, Fig.1) were administered the Montreal Cognitive Assessment (MoCA) for detection of cognitive dysfunction[4]. All were scanned on the 3T Connectome 2.0 MRI system (MAGNETOM Connectom, Siemens Healthcare) using a custom-built 72 channel head coil12, with a maximum gradient strength (G_{max}) of 500 mT/m[1]. Diffusion MRI data was acquired using a multi-shell acquisition scheme, with 8 b-values ranging from 0.05 to 6 ms/mm^2, linearly spaced up to G_{max}. T1-weighted images were acquired at 1 mm isotropic resolution. The SANDI model was fitted to the diffusion MRI data, and soma (f_{soma}) and neurite ($f_{neurite}$) volume fraction maps were generated[3]. Region-of-interest (ROI) medians were extracted. Participants were divided into a younger cohort (<50 years) and an older cohort (>50). Twenty-five healthy participants (19-49 years, 20F6M) and eleven older adults (51-83 years, 7F3M) were included (Fig. 1). Pearson's correlation test was used to assess the associations among f_{soma}, age, and MoCA. At each of 29 cortical ROIs, f_{soma} and $f_{neurite}$ in the younger and older cohorts were evaluated. In the older cohort, analysis focused on associations between age and MoCA versus f_{soma}.

Results

Maps of f_{soma} and $f_{neurite}$ in a representative older adult and young sex-matched control are shown in Figure 2. f_{soma} was reduced in the older cohort across ROIs (Fig. 3). One older subject who did not elect to complete cognitive testing was excluded from the older cohort used for analysis of cognition (n = 10). Within the older cohort, a trend toward decreased f_{soma} with increased age was noted overall, as well as within the four lobes, amygdala, and hippocampus (Fig. 4). A trend of decreased f_{soma} with greater cognitive impairment was observed in the whole brain and these areas, but was particularly weak in the hippocampus and entorhinal cortex (Fig. 5).

Conclusion

Significant reductions in soma fraction were observed with age, particularly in individuals over 50. Possible associations of age and cognitive impairment with soma volume fraction were noted. Of note, similar significant associations have been observed between soma fraction and age across the frontal, parietal and temporal lobes in 72 individuals scanned on Connectome 1.0[5]. Our results on Connectome 2.0 suggest that greater sensitivity of diffusion MRI with stronger gradients may enable detection of associations within a smaller cohort. Future work will focus on expanding the cohort, and including those with Alzheimer's disease.

References

1. Rutherford, S., Fraza, C., Dinga, R., Kia, S. M., Wolfers, T., Zabihi, M., ... & Marquand, A. F. (2022). Charting brain growth and aging at high spatial precision. *eLife*, *11*, e72904. https://doi.org/10.7554/eLife.72904.
2. Huang, S. Y., Witzel, T., Keil, B., et al. (2021). Connectome 2.0: Developing the next-generation ultra-high gradient strength human MRI scanner for bridging studies of the micro-, meso-and macro-connectome. *NeuroImage*, *243*, 118530. doi: 10.1016/j.neuroimage.2021.118530.
3. Palombo M, Ianus A, Guerreri M, et al. SANDI: A compartment-based model for non-invasive apparent soma and neurite imaging by diffusion MRI. Neuroimage. 2020 Jul 15;215:116835. doi: 10.1016/j.neuroimage.2020.116835.

4. Nasreddine, Z. S., Phillips, N. A., Bédirian, V., Charbonneau, et al. (2005). The Montreal Cognitive Assessment, MoCA: a brief screening tool for mild cognitive impairment. *Journal of the American Geriatrics Society*, *53*(4), 695-699. doi: 10.1111/j.1532-5415.2005.53221.x.
5. Lee, H., Lee, H. H., Ma, Y., et al. (2024). Age-related alterations in human cortical microstructure across the lifespan: Insights from high-gradient diffusion MRI. *Aging Cell*, e14267. doi: 10.1111/acel.14267.

Images/Tables

	Age (years)	Sex
Young N = 25	31±7.5	19 F 17 M
Older N = 11	67±9.6	8 F 3 M
(With MoCA: N = 10/11)	61±10.2	7 F 3 M

Figure 1: Demographics of younger and older participants (with N = 10/11 having cognitive scores).

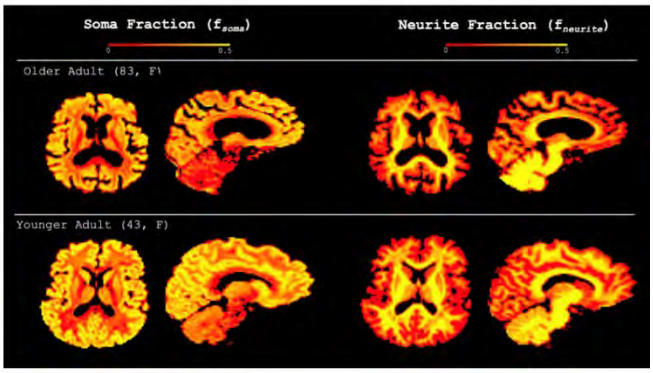

Figure 2: Representative maps of soma fraction and neurite fraction in an 83-year old female (older cohort) and a 43-year old female (younger cohort).

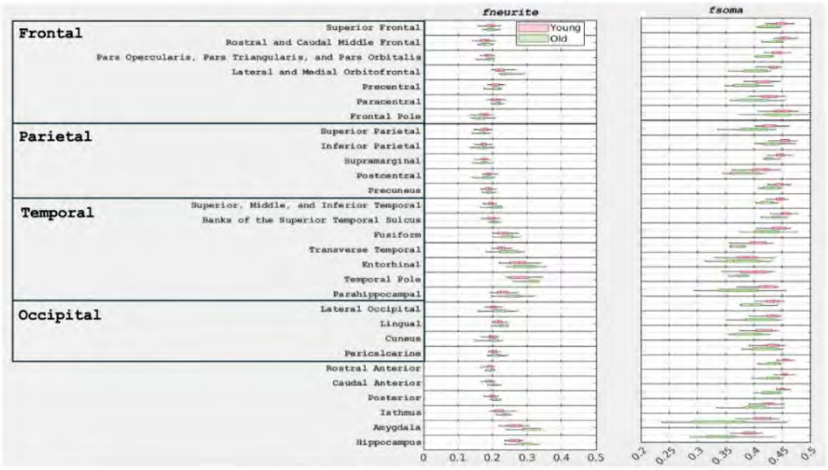

Figure 3: Boxplots of neurite and soma volume fractions between younger and older subjects, within specific ROIs.

Figure 4: Correlation plots of f_{soma} against age within the older cohort (N = 10).

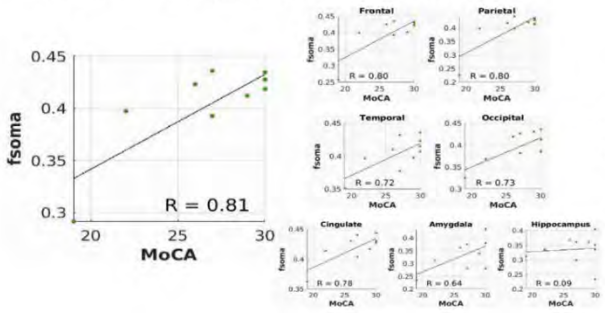

Figure 5: Correlation plots of f_{soma} against MoCA within the older cohort (N = 10).

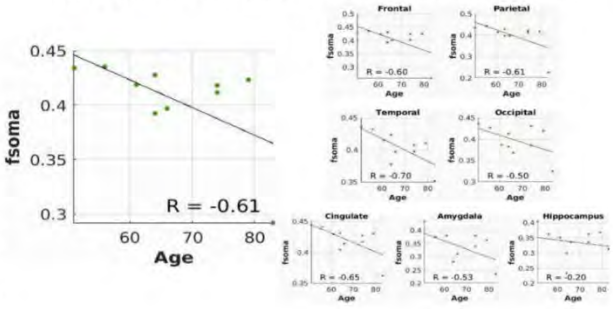

1158

Preoperative Cerebrospinal Fluid Volume as Predictor of Endoscopic Third Ventriculostomy with Choroid Plexus Cauterization (ETV/CPC) Outcomes

Marcia H Yoshikawa MD, Mingzhao Yu PhD, Hayleigh Tran, Henry Feldman PhD, Ariadna S Luviano, Julia Tatz, Jason Sutin PhD, Benjamin C Warf MD, PhD, P. Ellen Grant MD, Pei-Yi Lin PhD
Boston Children's Hospital, Boston, MA, USA

Abstract Category

Pediatrics

Purpose

Endoscopic third ventriculostomy with choroid plexus cauterization (ETV/CPC) prevents shunt dependence in infant hydrocephalus. However, about 30% of patients fail ETV/CPC and, so far, only age is an established predictor of failure. A recent study [1] suggested that the frontal occipital horn ratio (FOHR), a proxy of ventricle size, might also predict ETV/CPC failure. Given the limitations of FOHR in estimating ventricle volume, our aim was to determine if preoperative cerebrospinal fluid volume (CSFV) predicts long-term surgical outcomes after ETV/CPC in infant hydrocephalus.

Materials & Methods

Infants under one year of age who underwent ETV/CPC as the first operation for hydrocephalus between 2008 and 2021 at Boston Children's Hospital were included. Patients with brain MRI within 2 weeks prior to the surgery were included in the data analysis. Clinical and surgical data were retrieved from medical records. Brain parenchymal (BPV) and CSFV were estimated from the intracranial segmentation of preoperative MRI using a machine-learning based model. All segmentations were reviewed and corrected as needed for accuracy. BPV and CSFV z-scores (ZS) were generated from normative growth curves for age and sex from Peterson, et al[2]. Intracranial volume (ICV) was calculated as ICV=BPV+CSFV, while CSFV/ICV ratio is the ratio of CSFV/ICV. ETV/CPC treatment failure was defined as the need for any re-operation or death related to hydrocephalus. Once the ventriculoperitoneal shunt (VPS) is placed following ETV/CPC failure, the patient becomes shunt dependent. Cox regression analysis was used to identify independent predictors of failure and generate cumulative risk curves.

Results

A total of 191 infants (109 males and 82 females) were included, with a median(IQR) follow-up time of 47(66) months and median age at ETV/CPC of 56(150) days. Failure of initial ETV/CPC accounted for 93(48%) patients and among those, 69(36%) became shunt-dependent and 24(12%) were successfully managed with additional ETV. In the univariate analysis, age at ETV/CPC ($p=0.01$), prior CSF diversion ($p<0.0001$), FOHR ($p=0.02$), BPV ($p=0.007$), CSFV ZS ($p=0.04$), and CSFV/ICV ratio ($p=0.004$) were associated with shunt-dependence in the follow-up. When adjusted for age and prior CSF diversion, only CSFV ZS (HR 1.10; $p=0.01$) and CSFV/ICV ratio (HR 6.16; $p=0.01$) were independent predictors for shunt-dependence. Cumulative risk curves demonstrated that for patients 56-day-old at the time of ETV/CPC and with a CSFV ZS 1.89 (percentile 10th in this cohort), the risk of shunt dependence in one year after surgery was about 30%, while for patients of same age but with a CSFV ZS 8.24 (percentile 90th) the risk exceeded 40% (Figure).

Conclusion

Higher CSFV ZS and CSFV/ICV ratio were significantly associated with shunt dependence in infants who underwent first time ETV/CPC. The volumetric assessment was more accurate than FOHR in predicting shunt dependence when adjusted for age at intervention and prior temporary CSF diversion status. These findings suggest that CSFV can be a valuable tool for decision-making and family counseling.

References

[1] Warf BC, Weber DS, Day EL, et al. Endoscopic third ventriculostomy with choroid plexus cauterization: predictors of long-term success and comparison with shunt placement for primary treatment of infant hydrocephalus. *J Neurosurg Pediatr.* 2023 May 12;32(2):201-213. doi: 10.3171/2023.4.PEDS2310.

[2] Peterson MR, Cherukuri V, Paulson JN, et al. Normal childhood brain growth and a universal sex and anthropomorphic relationship to cerebrospinal fluid. *J Neurosurg Pediatr*. 2021 Jul 9;28(4):458-468. doi: 10.3171/2021.2.PEDS201006.

Images/Tables

Figure 1. Cumulative risk curves for patients 56-day-old and 160-day-old at the time of ETV/CPC and different CSFV z-score values. ETV/CPC: endoscopic third ventriculostomy with choroid plexus cauterization, CSFV: cerebrospinal fluid volume. Grey and blue areas indicate the standard error.

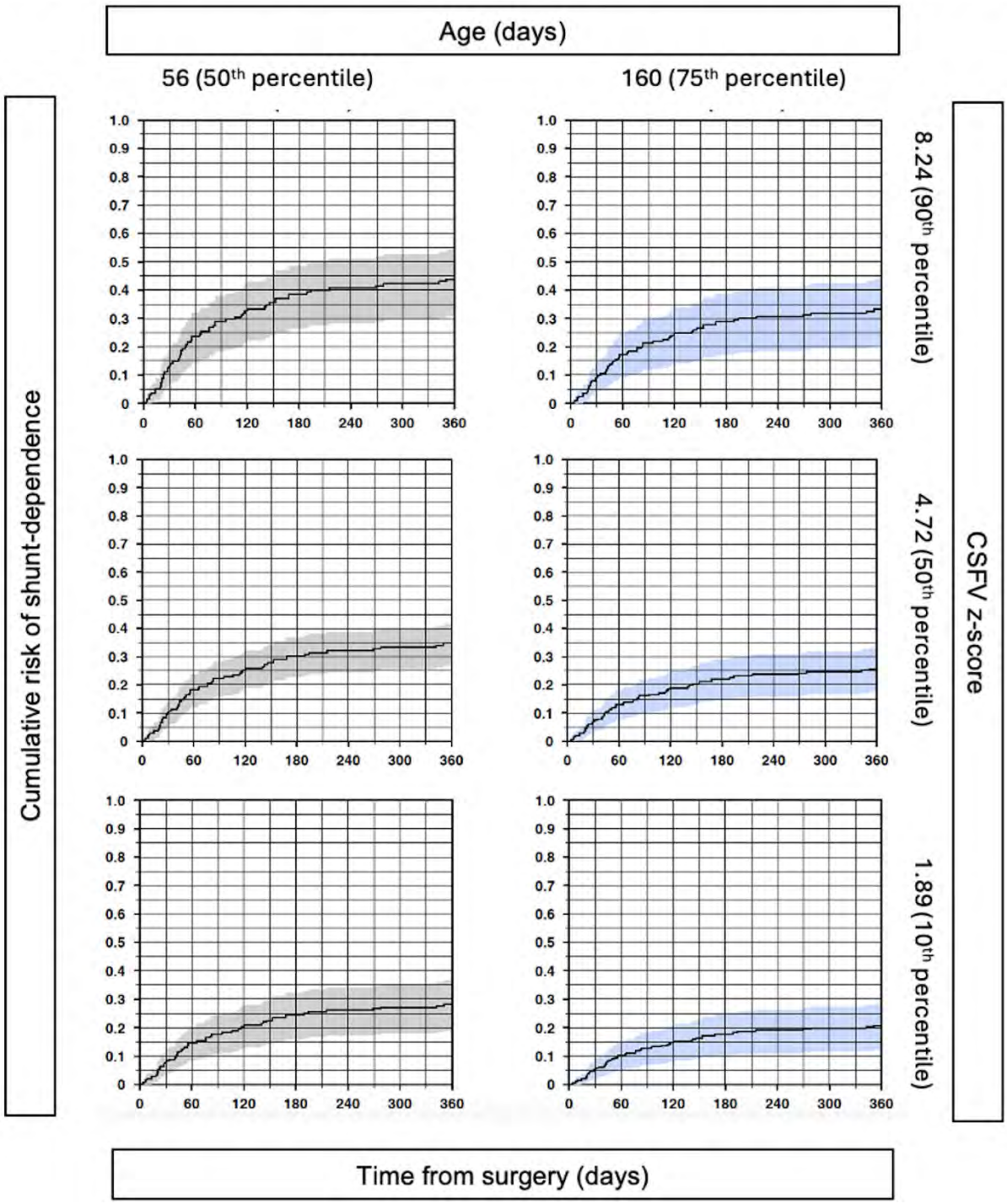

1163

Tumor Probability Map-Derived Peak Separation Index as a Prognostic Marker in Glioblastoma: Insights into Tumor-Edema Demarcation and Survival

Biprojit Nath MS, Samuel A. Bobholz PhD, Michael Flatley, Savannah R. Duenweg PhD, Aleksandra Winiarz BS, Benjamin Chao, Allison K. Lowman, Fitzgerald Kyereme, Jennifer Connelly, Kelly Mrachek MD, Elaine Tanhehco MD, Max Krucoff MD, Peter S. LaViolette PhD
Medical College of Wisconsin, Milwaukee, WI, USA

Abstract Category

Adult Brain

Purpose

Glioblastoma (GBM) is a highly aggressive brain tumor with poor survival and is significantly affected by various microenvironmental factors within the tumor core and the surrounding FLAIR-defined region due to its infiltrative nature [1]. This study investigates the prognostic value of the Peak Separation Index (PSI), a histogram-based feature derived from tumor probability maps (TPM), which quantifies the degree of separation between tumor and edema intensity peaks. We hypothesize that high PSI, reflecting a greater separation between edema and tumor peaks, is associated with improved survival in GBM and correlates with distinct microenvironmental features, such as cellularity, ECF, and cytoplasmic content.

Materials & Methods

We included all glioblastoma IDH-wildtype patients with gross total resection (GTR) from the UCSF-PDGM dataset (n=218) [3]. Using a pre-trained radio-pathomic model [2], we generated TPMs and spatial maps for cellular density (Cell), cytoplasmic content (Cyt), and extracellular fluid (ECF) from T1, T1C, FLAIR, and ADC MRI sequences. A Gaussian Mixture Model (GMM) was fitted to TPM intensities (within the FLAIR hyperintensity mask), with the assumption that the first peak is edema and the second is tumor. From this bimodal distribution, we derived the Peak Separation Index (PSI) as the standardized mean difference between these peaks, calculated for all patients (Figure 1). Mean Cell, ECF, and Cyt were extracted from all the spatial radio-pathomic maps (within the FLAIR defined mask). To determine an optimal PSI threshold, we used the PENN dataset [4], applying an iterative process to identify a threshold of 2.4 based on the greatest survival difference. This threshold was then applied to the UCSF-PDGM dataset to classify patients into high-PSI (PSI > 2.4) and low-PSI (PSI ≤ 2.4) groups, allowing for survival comparison using Kaplan-Meier analysis.

Results

Our analysis revealed that high-PSI patients (PSI > 2.4) had longer median survival (868 days) compared to low-PSI patients (599 days). High-PSI tumors showed significantly higher cell density (18.43 ± 0.94 vs15.25 ± 2.21, t= 9.34, $p<0.001$) and ECF (0.23 ± 0.04 vs. 0.15 ± 0.04, t=11.52, $p < 0.01$), along with lower cytoplasmic content (0.74 ± 0.04 vs 0.82 ± 0.04, t= -12.48, $p<0.001$) in the FLAIR region compared to low-PSI tumors.

Conclusion

This study highlights PSI, derived from tumor probability maps, as a valuable prognostic marker in GBM. It suggests that a higher PSI, indicating a more distinct separation between tumor and edema peaks, is associated with increased overall survival. Although high-PSI tumors exhibit elevated cell density and ECF, they show a more organized structure within the FLAIR region, where high TPM values allow clearer separation between tumor and edema. This organized profile could enhance the efficacy of targeted treatments, potentially contributing to the observed survival benefit in high-PSI patients. In contrast, low PSI indicates a diffusely infiltrative tumor architecture associated with poorer outcomes. Further studies are needed to validate PSI in diverse populations and assess its role in monitoring treatment response.

References

1. Erices JI, Bizama C, Niechi I, Uribe D, Rosales A, Fabres K, Navarro-Martínez G, Torres Á, San Martín R, Roa JC, Quezada-Monrás C. Glioblastoma Microenvironment and Invasiveness: New Insights and Therapeutic Targets. Int J Mol Sci. 2023 Apr 11;24(8):7047. doi: 10.3390/ijms24087047. PMID: 37108208; PMCID: PMC10139189.
2. Bobholz SA, Lowman AK, Connelly JM, Duenweg SR, Winiarz A, Nath B, Kyereme F, Brehler M, Bukowy J, Coss D, Lupo JM, Phillips JJ, Ellingson BM, Krucoff MO, Mueller WM, Banerjee A, LaViolette PS. Noninvasive Autopsy-Validated Tumor Probability Maps Identify Glioma Invasion Beyond Contrast Enhancement. Neurosurgery. 2024 Sep 1;95(3):537-547. doi: 10.1227/neu.0000000000002898. Epub 2024 Mar 19. PMID: 38501824; PMCID: PMC11302944.

3. Calabrese E, Villanueva-Meyer JE, Rudie JD, Rauschecker AM, Baid U, Bakas S, Cha S, Mongan JT, Hess CP. The University of California San Francisco Preoperative Diffuse Glioma MRI Dataset. Radiol Artif Intell. 2022 Oct 5;4(6):e220058. doi: 10.1148/ryai.220058. PMID: 36523646; PMCID: PMC9748624.
4. Bakas S, Sako C, Akbari H, Bilello M, Sotiras A, Shukla G, Rudie JD, Santamaría NF, Kazerooni AF, Pati S, Rathore S, Mamourian E, Ha SM, Parker W, Doshi J, Baid U, Bergman M, Binder ZA, Verma R, Lustig RA, Desai AS, Bagley SJ, Mourelatos Z, Morrissette J, Watt CD, Brem S, Wolf RL, Melhem ER, Nasrallah MP, Mohan S, O'Rourke DM, Davatzikos C. The University of Pennsylvania glioblastoma (UPenn-GBM) cohort: advanced MRI, clinical, genomics, & radiomics. Sci Data. 2022 Jul 29;9(1):453. doi: 10.1038/s41597-022-01560-7. PMID: 35906241; PMCID: PMC9338035.

Images/Tables

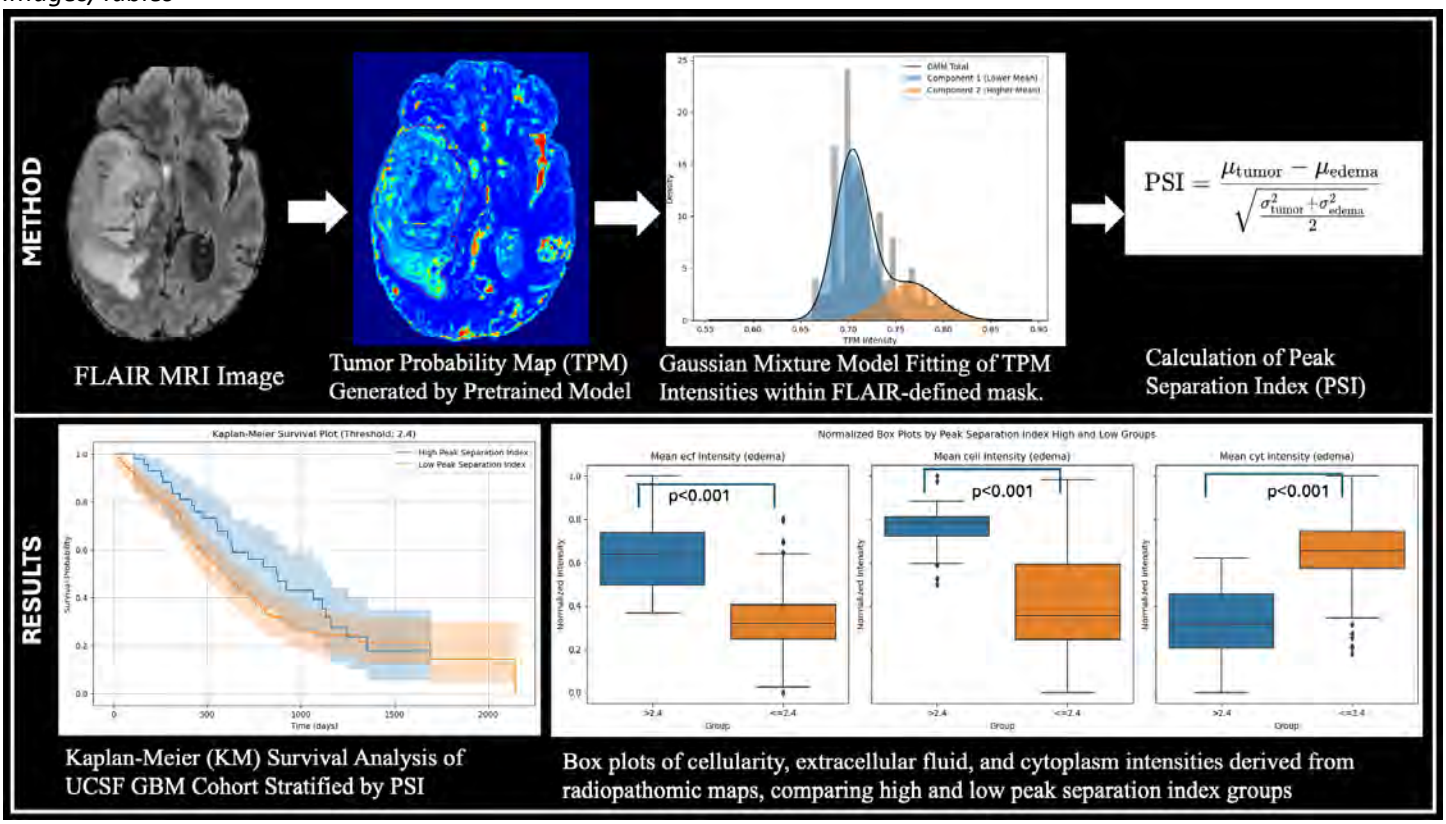

1165

SOX2 expression for locating tumor invasion in both standard of care treated and untreated glioblastoma patients

Aleksandra Winiarz BS, Samuel A Bobholz PhD, Allison K Lowman BS, Savannah R Duenweg PhD, Biprojit Nath MS, Benjamin Chao BS, Fitzgerald Kyereme BS, Jennifer Connelly MD, Kelly Mrachek MD, Max Krucoff MD, Peter S LaViolette PhD
Medical College of Wisconsin, Milwaukee, WI, USA

Abstract Category

Adult Brain

Purpose

Glioblastoma (GBM) patients have a poor overall survival (OS) of 15 months following standard of care [1] and a 5-year survival rate of 6.6% [2]. Tumor progression is monitored with MRI; however, it fails to visualize the full extent of tumor. Previous studies have found active tumor cells located as far as 4 cm away from contrast enhancement (CE), making detection of true tumor, and consequently, accurate localized treatment, difficult [3]. Sex determining region Y-box 2 (SOX2) is a transcription factor that regulates pluripotency and is expressed in glioma [4]. We investigated the extent of SOX2 expressing cells in autopsy brain samples from GBM patients who underwent standard treatment compared to those who did not.

Materials & Methods

This study included six GBM patients: 3 with no treatment and 3 age-matched controls who received standard of care, surgery, radiation, and temozolomide treatment. At autopsy, custom 3d-printed brain slicing jigs were used to align brain slices to the patient's final MRI scan prior to death. Large format tissue samples were taken from areas suspicious for infiltrative tumor, paraffin embedded, stained with hematoxylin and eosin (H&E) and SOX2 immuno-histochemistry (IHC), and digitized at 40x. The T1C and FLAIR images from the patient's final timepoint prior to death were manually annotated for regions of CE and FLAIR hyperintensity (FH). SOX2 slides were aligned to the patient's last FLAIR image using non-linear warping with custom in-house MATLAB software.

Results

Figure 1 shows representative samples from each patient. SOX2 expressing cells were found in normal (i.e. no CE or FH) regions in every patient, both treated and untreated. Overall, SOX2 positive cells were found further away from CE and FH in the treated group.

Conclusion

SOX2 expressing cells were found well outside CE and FH in all cases analyzed for this study. The distance from CE and FH varied between patients, but those that underwent standard of care tended to have SOX2 positive cells further from CE and FH suggesting infiltrative evolution. Additionally, because treated patients had longer OS, SOX2 cells could have spread farther by having more time to invade tissue, in addition to treatment affecting tumor growth dynamics. Future research should include tissue samples throughout the whole brain in addition to adding more patients that undergo a wide range of treatment regimens to further explore the extent of SOX2 expressing cells in both treated and untreated GBM.

References

[1] Stupp R, Mason WP, van den Bent MJ, et al. Radiotherapy plus concomitant and adjuvant temozolomide for glioblastoma. N Engl J Med. 2005;352(10):987-96. Epub 2005/03/11. doi: 352/10/987 [pii]10.1056/NEJMoa043330. PubMed PMID: 15758009.

[2] Ostrom QT, Cioffi G, Waite K, Kruchko C, et al. CBTRUS Statistical Report: Primary Brain and Other Central Nervous System Tumors Diagnosed in the United States in 2014-2018. Neuro Oncol. 2021;23(12 Suppl 2):iii1-iii105. Epub 2021/10/06. doi: 10.1093/neuonc/noab200. PubMed PMID: 34608945; PMCID: PMC8491279.

[3] Silbergeld DL, Chicoine MR. Isolation and characterization of human malignant glioma cells from histologically normal brain. J Neurosurg. 1997;86(3):525-31. Epub 1997/03/01. doi: 10.3171/jns.1997.86.3.0525. PubMed PMID: 9046311.

[4] Ben-Porath I, Thomson MW, Carey VJ, et al. An embryonic stem cell-like gene expression signature in poorly differentiated aggressive human tumors. Nat Genet. 2008 May;40(5):499-507. doi: 10.1038/ng.127. PMID: 18443585; PMCID: PMC2912221.

Images/Tables

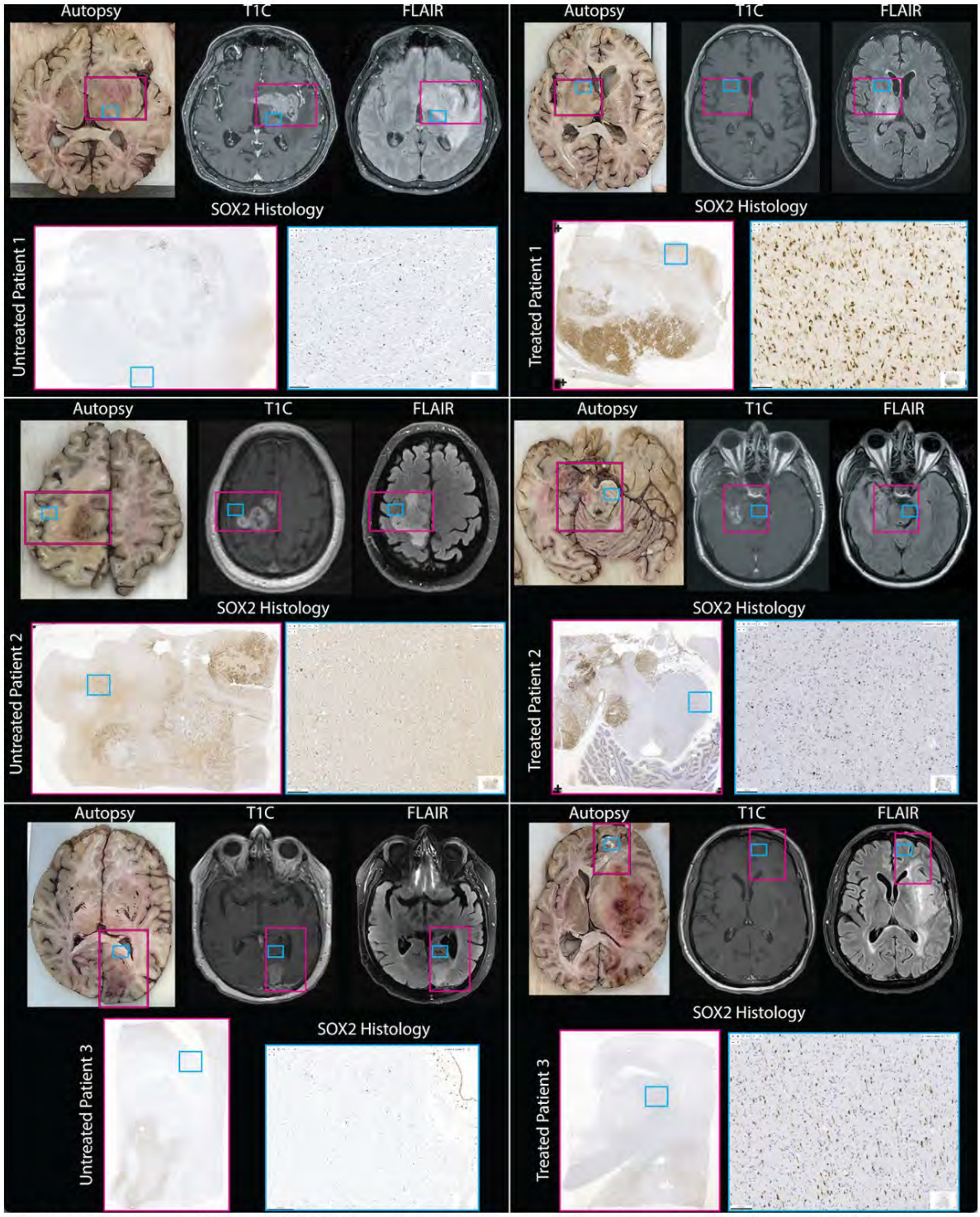

Figure 1: Autopsy tissue, T1C and FLAIR from last imaging timepoint, and corresponding SOX2 histology samples for untreated patients (left) and treated age-matched controls (right). Pink rectangles represent where the histology samples were taken from. Blue rectangles represent zoomed in areas of histology. Untreated patient 1 was a 76-year-old male with an OS of 25 days who opted out of treatment. Untreated patient 2 was a 48-year-old male with an OS of 148 days and untreated patient 3 was a 62-year-old male with an OS of 201 days who both opted out treatment after resection. Treated control 1 was a 75-year-old male with an OS of 399 days who underwent biopsy, chemotherapy, and radiation; treated control 2 was a 48-year-old male with an OS of 380 days who underwent 2 resections, chemotherapy, radiation, and TTFields; treated control 3 was a 60-year-old male with an OS of 430 days who underwent chemotherapy, radiation, TTFields, and bevacizumab.

1170

Recent Trends in Compensation and Clinical Productivity: Academic vs Non-academic Neuroradiologists

Dheeman Futela MBBS[1], Sam Payabvash MD[1], Dheeraj Gandhi MD FACR[2], Ajay Malhotra MD MMM[1]
[1]Department of Radioilogy, Yale School of Medicine, New Haven, CT, USA. [2]Department of Radiology, University of Maryland School of Medicine, Baltimore, MD, USA

Abstract Category

Socioeconomics & Health Policy

Purpose

Recent trends in compensation and clinical productivity among neuroradiologists are not well studied. In an environment of increasing radiology practice consolidation with continued assimilation of hospitals and healthcare systems, the divide between academics and non-academic practice has blurred. Despite increased imaging volumes, collections and unit prices may not be keeping up with increased workloads. When adjusted for inflation, reimbursement to radiologists per Medicare beneficiary declined, while wRVUs per beneficiary performed by radiologists increased. Further, reimbursement cuts may disproportionately affect neuroimaging, which relies more on MR studies and advanced imaging technology. This study aimed to assess recent trends in financial compensation and clinical productivity between academic and non-academic settings among neuroradiologists.

Materials & Methods

We studied de-identified data from the Medical Group Management Association (MGMA) for providers in the "Radiology: Neurological" specialty in academic and non-academic practices from 2014 to 2023. Median (and interquartile range) total compensation and wRVUs were compared with that of diagnostic radiologists overall. Trends were analyzed with simple linear regression and compounded annual growth rates.

Results

The MGMA Survey data from 2014 to 2023 included responses from 1784 neuroradiologists (1027 academic and 757 non-academic) and 24,623 diagnostic radiologists (8586 academic and 16,037 non-academic).

In 2023, the median compensation for academic neuroradiologists ($488,020 [IQR 415,478- 530,600]) was less than that for non-academic neuroradiologists ($611,621 [IQR 521,061-742,901]) by 22.5%. Median compensation for neuroradiologists was greater than that for diagnostic radiologists overall, by 6.6% in academics and 5.2% in non-academics. Median wRVUs for academic neuroradiologists (12,166 [IQR 9039- 15,234]) was marginally greater (by 3.5%) than that for non-academic neuroradiologists (11,741 [IQR 8320-14,186]). Median wRVUs performed by neuroradiologists was greater than that for diagnostic radiology overall by 30% in academics and 10.5% in non-academics.

Between 2014-2023, median compensation for academic neuroradiologists increased significantly and at a faster rate (4.1% annually) than non-academic (1.8% annually), which was similar to the trend for diagnostic radiologists overall. Throughout the period, median wRVUs for academic neuroradiologists remained greater (by 30-40%) than diagnostic radiology overall.

Conclusion

Non-academic neuroradiologists have a greater salary with similar productivity compared to their academic counterparts. Over the last decade, neuroradiologist compensation mirrored the increasing trend in diagnostic radiology overall, while median productivity for neuroradiologists remained substantially greater than in diagnostic radiology.

References

1. Rosenkrantz AB, Fleishon HB, Silva E, 3rd, Bender CE, Duszak R, Jr. Radiology Practice Consolidation: Fewer but Bigger Groups Over Time. J Am Coll Radiol. 2020;17(3):340-348.
2. Christensen EW, Nicola GN, Rula EY, Nicola LP, Hemingway J, Hirsch JA. Budget Neutrality and Medicare Physician Fee Schedule Reimbursement Trends for Radiologists, 2005 to 2021. J Am Coll Radiol. 2023;20(10):947-953.
3. Malhotra A, Futela D, Joshi R, et al. Academic Radiology Physician Financial Compensation in the United States: Trends and Distribution. *Radiology*. 2024;313(1):e241057.
4. Medical Group Management Association (MGMA). https://www.mgma.com/mgmadata. Accessed August 2, 2024.

Images/Tables

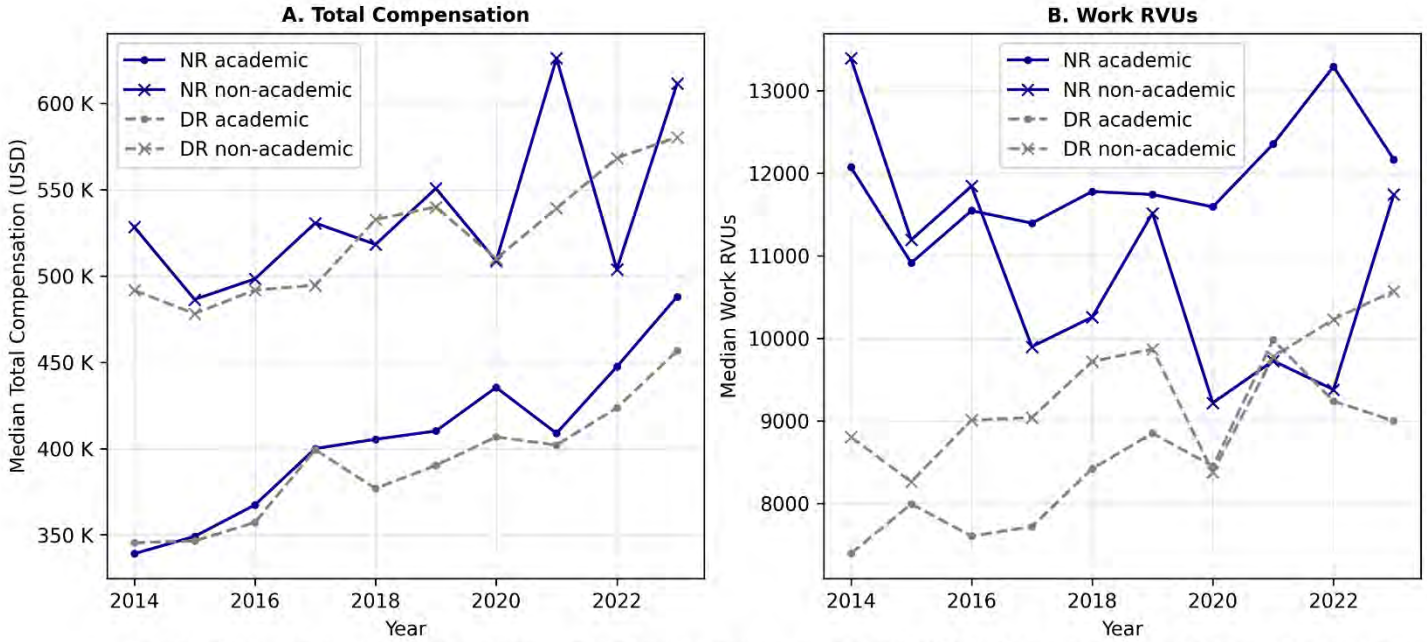

Figure. Trends in compensation and productivity for Neuroradiologists (NR) vs Diagnostic Radiologsts (DR) overall.

1177

Impact of AI-Based Detection and Tracking System on Follow-Up Adherence for Unruptured Intracranial Aneurysms Detected by CT Angiography

Hemdeep Kaur MS[1], Ichiro Yuki MD[1], Jennifer Soun MD[1], Tracy Nguyen BS[1], Rebecca Back BS[1], Beatrice Malvar BS[1], Jordan Xu MD[1], Kiarash Golshani MD[2], Frank P.K. Hsu MD PhD[1], Chloe Jin BA[1], Shuichi Suzuki MD PhD[1]
[1]UC Irvine Medical Center, Orange, CA, USA. [2]Orange, CA, USA

Abstract Category

AI/Informatics

Purpose

The increased use of CT angiography (CTA) for screening conditions such as stroke, TIA, headache, and head and neck trauma has led to more frequent incidental detection of unruptured intracranial aneurysms (UIAs) in clinical practice. Patients diagnosed with UIAs are generally advised to follow up with specialists, such as neuroradiologists, neurologists, or neurosurgeons; however, adherence to follow-up remains a challenge, with many patients lost to follow-up. Recently, AI-based software has been introduced as an adjunctive tool for detecting UIAs, incorporating tracking functions to support follow-up care. However, its effect on improving patient compliance is not yet fully understood. We conducted a retrospective analysis of patients with UIAs identified by this AI software to assess its role in enhancing follow-up adherence.

Materials & Methods

Between July 1, 2023, and May 1, 2024, patients who underwent CTA of the head at our institution were included in this study. Using the AI-based UIA detection software Viz Aneurysm®, we identified patients suspected of having UIAs during this period. After a thorough review of each patient's medical records, we selected those with a confirmed UIA diagnosis verified by neuroradiologists. For patients referred to specialists, we tracked adherence to follow-up, assessing whether they consulted specialists as instructed upon discharge. For those who missed follow-up appointments, we investigated reasons for non-adherence through direct contact. Finally, we compared follow-up compliance rates before and after implementing Viz Aneurysm®'s tracking system.

Results

A total of 4,793 CT angiograms were performed at our institution, among which 192 patients (4%) had at least one potential aneurysm detected by Viz Aneurysm®. The final radiology report confirmed aneurysms in 130 patients (68%), with 107 being newly diagnosed. Nine patients (7%) had ruptured aneurysms, with two cases (2%) resulting in mortality during hospitalization. Among patients with UIAs who opted for conservative management, 75 (58%) were advised to follow the standard post-diagnosis referral process for specialist follow-up. Despite these instructions, 48 patients (37%)

were lost to follow-up in the conventional referral system but were identified by Viz Aneurysm®. The main reasons for loss to follow-up were: 1) lack of appropriate referrals for 38 patients (29%), 2) insurance issues for 5 patients (4%), and 3) personal cancellation by 5 patients (4%). Patients without proper follow-up were contacted by the clinic and rescheduled, increasing the follow-up compliance rate from 58% to 91%.

Conclusion

The use of AI-based UIA detection software may improve follow-up adherence among patients with UIAs identified by CT angiography. This tool may help identify and track patients lost in the conventional referral process, addressing gaps due to missed referrals and potentially enhancing follow-up care for patients with UIAs.

References

1. Messina FC, McDaniel MA, Trammel AC, Ervin DR, Kozak MA, Weaver CS (2013) Improving specialty care follow-up after an ED visit using a unique referral system. Am J Emerg Med 31(10):1495-1500.
2. Steiner T, Juvela S, Unterberg A, Jung C, Forsting M, Rinkel G, European Stroke O (2013) European Stroke Organization guidelines for the management of intracranial aneurysms and subarachnoid haemorrhage. Cerebrovasc Dis 35(2):93-112.
3. Silva MA, Chen S, Starke RM (2022) Unruptured cerebral aneurysm risk stratification: Background, current research, and future directions in aneurysm assessment. Surg Neurol Int 13:182.
4. Khorasanizadeh M, Pettersson SD, Maglinger B, Garcia A, Wang SJ, Ogilvy CS (2023) Trends in the size of treated unruptured intracranial aneurysms over 35 years. J Neurosurg doi:10.3171/2023.2.JNS222919:1-11.

1183

Deep Learning in Vertebral Fracture Detection: A Systematic Review and Meta-Analysis Comparing Whole-Spine and Vertebra-Specific Imaging Approaches

Mohammad-Reza Hosseini-Siyanaki MD, Babak Ahmadi BS, Hakki Serdar Sagdic MD, Abheek Raviprasad MD, Antika Roy BS, Aysha Dogan BS, Sefat Munjerin MS, Evelyn Anthony MD, Keith Peters MD

University of Florida, Gainesville, FL, USA

Abstract Category

Spine

Purpose

To review current literature and assess the effectiveness of deep learning algorithms in detecting vertebral fractures, comparing their performance on whole-spine versus vertebra-specific images relative to diagnostic accuracy, with potential implications for optimizing clinical practice in vertebral fracture detection.

Materials & Methods

A systematic search of PubMed, Scopus, Embase, Web of Science, and Google Scholar was conducted to identify studies employing deep learning for vertebral fracture detection. A total of 39 studies met the inclusion criteria, with contingency tables extracted from 11 studies that reported relevant diagnostic metrics. Random-effects models were used to calculate pooled sensitivity, specificity, predictive values, summary ROC curves, and area under the curve (AUC), following the “Standards for Reporting Diagnostic Accuracy Studies” (STARD) guidelines. Heterogeneity among studies was assessed using Cochrane’s Q and I^2 tests. Studies were grouped by imaging type (whole-spine versus vertebra-specific), enabling comparison of deep learning performance across these categories.

Results

The systematic review included 39 studies, with diagnostic metrics extracted from 11 studies grouped by imaging type into whole-spine images and vertebra-specific images groups. For whole-spine images, the pooled sensitivity was *0.78 (95% CI: 0.70-0.86, I^2=99.20%)*, and the pooled specificity was *0.88 (95% CI: 0.83-0.94, I^2=99.81%)*. The summary ROC analysis for this group yielded an AUC of *0.92 (95% CI: 0.89-0.94)*. In the vertebra-specific images group, the pooled sensitivity was also 0.78 (95% CI: 0.72-0.85, *I^2=91.00%*), and the pooled specificity was *0.90 (95% CI: 0.85-0.94, I^2=98.79%).* The summary ROC AUC for vertebra-specific images was *0.93 (95% CI: 0.90-0.95).* Overall, both whole-spine and vertebra-specific groups showed high sensitivity and specificity, with no significant differences in performance between the two categories based on meta-regression and subgroup analyses.

Conclusion

In conclusion, this meta-analysis shows that deep learning models achieve high sensitivity and specificity in detecting vertebral fractures using both whole-spine and vertebra-specific images. Despite heterogeneity among studies, the

strong diagnostic accuracy across both approaches supports the reliability of deep learning for vertebral fracture detection. Future research should further refine these algorithms for clinical use.

References

Paik S, Park J, Hong JY, et al. Deep learning application of vertebral compression fracture detection using mask R-CNN. *Sci Rep* 2024;14:16308. DOI: https://doi.org/10.1038/s41598-024-16308

Images/Tables

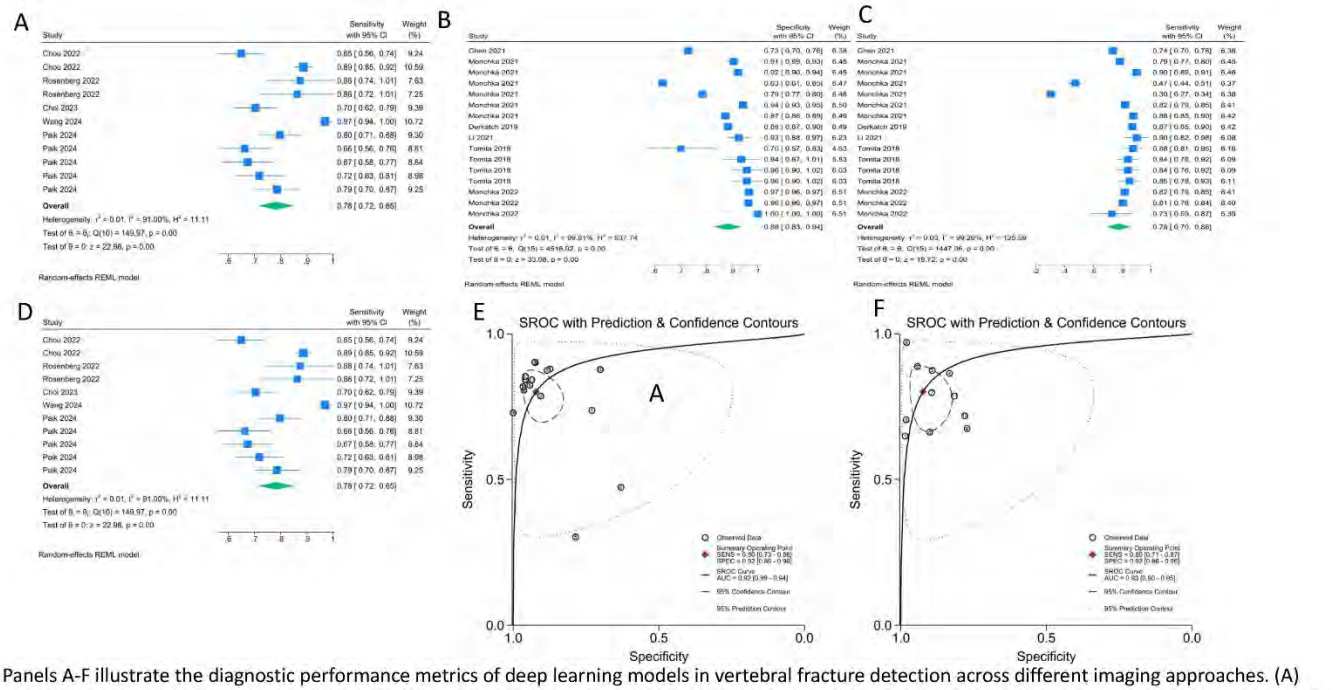

Panels A-F illustrate the diagnostic performance metrics of deep learning models in vertebral fracture detection across different imaging approaches. (A) Pooled sensitivity for vertebra-specific images, (B) pooled specificity for vertebra-specific images, (C) pooled sensitivity for whole-spine images, (D) pooled specificity for whole-spine images, (E) summary ROC curve for whole-spine images, and (F) summary ROC curve for vertebra-specific images. These plots highlight the high sensitivity and specificity achieved in both imaging modalities, supporting the utility of deep learning models in accurate vertebral fracture detection.

1189

Type 2 Diabetes (T2D) Related Abnormal Brain Area Prediction Performance of Quantitative Susceptibility Mapping (QSM) Magnetic Resonance Imaging (MRI) in the Boston Puerto Rican Healthy Study (BPRHS)

Huiyu Huang[1], Lea Bergeot[1], Fahad Salman[2], Nazmi Kurt[1], Serkan Akbas[1], Ferdinand Schweser[2], Salil Soman[1]

[1]Beth Israel Deaconess Medical Center and Harvard Medical School, Boston, MA, USA. [2]University at Buffalo, Buffalo, NY, USA

Abstract Category

Functional/Advanced Imaging

Purpose

Prior T2D studies revealed that occipital, temporal, frontal, limbic, parietal lobes, basal ganglia, ventricular system, and cerebellum were affected using non-QSM imaging techniques such as magnetoencephalography[1] and functional MRI[2]. This study aims to investigate the capabilities of multi-echo complex Total Field Inversion (mcTFI)[3] QSM in finding those abnormal regions.

Materials & Methods

A sample of 246 adults from the BPRHS was studied on T2D variables (HbA1c, blood glucose, medication, insulin) at baseline, approximately 2, 7, and 14 years. MRI scans (multi-echo gradient-recalled echo (mGRE) and T1-weighted) were acquired around year 14. mcTFI QSM images, derived from mGRE phase data, were segmented using the Joint Fusion Tool4 with T1-weighted and mGRE magnitude images to compute mean susceptibility values across various brain regions. Significant abnormalities ($p < 0.05$) were established using the Mann–Whitney U test and Bonferroni correction on the mean QSM values for DM groups categorized by DM variables. Then, linear and logistic regression was used to examine relationships of abnormal areas after controlling age.

Results

All areas differed significantly in the comparisons of DM (DM+) and non-DM patients. Starting from baseline, DM+ participants with HbA1c levels above 7 (A1c+) and without taking any DM medicine (Med-) exhibited higher susceptibility in the lateral occipital cortex until year ~2, likely due to iron accumulation. Med- patients with glucose levels above 126 (GLUC+) at year ~2 showed lower susceptibility in the fusiform, inferior temporal, and lateral orbitofrontal cortex due to myelin aggregation and higher susceptibility in the insula and transverse temporal gyrus. A1c+ and GLUC+ were associated with lower susceptibility in the anterior cingulate gyrus at year 7. Elder GLUC+ patients were affected in the fusiform and inferior temporal cortex, insula at year 2, and anterior cingulate gyrus at year 7. The above areas changed due to high blood sugar values and the rest areas are likely to be related to low blood sugar. DM+ patients with normal blood sugar (glucose levels and HbA1c under 126 and 7 and taking anti-diabetes first displayed higher susceptibility values in basal ganglia at year 2, and the insula, and lateral occipital cortex at year 14. Insulin above 20.7 (Insulin+) was linked to higher susceptibility values in the insula, parietal lobe, and an adverse susceptibility pattern in the ventricular system at baseline, then lower susceptibility values in the cerebellum while the insula remained to be influenced at year 2. Elder Insulin+ patients were affected in the ventricular system, insula, and cerebellum at baseline and year 2. Except for cerebellum and insula affected from previous years, Insulin+ at year 7 was related to higher susceptibility values in the medial orbitofrontal, supramarginal, and transverse temporal gyrus and lower susceptibility values in the posterior cingulate cortex.

Conclusion

Our work demonstrates patterns in susceptibility value differences in brain regions tied to high and low blood sugar over a ~14-year period before imaging, which may indicate trends in brain injury across time in DM. The findings suggest medical staff needs to monitor DM conditions timely and with multiple diagnoses and treatment methods.

References

1. Embury CM, Lord GH, Drincic AT, et al. Glycemic control level alters working memory neural dynamics in adults with type 2 diabetes. Cereb Cortex 2023;33:8333-8341

2. Guo X, Wang S, Chen YC, et al. Aberrant Brain Functional Connectivity Strength and Effective Connectivity in Patients with Type 2 Diabetes Mellitus. J Diabetes Res 2021;2021:5171618

3. Wen Y, Spincemaille P, Nguyen T, et al. Multiecho complex total field inversion method (mcTFI) for improved signal modeling in quantitative susceptibility mapping. Magn Reson Med 2021;86:2165-2178

4. Salman F TK, Adegbemigun A, et al. Bi-parametric Joint Label Fusion A Comprehensive Segmentation Tool for Deep Gray Matter in QSM. EMTP QMR 2024

1197

Visualizing White Matter Fiber Pathways in Non-enhancing Tumor Using Enhanced Modeling of Clinically Feasible Diffusion MRI

Drew Parker BS, Ehsan Golkar PhD, Ragini Verma PhD

University of Pennsylvania, Philadelphia, PA, USA

Abstract Category

Functional/Advanced Imaging

Purpose

Surgery is the current mainstay treatment for high grade gliomas (HGGs), which has primarily targeted the “visible” contrast-enhancing tumor (CET). However, recent research has shown that it is the “invisible” non-enhancing tumor (NET) which leads to progression or recurrence in HGGs by infiltrating the surrounding white matter (WM) tracts. This has led to the adoption of a supratotal resection (SpTR) approach [1], which includes resection of the ‘invisible’ (microscopic) cancer beyond the visible contrast enhanced margins, leading to longer progression free and overall survival. diffusion MRI (dMRI) based tractography has ushered in a new era in surgical planning, enabling the visualization of WM fibers and their relationship with the CE tumor margin, and has become a vital part in planning a safe brain tumor surgery [2]. However, infiltrative edema obscures the underlying WM pathways in NET in traditional modeling of dMRI. The goal of this work is to present an advanced modeling of clinically feasible dMRI data, that will provide an enhanced visualization in the NET compared to existing clinically feasible models.

Materials & Methods

We will use, from both patients and controls. We propose fitting a multi-compartment model, COMPARI, to the dMRI data, to characterize the NET as consisting of compartment that represents the edema, a second compartment that models the infiltrative edema (consisting largely of cancer cells intermixed with edema), and a compartment that captures the direction of the underlying white matter (WM) pathways. The model is expected to separate the cancerous and edematous components, enabling the visualization of complex white matter. This modeling will be fitted to clinically feasible multishell dMRI data (consisting of two shells: one low b value (b = 1000 s/mm^2) with 30 gradient directions, and one high b value (b = 2000 s/mm^2) with 64 gradient directions) from patients and controls. This model will be compared to various other models that are available in the literature, like SSST (single shell single tissue) and MSMT (multi shell multi tissue), on the basis of how well these models when combined with tractography, were able to visualize tracts in the NET. Fig. 1 provides the framework we adopted for the comparison across multiple combinations of models, acquisitions and tractography algorithms.

Results

Comprehensive comparisons showed that our model which had dedicated compartments for edema and infiltration performed better than other popular models. Fig. 2 and Fig. 3 show that the COMPARI model is able to provide a better visualization of the tracts in the peritumoral region, compared to a widely accepted multishell model, as well as a single shell model.

Conclusion

We demonstrate that an advanced modeling encompassing edema, infiltrating and tissue anisotropy, can provide a better visualization of the NET. Also, we have demonstrated that this is possible in a clinically feasible multishell acquisition (with two shells), that can be acquired in 5 minutes with multiband acceleration.

References

1. Giammalva, G.R., et al., *Brain Mapping-Aided SupraTotal Resection (SpTR) of Brain Tumors: The Role of Brain Connectivity.* Frontiers in oncology, 2021. **11**: p. 645854-645854.

2. Henderson Jr, F., et al., *Tractography and the connective in neurosurgical treatment of gliomas: the premise, the progress. and the potential.* Neurosurgical Focus, 2019. **48**(2)

Images/Tables

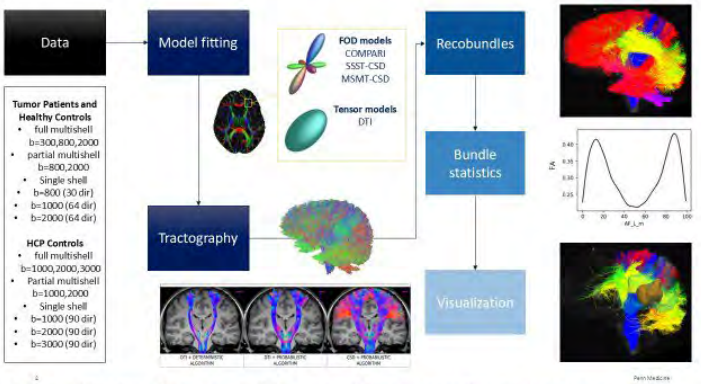

Fig. 1: Pipeline for model fitting and tractography, and comparative evaluationvc

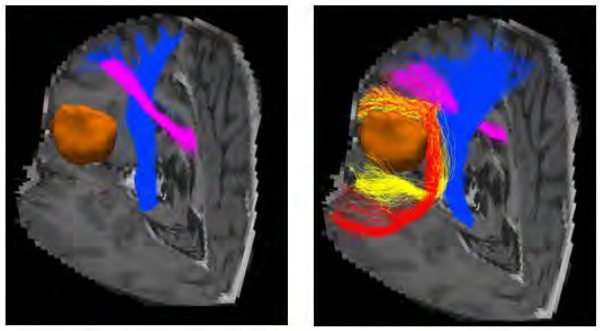

Fig. 2: Comparison of tractography using the MSMT model (left), and the COMPARI model (right), with the tumor being depicted in orange.

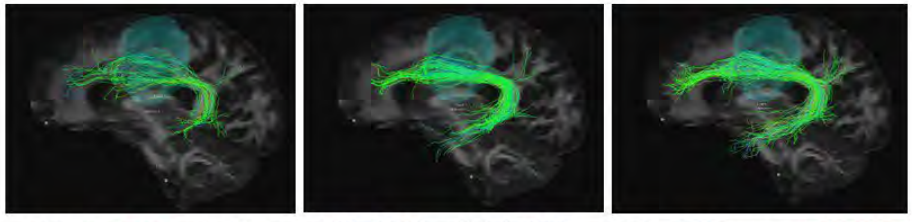

B1000 64 dir SSST probabilistic B800, B2000 multishell MSMT B800, B2000 multishell COMPARI

Fig. 3: Comparison of tractography using the SSST model (left), MSMT model (center), and the COMPARI model (right), with the edema being depicted in teal

1200

Comparison of Cadaveric MRI of the DRG with Dissection: Anatomic-Radiology Correlation

Mridhula Muthukumar
University Hospitals, Cleveland, OH, USA

Abstract Category

Functional/Advanced Imaging

Purpose

All spinal nerves, except C1, carry axons of sensory neurons with cell bodies in the dorsal root ganglion (DRG). The DRG carries somatosensory information from the PNS and CNS and is a significant neural structure in understanding pain mechanisms and treatment. The DRG is frequently evaluated by neuroradiologists, but its anatomic organization is not widely understood and current research focuses primarily on lumbar DRGs. Therefore, the purpose of this research is to characterize the anatomy of the human DRG at the cervical, thoracic and lumbar spinal levels on 3-Tesla (3T) MR imaging (MRI) and perform anatomic correlation after dissection.

Materials & Methods

We scanned 3 embalmed cadavers on a 3T MRI scanner at an isotropic resolution of 0.5-0.6 mm using CISS and VIBE sequences, prior to dissection. We conducted laminectomies on the MRI scanned cadavers at the C4, T4 and L4 levels and a total of 18 DRGs were studied. An anatomic-radiologic correlation using morphometric analysis (DRG cross sectional dimensions and distance from nerve root to spinal cord and spinal nerve) was performed to validate the findings on MRI.

Results

High resolution CISS of the cadaver demonstrates the differences in DRG anatomy at different spinal levels. In this work, we provide correlated MR images with anatomic dissection to aid the reader in better understanding the variations in DRG anatomy in the cervical, thoracic and lumbar levels.

Conclusion

Our findings reveal that the use of 3T CISS MRI allows for the precise characterization of the DRG within the neuroforamina at various spinal levels. Our results can aid in percutaneous interventions and surgical decision-making as anatomic position of the human DRG throughout the spinal column can be correlated to its location on MRI.

References

Silverstein, M. P., Romrell, L. J., Benzel, E. C., Thompson, N., Griffith, S., & Lieberman, I. H. (2015). Lumbar dorsal root Ganglia location: an anatomic and MRI assessment. *International journal of spine surgery*, *9*, 3. https://doi.org/10.14444/2003

Images/Tables

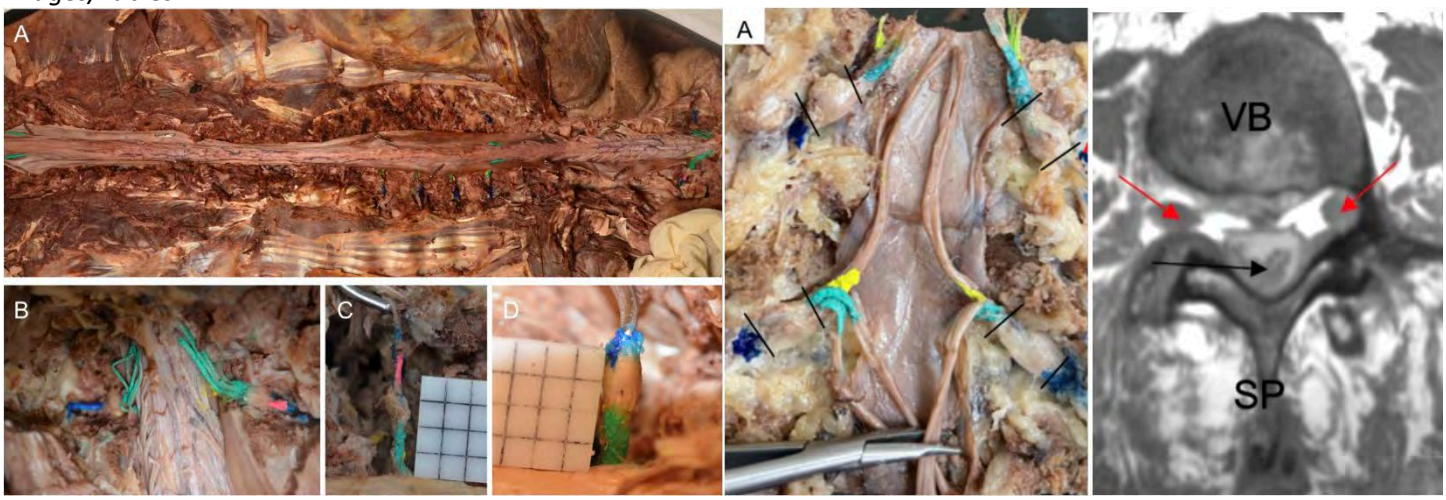

1203

Brain [68Ga]DOTATATE PET/MRI-Based Evaluation of Pituitary Neuroendocrine Tumors in the Context of Hormonal Subtypes

Sean H Kim MD[1], Jana Ivanidze MD, PhD[1], Arsalan Haghdel[2], Georgiana Dobri MD[2], David Pisapia MD[2], Arindam RoyChoudhury PhD[2], Nicolas Karakatsanis PhD[3], Theodore Schwartz MD[2]

[1]NewYork-Presbyterian Hospital Weill Cornell, New York, NY, USA. [2]Weill Cornell Medicine, New York, NY, USA. [3]Weill Cornell Medical College, New York, NY, USA

Abstract Category

Functional/Advanced Imaging

Purpose

Pituitary neuroendocrine tumors (pitNET) comprise up to 15% of all brain neoplasms and are most often treated surgically. Contrast-enhanced MRI is the gold standard for pitNET diagnosis and treatment planning. However, MRI can underestimate the extent of extrasellar disease, which has been implicated in the high propensity of pitNET for postoperative recurrence. PitNET express somatostatin receptor-2 (SSTR2), which can be targeted with [68Ga]DOTATATE. Histologically, differential SSTR2 expression has been demonstrated in different hormonal subtypes of pitNET. However, a broader role of PET imaging in clinical pitNET management remains to be established. Here, our purpose was to characterize [68Ga]DOTATATE PET avidity in a prospective cohort of patients with pitNET as a function of hormonal subtype and in comparison with the physiologically [Ga68]DOTATATE-avid normal pituitary gland.

Materials & Methods

Dedicated brain [68Ga]DOTATATE PET/MRI was performed in a prospective patient cohort as part of an IRB approved observational study of patients with SSTR2 positive brain tumors. All patients with biopsy proven pitNETs post resection with suspected postoperative residual or recurrent tumor were retrospectively identified and included in the study. Maximum Standardized Uptake Value (SUV) of the residual/recurrent pitNETs and of the normal pituitary gland were collected in each patient. SUV were then then compared across different hormonal pitNET subtypes as well as with SUV of the normal pituitary gland. Additionally, superior sagittal sinus (SSS) SUV was collected in each patient to allow for analysis of lesion SUV relative to SSS SUV (SUVR, conceptually based on prior studies in meningioma). Statistical analyses were performed using nonparametric Mann-Whitney and Kruskal-Wallis tests.

Results

Total of 20 patients met inclusion criteria; mean age was 55 and 9/20 (45%) were female. Six different hormonal subtypes of pitNETs were represented in the cohort (gonadotroph (n=7), thyrotroph (n=1), prolactinoma (n=9), mammosomatotroph (n=1), corticotroph (n=5), nonfunctioning adenoma (n=5)). SUVR of nonfunctioning adenomas was significantly lower than that of normal pituitary gland (p=0.02). Noting the sample size of one, the thyrotroph and mammosomatotroph demonstrated the highest and second highest SUV/SUVR, respectively. Excluding the two subtypes with a sample size of one, the lowest mean SUV and SUVR was observed in nonfunctioning adenomas and the highest mean SUV was observed in prolactinomas among the pitNETs, although the normal pituitary gland demonstrated the highest mean SUV and SUVR. Corticotrophs demonstrated the highest mean SUVR. SUV and SUVR differences between different pitNET subtypes, between functioning and nonfunctioning adenomas, and when comparing all pitNET to normal pituitary gland did not reach statistical significance.

Conclusion

We present pilot brain [68Ga]-DOTATATE PET/MRI findings in a prospective cohort. Despite the small sample size, we found decreased SUV and SUVR in nonfunctioning adenomas compared to hormonally active pitNET, replicating prior histologic findings and supporting a role for [68Ga]DOTATATE PET in clinical pitNET evaluation. Further studies in a larger prospective cohort will focus on systematic assessment of PET/MRI-guided tumor extent delineation for radiation treatment planning and response assessment. This work has the potential to improve postsurgical management, and thereby clinical outcomes, in patients with pitNET.

References

Tebani A, Jotanovic J, Hekmati N, Sivertsson Å, Gudjonsson O, Edén Engström B, Wikström J, Uhlèn M, Casar-Borota O, Pontén F. Annotation of pituitary neuroendocrine tumors with genome-wide expression analysis. Acta Neuropathol Commun. 2021 Nov 10;9(1):181. doi: 10.1186/s40478-021-01284-6. PMID: 34758873; PMCID: PMC8579660.

Taboada GF, Luque RM, Bastos W, Guimarães RF, Marcondes JB, Chimelli LM, Fontes R, Mata PJ, Filho PN, Carvalho DP, Kineman RD, Gadelha MR. Quantitative analysis of somatostatin receptor subtype (SSTR1-5) gene expression levels in

somatotropinomas and non-functioning pituitary adenomas. Eur J Endocrinol. 2007 Jan;156(1):65-74. doi: 10.1530/eje.1.02313. PMID: 17218727.
Tjörnstrand A, Casar-Borota O, Heurling K, Schöll M, Gjertsson P, Himmelman J, Itsenko O, Ragnarsson O, Filipsson Nyström H. Lower ^{68} Ga-DOTATOC uptake in nonfunctioning pituitary neuroendocrine tumours compared to normal pituitary gland-A proof-of-concept study. Clin Endocrinol (Oxf). 2020 Mar;92(3):222-231. doi: 10.1111/cen.14144. Epub 2020 Jan 9. PMID: 31868239.
Images/Tables

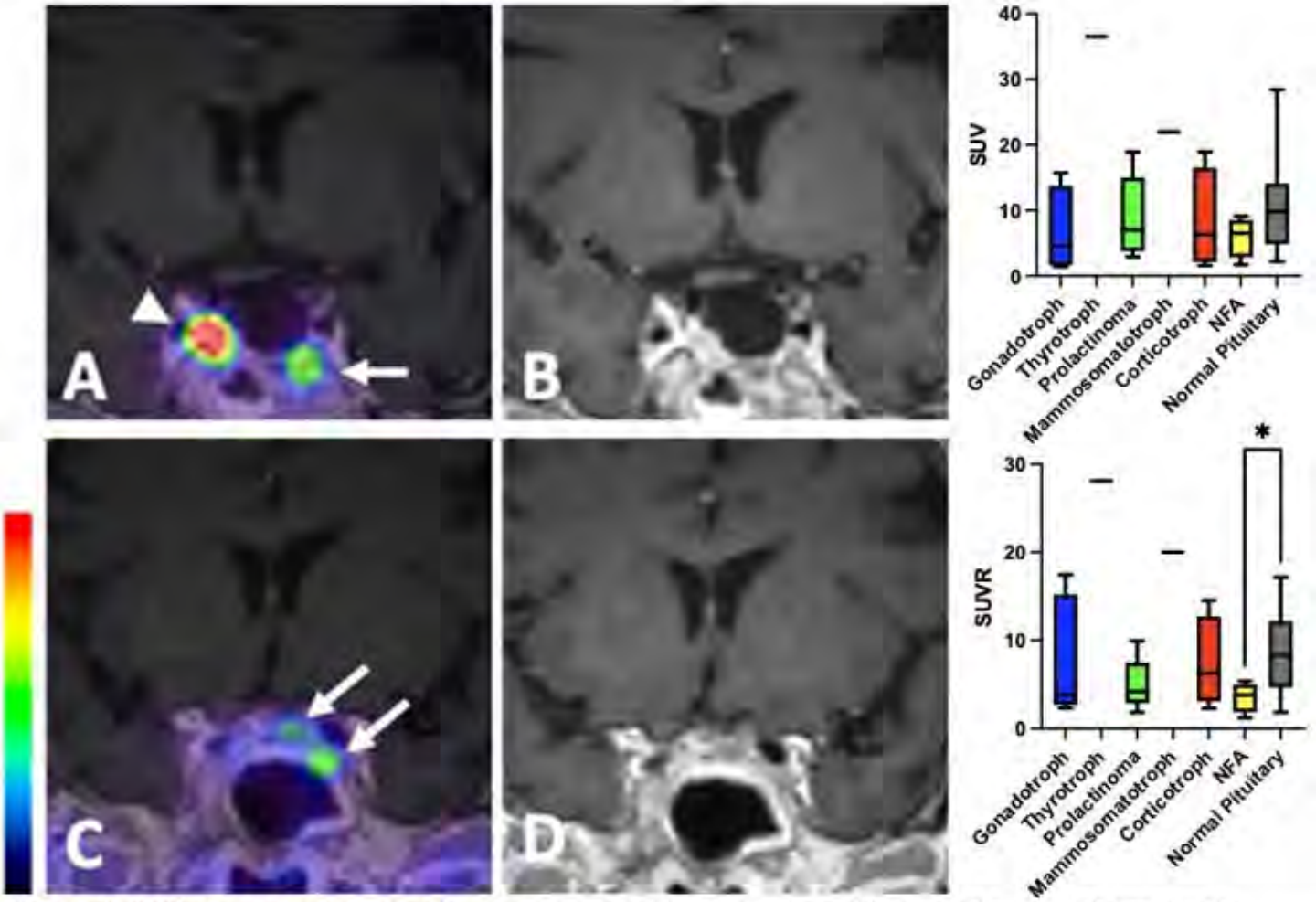

Figure: (Left) Representative patient from our prospective pilot cohort. 74-year-old male with previously resected gonadotroph adenoma who presented with suspected recurrence. Coronal fused PET/MRI windowed at SUV 0-15 shows mildly avid soft tissue compatible with residual tumor in the left cavernous sinus (arrow in A, SUV 4.2), less well delineated on corresponding postcontrast MRI alone (B). Arrowhead in A: normal pituitary gland. More anteriorly, mildly avid soft tissue along the anterosuperior margin of the sella (arrows in C, coronal fused PET/MRI with same windowing shown in A) is better delineated vs MRI alone (D). **(Right)** Box and Whiskers plots demonstrating distribution of SUV (top) and SUVR (bottom) of the normal pituitary gland and of the pitNETs by hormonal subtypes. Whiskers indicate minimum and maximum values.

1204

Disparities in Rates of Surgical Treatment for Patients with Idiopathic Intracranial Hypertension

Mihir Khunte[1], Dheeman Futela MBBS[1], Anuradha Rao MD[2], Dheeraj Gandhi MD, FACR[3], Ajay Malhotra MD, MMM[1]
[1]Yale, New Haven, CT, USA. [2]Richmond, VA, USA. [3]Baltimore, MD, USA

Abstract Category

Socioeconomics & Health Policy

Purpose

Purpose: Idiopathic intracranial hypertension (IIH) is an increasingly prevalent condition worldwide, with untreated cases potentially leading to severe headaches and irreversible vision loss due to sustained elevation of intracranial pressure (ICP). Recent studies have shown demographic disparities in prevalence, with Black and Hispanic patients having the largest prevalence with OR of IIH at 1.66 (95% CI 1.49–1.85) and 1.33 (95% CI 1.14–1.56), respectively.This study aims to investigate racial, socioeconomic, and geographic disparities in access to surgical treatment for IIH.

Materials & Methods

A retrospective analysis was conducted using data from the National Inpatient Sample (2016–2021) to identify adult inpatient admissions with idiopathic intracranial hypertension. Surgical interventions assessed included cerebral venous sinus stenting, cerebrospinal fluid (CSF) shunting, and optic nerve sheath fenestration (ONSF). Patients were identified using the International Classification of Diseases, Tenth Revision, Clinical Modification (ICD-10-CM) diagnosis and procedural coding system (PCS). Key patient demographics such as gender, age, race, and income quartile along with hospital characteristics such as region, rural/urban status, and hospital size were recorded. Logistic regression models were used to estimate the odds of receiving surgical treatment, adjusting for demographics and major IIH risk factors.

Results

A total of 54,900 patients with IIH were identified, of whom 9,145 (16.7%) underwent surgical treatment. The proportion of patients receiving surgical intervention increased marginally from 16.4% in 2016 to 18.2% in 2021, though this change was not statistically significant ($p = 0.281$). Patients receiving medical versus surgical management were similar in age (mean 36 years, $p = 0.633$) and gender distribution (92.3% female vs. 92.5%, $p = 0.807$). Patients who received surgical intervention were more likely to have obstructive sleep apnea (10.7% vs. 8.5%, $p = 0.003$) and papilledema (18.7% vs. 11.9%, $p < 0.001$). After adjusting for demographics and IIH risk factors, Black and Hispanic patients were significantly less likely to receive surgical treatment than White patients (OR 0.65 [95% CI 0.56–0.75], $p < 0.001$ and OR 0.64 [95% CI 0.52–0.79], $p < 0.001$, respectively). Medicaid-insured patients were also less likely to receive surgical intervention than those with private insurance (OR 0.77 [95% CI 0.68–0.88], $p < 0.001$). Regional disparities were identified, with patients in the Midwest (OR 1.31 [95% CI 1.06–1.63], $p = 0.014$), South (OR 1.70 [95% CI 1.40–2.05], $p < 0.001$), and West (OR 1.33 [95% CI 1.06–1.67], $p = 0.014$) having higher odds of receiving surgical treatment compared to those in the Northeast.

Conclusion

This study reveals substantial racial, socioeconomic, and geographic disparities in rates of surgical treatment for IIH, despite significantly higher prevalence in Blacks and Hispanics. These findings emphasize the need for targeted strategies to promote equitable access to surgical care for IIH across diverse patient populations.

References

Shaia JK, Sharma N, Kumar M, et al. Changes in Prevalence of Idiopathic Intracranial Hypertension in the United States Between 2015 and 2022, Stratified by Sex, Race, and Ethnicity. *Neurology.* 2024;102(3):e208036.

1208

Impact of AI-Assisted Detection on Aneurysm Call Rates in Head and Neck CT Angiography: A Retrospective Analysis

Pavan Khosla BA[1], Shadi Ebrahamian MD[2], Dheeman Futela MBBS[1], Ajay Malhotra MD, MM, FACR[1]
[1]Yale, New Haven, CT, USA. [2]Yale, New haven, CT, USA

Abstract Category

Socioeconomics & Health Policy

Purpose

The prevalence of intracranial aneurysms is reported to be 3.2% in the general population not at high risk. However, with increasing use on cross-sectional imaging, intracranial aneurysms are being reported more frequently. The purpose

of this study is to evaluate the call rate of intracranial aneurysms on head and neck computed tomography angiography (CTA) following the integration of artificial intelligence (AI) software in aiding neuroradiologists' diagnostic workflows.

Materials & Methods

We retrospectively analyzed 7,986 de-identified AI-aided CTA Head/Neck radiology reports for consecutively performed CTAs from January 1, 2023, to July 30, 2023. Meta-data was extracted using the OpenAI API with the GPT-4o-mini model. Cases involving infundibula, trifurcations, pseudoaneurysms, as well as aortic and pulmonary trunk aneurysms were excluded. Data analysis was performed in Python v3.8.3 and R v4.1.1 to extract data, calculate descriptive statistics, and visualize distributions.

Results

The call rate for aneurysms was 12.1%, with an average aneurysm size of 3.45 mm (SD=2.88 mm, median=3 mm). Figure 1 shows the distributions of aneurysm locations and sizes. AI-aided readings reported 970 head and neck aneurysms, with the location and frequency as follows: internal carotid artery (ICA) (n=464), common carotid artery (n=1), middle cerebral artery (n=127), anterior cerebral artery (n=70), posterior cerebral artery (n=7), posterior communicating artery (n=107), anterior communicating artery (n=110), basilar artery (n=36), vertebral artery (n=36), superior cerebellar artery (n=4), anterior inferior cerebellar artery (n=1), and posterior inferior cerebellar artery (n=7). Aneurysms were predominantly in the ICA and smaller vessels, with size distribution showing a high frequency of aneurysms at 2 mm (n=434) and 3 mm (n=217). Size counts revealed that aneurysms ≥4 mm were present in 278 cases, indicating a sizeable subset potentially warranting clinical follow-up.

Conclusion

AI implementation in CTA readings has shown a significant impact on aneurysm detection rates, particularly for small intracranial aneurysms. This automated support could enhance diagnostic accuracy in neuroradiology by increasing detection rates of smaller aneurysms, potentially refining patient management and surveillance protocols. Importantly, further studies are warranted to assess the impact of these AI-driven detection on clinical outcomes and resource utilization and assessment of cost-effectiveness.

References

Malhotra A, Wu X, Forman HP, Matouk CC, Gandhi D, Sanelli P. Management of Tiny Unruptured Intracranial Aneurysms: A Comparative Effectiveness Analysis. *JAMA Neurol.* 2018;75(1):27-34.

Images/Tables

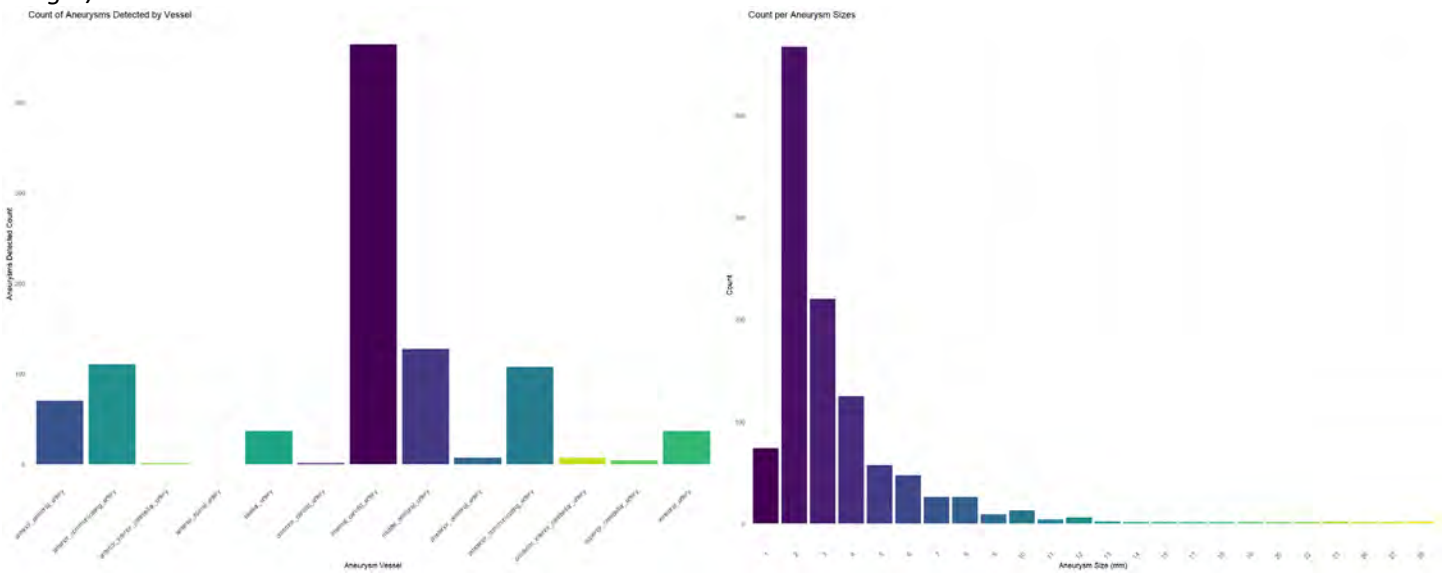

1209

Uncovering Vision and Motor Impairements Related Brain Areas in Type 2 Diabetes Through Quantitative Susceptibility Mapping (QSM) in the Multi-year Boston Puerto Rican Health Study (BPRHS)

Huiyu Huang[1], Lea Bergeot[1], Farhad Salman[2], Nazmi Kurt[1], Serkan Akbas[1], Ferdinand Schweser[2], Salil Soman[1]
[1]Beth Israel Deaconess Medical Center and Harvard Medical School, Boston, MA, USA. [2]University at Buffalo, Buffalo, NY, USA

Abstract Category

Adult Brain

Purpose

High blood sugar and insulin as Type 2 Diabetes (T2D) markers contribute to brain abnormalities, which can lead to cognitive decline[1]. This study investigates high-risk brain regions associated with cognitive deficits in T2D patients and explores their causal relationships with those T2D markers over time.

Materials & Methods

Data from 246 adults in the BPRHS includes T2D-related markers (e.g., HbA1c, blood glucose, medication, and insulin) and cognitive functions (Mini-Mental State Examination (MMSE), Digit Span Forward (DSF), and Clock Drawing (CD)) at baseline, and approximately 2, 7, and 14 years later. MRI scans (multi-echo gradient-recalled echo (mGRE) and T1-weighted) were acquired around year 14. Multi-echo complex Total Field Inversion (mcTFI)[2] QSM images, derived from mGRE phase data, were segmented using the Joint Fusion Tool[3] with T1-weighted and mGRE magnitude images to compute mean susceptibility values across brain regions. Statistical analyses included Mann–Whitney U tests, Bonferroni corrections, and both linear and logistic regression to examine susceptibility abnormalities and correlations with cognitive scores, considering T2D markers, age, and gender.

Results

Significant differences in susceptibility values ($p < 0.05$) were observed in three areas between non-T2D (DM-) and T2D (DM+) groups with cognitive decline (Cog-). At baseline, DM+ participants with DSF scores below 5 (DSF-) exhibited higher susceptibility in the lateral occipital cortex, likely due to iron accumulation, which may indicate vision loss. Higher susceptibility values in this area were associated with more severe vision impairment in younger male adults at baseline. This abnormality persisted in patients with blood glucose levels above 126 at year 2, suggesting that elevated blood sugar levels may have primarily caused the injury in this area. At year 14, MMSE scores below 25 and DSF scores below 5 were associated with higher susceptibility values in the basal ganglia. This finding was related to patients who had normal blood sugar levels and were taking anti-diabetes medication at year 2. Additionally, CT scores below 3 at year 14 were linked to lower susceptibility values in the cerebellum, suggesting iron loss. Lower susceptibility values were observed in DM+ patients with insulin levels above 20.7 starting from year 2. Thus, low blood sugar could contribute to motor control, coordination, and cognitive processing dysfunctions due to susceptibility changes in these two areas. Young male adults tended to experience more severe impairment when susceptibility values decreased in the basal ganglia and increased in the cerebellum.

Conclusion

Our findings demonstrate cognitive-related functional and structural injuries associated with blood glucose, medication use, and insulin in T2D over time. These insights may support the development of new drug targets and monitoring strategies. The persistence of blood glucose effects on the brain, even after cognitive decline, highlights the urgent need for timely treatment. Additionally, cognition-related brain changes emphasize the importance of considering the potential side effects of diabetes medications on brain health.

References

1. Damanik J, Yunir E. Type 2 Diabetes Mellitus and Cognitive Impairment. *Acta Med Indones* 2021;53:213-220
2. Wen Y, Spincemaille P, Nguyen T, et al. Multiecho complex total field inversion method (mcTFI) for improved signal modeling in quantitative susceptibility mapping. *Magn Reson Med* 2021;86:2165-2178
3. Salman F TK, Adegbemigun A, et al. Bi-parametric Joint Label Fusion A Comprehensive Segmentation Tool for Deep Gray Matter in QSM. *EMTP QMR* 2024

1210

Evaluation of Stereotactic Radiosurgery Response of Brain Hemangioblastomas with Arterial Spin- Labeling MRI

Banu Yagmurlu, Amit Persad, David J Park, Steven D Chang, Michael Iv
Stanford University School of Medicine, Palo Alto, CA, USA

Abstract Category

Adult Brain

Purpose

Hemangioblastomas (HB) show high signal on arterial spin-labeling (ASL) MRI due to their hypervascular nature. Stereotactic radiosurgery (SRS) is a non-invasive treatment that delivers precise, high-dose radiation to tumors, minimizing damage to surrounding tissues. This study sought to determine whether ASL-MRI can be used to monitor blood flow changes in brain HB treated with SRS over a three-year period.

Materials & Methods

This retrospective study included patients with von Hippel-Lindau associated brain HB who had ASL-MRIs before and after SRS. Total of 9 patients (median age 40 years, 6 females) with 26 HB were included. Median prescription SRS dose was 22 Gy and median maximum SRS dose was 29.9 Gy, with 17 lesions treated in a single fraction. Post-SRS MRI timepoints included: within the first 6 months, between 6 months and 1 year, between 1 and 3 years. Using region or volume of interest segmentation on 3D post-gadolinium and ASL-CBF images, the following metrics were obtained at each timepoint: maximum bidirectional diameters, lesion volumes, and mean and max CBF values. All variables were non-parametric. Continuous variables were compared by Mann-Whitney U test, and categorical variables compared by c^2 test for association. Spearman correlation was used to determine relations between variables.

Results

Median HB volumes at each timepoint were as follows: pre-SRS 0.22 cc, post-SRS 6-months 0.24 cc, post-SRS 1-year 0.16 cc, and post-SRS 3-years 0.14 ccm (p=0.066). Mean and max CBF changed significantly following SRS, with an initial decrease followed by an increase to 3-year follow-up (p=0.087, p=0.024). When screening for associated variables, marginal and max SRS dose correlated strongly with 3-year CBF (p=0.036, p=0.023, respectively). Follow-up CBF also correlated strongly with lower tumor volume at 3-year follow-up (p=0.03). Both factors correlated with chance of local tumor control (p=0.025). Finally, baseline CBF mean and CBF max correlated with lower 3-year tumor volume (p=0.002, p=0.004).

Conclusion

ASL-MRI can be used to evaluate SRS response in von Hippel-Lindau patients with brain HB. Specifically, our findings show that higher radiation dose leads to lower CBF on follow-up ASL-MRI, which is correlated with lower tumor volume.

References

1. Kano H, Shuto T, Iwai Y et al. Stereotactic radiosurgery for intracranial hemangioblastomas: a retrospective international outcome study. *J Neurosurg.* 2015;122(6):1469-78. doi: 10.3171/2014.10.JNS131602. Epub 2015 Mar 27. PMID: 25816088.
2. Haller S, Zaharchuk G, Thomas DL, Lovblad KO, Barkhof F, Golay X. Arterial Spin Labeling Perfusion of the Brain: Emerging Clinical Applications. *Radiology*. 2016;281(2):337-356. doi:10.1148/radiol.2016150789

Images/Tables

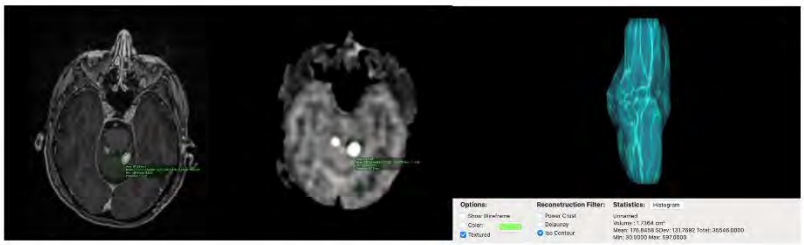

Measurement of volumetry and CBF metrics

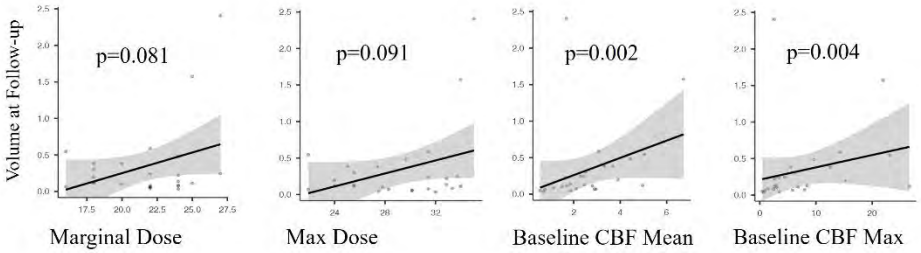

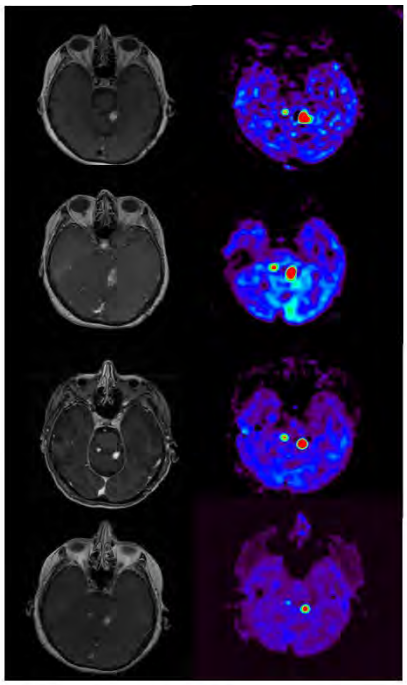

Temporal changes of the left vermian lesion (arrow), before SRS (1st row) and after SRS (6mo/6mo-1yr/1-3yrs) 2nd-4th rows from top to bottom respectively. Reduction in blood flow on ASL perfusion maps are noted. Although contrast enhanced T1 image showed an increase at the first time interval (2nd row left), ASL perfusion map indicates a decrease (2nd row right), attributable to radiation effects.

1211

Gender Differences in Medicare Practice and Payment of Neuroradiologists

Chris J Lee BS[1], Mihir Khunte BS[1], Dheeman Futela[1], Nagaraj Moily MD, PhD, MBA, MAM[1], Dheeraj Gandhi MD, FACR[2], Ajay Malhotra MD, MMM,FACR[1]

[1]Yale, New Haven, CT, USA. [2]Baltimore, MD, USA

Abstract Category

Socioeconomics & Health Policy

Purpose

Female neuroradiologists in clinical practice are outnumbered by their male counterparts. However, it is unknown whether there exist differences in practice patterns, and Medicare billings and payments between female and male neuroradiologists. The purpose of this study is to compare representation, practice range, clinical productivity, and Medicare payments for female and male neuroradiologists.

Materials & Methods

Retrospective cross-sectional study of Medicare provider and service data was conducted. Male and female neuroradiologists who received Medicare payments from 2017-2021, and the services rendered were analyzed. Primary outcome was gender representation, mean payments received by Medicare, charges submitted, and codes billed. T-tests and Mann-Whitney U tests were used to determine difference in payment and practice volume between male and female radiologists.

Results

From 2017-2021, a total of 2701 neuroradiologists, of whom 526 (19.5%) were female, with a higher proportion of women in academic than non-academic neuroradiology practice (23.3% vs 15.6% respectively). On average, female neuroradiologists charged less (mean [SE], $642,489 [$14,756] vs $738,416 [$7,800]; $p < .001$) and were paid less by Medicare (mean [SE], $92,834 [$1,877] vs $113,495 [$1,044]; $p < .001$) compared to their male counterparts. By contrast, female neuroradiologists had a higher payment-per-service ratio (mean [SE], 0.232 [0.001] vs 0.208 [0.0003]; $p < .001$). Females billed fewer median total services (1,802 [IQR, 925-4,726] vs 2,461 [IQR, 1,268-5,781]; $p < .001$), served fewer median beneficiaries (1,232 [IQR, 705-1,963] vs 1,697 [IQR, 990-2,682]; $p < .001$), and billed fewer median unique codes (19 [IQR, 13-26] vs 23 [IQR, 17-33]; $p < .001$). Temporal analysis of data across the 5-year study period showed

that men consistently received higher payments than women, although the difference in mean Medicare charge (p=0.03), mean Medicare payment (p=0.04), and median number of services provided (p=0.04) between the two cohorts is decreasing.

Conclusion

Female neuroradiologists were underrepresented, charged less, and received less overall payment compared to their male counterparts. Female neuroradiologists provided a smaller range and number of services, with higher payment-per-service ratio. Temporal analysis suggests that the difference in Medicare payment between the two genders are decreasing, providing a more positive outlook for gender equality in healthcare payment.

References

Ahmadi M, Khurshid K, Sanelli PC, et al. Influences for Gender Disparity in Academic Neuroradiology. *American Journal of Neuroradiology.* 2018;39(1):18-23.

1212

Clinical and Radiological Characterization of Metastatic Pituitary Neuroendocrine Tumors: Insights from a Retrospective Cohort Study

Sahar Alizada MD, Heba Al Qudah MD, Samir Dagher MD, Ahmed Msherghi MD, Ceylan Altintas Taslicay MD, Richard Dagher MD, Komal Shah MD, Rami Eldaya MD

MD Anderson Cancer Center, Houston, TX, USA

Abstract Category

Head & Neck

Purpose

Pituitary adenomas (PAs) are common benign tumors with an incidence of approximately 16.7%[1]. In contrast metastatic pituitary neuroendocrine tumor (PitNET), previously known as pituitary carcinoma, are exceedingly rare, comprising only 0.1–0.5% of pituitary, with poorly described imaging course[2]. Metastatic PitNET is defined as a tumor originating from adenohypophysial neuroendocrine cells, with metastasis to lymph nodes, distant sites, or discontinuous spread to central nervous system (CNS)[3]. Life expectancy in patients with metastatic PitNET has been shown to be markedly reduced[4,5]. Given the rarity and aggressive nature of metastatic PitNET, detailed case analysis is crucial for refining our knowledge and clinical approach. We present the clinical and radiological features of our patient cohort to enhance understanding of metastatic PitNET.

Materials & Methods

This retrospective study identified 38 consecutive patients with reported history of metastatic PitNET. Exclusion criteria were incomplete imaging, absence of pathology report at our institution, and lack of definite clinical and/or pathological confirmation of metastatic disease of pituitary origin. We collected clinical and imaging data on metastatic PitNET, including demographic information, tumor functionality and pathology, metastasis location, and patient follow-up duration. Imaging data covered initial and subsequent tumor size, Knosp grade, structural invasion, and PET avidity.

Results

In total 15 patients were identified, with complete imaging (initial and follow-up) available for 6 patients, and follow-up imaging only for the remaining 9 patients. Our results showed that the average age at diagnosis was 34.8 ± 14.7 years, with 40% of patients being female. The average time from initial diagnosis to carcinoma development was 9.7 ± 6.9 years. 80% of initial tumor and subsequent carcinoma were secreting. CNS metastasis was present in 11 (73.3%) patients, including 11 (73.3%) with brain metastasis and 3 (20%) with spinal metastasis. Multiple metastatic sites were present in 9 (60%) patients. Outside of the CNS, the most common metastasis was to the bone (6 patients), followed by the liver (4 patients). Survival outcomes showed that 7 (46.7%) patients were alive at the latest follow-up. For deceased patients, average time from diagnosis to death was 15.2 ± 7.1 years, while average time from metastasis diagnosis to death was 5.7 ± 4.1 years.

On the initial MRI (N = 6), the mean anteroposterior size was 3.5 ± 1 cm, transverse size was 2.7 ± 0.8 cm, and craniocaudal size was 2.7 ± 0.9 cm. On the subsequent MRI, 13 out of 15 patients showed residual/recurrent disease in the sella. On the initial MRI, 4 cases (66.7%) had Knosp grade 3 or more. On the subsequent MRI, 11 cases (73.3%) showed residual/recurrent disease in cavernous sinus. Local osseous or sphenoid sinus invasion was present in 3 cases (50%) on the initial MRI and in 7 cases (46.7%) on the subsequent MRI. PET imaging showed avidity in 80% of cases.

Conclusion

This study provides a comprehensive overview of the clinical and radiological characteristics of pituitary carcinomas. High CNS metastasis rates and frequent multi-site progression underscore their aggressive nature.

References

1. Ezzat S, Asa SL, Couldwell WT, et al. The prevalence of pituitary adenomas: a systematic review. *Cancer* 2004;101(3):613-619. https://doi.org/10.1002/cncr.20412
2. Sumislawski P, Rotermund R, Klose S, et al. ACTH-secreting pituitary carcinoma with TP53, NF1, ATRX and PTEN mutations Case report and review of the literature. *Endocrine* 2022;76(1):228-236. DOI: https://doi.org/10.1007/s12020-021-02954-0
3. Casar-Borota O, Burman P, Lopes MB. The 2022 WHO classification of tumors of the pituitary gland: An update on aggressive and metastatic pituitary neuroendocrine tumors. *Brain Pathol* Published online September 2024:e13302. DOI: https://doi.org/10.1111/bpa.13302
4. Dudziak K, Honegger J, Bornemann A, Horger M, Müssig K. Pituitary carcinoma with malignant growth from first presentation and fulminant clinical course--case report and review of the literature. *J Clin Endocrinol Metab* 2011;96(9):2665-2669. DOI: https://doi.org/10.1210/jc.2011-1166
5. McCormack A, Dekkers OM, Petersenn S, et al. Treatment of aggressive pituitary tumours and carcinomas: results of a European Society of Endocrinology (ESE) survey 2016. *Eur J Endocrinol* 2018;178(3):265-276. DOI: https://doi.org/10.1530/EJE-17-0933

Images/Tables

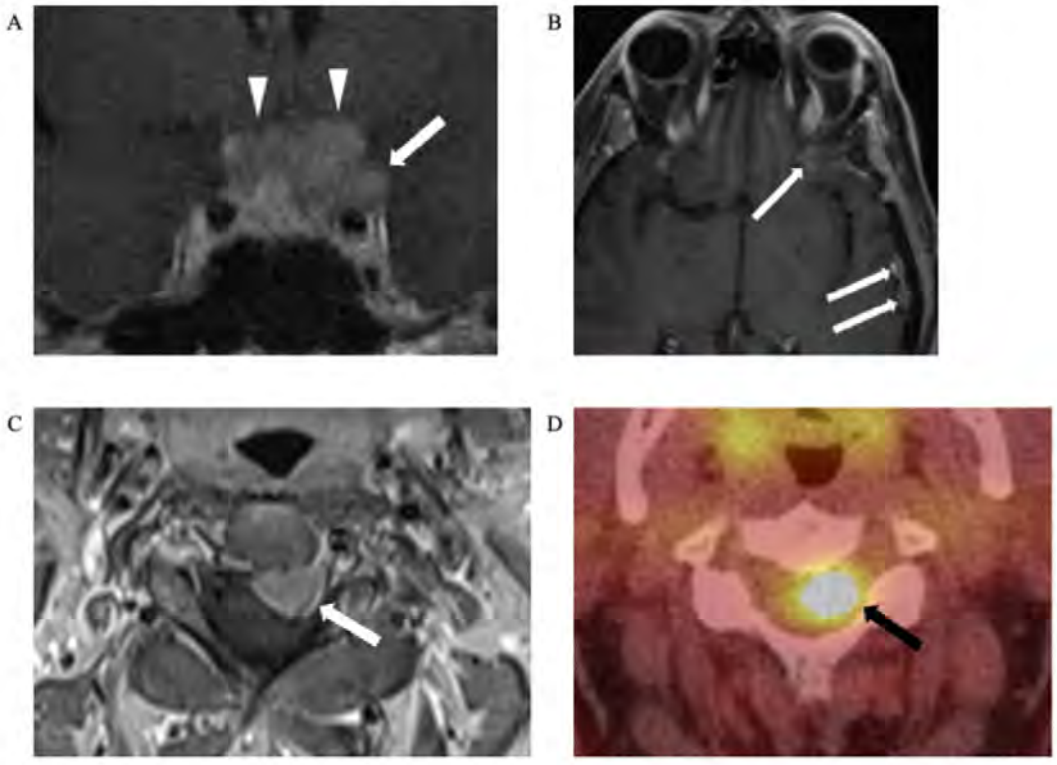

Figure 1: Initial (A) and 6-year follow-up (B, C, D) imaging of metastatic PitNET in a 60-year-old female

(A) Coronal delayed phase post-contrast MRI showing mass effect on the chiasm (arrowhead) and left cavernous sinus Knosp 3a lesion (arrow), associated with visual symptoms,

(B) Axial post-contrast brain MRI demonstrating multiple dural based metastatic deposits (arrows),

(C) Axial post-contrast cervical spine MRI depicting dural deposit along the ventral thecal sac (arrow),

(D) Fused axial FDG-PET showing PET avidity in the cervical spine dural metastasis (arrow).

1215

Radiomic shape analysis of contrast-enhancing tumor regions in glioblastoma is correlated with non-enhancing tumor spread.

Savannah R Duenweg PhD, Samuel A Bobholz PhD, Michael Flatley BS, Allison K Lowman BS, Aleksandra Winiarz BS, Benjamin Chao BS, Biprojit Nath MS, Fitzgerald Kyereme BS, Jennifer Connelly MD, Kelly Mrachek MD, Elaine Tanhehco MD, Max Krucoff MD, Peter S LaViolette PhD
Medical College of Wisconsin, Milwaukee, WI, USA

Abstract Category

Adult Brain

Purpose

Glioblastoma (GBM) is a highly aggressive, heterogenous primary brain tumor with a dismal median overall survival (OS) of 18 months[1]. Recently published radio-pathomic maps of tumor probability (TPM), created from autopsy tissue aligned with clinical MR imaging as ground truth, have been successful at identifying areas of non-enhancing tumor outside of contrast enhancement (TOC) and have been associated with decreased OS[2,3]. Radiomics, which is the process of extracting quantitative imaging features from medical scans using data-characterization algorithms, allows for the decoding of detailed tissue characteristics[4]. These radiomic features, when integrated with patient data, help in detecting and characterizing clinically relevant outcomes. Therefore, this study tested the hypothesis that radiomic shape features of the contrasting enhancing (CE) tumor would be associated with increased tumor outside CE.

Materials & Methods

The publicly available UCSF-PDGM dataset[5] was used for this study. A total of 218 patients diagnosed with GBM who underwent gross total resection (GTR) were analyzed for this study. Radio-pathomic tumor probability maps (TPM) were generated using a previously published model using pre-surgical T1, T1C, FLAIR and ADC images as input. Tumor segmentations were included in the dataset and include the CE, the necrotic core (NC), and FLAIR hyperintensity (FH). A mask of the tumor (i.e., CE and necrotic core) was used as the region of interest (ROI) for radiomic feature extraction. Radiomic shape features were calculated using Matlab. Additionally, the volume and proportion of high tumor probability, defined as TPM > 0.7, was calculated within the FH mask. Pearson correlations were then computed to determine the relationship between tumor shape and TOC.

Results

Of the total 41 shape features extracted, eight 3D features were ultimately found to be significantly correlated with increased volume and proportion of TOC (**Figure 1**). Volume mesh, volume voxel count, surface area mesh, minor axis length, least axis length (all $p < 0.05$, r range 0.25 – 0.29) elongation, and flatness (both $p = 0.01$, $r = 0.18$ and 0.19, respectfully) were all positively correlated with increased volume and proportion of TOC, whereas surface volume Ratio had a negative correlation ($p < 0.05$, $r = -0.21$).

Conclusion

This study demonstrates that specific 3D radiomic shape features of the contrast enhancing tumor in GBM patients are significantly correlated with an increased volume and proportion of TOC. Specifically, we found that tumors that are large, narrow, elongated, and smooth had an increase in TOC, providing insight into the morphological traits that may indicate tumor infiltration beyond the contrast-enhancing boundaries. Future research should focus on validating these shape features across larger and more diverse datasets, as well as integrating radiomic features with genomic and clinical data to build more robust predictive models.

References

1. Ostrom QT, Cote DJ, Ascha M, Kruchko C, Barnholtz-Sloan JS. Adult Glioma Incidence and Survival by Race or Ethnicity in the United States From 2000 to 2014. *JAMA Oncol*. Sep 01 2018;4(9):1254-1262. DOI:10.1001/jamaoncol.2018.1789
2. Bobholz SA, Lowman AK, Connelly JM, et al. Non-invasive tumor probability maps developed using autopsy tissue identify novel areas of tumor beyond the imaging-defined margin. *medRxiv*. 2022. DOI:https://doi.org/10.1101/2022.08.17.22278910
3. Bobholz SA, Lowman AK, Connelly JM, et al. Noninvasive Autopsy-Validated Tumor Probability Maps Identify Glioma Invasion Beyond Contrast Enhancement. *Neurosurgery*. Mar 19 2024. DOI:10.1227/neu.0000000000002898
4. Bobholz SA, Lowman AK, Barrington A, et al. Radiomic Features of Multiparametric MRI Present Stable Associations with Analogous Histological Features in Patients with Brain Cancer. *Tomography*. 2020/6// 2020;6(2). DOI:10.18383/j.tom.2019.00029

5. Calabrese E, Villanueva-Meyer JE, Rudie JD, et al. The University of California San Francisco Preoperative Diffuse Glioma MRI Dataset. *Radiol Artif Intell*. Nov 2022;4(6):e220058. DOI:10.1148/ryai.220058

Images/Tables

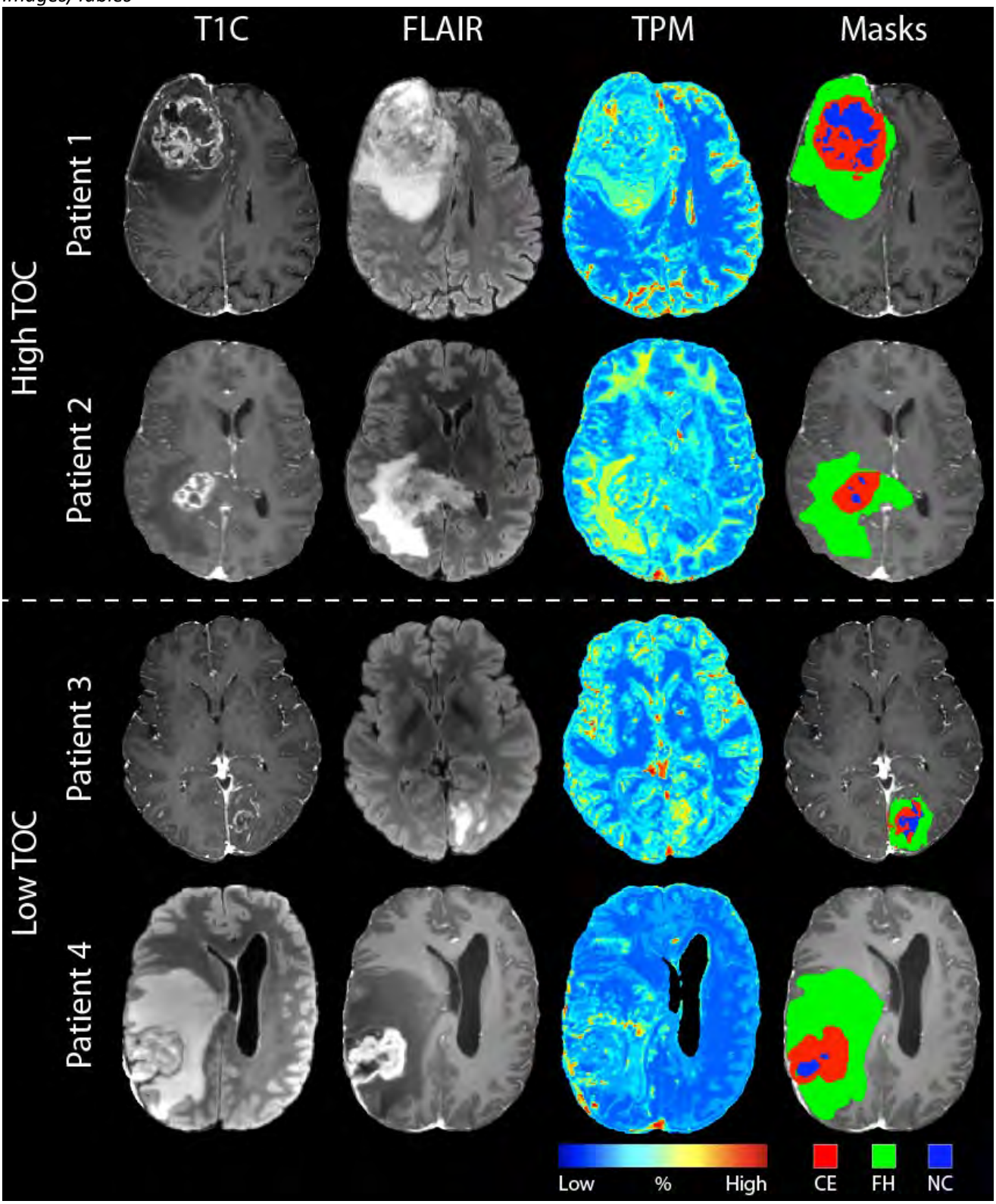

1216

Predicting Memory Outcome After Stereotactic Laser Ablation for Epilepsy using Task-Based fMRI.

Zofia M Lasiecka MD PhD[1], Jeremy L Smith PhD[1], Rebecca Roth[1], Kelsey C Hewitt Psy.D.[1], Daniel L Drane PhD[1], Jason W Allen MD PhD[2], Ranliang Hu MD[1]

[1]Emory University, Atlanta, GA, USA. [2]Indiana University, Indianapolis, IN, USA

Abstract Category

Functional/Advanced Imaging

Purpose

Stereotactic laser amygdalohippocampotomy (SLAH) is a minimally invasive technique for treating refractory epilepsy, showing promising results in seizure control and memory outcomes compared to open anterior temporal lobectomy (ATL) (Drane et al., 2021). Task-based functional MRI (t-fMRI) has replaced Wada testing for assessing memory decline risk after temporal lobe surgery, but its predictive value for memory outcomes post-SLAH remains unstudied. In this study we investigate the role of pre-surgical t-fMRI in predicting post-surgical memory outcome.

Materials & Methods

This is a retrospective single centered study on one of the largest SLAH cohorts in the country (n = 74, 41 left SLAH, 33 right SLAH). fMRI was done on one of 2 clinical 3T MRI scanners as part of presurgical planning (Magnetom Trio or Magnetom Skyra, Siemens Healthineers). fMRI was performed within 3 months before SLAH. Language tasks acquired during the session included verb generation, word generation, object naming, noun-verb and sentence completion. Non-verbal memory task - scene-encoding protocol - contrasted a visual scene-encoding paradigm (active condition) with a visual noise-encoding paradigm (control condition) (Binder et al., 2005). Neuropsychological tests were performed at 6-month and 1-year postsurgical time points and included both verbal memory and learning tests: Rey Auditory Verbal Learning Test (RAVLT) and the Logical Memory subtest of the 4th edition of the Wechsler Memory Scale (WMS-IV) and non-verbal memory tests: Rey Complex Figure Test (RCFT) and the Visual Reproduction subtest of the 4th edition of the Wechsler Memory Scale (WMS-IV). First- and second-level analyses were performed in FEAT, part of the FMRIB Free Software Library (FSL). Additional statistical analysis will be performed using IBM SPSS Statistics.

Results

Our preliminary results indicate that scene-recognition task activates posterior hippocampus, parahippocampal gyrus, fusiform gyrus, cingulate gyrus and precuneus cortex bilaterally in MTS patients however with right greater than left laterality. When comparing left versus right SLAH patients, both L and R-SLAH patients showed bilateral activation with greater activation on the right however R-SLAH had more activations on the left as compared to L-SLAH. When we divided SLAH patients based on the difference in their pre- and post-SLAH non-verbal memory performance, patients whose scores did not decline (n=43) after SLAH were showing overall increased activation on scene-recognition task as well as greater left activation on fMRI as compared to patients whose scores declined (n=17), although both groups' activations again had overall right lateralization. Our next analysis will correlate fMRI activations on scene-recognition task to non-verbal pre- and post-SLAH memory performance R-SLAH vs L-SLAH patients.

Conclusion

Scene recognition task fMRI in pre-surgical epilepsy patients showed activations in posterior hippocampus, parahippocampal gyrus, fusiform gyrus, cingulate gyrus and precuneus cortex bilaterally, however with right greater than left laterality. Preliminary analysis showed greater activation, especially on the left, was correlated with reduced non-verbal memory decline after SLAH. Further analysis is needed to evaluate how activation patterns can predict memory decline.

References

Drane DL, Willie JT, Pedersen NP, Qiu D, Voets NL, Millis SR, Soares BP, Saindane AM, Hu R, Kim MS, Hewitt KC, Hakimian S, Grabowski T, Ojemann JG, Loring DW, Meador KJ, Faught E Jr, Miller JW, Gross RE. Superior Verbal Memory Outcome After Stereotactic Laser Amygdalohippocampotomy. Front Neurol. 2021 Dec 9;12:779495.

Binder JR, Bellgowan PS, Hammeke TA, Possing ET, Frost JA. A comparison of two FMRI protocols for eliciting hippocampal activation. Epilepsia. 2005 Jul;46(7):1061-70.

Bigras C, Shear PK, Vannest J, Allendorfer JB, Szaflarski JP. The effects of temporal lobe epilepsy on scene encoding. Epilepsy Behav. 2013 Jan;26(1):11-21. doi: 10.1016/j.yebeh.2012.10.017. Epub 2012 Nov 30. PMID: 23207513; PMCID: PMC3529961.

1226

Augmenting Radiologist Assessment of Imaging Evident Dementias with Radiomic Analysis

Shreyas Puducheri BA[1], Olivia T Zhou BA[1], Krish Kapadia BS[1], Michael F Romano MD, PhD[2], V. Carlota Andreu-Arasa MD, PhD[3], Chad W Farris MD, PhD[3], Asim Z Mian MD[3], Aaron B Paul MD[4], Saurabh Rohatgi MD[4], Bindu N Setty MD[3], Juan E Small MD[5], Vijaya B Kolachalama PhD[6]

[1]Department of Medicine, Boston University Chobanian & Avedisian School of Medicine, Boston, MA, USA. [2]Department of Radiology and Biomedical Imaging, University of California, San Francisco, CA, USA. [3]Department of Radiology, Boston University Chobanian & Avedisian School of Medicine, Boston, MA, USA. [4]Department of Radiology, Massachusetts General Hospital, Boston, MA, USA. [5]Department of Radiology, Lahey Hospital & Medical Center, Burlington, MA, USA. [6]Department of Computer Science, Boston University, Boston, MA, USA

Abstract Category

AI/Informatics

Purpose

With the rising prevalence of dementia and advances in treatment options, the need for early and accurate differentiation of dementia etiologies has become increasingly critical [1,2]. While Alzheimer's disease (AD) is the most common form of dementia, other causes, such as vascular dementia, frontotemporal dementia, and prion disease, often present overlapping clinical and imaging features, complicating diagnosis and treatment [2]. MRI is an integral part of the standard dementia evaluation; however, assessments by radiologists can vary [3]. Integrating quantitative imaging analysis may help standardize these assessments, potentially allowing for earlier and more precise disease detection and intervention [2]. Our previous work has shown the potential of artificial intelligence (AI) to enhance neurodegenerative disease evaluation [4]. In this study, we aimed to expand upon this research by exploring the role of AI and radiomics in augmenting neuroimaging assessments to differentiate between Alzheimer's disease (AD) and other imaging-evident dementias (OIED).

Materials & Methods

We retrospectively analyzed 730 individuals with confirmed dementia and at least one T1 or T2/FLAIR MRI scan in the National Alzheimer's Coordinating Center (NACC) cohort. Using FastSurfer and a lesion prediction algorithm, we derived volumetric and lesion features and implemented eXtreme Gradient Boosting (XGBoost) models, as shown in figure (a). Model outputs were compared against assessments made by seven practicing neuroradiologists of 70 test cases, as well as against post-mortem neuropathological findings for AD in 27 cases. To evaluate feature contributions to model predictions, we employed tree-based feature importance metrics, such as feature weight and gain, as well as SHapley Additive exPlanations (SHAP), a widely used AI explainability method [5].

Results

Our model achieved cross-validated areas under the receiver operator characteristic curve (AUROC) of 0.79 and 0.66 for AD predictions and OIED predictions, respectively. Similarly, cross-validated average precision (AP) scores were 0.95 and 0.37, for AD and OIED, respectively. Our model could potentially improve the AUROC of AD assessments made by practicing neuroradiologists by 5.44% and the AUROC of OIED assessments by 7.64%. Model-predicted probability of AD was higher for cases with post-mortem evidence of neurofibrillary degeneration, and trained model trees appeared to be aligned with current clinical understanding of pathological patterns of neurodegeneration, as shown in figure (b). Model explainability SHAP values were aligned with clinicians' ratings of key atrophy measures and white matter hyperintensity artifacts.

Conclusion

Our AI model demonstrated strong performance in differentiating Alzheimer's disease and other imaging-evident dementias based on T1 and T2/FLAIR imaging. Our findings align with the current understanding of neurodegeneration, underscoring the model's relevance. Such models have the potential to enhance radiologists' approaches to neuroimaging assessment, supporting the role of AI's as an effective assistive tool in clinical practice.

References

1. *Global Status Report on the Public Health Response to Dementia*. 1st ed. Geneva: World Health Organization; 2021.
2. Langbaum JB, Zissimopoulos J, Au R, et al. Recommendations to address key recruitment challenges of Alzheimer’s disease clinical trials. *Alzheimer’s & Dementia* 2023;19:696–707. https://doi.org/10.1002/alz.12737

3. Bron EE, Smits M, van der Flier WM, et al. Standardized evaluation of algorithms for computer-aided diagnosis of dementia based on structural MRI: The CADDementia challenge. *NeuroImage* 2015;111:562–79. https://doi.org/10.1016/j.neuroimage.2015.01.048
4. Xue C, Kowshik SS, Lteif D, et al. AI-based differential diagnosis of dementia etiologies on multimodal data. *Nat Med* https://doi.org/10.1038/s41591-024-03118-z
5. Sathyan A, Weinberg AI, Cohen K. Interpretable AI for bio-medical applications. *Complex Eng Syst* 2022;2:18. https://doi.org/10.20517/ces.2022.41

Images/Tables

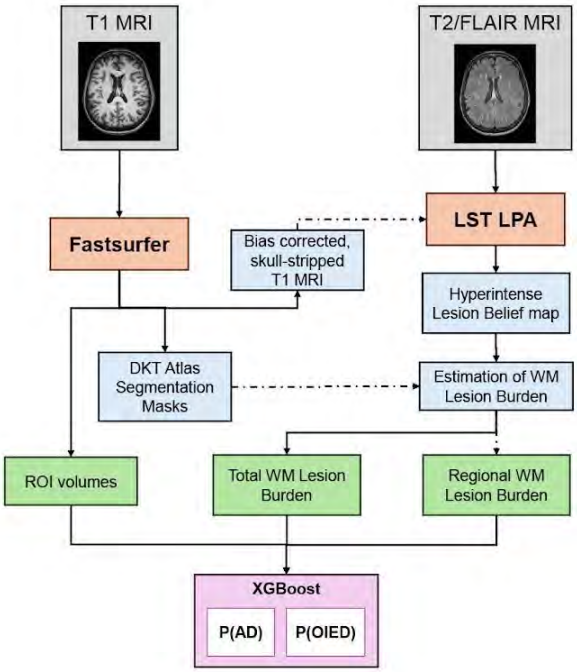

a - Image processing and modeling workflow

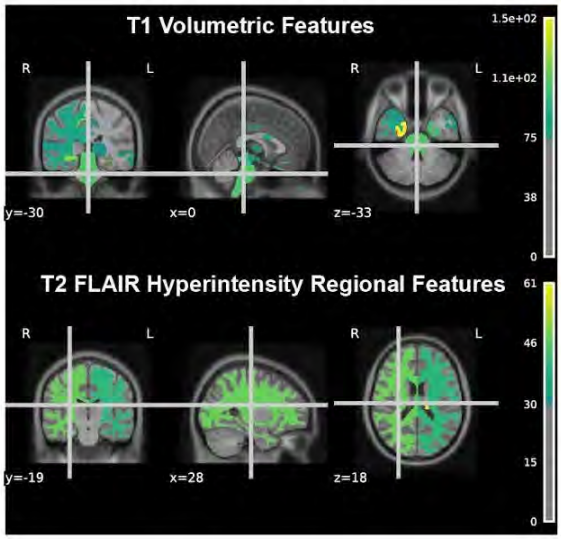

b - Feature importance heatmap for AD predictions

1228

Compensation and Clinical Productivity among Neurointerventional Radiologists

Dheeman Futela MBBS[1], Sam Payabvash MD[1], Dheeraj Gandhi MD FACR[2], Ajay Malhotra MD MMM[1]
[1]Department of Radiology, Yale School of Medicine, New Haven, CT, USA. [2]Department of Neurointerventional Radiology, University of Maryland School of Medicine, Baltimore, MD, USA

Abstract Category

Socioeconomics & Health Policy

Purpose

Recent trends in compensation and clinical productivity among neuro-interventional radiologists are not well studied, especially across different practice settings. In an environment of increasing radiology practice consolidation with continued assimilation of hospitals and healthcare systems, the divide between academics and non-academic practice has blurred. Despite increased imaging volumes, collections and unit prices may not be keeping up with increased workloads. When adjusted for inflation, reimbursement to radiologists per Medicare beneficiary declined, while wRVUs per beneficiary performed by radiologists increased. This study aimed to assess financial compensation and clinical productivity for neuro-interventional radiologists across practice types.

Materials & Methods

We studied deidentified data from the American Medical Group Association (AMGA) for providers in “Radiology: Neuro-interventional” specialty in academic and non-academic practices from survey year 2022. Median [interquartile range] clinical compensation, wRVUs (adjusted to 1.0 clinical full-time equivalent (FTE)), and compensation per unit work RVU were compared with that of interventional radiologists overall, and by practice’s academic affiliation, with non-parametric statistical analysis using Python (SciPy library).

Results

The AMGA Survey data from 2022 included responses from 146 neuro-interventional radiologists (NIR) and 894 interventional radiologists (IR). Median clinical compensation for NIRs was $528437 [IQR 457154, 602659], which was lower than that for IRs ($649363 [503506, 680493], P<0.001). Median work RVUs performed by NIRs (10640 [8362, 13306]) was greater than IRs (7119 [5183, 9375], P<0.001). Therefore, total clinical compensation per unit work RVU for NIRs ($46.5) was significantly lower than that for IRs ($81.6, P<0.001).

According to practice's academic affiliation, median compensation was greatest for NIRs without academic affiliation ($620000 [557676, 732668]), followed by teaching hospital or residency program ($530401 [491153, 604092]), and least for medical school ($495571 [383197, 557324]) (P<0.001). However, median work RVUs also showed a similar trend (P=0.03), and median clinical compensation per unit work RVU was similar across practices regardless of academic affiliation ($46-49 per unit RVU, P=0.76).

Conclusion

Our study quantified clinical compensation and productivity benchmarks for neurointerventional radiologists. Larger academic practices had lower median compensation with lower work RVUs, compared to non-academic practices. Compensation per work RVU was similar across practice types but was significantly lower than that for interventional radiologists for all practice types.

References

1. Rosenkrantz AB, Fleishon HB, Silva E, 3rd, Bender CE, Duszak R, Jr. Radiology Practice Consolidation: Fewer but Bigger Groups Over Time. J Am Coll Radiol. 2020;17(3):340-348.
2. Christensen EW, Nicola GN, Rula EY, Nicola LP, Hemingway J, Hirsch JA. Budget Neutrality and Medicare Physician Fee Schedule Reimbursement Trends for Radiologists, 2005 to 2021. J Am Coll Radiol. 2023;20(10):947-953.
3. Malhotra A, Futela D, Joshi R, et al. Academic Radiology Physician Financial Compensation in the United States: Trends and Distribution. *Radiology*. 2024;313(1):e241057.

Images/Tables

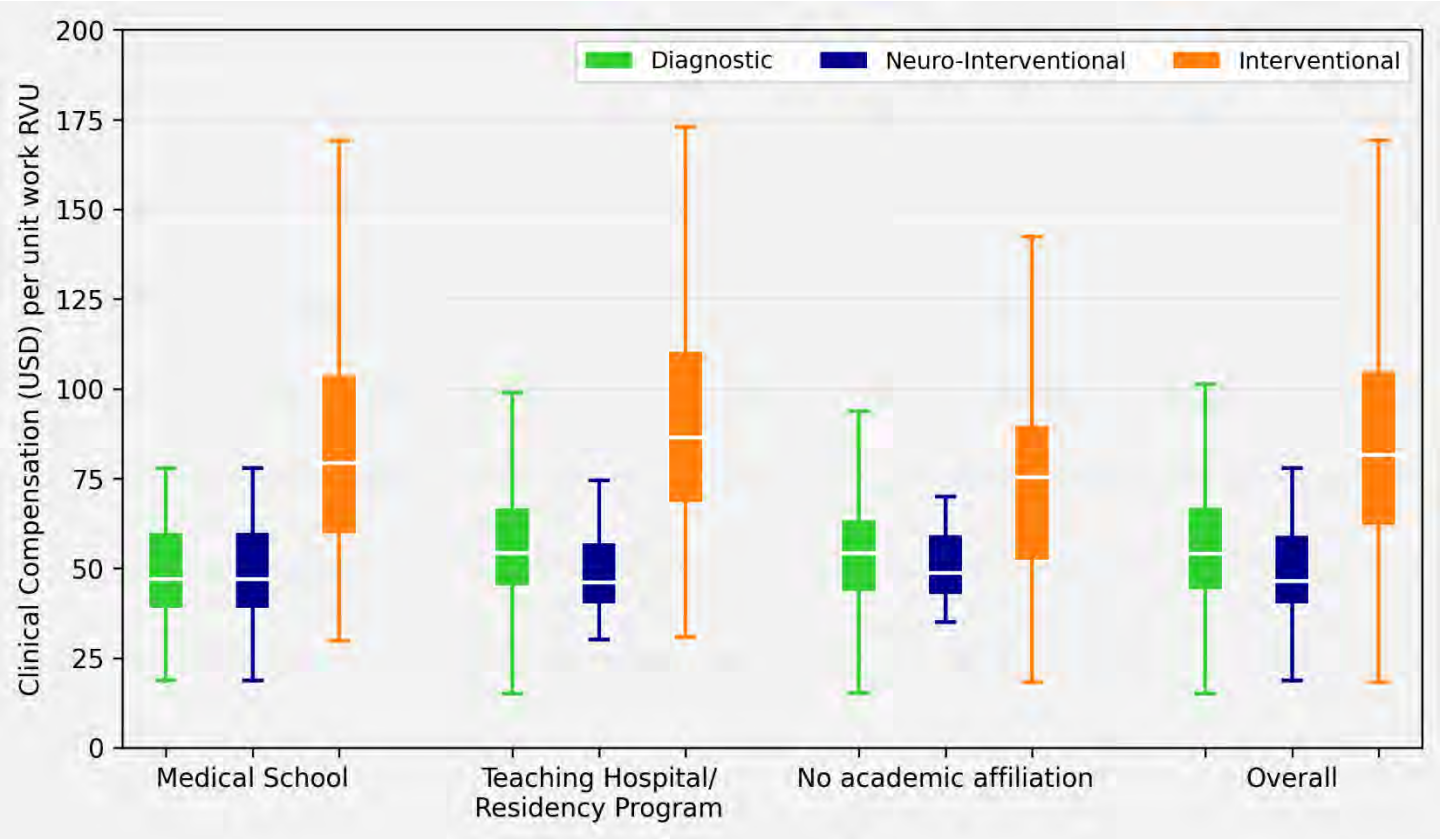

Electronic Scientific Posters

74

Carotid artery stenting intervention for enhancing blood flow in carotid disease – a prospective follow-up MRI study

Raminder Kaur[1], Paul Summers[2], William Siu[3], Xiaowei Song[1]
[1]Research and Evaluation Fraser Health Authority and Biomedical Physiology & Kinesiology Simon Fraser University, Burnaby, British Columbia, Canada. [2]ImageTech Lab, Simon Fraser University, Surrey, British Columbia, Canada. [3]Royal Columbian Hospital, New Westminister, British Columbia, Canada

Abstract Category

Functional/Advanced Imaging

Purpose

Carotid artery stenting (CAS) is an effective, less invasive alternative to carotid endarterectomy for reducing stroke risk in patients with significant stenosis,[1,2,3,4] but its impact on blood flow and brain function remains underexplored.[5] We investigated changes in internal carotid artery (ICA) blood flow pre- and post CAS to evaluate CAS effects.

Materials & Methods

This prospective MRI study enrolled patients with severe carotid stenosis (>70% occlusion) from May 2022 to July 2024. Patients underwent MRI scans pre- and post-CAS (at two and four months). CAS was performed within two weeks of baseline MRI by an experienced radiologist. The study was approved by the local institutional Research Ethics Board (H18-02495; FHA2018-058).

MRI examinations used a Philips Ingenia 3.0T with 32-channel head coil, including T1-weighted imaging and phase-contrast flow measurements, among the other sequences. Flow slices were oriented perpendicular to straight sections of both ICAs, with pulse plethysmography for cardiac synchronization. Parameters: VENC 90cm/s, 15 cardiac phases, flip angle 10°, TE/TR 5.3/9.0ms, FOV 150x100 mm, 5mm slice thickness, and 256 reconstruction matrix, 60x60 median filter for background correction.

Two raters independently drew ROIs for the right and left ICA. The mean velocity across each ROI and cardiac cycle was used to calculate the mean flow and averaged across raters.

Pre- and post-CAS digital subtraction angiography determined the degree of carotid stenosis. Lateralization of flow (Right ICA – Left ICA) was examined against stenosis differences between sides and the impact of CAS on flow ipsi- and contralateral to the treated stenosis.

Results

Of 14 participants, 11 (9 males, 5 females, aged 70–84 years (77.21 ± 4.7), with weights ranging from 59 to 127 kg (79.3 ± 17.3 kg) have returned for two-month and 4 completed the four-month follow-up, based on which further analyses were performed. Stenosis ranged from 70% to 95% (81.3% ± 7.4%), with right-sided in 3, left-sided in 7, and bilateral in 1 participant. Before CAS, flow lateralization was related to the difference in stenosis between sides, which was diminished after CAS (pre-CAS $R^2 = 0.65$; post-CAS $R^2 = 0.02$). There was a small but insignificant reduction in the mean absolute R-L flow difference (pre-CAS 59.49 ± 51.80 mL/min vs post-intervention 47.06 ± 43.40 mL/min; paired t-test $p = 0.279$). The mean extent of flow increases (seen in 5 or 45% patients) was greater than that of the decreases seen in 6 or 55% patients (increase: 25.87% ± 10.47% vs decrease: -7.45% ± 3.13%) (Figure 1a). The increase of the contralateral flows appeared to be slightly higher compared to ipsilaterally flows, although not significantly (contralateral 30.79 ± 30.64 mL/min vs ipsilateral 28.79 ± 19.92 mL/min, t-test; $p = 0.510$) (Figure 1b).

Conclusion

A pre-CAS stenosis-dependent reduction in ICA flow was aligning with previous studies. CAS eliminated the stenosis impact on the flow, though not completely. CAS maintained or increased total carotid artery blood flow, with contralateral arteries showing increases in half of participants, likely due to vascular recalibration from altered blood flow resistance. Further research is needed to understand measurement variability related to flow mapping and potential artifacts.

References

1. Kumar R, Chadha D, Chaddha A, Chauhan R, Singh N, Kamal P, et al. The safety and long-term efficacy of carotid artery stenting: an all-comers registry. Cureus 2022;14. https://doi.org/10.7759/cureus.32060
2. Piegza M, Jaworska I, Piegza J, Bujak K, Dębski P, Leksowska A, et al. Cognitive functions after carotid artery stenting—1-year follow-up study. J Clin Med 2022;11:3019. https://doi.org/10.3390/jcm11113019

3. Cremonesi A, Gieowarsingh S, Spagnolo B, Manetti R, Liso A, Furgieri A, et al. Safety, efficacy and long-term durability of endovascular therapy for carotid artery disease: the tailored-Carotid Artery Stenting Experience of a single high-volume centre (tailored-CASE Registry). EuroIntervention 2010;5:539–45. https://doi.org/10.4244/eijv5i5a95
4. Elserwi A, Amer T, Soliman N, Gaballa GM, Elmokadem AH. Efficacy and safety of carotid artery stenting for stroke prevention. Egypt J Radiol Nucl Med 2016;47:185–92. https://doi.org/10.1016/j.ejrnm.2015.10.007
5. Chinda B, Liang S, Siu W, Medvedev G, Song X. Functional MRI evaluation of the effect of carotid artery stenting: a case study demonstrating cognitive improvement. Acta Radiol Open 2021;10:2058460120988822. https://doi.org/10.1177/2058460120988822

Images/Tables

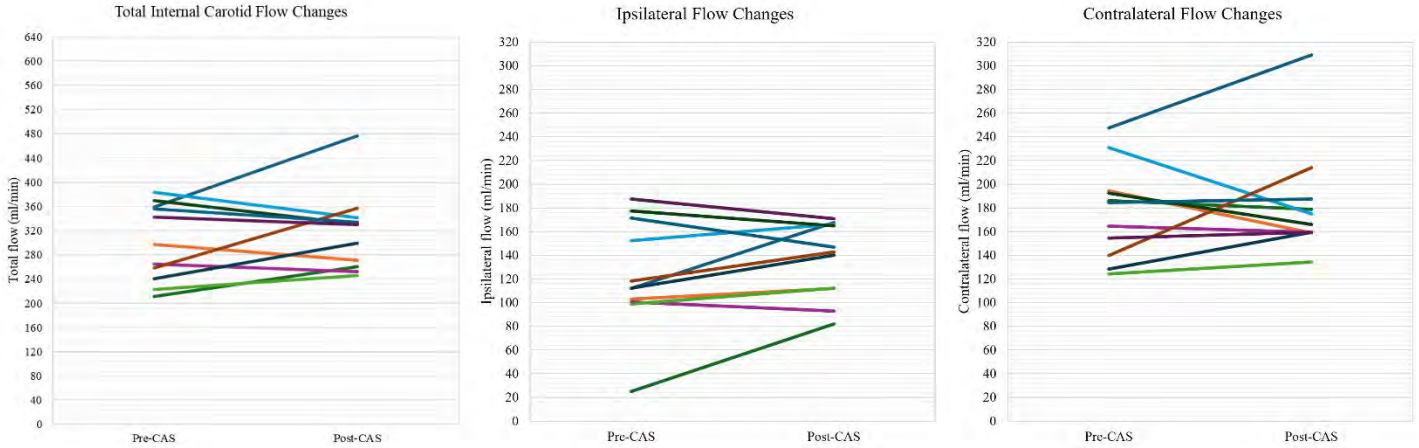

Figure 1: Total Internal Carotid and Ipsilateral/Contralateral Flow Changes Pre- and Post-CAS. (1a) The left panel shows individual changes in total internal carotid artery flow (mL/min) for each patient before and after carotid artery stenting (CAS). (1b) The middle panel illustrates flow changes on the ipsilateral side (mL/min) for each patient, and the right panel displays flow changes on the contralateral side, both measured before and after the CAS procedure.

92

EFFECT OF STRICT HEAD DOWN TILT BEDREST ON PITUITARY GLAND HEIGHT

Larry A Kramer MD[1], Dorsa Dayani MD[1], Khader M Hasan PhD[1], Eric M Bershad MD[2], Steven S Laurie PhD[3]
[1]UTHealth-Houston, Houston, Tx, USA. [2]Baylor College of Medicine, Houston, Tx, USA. [3]KBR, Houston, Texas, USA

Abstract Category

Adult Brain

Purpose

Pituitary gland deformity and loss of pituitary height have been identified in postflight astronauts (1), hypothesized to be related to increased intracranial pressure or intracranial pressure pulsatility. Microgravity-induced chronic headward fluid shift has been suggested as a root cause of intracranial compliance changes leading to altered intracranial pressure dynamics. Elevated intracranial pressure or pressure pulsatility is theorized to promote the development of an arachnoid diverticulum, which herniates into the pituitary fossa via a defect in the diaphragma sellae compressing the pituitary gland (2). We aimed to determine if chronic headward fluid induced by strict head-down tilt bed rest (HDTBR) can cause similar quantitative changes in pituitary gland height.

Materials & Methods

Control group data from two 6-degree HDTBR studies were analyzed. Study 1 collected MRI data at Baseline, 14 days into HDTBR (HDTBR-14), 52 days into HDTBR (HDTBR-52), and three days into Recovery (R+ 3), and included eight healthy adults, two women, age = 33 ± 8 years. Study 2 collected MRI data at Baseline, 15 days into HDTBR (HDTBR-15), 29 days into HDTBR (HDTBR-29), and 12 days into Recovery (R+12) and included 12 healthy adults, four women, age = 34 ± 9 years. Pituitary gland height was evaluated using a sagittal, 3D T1-MPRAGE sequence obtained on a dedicated 3T Siemens Biograph MRI scanner using a 32-channel head coil. Following the reconstruction of a true orthogonal sagittal plane of the pituitary gland using a 3D multiplanar reconstruction tool (Horosproject.org), the anterior pituitary mid-gland height at the pituitary stalk level was quantified. A paired t-test was used to evaluate changes from the baseline measurements.

Results

The pituitary baseline mean height was 6.5 ± 1.7 mm (Study 1) and 5.7 ± 1.6 mm (Study 2). From baseline measurements, Study 1 showed a decrease in mean pituitary height of 0.3 mm (p=.06) at HDTBR-14, 0.6 mm at HDTBR-52 (p<.002) and 0.2 mm at R+3 (p=.13). Study 2 from baseline measurements, showed a decrease in mean pituitary height of 0.3 mm (p=.011) at HDTBR-15, 0.5 mm at HDTBR-29 (p<.001) and 0.2 mm at R+12 (p=.02) (see scatter plot).
The pituitary baseline mean height was 6.5 ± 1.7 mm (Study 1) and 5.7 ± 1.6 mm (Study 2). From baseline measurements, Study 1 showed a decrease in mean pituitary height of 0.3 mm (p=.06) at HDTBR-14, 0.6 mm at HDTBR-52 (p<.002) and 0.2 mm at R+3 (p=.13). Study 2 from baseline showed a decrease in mean pituitary height of 0.3 mm (p=.011) at HDTBR-15, 0.5 mm at HDTBR-29 (p<.001) and 0.2 mm at R+12 (p=.02).

Conclusion

HDTBR results in progressive loss of pituitary height, which is most severe with the longest HDTBR exposure. The degree of pituitary height loss at HDTBR-52 replicates the 0.6 mm height loss found in long-duration astronauts after approximately six months of microgravity exposure. The hormonal effects of pituitary height loss are unknown in astronauts and HDTBR subjects and should be investigated in future studies.

References

1. Kramer LA, Hasan KM, Stenger MB, Sargsyan A, Laurie SS, Otto C, Ploutz-Snyder RJ, Marshall-Goebel K, Riascos RF, Macias BR. Intracranial Effects of Microgravity: A Prospective Longitudinal MRI Study. Radiology 2020;295(3):640-648. doi: 10.1148/radiol.2020191413

2. Yuh WT, Zhu M, Taoka T, Quets JP, Maley JE, Muhonen MG, Schuster ME, Kardon RH. MR imaging of pituitary morphology in idiopathic intracranial hypertension. Journal of magnetic resonance imaging : JMRI 2000;12(6):808-813.

Images/Tables

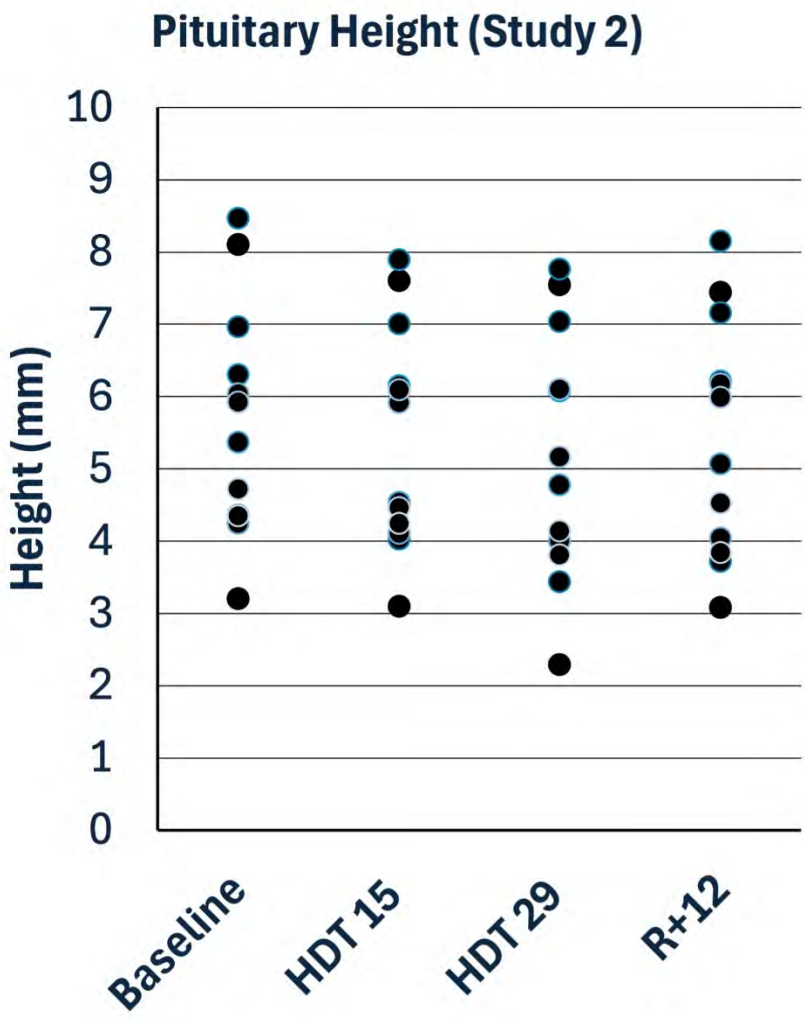

98

The cortical high-flow sign in oligodendroglioma, IDH-mutant and 1p/19q-codeleted: correlation with histological vascular density

Koji Yamashita[1], Osamu Togao[2], Kazufumi Kikuchi[1], Masaoki Kusunoki[1], Kousei Ishigami[1]
[1]Department of Clinical Radiology, Graduate School of Medical Sciences, Kyushu University, Fukuoka, Fukuoka, Japan. [2]Department of Molecular Imaging and Diagnosis, Graduate School of Medical Sciences, Kyushu University, Fukuoka, Fukuoka, Japan

Abstract Category

Adult Brain

Purpose

The presence of cortical high-flow sign with arterial spin labeling (ASL) can enhance the accuracy of preoperative diagnosis in oligodendroglioma, *IDH*-mutant, and 1p/19q-codeleted (ODG *IDHm-codel*) together with calcification, frontal lobe involvement, and cortical-based tumor. The cortical high-flow sign on ASL has been reported to be more frequent in ODG *IDHm-codel* than in diffuse glioma with *IDH*-wildtype or astrocytoma, *IDH*-mutant. Although higher glioma grades might also contribute to cortical high flow, it is unclear whether the histological vascular density or CNS WHO grade is responsible for the cortical high-flow sign. This study aimed to investigate whether the histological vascular density or CNS WHO grade was associated with the cortical high-flow sign in patients with ODG *IDHm-codel*.

Materials & Methods

This retrospective study consisted of pathologically confirmed 25 adult patients with ODG *IDHm-codel*. These 25 patients were divided into two groups based on the presence or absence of the cortical high-flow sign. MR imaging was performed on a 3.0-T unit. We implemented pseudo-continuous ASL technique with background suppression. Pair-wise subtraction of label images from control images was performed and relative perfusion maps were generated. Tumor-affecting cortices without intense contrast enhancement on conventional MR imaging were targeted for the determination of the cortical high-flow sign. Immunohistochemical staining of CD31 antibody was performed for the identification of vascular endothelial cells. A microscopic field of the most intense vascularization in each specimen under *a* ×100 objective field *was captured*. Statistical analysis included using the Mann–Whitney U test to compare the vessel number and the relative vascular density (%Vessel) between the positive and negative cortical high-flow sign groups. Next, we used Fisher's exact test to compare the difference between the presence or absence of cortical high-flow sign and CNS WHO grades. Finally, the Mann–Whitney U test was applied to compare the vessel number and %Vessel between CNS WHO grade 2 and CNS WHO grade 3 in the ODG *IDHm-codel*.

Results

A total of 25 adult patients with ODG *IDHm-codel* were divided into the positive (n =13) or negative (n = 12) cortical high-flow sign group. The vessel number and %Vessel were higher in patients with the positive cortical high-flow sign group than in patients with the negative cortical high-flow sign group ($p = 0.016$ and $p = 0.005$, respectively).

Nineteen patients were confirmed to have CNS WHO grade 2, while six were diagnosed with CNS WHO grade 3. We observed no significant differences ($p = 1.00$) in the frequency of cortical high-flow sign between CNS WHO grade 2 (10/19, 52.6%) and CNS WHO grade 3 (3/6, 50.0%). In addition, no significant differences are found in the vessel number and %Vessel between CNS WHO grade 2 and CNS WHO grade 3 ($p = 0.121$ and $p = 0.475$, respectively).

Conclusion

The cortical high-flow sign on ASL is associated with the histological vascular density in patients with ODG *IDHm-codel*. The CNS WHO grade is not associated with the histological vascular density of the cortex or the frequency of the cortical high-flow sign.

References

WHO Classification of Tumours Editorial Board. *Central Nervous System Tumours WHO Classification of Tumours, 5th Edition*. International Agency for Research on Cancer 2021

Yamashita K, Togao O, Kikuchi K, et al. Cortical high-flow sign on arterial spin labeling: a novel biomarker for IDH-mutation and 1p/19q-codeletion status in diffuse gliomas without intense contrast enhancement. *Neuroradiology* 2023;65:1415-1418

Yamashita K, Togao O, Kikuchi K, et al. The cortical high-flow sign of oligodendroglioma, IDH-mutant and 1p/19q-codeleted: comparison between arterial spin labeling and dynamic susceptibility contrast methods. *Neuroradiology* 2024;66:187-192

Images/Tables

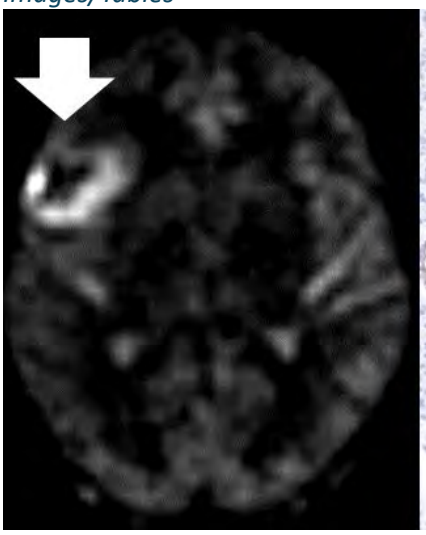

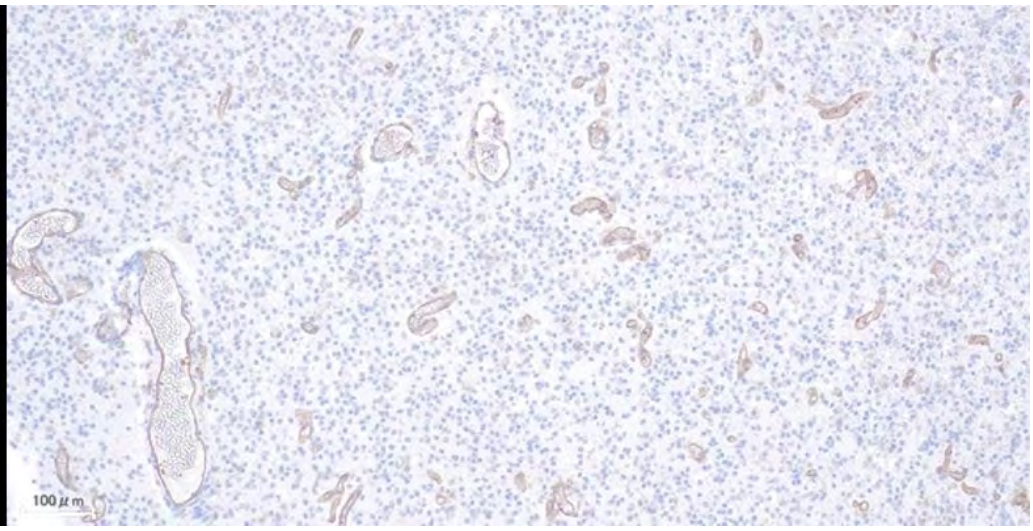

135

Physiologic steal in white matter structures of non-flow limited cerebral hemispheres as evidenced by observations of acetazolamide challenge arterial spin labeling MR

Rahim Ismail M.D.[1], Mark Manganaro D.O.[1], Pranay Rao M.D.[1], Tim Hoang B.S.[2], Matthew Bender M.D.[3], Henry Wang M.D. Ph.D.[1]

[1]University of Rochester Department of Imaging Sciences, Rochester, New York, USA. [2]University of Rochester School of Medicine and Dentistry, Rochester, New York, USA. [3]University of Rochester Department of Neurosurgery, Rochester, New York, USA

Abstract Category

Adult Brain

Purpose

Acetazolamide administration can allow for comparisons between cerebral blood flow (CBF) at baseline and after acetazolamide challenge to evaluate the cerebral vasculature. While effects of augmentation have been studied in vaso-occlusive hemispheres, little has been reported on physiologic, non-flow limited hemispheres.

Materials & Methods

Patients who underwent acetazolamide challenge MRI from 2014-2021 and a cerebral angiogram within one year were included. Patients with bilateral disease or non-diagnostic imaging artifacts were excluded. MRIs were obtained after 1 g of acetazolamide administered 5 and 10 minutes prior to acquisition. Augmentation and steal maps were generated by comparing pre and post acetazolamide CBF images. Regression analysis, Pearson correlation coefficient, two sample t-Test, Spearman and Mann Whitney U analyses were utilized for statistical evaluation.Patients who underwent acetazolamide challenge MRI from 2014-2021 and a cerebral angiogram within one year were included. Patients with bilateral disease or non-diagnostic imaging artifacts were excluded. MRIs were obtained after 1 g of acetazolamide administered 5 and 10 minutes prior to acquisition. Augmentation and steal maps were generated by comparing pre and post acetazolamide CBF images. Regression analysis, Pearson correlation coefficient, two sample t-Test, Spearman and Mann Whitney U analyses were utilized for statistical evaluation.

Results

38 Patients with unilateral cerebral vaso-occlusive disease underwent the acetazolamide challenge. Steal and T2 hyperintensities were assessed in non-flow limited hemispheres (NFLH) and flow limited hemispheres (FLH). A moderate correlation was demonstrated between NFLH steal and NFLH T2 hyperintensities (rs=0.48, p=0.0020). A weak correlation without statistical significance was demonstrated between ipsilateral T2 and contralateral T2 hyperintensities (rs= .27, p=.10). No correlation was found between steal severity or T2 hyperintensity and occlusion locations of stenosis.38 Patients with unilateral cerebral vaso-occlusive disease underwent the acetazolamide challenge. Steal and T2 hyperintensities were assessed in non-flow limited hemispheres (NFLH) and flow limited hemispheres (FLH). A moderate correlation was demonstrated between NFLH steal and NFLH T2 hyperintensities (rs=0.48, p=0.0020). A weak correlation without statistical significance was demonstrated between ipsilateral T2 and contralateral T2 hyperintensities (rs= .27, p=.10). No correlation was found between steal severity or T2 hyperintensity and occlusion locations of stenosis.38

Patients with unilateral cerebral vaso-occlusive disease underwent the acetazolamide challenge. Steal and T2 hyperintensities were assessed in non-flow limited hemispheres (NFLH) and flow limited hemispheres (FLH). A moderate correlation was demonstrated between NFLH steal and NFLH T2 hyperintensities (rs=0.48, p=0.0020). A weak correlation without statistical significance was demonstrated between ipsilateral T2 and contralateral T2 hyperintensities (rs= .27, p=.10). No correlation was found between steal severity or T2 hyperintensity and occlusion locations of stenosis.

Conclusion

Vascular steal phenomenon was demonstrated in the distal cerebral vasculature of cerebral white matter even in the absence of upstream flow limiting stenosis, suggesting an inherit vulnerability of these structures to hemodynamic fluctuations and possible contributing etiology to leukoaraiosis.

References

1. Vagal AS, Leach JL, Fernandez-Ulloa M, Zuccarello M. The acetazolamide challenge: techniques and applications in the evaluation of chronic cerebral ischemia. AJNR Am J Neuroradiol 2009;30:876–884.
2. Rowbotham GF, Little E. Circulations of the cerebral hemispheres. Br J Surg 1965;52:8–21.
3. Van den Bergh R. Centrifugal elements in the vascular pattern of the deep intracerebral blood supply. Angiology 1969;20:88–94.
4. Sleight E, et al. Cerebrovascular reactivity is a predictor of small vessel disease severity after one year in patients with mild stroke. Presented at: 2023; June 07; Toronto, Canada.

147

Exploring Ultra-Low-Field Portable Magnetic Resonance Imaging (MRI) for Brain Tumor Assessment in Low Middle Income Country: A Preliminary Study

Ahmed Altaf MBBS[1], Waqas Baqai[1], Sami Alam[1], Fatima Mubarak[1], Edmond Knopp MD[2], Khan Siddique[2]
[1]Aga Khan University, Karachi, Sindh, Pakistan. [2]Hyperfine Inc, New York, NY, USA

Abstract Category

Functional/Advanced Imaging

Purpose

This preliminary study aimed to evaluate the feasibility of Ultra Low Field portble MRI (ULF pMRI) for comprehensive assessment and volumetric analysis of brain tumors compared to conventional MRI (cMRI). To determine if ULF pMRI has adequate visualization and quantification of brain tumor morphology to guide neurosurgical decisions.

Materials & Methods

This preliminary study enrolled patients with suspected brain tumors who underwent neuroimaging from August to November 2022. Using a 0.06T ULF pMRI scanner (Hyperfine Swoop®) and a 1.5T cMRI system (General Electric Optima MR450w). The same imaging sequences were acquired on both scanners including T1-weighted, T2-weighted, FLAIR. pMRI scanning was conducted at the patient's bedside with a total protocol time of under 45 minutes. Brain tumor volumes were segmented manually on T2 and T1-weighted images and measured by a radiologist blinded to MRI type. Volumetrics were compared between pMRI and cMRI using Bland-Altman analysis and correlation coefficients to assess agreement.

Results

This study included 30 patients (mean age 41.3 ± 12.1 years) with brain tumors who underwent both ULF pMRI and cMRI. Comparative analysis revealed some variations in tumor dimensions between the two modalities among individual patients. However, a strong overall correlation was observed, with no clinically significant differences per Bland-Altman plots ($r = 0.96$, $p < 0.001$), with a mean difference of -1.2 cc (95% limits of agreement -3.4 to 0.9 cc). Importantly, ULF pMRI successfully delineated key features needed for surgical planning including tumor margins, edema, effects on the vasculature, and relationship with eloquent brain areas. Visualization of these characteristics was comparable to cMRI.

Conclusion

Our findings suggest that ULF pMRI is a viable alternative to diagnosing brain tumors. The strong correlation and negligible volumetric differences versus 1.5T MRI indicate reliable tumor delineation for surgical planning. Despite some individual variability, ULF pMRI successfully characterized tumor morphology, edema, vasculature, and eloquent area relations critical for management. Wider adoption of portable MRI could significantly improve access and outcomes in resource-limited regions lacking traditional scanners. Further validation is needed to solidify the role of ULF pMRI in the brain tumor imaging arsenal for underserved populations globally.

References

Bajwa MH, Shah MM, Khalid MU, Khan AA, Zahid N, Anis SB, et al. Distance travelled for brain tumour surgery: An low and middle income country's perspective. *J Pak Med Assoc.* 2022;72:S25–33.

2. Branco P, Ayres-Basto M, Portugal P, Ramos I, Seixas D. Brain magnetic resonance imaging: Perception and expectations of neurologists, neurosurgeons and psychiatrists. Neuroradiol J. 2014;27:261–7.

3. Brenner DJ, Hricak H. Radiation exposure from medical imaging: Time to regulate? *JAMA.* 2010;304:208–9.

4. Dewan MC, Rattani A, Fieggen G, Arraez MA, Servadei F, Boop FA, et al. Global neurosurgery: The current capacity and deficit in the provision of essential neurosurgical care. Executive summary of the global neurosurgery initiative at the program in global surgery and social change. J Neurosurg. 2018;130:1055–64.

Images/Tables

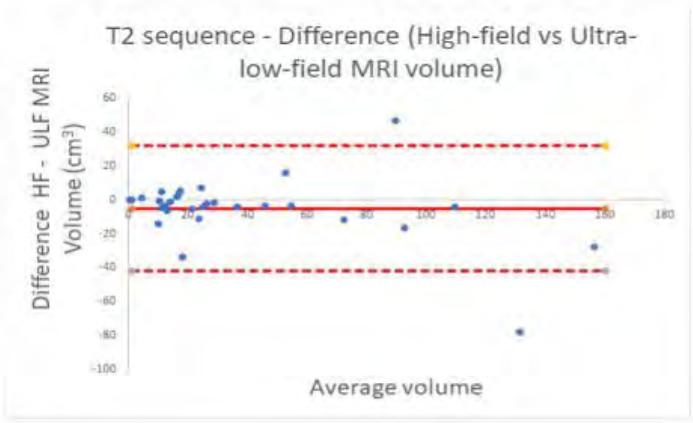

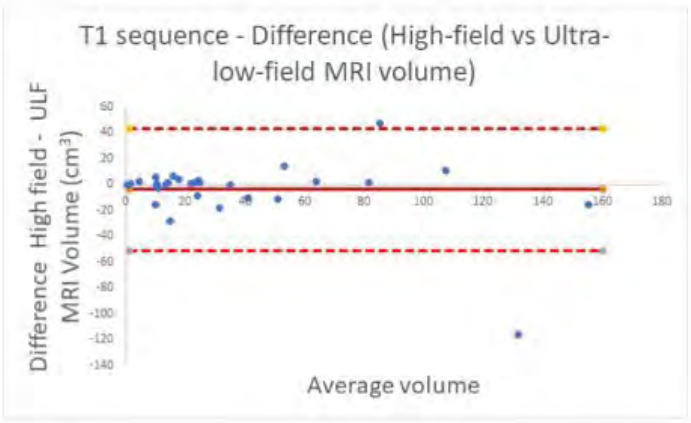

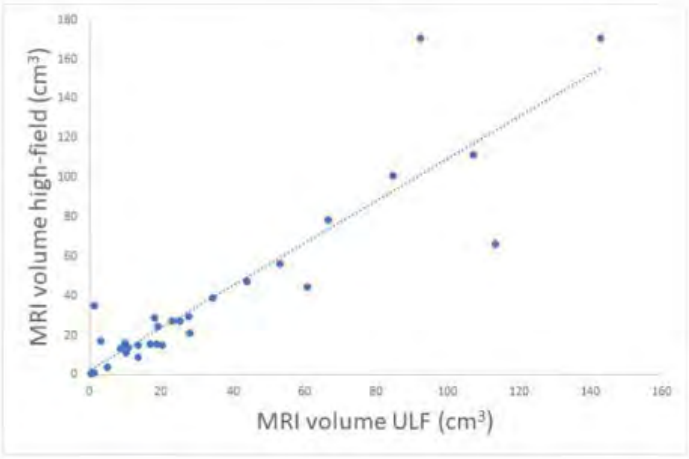

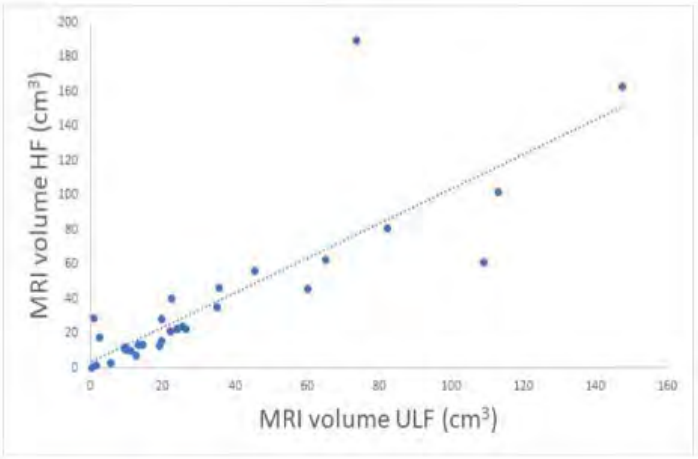

153

Characterizing the Brain Parenchymal Volume and Neurodevelopmental Outcomes of Neonates with Myelomeningocele

Marcia H Yoshikawa, Mingzhao Yu PhD, Ariadna Luviano, Henry Feldman PhD, Julia Tatz, Jason Sutin PhD, Benjamin C Warf MD, PhD, Jennifer Queally PhD, P. Ellen Grant MD, PhD, Pei-Yi Lin PhD

Boston Children's Hospital, Boston, MA, USA

Abstract Category

Pediatrics

Purpose

Myelomeningocele is the most common congenital defect of the central nervous system and is associated with long-term neurodevelopmental sequelae. Whole brain parenchymal volume (BPV) has shown to be a valuable proxy for neurocognitive outcomes in myelomeningocele patients older than 1 year of age [1], however, studies on the brain volume of neonates with myelomeningocele and its predictive value for long-term neurocognitive outcomes is still scarce. The main objective of this study is to characterize the BPV of neonates with myelomeningocele. Secondary aims include assessing whether neonatal BPV is associated with neurodevelopmental outcomes at 2 years of age.

Materials & Methods

Neonates admitted to Boston Children's Hospital for surgical management of myelomeningocele and who had a T2 brain MRI in the first 30 days of life were included. Clinical, surgical, and radiological data were collected from medical records. Neurodevelopment information was obtained from Bayley Scales Of Infant and Toddler Development (BSID) assessed at 2 years of age as part of clinical care. BSID composite scores < 85 were defined as scores at risk for neurodevelopmental delay. To obtain BPV and cerebrospinal fluid volume (CSFV), intracranial segmentation was performed by a deep-learning model. Manual ventricle segmentation served as ground truth for model training and all segmentations were reviewed and corrected for accuracy if necessary. Z-scores (zs) were generated from normative growth curves for age and sex from Peterson, et al [2].

Results

A total of 42 neonates were included (Fig 1). Females accounted for 18 (42.8%) and the mean (SD) birth weight was 3.02 (0.59) kg. Four (9.5%) patients were born preterm and 1 (2.3%) underwent prenatal myelomeningocele repair. The mean BPV zs was -0.65 (2.35) and 6 (14.3%) patients had a BPV zs two standard deviations below the norm (BPV zs ≤ -2). Female gender ($p<0.002$), prematurity ($p<0.0001$), and lower birth weight ($p=0.006$) were associated with decreased BV zs in the multivariate analysis adjusted for corrected age at MRI. At 2 years of age, 17 (53.1%) patients were at risk for cognitive delay, 15 (46.8%) were at risk for language delay, and 29 (90.6%) were at risk for motor delay. Among females, 10 (66.6%) had cognitive scores < 85, whereas among males, 7 (41.1%) had cognitive scores < 85. BV zs ≤ -2 was associated with cognitive scores at risk for delay ($p=0.04$, x2). There was no difference in gender or prematurity status between patients with BSID scores < 85 and ≥ 85.

Conclusion

In this cohort, 14.3% of the neonates with myelomeningocele had a remarkably low BV (BV zs ≤ -2). Females, low birth weight, and preterms were the subgroups at risk for decreased BV zs. At 2 years of age, most patients had neurodevelopmental scores at risk for delay when compared to the norm, with a trend towards higher frequency of 'at risk' cognitive scores in females. BV z-score ≤ -2 was the only neonatal feature associated with 'at risk' cognitive scores at 2 years of age. Our findings suggest that brain volume might be a useful predictor of long-term cognitive outcomes in a population in which the neurodevelopmental assessment is challenging.

References

[1] Mandell JG, et al. Volumetric brain analysis in neurosurgery: Part 2. Brain and CSF volumes discriminate neurocognitive outcomes in hydrocephalus. J Neurosurg Pediatr. 2015 Feb;15(2):125-32.

[2] Peterson MR, et al. Normal childhood brain growth and a universal sex and anthropomorphic relationship to cerebrospinal fluid. J Neurosurg Pediatr. 2021 Jul 9;28(4):458-468.

Images/Tables

Fig 1. Characteristics of the study population. CSF: Cerebrospinal Fluid.
*'Other' category includes thoracic and upper lumbar levels.

Clinical Variables	
Total n (%)	42 (100)
Female n (%)	18 (42.8)
Birth weight, kg (mean ± SD)	3.02±0.59
Preterm n (%)	4 (9.5)
Lesion level n (%)	
Mid lumbar	16 (38.1)
Low lumbar	17 (40.5)
Other*	9 (21.4)
Imaging variables	
Corrected age at MRI, days (mean ± SD)	7.90 ± 5.60
Brain Volume, cc (mean ± SD)	358.8 ± 57.7
Brain Volume z-score (mean ± SD)	-0.65 ± 2.35
CSF Volume, cc (mean ± SD)	133.3 ± 68.5
CSF Volume z-score (mean ± SD)	1.41 ± 1.92
Surgical variables	
Prenatal myelomeningocele closure n (%)	1 (2.3)
Postnatal surgical management n (%)	
Hydrocephalus	24 (80.9)
Tethered cord release	6 (14.3)
Posterior fossa decompression	4 (9.5)

154

Prolonged Venous Transit on Perfusion Imaging Is Associated With Prolonged Hospitalization in Acute Large Vessel Occlusion Strokes

Manisha Koneru[1], Dhairya Lakhani[2], Hamza Salim[3], Aneri Balar[3], Adam A Dmytriw[4], Adrien Guenego[5], Benjamin Pulli[6], Dylan Wolman[7], Jeremy Heit[6], Gregory Albers[6], Tobias Faizy[8], Kambiz Nael[9], Max Wintermark[10], Vivek Yedavalli[3]
[1]Cooper University Health Care, Camden, NJ, USA. [2]West Virginia University, Morgastown, WV, USA. [3]Johns Hopkins, Baltimore, MD, USA. [4]Mass Gen Brigham, Boston, MA, USA. [5]Centre Hospitalier Universitaire de Toulouse, Toulouse, Toulouse, France. [6]Stanford, Stanford, CA, USA. [7]Brown University, Providence, RI, USA. [8]Munster Hospital, Munster, Munster, Germany. [9]UCSF, San Francisco, CA, USA. [10]UT Houston, Houston, TX, USA

Abstract Category

Functional/Advanced Imaging

Purpose

Prolonged venous outflow (PVT+) is a surrogate marker for venous outflow. The PVT is defined as the presence or absence of time-to-maximum >= 10 seconds timing in either the superior saggital sinus or torcula on visual time-to-maximum maps from perfusion imaging. This novel metric has been shown to be associated with higher odds of mortality and lower liklihood of functional recovery, despite successful reperfusion with mechanical thrombectomy. The study aims to assess the relationship between PVT and length of hospitalization. We hypotheisze that PVT+ will be associated with longer lengths of stay.

Materials & Methods

Acute large vessel occlusion ischemic stroke patients successfully reperfused with thrombectomy between 01/2017-09/2022 were retrospectively reviewed. Primary outcome was length of hospitalization. Multivariable linear regressions were performed for the outcome of length of stay.

Results

Of 109 patients, the median age was 71 (IQR 62-80) years. PVT+ patients had significantly longer lengths of stay than PVT- patients (9 days (IQR 6-18) versus 6 days (IQR 4-12), p=0.03). In multivariable regressions adjusting for other clinical covariables, PVT+ was significantly associated with two additional days of hospitalization compared to PVT- patients (p=0.03).

Conclusion

Despite successful reperfusion, PVT+ was associated with two additional days of hospitalization on average comapred to PVT- patients. PVT is a simple, qualitative metric that demonstrates robustness in correlations with a range of short and long term clinical outcomes, and thus this novel surrogate of venous outflow may be informative for clinical practice.

References

Yedavalli VS, Koneru M, Hoseinyazdi M, et al. Prolonged venous transit on perfusion imaging is associated with higher odds of mortality in successfully reperfused patients with large vessel occlusion stroke. *J Neurointerv Surg* https://doi.org/10.1136/jnis-2024-021488.

Yedavalli VS, Koneru M, Balar AB, et al. Prolonged Venous Transit Is Associated With Lower Likelihood of Favorable Clinical Recovery in Reperfused Anterior Circulation Large-Vessel Occlusion Stroke. *Stroke: Vascular and Interventional Neurology* 0:e001412.

155

Lower Odds of Favorable Activity Measure Post Acute Care Scores With Prolonged Venous Transit in Reperfused Large Vessel Occlusion Strokes

Manisha Koneru[1], Dhairya Lakhani[2], Hamza Salim[3], Aneri Balar[3], Adam A Dmytriw[4], Adrien Guenego[5], Benjamin Pulli[6], Dylan Wolman[7], Jeremy Heit[6], Gregory Albers[6], Tobias Faizy[8], Kambiz Nael[9], Max Wintermark[10], Vivek Yedavalli[3]
[1]Cooper University Health Care, Camden, NJ, USA. [2]West Virginia University, Morganstown, WV, USA. [3]Johns Hopkins, Baltimore, MD, USA. [4]Mass Gen Brigham, Boston, MA, USA. [5]Centre Hospitalier Universitaire de Toulouse, Toulouse, Toulouse, France. [6]Stanford, Stanford, CA, USA. [7]Brown University, Providence, RI, USA. [8]Munster Hospital, Munster, Munster, Germany. [9]UCSF, San Francisco, CA, USA. [10]UT Houston, Houston, TX, USA

Abstract Category

Functional/Advanced Imaging

Purpose

The Activity Measure for Post-Acute Care (AM-PAC) score is commonly used in discharge planning for patients after hospitalization due to acute ischemic stroke from large vessel occlusions (AIS-LVO). Prolonged venous transit (PVT) is a binary, qualitative measure ascertained from time-to-maximum (Tmax) maps from post-processed perfusion imaging. PVT has been previously associated with 90-day mortality and unfavorable recovery. The objective to is explore the relationship between PVT on admission imaging and AM-PAC scores at discharge.

Materials & Methods

A retrospective review of a prospectively maintained database of consecutive adult AIS-LVO patients treated successfully with reperfusion therapy (modified Thrombolysis in Cerebral Infarction 2b/2c/3) was performed. PVT+ is defined as Tmax≥10s timing on Tmax maps in either the superior saggital sinus, torcula, or both venous outflow regions. The primary outcome was a favorable AM-PAC score at discharge, defined as having both Basic Mobility Score ≥17 and Daily Activity Score ≥19. Logistic regression analyses in unmatched and 1:1 propensity score-matched cohorts were performed.

Results

In 121 patients, median age was 72 (IQR 64-81) years. Favorable AM-PAC scores occurred less often in PVT+ than PVT- patients (10.5% vs. 45.8%). PVT+ was associated with a significantly reduced odds of favorable AM-PAC score in univariable (PVT+ vs. PVT- OR: 0.14, 95% CI: 0.05-0.43, p<0.001) and multivariable regressions (PVT+ vs. PVT- OR: 0.11, 95% CI: 0.03-0.48, p=0.01); the significant association furthermore persisted in the matched cohort analysis (PVT+ vs. PVT- OR: 0.73, 95% CI: 0.60-0.88, p<0.001).

Conclusion

PVT+ is independently associated with lower odds of favorable AM-PAC scores at discharge. Consistent associations with a variety of short-term and long-term clinical outcomes augment our understanding of PVT, and further establish the potential of this novel imaging parameter as an informative metric in clinical practice.

References

Yedavalli VS, Koneru M, Hoseinyazdi M, et al. Prolonged venous transit on perfusion imaging is associated with higher odds of mortality in successfully reperfused patients with large vessel occlusion stroke. *J Neurointerv Surg* https://doi.org/10.1136/jnis-2024-021488.

Yedavalli VS, Koneru M, Balar AB, et al. Prolonged Venous Transit Is Associated With Lower Likelihood of Favorable Clinical Recovery in Reperfused Anterior Circulation Large-Vessel Occlusion Stroke. Stroke: Vascular and Interventional Neurology 0:e001412.

162

Superior sagittal sinus dural arteriovenous fistula: Imaging characteristics and treatment strategies

Tze Phei Kee[1], Hong Wan Yap[1], Timo Krings[2]

[1]National Neuroscience Institute, Singapore, Singapore, Singapore. [2]Lahey Hospital & Medical Center, Massachusetts, Boston, USA

Abstract Category

Interventional

Purpose

Superior sagittal sinus dural arteriovenous fistula (SSS-DAVF) is an uncommon subset of dural arteriovenous fistulas. We aimed to explore the imaging characteristics and endovascular treatment strategies of SSS-DAVF.

Materials & Methods

Clinical and imaging data of 10 patients with SSS-DAVFs who underwent endovascular treatment in two different institutions from 2017-2022 and 2014-2023 respectively were retrospectively analyzed. The angiographic findings, endovascular treatment strategies and angiographic outcomes were evaluated and recorded.

Results

The patients with SSS-DAVFs were predominantly male with mean age at diagnosis of 54. None of these patients presented with intracranial haemorrhage. 6 out of 10 patients (60%) had previous known precipitating events. The fistulous points were located along the SSS wall or parallel parasinus wall in all cases. Bilateral cortical venous reflux was seen in 9 out of 10 cases (90%). Dural supply from the middle meningeal artery (MMA) and transosseous supply from the occipital artery (OA) or superficial temporal artery (STA) were seen in all cases, with pial-dural arterial supply in 8 out

of 10 (80%) of cases. 8 out of 10 (80%) of the SSS DAVFs were treated via transarterial access, with the remaining 20% via transvenous access. Balloon sinus protection during embolisation was used in 7 out of 10 (70%) cases. The average number of treatment sessions required for each case was 2.4, and 7 out of 10 (70%) cases achieved final complete angiographic occlusion. Complications include scalp necrosis in 2 out of 10 (20%) cases and reflux of liquid embolic material into the SSS in 1 out of 10 (10%) cases.

Conclusion

Our study found that SSS-DAVFs have shunt point(s) centred on the sinus or parallel para-sinus wall, with bilateral cortical venous reflux. Balloon sinus protection during embolisation is required in cases of SSS-DAVF with patent sinus. SSS-DAVFs appear to require complex treatment strategies and some with staged treatment sessions.

References

Chavan R, Sethi S, Sahu H, et al. Dural Arteriovenous Fistula within Superior Sagittal Sinus Wall with Direct Cortical Venous Drainage: A Systematic Literature Review. *Journal of Clinical Interventional Radiology ISVIR* 2022;06:119–30. DOI: https://doi.org/ 10.1055/s-0041-1731594

Zhang H, Su Y, Lv X. Transarterial embolization of sinus dural arteriovenous fistula using non-adhesive liquid embolic material. *Neuroradiol J.* 2023 Dec 27:19714009231224439. DOI: http://doi.org/10.1177/19714009231224439

Images/Tables

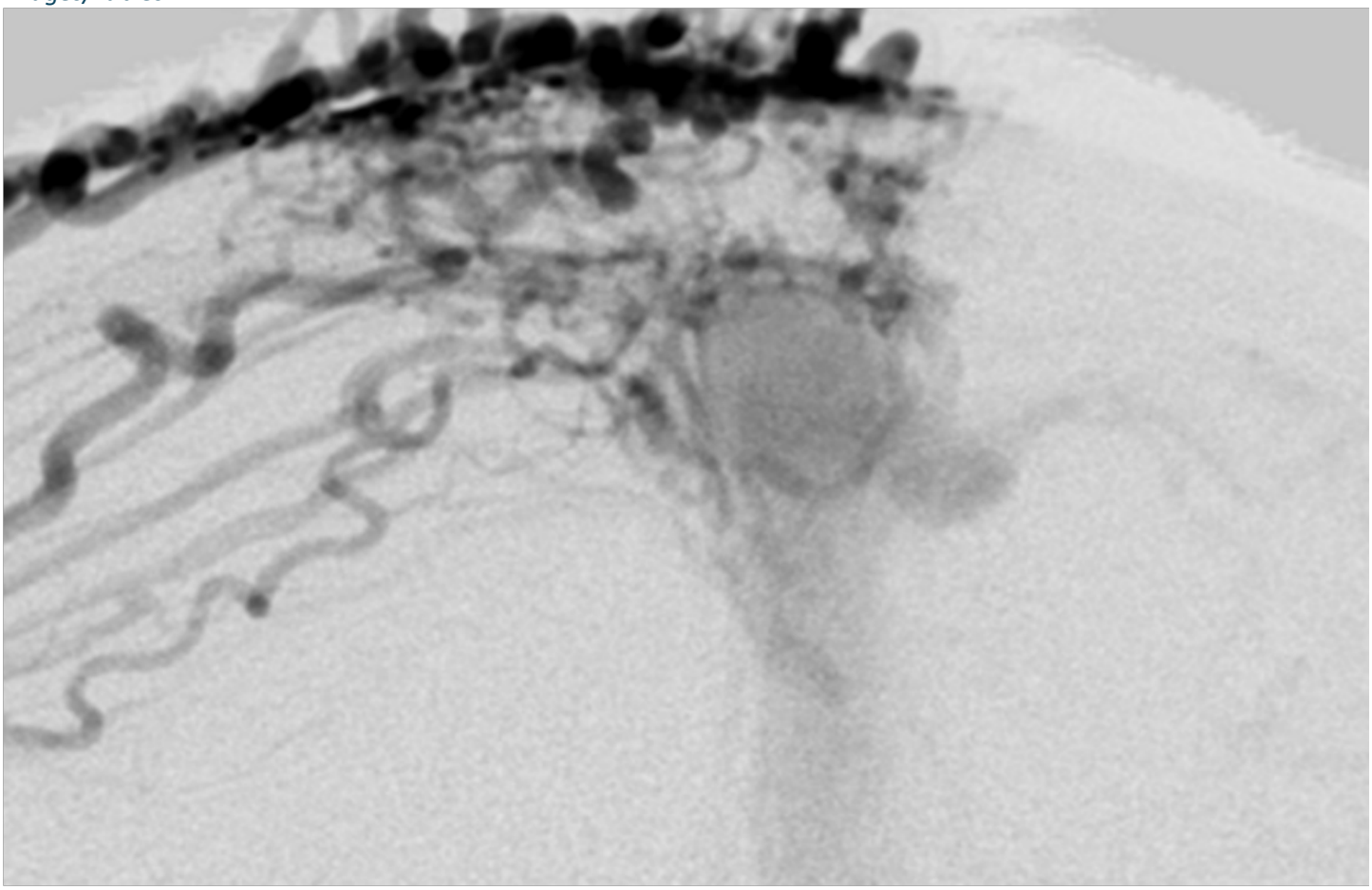

166

Selective Visualization of Perfusion of Meningiomas from the Internal and External Carotid Artery Systems by Super Selective Pseudo-Continuous Arterial Spin Labeling

Kazuhiro Tsuchiya MD[1], Miho Gomyo MD[1], Kenichi Yokoyama[1], Makoto Obara PhD[2]

[1]Kyorin University, Mitaka, Tokyo, Japan. [2]2) Philips Japan Ltd., Minato-ku, Tokyo, Japan

Abstract Category

Functional/Advanced Imaging

Purpose

Recently, 3D pseudo-continuous arterial spin labeling (pCASL) has been widely used as an arterial spin labeling (ASL) technique, with expanding applications in evaluating tumor hemodynamics. Meningioma is typically supplied by branches of the external carotid artery (ECA), although often also supplied by the internal carotid artery (ICA) branches. Predicting this vascular supply is crucial for surgical planning, and traditionally, selective DSA has been employed for this purpose. The super-selective (ss)-pCASL technique, which allows for separate labeling of the ICA and ECA, presents a potential non-invasive alternative to DSA. We present our initial experience of using ss-pCASL to attempt to separately visualize blood flow to meningiomas from the ECA and ICA systems. We also discuss the factors affecting the feasibility of distinguishing these two vascular pathways.

Materials & Methods

Since April 2024, we obtained super-selective ASL images of the ICA and ECA systems on the tumor side using ss-pCASL in addition to the conventional non-selective pCASL in 8 patients (age range: 58-88 years; 6 females and 2 males) who underwent preoperative or follow-up MR imaging at our institution. We reviewed the recorded cervical MRA used to determine the excitation pulse locations. Additionally, we evaluated patient-related factors (age, sex, tumor location, size, and histological type for surgically resected cases) that may influence the feasibility of separated blood flow visualization. The main imaging parameters for the ss-pCASL method were as follows: TR/TE, 4550/11 ms; sequence, FFE; FA, 90°; FOV, 240 x 240 mm; reconstructed matrix, 1.88 x 1.88 mm; slice thickness, 4 mm; NSA, 1; PLD, 1800 ms; acquisition time, 2:53.

Results

In 5 out of the 8 cases, blood flow from the ICA system was successfully visualized in addition to that from the ECA system. The tumors were in the convexity in 3 cases and at the lateral sphenoidal ridge in 2. The mean maximum diameter of the tumors was 48.6 mm. Surgical resection was performed in 2 cases, with the histological subtypes identified as transitional and angiomatous/microcystic meningioma, respectively. In terms of the blood flow, a predominant supply from the ECA system with minimal ICA involvement at the tumor margins in 3 cases. In 2 cases, the ECA supplied the anterior portion, while the ICA supplied the posterior portion of the tumor.

Conclusion

It is possible to super-selectively apply excitation pulses to the main trunks of the ICA and ECA using cervical MRA as a guide. In relatively large, superficially located meningiomas, such as those in the convexity or lateral sphenoid ridge, separated blood flow visualization from both the ECA and ICA systems can be observed. Due to the limited number of cases in this study, it was difficult to definitively determine the factors associated with the presence of blood flow from the ICA system. Nevertheless, this method allows for the non-invasive separation and visualization of blood flow from the ECA and ICA systems in meningiomas.

References

Yoshikane T, Hayashi K, Obara M, et al. The usefulness of super-selective arterial spin labeling for postoperative evaluation of pediatric moyamoya disease: technical note. Neuroradiology 2024;66:1391-95. doi:10.1007/s00234-024-03402-2

Images/Tables

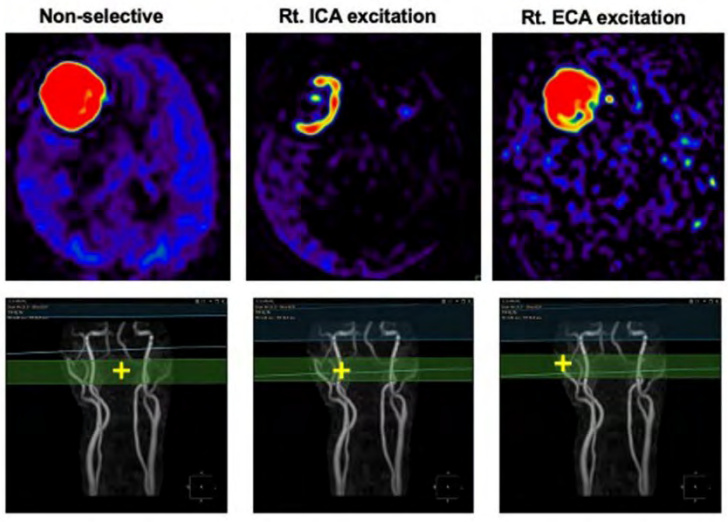

179

Improving Brain Metastasis Delineation in Radiotherapy: Comparative Volumetric Analysis of Black Blood vs. 3D T1 GRE Sequences in 1.5T MRI.

Zhao Hui Chen Zhou, Rafael D´Ambrosi, Amaya Hilario, Elena SalvadorÁlvarez, Agustín Cárdenas del Carre, Juan Romero Coronado, Carmen Lechuga Vázquez, Ana Ramos González
Hospital Universitario 12 de Octubre, Madrid, Madrid, Spain

Abstract Category

Adult Brain

Purpose

Brain metastases are the most common intracranial malignant tumors in adults, with an estimated incidence of 10-40% of patients with cancer. Because the central nervous system is a sanctuary protected by the blood-brain barrier, systemic treatments are not as effective, although new, more effective treatments are being developed. Currently, focal radiotherapy plays a central role in the management of brain metastases. Our aim is to evaluate how black blood sequences can modify radiotherapy treatment planning compared to 3D T1 post-contrast gradient-echo (GRE) sequences.

Materials & Methods

A retrospective review was performed of cranial MRI studies during a 9-month period (January 2023-September 2023) performed for the purpose of requesting simulation prior to radiotherapy treatment, including those metastases that had not previously been treated surgically. All patients were scanned on the same 1.5 T MRI GE Artist equipment, including 3D T1 post-contrast GRE (FSPGR) and 3D T1 post-contrast "black blood" sequences. A radiation oncologist and a neuroradiologist collaborated to plan radiotherapy treatment by determining the GTV and PTV volumes for each metastasis in each sequence, and comparing these volumes using statistical analysis (Wilcoxon test).

Results

During this period, 80 patients were simulated, of which only 36 patients (21 males:15 females) met the criteria of having both sequences and no previous surgical treatment. A total of 74 brain metastases were simulated. The mean GTV and PTV were 1.86cc and 3.28 cc in the 3D T1 GRE and 2.28cc and 3.78cc in the black blood sequences, with the difference being statistically significant (p value < 0.001). The mean volume differences were 0.28cc for the GTV and 0.71cc for the PTV.

Radiotherapy treatment planning volumes differ between 3D T1 GRE and black blood sequences. Black blood sequences are TSE-based sequences with the application of additional vascular suppression methods using techniques such as MSDE or DANTE. TSE sequences have a higher contrast ratio compared to GRE, which allows for better delineation of the margins of metastases and makes them appear larger. Although the differences in size may be only a few millimeters in a 2D plane, if we consider that metastases are spherical in morphology ($V = 4/3\ \pi\ r^3$), these are higher values in volume.

Conclusion

This study demonstrates that GTV and PTV volumes in brain metastasis planning are different between 3D T1 GRE and black blood sequences in a 1.5T MRI, being higher in black blood sequences.

References

Chkili, S., Lefebvre, Y., Chao, SL. et al. Optimization of workflow for detection of brain metastases at 3T: is a black-blood MTC prepared 3D T1 used alone robust enough to replace the combination of conventional 3D T1 and the black-blood 3D T1 MTC?. *Neuroradiology* 2023; 65:1133–1141. DOI: https://doi.org/10.1007/s00234-023-03143-8

Nagao E, Yoshiura T, Hiwatashi A, et al. 3D turbo spin-echo sequence with motion-sensitized driven-equilibrium preparation for detection of brain metastases on 3T MR imaging. *AJNR Am J Neuroradiol* 2011;32(4):664-70. DOI: https://doi.org/10.3174/ajnr.A2343.

Putz, F., Bock, M., Schmitt, D. et al. Quality requirements for MRI simulation in cranial stereotactic radiotherapy: a guideline from the German Taskforce “Imaging in Stereotactic Radiotherapy”. *Strahlenther Onkol* 2024; 200: 1–18 (2024). DOI:https://doi.org/10.1007/s00066-023-02183-6

Images/Tables

RESULTS: VOLUMES DIFFERENCES

	3D T1 GRE	3D T1 BLACK BLOOD	W of Wilcoxon	p value
Mean GTV	**1.86 cc (±3.21)**	**2.28 cc (±3.77)**	184	**<0.001**
Difference GTV	0,28 cc (DE 0,51)			
DICE	0.76			
Mean PTV	**3.28 cc (±4.81)**	**3.78 cc (±5.38)**	167	**<0.001**
Difference PTV	0.71 cc (DE 2.17)			
DICE	0.84			

185

Predictive Value of CT Perfusion in Identifying Ischemic Penumbra vis-à-vis final infarct size in Anterior Circulation Stroke with and without Successful Reperfusion

Rehab N Khalid MBBS, Sara DeGiorgi MD, Aman B Patel MD, Michael H Lev MD, Rajiv Gupta MD, PhD, Robert W Regenhardt MD, PhD, Quirin D Strotzer MD
Massachusetts General Hospital, Boston, MA, USA

Abstract Category

Functional/Advanced Imaging

Purpose

CT perfusion plays an important role for acute ischemic stroke imaging and treatment, but defining the ischemic penumbra and infarct core remains debated. This study examines the relationship between initial hypoperfused tissue and final infarct in patients with acute anterior circulation occlusion, with or without successful reperfusion, to assess CT perfusion's predictive spatial and volumetric accuracy and clinical value in penumbra identification.

Materials & Methods

This single-center study included patients diagnosed with acute ischemic stroke due to anterior circulation occlusion, who underwent CT perfusion scanning between 05/2021 and 02/2024. The initial imaging and follow-up non-contrast head CT scans were automatically co-registered. CT perfusion-derived ischemic core and penumbra segmentations were extracted and compared to manually segmented final infarcts on follow-up imaging. The comparison between groups with (endovascular thrombectomy [EVT] with modified Treatment in Cerebral Infarction (mTICI) score of ≥ 2b) and without successful reperfusion (no or unsuccessful EVT) were evaluated using the Dice similarity coefficient for spatial alignment and Pearson's correlation for volumetric agreement.

Results

A total of 121 patients met the inclusion criteria, of whom 49% were female (median age: 70 years, median NIHSS score: 14). Successful reperfusion was achieved in 37 patients, while 84 received no or unsuccessful EVT. Significant differences were observed between the non-reperfusion and reperfusion groups in terms of both spatial alignment (median Dice similarity coefficient: 0.52 vs. 0.29, $P < 0.001$) and volumetric agreement (Pearson's correlation between predicted and actual infarct volumes: 0.78 vs. 0.04, $P < 0.001$).

Conclusion

CT perfusion offers valuable insights into salvageable tissue in acute ischemic stroke, guiding treatments, predicting infarct volumes, and improving prognostication. Its ability to map the ischemic penumbra may enhance clinical care and aid in future stroke pathophysiology research in the large core era, potentially leading to better outcomes.

References

1. Regenhardt RW, Potter CA, Huang SS, Lev MH. Advanced Imaging for Acute Stroke Treatment Selection: CT, CTA, CT Perfusion, and MR Imaging. Radiol Clin North Am 2023;61(3):445–456. doi:10.1016/j.rcl.2023.01.003.
2. Albers GW, Marks MP, Kemp S, et al. Thrombectomy for Stroke at 6 to 16 Hours with Selection by Perfusion Imaging. N Engl J Med 2018;378(8):708–718. doi:10.1056/NEJMoa1713973.
3. Seners P, Oppenheim C, Turc G, et al. Perfusion Imaging and Clinical Outcome in Acute Ischemic Stroke with Large Core. Ann Neurol 2021;90(3):417–427. doi:10.1002/ana.26152.
4. Goyal M, Ospel JM, Menon B, et al. Challenging the Ischemic Core Concept in Acute Ischemic Stroke Imaging. Stroke 2020;51(10):3147–3155. doi:10.1161/STROKEAHA.120.030620.
5. Sarraj A, Campbell BCV, Christensen S, et al. Accuracy of CT Perfusion-Based Core Estimation of Follow-up Infarction: Effects of Time Since Last Known Well. Neurology 2022;98(21):e2084-e2096. doi:10.1212/WNL.0000000000200269.

Images/Tables

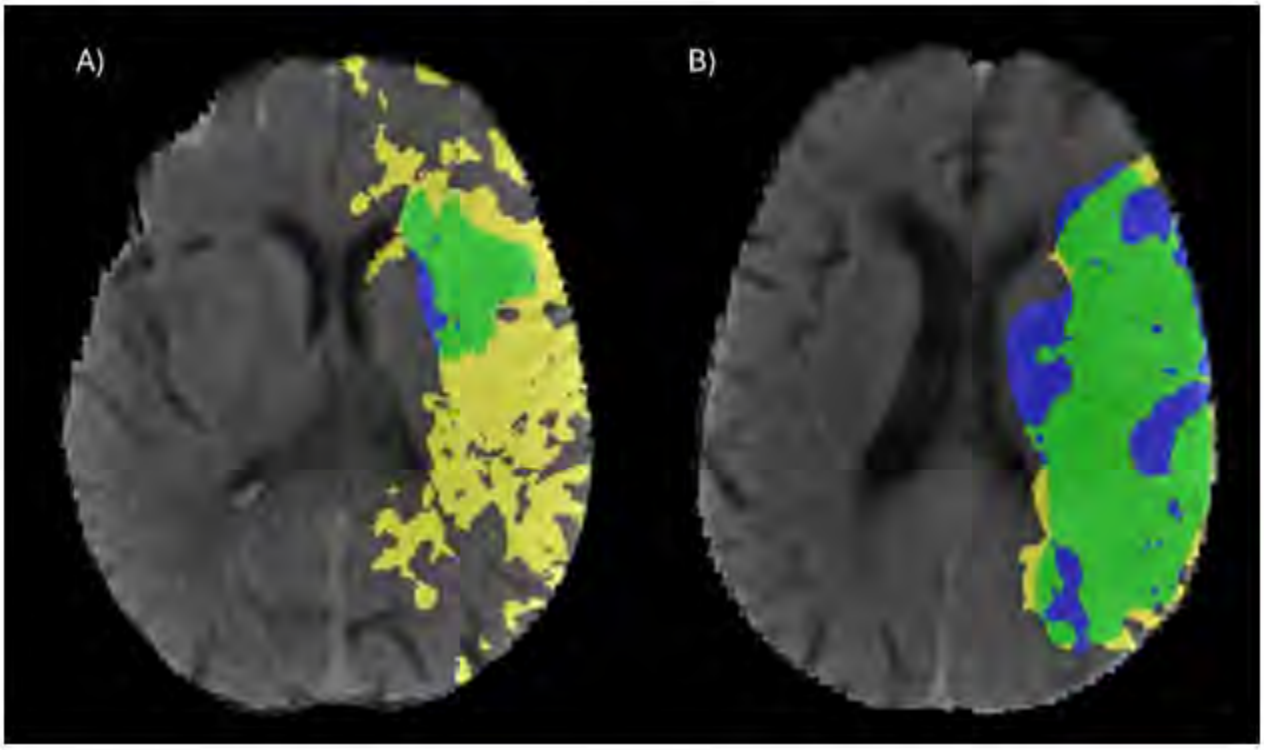

Figure 3: Example Cases. Two exemplary cases depicting the spatial overlap between the CTP-defined predicted and follow-up NCCT-defined final infarcts. CTP-defined ischemic penumbra and core were combined into a single binary segmentation. Segmentations are superimposed on brain-extracted axial sections of the follow-up NCCTs in the brain-tissue window. Color coding: green = true positive voxels, yellow = false positive voxels, blue = false negative voxels. A) A 70-year-old male patient with occlusion of the left middle cerebral artery who received endovascular thrombectomy (mTICI 3), resulting in a DSC of 0.2. B) A 93-year-old female with occlusion of the left middle cerebral artery who did not receive treatment, resulting in a relatively good spatial overlap (DSC: 0.73).

206

Telemedicine Radiology Provider Consultation Service After Outpatient Spine Imaging: A Pilot Study

Manisha Koneru[1], Hamail Iqbal[2], Lucinda Lau[2], Todd Siegal[1], Khuram Kazmi[1], Hamza A Shaikh[1]
[1]Cooper University Health Care, Camden, NJ, USA. [2]Cooper Medical School of Rowan University, Camden, NJ, USA

Abstract Category

Socioeconomics & Health Policy

Purpose

As the use of electronic medical records (EMR) increases, outpatient imaging results are now readily available to patients, often before their follow-up with the referring provider. The language within reports may cause confusion and stress from otherwise clinically insignificant findings. Furthermore, patients may feel they do not have an appropriate grasp on medical nomenclature to ask the right questions during their meeting with the provider. As patient understanding is paramount, radiology consultation services are a potential solution to allow patients to clarify questions regarding their imaging report. Still, little is known about the scale of potential benefit, optimal format, and barriers to implementing this service. The purpose of this pilot study is to explore how consultation services may enhance patient comprehension of their imaging, enabling them to make informed healthcare decisions.

Materials & Methods

Adult patients scheduled for a magnetic resonance imaging study of the lumbar spine with the complaint of “back pain” and associated diagnoses will be extracted and contacted via EMR messaging service prior to their scan and offered the opportunity to receive a free 30-minute virtual consultation with a neuroradiologist. A survey will be administered immediately following the consultation. The survey asked the following questions: patient understanding of their imaging, satisfaction with the service, preference for visit duration, and amount willing to pay for the service. Descriptive analyses were used to summarize survey responses.

Results

Of 7 participants, median age was 59 years (IQR 41-76), and 85.7% were female. 42.9% of patients listed bachelor’s degree as their highest level of education. Most were referred by pain management (42.9%). On a scale of 1 (none) to 5 (high), median rating of patient understanding of the imaging pre-consultation was 3 (IQR 2-4) and post-consultation was 5 (IQR 5-5). All agreed that the service was helpful and would opt for a similar service in the future. Majority had no preference whether on virtual or in-person meetings (57.1%). Patients noted that the highest they would pay was $40-$60 (28.6%) or $80-100 (28.6%), with a high degree of variation in reported preferences. Overall, all patients reported the highest satisfaction score with this experience.

Conclusion

Use of radiology consultation services enhance health competency, allowing for better patient satisfaction and care. The virtual setting allows for greater accessibility and is generally accepted by most patients. Furthermore, there is potential to enact this as a billable telemedicine service, as evident through patient willingness to pay for the service. However, the billing code for radiology interpretation should be evaluated to see if this additional service can be billed separately. This pilot study is limited by small sample size and extensive process of patient enrollment and scheduling through EMR review. Automation of scheduling through EMR integration to select pre-set time slots can optimize the workflow. Future studies with a larger cohort can explore the impact of this novel consultation service on patient experiences.

References

Suresh K, Hill PA, Kahn CE Jr, et al. Quality Improvement Report: Design and Implementation of a Radiology E-Consult Service. *Radiographics* 2023;43:e230139.

Freeman CW, O’Brien S, Levin D, et al. Striving to be of Value: Building a Virtual Radiology Consult Service for Patients. *Curr Probl Diagn Radiol* 2023;52:519–21.

217

Choroid plexus volume, CSF inflammatory markers, amyloid and tau burden in the Alzheimer's disease continuum: mediation and associations

Yoon Seong Choi MD PhD, Wenhao Han M.Sc, Megan Ching M.Sc
National University of Singapore, Singapore, Singapore, Singapore

Abstract Category

Adult Brain

Purpose

The purpose of this study is to investigate the mediating role of choroid plexus volume (ChPV) between CSF inflammatory markers, amyloid, and tau burden across the Alzheimer's disease (AD) spectrum. Additionally, the study aims to compare the correlation of ChPV with amyloid burden between CSF and PET imaging, and assess the diagnostic value of ChPV in detecting CSF amyloid-positive/PET amyloid-negative (CSF A+/PET A-) discrepancies among PET amyloid-negative individuals.

Materials & Methods

This study analyzed data from the Alzheimer's Disease Neuroimaging Initiative (ADNI) to examine the relationship between choroid plexus volume (ChPV), cerebrospinal fluid (CSF) inflammatory markers, and amyloid and tau burden in Alzheimer's disease (AD). A total of 1,507 participants with baseline T1-weighted MRI and CSF amyloid-beta-42 (Aβ42) levels were included. Two subcohorts were analyzed: ADNI-sc1, which focused on 17 CSF inflammatory markers, and ADNI-sc2, which focused on amyloid PET scans. ChPV and hippocampal volumes were normalized and adjusted for MRI scanner differences, and linear regression models were used to assess the associations between ChPV and CSF inflammatory markers. Mediation analysis explored ChPV's role between CSF markers and amyloid/tau burden. Kendall's correlation coefficients compared the relationships between ChPV, CSF Aβ42, and PET amyloid, and receiver operating characteristic (ROC) analysis evaluated ChPV's diagnostic performance in identifying CSF A+/PET A- discrepancies.

Results

ChPV was negatively associated with several CSF inflammatory markers, including soluble triggering receptor expressed on myeloid cells 2 (TREM2; $\beta = -0.65$, SE = 0.09, $P < 0.001$), soluble tumor necrosis factor receptors 1 (TNFR1; $\beta = -0.38$, SE = 0.08, $P < 0.001$) and 2 (TNFR2; $\beta = -0.29$, SE = 0.09, $P = 0.026$), transforming growth factor β1 (TGFβ1; $\beta = -0.42$, SE = 0.13, $P = 0.023$), soluble vascular cell adhesion molecule 1 (VCAM1; $\beta = -0.56$, SE = 0.15, $P = 0.004$), complement 3 (C3; $\beta = -0.58$, SE = 0.14, $P < 0.001$), and factor H (FH; $\beta = -0.37$, SE = 0.11, $P = 0.011$). Mediation analysis indicated that ChPV partially or fully mediated the effects of CSF inflammatory markers on Aβ42, the effects of CSF Aβ42 on inflammatory markers, and the effects of CSF Aβ42 on phosphorylated tau, with mediation proportions ranging from 18% to 45%. ChPV demonstrated stronger correlations with CSF Aβ42 (tau = -0.17, $P < 0.001$) than with amyloid PET centiloids (tau = -0.05, $P = 0.030$, $P = 0.006$ by Steiger's z-test). In non-demented, PET amyloid-negative individuals, ChPV improved the accuracy for identifying CSF A+/PET A- discordance, with a significant increase in the area under the ROC curve as compared to amyloid PET centiloids alone (AUC 0.591 vs. 0.643, $P = 0.022$).

Conclusion

Our study demonstrated that ChPV mediates the relationship between CSF inflammatory markers, amyloid, and tau pathology, and is more strongly correlated with CSF Aβ42 than amyloid PET centiloids. ChPV also improved the prediction of CSF/PET discordance in PET A- participants, highlighting its potential as a biomarker for early detection of AD pathology.

References

1. Li Y, Zhou Y, Zhong W, et al. Choroid Plexus Enlargement Exacerbates White Matter Hyperintensity Growth through Glymphatic Impairment. Annals of Neurology 2023;94:182-195.
2. Toledo JB, Korff A, Shaw LM, Trojanowski JQ, Zhang J. Low levels of cerebrospinal fluid complement 3 and factor H predict faster cognitive decline in mild cognitive impairment. Alzheimers Res Ther 2014;6:36.
3. Palmqvist S, Zetterberg H, Mattsson N, et al. Detailed comparison of amyloid PET and CSF biomarkers for identifying early Alzheimer disease. Neurology 2015;85:1240-1249.
4. Kleinberger G, Yamanishi Y, Suárez-Calvet M, et al. TREM2 mutations implicated in neurodegeneration impair cell surface transport and phagocytosis. Sci Transl Med 2014;6:243ra286

Images/Tables

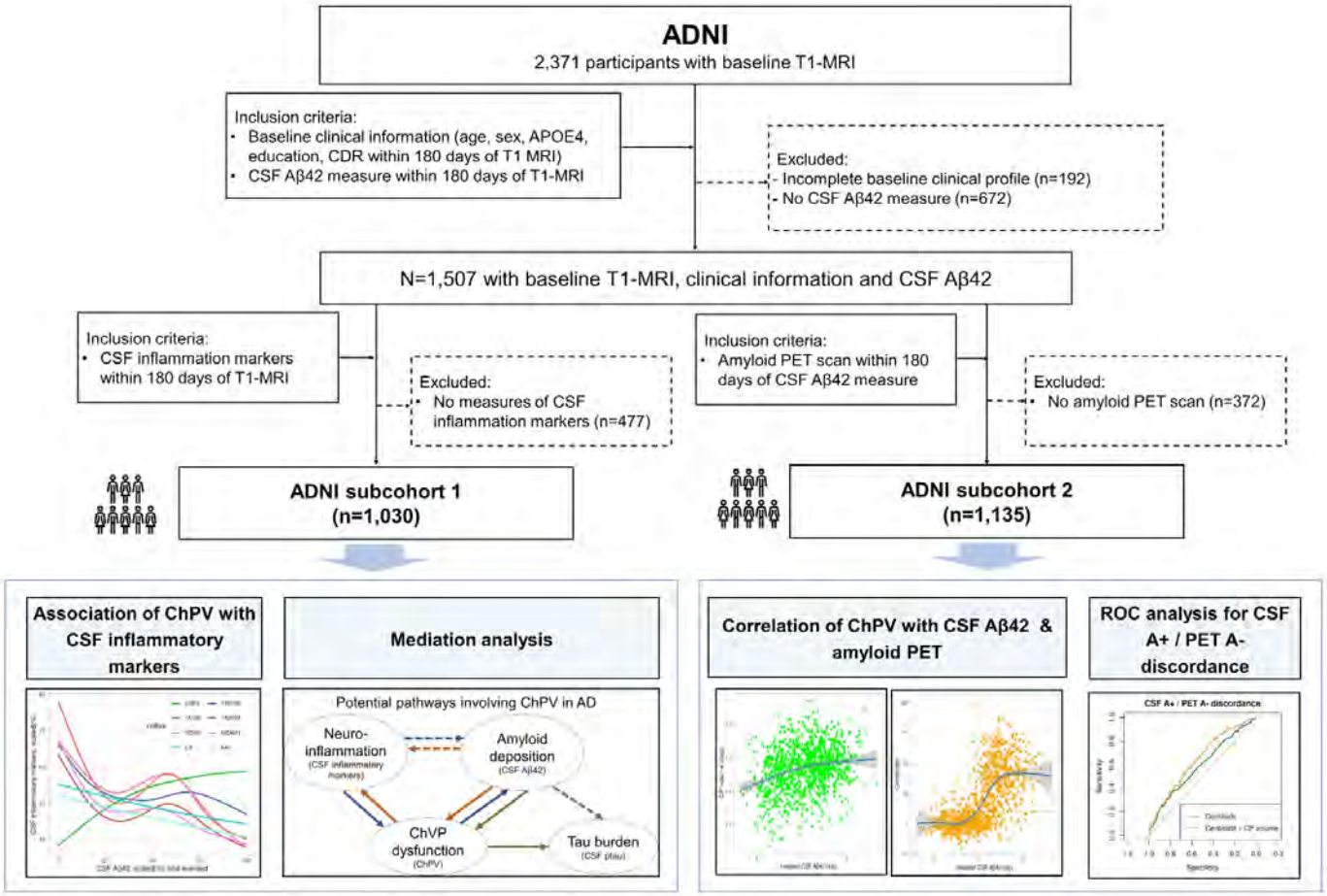

220

Postoperative [^{68}Ga]-DOTATATE-Guided Management in Patients with Gross Totally Resected WHO Grade 2 Meningioma

Kellen Vu BS[1], Se Jung Chris Chang MD[2], Hannah Otis BA[1], Benjamin Liechty MD[1], Arindam RoyChoudhury PhD[1], Rajiv S Magge MD[1], Susan C Pannullo MD[1], Jonathan PS Knisely MD[1], Theodore H Schwartz MD[3], Jana Ivanidze MD, PhD[1]
[1]Weill Cornell Medicine, New York, New York, USA. [2]Memorial Sloan-Kettering Cancer Center, New York, New York, USA. [3]New York, New York, USA

Abstract Category

Adult Brain

Purpose

Meningiomas are the most common primary intracranial neoplasms, primarily treated with surgical resection, with subsequent need for radiotherapy (RT) determined by WHO grade and resection extent. In WHO grade 2 meningiomas post gross total resection (GTR), there is no uniform standard of care; ongoing randomized prospective studies are evaluating the need for RT to the resection cavity. Resection extent has to date been primarily determined based on MRI alone. While MRI has excellent anatomic resolution, it lacks sensitivity and specificity in distinguishing residual or recurrent tumor from post-treatment scarring and inflammation.[1]

[^{68}Ga]-DOTATATE is a PET radiotracer targeting somatostatin receptor 2 (SSTR2), a highly sensitive and specific meningioma biomarker that has demonstrated clinical utility in meningioma diagnosis, radiotherapy planning, and response assessment.[2,3] We hypothesized that [^{68}Ga]-DOTATATE PET/MRI could confirm GTR more accurately than MRI alone, thereby obviating the need for resection cavity RT and increasing progression-free survival (PFS) in patients subsequently managed with active surveillance when compared to historical data of patients with GTR determined by MRI alone.

Materials & Methods

We selected patients from our prospective observational registry of individuals with meningioma and other SSTR2-positive brain tumors who underwent brain DOTATATE PET and met the inclusion criteria of (1) WHO grade 2 meningioma, (2) GTR demonstrated by postoperative brain PET/MRI or PET/CT with contemporaneous brain MRI, and (3) subsequent postoperative management through active surveillance alone (with serial contrast-enhanced MRI). Kaplan-Meier survival analysis was performed to determine PFS based on the Response Assessment in Neuro-Oncology (RANO) criteria.

Results

30 subjects met the inclusion criteria. The average preoperative RANO two-dimensional tumor size product was 11.5 cm^2 (range 3.0–28.6 cm^2). 15/30 (50%) of patients had tumors centered in the skull base, 9/30 (30%) had tumors located along the convexity, and 6/30 (20%) had tumors along the falx. 27/30 (90%) of patients underwent craniotomy, and 3/30 (10%) underwent endoscopic endonasal resection.

MRI follow-up data were available for a mean of 23 months after surgery (range 3–61 months). Kaplan-Meier analysis demonstrated a 30-month PFS of 100%. At maximum follow-up, our cohort demonstrated a 5-year PFS of 83.3%. This represents an increase in PFS compared to benchmark MRI-based studies such as Aghi et al. (p = 0.014), which reported a 5-year PFS of 59%, and Pan et al. (p = 0.069), which reported a 3-year PFS of 63%.[4,5]

Conclusion

We found that active surveillance after GTR as determined by [^{68}Ga]-DOTATATE PET/MRI resulted in excellent PFS in patients with WHO grade 2 meningiomas. Our findings lay the foundation for a paradigm shift in the management of WHO grade 2 meningiomas toward PET/MRI-guided decision making, obviating the need for RT in patients with PET-proven GTR and thereby decreasing morbidity, while increasing PFS compared to MRI-guided management alone.

References

1. Rachinger W, Stoecklein VM, Terpolilli NA, et al. Increased 68Ga-DOTATATE Uptake in PET Imaging Discriminates Meningioma and Tumor-Free Tissue. *J Nucl Med* 2015;56:347–53.
2. Mahase SS, O'Brien DAR, No D, et al. [68Ga]-DOTATATE PET/MRI as an adjunct imaging modality for radiation treatment planning of meningiomas. *Neuro-Oncol Adv* 2021;3:vdab012.
3. Ivanidze J, Chang SJ, Haghdel A, et al. [Ga68] DOTATATE PET/MRI-guided radiosurgical treatment planning and response assessment in meningiomas. *Neuro-Oncol* 2024;26:1526–35.
4. Aghi MK, Carter BS, Cosgrove GR, et al. Long-term recurrence rates of atypical meningiomas after gross total resection with or without postoperative adjuvant radiation. *Neurosurgery* 2009;64:56–60; discussion 60.
5. Pan PC, Pisapia DJ, Ramakrishna R, et al. Outcomes following upfront radiation versus monitoring in atypical meningiomas: 16-year experience at a tertiary medical center. *Neuro-Oncol Adv* 2021;3:vdab094.

Images/Tables

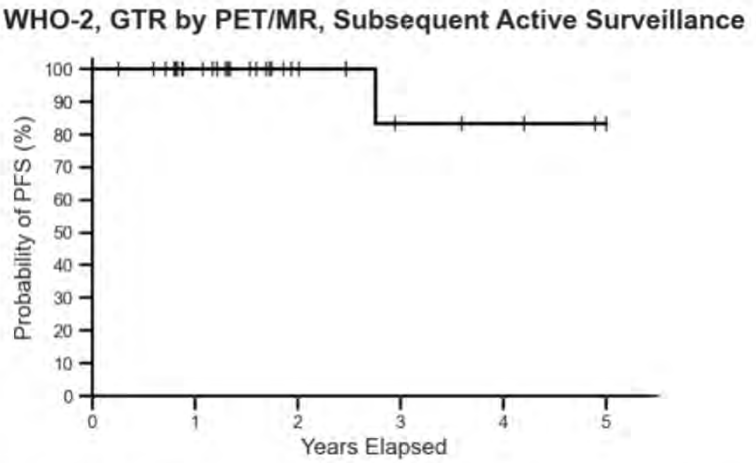

Figure 1. The PFS was 100% at 30 months, at which point one patient progressed. The 5-year PFS was 83.3%.

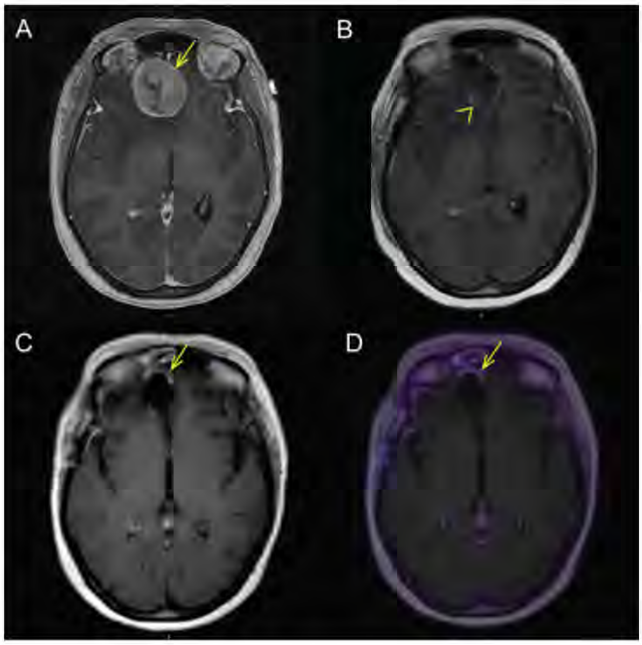

Figure 2. Representative images of a patient with WHO grade 2 meningioma who underwent a right frontotemporal craniotomy. **(A)** Preoperative axial T1-weighted postcontrast MRI demonstrating a heterogeneously enhancing extra-axial dural based mass (arrow) in the right anterior cranial fossa with surrounding edema and mass effect. **(B)** One-day postoperative axial T1-weighted postcontrast MRI demonstrating expected postoperative changes including linear enhancement along the resection cavity margin (arrow) and reduced mass effect. **(C, D)** Three-months postoperative axial T1-weighted postcontrast MRI (C) and corresponding fused [^{68}Ga]-DOTATATE PET/MRI (D) demonstrate interval near-resolution of linear enhancement along the posterior resection cavity margin, with slightly more conspicuous enhancement along the anterior margin (arrow). This demonstrates only minimal [^{68}Ga]-DOTATATE avidity with a standardized uptake value (SUV) up to 1.9, below the diagnostic threshold for meningioma. There is no intracranial focus of abnormal [^{68}Ga]-DOTATATE avidity to suggest residual or recurrent tumor. Fused PET/MR image utilizes a rainbow color scale with a maximum SUV range of 0 to 15.

226

Acquisition of Susceptibility-Sensitive Sequences for Central Vein Sign Detection: A Systematic Review of MRI Protocols

Ariel Kerpel MD[1], Shai Shrot MD[1], Gahl Greenberg MD[1], Shir Tal MD[1], Chen Hoffmann MD[1], Fang F Yu MD[2]
[1]Sheba Medical Center, Tel Hashomer, Israel, Israel. [2]University of Texas Southwestern Medical Center, Dallas, Texas, USA

Abstract Category

Adult Brain

Purpose

With the 2024 revision of the McDonald criteria, susceptibility-sensitive MRI sequences for detecting the central vein sign (CVS) have become increasingly important in the early diagnosis of multiple sclerosis.
This study aims to systematically review and consolidate data on susceptibility-sensitive sequence MRI protocols used in published research investigating the CVS, to identify standardized approaches and improve reproducibility.

Materials & Methods

A comprehensive search was conducted using PubMed databases. We included original research studies focused on brain CVS detection. Non-English studies were excluded. Following PRISMA guidelines, 460 abstracts were screened, 106 full-text articles were assessed, and 60 studies were included in the final review. Protocols from the selected studies were summarized and compared to identify commonalities and variations.

Results

The most commonly employed sequences were SWI, 3D T2* EPI, and SWAN-venule. However, variations in parameters such as resonance and echo times, voxel size, field strength, receiver coil, and contrast administration were frequently noted. Moreover, the lack of detailed protocol information across multiple studies hinders reproducibility. A direct comparison between SWI and T2* EPI at 7T demonstrated higher sensitivity to CVS with T2*, though inconsistencies in sequence protocols within this retrospective study limit the conclusions' strength. This comparison has yet to be explored at 3T, which holds greater clinical relevance for routine diagnostic use. Another study found that T2* EPI outperformed SWAN-venule and T2* GRE.

Conclusion

Different sequences were used for CVS detection, but inconsistencies in imaging parameters and a lack of detailed protocols limit reproducibility. Preliminary evidence suggests that 3D T2* EPI may be superior to SWAN-venule and T2* GRE for CVS detection on 3T MRI and to SWI on 7T MRI. However, further investigation is needed, particularly in comparing SWI with 3D T2* EPI on 3T MRI, to ensure broader clinical applicability.

References

1. Sati P, Oh J, Constable RT, Evangelou N, Guttmann CR, Henry RG, Klawiter EC, Mainero C, Massacesi L, McFarland H, Nelson F, Ontaneda D, Rauscher A, Rooney WD, Samaraweera AP, Shinohara RT, Sobel RA, Solomon AJ, Treaba CA, Wuerfel J, Zivadinov R, Sicotte NL, Pelletier D, Reich DS; NAIMS Cooperative. The central vein sign and its clinical evaluation for the diagnosis of multiple sclerosis: a consensus statement from the North American Imaging in Multiple Sclerosis Cooperative. Nat Rev Neurol. 2016 Dec;12(12):714-722. doi: 10.1038/nrneurol.2016.166. Epub 2016 Nov 11. PMID: 27834394.
2. Okromelidze L, Patel V, Singh RB, Lopez Chiriboga AS, Tao S, Zhou X, Straub S, Westerhold EM, Gupta V, Agarwal AK, Murray JV, Desai A, Sandhu SJS, Marin Collazo IV, Middlebrooks EH. Central Vein Sign in Multiple Sclerosis: A Comparison Study of the Diagnostic Performance of 3T versus 7T MRI. AJNR Am J Neuroradiol. 2023 Dec 29;45(1):76-81. doi: 10.3174/ajnr.A8083. PMID: 38164557; PMCID: PMC10756573.
3. Samaraweera AP, Clarke MA, Whitehead A, Falah Y, Driver ID, Dineen RA, Morgan PS, Evangelou N. The Central Vein Sign in Multiple Sclerosis Lesions Is Present Irrespective of the T2* Sequence at 3 T. J Neuroimaging. 2017 Jan;27(1):114-121. doi: 10.1111/jon.12367. Epub 2016 Jun 14. PMID: 27300318.
4. Montalban Xavier: "Revised McDonald criteria 2023", European Committee for Treatment and Research in Multiple Sclerosis (*ECTRIMS) Annual Congress 2024*. 18 September, 2024, Copenhagen, Denmark. Clinical Scientific Session.

229

Volume Contracted State, Mortality, and Functional Outcomes in Patients with Acute Ischemic Stroke due to Large Vessel Occlusion

Hamza Adel Salim MD[1], Mona Bahouth MD[2], Dhairya A. Lakhani MD[3], Janet Mei MD[2], Nathan Z. Hyson MD[2], Gregory W Albers MD[4], Tobias D. Faizy MD[5], Jeremy J. Heit MD PhD[4], Max Wintermark MD[1], Vivek Yedavalli MD[2]

[1]Department of Neuroradiology, MD Anderson Medical Center, Houston, TX, USA. [2]Department of Radiology, Division of Neuroradiology, Johns Hopkins Medical Center, Baltimore, MD, USA. [3]Department of Radiology, West Virginia University, Morgantown, WV, USA. [4]Department of Neuroimaging and Neurointervention, Stanford Medical Center, Palo Alto, CA, USA. [5]Department of Radiology, Neuroendovascular Program, University Medical Center Münster, Münster, Münster, Germany

Abstract Category

Head & Neck

Purpose

Acute ischemic stroke (AIS) is a leading cause of mortality and disability globally, with volume contracted state (VCS), as indicated by an elevated blood urea nitrogen to creatinine (BUN/Cr) ratio, potentially influencing outcomes. This study investigates the association between VCS and clinical outcomes in patients with AIS due to large vessel occlusion (LVO).

Materials & Methods

A retrospective cohort study was conducted involving 298 patients with LVO-AIS from two comprehensive stroke centers. Patients were divided into two groups based on BUN/Cr ratio: ≤20 (n = 205) and >20 (n = 93). Primary outcomes included 90-day mortality and favorable functional outcomes, defined as a modified Rankin Scale (mRS) score of 0-2. Secondary outcomes included the successful reperfusion, hemorrhagic transformation, and NIHSS score at discharge.

Results

Patients with a BUN/Cr ratio >20 had significantly higher 90-day mortality (35% vs. 13%, $p < 0.001$) and this association remained significant after adjusting for confounding factors (OR 2.20; 95% CI 1.11-4.39; $p = 0.024$). However, VCS was not significantly associated with favorable functional outcomes at 90 days (OR 1.28; 95% CI 0.67-2.51; $p = 0.46$). Age and initial stroke severity were more strongly associated with long-term functional outcomes.

Conclusion

An elevated BUN/Cr ratio >20, indicative of VCS, is associated with increased 90-day mortality in patients with LVO-AIS, but not with favorable functional outcomes. These findings suggest the need for further research into the role of hydration management in improving survival in AIS patients, potentially informing future treatment protocols.

References

Yedavalli V, Salim HA, Musmar B, et al. Pretreatment Predictors of Very Poor Clinical Outcomes in Medium Vessel Occlusion Stroke Patients Treated with Mechanical Thrombectomy. *Int J Stroke*. Published online July 29, 2024:17474930241270524. doi:10.1177/17474930241270524

Images/Tables

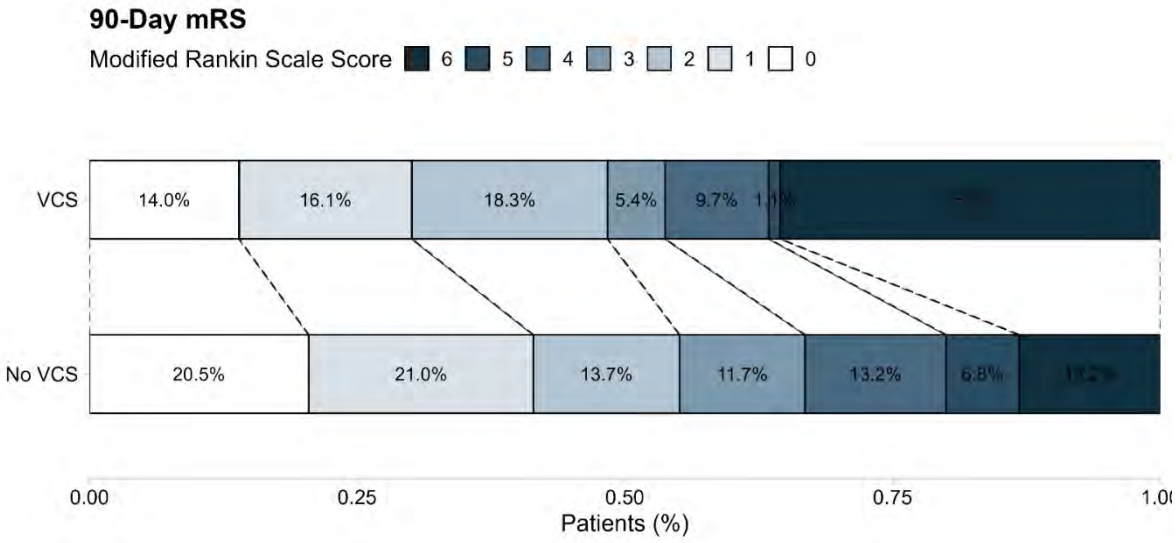

251

Harnessing Molecular Insights: A Systematic Review of Machine Learning Applications in Pediatric Brain Tumor Diagnosis and Prognosis

Negar Emamzadeh MD[1], Alireza Motamedi MD[2], Fatemeh Abbasi MD[3], Mahdi Zahmatyar MD[2], Saeid Hassanbaghlou MD[2], Sara Salehi MD[4], Shahriar Faghani MD[4]

[1]Iran University of Medical Sciences, Tehran, Tehran, Iran, Islamic Republic of. [2]Tabriz University of Medical Sciences, Tabriz, Azarbayjan Sharghi, Iran, Islamic Republic of. [3]Mazandaran University of Medical Sciences, Sari, Mazandaran, Iran, Islamic Republic of. [4]Mayo Clinic, Rochester, Minnesota, USA

Abstract Category

Pediatrics

Purpose

This systematic review evaluates molecular-based machine learning (ML) models in diagnosing and predicting outcomes for pediatric brain tumors. It aims to enhance clinical decision-making by integrating genetic, epigenetic, and imaging data into ML models, offering insights into their diagnostic and prognostic capabilities.

Materials & Methods

A comprehensive literature search was conducted across multiple databases including PubMed, Scopus, Web of Science, and IEEE Xplore, up to July 2024. Studies were included if they applied machine learning to pediatric brain tumors, incorporated molecular data, and met methodological standards such as cross-validation and external validation. Of 464 screened records, 15 studies met the inclusion criteria.

Results

Various machine learning models, including Support Vector Machines, Random Forests, and Neural Networks, demonstrated high diagnostic accuracy (up to 96.5%) for distinguishing tumor subtypes such as medulloblastomas, gliomas, and ependymomas. Incorporating molecular data like gene expression profiles and radiogenomic signatures significantly improved prognostic predictions, particularly for progression-free survival and overall survival. However, most studies were limited by small sample sizes and lack of external validation, impacting the generalizability of the results.

Conclusion

Molecular-based machine learning models hold great promise for improving the diagnosis and prognosis of pediatric brain tumors. Future research should focus on larger, multi-center studies with standardized methods to validate these models and facilitate their integration into clinical practice.

References

Das D, Mahanta LB, Ahmed S, et al. Study on Contribution of Biological Interpretable and Computer-Aided Features Towards the Classification of Childhood Medulloblastoma Cells. *J Med Syst* 2018;42:151.

Images/Tables

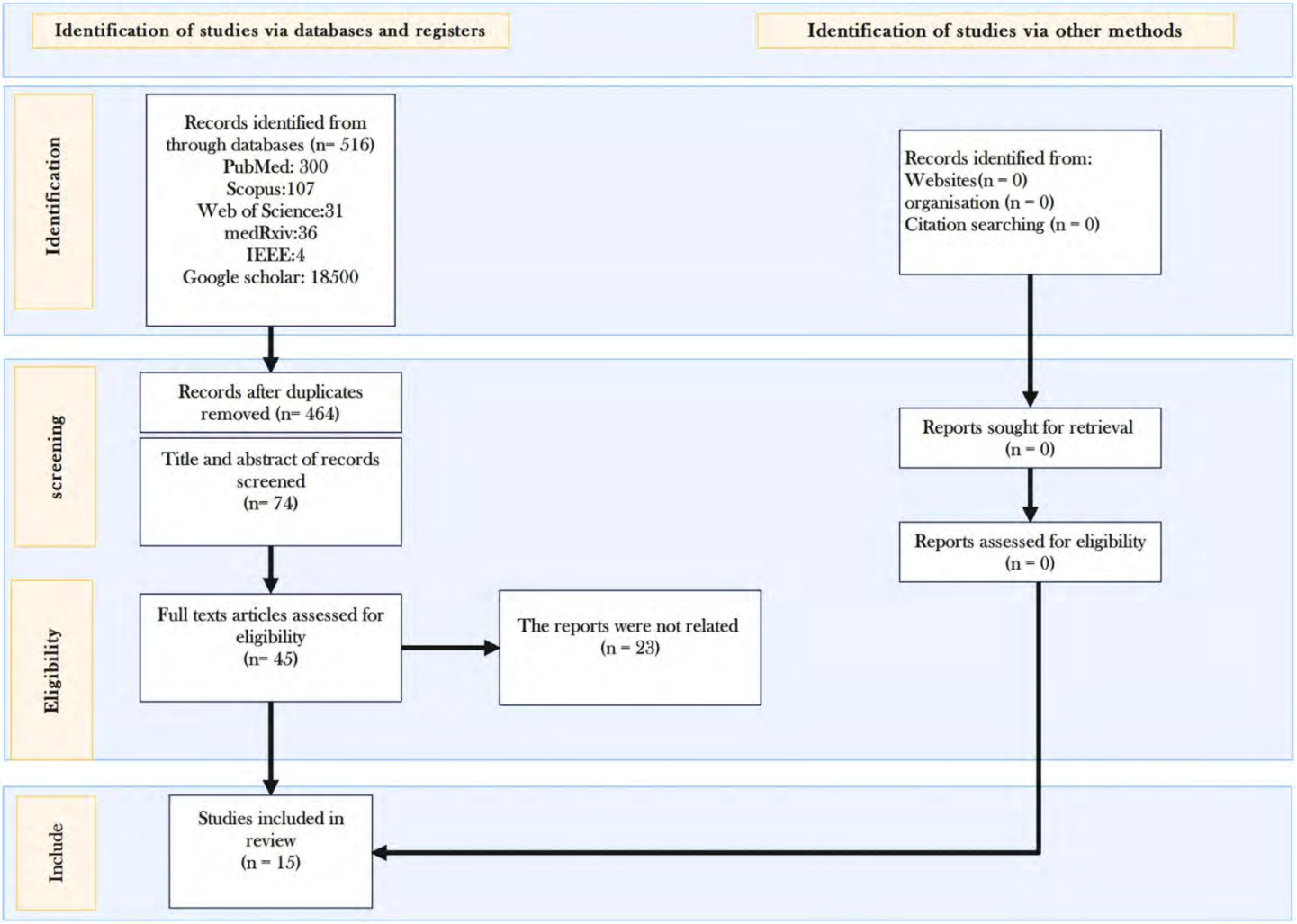

273

Estimation of Fat Content Using Chemical Shift Fat-Suppression MRI Predicts Mandibular Marrow Invasion in Oral Squamous Cell Carcinoma: a Radio-Histopathological Correlation Study

Finn D Begbie MBChB, MRCS, FRCR[1], Rachel McAllister[2], Robbie MacKinnon[3], Almaha Saleh[3], Neha Jose[3], Christopher R Pollard MBChB, FRCR[1], James A McCaul MBChB (Hons), PhD, FRCS (OMFS)[4]

[1]Department of Neuroradiology, Institute of Neurological Sciences, Glasgow, Scotland, United Kingdom. [2]Department of Oral and Maxillofacial Surgery, Institute of Neurological Sciences, Glasgow, Glasgow, Scottland, United Kingdom. [3]Department of Oral and Maxillofacial Surgery, Institute of Neurological Sciences, Glasgow, Glasgow, Scotland, United Kingdom. [4]Department of Oral and Maxillofacial Surgery, Institute of Neurological Sciences, Glasgow, Scotland, United Kingdom

Abstract Category

Head & Neck

Purpose

Oral squamous cell carcinoma (SCC) frequently presents with advanced disease and mandibular marrow infiltration(1). Marrow invasion has important prognostic and therapeutic implications(1,2) but it is difficult to confirm definitively on standard imaging(3). Estimation of marrow fat content is routinely used in the assessment of vertebral lesions to differentiate benign from sinister marrow-replacing lesions but is not established in the setting of oral SCC(4). Predicting marrow invasion on preoperative imaging can guide management and may allow mandible-sparing surgery. We assessed whether quantification of marrow fat content predicts mandibular invasion on histopathology.

Materials & Methods

Three-year retrospective review was undertaken in a tertiary oral and maxillofacial surgery centre. Included patients had locally advanced oral SCC with suspected mandibular invasion; had undergone major surgical resection with mandibulectomy; and had contrast-enhanced neck MRI including Dixon fat-suppression sequences available for study. Images were reviewed by two board-certified radiologists blinded to final histopathological results. Regions of interest were placed over areas of suspected marrow involvement on in- and out-of-phase T1-weighted, fat-suppressed sequences and percentage signal loss calculated. The cut-off value for suspected marrow infiltration was <20% signal loss(4). Postoperative histopathology reports were subsequently reviewed.

Results

Seventy-three patients were identified between 2021 and 2024. Thirteen patients were excluded who did not proceed to mandibulectomy. Of the remaining patients, seven had the required imaging available for evaluation. Five patients showed signal loss of <20% with confirmed postoperative histopathological marrow invasion. Two patients had >20% signal loss with postoperative histopathology showing no marrow invasion.

Conclusion

Preoperative estimation of mandibular fat content reliably predicts marrow invasion. We showed 100% correlation between estimated fat content and histopathological marrow invasion in this proof of concept study. This simple technique may allow preoperative selection of patients for significantly less morbid mandible-sparing surgery. To our knowledge, this is the first study to evaluate preoperative estimation of marrow fat content in the context of oral SCC.

References

1. Pandey M, Rao LP, Das SR, Mathews A et al. Patterns of mandibular invasion in oral squamous cell carcinoma of the mandibular region. *World J Surg Onc* 2007 Jan 30;5:12 DOI: https://doi.org/10.1186/1477-7819-5-12

2. Ord RA, Sarmadi M, Papdimitron J. A comparison of segmental and marginal bony resection for oral squamous cell carcinoma involving the mandible. *J Oral Maxillofac Surg* 1997;55:470-477. DOI: 10.1016/S0278-2391(97)90693-5

3. Nae A, O'Leary G, Feeley L, Fives C et al. Utility of CT and MRI in assessment of mandibular involvement in oral cavity cancer. *World J Otorhinolaryngol Head Neck Surg* 2019 Mar 22;5(2):71-75. DOI: 10.1016/j.wjorl.2019.02.001

4. Omoumi P. The Dixon method in musculoskeletal MRI: from fat-sensitive to fat-specific imaging. *Skeletal Radiol* 2022 51:1365–1369. DOI: https://doi.org/10.1007/s00256-021-03950-1

287

Volumetric Normalization: Evaluating the Application of Residual and Proportional Adjustment in Neuroimaging

Thrisha Reddy[1], Sabah Islam[2], Sabah Islam[1], Priya Santhanam PhD[3], Thomas Knoblauch MS[3], Alan Rodriguez MD[3], Cheryl Vanier PhD[1], Travis Snyder DO[3]

[1]College of Osteopathic Medicine, Touro University Nevada, Henderson, NV, USA. [2]Touro University Nevada, Henderson, NV, USA. [3]Imgen Research Group, Las Vegas, NV, USA

Abstract Category

Functional/Advanced Imaging

Purpose

Changes in brain volume are crucial factors when evaluating neurological alterations due to various diseases and covariates[1] and normalization allows for analysis of specific brain volumes or regions. Normalization of total intracranial volume (TIV) allows for comparisons of regions of interest during normal brain development, aging, and neurological pathologies[2]. Common normalization techniques include residual adjustment (RA) and proportional adjustment (PA) methods[3]. The RA adjusts for covariates such as headsize, brain size, or body size by using data from a control group, and comparing it with a region of interest (ROI). PA tests for group differences across proportionalized volumes, normalizing for intracranial brain volume[4] using a certain ROI which is divided by the TIV or the total brain volume (TBV); a group analysis is conducted via t-test or ANOVA[4]. This literature review compares both methods which have been used, particularly with magnetic resonance neuroimaging (MRI), to assess various characteristics and diseases in relation to TBV and ROI.

Materials & Methods

This review examines studies employing residual or PA methods. Research was identified through PubMed, Elsevier, and Google Scholar using keywords like ‘volumetric tracing,’ ‘total intracranial volume,’ ‘proportional adjustment,’ and ‘residual adjustment.’ Included studies adjusted for race/ethnicity, sex, age, or regions of interest, and analyzed cranial

volume normalization in pathologies like multiple sclerosis, Alzheimer's, and semantic dementia. Only studies with sample sizes larger than 10 using 1.5 T and 3T MRI were included to enhance statistical power and generalizability; case studies were excluded. This review compares PA and RA by analyzing studies using automated volumetric tracing techniques that utilize algorithms for MRI normalization and segmentation into gray matter, white matter, and cerebrospinal fluid.

Results

The results indicate distinct adjustment methods for neuroimaging analyses. RA relies on predicted values from linear regression within a control group, which are subtracted from dataset values. PA calculates ratios by dividing the volume of the ROI by the total brain volume, yielding proportional ratios.

For pathology analysis, RA is optimal for healthy patients to eliminate gender differences. For multiple sclerosis, PA is recommended. In Alzheimer's disease, RA removes gender differences, while both RA and PAs are applied for hippocampal normalization. These findings underscore the use of adjustment methods depending on the clinical context and neuroanatomical regions under study, highlighting the application of these techniques in different disease states.

Conclusion

The PA method is highly impacted by systematic error in intracranial volume (ICV) values, leading to inaccuracies in brain fraction measurements, whereas RA remains unaffected by the same error unless dependent forms are present[4]. PA tends to overcorrect gray matter volumes, indicating these structures are not directly proportional to ICV. When a ROI is highly correlated with ICV, the proportional method's reliability decreases, making it suitable when no correlation exists. In contrast, RA effectively removes ROI-ICV correlations[5], negating the influence of brain size. Both methods are valuable for volumetric normalization, but further research is needed to compare their effectiveness against newer methods and to address the common issues of overestimation and underestimation in each approach.

References

[1]Li X, Huang M, Hao X, Zhao Z, Xu D. Measuring variability of local brain volume using improved volume preserved warping. Comput Med Imaging Graph. 2022 Mar;96:102039. doi: 10.1016/j.compmedimag.2022.102039. Epub 2022 Jan 29. PMID: 35121376.

[2]Pengas G, Pereira JM, Williams GB, Nestor PJ. Comparative reliability of total intracranial volume estimation methods and the influence of atrophy in a longitudinal semantic dementia cohort. J Neuroimaging. 2009 Jan;19(1):37-46. doi: 10.1111/j.1552-6569.2008.00246.x. Epub 2008 May 19. PMID: 18494772.

[3]Wang J, Hill-Jarrett T, Buto P, Pederson A, Sims KD, Zimmerman SC, DeVost MA, Ferguson E, Lacar B, Yang Y, Choi M, Caunca MR, La Joie R, Chen R, Glymour MM, Ackley SF. Comparison of approaches to control for intracranial volume in research on the association of brain volumes with cognitive outcomes. Hum Brain Mapp. 2024 Mar;45(4):e26633. doi: 10.1002/hbm.26633. PMID: 38433682; PMCID: PMC10910271.

[4]O'Brien LM, Ziegler DA, Deutsch CK, Frazier JA, Herbert MR, Locascio JJ. Statistical adjustments for brain size in volumetric neuroimaging studies: some practical implications in methods. Psychiatry Res. 2011 Aug 30;193(2):113-22. doi: 10.1016/j.pscychresns.2011.01.007. PMID: 21684724; PMCID: PMC3510982.

5Voevodskaya O, Simmons A, Nordenskjöld R, Kullberg J, Ahlström H, Lind L, Wahlund LO, Larsson EM, Westman E; Alzheimer's Disease Neuroimaging Initiative. The effects of intracranial volume adjustment approaches on multiple regional MRI volumes in healthy aging and Alzheimer's disease. Front Aging Neurosci. 2014 Oct 7;6:264. doi: 10.3389/fnagi.2014.00264. PMID: 25339897; PMCID: PMC4188138.

290

Superior Detection of Paramagnetic Rim Lesions on Optimized 3D Echo Planar Imaging Versus Standard Susceptibility-Weighted Imaging

Joshua D Lee MD, PhD[1], Brian Renner MD[1], Sreekanth Madhusoodhanan Nair PhD[1], Kunio Nakamura PhD[2], Elaina Luskin MS[1], Meghan Kilbane BS[2], Meredith Dever MPH[2], Enrique Alvarez MD, PhD[3], Christina J Azevedo MD[4], Peter A Calabresi MD[5], Jeffrey A Cohen MD[2], Salim Chahin MD, MSCE[6], Léorah Freeman MD, PhD[7], Erin E Longbrake MD, PhD[8], Ruth Ann Marrie MD, PhD[9], Aaron E Miller MD[10], Nandita Mitra PhD[11], Ellen M Mowry MD[5], Jiwon Oh MD, PhD[12], Paulo Rodrigues PhD[13], Matthew K Schindler MD, PhD[11], Elias S Sotirchos MD[5], Emmanuelle L Waubant MD, PhD[14], Gary R Cutter PhD[15], Marwa Kaisey MD[1], Russell T Shinohara PhD[11], Daniel S Reich MD, PhD[16], Andrew J Solomon MD[17], Nancy L Sicotte MD[1], Daniel Ontaneda MD, PhD[2], Pascal Sati PhD[1]

[1]Cedars-Sinai, Los Angeles, CA, USA. [2]Cleveland Clinic, Cleveland, OH, USA. [3]University of Colorado, Aurora, CO, USA. [4]University of Southern California, Los Angeles, CA, USA. [5]Johns Hopkins University, Baltimore, MD,

USA. [6]Washington University, St. Louis, MO, USA. [7]University of Texas at Austin, Austin, TX, USA. [8]Yale University, New Haven, CT, USA. [9]Dalhousie University, Halifax, NS, Canada. [10]Icahn School of Medicine at Mount Sinai, New York, NY, USA. [11]University of Pennsylvania, Philadelphia, PA, USA. [12]University of Toronto, Toronto, ON, Canada. [13]QMENTA Inc., Boston, MA, USA. [14]University of California San Francisco, San Francisco, CA, USA. [15]University of Alabama at Birmingham, Birmingham, AL, USA. [16]National Institute of Neurological Disorders and Stroke, National Institutes of Health, Bethesda, MD, USA. [17]University of Vermont, Burlington, VT, USA

Abstract Category

Functional/Advanced Imaging

Purpose

Paramagnetic rim lesions (PRL) (Figure) have emerged as a highly specific imaging biomarker for multiple sclerosis (MS) and are proposed for incorporation into upcoming revisions to the McDonald diagnostic criteria[1]. PRL detection requires susceptibility-sensitive MRI sequences such as standard susceptibility-weighted imaging (SWI) or optimized 3D echo planar imaging (3D-EPI) with high isotropic resolution. However, consensus is lacking regarding the most sensitive MRI technique for PRL evaluation in the clinical setting. Here we perform a head-to-head, lesion-level comparative analysis of PRL detection on standard SWI versus optimized 3D-EPI.

Materials & Methods

3T brain MRI scans, including standard SWI (0.65 x 0.65 x 3 mm, 4-minute acquisition time) and optimized 3D-EPI (0.65 mm isotropic, 6-minute acquisition time), were acquired in 20 randomly selected participants from a multicenter prospective study involving 11 US and Canadian centers who were undergoing diagnostic evaluation for MS. The filtered phase images of standard SWI and optimized 3D-EPI were evaluated independently by two trained, blinded raters applying the 2024 consensus radiological criteria for PRL definition[2]: (a) hypointense rim surrounding an isointense lesion core; (b) co-localization with a non-enhancing T2-hyperintense lesion; (c) visible on at least two contiguous slices or two orthogonal planes. A third expert rater adjudicated any inter-rater disagreements. Differences in PRL counts between the two MRI sequences were evaluated with a McNemar test.

Results

In total, 112 PRL were identified across the 20 participants. Thirty (27%) of the 112 PRL were detected on SWI and 3D-EPI. Of the remaining 82 PRL, 69 (62%) were exclusively detected on 3D-EPI versus 13 (12%) exclusively detected on SWI ($p<0.001$). Of the 69 PRL that were exclusively detected on 3D-EPI, the primary reasons for non-detection on SWI were: (a) visibility limited to a single axial image (42%); (b) nodular appearance (20%); (c) indistinct rim (14%); (d) absence of rim (9%); (e) discontinuous rim (6%); (f) obscuration by vessels (4%); (g) partial rim (3%); (h) no corresponding lesion (1%). Of the 13 PRL exclusively detected on SWI, 8 (62%) were false-positives upon review of multiplanar images available on 3D-EPI, while the remainder were either obscured by vessels (23%) or had an indistinct rim (15%).

Conclusion

While a subset of PRL were detected on both standard SWI and optimized 3D-EPI, the vast majority of PRL were exclusively detected on 3D-EPI. Moreover, standard SWI was vulnerable to false-positive classification. The superior sensitivity of 3D-EPI is largely explained by its thinner image slices (0.65 mm) and multiplanar reconstructibility (isotropic voxels), facilitating adequate visualization for reliable application of the consensus radiological criteria for PRL definition. These results support integration of the 3D-EPI sequence into the brain MRI diagnostic protocol for MS.

References

1. Montalban X. Revised McDonald criteria 2023. Presented at the 40th Congress of the European Committee for Treatment and Research in Multiple Sclerosis, Copenhagen, Sep 2024.
2. Bagnato F, Sati P, Hemond CC, et al. Imaging chronic active lesions in multiple sclerosis: a consensus statement. *Brain* 2024; 147(9):2913-2933. DOI: 10.1093/brain/awae013.
3. Lee JD, Madhusoodhanan Nair S, Renner B, et al. Feasibility of Detecting Paramagnetic Rim Lesions at 3T Using Vendor-Provided Susceptibility Weighted Imaging. Presented at ACTRIMS Forum 2024, West Palm Beach, Feb 2024. DOI: 10.1177/13524585241248739

Images/Tables

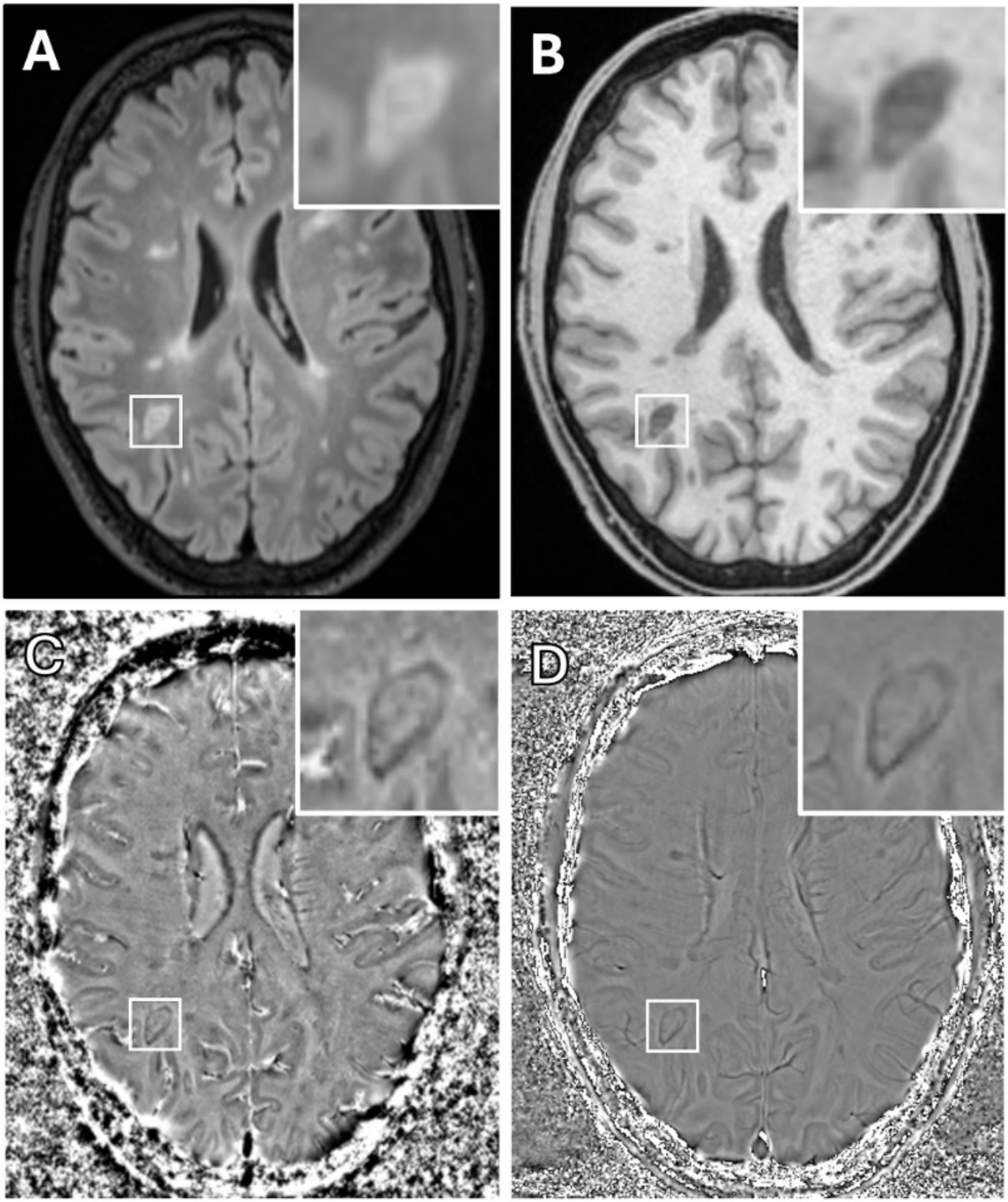

Figure. Axial brain MR images depicting a paramagnetic rim lesion (PRL) on (A) T2-FLAIR, (B) T1-weighted, (C) 3D echo planar imaging (3D-EPI) filtered phase, and (D) susceptibility-weighted imaging (SWI) filtered phase MRI sequences with magnified views shown as inset images.

293

Neuroanatomical Features of NAA10-related and NAA15-related Neurodevelopmental Syndromes

Rikhil Makwana[1], Rahi Patel[1], Gholson J Lyon MD, PhD[2], Matthew T Whitehead MD[3]
[1]Chicago Medical School, North Chicago, Illinois, USA. [2]Institute for Basic Research in Developmental Disabilities, Staten Island, New York, USA. [3]Children's Hospital of Philadelphia, Philadelphia, Pennsylvania, USA

Abstract Category

Pediatrics

Purpose

NAA10-related (Ogden Syndrome) and *NAA15*-related neurodevelopmental syndromes are ultra-rare genetic syndromes that present with varying degrees of intellectual disability, hypotonia, congenital cardiac abnormalities, seizures, and delayed speech and motor development. While there is much data on the clinical manifestations of these conditions, there are few radiologic reports describing the neuroanatomical abnormalities present on imaging. Our goal was to provide neuroimaging analyses for a subset of probands with *NAA10*- and *NAA15*-related neurodevelopmental symptoms and assess severity, common radiologic anomalies, and changes over time to better understand the pathophysiology of these disease processes as well as begin to develop a compendium of commonly seen neuroanatomical features in these syndromes to help increase their likelihood of diagnosis.

Materials & Methods

Neuroimaging studies from 26 probands (18 with pathogenic variants in *NAA10*, 8 with pathogenic variants in *NAA15*) were collected and analyzed. Size of the cerebrum, brainstem, and cerebellum, as well as myelination, brain malformations, globus pallidus hyperintensity, brain lesions, 4th ventricle size, tegmentovermian angle, cisterna magna size, pituitary size, olfactory tract, palate arch, number of vertebrae, and choroid plexus abnormalities were analyzed. In depth medical histories were also collected on all probands, including genetic testing results and social, cognitive, and developmental history. The Vineland 3 Adaptive Behavior Scale was also administered to the parents to assess functional status of the probands.

Results

On average, individuals with Ogden Syndrome had 5.7 anatomical abnormalities (standard deviation (SD) = 3.0), whereas those with NAA15 related neurodevelopmental syndrome had 2.8 (SD = 2.3) ($p = .02$). Probands who had more anatomical abnormalities tended to score worse on Vineland assessments, suggesting a possible correlation between the two. Structure and function were preserved such that individuals with greater defects on, for example, brain motor regions on MRI, tested worse on motor portions of the Vineland. Probands followed longitudinally demonstrated several changes between scans, most commonly in the cerebellum, brainstem, and degree of myelination. Such changes were only observed for probands with Ogden Syndrome in this cohort.

Conclusion

Despite clinical imaging being reported as being predominantly "normal" during routine clinical care, this analysis of a cohort of patients with Ogden Syndrome and *NAA15*-related neurodevelopmental syndrome has established a range of subtle abnormalities. When correlated with similar neurodevelopmental patterns, the anatomical differences can help increase the clinical suspicion of a diagnosis of *NAA10*-related and *NAA15*-related neurodevelopmental syndrome prior to genetic testing. Ultimately, we hope these findings help guide the development of future prospective and diagnostic studies for this under-served patient population.

References

Lyon GJ, Vedaie M, Besheim T, et al. Expanding the Phenotypic spectrum of Ogden syndrome (NAA10-related neurodevelopmental syndrome) and NAA15-related neurodevelopmental syndrome. https://doi.org/10.1101/2022.08.22.22279061.
Makwana R, Christ C, Marchi E, et al. Longitudinal adaptive behavioral outcomes in Ogden syndrome by seizure status and therapeutic intervention. *American J of Med Genetics Pt A* https://doi.org/10.1002/ajmg.a.63651.
Patel R, Park AY, Marchi E, et al. Ophthalmic manifestations of NAA10 -related and NAA15 -related neurodevelopmental syndromes: Analysis of cortical visual impairment and refractive errors. American J of Med Genetics Pt A https://doi.org/10.1002/ajmg.a.63821.
Patel R, Makwana R, Christ C, et al. Neuroanatomical Features of NAA10- and NAA15-Related Neurodevelopmental Syndromes. medRxiv https://doi.org/10.1101/2024.06.24.24309433.

Images/Tables

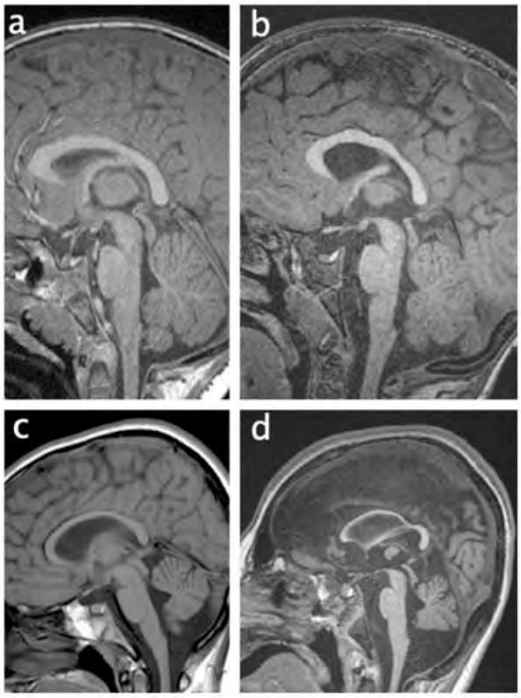

Figure 1a-d. Sagittal midline TI-weighted brain MRI collage demonstrating the phenotypic range of brain volume in 4 different probands with Ogden syndrome. a=normal (patient 15), b=mildly decreased cerebral volume with mild callosal thinning (patient 12), c=mildly diffusely decreased brain volume (patient 2), d=marked cerebral, moderate brainstem, and mild cerebellar volume reduction (patient 9).

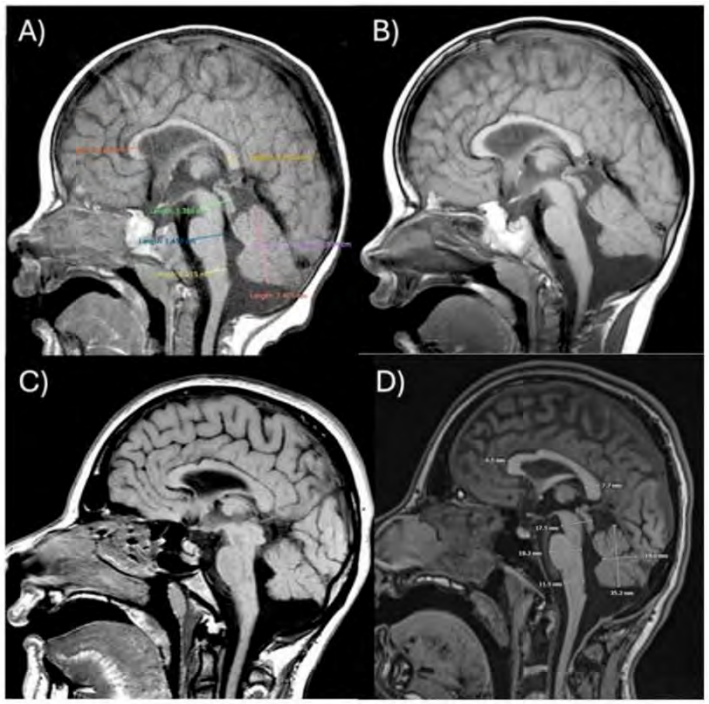

Figure 2. Sequential sagittal midline T1-weighted brain MR images from patient 13 at ages (a) 9 months, (b) 2 years, (c) 9 years, and (d) 16 years showing mild cerebral, cerebellar, and brainstem hypoplasia with lack of appropriate parenchymal growth over time.

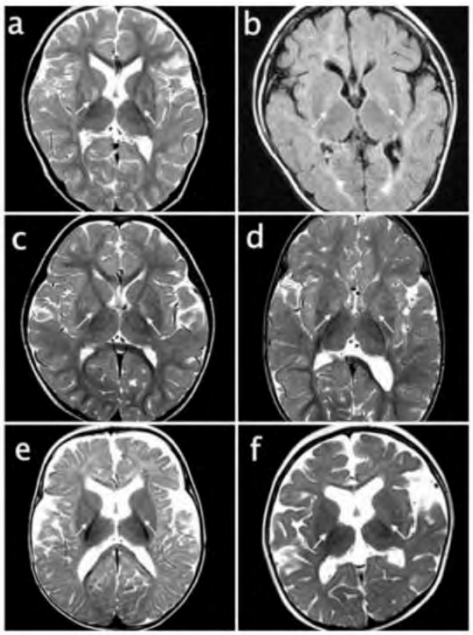

Figure 3. Brain MRI collage showing globus pallidus signal hyperintensity (arrows) on T2WI (a, c-f) and T2/FLAIR (b) in 5 patients with Ogden syndrome. Figures a and b are from the same patient (patient 13) at 4 years of age; the T2/FLAIR sequence reveals more widespread myelin deficiency abnormal white matter signal for age (b). Figure c=patient 4 (23 months), d=patient 8 (2 years), e=patient 5 (7 months), figure f=patient 7 (6 months).

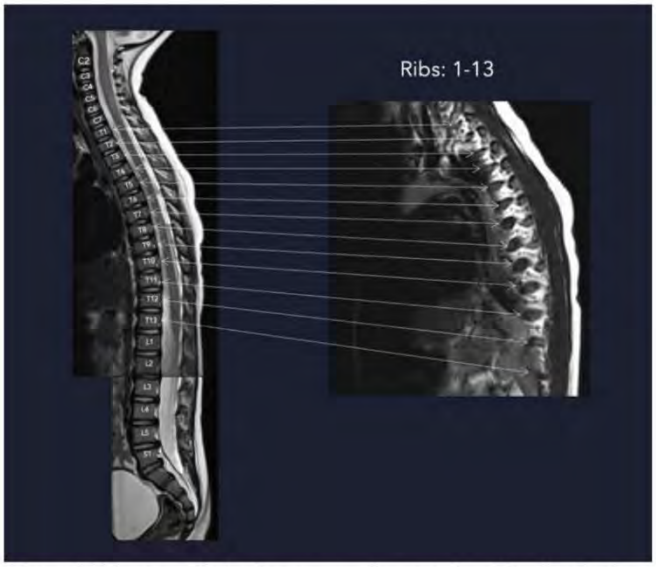

Figure 4. Minor vertebral column anomalies were found in all patients that underwent spine MRI (n=4). All had elements of transitional anatomy at the lumbosacral junction, including S1 partial lumbarization (n=2) and L5-S1 interval disk hypoplasia (n=2). One patient had 13 thoracic type rib bearing vertebrae. One patient had an underdeveloped L1 vertebral body that was beaked at its anteroinferior margin and associated with a gibbous deformity.

294

Post treatment MRI Markers of Collateral Status: Relationship to Adverse Stroke Events and Outcomes in Large Vessel Occlusion Acute Ischemic Stroke (LVO-AIS)

Cynthia Greene MD PhD[1], Dhairya Lakhani MD[2], Kevin Chen[1], Vivek Yedavalli MD[1]
[1]Johns Hopkins University, Baltimore, MD, USA. [2]West Virginia University, Morgantown, WV, USA

Abstract Category

Adult Brain

Purpose

On susceptibility weighted imaging (SWI) the brush sign (SBS) is related to ischemia(1, 2). The hyperintense vessel sign (FHVS) on fluid attenuated inversion recovery (FLAIR) is related to altered slow flow(3-5). Though these signs related to hemodynamics are well researched independently, in AIS their relationship to each other and combined utility is underexplored. Our purpose is to assess a) the relationship amongst FHVS and SBS in LVO-AIS and b) their utility as prognostic biomarkers of post-stroke complication and clinical outcomes.

Materials & Methods

This retrospective IRB approved study included 168 patients from 8/2017-6/2023 presenting with anterior circulation (ICA, MCA, ACA) LVO-AIS and who had follow-up MRI evaluation during their hospital stay. Clinical data: age, sex, hypertension (HTN), diabetes (DM), admission& discharge NIHSS, mechanical thrombectomy attempted (MT), IV TPA administration, mTICI scores, hemorrhagic transformation (HT), 90-day modified Rankin scores (mRS). FHVS and SBS were scored by a board certified neuroradiologist (VSY, 10 years of working experience). A pairwise complete case spearman correlation was performed; p value =<0.05 was statistically significant. Logistic regression analysis was performed with HT, NIHSS shift>=4 (admission NIHSS – discharge NIHSS), and 90-day mRS 0-2 as outcomes and FHVS and SBS as independent variables. Then a multivariable regression included age, sex, HT, DM, admission NIHSS, IV TPA, and MT as covariates. SBS was then also included a covariate in a second multivariate regression.

Results

Correlations: FHVS vs SBS ρ 0.5 p<0.001, FHVS vs NIHSS shift ρ = -0.22 p = 0.004, FHVS vs mTICI ρ -.25 p = 0.004, SBS vs Age ρ –0.22 p 0.005 and SBS vs mTICI ρ -.20 p =0.026.

Single variable regression: FHVS showed less favorable NIHSS shift with (odds ratio) OR 0.81, p = 0.028 and FHVS showed less risk of HT, OR 0.77 and p = 0.03.

Multiple covariate regression: FHVS showed less favorable NIHSS shift was OR 0.8 p = 0.027 and less risk of HT OR 0.73, p = 0.016.

With SBS covariate: FHVS showed less favorable NIHSS shift OR 0.72 p 0.031, less favorable mRS OR 0.76 p 0.039, and less risk of HT OR 0.71 p 0.032.

Conclusion

These preliminary results demonstrate significant but weak correlations between post-treatment imaging signs, FHVS and SBS, with clinical factors and outcomes; age and NIHSS shift. In the multivariable analysis, the predictive value of FHVS on NIHSS shift, was significant. When including SBS as a covariate FHVS was significant in predicting NIHSS shift, 90 day–mRS and HT. The multivariate regression with SBS covariate suggests cases with residual posttreatment FHVS had less favorable NIHSS shift, less favorable 90-mRS and decreased risk for HT in the absence of SBS. SBS on the other hand was not significant in this data. These mixed results demonstrate a predictive relationship between FHVS and LVO-AIS complications and outcomes when accounting for the presence of other MRI signs. Further investigation on how FHVS and SBS are related to nuances in underlying tissue properties may help inform how these signs may be used in further patient assessment and treatment.

References

1. Rascle L, Sadr BA, Amaz C, Mewton N, Buisson M, Hermier M, Ong E, Fontaine J, Derex L, Berthezène Y, Eker FO, Cho T-H, Nighoghossian N, Mechtouff L. Does the Brush-Sign Reflect Collateral Status and DWI-ASPECTS in Large Vessel Occlusion? Frontiers in Neurology 2022;13. doi: 10.3389/fneur.2022.828256

2. Haller S, Haacke ME, Thurnher MM, Barkhof F. Susceptibility-weighted Imaging: Technical Essentials and Clinical Neurologic Applications. Radiology 2021;299(1):3-26. doi: 10.1148/radiol.2021203071

3. Karadeli HH, Giurgiutiu DV, Cloonan L, Fitzpatrick K, Kanakis A, Ozcan EM, Schwamm HL, Rost SN. FLAIR Vascular Hyperintensity is a Surrogate of Collateral Flow and Leukoaraiosis in Patients With Acute Stroke Due to Proximal Artery Occlusion. Journal of Neuroimaging 2016;26(2):219-223. doi: 10.1111/jon.12274

4. Cheng B, Ebinger M, Kufner A, Köhrmann M, Wu O, Kang D-W, Liebeskind D, Tourdias T, Singer CO, Christensen S, Warach S, Luby M, Fiebach BJ, Fiehler J, Gerloff C, Thomalla G. Hyperintense Vessels on Acute Stroke Fluid-Attenuated Inversion Recovery Imaging. Stroke 2012;43(11):2957-2961. doi: 10.1161/STROKEAHA.112.658906
5. Shang WJ, Chen HB, Shu LM, Liao HQ, Huang XY, Xiao S, Hong H. The Association between FLAIR Vascular Hyperintensity and Stroke Outcome Varies with Time from Onset. American Journal of Neuroradiology 2019;40(8):1317-1322. doi: 10.3174/ajnr.A6142

Images/Tables

Figure 1: Example images of (top row) DWI with corresponding FLAIR HVS (yellow arrow) And (bottom row) DWI with corresponding SWI brush sign (red arrow).

ROC Curves for the Multivariable Regression

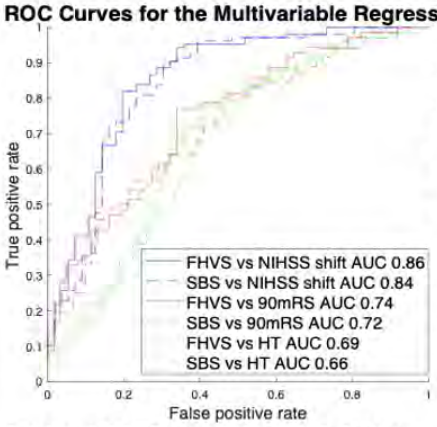

Single Variable Regression

	OR (95%CI)	P	AUC
FHVS vs NIHSS shift	0.81 (0.68-0.98)	0.028	0.60
SBS vs NIHSS shift	0.75 (0.35-1.62)	0.465	0.53
FHVS vs mRS	0.91 (0.75 - 1.1)	0.360	0.58
SWI vs mRS	1.52 (0.65 - 3.52)	0.334	0.53
FHVS vs HT	0.77 (0.60-0.98	0.030	0.57
SWI vs HT	0.49 (0.21-1.11)	0.088	0.56

Multivariable Regression, AIS factors only

	OR(95%CI)	P	AUC
FHVS vs NIHSS shift	0.74 (0.57 - 0.97)	0.027	0.86
SBS vs NIHSS shift	0.77 (0.26-2.24)	0.628	0.84
FHVS vs mRS	0.80 (0.63-1.01)	0.065	0.74
SWI vs mRS	1.13 (0.44-2.93)	0.795	0.72
FHVS vs HT	0.73 (0.57-0.94)	0.016	0.69
SWI vs HT	0.46 (0.19-1.14)	0.095	0.66

Multivariable Regression, Including SBS

	OR(95%CI)	P	AUC
FHVS vs NIHSS shift	0.72 (0.54-0.97)	0.031	0.85
SBS vs NIHSS shift	1.24 (0.37-4.12)	0.725	-
FHVS vs mRS	0.76 (0.59-0.99)	0.039	0.76
SWI vs mRS	1.43 (0.49-4.22)	0.515	-
FHVS vs HT	0.7 (0.51-0.97)	0.032	0.70
SWI vs HT	0.87 (0.28-2.75)	0.817	-

305

Imaging Features and Outcomes of Suspected Third and Fourth Branchial Cleft Cysts and Close Mimics

Joseph Kim MD, Jeffers Nguyen MD, Long Tu MD, PhD
Yale New Haven Hospital, New Haven, CT, USA

Abstract Category

Head & Neck

Purpose

Branchial cleft cysts (BCCs) are rare congenital lateral neck lesions. While second BCCs can represent up to 95% of BCCs, third and fourth BCCs are much less commonly encountered. Imaging remains a valuable tool to help identify the type of BCC and differentiate between similar pathologies. Differentiating between third and fourth BCCs is challenging due to their anatomical proximity, with definitive diagnosis often requiring surgical intervention. In our study, we present our institutional experience with suspected third and fourth BCCs, highlighting overall incidence, imaging features, differential considerations, and outcomes of management.

Materials & Methods

We collected cases from our tertiary referral center's database over the over 33 years (1992-2024), searching for reports with suspected third or fourth BCCs. We present descriptive statistics regarding patient sex, patient age, incidence, surgical management, and pathologic results. In our presentation, we discuss common imaging features and show representative and illustrative examples on CT and MRI.

Results

Over the 33-year study period, we found 781 imaging reports with mention of BCCs. 36 cases were further identified as specifically mentioning (or suspecting) third or fourth BCCs. 40% of patients were female, and 60% were male. Patients' ages ranged from 0.09 years to 60 years. Mean age was 22.3 years. Of these, 2 cases (2/36, 0.06%) went to surgery and were biopsied, finding 1 lymphangiomatous malformation (1/36, 0.03%) and 1 cystic lymph node with metastatic papillary thyroid cancer (1/36, 0.03%). 0 (0/36, 0%) cases were confirmed as BCCs. In the remaining 34 cases, third or fourth BCC remained a suspected but unconfirmed etiology. Most notable imaging characteristics that led to the suspicion of third or fourth BCCs include 1) hypodense, cystic structures, 2) location deep to the sternocleidomastoid muscle, and 3) location in close relation the thyroid gland.

Conclusion

At our tertiary institution, the paucity of surgically confirmed cases limits precise estimation of the incidence of these cysts. Patients who presented themselves in the acute setting, such as due to underlying neck infection, were generally lost to follow-up. Surgical management is not commonly pursued for suspected third or fourth BCCs. Third and fourth BCCs are elusive entities. Definitive diagnosis is surgical, though specific features may be suggestive on imaging.

References

1. Bajaj Y, Ifeacho S, Tweedie D, et al. Branchial anomalies in children. Int J Pediatr Otorhinolaryngol. 2011 Aug;75(8):1020-3. doi: 10.1016/j.ijporl.2011.05.008.
1. Maksimoski M, Maurrasse SE, Purkey M, et al. Combination Surgical Procedure for Fourth Branchial Anomalies: Operative Technique and Outcomes. Ann Otol Rhinol Laryngol. 2021 Jul;130(7):738-744. doi: 10.1177/0003489420971674.
1. Mattioni J, Azari S, Hoover T, et al. A cross-sectional evaluation of outcomes of pediatric branchial cleft cyst excision. Int J Pediatr Otorhinolaryngol. 2019 Apr;119:171-176. doi: 10.1016/j.ijporl.2019.01.030.
2. Rossi M, Moreddu E, Leboulanger N, et al. Fourth branchial anomalies: Predictive factors of therapeutic success. Journal of Pediatric Surgery. 2019 Aug;54(8):1702–1707. doi: 10.1016/j.jpedsurg.2019.02.005.

Images/Tables

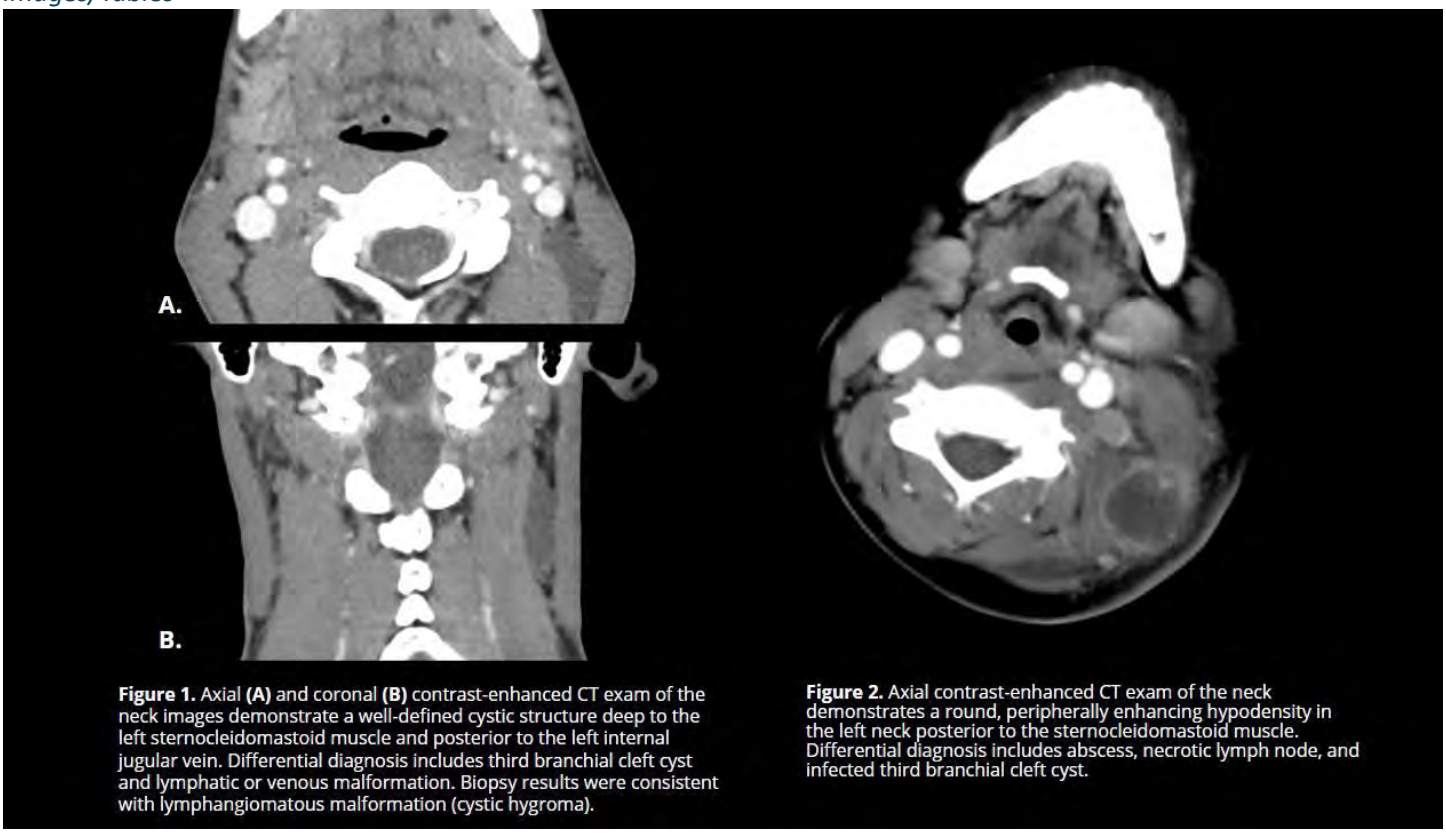

Figure 1. Axial **(A)** and coronal **(B)** contrast-enhanced CT exam of the neck images demonstrate a well-defined cystic structure deep to the left sternocleidomastoid muscle and posterior to the left internal jugular vein. Differential diagnosis includes third branchial cleft cyst and lymphatic or venous malformation. Biopsy results were consistent with lymphangiomatous malformation (cystic hygroma).

Figure 2. Axial contrast-enhanced CT exam of the neck demonstrates a round, peripherally enhancing hypodensity in the left neck posterior to the sternocleidomastoid muscle. Differential diagnosis includes abscess, necrotic lymph node, and infected third branchial cleft cyst.

327

Imaging and Genomic Features of Rosette-Forming Glioneuronal Tumor

Harrison T Lee MD, Soonmee Cha MD
University of California, San Francisco, San Francisco, CA, USA

Abstract Category

Adult Brain

Purpose

Rosette-forming glioneuronal tumor (RGNT) is a rare CNS WHO grade I neoplasm. Imaging characterization in literature is somewhat sparse, confined to small case reports and related meta-analyses. The purpose of this study is to present clinical, histopathologic, molecular genomic, and imaging features of a large series of RGNT from a single institution's experience.

Materials & Methods

A retrospective review was performed on all patients with RGNT at our institution using mPower (Nuance Healthcare, Burlington, MA). Patients were included only if they had both internally confirmed pathology as well as available pre-treatment MR imaging. Recorded demographic features included age and sex. Recorded imaging features included location, number of lesions, lesion size, composition, T1 intensity, T2 intensity, enhancement, perfusion, diffusivity, presence of surrounding edema, presence of susceptibility artifact, and presence of calcifications. Comprehensive histopathologic evaluation included immunohistochemistry and identified pathologic genetic mutations from an internal gene panel test of >500 cancer genes.

Results

A total of 25 patients, 11 males (44%) and 14 females (56%), was included in the study with average age of 26.69 years. In terms of location, 8 tumors (32%) were in the posterior fossa (including cerebral aqueduct, 4th ventricle, and cerebellar vermis), 6 tumors (24%) were in supratentorial ventricles (including lateral ventricles and 3rd ventricle), 5 tumors (20%) were in supratentorial parenchyma, and 6 tumors (24%) were multicompartment. 16 cases (64%) involved 1-5 lesions, 1 case (4%) involved 6-10 lesions, and 8 cases (32%) involved >10 lesions. Average lesion volume was 10.18 ml. All lesions (100%) were T1-hypointense and T2-hyperintense compared to cerebral cortex. 15 cases (60%) involved more solid-appearing components that were T1-hypointense/isointense and T2-isointense/hyperintense. 17 cases (68%) demonstrated enhancement, including all 15 cases with solid-appearing components, as well as 5 cases demonstrating mild enhancement of less solid-appearing components. Of the 6 cases with arterial spin labeling (ASL) imaging, 4 cases (67%) demonstrated hypervascularity. Average ADC value was 2065.78 with standard deviation 77.42, and average ADC value of solid-appearing components was 1276.41 with standard deviation 58.11. Overall, 7 cases (28%) demonstrated qualitative reduced diffusion, all involving solid-appearing components. 5 cases (20%) demonstrated perilesional edema. 11 cases (44%) demonstrated susceptibility artifact, possibly reflecting hemorrhage or calcifications. Of the 15 cases with CT imaging, 3 cases (20%) demonstrated calcifications. On histopathologic and genomic analyses, all tumors showed positive synaptophysin on immunohistochemistry. Of the 18 cases with gene panel testing, 14 cases (78%) demonstrated FGFR1 mutations (most common were p.N546K in 6 cases and p.K656E in 4 cases), 9 cases (50%) demonstrated PIK3CA mutations (most common were p.H1047R in 4 cases), and 6 cases (33%) demonstrated NF1 mutations (variable).

Conclusion

RGNT is a distinctive CNS grade I tumor with unique imaging patterns and molecular genomic features that can aid in its diagnosis. Its hallmark imaging characteristics include a mixed solid/cystic appearance, varying degree of enhancement, typical absence of reduced diffusion, and typical location in the fourth ventricle and adjacent vermis as well as supratentorial brain, including the lateral and third ventricles.

References

1. Komori T, Scheithauer BW, Hirose T. A rosette-forming glioneuronal tumor of the fourth ventricle. *Am J Surg Pathol* 2002;26(5):582-591. DOI: https://doi:10.1097/00000478-200205000-00004
2. Louis DN, Perry A, Wesseling P, et al. The 2021 WHO classification of tumors of the central nervous system: A summary. *Neuro Oncol* 2021;23(8):1231-1251. DOI: https://doi:10.1093/neuonc/noab106
3. Sievers P, Appay R, Schrimpf D, et al. Rosette-forming glioneuronal tumors share a distinct DNA methylation profile and mutations in FGFR1, with recurrent co-mutation of PIK3CA and NF1. *Acta Neuropathol* 2019;138(3):497-504. DOI: https://doi:10.1007/s00401-019-02038-4
4. Wilson CP, Chakraborty AR, Pelargos PE, et al. Rosette-forming glioneuronal tumor: An illustrative case and a systematic review. *Neuro Oncol Adv* 2020;2(1). DOI: https://doi:10.1093/noajnl/vdaa116

5. Anyanwu CT, Robinson TM, Huang JH. Rosette-forming glioneuronal tumor: an update. *Clin Transl Oncol* 2020;22(5):623-630. DOI: https://doi:10.1007/s12094-019-02179-8

Images/Tables

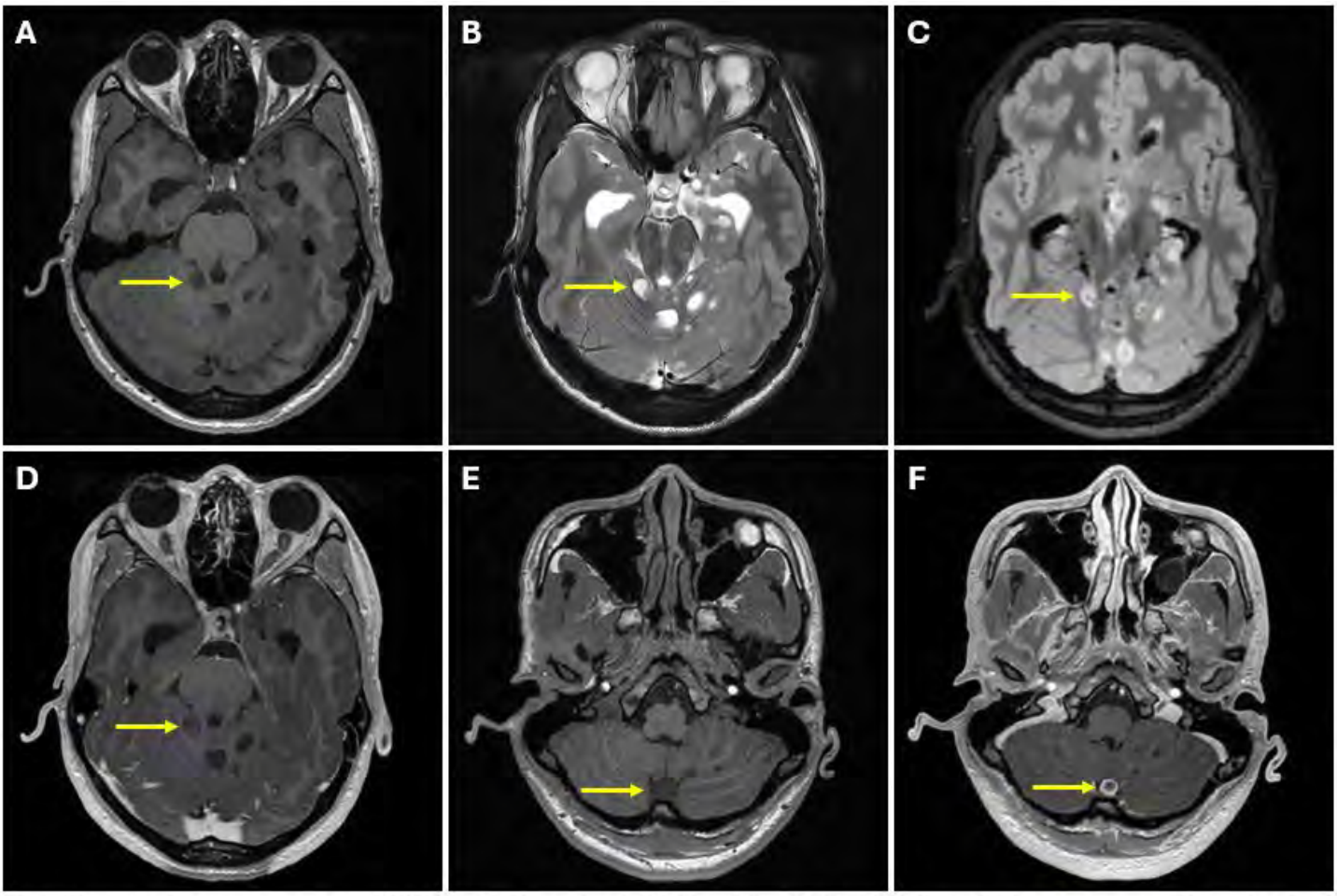

Fig 1. Characteristic appearance of RGNT on A) T1-weighted, B) T2-weighted, C) T2/FLAIR, and D) post-contrast T1-weighted sequences. Lesion with more pronounced enhancement on E) T1-weighted and F) post-contrast T1-weighted sequences.

338

The Impact of Sex on Mechanical Thrombectomy - an NVQI-QOD Study

Shyam Chandrasekar BS[1], Dayeong An PhD[1], Anas Al-Smadi MD[1], Ramez N Abdalla MD, PhD[1], Ali Shaibani MD, MBA[1], Joseph J Gemmete MD[2], Justin F Fraser MD[3], Donald R Cantrell MD, PhD[1], Sameer A Ansari MD, PhD[1]
[1]Department of Radiology, Neurosurgery, and Neurology, Northwestern University Feinberg School of Medicine, Chicago,, IL, USA. [2]Department of Radiology, Neurology, Neurosurgery, and Otolaryngology, University of Michigan Hospitals, Ann Arbor, MI, USA. [3]Department of Neurological Surgery, Radiology, Neurology, and Neuroscience, University of Kentucky School of Medicine, Lexington, KY, USA

Abstract Category

Interventional

Purpose

Women are relatively under-represented in thrombectomy trials, and female sex has been previously associated with poorer outcomes and lower treatment benefits. This study assesses the impact of patient sex on mechanical thrombectomy outcomes in the United States using the multi-center Neurovascular Quality Initiative-Quality Outcomes Database (NVQI-QOD) AIS Registry.

Materials & Methods

Patients who underwent mechanical thrombectomy (MT) for anterior circulation stroke were retrospectively identified from the multi-center NVQI database. Comorbidities, risk factors, procedural variables (e.g. reperfusion score), and clinical outcomes were subsequently compared between male and female cohorts. Favorable functional outcome was defined by a modified Rankin Scale (mRS) of 0 to 2 at 90 days post-operation. Demographic data was assessed using chi-

squared analysis and t-tests as indicated. Odds Ratios (OR) were generated with logistical regression and controlled multivariate regression analyses.

Results

Among 9,577 patients, 4,961 or 51.8% were female, with an average age of 68.4 years ± 15.3 (SD). Analysis showed males tended to be younger than females with mean ages of 65.8 and 70.8 years old respectively ($p<0.001$). There was no significant association between sex and reported race ($p=0.192$). Female patients had a greater likelihood of pre-existing hypertension (OR 1.23, $p<0.001$), Obesity (OR 1.11, $p=0.013$) and Atrial Fibrillation (OR 1.32, $p<0.001$), lesser likelihood of Severe CHF (OR 0.64, $p=0.008$), CAD (OR 0.64, $p<0.001$), and insulin-dependent diabetes (OR 0.85, $p<0.001$). Female patients had a greater mean last-known-well (LKW) to groin puncture time of 486 minutes versus 457 minutes for males, but no difference in ED arrival to groin puncture with overall mean of 85 minutes ($p=0.2548$). There was no association between sex and TICI score ($p=0.292$) or first pass successful recanalization ($p=0.127$). No difference in in-hospital/discharge mortality was seen (p-0.726).

Analysis of 90-day postoperative outcomes demonstrated females were 0.67 times as likely to achieve favorable functional outcomes ($p<0.001$) and 1.49 times as likely to die by 90 days. Multivariate regression analysis showed that female sex was an independent predictor of poorer functional improvement at 90 days but not mortality when controlled for factors including comorbidities, age, procedure time, and times from LWK and ED arrival. Symptomatic CHF (OR 1.79, $p<0.001$) and Diabetes (OR 1.56, $p=0.002$) were also associated with increased odds of 90-day mortality, whereas obesity was associated with decreased mortality (OR 0.67, $p<0.001$).

Every 10 minutes of procedure time reduced the likelihood of a favorable functional outcome by 7.9% and increased mortality odds by 7.2%. Additionally, each 10-minute increase from last-known-well to puncture decreased favorable outcomes by 0.36% and raised mortality odds by 0.3%. Each year of patient age reduced favorable outcomes by 3.5% and increased mortality odds by 6.3%.

Conclusion

This study identified sex-associated differences in risk factors as well as functional outcome and mortality outcome between females and males who underwent mechanical thrombectomy for anterior stroke. While increased likelihood of mortality was explained by clinical and procedural variables, female sex remained robustly associated with decreased odds of a favorable functional outcome. More research is required to better characterize the mediating variables that impact functional outcomes for female patients.

References

Casetta I, Fainardi E, Pracucci G, et al. Sex differences in outcome after thrombectomy for acute ischemic stroke. A propensity score-matched study. *Eur Stroke J*. 2022;7(2):151-157. doi:10.1177/23969873221091648

Fifi JT, Nguyen TN, Song S, et al. Sex differences in endovascular thrombectomy outcomes in large vessel occlusion: a propensity-matched analysis from the SELECT study. J Neurointerv Surg. 2023;15(2):105-112. doi:10.1136/neurintsurg-2021-018348

Carcel C, Harris K, Peters SAE, et al. Representation of Women in Stroke Clinical Trials: A Review of 281 Trials Involving More Than 500,000 Participants. Neurology. 2021;97(18):e1768-e1774.

Images/Tables

Table 1: Favorable Functional Improvement at 90 days Post-Operation – Logistic Regression with Odds Ratio

Variable	Odds Ratio	p-value	95% Conf. Interval
Female Sex*	0.7790	0.003	0.6621 - 0.9166
Obesity (BMI 30+)*	1.3721	0.000	1.1617 - 1.6206
Symptomatic CHF*	0.6544	0.001	0.5154 - 0.8309
Atrial Fibrillation	0.9053	0.292	0.7524 - 1.0894
Hypertension*	0.7780	0.011	0.6415 - 0.9436
Insulin-dependent Diabetes	0.8075	0.075	0.6383 - 1.0217
Smoking	0.9126	0.084	0.8226 - 1.0124
Coronary Artery Disease	1.0612	0.583	0.8581 - 1.3124
Age (years)*	0.9636	0.000	0.9572 - 0.9700
LKW to Groin Puncture (mins)*	0.9996	0.000	0.9994 - 0.9998
Procedure Time (mins)*	0.9925	0.000	0.9894 - 0.9956
ED to Groin Puncture (mins)	0.9994	0.346	0.9982 - 1.0006
Year of Procedure	0.9421	0.004	0.9046 - 0.9813

Table 2: Mortality at 90 days Post-Operation – Logistic Regression with Odds Ratio

Variable	Odds Ratio	p-value	95% Conf. Interval
Female Sex	1.1087	0.308	0.9092 - 1.3520
Obesity (BMI 30+)*	0.6908	0.000	0.5611 - 0.8505
Symptomatic CHF*	1.7819	0.000	1.3930 - 2.2794
Atrial Fibrillation	1.1884	0.102	0.9663 - 1.4614
Hypertension	1.1235	0.360	0.8756 - 1.4416
Insulin-dependent Diabetes	1.0988	0.493	0.8395 - 1.4382
Smoking	1.0007	0.992	0.8730 - 1.1470
Coronary Artery Disease	1.0629	0.614	0.8385 - 1.3474
Age (years)*	1.0639	0.000	1.0537 - 1.0742
LKW to Groin Puncture (mins)*	1.0003	0.007	1.0001 - 1.0005
Procedure Time (mins)*	1.0067	0.000	1.0036 - 1.0098
ED to Groin Puncture (mins)	1.0006	0.427	0.9992 - 1.0020
Year of Procedure*	1.1228	0.000	1.0680 - 1.1805

343

Genetic Influences on Subcortical Structures and on Depression and Anxiety in a Bivariate Twin Model

Safiya I. Lahlaf MD, J. Eric Schmitt MD, PhD
Hospital of the University of Pennsylvania, Philadelphia, PA, USA

Abstract Category

Adult Brain

Purpose

Depressive and anxiety disorders are ubiquitous in the general population, but the underlying causes that lead to the development of these disorders are still largely unknown. Previous studies have shown that changes in multiple subcortical structures, particularly the hippocampus and amygdala, are related to depression, and small changes have also been seen in anxiety. Additionally, both depression and anxiety are moderately heritable. The purpose of this study was to examine the genetic influences on subcortical structures and on depression and anxiety using a bivariate twin model.

Materials & Methods

This study used Human Connectome Project (HCP) data, which includes behavioral and 3T MRI neuroimaging data on 1,200 subjects aged 22 to 35, including N=349 monozygotic and N=233 dizygotic twins. FreeSurfer-derived subcortical volumes (thalamus, putamen, pallidum, amygdala, hippocampus, and nucleus accumbens) were examined. Behavioral measures included the Achenbach Adult Self-Report (ASR) Anxious/Depressed, ASR DSM Depressive, and ASR DSM Anxiety Problems Raw Scores and Gender and Age Adjusted T-scores, as well as the Depressive Episode and Depressive

Symptoms measures. We first assessed phenotypic associations between measures of depression and anxiety via logistic regression after controlling for the confounds of age and gender. Logistic regression was also performed on female and male participants individually. Genetically informative structural equation models (univariate ACE and bivariate Cholesky decomposition) were then applied in OpenMx in order to quantify the strength of genetic effects on both brain and behavioral measures, as well as to assess if genetic factors contribute to brain-behavioral associations.

Results

Individuals who had a prior depressive episode had statistically significant volumetric differences in the left thalamus ($p=0.005$), right putamen ($p=0.01$), bilateral hippocampi ($p<0.005$), bilateral amygdalae ($p<0.002$), and right nucleus accumbens ($p=0.002$). When separated by gender, the most significant volumetric differences were seen in the left caudate ($p=0.003$), right caudate ($p=0.004$), and right putamen ($p=0.005$) in female participants, while the left amygdala ($p=0.001$) showed the most significant difference in male participants. Measures of anxiety and depression were modestly heritable (0.18-0.34), and subcortical volumes were significantly heritable (0.49-0.86). Bivariate twin models showed significant genetically mediated associations between measures of depression and anxiety and subcortical volumes. For example, age and gender-adjusted anxiety/depression (ASR_Anxd_Pct) demonstrated statistically significant genetic correlations with the left hippocampus ($r_G=0.73$; $p<0.003$), right hippocampus ($r_G=0.40$; $p<0.003$), and left amygdala ($r_G=0.45$; $p=0.018$). Environmental effects were generally less striking, although individual-specific environmental factors significantly influenced the relationship between depression and hippocampal volumes ($p<0.005$).

Conclusion

These findings support prior work suggesting differences in subcortical volumes between individuals with depression and anxiety. The results also suggest that there may be gender-specific structural changes. Furthermore, quantitative models provide evidence that at least some of the observed phenotypic associations are genetically mediated, including those observed in the hippocampus and amygdala. These findings further our understanding of the etiologies behind depression and anxiety and suggest avenues of continued research in a variety of directions, such as the development of more targeted treatments or neuroimaging correlates to help identify individuals at risk.

References

Gottschalk MG, Domschke K. Genetics of generalized anxiety disorder and related traits. *Dialogues in Clinical Neuroscience* 2017;19(2):159-168. doi:10.31887/dcns.2017.19.2/kdomschke

Groenewold NA, Bas-Hoogendam JM, Amod AR, et al. Volume of subcortical brain regions in social anxiety disorder: Mega-analytic results from 37 samples in the enigma-anxiety working group. *Molecular Psychiatry* 2023;28(3):1079-1089. doi:10.1038/s41380-022-01933-9

Hamilton JP, Siemer M, Gotlib IH. Amygdala volume in major depressive disorder: A meta-analysis of Magnetic Resonance Imaging Studies. *Molecular Psychiatry* 2008;13(11):993-1000. doi:10.1038/mp.2008.57

Kendall KM, Van Assche E, Andlauer TF, et al. The genetic basis of major depression. *Psychological Medicine* 2021;51(13):2217-2230. doi:10.1017/s0033291721000441

Videbech P, Ravnkilde B. Hippocampal volume and depression: A meta-analysis of MRI studies. *American Journal of Psychiatry* 2004;161(11):1957-1966. doi:10.1176/appi.ajp.161.11.1957

347

Sensitivity and Specificity of the Skull base Jagged Sign in Adults with Seizures and Intracranial Hypertension.

Kamand Khalaj MD-MPH, Elham Tavakkol MD, Andres Rodriguez MD, David Timaran-Montenegro MD, Arash Kamali MD
UTHealth Houston, Houston, Texas, USA

Abstract Category

Adult Brain

Purpose

Our study aims to assess the sensitivity and specificity of the Skull Base Jagged Sign (SJS) on brain MRI and CT scans in adult patients with normal or elevated intracranial pressure (ICP), presenting to the ER with or without idiopathic unprovoked seizures. Building on previous research highlighting bone remodeling, such as the empty sella, in response to ICP changes, we seek to further understand structural alterations associated with elevated ICP. We compared the frequency of SJS across four distinct patient groups to evaluate its diagnostic value and potential as an imaging marker for increased ICP.

Materials & Methods

This IRB-approved retrospective study included adults aged 18-40 who underwent lumbar puncture and MRI or CT scan at our institution. Participants were categorized into four groups: Group 1 (increased ICP + Seizure, n=27), Group 2 (Normal ICP + Seizure, n=39), Group 3 (increased ICP without Seizure, n=52), and Group 4 (Control group, n=39). The control group included patients with normal opening pressure, normal clinical, MRI, and CSF exams. Radiologic analysis focused on detecting SJS, identified as sharp bony remodeling in the posterior medial cranial fossa on coronal T2-weighted MRI sequences or coronal CT views of the brain, with assessments performed by two independent observers. Statistical analyses evaluated sensitivity, specificity, and predictive values for SJS.

Results

The presence of SJS varied significantly across groups, showing distinct diagnostic patterns. In Group 1 (elevated ICP + Seizure), SJS was present in 88.9% of cases, compared to 71.2% in Group 3 (elevated ICP without Seizure) ($p=0.07$). SJS was also significantly more frequent in Group 1 (88.9%) than in Group 2 (Normal ICP + Seizure) at 46.2% ($p<0.001$). Similarly, in the comparison between patients with elevated ICP without seizure (Group 3) and the control group (Group 4), SJS positivity was markedly higher at 71.2% versus 30.8%, respectively ($p<0.001$). SJS was found in 46.2% of patients in Group 2, compared to 30.8% in the control group (Group 4) ($p=0.16$).

For predicting seizure in patients with elevated ICP (Groups 1 & 3, N=79), SJS achieved a sensitivity of 88.9% and a specificity of 28.8%. For diagnosing increased ICP in seizure patients (Groups 1 & 2, N=66), SJS sensitivity was 88.9%, with a specificity of 53.8%. In predicting seizure in patients with normal ICP (Groups 2 & 4, N=78), SJS sensitivity and specificity were 46.2% and 69.2%, respectively ($p=0.16$). Finally, for diagnosing elevated ICP in patients without seizure (Groups 3 & 4, N=91), SJS demonstrated a sensitivity of 71.2% and specificity of 69.2%.

Conclusion

The Skull Base Jagged Sign demonstrates high sensitivity and may serve as a screening tool on brain MRI or CT scans for diagnosing elevated intracranial pressure (ICP) in patients presenting to the Emergency Room with or without seizures.

References

Kamali A, Park ES, Lee SA, Nunez LC, Butler IJ, Sitton CW, Riascos RF, Shah MN, Zhang X, Huisman TAGM. Introducing the "Temporal Thumb Sign" in Pediatric Patients With New-Onset Idiopathic Seizures With and Without Elevated Cerebrospinal Fluid Opening Pressure. Pediatr Neurol. 2022 140:52-58. PMID: 36640519.

Kamali A, Aein A, Naderi N, et al. Neuroimaging features of intracranial hypertension in pediatric patients with new-onset idiopathic seizures, a comparison with patients with confirmed diagnosis of idiopathic intracranial hypertension: a Preliminary study. J Child Neurol. 2021;36:1103e1110.

Images/Tables

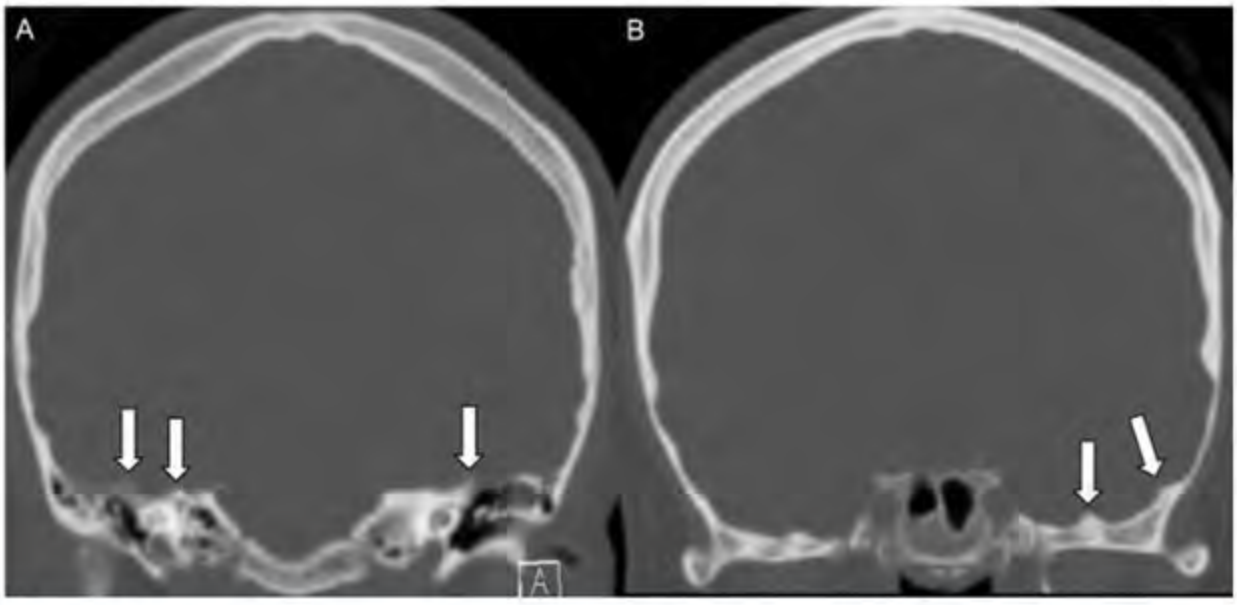

Figure 1: Coronal Head CT scans of a 30-year-old (A) and a 26-year-old (B) female presenting with headaches and diagnosed with idiopathic intracranial hypertension. Skull base Jagged Sign is seen in the bilateral petrous bones (white arrows in A) in the first subject and in the left petrous bone in the second subject (white arrows in B).

356

Association of Early Life Air Pollutants with Adolescent Magnetic Resonance Spectroscopy Concentrations

Chloe Dunseath BS[1], Yingying Xu PhD[2], Kimberly Yolton PhD[2], Patrick Ryan PhD[2], Kim M Cecil PhD[2]
[1]University of Cincinnati College of Medicine, Cincinnati, OH, USA. [2]Cincinnati Children's Hospital Medical Center, Cincinnati, OH, USA

Abstract Category

Pediatrics

Purpose

An ever-increasing number of studies document the neurotoxicity and contribution of air pollution to several conditions including autism spectrum disorder, deficits in attention-related behaviors, and increased anxiety and depressive symptoms in childhood (1, 2). Early life exposure to pollutants may contribute to atypical neurodevelopment resulting in altered intrinsic neurochemistry. We estimated the association of key air pollutants at multiple timepoints and proton magnetic resonance spectroscopy (MRS)-derived metabolite concentrations from participants in a prospective cohort longitudinally followed to adolescence.

Materials & Methods

We applied validated spatiotemporal models to estimate daily exposures to particulate matter less than 2.5 microns ($PM_{2.5}$), nitrogen dioxide (NO_2) and ozone (O_3) at the homes of participants. Daily exposure estimates for each pollutant were aggregated to derive average gestational, first year of life and annual timepoints.

During the 12-year study visit, participants completed anatomical T1-weighted imaging using a 3 Tesla MR scanner. Short echo point resolved spectroscopy (PRESS) was acquired within a single voxel (8 cc) positioned bilaterally within the frontal lobe cortex. Raw spectra were quantified using LCModel software. Adjustments for fractional tissue volumes, water and metabolite relaxation rates were applied to generate metabolite concentrations.

We developed linear regression models to evaluate associations between exposure concentrations of each pollutant and metabolite concentrations for the participants (n=334, 167 female, mean (SD) age 12.2 (0.7) years). All effect estimates are presented corresponding to each unit increase in exposure concentration. Final models were adjusted for child sex, maternal education, neighborhood deprivation index and greenspace.

Results

Adjusted models found composite glutamate and glutamine concentrations were inversely associated with NO_2 (ß -0.076 (95% confidence interval (CI): -0.11, -0.042) for gestational, -0.061 (95% CI: -0.1, -0.021) for year 1) and $PM_{2.5}$ (ß -0.115 (95% CI: -0.19, -0.039) for gestational, -0.46 (95% CI: -0.61, -0.311) for year 1) and ozone (ß -0.048 (95% CI: -0.085, -0.011 for gestational) concentrations.

Conclusion

Higher concentrations of NO_2, $PM_{2.5}$ and O_3 during early life are associated with reduced brain glutamate concentrations age 12. This may reflect reduced numbers of glutamatergic receptors arising from early-life exposure to air pollutants perturbing intrinsic neurochemistry.

References

1. Yolton, K., et al., 2019. lifetime exposure to traffic-related air pollution and symptoms of depression and anxiety at age 12 years. Environ Res. 173**,** 199-206.
2. Iyanna, N., et al., 2023. Air pollution exposure and social responsiveness in childhood: The cincinnati combined childhood cohorts. Int J Hyg Environ Health. 251**,** 114172.

Images/Tables

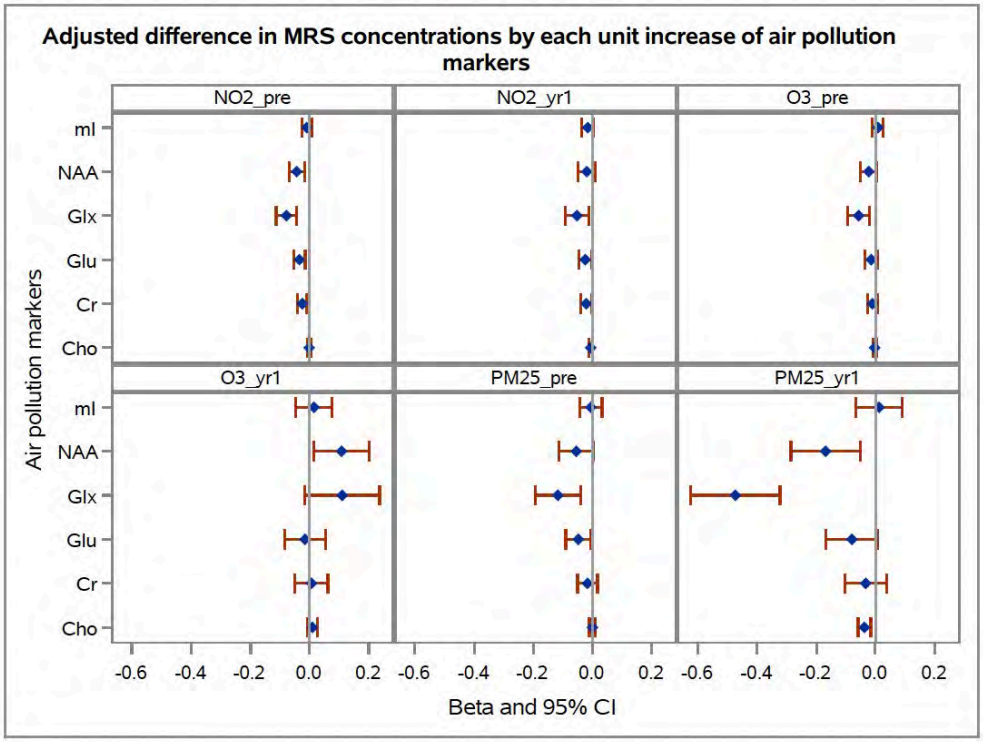

362

Enhanced Grey White Differentiation Utilizing an Investigational Photon Counting CT, a Multicenter Pilot Study

Gregory Avey MD[1], Hakan Almqvist MD[2], Brian Nett PhD[3], Meghan Yue B.S. Biomedical Engineering[4], Nicholas Mathew MS[4], Aaron Field MD[1], Tabassum Kennedy MD[1], Aria Salypongse PhD[1], Sean Rose PhD[5], Staffan Holmin MD, PhD[2], Timothy Szczykutowicz PhD[1]

[1]University of Wisconsin, Madison, WI, USA. [2]Karolinska University Hospital, Stockholm, Uppland, Sweden. [3]GE Healthcare, Wauwatosa, WI, USA. [4]GE Healthcare, Waukesha, WI, USA. [5]University of Texas Health Science Center at Houston, Houston, TX, USA

Abstract Category

Functional/Advanced Imaging

Purpose

To evaluate the effectiveness of an investigational photon counting CT (PCT) system combined with a novel deep learning processing algorithm designed to enhance grey-white matter differentiation compared to current clinical standard energy integrating detector (EID) and PCT CT systems.

Materials & Methods

A convenience sample of 7 patients who received a nonenhanced head CT on a clinical standard CT device and a subsequent head CT on an investigational silicon detector based photon counting CT system were evaluated. The novel PCT mages were processed both conventionally and with 2 strengths of a deep learning algorithm designed to capitalize on the improved low contrast properties of photon counting CT to increase the perceived grey-white delineation in these images.

Qualitative analysis of images was independently performed by 4 subspecialty-certified readers from two sites. Image sets were presented in a randomized and blinded manner to the reviewers.

Subjective image quality was assessed in terms grey matter - white matter differentiation and overall diagnostic acceptability on a 1 to 5 likert scale. Grey white matter differentiation was assessed in the central ASPECTS territories (caudate head, insular ribbon, lentiform nuclei, internal capsule) with one additional score encompassing overall differentiation in the M1 to M6 cortical areas. Overall low contrast detectability, noise magnitude, noise texure, spatial resolution and diagnostic confidence were also graded on a 1 to 5 scale.

Results

The investigational PCT images processed with the deep learning algorithm demonstrated significantly higher grey-white matter differentiation when compared to the clinical standard CT images across all anatomic regions, with Bonferroni-adjusted p values ranging from p=0.002 to p=0.03. Averaged across the regions, the mean grey-white matter likert score of the clinical standard, novel PCT, novel PCT with DL level 2 and novel PCT with DL level 3 were 3.01, 3.25, 4.0, and 4.59, respectively (out of a maximum of 5).

Subjective low-contrast detectability was rated as higher for the investigational system baseline images and the two deep learning image sets with likert scores of 3.11 (p=0.02), 3.71 (p<0.001), and 3.82 (p=0.009) vs the clinical standard images (2.68). Overall diagnostic image quality was higher in both levels of the deep learning processed novel PCT images compared to the clinical standard, (3.96 and 4.25 vs 2.89, p=0.002 and p=0.016).

Inter-rater agreement was considered moderate in the assessment of grey-white contrast in the anatomic regions, with weighted kappa scores averaged over rater pairs, ranging from 0.44 to 0.57. Kappa scores for overall diagnostic quality and low contrast detectability were also moderate at 0.46 and 0.47.

Conclusion

The combination of the experimental PCT system and the deep learning processing algorithm significantly improves grey-white matter perception and subjective diagnostic quality compared to current clinical standard CT systems. The superior visualization of grey-white matter boundaries has the potential to facilitate more accurate ASPECTS scoring, which is crucial for assessing early ischemic changes in stroke patients. The improved tissue contrast also has the potential to decrease perceptual errors and increase diagnostic confidence while maintaining current CT radiation doses.

References

1) Pexman JH, Barber PA, Hill MD, Sevick RJ, Demchuk AM, Hudon ME, Hu WY, Buchan AM. Use of the Alberta Stroke Program Early CT Score (ASPECTS) for assessing CT scans in patients with acute stroke. AJNR Am J Neuroradiol. 2001 Sep;22(8):1534-42

2) Pourmorteza A, Symons R, Reich DS, Bagheri M, Cork TE, Kappler S, Ulzheimer S, Bluemke DA. Photon-Counting CT of the Brain: In Vivo Human Results and Image-Quality Assessment. AJNR Am J Neuroradiol. 2017 Dec;38(12):2257-2263.

3) Douek PC, Boccalini S, Oei EHG, Cormode DP, Pourmorteza A, Boussel L, Si-Mohamed SA, Budde RPJ. Clinical Applications of Photon-counting CT: A Review of Pioneer Studies and a Glimpse into the Future. Radiology. 2023 Oct;309

Images/Tables

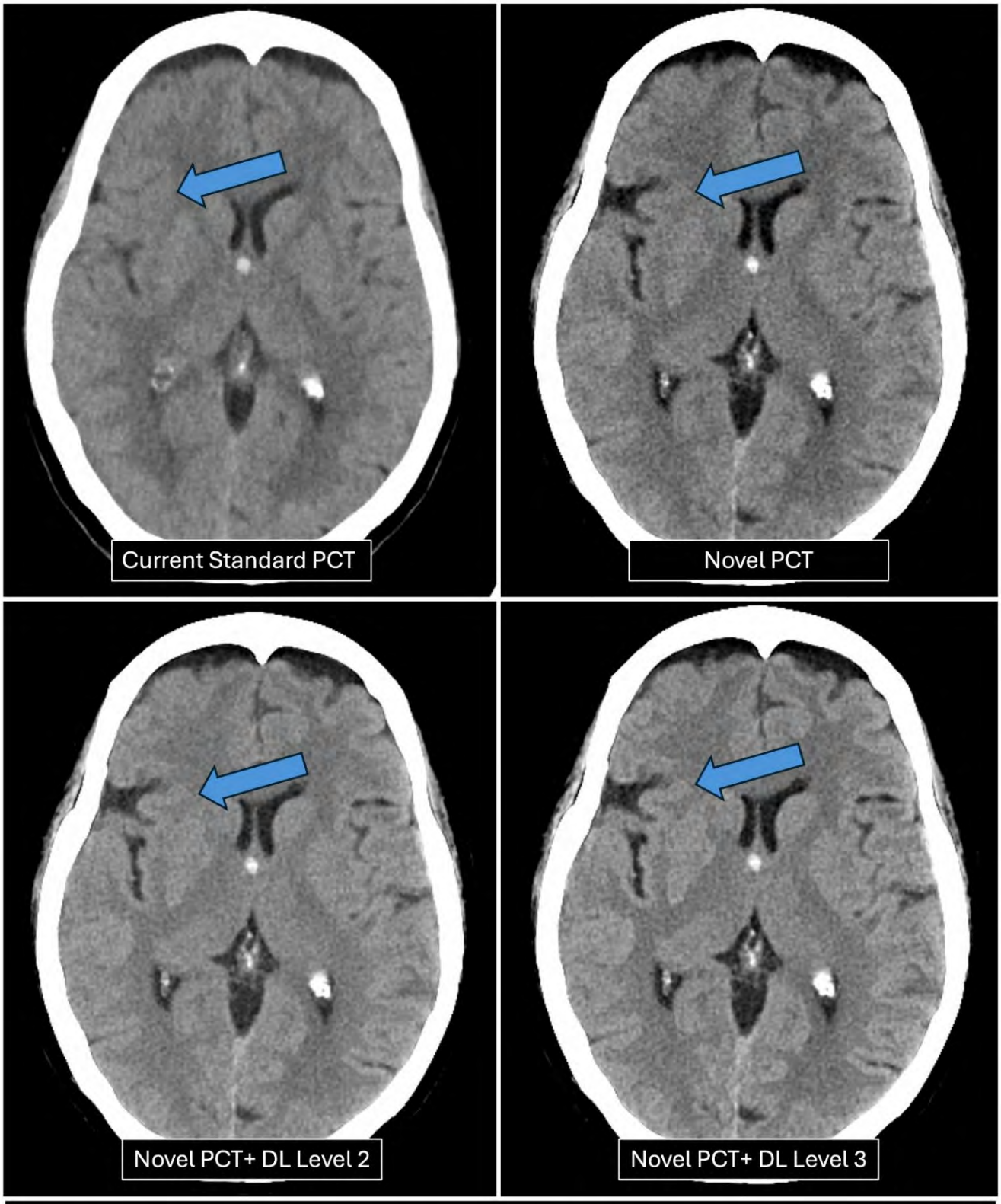

Comparison of current clinical standard PCT, novel PCT, and novel PCT with medium and high levels of deep learning algorithm applied. There is improved grey white visualization with the novel PCT, along with improved visualization of the right insular ribbon (blue arrow). A colloid cyst is also noted centrally within the image.

379

Localization of Diffuse Axonal Injury Lesions using Machine Learning Segmentation and Anatomic Parcellation

Peter I Kamel MD, Annie Trang, Jamie Podell MD, Uttam Bodanapally MBBS
University of Maryland, Baltimore, MD, USA

Abstract Category

AI/Informatics

Purpose

Diffuse axonal injury is a severe form of traumatic brain injury that leads to numerous lesions which characteristically involve the grey-white interface, corpus callosum, and brainstem. The number and small size of the lesions can make it challenging for automated quantification, localization, and subsequent prognostication. The purpose of this study was to develop and evaluate a machine learning-based segmentation neural network and parcellation algorithm to localize hemorrhagic lesions in diffuse axonal injury.

Materials & Methods

Initial training data consisted of 98 MRI examinations with known traumatic brain injury. Hemorrhagic lesions on SWI images were manually segmented by a board-certified neuroradiologist, critical care neurologist, and trauma radiologist. A 3D full-resolution nnU-Net was trained for 150 epochs with 5 folds for cross-validation with multiple iterations of training correction. Segmentation inference was performed on a separate set of 132 MRI examinations with diffuse axonal injury without midline shift or significant parenchymal distortion. Images were registered to a standard anatomic atlas with anatomic parcellation performed with TorchIO and HighRes3DNet. Segmentation was correlated with anatomic parcellation to localize the lesions. Localization was compared to ground truth radiologist determination of the presence or absence of lesion in the specified territory.

Results

For all locations, the algorithm demonstrated an overall accuracy of 81.4% with sensitivity of 79.7% and specificity of 83.2%. Accuracy was highest for the lobar white matter (95.5%), thalamus (87.7%), and frontal cortex (87.1%) with lowest accuracy for the basal ganglia (72.3%), corpus callosum (74.2%), and brainstem (76.8%). The algorithm demonstrated lower sensitivity with higher specificity for posterior fossa lesions with higher sensitivity and lower specificity for supratentorial lesions with common limitations related to ventriculostomy catheters and from other areas of susceptibility such as mineralization in the basal ganglia.

Conclusion

Machine learning-based segmentation and anatomic parcellation serves as a viable method for localizing traumatic brain injury lesions though with limitations, particularly with the sensitivity of posterior fossa lesions and specificity of basal ganglia lesions.

References

Humble SS, Wilson LD, Wang L, Long DA, Smith MA, Siktberg JC, Mirhoseini MF, Bhatia A, Pruthi S, Day MA, Muehlschlegel S, Patel MB. Prognosis of diffuse axonal injury with traumatic brain injury. J Trauma Acute Care Surg. 2018 Jul;85(1):155-159. doi: 10.1097/TA.0000000000001852. PMID: 29462087; PMCID: PMC6026031.

Images/Tables

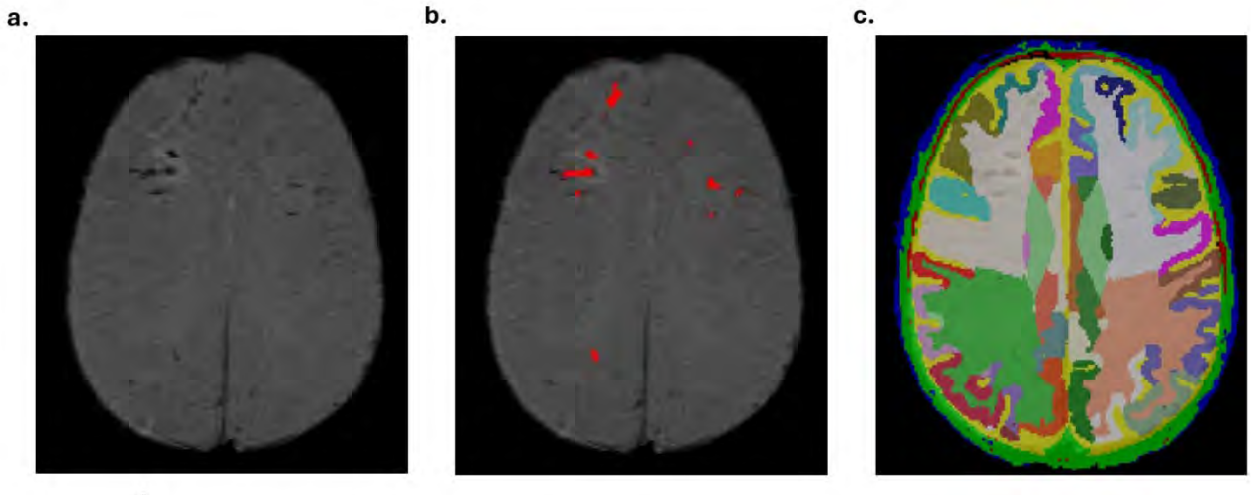

d.

Location	Hemorrhage Volume (cc)	Percent Hemorrhage
Right-Frontal-White-Matter	1.472	1.93%
Right-PIns-posterior-insula	0.523	23.32%
Left-Frontal-White-Matter	0.519	0.69%
Right-Temporal-White-Matter	0.51	1.52%
Right-MFG-middle-frontal-gyrus	0.327	2.22%
Right-LiG-lingual-gyrus	0.303	3.54%
Right-Claustrum	0.234	8.55%
Right-Insula-White-Matter	0.225	1.78%

Figure 1. (**a**) SWI image of a patient with diffuse axonal injury (DAI). (**b**) Segmentation map of DAI lesions automatically performed by a machine learning algorithm. (**c**) Anatomic parcellation map overlaid on the brain parenchyma. (**d**) Quantified analysis of the DAI lesion location and volume.

384

Prediction of HPV-positive Squamous Cell Carcinoma using Self-Supervised Learning

John D Mayfield M.D., Ph.D., M.Sc., Karen Buch M.D., Vrushab Gowda J.D., M.D., Edwin Qiu B.S., Osamu Sakai M.D., Ph.D.
Massachusetts General Hospital, Boston, MA, USA

Abstract Category

AI/Informatics

Purpose

There has been a progressive increase in the prevalence of head and neck cancers (HNCs) in the past decade, with more than 660,000 newly diagnosed cases and over 300,000 deaths per year globally, largely driven by squamous cell carcinoma (SCC). Human papillomavirus (HPV)-associated SCCs, a subset of SCCs, have seen the greatest rise in incidence affecting a younger patient population. This trend is a critical public health concern at national and supranational levels, a fact compounded by the small numbers of subspecialty-trained head and neck radiologists needed to evaluate these patients. Machine learning techniques can play a crucial role in both extending their capabilities and assisting their colleagues in lower resource settings. We propose the comparison of two feature extraction methods for self-supervised learning: SwinUNETr and Clustering-constrained Attention Multiple Instance Learning (CLAM). These were benchmarked against a 3D DenseNet121-based architecture. A subsequent linear classifier was used to identify HPV-positive cancer on single timepoint volumetric CT for each SSL model.

Materials & Methods

From the TCIA oropharyngeal radiomics (OP-Radiomics) dataset, 440 of the 606 patients reported p16 positivity, indicating HPV-positive status with 121 negative and 319 positive cases. Class balancing was achieved through data augmentation and weight balancing. Aerodigestive tract was identified as the origin and volumes were center cropped

to size 128x128x60 to involve surrounding soft tissues. Volumes were then passed into each model following a 5-fold cross-validation split for feature extraction into a latent representation. A subsequent linear classifier predicted HPV status on training and validation datasets. The 3D DenseNet121 was modified for the volume sizes and run following manual hyperparameter optimization.

Results

The SwinUNET model achieved 0.82 validation AUC (95% CI: 0.72-0.88). CLAM model resulted in a 0.79 validation AUC (95%CI: 0.65-0.84). The benchmark 3D DenseNet121 resulted in a 0.81 validation AUC (95%CI: 0.55-0.89).

Conclusion

SSL models performed similarly to the 3D DenseNet121 with the SimSiam model demonstrating noninferior performance (p-value 0.199, ANOVA mean AUC). Their application can provide decreased reliance on segmentation and large CNN architectures to differentiate HPV-related HNC on CT, a potential benefit in practice settings lacking head and neck radiologists.

References

1. Kwan JYY, Su J, Huang SH, Ghoraie LS, et al. (2019). **Data from Radiomic Biomarkers to Refine Risk Models for Distant Metastasis in Oropharyngeal Carcinoma**. The Cancer Imaging Archive. https://doi.org/10.7937/tcia.2019.8dho2gls
2. Cao, H., Wang, Y., Chen, J., et al, 2022, October. Swin-unet: Unet-like pure transformer for medical image segmentation. In *European conference on computer vision* (pp. 205-218). Cham: Springer Nature Switzerland.
3. Ryan, S., Carlson, N., Butler, H., et al. 2020. Cluster activation mapping with applications to medical imaging. *arXiv preprint arXiv:2010.04794*.

386

Role of Hybrid PET-MRI in Pre-surgical Evaluation of Refractory Epilepsy

Sanidhya S Karve MD[1], Rajesh R Kannan MD[1], Suresh K Mukherji MD[2]
[1]Amrita Institute Of Medical Sciences and Research Center, Kochi, Kerala, India. [2]University of Louisville, Louisville, Kentucky, USA

Abstract Category

Functional/Advanced Imaging

Purpose

One-third of epilepsy patients do not improve on medications alone, and surgery is the most successful method of treating medically unresponsive epilepsy. Hybrid PET-MRI is an emerging technique that increases the detection of epileptogenic structural lesions. The purpose of our study is to determine the role of PET-MRI in the pre-surgical evaluation of refractory epilepsy.

Materials & Methods

The study population consisted of 51 patients with medical refractory epilepsy (ages 1yo-43yo) with abnormal intracranial findings detected on Hybrid PET-MRI performed using a dedicated seizure protocol. All patients underwent surgery and the PET-MRI abnormalities were directly compared with histopathology. The ability of PET-MRI to localize and lateralize the surgically confirmed lesions was also compared with stand-alone PET and MRI using histopathology as the gold standard. McNemar's Chi-Square test (IBM SPSS 20.0 software) was used to calculate sensitivity, specificity, predictive values, and accuracy.

Results

Hybrid PET-MRI detected different structural lesions. 17(33.3%) patients had MTS, 21(41.2%) patients had FCD, 8(15.7%) patients had gliosis, 3(5.9%) patients had tumors, 1 had a cavernoma, and one was negative. PET-MRI detected single pathology in 44 patients and dual pathology in 6 patients. Histopathology confirmed the presence of single pathology in 43 patients and dual pathology in three. Hybrid PET-MRI is 84.8% sensitive, 78% accurate, and 20% specific in diagnosing epileptogenic lesions when compared with histopathology. Hybrid PET-MRI was found to be superior in lesion lateralization, where sensitivity, specificity, and accuracy of hybrid PET-MRI were 93.1%, 94.7%, and 93.8%, respectively, when compared to MRI's 82.8%, 78.9%, and 81.3% and stand-alone PET's 72.4%, 73.7%, 72.9% respectively.

Conclusion

Hybrid PET-MRI is an important modality to help identify intra-cranial abnormalities in patients with medically refractory epilepsy. Hybrid PET-MRI is superior to stand-alone MRI / PET in detecting and diagnosing epileptogenic lesions in patients with intractable epilepsy.

References

1. Friedman E. Epilepsy Imaging in Adults: Getting It Right. American Journal of Roentgenology. 2014 Nov 1;203(5):1093–103.
2. Shin, H. W., Jewells, V., Sheikh, A., et al. (2015). Initial experience in hybrid PET-MRI for evaluation of refractory focal onset epilepsy. *Seizure*, *31*, 1-4. https://doi.org/10.1016/j.seizure.2015.06.010
3. Oldan JD, Shin HW, Khandani AH, et al. Subsequent experience in hybrid PET-MRI for evaluation of refractory focal onset epilepsy. Seizure. 2018 Oct;61:128–34.
4. Kun Guo, Cui B, Shang K, et al. Assessment of localization accuracy and postsurgical prediction of simultaneous 18F-FDG PET/MRI in refractory epilepsy patients. EurRadiol. 2021 Sep;31(9):6974–82.
5. Sanidhya S. Karve, R Rajesh Kannan. Role of PET-MRI in detecting and diagnosing Focal Cortical Dysplasias. International Journal of Health Sciences and Research [IJHSR] DOI: https://doi.org/10.52403/ijhsr.20221219

Images/Tables

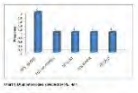

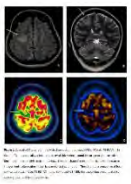

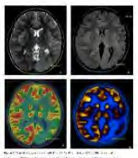

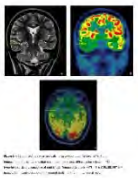

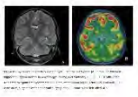

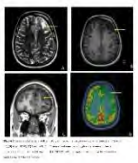

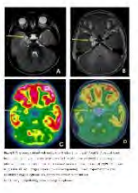

393

Analysis of Relative Cerebral Blood Volume in Patients Over the Course of Pembrolizumab Treatment

Jared Stoller MS[1], Daniel L Schwartz BS[1], Doonyaporn Wongsawaeng MD[2], Leslie L Muldoon PhD[1], Rochelle Fu PhD[1], Ramon F Barajas MD[1], Prakash Ambady MD[3]

[1]Oregon Health and Science University, Portland, Oregon, USA. [2]Siriraj Hospital, Mahidol University, Bangkok, THAILAND, Thailand. [3]Providence Portland Medical Center, Portland, Oregon, USA

Abstract Category

Functional/Advanced Imaging

Purpose

The current standard of care based on gadolinium (Gd) MRI cannot reliably distinguish true progression from treatment-related imaging changes (TRIC) after chemo-radiation (CRT) in high-grade glioma. Not feasible with Gd-MRI, Ferumoxytol, a blood pool contrast agent, enables 'steady-state imaging' . This open-label single arm phase 2 trial (NCT03347617) evaluated the longitudinal trend of tumor steady-state Ferumoxytol (Fe) [DS1] relative cerebral blood volume (Fe-SS rCBV) and whether Fe-SS rCBVs differed between glioblastoma patients who experienced TRIC and true progression (TP) post-CRT. We hypothesize that TRIC will exhibit lower Fe-SS rCBV than in TP due to the absence of neoangiogenesis.

Materials & Methods

This trial enrolled patients with newly diagnosed histologically confirmed (WHO 2007) grade 4 glioma who were scheduled to start standard CRT followed by 6 cycles of adjuvant temozolomide (TMZ). They received upfront pembrolizumab (200 mg IV every 3 weeks starting +/- 10 days from start of CRT and continued for up to two years, dose limiting toxicity or confirmed progression. Patients underwent Fe-MRI (early phase and 24-hour delayed phase) at four predetermined imaging sessions: 1. pre-radiation, 2. post-radiation, 3. suspected progression (SP), and 4. one-month post-SP. Clinical response (TRIC vs. TP) was assessed by biopsy or modified RANO criteria. Difference in Fe-rCBV between TRIC vs. TP was tested using two sample t-test between imaging sessions and association between overall survival (OS) and Fe-rCBV was analyzed using Cox regression.

Results

A total of 52 patients were enrolled and 43 patients with at least one follow-up response assessment Fe- MRI scan were evaluable (15 female, median age, 58 years (range,22-77) . At the end of the two-year treatment period, 14 patients had TRIC (1 patient had two instances of TRIC and 1 patient had 3 instances), 25 patients had TP without TRIC, and 4 patients had neither. The median time from consent to TRIC was 4.2 months, and from consent to TP was 8.8 months. A total of 18 Fe-SS scans were evaluable at SP by RANO criteria (11 TP, 7 TRIC).

At pre-radiation and post-radiation, no difference in Fe ss-rCBV was observed between TP and TRIC patients, although ss-rCBV decreased from pre-radiation to post-radiation in both groups. At the time of SP, ss-rCBV increased in TP patients but decreased in TRIC patients. TRIC patients had an mean ± SD rCBV of 1.64 ± 0.57, while those with TP had a mean(SD) rCBV of 2.53 ± 1.93; the difference was not significant (P = 0.18), partly due to small sample size. At post-radiation, a lower rCBV was significantly associated with longer OS (P = 0.0058). With the decrease of one unit of rCBV, the risk of mortality decreased by 32% (HR = 0.68; 95% CI, 0.51, 0.89). The association remained after adjusting for age and KPS.

Conclusion

We presented a prospective longitudinal trend in rCBV values over the course of treatment. The substantial mean difference observed between TRIC and TP patients' needs to be confirmed in a larger study. This work presents significant prognostic evidence that lower Fe-ss-rCBV at post radiation is predictive for overall survival.

References

Barajas RF Jr, Schwartz D, McConnell HL, Kersch CN, Li X, Hamilton BE, Starkey J, Pettersson DR, Nickerson JP, Pollock JM, Fu RF, Horvath A, Szidonya L, Varallyay CG, Jaboin JJ, Raslan AM, Dogan A, Cetas JS, Ciporen J, Han SJ, Ambady P, Muldoon LL, Woltjer R, Rooney WD, Neuwelt EA. Distinguishing Extravascular from Intravascular Ferumoxytol Pools within the Brain: Proof of Concept in Patients with Treated Glioblastoma. AJNR Am J Neuroradiol. 2020 Jul;41(7):1193-1200. doi: 10.3174/ajnr.A6600. Epub 2020 Jun 11. PMID: 32527840; PMCID: PMC7357650.

Images/Tables

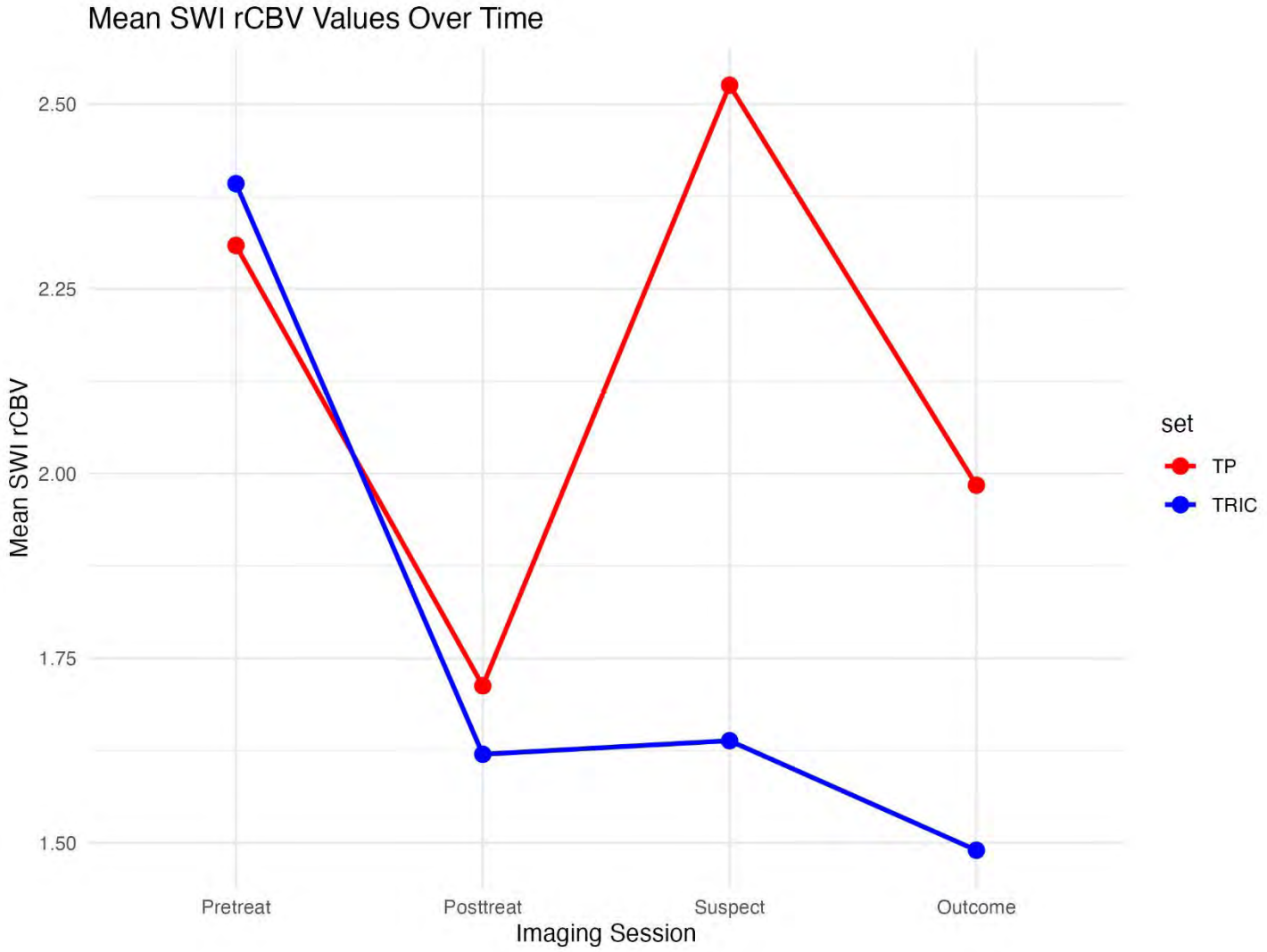

406

Disability & Accessibility in Neuroradiology: Where Are We Now and Future Directions

Karen Buch MD, William Mehan MD
Massachusetts General Hospital, Boston, MA, USA

Abstract Category

Socioeconomics & Health Policy

Purpose

To discuss new legislation and regulation published in August 2024 related to Title II of the American Disabilities Act (ADA) with a specific focus on imaging equipment accommodations and accessibility for patients with disabilities. With this discussion of legislation, survey-based data amongst neuroradiology fellows and attendings at a large level I stroke/trauma center in New England assessing their knowledge of Title II of the ADA, formal education in caring for patients with disabilities, and comfort with providing clinical care for patients with disabilities was assessed.

Materials & Methods

This was an IRB-approved, voluntary survey conducted at a level I trauma/stroke center in New England which is part of a large integrated healthcare network. Surveys were administered to neuroradiology attendings and fellows to assess level of knowledge of Title II of the ADA preparedness, comfort with providing care for patients with disabilities, experience with formal training on caring for patients with disabilities, and knowledge of resources for accommodating patients with disabilities presenting to Radiology for imaging or imaging-guided procedures. Surveys were conducted on a 5-part Likert scale ranging from (0= no knowledge/completely uncomfortable up to 5 = expert level

knowledge/completely comfortable). Basic descriptive statistics/frequencies from the completed surveys were performed.

Results

A combined total of 35 individuals responded comprising of 21 neuroradiology fellows and 14 neuroradiology faculty responded to the voluntary survey. On average radiology attendings and trainees had little knowledge of the details of Title II (mean 1.4), felt uncomfortable providing care for patients with disabilities (mean 2.3), and had little knowledge of resources available for patients with disabilities (mean 2.2). There was no significant difference between responses from attending radiologists and radiology fellows (P = 0.66).

Conclusion

Current survey-based data of neuroradiology attendings and trainees at a single institution shows that there remains significant barriers to imaging access for patients with disabilities. The results of this study highlight the needs to initiatives, multi-disciplinary collaboration, and resources to augment the current experience and accessibility of imaging for patients with disability. With new legislation and regulations for improving disability access to medical imaging equipment required by hospitals, this topic of accessibility is more relevant than ever.

References

1. Okoro CA, Hollis ND, Cyrus AC, Griffin-Blake S. Prevalence of disabilities and health care access by disability status and type among adults - United States, 2016. MMWR Morb Mortal Wkly Rep. 2018;67(32):882-887.
2. Net JM, Feliciano YZ, Podsiadlo V, Dialani V, Grimm LJ. Optimizing the Patient Experience for Women With Disabilities in the Breast Imaging Clinic. J Breast Imaging. 2024 Apr 1;6(2):183-191. doi: 10.1093/jbi/wbad106. PMID: 38401130.
3. Klassen AC, Yudell M. Barriers and facilitators to mammography among women with intellectual disabilities: a qualitative approach. Disabil Soc. 2020;35(8):1290-1314.
4. Centers for Disease Control and Prevention. Disability barriers to inclusion. Updated September 16, 2020. Accessed June 13, 2024. https://www.cdc.gov/ncbddd/disabilityandhealth/ disability-barriers.html.
5. CDC. Disability and health promotion. CDC's commitment to disability inclusion. Updated July 17, 2023. Accessed June 13, 2024.

419

Cavernoma as a Cause of Tremor: Case Report and Literature Review

Tiffany A Rodrigues MEng[1], Andrew Z Yang MA (Philosophy)[1], Sriranga Kashyap PhD[2], Can Sarica MD[1], Rafael E Buongermini MD[1], Artur Vetkas MD, PhD[1], Jurgen Germann PhD[1], Alfonso Fasano MD, PhD[1], Suneil K Kalia MD, PhD[1], Andres M Lozano MD, PhD[1], Marie Slegr MD[1], Alexandre Boutet MD, PhD[1]

[1]University of Toronto, Toronto, Ontario, Canada. [2]University Health Network, Toronto, Ontario, Canada

Abstract Category

Adult Brain

Purpose

Cavernomas are vascular malformations of the central nervous system that can cause focal neurological deficits[1,2]. The present study reports an individual presenting with tremor concurrently with a cavernoma in the cerebellar dentate nucleus. We hypothesize that her cavernoma is disrupting neurocircuitry involved in motor control, such as the dentatorubrothalamic tract (DRTT), thereby causing tremor. The aims of this study are to 1) demonstrate volume change of the patient's cavernoma over time; 2) confirm impingement on critical motor circuits; and 3) review the literature of cavernoma causing movement disorder. Understanding the relationship between cavernoma and tremor is critical to prevent misdiagnosis, incorrect treatment, or delay in care.

A 59-year-old right-handed woman presented with a new mild, intermittent right-hand rest tremor, which was also observed while walking, that started four months prior. She also reported right arm stiffness and right shoulder pain. The woman was known to have a cavernoma in the right dentate since 2008. Work-up included a repeat MRI of the brain revealing progressive growth of the cavernoma.

Materials & Methods

First, the patient's serial MRIs were skull-stripped, bias-field corrected, co-registered to a high-resolution T1-weighted MRI, and in-plane interpolated to ensure consistent orientation and spatial resolution. Then, cavernoma was manually segmented on each MRI (FSL; https://fsl.fmrib.ox.ac.uk/). Next, to assess the impact of the cavernoma on motor pathways, tractography analysis was conducted to examine the dentatorubrothalamic tract (DRTT), a critical pathway

for motor control. Diffusion-weighted images were acquired on a 3T MRI scanner using a 64-direction DWI sequence, and deterministic fiber tracking was performed, where the DRTT was reconstructed using seeds in the dentate, red nucleus, and thalamus (DSI Studio; https://dsi-studio.labsolver.org). In addition, a systematic review was conducted according to PRISMA guidelines to identify other cases of cavernomas causing movement disorders.

Results

Lesion segmentation confirmed progressive lesion growth since 2008. The volumes of 2008, 2016, 2018, and 2024 lesions were 43.39 mm^3, 717.04 mm^3, 744.42 mm^3, and 843.09 mm^3, respectively (Figure 1). Patient-specific reconstruction of the DRTT indicated that while the lesion did not impinge on the tract in 2008, it did in 2024 (Figure 1). The literature search (48 articles screened) resulted in 8 articles reporting cavernoma causing Parkinsonism. This case highlights the importance of secondary causes of movement disorders. Crucially, in our case, the radiological interpretations reported stable findings from 2016 until 2024, which did not raise the possibility of the cavernoma as a cause of tremor. At this early stage, the exact type of secondary tremor remains to be differentiated to tailor the optimal treatment. Neuroradiologists should be familiar with key motor pathways and lesions mimicking movement disorders.

Conclusion

In conclusion, this case highlights the potential of a cavernoma in the dentate nucleus to disrupt motor pathways, thereby contributing to tremor onset. Recognizing progressive lesion growth and its anatomical impact is essential to distinguishing secondary tremors from primary movement disorders. Early and accurate identification of such cases may lead to more targeted interventions, emphasizing the importance of detailed radiological assessment and awareness of secondary causes of movement disorders among clinicians.

References

1. Flemming KD, Lanzino G. Cerebral cavernous malformation: what a practicing clinician should know. *Mayo Clin Proc* 2020;95:2005–20. https://doi.org/10.1016/j.mayocp.2019.11.005
2. Kuroedov D, Cunha B, Pamplona J, et al. Cerebral cavernous malformations: typical and atypical imaging characteristics. *J Neuroimaging* 2023;33:202–17. https://doi.org/10.1111/jon.13072

Images/Tables

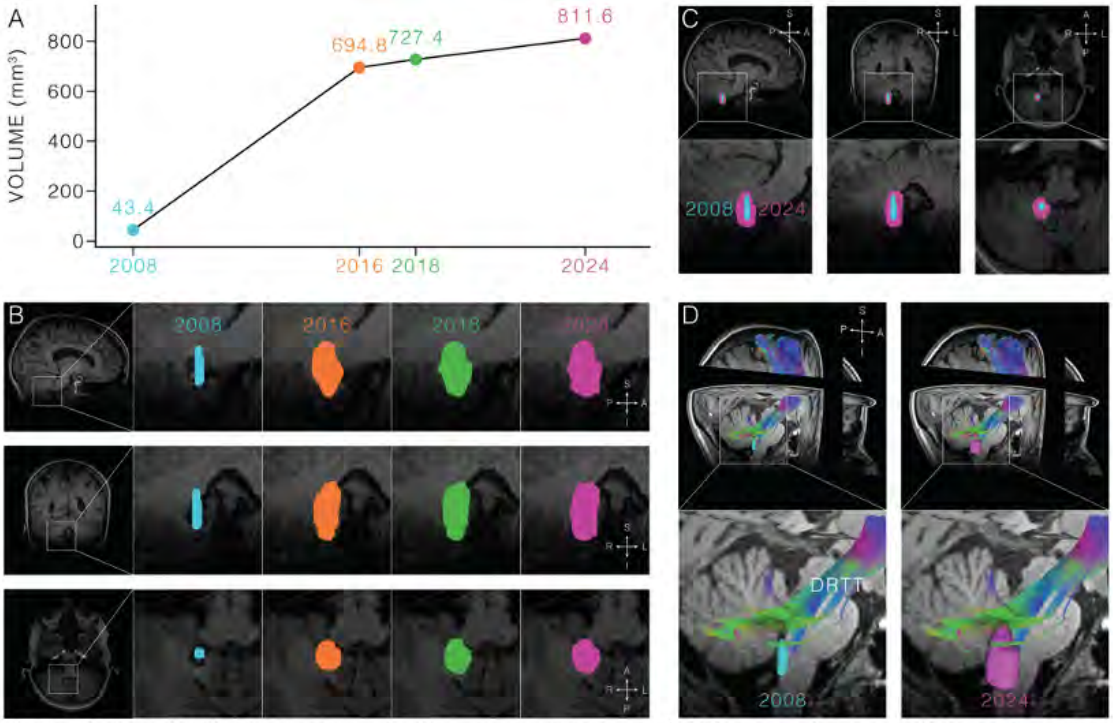

Figure 1: Longitudinal assessment of cavernoma lesions. (A) Volume changes of the cavernoma lesion over time, indicating significant growth from 2008 (cyan), 2016 (orange), 2018 (green), to 2024 (magenta). (B) T1 images showing the evolution of the cavernoma from 2008 (cyan) to 2024 (magenta). (C) T1 image comparing the cavernoma lesion in 2008 (cyan) to 2024 (magenta). (D) T1 image with 3D reconstructions of the cavernomas showing the relationship of the lesion to the dentato-rubrothalamic tract (DRTT), where in 2008 (cyan) there is no impingement of the DRTT in contrast to 2024 (magenta).

432

Endovascular treatment strategies for carotid blowout syndrome and outcomes: single centre experience

Hong Wan Yap, Tze Phei Kee
National Neuroscience Institute, Singapore, Singapore, Singapore

Abstract Category

Interventional

Purpose

Carotid blowout syndrome (CBS) is a challenging complication that arises in patients treated with head and neck cancer as a result of arterial wall necrosis from irradiation or direct tumor invasion. This retrospective review aims to identify factors affecting the endovascular treatment decision of CBS between reconstruction and deconstruction techniques.

Materials & Methods

We conducted a retrospective review of all CBS cases with either internal carotid artery (ICA) or common carotid artery (CCA) as culprit vessel, treated endovascularly at our institution from January 2015 to June 2024. A total of 8 cases were identified. CBS was classified as type 1 (impending rupture), type 2 (sentinel bleeding) and type 3 (active massive bleeding).

Results

Out of the 8 cases, 4 underwent parent artery reconstruction with covered stent while the other 4 underwent parent artery sacrifice.

Of the 4 patients treated with covered stent, 2 had type 3 CBS while the other 2 had type 1 CBS. Balloon test occlusion (BTO) was not performed. 3 out of 4 patients had delayed complications. 1 patient had multiple rebleeding episodes over the next few months from unknown source with development of mild in-stent stenosis; 2 developed delayed stent occlusion with ipsilateral MCA infarct.

Of the 4 patients treated with parent artery sacrifice, all presented with type 1 CBS. One patient failed BTO and had external carotid artery-ICA bypass prior to occlusion of the offending ICA. The other 3 demonstrated good cross flow from contralateral ICA injection, of which 1 was performed with BTO and another was performed with compression of the ipsilateral ICA. 3 out of 4 patients had complications. 2 developed infarcts of the occluded ICA territory (1 immediate, 1 delayed), where the patient who developed immediate infarct passed BTO the day prior. 1 other patient had further bleeding episodes from the ipsilateral CCA (post ICA occlusion) necessitating additional sacrifice of the ipsilateral ECA and CCA.

Conclusion

Endovascular treatment for CBS carries high complication rates regardless of treatment strategies. Formal BTO would be of value to determine cross flow, with quick alternative surrogates being estimation of cross flow with manual compression or assessment of the size of ACOM. For patients who passed BTO, parent artery sacrifice may be a more favorable option, as it does not require institution of dual antiplatelet therapy to maintain stent patency, which may complicate future bleeding. For patients who failed BTO, covered stent placement would be more favorable given the high risk of ischaemic event in the absence of adequate cross flow intracranially. Careful consideration of various factors involved is essential before deciding on treatment strategy to balance the risks of developing ischaemic or haemorrhagic events.

References

Chang FC, Lirng JF, Luo CB, Guo WY, Teng MM, Tai SK, Chang CY. Carotid blowout syndrome in patients with head-and-neck cancers: reconstructive management by self-expandable stent-grafts. AJNR Am J Neuroradiol. 2007 Jan;28(1):181-8.

Suárez C, Fernández-Alvarez V, Hamoir M, Mendenhall WM, Strojan P, Quer M, Silver CE, Rodrigo JP, Rinaldo A, Ferlito A. Carotid blowout syndrome: modern trends in management. Cancer Manag Res. 2018 Nov 13;10:5617-5628.

Kikuchi K, Yoshiura T, Hiwatashi A, Togao O, Yamashita K, Honda H. Balloon test occlusion of internal carotid artery: Angiographic findings predictive of results. World J Radiol. 2014 Aug 28;6(8):619-24.

Imai T, Asada Y, Matsumoto K, Sato I, Goto T, Matsuura K. Neck dissection with carotid artery resection after insertion of a protective endovascular covered stent for recurrent head and neck cancer: a case report. Int Cancer Conf J. 2022 Feb 1;11(2):119-123.

Images/Tables

Parent artery sacrifice for type 1 CBS of the left ICA, subsequently developed another type 1 CBS of the left CCA which was treated by sacrificing the left CCA and ECA

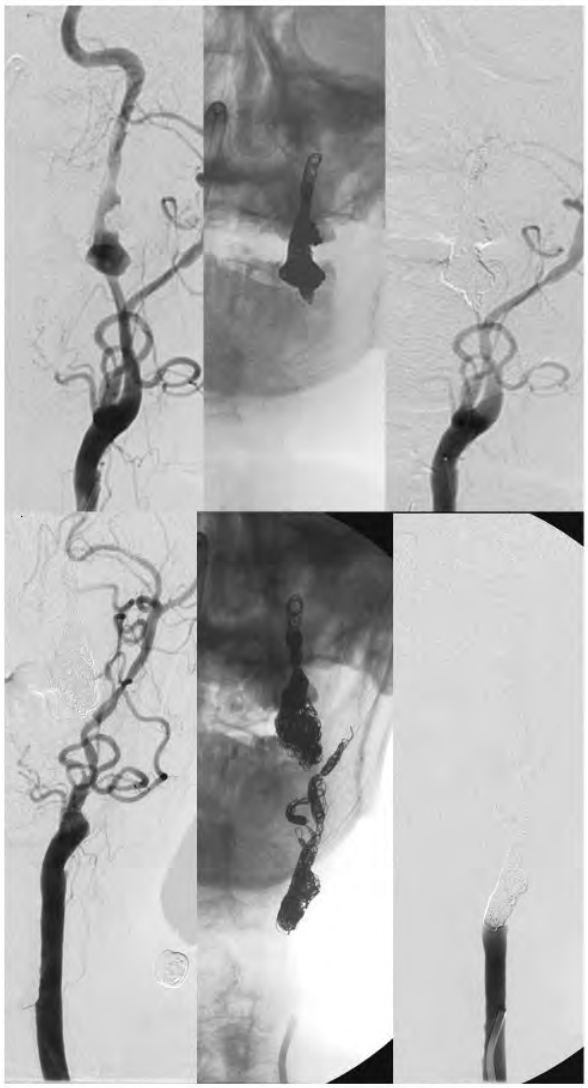

Covered stent treatment for type 3 CBS of the right ICA, complicated by delayed stent occlusion 3 years post stenting with ipsilateral haemodynamic infarct

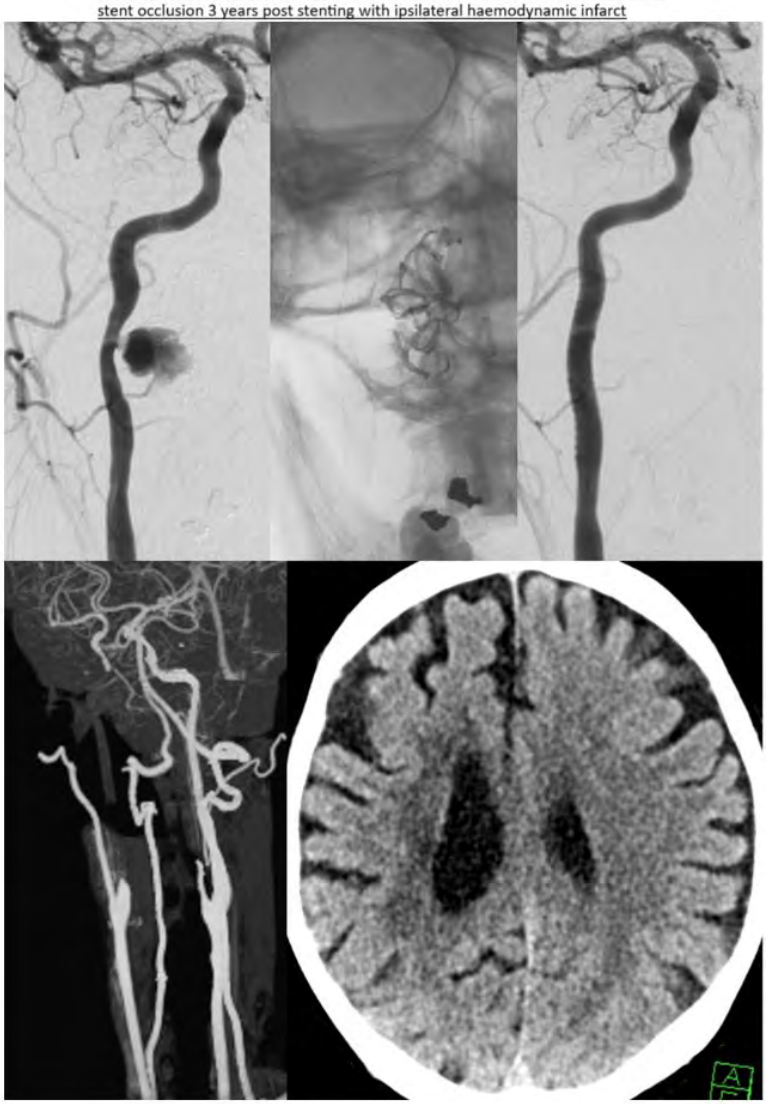

435

Comparison of Deep Learning segmentation algorithms for delineating cellular Gioblastoma on post-operative MRI

Andrew Forester[1], Laura Beltran[1], Aurélie Beaudoin[1], Taha Belbadaoui BS[1], Louis Gagnon MD-PhD[2]
[1]Laval University, Quebec City, Qc, Canada. [2]Quebec City, Qc, Canada

Abstract Category

AI/Informatics

Purpose

For glioblastoma (GBM) patients, distinguishing residual and/or recurrent tumors from treatment-related changes and pseudoprogression is essential for determining appropriate follow-up treatment strategies. Additionally, accurately delineating infiltrative (non-enhancing) tumor from peri-tumoral edema is crucial for implementing emerging surgical techniques, such as supramarginal resection[1]. However, this task is challenging[2] and can benefit from deep learning (DL) algorithms combined with multishell diffusion MRI. While DL algorithms are effective at accurately segmenting enhancing cellular tumors, the delineation of infiltrative disease remains a significant challenge[3]. The aim of this study is to evaluate whether specific DL algorithms outperform others in two key areas: (1) segmentation of non-enhancing cellular tumors, and (2) differentiation of recurrent disease from post-treatment changes.

Materials & Methods

Multimodal MRI from a UCSD cohort of 178 patients (mean age, 56 years ± 13 [SD]; 116 male, 62 female) with 243 MRI timepoints was used. Sequences included T1pre- and post-contrast, FLAIR, T2, Restricted Spectrum Imaging (RSI) Cellularity maps, and Dynamic Susceptibility Contrast (DSC)-derived Cerebral Blood Volume (CBV) maps. Cellular tumor (both enhancing and non-enhancing) were manually annotated by a neuroradiologist and a radiology fellow following the procedure described in Gagnon et al[3].

Three different DL algorithms were tested: nnUNet[4], U-MambaBot[5] and SegResNet[6]. Each algorithm was trained (80% of dataset) and validated (20% of dataset) using 5 fold cross validation with the standard out of the box 3D full-resolution configuration.

The predicted enhancing and nonenhancing cellular tumor volumes were compared to the ground truth segmentations using Dice score and Volume Similarity (VS). A threshold was applied to the volume of segmented cellular tumor to differentiate residual disease from post-treatment changes. The receiver operating characteristic (ROC) curve was obtained by varying the threshold volume and the performance of each algorithm was defined as the area under the curve (AUC) of ROC.

Results

Fig 1A presents the Dice score and VS of the three DL algorithms. Dices and VS were comparable for all three algorithms but nnU-Net was slightly higher (mean Dice score: 0.44 ± 0.26, mean VS: 0.66 ± 0.29, $p<0.05$). Fig 1B displays the ROC curve for each algorithm along with their respective AUC. nnU-Net and U-MambaBot (AUC 0.837 and 0.830) were slightly higher than SegResNet (AUC: 0.811, $p<0.05$ n=10 000 random permutation).

Conclusion

All three algorithms performed well in distinguishing recurrent glioblastoma from post-treatment changes. However, their performances in delineating non-enhancing cellular tumor were similarly suboptimal. The lack of significant difference in performance among the three DL algorithms suggests that the primary cause of poor results lies in the ground truth segmentations of the dataset. The ambiguous boundaries of non-enhancing regions makes it difficult to annotate a clear and reliable volume with confidence.

A potential hypothesis is that the features extracted by the DL algorithms may not align well with the manually segmented ground truth masks. Improvements in performance could be achieved through several approaches: using segmentation masks generated from a consensus of a larger group of experts, fine-tuning the parameters of the current DL algorithms, developing new algorithms, and employing optimized multishell diffusion MRI sequences with higher b-values.

References

Vivas-Buitrago T, Domingo RA, Tripathi S, et al. Influence of supramarginal resection on survival outcomes after gross-total resection of IDH–wild-type glioblastoma. *J Neurosurg*. 2021;136(1):1-8. doi:10.3171/2020.10.JNS203366

2. Taylor C, Ekert JO, Sefcikova V, Fersht N, Samandouras G. Discriminators of pseudoprogression and true progression in high-grade gliomas: A systematic review and meta-analysis. *Sci Rep*. 2022;12(1):13258. doi:10.1038/s41598-022-16726-x

3. Gagnon L, Gupta D, Mastorakos G, et al. Deep Learning Segmentation of Infiltrative and Enhancing Cellular Tumor at Pre- and Posttreatment Multishell Diffusion MRI of Glioblastoma. *Radiol Artif Intell*. 2024;6(5):e230489. doi:10.1148/ryai.230489

4. Isensee F, Jaeger PF, Kohl SAA, Petersen J, Maier-Hein KH. nnU-Net: a self-configuring method for deep learning-based biomedical image segmentation. *Nat Methods*. 2021;18(2):203-211. doi:10.1038/s41592-020-01008-z

5. Ma J, Li F, Wang B. U-Mamba: Enhancing Long-range Dependency for Biomedical Image Segmentation. Published online January 9, 2024. doi:10.48550/arXiv.2401.04722

6. Myronenko A. 3D MRI brain tumor segmentation using autoencoder regularization. Published online November 19, 2018. doi:10.48550/arXiv.1810.11654

Images/Tables

A)

Algorithms	Dice Score		Volume similarity	
	Mean ± SD	Median and IQR	Mean ± SD	Median and IQR
Total cellular tumor				
nnU-Net	0.68 ± 0.23	0.77 (0.60–0.85)	0.81 ± 0.22	0.89 (0.72–0.95)
U-MambaBot	0.65 ± 0.24*	0.73 (0.55–0.83)	0.77 ± 0.26*	0.88 (0.73–0.95)
SegResNet	0.66 ± 0.25*	0.75 (0.55–0.83)	0.78 ± 0.26*	0.88 (0.73–0.95)
Enhancing cellular tumor				
nnU-Net	0.73 ± 0.27	0.84 (0.64–0.92)	0.79 ± 0.26	0.91 (0.72–0.96)
U-MambaBot	0.69 ± 0.30*	0.82 (0.57–0.92)	0.75 ± 0.30*	0.89 (0.69–0.96)
SegResNet	0.70 ± 0.30*	0.84 (0.57–0.92)	0.76 ± 0.30*	0.91 (0.68–0.96)
Nonenhancing cellular tumor				
nnU-Net	0.44 ± 0.26	0.51 (0.23–0.67)	0.66 ± 0.29	0.75 (0.52–0.89)
U-MambaBot	0.41 ± 0.26*	0.47 (0.13–0.64)	0.64 ± 0.31*	0.74 (0.47–0.89)
SegResNet	0.40 ± 0.26*	0.45 (0.15–0.63)	0.63 ± 0.31*	0.75 (0.42–0.89)

B)

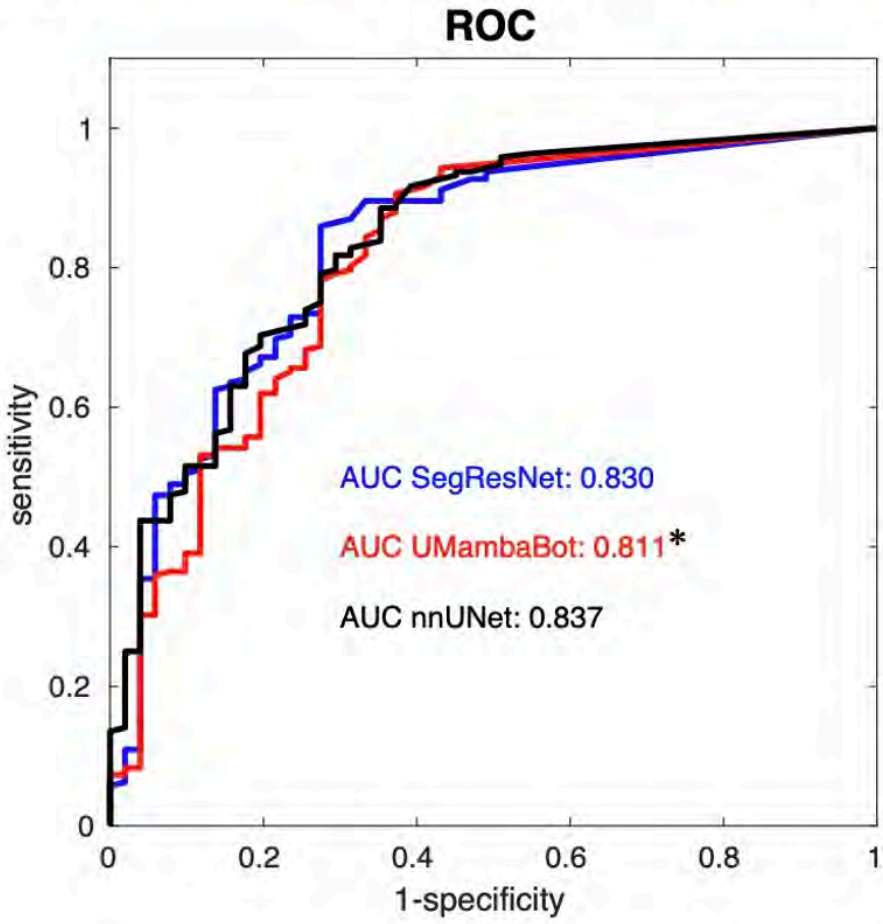

436

Atrial Fibrillation is Associated with Lower Likelihood of First Pass Effect in Thrombectomy for Medium Vessel Occlusion Acute Ischemic Stroke

Omnea Elgendy[1], Michael Dubinski[1], Jane Khalife[2], Jesse Thon[2], Hermann Schumacher[2], Khalid Hanafy[2], Hamza Shaikh[2], Manisha Koneru[2]

[1]Cooper Medical School of Rowan University, Camden, NJ, USA. [2]Cooper Neurological Institute, Camden, NJ, USA

Abstract Category

Interventional

Purpose

First pass effect (FPE), defined as achieving complete reperfusion following a single pass in endovascular thrombectomy (EVT), is associated with clinically favorable outcomes following an acute ischemic stroke. Atrial fibrillation (AF) has been shown to be associated with greater rates of FPE in acute large vessel occlusions; however, the association between AF and FPE in medium vessel occlusions (MeVO) remains unknown.[1] We aimed to assess the association between AF and achieving FPE in MeVO.

Materials & Methods

We retrospectively reviewed a prospectively maintained registry of adult acute ischemic stroke patients at a comprehensive stroke center between 10/2019 and 10/2023. Patients undergoing EVT for a MeVO in a middle cerebral artery segment (M2/M3) were included. Univariable and multivariable logistic regressions were performed for FPE (defined as modified Treatment in Cerebral Infarction [mTICI] 2C/3) and modified FPE (mFPE, mTICI 2B/2C/3) using clinically or statistically significant covariables. Model performance was assessed using receiver operating characteristic curve analysis.

Results

Of 67 patients included patients (median age 70 years, IQR 63-82), 23 had AF. Most occlusions (88.1%) were in the distal M2 segment. FPE and mFPE rates were 34.3% and 58.2%, respectively. In multivariable regressions, AF was independently associated with a lower likelihood of FPE (adjusted OR 0.08, 95% CI 0.01-0.63, p=0.02) and mFPE (adjusted OR 0.04, 95% CI 0.01-0.49, p=0.01). Prior antiplatelet/anticoagulant use was also associated with a lower likelihood of mFPE (adjusted OR 0.05, 95% CI 0.01-0.71, p=0.03). Models for FPE and mFPE showed good discrimination (AUC 0.80 and 0.86, respectively).

Conclusion

AF was associated with a significantly lower likelihood of FPE and mFPE in thrombectomy for MeVOs. These findings highlight the potential need to prepare for additional passes and rescue intraprocedural strategies in EVT for MeVO patients with AF.

References

1. Pillai P, Bush SJ, Kusuma Y, et al. Atrial fibrillation is associated with higher first pass effect following thrombectomy for large vessel occlusion. *J Neurointerv Surg*; 16. Epub ahead of print 17 June 2024. DOI: 10.1136/jnis-2023-020512.

438

Utility of Imaging in the Diagnosis and Successful Treatment of Pulsatile Tinnitus

Ricardo Reyes MS[1], Carleton E Corrales MD[2], Jeffrey P Guenette MD, MPH[1]

[1]Division of Neuroradiology, Brigham and Women's Hospital, Harvard Medical School, Boston, MA, USA. [2]Department of Otolaryngology-Head and Neck Surgery, Brigham and Women's Hospital, Harvard Medical School, Boston, MA, USA

Abstract Category

Head & Neck

Purpose

Pulsatile tinnitus (PT), the perception of a rhythmic sound without an extracorporeal stimulus, affects over 3.4 million people in US every year[1]. The utility of imaging in the setting of PT is unclear. The American Academy of Otolaryngology strongly recommends against imaging unless patients meet stringent criteria[2] while the American College of Radiology recommends either CT or MRI as appropriate for initial workup[3]. This study aims to explore the yield of imaging in the setting of PT.

Materials & Methods

We retrospectively reviewed charts for patients with an ICD-10 code (H93.A) for “Pulsatile Tinnitus” spanning 10 years across our multi-institution healthcare system. Clinical, radiologic, and otologic characteristics were reviewed as well as outcomes with and without treatment.

Results

We randomly sampled 100 patients. 93% (93/100) had tinnitus that was pulsatile. 80% (74/93) of those with documented PT had CT, MR, or ultrasound imaging performed with the majority undergoing MR imaging only (51/74). Potentially life-threatening diagnosis was reported on imaging in 4/74 patients: ICA aneurysm, fibromuscular dysplasia, an arteriovenous fistula, and a clival mass. Treatments for PT included medical and surgical interventions. Of those without imaging, 11% (2/19) received treatment with symptom resolution. Of those with imaging, only 5% (4/74)

received treatment with symptom resolution. Overall, 7% (6/93) of patients with PT received treatment with symptom resolution, 24% (22/93) received treatment without symptom resolution, 16% (15/93) experienced symptom resolution without treatment, and 20% (19/93) did not receive treatment nor did their symptoms improve. 33% (31/93) had unclear outcomes based on available charting data.

Conclusion

Despite the varying recommendations for the workup of PT, imaging has been a prevalent diagnostic tool in our healthcare system. A small number of patients with PT who undergo imaging were diagnosed with a life-threatening etiology while a similarly small number received a successful treatment with resolution of symptoms. Furthermore, ICD coding errors and unclear charting in electronic records makes it challenging to assess PT outcomes.

References

1. Bhatt JM, Lin HW, Bhattacharyya N. Prevalence, Severity, Exposures, and Treatment Patterns of Tinnitus in the United States. *JAMA Otolaryngology–Head & Neck Surgery*. 2016;142(10):959-965. DOI: https://doi.org/10.1001/jamaoto.2016.1700

2. Tunkel DE, Bauer CA, Sun GH, et al. Clinical Practice Guideline: Tinnitus. *Otolaryngology– Head and Neck Surgery*. 2014;151(S2):S1-S40. DOI: https://doi.org/10.1177/0194599814545325

3. Jain V, Policeni B, Juliano AF, et al. ACR Appropriateness Criteria® Tinnitus: 2023 Update.*Journal of the American College of Radiology*. 2023;20(11):S574-S591. DOI: https://doi.org/10.1016/j.jacr.2023.08.017

439

Including clinical information and Radiomics features to detect recurring Glioblastoma in post-operative MRI with Deep Learning

Taha Belbadaoui BS[1], Andrew Forester[1], Laura Beltran[1], Aurélie Beaudoin[1], Farzard Khalvati PhD[2], Louis Gagnon MD-PhD[1]
[1]Laval University, Quebec City, Qc, Canada. [2]University of Toronto, Toronto, On, Canada

Abstract Category

AI/Informatics

Purpose

Distinguishing recurrent glioblastoma from post-treatment changes in post-operative MRI is a significant challenge due to the overlapping imaging features of these conditions[1]. Accurate differentiation is essential for informing patient management and therapeutic planning. Advanced imaging analysis techniques, including radiomics[2] and deep learning-based segmentation methods[3], offer promising potential to improve diagnostic accuracy. However, a direct comparison of these two approaches has not yet been conducted. Additionally, the impact of incorporating clinical data, such as chemotherapy status, on predictive performance remains unclear[4].

Materials & Methods

A retrospective analysis was performed on the UCSD post-operative GBM dataset, which included 136 glioblastoma patients with available clinical data, including chemotherapy status. The imaging modalities used were T1 post-contrast (T1post), fluid-attenuated inversion recovery (FLAIR), and cellularity maps (CELL) from Restricted Spectrum Imaging (RSI). Two main approaches were evaluated: a Radiomics-Based Model and a volume thresholding method from an nnUNet cellular tumor segmentation model[3].

Radiomics features were extracted using PyRadiomics[5] as illustrated in Fig 1A. An Extremely Randomized Trees classifier was then trained on these features, utilizing a five-fold cross-validation to ensure that each patient served as a test case exactly once, with balanced distributions of positive and negative cases. Chemotherapy status was also included as an additional feature to evaluate its influence on model performance.

The nnUNet model was used to directly segment the cellular tumor volume from MRI images[3]. To differentiate between recurrent disease and post-treatment changes, a threshold was applied to the predicted cellular tumor volumes as described in Gagnon et al[3].

The primary performance metric was the Area Under the Receiver Operating Characteristic Curve (AUC).

Results

Figure 1B summarizes the primary results. The radiomics-based model, excluding chemotherapy data, achieved a maximum AUC of 0.72 when using T1post + CELL, T1post alone, or in combination with FLAIR. Adding chemotherapy status enhanced performance across all imaging combinations, with the highest AUC of 0.81 observed using T1post + CELL images. The nnUNet segmentation approach reached an AUC of 0.79.

Conclusion

The integration of chemotherapy status enhanced the performance of the radiomics model, underscoring the importance of clinical context in predictive modeling. This improvement was anticipated, as chemotherapy can influence tumor appearance on MRI[1,4]. The radiomics model, which included clinical data, demonstrated slightly better performance than the nnUNet segmentation model, which can be attributed to several factors. First, radiomics enriches feature representation by capturing detailed texture and intensity characteristics, which, when combined with clinical variables, offer a more thorough characterization of tumor status. Second, incorporating clinical context, such as chemotherapy status, may correlate with specific imaging features that signal treatment response or recurrence, thereby improving the model's discrimination ability. Finally, segmentation models like nnUNet have limitations, as they rely mainly on spatial and morphological features, potentially overlooking the subtle textural variations that radiomics can capture.

Expanding the dataset could improve the robustness and generalizability of the models. Moreover, the limited inclusion of clinical variables might have restricted the model's performance, suggesting that incorporating additional clinical factors could further strengthen its predictive accuracy.

References

1. Taylor C, Ekert JO, Sefcikova V, Fersht N, Samandouras G. Discriminators of pseudoprogression and true progression in high-grade gliomas: A systematic review and meta-analysis. Sci Rep. 2022 Aug 2;12(1):13258. doi: 10.1038/s41598-022-16726-x. PMID: 35918373; PMCID: PMC9345984

2. Park JE, Kim HS, Jo Y, et al. Radiomics prognostication model in glioblastoma using diffusion- and perfusion-weighted MRI. Sci Rep-uk. 2020;10(1):4250. doi: 10.1038/s41598-020-61178-w.

3. Gagnon L, Gupta D, Mastorakos G, et al. Deep Learning Segmentation of Infiltrative and Enhancing Cellular Tumor at Pre- and Posttreatment Multishell Diffusion MRI of Glioblastoma. *Radiol Artif Intell*. 2024;6(5):e230489. doi:10.1148/ryai.230489

4. Wolfgang W, Thierry G, Martin B, et al. Lomustine and Bevacizumab in Progressive Glioblastoma. New Engl J Med. 2017;377(20):1954–1963. doi: 10.1056/nejmoa1707358.

5. van Griethuysen JJM, Fedorov A, Parmar C, Hosny A, Aucoin N, Narayan V, Beets-Tan RGH, Fillion-Robin JC, Pieper S, Aerts HJWL. Computational Radiomics System to Decode the Radiographic Phenotype. Cancer Res. 2017 Nov 1;77(21):e104-e107. doi: 10.1158/0008-5472.CAN-17-0339. PMID: 29092951; PMCID: PMC5672828.

Images/Tables

A)

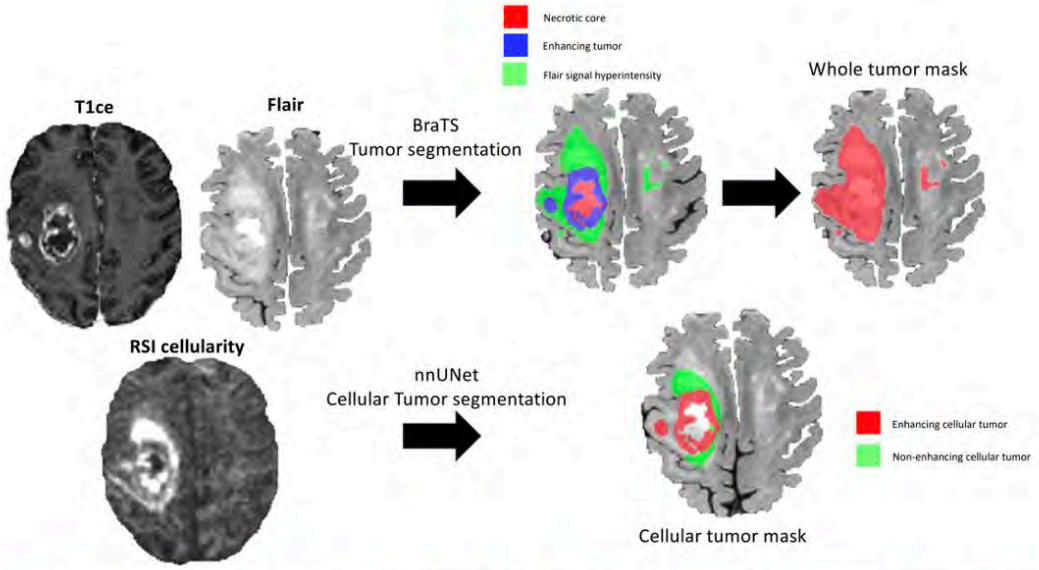

B)

nnUNet segmentation and thresholding		Radiomics Features without Chemotherapy		Radiomics Features with Chemotherapy	
T1, T1post, T2, FLAIR, CELL	0.79 ±0.06	T1post	0.72 ±0.13	T1post	0.73 ±0.14
		FLAIR	0.65 ±0.13	FLAIR	0.61 ±0.18
		CELL	0.69 ±0.08	CELL	0.61 ±0.11
		CELL+T1post	0.72 ±0.13	CELL+T1post	0.81 ±0.10
		FLAIR+T1post	0.72 ±0.17	FLAIR+T1post	0.76 ±0.15
		FLAIR+T1post+ CELL	0.68 ±0.14	FLAIR+T1post+ CELL	0.75 ±0.15

448

Adult Spinal Atypical Teratoid Rhabdoid Tumor with Cerebral Leptomeningeal Involvement; When Rarity Meets Complexity

Kidist T Arficho MD, Jeffry Lin MD, Abraham Mengstu MD, Rani Bashiti MD
Henry Ford Providence Hospital, MSUCHM, Southfield, Michigan, USA

Abstract Category

Spine

Purpose

Atypical teratoid rhabdoid tumor (ATRT) is a highly malignant, aggressive tumor typically found in the posterior fossa of the brain in pediatric patients, particularly in children under three years of age [1]. Its occurrence in adults, especially within the spine and subsequent leptomeningeal spread to the brain, is exceptionally rare and remains poorly understood [2, 3].

This case report underscores the diagnostic challenges posed by ATRT of the spine in adults, highlighting issues such as nonspecific clinical presentation, absence of definitive imaging characteristics, and histopathological overlap with other tumors.

The purpose of this study is to present a rare and diagnostically complex case of adult onset lumbar spinal ATRT who developed leptomeningeal dissemination to the brain, cervical and thoracic spine.

Materials & Methods

A case report of a 30-year-old female with progressive neurological symptoms underwent MRI in August, 2024, revealing a lumbar intradural mass. Surgical resection was performed, and histopathological examination confirmed ATRT with characteristic immunohistochemical staining. Postoperative complications delayed further treatment. Follow-up MRI demonstrated leptomeningeal spread to the brain, cervical and thoracic spine underscoring diagnostic and therapeutic challenges.

Results

A 30-year-old female presented to the emergency department (ED) multiple times over several weeks with intermittent lower extremity pain. As her symptoms worsened, she returned with complaints of lower extremity weakness, difficulty walking and perianal numbness.

Initial MRI of the lumbar spine revealed a well-defined, T1 and T2 hypointense (Fig A), heterogeneously enhancing intradural extramedullary mass (Fig B), from L2 to L5, with thickening and enhancement of the nerve roots (Fig C), but no bone involvement. Concurrent MRIs of the brain (Fig D), cervical, and thoracic spine showed no enhancing lesions at that time.

During surgery, the mass was observed to be partially encapsulated, with extensive involvement of the right L5 nerve root and indistinct margins near the cauda equina. Given its close proximity to the conus, a small portion of the tumor was intentionally left at the superior pole to minimize the risk of nerve damage.

Histopathological analysis confirmed ATRT with characteristic INI1 loss. The postoperative course was complicated by infection and pulmonary embolism, delaying the initiation of further treatment.

Follow-up MRI demonstrated interval development of a new enhancing mass in the right mesial temporal lobe (Fig E), nodular leptomeningeal enhancement, particularly in the peri mesencephalic cistern (Fig F), and diffuse enhancement in the cerebellar hemispheres. Additional findings included new enhancement in the right internal auditory canal, thickening and enhancement of Meckel's cave, and a focal T1 hyperintensity in the prepontine space, suggestive of hemorrhage. There was also evidence of tumor spread to the cervical (Fig G) and thoracic spine and increased enhancement of the residual lumbar tumor (Fig H). Radiation therapy was promptly initiated to target both spinal and cerebral lesions.

Conclusion

This case highlights the rarity and aggressive nature of atypical teratoid/rhabdoid tumor (ATRT) with leptomeningeal spread to the brain in adult patients, presenting significant diagnostic challenges. It emphasizes the crucial need to include ATRT in the differential diagnosis of atypical spinal tumors in adults, particularly when leptomeningeal dissemination is present.

References

- 1.*Broggi G, Gianno F, Shemy DTet al. . Atypical teratoid/rhabdoid tumor in adults: a systematic review of the literature with meta-analysis and additional reports of 4 cases. J. Neurooncol. 157(1), 1–14 (2022).* [DOI] [PubMed] [Google Scholar]
- 2. Li L, Patel M, Nguyen HS, Doan N, Sharma A, Maiman D. Primary atypical teratoid/rhabdoid tumor of the spine in an adult patient. Surgl. Neurol. Int. 7, 27 (2016). [DOI] [PMC free article] [PubMed] [Google Scholar]
- 3.*Amit A, Vats A, Shoakazemi A, Herron B, McCarthy A, McConnell RS. Dumbell atypical teratoid/rhabdoid tumour (AT/RT) of the cervical spine. Br. J. Neurosurg. 34(3), 339–341 (2020).*[DOI] [PubMed] [Google Scholar]

Images/Tables

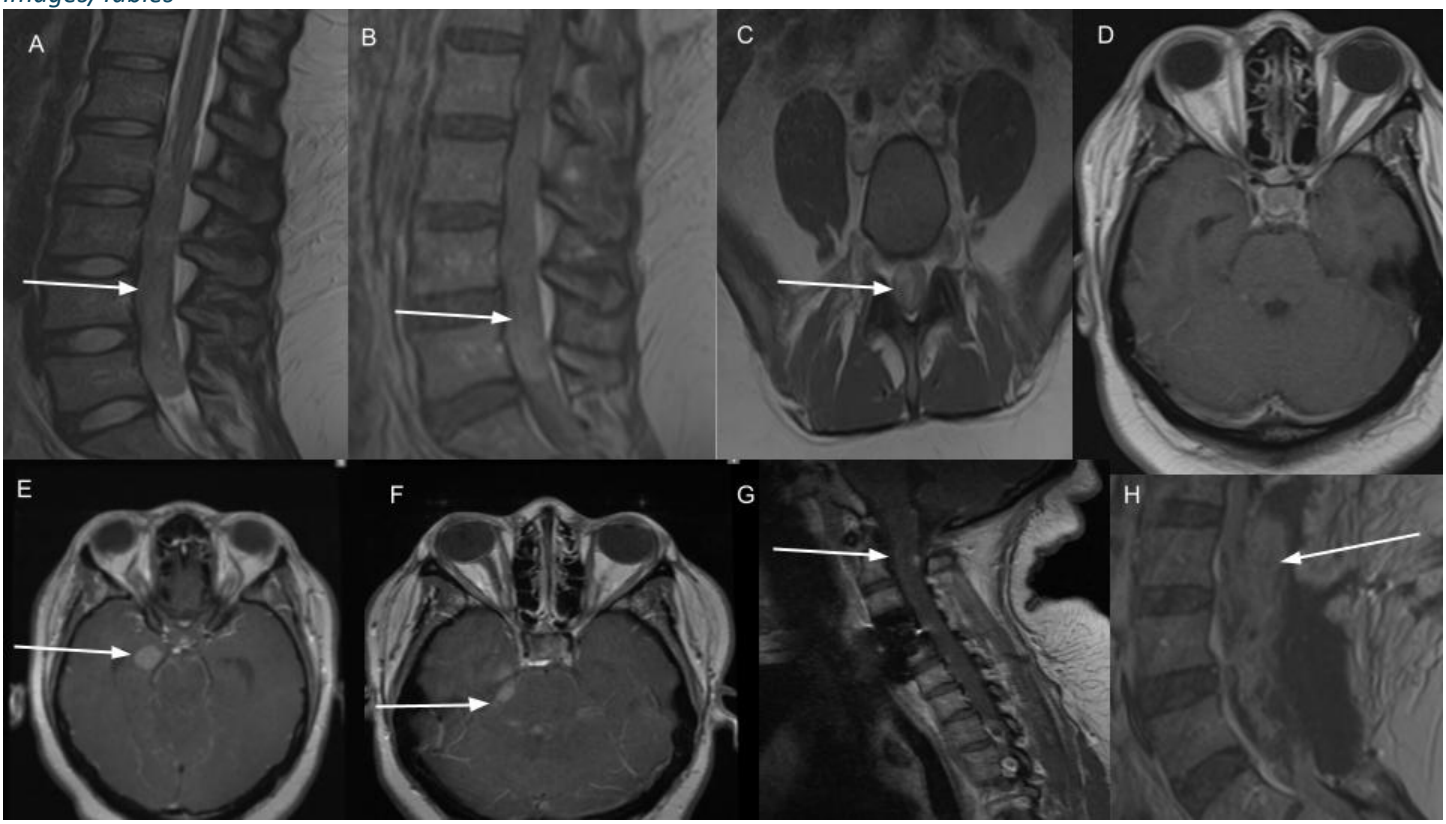

450

Multi-reader Comparison of Photon-Counting Detector CT Reconstructions for Evaluation of Temporal Bone Cochlear Implants

Siddhant Dogra[1], Thomas O'Donnell[2], Gopi Nayak[1], Mari Hagiwara[1], Gul Moonis[1]
[1]NYU Langone Health, New York, NY, USA. [2]Siemens Healthineers, Malvern, PA, USA

Abstract Category

Head & Neck

Purpose

Photon counting CT (PCCT) has steadily grown in popularity since approved for clinical use, including for visualization of temporal bone pathology and implants.[1] Many studies have shown improved image quality and reduced artifacts in cadavers and phantom studies but there is limited data of temporal bone PCCT in live clinical patients.[2, 3] Moreover, evaluations of different PCCT reconstructions are lacking but important for protocol development. We performed a reader-study comparing six different reconstruction strategies in a population of 17 live patients with cochlear implants.

Materials & Methods

Temporal bone imaging was performed in 17 patients who previously had received cochlear implants. Scanning was performed at 120 kV, using 120x0.2 mm collimation, 1 second rotation time, and a pitch of 0.5.

The raw data was reconstructed using six different algorithms, as follows: Hr84 0.2 mm (full spectrum, ultra-high-resolution, head-regular, sharpness level 84), Hr84 0.4 mm T3D (energies of 25 keV and below removed), Qr56 iMAR 0.4 mm T3D (quantitative-regular, iterative metal artifact reduction), Qr76 M140 0.4 mm (virtual monoenergetic 140 keV), Qr76 M70 0.4 mm, and Qr76 T3D 0.4 mm (full spectrum with energies of 25 keV and below removed). All were performed with quantum iterative reconstruction strength 3. The ultra-high-resolution reconstructions used a 1024x1024 matrix while the others used 512x512.

Two head-and-neck radiologists evaluated reconstructions for each patient. Using a 0-2 Likert scale, they evaluated electrode visibility (0=significant blooming artifact, 1=mild artifact, 2= minimal to no artifact), wire visibility (0=not visible, 1=wire is blurry with some artifact, 2=clearly visible), and overall image quality (0=poor, 1=diagnostic but some interpretation difficulty, 2=superb). Mean scores for each type of reconstruction were compared. A repeated measures

ANOVA was performed for each metric and then Tukey's test was used to assess every pairwise reconstruction comparison to assess for significant differences. Significance was set at p-value <0.05.

Results

Hr84 0.2 mm Q3 and Hr84 0.4 mm T3D both had the highest mean score of 1.91 for electrode visibility and were statistically higher than all other reconstructions. Hr84 0.4 mm T3D had the highest mean score of 1.38 for wire visibility but was only statistically significantly higher than the Qr56 iMAR 0.4 mm T3D score. Hr84 0.2 mm Q3 had the highest mean overall image quality of 1.97 but statistically was again only significantly higher than the Qr56 iMAR 0.4 mm T3D. Table 1 lists mean scores and standard deviations for each reconstruction.

Qr56 iMAR 0.4 mm T3D performed the worst in all three metrics (mean scores of 0.15 for electrode visibility, 0.33 for wire visibility, and 0.03 for overall image quality) and was statistically worse than every other reconstruction for all metrics.

Conclusion

Ultra-high-resolution reconstructions were rated the best across electrode visibility, wire visibility, and overall image quality in a population of patients with cochlear implants who underwent PCCT. The reconstruction using iterative metal artifact reduction was rated the lowest in all three metrics. The ultra-high-resolution reconstructions may be preferred due to more detail due to sharper kernels and larger matrices.

References

1. Takahashi Y, Higaki F, Sugaya A, et al. Evaluation of the ear ossicles with photon-counting detector CT. *Jpn J Radiol* 2023

2. Zhou W, Lane JI, Carlson ML, et al. Comparison of a Photon-Counting-Detector CT with an Energy-Integrating-Detector CT for Temporal Bone Imaging: A Cadaveric Study. *AJNR Am J Neuroradiol* 2018;39:1733-1738

3. Rajagopal JR, Farhadi F, Solomon J, et al. Comparison of Low Dose Performance of Photon-Counting and Energy Integrating CT. *Acad Radiol* 2021;28:1754-1760

Images/Tables

Table 1. Mean rater scores for each of the six reconstructions across electrode visibility (0=significant blooming artifact, 1=mild artifact, 2= minimal to no artifact), wire visibility (0=not visible, 1=wire is blurry with some artifact, 2=clearly visible), and overall image quality (0=poor, 1=diagnostic but some interpretation difficulty, 2=superb). Each value is reported as mean (standard deviation).

Reconstruction	Electrode Visibility	Wire Visibility	Image Quality
Hr84 0.2 mm Q3	**1.91 (0.28)**	1.35 (0.88)	**1.97 (0.17)**
Hr84 0.4 mm T3D	**1.91 (0.38)**	**1.38 (0.88)**	1.94 (0.34)
Qr56 iMAR 0.4 mm T3D	0.15 (0.36)	0.33 (0.47)	0.03 (0.17)
Qr76 M140	0.91 (0.45)	0.97 (0.72)	0.71 (0.46)
Qr76 M70	1.24 (0.43)	1.15 (0.82)	1.74 (0.45)
Qr76 T3D	1.24 (0.43)	1.24 (0.85)	1.68 (0.47)

458

Complex Deep Venous Abnormalities in Patients with Sturge-Weber syndrome

Ajay Kumar, MD,PhD[1], Fatimah M Albazron, MS[2], Csaba Juhasz, MD,PhD[2]

[1]University of Pennsylvania, Perelman School of Medicine, Philadelphia, PA, USA. [2]Wayne State University School of Medicine, Detroit, MI, USA

Abstract Category

Pediatrics

Purpose

Sturge-Weber syndrome (SWS) is a rare neurocutaneous disorder with intracranial venous abnormalities, such as leptomeningeal venous malformation (LVM) and enlarged medullary veins. Small studies reported absent deep veins, most commonly the internal cerebral vein (ICV), in some SWS patients (1), but the prevalence and extent of ICV and other deep vein abnormalities in SWS remain unknown. Post-contrast T1-weighted or fluid-attenuated inversion

recovery (FLAIR) images are considered to be the gold standard to diagnose the LVM, but susceptibility-weighted imaging (SWI) is more sensitive to identify small vein abnormalities, such as those in medullary and deep veins (2,3). The purpose of this study was to evaluate deep vein abnormalities and their relation to enlarged medullary veins and parenchymal abnormalities in patients with SWS.

Materials & Methods

Thirty young patients with SWS and unilateral LVM (age 1-25 years, median age: 13 years) underwent 3T brain MRI prospectively including native SWI, T2, FLAIR, T1 and post-contrast T1-weighted images. Abnormalities (absence or enlargement) of three major deep cerebral veins (internal cerebral vein (ICV), thalamostriate vein (TSV), septal vein (SV)), readily identifiable on SWI (left image: SWI in a healthy control showing normal SV, TSV and ICV), as well as extent of enlarged medullary veins (as reported in ref 3) were evaluated on SWI minimal intensity projection (MIP) images based on consensus by three investigators and compared with the side and extent of the LVM (assessed on post-contrast T1) and lobar atrophy.

Results

Abnormal (absent or enlarged) deep cerebral veins were observed in 22 SWS patients (73%): absent ICV in 17 (57%; including 5 with bilateral absence), TSV in 14 (47%, 5 bilateral absence), SV in 13 (43%, 3 bilateral) patients (right image: SWI showing bilateral absent SV, TSV and ICV in a patient with right hemispheric SWS). These deep vein abnormalities were often missed or underestimated by post-contrast images that readily detected the LVM. Unilateral enlargement was clearly present in 8 SVs, 4 TSVs and 1 ICV; enlarged intra- or peri-thalamic veins were also detected in conjunction with absent ICV. Enlarged medullary veins ipsilateral to the LVM, present in 26 patients, were more extensive in those with absent ICV ($p<0.05$). Lobar atrophy, present in 27 patients and involving 1-4 cerebral lobes, was always unilateral including those with bilateral deep vein abnormality.

Conclusion

Absent and/or enlarged deep cerebral veins are common in SWS, detected by SWI but may be missed by post-contrast T1. Absent ICV is associated with more extensive enlarged medullary, intra-/perithalamic veins that may provide collateral venous outflow. Extension of deep vein abnormalities contralateral to the leptomeningeal venous malformation may indicate a complex deep venous abnormality that can involve both absent and enlarged deep veins along with collaterals that may limit the extent of SWS-induced brain injury.

References

1. Slasky SE, Shinnar S, Bello JA. Sturge-Weber syndrome: deep venous occlusion and the radiologic spectrum. Pediatr Neurol. 2006; 35(5):343-7.
2. Hu J, Yu Y, Juhasz C, et al. MR susceptibility weighted imaging (SWI) complements conventional contrast enhanced T1 weighted MRI in characterizing brain abnormalities of Sturge-Weber Syndrome. J Magn Reson Imaging. 2008; 28(2):300-7.
3. Juhász C, Luat AF, Behen ME, et al. Deep Venous Remodeling in Unilateral Sturge-Weber Syndrome: Robust Hemispheric Differences and Clinical Correlates. Pediatr Neurol. 2023; 139:49-58.

Images/Tables

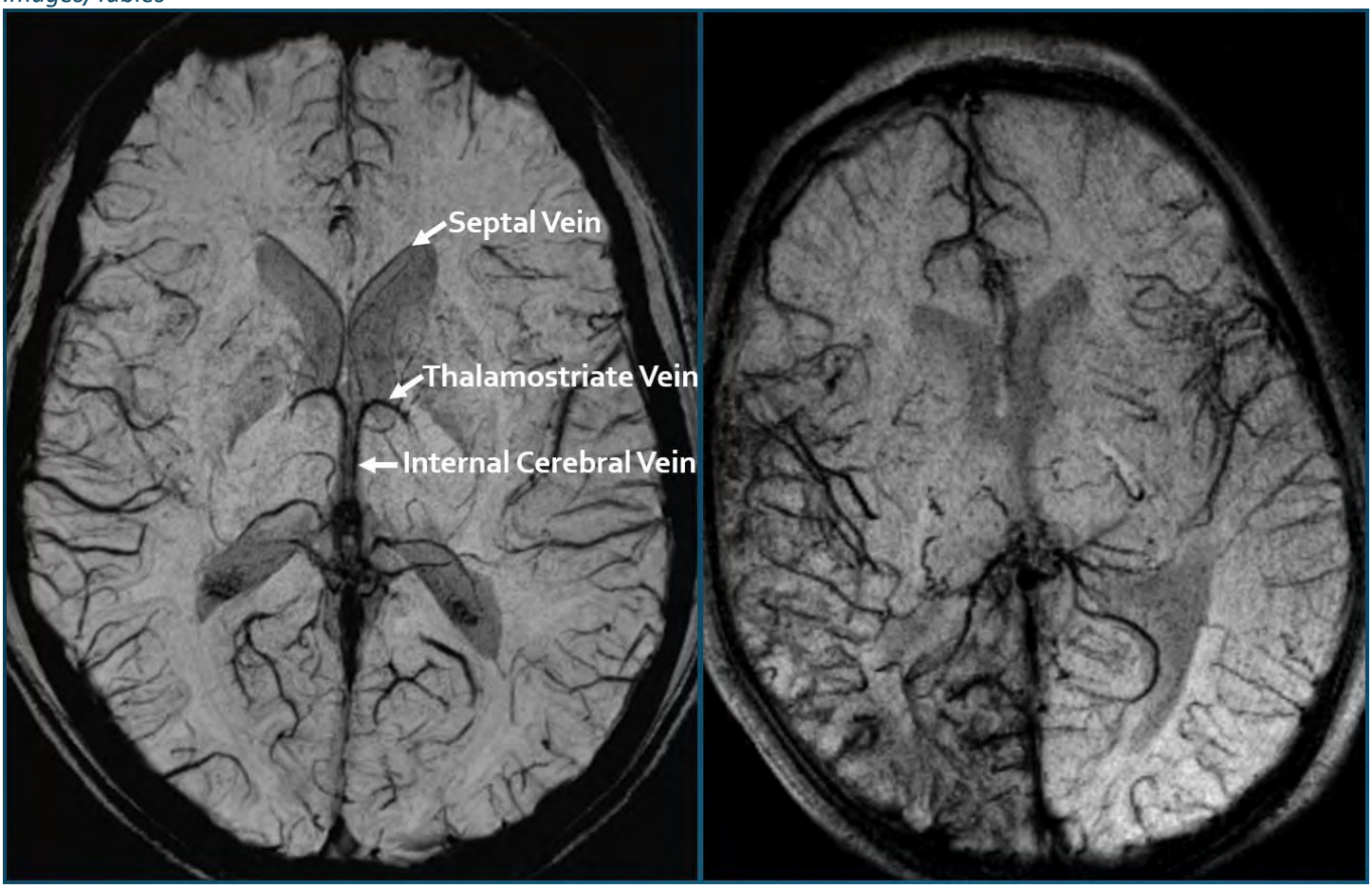

469

White Matter Hyperintensities in Progressive Supranuclear Palsy and Parkinson's Disease

Yash Patel[1], Nathaniel Bendahan[2], Sarah Zaheer[3], Maziar Abarghouei Emamikhah[3], Richard Zou[1], Mikail Malik[1], Nicole Owsicki[1], Alexandre Boutet[4], Anthony Lang[5]

[1]University of Toronto, Toronto, ON, Canada. [2]Edmond J. Safra Program in Parkinson's Disease, Division of Neurology, Toronto Western Hospital, Toronto, ON, Canada. [3]Edmond J. Safra Program in Parkinson's Disease, the Rossy PSP Centre, Division of Neurology, Toronto Western Hospital, Toronto, ON, Canada. [4]Krembil Research Institute, Toronto Western Hospital, Toronto, ON, Canada. [5]Edmond J. Safra Program in Parkinson's Disease, the Rossy PSP Centre, Krembil Research Institute, Division of Neurology, Toronto Western Hospital, University Health Network, Toronto, ON, Canada

Abstract Category

Adult Brain

Purpose

Progressive supranuclear palsy (PSP), is a form of parkinsonian syndrome that may be difficult to distinguish from Parkinson's disease, especially in the early stages of the disease due to extensive clinical heterogeneity and overlap in disease presentation. Here, we assess the difference in white matter hyperintensity (WMH) burden between PSP and PD patients, in the hopes of aiding clinical diagnosis and understanding pathogenesis.

Materials & Methods

We evaluated the MRI scans of 67 PSP, and 67 age and sex-match PD patients from the Movement disorders clinic and the Rossy PSP Centre, Krembil Brain Institute, Toronto Western Hospital, Toronto Canada. The total sample consisted of 134 patients with a mean age 70 years, 67% males and 33% females. Multiple scanners (1.5T, 3T) and manufactures (Philips, Siemens, GE) were used to acquire 3D T1w (1 mm isotropic), and 2D FLAIR (0.43x0.43x5.0mm) as per our movement disorder protocol. T1w and FLAIR images were co-registered using rigid body registration, and WMH were quantified using a convolutional neural network-based tool (segcsvd-WMH) specifically designed for diverse clinical patient datasets (Figure 1a)[1]. WMH volumes were adjusted by intracranial volume (ICV), and log10 normalized. Linear

regression was used to test difference in WMHvol/ICV between PSP and PD, while accounting for age, sex, MR field strength and MR manufacturer.

Results

Patients with PSP had a significantly higher WMH burden than PD (0.55% vs 0.29% of total ICV, respectively, Wilcoxon rank sum p-vale = 0.001, Figure 1b). Multivariable linear regression confirmed the main effect of diagnosis (beta estimate = 0.28, se = 0.079, p = 0.00041, PSP > PD), and age (beta = 0.09, se = 0.04, p = 0.017) on WMH volume (Figure 1c).

Conclusion

In summary, we found greater WMH volumes in PSP patients compared with PD, suggesting an increased role of white matter structural abnormalities in PSP. These findings may provide a supportive role in diagnosis as well as expand an understanding of pathogenesis including a proposed association between PSP and hypertension[2].

References

1. Gibson, E. *et al.* SegcsvdWMH: A convolutional neural network-based tool for quantifying white matter hyperintensities in heterogeneous patient cohorts. 2024.06.20.24309230 Preprint at https://doi.org/10.1101/2024.06.20.24309230 (2024).

2. Rabadia, S. V. *et al.* Hypertension and progressive supranuclear palsy. *Parkinsonism Relat Disord* **66**, 166–170 (2019).

Images/Tables

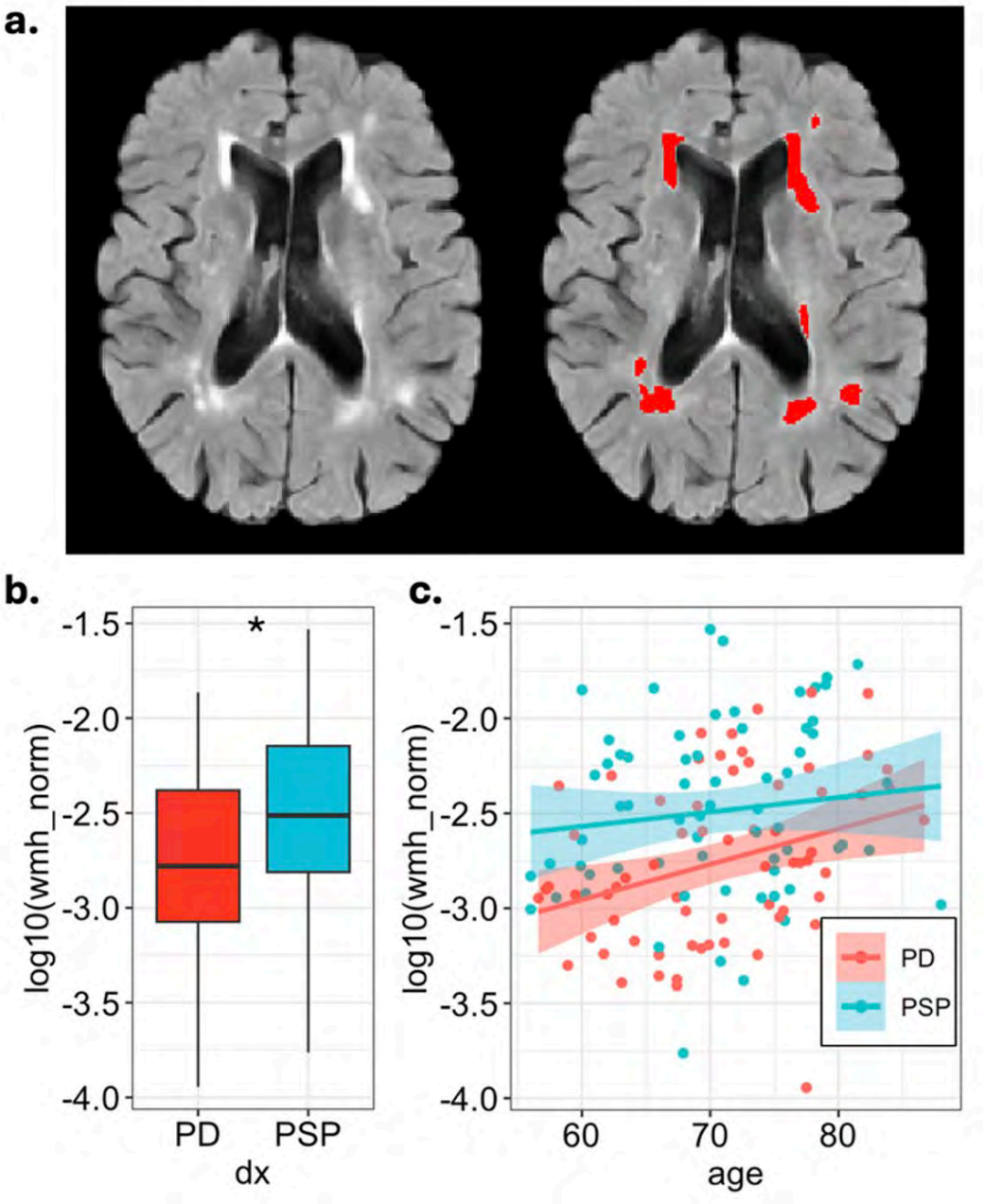

470

Predictive Value of Clinical Features and Pre-treatment to Post-treatment MRI Radiomics Differences for Response Assessment Following Stereotactic Body Radiation Therapy in Patients with Spinal Metastasis

Kamyar Afshin MD, Chinthaka Heyn MD, PhD, Arjun Sahgal MD, Pejman Jabehdar Maralani MD
Sunnybrook Health Sciences Center, Toronto, ON, Canada

Abstract Category

Spine

Purpose

The aim of this study was to assess if the changes in radiomics features from pre-treatment to post-treatment MRI alone or in combination with clinical and basic imaging parameters can predict local progression in patients with spinal metastasis receiving stereotactic body radiotherapy (SBRT).

Materials & Methods

Patients with spinal metastases who underwent SBRT and had both pre-treatment and post-treatment MRI at our center from July 2008 to June 2021 were included in this retrospective study. The treated spinal segments were classified into local progression (LP) and non-local progression (non-LP). LP was defined according to SPINO[1] guidelines documented in radiation-oncology clinic notes using electronic medical records (EMR). Clinical and basic imaging parameters were extracted from imaging reports and EMR and are referred to as non-radiomics data summarized in table 1. Radiomic features were extracted from T1-weighted images by manually drawing regions of interest over the tumors. Radiomics feature selection involved first order radiomics extraction from pre- and post-treatment MRI using PyRadiomics[2] using in-house developed scripts in Python. Next, the change between pre- and post-treatment extracted radiomics feature were considered as parameters of interest. Pre-processing and feature engineering steps included data cleaning, intensity normalization, and label-encoding to convert categorical data into numerical values and robust scaler to standardize and normalize features.

Four ML algorithms including Random Forest (RF), Neural Network (NN), Extreme Gradient Boosting (XGboost), and Logistic Regression (LR) were applied to each radiomics data, non-radiomics data and the combination of both to construct the prediction models. Model performance was evaluated using accuracy and AUC (area under the ROC cure).

Results

688 segments from 369 patients (52% male, 48% female) were included. 69% of segments had LP and 31% had non-LP. The average length of follow-up was 976.75 days. Each region of interest generated 43 features including 19 first order radiomics combined with 24 non-radiomics. The XGboost model with non-radiomics data exhibited a moderate predictive value (AUC = 0.852), while with the first order radiomics demonstrated less predictive value (AUC = 0.479). The combined model achieved the second-best performance (AUC = 0.753).

Conclusion

The predictive value of MRI-based radiomics was less than non-radiomics in all models to predict local progression in patients with spinal metastasis treated with SBRT.

References

1. Thibault, I., Chang, E. L., Sheehan, J. P., Ahluwalia, M., Guckenberger, M., Sohn, M. J., Ryu, S., Foote, M., Lo, S. S., Muacevic, A., Soltys, S. G., Chao, S. T., Gerszten, P. C., Lis, E., Yu, E., Bilsky, M. H., Fisher, C. G., Schiff, D., Fehlings, M. G., … Sahgal, A. (2015). Response assessment after stereotactic body radiotherapy for spinal metastasis: a report from the SPIne response assessment in Neuro-Oncology (SPINO) group. *Lancet Oncology*, *16*(16), 595–603. https://doi.org/10.1016/S1470-2045(15)00166-7
2. Van Griethuysen, J. J. M., Fedorov, A., Parmar, C., Hosny, A., Aucoin, N., Narayan, V., Beets-Tan, R. G. H., Fillon-Robin, J. C., Pieper, S., Aerts, H. J. W. L. (2017). Computational Radiomics System to Decode the Radiographic Phenotype. Cancer Research, 77(21), e104–e107. `https://doi.org/10.1158/0008-5472.CAN-17-0339 <https://doi.org/10.1158/0008-5472.CAN-17-0339>`

Images/Tables

Table 1 Non-radiomic features and their definition

FEATURE	DEFINITION
AgeAtTx	Age at treatment
NumScg	Number of spinal metastases that the patient has
PRIM_SITE	Primary cancer site
SINS_TOT	SINS total score
OLIGO_NUMBER	Number of involved segments in oligometastatic patients
NUM_SPINE_M	Number of spinal metastases that the patient has (including treated and untreated segments)
INDIC	Indication for spine SBRT (including pain, Oligometastasis, pain and oligometastasis, previous EBRT and pain, previous EBRT/SBRT and progression, progression despite systemic treatment, pain and progression despite systemic treatment, and induction/consolidation prior to systemic therapy)
PRVdose	Previous dose of radiation
Resp_PAIN	Response to pain after SBRT
DOSEFRAC	Dose fractions of SBRT
GRAD_EPIDURAL	Bilsky grade of epidural disease at baseline
CHEMO	Did the patient receive chemotherapy or target therapy prior to SBRT?
ECOG	ECOG performance status score
OLIGO_DISEASE	Is it an oligometastatic cancer?
SPINE_MET_ONLY	Does the patient have only spine metastases?
TX_R_DISEASE	Is this spine tumor considered a resistant disease?
OR	Did the patient have spine surgery for this segment (before SBRT)?
SEX	Gender
EPIDURAL	Presence of epidural disease
PARASPINAL	Presence of paraspinal involvement
P_CA_TYPE	Type of past medical history of cancer (not related to SBRT)
TxCategory	Denovo Or Postop Or Retreat
BASE_VCF	Presence of vertebral compression fracture at baseline (before SBRT)
PR_SPINE_SAME	Did the patient receive previous palliative EBRT at the same vertebral segment (retreatment of the same target)?

Table 2 Comparison of different models with different input

	Radiomics only	Clinical only	Combination
XGboost	**Accuracy: 0.58**	**Accuracy: 0.77**	**Accuracy: 0.72**
	AUC: 0.479	**AUC: 0.852**	**AUC: 0.753**
RF	**Accuracy: 0.63**	**Accuracy: 0.75**	**Accuracy: 0.70**
	AUC: 0.48	**AUC: 0.83**	**AUC: 0.70**
LR	**Accuracy: 0.66**	**Accuracy: 0.68**	**Accuracy: 0.68**
	AUC: 0.46	**AUC: 0.82**	**AUC: 0.69**
NN	**Accuracy: 0.68**	**Accuracy: 0.67**	**Accuracy: 0.68**
	AUC: 0.51	**AUC: 0.70**	**AUC: 0.57**

Figures 1: ROC curve for XGB model

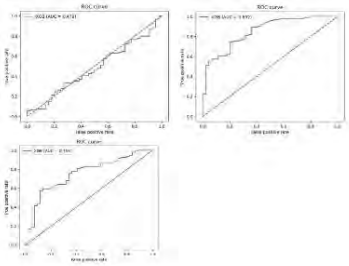

Figure 2: Heatmap for non-radiomics and radiomics features

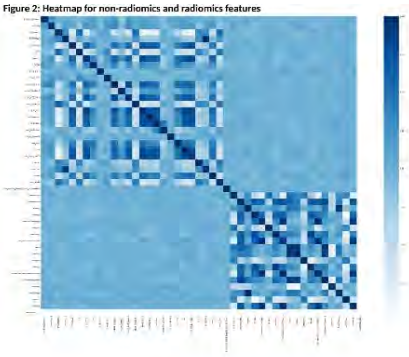

475

Computed Tomography Perfusion Quantitative Diagnosis of Carotid Blowout Syndrome

Chia-Hung Wu MD, PhD[1], Shan-Su Huang MS[1], Kan Ling MD[2], Te-Ming Lin MD, MS[1], Feng-Chi Chang MD[1]
[1]Department of Radiology, Taipei Veterans General Hospital, Taipei, Taipei, Taiwan. [2]Department of Radiology, Taipei Medical University-Shuang Ho Hospital, New Taipei City, Taipei, Taiwan

Abstract Category

Head & Neck

Purpose

This study aimed to investigate the computed tomography perfusion (CTP) quantitative diagnosis of the carotid blowout syndrome (CBS).

Materials & Methods

This study prospectively recruited subjects with CBS between 2015 and 2023. CTP and digital subtraction angiography (DSA) were performed and patients were classified into 3 different groups (threatened, impending and acute CBS). Pericarotid soft-tissues (PSCT) were evaluated by CTP in 3 different models as small focal lesion in 1cm of PSCT, 1cm surrounding PSCT and the whole PSCT respectively. CTP parameters including blood flow (BF), blood volume (BV), mean transit time (MTT) and flow extraction product (FEP) were calculated.

Results

CTP data of 110 subjects (45 threatened, 32 impending and 33 acute CBS) were included and evaluated. PSCT BV (1.8 ± 1.2vs.3.5 ± 2.0; $p < 0.001$) in 1cm of PSCT and BF in 1cm surrounding PSCT (42.6 ± 11.0vs.50.9 ± 20.4; $p = 0.031$) were lower in acute than threatened and impending CBS patients. Lower BV in acute (1.8 ± 1.2) compared with threatened (3.7 ± 2.3; $p < 0.001$; $p < 0.001$) and impending (3.2 ± 1.6; $p = 0.009$) CBS patients in 1cm of PSCT.

Conclusion

CTP parameters, especially BV, may be used as an imaging biomarker to differentiate acute CBS from others quantitatively. The PSCT perfusion plays a significant role in CBS severity.

References

1. Chang FC, Lirng JF, Luo CB, et al. Carotid blowout syndrome in patients with head-and-neck cancers: reconstructive management by self-expandable stent-grafts. *AJNR Am J Neuroradiol* 2007;28:181-188
2. Lee CW, Yang CY, Chen YF, et al. CT angiography findings in carotid blowout syndrome and its role as a predictor of 1-year survival. *AJNR Am J Neuroradiol* 2014;35:562-567
3. Chang FC, Lirng JF, Luo CB, et al. Patients with head and neck cancers and associated postirradiated carotid blowout syndrome: endovascular therapeutic methods and outcomes. *J Vasc Surg* 2008;47:936-945
4. Chang FC, Luo CB, Lirng JF, et al. Complications of carotid blowout syndrome in patients with head and neck cancers treated by covered stents. *Interv Neuroradiol* 2008;14 Suppl 2:29-33
5. Chang FC, Luo CB, Lirng JF, et al. Endovascular Management of Post-Irradiated Carotid Blowout Syndrome. *PLoS One* 2015;10:e0139821

Images/Tables

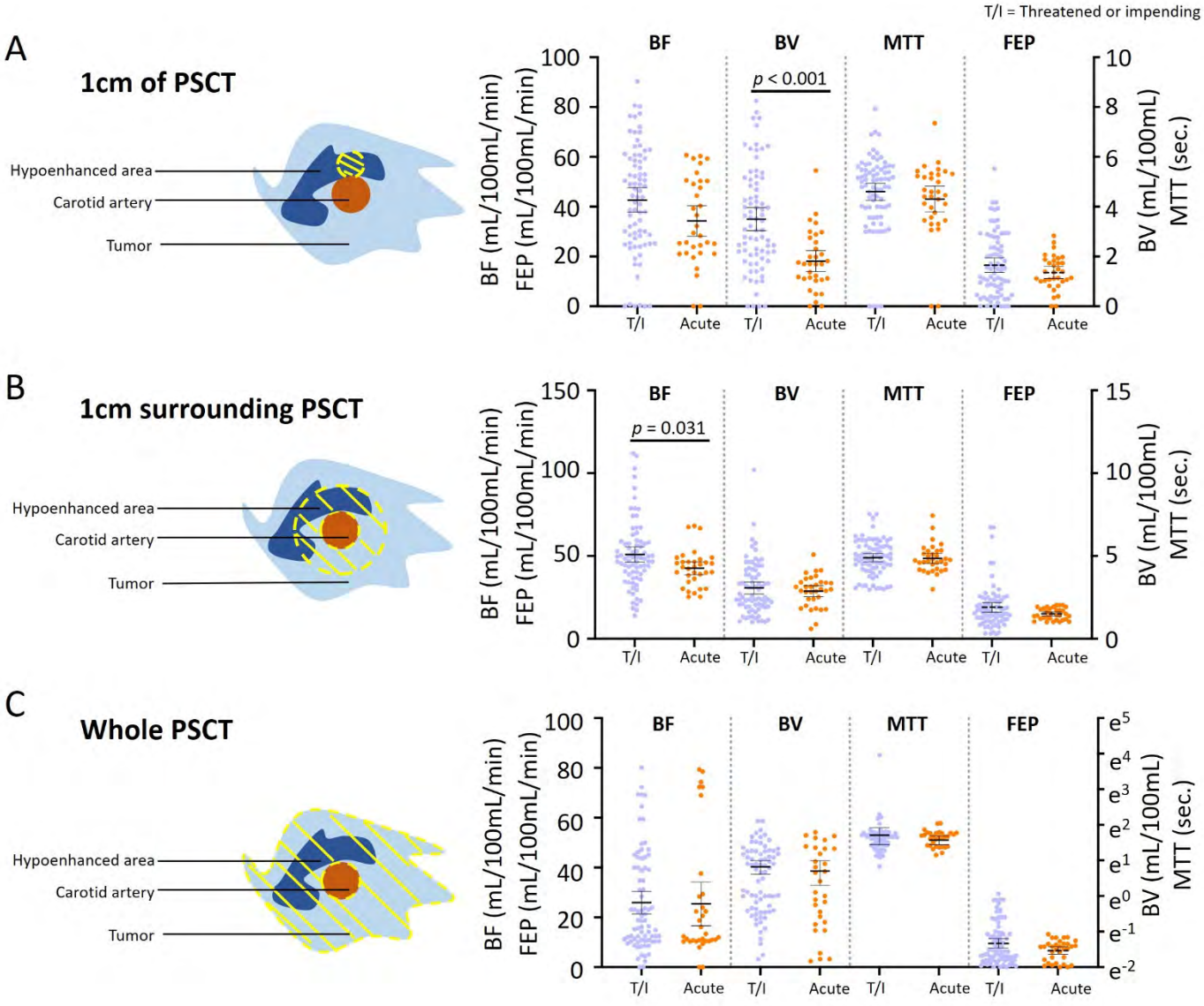

477

Lower Cerebral Small Vessel Disease Burden in Superagers: A Combined White Matter Hyperintensity and DTI Approach

Laiz Laura de Godoy MD, PhD[1], Carole Sudre MSc, PhD[2], Adalberto Studart-Neto MD, PhD[3], Bruno Pastorello PhD[3], Natália Cristina Moraes MSc[3], Mônica Sanches Yassuda PhD[3], Ricardo Nitrini MD, PhD[3], Claudia da Costa Leite MD, PhD[3], Francesco Carletti MD, PhD[2], Sotirios Bisdas MD, PhD[2], Hans Rolf Jäger MD[2]

[1]Perelman School of Medicine at the University of Pennsylvania, Philadelphia, PA, USA. [2]University College London, London, -, United Kingdom. [3]University of Sao Paulo, Sao Paulo, SP, Brazil

Abstract Category

Adult Brain

Purpose

Older adults with youthful memory performance are defined as superagers.[1] Cerebral small vessel disease (CSVD) is commonly identified in neuroimaging of elderly patients and is believed to contribute to the pathogenesis of cognitive dysfunctions.[2] In this study, we used a regional-zonal analysis to map white matter hyperintensities (WMH), the most common and reliable marker of age-related neurovascular damage,[3] and employed diffusion tensor imaging (DTI) to examine microstructural integrity in normal appearing white matter (NAWM).

Materials & Methods

A cohort of 31 older adults, 80 or older, were grouped as superagers (n=14) and age-matched healthy older adults (n=17) and scanned in a 3T MRI. **WMH Image processing:** Using T1-WI, the cortical gray matter was automatically parcellated into lobes using Geodesic Information Flows. The segmentation algorithm models tissues as a Gaussian Mixture Model under multivariate data (T1-WI, FLAIR) and automatically determines the number of Gaussian components required to jointly model healthy tissues and abnormal signals. After convergence, the optimized model is used to produce a probabilistic lesion map that is integrated to produce lesion volume measurements. To spatially localize WMH, a subject-specific coordinate frame was used to divide the white and deep gray matter by cortical lobes and distance from the ventricular surface. Cortical lobes were defined by solving the Laplace equation between the ventricular surface, and aggregate Geodesic Information Flows lobar regions, dividing the brain into five lobes and four radial layers. Spatial localization was illustrated in a "bullseye's representation" of WMH as described previously.[4] Finally, WMH volumes were estimated per region, providing regional summary measures and allowing the 3-dimensional WMH distribution to be displayed as a 2-dimensional plot.[4]

DTI Image processing: Diffusion images were preprocessed using the Functional Magnetic Resonance Imaging of the Brain (FMRIB) Diffusion Toolbox from FMRIB's Software Library (FSL).[5] The diffusion tensor model was then fitted to independent voxels for fractional anisotropy (FA) and mean diffusivity (MD) measurements,[5] with measurements missing in 2 control cases. Diffusion measures were aggregated over the NAWM defined as the WM segmentation mask to which WMH lesion map are subtracted and morphologically eroded by one voxel to remove possible penumbra and partial volume area.

Statistical comparisons were performed using Mann-Whitney U test with WMH volumes considered as proportion of total intracranial volume.

Results

The overall burden of WMH was 3.52mL [2.13, 8.45] (median / IQR) in the superagers compared to 8.52 [3.23, 19.36] in the age-matched healthy older adults. There was a trend towards an overall lower load in superagers compared to age-matched healthy older adults (p=0.197) particularly in the frontal lobes (p=0.099). In this area, mid to outer layers were more affected in the control group (p=0.065, p=0.025, p=0.108 for layers 2 to 4 respectively). Figure 1 present the violin distribution of global WMH and the median of regional frequency load for the superagers and controls represented by bullseyes. DTI Analysis of the NAWM showed similar FA (median 0.42 for both) and MD (median 0.000778) in the superagers and controls (FA, p=0.913; MD, p=0.743).

Conclusion

A lower burden of CSVD may contribute to the superagers' phenotype.

References

1.Rogalski EJ, Gefen T, Shi J, Samimi M, Bigio E, Weintraub S, et al. Youthful memory capacity in old brains: anatomic and genetic clues from the Northwestern SuperAging Project. J Cogn Neurosci. 2013;25: 29–36.

2.Elahi, F. M., Wang, M. M. & Meschia, J. F. Cerebral Small Vessel Disease-Related Dementia: More Questions Than Answers. *Stroke* **54**, 648–660 (2023).

3.Cardoso, M. J. *et al.* Geodesic Information Flows: Spatially-Variant Graphs and Their Application to Segmentation and Fusion. *IEEE Transactions on Medical Imaging* vol. 34 1976–1988 Preprint at https://doi.org/10.1109/tmi.2015.2418298(2015).

4. Sudre, C. H. *et al.* Bullseye's representation of cerebral white matter hyperintensities. *J. Neuroradiol.* **45**, 114–122 (2018).

5. Smith, S. M. *et al.* Advances in functional and structural MR image analysis and implementation as FSL. *NeuroImage* vol. 23 S208–S219 Preprint at https://doi.org/10.1016/j.neuroimage.2004.07.051(2004).

Images/Tables

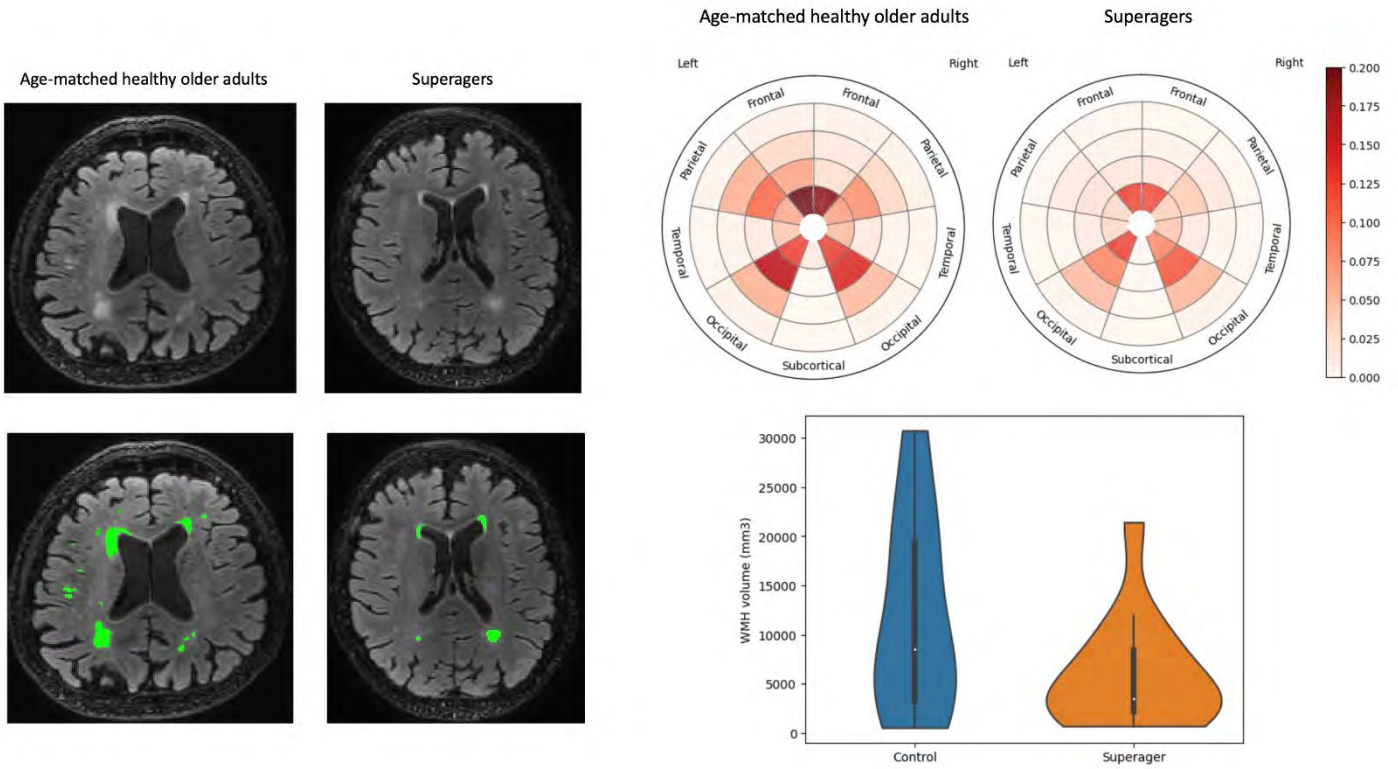

491

Role of Dynamic Magnetic Resonance Imaging in Hirayama Disease, a Rare Motor Neuron Disease

Dhanush Jayananda Amin MD[1], Jyotsna Yarlagadda DNB[2], Bhargavi Paladi MD[2], Siddhartha Gaddamanugu MD[1]
[1]University of Alabama at Birmingham, Birmingham, AL, USA. [2]Nizam's Institute of Medical Sciences, Hyderabad, Telangana, India

Abstract Category

Spine

Purpose

Hirayama disease (HD) is a benign self-limiting motor neuron disease, most commonly occurring in young males. HD is more common in Japan and Asian countries, and rare in the western population. Magnetic resonance imaging (MRI) is the best technique for the diagnosis of this entity. Early diagnosis is important as the patients can be advised to limit neck flexion movements to arrest the progression of the disease. Any clinically suspected case of Hirayama disease should undergo flexion MRI as conventional neutral MRI may miss findings in a few cases. The purpose of the present study is to evaluate the usefulness of flexion MR imaging and laminodural space (LDS) measurement in young patients with clinical and electroneuromyography (ENMG) definite Hirayama disease.

Materials & Methods

This is a retrospective observational study of 22 patients with clinical and ENMG definite Hirayama disease during the period of 2019-2022 These patients underwent MRI of cervical spine in neutral position and with neck flexion of 30°-40°. In neutral MRI, atrophy and T2-weighted hyperintensities in the cord were noted. In flexion MRI, the maximum forward shifting of the posterior dural sac, also known as the LDS, was noted along with other parameters.

Results

- Out of 22 patients, 20 (90.9 %) were males and 2 (9.1%) were females. The age of presentation varied from 17 to 27 years, with a mean age of 21 ± 3.36 years.
- 20 patients (90.9 %) had an involvement of unilateral upper extremity while 2 patient (9.1 %) had bilateral involvement.

- All 22 patients (100 %) had weakness and wasting of the affected hand muscles and 12 patients (54.54%) had wasting of forearm muscles.
- Neutral-position cervical MR imaging showed loss of cervical lordosis in 20 patients (90.9%) and localized lower cervical cord atrophy in 18 patients (81.8%).
- Intramedullary cervical cord T2-weighted hyperintensities were noted in 12 patients (54.54 %).
- Flexion MR imaging showed loss of the dural attachment, forward shifting of the posterior dural sac, a prominent posterior epidural space in all 22 patients (100%) and flow voids in posterior epidural space in 19 patients (86.36%).
- The mean LDS in our study was 5.4 mm.
- The mean AP diameter of the cord in neutral and flexion MRI was 4.64 mm and 4.18 mm respectively suggestive of cord compression during flexion.
- The mean AP diameter of the spinal canal in neutral and flexion MRI was 9.72 mm and 6.22 mm respectively suggestive of decrement in antero-posterior diameter of the spinal canal during flexion.

Conclusion

Flexion MRI plays a very important role in confirming the diagnosis of Hirayama disease in clinically suspected cases. Anterior displacement of posterior dura mater and widening of LDS was noted in all cases in our study. Even in conventional neutral MRI, findings like cord atrophy and T2 hyperintensities are seen but not in all the cases. So, flexion MRI increases diagnostic confidence by showing increased LDS, which is a characteristic finding in HD.

References

1. Huang YL, Chen CJ: Hirayama disease. Neuroimaging Clin N Am. 2011, 21:939-50, ix-x. 10.1016/j.nic.2011.07.009
2. Pradhan S: Bilaterally symmetric form of Hirayama disease . Neurology. 2009, 72:2083-9. 10.1212/WNL.0b013e3181aa5364
3. Guo XM, Qin XY, Huang C: Neuroelectrophysiological characteristics of Hirayama disease: report of 14 cases. Chin Med J (Engl). 2012, 125:2440-3.
4. Hirayama K: Juvenile muscular atrophy of unilateral upper extremity (Hirayama disease)—half-century progress and establishment since its discovery (Article in Japanese). Brain Nerve. 2008, 60:17-29.
5. Boruah DK, Prakash A, Gogoi BB, Yadav RR, Dhingani DD, Sarma B: The importance of flexion MRI in Hirayama disease with special reference to laminodural space measurements. AJNR Am J Neuroradiol. 2018, 39:974-80. 10.3174/ajnr.A5577

Images/Tables

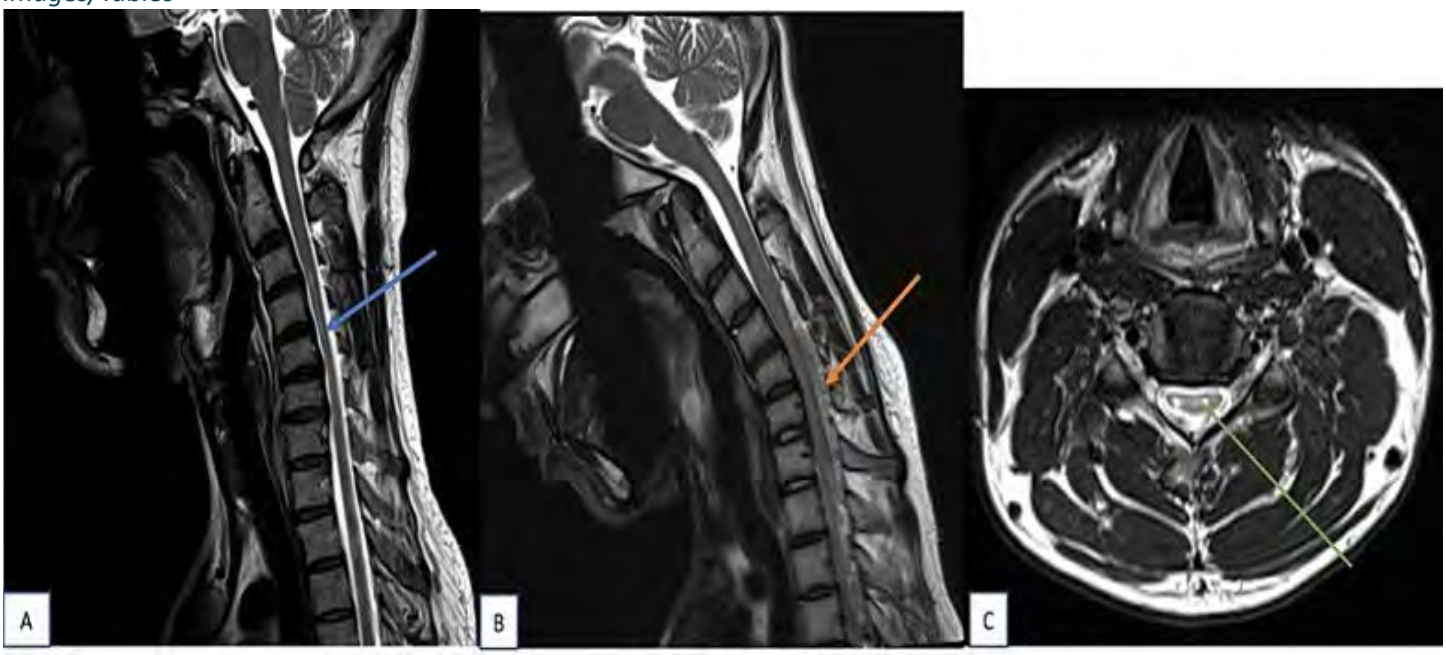

494

How Effectively Can Multi-Institutional MRI-Based Radiomics Analysis Distinguish Between Primary CNS Lymphoma, Glioblastoma, and Brain Metastases?

Mohammadreza Amjadzadeh MD[1], Matthew Pease MD[2], Murat Ak MD[3], Priyadarshini Mamindla[1], Serafettin Zenkin MD[3], Vishal Peddagangireddy[1], Mira Ayoub MD[3], Yassine Alami Idrissi MD[3], Walaa Hamza MD[3], Afrooz Zandifar MD[3], Abdallah Kamal MD[3], Nursima Ak MD[3], Mahir Yilmaz MD[3], Nasim Batavani MD[3], Ghazaleh Amjad MD[3], Pascal O. O. Zinn MD[3], Fanny E. Moron MD[4], Rivka Rachel Colen MD[1]

[1]Hillman Cancer Center, University of Pittsburgh Medical Center, Pittsburgh, Pennsylvania, USA. [2]Department of Neurosurgery, University of Pittsburgh Medical Center, Pittsburgh, PA, USA. [3]Hillman Cancer Center, University of Pittsburgh Medical Center, Pittsburgh, PA, USA. [4]Department of Radiology; Baylor College of Medicine, Houston, Texas, USA

Abstract Category

AI/Informatics

Purpose

This study examines the potential of radiomics to differentiate between Primary CNS Lymphoma (PCNSL), Glioblastoma (GB), and Brain Metastasis (BM), which together make up nearly 75% of all brain tumors, and present significant diagnostic challenges due to overlapping radiographic characteristics, often requiring invasive biopsies.

Materials & Methods

This multi-institutional retrospective study analyzed 1,075 patients (mean age: 64 ± 11.84 [SD] years; 52% male; PCNSL: *n* = 133, GB: *n* = 433, and BM: *n* = 509). By applying co-registration, axial T2-FLAIR and non-contrast and contrast-enhanced T1-weighted sequences were used for manual segmentation in 3D-Slicer software. Regions of interest (ROIs) included enhanced tumor, necrosis, peri-tumoral edema/invasion, and contralateral white matter (cWM).

After skull stripping, we used our in-house radiomic extraction pipeline, first-order features (e.g., skewness, kurtosis) were extracted using the intensity-level histogram, while second-order features, derived from the Grey-Level Co-occurrence Matrix (GLCM), capturing pixel spatial relationships at four angles (0°, 45°, 90°, 135°). Variance, range, and average were calculated across these angles to generate rotation-invariant features. To reduce the signal-to-noise ratio, we quantized images into 8, 16, 32, 64, and 256 gray-level numbers. At each quantization, 13 features were calculated across the four angles, followed by computing three rotation-invariant measures for each feature, resulting in 195 second-order features for each ROI. We further normalized features using the normal, patient-specific cWM and computed volume-independent features by dividing the original 195 features by each ROI volume. This resulted in 390 total second-order and 10 first-order features per ROI per sequence.

Machine learning analysis in R software involved a 70% training and 30% independent validation split. Features with high multicollinearity (Pearson's correlation > 0.85) were removed, and LASSO regression refined the set to 30 significant features. These were incorporated into an eXtreme Gradient Boosting (XGBoost) model, trained using 10-fold cross-validation. The model's performance was evaluated using the independent cohort.

Results

When evaluated on the independent cohort, the model robustly distinguished between tumor types, achieving a significant performance ($p < 0.001$) with an accuracy of 89%. The model's efficacy was further supported by the AUC values from the ROC curves, which reflected strong discriminatory power. The AUC values for distinguishing PCNSL from non-PCNSL (96.95%), GB from non-GB (98.38%), and BM from non-BM (96.74%) were exceptionally high, indicating model's near-perfect ability to correctly classify these tumors.

Sensitivity rates were 74% for PCNSL, 88% for GB, and 94% for BM, while specificity was 98% for PCNSL, 96% for GB, and 87% for BM, indicating reliable true-positive and true-negative identification. The positive predictive values were high for GB (0.93), PCNSL (0.85), and BM (0.87), demonstrating the reliable predictive performance of the model. The negative predictive values were also exceptionally high for PCNSL (0.97), GB (0.92), and BM (0.94), demonstrating model's accurate performance in ruling out these tumors when they are not present.

Conclusion

We successfully developed and validated a robust radiomics signature capable of distinguishing between PCNSL, GB, and BM, which highlights the potential of radiomics as an effective, non-invasive, and cost-efficient diagnostic tool for differentiating between these tumor types, utilizing only standard-of-care MRI.

References

1. Ferlay J, Soerjomataram I, Dikshit R, et al. Cancer incidence and mortality worldwide: Sources, methods and major patterns in GLOBOCAN 2012. Int J Cancer. 2015;136(5):E359-86. DOI: https://doi.org/10.1002/ijc.29210.
2. Nyul LG, Udupa JK, Zhang X. New variants of a method of MRI scale standardization. IEEE Trans Med Imaging. 2000;19(2):143-50. DOI: https://doi.org/10.1109/42.836373.
3. Haralick RM, Shanmugam K, Dinstein IH. Textural features for image classification. IEEE Trans Syst Man Cybern. 1973;(6):610-21. DOI: https://doi.org/10.1109/TSMC.1973.4309314.
4. Tibshirani R. Regression shrinkage and selection via the lasso. J R Stat Soc Series B Stat Methodol. 1996;58(1):267-88.

Images/Tables

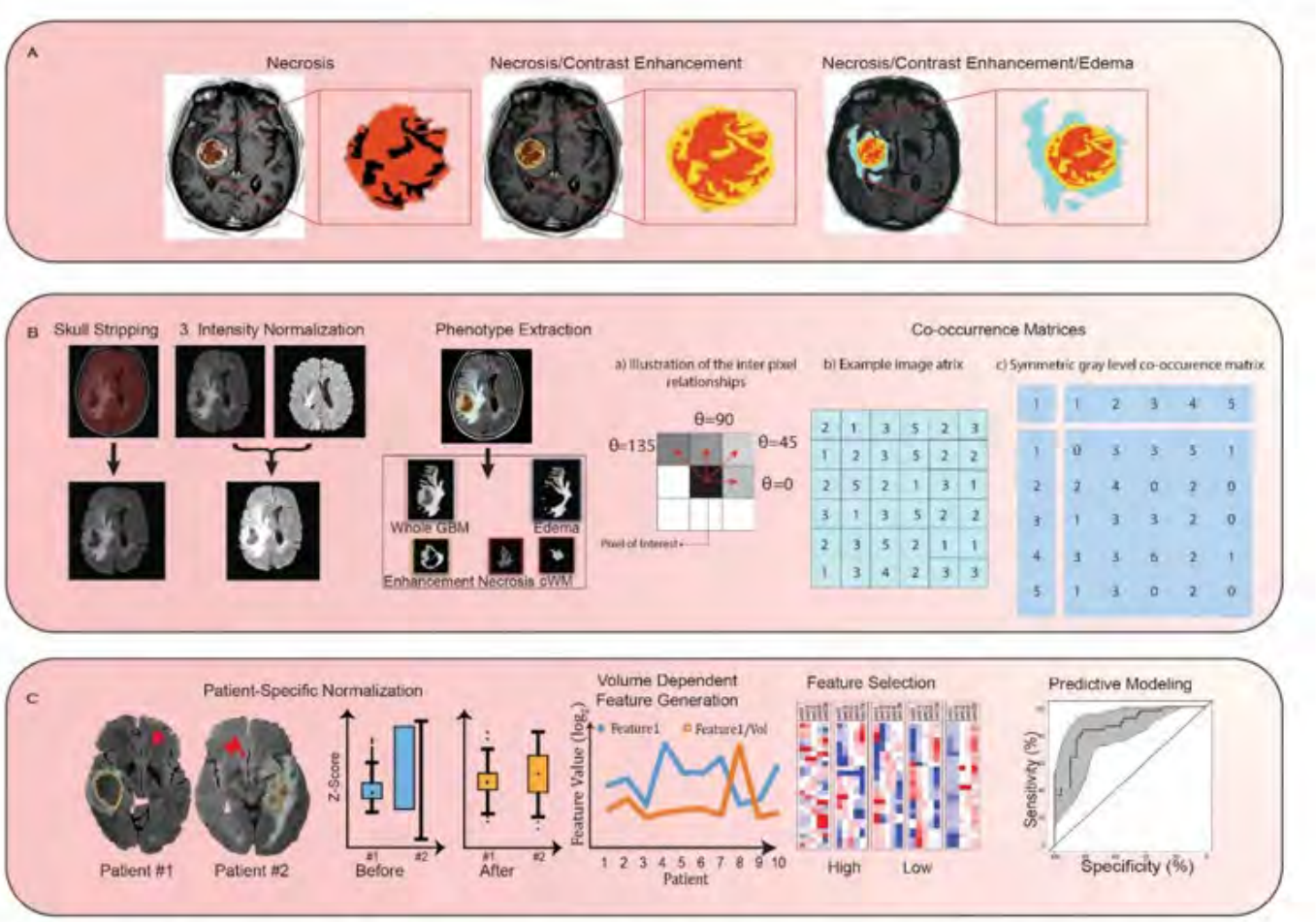

Radiomics Pipeline Outline. A. Segmentation of various phenotypes and regions of interest. B & C. Steps for extracting radiomics features and developing the predictive model.

496

Fractional Tumor Burden (FTB): An Early Predictor of Response to Tumor Treating Fields (TTFields) in Glioblastoma

Kathleen M Schmainda PhD, Melissa A Prah, Jennifer M Connelly MD
Medical College of Wisconsin, Milwaukee, WI, USA

Abstract Category

Adult Brain

Purpose

To determine if perfusion derived FTB maps provide an earlier indicator of response to TTFields compared to conventional MRI

Materials & Methods

88 patients provided informed written consent to this IRB-approved and HIPAA-compliant study. Inclusion criteria consisted of a diagnosis of new or recurrent IDH wild-type glioblastoma and treatment with TTFields with an average compliance of >70%. An MRI that included DSC (dynamic susceptibility contrast) perfusion imaging at baseline and at least one post-initiation time point of 1-2, 3-4 or 5-6 months was also required for analysis. An analysis workflow (IB RadTech™, Imaging Biometrics LLC, Elm Grove, WI) was used to create FTB maps.[1,2] The workflow incorporates the creation of delta T1 (dT1) images, created from registered and calibrated pre- and post-contrast T1w images, for the purpose of delineating contrast-enhancing lesion volumes (CELV). Leakage-corrected, standardized maps of relative cerebral volume (sRCBV) are generated from the DSC-MRI data.[3] Together dT1 and sRCBV are used to generate perfusion class maps, using previously determined tissue-validated sRCBV thresholds.[4] The thresholds distinguish highly vascular (red), mixed or intermediate vascular (yellow) and avascular/treatment-effect (blue) regions within CELV. Consistent with previous use[1], fractional tumor burden (FTB) is defined as the volume fraction of red+yellow regions. The ability to predict overall survival (OS) and progression free survival (PFS) was determined according to increases vs decreases in CELV, mean sRCBV and FTB, relative to pre-treatment values, using the Kaplan-Meier method.

Results

N=21 patients, ranging in age from 29-85y, satisfied the inclusion criteria. FTB results are shown in **Figure 1** for a patient whose FTB decreased despite an increase in CELV. This example may explain a previous finding that 44% of responders had initial growth on standard imaging despite a later clinical response.[5] The OS and PFS results for all metrics at 1-2 months are shown in **Figure 2.** The FTB fraction was found to be predictive of OS (p=0.02) and PFS (p=0.03) at 1-2 months, but not at later time points. The CELV was not predictive of OS at any time point, consistent with the reported delay of 5.2 months before an objective response can be confirmed with conventional imaging.[5] Changes in mean rCBV were not predictive of OS at any time point, which may reflect the spatial averaging of the sRCBV from both tumor and non-tumor regions within the CELV.

Conclusion

The results suggest that FTB, a more accurate indicator of true tumor burden, may serve as an early indicator of response to TTFields, whereas conventional post-contrast MRI and spatially averaged sRCBV do not. However, the study sample size is small, requiring a larger study for confirmation.

References

1. Hoxworth JM, Eschbacher JM, Gonzales AC, et al. Performance of standardized relative CBV for quantifying regional histologic tumor burden in recurrent high-grade glioma: Comparison against normalized relative CBV using image-localized stereotactic biopsies. *American Journal of Neuroradiology* 2020;41:408–15.

2. Connelly JM, Prah MA, Santos-Pinheiro F, et al. Magnetic Resonance Imaging Mapping of Brain Tumor Burden: Clinical Implications for Neurosurgical Management: Case Report. *Neurosurgery Open* 2021;2:2–5.

3. Bedekar D, Jensen TR, Schmainda KMKM. Standardization of relative cerebral blood volume (rCBV) image maps for ease of both inter and intra-patient comparisons. *Magn Reson Med* 2010;64:907–13.

4. Prah MA, Al-Gizawiy MM, Mueller WM, et al. Spatial discrimination of glioblastoma and treatment effect with histologically-validated perfusion and diffusion magnetic resonance imaging metrics. *J Neurooncol*2018;136:13–21.

5. Vymazal J, Wong ET. Response patterns of recurrent glioblastomas treated with tumor-treating fields. *Semin Oncol* 2014;41.

Images/Tables

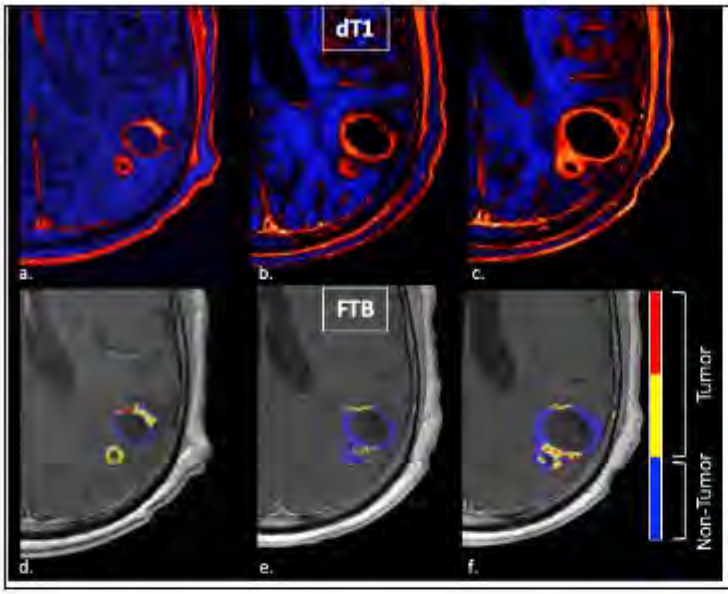

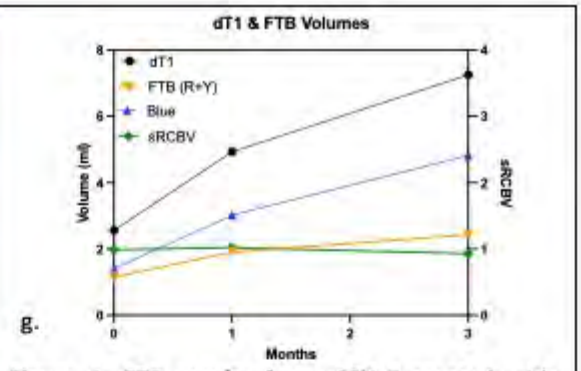

Figure 1: **FTB results for a 62Y F** treated with TTFields. (a-c) Delta T1 (dT1) maps show an increase in contrast enhancing volume largely due to a corresponding increase in the non-tumor (blue) fraction of tumor (d-f). Longitudinal changes in dT1, FTB, non-tumor (blue) volumes and sRCBV are shown for this patient.

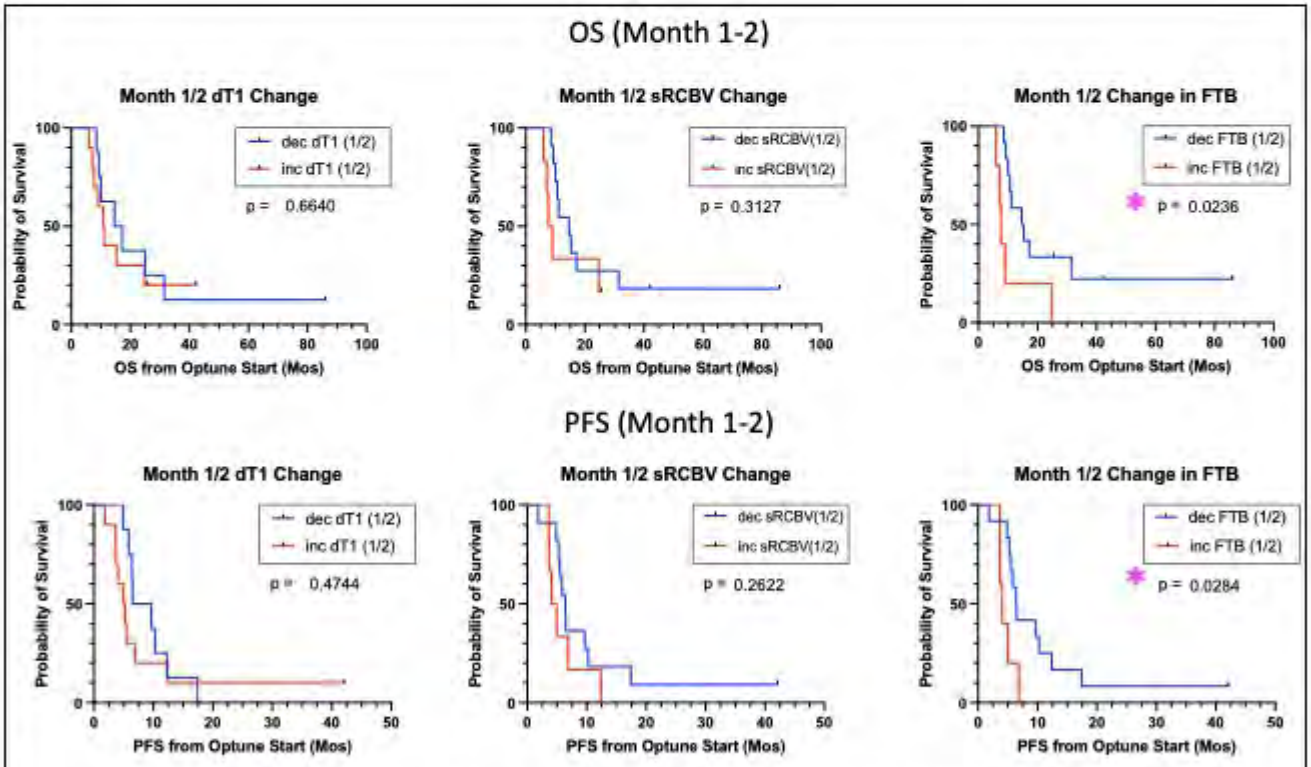

Figure 2: (a) Overall survival (OS) and (b) progression free survival (PFS) for dT1, sRCBV and FTB at 1-2 months after TTFfield initiation. Significant predictors or response (*) were observed for the FTB for both OS and PFS .

498

Role of MRI Spine in predicting AQP4 positivity in NMOSD patients

Abhishek Jagdishchander Arora MD, FRCR, Mohit Kapoor MBBS, Amit Patle MBBS
All India Institute of Medical Sciences, Bibinagar, Hyderabad, Telangana, India

Abstract Category

Spine

Purpose

To evaluate Spine MR characteristics of neuromyelitis optica which are strongly associated with aquaporin 4 antibody positivity by using clinicoradiological scoring system.

A long turnaround time (days to weeks) for serologic assay results for the AQP4 antibody further delays the diagnosis of NMOSD. Recent studies demonstrated the beneficial effects of rituximab, plasma exchange, or lymphocytapheresis combined with steroid therapy, in timely treatment of NMOSD.

To correlate the MR Spine imaging features of neuromyelitis optica spectrum disorder which are strongly associated with aquaporin 4 antibody positivity, and to calculate score of each NMOSD patient based on MRI features and then correlate the Score with Aquaporin 4 antibody positivity.

Materials & Methods

Inclusion Criteria: All patients diagnosed with NMOSD, based on the international consensus criteria developed by International panel for NMOSD diagnosis (IPND) who underwent MRI study of whole spine (plain and contrast) and with aquaporin-4 antibody test report at the time of scan or obtained subsequently, (n=30) were included.

Exclusion criteria : 1) Any patient not having either aquaporin -4 antibody or MRI were excluded. 2) Any partially treated patients before MRI were excluded including cases with relapse of previously treated disease. 3) Any patients with contraindication to MRI were excluded.

We evaluated the following parameters in MRI Spine. cervicomedullary junction involvement, cord expansion ratios in LETM, bright spotty lesions, the number of involved segments, enhancement patterns, and axial distribution patterns using spinal MR imaging and gave score to each patient based on above parameters and based on the gender as shown in subsequent slides.

Statistical analysis was performed to identify the threshold score with best sensitivity and specificity.

Also each MRI parameter in NMOSD was separately correlated with aquaporin-4 antibody seropositivity.

Results

17 out of 30 patients with MRI Spine were aquaporin-4 antibody–positive.

The sensitivity and specificity of each parameter are as follows: female gender (sensitivity, 88%; specificity, 84%), cervicomedullary junction involvement (sensitivity 94.12%; specificity, 84.62%), cord expansion ratio 1.4 (sensitivity, 47.06%; specificity, 80%),enhancement on post contrast (sensitivity 69.3%,specificity 87%) and bright spotty lesions (sensitivity, 93%; specificity, 89%).

Most sensitive and specific parameter to predict AQP4 antibody seropositivity is cervicomedullary junction involvement and bright spotty lesions respectively

With a score threshold of ≥3, the sensitivity of the scoring system was 83.3% and the specificity was 86.2% .

Conclusion

Score threshold ≥3 in the scoring system best predicts AQP4 antibody seropositivity in patients with LETM and helpful in diagnosis of NMOSD (with sensitivity of 85% and specificity of 76%, increasing the threshold score to >/=4 decreased the sensitivity to 65% but increased specificity to 94%)

Most sensitive and specific parameter to predict AQP4 antibody seropositivity is cervicomedullary junction involvement and bright spotty lesions respectively on MR Spine

References

Jarius S, Wildemann B. Aquaporin-4 antibodies (NMO-IgG) as a serological marker of neuromyelitis optica: a critical review of the literature. Brain Pathol 2013;23:661–83 CrossRef Medline

Pekcevik Y, Mitchell CH, Mealy MA, et al. Differentiating neuromyelitis optica from other causes of longitudinally extensive transverse myelitis on spinal magnetic resonance imaging. Mult Scler 2016;22:302–11 CrossRef Medline

Waters P, Jarius S, Littleton E, et al. Aquaporin-4 antibodies in neuromyelitis optica and longitudinally extensive transverse myelitis. Arch Neurol 2008;65:913–19 Medline

Cassinotto C, Deramond H, Olindo S, et al. MRI of the spinal cord in neuromyelitis optica and recurrent longitudinal extensive myelitis. J Neuroradiol 2009;36:199 –205 CrossRef Medline

Jarius S, Franciotta D, Bergamaschi R, et al. NMO-IgG in the diagnosis of neuromyelitis optica. Neurology 2007;68:1076–77 CrossRef Medline

500

Where Do CSF-Venous Fistulas Occur? A Systematic Review and Meta-Analysis

Zaid Saadeh, Sherief Ghozy, Ajay Madhavan, John Benson, Jared Verdoorn, Jeremy Cutsforth-Gregory, DK Kim MD, Jodie Serum, Ian Mark
Mayo Clinic, Rochester, MN, USA

Abstract Category

Spine

Purpose

CSF-venous fistulas (CVFs) are an important and underrecognized cause of spontaneous intracranial hypotension. They are a direct communication between the subarachnoid space and paraspinal vein resulting in loss of CSF. No large volume studies have evaluated the prevalence of affected laterality or spinal levels. We performed a systematic review and meta-analysis to answer this question.

Materials & Methods

A literature review identified 587 studies for possible inclusion and 105 were selected as relevant by two screeners. Studies from the same institution with data overlap and <3 subjects were removed. The side of involvement and spinal levels affected for patients with CVFs were collected when available and submitted for analysis. Pooled prevalence rates were computed. Pairwise meta-regression was used to assess for statistically significant difference when $p<0.05$.

Results

CVFs were most common on the right compared to the left with this laterality reported in 394/628 cases (63%; $p<0.001$). Nearly all were in the thoracic spine (565/600 or 94%). T9 demonstrated the highest prevalence rate for a specific spinal level out of the pooled CVFs at 14%. Note that this prevalence was determined after excluding cases where the CVF was categorized into a spinal region without level or multifocal. T7 and T10 also showed high prevalence rates of 12% and 13%, respectively. The lumbar and cervical spine demonstrated significantly lower prevalence when compared to the thoracic region ($P<0.001$).

Conclusion

Localization of CVFs is crucial in therapeutic planning and intervention. Our meta-analysis sought to augment this by identifying common areas of involvement. Although CVFs are a new discovery with a relatively small patient pool, we found significantly more on the right. The greatest prevalence rates by level were in the lower thoracic spine at T7, T9, and T10. One possible etiology could be pulsatile flow related to diaphragmatic motion.

References

Kranz, P. G., Gray, L., Malinzak, M. D., Houk, J. L., Kim, D. K., & Amrhein, T. J. (2021). CSF–venous fistulas: Anatomy and diagnostic imaging. *American Journal of Roentgenology*, *217*(6), 1418–1429. https://doi.org/10.2214/ajr.21.26182

501

Endovascular management of intracranial carotid blowout syndrome in patients with head and neck cancers

Feng-Chi Chang MD, Kai-Wei Yu, Chia-Hung Wu
Department of Radiology, Taipei Veterans General Hospital; National Yang Ming Chiao Tung University, Taipei, Taiwan, Taiwan

Abstract Category

Interventional

Purpose

Carotid blowout syndrome is a serious complication of head and neck cancer (HNC) that may involve intracranial or extracranial internal carotid artery (ICA). Although parent artery occlusion (PAO) is the major endovascular treatment for intracranial carotid blowout syndrome (iCBS), the efficacy of using a balloon-expandable coronary stent-graft (BES) remains unclear.

Materials & Methods

This was a quasi-randomized trial, prospective study included patients with iCBS treated by BES or PAO between 2018 and 2024. Patients were allocated to either group based on the last digit of their chart number. The even number went

to BES group and the odd number went to PAO group. The inclusion criteria of iCBS included pathological process of CBS involving petrous and/or cavernous ICA detected by both imaging and clinical features. The primary outcome was defined as rebleeding events after intervention. The secondary outcome was defined as neurological complication after intervention.

Results

Fifty-nine patients with 61 iCBS lesions were enrolled. Thirty-three iCBS lesions were treated with BES, and 28 underwent PAO. The results for the BES group versus the PAO group were as follows: rebleeding events, 5/33 (15.1%) vs. 5/28 (17.8%) (p = .78); neurological complication, 5/33 (15.1%) vs. 5/28 (17.8%) (p = .78); median hemostatic time (months), 10.0 versus 11.5 (p = 0.22) and median survival time (months), 10.0 versus 11.5 (p =0.39).

Conclusion

No significant difference in rebleeding risk or neurological complication was observed between the BES and PAO groups. Our study confirmed the safety and effectiveness of applying BES for iCBS in HNC patients.

References

Chang FC, Lirng JF, Luo CB, et al. Patients with head and neck cancers and associated postirradiated carotid blowout syndrome: endovascular therapeutic methods and outcomes. J Vasc Surg 2008;47:936–45. doi: 10.1016/j.jvs.2007.12.030

Chang FC, Luo CB, Lirng JF, et al. Endovascular management of post-irradiated carotid blowout syndrome. PLoS One 2015;10:e0139821. doi: 10.1371/journal.pone.0139821

Yu KW, Wu CH, Lin TM, et al. Endovascular management of post-irradiated carotid blowout syndrome in patients with lower neck cancers. Eur J Vasc Endovasc Surg 2024;67:708–16. doi: 10.1016/j.ejvs.2023.12.036

Images/Tables

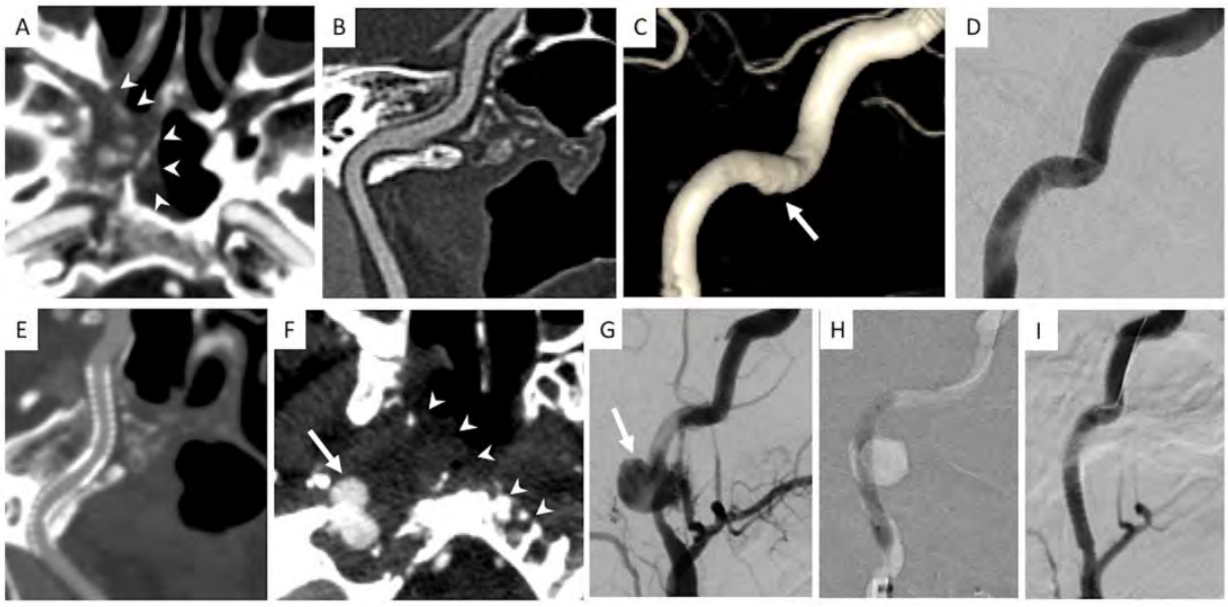

504

Minimal Impact of Embolization to New Territory on Outcomes in Medium Vessel Occlusion Strokes Treated with Mechanical Thrombectomy: A Multicenter Study

Hamza Adel Salim MD[1], Dhairya A. Lakhani MD[2], Basel Musmar MD[3], Tobias D. Faizy MD[4], Jeremy J. Heit MD PhD[5], Adrien Guenego MD[6], Adam A. Dmytriw MD[7], Max Wintermark MD[1], Vivek S Yedavalli MD[8]

[1]MD Anderson Cancer Center, Houston, TX, USA. [2]West Virginia University, Morgantown, WV, USA. [3]Thomas Jefferson University Hospital, Philadelphia, PA, USA. [4]University Medical Center Münster, Münster, Germany, Germany. [5]Stanford Medical Center, Palo Alto, CA, USA. [6]Department of Diagnostic and Interventional Neuroradiology, Erasme University

Hospital, Brussels, Brussels, Belgium. [7]Neuroendovascular Program, Massachusetts General Hospital, Harvard University, Boston, MA, USA. [8]Johns Hopkins Medical Center, Baltimore, MD, USA

Abstract Category

Head & Neck

Purpose

Mechanical thrombectomy (MT) is established as an effective treatment for large vessel occlusion strokes, but its efficacy and safety for medium vessel occlusions (MeVO) remain less clear. This study examines the impact of periprocedural embolization to a new vascular territory (ENT) on clinical outcomes in MeVO stroke patients treated with MT.

Materials & Methods

We conducted a multicenter, retrospective analysis using the MAD-MT registry, including 2,122 MeVO stroke patients who underwent mechanical thrombectomy (MT) between September 2017 and July 2023. ENT was defined as filling defects in previously unaffected territories, excluding embolization in the vascular bed distal or proximal to the original occlusion, observed on final angiographic runs after retrieval of the primary thrombus. We evaluated the associations between ENT, procedural variables, and 90-day clinical outcomes, including functional independence (modified Rankin Scale [mRS] scores of 0-2), excellent outcomes (mRS 0-1), mortality, and hemorrhagic complications.

Results

ENT occurred in 2.9% (63/2,122) of patients. Multivariable analysis found that a longer onset-to-arterial puncture time (in hours) (adjusted OR [aOR], 1.03; 95% CI, 1.01-1.05; p = 0.002) and a greater total number of passes (aOR, 1.15; 95% CI, 1.01-1.32; p = 0.032) were associated with an increased risk of ENT. In contrast, excellent recanalization (TICI 2c-3) was associated with a reduced risk of ENT (aOR, 0.41; 95% CI, 0.23-0.72; p = 0.002). Additionally, functional independence at 90 days (mRS 0-2) in the ENT group was not lower than in the non-ENT group (aOR, 0.87; 95% CI, 0.48-1.60; p = 0.66). Moreover, ENT was not significantly associated with mortality (aOR 1.80; 95% CI 0.91-3.58; p = 0.093). Similarly, no significant association was found with hemorrhagic complications (aOR 1.51; 95% CI 0.67-3.42; p = 0.32).

Conclusion

ENT during MT for MeVO stroke occurs infrequently and does not significantly affect 90-day clinical outcomes, mortality, or hemorrhagic complications. These findings indicate that the potential risk of ENT should not discourage clinicians from performing MT in MeVO cases. Further prospective studies are needed to validate these results.

References

Salim HA, Yedavalli V, Musmar B, Adeeb N, E L Naamani K, Henninger N, Sundararajan SH, Kühn AL, Khalife J, Ghozy S, Scarcia L, Tan BYQ, Heit JJ, Regenhardt RW, Cancelliere NM, Bernstock JD, Rouchaud A, Fiehler J, Essibayi MA, Sheth SA, Puri AS, Barreau X, Colasurdo M, Renieri L, Dyzmann C, Marotta T, Spears J, Mowla A, Jabbour P, Filipe JP, Biswas A, Harker P, Clarençon F, Radu RA, Siegler JE, Nguyen TN, Varela R, Ota T, Gonzalez N, Moehlenbruch MA, Altschul D, Gory B, Costalat V, Stracke CP, Aziz-Sultan MA, Hecker C, Shaikh H, Liebeskind DS, Baker A, Pedicelli A, Alexandre A, Faizy TD, Tancredi I, Kalsoum E, Lubicz B, Patel AB, Mendes Pereira V, Guenego A, Dmytriw AA; MAD MT Investigators. Endovascular therapy versus best medical management in distal medium middle cerebral artery acute ischaemic stroke: a multinational multicentre propensity score-matched study. J Neurol Neurosurg Psychiatry. 2024 Jul 23:jnnp-2024-333669. doi: 10.1136/jnnp-2024-333669. Epub ahead of print. PMID: 39043567.

Images/Tables

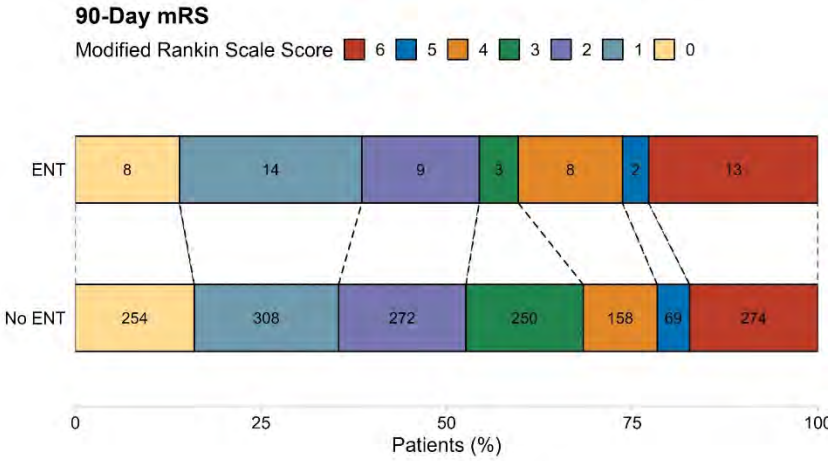

505

Comparison of an automated DSC MR perfusion platform vs a manual DSC MR perfusion platform for surveillance of High Grade Glioma status post surgical resection on Chemotherapy and Radiation.

James Thomas MD, Mara M Kunst MD, Juan E Small MD
Lahey Hospital and Medical Center, Burlington, MA, USA

Abstract Category

Functional/Advanced Imaging

Purpose

It is well known that DSC MR Perfusion is very useful in High Grade Gliomas compared to standard MR imaging particularly for surveillance of postoperative patients on chemoradiation therapy to help in differentiating between tumor progression and post treatment related effects. However processing of DSC may not be readily available at all times in facilities with around the clock MR scanning because a trained MR technologist or Radiologist needs to process the rCBV maps and send it to PACS. An automated DSC Perfusion pipeline creating normalized rCBV maps could be very useful for serial surveillance in a busy practice. We retrospectively compared the performance of a recently FDA approved, commercially available, automated DSC MR Perfusion platform with a manual DSC MR perfusion platform using no preload GRE DSC.

Materials & Methods

23 patients with High Grade Glioma status post surgical resection on chemotherapy and radiation therapy were evaluated for a total of 57 studies were acquired with no preload GRE DSC utilizing Boxerman et al. Consensus recommendations with flip angle of 30 were processed using two MR perfusion processing pipelines. Weight based Gadobutrol was utilized for intravenous contrast. MR Brain with and without contrast was obtained.

One processing pipeline is a recently FDA approved automated commercially available DSC MR perfusion program, Nordic Mediva, and is compared with a commercially available FDA approved manual DSC processing platform, Dynasuite. Raw DSC data, from prior studies, was pushed to the automated platform to facilitate serial comparison. Both utilize Leakage Correction, motion correction and both generate relative CBV maps. The automated platform uses a previously reported patented technique for normalizing CBV maps by comparing the concentration time curves of the tumor divided by the mean CBV concentration time curve of the normal appearing white matter and gray matter by automated exclusion of vessels, noise, tumor and non brain pixels creating quantitative normalized rCBV maps. Two experienced Neuroradiologists evaluated PowerPoint side by side screenshots of a representative area of enhancement , the automated normalized rCBV image and manual rCBV image evaluating the rCBV map in the area of enhancement, background, SNR, ease of comparison and diagnostic confidence.

Results

The automated DSC processing pipeline demonstrated increased conspicuity of the areas of rCBV related to the enhancing mass , more background suppression and motion correction seemed to be more robust with less missing data on motion limited studies. Moreover automated DSC facilitated faster interpretation with rCBV maps available nearly contemporaneously provided prior study raw data for DSC was available to be processed on the automated platform. Same vendor serial comparison was relatively easy. Serial comparison between vendor maps was challenging because the maps looked different from each other. It was easier to tell whether there was treatment response/ failure on serial review of the automated rCBV maps.

Conclusion

Automated normalized rCBV maps can be useful for patient care with nearly contemporaneous availability of images on PACS with increased visibility of rCBV in areas of enhancement , better background suppression thereby increasing the diagnostic confidence in assessing residual tumor vs post treatment effects on serial imaging .

References

1. Bjørnerud A, Emblem KE. A fully automated method for quantitative cerebral hemodynamic analysis using DSC–MRI. *J Cereb Blood Flow Metab*. 2010;30(5):1066-78. doi:10.1038/jcbfm.2010.4.
2. Emblem KE, Bjornerud A. An automatic procedure for normalization of cerebral blood volume maps in dynamic susceptibility contrast−based glioma imaging. *AJNR Am J Neuroradiol*. 2009;30(10):1929-32. doi:10.3174/ajnr.A1680.
3. Emblem KE, Due-Tonnessen P, Hald JK, et al. Automatic vessel removal in gliomas from dynamic susceptibility contrast imaging. Magn Reson Med. 2009;61:1210-17.

4. Jafari-Khouzani K, Emblem KE, Kalpathy-Cramer J et al. Repeatability of cerebral perfusion using dynamic susceptibility contrast MRI in glioblastoma patients. *Transl Oncol*. 2015;8(3):137-46. doi:10.1016/j.tranon.2015.03.002
5. Boxerman JL, Quarles CC, Hu LS, et al. Consensus recommendations for a dynamic susceptibility contrast MRI protocol for use in high-grade gliomas. *Neuro-Oncology*. 2020;22(9):1262-75. doi:10.1093/neuonc/noaa141.

Images/Tables

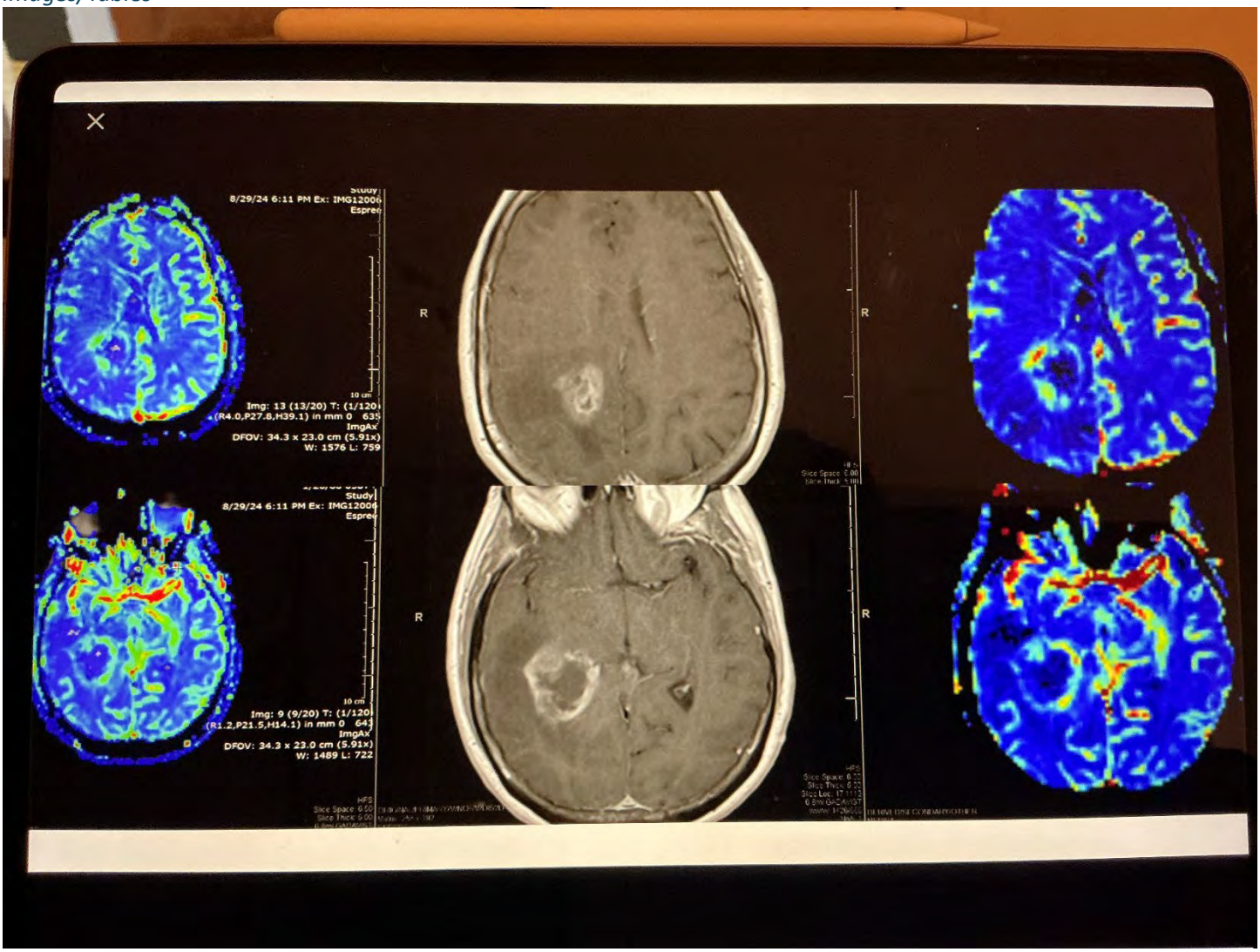

511

Prolonged Venous Transit and Clinical Outcomes in Anterior Circulation Large-Vessel Occlusion Stroke With Complete or Near-Complete Reperfusion

Hamza Adel Salim MD[1], Dhairya A. Lakhani MD[2], Janet Mei MD[3], Nathan Z. Hyson MD[3], Vaibhav Vagal MD[4], Kambiz Nael MD[5], Gregory W Albers MD[6], Tobias D. Faizy MD[7], Jeremy J. Heit MD PhD[6], Max Wintermark MD[1], Vivek Yedavalli MD[3]
[1]MD Anderson Cancer Center, Houston, TX, USA. [2]Department of Radiology, West Virginia University, Morgantown, WV, USA. [3]Johns Hopkins Medical Center, Baltimore, MD, USA. [4]Renaissance School of Medicine at Stony Brook University, New York, NY, USA. [5]University of California San Francisco, San Francisco, CA, USA. [6]Stanford Medical Center, Palo Alto, CA, USA. [7]University Medical Center Münster, Münster, Münster, Germany

Abstract Category

Head & Neck

Purpose

Prolonged venous transit (PVT), indicating impaired venous outflow, has been associated with poor outcomes in patients with acute ischemic stroke due to large-vessel occlusion (AIS-LVO) undergoing mechanical thrombectomy (MT). The prognostic significance of PVT in patients achieving complete or near-complete reperfusion is not well established. This

study aimed to determine whether PVT is associated with unfavorable functional outcomes and increased mortality at 90 days in AIS-LVO patients with excellent recanalization (modified Thrombolysis in Cerebral Infarction [mTICI] score of 2c or 3).

Materials & Methods

We retrospectively analyzed data from a prospective registry of AIS-LVO patients treated between September 2017 and September 2022. Inclusion criteria were anterior circulation LVO, complete or near-complete reperfusion after MT (mTICI 2c or 3), and available 90-day modified Rankin Scale (mRS) scores. PVT was assessed on pretreatment CT perfusion Tmax maps, defined as Tmax ≥ 10 seconds in the posterior superior sagittal sinus or torcula. The primary outcome was favorable functional recovery (90-day mRS 0–2). Secondary outcomes included excellent recovery (90-day mRS 0–1) and 90-day mortality.

Results

Among 81 patients, 25 (31%) had PVT+ and 56 (69%) had PVT− profiles. Baseline characteristics were similar between groups. PVT+ patients had significantly higher discharge NIH Stroke Scale scores and worse 90-day mRS scores compared to PVT− patients (median mRS, 4.00 vs. 1.00; P < 0.001). Multivariable analysis showed that PVT+ was independently associated with lower odds of favorable outcome (odds ratio [OR], 0.18; 95% confidence interval [CI], 0.04–0.65; P = 0.013) and excellent outcome (OR, 0.12; 95% CI, 0.02–0.52; P = 0.008). PVT+ was also associated with higher odds of 90-day mortality (OR, 4.11; 95% CI, 1.08–17.0; P = 0.041).

Conclusion

In AIS-LVO patients achieving complete or near-complete reperfusion after MT, PVT is a strong negative prognostic marker associated with decreased likelihood of favorable functional outcomes and increased 90-day mortality. PVT assessment may help identify patients at higher risk of poor outcomes despite successful reperfusion therapy.

References

Yedavalli VS, Lakhani DA, Koneru M, Balar AB, Greene C, Hoseinyazdi M, Nabi M, Lu H, Xu R, Luna L, Caplan J, Dmytriw AA, Guenego A, Heit JJ, Albers GW, Wintermark M, Urrutia V, Huang J, Nael K, Leigh R, Marsh EB, Hillis AE, Llinas RH. Simplifying venous outflow: Prolonged venous transit as a novel qualitative marker correlating with acute stroke outcomes. Neuroradiol J. 2024 Jul 27:19714009241269475. doi: 10.1177/19714009241269475. Epub ahead of print. PMID: 39067016.

Images/Tables

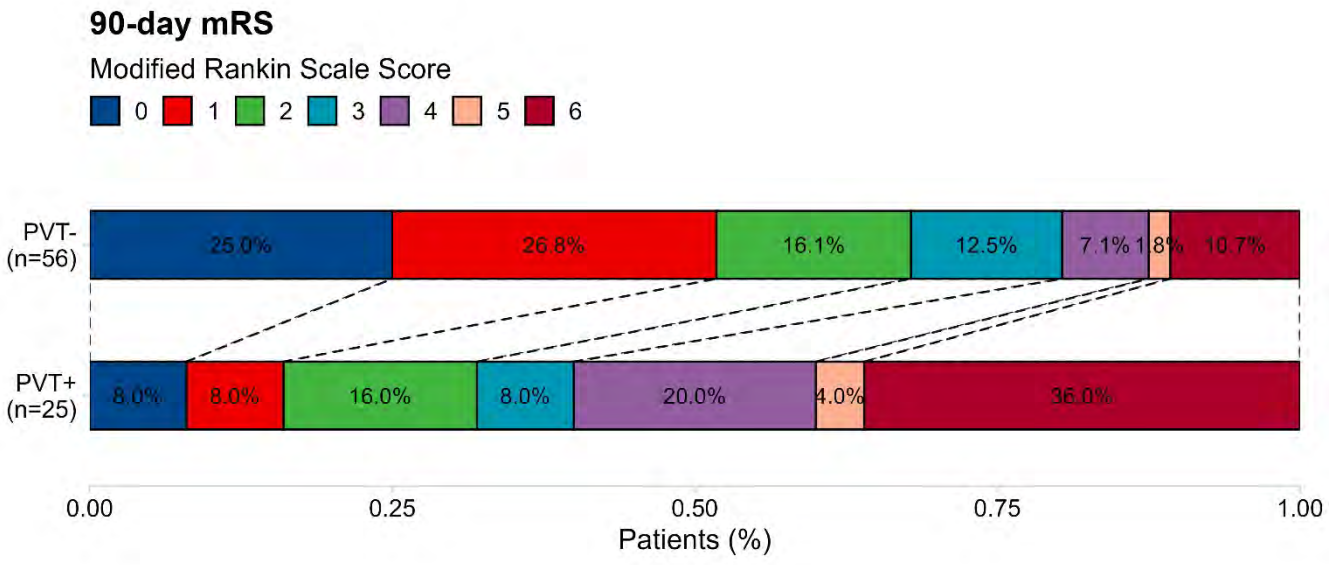

516

Generative AI for Automated Time-to-Maximum and Cerebral Blood Flow Mapping from Non-Contrast Head Computed Tomography Images

Nicholas J Primiano MD MS[1], Abhinav Changa MD[1], Jacky Cheung MD[2], Benjamin Kummer MD[2]

[1]Mount Sinai, New York, NY, USA. [2]New York, NY, USA

Abstract Category
AI/Informatics
Purpose
Endovascular thrombectomy (EVT) is the standard of care for treating patients with acute ischemic stroke (AIS) caused by large-vessel occlusions (LVO). While the utility of CT perfusion (CTP) imaging has recently come under scrutiny for patient selection, CTP is still widely used for selecting EVT candidates in the clinical community, which can delay care and potentially worsen outcomes. We trained a deep learning model to generate time-to-maximum (Tmax) and cerebral blood flow (CBF) maps from non-contrast CT head (NCCTH) images obtained during routine stroke evaluations.
Materials & Methods
We retrospectively reviewed patients presenting with AIS due to LVO at a multi-site academic medical center between May 2019 and June 2021 that had both NCCTH and CTP imaging within a 30-minute interval. Using NCCTH and CTP images from our institutional radiology database, we manually extracted Tmax and CBF maps generated by third-party post-processing software, Viz.ai, to serve as ground truth labels. Brain structures were segmented from NCCTH images using the TotalSegmentator package. NCCTH slices were co-registered to their corresponding CTP images. We then trained a pix2pix-turbo model to predict Tmax and CBF map slices from co-registered NCCTH images. Pix2pix-turbo is a conditional generative adversarial network based on Sable Diffusion Turbo that performs paired image-to-image translation.
Results
After applying pre-specified exclusionary criteria, we included 101 (90% train, 10% test) patients in our study. For Tmax map generation, the pix2pix-turbo model achieved a Fréchet Inception Distance (FID) of 62.21, a Peak Signal-to-Noise Ratio (PSNR) of 16.99, and a Structural Similarity Index (SSIM) of 0.827. For CBF map generation, corresponding metrics were FID 59.58, PSNR 16.38, and SSIM 0.787.
Conclusion
Using a deep learning, cross-modality approach, we trained a generative AI model that demonstrated moderate efficacy in directly producing Tmax and CBF maps from NCCTH images. Given the relatively small sample size, future work will validate our findings in larger cohorts and focus on predicting estimates of Tmax and CBF volumes. If successful, our approach could enable earlier, more informed triage and treatment decisions in clinical scenarios that require advanced neuroimaging.
References
Raul G. Nogueira, M.D., Ashutosh P. Jadhav, M.D., Ph.D., Diogo C. Haussen, M.D., et al. “Thrombectomy 6 to 24 hours after stroke with a mismatch between deficit and infarct.” New England Journal of Medicine, vol. 378, no. 1, 4 Jan. 2018, pp. 11–21, https://doi.org/10.1056/nejmoa1706442.

Images/Tables

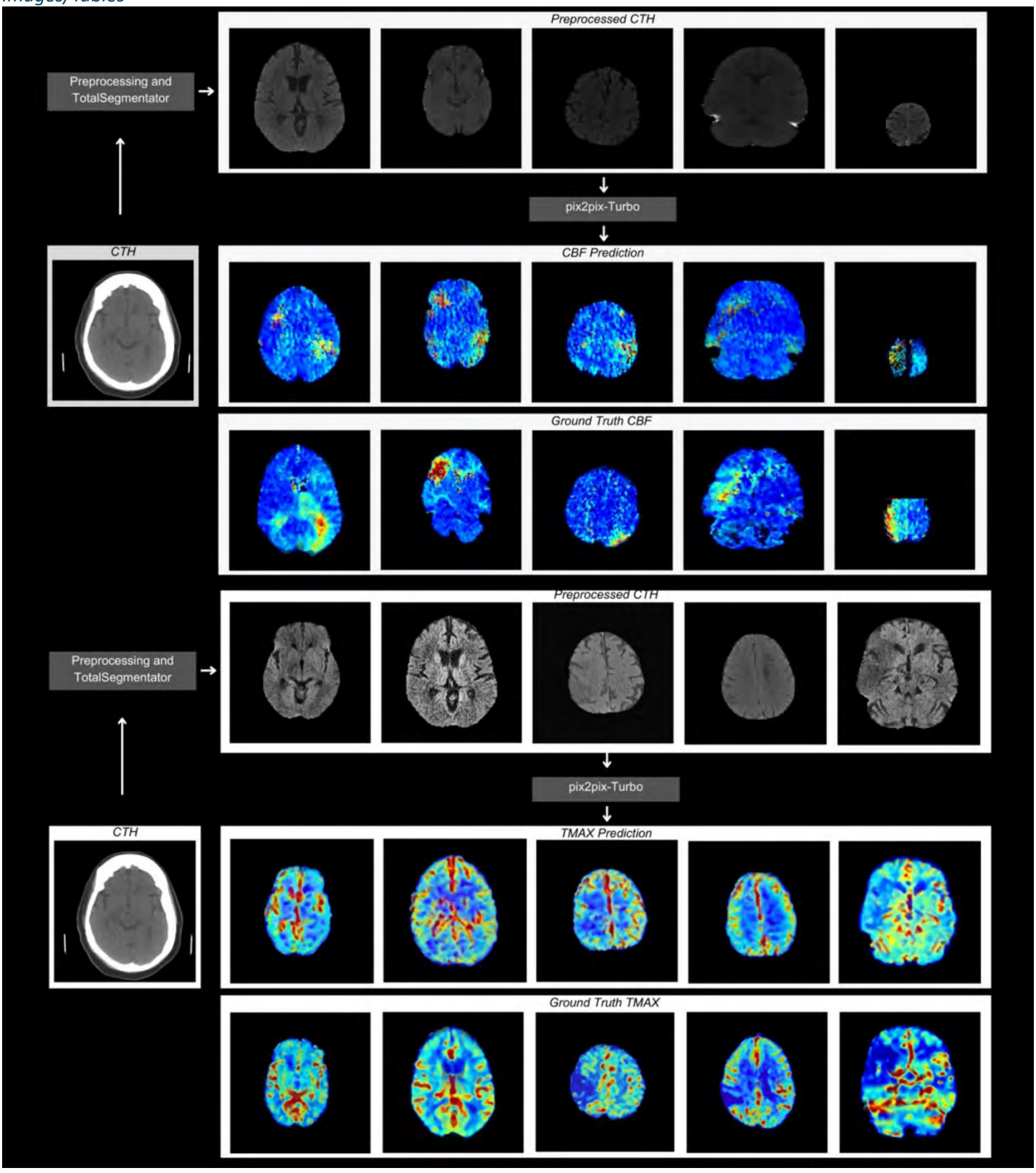

528

Correlating ALPS Index with DTI Indices of Projection and Association Fibers with Respect to the Laterality of Disease in Tremor Dominant Movement Disorder Patients Selected for DBS Therapy

Joshua Estin BS[1], Mahdi Alizadeh PhD[2], Teresita DeVera APN[2], Ron Gefen MD[2], Thomas Ross PhD[2], Islam Fayed MD[2]
[1]Cooper Medical School of Rowan University, Camden, NJ, USA. [2]Cooper University Health Care, Camden, NJ, USA

Abstract Category

Functional/Advanced Imaging

Purpose

Glymphatic dysfunction has been shown to be important in the pathophysiology of Parkinson's Disease (PD). Recent advancements in MR imaging now enable the measurement of diffusion along the perivascular space (ALPS), which has shown a correlation with Parkinson's disease (PD). Diffusion Tensor Imaging (DTI) indices of diffusion in association and projection fibers have separately been proven to be abnormal in PD. The objective of this study is to examine the relationship between ALPS index and DTI indices such as Fractional Anisotropy (FA) and mean, axial and radial diffusivities (MD, AD, and RD) in a group of 7 patients who were subsequently treated with Deep Brain Stimulation (DBS). We hypothesize the possible utility for future DBS candidates both in terms of strengthening indications and following outcomes.

Materials & Methods

This study enrolled patients diagnosed with movement disorders (Parkinson's Disease or Essential Tremor) who were selected for bilateral DBS placement in 2024. All patients had tremor dominant disease. The patients underwent MRI DTI imaging to measure DTI indices such as FA, MD, AD, RD along association and projection fibers as well as DTI-ALPS index. The index was calculated as a ratio of diffusivities along the x-axis in the region of neural fibers passing vertically to the diffusivities perpendicular to them, which reflected perivascular water motion at the lateral ventricular body level. The analysis was performed using a Spearman correlation, followed by FDR correction. Laterality was analyzed using the Wilcoxon signed-rank test.

Results

7 total patients (5 men, 2 women; mean age, 69 7.46 years) were analyzed, 5 with Parkinson's Disease (5 men) and 2 with Essential Tremor (2 women). DBS targets included the subthalamic nucleus (STN) in 3 patients, Globus Pallidus Internus (GPi) in 2 patients, Ventral Intermediate Nucleus (VIM) in 1 patient, and both VIM and Zona Incerta (ZI) in 1 patient. We found a significant positive correlation between ALPS index and FA value of association fibers on the ipsilateral side/ diseased hemisphere (P = 0.012). The contralateral ALPS index also showed a strong positive correlation with both FA measures of association and projection fibers (P = 0.007 and P = 0.034, respectively). It further demonstrated a statistically nonsignificant trend with both AD and MD values of projection fibers. In terms of the laterality analysis, a statistically nonsignificant trend was seen with the RD value of association fibers. Correlating with disease onset, there was a moderate to strong negative correlation between the MD value of association fibers in both the ipsilateral and contralateral sides; however neither was statistically significant. No significant correlation between these measures and disease onset was observed.

Conclusion

Advancements in MRI post-processing have allowed measurement of DTI indices and ALPS index which are here shown to correlate with laterality and onset and demonstrate dysfunction of diffusion in movement disorders such as PD and ET. This suggests possible utility in the future as a quantitative noninvasive biomarker of disease severity, laterality, and possibly predictors of the DBS outcomes.

References

Bae YJ, Kim JM, Choi BS et al. Glymphatic function assessment in Parkinson's disease using diffusion tensor image analysis along the perivascular space. *Parkinsonism Relat Disord* 2023 Sep;114:105767.
DOI: https://doi.org/10.1016/j.parkreldis.2023.105767. https://doi.org/
Wood KH, Nenert R, Miften AM et al. Diffusion Tensor Imaging-Along the Perivascular-Space Index Is Associated with Disease Progression in Parkinson's Disease. *Mov Disord* 2024 Sep;39(9):1504-1513.
DOI: https://doi.org/10.1002/mds.29908.

McKnight CD, Trujillo P, Lopez AM et al. Diffusion along perivascular spaces reveals evidence supportive of glymphatic function impairment in Parkinson disease. *Parkinsonism Relat Disord* 2021 Aug;89:98-104. DOI: https://doi.org/10.1016/j.parkreldis.2021.06.004.
Qin Y, He R, Chen J et al. Neuroimaging uncovers distinct relationships of glymphatic dysfunction and motor symptoms in Parkinson's disease. *J Neurol* 2023 May;270(5):2649-2658. DOI: https://doi.org/10.1007/s00415-023-11594-5.

531

Large Vessel Occlusion Mechanical Thrombectomy Outcomes in the Setting of Preexisting Intracranial Atherosclerotic Disease.

Adam M Basiago MD[1], Deep K Pujara MBBS[2], Amrou Sarraj MD[2], Clark W Sitton MD[1]
[1]UTHealth Houston, Houston, TX, USA. [2]University Hospital Cleveland Medical Center - Case Western Reserve University, Cleveland, OH, USA

Abstract Category

Interventional

Purpose

Mechanical thrombectomy (MT) is the mainstay of treatment of acute large vessel occlusion (LVO) in the 6-24h with superiority over medical management demonstrated in multiple recent trials.[1-5] Intracranial atherosclerotic disease (ICAD) is a less common but significant primary cause of stroke, especially amongst black and Asian patients, and is a common comorbidity in LVO.[6-8] A single multicenter retrospective study showed worse outcomes in ICAD patients with successful MT.[9] We investigated the effect of ICAD on the outcomes of patients in the SELECT database.

Materials & Methods

We retrospectively analyzed the digital subtraction angiograms (DSA) of 117 MT patients with TICI3 recanalization from 9 different institutions (SELECT)[1] for evidence of ICAD. We defined ICAD as convincing evidence of atherosclerotic irregularity outside the region of recanalization and not morphologically likely to represent spasm or dissection.[10] All DSAs were evaluated by both a neuroradiology fellow and a neuroradiology attending with 22 years of experience. ICAD patients were compared to similar patients without ICAD, and outcomes were analyzed using the metrics of mRS shift, mortality, symptomatic intracranial hemorrhage, neurological worsening, final infarct volume (on DWI), and growth in infarct size from baseline. All p-values were calculated using multivariable logistic regression models, which were adjusted for age, NIHSS score, tPA administration, time to procedure, ASPECT score, and CT perfusion core volume (prior to intervention).

Results

We found 13 cases out of 117 with evidence of ICAD. ICAD patients had significantly increased incidence of hypertension (p-value: 0.019) and diabetes (p-value: 0.048), particularly poorly controlled diabetes with elevated glucose (p-value: 0.015) – table 1. There was no significant association with clot location, NIHSS score, ASPECT Score, or CT perfusion core volume.

Outcomes for ICAD patients (figure1) were worse than for those without ICAD (figure 2), with lower overall functional status by mRS (acOR: 0.19, 95% CI: 0.06 to 0.60, p-value: 0.005), a lower percentage of good (aOR: 0.06, 95% CI: 0.01 to 0.42, p-value: 0.005) or excellent outcomes (aOR: 0.06, 95% CI: 0.01 to 0.53, p-value: 0.011) – table 2. Final infarct volumes were larger (adj Coeff: 38.02, 95% CI: 12.19 to 63.84, p-value: 0.004), infarcts demonstrated larger growth from baseline (adj Coeff: 38.02, 95% CI: 12.19 to 63.84, p-value: 0.004), and more patients experienced neurological worsening (aOR: 9.55, 95% CI: 1.40 to 65.28, p-value: 0.021) – table 2. There was no significant difference in symptomatic intracranial hemorrhage. The association with poor outcomes persisted even when adjusting for hypertension and diabetes, although the association was not as strong.

Limitations of the study include the relatively small percentage of patients with ICAD in this cohort, and the limitations of cerebral angiography to detect non-caliber-changing ICAD, and to reliably distinguish it from spasm or other post-procedural changes in a single vessel.

Conclusion

In our cohort of randomized to MT, ICAD was associated with concomitant hypertension and diabetes, worse functional outcomes, and larger final infarct volumes that demonstrated larger growth from baseline. ICAD appears to be an important prognostic indicator in the setting of MT for LVO.

References

1. Sarraj A, Hassan AE, Grotta J, et al. Optimizing Patient Selection for Endovascular Treatment in Acute Ischemic Stroke (SELECT): A Prospective, Multicenter Cohort Study of Imaging Selection. *Ann Neurol*. Mar 2020;87(3):419-433. doi:10.1002/ana.25669
2. Sarraj A, Hassan AE, Savitz S, et al. Outcomes of Endovascular Thrombectomy vs Medical Management Alone in Patients With Large Ischemic Cores: A Secondary Analysis of the Optimizing Patient's Selection for Endovascular Treatment in Acute Ischemic Stroke (SELECT) Study. *JAMA Neurol*. Oct 01 2019;76(10):1147-1156. doi:10.1001/jamaneurol.2019.2109
3. Sarraj A, Hassan AE, Abraham MG, et al. Trial of Endovascular Thrombectomy for Large Ischemic Strokes. *N Engl J Med*. Apr 06 2023;388(14):1259-1271. doi:10.1056/NEJMoa2214403
4. Yoshimura S, Sakai N, Yamagami H, et al. Endovascular Therapy for Acute Stroke with a Large Ischemic Region. *N Engl J Med*. Apr 07 2022;386(14):1303-1313. doi:10.1056/NEJMoa2118191
5. Goyal M, Menon BK, van Zwam WH, et al. Endovascular thrombectomy after large-vessel ischaemic stroke: a meta-analysis of individual patient data from five randomised trials. *Lancet*. Apr 23 2016;387(10029):1723-31. doi:10.1016/S0140-6736(16)00163-X
6. Banerjee C, Chimowitz MI. Stroke Caused by Atherosclerosis of the Major Intracranial Arteries. *Circ Res*. Feb 03 2017;120(3):502-513. doi:10.1161/CIRCRESAHA.116.308441
7. Kim JS, Kang DW, Kwon SU. Intracranial atherosclerosis: incidence, diagnosis and treatment. *J Clin Neurol*. Apr 2005;1(1):1-7. doi:10.3988/jcn.2005.1.1.1
8. Bala F, Singh N, Moreau F, et al. Prevalence of Intracranial Atherosclerotic Disease in Patients with Low-Risk Transient or Persistent Neurologic Events. *AJNR Am J Neuroradiol*. Mar 2022;43(3):376-380. doi:10.3174/ajnr.A7429
9. Kass-Hout T, Morsi RZ, Thind S, et al. Underlying intracranial atherosclerotic disease is associated with worse outcomes in acute large vessel occlusion undergoing endovascular thrombectomy. *J Stroke Cerebrovasc Dis*. Aug 2023;32(8):107227. doi:10.1016/j.jstrokecerebrovasdis.2023.107227
10. Samuels OB, Joseph GJ, Lynn MJ, Smith HA, Chimowitz MI. A standardized method for measuring intracranial arterial stenosis. *AJNR Am J Neuroradiol*. Apr 2000;21(4):643-6.

Images/Tables

Table 1:

Table 2:

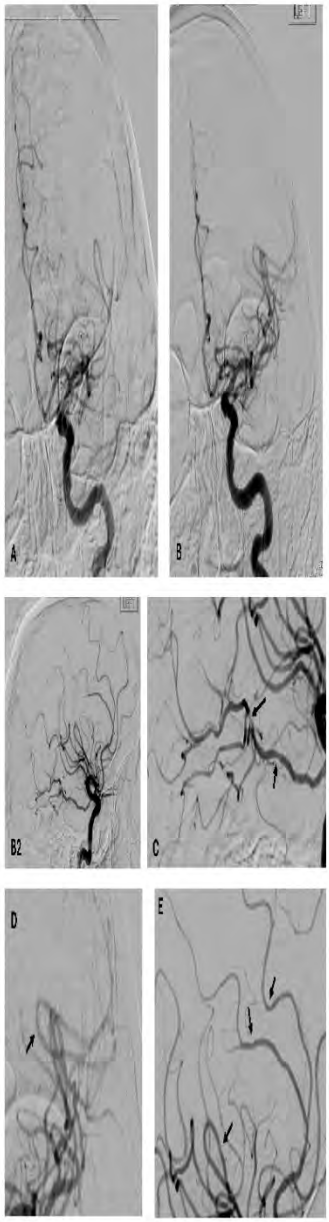

Fig 1: LVO patient before (A) and after (B1, B2) TICI3 MT. Magnified views of PCA (C), MCA (D), and ACA (E) branches show diffuse ICAD (arrows).

Fig 2: TICI3 post MT with completely smooth vessel morphology.

533

Geographic Assessment of Post-Appointment Neurosurgical Imaging Completed at External Facilities

Hamail Iqbal BA[1], Manisha Koneru MS[1], Clint Badger DO[2], Hamza Shaikh MD[2]
[1]Cooper Medical School of Rowan University, Camden, NJ, USA. [2]Department of Neurosurgery, Cooper University Hospital, Camden, NJ, USA

Abstract Category

Socioeconomics & Health Policy

Purpose

Effectively transferring imaging studies between radiology practices can be challenging given numerous logistical processes. These challenges are particularly evident when critical result alerts must be communicated between radiology practices with limited interoperability, presenting as a significant patient safety concern. Such pitfalls are crucial to address among neurosurgical studies, in which time-sensitive delivery of results are necessary to facilitate potentially life-saving interventions. Here, we aim to identify whether proximity to radiology facilities among a single health system in Southern New Jersey may be a barrier to access by examining the patient population obtaining neurosurgical imaging at an external facility.

Materials & Methods

A retrospective study was conducted using an Epic data query with appropriate IRB approval. All patients ≥18 years who completed an imaging study between January 1, 2021, and July 31, 2023, ordered by a neurosurgeon at Cooper University Hospital following the initial consultation were included. Only patients who completed studies at an external radiology facility were further analyzed. Patients were stratified based on (1) whether they completed the imaging study on the same day as the consult or sometime after, and (2) their home zip code. Latitudes and longitudes based on zip codes of seven Cooper Radiology facilities (CRFs) were used to calculate distances between the residential zip codes and the facilities. Distances were categorized as <10 miles, 10-15 miles, and 16-20 miles. All analysis was completed in Microsoft Excel Version 16.90.2.

Results

Of 2932 patients, 2137 (72.9%) completed imaging studies at a CRF. Of the 795 (27.1%) patients who completed studies externally, 78 had completed them same-day, and 717 were completed at a later date. 488 (61.4%) patients lived within 10 miles of a CRF, with 449 having non-same-day and 39 having same-day imaging. 150 (18.8%) patients lived between 11 and 15 miles, with 141 having non-same-day and 9 having same-day imaging. 34 (4.3%) patients lived between 16 and 20 miles, with 29 having non-same-day and 5 having same-day imaging.

Conclusion

Most patients who completed imaging studies externally live within 10 miles of a CRF. While proximity of a CRF to patients may not be a primary barrier, factors such as patient preference, scheduling delays, or other logistical inefficiencies warrant further study through both quantitative and qualitative methods. Identifying such barriers can improve patient access and better align services with patient need, facilitating timely interventions in neurosurgical care. These findings further underscore the importance of developing efficient data-sharing capabilities between radiology practices such that urgent studies can be communicated securely without significantly delaying patient care.

References

1. Vreeland A, Persons KR, Primo HR, et al. Considerations for Exchanging and Sharing Medical Images for Improved Collaboration and Patient Care: HIMSS-SIIM Collaborative White Paper. *J Digit Imaging*. 2016;29(5):547-558.
2. Kotter E. Basic Workflow of Medical Imaging. *Basic Knowledge of Medical Imaging Informatics, Springer International Publishing.* 2021.doi:10.1007/978-3-030-71885-5_4.

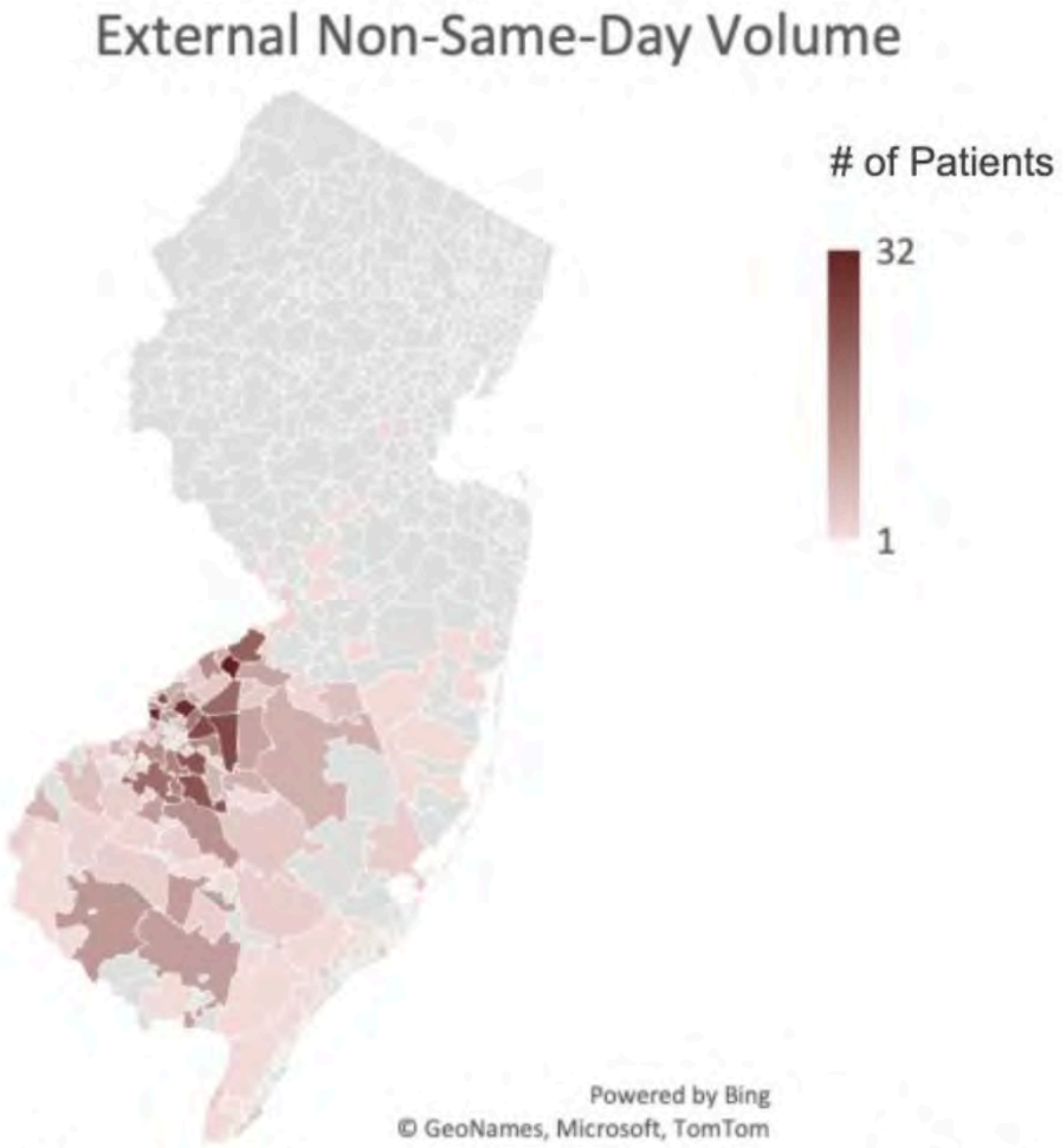

Figure 2. Choropleth map indicating the number and county of residence of patients who completed a non-same-day external imaging study.

536

Acute thoracolumbar spine trauma evaluation and role of TLICS in decision making.

Abhishek Arora MD FRCR[1], Chandrika Kandur MD[1], Iram Fathima DMRD, DNB[2], Dhanush Amin MD[3]
[1]All India Institute of Medical Sciences, Bibinagar, Hyderabad, Telangana, India. [2]Hyderabad, Telangana, India. [3]University of Alabama, Birmingham, Alabama, USA

Abstract Category

Spine

Purpose

To describe all the TLICS components (injury morphology, integrity of posterior ligamentous complex and imaging neurological status) traumatic thoracolumbar spine with CT and MRI imaging studies, and to calculate the score of these injuries as per TLICS (Thoracolumbar Injury Classification and Severity Score) and correlate them with AIS grades (Calculated by Surgeons)

To correlate the treatment given and treatment suggested based on TLICS score.

Materials & Methods

•This study was prospective analysis of data of 39 patients, who presented with acute thoracolumbar spine trauma. All CT examinations were performed using a helical CT scanner (Somatom Plus-S; Siemens, Erlangen, Germany) and isotropic dataset acquired. MR imaging of the injured spine was performed within 72hrs of injury on the Siemens 3.0T MR scanner.

•EXCLUSION CRITERIA

Patients not willing to give written consent.

Patients with the rigid spine (DISH, RA, AS)

Patients with congenital anomalies of the spine

Patients who were lost to follow-up

•FOLLOW UP: All the patients were followed up for an average 4.2 months. The first follow-up was at 4 weeks post-procedure to assess the clinical outcome and evaluate the need for further treatment. Imaging evaluation by CT and/or MRI was done if indicated.

•OUTCOME MEASURES:

•Technical success: Fracture reduction with stabilization of the spine.

•Clinical success: Resolution of the symptoms and signs that prompted surgical/ conservative management and improvement of neurological status.

Results

•In 33 of 39 patients treatment decision matched as per the TLICS score obtained, (TLICS ≥4- surgery ,TLICS<4- conservative) whereas in 6 patients clinical (pain, ambulation, and age) and radiological parameters(spinal canal stenosis, kyphotic angle)were taken into account for decision making.

•36 (92.3%) patients were treated surgically by posterior fusion with instrumentation.

•3 (7.7%) patients were given conservative management.

•7 patients had a TLICS of <4 of which 5 underwent surgery and 2 were treated conservatively, as per TLICS.

•All 5 of them had burst morphology patterns with intact neurological status and intact PLC.

•The decision for surgery in those 5 patients was based on the surgeon's concerns of, reduction of spinal canal dimension of more than 50%, retropulsion of burst fracture fragments into the spinal canal that can cause progressive neurologic deterioration, kyphosis angle and individual surgeons experiences of pain relief at the long term.

•There was a significant difference in canal stenosis and kyphosis angle in operative and conservative groups of burst fractures.

Conclusion

TLICS was useful in 84% of cases in our study for decision making.

No patient experienced neurological worsening during the follow-up, thus consolidating evidence regarding usefulness of TLICS.

ASIA sensory scores and motor scores improved significantly at last follow-up.

Out of 39 patients presented with spinal trauma, ten patients had complete paralysis at the time of presentation. The last follow-up examination did not show any improvement with respect to the neurological status of the patients with complete paralysis.

References

Azhari S, Azimi P, Shahzadi S, Mohammadi HR, Kashani HR. Decision-making process in patients with thoracolumbar and lumbar burst fractures with thoracolumbar injury severity and classification score less than four. Asian spine journal. 2016 Feb;10(1):136.

546

Correlation Between Early Brain Development and Later Diagnostic and Cognitive Development Outcomes, Using Structural and Diffusion Neuroimaging Tools

Eun Soo Kim

Hallym University Sacred Heart Hospital, Anyang-si, Gyeonggi-do, Korea, Republic of

Abstract Category

Pediatrics

Purpose

The first two years of life are critical for brain development, marked by rapid myelination in white matter tracts like the posterior limb of the internal capsule (PLIC), optic radiation (OR), and corpus callosum (CC) splenium. This period involves dynamic changes in white matter microstructure, assessed using diffusion tensor imaging (DTI) metrics like fractional anisotropy (FA), axial diffusivity (AD), and radial diffusivity (RD). This study aims to correlate early brain development with cognitive outcomes by measuring FA, AD, and RD in various fiber tracts from 2 weeks to 3 months post-birth in a cohort of 23 infants.

Materials & Methods

Participants were recruited as part of the UNC Brain Connectome Project, and MRI scans were conducted using a 3T Siemens scanner during natural sleep. Image processing involved creating brain masks with ITK-SNAP, constructing an atlas with DTI Atlas Builder, and performing tractography with 3D Slicer. Cognitive assessments were conducted using the Mullen Scales of Early Learning (MSEL). Statistical analysis revealed significant associations between FA, AD, and RD in specific tracts and cognitive abilities such as gross motor, fine motor, visual reception, and language skills.

Results

Significant correlations were found between cognitive development and white matter tracts. Key findings include significant FA, RD, and AD results for gross and fine motor skills in the corticothalamic tract and fornix, visual reception in the optic tract and radiation, and language skills in arcuate and uncinate fasciculi. The corpus callosum regions also correlate with early learning outcomes.

Conclusion

These findings highlight the importance of early white matter development in cognitive outcomes and underscore the utility of DTI in studying infant brain maturation.

References

1. Howell BR, Styner MA, Gao W, et al. The UNC/UMN Baby Connectome Project (BCP): An overview of the study design and protocol development. *Neuroimage* 2019;185:891-905

2. Rose J, Vassar R, Cahill-Rowley K, et al. Brain microstructural development at near-term age in very-low-birth-weight preterm infants: an atlas-based diffusion imaging study. *Neuroimage* 2014;86:244-256

3. Dubois J, Dehaene-Lambertz G, Kulikova S, et al. The early development of brain white matter: a review of imaging studies in fetuses, newborns and infants. *Neuroscience* 2014;276:48-71

4. Kipping JA, Tuan TA, Fortier MV, et al. Asynchronous development of cerebellar, cerebello-cortical, and cortico-cortical functional networks in infancy, childhood, and adulthood. *Cerebral cortex* 2017;27:5170-5184

5. Geng X, Gouttard S, Sharma A, et al. Quantitative tract-based white matter development from birth to age 2 years. *Neuroimage* 2012;61:542-557

Images/Tables

Figure 1

ITK-SNAP tool after completion of the brain mask (red)

ITK-SNAP (Version 3.8) with four MRI sequences from BCP brain dataset loaded

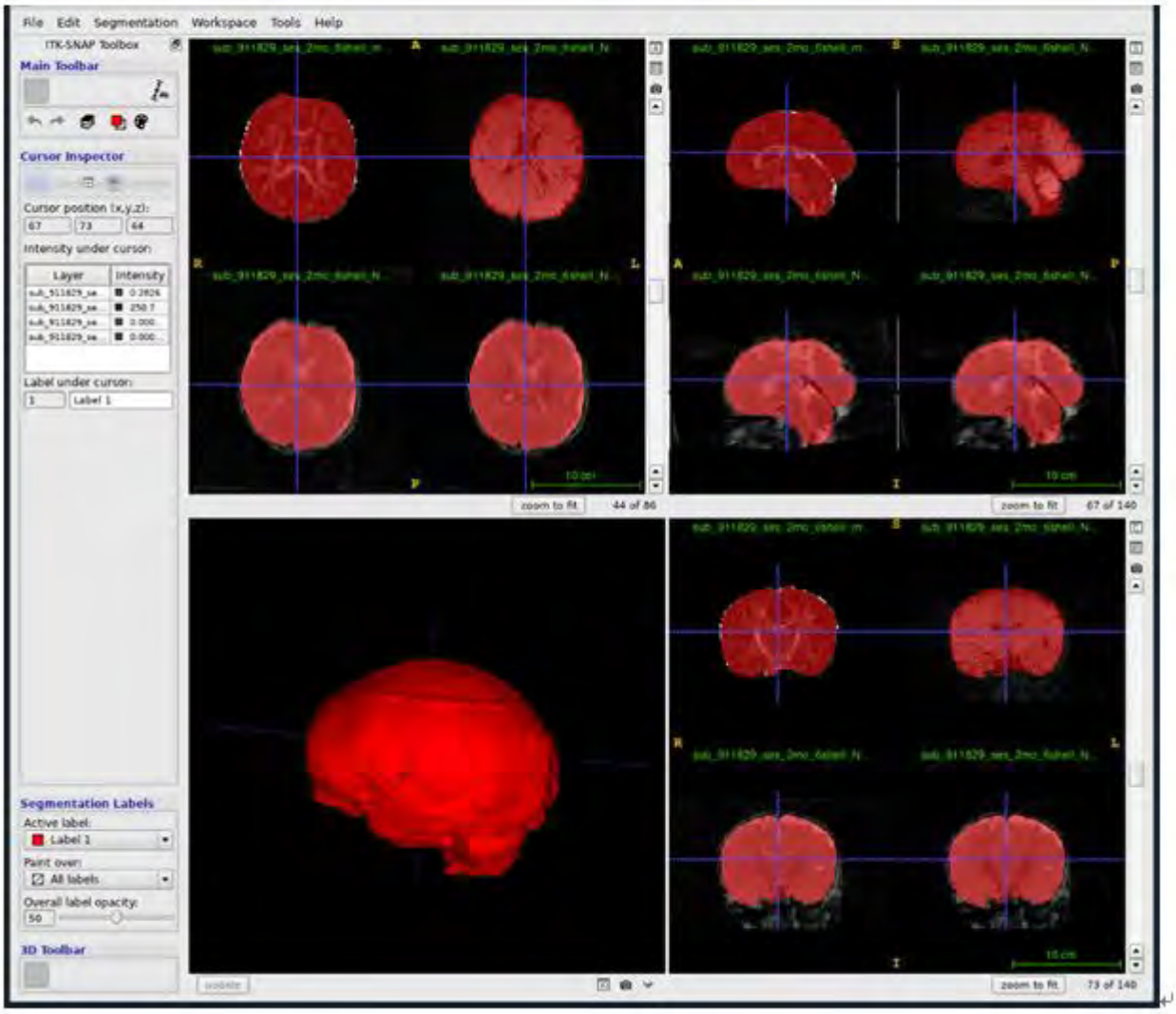

547

Digital twins for stroke treatment selection support: enhancing personalized care through patient-specific modelling

Wiktor Olszewski[1], Praneeta R. Konduri Dr[1], Charles B.L.M. Majoie Prof. Dr[2], Alfons G. Hoekstra Prof. Dr[3], Henk A. Marquering Prof. Dr[1]

[1]Department of Biomedical Engineering and Physics, Amsterdam UMC - location University of Amsterdam, Amsterdam, North Holland, Netherlands. [2]Department of Radiology and Nuclear Medicine, Amsterdam UMC - location University of Amsterdam, Amsterdam, North Holland, Netherlands. [3]Computational Science Laboratory, Informatics Institute, Faculty of Science, University of Amsterdam, Amsterdam, North Holland, Netherlands

Abstract Category

AI/Informatics

Purpose

Digital twins in healthcare are personalized virtual simulations of patients and treatments, which can be used to predict individual treatment responses and clinical outcomes. There are a variety of factors that influence stroke treatment outcomes, including baseline tissue and thrombus characteristics, intracranial artery geometry, patient age, and time of treatment for ischemic stroke (1). A multitude of treatment options is now available for treating patients with large vessel occlusion acute ischemic stroke, making it difficult for the interventionist to decide which device or combination of devices should be used in which patient to achieve first pass reperfusion. Computational modeling allows us to replicate, or simulate, complex biological processes, making digital twins a promising support tool for treatment planning. Previous research has shown that we can successfully predict treatment outcomes on the population level, however, reliable patient-specific models for tailored treatment planning are still lacking. (2). The GEMINI consortium aims to develop and evaluate digital twins for both ischemic and hemorrhagic strokes allowing support in treatment decision-making. We will validate the added clinical value of digital twins in a clinical trial, evaluating whether ischemic stroke treatment choices supported by the availability of the digital twin tool result in a higher rate of first pass reperfusion.

Materials & Methods

The envisioned digital twins will comprise mechanistic computational models of various aspects of stroke etiology and treatment including but not limited to blood flow, brain perfusion, metabolism, thrombosis, and thrombectomy. These computational models have proven valuable in in-silico trials as shown in previous studies (3). The population-based thrombectomy models will be optimized to predict outcomes on a patient-specific level by incorporating patient's own imaging characteristics and clinical data. In this process, the model will be updated to reflect the unique characteristics of the individual, making predictions and treatment recommendations more accurate and tailored to that patient. By integrating digital twins into software that is already used in clinical practice (StrokeViewer, NicoLab) (4), clinicians will be able to quickly analyze patient’s imaging and clinical data in tandem by evaluating treatment simulations for various devices and scenarios provided by the digital twin. The clinical trial will compare first-pass recanalization rates and clinical outcomes for patients with acute ischemic stroke in scenarios where the treating physician performs thrombectomy with and without access to the digital twin tool.

Results

GEMINI will deliver five personalized digital twin tools. For ischemic stroke, the project will generate models to: 1) predict outcomes of thrombectomy, and 2) simulate the progression of ischemic lesions for up to one week after treatment. For aneurysm management, GEMINI will develop and validate models to: 3) optimize treatment strategies, 4) simulate the healing progress up to two years post-treatment, and 5) manage unruptured aneurysms.

Conclusion

The GEMINI consortium aims to develop personalized digital twins for managing both ischemic and hemorrhagic strokes, as well as predicting disease progression. By incorporating patient-specific data into mechanistic and data-driven models, these digital twins have the potential to assist physicians in tailoring stroke treatments to individual patients.

References

1. Nguyen TN, Abdalkader M, Fischer U, Qiu Z, Nagel S, Chen HS, et al. Endovascular management of acute stroke. Lancet. 2024;404(10459):1265-78.

2. Konduri PR, Marquering HA, van Bavel EE, Hoekstra A, Majoie C, Investigators I. In-Silico Trials for Treatment of Acute Ischemic Stroke. Front Neurol. 2020;11:558125.

3. Miller C, Konduri P, Bridio S, Luraghi G, Arrarte Terreros N, Boodt N, et al. In silico thrombectomy trials for acute ischemic stroke. Comput Methods Programs Biomed. 2023;228:107244.

4. Boers AM, Marquering HA, Jochem JJ, Besselink NJ, Berkhemer OA, van der Lugt A, et al. Automated cerebral infarct volume measurement in follow-up noncontrast CT scans of patients with acute ischemic stroke. AJNR Am J Neuroradiol. 2013;34(8):1522-7.

Images/Tables

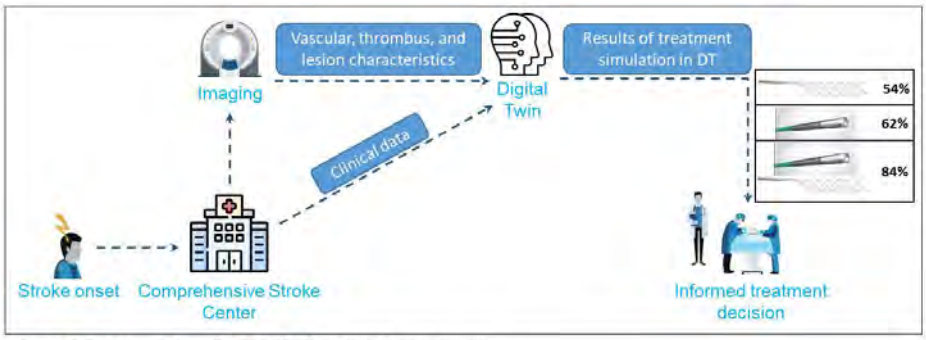

Figure 1: Implementation of a digital twin in stroke management.

551

Global and Regional Connectivity in Intracranial Dural Arterio-Venous Fistula Using Resting State fMRI - A Graph Theory Analysis

Jithin Sivan Sulaja MSc, Bejoy Thomas MD, DNB, PDCC, Smitha K Achuthan PhD, Santhosh Kumar Kannath MD, PDCC
Sree Chitra Tirunal Institute for Medical Sciences and Technology, Thiruvananthapuram, Kerala, India

Abstract Category

Functional/Advanced Imaging

Purpose

The resting state functional changes and wide spread network alterations in dural arterio-venous fistula (DAVF) brain are not fully explored[1]. The study aims to investigate the brain network connectivity alterations in patients with DAVF using resting-state functional MRI (rsfMRI) and graph theory analysis[2]. DAVF is a neurovascular disorder characterized by abnormal connections between dural arteries and veins, leading to disrupted cerebral blood flow and resultant neurological symptoms[3]. Studying brain functional connectivity through rsfMRI and graph-theoretical methods offers valuable insights into the network-level alterations associated with DAVF. By comparing functional connectivity and network properties in DAVF patients and healthy controls (HC), this study aims to identify network-based indicators which may improve decisions on treatment strategies for DAVF.

Materials & Methods

The study prospectively recruited 50 DAVF patients from an interventional neuroradiology department of a tertiary referral and 50 age-matched healthy controls(HS) from the community. All participants underwent rsfMRI scans on a 3T. Image preprocessing followed a standardized pipeline using SPM12 and GRETNA, including steps like slice timing correction, realignment, normalization, and temporal filtering. Functional connectivity networks were constructed for each participant based on 160 regions of interest (ROIs) from the Dosenbach atlas. Using Pearson correlations, 160x160 connectivity matrices were generated, and functional networks were constructed across a range of sparsity thresholds. Global and nodal network metrics, including assortativity, hierarchy, synchronization, clustering coefficient, nodal efficiency and shortest path length, were computed to characterize functional connectivity in DAVF patients compared to HC.

Results

DAVF patients showed significant alterations in global network metrics, particularly higher assortativity and synchronization than in healthy controls. However, network hierarchy was reduced in DAVF patients, suggesting impaired information flow between regions. Nodal analysis revealed region-specific changes: DAVF patients had decreased clustering coefficients and nodal efficiency in occipital and default mode network (DMN) areas (Fig.1). Also increased betweenness centrality and shortest path length were observed in the posterior occipital and posterior cingulate regions.

Conclusion

The findings reveal distinct global and nodal connectivity patterns in DAVF patients, marked by increased assortativity and synchronization alongside reduced hierarchy, which collectively may suggest a compensatory network reorganization in response to vascular and hence neural disruptions. The reduced clustering and nodal efficiency in occipital and DMN regions imply local connectivity deficits, while the elevated betweenness centrality in specific regions

may represent structural adaptations or critical areas of compensatory activity. These network properties have the potential to serve as indicators of neural dysfunction in DAVF, providing insights into disease severity which in turn may guide therapeutic interventions. Future work could expand these observations to explore how DAVF treatment outcomes, such as post-embolization recovery, impact functional connectivity and network properties, enhancing our understanding of brain network reorganisation in response to treatment of this complex disease.

References

1. Sekar S, Kannath SK, Ramachandran S, Menon RN, Thomas B. Alterations in Resting-State Functional MRI Connectivity Related to Cognitive Changes in Intracranial Dural Arteriovenous Fistulas Before and After Embolization Treatment. *J Magn Reson Imaging* 2022; 55(4):1183-1199 https://doi.org/10.1002/jmri.27936
2. Bullmore, E., & Sporns, O. Complex brain networks: graph theoretical analysis of structural and functional systems. *Nature reviews. Neuroscience* 2009; *10*(3), 186–198. https://doi.org/10.1038/nrn2575
3. Cognard, C., Gobin, Y. P., Pierot, L., Bailly, A. L., Houdart, E., Casasco, A., Chiras, J., & Merland, J. J. Cerebral dural arteriovenous fistulas: clinical and angiographic correlation with a revised classification of venous drainage. *Radiology* 1995; *194*(3), 671–680. https://doi.org/10.1148/radiology.194.3.7862961

Images/Tables

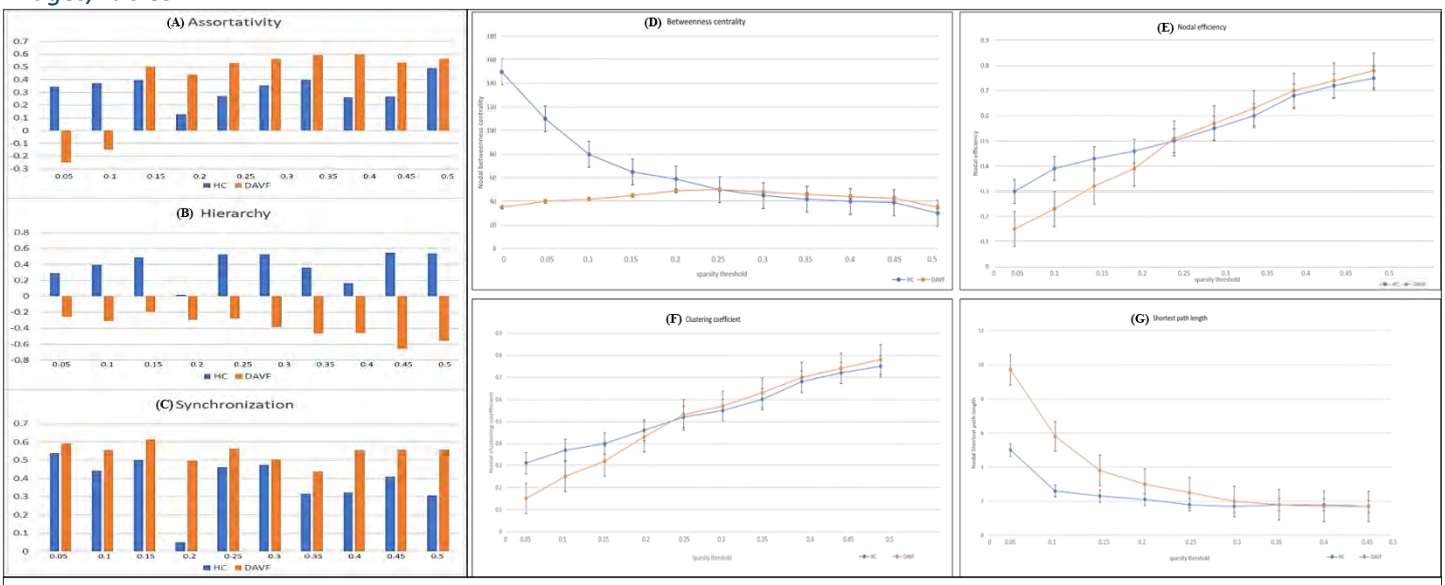

Figure 1. Distribution of global and nodal topological parameters of the functional connectome among different sparsity thresholds (0.05–0.5). Orange colour denotes DAVF data, and blue denotes HC data. (A) Assortativity of functional connectomes. (B) Hierarchy of functional connectomes. (C) Synchronization of functional connectomes. (D) Betweenness centrality. (E) Nodal efficiency. (F) Clustering coefficient. (G) Shortest path length.

558

Head-to-Head Comparison of Two AI Software Solutions for Detecting Vessel Occlusions in Stroke Code Patients Using Head and Neck CTA Scans

Han Zhong MD[1], Christopher Ciasullo DO[1], Kevin Pham DO[2], Devon Klein MD[1]

[1]Overlook Medical Center, Summit, NJ, USA. [2]Overlook Medical Center, SUmmit, NJ, USA

Abstract Category

AI/Informatics

Purpose

Artificial intelligence (AI) is increasingly leveraged by stroke care teams for the detection and management of vessel occlusions (VO) in acute ischemic stroke, offering potential for faster diagnosis, improved accuracy, and optimized patient outcomes. By enabling rapid identification of VO on imaging, AI tools can support timely clinical decisions in stroke cases. This study aims to provide a comprehensive comparison of the performance and reproducibility of two commercially available AI software solutions, Vendor A (Aidoc, Tel Aviv) and Vendor B (RapidAI-IschemaView, Menlo Park), for the detection of VO on head and neck computed tomography angiography (CTA) scans.

Materials & Methods

A retrospective review was conducted on all head and head & neck CTA scans (01/17/2024 - 04/01/2024), including non-dedicated stroke exams for patients with non-classical stroke symptoms, at a large academic site. Initial classification was performed using natural language processing (NLP) of the radiological reports. For cases where NLP results and AI classifications were discordant, an independent Neuroradiologist review was conducted to establish a ground truth reference standard. The performance of both AI solutions was then evaluated against this reference standard to assess their diagnostic accuracy.

Results

A total of 612 cases were analyzed for the detection of vessel occlusions (VO), with a prevalence of 13.4%. Vendor A exhibited a sensitivity of 94.0% (86.5% - 98.0%) and specificity of 94.1% (91.7% - 95.9%) (Table 1). The positive predictive value (PPV) was 70.9% (63.4% - 77.4%), while the negative predictive value (NPV) reached 99.0% (97.7% - 99.6%). The overall Vendor A accuracy was 94.0% (91.9% - 95.8%). In comparison, Vendor B demonstrated a sensitivity of 83.1% (73.3% - 90.5%) and specificity of 84.9% (81.6% - 87.9%). The PPV for Vendor B was 46.0% (40.5% - 51.6%), with an NPV of 97.0% (95.3% - 98.1%). The overall accuracy for Vendor B was 84.7% (81.6% - 87.4%). Further performance details, including across vessel subtypes are presented in Table 2.

Conclusion

This study highlights the importance of a reliable ground truth dataset for assessing AI performance in VO detection. The performance differences between Vendor A and Vendor B underscore the variability across AI solutions, even for similar clinical goals. By using an independently verified reference standard, we established a robust comparison, enabling healthcare providers to better understand the relative value of each tool. As AI adoption grows, such standardized benchmarks are essential for guiding informed decision-making and enhancing patient care in stroke management.

References

1. Parvathy G, Kamaraj B, Bikikumar S, Aakanshrahul M, Aiswariyanna A, Vindhesh D, Hassan M, Muhammad S. Emerging artificial intelligence-aided diagnosis and management methods for ischemic strokes and vascular occlusions: A comprehensive review. World Neurosurg X. 2024;22:100303. doi:10.1016/j.wnsx.2024.100303.
2. Murray NM, Unberath M, Hager GD, Hui FK. Artificial intelligence to diagnose ischemic stroke and identify large vessel occlusions: a systematic review. J Neurointerv Surg. 2020 Feb;12(2):156-164. doi: 10.1136/neurintsurg-2019-015135. Epub 2019 Oct 8. PMID: 31594798.
3. Amukotuwa SA, Straka M, Dehkharghani S, Bammer R. Fast Automatic Detection of Large Vessel Occlusions on CT Angiography. Stroke. 2019 Dec;50(12):3431-3438. doi: 10.1161/STROKEAHA.119.027076. Epub 2019 Nov 4. PMID: 31679501; PMCID: PMC6878187.

Images/Tables

Table 1: Comparative Performance Metrics for Stroke Code and non-Stroke Code patients for Vessel Occlusion Detection

Metric	Stroke Code	Non-Stroke Code
Total Patients Analyzed	621	949
Vessel Occlusion Prevalence	13.4% (83/621)	3.3% (31/949)
Sensitivity	94.0% (95% C.I: 86.5% - 98.0%)	83.9% (95% C.I: 66.3% - 94.5%)
Specificity	94.1% (95% C.I: 91.7% - 95.9%)	98.5% (95% C.I: 97.5% - 99.2%)
Positive Predictive Value (PPV)	70.9% (95% C.I: 63.4% - 77.4%)	65.0% (95% C.I: 51.9% - 76.2%)
Negative Predictive Value (NPV)	99.0 (95% C.I: 97.7% - 99.6%)	99.4% (95% C.I: 98.8% - 99.8%)
Accuracy	94.0% (95% C.I: 91.9% - 95.8%)	98.0% (95% C.I: 96.9% - 98.8%)

Table 2: Prevalence for Stroke Code and non-Stroke Code findings across Vessel Occlusion Locations

Vessel type	Stroke Code	Non-Stroke Code
Total Vessel Occlusions	90	28
MCA-M1, ICA	53% (53/90)	39% (11/28)
PCA-P1, ACA-A1, Basilar	8% (7/90)	7% (2/28)
MCA-M2, MCA-proximal M3, PCA-P2, PCA-proximal P3, ACA-A2, ACA-proximal A3, and Vertebral-V4	33% (30/90)	54% (15/28)

565

Enabling Rapid Adoption of Deep Learning in Radiology Training: Leveraging Open-Source Pre-trained Models and Ensemble Architectures for Lumbar Spine Degeneration Classification

Bryson J Hewins MD, MS[1], Jonathan Wang[2], Anne Sidwell[3], William Hartter[4], Aaron Cho MD[1], Amy Condos MD[1]
[1]Naval Medical Center San Diego, San Diego, CA, USA. [2]Uniformed Services University of the Health Sciences, Bethesdsa, MD, USA. [3]Uniformed Services University of the Health Sciences, Bethesda, MD, USA. [4]Uniformed Services University of the Health Sciences, San Diego, MD, USA

Abstract Category

AI/Informatics

Purpose

Lumbar spine degeneration is a leading cause of chronic low back pain and disability, posing a significant health burden. Deep learning–based computer-aided detection (CAD) models can enhance diagnostic accuracy in lumbar spine MRI. However, model development is hindered by high computational demands and limited expertise among radiology trainees, with few training opportunities currently available[1]. This study aims to demonstrate how trainees can rapidly develop effective deep learning models for clinically relevant applications using accessible open-source pre-trained models and ensembling techniques, thereby lowering barriers to artificial intelligence (AI) integration in radiology training and practice.

Materials & Methods

In this retrospective study, we used a publicly available, multi-institutional dataset from the RSNA 2024 Lumbar Spine Degenerative Classification Challenge[2], consisting of de-identified lumbar spine MRI scans from 1,945 patients annotated for five degenerative conditions across five lumbar levels (L1/L2 to L5/S1). Following the Checklist for Artificial Intelligence in Medical Imaging (CLAIM) guidelines[3] with ASNR Evidence Level 5b for AI modeling[4], we performed data preprocessing, model selection, training, and evaluation optimized for environments with limited computational resources.

We implemented an ensemble of three open-source, pre-trained deep learning models:

1. **YOLOv8** for object detection, identifying regions of interest within MRI scans.
2. **EfficientNet-B5** for image classification of localized regions.
3. **3D Vision Transformer** for volumetric analysis, capturing spatial relationships in three-dimensional data.

Model training, validation and testing were all performed using freely available Kaggle servers for machine learning, which offers NVIDIA Tesla P100 GPUs with 16GB of memory. Models were initialized with pre-trained weights from ImageNet and fine-tuned using transfer learning. Predictions were combined using weighted averaging: 0.25 for YOLOv8, 0.20 for EfficientNet-B5, and 0.55 for the 3D Vision Transformer. Model performance was evaluated using weighted log loss.

Results

The ensemble model achieved a weighted log loss of **0.532**, significantly improving over our initial single-model approach (weighted log loss **1.182**), representing a **55% reduction**. This improvement indicates enhanced classification accuracy across degenerative conditions and severity levels (normal/mild, moderate, severe). The ensemble outperformed individual models, demonstrating the effectiveness of combining open-source pre-trained architectures in resource-limited settings.

Conclusion

This study demonstrates that radiology trainees can overcome on-site computational and domain expertise limitations to develop high-performing deep learning models for clinically relevant computer-aided detection tasks such as lumbar spine degeneration classification. By leveraging transfer learning from large task-specific pre-trained open-source models integrating object detection, image classification, and volumetric analysis, we established a structured and accessible pipeline that facilitates engagement with AI among trainees and accelerates deep learning integration into medical training. Limitations of this study include reliance on existing model architectures and the ongoing need for external validation across diverse patient populations. Future work will focus on external validation and include common measures of diagnostic accuracy (F1-score, accuracy, precision, recall etc.), and adapting this framework for broader clinical and training applications.

DISCLAIMER

The opinions and assertions expressed herein are those of the authors and do not reflect the official policy or position of the Uniformed Services University of the Health Sciences or the Department of Defense.

References

1. Van Kooten MJ, Tan CO, Hofmeijer EIS, et al. A framework to integrate artificial intelligence training into radiology residency programs: preparing the future radiologist. **Insights Imaging** 2024;15:100. DOI: https://doi.org/10.1186/s13244-023-01595-3

2. RSNA 2024 Lumbar Spine Degenerative Classification. Kaggle website. https://kaggle.com/competitions/rsna-2024-lumbar-spine-degenerative-classification. Accessed October 20, 2024.

3. Tejani AS, Klontzas ME, Gatti AA, et al. Checklist for Artificial Intelligence in Medical Imaging (CLAIM): 2024 update. **Radiol Artif Intell** 2024;6. DOI: https://doi.org/10.1148/ryai.240300

4. Pham N, Hill V, Rauschecker A, et al. Critical appraisal of artificial intelligence–enabled imaging tools using the levels of evidence system. **AJNR Am J Neuroradiol** 2023;44–E28. DOI: https://doi.org/10.3174/ajnr.A7850

587

MRI Defines Baicalein Enhanced Immunotherapy in a Rat Model of Medulloblastoma

Cooper L Stateler MD[1], Sara A Biju[1], Samantha Holland BS[1], Jared Stoller BS[1], Doonyaporn Wongsawaeng MD[1], Leslie L Muldoon PhD[1], Prakash Ambady MD[2], Ramon F Barajas MD[1]

[1]Oregon Health and Science University, Portland, Oregon, USA. [2]Providence, Portland, Oregon, USA

Abstract Category

Pediatrics

Purpose

Medulloblastoma is the most common malignancy of the central nervous system in pediatric patients. Current treatments achieve long-term survival, but often leave individuals prone to irreversible CNS damage.[1] Clinical immunotherapies struggle to show efficacy due to difficulty traversing the blood-brain-barrier and the immunosuppressive nature of the tumor microenvironment.[2] This study aims to explore the efficacy and MRI features of preclinical targeted therapy leveraging the innate immune system. Specifically, we assessed the immunomodulatory drug Baicalein (Bac), which has not been previously explored in medulloblastoma. 3

Materials & Methods

A group of 15 adult nude female rats were implanted with serially passaged human medulloblastoma cells from the MB002 line. On day 12 after tumor implantation, baseline gadolinium enhanced 12T MRI (Gd-MRI) T1 and T2 images were used to estimate pre-treatment tumor volumes. The treatment cohorts consisted of untreated controls, 2Gy irradiation to the tumor-bearing hemisphere with 20mg/kg temozolomide (CRT) PO x1, and CRT combined with Bac 100mg/kg PO QD daily x8. After the elapsed treatment period, Gd-MRI and histology were used to analyze tumor volume change prior to euthanasia. Statistical significance was defined by t-tests with a p-value of less than 0.05.

Results

Both the T1 post-gadolinium volume and T2 volume demonstrate post-treatment changes when compared to controls, shown in Figure 1, section a and b. After treatment, the control group had an average growth of 108.9 +/- 26.6 (mean +/- StDev) mm^3 and 109.7 +/- 6.7 mm3 in T1 and T2 volumes respectively. The CRT alone group had an average growth of 31.9 +/- 15.6 mm^3 (T1) and 43.8 +/- 7.5 mm^3 (T2), while the CRT + Baicalein group (n = 2) had the smallest average growth post-treatment, with volumes of 18.0 mm^3 (T1) and 12.0 mm3 (T2).

In terms of tumor volume histology (Figure 1, c), the control group had a significantly increased volume of 154.3 +/- 14 mm^3 compared to CRT alone (51.2 +/- 12 mm^3) and CRT + Bac (20.5 +/- 11.2 $mm^{3;}$ $P < 0.05$).

Conclusion

These results suggest that the combination of traditional cancer therapies with immune response-inducing treatments may improve efficacy in preclinical medulloblastoma models, demonstrated by MRI and histology. Further studies will increase the sample size and diversify treatment route as well as dosage of the treatment cohorts for more conclusive data, with the eventual goal of progressing to the clinical environment.

References

1. Millard, N. E., & De Braganca, K. C. (2016). Medulloblastoma. J Child Neurol, 31(12), 1341-1353. https://doi.org/10.1177/0883073815600866

2. Voskamp, M. J., Li, S., van Daalen, K. R., Crnko, S., Ten Broeke, T., & Bovenschen, N. (2021). Immunotherapy in Medulloblastoma: Current State of Research, Challenges, and Future Perspectives. Cancers (Basel), 13(21). https://doi.org/10.3390/cancers13215387

3. He, S., Wang, S., Liu, S., Li, Z., Liu, X., & Wu, J. (2021). Baicalein Potentiated M1 Macrophage Polarization in Cancer Through Targeting PI3Kγ/ NF-κB Signaling. Front Pharmacol, 12, 743837. https://doi.org/10.3389/fphar.2021.743837

Images/Tables

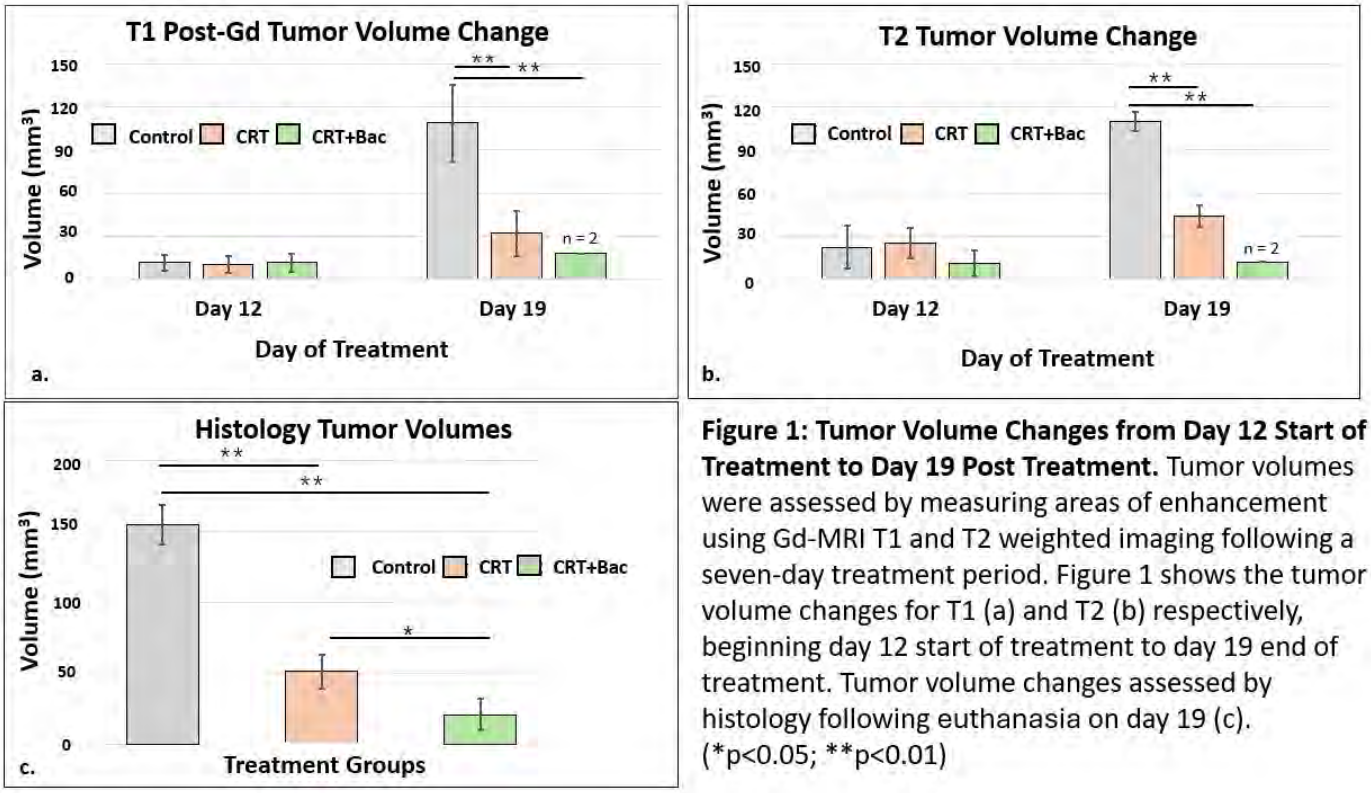

Figure 1: Tumor Volume Changes from Day 12 Start of Treatment to Day 19 Post Treatment. Tumor volumes were assessed by measuring areas of enhancement using Gd-MRI T1 and T2 weighted imaging following a seven-day treatment period. Figure 1 shows the tumor volume changes for T1 (a) and T2 (b) respectively, beginning day 12 start of treatment to day 19 end of treatment. Tumor volume changes assessed by histology following euthanasia on day 19 (c). (*p<0.05; **p<0.01)

588

ENHANCING DETECTION OF LARGE VESSEL AND MEDIUM VESSEL OCCLUSIONS IN HEAD CT ANGIOGRAMS: A STUDY ON THE EFFICACY OF ACOMMERCIAL AI ALGORITHM

Kevin Pham DO, Han Zhong MD, Devon Klein MD
Overlook, Medical Center, Summit, NJ, USA

Abstract Category

AI/Informatics

Purpose

The purpose of this study is to evaluate the added value of using a commercially available AI algorithm for the detection of Vessel Occlusion (VO) in CT angiograms (CTA) of the head.

Materials & Methods

Head CTAs and their retrospective reports were collected from 09/07/2023 to 12/31/2023 prior to the implementation of the AI algorithm. All reports identified as negative by natural language processing were analyzed by the image-based AI algorithm. Any discordant cases between the report (NLP-) and AI (AI+) were further adjudicated by a neuroradiologist to provide a ground truth interpretation. From the discordant case review the enhanced detection rate of VO enabled by the AI algorithm was calculated.

Results

A total of 1,907 head CTAs and reports were analyzed for the study. The prevalence of VO was 10.6% (203/1,907). A total of 22 discordances(NLP-/AI+) were identified, of which 63.6% (14/22) proved to be true positives by independent review. This resulted in a measured enhanced detection rate of6.9% (14/203). Upon further analysis 14.3% (2/14) of the overlooked findings were large vessel occlusions (MCA-M1, ICA; PCA-P1, ACA-A1, ICA, Basilar) and85.7% (12/14) of the findings were medium vessel occlusions (MCA-M2, MCA-proximal M3, PCA-P2, PCA-proximal P3, ACA-A2, ACA-proximal A3, and Vertebral-V4).

Conclusion

This study highlights the potential of a commercially available AI algorithm in enhancing the detection of Vessel Occlusion in head CT angiograms. The AI successfully identified an additional 6.9% of true positives that were missed in initial readings, encompassing both large and medium vessel occlusions. These results suggest that integrating AI into

diagnostic processes can significantly improve accuracy and potentially patient outcomes by ensuring more timely and accurate detections. Future work should explore the integration of these AI tools into routine clinical workflows to maximize their benefits.

References

1. Chandrabhatla AS, Kuo EA, Sokolowski JD, et al. Artificial Intelligence and Machine Learning in the Diagnosis and Management of Stroke: A Narrative Review of United States Food and Drug Administration-Approved Technologies. J Clin Med. 2023 May 30;12(11):3755. doi: 10.3390/jcm12113755. PMID: 37297949; PMCID: PMC10253618.
2. Soun JE, Chow DS, Nagamine M, Takhtawala RS, Filippi CG, Yu W, Chang PD. Artificial Intelligence and Acute Stroke Imaging. AJNR Am J Neuroradiol. 2021 Jan;42(1):2-11. doi: 10.3174/ajnr.A6883. Epub 2020 Nov 26. PMID: 33243898; PMCID: PMC7814792.
3. Matsoukas S, Morey J, Lock G, Chada D, Shigematsu T, Marayati NF, Delman BN, Doshi A, Majidi S, De Leacy R, Kellner CP, Fifi JT. AI software detection of large vessel occlusion stroke on CT angiography: a real-world prospective diagnostic test accuracy study. J Neurointerv Surg. 2023 Jan;15(1):52-56. doi: 10.1136/neurintsurg-2021-018391. Epub 2022 Jan 27. PMID: 35086962.

603

Obesity and Insulin Resistance Mediate Amyloid Burden in Midlife

Soheil Mohammadi[1], Mahsa Dolatshahi[1], Paul K. Commean[1], Farzaneh Rahmani[1], Caitlyn Nguyen[1], LaKisha Lloyd[1], Sara Hosseinzadeh Kasani[1], Mahshid Naghashzadeh[1], Bettina Mittendorfer[2], Claude Sirlin[3], Tammie L.S. Benzinger[1], Joseph E. Ippolito[1], John C. Morris[1], Cyrus A. Raji[1]

[1]Mallinckrodt Institute of Radiology, Washington University in St. Louis, St. Louis, MO, USA. [2]Departments of Medicine and Nutrition & Exercise Physiology, School of Medicine, University of Missouri, Columbia, MO, USA. [3]Liver Imaging Group, Department of Radiology, University of California, San Diego, CA, USA

Abstract Category

Adult Brain

Purpose

Midlife obesity and insulin resistance are recognized contributors to Alzheimer's disease, yet it remains unclear whether their interaction influences amyloid and tau burden in the brain. This study aimed to investigate the associations between obesity (BMI ≥ 30 kg/m²) and insulin resistance, measured by the homeostatic model (HOMA-IR), with PET-derived whole-brain amyloid burden, as well as region-specific amyloid and tau burdens.

Materials & Methods

A total of 65 cognitively normal middle-aged subjects (49.17 ± 5.94 years, male: 24 (36.92%), obesity: 32 (49.23 %), BMI: 31.95 ± 7.32 kg/m²) underwent amyloid and tau PET scans and 3T MRI, along with metabolic assessments. Insulin resistance was measured using HOMA-IR, with values ≥ 1.9 classified as IR+. Dynamic amyloid imaging was conducted using a bolus injection of approximately 15 mCi [11C] PiB, followed by a 60-minute scanning period. Data collected from the 30 to 60 minutes post-injection were utilized to compute the whole-brain amyloid Centiloid. For tau PET imaging, participants received a single intravenous bolus of 7.2–10.8 mCi of AV-1451, followed by a 105-minute scan. Analyses were conducted using the PET Unified Pipeline (PUP, https://github.com/ysu001/PUP)[1]. Standardized uptake value ratios (SUVRs) were calculated from FreeSurfer-defined ROIs, using the cerebellar cortex as the reference region and a post-injection window of 30–60 minutes for PiB and 50–70 minutes for AV-1451. Based on HOMA-IR and obesity status, participants were divided into four groups: metabolically normal non-obese (MNNO), metabolically abnormal non-obese (MANO), metabolically normal obese (MNO), and metabolically abnormal obese (MAO). One-way ANOVA was conducted to investigate between-group differences in whole brain amyloid burden, as well all region-specific amyloid and tau burdens in regions of interest (ROI) related to Alzheimer's disease, adjusted for age and sex. Post-hoc analyses were performed, with p-values adjusted for multiple comparisons using the Bonferroni method.

Results

The one-way ANOVA revealed significant between group differences in whole brain amyloid Centiloid and total inferior temporal cortex amyloid. ANCOVA post-hoc analysis indicated a significantly higher whole brain amyloid Centiloid and total inferior temporal cortex amyloid in the MAO compared to the MNNO. The ANOVA analysis did not show a between group difference in tau burden in the ROIs.

Conclusion

Our findings highlight a link between midlife obesity and insulin resistance with increased whole-brain amyloid Centiloid as well as higher amyloid burden in the inferior temporal cortex. Given the convincing evidence implicating whole-brain and inferior temporal amyloid burden in Alzheimer's pathology, these results suggest that midlife obesity and insulin resistance may mediate Alzheimer's disease risk. The lack of significant between-group differences in tau burden aligns with the subclinical stage of Alzheimer's in our participants.

References

1. Su Y, D'Angelo GM, Vlassenko AG, et al. Quantitative analysis of PiB-PET with freesurfer ROIs. *PloS one* 2013; **8**(11): e73377.

Images/Tables

Table 1. demographic and clinical characteristics by group

		Metabolically normal non-obese	Metabolically abnormal non-obese	Metabolically normal obese	Metabolically abnormal obese	P-value
N		20	13	9	23	
Age (mean (SD))		47.50 (5.65)	48.54 (5.58)	49.56 (7.02)	49.91 (6.58)	0.62
Education (mean (SD))		15.85 (1.98)	15.85 (2.51)	15.11 (1.96)	15.04 (2.33)	0.566
Sex (%)	Male	6 (30.0)	8 (61.5)	2 (22.2)	8 (34.8)	0.197
	Female	14 (70.0)	5 (38.5)	7 (77.8)	15 (65.2)	
BMI (mean (SD))		24.02 (2.75)	27.52 (2.34)	35.17 (6.14)	37.73 (5.55)	**<0.001**
Obesity (%)	Non-obese	20 (100.0)	13 (100.0)	0 (0.0)	0 (0.0)	**<0.001**
	Obese	0 (0.0)	0 (0.0)	9 (100.0)	23 (100.0)	
Cholesterol (mean (SD))		183.20 (25.39)	176.62 (30.42)	187.44 (43.93)	183.96 (29.59)	0.858
Triglyceride (mean (SD))		64.40 (23.11)	107.15 (44.37)	87.11 (34.54)	109.57 (38.59)	**<0.001**
HDL (mean (SD))		71.10 (12.42)	50.08 (9.01)	55.67 (15.41)	50.13 (12.75)	**<0.001**
LDL (mean (SD))		99.25 (21.82)	105.08 (26.50)	114.22 (35.08)	111.91 (27.21)	0.373
NON-HDL Cholesterol (mean (SD))		112.10 (24.29)	126.54 (30.61)	131.78 (32.60)	133.83 (30.91)	0.1
Chol/HDL ratio (mean (SD))		2.65 (0.75)	3.77 (1.09)	3.44 (0.73)	3.83 (1.15)	**0.001**
HbA1C (mean (SD))		5.36 (0.40)	5.61 (0.45)	5.48 (0.50)	5.84 (0.63)	**0.025**
HOMA IR (mean (SD))		1.03 (0.51)	2.95 (1.07)	1.52 (0.37)	6.59 (3.87)	**<0.001**
MMSE (mean (SD))		29.41 (0.71)	29.30 (0.32)	29.67 (0.82)	29.00 (1.29)	0.094
Amyloid status (%)	Neg	20 (100.0)	12 (92.3)	9 (100.0)	22 (95.7)	0.578
	Pos	0 (0.0)	1 (7.7)	0 (0.0)	1 (4.3)	
Race (%)	White	14 (70.0)	10 (76.9)	4 (44.4)	14 (60.9)	0.591
	African/American	3 (15.0)	1 (7.7)	4 (44.4)	7 (30.4)	
	Asian	1 (5.0)	1 (7.7)	0 (0.0)	0 (0.0)	
	Other	2 (10.0)	1 (7.7)	1 (11.1)	2 (8.7)	
SAT (mean (SD))		1526.09 (589.94)	2038.04 (502.76)	3492.92 (932.95)	3788.19 (1504.86)	**<0.001**
VAT (mean (SD))		479.85 (213.99)	773.04 (279.99)	893.08 (298.19)	1463.74 (569.99)	**<0.001**

BMI: Body Mass Index, MMSE: Mini-mental state examination, HDL: High Density Lipoprotein, LDL: Low Density Lipoprotein, HbA1C: Hemoglobin A1C, HOMA-IR: Homeostatic Model Assessment for Insulin Resistance, SAT: subcutaneous adipose tissue, VAT: visceral adipose tissue. Significant p-values are emboldened.

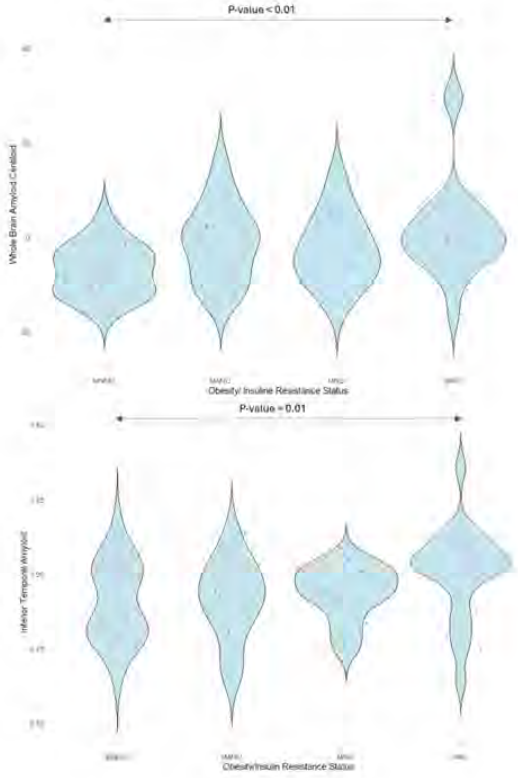

604

Comparison of Diffusion Tensor Imaging Analysis Along Perivascular Space (DTI-ALPS) Indices Based on DTI Data with Different Protocols

Enchao Qiu MD, PhD[1], Phillip Phan BS[1], Areeba Nisar MD[1], Nikolaos Mouchtouris MD[2], Mahdi Alizadeh PhD[2], Devon Middleton PhD[3], Feroze Mohamed PhD[3], Joga Chaganti MD[3], Kiran Talekar MD[3], Prabath Mondel MD[3], Scott Faro MD[3], Hsiangkuo Yuan MD, PhD[1]

[1]Department of Neurology, Thomas Jefferson University, Philadelphia, PA, USA. [2]Department of Neurological Surgery, Thomas Jefferson University, Philadelphia, PA, USA. [3]Department of Radiology, Thomas Jefferson University, Philadelphia, PA, USA

Abstract Category

Functional/Advanced Imaging

Purpose

While the initial diffusion tensor imaging analysis along perivascular space (DTI-ALPS) study employed a b-value of 1000 s/mm² with 30 directions, some subsequent DTI-ALPS studies utilized different DTI protocols. (Taoka et al, 2017; Andica et al, 2023) This study aims to evaluate whether DTI-ALPS analysis based on DTI data with b-values of 800 s/mm² and 64 diffusion directions is comparable to DTI data acquired with b-values of 1000 s/mm² and 30 diffusion directions.

Materials & Methods

The study compared DTI-ALPS indices between 10 right-handed subjects (DTI data with b=1000 s/mm², 30 directions, TOPUP and Eddy current correction) and 6 right-handed subjects (DTI data with b=800 s/mm², 64 directions, Eddy current correction only). The processing pipeline included DTI map generation (fractional anisotropy [FA] and tensor) using DTIFIT, followed by FA color map registration to the FMRIB58_FA (1mm) template. Spherical ROIs with 5-mm diameters were placed based on the Montreal Neurological Institute (MNI) coordinates in left and right projection fibers and association fibers on the template. Left and right ALPS indices were calculated and compared between groups using independent *t*-tests.

Results

No statistically significant demographic differences in sex and age were observed between groups ($P > 0.05$, see Table 1). Analysis revealed no statistical differences in left and right ALPS indices between the two groups (Left: 1.655 vs. 1.586, $P = 0.271$, 95% confidence interval: -0.060~0.198; Right: 1.560 vs. 1.581, $P = 0.761$, 95% confidence interval: -0.169~0.126. See Table 1), suggesting possible compatibility despite different acquisition parameters.

Conclusion

DTI data with b-values of 800 s/mm² and 64 directions can yield statistically similar ALPS indices compared to the DTI data with b-values of 1000 s/mm² and 30 directions. DTI inhomogeneities do not seem to influence the outcome of ALPS value. The ALPS, being an index, is able to override these distortions. This finding suggests that there is potential consistency of ALPS indices across the two DTI protocols. Future larger studies are needed to validate the results.

References

1. Taoka T, Masutani Y, Kawai H, Nakane T, Matsuoka K, Yasuno F, Kishimoto T, Naganawa S. Evaluation of glymphatic system activity with the diffusion MR technique: diffusion tensor image analysis along the perivascular space (DTI-ALPS) in Alzheimer's disease cases. Japanese journal of radiology. 2017;35:172-178.

2. Andica C, Kamagata K, Takabayashi K, Kikuta J, Kaga H, Someya Y, Tamura Y, Kawamori R, Watada H, Taoka T, Naganawa S. Neuroimaging findings related to glymphatic system alterations in older adults with metabolic syndrome. Neurobiology of Disease. 2023;177:105990.

Images/Tables

Table 1. Comparison of Demographic data and DTI-ALPS indices between 10 subjects and 6 subjects with different b values and directions

	10 subjects	6 subjects	Statistical results
Hand dominance	Right	Right	-
Sex (F/M)	6/4	1/5	$\chi^2 = 2.861$, P = 0.091
Age (mean ± SD)	28.7±6.57	29.4±2.70	t = -0.046, P=0.964
DTI data	b =1000 s/mm², 30 diffusion directions	b= 800 s/mm², 64 diffusion directions	-
Left ALPS indices	1.655±0.137	1.586±0.067	t = 1.146, P=0.271, 95% CI: -0.060~0.198
Right ALPS indices	1.560±0.148	1.581±0.102	t = -0.311, P=0.761, 95% CI: -0.169~0.126

DTI-ALPS: diffusion tensor imaging analysis along perivascular space; CI: confidential interval.

606

Advancing Neurovascular Imaging: Optimization of Reconstruction Kernel and Quantum Iterative Reconstruction for Ultra-High-Resolution Photon-Counting Detector CT Angiography

Justin Chetta MD[1], Adrienn Tóth MD[2], Yongjoo (Jennifer) Cho[2], Evan Wilson[2], John Crow MD[2], Eric Bass DO[2], Maria Gisele Matheus MD[2], Jennifer Joyce DO[2], Sameer Tipnis PhD[2], Maria Vittoria Spampinato MD[2]

[1]Medical University of South Carolina, Charleston, SC, USA. [2]Medical University of South Carolina, Charleston, South Carolina, USA

Abstract Category

Adult Brain

Purpose

Effective imaging of intracranial aneurysms, particularly those smaller than 3 mm, can be challenging with conventional CT technologies[1]. Photon-counting detector (PCD)-CT offers improved spatial resolution and image quality compared to conventional energy-integrating detector CT[2-4]. We aimed to find the optimal combination of sharp reconstruction kernels and quantum iterative reconstruction (QIR) for ultra-high-resolution (UHR) PCD-CT with a special focus on imaging intracranial aneurysms.

Materials & Methods

Eighteen patients diagnosed with intracranial aneurysms were prospectively enrolled in this study. CT angiograms were acquired in UHR mode on a clinical dual-source PCD-CT. Images were reconstructed at 0.2 mm slice thickness, with six strength levels of a dedicated neurovascular kernel (Hv48 / 56 / 64 / 72 / 80 / 89) in combination with four QIR levels (1-4) and corresponding matrix sizes (512 × 512 / 768 × 768 / 1024 × 1024). Image noise, signal-to-noise ratio (SNR), contrast-to-noise ratio (CNR) and vessel sharpness were determined for all reconstructions. Qualitative image quality was assessed by three readers using a 5-point Likert scale, focusing on the top-performing kernels (Hv56, 64, 72) across all QIR levels (1-4). The evaluation was conducted in a blinded, randomized manner, evaluating vessel sharpness, image noise, artifacts, aneurysm characterization, delineation of the carotid bifurcation, and overall image quality.

Results

Increased kernel sharpness and lower QIR levels were associated with a continuous rise in image noise. The reconstructions that exhibited the highest CNR values were identified as Hv48 (512 × 512 pixels) and Hv72 (768 × 768 pixels) in combination with QIR level 4. Vessel sharpness improved with higher kernel strengths, reaching a plateau at Hv64 and Hv72 reconstructions, as observed in the small intracranial arteries, with maximum ΔHU values of 260.59 and 255.11, respectively. Our qualitative image quality analysis demonstrated a consistent preference for QIR level 4 across all kernels in each evaluated category ($P < 0.001$). Among the kernels, Hv72 was the most frequently preferred, although it exhibited a higher incidence of image artifacts compared to the other kernels.

Conclusion

Our study provides valuable insights into the quantitative and qualitative properties of image quality achieved with ultra-high-resolution photon-counting detector CT angiography in a cohort of patients with intracranial aneurysms. Although the ultra-sharp neurovascular kernels exhibited increased image noise, our findings suggest that employing the highest level of iterative reconstruction can enhance the overall quantitative image quality. Correspondingly, our qualitative image quality analysis consistently revealed a preference for QIR level 4 when utilizing ultra-sharp kernels, emphasizing its effectiveness in improving image quality. Among the configurations evaluated, the combination of the Hv72 kernel with QIR level 4 demonstrated the most significant advantages, making it the recommended parameter for ultra-high-resolution PCD-CT in neurovascular imaging.

References

1. Allaw S, Khabaz K, Given TC, et al. A review of intracranial aneurysm imaging modalities, from CT to state-of-the-art MR. AJNR Am J Neuroradiol. 2024.
2. Tóth A, Chetta JA, Yazdani M, et al. Neurovascular Imaging with Ultra-High-Resolution Photon-Counting CT: Preliminary Findings on Image Quality Evaluation. AJNR Am J Neuroradiol. 2024.
3. Diehn FE, Zhou Z, Thorne JE, et al. High-Resolution Head CTA: A Prospective Patient Study Comparing Image Quality of Photon-Counting Detector CT and Energy-Integrating Detector CT. AJNR Am J Neuroradiol. 2024;45(10):1441-9.
4. Booz C, Bucolo GM, D'Angelo T, et al. Carotid artery assessment in dual-source photon-counting CT: impact of low-energy virtual monoenergetic imaging on image quality, vascular contrast and diagnostic assessability. Radiol Med. 2024.

Images/Tables

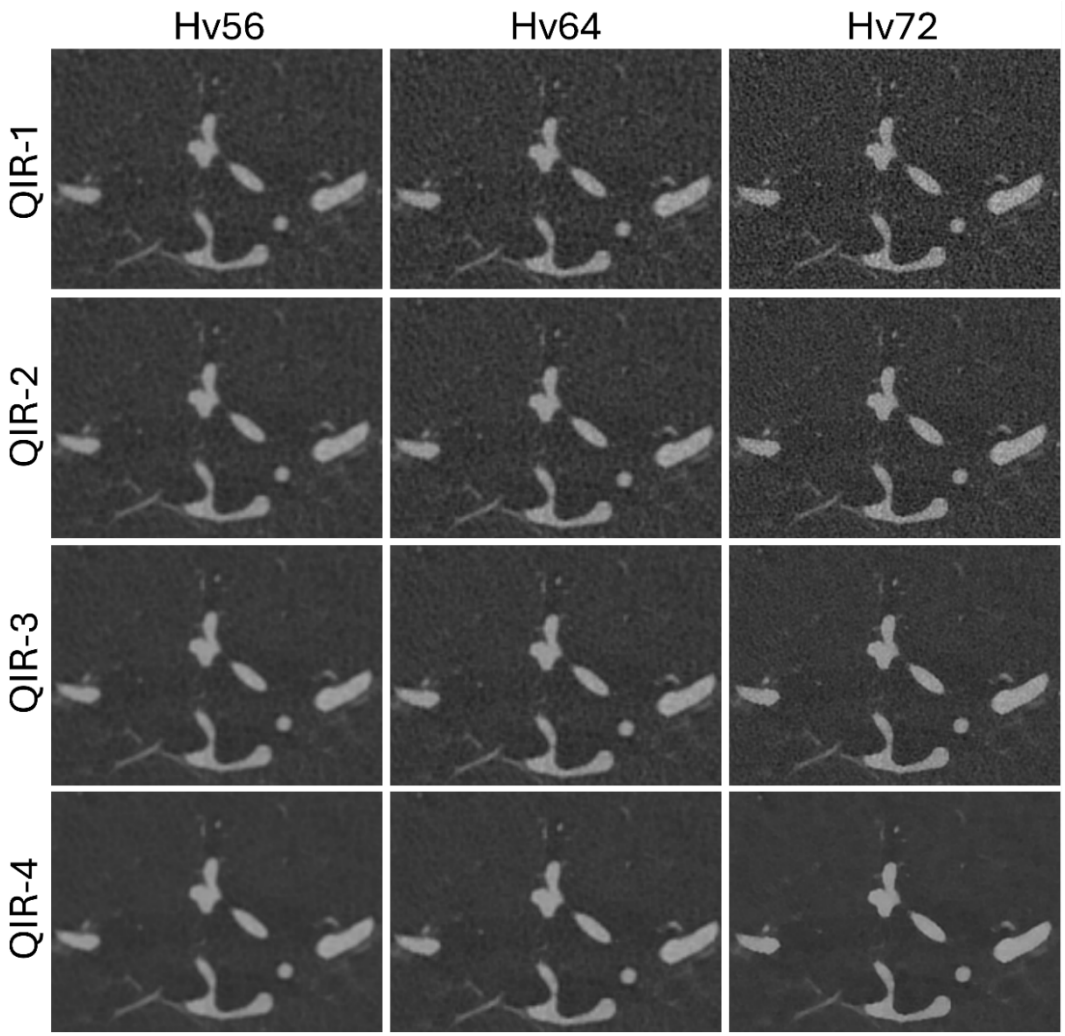

612

The Cervical Spine MRI Dataset for Vertebral Segmentation

Longfei Zhou PhD[1], Walter Wiggins MD, PHD[2], Jikai Zhang Master of Biostatistics[3], Roy Colglazier MD[4], Jay Willhite MD[4], Austin Dixon MD[4], Michael Malinzak MD[4], Hanxue Gu[3], Maciej A. Mazurowski PhD[3], Evan Calabrese MD PhD[4]
[1]Gannon University, Erie, PA, USA. [2]Greensboro Radiology, Greensboro, NC, USA. [3]Duke University, Durham, NC, USA. [4]Duke University School of Medicine, Durham, NC, USA

Abstract Category

Spine

Purpose

MRI is essential for diagnosis of cervical spine diseases[1]. Recently, there has been considerable interest in quantitative analysis of MRI to improve and standardize radiologic assessment of cervical spine diseases including degenerative spondylosis. Unfortunately, detailed anatomic segmentation is required for many such analyses and can be prohibitively time consuming to perform manually. Deep learning enabled automated segmentation could greatly facilitate cervical spine MRI analysis tasks such as quantification of degenerative disc disease. However, only a limited number of studies in literature have explored automated methods for cervical spine MRI segmentation. In this study, we present a novel MRI dataset comprising sagittal T2-weighted cervical spine images, along with expert segmentations of vertebral bodies and intervertebral discs and a deep learning segmentation model for generating segmentations on new data.

Materials & Methods

We retrospectively collected 1,232 patients with 1,255 cervical spine MRI exams at a single academic medical center. Associated demographical data, including age, sex, primary self-reported race, and ethnicity, were also collected. 491 MRI exams were pseudo-randomly selected for manual annotation. Six board-certified neuro or musculoskeletal radiologists and a postdoctoral fellow annotated the dataset. Annotators used the ITK-Snap software tool to create

annotation masks (**Figure 1**) for vertebral bodies (Label 1 in red) and intervertebral discs (Label 2 in green). We trained and validated a deep learning segmentation model using nnU-Net[2] on the manually annotated exams including 391 exams for model development and 100 exams for internal validation using the Disc coefficients (DSC) as the performance metric. The remaining unlabeled exams were automatically labeled using the fully trained model.

Results

Each exam in the final dataset includes the three following components: (1) de-identified DICOM files that represent the initial MRI, (2) a NIfTI file converted from (1) using dcm2niix toolkit, (3) a NIfTI file for the segmentation, completed by either readers or the segmentation model. Initial DICOM files underwent thorough de-identification using the MIRC RSNA DICOM anonymizer tool. The deep learning segmentation model trained on 391 exams yielded an average validation set DSC of 0.929 on vertebral bodies and 0.904 on intervertebral discs. The complete dataset and segmentation model will be shared publicly on the Medical Imaging and Data Resource Center (MIDRC), an NIH funded image data repository.

Conclusion

In this work, we present a cervical spine segmentation dataset of 1,255 sagittal T2 MRI exams. Approximately 40% of the data were manually labeled by domain experts. A deep learning segmentation model trained on this data achieved state-of-the-art performance, demonstrating the utility of our dataset to further aid the process of cervical spine MRI analysis. While prior related work has primarily focused on spine segmentation on CT[3,4], this work extends these capabilities to MRI, which is critical for analysis of cervical spine pathology. Future work will include classifications of C1-C7 vertebral bodies and discs, manual verification of automatically labeled exams, and external validation.

References

1. Kaiser, Jay A. MD; Holland, Betsy A. MD. Imaging of the Cervical Spine. Spine 23(24):p 2701-2712, December 15, 1998.
2. Isensee, F., Jaeger, P.F., Kohl, S.A.A. et al. nnU-Net: a self-configuring method for deep learning-based biomedical image segmentation. Nat Methods 18, 203–211 (2021). https://doi.org/10.1038/s41592-020-01008-z
3. Lin, H. M., Colak, E., Richards, T., Kitamura, F. C., Prevedello, L. M., Talbott, J., Ball, R. L., Gumeler, E., Yeom, K. W., Hamghalam, M., Simpson, A. L., Strika, J., Bulja, D., Angkurawaranon, S., Pérez-Lara, A., Gómez-Alonso, M. I., Ortiz Jiménez, J., Peoples, J. J., Law, M., Dogan, H., … RSNA-ASSR-ASNR Annotators and the Dataset Curation Contributors (2023). The RSNA Cervical Spine Fracture CT Dataset. *Radiology. Artificial intelligence*, *5*(5), e230034. https://doi.org/10.1148/ryai.230034
4. Deng, Y., Wang, C., Hui, Y., Li, Q., Li, J., Luo, S., ... & Zhou, S. K. (2021). CTSpine1K: a large-scale dataset for spinal vertebrae segmentation in computed tomography. *arXiv preprint arXiv:2105.14711*.

Images/Tables

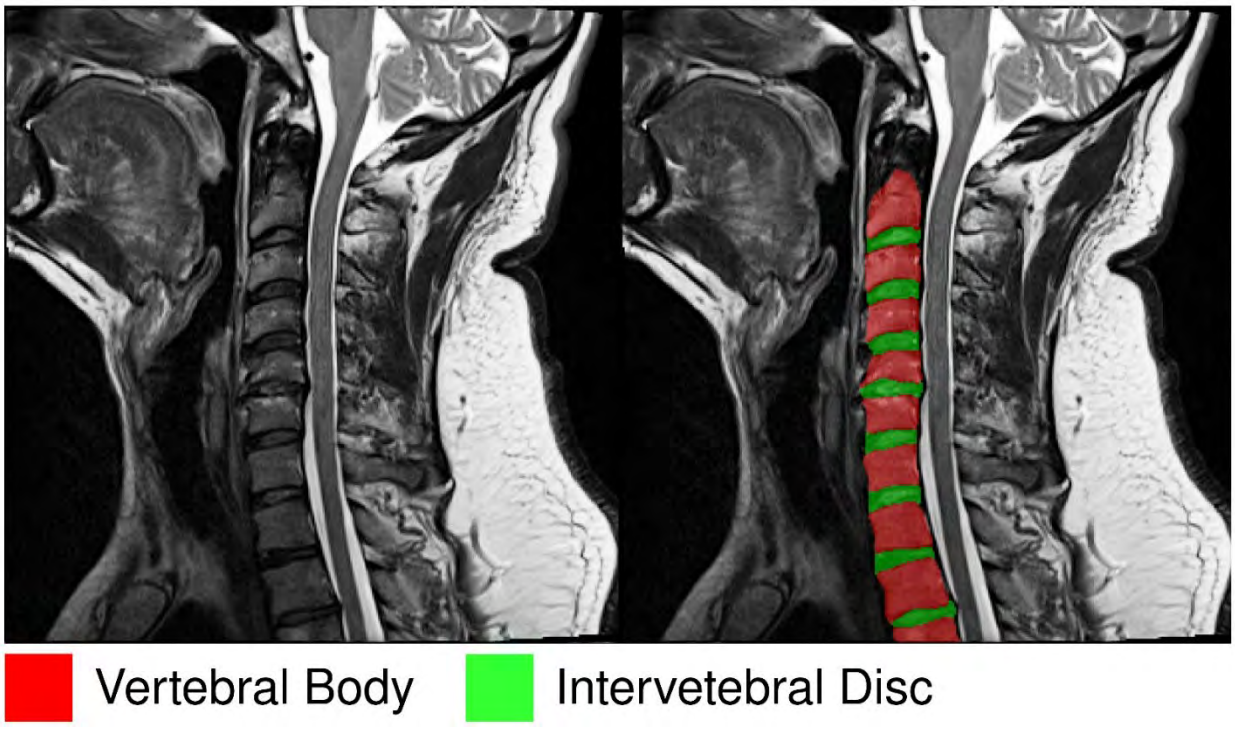

614

18F-FNOS PET Measures Neuroinflammation in Alzheimer's Disease

Ajay Kumar, MD,PhD[1], Anthony Young, BS[2], David A Wolk, MD[3], Hsiaoju Lee, PhD[4], Robert Mach, PhD[4], Jacob Dubroff, MD,PhD[5], Ilya M Nasrallah, MD,PhD[1]

[1]Neuroradiology, University of Pennsylvania Perelman School of Medicine, Philadelphia, PA, USA. [2]PET Analysis Lab, University of Pennsylvania Perelman School of Medicine, Philadelphia, PA, USA. [3]Neurology, University of Pennsylvania Perelman School of Medicine, Philadelphia, PA, USA. [4]Radiology, University of Pennsylvania Perelman School of Medicine, Philadelphia, PA, USA. [5]Nuclear Medicine, University of Pennsylvania Perelman School of Medicine, Philadelphia, PA, USA

Abstract Category

Functional/Advanced Imaging

Purpose

Alzheimer's disease (AD) is a progressive neurodegenerative disorder, characterized by misfolded tau and amyloid protein aggregates. Previous findings suggest these protein aggregates are associated with increased neuroinflammation.[1] Therefore, *in vivo* markers of neuroinflammation are of interest for insights into AD pathology and progression. The inducible form of nitric oxide synthase, iNOS, is upregulated during inflammatory states by activated microglia and is a key marker of oxidative stress and the immune response. ^{18}F-FNOS is a positron emission tomography (PET) probe developed to bind to iNOS, and ^{18}F-FNOS has been used to image both acute[2] and chronic[3,4] inflammation. In this study, we prospectively evaluated a small cohort of AD patients for presence of neuroinflammatory changes using ^{18}F-FNOS PET and compared with healthy control group (HC).

Materials & Methods

Four AD patients (mean age: 78±7 year; range: 70-86) and 4 HC (mean age: 68±13 year; range: 54-83) underwent 60-minutes dynamic PET scan after intravenous injection of 213±18 MBq of ^{18}F-FNOS. Metabolite corrected plasma input functions were measured from arterial sampling. MRI segmentation and PET time-activity curve extraction were performed in MRICloud and Integrative Data Analysis Environment, respectively, as described in Doot et. al. Regional total volume of distribution (V_T) was calculated, and V_T parameter maps were generated in PMOD v3.7 using graphical Logan Plots analysis with individual arterial inputs. Voxel-wise analysis was performed in SPM12 using 2-tailed t-test and t-score maps were generated with $p<0.005$, without corrections for multiple comparisons, and a size threshold of 50 voxels. Regional and whole-brain V_T were compared using two-sample t-tests in Prism GraphPad 8. Age as a potential confounder was investigated by applying a linear regression to whole-brain V_T.

Results

Whole-brain V_T appeared to be slightly increased in AD group compared to HC; 2.8±0.2 vs 2.6±0.2 ml/ccm ($p=0.08$). Further, there were significant regional differences between AD and HC with higher V_T noted in 9/19 brain regions, including temporal lobe, temporal pole, amygdala, parahippocampus, ventral striatum, midbrain, pons, medulla and cerebellum (top panel of the **Figure**). Voxel-wise whole brain analysis result is shown in the bottom panel of the **Figure**. While there was a significant age-related increase in ^{18}F-FNOS whole-brain V_T in HC ($y= 0.012x +1.77$, $r^2=0.96$, $p<0.02$), no such age-related changes were noted in AD group ($p=0.73$), suggesting that the altered V_T seen in AD group was likely disease related.

Conclusion

^{18}F-FNOS PET showed both global and regional increases in neuroinflammatory changes in patients with AD, and therefore, may be useful in the evaluation of pathogenesis, progression, monitoring of treatment effect and prognostication in this condition.

References

1. Leng F, Edison P. Neuroinflammation and microglial activation in Alzheimer disease: where do we go from here? Nature reviews Neurol 2021; 17(3): 157-172. https://doi.org/10.1038/s41582-020-00435-y
2. Huang HJ, Isakow W, Byers DE, et al. Imaging pulmonary inducible nitric oxide synthase expression with PET. JNM 2015; 56(1): 76-81. https://doi.org/10.2967/jnumed.114.146381
3. Doot RK, Young AJ, Nasrallah IM, et al. [18F]NOS PET Brain Imaging Suggests Elevated Neuroinflammation in Idiopathic Parkinson's Disease. Cells 2015; 11(19), 3081. https://doi.org/10.3390/cells11193081
4. Wetherill RR, Doot RK, Young AJ, et al. Molecular Imaging of Pulmonary Inflammation in Users of Electronic and Combustible Cigarettes: A Pilot Study. JNM 2023;64(5),797-802. https://doi.org/10.2967/jnumed.122.264529

Images/Tables

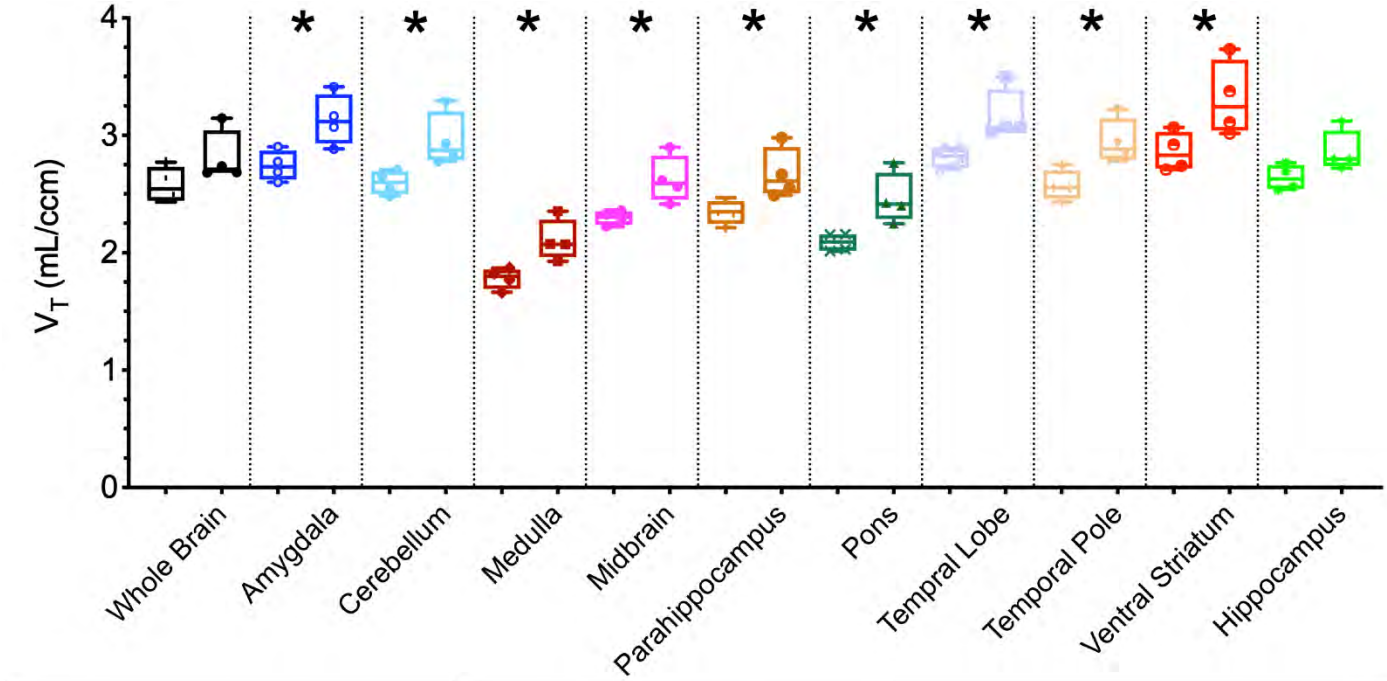

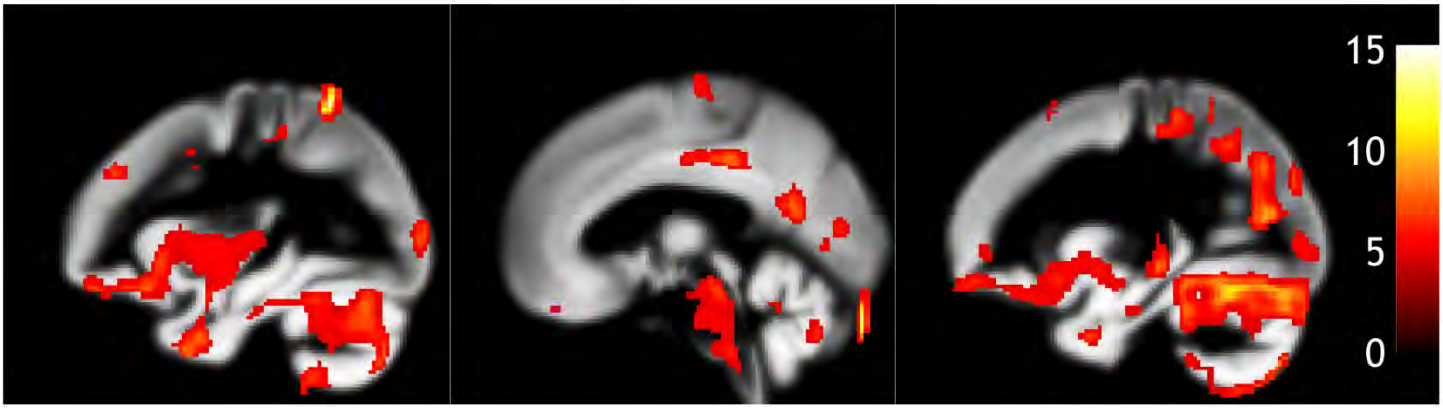

619

Racial and gender disparities in percutaneous ablation treatment for vertebral metastases: Multinational and Multicenter Database Study

Abdul AL halak DO[1], Aneri B Balar MD[2], Hamza Adel Salim MD[2], Vivek S Yedavalli MD[2], Majid Khan MD[2], Dhairya Lakhani MD[1]

[1]WVU Medicine, Morgantown, WV, USA. [2]John Hopkins, Baltimore, MD, USA

Abstract Category

Spine

Purpose

Vertebral metastases are a common and serious complication of advanced cancer, often resulting in pain, spinal instability, and neurological issues. Percutaneous ablation therapies, including radiofrequency and cryoablation, have emerged as minimally invasive options for managing these metastases, providing symptom relief and enhancing spinal stability1-4. This study aims to investigate sex and racial disparities among patients with vertebral metastases who are offered ablation therapy.

Materials & Methods

We utilized the TriNetX Research Network, which provides access to de-identified health records from over 275 million patients, from 19 countries and over 120 health organizations. Our study included patients aged ≥ 18 years diagnosed with vertebral metastasis, stratified by gender and race. We identified patients who underwent ablation therapy, using CPT codes 20982 for radiofrequency ablation and 20983 for cryoablation, and examined the demographic distribution of

this treatment. Patients with missing sex data (n=9,195) and unknown race (n=48,454) were excluded from the respective analyses. Chi-squared tests were employed to compare group differences.

Results

As shown in Table 1, a total of 301,965 patients with vertebral metastases were included in the study, of whom 1,426 received ablation therapy. The mean age of patients with vertebral metastasis was 72.4 years (±13.3), while the mean age of those treated with ablation was 68.1 years (±12.8). Females were significantly underrepresented in the ablation cohort (n=288, 20.2%) compared to the overall vertebral metastasis cohort (n=131,040, 43.41%; p<0.001). Similarly, Black or African American patients constituted a smaller proportion of the ablation cohort (n=125, 8.76%; p<0.001) compared to the main cohort (n=33,337, 11.04%).

Conclusion

This analysis highlights significant sex and racial disparities among patients with vertebral metastases who receive percutaneous ablation therapy. Both females and Black patients were underrepresented in the treatment cohort. This multi-institutional and multinational database study underscores the need for strategies to ensure equitable care and improve access to effective treatment options.

References

1. Tomasian A, Jennings JW. Vertebral Metastases: Minimally Invasive Percutaneous Thermal Ablation. Tech Vasc Interv Radiol 2020;23:100699.
2. Chen L, Hou G, Zhang K, et al. Percutaneous CT-Guided Microwave Ablation Combined with Vertebral Augmentation for Treatment of Painful Spinal Metastases. AJNR Am J Neuroradiol 2022;43:501-506.
3. Tomasian A, Khan MA, Jennings JW. Percutaneous Treatment of Spinal Metastases. Neuroimaging Clin N Am 2023;33:499-506.
4. Tmasian A, Levy J, Jennings JW. Percutaneous Vertebral Augmentation and Thermal Ablation in Patients with Spinal Metastases. Semin Intervent Radiol 2024;41:170-175.

Images/Tables

Table 1: Demographic Characteristics of Patients with Vertebral Metastases and the Ablation Treatment Cohort.

Category	Vertebral metastases (n=301,965)	Vertebral metastases with Ablation Treatment (n=1,426)	P value
Age (Mean +/- SD)	72.4 ± 13.3	68.1 ± 12.8	NA
Sex			
Male	161,768 (53.57%)	632 (44.32%)	<0.001
Female	131,040 (43.41%)	288 (20.2%)	<0.001
Unknown	9,157 (3.03%)	38 (2.66%)	NA
Race			
White	189,554 (62.77%)	1,104 (77.41%)	<0.001
Black or African American	33,337 (11.04%)	125 (8.76%)	<0.001
Asian	19,332 (6.41%)	44 (3.08%)	<0.001
Other Race	11,394 (3.79%)	62 (3.94%)	NA
Unknown Race	48,348 (16.01%)	106 (7.43%)	NA

622

Unveiling Patterns of Peri-Lead Edema After DBS: A Retrospective Review of Clinical and Demographic Factors

Coplen D Johnson[1], Garret Miller[1], Shivam S Shah[1], Christopher Stevens[1], Nicholas L Thomas[1], Octavio Arevalo[2]
[1]LSU Health Shreveport School of Medicine, Shreveport, LA, USA. [2]LSU Health Shreveport School of Medicine Department of Radiology, Shreveport, LA, USA

Abstract Category

Adult Brain

Purpose

Postoperative peri-lead edema (PLE) is an increasingly recognized adverse effect of deep brain stimulation (DBS), a treatment used for neurological disorders such as Parkinson's disease (PD), essential tremor (ET), intractable focal epilepsy, and dystonia[1-5]. We conducted a retrospective chart review to assess the incidence of PLE and identify potential clinical and demographic risk factors.

Materials & Methods

A single physician performed DBS electrode placements. To check for complications, postoperative computed tomography (CT) scans were conducted on the day of surgery and approximately two weeks afterward. Data on age, gender, complications, edema size, electrode laterality, lead target, lead brand, indication, and use of robotic assistance versus Starfix were collected and analyzed statistically.

Results

133 leads were implanted in 63 patients, with peri-lead edema (PLE) observed in 65 electrodes (48.87%). Minor postoperative complications, such as subarachnoid hemorrhage (SAH) and subdural hematoma (SDH), were noted in some patients. A few cases of severe PLE were recorded, with the most significant volume of edema reaching 85.11 cm^3. No statistically significant differences were found between PLE-positive and PLE-negative patients based on age, sex, lead target, indication, or robotic assistance versus Starfix. However, the use of Boston Scientific electrodes was significantly associated with PLE, with a p-value of 0.047.

Conclusion

PLE appears more prevalent than previously reported and generally presents with delayed onset post-surgery. This retrospective analysis identified the use of Boston Scientific electrodes as a potential risk factor for PLE. Further research, particularly more extensive studies, is necessary to clarify the underlying mechanisms of PLE, improve prevention strategies, and enhance our understanding of this complication.

References

1. Malek N. Deep Brain Stimulation in Parkinson’s Disease. *Neurol India*. 2019;67(4):968-978. doi:10.4103/0028-3886.266268
2. Whiting AC, Catapano JS, Walker CT, et al. Peri-Lead Edema After Deep Brain Stimulation Surgery: A Poorly Understood but Frequent Complication. *World Neurosurg*. Published online December 28, 2018:S1878-8750(18)32915-2. doi:10.1016/j.wneu.2018.12.092
3. Tian Y, Wang J, Jiang L, et al. The need to be alert to complications of peri-lead cerebral edema caused by deep brain stimulation implantation: A systematic literature review and meta-analysis study. *CNS Neurosci Ther*. 2022;28(3):332-342. doi:10.1111/cns.13802
4. Giordano M, Innocenti N, Rizzi M, et al. Incidence and management of idiopathic peri-lead edema (IPLE) following deep brain stimulation (DBS) surgery: Case series and review of the literature. *Clin Neurol Neurosurg*. 2023;234:108009. doi:10.1016/j.clineuro.2023.108009
5. Deogaonkar M, Nazzaro JM, Machado A, et al. Transient, symptomatic, post-operative, non-infectious hypodensity around the deep brain stimulation (DBS) electrode. *J Clin Neurosci*. 2011;18(7):910-915. doi:10.1016/j.jocn.2010.11.020

Images/Tables

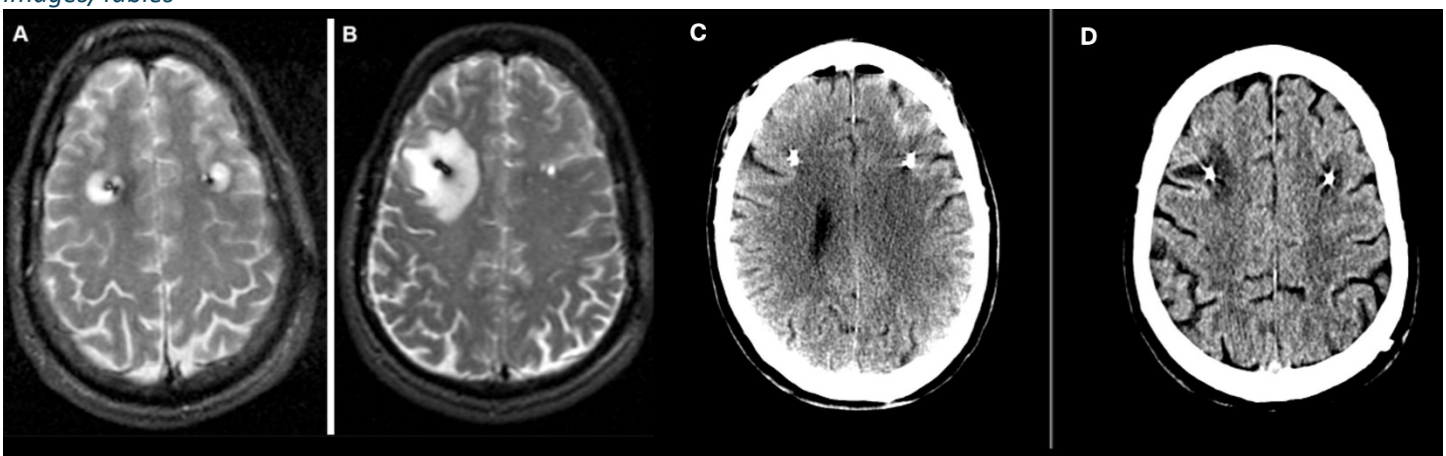

Figure 1. Postoperative T2-weighted MRI images display mild peri-lead edema (PLE) in panel **A** and moderate-to-severe PLE in panel **B**. A same-day postoperative CT scan (**C**) shows no PLE, while a follow-up CT scan taken weeks later (**D**) demonstrates the presence of PLE. The PLE appears as hyperintense on T2-weighted MRI and hypodense on CT, surrounding the electrode, consistent with vasogenic edema in the white matter.

626

A versatile virtual approach to Neuroradiology Education: ASNR MICCAI BraTS–METS Challenge Experience

Raisa Amiruddin MBBS[1], Nazanin Maleki MD[1], Nikolay Yordanov[2], Anastasia Janas[3], Athanasios Gkampenis MD[4], Pascal Fehringer[5], Ahmed Moawad MD[6], Sanjay Aneja[7], Spyridon Bakas PhD[8], Mariam Aboian MD PhD[1]
[1]Children's Hospital of Philadelphia, Philadelphia, Pennsylvania, USA. [2]Sofia, Bulgaria, Bulgaria. [3]Berlin, Germany, Germany. [4]Athens, Greece, Greece. [5]Jena, Germany, Germany. [6]Philadelphia, Pennsylvania, USA. [7]Yale University School of Medicine, New Haven, Connecticut, USA. [8]Indiana University, Bloomington, Indiana, USA

Abstract Category

Professional Development

Purpose

Social media has helped build and share content in the medical community. Being part of users' daily routines, it promotes engagement in learning and inspires interactions between learners and mentors. We sought to create a resourceful educational platform for the ASNR MICCAI BraTS Challenge, a landmark community benchmark event for brain tumor segmentation and analysis.

Materials & Methods

We launched a social media initiative in 2023 on X, LinkedIn, Instagram and WhatsApp to help learners build foundational knowledge of neuroimaging. We leveraged these platforms to host our lecture series and upload them onto YouTube, summarize concepts as bite-sized information, relay the process of image annotation and algorithm development, and guide learners towards open access resources for education. We utilized Hootsuite, Iconosquare, and Chatilyzer to calculate metrics and analyze the impact of our online presence.

Results

We published 55 posts on X through 3 iterations (2023, 2024, 2025) of BraTS since February 2023 and garnered 112,460 impressions, with average engagement rate of 3.96% per post. The highest engagement rate for a post is 8.97%. There has been 264% growth of users viewing our content, 478% growth of users amplifying our posts, and audience growth rate of 8.45% since the day of broadcast of the 2025 Challenge. We published 8 LinkedIn and 8 Instagram posts for the 2025 Challenge, having average engagement rates of 11% and 2.99% per post respectively. We set up a WhatsApp community to support student coordinators through the 2025 image annotation pipeline with faculty annotators. We have exchanged 495 messages here, with an average of 12 messages/day. This annotation protocol is a unique opportunity for students to interact, learn and develop professional relationships with faculty while also simulating the experience of an MR image analysis internship.

Conclusion

Our initiative is using a dynamic learning framework to foster an expanding network of committed learners and mentors and increase awareness on the necessity of meticulously curated public databases for the development of precise and

accurate algorithms for brain tumor analysis. This approach has become valued by our internationally distributed community of students and faculty for enhancing educational and professional growth in the world of neuroimaging and acknowledging their contributions to a revolutionary undertaking in the domains of open science and artificial intelligence.

References

1. PURWANTO, A., Fahmi, K., & Cahyono, Y. (2022). The Benefits of Using Social Media in the Learning Process of Students in the Digital Literacy Era and the Education 4.0 Era. Journal of Information Systems and Management (JISMA), 2(2), 1–7. https://doi.org/10.4444/jisma.v2i2.296

2. Williams, R. (2020). An Exploration into the Pedagogical Benefits of Using Social Media: Can Educators Incorporate Social Media into Pedagogy Successfully? A work in progress. ABC Journal of Advanced Research, 9(2), 69-78. https://doi.org/10.18034/abcjar

Images/Tables

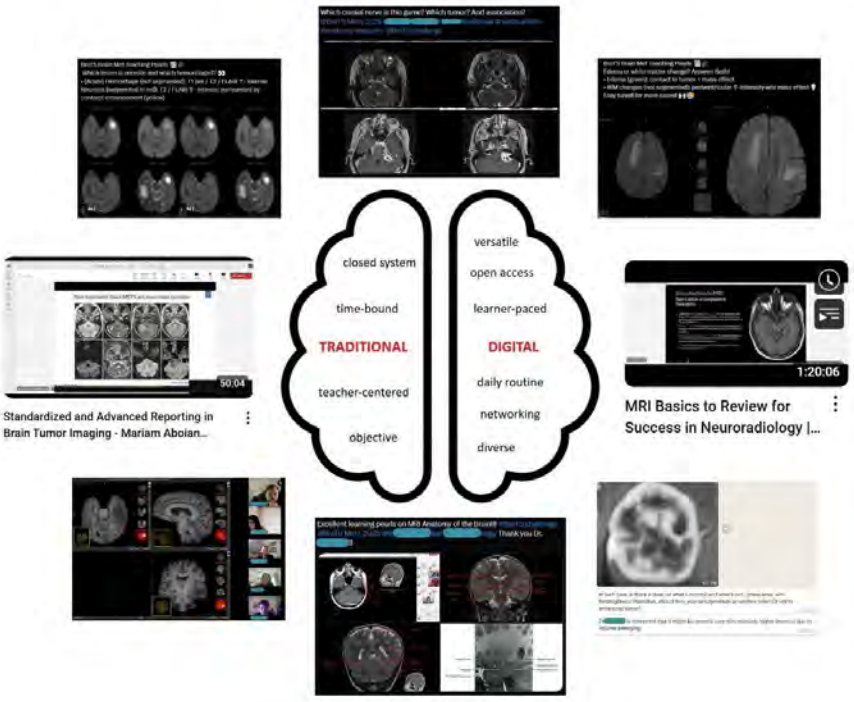

632

Assessing Metabolic Dysfunction at Cerebral Microbleed Sites using MRI-based Quantitative Oxygen Extraction Fraction Mapping

Dan Zlatopolsky BS[1], Isabel Hagger BS[2], Nazmi Kurt MD[3], Daniel Hsu[4], Junghun Cho PhD[4], Salil Soman MD, MS[5]

[1]Medical College of Georgia Augusta University / University of Georgia Medical Partnership, Athens, Georgia, USA. [2]Northeastern University, Boston, Massachussetts, USA. [3]Beth Israel Deaconess Medical Center / Harvard Medical School, Boston, Massachussetts, USA. [4]University at Buffalo, Buffalo, New York, USA. [5]Beth Israel Deaconess Medical Center / Harvard Medical School, Boston, Massachusetts, USA

Abstract Category

Functional/Advanced Imaging

Purpose

Cerebral microbleeds (CMBs) are hemosiderin deposits in the brain[1-4] detected on brain MRI consisting of red blood cell breakdown products like hemosiderin, erythrocytes, and iron within macrophages that can persist in perivascular space for years.[5, 6] These deposits are linked to conditions like cerebral amyloid angiopathy and traumatic brain injury,[3, 4] and Alzheimer's disease anti-amyloid therapies (ARIA).[7] Traditionally associated with hypertensive vasculopathy [8] or cerebral amyloid angiopathy,[9] CMBs also appear in healthy individuals,[10] prompting further investigation into their mechanisms.

CMBs are associated with vascular remodeling,[11] vessel calcification,[12] blood-brain barrier dysfunction,[13] and neuronal signaling alterations.[15] Studies show high activity of macrophages and pericytes at CMBs.[14] Given these varied findings, assessing the metabolic activity at CMBs could reveal important in vivo processes.

A recent MRI-based OEF model has been developed by integrating quantitative susceptibility mapping and quantitative blood oxygen level-dependent magnitude (QQ)[16-20]. The QQ-based OEF aligns well with ^{15}O-PET[19] and requires only routine MRI sequences without tracers. In this study, we applied QQ to assess OEF values at CMB sites compared to non-CMB sites, aiming to identify metabolic dysfunction.

Materials & Methods

This IRB-approved study included 196 patients with suspected dementia who underwent MRI imaging that included a 3D multiecho GRE on a 3.0 T MR system (Signa Premier; GE Healthcare) using a 48-channel head coil with the following scan parameters: TE 3.648 – 47.424 ms, echo spacing 3.984 ms, 11 echoes, bandwidth 62.5 kHz, voxel size 0.5 × 0.5 × 1 mm3, flip angle 12, acquisition matrix 256 × 256, reconstruction matrix 512 × 512, total scan time, 4 minutes 30 seconds. MEDI+0 QSM,[21] SWI[22] and QQ[19] images were produced for subjects. A board-certified neuroradiologist and a trained research assistant reviewed SWI and QSM images to identify CMBs using a Change Healthcare viewing environment. For each CMB, regions of interest (ROIs) were drawn on QSM and QQ to measure ppb and OEF values. Additional ROIs were drawn at four locations surrounding the CMB site and in contralateral brain tissue without CMBs on the QQ image and OEF values were recorded (figure 1). T-tests assessed OEF differences, and simple linear regression was used to predict OEF values from CMB QSM measurements.

Results

Of the 191 subjects, 48 had CMBs, yielding 69 CMBs for analysis. We found the OEF values to systematically decrease with increasing CMB ppb value (figure 2). ROIs containing CMBs exhibited significantly lower OEF compared to surrounding and contralateral parenchyma ($p < 0.01$) (figure 3, 4). QSM values stratified at 75, 100, 200, and 300 ppb, demonstrated increasing significant differences (figures 3, 4).

Conclusion

Our results show significant CMB site OEF reduction, particularly in areas with high QSM values, which indicate higher iron concentrations from red blood cells or iron-rich activated macrophages. These findings suggest decreased metabolic activity within the parenchyma where CMB's are detected. The relationship between OEF and QSM value supports the presence of greater vascular remodeling, BBB dysfunction or inflammation to be related to metabolic dysfunction. These results provide evidence for potential neurodegeneration therapeutic targets focusing on restoring metabolic function.

References

1. Greenberg SM, Vernooij MW, Cordonnier C, et al. Cerebral microbleeds: a guide to detection and interpretation. *Lancet Neurol* 2009;8:165-174

15. Yang Q, Vazquez AL, Cui XT. Revealing in vivo cellular mechanisms of cerebral microbleeds on neurons and microglia across cortical layers. *iScience* 2024;27:109371

19. Cho J, Lee J, An H, et al. Cerebral oxygen extraction fraction (OEF): Comparison of challenge-free gradient echo QSM+qBOLD (QQ) with (15)O PET in healthy adults. *J Cereb Blood Flow Metab* 2021;41:1658-1668

21. Liu Z, Spincemaille P, Yao Y, et al. MEDI+0: Morphology enabled dipole inversion with automatic uniform cerebrospinal fluid zero reference for quantitative susceptibility mapping. *Magn Reson Med* 2018;79:2795-2803

22. Haacke EM, Xu Y, Cheng YC, et al. Susceptibility weighted imaging (SWI). *Magn Reson Med* 2004;52:612-618

Images/Tables

FIGURE 1: Example CMB on SWI(A), QSM (B)and QQ (C)Images. CMBs were identified on SWI and QSM images, then ppb for CMB was measured on the QSM, and then OEF values on, around, and contralateral to the CMB were recorded from the OEF images.

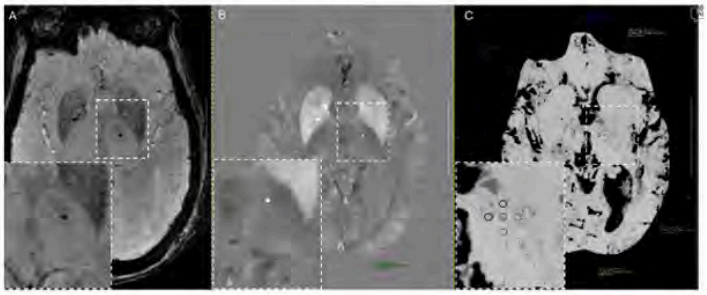

FIGURE 2: Relationship between CMB OEF and QSM values. Note OEF values decrease with increasing susceptibility, suggestive of decreased metabolic activity at higher susceptibility CMBs.

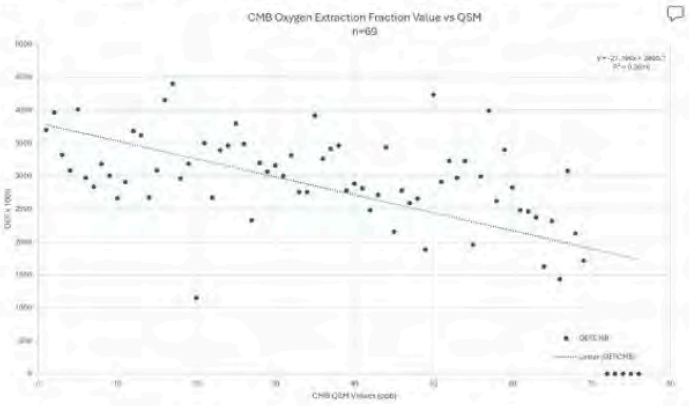

FIGURE 3: Box and Whisker Plots of Observed OEF Values by ROI Group. A) For all QSM Value CMBs, B) evaluating CMBs with QSM value of > 75 ppb, C) evaluating CMBs with QSM value of > 100 ppb, D) evaluating CMBs with QSM value of > 200 ppb, E) evaluating CMBs with QSM value of > 300 ppb.

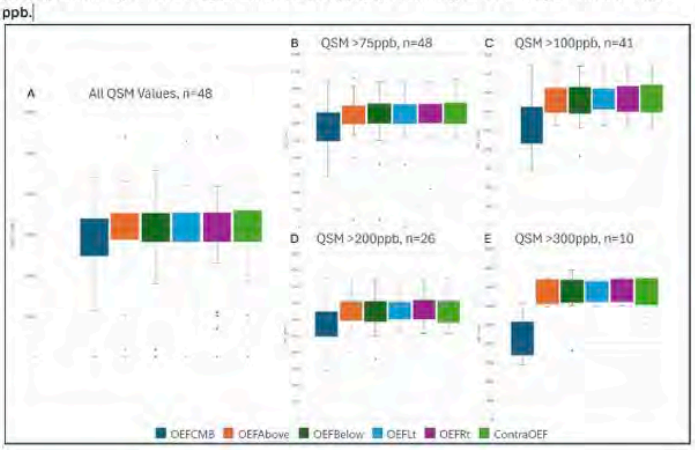

Figure 4: T-test Results for CMBs Relative to Other ROIs When Stratifying By Minimum ppb Value. Note significant differences (bold) between CMB region and all other ROIs when stratifying by minimum CMB ppb value.

QSM ppb	CMB vs Above	CMB vs Below	CMB vs Lt	CMB vs Rt	CMB vs Contralateral	n
All	**0.043242677**	0.090498	**0.001446619**	0.084376952	0.07939675	69
>75	0.086285393	0.10919	**0.027803629**	**0.03276025**	**0.025002146**	48
>100	**0.00066359**	**0.001832**	**9.91386E-05**	**0.000131823**	**0.000722375**	41
>200	**0.000264544**	**0.002591**	**0.000203952**	**0.000156803**	**0.042673373**	26
>300	**5.16423E-05**	**0.001055**	**3.27695E-05**	**2.42146E-05**	**4.45912E-05**	10

637

Perfusion Imaging Prolonged Venous Transit is Associated With Lower Odds of Favorable Recovery After Successful Reperfusion in Anterior Circulation Large Vessel Occlusions

Manisha Koneru[1], Dhairya Lakhani[2], Hamza Salim[3], Aneri Balar[3], Adam A Dmytriw[4], Adrien Guenego[5], Benjamin Pulli[6], Dylan Wolman[7], Jeremy Heit[6], Gregory Albers[6], Tobias Faizy[8], Kambiz Nael[9], Max Wintermark[10], Vivek Yedavalli[3]
[1]Cooper University Health Care, Camden, NJ, USA. [2]West Virginia University, Morgantown, WV, USA. [3]Johns Hopkins, Baltimore, MD, USA. [4]Mass Gen Brigham, Boston, MA, USA. [5]Centre Hospitalier Universitaire de Toulouse, Toulouse, Toulouse, France. [6]Stanford, Stanford, CA, USA. [7]Brown University, Providence, RI, USA. [8]Munster Hospital, Munster, Munster, Germany. [9]UCSF, San Francisco, CA, USA. [10]UT Houston, Houston, TX, USA

Abstract Category

Functional/Advanced Imaging

Purpose

Unfavorable clinical outcomes in patients with acute ischemic stroke caused by large-vessel occlusions despite successful reperfusion have been associated with poor venous outflow. The objective of this study is to assess the relationship between prolonged venous transit (PVT), a novel perfusion imaging surrogate for poor venous outflow, and likelihood of favorable clinical recovery.

Materials & Methods

Consecutive patients (2017–2022) with successfully reperfused, anterior circulation acute ischemic stroke caused by large-vessel occlusions were retrospectively reviewed. We assessed the association between PVT+, defined as time to maximum ≧10-second timing delays within either the posterior superior sagittal sinus, torcula, or both regions on pretreatment perfusion imaging, and favorable clinical outcomes defined as 90-day modified Rankin Scale score of 0 to

2. Patients were dichotomized into PVT+ and PVT− for analysis. Multivariable logistic regression analyses for favorable recovery were performed with demographic variables and stroke characteristics.

Results

A total of 127 consecutive patients (median age, 71 [interquartile range 61—77] years; 59.1% female) were included, and 40 of 127 (31.5%) were PVT+. PVT+ (adjusted odds ratio [aOR], 0.23 [95% CI, 0.07–0.81]; p=0.02) and advanced age (aOR, 0.92 [95% CI, 0.88–0.97]; p=0.01) were significantly associated with the primary outcome.

Conclusion

PVT+ was associated with a lower likelihood of achieving favorable clinical recovery in successfully reperfused patients with acute ischemic stroke caused by large vessel occlusion. PVT may serve as a clinically useful adjunctive imaging parameter.

References

1. Yedavalli VS, Koneru M, Balar AB, et al. Prolonged Venous Transit Is Associated With Lower Likelihood of Favorable Clinical Recovery in Reperfused Anterior Circulation Large-Vessel Occlusion Stroke. *Stroke: Vascular and Interventional Neurology* 0:e001412.
2. Yedavalli VS, Lakhani DA, Koneru M, et al. Simplifying venous outflow: Prolonged venous transit as a novel qualitative marker correlating with acute stroke outcomes. *Neuroradiol J* https://doi.org/10.1177/19714009241269475.
3. Faizy TD, Heit JJ. Cerebral Venous Outflow in Acute Ischemic Stroke Patients–Out Through the Middle! *Acad Radiol* 2024;31:1558–9.

645

Evaluating Clinical and DTI Metrics for Classifying Blast Exposure Levels in Special Operations Forces:Insights into Neurostructural Integrity and Cognitive Function

Andrea diociasi MD[1], Sara De Giorgi MD[2], Luca Roccatagliata MD, PhD[3], Rajiv Gupta MD, PhD[2]
[1]IRCCS Ospedale Policlinico San Martino, Genova, Liguria, Italy. [2]Mass General Brigham Inc, Boston, MA, USA. [3]Department of Health Science (DISSAL), University of Genoa, Genova, Liguria, Italy

Abstract Category

Functional/Advanced Imaging

Purpose

This study takes a unique approach by exploring the predictive value of clinical and Diffusion Tensor Imaging (DTI) metrics for classifying blast exposure levels in Special Operations Forces (SOF) personnel. We aimed to identify the optimal Generalized Blast Exposure Value (GBEV) threshold— a score reflecting cumulative blast impacts throughout their careers. Additionally, we examined how changes in Fractional Anisotropy (FA), cumulative blast burden, and age correlate with neurostructural integrity and cognitive function.

Materials & Methods

We analyzed clinical and diffusion MRI data from 95 SOF personnel with documented blast exposure histories. T-tests or Mann-Whitney U tests, adjusted with False Discovery Rate (FDR) correction, were used to determine the optimal GBEV threshold for separating participants into low and high-exposure groups, maximizing differences in clinical metrics. After establishing the GBEV threshold, we used Multivariate Analysis of Covariance (MANCOVA) to assess differences in FA across 42 white matter tracts identified through TRACULA. Linear regression assessed the relationships between FA, GBEV classification, and age in tracts showing significant group differences.

We also developed logistic regression models to classify exposure groups based on (1) clinical metrics alone, (2) DTI metrics alone, and (3) a combined model incorporating both clinical and DTI metrics. Clinical metrics included the General Ability Index (GAI), derived from the Verbal Comprehension Index (VCI) and Perceptual Reasoning Index (PRI); Full-Scale Intelligence Quotient (FSIQ); and the Patient Health Questionnaire-8 (PHQ-8), used to measure depression severity

Results

We identified a GBEV threshold of 9.5 million, where the separation between low and high-exposure groups was most pronounced in clinical metrics. After FDR correction, participants in the high exposure group showed significantly higher PHQ-8 scores ($p = 0.003$) and lower cognitive performance, including FSIQ ($p < 0.001$), VCI ($p = 0.006$), PRI ($p < 0.001$), and GAI ($p < 0.001$). MANCOVA analysis revealed significant differences in FA between groups, particularly in the left arcuate fasciculus ($p = 0.017$) and left corticospinal tract ($p = 0.009$). Linear regression analyses indicated a significant negative relationship between GBEV and FA in the left arcuate fasciculus ($p = 0.023$) and left corticospinal tract ($p =$

0.009). At the same time, age was not a significant predictor of FA. The logistic regression model combining clinical and DTI metrics achieved the highest classification accuracy (79%) and area under the curve (AUC = 0.814), outperforming the clinical-only model (accuracy = 74%, AUC = 0.775) and the DTI-only model (accuracy = 73%, AUC = 0.697).

Conclusion

This study highlights the utility of combining clinical and DTI metrics to classify blast exposure levels in SOF personnel. Significant differences in clinical performance and FA values between low and high-exposure groups indicate these combined metrics are reliable indicators of blast-related neurostructural changes. These findings emphasize the association between higher blast exposure, cognitive decline, and brain structural alterations in key white matter tracts. These insights not only support the use of comprehensive assessment models for early identification of individuals at risk of blast-related cognitive and neurological deficits but also inspire further research in this area, paving the way for targeted interventions and improved long-term outcomes.

References

Modica LCM, Egnoto MJ, Statz JK, Carr W, Ahlers ST. Development of a Blast Exposure Estimator from a Department of Defense-Wide Survey Study on Military Service Members. J Neurotrauma. J Neurotrauma; 2021;38(12):1662–1669. doi: 10.1089/NEU.2020.7405.

Images/Tables

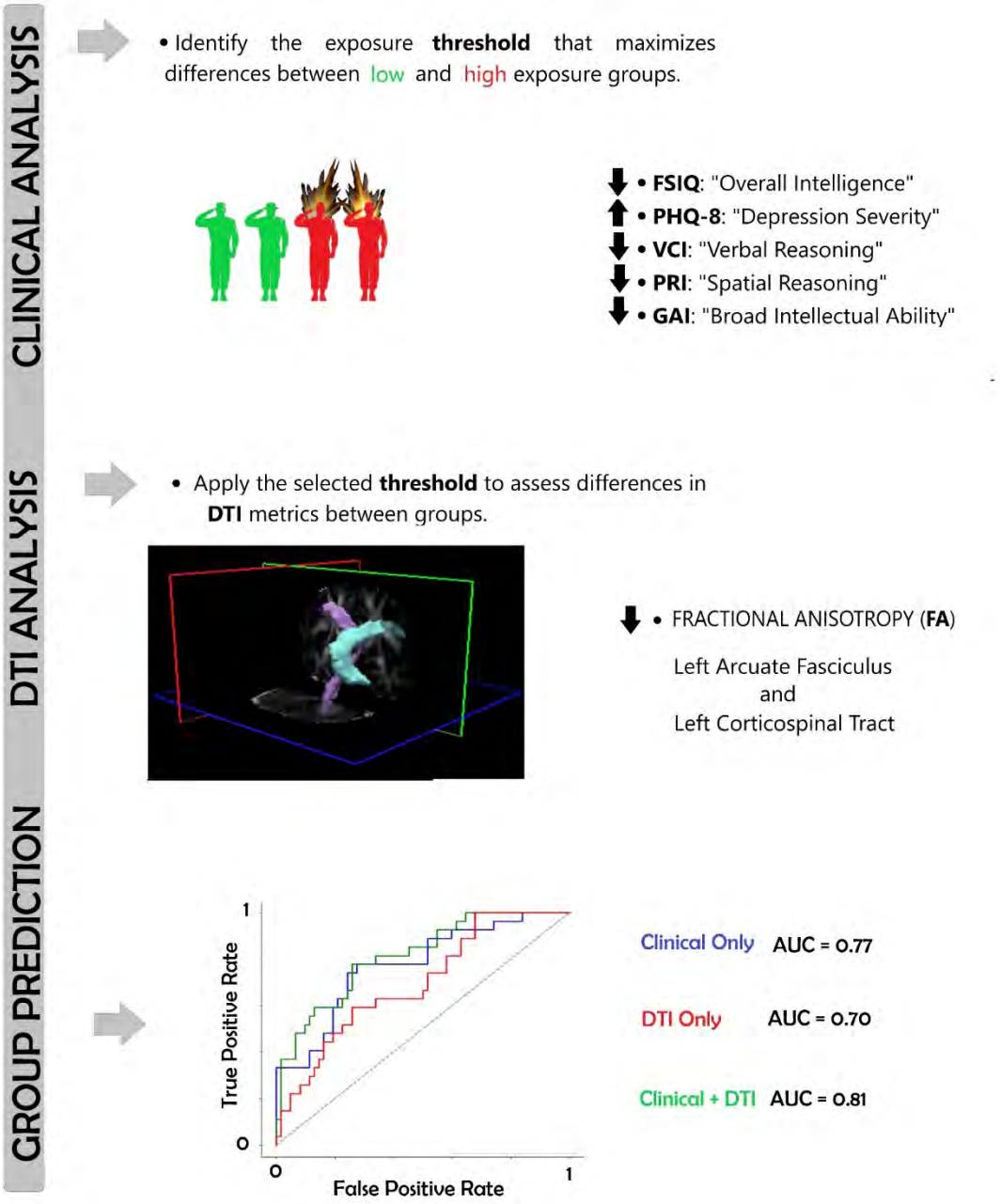

668

Evaluating Sociodemographic Biases in an Automated Artificial Intelligence-Based Glioblastoma Response Assessment Algorithm

Rachel S Lee BS[1], Dominic LaBella MD[2], Evan Calabrese MD PhD[2]
[1]Duke University School of Medicine, Durham, NC, USA. [2]Duke University Medical Center, Durham, NC, USA

Abstract Category

AI/Informatics

Purpose

Brain MRI plays a crucial role in monitoring glioblastoma disease progression and treatment response. Existing treatment response tools are subject to inter-rater reliability due to subjective interpretations and variable linear tumor measurements. Recently, several automated artificial intelligence (AI)-based volumetric brain tumor MRI segmentation tools have been developed to provide objective, volumetric measurements of tumor sub-compartment volume, which can aid radiologists' response assessments. A rising concern regarding the use of AI is potential biases in the AI model, especially across sociodemographic factors such as sex, race, and insurance type. This raises the concern for introducing and further propagating pre-existing health disparities. To investigate this concern, we evaluated sociodemographic biases in a custom glioblastoma MRI segmentation model trained on a large multi-institution dataset.

Materials & Methods

498 brain MRIs from 139 patients with glioblastoma from 2017-2022 at a single center were analyzed retrospectively. MRI data underwent skull removal using a previously published deep learning method. Enhancing tumor volume and surrounding non-enhancing T2-FLAIR signal abnormality compartments were extracted by a 3D AI segmentation algorithm implemented in nnU-Net and trained on the 2024 BraTS glioma dataset (>2000 exams). Automated segmentations were compared to manually corrected segmentations performed by a neuroradiologist using quantitative Dice overlap. For patients who had multiple MRI exams, one MRI was randomly selected for analysis to avoid statistical complexity with correlated data. Sociodemographic factors, including sex, race, age, address with zip code (which were then geocoded to area deprivation index), marital status, and insurance status were extracted from patients' medical charts. Subgroup analyses were performed using one-way ANOVA, t-test, and Spearman correlation.

Results

Our retrospective cohort was 60% male and 91% White, with a median age of 59. There was a statistically significant difference of 0.013 in Dice overlap across sex for FLAIR segmentation. There were no statistically significant differences across race, area deprivation index, smoking status, marital status, and age. There were statistically significant differences seen across insurance types for FLAIR segmentation, with Dice overlap greater in those with Medicare and government insurance compared to private by 0.014 and 0.017, respectively.

Conclusion

Statistically significant differences across sex and insurance type were seen in this AI model for FLAIR segmentation. However, the observed Dice overlap differences were between 0.013 and 0.017 and are unlikely to be clinically significant.

References

Ellingson BM. On the promise of Artificial Intelligence for standardizing radiographic response assessment in gliomas. *Neuro-Oncology* 2019;21:1346–7.
Rudie JD, Calabrese E, Saluja R, et al. Longitudinal assessment of posttreatment diffuse glioma tissue volumes with three-dimensional convolutional neural networks. *Radiology: Artificial Intelligence* 2022;4.
Tejani A, Rayan J, Xi Y, et al. Understanding and mitigating bias in Imaging Artificial Intelligence. *RadioGraphics* http://doi.org/10.1148/rg.230067.q2.

Images/Tables

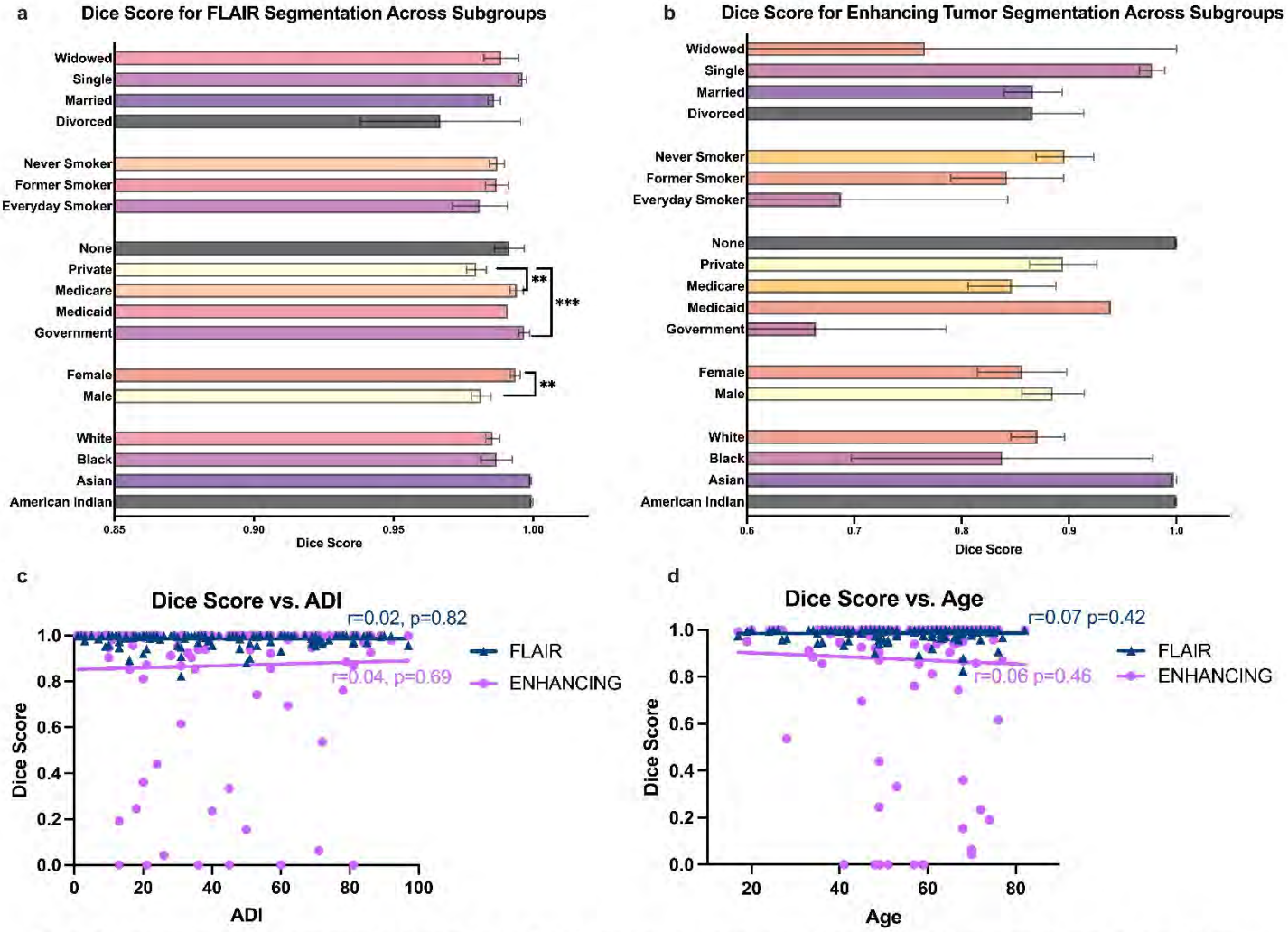

Fig 1: Dice score across sociodemographic factors for (a) FLAIR and (b) enhancing tumor. Dice score by (c) area deprivation index and (d) age. *** = p<0.001, ** = p<0.01

678

After Chemotherapy, Apparent Diffusion Coefficient Values are raised in the Choroid Plexus

Anja Hohmann[1], Ke Zhang[1], Johann M.E. Jende[2], Felix T. Kurz[3]

[1]University Hospital Heidelberg, Heidelberg, Germany, Germany. [2]German Cancer Research Center, Heidelberg, Germany, Germany. [3]University Hospital Geneva, Geneva, Switzerland, Switzerland

Abstract Category

Adult Brain

Purpose

The choroid plexus (CP) not only secretes the cerebrospinal fluid (CSF), it also serves as a highly vascularized and regulated interface between blood and CSF that has recently gained attention for its role in neurodegeneration and neuroimmunology, like Alzheimer's Disease and Multiple Sclerosis.[1,2] While it modulates passage of drugs and toxins into the central nervous system as part of the blood-CSF-barrier,[3] therapy effects on the CP itself have not been investigated. Apparent diffusion coefficient (ADC) has been used in brain tumor diagnostics and therapy monitoring, with ADC values increasing in tumor tissue after chemotherapy.[4] We aimed to investigate the effect of chemotherapy on ADC values in the CP of brain tumor patients.

Materials & Methods

We compared 200 ADC maps from 100 individual patients with low grade glioma (LGG) who had received standard chemotherapy, with 100 age-matched LGG-patients who had not received any therapy other than surgical resection. CP

VOIs were manually segmented on 3D anatomical T1 images (**Fig. 1a**), and shrunk by one voxel at the borders using Matlab in order to reduce potential partial volume effects from CSF. DWI with ADC maps were obtained at 3 Tesla (Prisma, Siemens) with parameter values of b = 0 s/mm^2 and b = 1000 s/mm^2. Further sequence parameters for DWI were: TR/TE 3630/55ms, FoV 219*219mm^2, matrix 192 × 192, slice thickness/interval: 5 mm/0.5 mm. ADC maps were coregistered using SPM12 to T1 images and analysed in Matlab. T-tests were used to compare groups, and correlation analysed was performed using Spearman's rank correlation.

Results

A total of 200 scans was analyzed from 100 subjects after chemotherapy (43 females, mean age 41.8 years) and 100 subjects without tumor-specific therapy (48 females, mean age 41.5 years). Volume of CP VOIs did not differ between groups (44.5 vs. 42.6 voxels, p=0.16). Following chemotherapy, ADC values in the CP were higher compared to subjects who had never received chemotherapy (2.69±0.22 10^{-3}mm^2/s vs. 2.56±0.28 10^{-3}mm^2/s, p<0.001), **Fig. 1b**. ADC values did not differ between women and men for both therapy (p=0.41) and control group (p=0.11). Subjects had undergone an average of 7.9±4.7 cycles of chemotherapy [range: 1-25 cycles], with more cycles of chemotherapy associated with higher ADC values, when controlling for age (r=0.34, p<0.001). Scans were acquired on average 24±34 months after the last treatment cycle [range: 0-183 months], which did not correlate with ADC values (r=0.10, p=0.34).

Conclusion

Our study shows that ADC values in the CP, a highly vascularized interface between blood and CSF, are increased following chemotherapy. Subjects were scanned on average 2 years after receiving their last chemotherapy cycle. Total number of chemotherapy cycles was associated with higher ADC, whereas the time interval since last treatment showed no correlation. This indicates that chemotherapy not only changes diffusion parameters in the CP, but that therapy-associated effects are related to the total amount of chemotherapy administered and can be detected years after treatment. These results are particularly relevant to future clinical application, such as estimation and monitoring of treatment-related toxicity in brain tumor patients.

References

1. Choi JD, Moon Y, Kim H-J, et al. Choroid Plexus Volume and Permeability at Brain MRI within the Alzheimer Disease Clinical Spectrum. *Radiology* 2022;304:635–45.
2. Ricigliano VAG, Morena E, Colombi A, et al. Choroid Plexus Enlargement in Inflammatory Multiple Sclerosis: 3.0-T MRI and Translocator Protein PET Evaluation. *Radiology* 2021;301:166–77.
3. Strazielle N, Ghersi-Egea JF. Choroid plexus in the central nervous system: biology and physiopathology. *J Neuropathol Exp Neurol* 2000;59:561–74.
4. Lun MP, Monuki ES, Lehtinen MK. Development and functions of the choroid plexus-cerebrospinal fluid system. *Nat Rev Neurosci* 2015;16:445–57.

Images/Tables

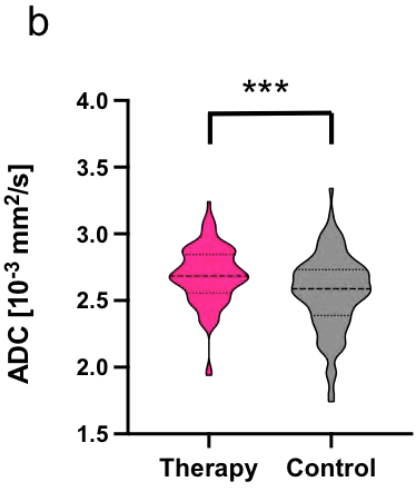

682

CT Image Findings of Double-hit Lymphoma of the Head and Neck

Inseon Ryoo MD, PhD[1], Yu Chen MD[2], Vrushab Gowda MD[3], Edwin Qiu[4], Karen Buch MD[3], Osamu Sakai MD, PhD[3]
[1]Department of Radiology, Korea University Guro Hospital, Korea University College of Medicine, Seoul, N/A, Korea, Republic of. [2]Department of Radiology, Peking Union Medical College Hospital, Chinese Academy of Medical Sciences & Peking Union Medical College, Beijing, N/A, China. [3]Department of Radiology, Massachusetts General Hospital, Harvard Medical School, Boston, MA, USA. [4]Boston University Chobanian & Avedisian School of Medicine, Boston, MA, USA

Abstract Category

Head & Neck

Purpose

Double-hit lymphoma (DHL) is a type of high-grade diffuse large B-cell lymphoma (DLBCL) with a dual rearrangement of MYC and either B-cell CLL/lymphoma 2 (BCL2) and/or BCL 6 genes. DHL is an uncommon subset accounting for 5-7 % of all DLBCLs. Patients with DHL frequently present with aggressive clinical features, and long-term survivors are rare. Previous reports showed that high-grade lymphomas such as Burkitt's lymphoma had infiltrative imaging findings of tumor mass, unlike non-double-hit DLBCLs. As DHL is also a high-grade, aggressive B-cell lymphoma, we evaluated the differences in neck CT imaging findings between patients with DHL and non-double-hit DLBCL.

Materials & Methods

This IRB-approved retrospective study included 13 DHL patients and age and sex-matched 26 non-double-hit DLBCL patients who underwent contrast-enhanced neck CTs at a tertiary hospital. The size of the largest tumor mass (measured in long and short axis), presence/absence of gross internal necrosis, infiltrative patterns, and matted patterns of lymph nodes were evaluated and compared between the DHL and non-double-hit DLBCL groups. Multiple logistic regression analyses were conducted to determine which factors independently discriminated DHL from non-double-hit DLBCL.

Results

The long and short diameters of the largest tumor mass showed no significant difference between the two groups (p = 0.503 and 0.976, respectively). The DHL patients showed more gross internal necrosis and infiltrative patterns on the neck CTs than the non-double-hit DLBCL patients (p = 0.001 and 0.008, respectively). The DHL patients had more matted patterns of lymphadenopathy than the non-double-hit DLBCL patients. However, statistical significance for this finding was not achieved (p = 0.253). The presence of gross internal necrosis independently distinguished DHL from non-double-hit DLBCL (p = 0.024; odds ratio, 16.533; 95 % confidence interval, 1.447-188.889).

Conclusion

DHL patients had more gross internal necrosis and infiltrative patterns on the neck CT than the non-double-hit DLBCL patients. Analysis of lymphoma patients' neck CT imaging findings may help predict the high-grade DHL.

References

1. Riedell PA, Smith SM. Double hit and double expressors in lymphoma: Definition and treatment. *Cancer* 2018;124:4622-4632
2. Grubstein A, Givon-Madhala O, Morgenstern S, et al. Extranodal primary B-cell non-Hodgkin lymphoma of the breast mimicking acute mastitis. *J Clin Ultrasound* 2005;33:140-142
3. Hama Y. Sporadic Burkitt's lymphoma of the axilla: CT and MR imaging findings. *BJR Case Rep* 2016;2:20150481
4. Aiken AH, Glastonbury C. Imaging Hodgkin and non-Hodgkin lymphoma in the head and neck. *Radiol Clin North Am* 2008;46:363-378, ix-x
5. Harnsberger HR, Bragg DG, Osborn AG, et al. Non-Hodgkin's lymphoma of the head and neck: CT evaluation of nodal and extranodal sites. *AJR Am J Roentgenol* 1987;149:785-791

Images/Tables

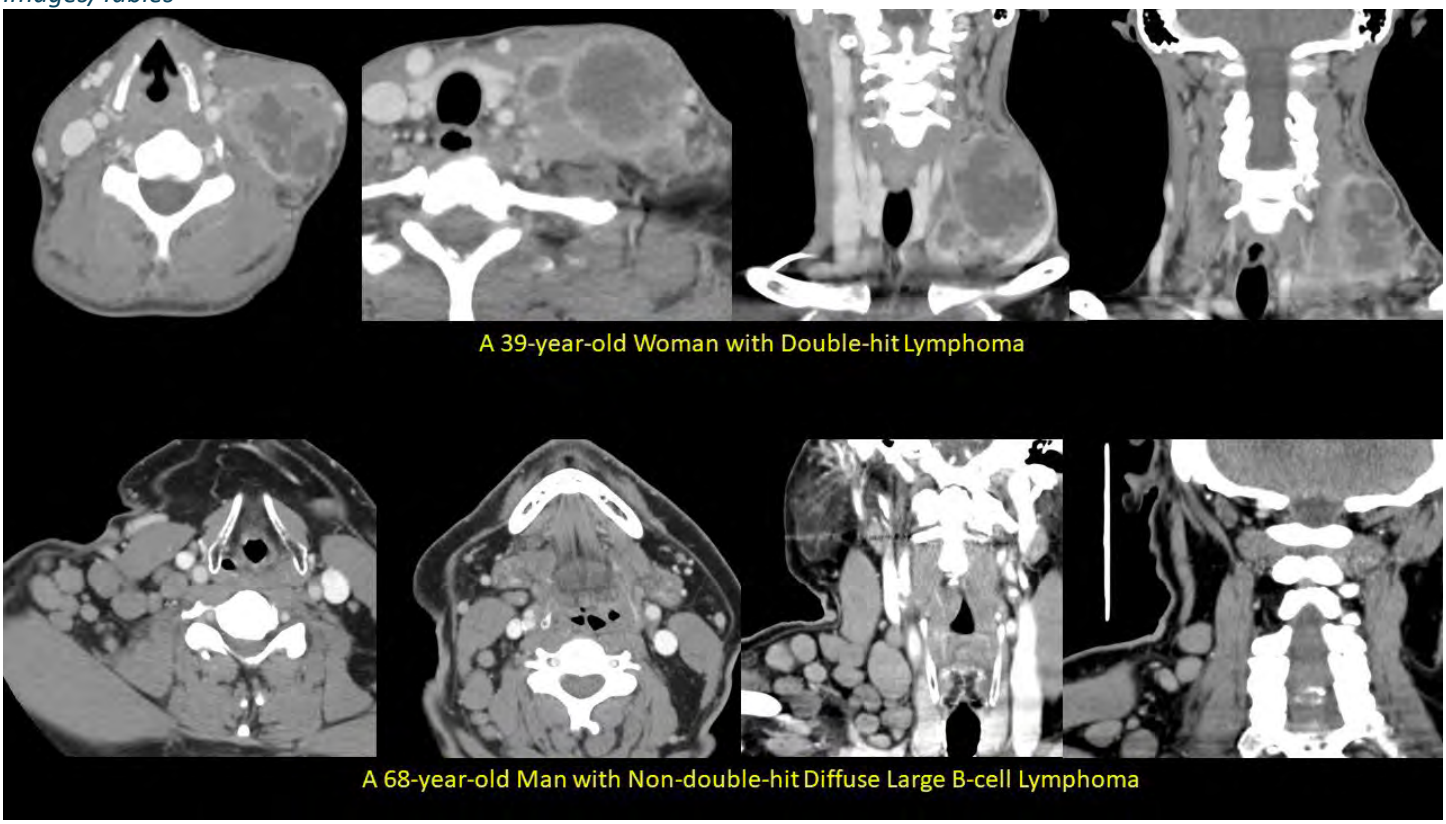

683

Multi-Reader Comparison of Standard and Joint Brain FDG PET/MRI Reconstructions for Dementia Diagnoses

Siddhant Dogra, Kevin Hsu, Timothy M Shepherd
NYU Langone Health, New York, NY, USA

Abstract Category

Functional/Advanced Imaging

Purpose

The volume of fluorodeoxyglucose-18 positron emission tomography (FDG PET) / MRI scans ordered by clinicians for indications of suspected dementia is rapidly increasing as the US population ages.[1] Keeping pace with the increasing number of requests will be challenging; one solution is to increase throughput and reduce the time taken per scan. Typically, brain FDG PET list-mode data acquisition on an integrated PET/MRI system occurs over a 20-minute interval starting at 40 minutes post-injection. Standard data reconstruction reconstructs the MRI and PET data separately ("standard reconstruction"). Techniques that produce anatomically guided PET reconstructions using structural MRI are more accurate but too time consuming for clinical practice. We have implemented a deep learning-based approach to transform PET and high-resolution MR images into an anatomically guided reconstructions ("joint reconstruction"), with comparable image quality to anatomically guided PET images and extremely fast prediction times.[2] We expect that the improved image quality of joint reconstructions will allow for shorter acquisition times that still result in diagnostic images.

Here, we performed a pilot multi-reader study to assess image and diagnostic quality of FDG PET/MRI studies reconstructed from shorter intervals in both normal and Alzheimer's disease (AD) cases.

Materials & Methods

Nine patients (three ultimately not diagnosed with any dementia and six diagnosed with AD) underwent 20-minute FDG PET data acquisition. Standard and joint PET/MRI reconstructions were made for each case using the initial 4, 2, and 1 minute of acquired PET data, ultimately resulting in 54 total studies (Figure 1).

Two fellowship-trained neuroradiologists who read brain PET/MRI in clinical practice evaluated all studies in a randomized order. For each study, each reader was asked to give a diagnosis of normal or AD, grade their confidence in

the diagnosis on a 4-point Likert scale (1 = nondiagnostic; 2 = low; 3 = average; 4 = high), and grade image quality on a 4-point Likert scale (1 = nondiagnostic; 2 = poor; 3 = average; 4 = excellent).

Results

Both readers gave the correct diagnosis for 100% of cases. Diagnostic confidence was significantly higher for the joint reconstruction compared to the standard reconstruction across all studies, as well as when specifically comparing just among 2-minute reconstructions and 1-minute reconstructions (Figure 2). Confidence was also higher for comparing 4-minute reconstructions but did not reach statistical significance. Image quality was significantly higher for the joint reconstruction across all studies as well as when separately compared between 4-minute, 2-minute, and 1-minute reconstructions (Figure 3).

Conclusion

Both readers were able to make the correct diagnoses in all cases even when reconstructions used only the first minute of acquired PET data (a simulated 95% time *or dose* reduction for PET). We did see significant improved diagnostic confidence and perceived image quality with joint reconstructions versus standard reconstructions, most pronounced when using the initial 1-2 minutes of data. Although a preliminary study, our results support the hypothesis that we could shorten the interval we used for joint reconstruction. We are currently expanding our work to more subjects, time intervals, dementias and raters.

References

1. Olivari BS, French ME, McGuire LC. The Public Health Road Map to Respond to the Growing Dementia Crisis. *Innov Aging* 2020;4:igz043

2. Schramm G, Rigie D, Vahle T, et al. Approximating anatomically-guided PET reconstruction in image space using a convolutional neural network. *Neuroimage* 2021;224:117399

Images/Tables

Figure 1. Representative images of a patient with Alzheimer's disease who underwent FDG PET/MRI. The top row shows joint reconstructions using only the initial 4, 2, and 1 minutes of list-mode data. The bottom row shows standard reconstructions using the same intervals of list-mode data.

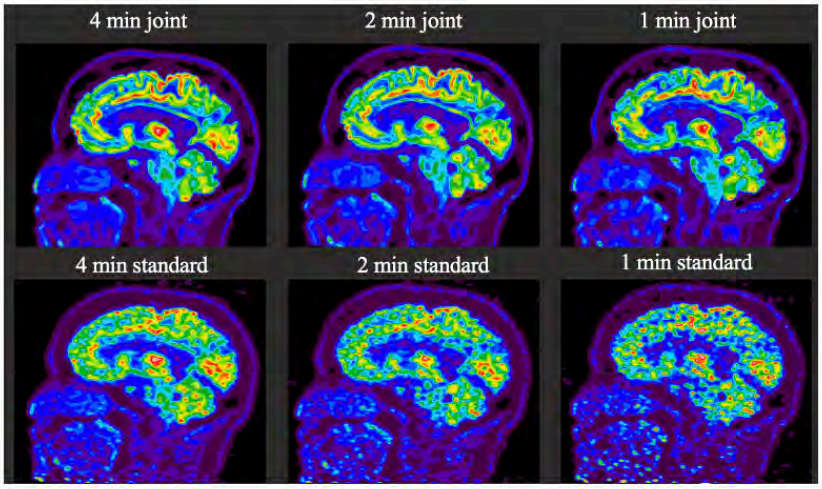

Figure 2. Diagnostic confidence and image quality comparisons between joint and standard reconstructions according to time interval as well as overall. The difference in diagnostic confidence using 4 minutes did not reach statistical significance while all other differences were statistically significant at p-value less than 0.05.

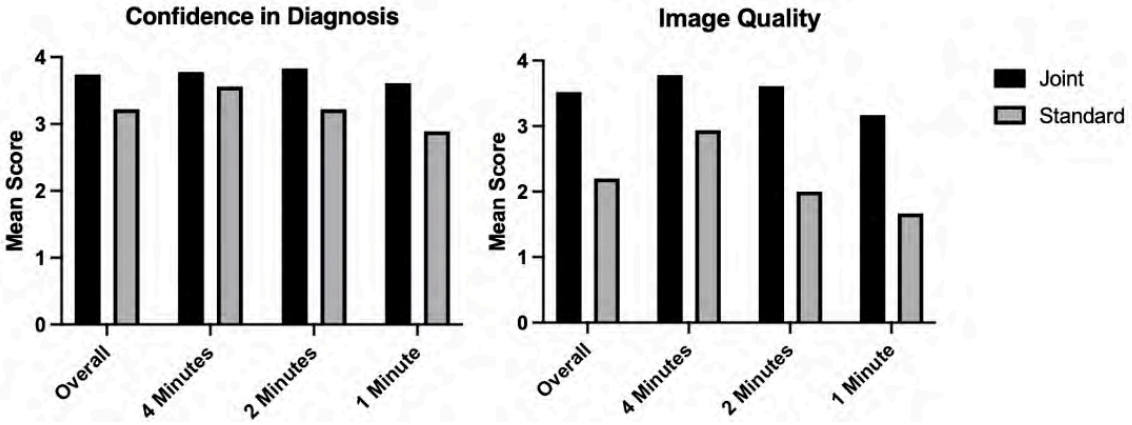

692

Comprehensive Radiomics and Radiogenomics Analysis of Skull Base Chordoma: Classifying Novel Radiomic Subgroups and Predicting Genetic Signatures and Clinical Outcomes Using Advanced Classifiers and Feature Selection Techniques

Mohammadreza Amjadzadeh MD[1], Zachary C Gersey MD[2], Serafettin Zenkin MD[3], Priyadarshini Mamindla[1], Murat Ak MD[3], Vishal Peddagangireddy[1], Tritan Plute[4], Hussein Abdallah[4], Nallammai Muthiah[5], Eric W. Wang MD[6], Carl H. Snyderman MD[6], Paul A. Gardner MD[7], Georgios Zenonos MD[1], Rivka R Colen MD[1]

[1]Hillman Cancer Center, University of Pittsburgh Medical Center, Pittsburgh, Pennsylvania, USA. [2]Department of Neurological Surgery, Pittsburgh, Pennsylvania, USA. [3]Hillman Cancer Center, University of Pittsburgh Medical Center, Pittsburgh, PA, USA. [4]University of Pittsburgh School of Medicine, Pittsburgh, PA, USA. [5]Department of Neurological Surgery, Pittsburgh, PA, USA. [6]Department of Otolaryngology, University of Pittsburgh, Pittsburgh, PA, USA. [7]Department of Neurosurgery, University of Pittsburgh Medical Center, Pittsburgh, PA, USA

Abstract Category

AI/Informatics

Purpose

Evaluation of different radiomic classifiers and feature selection methods for predicting Overall Survival (OS), Progression-Free Survival after Surgery (PFSS), and chromosomal subgrouping in Skull Base Chordoma (SBC) patients.

Materials & Methods

We studied 193 patients (mean age: 43.61 years±19.08[SD]; 56% male; 104: treatment- naïve) who underwent 269 resections, with preoperative MRIs available for 250 cases. After co-registration of axial contrast-enhanced T1-weighted (T1POST) and pre-contrast T2 sequences, primary tumors were segmented using 3D-Slicer. Following skull stripping, Intensity-level histograms and gray-level co-occurrence matrix (GLCM) were extracted for each region of interest using our in-house radiomic extraction pipeline, resulting in 800 radiomic features per voxel of interest (400 each sequence: 10 intensity-level, 195 GLCM, 195 volume-dependent features).

Univariate Cox regression was performed for OS and PFSS to identify significant features, followed by multivariate Cox regression for confounder adjustment. Kaplan-Meier curves were generated to compare survival outcomes based on feature intensities.

Classifiers (SVM, Random Forest, Naïve Bayas, Decision Tree, eXtreme Gradient Boosting [XGBoost]) combined with feature selection methods (LASSO, Ridge, ElasticNet) were applied for two-way classification of OS and PFSS, and three-way classification of molecular subgroups predictions. We performed an unsupervised analysis through consensus clustering techniques to further correlate molecular subgroups with PFSS.

Results

Univariate analysis of features from 104 treatment-naïve scans identified 32 significant features for OS and 38 for PFSS. Multivariate analysis yielded three significant features (T1POST-F39, T2-FOF10, T2-F191) for predicting OS, and three features (T1POST-FV36, T1POST-F172, T2-FOF10) for predicting PFSS. Kaplan-Meier revealed that low presence of T1POST-F39 was significantly correlated with poorer OS ($p=0.042$), while high presence of T1POST-F172 was significantly associated with better PFSS ($p=0.017$).

XGBoost with ElasticNet applied on features from 104 treatment-naïve scans achieved a high accuracy of 90.91%, sensitivity of 100%, specificity of 80%, and AUC of 83.33% utilizing 12 radiomic features for predicting OS. XGBoost with Ridge, applied on features from 250 scans yielded an accuracy of 80.77%, sensitivity of 75%, specificity of 85.71%, and AUC of 80.36% using 8 radiomic features for predicting PFSS.

For molecular subgroup prediction (one vs others), XGBoost with ElasticNet, achieved an accuracy of 100% for group A, 80% for group B, and 80% for group C using 19 radiomic features.

Unsupervised clustering using 400 T1POST features indicated two optimal clusters through 22 clustering paradigms, elbow method, and consensus clustering. Kaplan-Meier indicated cluster one had longer PFSS ($p < 0.01$). Chromosomal analysis showed cluster two having significantly higher mean in both 9p21 ($p < 0.01$) and 1p36 ($p < 0.05$) deletions. T2 scans followed the same process, confirming two clusters, with cluster one having longer PFSS ($p < 0.05$) and cluster two showing a higher mean in 9p21 deletions. Combined T1POST and T2 analysis reaffirmed two clusters, with cluster one showing better PFSS ($p < 0.01$) and cluster two showing a higher mean in 9p21 deletions.

Conclusion

Radiomics analysis using XGBoost with various feature selection methods, achieved the highest classification accuracy, indicating its robustness in handling two-way and three-way classification problems inherent in our dataset. These findings suggest XGBoost's ability to model complex relationships, making it a suitable classifier.

References

Zinn PO, Majadan B, Sathyan P, Singh SK, Majumder S, Jolesz FA, Colen RR. Radiogenomic mapping of edema/cellular invasion MRI-phenotypes in glioblastoma multiforme. PLoS One. 2011;6(10). DOI: 10.1371/journal.pone.0025451

693

Subjective Adjudication Compared to Objective Quantification of Plaque Enhancement

Carlos Dier MD[1], Sultan Alhajahjeh MD[1], Abdallah Alqudah MD[1], Andres Gudino MD[1], Navami Shenoy BA[1], Elena Sagues MD[1], Martin Cabarique MD[1], Sebastian Sanchez MD[2], Bruno A Policeni MD[1], Minako Hayakawa MD[1], Edgar A Samaniego MD, MS[1]

[1]University of Iowa, Iowa, IA, USA. [2]Yale University, New Haven, CT, USA

Abstract Category

Adult Brain

Purpose

In clinical practice, plaque enhancement is assessed subjectively, which can introduce potential bias. Three-dimensional voxel-based signal intensity (SI) quantification offers an objective measure of plaque enhancement distribution. The inter-reader agreement and the reliability of a consensus-based subjective determination of plaque enhancement were evaluated in comparison to this objective method.

Materials & Methods

Patients with stroke secondary to intracranial atherosclerotic disease were prospectively assessed using 7T high-resolution MRI. Subjective assessment: two adjudicators determined that a plaque was enhancing if its degree of enhancement was greater than that of the pituitary stalk, with any disagreements resolved by an experienced neuroradiologist. For objective assessment, the distribution of SI across the plaque was normalized to that of the corpus callosum using a 3D voxel-based in-house code. The normalized mean SI on post-contrast T1 MRI was defined as the mean enhancement ratio (MER).[1] A plaque was classified as objectively "enhancing" if the MER exceeded one. Inter-rater agreement was analyzed using the kappa coefficient, and the agreement between the subjective and objective determinations was also evaluated with kappa statistics. Univariate regression analysis was conducted to identify which morphological characteristics influenced the subjective adjudication of plaque enhancement.

Results

A total of 41 patients with 75 plaques were evaluated. The inter-rater agreement for the presence of enhancement was minimal (k = 0.34). After consensus, 43% of plaques (32/75) were classified as "enhancing", while 57% (43/75) were classified as "non-enhancing". There was moderate agreement between subjective consensus adjudication and objective MER (k = 0.39, $p < 0.001$). Subjective assessment was more likely to reliably adjudicate enhancement when evaluating stenotic plaques (OR 1.04; 95% CI 1.01 – 1.08, *p 0.02*) and plaques with positive remodeling (OR 2.20; 95% CI 1.17 – 4.54, *p* 0.021). However, it was less likely to reliably determine enhancement for plaques in the posterior circulation (OR 0.23; 95% CI 0.06–0.73, *p* 0.018), despite these plaques being objectively classified as "enhancing."

Conclusion

Subjective assessment of plaque enhancement exhibits poor inter-rater agreement and moderate agreement when compared to a 3D voxel-based method for quantifying plaque enhancement. This voxel-based approach may be particularly useful for evaluating enhancement in non-stenotic plaques without remodeling, particularly in the posterior circulation.

References

Sanchez S, Raghuram A, Fakih R, et al. 3D Enhancement Color Maps in the Characterization of Intracranial Atherosclerotic Plaques. *AJNR Am J Neuroradiol*. 2022;43:1252-1258. doi: 10.3174/ajnr.A7605

Images/Tables

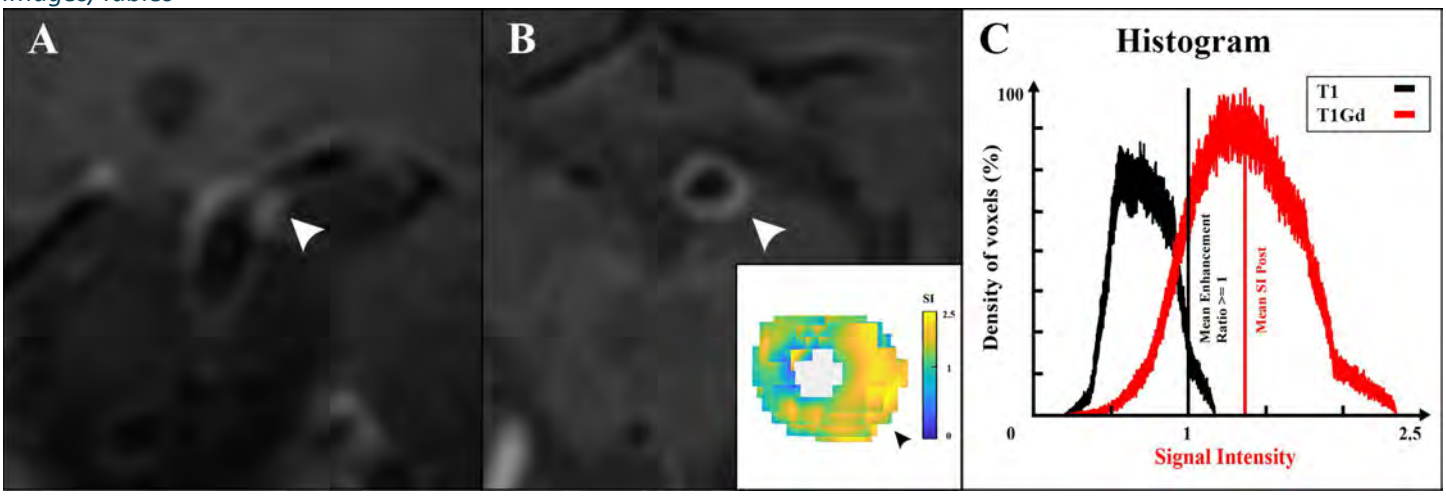

698

Three-Dimensional Voxel-Based Signal Intensity Quantification of Symptomatic Intracranial Plaques

Carlos Dier MD[1], Andres Gudino MD[1], Navami Shenoy BA[1], Elena Sagues MD[1], Martin Cabarique MD[1], Gustavo Chiriboga MD[1], Shubhangi Setia MD[1], Sebastian Sanchez MD[2], Connor Aamot BS[1], Minako Hayakawa MD[1], Bruno A Policeni MD[1], Edgar A Samaniego MD, MS[1]

[1]University of Iowa, Iowa, IA, USA. [2]Yale University, New Haven, CT, USA

Abstract Category

Adult Brain

Purpose

High-resolution MRI facilitates the identification of symptomatic intracranial plaques following gadolinium administration. Current objective assessment methods depend on 2D multiplanar imaging, which can introduce bias due to manual sampling of regions of interest. Voxel-based signal intensity (SI) quantification may enhance the evaluation of these plaques.

Materials & Methods

Patients with stroke or transient ischemic attacks due to intracranial atherosclerotic disease underwent prospective imaging with 7T high-resolution MRI. Three-dimensional plaque segmentations were generated using 3D Slicer, and the SI distribution within plaques was analyzed using an in-house MATLAB 2020a code. This method normalized SI to the corpus callosum (CC) and generated voxel-based enhancement colormaps, correlating with pre- and post-contrast SI curves. Three plaque enhancement metrics were obtained: mean enhancement ratio (MER: mean SI post / mean SI CC), gadolinium uptake ([mean SI post - mean SI pre] / standard deviation SI pre), and contrast-enhancement ratio (CER: [mean SI post - mean SI pre] / mean SI post). Plaques were classified as symptomatic if they were located in the ipsilateral vascular territory corresponding to the localized symptoms.[1] The Mann-Whitney test was used to compare enhancement metrics between symptomatic and asymptomatic plaques, and univariate regression analysis was conducted to identify predictors of symptomatic plaques. An ROC curve analysis was conducted to evaluate the accuracy of plaque enhancement metrics in detecting symptomatic plaques.

Results

A total of 41 patients with 75 plaques were analyzed, of which 40 plaques (53%) were classified as symptomatic. Symptomatic plaques demonstrated significantly different enhancement patterns compared to asymptomatic plaques, including MER (1.16 ± 0.48 vs. 0.97 ± 0.33, $p\ 0.03$), gadolinium uptake ratio (5.6 ± 4.13 vs 3.43 ± 2.48, $p < 0.001$), and CER (1.09 ± 0.69 vs. 0.77 ± 0.67, $p\ 0.01$). Symptomatic plaques were more likely to show increased gadolinium uptake ratio (OR 1.25, 95 CI 1.05 – 1.49, $p\ 0.01$). Although not statistically significant, there was a trend toward higher MER (OR 3.07, 95 CI 0.92 – 10.26, $p\ 0.06$) and CER (OR 2.03, 95 CI 0.95 – 4.33, $p\ 0.06$) in symptomatic plaques. A gadolinium uptake ratio above 3.7 demonstrated an area under the curve of 0.70 for detecting symptomatic plaques.

Conclusion

Voxel-based SI quantification may enhance the symptomatic stratification of intracranial plaques by objectively identifying increased enhancement.

References

Sanchez S, Raghuram A, Fakih R, et al. 3D Enhancement Color Maps in the Characterization of Intracranial Atherosclerotic Plaques. *AJNR Am J Neuroradiol*. 2022;43:1252-1258. doi: 10.3174/ajnr.A7605

Images/Tables

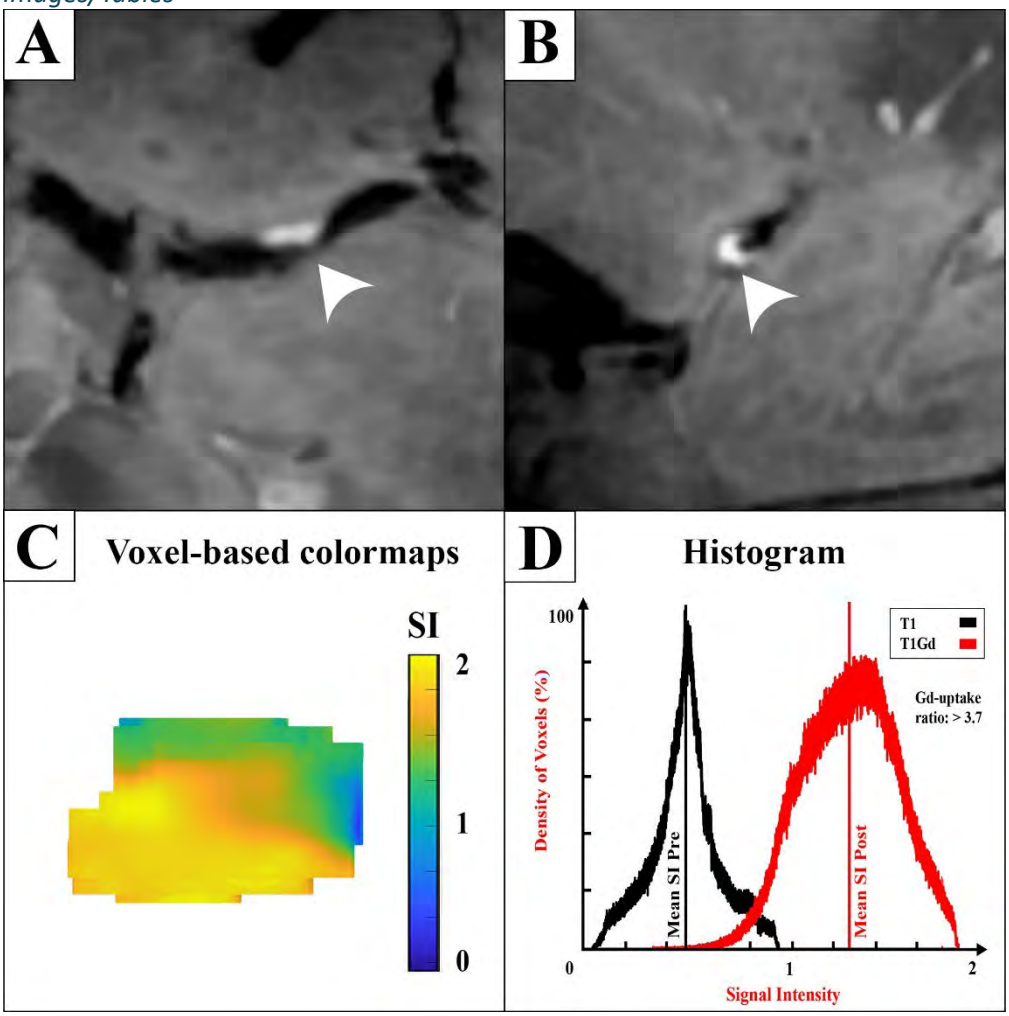

699

Exploring the Potential of Multimodal Large Language Models in Classifying Spinal Degenerative Conditions: A Comparative Analysis

Dhruv Patel BHSc, Jack Lott MSc
Queen's University, Kingston, Ontario, Canada

Abstract Category

AI/Informatics

Purpose

MRIs are commonly used in the evaluation of patients with low back pain, often revealing underlying spinal degeneration that is critical to diagnose for effective management. Deep learning algorithms have enhanced computer-aided diagnosis of such conditions but require extensive model training, and face interpretability issues due to their “black box” nature. Multimodal Large Language Models (LLMs), such as GPT-4o, offer a unique solution to these challenges without extensive training through its ability to interpret MRIs and perform visual question answering. Our research aims to assess the capabilities of multimodal LLMs, such as ChatGPT, Gemini and Claude, for diagnosis and severity predictions when applied to a database of degenerative spine MRIs.

Materials & Methods

Axial T2 and Sagittal T1 and T2 lumbar spinal MRIs were obtained from the RSNA 2024 Lumbar Spine Degenerative Classification database, covering five spine conditions (right and left neural foraminal narrowing, right and left subarticular stenosis, and spinal canal stenosis) across four severity levels: mild, moderate, severe, and normal. A balanced dataset of 1000 images (100 per condition and severity) was created. GPT-4o, Gemini 1.5 Pro, and Claude 3.5 Sonnet were prompted to diagnose a spinal degenerative condition and rate severity using a standardized Zero-Shot Chain-of-Thought schema. Additionally, a fine-tuned GPT-4o model, trained on a separate 1000-image dataset from the

original source, was evaluated. Model outputs were compared to established diagnoses, with performance measured by accuracy, sensitivity, precision, and F1-score.

Results

Baseline LLM performance in disease classification demonstrated limited overall accuracy (21-24%) and low F1 scores (0.09-0.14). Claude and GPT-4o showcased stronger performances for severity assessment, with accuracies of 49-51% and F1 scores of 0.46-0.49. The fine-tuned GPT-4o model outperformed baseline models, achieving the highest diagnostic and severity assessment accuracy (39% and 52% respectively), and particularly excelled in detecting left-sided conditions. When conducting sub-analyses, Claude exhibited better results with more severe cases, while GPT-4o showed stronger results in classifying moderate severity cases. While all models exhibited a bias towards predicting spinal canal stenosis, this was most pronounced in Claude. Interestingly, the fine-tuned GPT-4o model in the orientation-agnostic condition —where left and right distinctions were ignored—showed a notable increase in both accuracy and F1 scores (79.5% and 0.7131 respectively).

Conclusion

To our knowledge, this study represents the first application of multimodal LLMs to the classification of spinal pathologies on MRI. Our analysis shows that, despite promising outcomes in specific cases, the overall accuracy of multimodal LLMs remains too limited to be considered a reliable tool for the interpretation of MRIs in the context of degenerative spinal conditions.

References

1) Brinjikji W, Luetmer PH, Comstock B, et al. Systematic literature review of imaging features of spinal degeneration in asymptomatic populations. *AJNR Am J Neuroradiol*. 2015;36(4):811-816. doi:10.3174/ajnr.A4173

2) Zhang D, Ma Z, Gong R, et al. Using natural language processing (GPT-4) for computed tomography image analysis of cerebral hemorrhages in radiology: retrospective analysis. *J Med Internet Res*. 2024;26
. doi:10.2196/58741

3) Hayden N, Gilbert S, Poisson LM, et al. Performance of GPT-4 with vision on text- and image-based ACR diagnostic radiology in-training examination questions. *Radiology*. 2024;312(3). doi:10.1148/radiol.240153

4) Richards T, Talbott J, Ball R, et al. RSNA 2024 Lumbar Spine Degenerative Classification. http://www.kaggle.com/competitions/rsna-2024-lumbar-spine-degenerative-classification. Accessed November 6, 2024.

Images/Tables

Table 1: Condition Metrics for Spine Degeneration Research Models

Model	Accuracy	Precision	Recall	F1 Score	Sensitivity
GPT	0.2362	0.5224	0.2362	0.1439	0.2362
GPT_FineTune	0.3902	0.2229	0.3902	0.2682	0.3902
Claude	0.2123	0.2367	0.2123	0.0965	0.2123
Gemini	0.2352	0.0916	0.2352	0.1282	0.2352

Table 2: Severity Metrics for Spine Degeneration Research Models

Model	Accuracy	Precision	Recall	F1 Score	Sensitivity
GPT	0.4870	0.5218	0.4870	0.4605	0.4870
GPT_FineTune	0.5245	0.5255	0.5245	0.5240	0.5245
Claude	0.5088	0.5148	0.5088	0.4894	0.5088
Gemini	0.2674	0.7366	0.2674	0.2541	0.2674

Table 3: Orientation-agnostic Condition Metrics for Spine Degeneration Research Models

Model	Accuracy	Precision	Recall	F1 Score	Sensitivity
GPT	0.2799	0.7089	0.2799	0.2142	0.2799
GPT_FineTune	0.7950	0.6586	0.7950	0.7131	0.7950
Claude	0.2216	0.4289	0.2216	0.1124	0.2216
Gemini	0.2758	0.1826	0.2758	0.1939	0.2758

Figure 1: LLM Diagnosis Pipeline

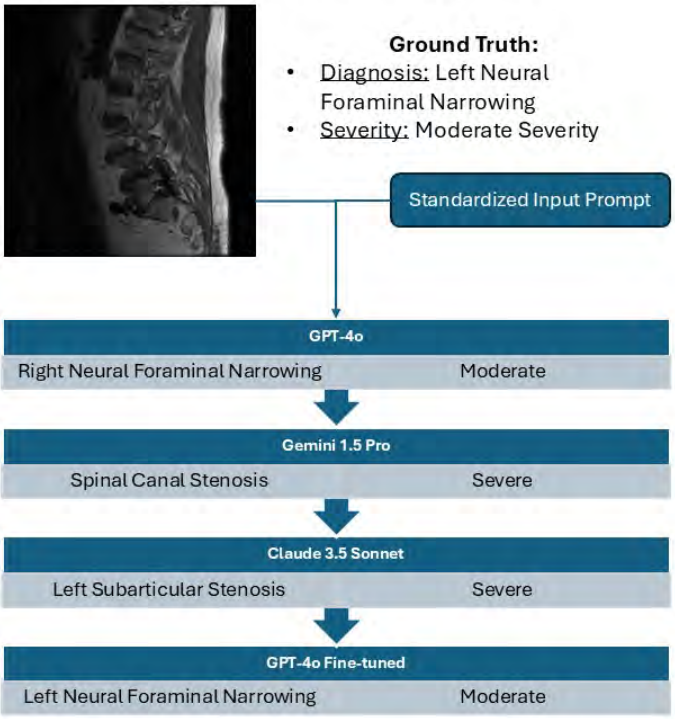

701

Inter-Rater Variability of Manual Brain Metastasis Measurements and Role of PACS-Based AI Tool for Measurement Improvement

David Weiss[1], Nazanin Maleki MD[2], Cornelius Deuschl MD[3], Klara Osenberg[1], Sven Schoenherr PhD[4], Julian Lautenschlager MS[4], Wolfgang Holler MS[4], Malte Westerhoff PhD[4], Spyridon Bakas PhD[5], Ajay Malhotra MBBS, MD, MMM[1], Nagaraj Moily MD, PhD, MBA, MAM[1], Veronica Chiang MD[6], Sanjay Aneja MD[7], Elizabeth Schrickel MD[8], Fatima Memon MD[9], MingDe Lin PhD[10], Mariam Aboian MD, PhD[2]

[1]Department of Radiology and Biomedical Imaging, Yale School of Medicine, New Haven, CT, USA. [2]Department of Radiology, Children's Hospital of Philadelphia, Philadelphia, PA, USA. [3]Department of Diagnostic and Interventional Radiology and Neuroradiology, Essen University Hospital, Essen, North Rhine-Westphalia, Germany. [4]Visage Imaging, GmbH, Berlin, Berlin, Germany. [5]Department of Pathology, Indiana University, Indianapolis, IN, USA. [6]Department of Neurosurgery, Yale School of Medicine, New Haven, CT, USA. [7]Department of Therapeutic Radiology, Yale School of Medicine, New Haven, CT, USA. [8]Department of Neuroradiology, Wexner Medical Center, Ohio State University, Columbus, OH, USA. [9]Carolina Radiology, Myrtle Beach, SC, USA. [10]Visage Imaging, Inc., San Diego, CA, USA

Abstract Category

AI/Informatics

Purpose

Accurate measurement, assessment, and reporting of brain metastases (BM) are prerequisites for precision neuro-oncological care[1, 2]. However, these processes are laborious and exhibit inter-observer variability[3-5]. This study aimed to evaluate the differences between manual BM measurements performed by two board-certified neuroradiologists (R1 and R2) on pre- and post-Gamma Knife radiosurgery (GKR) patients and the role of an AI-enabled Lesion Tracking Tool (AI-LTT) for measurement improvement.

Materials & Methods

In this retrospective study, GKR planning and follow-up images of patients with BM who underwent GKR at our institution were de-identified and examined on a research instance of our PACS (AI Accelerator, Visage Imaging, Inc.). R1 and R2 displayed up to eight longitudinal studies of each patient chronologically and measured maximum BM diameters (DMAX) manually on T1 post-gadolinium sequences of the same dataset while reviewing other available MR sequences of each patient in manual workflow. If a BM was detected from only one reader, third board-certified neuroradiologist verified lesion and determined DMAX to define final reference standard annotations. Manual measurements from R1 and R2 were recorded and compared. Clinically relevant characteristics of lesions that only one of the two readers detected were recorded. In AI-LTT workflow, the tool automatically selected, displayed, and 3D registered T1 gadolinium-enhanced MR sequences in up to eight longitudinal studies. AI-LTT-integrated segmentation model, validated on 156 MRIs, automatically 3D-segmented the BMs from which DMAX were extrapolated per RANO-BM criteria and presented in a chart. AI measurements were revised by R1 and R2 as needed. Time and number of mouse clicks needed for each patient from study open until measurement completion were recorded separately for both readers and workflows.

Results

A total of 50 studies in 10 patients were included in workflow experiments. Mean numbers of seconds and mouse clicks of R1 and R2 for manual measurement of each patient were 708.8vs.648.1 seconds (P=0.853) and 201.2vs.201.7 clicks (P=0.971). Mean numbers of seconds and clicks per lesion of R1 and R2 for each patient were 106.4vs.100.8 seconds per lesion (P=0.684) and 29.0vs.29.3 clicks per lesion (P=0.912) (Fig1). Mean absolute and relative differences of recorded DMAX measurements were 1.733mm and 0.452, respectively. Intra-class correlation coefficient was 0.922 and Spearman correlation coefficient was 0.881. Both readers disagreed on 72 lesions regarding presence of a metastatic brain tumor. Here, mean DMAX was 2.74±1.56mm (Table1, Fig2). In loading and displaying of studies, AI-LTT accelerated the workflow by providing mean reduction of 25.1% and 30.8% in seconds and 21.0% and 27.0% in clicks for R1 and R2, respectively. In manual BM measurement workflow, R1 needed, on average, 665.8 seconds (191.2 clicks) and R2 602.9 seconds (191.7 clicks), whereas R1 needed, on average, 264.6 seconds (47.5 clicks) and R2 403.0 seconds (63.6 clicks) in AI-LTT workflow (Fig3). In validation of segmentation model, 156 studies in 40 patients were included. In BM detection, precision and sensitivity were 0.96 and 0.91 for lesions ≥ 5mm (Table2).

Conclusion

The findings of this study confirm inter-observer variability of manual BM measurements and the opportunity for an AI-LTT-facilitated workflow that can help improve the measurement process.

References

1. Le Rhun, E., et al., *EANO-ESMO Clinical Practice Guidelines for diagnosis, treatment and follow-up of patients with brain metastasis from solid tumours.* Ann Oncol, 2021. **32**(11): p. 1332-1347.
2. Bink, A., et al., *Structured Reporting in Neuroradiology: Intracranial Tumors.* Front Neurol, 2018. **9**: p. 32.
3. Nobel, J.M., K. van Geel, and S.G.F. Robben, *Structured reporting in radiology: a systematic review to explore its potential.* Eur Radiol, 2022. **32**(4): p. 2837-2854.
4. Bauknecht, H.C., et al., *Intra- and interobserver variability of linear and volumetric measurements of brain metastases using contrast-enhanced magnetic resonance imaging.* Invest Radiol, 2010. **45**(1): p. 49-56.
5. Erasmus, J.J., et al., *Interobserver and intraobserver variability in measurement of non-small-cell carcinoma lung lesions: implications for assessment of tumor response.* J Clin Oncol, 2003. **21**(13): p. 2574-82.

Images/Tables

A

Parameter	Value
BM detection – neuroradiologist 1 (R1)	
Precision	1
Sensitivity	0.953
F1-Score	0.975
BM detection – neuroradiologist 2 (R2)	
Precision	1
Sensitivity	0.850
F1-Score	0.919
Mean absolute difference (R1-R2) ± SD (in mm)	**1.733 ± 1.878**
95% CI	[-1.948, 5.414]
Mean relative difference (R1-R2) ± SD	**0.452 ± 0.845**
95% CI	[-1.204, 2.108]
Intra-class correlation coefficient	**0.922**
Spearman correlation coefficient	**0.881**

B

Tumor characteristic	n = 72
Anatomical location	
Cerebellar (%)	33 (45.8)
Parietal lobe (%)	16 (22.2)
Temporal lobe (%)	9 (12.5)
Pons (%)	7 (9.7)
Frontal lobe (%)	3 (4.2)
Occipital lobe (%)	3 (4.2)
Thalamus (%)	1 (1.4)
DMAX (in mm)	
Mean ± SD	2.74 ± 1.56
Field strength of MRI scanner	
1.5 T (%)	58 (80.6)
3 T (%)	14 (19.4)
Slice thickness of MRI study (in mm)	
Mean ± SD	1.63 ± 0.66
On SRS planning study, irradiated (%)	**2 (2.8)**
Increase (%)	1 (50)
Decrease (%)	1 (50)
On SRS planning study, non-irradiated (%)	**2 (2.8)**
Decrease (%)	2 (100)
On follow-up study (%)	**37 (51.4)**
Increase (%)	12 (32.4)
Stable (%)	11 (29.7)
Decrease (%)	14 (37.9)
On last follow-up study (%)	**31 (43.0)**

Table 1. Inter-rater variability in measuring BMs and characterization of indeterminate brain lesions.
(A) Based on the two-dimensional measurements performed by the two neuroradiologists, the inter-observer variability in detecting and measuring 352 cerebral metastases was analyzed. A total of 72 lesions that were detected by only one of the two readers are characterized in Table **B**.

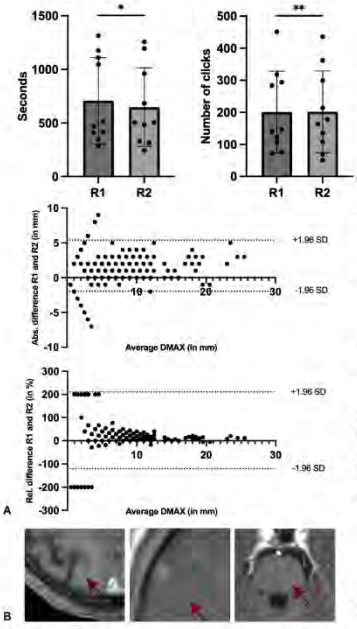

Figure 2. Inter-rater variability in measuring BMs and imaging of indeterminate lesions.
(A) The absolute and relative differences of the 2D measurements performed by R1 and R2 are visualized. **(B)** Three representative examples of the 72 indeterminate BMs are outlined on axial planes.

Figure 1. Comparison of manual BM measurement effort by two neuroradiologists.
The seconds and number of mouse clicks (correlation with lesions per patient) needed for each patient from study open until measurement completion were recorded separately for both readers. * = P = 0.853; ** = P = 0.971; *** = P = 0.684; **** = P = 0.912

Parameter	All identified lesions	Lesions ≥5mm	Lesions <5mm
True positive lesions	501	366	135
False negative lesions	106	35	71
False positive lesions	43	15	28
Precision	0.92	0.96	0.83
Sensitivity	0.82	0.91	0.66
F1-Score	0.87	0.93	0.73

Parameter	Mean	Standard deviation	Variance
Dice Similarity Coefficient	0.743	0.254	0.065

Table 2. Performance metrics of segmentation model. The accuracy in BM detection and 3D segmentation is outlined.

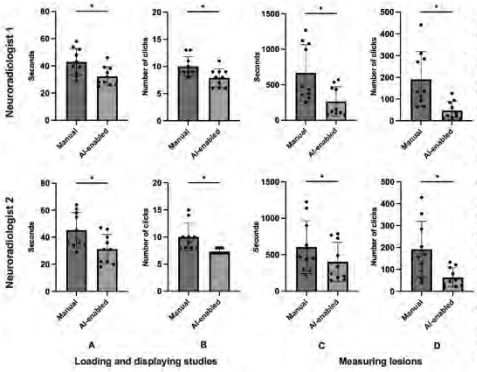

Figure 3. Comparison of manual vs. AI-LTT-assisted loading, displaying, and measuring of longitudinal BM studies. The time and necessary clicks of the fully manual workflow were compared with the AI-LTT-assisted workflow. A significant reduction across all bar graphs was demonstrated. * = $P < 0.01$

715

MRI Brain Biomarkers in Predicting Late-Onset Epilepsy in Cerebral Amyloid Angiopathy

Jisoo Kim MD[1], Michael Buckner MD[2], Majed Alzahrany MD[3], Alexis Hankerson MPH[1], Geoffrey S Young MD[1], Rani Sarkis MD MSc[1]

[1]Brigham and Women's Hospital, Boston, MA, USA. [2]South Shore Hospital, Weymouth, MA, USA. [3]King Abdulaziz University, Jeddah, n/a, Saudi Arabia

Abstract Category

Adult Brain

Purpose

Cerebral amyloid angiopathy (CAA) results from beta-amyloid deposition in the walls of the leptomeningeal and cortical arteries and arterioles of the brain. It often manifests with hemorrhagic lesions including lobar macro and microhemorrhage, subarachnoid hemorrhage, and/or superficial siderosis. CAA is also associated with a higher rate of late-onset epilepsy (1) ,(2). In this study we sought to identify neuroimaging features associated with interictal epileptiform abnormalities (IEAs) on EEG and the development of late-onset epilepsy in those with CAA.

Materials & Methods

Patients with assigned ICD codes for CAA, and procedure codes for EEG, between 2012 and 2023, were identified retrospectively from our institutional research patient data registry. We excluded patients with inflammatory CAA and

patients without brain MRI in our PACS. A neuroradiology fellow assessed each MRI using the Boston criteria v2 (3), Microbleed Anatomic Rating Scale (MARS) (4), and Fazekas scale (5). A faculty board-certified neuroradiologist reviewed challenging cases. The following variables were extracted - number of infratentorial microhemorrhage (brainstem, cerebellum), deep microhemorrhage (basal ganglia, thalamus, internal capsule, external capsule, corpus callosum, deep peri-ventricular white matter), cortical and juxtacortical microhemorrhage, subcortical microhemorrhage; focal or multifocal superficial siderosis; number of peri-vascular spaces in the centrum semiovale and basal ganglia; Fazekas score and presence of multifocal subcortical white matter pattern. Fisher's Exact and Chi Squared tests were used as appropriate.

Results

Of 59 patients meeting eligibility criteria, 36 (61.0%) were female. Average age at MRI and EEG was 76.5 ± 7.1 years. Average time between MRI and EEG was 1.5 7.6 months. 49/59 (83%) of EEGs were performed as routine, 7/59 (12%) long-term inpatient monitoring, and 3/59 (5%) ambulatory. EEG abnormalities seen in 51/59 (86%) patients included IEAs in 13/19 (22%) and diagnosis of epilepsy in 23 (39%). Focal superficial siderosis was the only imaging marker significantly correlated with diagnosis of epilepsy (p=0.033, OR 3.88). Subgroup analysis of routine EEGs revealed presence of infratentorial microhemorrhages (p=.0.042, OR 4.67) and cortical microhemorrhages (p=0.025, OR with correction 7.22), to be significant predictors of epilepsy in this group.

Conclusion

Among CAA patients who underwent an EEG, presence of focal superficial siderosis was significantly correlated with diagnosis of epilepsy. In the subgroup of patients diagnosed on routine EEG, presence of cortical and infratentorial microhemorrhages both correlated with epilepsy. While it is possible that both focal hemorrhage and seizures were caused by a third factor, these findings suggest a strong association of focal small hemorrhages with seizures in CAA. Further study is indicated to confirm these findings in CAA; look for similar associations in patients with focal hemorrhage from microvascular disease, trauma, etc; investigate variation in the association related to hemorrhage location; and investigate causality.

References

1. Marsico O, Pascarella A, Gasparini S, et al. The hidden link between late-onset seizures and cerebral amyloid angiopathy: A case-control study. Epilepsia Open. 2024 Oct;9(5):1723-1730. doi: 10.1002/epi4.12976. Epub 2024 Jul 6.
2. Tabaee Damavandi P, Storti B, Fabin N, et al. Epilepsy in cerebral amyloid angiopathy: an observational retrospective study of a large population. Epilepsia. 2023 Feb;64(2):500-510. doi: 10.1111/epi.17489. Epub 2023 Jan 2.
3. Charidimou A, Frosch MP, Al-Shahi Salman R, et al; International CAA Association. Advancing diagnostic criteria for sporadic cerebral amyloid angiopathy: Study protocol for a multicenter MRI-pathology validation of Boston criteria v2.0. Int J Stroke. 2019 Dec;14(9):956-971. doi: 10.1177/1747493019855888. Epub 2019 Sep 12.
4. Gregoire SM, Chaudhary UJ, Brown MM, et al. The Microbleed Anatomical Rating Scale (MARS): reliability of a tool to map brain microbleeds. Neurology. 2009 Nov 24;73(21):1759-66. doi: 10.1212/WNL.0b013e3181c34a7d.
5. Fazekas F, Chawluk JB, Alavi A, et al. MR signal abnormalities at 1.5 T in Alzheimer's dementia and normal aging. AJR Am J Roentgenol. 1987 Aug;149(2):351-6. doi: 10.2214/ajr.149.2.351.

Images/Tables

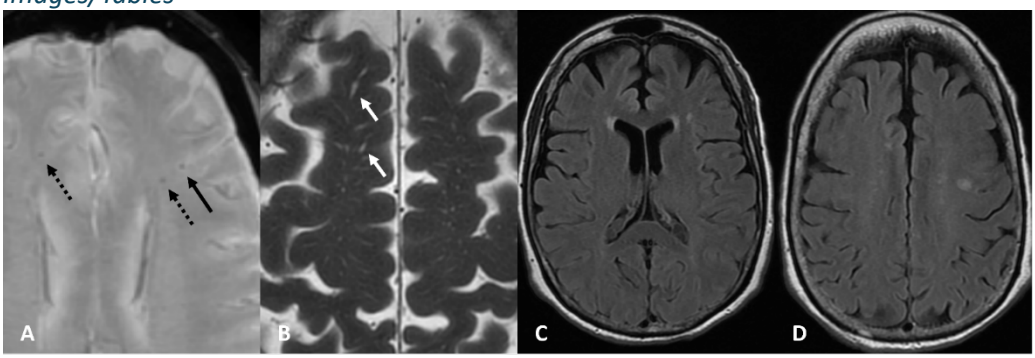

Fig 1. MRI brain of a patient with seizure in the setting of CAA. A) Susceptibility-weighted imaging demonstrates a cortical/juxtacortical microhemorrhage in the left frontal lobe (solid arrow) and subcortical microhemorrhage in both frontal lobes (dashed arrows). B) Fast-spin echo T2-weighted sequence demonstrates multiple peri-vascular spaces in the centrum semiovale. C) FLAIR sequence demonstrates a Fazekas grade 1 white matter signal abnormality. D) Several distinct foci of signal abnormality are seen but this did not meet criteria for multifocal spot pattern since there are fewer than 10 spots on one side.

732

Imaging of Fetal Hydrocephalus

Marwa Abdelrasoul MD., PhD., John Crow MD, Maria Gisele Matheus MD.
Medical University of South Carolina, Charleston, SC, USA

Abstract Category

Pediatrics

Purpose

Hydrocephalus is caused by imbalance between CSF production and absorption. Prenatal imaging using MRI is being widely used to determine underlying etiology, identify associated congenital anomalies, and plan obstetric management. The main MR sequences utilized are T2-weighted Haste sequences in axial, coronal and sagittal planes. Complimentary DWI, T1 and gradient echo sequences are also added. This presentation aims to review MR findings of fetal hydrocephalus and review underlying etiologies which can help predict prognosis and guide fetal care.

Materials & Methods

Illustrative cases from our institution and review of literature to show key findings of hydrocephalus and the most common underlying etiologies. We will include ventricular atrial width measurements, assessment of aqueduct of Sylvius patency and assessment of associated congenital anomalies (e.g. posterior fossa anomalies).

Results

Identify signs of fetal hydrocephalus and discussing possible underlying neurological etiologies using our institutional cases in conjunction with review of current literature.

Conclusion

Adequate MR evaluation of hydrocephalus and assessing can have significant impact on postnatal fetal care and improve clinical outcome.

References

1. Mirsky DM, Stence MV, Powers AM, et al. Imaging of Fetal Ventriculomegaly. Pediatr Radiol 2020; 50: 1948-1958
2. Oi S, Diagnosis, outcome, and management of fetal abnormalities: fetal hydrocephalus. Childs Nerv Syst 2003; 19: 508–516
3. Krishnan P, Raybaud C, Palasamudram S, et al. Neuroimaging in Pediatric Hydrocephalus. Indian J Pediatr 2019; 86: 952–960

743

Vertebral Artery Impingement: A Case Series

Emilio P. Supsupin MD[1], Christopher B. Reyes MD[2], Abdul-Aziz Ontok MD[2], Rhoby U. Orata MD[2]
[1]UFHealth College of Medicine, Jacksonville, Florida, USA. [2]Victoriano Luna Medical Center - AFP Health Service Command, Quezon City, Metro Manila, Philippines

Abstract Category

Spine

Purpose

Extrinsic bony compression or vertebral artery impingement related to fractures of the arch of C1 (atlas) is rare. The incidence of arterial impingement is disproportionately small as compared to other vascular injuries such as traumatic dissection. This presentation aims to illustrate the findings of vertebral artery impingement on CT angiography (CTA).

Materials & Methods

Displaced fractures of C1 with subsequent diagnosis of vertebral artery impingement documented on CTA were retrospectively reviewed from May 2023 through June 2024.

Results

Three consecutive cases of vertebral artery impingement associated with displaced fractures of C1 presented at our institution within the specified time frame. All subjects (three males aged 90, 89, and 86) sustained displaced fractures of the C1 arch following a ground level fall. Subsequent CTAs disclosed vertebral artery impingement. In all cases, arterial impingement resulted from extrinsic bony compression of a short segment of the vertebral artery (i.e., V3 segment), caught between the lateral mass and displaced fracture segments at the posterior arch of the atlas in the area of the sulcus arteriosus. The distal V3 segment of the vertebral artery sits

at the sulcus arteriosus. All subjects complained of severe neck pain but were otherwise neurologically stable and without focal deficits upon admission. They were managed conservatively, and follow-up CTA revealed stable findings.

Conclusion

Displaced fractures particularly involving the sulcus arteriosus of the atlas should raise concern for possible vertebral arterial impingement. CTA offers excellent depiction of vertebral artery impingement and associated bony injuries and may help guide management.

References

Matsuzaki R, Nakada C, Kondo K, et.al. Diagnosis and treatment of vertebral artery injuries due to blunt trauma: A case series, Trauma Case Reports, Volume 44, 2023, 100780, ISSN 2352-6440, https://doi.org/10.1016/j.tcr.2023.100780

Images/Tables

Case 1: 90-year-old male with ground level fall while gardening

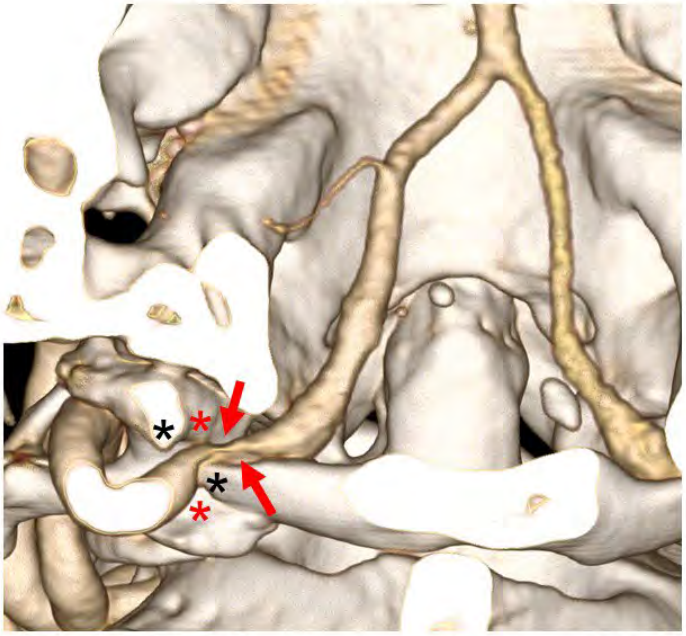

CTA with 3D rendering showing severe irregular narrowing (red arrows) of the V3 segment of the right vertebral artery (RVA) from extrinsic bony compression, caught between the displaced posterior arch fracture in the area of the sulcus arteriosus (black asterisks) and the lateral mass of C1 (red asterisks), consistent with arterial impingement

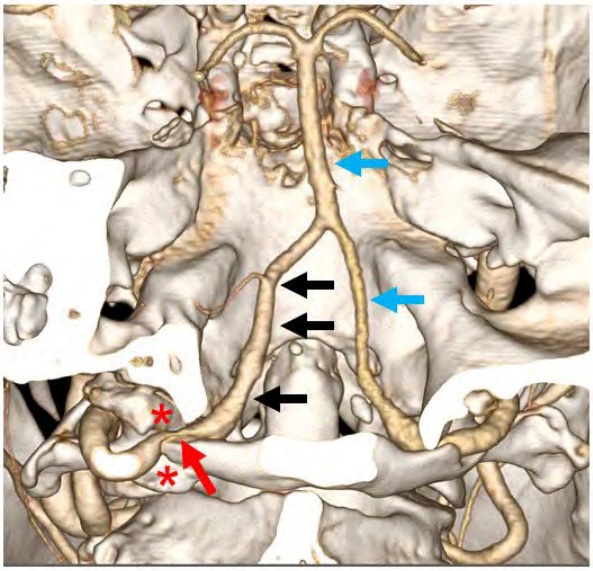

There is resumption of normal caliber and normal filling of the RVA (black arrows) distal to its impinged V3 segment (red arrow). There is normal filling of the left vertebral artery and basilar artery (blue arrows).

753

Single Level Spinal Fusions: Does Postoperative Alignment Matter?

Matthew E Rosenthal BA[1], Madeline Kimble BS[2], Dane Donich BS[3], Matthew Patterson BS[3], Rohit Mauria MD[4], Eric Z Herring MD[4], Collin M Labak MD[4], Gabriel A Smith MD[4]

[1]Case Western Reserve University School of Medicine, Cleveland, Ohio, USA. [2]Lincoln Memorial University College of Osteopathic Medicine, Harrogate, Tennessee, USA. [3]Northeast Ohio Medical University, Rootstown, Ohio, USA. [4]University Hospitals Department of Neurological Surgery, Cleveland, Ohio, USA

Abstract Category

Spine

Purpose

Factors contributing to lumbar fusion revision remain unclear, with causes including recurrence of stenosis, non–union, and adjacent segment disease (ASD).1 The primary objective of this study was to characterize the postoperative alignment of adjacent segments after single-level lumbar interbody fusions and evaluate predictors of ASD development within the first 2 years after fusion surgery.

Materials & Methods

This retrospective review examined 40 patients treated with single-level lumbar interbody fusion between 2018 and 2023. Patients were divided by radiographic changes at adjacent segments (ASD) around a spinal fusion (n=18) and non-

ASD (n=22). The criteria for ASD was defined as a decrease in adjacent disc height of >3mm, intervertebral angle changes in flexion of >5 degrees, and listhesis of >2mm when compared to preoperative films between 3 months and 2 years after surgery. Clinical data collected included demographics, operative details, and pre- and post-operative deformity measurements. T-test and logistic regressions were used to evaluate variables as predictors for development of ASD.

Results

Mean postoperative spinopelvic parameters showed no statistical difference between patients who developed ASD and those who did not. Patients with radiographic ASD underwent TLIF procedures 100% of the time compared to 86% for Non-ASD patients (p=0.05). Logistic regression revealed significantly higher rate of reoperation within 2 years for radiographic ASD patients compared to Non-ASD patients (OR: 40.25, 95% CI: 3.84 - 421.6, p=0.02) as well as when corrected for patient BMI and Age (OR: 6.79, 95% CI: 0.99 - 46.6, p=0.05). Additionally, BMI was associated with increased risk of radiographic ASD (OR: 1.18, 95% CI: 1.03 - 1.36, p=0.01).

Conclusion

Patients undergoing anterior fusion procedures may have a lower risk of ASD within the first 2 years after surgery whereas elevated BMI may increase risks of ASD. Single level lumbar interbody fusion patients with radiographic ASD have an increased risk of reoperation within 2 years.

References

1. Lee YC, Lee R. Minimal invasive surgical algorithm for revision lumbar spinal surgery. J Spine Surg. 2019;5(4):413-424. doi:10.21037/jss.2019.09.08

2. Chapin L, Ward K, Ryken T. Preoperative Depression, Smoking, and Employment Status are Significant Factors in Patient Satisfaction After Lumbar Spine Surgery. Clin Spine Surg. 2017;30(6):E725. doi:10.1097/BSD.0000000000000331

3. Zheng F, Cammisa FPJ, Sandhu HS, Girardi FP, Khan SN. Factors Predicting Hospital Stay, Operative Time, Blood Loss, and Transfusion in Patients Undergoing Revision Posterior Lumbar Spine Decompression, Fusion, and Segmental Instrumentation. Spine. 2002;27(8):818

4. Harada, T., Hashizume, H., Taniguchi, T. et al. Association between acetabular dysplasia and sagittal spino-pelvic alignment in a population-based cohort in Japan. Sci Rep 12, 12686 (2022). https://doi.org/10.1038/s41598-022-16865-1

765

Asymmetrically Effaced Pyriform Sinuses: Prevalence and Clinical Implications

Yu Chen MD[1], Inseon Ryoo MD, PhD[2], Vrushab Gowda MD[3], Karen Buch MD[3], Osamu Sakai MD, PhD[3]

[1]Department of Radiology, Peking Union Medical College Hospital, Chinese Academy of Medical Sciences & Peking Union Medical College, Beijing, N/A, China. [2]Department of Radiology, Korea University Guro Hospital, Korea University College of Medicine, Seoul, N/A, Korea, Republic of. [3]Massachusetts General Hospital, Harvard Medical School, Boston, MA, USA

Abstract Category

Head & Neck

Purpose

Pyriform sinus lesions are difficult to detect clinically. CT could be the first to identify unrevealed lesions. This study assessed the prevalence of asymmetric pyriform sinus effacement on CT, exploring its clinical implications.

Materials & Methods

We retrospectively reviewed patients who underwent neck PET/CT in 2023 on non-contrast-enhanced attenuation-correction (AC) and diagnostic contrast-enhanced (CE) CTs. Effacement degree was categorized into four grades: no effacement (0%), mild (<50%), moderate (50-90%), and severe/complete effacement (>90%) (Fig.). Radiotracer uptake in the hypopharynx/larynx was recorded. The presence of cervical lymphadenopathy was documented.

Results

554 patients were included: 114 head and neck cancer (HNC) and 440 non-HNC patients.

On AC-CT, pyriform sinus effacement was seen at 35% on the left (n=192), 10% on the right (n=55), and 34% bilaterally (n=188). CECT demonstrated left-sided effacement in 27% (n=148), right-sided in 10% (n=56), and bilateral in 26% (n=144). Of note, 21% (25/119) of patients without effacement on AC-CT subsequently developed effacement on CECT. Conversely, many patients with effacement on AC-CT did not display effacement on CECT: 31% (59/192) in the left-sided effacement group, 27% (15/55) in the right-sided effacement group, and 20% (38/188) in the bilateral effacement group.

Among those with mild effacement on AC-CT, 50.5% (46/91) maintained their degree of effacement on CECT, while 38.5% (35/91) no longer displayed effacement. Similarly, in the moderate effacement group, 31.1% (38/122) maintained their grading, while 64.7% (79/122) demonstrated a decreased degree. Among subjects with complete effacement, 60.8% (135/222) remained unchanged, while 39.2% (87/222) displayed a reduced level.
In the HNC group, 35.1% (n=40) demonstrated left-sided involvement, 7.9% (n=9) right-sided, 43.9% (n=50) bilaterally, and 13.2% (n=15) revealed no effacement. By contrast, the non-HNC group featured left-sided effacement among 34.5% (n=152) of subjects, right in 10.5% (n=46), and bilateral effacement in 31.4% (n=138). No effacement was observed in 23.6% (n=104) of subjects. Moreover, the location of effacement differed significantly between the two groups (p=0.024).
On diagnostic CT, 67.5% (n=77) of subjects in the HNC group maintained their degree of effacement, while 26.3% (n=30) demonstrated a deceased level, and 6.1% (n=7) featured an increased extent. Among non-HNC subjects, 53.5% (n=236) patients maintained their degree of effacement, 39% (n=171) decreased, and 7.5% (n=33) increased. These differences were found to be statistically significant (p=0.028).
Sixteen subjects displayed hypopharyngeal/laryngeal ^{18}F-FDG uptake. All eight HNC patients with uptake had due to known head and neck cancer, while five of the eight non-HNC patients had contralateral vocal cord paralysis. Lymphadenopathy was observed in 13.2% (n=15) of the HNC group and 18.4% (n=81) of the non-HNC group, without a significant difference between the two (p=0.117).

Conclusion

Asymmetric pyriform sinus effacement is a frequent finding on CT. Left-sided effacement was more commonly identified in patients without lesions. Additionally, the degree and laterality of effacement can vary within the same individual between AC-CT and CECT performed on the same day.

References

1. Price DB, Miller LJ, Price AP. Evaluation of nondistended pyriform sinus without respiratory maneuvers. J Comput Assist Tomogr. 1993 Jan-Feb;17(1):163-5.

Images/Tables

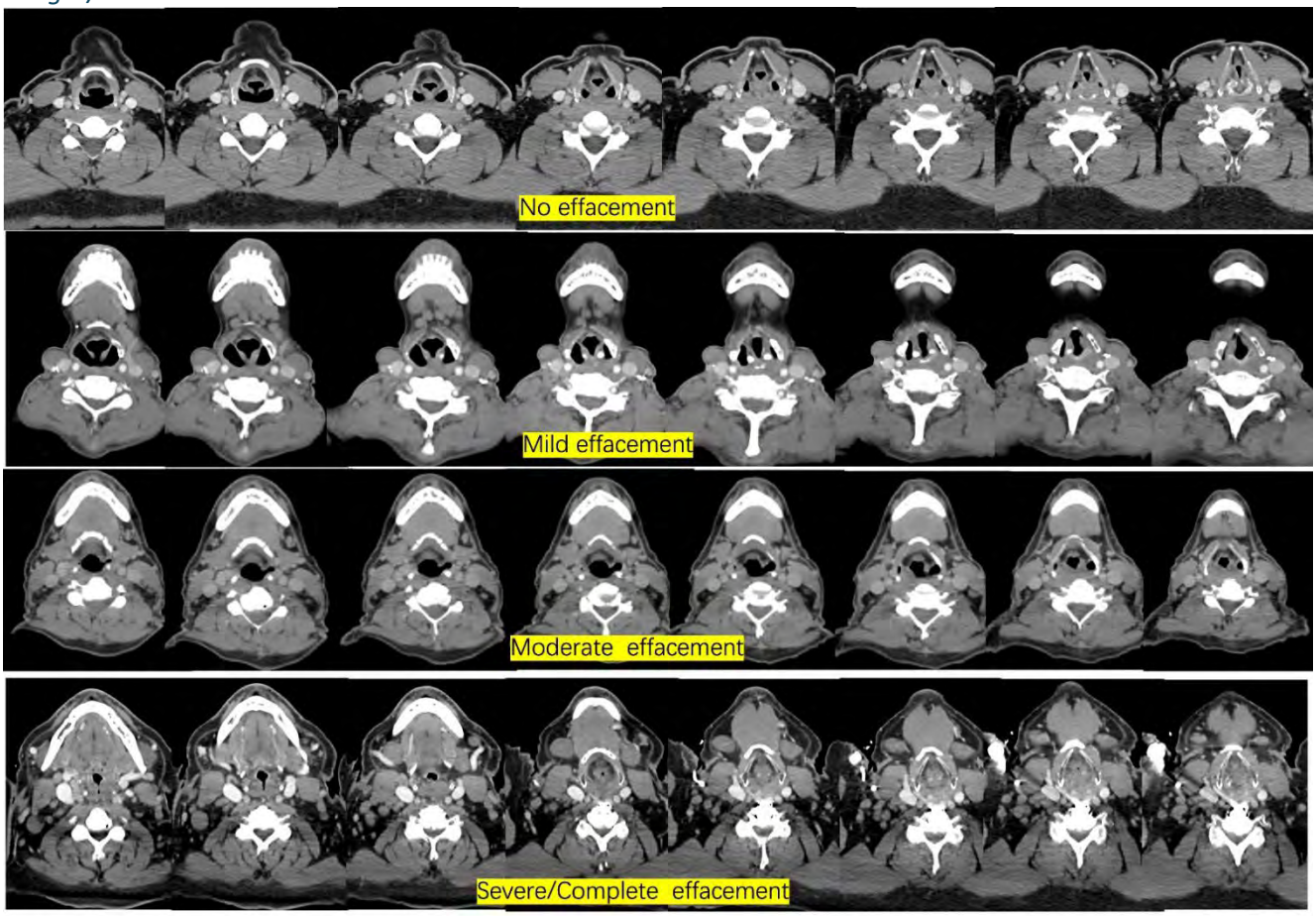

772

Association of Lipid Profile Composite Score with Brain Amyloid Deposition

Sara Hosseinzadeh Kassani[1], Paul K. Commean[1], Mahsa Dolatshahi[1], Soheil Mohammadi[1], Mahshid Naghashzadeh[1], Caitlyn Nguyen[1], LaKisha Lloyd[1], Nancy Hantler[1], Abby McBee-Kemper[1], Farzaneh Rahmani[1], Bettina Mittendorfer[2], Joseph E. Ippolito[3], Claude Sirlin[4], John C. Morris[5], Tammie L.S. Benzinger[1], Cyrus A. Raji[1]
[1]Mallinckrodt Institute of Radiology, Washington University in St. Louis, St. Louis, MO, USA. [2]Missouri University School of Medicine, St. Louis, MO, USA. [3]Washington University in St. Louis, St. Louis, MO, USA. [4]University of California, San Diego, St. Louis, MO, USA. [5]Washington University School of Medicine in St. Louis, St. Louis, MO, USA

Abstract Category

AI/Informatics

Purpose

Lipid profile markers, including HDL, LDL, total cholesterol, and triglycerides, are recognized as potential contributors to the progression of neurodegenerative diseases, such as Alzheimer's disease (AD)[1]. We examined the link between the lipid profile components and brain amyloid deposition through training a machine learning-based method that characterizes relative importance of each lipid component.

Materials & Methods

In an IRB-approved study, a total of 57 middle-aged cognitively normal participants (age: 49.5±6.2 years, females: 64.9%, obesity (BMI of 30 kg/m^2 or higher): 52.6 %, BMI: 31.3±6.4 kg/m2) underwent brain [11C]PiB and AV-1451 PET, body MRI, metabolic and cognitive assessment and adiposity metrics. We constructed a composite lipid score by training a Kernel Ridge Regression (KRR) model with a radial basis function (RBF) kernel to predict amyloid deposition (Centiloid values) using HDL, LDL, total cholesterol, and triglyceride levels. The composite score was derived by normalizing and combining the feature importance values of each lipid component. We assessed the association between whole-brain amyloid centiloid, lipid markers, and the composite score using Spearman correlation test.

Results

Spearman’s correlation analysis showed a significant negative correlation between HDL and amyloid centiloid values (ρ = -0.419, p = 0.001), but not other lipid metrics (p > 0.05). The KRR-based composite lipid score achieved a stronger and significant positive correlation with amyloid centiloid (ρ = 0.463, p = 0.0003). The obtained results suggest that the nonlinear associations among lipid metrics, as captured by the KRR-derived composite score, may provide a meaningful association with amyloid deposition patterns in the brain. These findings highlight the potential of a lipid composite score to predict amyloid deposition more effectively than individual lipid measures. The significant associations found for HDL and the composite score suggest that lipid profile could play a role in amyloid burden and influence neurodegenerative diseases such as Alzheimer's disease. These findings highlight the potential of a lipid composite score to predict amyloid deposition more effectively than individual lipid measures.

Conclusion

The significant associations found for HDL and the composite score suggest that lipid profile could play a role in amyloid burden and influence neurodegenerative diseases such as Alzheimer's disease. Future work will explore the use of composite score in longitudinal studies and its potential role in predicting clinical outcomes related to AD.

References

Yin F. Lipid metabolism and Alzheimer's disease: clinical evidence, mechanistic link and therapeutic promise. FEBS J. 2021;288(13):3825-3840.

Images/Tables

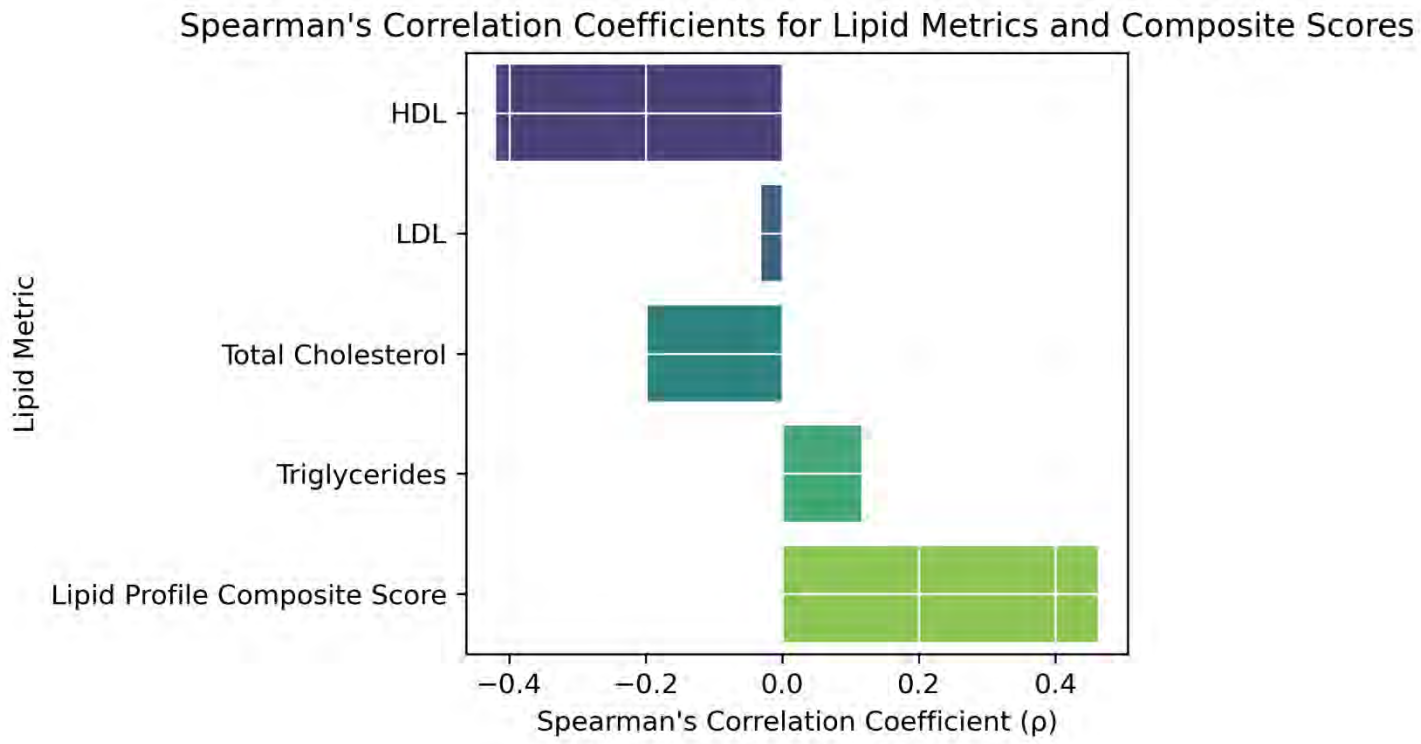

775

Artificial Intelligence in Head and Neck Cancers: A Scoping Review of Current Applications and Future Directions

Rafail Christodoulou MD, Nancy Pham MD
Department of Radiology Stanford University School of Medicine, Palo Alto, California, USA

Abstract Category

Head & Neck

Purpose

Head and neck cancer clinical management relies on integrating imaging, histologic, and molecular data to inform decision-making. Artificial intelligence (AI), with its capacity to efficiently process large-volume, multi-modal data, can augment this decision-making process by identifying patterns that are not readily apparent to human observers. Thus, AI-based tools and predictive models have the potential to guide diagnosis, prognosis, and treatment, as well as personalize treatment to the individual patient in the future. This review provides a comprehensive analysis of the existing literature on AI applications in head and neck cancers, highlighting the most common clinical tasks, current challenges and potential future directions.

Materials & Methods

A systematic literature search was conducted across PubMed, IEEE Xplore, Scopus, and Google Scholar yielding a total of 21,060 studies. After removing duplicates and applying filters to limit studies to the 2014-2024 timeline and primary peer-reviewed research data, 123 studies met our inclusion criteria. This protocol was registered on open science framework (OSF).

Results

The 123 included studies mainly focused on five domains of the head and neck cancer patient care pathway: staging, diagnosis, prognosis, treatment response, and survival outcomes. Our findings reveal significant progress in AI-based methodologies, especially deep learning and radiomics for head and neck cancer. For staging, an important prognostic factor for head and neck cancer is determining lymph node metastasis and extranodal extension of disease (ENE). AI-based models for lymph node metastasis and ENE have shown to surpass human readers. For diagnosis, AI-based prediction models have reported accuracy levels reaching up to 99% across various imaging modalities for distinguishing benign and malignant lesions. For prognosis and treatment, deep learning and radiomics-based approaches can enhance risk and treatment stratifications beyond conventional staging systems.

Conclusion

AI-based tools have the potential to improve head and neck cancer management, from clinical tasks related to diagnosis to personalized treatment planning. With continued advancements and validation, AI can be more readily translated from the research to clinical setting. However, challenges remain in clinical implementation, such as data standardization and model reproducibility. Additionally, most reviewed studies were single institution investigations, which may limit the generalizability of findings. Future research should prioritize multicenter trials and standardization to support broader clinical applicability.

References

- Loperfido A, Celebrini A, Marzetti A, Bellocchi G. Current role of artificial intelligence in head and neck cancer surgery: a systematic review of literature. *Explor Target Anti-tumor Ther*. 2023;933–940. https://doi.org/10.37349/etat.2023.00174
- Mahmood H, Shaban M, Rajpoot N, et al. Artificial Intelligence-based methods in head and neck cancer diagnosis: an overview. *Br J Cancer*. 2021;124:1934–1940. https://doi.org/10.1038/s41416-021-01386-x
- Giannitto C, Carnicelli G, Lusi S, et al. The use of artificial intelligence in head and neck cancers: a multidisciplinary survey. *J Pers Med*. 2024;14(4):341. https://doi.org/10.3390/jpm14040341
- Pham N, Ju C, Kong T, Mukherji SK. Artificial intelligence in head and neck imaging. *Semin Ultrasound CT MRI*. 2022;43(2):170–175. https://doi.org/10.1053/j.sult.2022.02.006
- Kazmierski M, Welch M, Kim S, et al. Multi-institutional prognostic modeling in head and neck cancer: evaluating impact and generalizability of deep learning and radiomics. *Cancer Res Commun*. 2023;3(6):1140–1151. https://doi.org/10.1158/2767-9764.crc-22-0152

Images/Tables

Artificial Intelligence in Head and Neck Cancers: A Scoping Review of Current Applications and Future Directions

Rafail Christodoulou,MD, Nancy Pham ,MD, Department of Radiology Stanford University School of Medicine

INTRODUCTION

Head and neck cancers (HNC), particularly squamous cell carcinomas, pose complex challenges due to their heterogeneous nature and critical anatomical locations. AI holds promise for improving HNC management through advancements in imaging, diagnosis, treatment planning, and patient monitoring.[1]

METHODS

This scoping review conducted a systematic search of PubMed, IEEE Xplore, Scopus, and Google Scholar for studies from January 2014 to December 2024, identifying 21,060 records on AI applications in head and neck cancer (HNC). After applying filters (English, past decade, primary research) and removing duplicates, 123 studies met inclusion criteria(see Figure 1). . This protocol was registered on open science framework (OSF).We proceeded to data extraction by two reviewers focusing on study characteristics, AI techniques, and HNC outcomes.

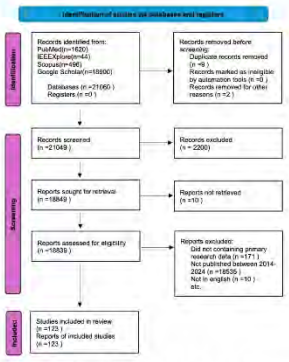

Figure 1:Literature search based on PRISMA scoping review guidelines

RESULTS

AI models in head and neck cancer (HNC) achieved high diagnostic accuracy, with rates up to 99% in distinguishing benign and malignant lesions across various imaging modalities(see Figure 2). Radiomics improved treatment stratification and prognostic assessments, aiding in personalized care(see Figure 3).[3] AI-driven auto-segmentation optimized radiotherapy planning by reducing manual contouring time and enhancing consistency(see Figure 4). However, most studies were single-institution, highlighting a need for multi-center research to confirm findings.[2]

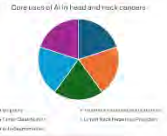

Figure 2: Core Applications of AI in head and neck cancers

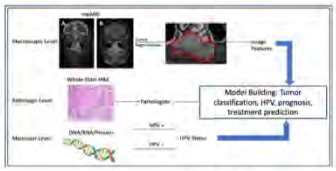

Figure 3: Pathologic, Genetic, and Imaging Data for AI Model to Classify Tumors, Predict Treatment, Prognosis, and HPV Status [4]

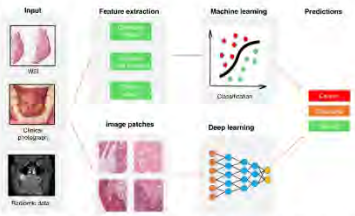

Figure 4: AI Model Workflow for Cancer Classification Using Imaging, Pathology, and Radiomic Data [2]

CONCLUSION

AI shows strong potential to improve head and neck cancer management, enhancing diagnostic accuracy, treatment planning, and personalized care. However, challenges like data standardization and model reproducibility limit clinical implementation. Most studies are single-institution, highlighting the need for multi-center validation. Future work should focus on addressing these gaps for broader applicability.[4]

References

1. Loperfido, A., Celebrini, A., Marzetti, A., & Bellocchi, G. (2023). Current role of artificial intelligence in head and neck cancer surgery: a systematic review of literature. *Exploration of Targeted Anti-tumor Therapy*, 933–940. https://doi.org/10.37349/etat.2023.00174

2. Mahmood, H., Shaban, M., Rajpoot, N. *et al* Artificial Intelligence-based methods in head and neck cancer diagnosis: an overview. *Br J Cancer* **124**, 1934–1940 (2021). https://doi.org/10.1038/s41416-021-01386-x

3. Giannitto, C., Carnicelli, G., Lusi, S., Ammirabile, A., Casiraghi, E., De Virgilio, A., Esposito, A. A., Farina, D., Ferreli, F., Franzese, C., Frigerio, G. M., Lo Casto, A., Malvezzi, L., Lorini, L., Othman, A. E., Preda, L., Scorsetti, M., Bossi, P., Mercante, G., . . . Francone, M. (2024). The use of artificial intelligence in head and neck cancers: a multidisciplinary survey. *Journal of Personalized Medicine*, *14*(4), 341. https://doi.org/10.3390/jpm14040341

4. Pham, N., Ju, C., Kong, T., & Mukherji, S. K. (2022b). Artificial Intelligence in head and neck imaging. *Seminars in Ultrasound CT and MRI*, *43*(2), 170–175. https://doi.org/10.1053/j.sult.2022.02.006

5. Kazmierski, M., Welch, M., Kim, S., McIntosh, C., Rey-McIntyre, K., Huang, S. H., Patel, T., Tadic, T., Milosevic, M., Liu, F., Ryczkowski, A., Kazmierska, J., Ye, Z., Plana, D., Aerts, H. J., Kann, B. H., Bratman, S. V., Hope, A. J., & Haibe-Kains, B. (2023). Multi-institutional prognostic modeling in head and neck cancer: Evaluating impact and generalizability of deep learning and radiomics. *Cancer Research Communications*, *3*(6), 1140–1151. https://doi.org/10.1158/2767-9764.crc-22-0152

6 Y, D., Ramalingam, K., Ramani, P., & Deepak, R. M. (2023). Machine learning in the detection of oral lesions with clinical intraoral images. *Cureus*. https://doi.org/10.7759/cureus.44018

Created with BioRender Poster Builder

793

Prevalence of Cerebral Tau Deposition in Community-Dwelling Older Adults Using [18F]MK-6240 PET and Cognitive Implications

Shama Jaswal[1], Bardiya Yazdi[2], Sindy Ozoria Blake[1], Peter Chernek[2], Jenseric Claimag[2], Qolamreza Razlighi[2], Gloria Chia-Yi Chiang[1]

[1]New York Presbyterian/ Weill Cornell Medicine, New York, NY, USA. [2]Brain Health Imaging Institute/ Weill Cornell Medicine, New York, NY, USA

Abstract Category

Functional/Advanced Imaging

Purpose

[18F]MK-6240 is a second-generation PET tracer used to detect tau neurofibrillary tangles in vivo, one of the pathologic hallmarks of Alzheimer's disease. This study aimed to determine the prevalence of early tau deposition in a cognitively normal cohort.

Materials & Methods

One hundred seventy-three community-dwelling older adults (ages 60-80 years, 49% female) were recruited prospectively to undergo tau PET imaging with the second-generation tau tracer, [18F]MK-6240. Two radiologists, blinded to amyloid PET positivity and cognitive assessments, reviewed the images, and regions of tau deposition were recorded. Participants were classified according to a Braak staging scheme. Multidomain cognitive assessments were also performed.

Results

Fifty-nine (34%) participants were found to be Braak-positive. Of these, 30 (51%) were Braak stage I/II, 7 (12%) were Braak stage III/IV, and 7 (12%) were Braak stage V/VI. Notably, 15 (25%) had atypical patterns of tau deposition that did not conform to Braak staging, such as having higher stage cortical tau deposition without tau in the mesial temporal lobe. 45.8% of the tau positive cognitively normal participants were amyloid-positive on PET. Participants with tau deposition had more impaired delayed recall on the Craft Story ($p=0.037$) and Auditory Verbal Learning ($p=0.039$) tests, despite no statistical difference in Montreal Cognitive Assessment scores ($p>0.05$).

Conclusion

A significant proportion of cognitively normal older adults have tau deposition in the brain, particularly in Braak I/II regions. Further follow-up is warranted in those do not conform to traditional Braak staging, as the distribution of tau may predict atypical forms of Alzheimer's disease or primary tauopathies.

References

1- Braak H, Braak E. Neuropathological staging of Alzheimer-related changes. Acta Neuropathol 82(4):239-59.

2- Scholl M, Lockhart NS, Schonhaut RD, et al. PET Imaging of Tau Deposition in the Aging Human Brain. Neuron. 2016 Mar 2;89(5):971–982

Images/Tables

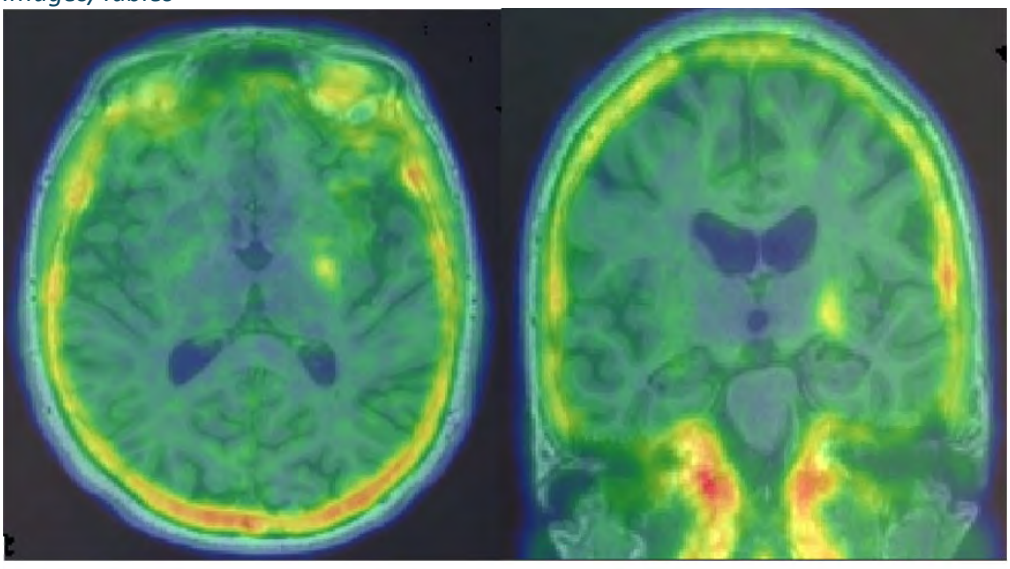

Fig.1: Atypical Tau pattern in Left Basal Ganglia.

798

Subarachnoid Hemorrhage (SAH) Management: Establishing a Safe Threshold for Imaging Based on SAH Size

Caline Azzi MD[1], Mahla Radmard[1], Armin Tafazolimoghadam MD[2], Jee Moon MD[1], Soyeb Aftab MBBS[3], Tej Azad MD[1], Shahram Hadidchi MD[1], Joyce Hsu MD[1], Luke Miller MD[1], Sam Speer MD[1], Chi Trinh BA[1], David M. Yousem MD, MBA[1]

[1]Johns Hopkins, Baltimore, MD, USA. [2]Tehran University of Medical Sciences, Tehran, Iran, Iran, Islamic Republic of. [3]All India Institute of Medical Sciences, New Delhi, India, India

Abstract Category

Adult Brain

Purpose

This study aims to establish a hemorrhage size threshold for safely managing SAH patients without follow-up imaging. It examines factors associated with hemorrhage enlargement, SAH type (post-traumatic vs. aneurysmal), and clinical outcomes, including hydrocephalus risk.

Materials & Methods

We conducted a retrospective analysis of non-contrast head CT scans (NCCT) in 85 SAH patients. Patient data, including demographics (age, gender, race), comorbidities, and NCCT findings, were obtained from electronic medical records. Variables assessed included the maximal linear SAH measurement, Glasgow Coma Scale (GCS) scores, presence of other intracranial bleeds, and clinical outcomes (e.g., hydrocephalus development, external ventricular drainage [EVD] placement, mortality, and length of hospitalization). We analyzed basal cistern involvement and intraventricular extension to understand their association with hydrocephalus. Statistical analyses (Chi-square and Mann-Whitney U tests) were used to identify associations, and subset analysis on 36 patients with isolated SAH (no other bleeds) was conducted to identify potential thresholds for safely omitting follow-up imaging.

Results

Among the patients, 79 had post-traumatic SAH, and 6 had aneurysmal SAH. The cohort's mean age was 70.6 years (SD: 3.6), with 51 (50%) males and 34 (40%) females. The racial/ethnic breakdown was 59 (69.4%) white, 24 (28.2%) black, and 2 (2.4%) of other races. Falls were the primary cause (78.8%), followed by motor vehicle accidents (11.8%), assault (1.2%), and other causes (8.2%). Aneurysmal SAH cases had a larger initial hemorrhage size ($P < 0.001$), with a median size of 40 mm for aneurysmal cases compared to 17.5 mm in post-traumatic cases, and basal cistern hemorrhage was significantly more common in aneurysmal SAH (85.7%) than in post-traumatic cases (8.4%; $p < 0.001$).

Among the 10 patients who developed hydrocephalus, 5 were post-traumatic and 5 aneurysmal. The mean age was 68.2 years (SD: 5.99), with 7 males and 3 females. The racial distribution was 5 white, 4 black, and 1 of other ethnicity. There was a higher association between hydrocephalus and both intraventricular hemorrhage (90%) and basal cistern involvement (70%) ($P < 0.001$ for both). This indicates that IVH and basal cistern hemorrhage are significant risk factors for hydrocephalus.

In the isolated SAH subset (n=36), only 3 patients experienced hemorrhage enlargement, all with initial measurements above 15 mm or complicating factors like fractures.

Conclusion

For isolated SAH patients, a 15 mm maximal linear measurement threshold may serve as a guideline for determining the necessity of follow-up imaging, particularly when there are no complicating factors (e.g., fractures, IVH, or basal cistern involvement). The presence of IVH and basal cistern hemorrhage significantly increases the risk of post-SAH hydrocephalus in both post-traumatic and aneurysmal cases. Further studies are recommended to validate these findings, refine imaging recommendations, and improve SAH patient management by understanding risk factors better.

References

Marcolini E, Hine J. Approach to the Diagnosis and Management of Subarachnoid Hemorrhage. West J Emerg Med. 2019 Mar;20(2):203-211. doi: 10.5811/westjem.2019.1.37352. Epub 2019 Feb 28. PMID: 30881537; PMCID: PMC6404699.

802

Incidental Vascular Pathologies on CT Soft Tissue Neck

Manisha Mangla MBBS MPH[1], Aditya Duhan MBBS[2], Rajiv Mangla MD[2], Amar Swarnkar MBBS[2]
[1]SUNY UPstate, Syracuse, NewYork, USA. [2]SUNY Upstate, Syracuse, NewYork, USA

Abstract Category

Head & Neck

Purpose

Vascular pathologies involving the carotid, vertebral and intracranial arteries can be asymptomatic. These conditions can lead to significant morbidity and mortality, including stroke, intracranial hemorrhage, oropharyngeal bleeding, and carotid blowouts. CT soft tissue imaging of the neck is frequently performed for diagnosing non-vascular soft tissue head and neck pathologies and is the modality of choice for monitoring patients with head and neck cancers. Radiation and surgery for these cancers can damage blood vessels, leading to conditions such as radiation vasculitis.

Various other vascular conditions, including arterial dissections, pseudoaneurysms, fibromuscular dysplasia, connective tissue disorders, autoimmune vasculitis, mycotic aneurysms, and vasculopathy in drug abusers, have been described in the literature. These pathologies can affect the vessel wall, lumen, or both. Although CT soft tissue imaging is not optimized for vascular evaluation, it can often can be seen albeit suboptimally on CT soft tissue neck studies. It is important to identify these to prevent adverse outcome and recommend further dedicated vascular imaging.

This review will discuss the imaging features of clinically critical arterial pathologies, which are categorized into atherosclerotic and non-atherosclerotic types as incidentally detected on CT soft tissue neck studies. Additional imaging characteristics that assist in prognosis and management will also be highlighted.

Materials & Methods

We will review the CT soft tissue neck of the patients diagnosed with various vascular pathologies at our institution , which includes pseudoaneurysms, aneurysm , AV fistula , hemodynamically significant stenosis and thrombus .

Results

CT soft tissue neck is not optimized for evaluation of the vascular pathologies , since the study is usually obtained in the late arterial phase and there is suboptimal opacification of the blood vessels . Imaging features such as vessel wall irregularity , abrupt cut off , intimal flap , carotid web , flame sign can raise the suspicion of vascular pathology , which can help in early diagnosis and management to reduce the significant morbidity and mortality .Beaded appearance of carotid arteries can help in establishing the early diagnosis of fibromuscular dysplasia .Early detection of Pseudoaneurysms associated with branches of external carotid artery , sequelae of radiation treatment in head and neck cancer can potentially prevent a catastrophic oropharyngeal bleeding .

Conclusion

CT soft tissue neck is not an ideal imaging modality to assess the vascular pathologies in the neck but these can be seen on careful observation. Identification of these vascular lesions is important to avoid adverse outcome. We recommend to include assessment of blood vessel in routine search pattern while reading soft tissue neck CT studies and recommend appropriate vascular studies.

References

Agarwal A, Bathla G, Kanekar S. Imaging of Non-atherosclerotic Vasculopathies. J Clin Imaging Sci. 2020 Oct 13;10:62. doi: 10.25259/JCIS_91_2020. PMID: 33194304; PMCID: PMC7656038.

Images/Tables

Faint blush missed on CT STN, later presented
With intraventricular bleed secondary to miss
Thalamic AVM

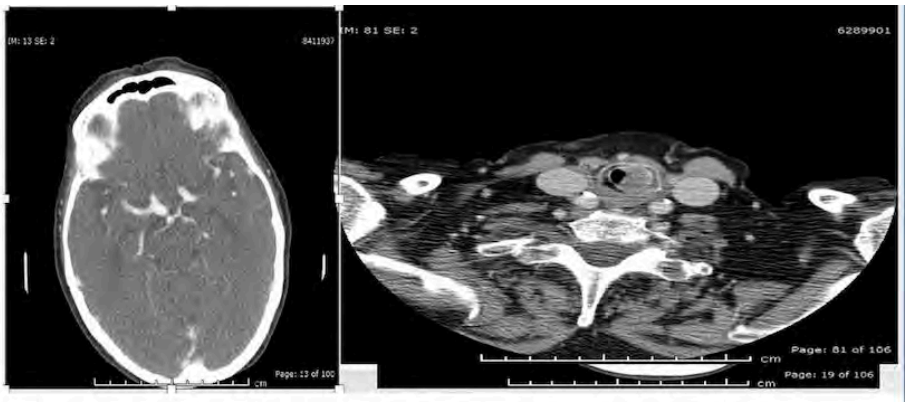

Fig 1: patient with subglottic carcinoma with incidental Right ICA Aneurysm

Fig2: Patient with carcinoma of posterior pharyngeal wall with hemodynamically significant stenosis of right innominate and left subclavian artery

804

Prevalence of Dilated Condylar and Mastoid Emissary Veins in Patients with Pulsatile Tinnitus

Ben Soares B.A., Bindu N. Setty M.D., Piers Klein B.A., Mohamad Abdalkader
Boston University Chobanian and Avedisian School of Medicine, Boston, MA, USA

Abstract Category

Head & Neck

Purpose

Emissary veins are common incidental radiological findings and enlarged emissary veins have been associated with the development of pulsatile tinnitus. The purpose of this study is to further investigate the prevalence and distribution of emissary veins in patients with and without pulsatile tinnitus.

Materials & Methods

We conducted a single- center case-control study of consecutive patients with pulsatile tinnitus who received imaging evaluation with CT venogram imaging between February 2018 and February 2022. Age and sex- matched controls who received CTV for different reasons, excluding those with headache, visual disturbance, or pulsatile tinnitus were selected during the same study period. 148 patients were evaluated in the pulsatile tinnitus cohort with 100 patients in the control cohort. Radiological evaluation was performed by two radiologists and measurements were performed at the point of maximal diameter. For statistical analyses, Mann-Whitney U test was used to compare vein diameters, and Fisher's exact test was used to compare vein frequencies

Results

In the pulsatile tinnitus group, condylar emissary veins were noted in 194 of 296 total sides (0.66) and in the control group 155 of 200 total sides (0.78). Mastoid emissary veins were noted in 153 of 296 total sides (0.52) in the pulsatile tinnitus group and 129 of 200 total sides (0.65) in the control group. Condylar and mastoid emissary veins were significantly less frequent in the pulsatile tinnitus group.

In the pulsatile tinnitus group there were 21 total dilated condylar veins (>5 mm) versus 6 in the control group. There were 45 dilated mastoid veins (>2 mm) in the PT group versus 17 in the control group. Dilated condylar and mastoid emissary veins were significantly more common in the pulsatile tinnitus group.
There was no significant difference in the total frequency of condylar and mastoid emissary veins or dilated condylar and mastoid emissary veins when comparing patients with and without jugular stenosis, transverse sinus stenosis, and sigmoid sinus wall abnormalities. Additionally there was no significant difference in condylar/mastoid vein frequency or dilated condylar/mastoid vein frequency when comparing patients with and without radiologic or clinical diagnoses of idiopathic intracranial hypertension.

Conclusion

Dilated condylar emissary veins and mastoid emissary veins are more common in patients with pulsatile tinnitus. Enlarged emissary veins could be considered as primary or contributing etiology when evaluating CT angiogram/venograms for PT. A direct correlation between occlusive venous anatomical features and the frequency of dilated emissary veins wasn't observed. Dilated emissary veins are an important radiologic finding that may assist in the diagnosis of PT.

References

Sismanis A. Pulsatile tinnitus: contemporary assessment and management. *Curr Opin Otolaryngol Head Neck Surg*. 2011 Oct;19(5):348.
Friedman DI, Jacobson DM. Diagnostic criteria for idiopathic intracranial hypertension. *Neurology* 2002 Nov 26;59(10):1492–5.
Kizildag B, Bilal N, Yurttutan N, et al. The relationship between tinnitus and vascular anomalies on temporal bone CT scan: a retrospective case control study. *Surg Radiol Anat* 2016 Sep 1;38(7):835–41.
Reardon MA, Raghavan P. Venous Abnormalities Leading to Tinnitus: Imaging Evaluation. *Neuroimaging Clin N Am* 2016 May 1;26(2):237–45.
Mattox DE, Hudgins P. Algorithm for evaluation of pulsatile tinnitus. *Acta Otolaryngol (Stockh)* 2008 Jan 1;128(4):427–31.

807

Causes of Misdiagnosed Bleeds on RAPID ICH

Matthew Steritz DO, Timothy Naney DO, Jon Hallstrom MD, Ashish Gandhe MD
University of New Mexico, Albuquerque, NM, USA

Abstract Category

AI/Informatics

Purpose

With a steadily increasing number of radiology studies and a relatively constant number of radiologists there has been increasing demand for new and improved AI programs to offset the increasing workload. This is especially needed in areas where critical findings need be identified and passed along to the managing clinicians expediently. Intracranial hemorrhage (ICH) in the emergency and inpatient setting is one such area where swift identification of critical finings and subsequent notification to providers is imperative. The non-contrast head CT (NCCT) is the primary imaging modality used to identify ICH. RAPID ICH is an automated intelligence software designed to detect the presence or absence of ICH to more efficiently identify or exclude this diagnosis. This program can also notify providers of positive findings. An accurate program with notification capabilities can be especially helpful in busy level 1 trauma centers. However, the high acuity and comorbidities of the patients at level 1 trauma centers lead to many suboptimal exams. Our goal for this project was to evaluate the accuracy of RAPID ICH at a level 1 trauma center and to investigate if there were inaccuracies, what could be contributing factors.

Materials & Methods

We collected all of the NCCTs from January 1^{st,} 2024 to January 31^{st,} 2024, and analyzed if the radiologist report aligned with the RAPID report. The radiologist's read was considered the gold standard. At least two fellowship trained neuroradiologists reviewed all the mismatched cases. A reason was given for the discrepancy between the two reports was given the neuroradiologist.

Results

In total, there were 1,991 NCCT analyzed. 351 of those did not contain a RAPID ICH report and were excluded from analysis. Of the remaining 1,640 NCCT, 83% (1364 of 1640) were congruent between the RAPID ICH report and radiologist report. There were 276 exams with discrepancies between the two reports. Of the unmatched cohort, there

were 59 RAPID ICH false positives and 217 RAPID ICH false negatives. From this dataset the RAPID ICH software had a sensitivity of 82.6% and specificity of 79%. Streak artifact accounted for 53% of the were streak account for 24.3% overcalled for streak . Streak and motion accounted for the largest percentage of false positives. Small isodense bleeds not detected by RAPID accounted for 91% of the false negatives.

Conclusion

Of the cases with discrepancies between the RAPID ICH and the radiologist's report, there were many more false positives than false negatives. The sensitivity and specificity from this data set was substantially lower than what had been previously reported in the literature and the RAPID ICH website. The results from this study may be more representative of how this software performs under non-ideal conditions such as level 1 trauma centers.
In high acuity settings with increasing study volumes, finding AI programs that can expedite reporting without sacrificing accuracy is invaluable. With the advent of more and more AI software it is important to assess and provide feedback on how these programs affect reporting and ultimately find ways to better AI and thus improve patient care.

References

1. Heit JJ, Coelho H, Lima FO, Granja M, Aghaebrahim A, Hanel R, Kwok K, Haerian H, Cereda CW, Venkatasubramanian C, Dehkharghani S, Carbonera LA, Wiener J, Copeland K, Mont'Alverne F. Automated Cerebral Hemorrhage Detection Using RAPID. AJNR Am J Neuroradiol. 2021 Jan;42(2):273-278. doi: 10.3174/ajnr.A6926. Epub 2020 Dec 24. PMID: 33361378; PMCID: PMC7872180.
2. Eldaya, Rami W. MD, MBA∗; Kansagra, Akash P. MD, MS∗,†,§; Zei, Markus MD∗; Mason, Evan DO∗; Holder, Derek MD, MS†; Heitsch, Laura MD†,‡; Vo, Katie D. MD∗; Goyal, Manu S. MD, MSc∗,†. Performance of Automated RAPID Intracranial Hemorrhage Detection in Real-World Practice: A Single-Institution Experience. Journal of Computer Assisted Tomography 46(5):p 770-774, 9/10 2022. | DOI: 10.1097/RCT.0000000000001335

809

Factors Associated with Time to Resolution of Amyloid-Related Imaging Abnormalities Following Cessation of Lecanemab

Jarrel CY Seah MBBS[1], JEREMY N FORD MD[1], Esteban C Cadavid MD[2], Odette G Chagui[2], Benjamin M Kozak MD[2], Hana Farzaneh MD[2], Nima Omid-Fard MD[2], Shenghua Zhu MD, PhD[2], Maryam Vejdani-Jahromi MD, PhD[2], Harry R Griffin MD[2], Javier M Romero MD[2], Saurabh Rohatgi MD[1]

[1]MGH, BOSTON, MA, USA. [2]MGH, Boston, MA, USA

Abstract Category

Adult Brain

Purpose

The natural course of Amyloid-related Imaging Abnormalites (ARIA) following cessation of lecanemab is still not well understood given the relative novelty of the drug in routine clinical practice. This study reports on the mean time to resolution of both ARIA-H (hemorrhage) and ARIA-E (edema/effusion) in a real-world clinical cohort and examines the factors associated with increased time-to-resolution.

Materials & Methods

A cohort of 21 patients with ARIA-H and/or ARIA-E in this single-center study were identified retrospectively and detailed information about the severity and type of ARIA was extracted from the radiology reports as well as cross-checked against the imaging. Both symptomatic and asymptomatic patients were included. Stabilization of ARIA-H was defined as having no new microhemorrhages or superficial siderosis after 30 days. Resolution of ARIA-E was defined as having complete resolution of T2 FLAIR changes. The time between the first MRI demonstrating ARIA, and the first MRI demonstrating resolution / stability of ARIA was measured. Demographics, ApoE genotype, as well as comorbidities such as type 2 diabetes mellitus and hyperlipidemia were extracted from the electronic medical record. A Cox proportional hazards model was used to model the association between these factors and the time to resolution / stabilization of ARIA.

Results

The mean time to resolution / stabilization was 53 days with mean time to stabilization of ARIA-H being 53 days and mean time to resolution of ARIA-E being 55 days. 15 cases had ARIA-H and 18 cases had ARIA-E, with 12 cases having both ARIA-H and ARIA-E. 13 out of 21 cases had hyperlipidemia. In the full Cox model, the only statistically significant factor was hyperlipidemia. Patients without hyperlipidemia demonstrated the fastest mean time to resolution / stabilization of 42.5 days (p=0.05).

Fig 1: Kaplan-Meier curve showing fraction of unresolved/non-stabilized ARIA cases in all cases as well as cases without hyperlipidemia.
Fig 2: Axial T2 FLAIR images of A) Patient with hyperlipidemia with ARIA-E. B) Patient with hyperlipidemia with resolved ARIA-E. C) Patient without hyperlipidemia with ARIA-E. D) Patient without hyperlipidemia with resolved ARIA-E.

Conclusion

In conclusion, while limited due to its small size, this study provides valuable insights into the time to resolution or stabilization of Amyloid-related Imaging Abnormalities (ARIA) following the cessation of lecanemab in a real-world clinical cohort. With a mean time of approximately 53 days to achieve stability or resolution, this data supports the notion that ARIA-E may often resolve within a few months post-cessation. Notably, hyperlipidemia status emerged as a statistically significant factor associated with slower resolution or stabilization, suggesting a potential metabolic influence on ARIA recovery. These findings contribute to the growing understanding of ARIA's natural course and could inform monitoring and management strategies in clinical practice. Further studies with larger cohorts are warranted to confirm these findings and to explore other potential factors influencing ARIA resolution.

References

Hampel H, Elhage A, Cho M, Apostolova LG, Nicoll JAR, Atri A. Amyloid-related imaging abnormalities (ARIA): radiological, biological and clinical characteristics. Brain. 2023;146(11):4414-4424.
Agarwal A, Gupta V, Brahmbhatt P, et al. Amyloid-related Imaging Abnormalities in Alzheimer Disease Treated with Anti-Amyloid-β Therapy. Radiographics. 2023;43(9):e230009.

Images/Tables

Figure 1

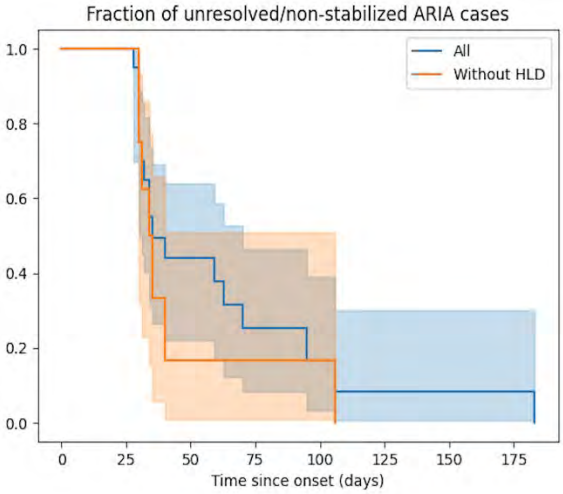

Figure 2

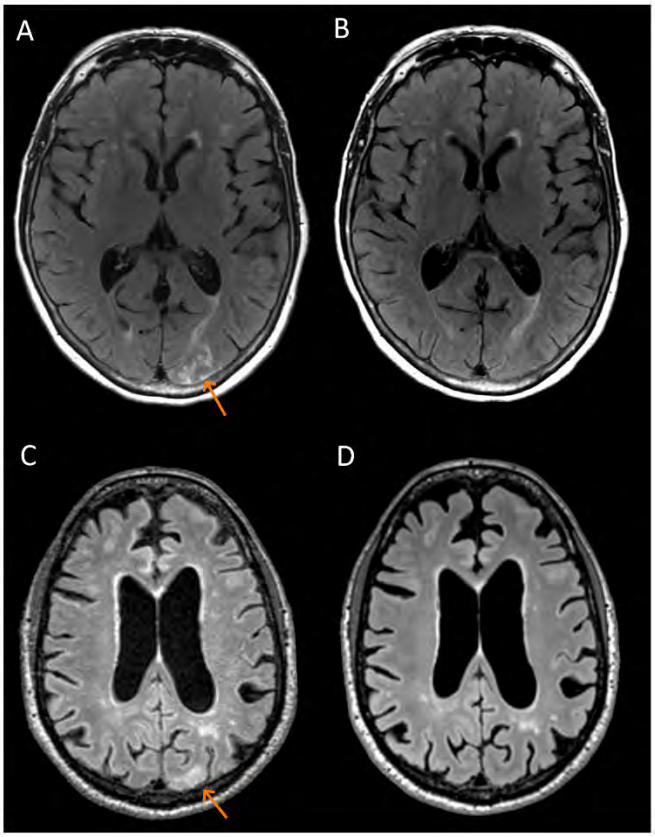

810

Association of Methylation Grade in IDH-Mutant Astrocytomas with MRI Features and Volumetrics.

Kanwar Singh[1], Matthew Lee[2], Matthew Young DO[2], Rajan Jain MD[2]

[1]NYU Grossman School of Medicine, New York, NY, USA. [2]NYU Grossman School of Medicine School Of Medicine, New York, NY, USA

Abstract Category

Adult Brain

Purpose

DNA methylation serves as a biomarker for stratifying IDH mutant astrocytomas, allowing differentiation between low- and high-grade molecular subtypes.[1] Low-grade methylation subclass indicates a better prognosis and is associated with fewer genetic abnormalities compared to high-grade methylation subclass astrocytomas. This study aimed to investigate the associations between imaging features, volumetric data, and methylation grade for IDH-mutant astrocytomas.

Materials & Methods

A retrospective review of 108 patients diagnosed with IDH-mutant astrocytoma with DNA methylation subclassification between 2014–2022 was done, of whom 71 met inclusion criteria after excluding cases with insufficient imaging or age less than 18. Histologic diagnosis followed the 2021 WHO CNS Tumor Classification. Preoperative MRIs (T2-weighted, T2-FLAIR, pre-/post-contrast T1) were preprocessed and segmented into edema, non-enhancing and enhancing tumor using the Federated Tumor Segmentation (FeTS) tool.[2] These images were reviewed to collect VASARI MRI features by a radiology research associate and a neuroradiology fellow, both blinded to pathology and DNA methylation data. Statistical analysis comparing the imaging features between the patient groups was performed with significance level < 0.05. Median follow-up time, progression-free and overall survival data were also collected.

Results

45 cases belonged to the low-grade methylation group while 26 belonged to the high-grade methylation group. 28 cases exhibited tumor enhancement while the rest were non enhancing. VASARI features such as enhancement quality ($X^2 = 14.73$, $p = 0.0006$), proportion enhancing ($X^2 = 14.64$, $p = 0.0007$), necrosis ($X^2 = 17.71$, $p = 0.0005$), diffusion characteristics ($X^2 = 14.08$, $p = 0.0009$), multifocality ($X^2 = 10.53$, $p = 0.015$) and nCET crossing the midline ($X^2 = 6.44$, $p = 0.040$) demonstrated significant associations with methylation grade. Volumetric analysis revealed edema volume differed significantly by methylation subgroup ($t = -3.7852$, $p = 0.0003$). The low-grade methylation subgroup had a mean edema volume of 32.39 cm^3 (SD = 42.77; range = 0.823 to 142.798 cm^3), while the high-grade methylation subgroup had a mean of 78.25 cm^3 (SD = 55.21; range = 9.43 to 135.26 cm^3). The median follow-up time for all patients was 32 months. There were 36 progression events (18 with low methylation grade and 18 with high methylation grade) and 7 deaths, all of which occurred in patients with high methylation grade.

Conclusion

This study reports significant associations between imaging features and methylation grades in IDH-mutant astrocytomas, suggesting that specific MRI characteristics may serve as valuable indicators of methylation status. Our volumetric analysis further supports that high methylation grade is associated with significantly larger edema volumes, providing a quantitative dimension to the imaging assessment that correlates with a poorer prognosis.

References

1. Lee MD, Jain R, Galbraith K, et al. T2-FLAIR Mismatch Sign Predicts DNA Methylation Subclass and CDKN2A/B Status in IDH-Mutant Astrocytomas. *Clinical Cancer Research* 2024;30:3512–9.
2. Pati S, Baid U, Edwards B, et al. Federated learning enables big data for rare cancer boundary detection. *Nat Commun* 2022;13:7346.

Images/Tables

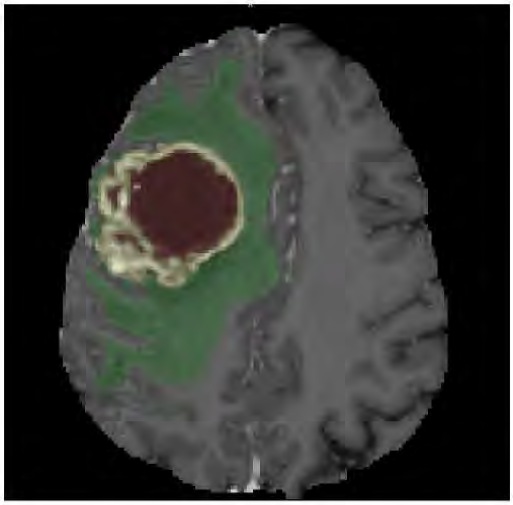

Figure 1: Post-contrast T1 image showing segmented tumor regions: Edema (Green), Contrast-Enhancing Tumor (Yellow), and Necrosis/Non-Contrast-Enhancing Tumor (Red).

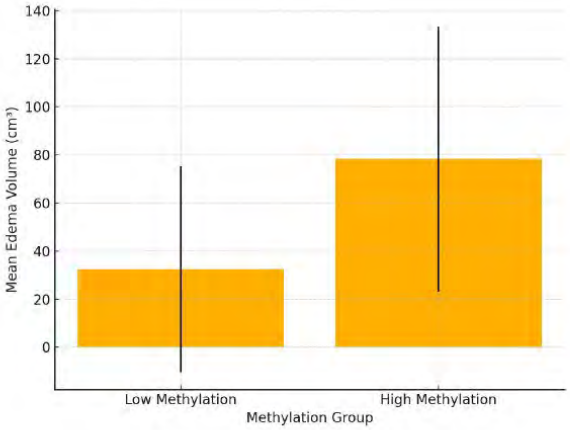

Figure 2: Mean edema volume by methylation group.

819

Association Between Intracranial Atherosclerotic Disease High-Resolution Vessel Wall Magnetic Resonance Imaging Findings with Multifocal Ischemic Infarcts and Overall Survival

David Timaran Montenegro MD, Abdulla A Alhashmi MD, Elham Tavakkol MD, Kamand Khalaj MD, Andres F Rodriguez, Arash Kamali MD, Jose Gavito Higuera MD, Roy Riascos MD
University of Texas Health Science Center at Houston, Houston, Texas, USA

Abstract Category

Adult Brain

Purpose

High-resolution vessel Wall Magnetic Resonance Imaging (HR-VW MRI) allows for detailed visualization of vessel wall abnormalities and plaque morphology, which are hypothesized to contribute to infarct formation in individuals with atherosclerotic disease. We specifically examine whether patients with intracranial atherosclerotic disease present vessel wall changes on HR-VW MR associated with multifocal ischemic infarct on DWI and the impact on overall survival.

Materials & Methods

A retrospective review of 339 patients studied with MRI vessel wall imaging over 7 years. Patients with suboptimal imaging quality and nonconclusive results of vessel wall imaging were excluded from the study. In total, 179 (52.8%) patients were included in the study. Vessel imaging was obtained using 3T scanners for all patients. The imaging protocol included DWI, 3D TOF MRA, and HR-VWI with and without contrast agent administration. The presence of plaque hemorrhage, plaque/wall signal intensity, and enhancement were collected. Chi-square and Fisher tests were used for univariate analysis. Kaplan Meier curve and Log-rank test were used for survival analysis.

Results

In 68 patients (38%) were diagnosed with intracranial atherosclerotic disease. In 24 patients (35.2%), the left PCA was affected, in 21 (30.8%), the right MCA was compromised, in 18 patients, the left MCA (26.4%) was affected, the right ICA in 12 patients (17.6%), the left ICA in 13 patients (19.1%), left ACA in 12 patients (17.6%), right PCA in 13 patients (19.1%), and right ACA in 10 patients (14.7%). Involvement of multiple vessels was identified in 47 patients (69.1%). Acute ischemia on DWI was identified in 54 patients (79.4%). Multifocal ischemia was identified in 20 patients (37%). Intracranial occlusive disease was observed in 10 patients (14.7%) and greater than 50% in 47 patients (69.1%). ON HR-VW MR, 32 patients showed intracranial vessel wall enhancement (47%); in 3 patients (4.4%), plaque hemorrhage was identified. Eccentric enhancement was identified in 19 patients (27.9) and concentric enhancement in 7 patients (10.2%). In patients with infarct compromising more than one vascular territory, 8 (40%) presented wall enhancement (p=0.3). Among them, eccentric wall enhancement was observed in (10%) (p=0.02). The survival rate of patients with vessel enhancement at 48 months was 100% versus 86% in patients without vessel wall enhancement (p=0.04). Vessel wall enhancement was not associated with recurrent stroke-free survival.

Conclusion

Among patients with ICAD and multifocal ischemic infarcts, the incidence of vessel wall enhancement reached 40%. There was a significant association between eccentric enhancement and multifocal ischemia, present in up to 10% of the patients. Interestingly, better overall survival rates were observed in patients with vessel wall enhancement at 48 months.

References

1. Mazzacane, F.; Mazzoleni, V.; Scola, E.; Mancini, S.; Lombardo, I.; Busto, G.; Rognone, E.; Pichiecchio, A.; Padovani, A.; Morotti, A.; et al. Vessel Wall Magnetic Resonance Imaging in Cerebrovascular Diseases. Diagnostics2022,12,258. https:// doi.org/10.3390/diagnostics12020258
2. Kim, J.-M.; Jung, K.-H.; Sohn, C.-H.; Moon, J.; Shin, J.-H.; Park, J.; Lee, S.-H.; Han, M.H.; Roh, J.-K. Intracranial plaque enhancement from high resolution vessel wall magnetic resonance imaging predicts stroke recurrence. Int. J. Stroke 2016, 11, 171–179.
3. Fakih, R.; Roa, J.A.; Bathla, G.; Olalde, H.; Varon, A.; Ortega-Gutierrez, S.; Derdeyn, C.; Adams, H.P.; Hasan, D.M.; Leira, E.C.; et al. Detection and Quantification of Symptomatic Atherosclerotic Plaques With High-Resolution Imaging in Cryptogenic Stroke. Stroke 2020, 51, 3623–3631.

Images/Tables

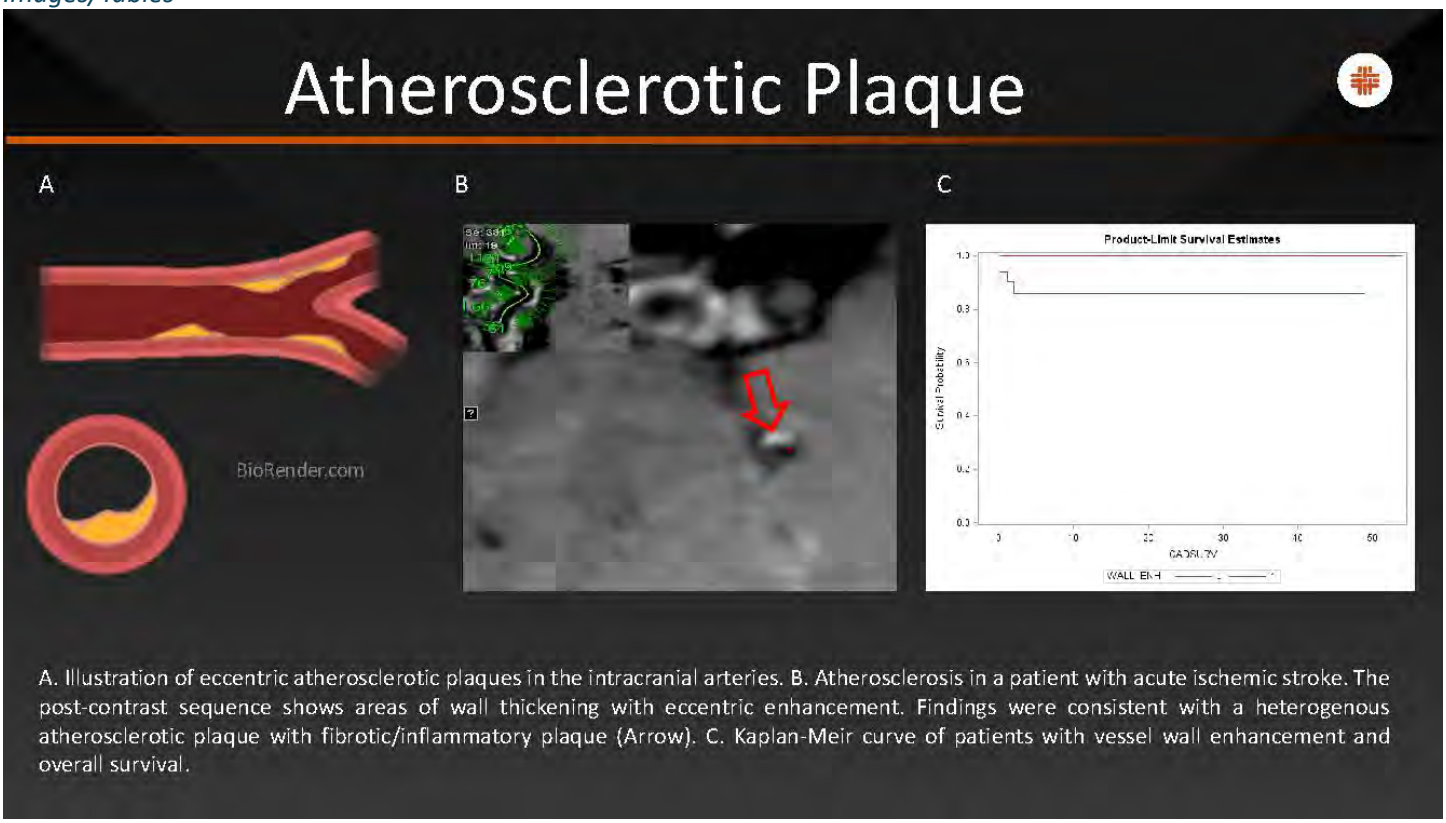

A. Illustration of eccentric atherosclerotic plaques in the intracranial arteries. B. Atherosclerosis in a patient with acute ischemic stroke. The post-contrast sequence shows areas of wall thickening with eccentric enhancement. Findings were consistent with a heterogenous atherosclerotic plaque with fibrotic/inflammatory plaque (Arrow). C. Kaplan-Meir curve of patients with vessel wall enhancement and overall survival.

828

Neuroradiological and Accessibility Barriers to Lecanemab Administration in Alzheimer's Disease

Samantha L. Watts
Boston University School of Medicine, Boston, MA, USA

Abstract Category

Socioeconomics & Health Policy

Purpose

Lecanemab, a monoclonal antibody for early-stage Alzheimer's disease (AD), shows promise as a treatment but may impose significant burdens on patients, neuroradiologists, and healthcare systems due to its complex imaging requirements, administration schedule, and high costs. These challenges could exacerbate health disparities, particularly among underserved or resource-limited populations. This study examines Lecanemab administration in relation to its financial and operational challenges and how these may affect the accessibility and feasibility of widespread treatment.

Materials & Methods

This review synthesized clinical guidelines, observational studies, and institutional case reports retrieved from PubMed and NIH databases, focusing on patient costs, operational requirements within radiology and infusion services, and overall healthcare utilization related to Lecanemab administration. Literature contributions from multidisciplinary teams in radiology, neurology, and case management were incorporated to further assess the systemic resource demands and accessibility inequities.

Results

Lecanemab's projected $5 billion annual cost to Medicare raises significant concerns about patient access and healthcare affordability. Initial treatment eligibility requires genetic testing, cognitive evaluations, and extensive imaging—factors that, combined with inconsistent insurance coverage, may deter patients from starting or continuing treatment. The estimated annual cost per patient is $19,500, including $11,000 in out-of-pocket expenses, plus additional costs for MRI screenings, infusion visits, and related care. The need for frequent brain MRIs to monitor amyloid-related imaging abnormalities (ARIA), especially for those with APOE4 genetic predispositions, adds both

financial and logistical challenges. Advanced imaging access, particularly for rural or underserved patients, often requires travel to specialized facilities, placing additional financial and time burdens on patients and caregivers. Healthcare providers report significant operational and staffing challenges. Radiology departments are tasked with managing specialized MRI reporting for drug approval, handling increased volumes of routine imaging, and monitoring for ARIA. Infusion centers are facing bottlenecks due to the intravenous administration of Lecanemab every 2 weeks for at least 18 months, necessitating additional space, equipment, and trained staff. Furthermore, facilities without the infrastructure to manage adverse events related to ARIA may face increased liability risks and potential emergency interventions, which stretch hospital resources and further complicate the delivery of care.

Conclusion

Lecanemab's financial and logistical demands create significant barriers for both patients and healthcare systems, exposing critical gaps in accessibility and infrastructure. High treatment costs, frequent MRI visits, travel to specialized centers, and genetic testing may limit access to those with sufficient resources, excluding many who could benefit. Radiology and infusion services face increased demands that require investment in hiring and training additional personnel, acquiring equipment, and establishing new protocols. This strain on healthcare systems, particularly those with limited resources, could lead to delays, longer wait times, and compromised care quality. As Lecanemab is rolled out more widely, these challenges may worsen, reducing its efficacy in slowing disease progression and potentially disqualifying patients who may have previously qualified due to disease progression beyond the inclusionary range. Neuroradiologists and neurologists are well-positioned to help develop solutions that increase access and prepare healthcare systems for the increased demand. Addressing these challenges will maximize Lecanemab's impact on Alzheimer's treatment, improving patient outcomes and reducing healthcare disparities.

References

1. Cummings J, Apostolova L, Rabinovici GD, et al. Lecanemab: Appropriate Use Recommendations. J Prev Alzheimers Dis. **2023**;10(3):362-377.
2. Moonis G, et al. ACR Appropriateness Criteria® Dementia. J Am Coll Radiol. **2020**;17(5).
3. Herpen R, Palekar N. Q&A: Cost is largest "roadblock" to lecanemab treatment for Alzheimer's. Healio. **July 2024**. Accessed November 6, 2024. https://www.healio.com/news/neurology/20240718/qa-cost-is-largest-roadblock-to-lecanemab-treatment-for-alzheimers#:~:text=Palekar%3A%20Lecanemab%20is%20the%20first,%2C%20MRIs%2C%20infusion%20costs).
4. Hudnall CE. Radiology Takes on Alzheimer's Disease. Am Coll Radiol. **October 2023**. Accessed November 6, **2024**. https://www.acr.org/Practice-Management-Quality-Informatics/ACR-Bulletin/Articles/October-2023/Radiology-Takes-on-Alzheimers-Disease.

831

Hyperechoic Ependyma in Premature Infants: A Potential Clue to Future Complications

Mika Shapira Rootman MD/PhD, Goni Merhav MD, Firas Srour MD
Rambam health care Campus, Haifa, Israel, Israel

Abstract Category

Pediatrics

Purpose

Major brain injuries associated with prematurity, such as germinal matrix hemorrhage/intraventricular hemorrhage (IVH), periventricular hemorrhagic infarction (PVHI), and white matter injury, have significant long-term neurological consequences. In the NICU, early detection and prediction of these complications typically rely on head ultrasound (HUS). While HUS can identify some risk factors, specific markers like hyperechoic ependyma (Figure 1) are underexplored as potential predictors of adverse outcomes, including post-hemorrhagic hydrocephalus of prematurity (PHHP) and severe white matter injury. This study aims to characterize hyperechoic ependyma on HUS in premature neonates and evaluate its association with the development of PHHP, the need for repeated neurosurgical interventions, and progression to advanced-grade periventricular leukomalacia (PVL).

Materials & Methods

We conducted a retrospective analysis of 184 preterm infants (<37 weeks gestation) who underwent HUS within the first 10 days of life, with a follow-up HUS after 10 days when available, supplemented by brain MRI obtained after the acute phase. Two certified radiologists independently evaluated HUS images, focusing on ependymal echogenicity and IVH grading. MRI assessments included ventriculomegaly, detailed hydrocephalus features (such as the requirement for

shunt placement, including cases necessitating multiple shunts, intraventricular septations, and ventricular compartment entrapment), and the severity of PVL. Statistical analyses utilized Spearman's rank and Chi-square tests, with Cramer's V to assess effect sizes, and statistical significance was set at $p<0.05$.

Results

Hyperechoic ependyma was identified in 7.6% of the cohort, predominantly on late HUS performed after 10 days of life. There was a strong positive correlation between late ependymal echogenicity and the subsequent development of PHHP requiring shunt placement ($r = 0.415$, $p < 0.01$, Cramer's $V = 0.297$), especially in cases without early hemorrhage (within the first 10 days). Additionally, late ependymal echogenicity significantly correlated with intraventricular septations ($r = 0.493$, $p < 0.01$), which are associated with more complex cases of hydrocephalus. Among patients with echogenic ependyma, 85.7% developed PVL, with a notable association for severe PVL ($r = 0.255$, $p < 0.05$, Cramer's $V = 0.214$). Furthermore, higher-grade IVH was significantly associated with echogenic ependyma. The relationship between ependymal echogenicity and hemorrhagic severity was consistent, with significant correlations found for grade 3 and PVHI hemorrhages across different phases of assessment.

Conclusion

Hyperechoic ependyma on late HUS strongly associates with severe neurological outcomes in preterm infants, including PHHP requiring shunt intervention and high-grade PVL. This finding suggests that hyperechoic ependyma may serve as a valuable early imaging marker of severe neonatal brain injury, likely linked to inflammatory or other injury-related pathways. Recognizing hyperechoic ependyma on HUS could improve early risk stratification, guiding closer monitoring and more proactive clinical management for high-risk neonates. Further research is warranted to elucidate the mechanisms underlying these associations and to validate hyperechoic ependyma as a reliable predictor in neonatal neuroimaging.

References

1. Rypens E, Avni EF, Dussaussois L, et al. Hyperechoic thickened ependyma: sonographic demonstration and significance in neonates. *Pediatr Radiol*. 1994;24(8):550-553.

2. Robinson S, Jantzie LL. Pathogenesis of posthemorrhagic hydrocephalus of prematurity: New horizons. *Semin Perinatol*. 2022;46(5):151596.

Images/Tables

832

Changes in Arachnoid Granulations in the Absence of Intracranial Pressure Alterations

Andrew W K Ko MD, Dipakkumar Thakor MD, Nada Aboudahab MD, Ali Sheikhy MD, M. Reza Taheri MD, PhD
George Washington University Hospital, Washington, DC, USA

Abstract Category

Adult Brain

Purpose

Changes in visible arachnoid granulations on imaging (VAGs) have been implicated in clinical outcome and severity of disease. For instance, patients with idiopathic intracranial hypertension (IIH) were noted to have a lower number of VAGs after age, BMI, and sex matching[1]. Concordantly, the number of VAGs was also inversely associated with imaging markers of severe disease in IIH[2]. Patients with chronic hydrocephalus from subarachnoid hemorrhage that had more VAGs tended to not require ventriculoperitoneal shunting[3]. However, to our knowledge, no studies have looked at changes in VAGs in patients without known intracranial pressure (ICP) alterations. In this study, we test the null hypothesis that there are no significant variations in VAG number or volume in patients with no acute intracranial abnormalities expected to impact ICP.

Materials & Methods

In this IRB-approved study, we retrospectively reviewed patients with at least 2 consecutive CTA studies, VAGs on either study, and no acute intracranial abnormalities. We included 88 patients based on these criteria, with average time between imaging of 150 (range 60-365) days. The mean age was 60 (range 30-90) years with 48% females and 52% males. We used paired t-test to compare number and volume of visible AGs both at an initial time point A and follow-up time point B.

Results

We found a range 0 to 7 VAGs in patients included in this study. We found a significant difference in number of VAGs between time points A and B (A: 0.99±1.42, B: 0.92±1.42, p=0.033). When comparing individual VAGs, a small volume difference with a borderline in statistical significance (A: 42.7±53.6 mm^3, B: 45.7±56.9 mm^3, p=0.053) is also observed.

Conclusion

VAGs undergo small changes in number and volume over time, which support the idea that arachnoid granulations are dynamic. These changes are markedly smaller than those suggested by prior studies in settings of altered ICP.

References

1. Huda F, Abdelmonem A, Dehghani Firouzabadi F, Srinivas Dola VN, Sheikhy A, Taheri MR. The role of arachnoid granulations in idiopathic intracranial hypertension. *Neuroradiol J*. 2023;36(6):651-656. DOI: https://doi.org/10.1177/19714009231173109
2. Watane GV, Patel B, Brown D, Taheri MR. The Significance of Arachnoid Granulation in Patients With Idiopathic Intracranial Hypertension. *J Comput Assist Tomogr*. 2018;42(2):282-285. DOI: https://doi.org/10.1097/RCT.0000000000000668
3. Almohaimede K, Zaccagna F, Kumar A, et al. Arachnoid granulations may be protective against the development of shunt dependent chronic hydrocephalus after aneurysm subarachnoid hemorrhage*. *Neuroradiol J*. 2023;36(2):189-193. DOI: https://doi.org/10.1177/19714009221122249

833

Changes in Arachnoid Granulations in Acute Hydrocephalus

Andrew W K Ko MD, Nada Aboudahab MD, Dipakkumar Thakor MD, Ali Sheikhy MD, M. Reza Taheri MD, PhD
George Washington University Hospital, Washington, DC, USA

Abstract Category

Adult Brain

Purpose

Changes in visible arachnoid granulations on imaging (VAGs) have been implicated in clinical outcome and severity of disease. For instance, patients with idiopathic intracranial hypertension (IIH) were noted to have a lower number of VAGs after age, BMI, and sex matching[1]. Concordantly, number of VAGs was also inversely associated with imaging markers of severe disease in IIH[2]. Patients with chronic hydrocephalus from subarachnoid hemorrhage that had more VAGs tended to not require ventriculoperitoneal shunting[3]. In animal studies, arachnoid granulations were observed to be smaller and flattened, with decreased microvilli and vacuoles reflective of decreased CSF transport in settings of

rapidly decreased ICP[4]. However, to our knowledge, no studies have looked at changes in VAGs in cases of rapidly increased ICP. In this study, we test the null hypothesis that there are no significant variations in VAGs number or volume in patients with acute hydrocephalus.

Materials & Methods

In this IRB-approved study, we retrospectively reviewed patients with at least 2 consecutive CTA studies, VAGs on either study, and acute hydrocephalus on initial study. We included 9 patients based on these criteria, with average time between imaging of 9.5 (range 6-192) days. The mean age was 61 (range 29-90) years with 49% females and 51% males. We used paired t-test to compare number and volume of VAGs both at an initial time point A and follow-up time point B.

Results

We found a range 0 to 5 VAGs in patients included in this study. In comparison to the initial exam, which was obtained at a time of an acute intracranial abnormality and evidence of elevated ICP, the number of VAGs in the follow-up group, in which measures had been taken to decrease the ICP, were significantly lower (A: 1.93±1.16, B: 0.73±1.35, $p<0.001$). We found no significant difference in mean volume of VAG from time point A compared to time point B (A: 56.4±41.7 mm^3, B: 65.5±51.7 mm^3, $p=0.476$), likely due to the range of volumes (0-410 mm^3) of VAGs in different patients. In an ongoing analysis, we have noticed that in two separate patients, the volume of a VAG on the second study is less than on initial presentation. For instance, a left transverse sinus VAG, shown in Figure 1, decreased from 6.2 x 5.0 x 6.0 mm to 2.9 x 2.1 x 2.5 mm. Another left transverse sinus VAG, shown in Figure 2, decreased from 4.6 x 5.1 x 4.9 mm to 3.8 x 3.9 x 4.0 mm. We are continuing our investigation of comparative changes in other individual VAGs at the two time points.

Conclusion

Our findings suggest that the number and potentially volume of VAGs decrease once measures are performed to normalize the acutely elevated ICP.

References

1. Huda F, Abdelmonem A, Dehghani Firouzabadi F, Srinivas Dola VN, Sheikhy A, Taheri MR. The role of arachnoid granulations in idiopathic intracranial hypertension. *Neuroradiol J*. 2023;36(6):651-656. DOI: https://doi.org/10.1177/19714009231173109
2. Watane GV, Patel B, Brown D, Taheri MR. The Significance of Arachnoid Granulation in Patients With Idiopathic Intracranial Hypertension. *J Comput Assist Tomogr*. 2018;42(2):282-285. DOI: https://doi.org/10.1097/RCT.0000000000000668
3. Almohaimede K, Zaccagna F, Kumar A, et al. Arachnoid granulations may be protective against the development of shunt dependent chronic hydrocephalus after aneurysm subarachnoid hemorrhage*. *Neuroradiol J*. 2023;36(2):189-193. DOI: https://doi.org/10.1177/19714009221122249
4. Takahashi Y, Shigemori M, Inokuchi T, et al. Scanning electron microscopic observations of the arachnoid granulations in monkeys with cerebrospinal fluid hypotension. *Kurume Med J*. 1993;40(4):201-211. DOI: https://doi.org/10.2739/kurumemedj.40.201

Images/Tables

Figure 1)

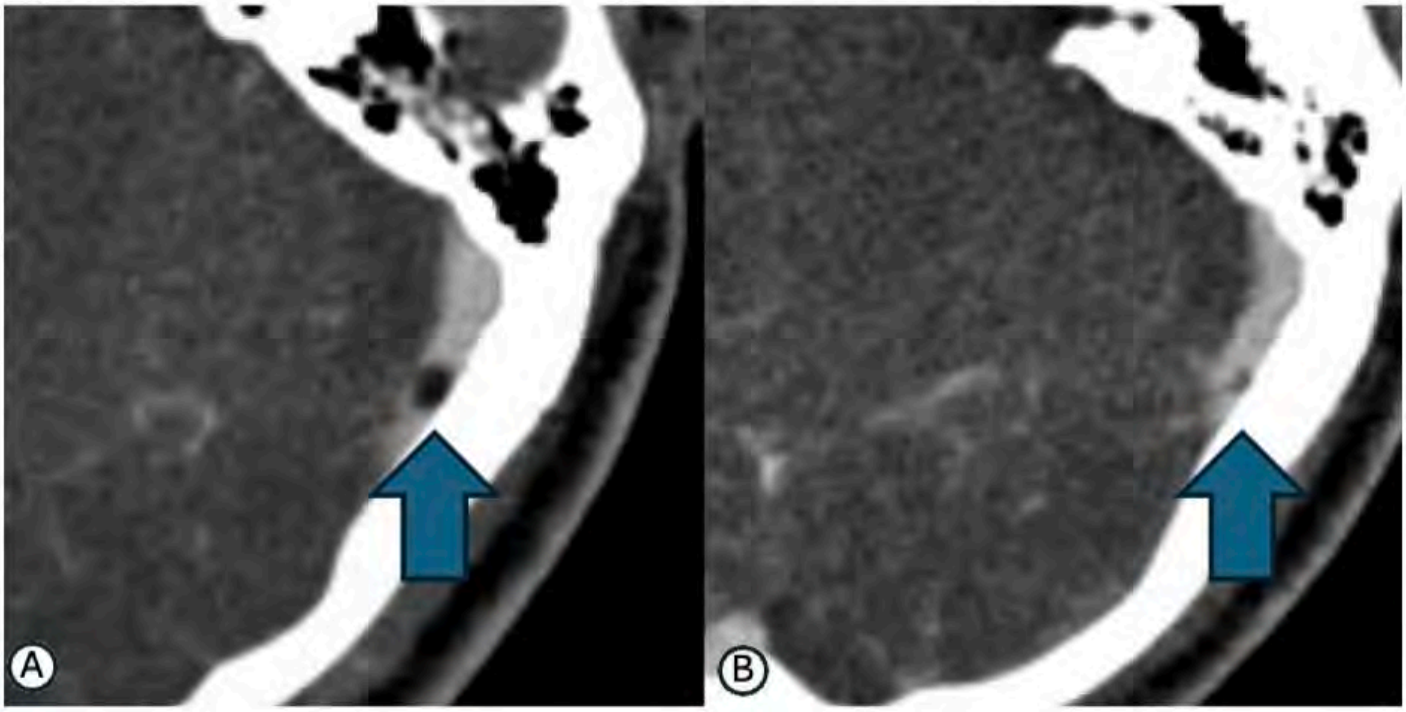

Initial imaging on a patient with multiple acute intracranial hemorrhages and acute hydrocephalus shows a VAG (arrow) on the left transverse sinus (A). The VAG decreased in volume after the patient underwent external ventricular drain placement (B).

Figure 2)

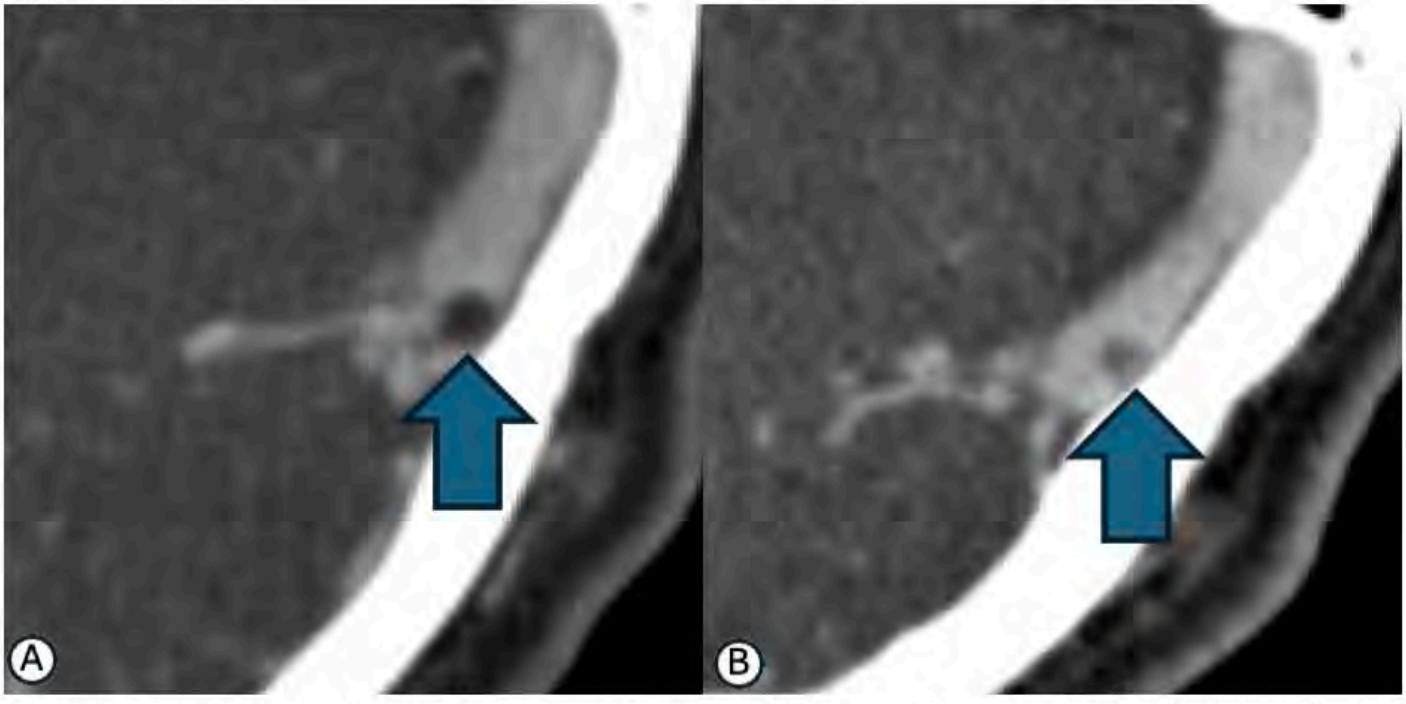

Initial imaging on a patient with an acute intracranial hemorrhage and acute hydrocephalus shows a VAG (arrow) on the left transverse sinus (A). The VAG decreased in volume after the patient underwent hemicraniectomy and external ventricular drain placement (B).

835

Nigrosome and Neuromelanin Volume Analysis in Parkinson's Disease: Diagnostic Utility and SUVR Correlation

Hwan Heo MS[1], ALeum Lee MD, Ph.D[2], Myeongoh Lee MS[1], Jeongwon Jo MS[1], Intae Shin MS[1], Minseung Kim MD[3], Seokjong Chung MD[4], Sukyun Kang MD, Ph.D[3], Soohwa Song Ph.D[1]
[1]Heuron Co., Ltd.,, Seoul, Seoul, Korea, Republic of. [2]Soon Chun Hyang University Hospital Bucheon, Bucheon-si, Gyeonggi-do, Korea, Republic of. [3]Department of Neurology, Dongtan Sacred Heart Hospital, Hallym University College of Medicine, Hwaseong, Gyeonggi-do, Korea, Republic of. [4]Department of Neurology, Yongin Severance Hospital, Yonsei University Health System, Yongin, Gyeonggi-do, Korea, Republic of

Abstract Category

AI/Informatics

Purpose

Parkinson's disease (PD) is characterized by dopaminergic neuron loss in the substantia nigra pars compacta (SNpc), where nigrosome-1 (N1) is most vulnerable to degeneration.[1,2] This process involves neuromelanin (NM) release and iron accumulation. Susceptibility map-weighted imaging (SMWI) and sandwich NM sequences can detect these changes[3,4], and quantitative information can be analyzed using Heuron NI and NM tools. We evaluated how combining these quantitative markers improves diagnostic accuracy and analyzed their correlation with standardized uptake value ratio (SUVR).

Materials & Methods

Data acquisition: We prospectively enrolled 142 participants (72 PD patients, 70 Normal Controls) from two hospitals between December 2023 and July 2024. PD diagnosis was confirmed by experienced neurologists using United Kingdom Parkinson's Disease Society Brain Bank Diagnostic Criteria. All participants underwent 3T MRI scanning (Siemens VIDA and Philips Ingenia Elition X) with a 32-channel coil. We performed 3D multi-echo GRE sequence for N1 analysis, sandwich NM sequence, and 3D T1-weighted imaging for NM quantification and intracranial volume normalization. The MRI protocols included: 3D multi-echo GRE (FOV=192×192×32, voxel size=0.5×0.5×1.0mm, FA=20°, 3 echoes, TR=48ms, TE=14/26.5/39ms), sandwich NM (FOV=320×320×32, voxel size=0.8×0.8×1.2mm, FA=14°, TR=30ms, TE=4.2ms), and 3D T1w (TR=2300ms, TE=2.3ms, TI=1100ms, voxel size=1mm³, FA=8°). Additionally, 33 PD patients underwent 18F-FP-CIT PET scanning(Biograph mCT, Siemens Healthineers).
Image processing : we utilized Heuron's commercial deep learning-based tools. Heuron NI for N1 quantification and volume measurement, Heuron NM for NM volume quantification, and Heuron BrainPET for PET-CT analysis. N1 diagnostic performance was evaluated using ROC-derived cut-off values. NM volume measurements were used as weights for N1 volume analysis. We analyzed correlations between NM volume and SUVR to assess PD-related NM signal changes.

Results

Diagnostic performance of Heuron NI based on N1 volume yielded an AUC of 0.932, with 93.06% sensitivity and 82.86% specificity. Adding NM volume as a weight improved AUC to 0.956, showing statistically significant enhancement ($p = 0.021$). Using NM volume alone showed low diagnostic performance (AUC = 0.735). Correlations were significant between NM volume and SUVR in basal ganglia subregions.

Conclusion

In this study, we found that (NM) volume segmented from Sandwich NM images showed significant correlation with SUVR from various subregions of basal ganglia, particularly in the putamen and caudate nucleus, consistent with previous findings.[5] The NM volume, while not effective as an independent diagnostic marker, improved diagnostic accuracy when used as a weighting factor for the N1 region. The NM-weighted model demonstrated better performance for PD diagnosis, with an AUC of 0.956 compared to the unweighted model (AUC 0.932). These results suggest potential clinical utility of NM in improving PD diagnostic accuracy.

References

1. Dickson, Dennis W. "Parkinson's Disease and Parkinsonism: Neuropathology." *Cold Spring Harbor Perspectives in Medicine* 2, no. 8 (August 2012): a009258.
2. Cosottini, Mirco, Daniela Frosini, Ilaria Pesaresi, et at. "MR Imaging of the Substantia Nigra at 7 T Enables Diagnosis of Parkinson Disease." *Radiology* 271, no. 3 (June 2014): 831–38.
3. Ji, Sooyeon, Eun-Jung Choi, Beomseok Sohn, et al. "Sandwich Spatial Saturation for Neuromelanin-Sensitive MRI: Development and Multi-Center Trial." NeuroImage 264 (December 2022): 119706.

4. Nam, Yoonho, Sung-Min Gho, Dong-Hyun Kim, et al. “Imaging of Nigrosome 1 in Substantia Nigra at 3T Using Multiecho Susceptibility Map-weighted Imaging (SMWI).” Journal of Magnetic Resonance Imaging 46, no. 2 (August 2017): 528–36.
5. Isaias, Ioannis U., Paula Trujillo, Paul Summers, et al. “Neuromelanin Imaging and Dopaminergic Loss in Parkinson’s Disease.” *Frontiers in Aging Neuroscience* 8 (2016): 196.

Images/Tables

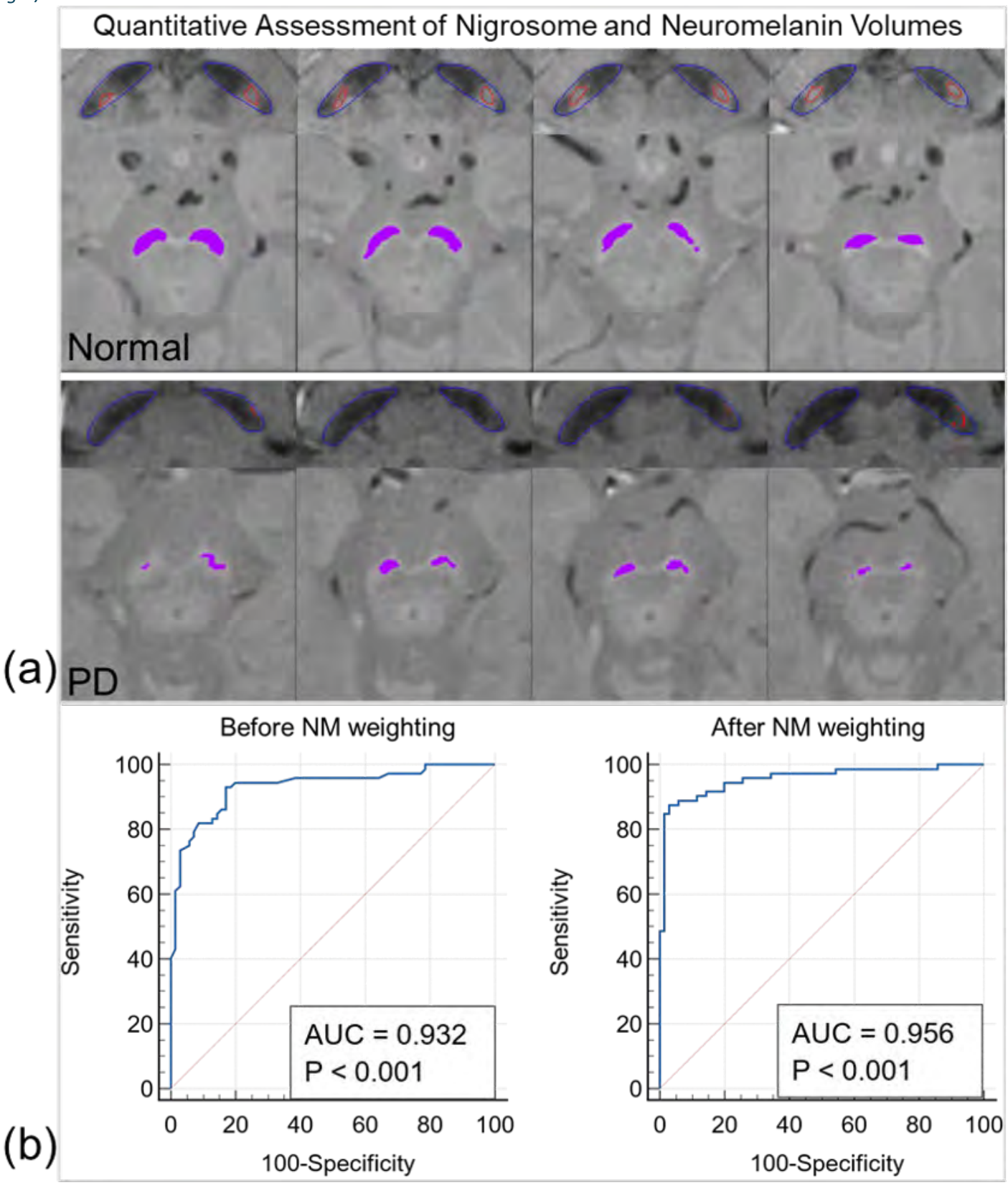

844

The Vertical Triband Flag Sign: A Novel MRI Marker for Rathke Cleft Cyst Differentiation

Elham Paraandavaji MD[1], Guive Sharifi Professor[1], Mohammad Ali Kazemi Associate Professor[2], Nader Akbari Dilmaghani Associate Professor[1]

[1]Skull Base Research Center, Loghman Hakim Hospital, Shahid Beheshti University of Medical Sciences, Tehran, Tehran, Iran, Islamic Republic of. [2]Department of Radiology, Amiralam Hospital, Tehran University of Medical Sciences, Tehran, Tehran, Iran, Islamic Republic of

Abstract Category

Adult Brain

Purpose

Rathke cleft cysts (RCC) are benign cystic lesions commonly located in the sellar and suprasellar regions, with an approximate prevalence of 4% (1, 2). Differentiating RCC from other cystic lesions in this area is challenging due to similar imaging characteristics (3). This study introduces the "vertical triband flag sign" as a novel MRI marker to improve RCC differentiation.

Materials & Methods

We retrospectively reviewed MRI data from 42 patients with confirmed RCC treated between 2016 and 2023. Imaging was performed using a 1.5-T MRI scanner, and all scans were independently reviewed by a neurosurgeon and neuroradiologist for the presence of the flag sign in T1 and T2-weighted images.

Results

The vertical triband flag sign was identified in 90.5% of cases, appearing most frequently in T1-weighted images (71.5%). This sign, characterized by three distinct vertical bands across the cyst, was absent in cases with small sellar or suprasellar RCC. In contrast, the dot sign, often noted as characteristic of RCC, was observed in only one case (4).

Conclusion

The vertical triband flag sign could serve as a valuable diagnostic tool for RCC, enhancing specificity and aiding radiologists and neurosurgeons in differentiating RCC from other cystic lesions. This sign has promising potential for RCC diagnosis, though further multicenter studies are recommended to confirm its diagnostic accuracy.

References

1. Wang S, Nie Q, Wu Z, Zhang J, Wei L. MRI and pathological features of Rathke cleft cysts in the sellar region. Exp Ther Med 2020;19:611–18. DOI: https://doi.org/10.3892/etm.2019.8272.
2. Jung JE, Jin J, Jung MK, et al. Clinical manifestations of Rathke's cleft cysts and their natural progression during 2 years in children and adolescents. Ann Pediatr Endocrinol Metab 2017;22:164–69. DOI: https://doi.org/10.6065/apem.2017.22.3.164.
3. Kim JE, Kim JH, Kim OL, et al. Surgical treatment of symptomatic Rathke cleft cysts: clinical features and results with special attention to recurrence. J Neurosurg 2004;100:33–40. DOI: https://doi.org/10.3171/jns.2004.100.1.0033.
4. Tominaga JY, Higano S, Takahashi S. Characteristics of Rathke's cleft cyst in MR imaging. Magn Reson Med Sci 2003;2:1–8. DOI: https://doi.org/10.2463/mrms.2.1.

Images/Tables

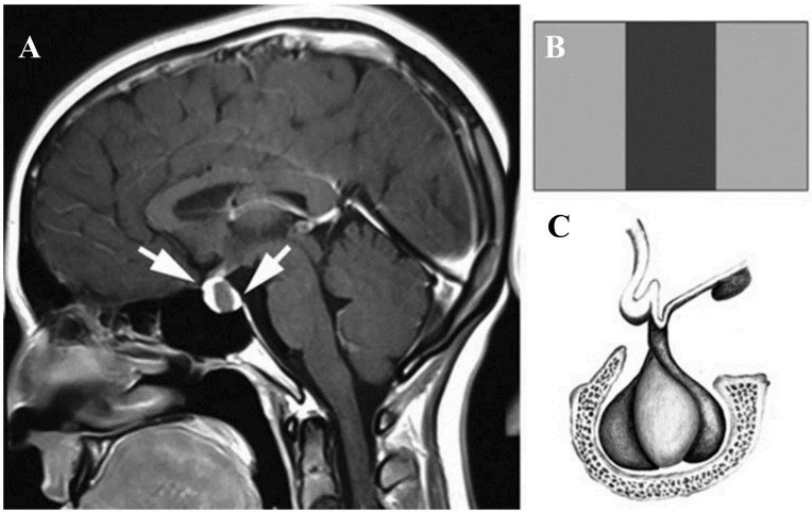

860

Biochemical Metric Correlates to Parathyroid Scintigraphy for the Pre-Surgical Evaluation of Hyperparathyroidism

Ryan Smith, Victoria Linehan, Steve Burrell, Ian R Macdonald
Dalhousie University, Halifax, Nova Scotia, Canada

Abstract Category

Head & Neck

Purpose

To compare parathyroid scintigraphy results with patient biochemistry, surgery, and pathology to inform appropriateness criteria and assess biochemical metrics in the imaging workup of hyperparathyroidism (HPT).

Materials & Methods

This retrospective study included 421 patients who underwent parathyroid scintigraphy at our institution from 2016 to 2020. Patients were grouped based on study indication (primary vs. secondary HPT) and their clinical profiles were reviewed for scan result, parathyroid-related blood work, surgical results, location of adenomas, and pathology. Performance metrics of scintigraphy were analyzed. Demographics, bloodwork, and location were compared between positive and negative scans using univariate analysis (t-tests and Fisher tests, as appropriate). Positive scintigraphy, primary HPT group, and bloodwork were analysed with two-way ANOVAs. Multivariate logistic regression analysis was employed to identify predictors positive scans. ROC analysis was conducted to evaluate the performance of biochemistry in predicting scan results.

Results

Positive tests—occurring in 52% of patients—were associated with higher parathyroid hormone (PTH) and corrected calcium. However, PTH level was only predictive of a positive test in patients with secondary HPT. Scintigraphically, abnormal glands were identified in equal proportions in the left and right neck with 66% located to the inferior parathyroid glands, 9% ectopically located, and 7% demonstrating multifocal abnormal glands. Sensitivity of scintigraphy for pathology-proven parathyroid adenomas was overall 77% however, of these, only 67% were concordant with the surgically documented location. The positive predictive value for adenomas was 100% with no false positive scans, however the negative predictive value was only 13%. On multivariate analysis, male sex, corrected calcium, and phosphorus were predictors of a positive scan. Corrected calcium was deemed the most predictive with an OR of 1.28 for every 0.1 mmol/L increase. Based on ROC analysis, corrected calcium had an AUC of 0.628 and a cutoff of 2.65 mmol/L maximized sensitivity (79%) and specificity (42%) for a positive test.

Conclusion

In this large retrospective cohort, several biochemical metrics such as corrected calcium levels were predictive of a positive study. Furthermore, PTH levels significantly differed between primary and secondary HPT suggesting that a tailored biochemical metric may be the optimal approach for selecting HPT patients for imaging work up. Scintigraphy has a very high positive predictive value, however for those with a negative scan or secondary HPT, further investigation into the concurrent use of additional imaging techniques (US, 4D-CT) is warranted.

References

1. Zhu M, He Y, Liu T, et al. Factors That Affect the Sensitivity of Imaging Modalities in Primary Hyperparathyroidism. Int J Endocrinol. 2021 Feb 20;2021:3108395.
2. Galvin L, Oldan JD, Bahl M, et al. Parathyroid 4D CT and Scintigraphy: What Factors Contribute to Missed Parathyroid Lesions? Otolaryngol Head Neck Surg. 2016 May;154(5):847-533.
3. Durmuş ET, Atmaca A, Kefeli M, et al. Clinicopathological variables that correlate with sestamibi positivity in uniglandular parathyroid disease: a retrospective analysis of 378 parathyroid adenomas. Ann Nucl Med. 2022 Jan;36(1):33-42

Images/Tables

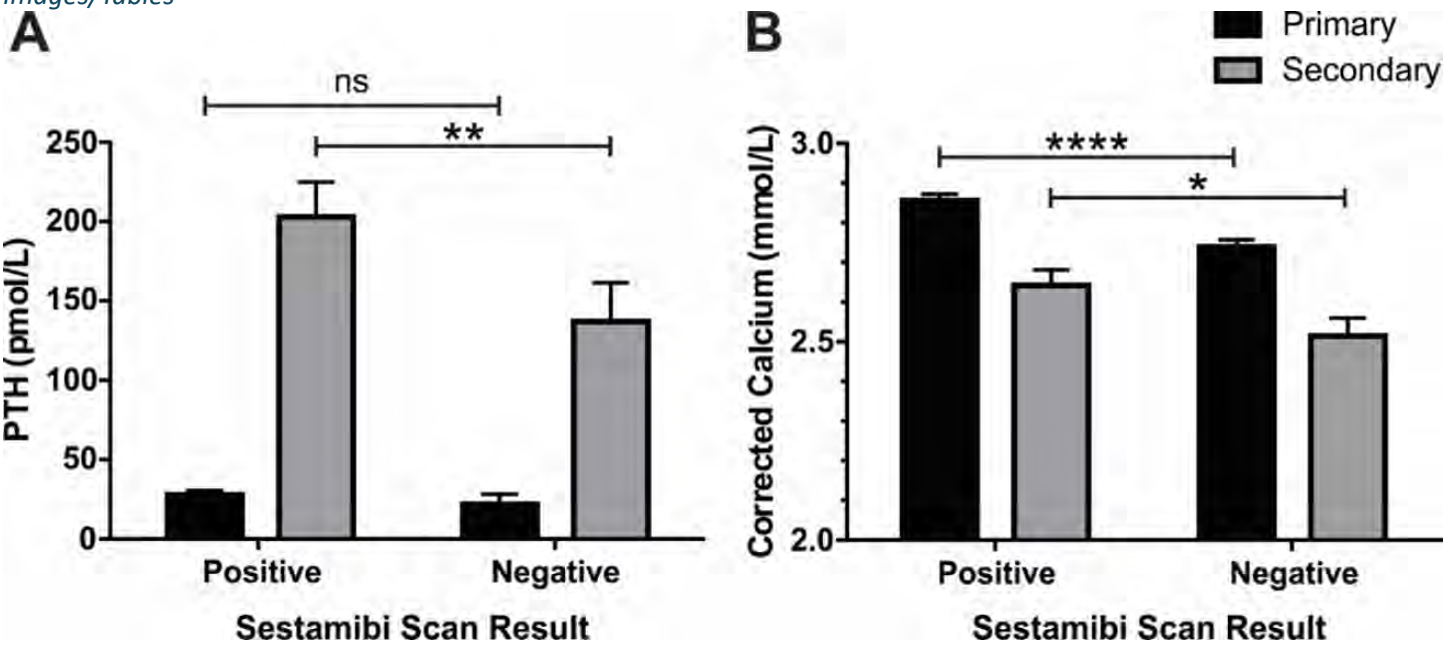

862

CT Angiography of the Head for the Initial Assessment of Giant Cell Arteritis: Presenting Symptoms, Biopsy Outcomes and Alternative diagnosis

Arsalan Rizwan MD, PhD, Supriya Khatri BSc, Sana Basseri MD, PhD, John Rossiter MD, PhD, Martin ten Hove MD, Omar Islam MD, Benjamin Kwan MD
Queen's University, Kingston, Ontario, Canada

Abstract Category

Head & Neck

Purpose

Giant cell arteritis (GCA), a form of large vessel vasculitis, carries the risk of irreversible loss of vision due to involvement of arteries supplying optic nerve, retina and choroid. As such, timely diagnosis of GCA is crucial. The study examines the presenting symptoms among suspected GCA patients with both positive and negative biopsy results and the association of CTA findings of the suspected GCA patients with STA biopsy results.

Materials & Methods

A retrospective study involving 22 patients who underwent superficial temporal artery (STA) biopsy and computed tomography angiography (CTA) at Kingston Health Science Center. The CTA images of the patients were analyzed for the following imaging signs: blurred superficial temporal artery wall, perivascular enhancement, presence of stenosis or occlusion of STA and calcification. The association between imaging signs and STA biopsy (positive if histopathology consistent with GCA) results was assessed using odds ratios (ORs). Additionally, the final alternative diagnosis for the patients with negative biopsy results was also investigated.

Results

There was a strong association between the presence of two CTA imaging findings—blurred STA wall and perivascular enhancement—and positive STA biopsy results (OR: 29 , p: 0.001). Suspected GCA patients with negative STA biopsy results had no single unifying alternative diagnosis.

Conclusion

This study provides evidence for the potential role of CTA in the initial assessment of suspected GCA patients.

References

Dejaco C, Ramiro S, Bond M, et al. EULAR recommendations for the use of imaging in large vessel vasculitis in clinical practice: 2023 update. *Ann Rheum Dis*. 2024;83(6):741-751. doi:10.1136/ARD-2023-224543

863

Clinical Experience with Gadopiclenol in Patients with Brain Metastases: Single and Double Doses, Comparison of Standard and Delayed Imaging

Josef Vymazal MD, PhD, Zuzana Ryznarova MD, PhD, Aaron Rulseh MD, PhD
Na Homolce Hospital, Prague, NA, Czech Republic

Abstract Category

Adult Brain

Purpose

To demonstrate the role of gadopiclenol in MR imaging of brain metastases at standard (0.05 mmol/kg) and double dose (0.1 mmol/kg), including delayed examination (ca 15 minutes after contrast administration).

Materials & Methods

Ninety-one subjects with known brain metastases underwent MRI prior to radiosurgery (44 female, mean age 64.2 12 years). A standard T1W 3D SPACE sequence was acquired in all subjects (3 subjects at 1.5T, 88 at 3T) post-contrast, followed by a delayed acquisition. In roughly half of subjects (n=47), the delayed acquisition was preceded by additional contrast administration (cumulative double dose). After randomization, 3 blinded readers evaluated the number of lesions for each patient in 2 sessions, 1 month apart. A paired t-test was used to compare early and late evaluations in the two groups (subjects with cumulative single dose or double dose), the Welch t-test was used to compare differences in (late-early) single versus (late-early) double doses.

Results

Agreement between all three blinded readers was used for evaluation. The late single dose exam revealed 170 metastatic lesions compared to 161 metastatic lesions on the early exam. The late double-dose exam revealed 138 metastatic lesions compared to 121 metastatic lesions on the single dose early exam. The number of lesions on early versus late (single/double dose) exams did not differ significantly (p=0.4 and p=0.11, respectively). No significant difference was detected between double dose and delayed single dose.

Conclusion

Although relatively more lesions were detected on delayed exam (single/double dose), the difference did not reach significance, likely reflecting small effect size. Furthermore, no significant difference was found between late single and double dose.

References

1. Robic C, Port M, Rousseaux O, Louguet S, Fretellier N, Catoen S, Factor C, Le Greneur S, Medina C, Bourrinet P, Raynal I, Idée JM, Corot C. Physicochemical and Pharmacokinetic Profiles of Gadopiclenol: A New Macrocyclic Gadolinium Chelate With High T1 Relaxivity. Invest Radiol. 2019 Aug;54(8):475-484. doi: 10.1097/RLI.0000000000000563. Erratum in: Invest Radiol. 2019 Dec;54(12):810. doi: 10.1097/RLI.0000000000000632. PMID: 30973459; PMCID: PMC6661244.
2. Loevner LA, Kolumban B, Hutóczki G, Dziadziuszko K, Bereczki D, Bago A, Pichiecchio A. Efficacy and Safety of Gadopiclenol for Contrast-Enhanced MRI of the Central Nervous System: The PICTURE Randomized Clinical Trial. Invest Radiol. 2023 May 1;58(5):307-313. doi: 10.1097/RLI.0000000000000944. Epub 2022 Dec 19. PMID: 36729404; PMCID: PMC10090311.

875

Clinical Determinants of White Matter Hyperintensities in a Population-Based Cohort

Yash Patel PhD[1], Jean Shin[2], Richard Zou[1], Alexandre Boutet[3], Tomas Paus[4], Zdenka Pausova[5]
[1]University of Toronto, Toronto, ON, Canada. [2]Centre hospitalier universitaire Sainte-Justine, University of Montreal, Montreal, QC, Canada. [3]Krembil Research Institute, Toronto Western Hospital, University Health Networ, Toronto, ON, Canada. [4]Departments of Psychiatry and Neuroscience, Faculty of Medicine, University of Montreal and Centre hospitalier universitaire Sainte-Justine, University of Montreal, Montreal, QC, Canada. [5]Department of Pediatrics, Faculty of Medicine, University of Montreal, and Centre hospitalier universitaire Sainte-Justine, University of Montreal, Montreal, QC, Canada

Abstract Category

Adult Brain

Purpose

White matter hyperintensities (WMH) index structural abnormalities within periventricular and deep white matter, with WM tissue appearing hyperintense on T2 or FLAIR magnetic resonance imaging. WMH are associated with a higher risk of stroke, dementia, and with vascular risk factors, such as hypertension[1,2]. Herein, we aim to characterize the relative effects of common clinical and bloodwork-based measures on WMH.

Materials & Methods

We used data from 36,320 stroke-free, dementia-free, individuals from the UK Biobank, with an average age of 64 years (age range of 45 – 81 years, 53% female sex). T1w and FLAIR images (3T Siemens Skyra) were co-registered using 6 degrees of freedom rigid registration, and WMH were quantified using a convolutional neural network-based tool (segcsvd-WMH)[3]. WMH volumes were extracted using regional WMH segmentation[4]. We used a multivariable linear regression model to assess the effects of age, sex, BMI, systolic blood pressure (BP), diastolic BP, HbA1c, total triglycerides, low density lipoprotein (LDL)-cholesterol, high density lipoprotein (HDL)-cholesterol, and smoking status on WMH. The 'relaimpo' R package was used to calculate the relative variance explained for each of these predictors using the averaging over orders method ('lmg')[5].

Results

The multivariable linear model explain a total of 24% of variation in total WMH, with age contributing to 19%, while systolic BP, diastolic BP and HbA1c explaining 3.30%, 0.53% and 0.67% of additional variance, respectively (Figure 1). These findings do not vary as a function of regional WMH; nonetheless, the regional models explain the lowest variance in WMH in the temporal (R^2 = 14.5%) WM and the highest in the frontal (R^2 =23.1%) WM (Figure 1).

Conclusion

In summary, WMH are predominately associated with age and, to a lesser degree, with modifiable risk factors such as systolic BP and glycemic control (HbA1c). These associations do not vary substantially across brain regions, suggesting a region-independent pathophysiology.

References

1. Wardlaw, J. M., Smith, C. & Dichgans, M. Small vessel disease: mechanisms and clinical implications. *The Lancet Neurology* **18**, 684–696 (2019).

2. Patel, Y. *et al.* Genetic risk factors underlying white matter hyperintensities and cortical atrophy. *Nat Commun* **15**, 9517 (2024).

3. Gibson, E. *et al.* SegcsvdWMH: A convolutional neural network-based tool for quantifying white matter hyperintensities in heterogeneous patient cohorts. 2024.06.20.24309230 Preprint at https://doi.org/10.1101/2024.06.20.24309230 (2024).

4. Sudre, C. H. *et al.* Bullseye's representation of cerebral white matter hyperintensities. *Journal of Neuroradiology* **45**, 114–122 (2018).

5. Grömping, U. Relative importance for linear regression in R: the package relaimpo. *Journal of statistical software* **17**, 1–27 (2007).

Images/Tables

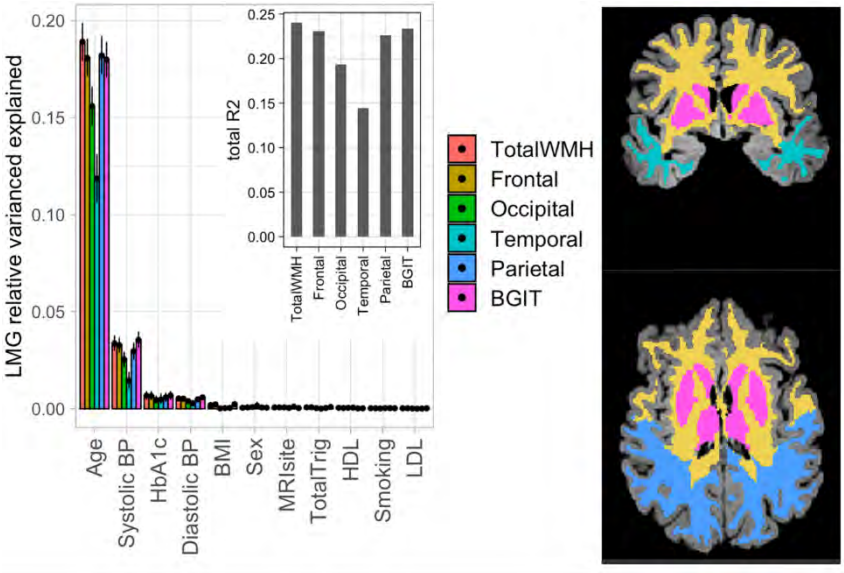

879

Deep Learning-Driven Prediction of Pediatric Spinal Cord Injury Severity Using Comprehensive Structural MRI Analysis

Zahra Sadeghi Adl MSc[1], Sara Naghizadehkashani Md[2], Laura Krisa Phd[2], Devon Middleton Phd[2], Mahdi Alizadeh Phd[2], Adam Flanders Md[2], Scott H Faro Md[2], Feroze B Mohamed Phd[2]

[1]Temple university, Philadelphia, PA, USA. [2]Thomas Jefferson University, Philadelphia, PA, USA

Abstract Category

AI/Informatics

Purpose

Spinal cord injury (SCI) in the pediatric population presents a unique challenge in diagnosis and prognosis due to the complexity of performing clinical assessments on children. Accurate evaluation of structural changes in the spinal cord is essential, as clinical tests can be difficult to perform reliably in pediatric population. The purpose of this study was to evaluate structural characteristics of the spinal cord by comparing cross-sectional area (CSA), anterior-posterior (AP) width, and right-left (RL) width across all vertebral levels between typically developing (TD) children and those with SCI. We aimed to use these structural measurements, alongside deep learning methods, to detect SCI and predict the American Spinal Injury Association (ASIA) Impairment Scale (AIS) categories.

Materials & Methods

Sixty-one pediatric participants, aged 6-18, were enrolled in this study, including 20 children diagnosed with SCI and 41 typically developing (TD) children as controls. All participants underwent spinal MRI scanning using a 3T MRI scanner, capturing high-resolution T2-weighted images along the cervical and thoracic spinal cord. SCI participants also underwent the International Standards for Neurological Classification of Spinal Cord Injury (ISNCSCI) assessment, which determines the AIS category and provides a standardized evaluation of neurological function. For each subject, CSA, AP width, and RL width were measured across all vertebral levels (from C1 through T11) using the Spinal Cord Toolbox (SCT), an automated processing tool designed to extract structural parameters from spinal MRI data accurately. To classify SCI presence and severity, a custom deep convolutional neural network (CNN) model was developed. The CNN was trained to classify subjects as SCI or TD and to predict the AIS categories of SCI subjects based on extracted structural parameters, including CSA, AP width, and RL width, along with demographic information such as age and height. For comparison, traditional machine learning models, including support vector machine (SVM) and random forest classifiers, were also trained on the extracted structural features to benchmark the CNN model's performance.

Results

Significant structural differences ($P<0.05$) were found in CSA, AP, and RL widths between the SCI and TD groups, indicating pronounced changes in spinal cord morphology due to SCI and suggesting these structural parameters as effective biomarkers for SCI in pediatric populations. The CNN-based model demonstrated superior performance, achieving a classification accuracy of 96.59% in distinguishing SCI from TD participants. In addition to classifying SCI presence, the CNN accurately predicted AIS impairment categories, reaching an accuracy of 94.92%. The model exhibited high precision, recall, and F1 scores across AIS categories, particularly for severe injury categories. In contrast, traditional machine learning models achieved lower classification accuracy, with SVM and random forest models reaching only 68.89% and 74.00%, respectively.

Conclusion

This study highlights the effectiveness of integrating cross-sectional spinal cord measurements with deep learning models for the diagnosis and prognosis of pediatric SCI. The CNN-based approach outperformed traditional machine learning models in diagnostic task, emphasizing the advantages of deep learning in capturing complex structural patterns that characterize SCI.

References

1. Cunha, N.S., et al., *Pediatric spinal cord injury: a review.* Children, 2023. **10**(9): p. 1456.

2. Yousefifard, M., et al., *Severity assessment of impairment in spinal cord injury; a systematic review on challenging points about International Standards for Neurological Classification of Spinal Cord Injury.* Frontiers in Emergency Medicine, 2021.

3. Anjum, A., et al., *Spinal Cord Injury: Pathophysiology, Multimolecular Interactions, and Underlying Recovery Mechanisms.* International Journal of Molecular Sciences, 2020. **21**(20): p. 7533.

4. Mulcahey, M.J., et al., *Interrater reliability of the international standards for neurological classification of spinal cord injury in youths with chronic spinal cord injury.*Archives of physical medicine and rehabilitation, 2011. **92**(8): p. 1264-1269.
5. Kirshblum, S.C., et al., *International standards for neurological classification of spinal cord injury (revised 2011).* The journal of spinal cord medicine, 2011. **34**(6): p. 535-546.
6. De Leener, B., et al., SCT: Spinal Cord Toolbox, an open-source software for processing spinal cord MRI data. Neuroimage, 2017. 145: p. 24-43.

Images/Tables

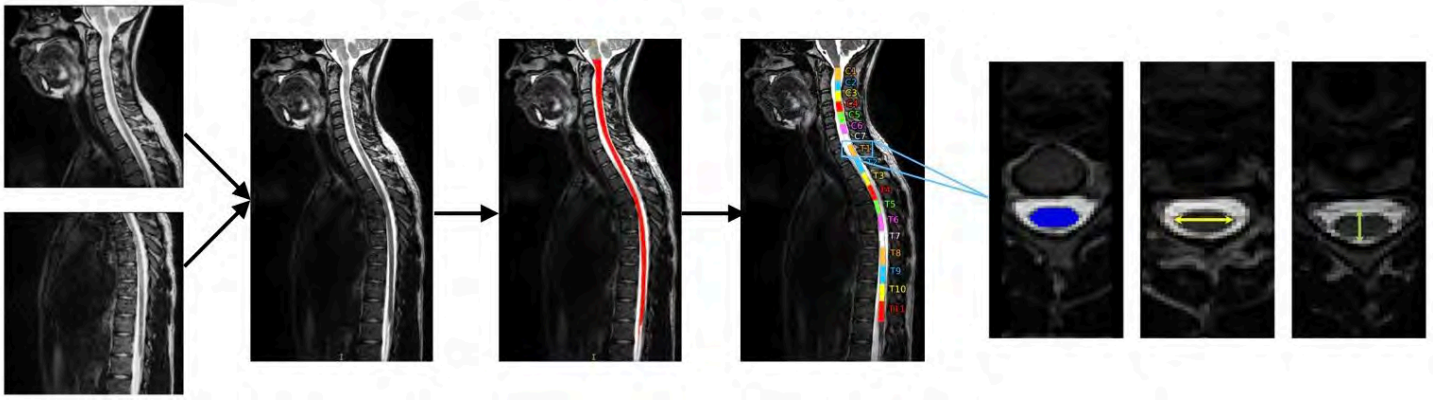

888

How Often Does Temporal bone CT Confirm Suspected Superior Semicircular Canal Dehiscence Detected on MRI?

David Petrover MD, Gul Moonis MD
NYU Grossman School of Medicine, New York, NY, USA

Abstract Category

Head & Neck

Purpose

It is not uncommon for patients presenting for an MRI brain or IAC to have possible dehiscence of the superior semicircular canal. Evaluation of superior semicircular canal dehiscence (SSCD) is challenging on MR technique due to poor spatial resolution and difficulty in discerning bony detail; a follow up temporal bone CT is usually recommended. This study's purpose was to gauge whether patients obtain follow up CT studies, and if so, whether the SCCD is confirmed.

Materials & Methods

At our multisite tertiary care center, a retrospective review of prior MRI brain and IAC studies was conducted by searching the keyword of "superior semicircular canal dehiscence" in the impression of radiology reports. No timeframe or other filters were used. The studies were then screened for whether superior semicircular canal dehiscence was suggested in the report. Subsequently, each study was reviewed for whether a follow up CT temporal bone study was obtained. CT temporal bone was considered as the gold standard for the diagnosis.

Results

A total of 292 unique patients who underwent MRI brain or IAC studies were identified with the suggestion of SSCD in the impression. The oldest study was from 2012, and the newest was from 2024. 286 (96%) of the studies were IAC protocol, utilizing a 3D, heavily-T2-weighted sequence (e.g., CISS, FIESTA, or SPACE) through the IAC. Of the 6 cases in which the suggestion of SCCD was made on conventional MR brain sequences, none underwent a follow up CT. 208 (72%) patients underwent no follow up CT temporal bone at our facility, despite the recommendation on MRI report. Of the 84 who did undergo a follow up CT temporal bone, 30 (36%) were confirmatory of a SSCD. Of all cases, 256 (88%) contained an indication with a symptom seen in SCCD, most commonly hearing loss, tinnitus, and vertigo and 76 (30%) of these had follow up CT's. Of the 34 with indications not suspicious for SCCD, 7 (21%) had follow up. 1 case had no clinical information available.

Conclusion

A substantial majority of patients or their providers did not follow recommendation for a CT temporal bone after suggestion of a SSCD on MRI. Some possible reasons as to this result include loss to follow up and the clinical history and

symptomatology not suggestive of SSCD. Although there is a prior study which showed that MRI using heavily T2 weighted sequences was highly sensitive and specific for diagnosis of SSCD, this was not borne out in our study. The results of this study raise the question as to the sensitivity of detecting SSCD on MRI using a 3D, heavily-T2-weighted sequence and the utility of recommending a follow up Temporal Bone CT especially in asymptomatic individuals.

References

1. Mau C, et al. Superior semicircular canal dehiscence: Diagnosis and management. J Clin Neurosci. 2018 Feb;48:58-65. doi: 10.1016/j.jocn.2017.11.019. Epub 2017 Dec 7. PMID: 29224712.
2. Beyazal Ç et al. The Efficacy of Magnetic Resonance Imaging for the Diagnosis of Superior Semicircular Canal Dehiscence. J Int Adv Otol. 2018 Apr;14(1):68-71. doi: 10.5152/iao.2017.4103. Epub 2017 Dec 14. PMID: 29283100; PMCID: PMC6354492.
3. Browaeys P et al. Can MRI replace CT in evaluating semicircular canal dehiscence? AJNR Am J Neuroradiol. 2013 Jul;34(7):1421-7. doi: 10.3174/ajnr.A3459. Epub 2013 Mar 21. PMID: 23518357; PMCID: PMC8051493.

Images/Tables

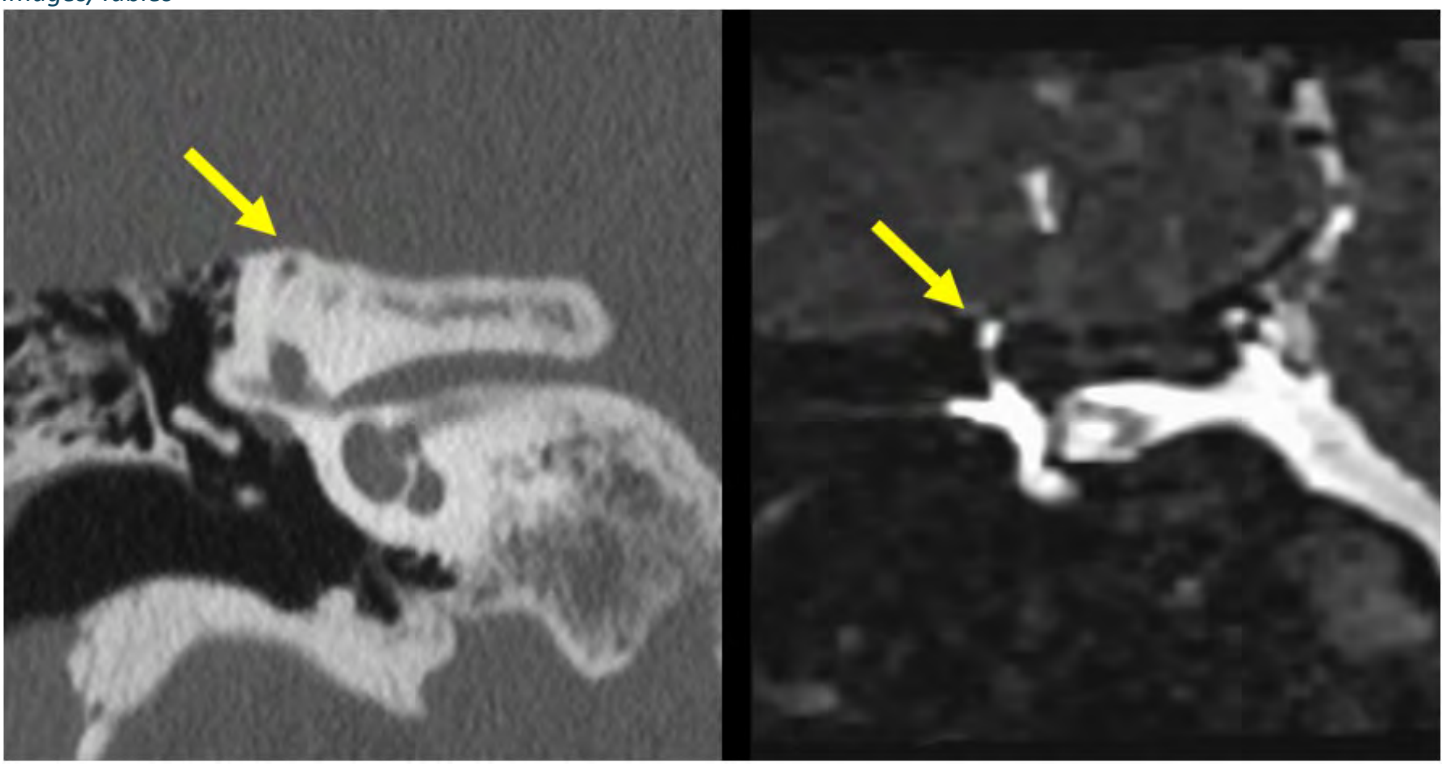

890

Improved Radiology Review Time and Accuracy with the Rapid DeltaFuseTM Platform For Head CT Scan Comparisons

James Montuori[1], Justin Honce[2], Vincent Timpone[3], Chris Song[4], Jeremy Heit[5], Seena Dehkharghani[6]
[1]Pennington, New Jersey, USA. [2]University of Colorado Hospital, Aurora, Colorado, USA. [3]Mayo Clinic Hospital, Phoenix, Arizona, USA. [4]Edison, New Jersey, USA. [5]Stanford, CA, USA. [6]New York, New York, USA

Abstract Category

Functional/Advanced Imaging

Purpose

Identifying Hounsfield unit (Hu) changes between two CT images acquired at different times for the same patient is often challenging and time-consuming. Rapid DeltaFuse™ (iSchemaView, Menlo Park, CA) is an AI software that automatically co-registers serial head CT scans from the same patient across time. In addition, any significant change in Hu is color-coded so changes can be quickly and easily detected. The aim of this study was to assess the impact of Rapid DeltaFuse™ on the time to review CT scans and assess the accuracy of reading complex scans by both general radiologists and neuroradiologists.

Materials & Methods

Six physicians (2 radiologists and 4 neuroradiologists) participated in this study, which was conducted using a study-specific Qualtrics survey tool. Participants were provided NCCT scans (baseline and follow-up scans) for 20 patients. Most scans had either hydrocephalus, brain hemorrhage, or both conditions. Physicians were asked to compare the scans between baseline and follow-up, and answer three questions in a survey setting:

1. *Is there a change in ventricular size?*
2. *Is there a new ICH or extra-axial hemorrhage or a change in a prior hemorrhage?*
3. *Is there a new or changing parenchymal abnormality (other than ICH/subdural, such as a brain mass, or a surgical change like a device insertion or removal, such as a shunt)?*

In half of the cases (Non-Rapid cases) participants compared the scans as they would in routine clinical practice. In the other half, they were provided with the Rapid DeltaFuse™ output, which highlighted differences in Hu values between the scans (Rapid cases). Participants were instructed to complete the review of the scans as efficiently and quickly as possible. Each case review was timed. One month after the completion of the first phase, the participants completed the Follow-up phase, where they were asked to review the same cases, but the Rapid and Non-Rapid cases were switched. The time to review scans was compared between Rapid and Non-Rapid cases, as well as the accuracy of the participants' answers, both for Phase 1 and the Follow-up phase. The Ground Truth was based on the NCCT scans comparison assessment which was determined by a consensus of one expert neuroradiologist and one expert vascular neurologist.

Results

Physicians were significantly faster in reviewing 20 scans while using Rapid DeltaFuse™ (mean time to review: 30 minutes (mean time/case: 1.6 minutes)) as compared to when reviewing scans as they would in routine practice (mean time to review: 50 minutes (mean time/case: 2.5 minutes); p=0.02). Participants were also more accurate in correctly identifying changes between baseline and follow-up scans while using Rapid DeltaFuse™ (96% accuracy) versus the routine method of clinical review (91%, p=0.04).

Conclusion

In a simulated Head CT reading study, the use of the Rapid DeltaFuse™ platform led to significantly faster reading times (40% relative reduction) and significantly increased accuracy for detecting radiographic differences between two scans. This AI platform appears promising for improving both speed and accuracy when comparing complex Head CT scans.

References

Erickson BJ, Mandrekar J, Wang L, et al. Effect of automated image registration on radiologist interpretation. *J Digit Imaging*. 2007;20(2):105-113. doi:10.1007/s10278-007-9023-x

Images/Tables

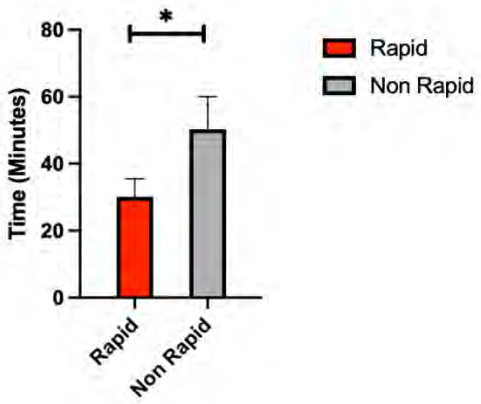

Figure 1. Mean time (±SEM) to review 20 cases using Rapid DeltaFuse™ (red) compared to routine practice (grey)

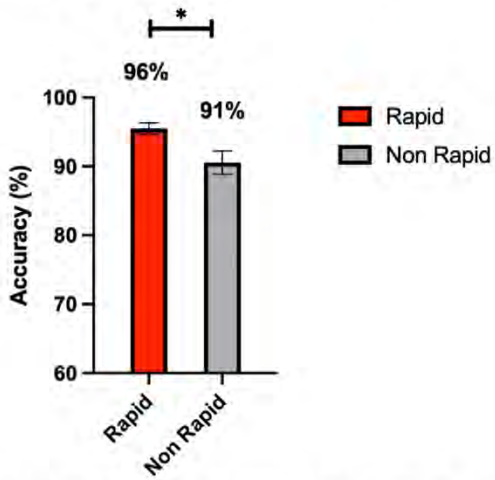

Figure 2. Mean accuracy (±SEM) for detecting radiographic differences between two scans using Rapid DeltaFuse™ (red) compared to routine practice (grey)

895

Evaluation of Open Small Language Models for Privacy-Preserving Structured Data Extraction from Neuroradiology Reports

Mohamed Sobhi Jabal MD, MS, Jikai Zhang MS, Evan Calabrese MD, PhD
Duke University, Durham, NC, USA

Abstract Category

AI/Informatics

Purpose

Open small language models (SLMs) offer secure local deployment in healthcare settings with lower computational requirements, ensuring privacy and reducing infrastructure costs and environmental impact. This study aimed to assess the potential of recently released state-of-the-art open-weight SLMs for structured data extraction from neuroradiology reports.

Materials & Methods

We analyzed a dataset of 7,294 brain MRI radiology reports annotated for Brain Tumor Reporting and Data System (BT-RADS) follow-up scores. An automated pipeline was developed to benchmark the performance of open SLMs and large language models (LLMs) in extracting BT-RADS scores from unstructured text, as well as the impact of prompting on performance. We compared the performance of 4 SLMs (Llama3.2:3b, Llama3.2:1b, Phi3:3.8b, Ph3.5:3.8b) and 4 LLMs (Llama3:70b, Openbiollm-llama-3:70b, Mixtral:8x7b, Biomistral:7b). Performance metrics included accuracy, F1 score, precision, and recall. Statistical analyses using Mann-Whitney U test and paired t-test were conducted to determine the significance of observed performance differences.

Results

Small language models demonstrated comparable performance to LLMs with mean accuracy of 85.0% ± 22.8% versus 81.0% ± 19.9% respectively (p=0.42, effect size=-0.36). The best-performing SLM (Phi3:3.8b) achieved 94.98% accuracy, approaching the performance of the best LLM (Openbiollm-llama-3:70b) at 98.68%. Macro F1 scores showed similar trends, with SLMs averaging 80.9% ± 9.6% compared to 66.4% ± 25.6% for LLMs. Detailed prompting strategies showed modest improvements over simple prompting (mean accuracy of 77.5% vs 66.0%, however this difference was not statistically significant (p=0.24, effect size=0.46).

Conclusion

SLMs demonstrated competitive performance, approaching those of larger models, making them a viable alternative for structured healthcare data extraction from diagnostic reports. Potential advantages of open SLMs include secure local on-device deployment in low-resource settings, faster inference on consumer grade hardware, lower compute costs, reduced environmental impact, ability to perform custom fine-tuning for domain specific tasks, and increased control over model versioning and deprecation compared to commercial model providers.

References

- Huang J, Yang DM, Rong R, et al. A critical assessment of using ChatGPT for extracting structured data from clinical notes. *NPJ Digit Med* 2024;7.
- Dagdelen J, Dunn A, Lee S, et al. Structured information extraction from scientific text with large language models. *Nat Commun* 2024;15:1418.

Images/Tables

Figure 1. Model performance across all assessed models for structured data extraction from neuroradiology reports.

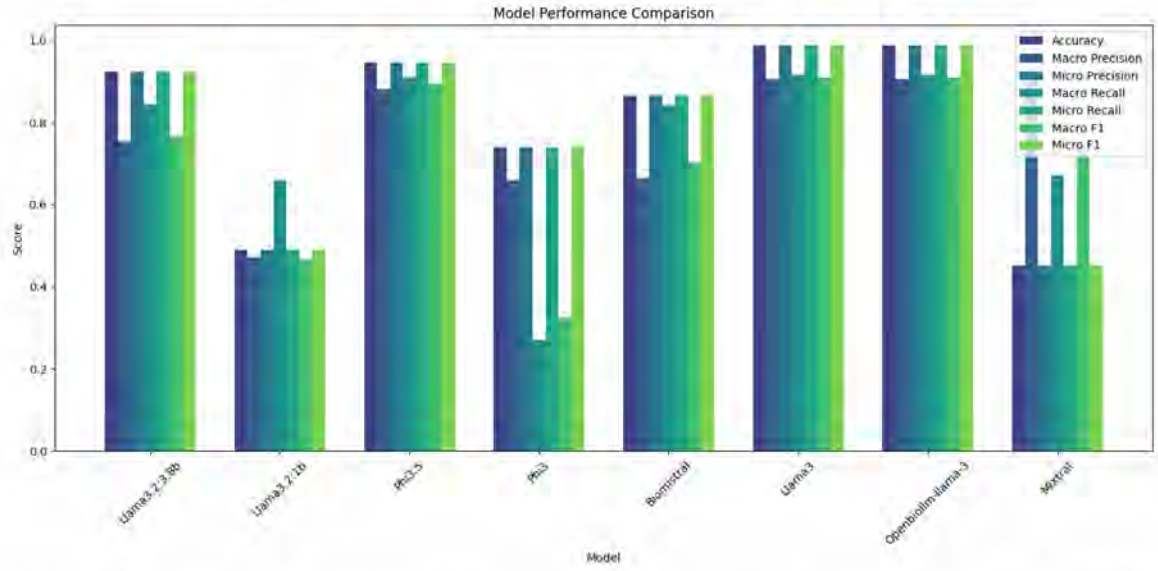

Table 1. Performance comparison of small and large language models as well as impact of SLM prompting strategies for structured data extraction from neuroradiology reports.

Model	Accuracy			Macro F1 Score		
	Mean ± SD	Median [IQR]	Range	Mean ± SD	Median [IQR]	Range
Model Size						
SLM	85.0% ± 22.8%	96.2% [12.2%]	45.2%–98.7%	80.9% ± 9.6%	77.9% [16.5%]	70.3%–91.0%
LLM	81.0% ± 19.9%	92.3% [20.6%]	48.9%–95.0%	66.4% ± 25.6%	76.6% [40.7%]	32.4%–89.4%
Prompting						
Simple	66.0% ± 27.9%	68.1% [26.1%]	30.4%–97.2%	59.1% ± 22.2%	55.3% [15.2%]	36.2%–89.4%
Detailed	77.5% ± 21.1%	83.2% [25.2%]	48.9%–94.6%	61.2% ± 26.3%	61.6% [36.7%]	32.4%–89.4%

905

Unveiling the Neuroimaging Spectrum of Snake Bite Injury and Flagging the Lessons Learnt

Charu Paruthi DM Neuroradiology, MD Radiodiagnosis, EBIR, M Sarthak Swarup MD Radiodiagnosis, Reeta Kanaujiya MD Radiodiagnosis
VMMC and Safdarjung Hospital, New Delhi, Delhi, India

Abstract Category

Adult Brain

Purpose

Background

Snake bite envenomation is an important global concern. According to the WHO fact sheet, majority of these cases occur in South-east Asia, Africa and Latin America.

In India, over 200 species of snakes are found, out of which only three families are poisonous. These include Elapidae (neurotoxic), Viperidae (vasculotoxic) and Hydrophidae (musculotoxic).

Data regarding the neuroimaging manifestations of snake bite envenomation is scanty and is limited to scattered case reports.

Purpose

The purpose of our study was to describe the spectrum of neuroimaging features in snake bite envenomation and look for imaging findings that may point towards an adverse clinical outcome and thus require urgent management.

Materials & Methods

A retrospective review of clinical and imaging records of 12 patients with confirmed history of snake bite, seen over last 18 months (encompassing two monsoons, April 2023- September 2024) was done. MRI brain studies were available in all. Those with a known underlying neurological disorder were excluded. Clinical records were obtained and details regarding type of snake bite, treatment given, clinical details and final outcome were recorded if available. MRI images were analysed independently by 2 radiologists and correlated with the available clinical details.

Results

The age of the affected patients ranged from 19 to 56 years. Mean age of the study group was 34.4 years. Male to female ratio was 1.4:1 (7 males and 5 females).

The MRI spectrum was wide and ranged from diffuse cerebral edema (3) to encephalopathy involving bilateral basal ganglia, thalami and cerebral cortex (10), sub-arachnoid haemorrhage (1), micro-hemorrhagic foci (1) and multiple parenchymal hemorrhages (1). Identification of the snake species was possible in 8 cases, out of which 3 were vasculotoxic and 5 neurotoxic. Both varieties of snake bite envenomation were found to present more frequently with overriding imaging features of encephalopathy. Haemorrhagic manifestations were mostly seen in vasculotoxic snake bites. However, severe cerebral edema was the most life-threatening complication as it led to fatal tentorial herniation. Sustained supportive therapy led to recovery of 10 patients in 4-6 weeks. Two patients with severe cerebral edema succumbed.

Conclusion

Though neuroimaging features of snake bite envenomation vary depending upon the type of snake, it is not possible to know the snake type in all cases. Encephalopathy is a common finding seen in most of the snake bite cases. Depending on the imaging findings, hypoxia seems to be a major cause of encephalopathy in these cases. This may be due to respiratory paralysis caused by the neurotoxic venom or a direct effect of the venom itself, which can explain these findings in vasculotoxic snake bites. Prompt supportive management and active measures to prevent brain edema may lead to a decrease in mortality.

Take home message

In cases of snake bite envenomation presenting with neurological manifestation, MRI is helpful in detecting the severity of brain involvement and complications like brain herniations. This in turn can help in initiating timely treatment

References

Sharma V, Nayak S, Pattnaik SS, Mohanty AP, Patro S. Snake Bite-Induced Leukoencephalopathy: A Rare Case. Cureus. 2024 Feb 28;16(2):e55116. doi: 10.7759/cureus.55116. PMID: 38558597; PMCID: PMC10979323.

Huang YK, Chen YC, Liu CC, Cheng HC, Tu AT, Chang KC. Cerebral Complications of Snakebite Envenoming: Case Studies. Toxins (Basel). 2022 Jun 27;14(7):436. doi: 10.3390/toxins14070436. PMID: 35878174; PMCID: PMC9320586.

Gutiérrez JM, Calvete JJ, Habib AG, Harrison RA, Williams DJ, Warrell DA. Snakebite envenoming. Nat Rev Dis Primers. 2017 Sep 14;3:17063. doi: 10.1038/nrdp.2017.63. Erratum in: Nat Rev Dis Primers. 2017 Oct 05;3:17079. doi: 10.1038/nrdp.2017.79. PMID: 28905944.
Ranawaka UK, Lalloo DG, de Silva HJ. Neurotoxicity in snakebite--the limits of our knowledge. PLoS Negl Trop Dis. 2013 Oct 10;7(10):e2302. doi: 10.1371/journal.pntd.0002302. PMID: 24130909; PMCID: PMC3794919.
Young PM, Bancroft LW, Peterson JJ, Roberts CC, Liu PT, Zaleski CG. Imaging spectrum of bites, stings, and their complications: pictorial review. AJR Am J Roentgenol. 2009 Sep;193(3 Suppl):S31-41, Quiz S42-5. doi: 10.2214/AJR.07.7123. PMID: 19696242.

Images/Tables

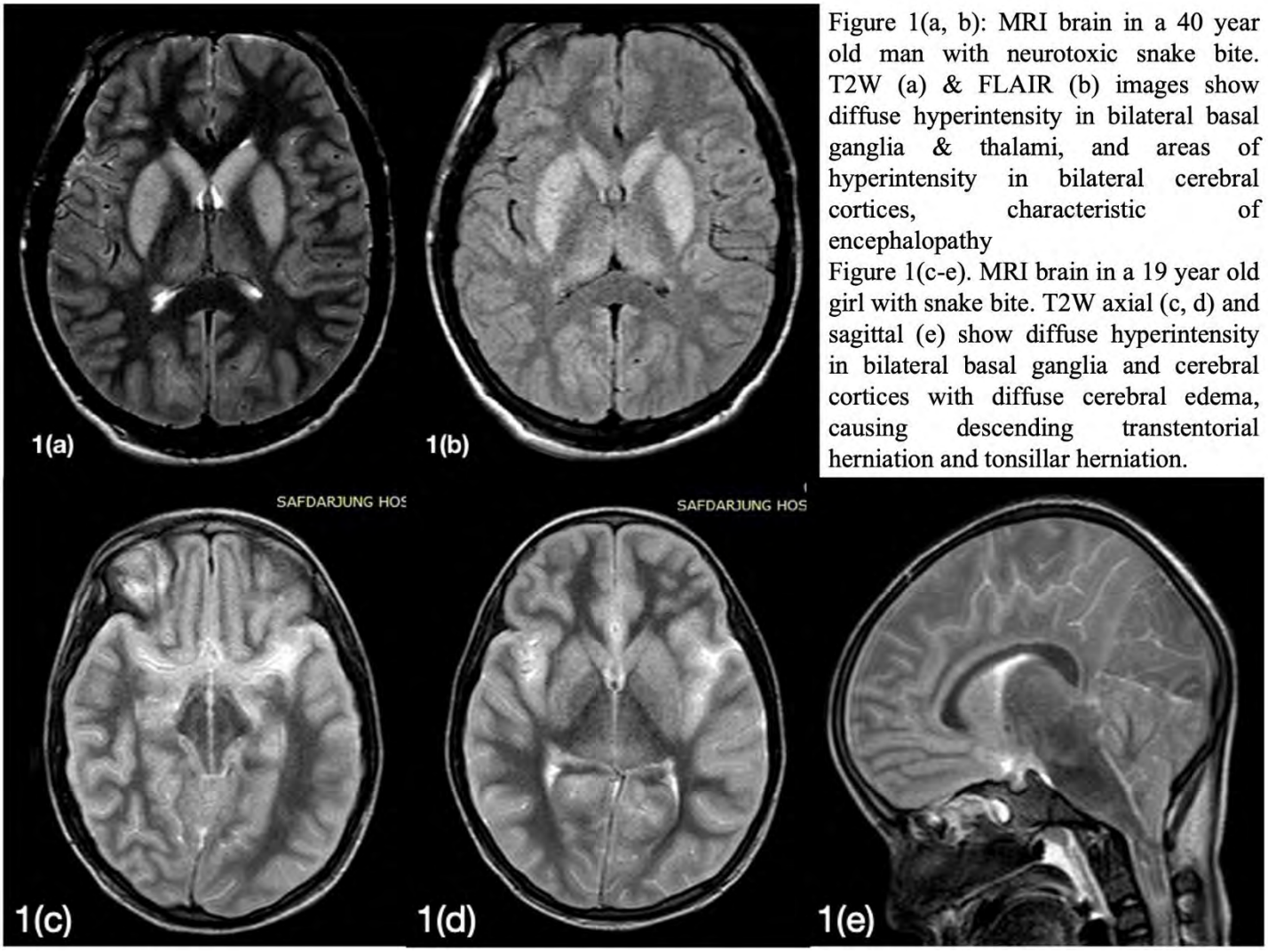

Figure 1(a, b): MRI brain in a 40 year old man with neurotoxic snake bite. T2W (a) & FLAIR (b) images show diffuse hyperintensity in bilateral basal ganglia & thalami, and areas of hyperintensity in bilateral cerebral cortices, characteristic of encephalopathy

Figure 1(c-e). MRI brain in a 19 year old girl with snake bite. T2W axial (c, d) and sagittal (e) show diffuse hyperintensity in bilateral basal ganglia and cerebral cortices with diffuse cerebral edema, causing descending transtentorial herniation and tonsillar herniation.

909

Prospective Evaluation of Two Artificial Intelligence–Enabled Large Vessel Occlusion Detection Software Solutions in a Comprehensive Stroke Center

Subtain Ali MD[1], Dhairya Lakhani MD[1], Davide Carone MD, DPhil[2], George Harston MBBChir, DPhil[2], Alistair Perry PhD[3], Musharaf Khan DO[1], Abdulrahman Al Halak DO[1], Ansaar T. Rai MD[1]
[1]West Virginia University, Morgantown, WV, USA. [2]Oxford University Hospitals NHSFT, Oxford, Oxfordshire, United Kingdom. [3]Brainomix Limited, Oxford, Oxfordshire, United Kingdom

Abstract Category

AI/Informatics

Purpose

Prompt identification of stroke patients with a large vessels occlusion (LVO) for mechanical thrombectomy is crucial to maximize treatment outcomes. Artificial intelligence (AI)–enabled automated LVO detection has been recommended as

a possible solution to improve hospitals workflow, and different solutions are now commercially available.[1] This ongoing study aims to prospectively evaluate the performance of two different AI solutions to support identification of large vessel occlusions using CT angiography (CTA).

Materials & Methods

Consecutive patients, presenting to a US comprehensive stroke center with suspected stroke, were enrolled in a prospective observational study. To be included, patients had to present with an acute stroke syndrome and undergo a stroke imaging protocol of non-contrast-CT (NCCT) and CTA as a minimum. All patient imaging was processed in real time using two different AI solutions: Brainomix360 and Viz.ai. Ground truth information on vessel occlusion (presence and location) was extracted from radiology reports. The performance of each solution was assessed in terms of sensitivity and specificity for anterior circulation vessel occlusion.

Results

Of the 302 patients meeting the inclusion criteria, 12 were excluded due to the presence of intracranial hemorrhage and 5 due to the presence of artefacts severely compromising image quality. The median (Q1-Q3) age was 67 years (55-77). 147 patients were female. 28 patients had an intracranial occlusion affecting the anterior circulation. Of these,18 patients had a proximal occlusion (intracranial ICA or M1 segment of the MCA), whilst 10 had more distal occlusions (n=7 involving the M2 segment, and n=3 involving the M3 segment). Both Brainomix360 and Viz.ai successfully identified all proximal large vessel occlusion (sensitivity 100%). Sensitivity remained high when including more distal occlusions (sensitivity after including M2 occlusions: Brainomix360: 96%; Viz.ai: 84%; sensitivity after including M2 and M3 occlusions: Brainomix360: 89%, Viz.ai: 79%). Anterior circulation occlusions were detected with a 92% specificity when using Brainomix360 and a 96% specificity when using Viz.ai.

Conclusion

The results from this analysis demonstrate that both AI solutions accurately identified intracranial LVO. Compared to Viz.ai, Brainomix360 showed higher sensitivity for more distal occlusions with a small reduction in specificity.

References

Dusenbury W, Mathiesen C, Whaley M, Adeoye O, Leslie-Mazwi T, Williams S, et al. Ideal Foundational Requirements for Stroke Program Development and Growth: A Scientific Statement From the American Heart Association. *Stroke*. 2023

Images/Tables

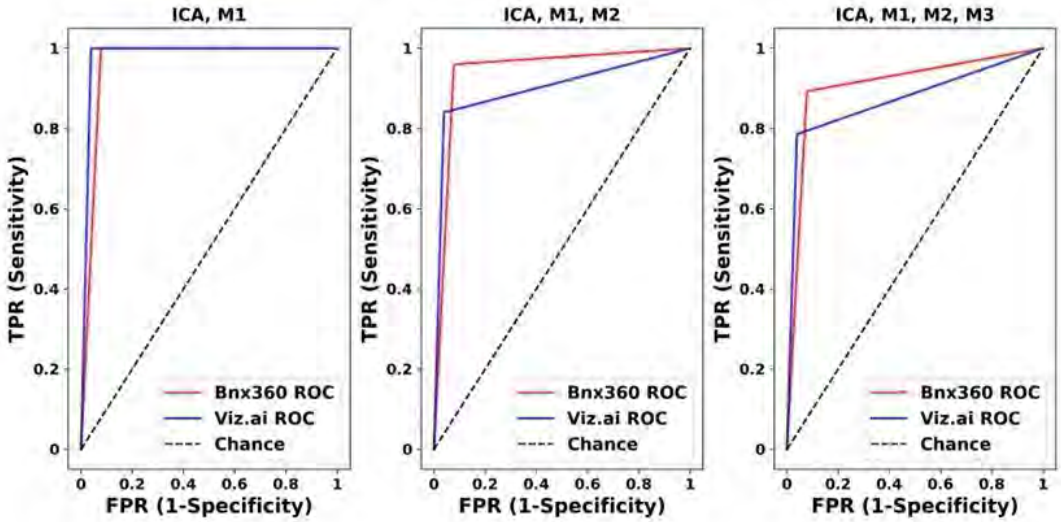

Occlusion Site	Device	Sensitivity	Specificity	AUC	f1-score
ICA, M1	Brainomix 360	1.00	0.92	0.96	0.97
	Viz.ai	1.00	0.96	0.98	0.97
ICA, M1, M2	Brainomix 360	0.96	0.92	0.94	0.95
	Viz.ai	0.84	0.96	0.90	0.89
ICA, M1, M2, M3	Brainomix 360	0.89	0.92	0.91	0.92
	Viz.ai	0.79	0.96	0.87	0.86

911

Neural Network-Driven Radiomic Signatures for Predicting NF1, NF2, and TERT Mutations in Glioblastoma

Priyadarshini Mamindla[1], Mohammadreza Amjadzadeh MD[1], Vishal Peddagangireddy[1], Sinef Huvaj Aksoy MD[2], Ayla Buyukkaya MD[2], Ozlem Tugce Kalayci MD[2], Teke Memik MD[2], Pascal O. Zinn MD[1], Rivka R Colen MD[1]
[1]Hillman Cancer Center, University of Pittsburgh Medical Center, Pittsburgh, Pennsylvania, USA. [2]Hillman Cancer Center, University of Pittsburgh Medical Center, Pittsburgh, PA, USA

Abstract Category

AI/Informatics

Purpose

To present a novel neural network-based radiomic approach for identifying key radiomic signatures that predict the presence or absence of gene mutations, such as NF1, NF2, and TERT, detected using Next-Generation Sequencing (NGS) in Glioblastoma (GB) patients.

Materials & Methods

This retrospective study included 375 pathologically confirmed GB patients. Post-contrast T1-weighted and FLAIR MRI sequences were segmented using 3D-Slicer to create a volume of interest. Regions of interest (ROIs) encompassed tumor enhancement, necrosis, edema, and contralateral white matter (cWM). After skull stripping, feature extraction was performed where, first-order features such as skewness and kurtosis were extracted, and second-order features were calculated from the Gray-Level Co-occurrence Matrix (GLCM) at various angles (0°, 45°, 90°, and 135°). Image quantization at different gray levels (8, 16, 32, 64, and 256) resulted in 195 second-order features per ROI. Features were normalized against the patient-specific cWM, and volume-independent features were derived by dividing the 195 original features by each ROI volume. This pipeline resulted in 390 total second-order and 10 first-order features per ROI per sequence.

To reduce dimensionality and select relevant features, Random Forest method was employed for feature selection, isolating significant radiomic signatures for each mutation. Radiomic-based predictive models were developed using neural network classifiers consisting of multiple dense layers and a sigmoid-activated output layer. Using neural networks, we captured complex, non-linear patterns within our radiomic data to identify correlations between radiomic signatures and gene mutations. This approach leveraged the neural network's capacity for feature representation learning and generalization. The dataset was split into 70:30 for training and independent validation cohorts, with 3-fold cross-validation applied to the training cohort. Regularization techniques, including dropout and early stopping, were incorporated to reduce overfitting and optimize the model. Performance of the models were assessed using metrics such as accuracy, sensitivity, specificity, and the Area Under the Curve (AUC) of the Receiver Operating Characteristic (ROC) curve.

Results

The Random Forest-based feature selection method successfully reduced feature space and importantly, this reduction in features did not compromise the predictive performance and computational efficiency of the neural network classifiers across target genes, as evidenced by the maintained accuracy, sensitivity, specificity, and AUC metrics for each gene model.

For NF1, the neural network model identified 10 significant radiomic features, achieving 73.21% accuracy, 72.63% sensitivity, 76.47% specificity, and an AUC of 75.54%. For NF2, 5 key features were selected, yielding 80.36% accuracy, 72.72% sensitivity, 81.18% specificity, and an AUC of 73.9%. TERT mutation prediction utilized 8 features, with performance metrics of 72.32% accuracy, 73.08% sensitivity, 72.09% specificity, and an AUC of 73.75%.

Conclusion

These findings highlight the potential of neural networks, combined with targeted feature selection through Random Forest method, as an effective strategy for predicting gene mutation status in GB patients. Our robust approach hold potential for clinical applications in gene mutation risk assessment, contributing to personalized treatment planning and improved patient outcomes.

References

Breiman L. Random forests. Mach Learn. 2001;45(1):5-32. DOI: 10.1023/A:1010933404324

913

SOX-2 Expression Across Whole Brain Slices Identifies Tumor Well Beyond Contrast Enhancement and Flair Hyperintense Regions in Glioblastoma Patients

Benjamin E Chao BS, Aleksandra Winiarz BS, Samuel Bobholz PhD, Allison Lowman BS, Savannah Duenweg PhD, Biprojit Nath MS, Fitzgerald Kyereme BS, Jennifer Connelly MD, Kelly Mrachek MD, Max Krucoff MD, Peter LaViolette PhD
Medical College of Wisconsin, Milwaukee, WI, USA

Abstract Category

Adult Brain

Purpose

Glioblastoma (GBM) is a universally recurring brain tumor, with only 17% of patients surviving two years past initial diagnosis.[1] This is due in part to rapid spread of non-enhancing tumor, and the inability to completely resect the tumor volume. The extent of tumor invasion has been shown to exist several centimeters away from contrast enhancement (CE) on clinical MRI,[2] and even as far as the contralateral hemisphere via white matter tract invasion.[3] This study uses SRY-Box 2 (SOX2)[4], a marker for cell pluripotency, to locate infiltrative tumor cells in large whole brain slices obtained at autopsy. Here, we align and visualize the percent of SOX2 positive cells compared to total cell density both within and outside CE and FLAIR hyperintense regions. We hypothesize that SOX2 positivity will be present well beyond the boundaries of both regions.

Materials & Methods

This study investigated two GBM patients. Patients 1 and 2 had imaging 12 and 15 days prior to death respectively. Patient 1 received standard of care, including surgical resection, temozolomide, and radiation therapy with an overall survival (OS) of 1601 days past initial diagnosis. Patient 2 underwent an initial surgery, then denied additional treatment (OS: 148 days). During autopsy, brains were sliced with patient specific axial-MRI aligned slicing jigs. Large format tissue samples covering three entire brain slices were paraffin embedded, sliced, SOX2 stained, and digitized at 40x. Digitized histology was aligned to MRI and visualized in space with T1C and FLAIR images. MRI scans were collected sequentially near the end of life at the patient's preference on timing. A 3D surface-based model for growth of contrast enhancement volume and FLAIR hyperintensity volume was developed using hand drawn regions of interest. The model linearly inflated these regions to predict ROIs for the time of death. Volume rendering and smoothing was done using 3DSlicer and Blender.

Results

SOX2 positive cells were detected greater than 6 centimeters beyond CE and greater than 5 centimeters outside of FLAIR hyperintensity. CE and FLAIR hyperintensity volume predictions failed to fully capture the extent of SOX2 positive cell invasion.

Conclusion

This analysis allowed us to visualize in MRI space the true extent of tumor volume using SOX2 as a marker. These results suggest CE and FLAIR fail to characterize true tumor extent, even when accounting for time between last MRI scan and death.

References

1. Ostrom QT, Price M, Neff C, et al. CBTRUS Statistical Report: Primary Brain and Other Central Nervous System Tumors Diagnosed in the United States in 2016—2020. *Neuro-Oncol*. 2023;25(Supplement_4):iv1-iv99. doi:10.1093/neuonc/noad149

2. Giese A, Bjerkvig R, Berens ME, Westphal M. Cost of Migration: Invasion of Malignant Gliomas and Implications for Treatment. *J Clin Oncol*. 2003;21(8):1624-1636. doi:10.1200/JCO.2003.05.063

3. Brooks LJ, Clements MP, Burden JJ, et al. The white matter is a pro-differentiative niche for glioblastoma. *Nat Commun*. 2021;12(1):2184. doi:10.1038/s41467-021-22225-w

4. Zhang S, Cui W. Sox2, a key factor in the regulation of pluripotency and neural differentiation. *World J Stem Cells*. 2014;6(3):305-311. doi:10.4252/wjsc.v6.i3.305

Images/Tables

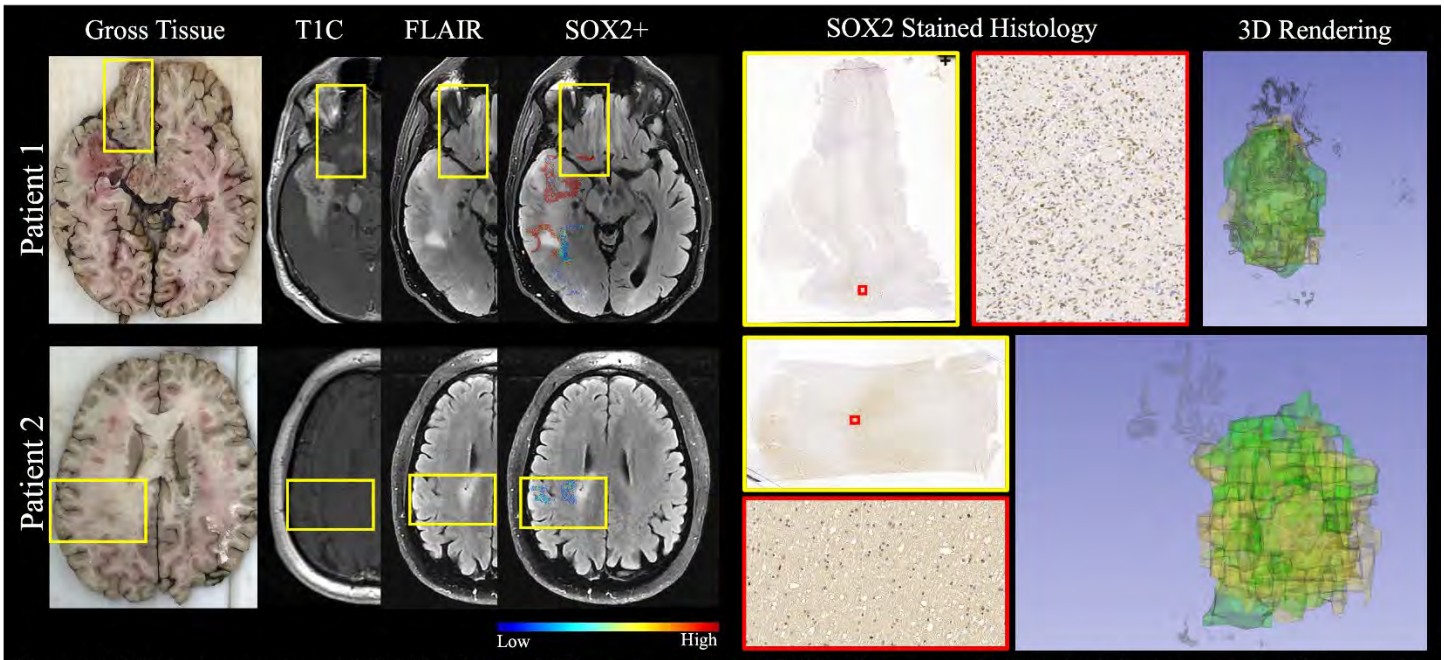

Figure 1. Left: Patient's autopsy tissue, T1C, FLAIR, and aligned SOX2+ intensity map (ratio of SOX2+ cells to normal cells). Yellow box indicates chosen region of interest, outside of FLAIR hyperintensity and CE. **Middle:** Screen captures of chosen histology samples highlighting SOX2+ tumor cells. **Right:** 3D rendering of SOX2+ histology aligned to MRI space, with CE (yellow) and FLAIR hyperintensity (green) growth predictions.

916

Automated FTB Maps: Quantitative Assessment of Brain Tumor Burden

Michael Schmainda, Timothy Dondlinger
Imaging Biometrics, LLC, Elm Grove, WI, USA

Abstract Category

Adult Brain

Purpose

To create a post-processing pipeline that automatically generates quantitative FTB maps for the rapid, consistent, and accurate assessment of brain tumors.

Materials & Methods

The diagnosis and treatment of patients with brain tumors and other diseases relies on accurate imaging that can non-invasively provide timely feedback to clinicians. Conventional imaging, such as contrast-enhanced MRI (CE-MRI), cannot reliably distinguish tumor growth from pseudo-progression or post-treatment radiation effect (PTRE), which can mimic tumor on CE-MRI. The ability to distinguish these tissue types is necessary to determine if a patient should continue with their current treatment course, return to surgery, or if they are eligible to enroll in a clinical trial. Yet no standard method exists to make this distinction other than using a wait and see approach that requires costly longitudinal imaging and/or tissue confirmation that requires surgical biopsy.

Results

Imaging Biometrics, LLC (Elm Grove, WI) has developed and validated an automated FTB processing platform that overcomes these challenges for brain tumor management[1,2]. The core of the platform has two foundational applications: IB Delta T1 maps and IB Neuro.

IB Delta T1 maps automatically quantify regions of true contrast enhancement, making subtle regions of enhancement easy to see while removing confounding factors, such as post-surgical blood product. The generation of Delta T1 maps include an exclusive calibration step that translates the relative MR intensities to a fixed and consistent scale. When the pre- and post-contrast T1 weighted images are calibrated, co-registered, and subtracted, bright signal on pre-contrast images is removed while subtle regions of contrast enhancement are made visible. The result is an objective delineation of true regions of contrast enhancement.

IB Neuro is an MRI Dynamic Susceptibility Contrast (DSC) perfusion platform that generates accurate quantitative measurements of cerebral blood volume called standardized relative cerebral blood volume (sRCBV).[3] The generation of sRCBV values employ the same exclusive calibration technology as IB Delta T1 maps. This eliminates the need to apply

"tissue normalization" techniques which are inherently variable and time-consuming. The sRCBV values are more consistent and apply across vendor platforms, field strengths, patients, or time points. Thus, the ability to directly quantify changes across time is made possible. Furthermore, the sRCBV values have been independently validated by multiple sites using tissue biopsy samples to establish cutoff thresholds that differentiate tumor from PTRE.[4]

Conclusion

When using these two approaches, the fraction of tumor burden within the true enhancing region can be computed. As shown in Fig. 1, these FTB maps enable rapid and objective assessment of brain tumor progression and treatment efficacy and provide quantitative longitudinal assessment of treatment response. The maps can be imported into surgical navigation systems to target biopsies, plan surgical resection and radiation, and plan laser ablation treatment. The use of IB's FTB maps has recently been shown to result in greatest confidence and inter-reader agreement for brain tumor response assessment as compared DSC perfusion or arterial spin labeling (ASL) alone.[5]

References

1. Hoxworth JM, Eschbacher JM, Gonzales AC, et al. Performance of standardized relative CBV for quantifying regional histologic tumor burden in recurrent high-grade glioma: Comparison against normalized relative CBV using image-localized stereotactic biopsies. *American Journal of Neuroradiology* 2020;41:408–15.
2. Connelly JM, Prah MA, Santos-Pinheiro F, et al. Magnetic Resonance Imaging Mapping of Brain Tumor Burden: Clinical Implications for Neurosurgical Management: Case Report. *Neurosurgery Open* 2021;2:2–5.
3. Bedekar D, Jensen TR, Schmainda KMKM. Standardization of relative cerebral blood volume (rCBV) image maps for ease of both inter and intra-patient comparisons. *Magn Reson Med* 2010;64:907–13.
4. Prah MA, Al-Gizawiy MM, Mueller WM, et al. Spatial discrimination of glioblastoma and treatment effect with histologically-validated perfusion and diffusion magnetic resonance imaging metrics. *J Neurooncol* 2018;136:13–21.
5. Ghiam Yamin, Eric Tranvinh, Bryan A. Lanzman, et al. Arterial Spin-Labeling and DSC Perfusion Metrics Improve Agreement in Neuroradiologists' Clinical Interpretations of Posttreatment High-Grade Glioma Surveillance MR Imaging—An Institutional Experience. *American Journal of Neuroradiology* March 2024, DOI: https://doi.org/10.3174/ajnr.A8190.

Images/Tables

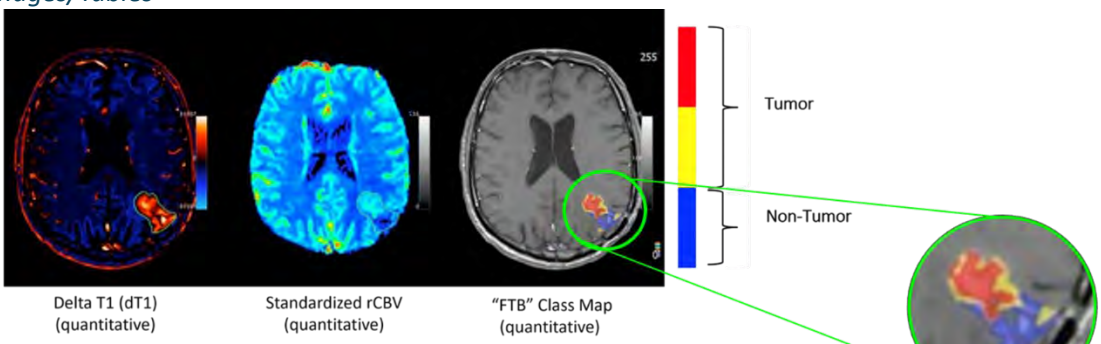

Fig 1. (left) quantitative Delta T1 map identifies regions of contrast enhancement, (center) sRCBV map from IB Neuro, (right) a DSC-perfusion derived class (FTB) map delineating tumor (red and yellow regions) from non-tumor (blue regions) tissue.

918

Conventional and Advanced Imaging Features of CNS Lymphoid Pathologies: A multi-institutional study and literature review.

Sunpob Cheewadhanaraks, Otto Rapalino
Massachusetts General Hospital, Boston, MA, USA

Abstract Category

Adult Brain

Purpose

The purpose of this study was to provide an update on the imaging findings of lymphoid pathologies affecting the central nervous system (CNS) following their revised 2022 classification and assess the diagnostic value of advanced

imaging techniques such as Dynamic Susceptibility Contrast (DSC) perfusion, Magnetic Resonance Spectroscopy (MRS), and Fluorine-18 (F-18) fluorodeoxyglucose positron emission tomography (FDG-PET).

Materials & Methods

Conventional and advanced imaging findings were analyzed in 332 confirmed cases of CNS lymphoid pathologies, including cases with DSC perfusion (n=41), MR spectroscopy (n=31), and FDG-PET (n=46) studies.

Results

Most of the lymphoma cases were primary (85%) and classified as diffuse large B-cell lymphoma (DLBCL) (76%). Intravascular lymphoma and immunodeficiency-associated CNS lymphoma were less frequent (6% and 4%, respectively). MRI abnormalities were found in the brain in 95% of cases and in the intradural spinal compartment in 14% of cases. The most common MRI brain pattern was an intraparenchymal mass (69%), followed by an ill-defined enhancing lesion without mass effect (15%) and a ring-like peripherally enhancing pattern (7%). The spinal intradural involvement more frequently presented with nerve root/cauda equina enhancement (58%). DSC perfusion revealed mildly elevated cerebral blood volume (CBV) values in 60% of patients. MRS showed variable elevation of choline/creatine (Cho/Cr) ratios in 87% and abnormal lipid elevation in 68% of cases. FDG PET showed increased metabolic uptake compared to the background parenchyma in 89% of patients.

Conclusion

CNS lymphoid pathologies have a broad spectrum of radiological presentations but have characteristic findings that could help differentiate them from other pathologies. Multimodal imaging, including advanced MRI techniques and FDG PET, can increase the diagnostic accuracy of the radiological assessment.

References

Pons-Escoda A, Naval-Baudin P, Velasco R, et al. Imaging of Lymphomas Involving the CNS: An Update-Review of the Full Spectrum of Disease with an Emphasis on the World Health Organization Classifications of CNS Tumors 2021 and Hematolymphoid Tumors 2022. AJNR Am J Neuroradiol 2023 Feb 23. [Epub ahead of print]

Images/Tables

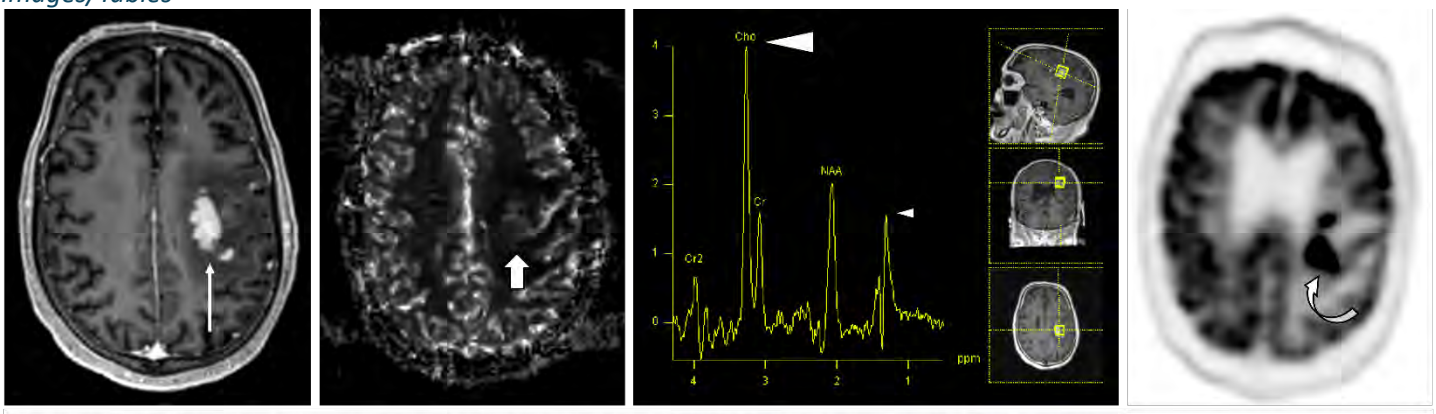

72-year-old male patient with primary CNS lymphoma. Axial gadolinium-enhanced T1-weighted image (A) shows a homogeneously enhancing mass-like lesion in the left frontoparietal white matter (thin white arrow). The lesion demonstrated mild elevation of rCBV values on the leakage-corrected CBV image (B) (short thick white arrow), as well as prominent choline/creatine elevation (larger white arrowhead), moderate decrease of NAA/creatine, and significant increase of lactate and lipid peaks on MR spectroscopy (C) (smaller white arrowhead). Focal hypermetabolism was found within the lesion on FDG PET (D) (curved white arrow).

920

Optimizing CSF leak imaging utilizing pledgets only

Carlos Kuria MD[1], Alex Ocana MD[1], Cindy Yuan MD[1], Tann Mark MD[2]

[1]Indiana University, Indianapolis, Indiana, USA. [2]Indiana University, Indianapolis, Indianaplis, USA

Abstract Category

Adult Brain

Purpose

The objective of this report is to improve the diagnostic efficiency of imaging protocols for the detection of cerebrospinal (CSF) fluid leaks by evaluating the relative sensitivities of computed tomography (CT) cisternography, radionuclide cisternography (RC) imaging and radionuclide pledget analysis.

Materials & Methods

We retrospectively reviewed 69 patients who had RC performed with or without same day CT cisternography for the evaluation of CSF leaks between 2024 and 2016 at our institution. RC utilized intrathecal Tc-99m DTPA while CT

cisternography utilized intrathecal iodinated contrast which were administered via lumbar puncture. RC reviewed included a mix of planar imaging and Single Photon Emission Computed Tomography (SPECT)/CT imaging. All images were reviewed using standard diagnostic radiology monitors.

Results

A total of 13 RC was positive for CSF leak, 5 of which had planar imaging (0% sensitive) and 8 had SPECT/CT (37.5% sensitive). Planar imaging did not show CSF leak in any of the five positive cases. SPECT/CT was positive in 3 of the 8 cases. Ear and nasal pledgets were used in only 12 positive cases for radiation count analysis in addition to planar imaging or SPECT/CT. All these 12 studies were positive on pledget radiation counts. Same day CT cisternograms were available for the 12 positive RC exams for comparison. Only 8 CT cisternograms (67% sensitive) were found to be positive for CSF leak.

One positive RC exam did not utilize pledgets but demonstrated CSF leak on RC SPECT/CT as well as same day CT cisternogram.

Conclusion

Our results demonstrated that performing nuclear medicine cisternography imaging, as well as inclusion of nasal and ear pledgets analysis is unnecessary due to low sensitivity. We recommend utilizing only nasal and ear pledgets for radiation count analysis in combination with same day CT or MR cisternography for evaluating CSF leaks. CT cisternography was also found to be less sensitive compared to pledgets for detection of CSF leaks but adds the advantage of anatomical detail which may be key for surgical planning or management decision.

References

Bergstrand, G., Oxenstierna, G., Flyckt, L. *et al.* Radionuclide cisternography and computed tomography in 30 healthy volunteers. *Neuroradiology* **28**, 154–160 (1986). https://doi.org/10.1007/BF00327889

Hablas, L.T., Ammar, A.M. et al. CSF rhinorrhea: non-contrast CT, contrast-enhanced CT cisternography or combined?. *Egypt J Radiol Nucl Med* **53**, 201 (2022). https://doi.org/10.1186/s43055-022-00889-8

Porubcin, Stefan, Alena Rovnakova et al . Diagnostic Value of Radioisotope Cisternography Using ^{111}In-DTPA in a Patient with Rhinorrhea and Purulent Meningitis. *Medicina* 2022, 58, 714. https://doi.org/10.3390/medicina58060714

Xie M, Zhou K, Kachra S et al. Diagnosis and Localization of Cerebrospinal Fluid Rhinorrhea: A Systematic Review. *American Journal of Rhinology & Allergy*. 2022;36(3):397-406. doi:10.1177/19458924211060918

922

The association between cerebral amyloid angiopathy and quantitative MRA features

Mohamad H Mosi, Mona Kharaji, KAIYU ZHANG, Charles Watt, Mahmud Mossa-Basha

University of Washington, Seattle, WA, USA

Abstract Category

Adult Brain

Purpose

Cerebral amyloid angiopathy (CAA) is a prevalent condition among the elderly, affecting 4.7–9% of patients aged 60–69 years and 43–58% of patients over 90 years1. The significance of CAA lies in its pathophysiology, which renders brain arteries fragile and prone to bleeding, thereby increasing the risk of macro and micro hemorrhages and resulting in a mortality rate of 50%2. This study aims to explore the association between CAA, vascular risk factors, and quantitative MRA.

Materials & Methods

In this cross-sectional study, patients with possible and probable CAA and matched controls were included3. Clinical and demographic data (sex, age, diabetes, smoking, hypertension and atrial fibrillation) were collected. Using in-house developed semi-automated software (Vessel Voyager), center-line tracing and segment labeling for the entire intracranial arterial tree was performed on 3D_TOF images. Quantitative MRA features such as total length of the arteries, number of branches and tortuosity were extracted. MRA features and vascular risk factors were compared between CAA and no CAA cohorts.

Results

79 patients, including 54 without CAA and 25 with CAA, were included. In the CAA cohort, 4 cases were classified as possible and 21 as probable. Using logistic regression, including vascular risk factors and quantitative MRA measures, we found a decrease in the likelihood of CAA diagnosis by 4.2% for each increase of 1 unit in the number of branches in an arterial territory (p=0.005). Additionally, there was a decrease in likelihood of CAA of 12.6% with each 1 unit increase in

BMI, although this was not statistically significant (p=0.08). No significant differences were found between cohorts in terms of all other vascular risk factors.

Conclusion

The number of arterial branches on quantitative MRA is inversely associated with CAA diagnosis. Further investigation establishing CAA diagnosis and imaging features is needed to potentially improve diagnosis.

References

1. Walker DA, Broderick DF, Kotsenas AL, Rubino FA. Routine Use of Gradient-Echo MRI to Screen for Cerebral Amyloid Angiopathy in Elderly Patients. American Journal of Roentgenology. 2004;182(6):1547-1550. doi:10.2214/ajr.182.6.1821547

2. Kaiser J, Schebesch KM, Brawanski A, Linker RA, Schlachetzki F, Wagner A. Long-Term Follow-Up of Cerebral Amyloid Angiopathy-Associated Intracranial Hemorrhage Reveals a High Prevalence of Atrial Fibrillation. Journal of Stroke and Cerebrovascular Diseases. 2019;28(11):104342. doi:https://doi.org/10.1016/j.jstrokecerebrovasdis.2019.104342

3. Sotoudeh H, Sarrami AH, Wang JX, et al. Susceptibility-Weighted Imaging in Neurodegenerative Disorders: A Review. J Neuroimaging. 2021;31(3):459-470. doi:10.1111/jon.12841

Images/Tables

	Odds Ratio (OR)	95% Confidence Interval	p-value
Total Length (mm)	1.000	(0.999, 1.001)	0.792
Total Branch Number(unit)	0.958	(0.925, 0.984)	0.005**
Average Tortuosity	1.603	(0.925, 0.984)	0.683
BMI (kg/m2)	0.874	(0.738, 1.003)	0.080
Age	1.041	(0.959, 1.138)	0.336
Sex	0.902	(0.183, 4.343)	0.896
smoking	4.055	(0.829, 2.723)	0.104
Hypertension	3.003	(0.347, 3.310)	0.325
Diabetes	0.784	(0.120, 4.747)	0.789
Afib	1.873	(0.408, 8.314)	0.421

Logistic regression table reveals the difference between the cohort with CAA vs cohort with no evidence for CAA with correcting to vascular risk factors..

925

Investigating the causative effects of tinnitus of different severity and stages on the white matter microstructural integrity

Xinghao Wang

Beijing Friendship Hospital, Capital Medical University, Beijing, Beijing, China

Abstract Category

Adult Brain

Purpose

To explore the impact of idiopathic tinnitus on the brain white matter (WM) integrity of different severity and stages at a causal level.

Materials & Methods

A directed bilateral Mendelian Randomization (MR) analysis based on genome-wide association studies (GWAS) has been implemented. The tinnitus-related GWAS is derived from the research of 117882 European participants, which contains accounts of tinnitus at different severity and stages. WM diffusion indices, which come from GWAS of 3144

brain imaging phenotypes from the UK Biobank, based on tract-based spatial statistics and neurite orientation dispersion and density imaging represent its integrity in this study. The primary estimate was inverse-variance weighted, with heterogeneity and pleiotropy detected using MR Pleiotropy Residual Sum and Outlier and MR-Egger.

Results

This study revealed a significant causal relationship between tinnitus and brain WM microstructural alterations, including changes primarily within the thalamic and acoustic radiation, limbic-related fiber bundles, as well as fibers along the transmission pathways of auditory information from peripheral to central. Interestingly, we found that individuals exhibiting WM changes in the internal capsule, corticospinal tract, and tapetum might have previously experienced tinnitus. Furthermore, moderate tinnitus patients exhibit the most pronounced WM integrity changes.

Conclusion

This study substantiates that tinnitus can instigate substantial WM microstructural alterations mainly within the auditory-thalamic-limbic system and the auditory information transmission pathway from peripheral to central, while the reciprocal causality is not supported. Moreover, the data underscores that WM integrity changes vary depending on the severity and stages, and moderate tinnitus precipitates the most significant. Alterations in several specific WM fiber bundles indicate a history of tinnitus.

References

1.Bauer, C.A. (2018). Tinnitus. N. Engl. J. Med. 378, 1224-1231. doi: 10.1056/NEJMcp1506631.
Bledsoe, I.O., Stebbins, G.T., Merkitch, D., & Goldman, J.G. (2018). White matter abnormalities in the corpus callosum with cognitive impairment in Parkinson disease. Neurology 91, e2244-e2255. doi: 10.1212/WNL.0000000000006646.
2.Burgess, S., Dudbridge, F., & Thompson, S.G. (2016). Combining information on multiple instrumental variables in Mendelian randomization: comparison of allele score and summarized data methods. Stat. Med. 35, 1880-1906. doi: 10.1002/sim.6835.
3.Burgess, S., & Thompson, S.G. (2017). Interpreting findings from Mendelian randomization using the MR-Egger method. Eur. J. Epidemiol. 32, 377-389. doi: 10.1007/s10654-017-0255-x.
4.Catani, M., Howard, R.J., Pajevic, S., & Jones, D.K. (2002). Virtual in Vivo Interactive Dissection of White Matter Fasciculi in the Human Brain. Neuroimage 17, 77-94. doi: 10.1006/nimg.2002.1136.
5.Chen, Q., Lv, H., Chen, Y., Song, J., & Wang, Z. (2021a). Editorial: Neuroimaging Approaches to the Study of Tinnitus and Hyperacusis. Front. Neurosci. 15, 700670. doi: 10.3389/fnins.2021.700670.

Images/Tables

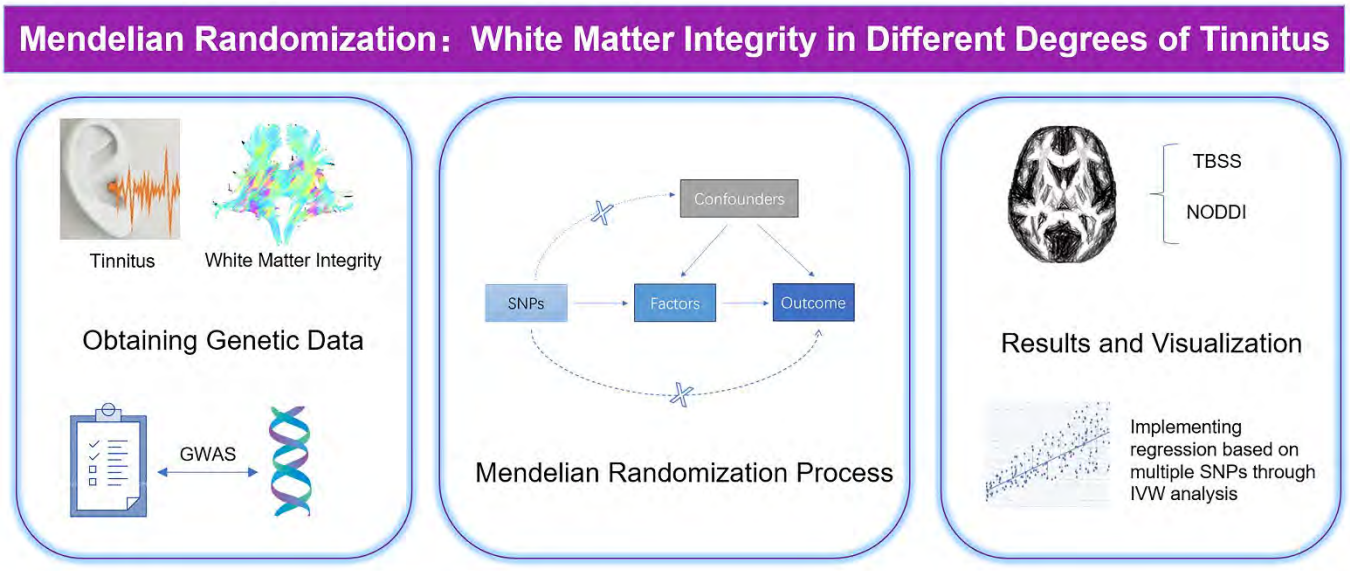

926

The Genetic Architecture of Multimodal Brain Age and Application to Neurological and Psychiatric Disorders

Xinghao Wang
Beijing Friendship Hospital, Capital Medical University, Beijing, Beijing, China

Abstract Category

AI/Informatics

Purpose

To develop a brain age model using multimodal MRI data and analyze its genetic associations and clinical relevance.

Materials & Methods

We developed a brain age model using multimodal MRI data from 27,799 participants in the UK Biobank. The model integrated structural, diffusion, SWI, T2Flair, and perfusion imaging features, applying an XG-Boost machine learning approach. We calculated brain age delta, the difference between predicted and actual age, and conducted genome-wide association studies (GWAS) on brain age delta to explore its genetic architecture. Additionally, plasma drug gene targets and brain region-specific gene co-localization were examined to provide insights into genetic mechanisms of brain aging.

Results

Brain age model achieved a mean absolute error of 3.12 years. Over a 9-year follow-up, accelerated brain aging was associated with increased risk of transient ischemic attack (TIA), depression, and anxiety, with a weaker link to insomnia. GWAS analysis identified new genetic markers related to brain age, including potential plasma drug gene targets and gene co-localization in specific brain regions. Mediation analysis suggested immune-related pathways as potential mechanisms underlying these associations, offering insights into the biological processes involved in neurodegeneration and mental health.

Conclusion

The study underscores brain age as a relevant biomarker for aging and mental health, identifying genetic and immune pathways that may drive neurodegeneration. These findings offer novel insights into brain aging and potential therapeutic targets.

References

1.Soumya Kumari, L K, and R Sundarrajan. “A review on brain age prediction models.” Brain research vol. 1823 (2024): 148668. doi:10.1016/j.brainres.2023.148668

2.Hu, Lianting et al. “MRI-based brain age prediction model for children under 3 years old using deep residual network.” Brain structure & function vol. 228,7 (2023): 1771-1784. doi:10.1007/s00429-023-02686-z

928

Are Venostenotic Features of Jugular Bulbs and their Tributaries Associated with Artifactual ASL-MRI Skull Base Venous Hyperintensity? A Comprehensive MR Image Analysis

Periakaruppan V Manickam MD, Thomas R Geisbush MD, Siddhant S Dhawan MS, Tarik F Massoud MD, PhD
Stanford University School of Medicine, Palo Alto, CA, USA

Abstract Category

Head & Neck

Purpose

The infrequent demonstration of MRI arterial spin-labeling (ASL) signal hyperintensity typically at the left jugular bulb (JB) often creates a diagnostic dilemma. This is usually ascribed to artifact from “benign jugular venous stasis”, presumed from anatomical-physiological asymmetries in internal jugular veins (IJVs), or a much less common skull base dural AVF requiring additional imaging work-up. The mechanisms for JB stasis/recirculation of labeled venous blood and consequent ASL artifact are not fully understood. Just as patients with craniosynostosis have significantly smaller jugular foramina in conjunction with raised intracranial pressure, we hypothesized that jugular venous outflow tract obstruction owing to unfavorable venostenotic morphologies of JBs and their tributaries may predispose to venous stasis and thus be associated with this artifact. We investigated potential mechanistic links between JB morphology and ASL-MRI signal by image analysis and comparisons of patients with/without artifact.

Materials & Methods

We retrospectively reviewed brain post-contrast MRI-BRAVO images of 49 age/sex matched adult patients (25 with focal left-sided skull base ASL hyperintensity and no imaging evidence of an AVF [ASL+ group], and 24 control subjects with no skull base ASL hyperintensity [CSs group]). We noted IJV dominance, and on axial images for both cohorts we measured left-sided (a) diameters of sigmoid sinuses, inferior petrosal veins, and posterior condylar veins, all at vessel confluences with JBs; and maximum cross-sectional JB areas. We then used reformatted parasagittal images to measure dimensions of narrowest points of inflow, outflow, and midportion of each JB; and any presence of JB diverticula. Lastly, we obtained 3D volumes of JBs after segmentations in orthogonal planes. We performed inter-group comparisons of independent means using a t-test to assess for associations between venostenotic features of JBs and presence/absence of ASL hyperintensity, and Pearson correlation for age associations. Significance was set at $p<0.05$.

Results

There were almost equal numbers of males and females in both groups (mean age 67.8±13.9 years). Mean diameters of posterior condylar veins were significantly smaller (p=0.013) in ASL+ (2.1mm) than in CSs (2.7mm). Mean lengths of midportions of JBs viewed parasagittally were significantly smaller (p=0.03) in ASL+ (9.1mm) than in CSs (11.3mm). Mean lengths of the narrowest points of outflow of JBs viewed parasagittally were significantly smaller (p=0.006) in ASL+ (2.14mm) than in CSs (2.7mm). There were no other significant differences or correlations, including with patient sex and age. JB diverticula were observed in similar numbers in both groups (five in ASL+, four in CSs).

Conclusion

This is the first report that significantly links morphological venostenotic features in left-sided JBs with an observation of associated ASL-MRI hyperintensity. We speculate that JBs with relatively smaller midportions, and especially with smaller outflows into IJVs, may possess configurations that favor stasis/recirculation of labeled venous blood to help explain the origin of ASL-MRI hyperintensity. The presence of significantly smaller posterior condylar veins in ASL+ individuals would also add to relative stasis by diminishing JB outflow via this emissary vein. We demonstrate that JB morphological and venostenotic features may contribute to development of artifactual ASL-MRI hyperintensity at the skull base.

References

1. Caton MT, Callen AL, Copelan AZ, Narsinh KH, Smith ER, Amans MR. Jugular venous reflux can mimic posterior fossa dural arteriovenous fistulas on MRI-MRA. AJR Am J Roentgenol 2021;216:1626-1633.
2. Iwamura M, Midorikawa H, Shibutani K, et al. High-signal venous sinuses on MR angiography: discrimination between reversal of venous flow and arteriovenous shunting using arterial spin labeling. Neuroradiology 2021;63:889-896.
3. Florisson JM, Barmpalios G, Lequin M, et al. Venous hypertension in syndromic and complex craniosynostosis: the abnormal anatomy of the jugular foramen and collaterals. J Craniomaxillofac Surg 2015;43:312-318.

934

Is Transient Global Amnesia Linked to Styloidogenic Jugular Venous Compression? An Imaging-Morphometric Correlative Study of Potential Impaired IJV Drainage in Patients with Focal Hippocampal DWI Lesions

Mohamed S Muneer MD, Thomas R Geisbush MD, Siddhant S Dhawan MS, Tarik F Massoud MD, PhD
Stanford University School of Medicine, Palo Alto, CA, USA

Abstract Category

Adult Brain

Purpose

The diagnosis of transient global amnesia (TGA) is clinical, although associated mesiotemporal punctate diffusion-weighted imaging (DWI) lesion(s) are reported with variable incidence. The pathogenetic mechanisms for these foci of restricted diffusion are unresolved but abnormal brain venous drainage leading to intracranial hypertension may play a role. Although disputed, various causes of internal jugular vein (IJV) obstruction with or without flow reversal may occur, e.g. transiently during Valsalva in presence of valvular incompetence or IJV stenosis. Styloidogenic jugular venous compression (SJVC) between C1 transverse process, styloid process, and posterior belly of digastric is a common and usually asymptomatic anatomical variant, though it too has been associated with idiopathic intracranial hypertension. A potential contribution of SJVC to venous drainage impairment in TGA patients has not been evaluated previously. We studied this possible mechanistic link by image analysis of IJV percentage stenosis in patients exhibiting focal hippocampal DWI lesions.

Materials & Methods

We retrospectively reviewed post-contrast MRIs and CTs of 80 age and sex matched adult patients (20 with clinical TGA and restricted DWI [TGA+/MRI+], 20 with clinical TGA and no restriction [TGA+/MRI-], 20 without clinical TGA but with hippocampal punctate restriction similar to TGA [TGA-/MRI+], and control subjects [CSs, TGA-/MRI-]. For all cohorts, we measured anteroposterior and transverse dimensions of each IJV in sagittal and axial planes, both at the styloidogenic compression and 2 cm more proximally. From these we calculated the cross-sectional areas at both points and consequent degree of SJVC stenosis, categorizing this as mild (0-50%), moderate (51-80%), or severe (81-100%). We performed within group category comparisons using a non-parametric Kruskal-Wallis test to assess for any associations between percentage/grade of SJVC stenosis and characteristics of patients/IJVs/hippocampal lesions, as well as type of experimental cohort. We also noted SJVC sidedness and relative IJV dominance. Significance was set at $p<0.05$.

Results

There were equal numbers of males and females, with a mean age of 65.6+/-11.8 years. The right SJVC was greater (88.9% stenosis) than left (64.2%) across all four cohorts. The type of experimental cohort was significantly associated with occurrence of right-sided SJVC stenosis (p=0.001). Right stenosis was present significantly more in TGA+/MRI+ patients (mean stenosis 91.9%, p=0.007) and TGA+/MRI- patients (mean stenosis 91.5%, p=0.02) than in CSs (85.2% stenosis). However, there was no statistical difference in percentage/grade stenosis between TGA+/MRI+ and TGA+/MRI- patients, and no other significant associations.

Conclusion

This is the first report that links right-sided proximal IJV stenosis owing to SJVC with a clinical presentation/suspicion of TGA in patients having focal hippocampal restricted DWI lesions. A similar association in patients with clinical TGA but apparent normal hippocampi may reflect the presence of MRI-occult lesions or possible imaging outside the time course for detection of restricted diffusion. Further larger-sized investigations of pathogenetic factors contributing to this clinically important entity are ongoing, including considerations of scan timing versus symptoms onset to better detect DWI lesions. We recommend that MRI assessment of TGA patients include imaging of presence and severity of right-sided SJVC.

References

1. Han K, Hu HH, Chao AC, et al. Transient global amnesia linked to impairment of brain venous drainage: An ultrasound investigation. Front Neurol 2019;10:67.

2. Jan K, Saini M, Sng G, et al. Transient global amnesia and focal diffusion weighted imaging lesions in mesiotemporal region: A ten-year experience. Clin Neurol Neurosurg 2021;202:106522.

3. Zhao X, Cavallo C, Hlubek RJ, et al. Styloidogenic jugular venous compression syndrome: Clinical features and case series. Oper Neurosurg 2019;17:554-561.

937

Development of NM-MRI and SMwI templates for Simultaneous Multimodality Analysis of Parkinson's Disease

Jeongwon Jo MS[1], Aleum Lee MD, PhD[2], Hwan Heo MS[1], MyeonOh Lee MS[1], Intae Shin MS[1], Min Seung Kim MD[3], Seok Jong Chung MD[4], Suk Yun Kang MD, PhD[3], Soohwa Song PhD[1]

[1]Heuron, Seoul, Seoul, Korea, Republic of. [2]Soon Chun Hyang University Hospital, Bucheon-si, Gyeonggi-do, Korea, Republic of. [3]Dongtan Scred Heart Hospital, Hwaseong-si, Gyeonggi-do, Korea, Republic of. [4]Yongin Severance Hospital, Yongin-si, Gyeonggi-do, Korea, Republic of

Abstract Category

Functional/Advanced Imaging

Purpose

Simultaneous multimodality analysis is increasingly needed for MR imaging of brain diseases. While NM-MRI and SMwI are useful for capturing NM and Nigrosome1 in PD studies, their unique characteristics complicate combined analysis[5]. This study proposes a multi-modality template method for targeted regions using whole-brain 3D T1 images.

Materials & Methods

The dataset consisted of scans from 29 NC subjects, acquired using a 3T scanner. The MRI protocol included: whole-brain 3D T1w imaging with MPRAGE; SandwichNM[1] protocol for NM-sensitive imaging; and 3D multi-echo GRE for SMwI[2]. T1w images were skull-stripped. For T1w images, the tissue masks were generated and used as priors for N4 bias field correction. For NM-MRIs, 4 slices located on adjacent cross sections were eliminated to avoid intensity

artifacts. Then, the bias field was corrected without prior. SMwI images were reconstructed from the 3-echo data using the previous study[2].

The template construction method uses three strategies: 1. restricting the image to the ROI, which is centered in the midbrain, minimally affected by capture angle. 2. applying Gaussian-weighted averaging to reduce cross-sectional artifacts on the template caused by capture angle. 3. applying a multimodal template-building approach[3] to enhance midbrain subregion clarity, including the SNpc. The proposed iterative template construction includes three steps (Fig. 1, a). Initially, T1w images are spatially normalized to MNI space to crop the midbrain-centered ROI and create an unbiased initial T1w template. In the first step, a T1w template is generated, using spatial normalization across 29 subjects; transformations are then applied to NM-MRI and SMwI data. The second step builds an NM-MRI template, driven by NM-MRI data, with transformations applied to T1w and SMwI data. The third step constructs an SMwI template using SMwI data, with transformations applied to T1w and NM-MRI data. Spatial normalization of iteration 1, and 2 follow the SyN method from ANTs and multiGradICON4, respectively. To enhance structure information of NM-MRI and SMwI, exponential operation is applied to NM-MRI and SMwi before normalization. The final templates were compared with previous templates.[5]

Results

The average cross correlation between template and spatially normalized image is increased at both modalities (NM-MRI: 0.902 -> 0.965; SMwI: 0.848 -> 0.956) (Fig. 1, c). The contrast to noise ratio (CNR) between Nigrosome1 and SNpr of SMwI template is increased. (14.268 -> 22.64) The proposed method enhances the spatial matching of the NM-MRI and SMwI data used to create the templates, as seen in (Fig. 1, c), which indicates the quality of the templates also improved (Fig. 1, b).

Conclusion

We confirmed that the SNpc region in NM-MRI was consistently aligned and undistorted in any one area. Also, we observed the quality of the Nigrosome1 region in the SMWI template was improved. We expect that the development of high-quality templates located in the same space will enable simultaneous analysis of NM-MRI and SMwI in PD studies.

References

1. Ji, Sooyeon, et al. "Sandwich spatial saturation for neuromelanin-sensitive MRI: Development and multi-center trial." NeuroImage 264 (2022): 119706.
2. Gho, Sung-Min, et al. "Susceptibility map-weighted imaging (SMWI) for neuroimaging." *Magnetic resonance in medicine* 72.2 (2014): 337-346.
3. Wu, Yingjuan, et al. "Development of High Quality T1w and DTI Templates of the Older Adult Brain in a Common Space." *Proc. Intl. Soc. Mag. Reson. Med*. Vol. 27. 2019.
4. Demir, Başar, et al. "MultiGradICON: A Foundation Model for Multimodal Medical Image Registration." *International Workshop on Biomedical Image Registration*. Cham: Springer Nature Switzerland, 2024.
5. Sung, Young Hee, et al. "Early-stage Parkinson's disease: Abnormal nigrosome 1 and 2 revealed by a voxelwise analysis of neuromelanin-sensitive MRI." Human Brain Mapping 42.9 (2021): 2823-2832.

Images/Tables

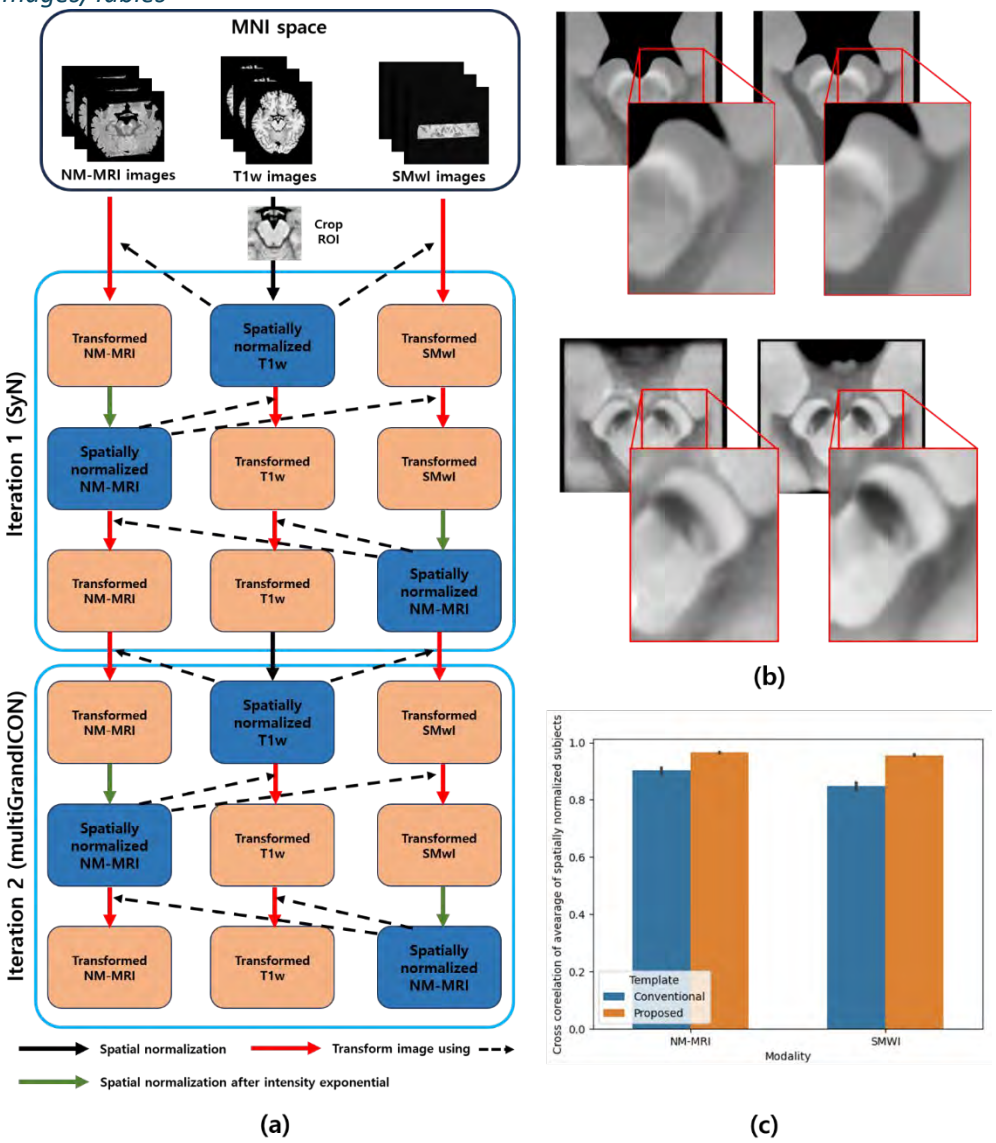

939

Evaluation of Publicly Available Deep Learning Lumbar Spine MRI Analysis Tool for Prioritizing MRI Evaluation

Nazmi Kurt MD, Serkan Akbas MD, Raphael Russo BS, Salil Soman MD, MS
Beth Israel Deaconess Medical Center / Harvard Medical School, Boston, MA, USA

Abstract Category

Spine

Purpose

Among the etiologies warranting urgent intervention on lumbar spine MRI are ones where the spinal canal is severely narrowed. In the setting of radiologist shortages,[1] clinician accessibility to a tool that can identify this spinal canal narrowing would help prioritize exams, or alert non-radiologist clinicians to their presence would benefit patient care. Recently, multiple deep learning models have been shown to perform detailed lumbar spine MRI analysis.[2-4] In this study we assess the performance of the publicly available SpineNetV2[5] (https://github.com/rwindsor1/SpineNet) package on a dataset of lumbar spine MRIs, relative to a neuroradiology attending and fellows.

Materials & Methods

The Mendeley lumbar spine data set with 512 subjects (https://data.mendeley.com/datasets/k57fr854j2/2) was analyzed using SpineNetV2[5] to generate spinal canal (grading scale 1-4, from normal to severe) and bilateral neural foraminal (present / absent) stenosis, and spine level labels (figure A).

The images were next reviewed by a board certified neuroradiologist with 14 years experience and 2 neuroradiology fellows. Reviewers score spinal canal and neural foraminal stenosis using the same scale as SpineNetV2. A consensus reading for these categories across all 3 readers was generated using a 2/3 majority method. The CC_3-4 score, indicating if a study had moderate or severe spinal canal stenosis, was generated from reader and algorithm spinal canal stenosis scores.

Interrater reliability for the spinal canal, left, and right neural foraminal stenosis using Fleiss Kappa was generated for the three readers, and again including the algorithm's scores as a fourth rater. Fleiss Kappa was calculated for the readers and using the algorithm as a 4th reader for the CC_3-4 scores. Cohen's Kappa between the scores for spinal canal stenosis, as well as for CC_3-4, for the algorithm and the consensus reading was calculated. Bland Altman plot of the consensus spinal canal stenosis relative to the algorithm. All analyses were performed using python 3, at the level of individual spine levels, resulting in a total of 3032 levels evaluated.

Results

Fleiss and Cohen's Kappa scores are in figure B. Agreement among the readers are seen on figures C and D. Agreement between the readers and the algorithm are on figures E and F.

Conclusion

Our results show that our readers had moderate agreement by Fleiss Kappa for spinal canal stenosis, which was slightly improved when including the algorithm's scores. The CC_3-4 scores also only showed moderate agreement for the readers, made slightly worse, but still moderate, when including algorithm's scores. These findings suggest this algorithm reviewing lumbar spine MRI would have comparable agreement with radiologists as a screening tool for lumbar spine emergencies. While the need for surgical intervention would still need to be evaluated by a clinician, this software could serve as a reasonable tool for prioritize studies for review, especially when multiple feeder sites are sending studies to radiologists for review at locations across the enterprise.

The SpineNetV2 publicly available deep learning software has potential to serve as a prioritization tool for moderate to severe vertebral canal narrowing, which can aid in screening for patients with potentially critical spinal stenosis.

References

Radiologist Workforce. *AJR Am J Roentgenol* 2024;222:e2430920

2. Bharadwaj UU, Christine M, Li S, et al. Deep learning for automated, interpretable classification of lumbar spinal stenosis and facet arthropathy from axial MRI. *Eur Radiol* 2023;33:3435-3443

3. Grob A, Loibl M, Jamaludin A, et al. External validation of the deep learning system "SpineNet" for grading radiological features of degeneration on MRIs of the lumbar spine. *Eur Spine J* 2022;31:2137-2148

4. Windsor R, Jamaludin A, Kadir T, et al. Automated detection, labelling and radiological grading of clinical spinal MRIs. *Sci Rep* 2024;14:14993

5. Windsor R, Jamaludin A, Kadir T, et al. SpineNetV2: Automated Detection, Labelling and Radiological Grading Of Clinical MR Scans. 2022:arXiv:2205.01683

Images/Tables

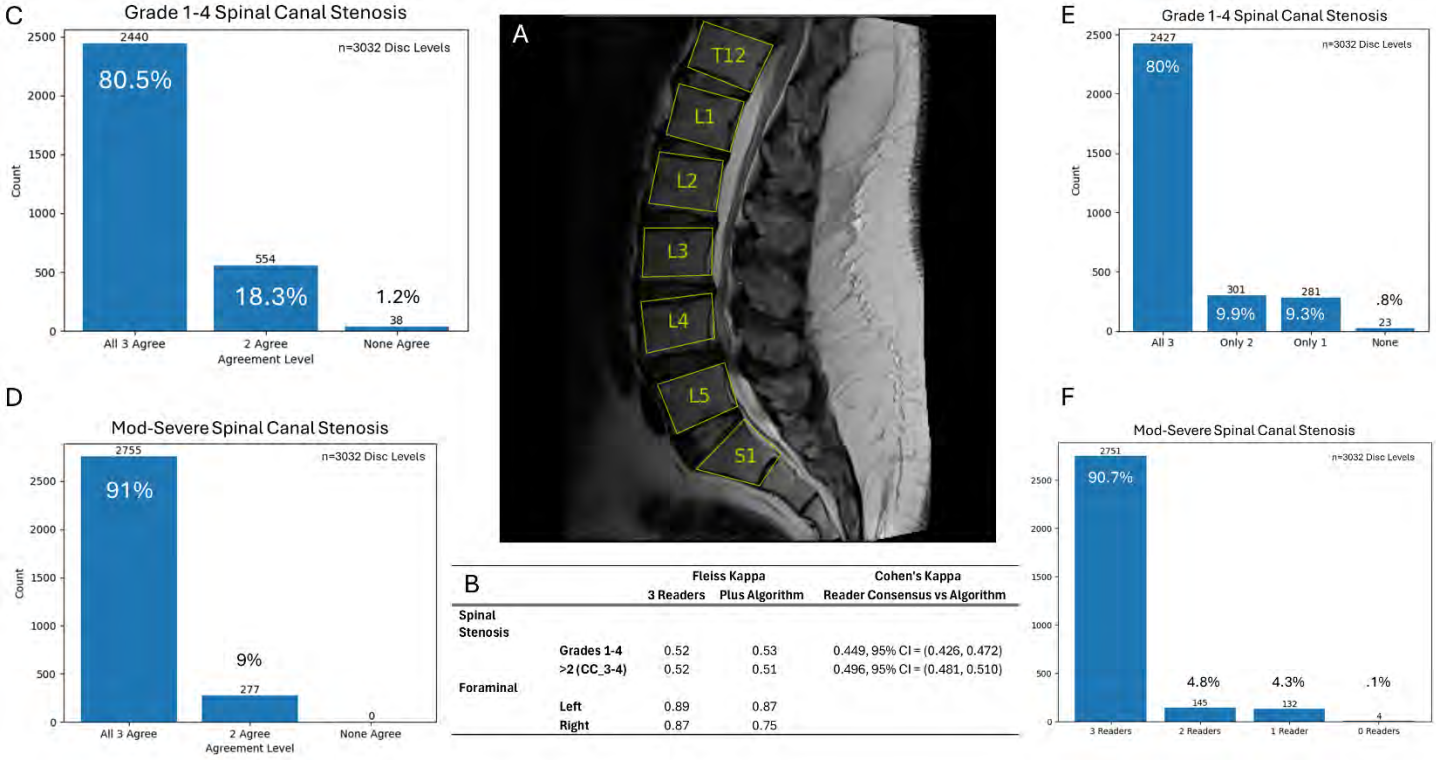

B

		Fleiss Kappa		Cohen's Kappa
		3 Readers	Plus Algorithm	Reader Consensus vs Algorithm
Spinal Stenosis				
	Grades 1-4	0.52	0.53	0.449, 95% CI = (0.426, 0.472)
	>2 (CC_3-4)	0.52	0.51	0.496, 95% CI = (0.481, 0.510)
Foraminal				
	Left	0.89	0.87	
	Right	0.87	0.75	

963

Transverse Sinus Stenosis and Sigmoid Sinus Wall anomalies: Causality or Coincidence

Pamela Semaan MD, Bindu Setty MD, Christopher Shin MD, Anvitha Sathya BA, Mathiew Miller, Mohamad Abdalkader MD

Boston Medical Center, Boston, MA, USA

Abstract Category

Adult Brain

Purpose

Pulsatile tinnitus (PT) can be debilitating and can impact patients' quality of life. Venous abnormalities, such as transverse sinus stenosis (TSS) and sigmoid sinus wall anomalies (SSWA), are the leading causes of pulsatile tinnitus. Although each of these conditions has been independently studied as contributors to PT, their relationship has not been well established. This study aims to evaluate the relationship between TSS and SSWA in patients presenting with PT.

Materials & Methods

We conducted a retrospective cohort study, reviewing patients with PT and age- gender- matched controls from January 2018 to March 2022. Inclusion criteria for the PT group included patients with PT who underwent CT Angiogram/Venogram. The control group consisted of patients who underwent the same imaging modalities for other indication unrelated to PT. Descriptive statistics were used to characterize patients with and without SSWAs in each group as well as patients with and without TSS, using the student's t-test.

Results

We identified a total of 150 patients with PT and 100 control patients. Among the PT group, the prevalence of TSS was 70/150 (46.7%, bootstrap 95% confidence interval: [45.8%-48.5%]), and the prevalence of SSWA was 71 out of 150 (47.3%, 95% confidence interval: 46.7%-49.7%). In the control group, the prevalence of TSS was 27/100 (27.0%, bootstrap 95% confidence interval: [25.9%-28.4%], and the prevalence of SSWA was 26 out of 100 (26.0%, bootstrap 95% confidence interval: 24.2%-26.4%). Patients with PT demonstrated a significantly higher prevalence of both TSS and SSWA compared to controls ($p < 0.001$). In patients with both PT and TSS, the prevalence of SSWA was 59 out of 97 (60.8%, bootstrap 95% confidence interval: 57.8%-60.9%). In contrast, among control patients without PT and without TSS, the prevalence of SSWA was 38 out of 153 (24.8%, bootstrap 95% confidence interval: 24.0%-26.6%). Overall, the prevalence of SSWA in patients with both PT and TSS was significantly higher than in patients without PT and without TSS.

Conclusion

In our series, TSS and SSWAs were the most frequently identified causes of PT. The significantly higher prevalence of SSWA in patients with both PT and TSS, compared to those without PT and TSS, suggests that TSS may play a primary role in the development of SSWA in the context of PT. Therefore, in patients presenting with PT and SSWAs, an active search for TSS and IIH is recommended. When managing patients with PT, TSS, and SSWAs, addressing TSS should be the mainstay treatment, as dedicated treatment of SSWAs may not be necessary. Larger comparative studies are needed to further evaluate these findings.

References

1. Erlandsson SI, Hallberg LR. Prediction of quality of life in patients with tinnitus. Br J Audiol. 2000 Feb;34(1):11-20. doi: 10.3109/03005364000000114. PMID: 10759074.
2. Abdalkader M, Sakai O et al. State of the Art: Venous Causes of Pulsatile Tinnitus and Diagnostic Considerations Guiding Endovascular Therapy. Radiology. 2021 Jul;300(1):2-16. doi: 10.1148/radiol.2021202584. Epub 2021 May 25. PMID: 34032509.
3. Reardon MA, Raghavan P. Venous Abnormalities Leading to Tinnitus: Imaging Evaluation. Neuroimaging Clin N Am. 2016 May;26(2):237-45. doi: 10.1016/j.nic.2015.12.006. Epub 2016 Mar 5. PMID: 27154606.
4. Hsieh YL, Wang W. Sigmoid Sinus Wall Anomalies Can Progress and May Not Be Congenital. Laryngoscope. 2024 Nov;134(11):4707-4715. doi: 10.1002/lary.31538. Epub 2024 May 28. PMID: 38804647.

967

Do Lesion Size, Shape and Location limit the ability of Susceptibility Weighted Imaging to Differentiate Intracranial Hemorrhages from Calcifications?

Adrija Krishnamoorthy[1], Einat Slonimsky MD[2], Scott Hwang MD, PhD[2], Jonathon Maffie MD, PhD[2]

[1]Penn State University, University Park, PA, USA. [2]Penn State Health, Hershey, PA, USA

Abstract Category

Adult Brain

Purpose

To differentiate intracranial hemorrhage from calcification, SWI phase signal analysis has been applied mainly to intraparenchymal, subcentimeter foci that are approximately spherical in shape. Aliasing particularly near the central regions have hindered the ability of SWI phase signal to accurately classify large size susceptibility foci. The ability of phase images to distinguish susceptibility foci irrespective of their location, size and shape as well as the influence of known sites of physiologic calcifications, without recourse to CT, remains an unexplored area.

Materials & Methods

In this retrospective study, 50 consecutive cases were selected who underwent MRI brain with SWI sequence and CT head within 24 hours of completing each modality. Prior authorization from the institutional review board was obtained for the study. Two reviewers independently analyzed SWI sequence with blinding to all other MR sequences and CT. Phase signals of susceptibility foci were segmented into three sectors: cranial polar, caudal polar and central regions. To overcome the phase aliasing effects near the central regions, phase halo was used. No restrictions were placed on the size, shape or location of susceptibility foci except for the exclusion of basal ganglia calcifications. Discrepancy in analyzing phase images was resolved with consensus to obtain the final phase input from each of the three sectors. CT images were independently assessed by a third reviewer and ≥ 100 HU was used to differentiate hemorrhage from calcification. Appropriate statistical analysis was performed and p value less than 0.05 was considered significant

Results

In the study cohort, there were 22 males and 28 females ranging in age from 2 to 90 years old (mean 61.19±21.13). In total, 639 intracranial susceptibility foci were identified. Among 406 hemorrhages identified, 305 were intraparenchymal, 45 subdural, 22 subarachnoid, 15 intraventricular and 19 cortical vein thrombosis. Among 233 calcifications identified, 36 were intraparenchymal, 44 pineal, 84 choroid plexus, 17 dural and 52 arachnoid granulations. The size of all hemorrhages ranged from 1.5mm to 145.2mm (mean 11.5±15.81). The size of calcifications ranged from 1.5mm to 71.9mm (mean 8.16±7.13mm). The shape of hemorrhagic lesions was spheroid in 300, linear in 75 and irregular in 31. The shape of calcifications was spheroid in 135, linear in 94 and irregular in 1. Depending on the location, the sensitivity to identify hemorrhages ranged from 79% to 100%, specificity from 82% to 100%, positive predictive value from 95% to 100%, negative predictive value from 76% to 98% and accuracy from 93% to 99%. Inter-rater agreement for the detection of susceptibility lesions on SWI was k=0.79 (CI 0.66-0.92) and for the characterization of phase signals was

k=0.62 (CI 0.55-0.69). AUC measured >0.90 (p<0.001) for all three sectors in phase images to detect hemorrhages. For the detection of calcifications, AUC from the caudal sector and halo measured >0.90 (p<0.001), whereas from the cranial sector, it measured 0.80 (p<0.001).

Conclusion

Evaluation of SWI phase signal across three sectors can effectively distinguish between intracranial hemorrhage and calcification in a majority of cases, regardless of their size, shape, or location.

References

Weng CL, Jeng Y, Li YT, Chen CJ, Chen DY. Black Dipole or White Dipole: Using Susceptibility Phase Imaging to Differentiate Cerebral Microbleeds from Intracranial Calcifications. AJNR Am J Neuroradiol. 2020;41:1405-1413. DOI: 10.3174/ajnr.A6636

Tay KL, Leason SR, Dawes LC, Thomas SL, Hillenbrand CM. Haemorrhage and Calcification on Susceptibility-Weighted Imaging: A Quick and Reliable Qualitative Technique for Differentiating Lesions with Ambiguous Phase. Clin Neuroradiol. 2022;32:705-715. DOI: 10.1007/s00062-021-01094-2

Gumus K, Koc G, Doganay S, Gorkem SB, Dogan MS, Canpolat M, Coskun A, Bilgen M. Susceptibility-Based Differentiation of Intracranial Calcification and Hemorrhage in Pediatric Patients. J Child Neurol. 2015;30:1029-36. DOI: 10.1177/0883073814552439

968

Deep learning-based CT volume and density measures are associated with infarct growth rate and functional outcome before transfer for thrombectomy from a primary stroke center

Henk van Voorst MD, PhD[1], Yongkai Liu PhD[1], Aroosa Zamarud MD[1], Anke Wouters MD, PhD[2], Pierre Seners MD[1], Abdelkader Mahameddi MD[1], Benjamin FJ Verhaaren MD[1], Soren Christensen PhD[1], Michael Mlynash MD, PhD[1], Gregory Zaharchuk MD, PhD[1], Maarten G Lansberg MD, PhD[1], Gregory W Albers MD[1], Jeremy J Heit MD, PhD[1]
[1]Stanford, Stanford, CA, USA. [2]KU Leuven, Leuven, Belgium, Belgium

Abstract Category

AI/Informatics

Purpose

Even after a successful thrombectomy for acute ischemic stroke, a large portion of patients have poor outcomes. New imaging metrics that predict outcomes could help to identify patients who might benefit from neuroprotective therapies before they are transferred for thrombectomy treatment from a primary to a comprehensive stroke center (PSC/CSC). We determined if CT perfusion (CTP) or deep learning-based CT (DLCT) (1) volume and density measures determined in the PSC are associated with the infarct growth rate during transfer to a CSC and functional outcomes after thrombectomy.

Materials & Methods

Patients from the prospective CRISP2 cohort study with CT and CTP in a PSC were included(2,3). Infarct growth was determined at admission using the CTP core volume in the PSC and CTP core or DWI lesion volume in the CSC. Functional outcome was measured using the modified Rankin Scale (mRS) 90 days after CSC admission. We considered the following outcome measures: infarct growth rate (mL/h), fast infarct growth (≥5mL/h) (2,3), ordinal mRS, and functional independence (mRS≤2). DLCT and CTP measures were selected using stepwise variable selection in addition to a predetermined set of clinical and imaging variables (table 1). DLCT measures we considered were: lesion volume, hypodense (<26HU) lesion volume (4), net water uptake (NWU) (5), average density, median density, and standard deviation of density in the lesion. CTP measures we considered were: CBV index, Hypoperfusion Intensity Ratio, ischemic core, and Tmax>6s volume, excluding Tmax>10s volume. We report adjusted coefficients and odds ratios with 95% confidence interval (aB/aOR[95%CI]) for models using DLCT and CTP variables as input and infarct growth rate (robust regression) and 90-day ordinal mRS (shift analysis) as outcomes. Predictive performance for fast infarct growth rate and mRS≤2 is reported with the AUC for models using DLCT, CTP, and both imaging (CTP+DLCT) variables as input. Multiple imputation was used to handle missing variables with five imputed datasets (R 4.4.2, Hmisc: AregImpute).

Results

We included 134/105 men/women with a mean age of 69(SD:15) years. Larger DLCT lesion volume (aB/10mL: 1.55[1.03;2.07] mL/h) and smaller CTP Tmax>6s volume (aB/10mL: -0.44[-0.76;-0.12] mL/h) were associated with higher infarct growth rates. Functional outcomes were worse when a larger volume of hypodense tissue (<26HU) was observed with DLCT (aOR/10mL: 0.65[0.44;0.96]). Models using DLCT and/or CTP variables had comparable AUCs for fast infarct

growth rate (AUC ≥5mL/h DLCT: 0.82, CTP: 0.76, DLCT+CTP: 0.85) and functional independence (AUC mRS≤2 DLCT: 0.84, CTP: 0.83, DLCT+CTP: 0.84).

Conclusion

DLCT-based lesion volume and density measured in a primary stroke center were associated with the infarct growth rate during transfer and 90-day functional outcome. Predictive performances of models using DLCT and CTP were comparable. Therefore, DLCT measures could be considered as a prognostic marker in the PSC in addition to or as a substitute for CTP.

References

1. Ostmeier, Sophie, et al. "Random expert sampling for deep learning segmentation of acute ischemic stroke on non-contrast CT." Journal of NeuroInterventional Surgery (2024).
2. Wouters, Anke, et al. "Clinical and Imaging Features Associated With Fast Infarct Growth During Interhospital Transfers of Patients With Large Vessel Occlusions." *Neurology* 103.6 (2024): e209814.
3. Seners, Pierre, et al. "Clinical change during inter-hospital transfer for thrombectomy: Incidence, associated factors, and relationship with outcome." *International Journal of Stroke* (2024): 17474930241246952.
4. Yogendrakumar, Vignan, et al. "Abstract TMP93: Severe Non-Contrast CT Hypodensity Modifies EVT Treatment Effect and is Associated With Worse Outcomes Independent of Ischemic Core Volume: A Secondary Analysis of the SELECT2 Trial." *Stroke* 55.Suppl_1 (2024): ATMP93-ATMP93.
5. Minnerup, Jens, et al. "Computed tomography–based quantification of lesion water uptake identifies patients within 4.5 hours of stroke onset: a multicenter observational study." *Annals of neurology* 80.6 (2016): 924-934.

Images/Tables

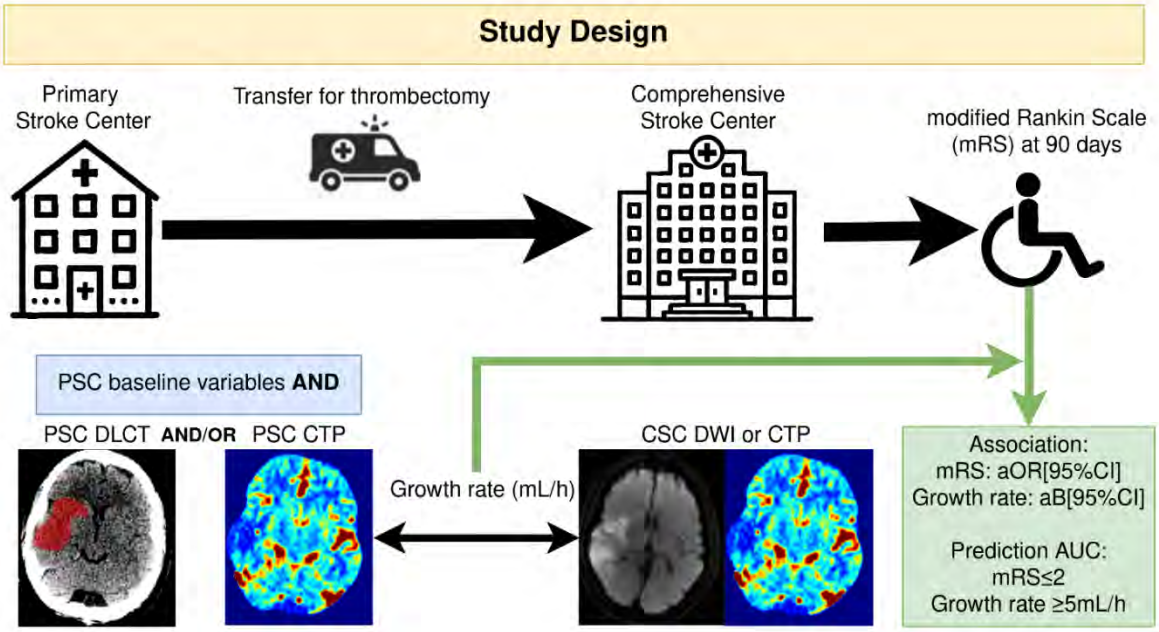

Results

Variable measured in the primary stroke center	Growth rate (mL/h) aB[95%CI]	modified Rankin Scale (mRS) aOR[95%CI]
DLCT: lesion volume (per 10mL)	1.55 (1.03; 2.07)***	Not selected
DLCT: Volume in Lesion with <26HU (per 10mL)	Not selected	0.65 (0.44; 0.96)*
DLCT: Net Water Uptake (per %)	-0.22 (-0.46; 0.02)	0.93 (0.88; 0.99)
DLCT : Density standard deviation in lesion (HU)	1.48 (0.2; 2.75)*	0.72 (0.52; 1.01)
CTP: Tmax>6s volume without Tmax>10s volume (per 10mL)	-0.44 (-0.76; -0.12)*	Not selected
CTP: Hypoperfusion Intensity Ratio (per 0.1)	0.47 (-0.15; 1.09)	0.88 (0.78; 1.0)

Table 1. Associations of DLCT and CTP measures with outcomes. DLCT and CTP variables were selected using stepwise selection optimized for Akiake Infromation Criterion. Baseline confounding variables that were used are not included in the table. *:p<0.05, **:p<0.001, ***:p<0.00001.

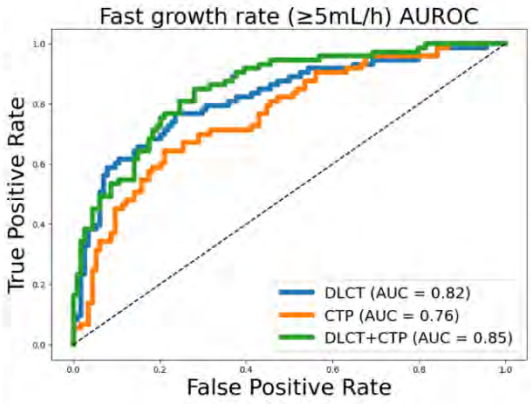

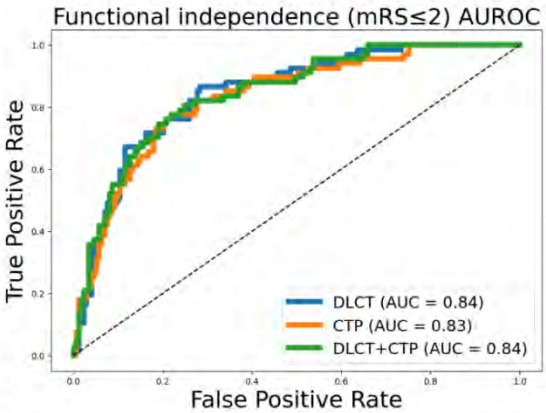

978

Initial Impression of MR Guided PET Reconstruction in Detecting Focal Cortical Hypometabolism in Epilepsy Patients

Chen Lin PhD[1], Matthew Spangler-Bickell[2], Daniel Litwiller[2], Alex Smith[3], Robert A Pooley[1], Erik H Middlebrooks[1]
[1]Mayo Clinic, Jacksonville, FL, USA. [2]GE Healthcare, Waukesha, Wi, USA. [3]GE Healthcare, Waukesha, WI, USA

Abstract Category

Functional/Advanced Imaging

Purpose

Focal cortical dysplasia (FCD) is one of the most common causes of epilepsy, yet one of the most difficult lesional causes to identify on imaging. Identification of lesions is critical as it is perhaps the greatest individual predictor of seizure freedom after surgery. FDG-PET is a relatively underutilized tool identification of FCD, likely in part due to difficulty with confidently detecting smaller cortical lesions. Incorporating anatomical information from high resolution MR images into the PET reconstruction through regularization has the potential to improve the PET image quality, particularly in regions where differentiation between white and grey matter is critical. We highlight a number of impactful cases.

Materials & Methods

Five patients with FCD who had previously undergone FDG-PET MR were retrospectively evaluated. PET MR exams were performed on a SIGNA 3T PET/MR (GE HealthCare, Waukesha, WI). 3D T1 IR FSPGR and T2 FLAIR CUBE images were acquired simultaneously with PET. PET images were originally reconstructed using conventional TOF-OSEM reconstruction with 28 subsets and 4 iterations using 3 mm FWHM spatial filter and standard Z-filter as the standard of care. The algorithm implemented in the retrospective MR guided PET reconstruction is a modified asymmetrical Bowsher's. 3D T1 and T2 MR images are used as "priors" for the reconstruction. The algorithm uses the MR images to identify similar neighborhoods around each pixel and penalizes over those neighborhoods during reconstruction. The algorithm is implemented within a list-mode block sequential regularized expectation maximization (BSREM) framework and incorporates data-driven event-by-event motion correction. The motion correction removes any blurring in the PET image, ensures alignment with the attenuation map, and, since the PET and MR priors are acquired simultaneously, the priors can be transformed according to the estimated motion to ensure alignment between the PET data and MR priors. Images of conventional FDG-PET reconstructions and MRI were qualitatively compared with the proposed MR-guided PET reconstruction by a neuro-radiologist.

Results

In all five patients, the MR-guided PET reconstruction algorithm produced enhanced differentiation of gray matter and white matter. In particular, there was improved delineation of the cortex. All lesions showed cortical hypometabolism that was better visualized on the MR-guided PET reconstruction. Two of the five target lesions were not initially identified on interpretation of the standard FDG-PET reconstruction. There were no imaging artifacts identified in any of the image reconstructions, nor detection of any false positive areas of hypometabolism on the MR-guided PET reconstruction. As shown by the examples in Figure 1, MR-guided PET reconstruction may enable improved visualization and more confident detection of focal cortical hypometabolism than conventional PET reconstruction.

Conclusion

FDG-PET may enhance lesion detection over MRI alone but is limited by anatomical definition, resolution, and blurring that make detection of small cortical areas of hypometabolism difficult to identify. We show that improvement in cortical definition and anatomic fidelity in the MRI-guided PET reconstruction algorithm has the potential to improve detection of small lesions due to improved visual conspicuity. Future studies will be needed to further assess diagnostic performance and advantages over existing techniques.

References

Bing Bai, Quanzheng Li, Richard M Leahy. "MR Guided PET Image Reconstruction" Se min Nucl Med. 2013 Jan;43(1):30-44.

Khalighi, Mohammad Mehdi, Timothy Deller, Matthew Spangler-Bickell, Kristen Wangerin, Dawn Holley, Kim Halbert, Michael Zeineh et al. "High Quality Isotropic Whole-body PET Imaging Using MR Priors." (2020): 1477-1477.

Bowsher, James E., Hong Yuan, Laurence W. Hedlund, Timothy G. Turkington, Gama I Akabani, Alexandra Badea, William C. Kurylo et al. "Utilizing MRI information to estimate F18-FDG distributions in rat flank tumors." In IEEE Symposium Conference Record Nuclear Science 2004., vol. 4, pp. 2488-2492. IEEE, 2004.

Spangler-Bickell M, Hurley S, Pirasteh A, Perlman S, Deller T, McMillan A. Evaluation of Data-Driven Rigid Motion Correction in Clinical Brain PET Imaging. J Nucl Med. 2022; DOI: 10.2967/jnumed.121.263309
Chassoux F, Rodrigo S, Semah F, Beuvon F, Landre E, Devaux B, Turak B, Mellerio C, Meder JF, Roux FX, Daumas-Duport C, Merlet P, Dulac 0, Chiron C. FDG-PET improves surgical outcome in negative MRI Taylor-type focal cortical dysplasias. Neurology. 201 0 Dec 14;75(24):2168-75. doi: 10.1212/WNL.Ob013e31820203a9. PMID: 21172840

Images/Tables

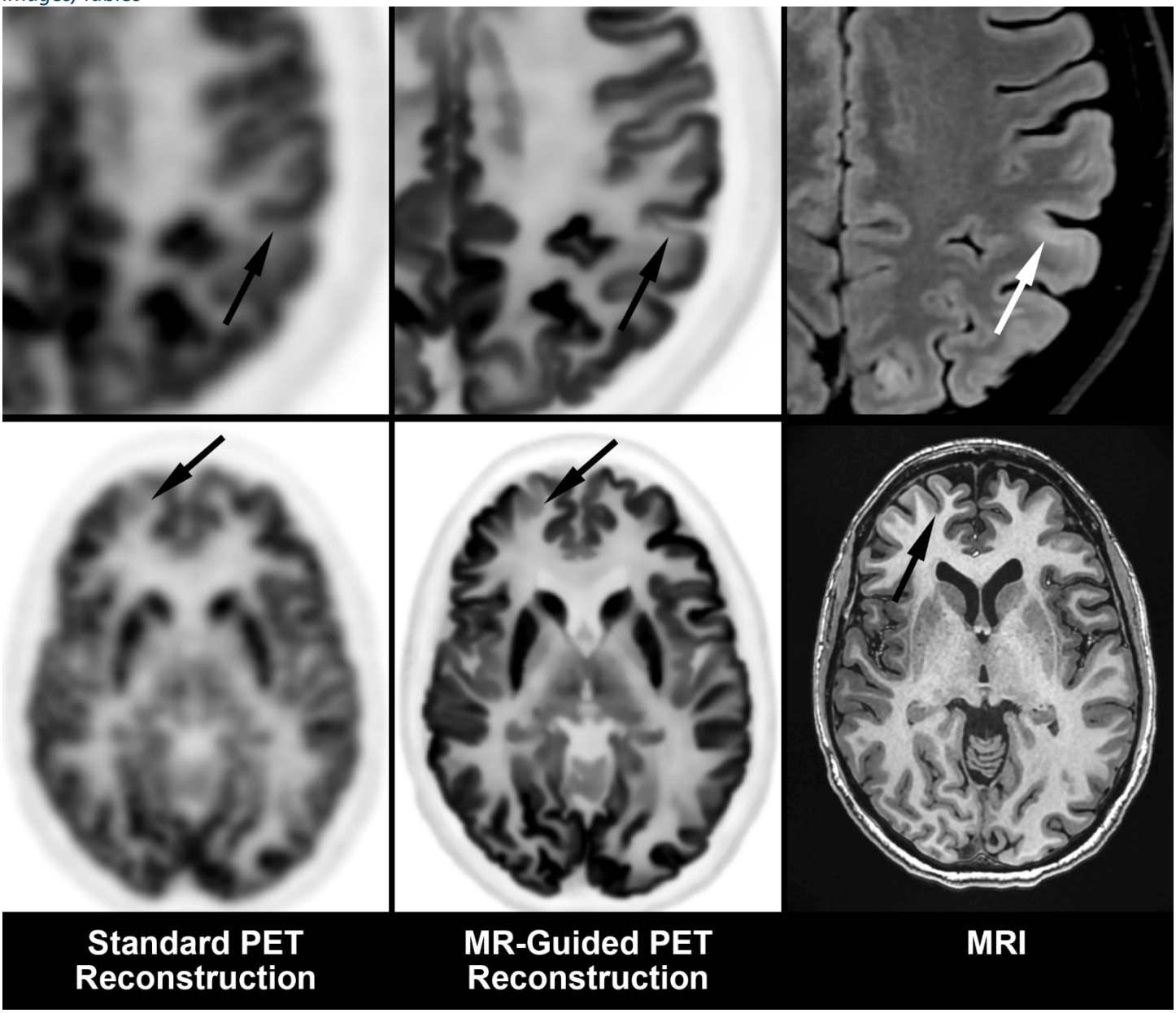

1006

Diffusion MRI of the spinal cord as a biomarker of ALS disease progression in individuals carrying *C9orf72*

Sara Naghizadehkashani, Spandana Tammiraju M.B.B.S., Zahra Sadeghi Adl, Laura Krisa PhD, Devon Middleton PhD, Piera Pasinelli PhD, Dana Johnson, Thomas Hulcher, Kiran Talekar MD, Hristelina Ilieva MD, PhD, Feroze Mohamed PhD, Jayakrishnan Nair PT, PhD
Thomas Jefferson University, Philadelphia, PA, USA

Abstract Category

Spine

Purpose

Amyotrophic lateral sclerosis (ALS) is the most common adult-onset progressive neurodegenerative disease. The absence of early markers of disease progression between cellular onset and clinically observable muscle weakness greatly compromises timely diagnosis and intervention. Among cases of familial ALS, the most prevalent mutation involves the pathogenic expansion of *C9orf72*. While cervical motor function is a good prognosticator of survival, the predictive role of neuroimaging in asymptomatic at-risk individuals remains of interest. This pilot study aims to evaluate diffusion tensor imaging (DTI) metrics in the cervical spinal cord as potential early prognostic biomarkers of latent progression of ALS in asymptomatic *C9orf72* carriers (C9+).

Materials & Methods

Clinical and DTI data were obtained from four *C9orf72* carriers and six age- and sex-matched, neurologically intact controls (mean age 41 years). Images of the cervical spinal cord (C1-C7) were acquired using a 3.0T Siemens Prisma MRI scanner system and a 24-channel spine array coil with anatomical sequences (T1 and T2) as well as a custom, inner field-of-view hybrid diffusion (iFOV-HYDI) MR sequence. Fractional anisotropy (FA) and mean, axial, and radial diffusivity (MD, AD, RD) of both gray and white matter in the cervical cord were quantified. DTI measurements were analyzed using a general linear model, with linear regression to assess the relationship between group status, spinal level, and diffusion metrics at two time points (at enrollment and after six months). Bonferroni adjustment was applied to correct for multiple comparisons.

Results

Subjects with C9+ demonstrated an overall significant decrease in RD of gray matter at the C3 level ($p = 0.017$) on follow-up scans with no accompanying change in clinical evaluation. There was also a minimal but statistically significant difference in RD of the white matter at the C2 level ($p = 0.023$), and in AD of the gray matter at the C4 level ($p = 0.024$) in this group. For all the examined diffusivity metrics (FA, MD, RD, AD), the magnitude of difference between the two time points varied across individual subjects, likely contributing to the minimal average differences observed. There was no significant change in FA or MD for either group between the two time points.

Conclusion

Our preliminary findings suggest a predictive role of spinal cord DTI as a non-invasive method for identifying and monitoring subclinical disease progression in *C9orf72* carriers at risk for ALS. Despite the small sample size and the data variability in this pilot study, significant changes were observed in DTI measures like RD and AD over a six-month period. However, larger studies and extended follow-up are needed to further validate these findings.

References

- Nakamura R, Atsuta N, Watanabe H, Hirakawa A, Ito M, Senda J *et al.* Neck weakness is a potent prognostic factor in sporadic amyotrophic lateral sclerosis patients. *J Neurol Neurosurg Psychiatry* 2013; 84(12)**:** 1365-71
- Bertrand A, Wen J, Rinaldi D, et al. Early Cognitive, Structural, and Microstructural Changes in Presymptomatic *C9orf72* Carriers Younger Than 40 Years. *JAMA Neurol.* 2018;75(2):236–245. doi:10.1001/jamaneurol.2017.4266
- Behler A, Müller HP, Ludolph AC, Kassubek J. Diffusion Tensor Imaging in Amyotrophic Lateral Sclerosis: Machine Learning for Biomarker Development. *Int J Mol Sci*. 2023;24(3):1911. Published 2023 Jan 18. doi:10.3390/ijms24031911
- Kamagata K, Andica C, Kato A, et al. Diffusion Magnetic Resonance Imaging-Based Biomarkers for Neurodegenerative Diseases. *Int J Mol Sci*. 2021;22(10):5216. Published 2021 May 14. doi:10.3390/ijms22105216

Images/Tables

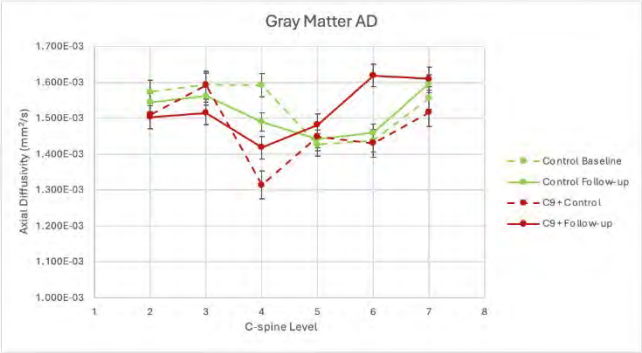

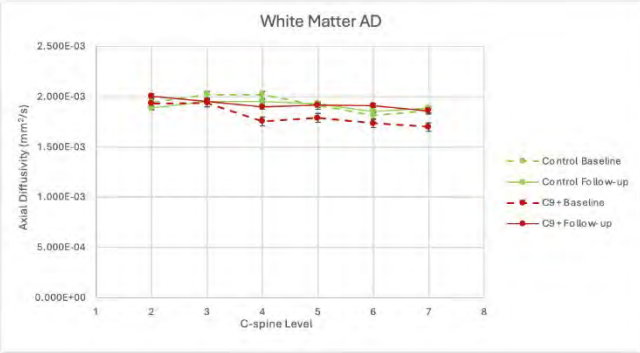

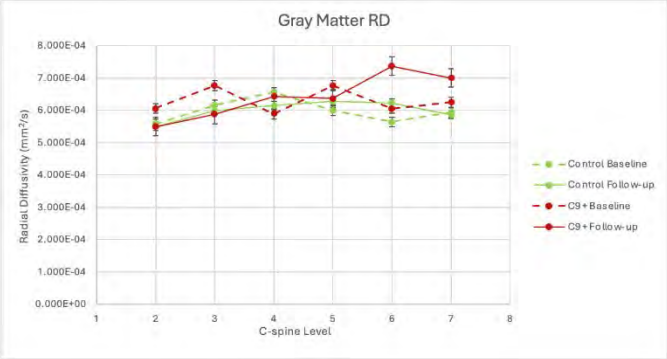

1009

Radiologists' Confidence in Diagnosing Parathyroid Adenomas: Impact of 4D-CT with Ultrasound

Soha Mohammadi MD[1], Mary Elizabeth Cunnane MD[1], Katherine L Reinshagen MD[1], Yuh-Shin Chang MD, PhD[1], Manuel Patino Galindo MD[1], Amy F. Juliano MD[1], Hillary R. Kelly MD[2]

[1]Department of Radiology, Massachusetts Eye and Ear, Harvard Medical School, Boston, MA, USA. [2]Department of Radiology, Massachusetts General Hospital, Massachusetts Eye and Ear, Harvard Medical School, Boston, MA, USA

Abstract Category

Head & Neck

Purpose

Four-dimensional CT (4D-CT) is often used as a stand-alone test for preoperative localization of parathyroid adenomas. In a concurrent study, we demonstrated that adding ultrasound (US) to 4D-CT does not significantly change the accuracy of parathyroid adenoma identification. However, radiologists make diagnoses with varying levels of confidence, and the radiologist's level of confidence may influence the likelihood of surgical intervention as well as the choice of minimally invasive parathyroidectomy versus four-gland exploration. We aimed to evaluate the effect of adding US to 4D-CT on radiologists' confidence in diagnosing parathyroid adenomas.

Materials & Methods

Four Neuroradiologists independently retrospectively reviewed 20 cases each, with 10 cases assessed using 4D-CT alone and 10 assessed using 4D-CT combined with US. For each case, radiologists assigned a confidence score on a 5-point Likert scale: a score of 5 indicated "Consistent with" parathyroid adenoma (the lesion is certainly parathyroid), 4 was "Highly suggestive of" (likely parathyroid adenoma, one feature may be atypical), 3 was "Probable" (more likely than not to be parathyroid adenoma), 2 was "Possible" (equal chance of being parathyroid or another structure), and 1 was "Unlikely" (most features suggest the lesion is not parathyroid). A total of 49 histologically confirmed lesions were included as the reference standard for accuracy. Receiver operating characteristic (ROC) curve analysis identified an optimal confidence cutoff for accurate lesion identification, and confidence scores for correctly identified lesions (True Positives) were compared between groups using the Mann-Whitney U test. Additionally, within the 4D-CT + US group, a Wilcoxon matched-pairs signed-rank test was used to assess changes in confidence for each radiologist by comparing confidence scores assigned after viewing 4D-CT alone and another after subsequently viewing US for the same cases.

Results

The ROC curve analysis suggested an optimal diagnostic cutoff at a Likert score of 3, balancing sensitivity and accuracy for identifying candidate lesions. The 4D-CT and 4D-CT+US groups showed high confidence in diagnosing true positive lesions, with a median Likert score of 5. Although the difference in confidence scores between groups was not statistically significant (p-value = 0.0706), the Wilcoxon matched-pairs signed-rank test in the 4D-CT + US group indicated a significant increase in confidence with US (p-value = 0.003). Overall confidence scores improved with US, suggesting that radiologists may feel more confident about their diagnoses when US is employed with 4D-CT. The discrepancy between the non-significant group comparison and the significant paired analysis may be attributed to the sensitivity of the statistical tests. The group comparison could have been impacted by variability among radiologists and a ceiling effect, as baseline confidence levels were high. In contrast, the paired analysis clearly highlighted individual improvements in confidence when US was added.

Conclusion

Adding US to 4D-CT increased radiologists' confidence in diagnosing parathyroid adenomas. Furthermore, a Likert score cutoff of 3 provided the optimal balance of sensitivity and accuracy in lesion identification. Although the overall confidence increase across groups was not statistically significant, individual radiologists consistently reported higher confidence after US was incorporated.

References

1. Bunch PM, Randolph GW, Brooks JA, et al. Parathyroid 4D CT: What the Surgeon Wants to Know. Radiographics 2020;40(5):1383-94. DOI: https://doi.org/10.1148/rg.2020190190

Images/Tables

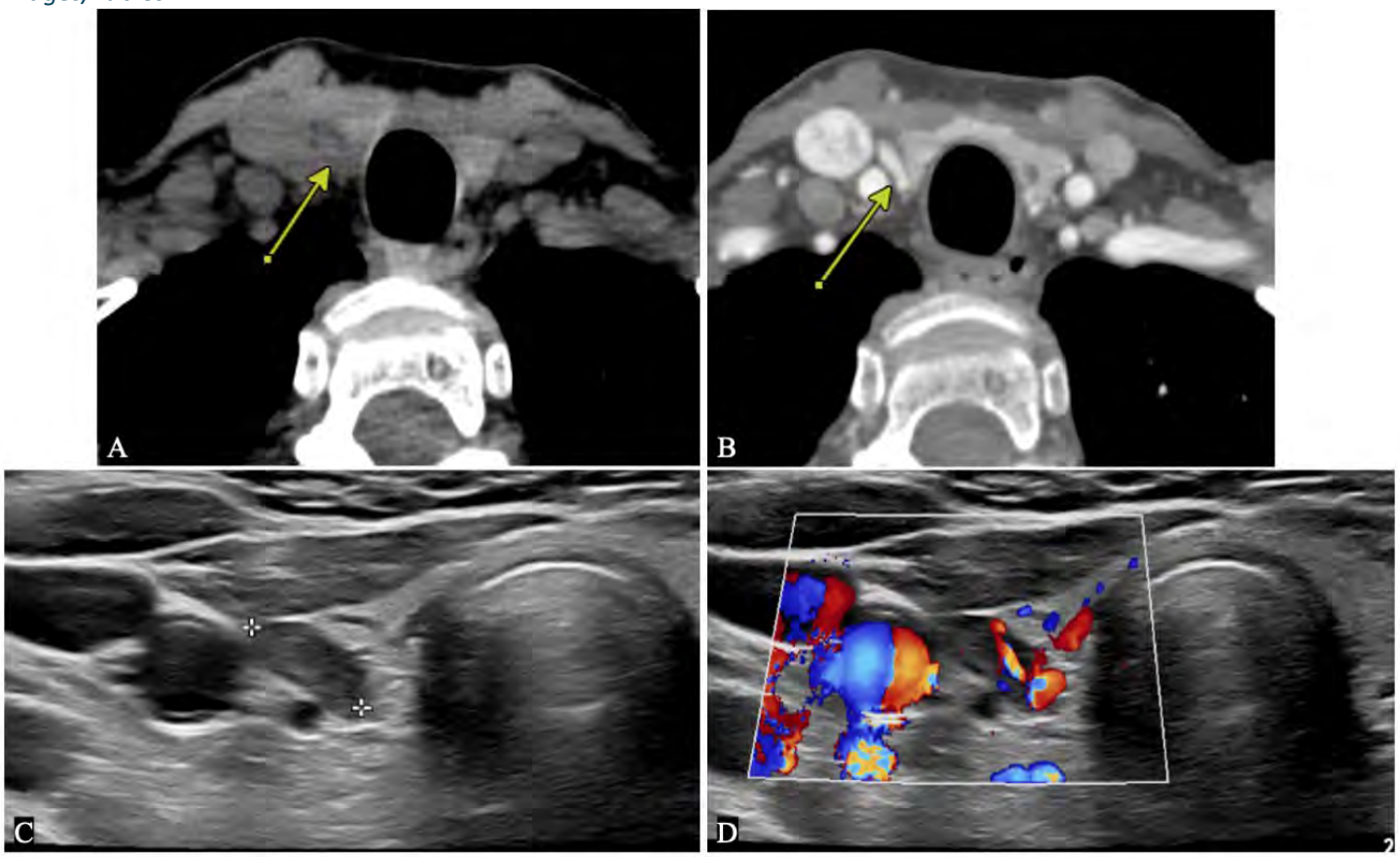

In this patient with a history of hyperparathyroidism, 4D-CT imaging demonstrates a small lesion along the right lower pole of the thyroid gland. This lesion is challenging to detect on pre-contrast images due to the reduced intrinsic density of the thyroid tissue (A). However, on arterial phase image, the lesion exhibits hyperattenuation relative to the thyroid (B). The ultrasound examination further characterizes the lesion. In the transverse view, without and with color Doppler, the lesion is well-defined and shows excellent conspicuity and significant color Doppler flow (C and D).

1012

Trans-foraminal Fibrin Glue Injection Utilizing a Curved Needle System for Treatment of Ventral Spinal CSF Leaks

Yi Xiang Zhan DO, Prateek Chintalapati MD, Horia Marin MD, Arafat Y Ali DO
Henry Ford Hospital, Detroit, MI, USA

Abstract Category

Interventional

Purpose

The diagnosis and management of spontaneous intracranial hypotension (SIH) and spinal CSF leaks has rapidly evolved with diagnosis now guided by advanced myelographic techniques and minimally invasive treatment options including transvenous embolization and CT-guided fibrin glue injection. Ventral dural leaks are particularly challenging to treat by percutaneous methods due to technically challenging needle trajectories necessary to administer patch material into the ventral epidural space. Alternative surgical repair options can be similarly challenging. We introduce a novel technique for percutaneous ventral epidural access by utilizing a curved needle system (Pakter, Cook) in treatment of ventral epidural CSF leak.

Materials & Methods

We describe two cases of ventral CSF leaks secondary to dural tears which we successfully treated with fibrin glue occlusion utilizing a curved needle system for transforaminal access.

Procedure technique:

Dynamic digital subtraction fluoroscopy and/or CT myelography is performed for diagnosis and localization of the presumed dural defect. Upon localization of a ventral tear, ventral epidural space can be accessed using a curved needle in a coaxial system. A 21 G introducer needle is advanced to the anterior inferior margin of the neural foramen using intermittent CT fluoroscopy. A 25 G curved needle is advanced through the introducer in a coaxial fashion. When positioned properly, the curved margin of the posterior wall of the vertebral body guides the 25G inner curved needle to the ventral most epidural space. Proper positioning is confirmed via epidurogram with small volume air or contrast. Subsequently, fibrin glue is slowly injected, effectively occluding the dural defect.

Results

Patient 1 is a 68-year-old female who presented to the emergency room with a 3-day severe headache without preceding trauma or anticoagulation use, exacerbated by coughing. Imaging demonstrates bilateral subacute subdural hematomas with findings suggestive of SIH. Empiric epidural blood patch was initially performed without significant improvement. CT myelogram demonstrated a longitudinally extensive epidural collection with a dural tear at T5-T6. CT guided fibrin glue injection via trans-foraminal approach with a curved needle was performed. On clinical follow-up, the patient endorses resolution of symptoms. Follow-up CT head demonstrates near complete resolution of subdural collections.

Patient 2 is a 62-year-old male with worsening postural headaches due to CSF leak with a large epidural collection and MRI brain findings of superficial siderosis. CT myelogram was performed demonstrating ventral dural tear at C7-T1 secondary to a disc osteophyte complex. Subsequent fibrin glue injection was performed via a transforaminal approach using a curved needle. Patient endorsed resolution of symptoms following the procedure.

Conclusion

Targeted CT guided ventral epidural fibrin glue injection using transforaminal approach with a coaxial curved needle system is an effective method for treatment of CSF leak due to ventral dural tear.

References

1. Mamlouk MD, Callen AL, Madhavan AA, et al. Spinal CSF leaks: The Neuroradiologist transforming care. AJNR Am J Neuroradiol November 2024;45(11):1613-1620. DOI: https://doi.org/10.3174/ajnr.a8484
2. Mamlouk MD, Shen PY, Sedrak MF, et al. CT-guided fibrin glue occlusion of cerebrospinal Fluid–Venous fistulas. Radiology 2021;299(2):409–418. DOI: https://doi.org/10.1148/radiol.2021204231

Images/Tables

A = Axial T2WI showing ventral extradural collection, B = axial CT myelogram showing extradural air confirming needle position, C = curved needle in place with fibrin injection, access would be challenging with a straight needle.

1014

Incidental T1 Hypointense Spinal Bone Lesions: A Large Institutional Analysis of Management Practices and Validation of SSR Guidelines.

Aoife M Haughey MB BCH BAO MRCPI FFR[1], Paddy Nicholson[2]
[1]JDMI University Hospital Network, Toronto, Ontario, Canada. [2]RCSI, Beaumont Hospital, Dublin, Dublin, Ireland

Abstract Category

Spine

Purpose

Incidental T1 hypointense bone lesions are frequently encountered findings on spinal MRI1. Determining appropriate follow-up for these lesions is crucial for both patient care and resource management. The 2022 Society of Skeletal Radiology (SSR) guidelines2 offer a framework for managing incidental bone lesions, but their real-world application and impact on spinal lesion management, specifically, warrant further investigation.

This study builds upon existing literature by providing a comprehensive analysis of incidental T1 hypointense spinal lesions at a large tertiary referral centre over a decade of practice. We evaluate current practice patterns, retrospectively assess adherence to the SSR guidelines, identify clinical and demographic factors associated with follow-up recommendations, and quantify the potential cost savings associated with guideline-based management. Our objectives are to: (1) determine the long-term outcomes of these lesions in patients without a known history of active malignancy; (2) evaluate the concordance between follow-up practices and SSR recommendations; (3) explore the influence of patient and lesion characteristics on management decisions; and (4) assess the potential economic impact of optimised, guideline-driven follow-up strategies.

Materials & Methods

This retrospective cohort study was approved by our institutional Research Ethics Board with waiver of informed consent due to the retrospective nature of the analysis. The study analysed MRI examinations performed between May 2013 and May 2023. We identified 276 MRI spine reports fulfilling our inclusion criteria, in which an indeterminate and incidental T1 hypointense bone lesion was identified and follow up imaging recommended.

Results

MRI of the spine was performed in 256,989 patients during the 10-year period. Reports of 6,709 of these patients contained the term “T1 hypointense”. Following review of the reports of all 6,709 patients, 276 patients had varying numbers of follow-up studies and follow-up with varying modalities, without tissue sampling or histopathological diagnosis. The lesions ranged in size from 3 mm – 28 mm, median size 12 mm. 186 were classified as Bone RADS 1, where no follow-up is recommended, while 23 were classified as Bone RADS 2/3, for which follow-up or further imaging is advised. In practice, all 186 Bone RADS 1 lesions (100%) received follow-up imaging despite the SSR recommendation to leave these lesions alone. Conversely, the majority of Bone RADS 2/3 lesions were managed in alignment with the guidelines, receiving appropriate follow-up.

Conclusion

Based on our results, we recommend a conservative, evidence-based approach to the management of incidental T1 hypointense spinal lesions. For lesions classified as Bone RADS 1, routine follow-up imaging should be avoided unless clinical changes arise, while Bone RADS 2/3 lesions may benefit from further imaging to monitor for potential changes. Adopting these recommendations in routine practice could reduce variability in follow-up decisions, promote consistency across experience levels, and support more efficient resource allocation.

References

1. Miller BJ. Use of imaging prior to referral to a musculoskeletal oncologist. J Am Acad Orthop Surg 2019;27:e1001–e1008.

2. Chang CY, Garner HW, Ahlawat S, et al. Society of Skeletal Radiology–white paper. Guidelines for the diagnostic management of incidental solitary bone lesions on CT and MRI in adults: bone reporting and data system (Bone-RADS). Skeletal Radiol 2022;51:1743–1764.

Images/Tables

1015

Belzutifan Decreases Contrast-enhancing Volume and Cerebral Blood Flow of Von Hippel-Lindau-Associated Hemangioblastoma

Amit RL Persad[1], Banu Yagmurlu[2], David Park[2], Aroosa Zamarud[2], Yuhao Huang[2], Eva Liu[3], Yusuke Hori[2], Steven D Chang[2], Michael Iv[2]

[1]Western University, London, ON, Canada. [2]Stanford University, Palo Alto, CA, USA. [3]University of Saskatchewan, Saskatoon, SK, Canada

Abstract Category

Adult Brain

Purpose

Hemangioblastoma is a vascular tumor that is frequently associated with von Hippel-Lindau (vHL) disease. Mutations in vHL lead to dysregulation of the hypoxia inducible factor 2 alpha (HIF-2a) pathway. Belzutifan is a novel drug that targets HIF-2a and has shown efficacy in hemangioblastoma treatment. The mechanism of action of this drug is not well understood. No prior studies of hemangioblastoma treatment with Belzutifan have investigated tumor blood flow using MRI perfusion.

Materials & Methods

This was a retrospective analysis of a cohort of patients treated for CNS hemangioblastoma using Belzutifan. All patients had MRI with arterial spin labeling perfusion imaging for quantification of cerebral blood flow (CBF) at three time points: pre-treatment baseline and post-treatment midpoint (5 months) and final (greater than a year) follow-up. At each time point, tumor size, volume, and absolute and normalized CBF values were obtained.

Results

A total of 7 patients (median age 40 years, 3 female) with 31 tumors were identified. The median time duration on Belzutifan was 16 months. A total of 28 lesions had partial response, and 3 had stable disease based on RECIST 1.0. Statistically significant decreases were seen in tumor volume, tumor diameter, , and absolute and normalized CBF_{mean} and CBF_{max} (all $p<0.001$) and cyst volume ($p=0.016$) on final follow-up. Baseline CBF was predictive of tumor response to treatment (AUC=0.905) moreso than tumor volume (AUC=0.214).

Conclusion

Belzutifan decreases tumor volume and CBF in CNS hemangioblastomas. There is a significant association between these decreases, implying that the regression in hemangioblastoma might be associated with a decrease in tumor blood supply.

References

1. Klingler JH, Gläsker S, Bausch B, Urbach H, Krauss T, Jilg CA, Steiert C, Puzik A, Neumann-Haefelin E, Kotsis F, Agostini H, Neumann HPH, Beck J. Hemangioblastoma and von Hippel-Lindau disease: genetic background, spectrum of disease, and neurosurgical treatment. Childs Nerv Syst. 2020 Oct;36(10):2537-2552.
2. Zamarud A, Marianayagam NJ, Park DJ, Yener U, Yoo KH, Meola A, Chang SD. The outcome of central nervous system hemangioblastomas in Von Hippel-Lindau (VHL) disease treated with belzutifan: a single-institution retrospective experience. J Neurooncol. 2023 Nov;165(2):373-379.
3. Neska-Matuszewska M, Zimny A, Bladowska J, Czarnecka A, Sąsiadek M. The role of diffusion and perfusion magnetic resonance imaging in differentiation of haemangioblastomas and pilocytic astrocytomas. Pol J Radiol. 2018 May 10;83:e197-e203.

Images/Tables

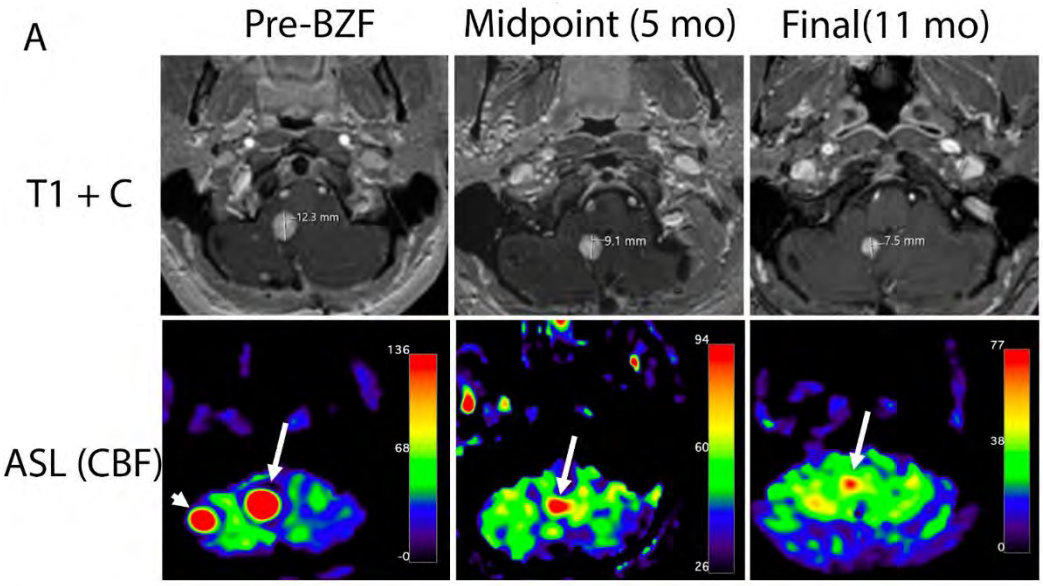

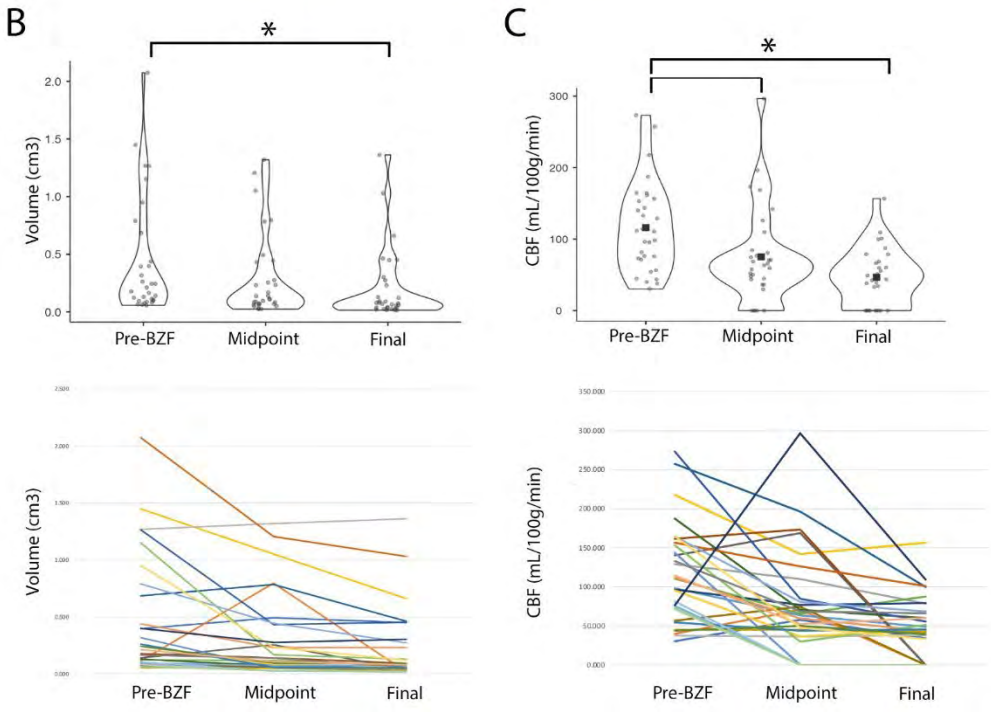

1025

Machine Learning-Derived Carotid Vascular Risk is Associated with Stroke, Retinal Microvascular Density, and MRI-Extracted Brain Atrophy in UK Biobank Participants

Saman Doroodgar Jorshery MD, MPH[1], Saurabh Rohatgi MD[1], Seyedeh Maryam Zekavat MD, PhD[2], Vineet Raghu PhD[1], Pradeep Natarajan MD[1], Michael T. Lu MD, MPH[1], Javier Romero MD[1]
[1]MGH, Boston, MA, USA. [2]MEEI, Boston, MA, USA

Abstract Category

AI/Informatics

Purpose

Current research lacks large-scale human studies using non-invasive clinical imaging to simultaneously study the macrovasculature and microvasculature. Machine learning applied to carotid ultrasound images and retinal fundus photos can offer valuable insights into both macro- and microvascular health.

Materials & Methods

We investigated the relationship between the macro- and micro- vasculature using imaging data from the UK Biobank, a prospective study of adult volunteers aged 40-69 years. We estimated carotid macrovascular risk by leveraging deep learning using DenseNet121 architecture across right side longitudinal carotid ultrasound images from 64,574 individuals. 80% of the dataset was divided for model training to predict carotid vascular age which is an estimate of biological age defined as an individual's chronologic age at the time of the ultrasound, adjusted for the presence of cardiovascular risk factors, comorbidities, and observed all-cause mortality and major cardiovascular events during follow-up. First, in the testing dataset we assessed the association of standardized Carotid-Risk with observed incident stroke over median 3.8 years of follow-up stroke (based on International Classification of Disease codes). Second, we associated standardized Carotid-Risk with retinal vascular density (calculated using machine learning-derived vascular segmentations of retinal fundus photos) across individuals with both imaging modalities available. Third, we evaluated the association of carotid-risk with brain volume of cortical grey matter (derived from T1 structural brain MRI via FreeSurfer software and normalized for head size). Analyses were performed using linear regression models adjusted for age, sex, smoking, hypertension, type 2 diabetes mellitus, and principal components of genetic ancestry.

Results

11,832 participants from testing set had carotid imaging, of which 7,559 also had brain MRI, and 6,500 had retinal imaging. The overall dataset had mean age of 65.5 (SD: 7.7), 48.2% male, 62.4% never smokers, mean BMI of 26.6 (SD: 4.5). After adjusting for the aforementioned covariates, each standard deviation increase in Carotid-Risk was significantly associated with incident stroke (aHR: 1.37 (CI: 1.03 to 1.82), P=0.03, N=11,832). Across individuals with retinal imaging, there was a significant association between right carotid risk and right retinal vascular density, with each standard deviation increase in carotid risk being associated with reduced retinal vascular density (Beta -0.1 SD, P=0.02), independent of the specified risk factors. Carotid-Risk was significantly associated with cortical grey matter volume (-0.05 SD decrease in grey matter per SD increase in Carotid-Risk, 95% CI [-0.02 to -0.07], P< 0.001, N=7,559). There was no significant association between Carotid-Risk and white matter volume (P=0.27).

Conclusion

Accelerated carotid biological aging is associated with increased risk of future stroke, lower retinal vascular density, and cortical grey matter atrophy, independent of other cardiometabolic risk factors. Poor macrovascular flow may contribute to ischemia and subsequent microvascular pruning downstream, with resulting loss of cortical grey matter volume over time. Our study highlights the potential of machine learning applied to population-based imaging for understanding the interplay between macro- and micro- vasculature with stroke and anatomical changes in the brain.

References

1- Zekavat SM, Raghu VK, Trinder M, Ye Y, Koyama S, Honigberg MC, Yu Z, Pampana A, Urbut S, Haidermota S, O'Regan DP, Zhao H, Ellinor PT, Segrè AV, Elze T, Wiggs JL, Martone J, Adelman RA, Zebardast N, Del Priore L, Wang JC, Natarajan P. Deep Learning of the Retina Enables Phenome- and Genome-Wide Analyses of the Microvasculature. Circulation. 2022 Jan 11;145(2):134-150. doi: 10.1161/CIRCULATIONAHA.121.057709. Epub 2021 Nov 8. PMID: 34743558; PMCID: PMC8746912.

2- Weiss J, Raghu VK, Bontempi D, Christiani DC, Mak RH, Lu MT, Aerts HJWL. Deep learning to estimate lung disease mortality from chest radiographs. Nat Commun. 2023 May 16;14(1):2797. doi: 10.1038/s41467-023-37758-5. PMID: 37193717; PMCID: PMC10188525.

Images/Tables

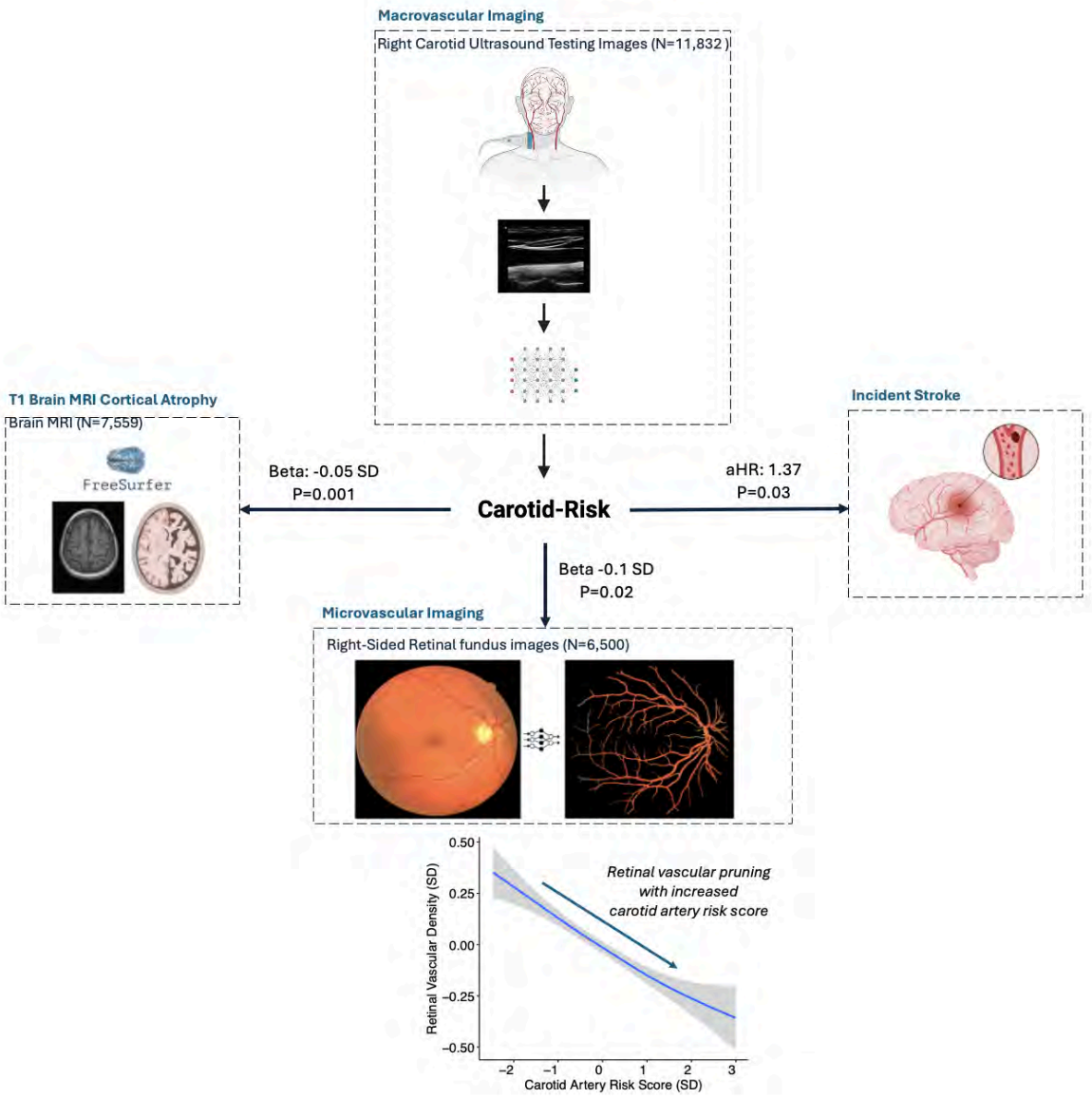

1037

Representation of International Medical Graduates among Diagnostic Radiology Chairs, Neuroradiology Chiefs, and Program Directors

Fatemeh Dehghani Firouzabadi[1], Mina Hesami[2], Ali Sheikhy[3], Mahla Radmard[4], Mona Dabiri[4], Sara Ramezanpour[5], David M. Yousem[4]

[1]San Francisco, California, USA. [2]New Haven, Connecticut, USA. [3]National Institutes of Health, Bethesda, Maryland, USA. [4]Russell H. Morgan Department of Radiology and Radiological Science, Johns Hopkins Medical Institution, Baltimore, Maryland, USA. [5]South Miami, Florida, USA

Abstract Category

Socioeconomics & Health Policy

Purpose

The number of international medical graduates (IMGs) entering radiology residencies and neuroradiology fellowships averaged 9.7% and 20.9% from 2021-2023 respectively. We aimed to determine whether IMG graduates are populating leadership roles at a proportionate rate in diagnostic radiology (DR) and neuroradiology (NR).

Materials & Methods

We surveyed 191 DR program directors (PDs), 94 NR PDs, 192 chairs of DR and 91 directors of NR inquiring about their original citizenship and medical school [American Medical Graduates (AMG) vs IMG]. We reviewed institutional web sites to obtain missing data and recorded H indices for each person using Scopus.

Results

We confirmed the original citizenship and medical school location in 61 75% and 93-98% of each leadership group. We found that 19/119 (16.2%) DR PDs, 31/71 (43.7%) NR PDs, 33/116 (28.5%) DR Chairs and 28/69 (40.6%) NR Chiefs were not originally US citizens. The IMG rate was 18/188 (9.6%), 20/90 (22.2%), 26/186 (14.0%), and 19/85 (22.4%) for DR PDs, NR PDs, Chairs and NR Chiefs respectively. The most common country of origin and medical school cited was India for all leadership groups. IMGs had a median H index of 14 while AMGs 10, significantly different (p=0.021)

Conclusion

Compared to the rate of DR/NR trainees entering from 2021-2023, IMGs are proportionately represented at the NR PD), NR chief, DR Chairs, and DR PDs positions. The H index of the IMGs was higher than AMGs. We conclude that IMGs have made substantial and proportionate inroads in radiology and neuroradiology leadership. The proportional presence of IMGs in critical leadership roles within DR and NR, alongside their notably higher academic productivity, signifies a promising trend towards a more inclusive and dynamic leadership paradigm. This advancement not only enriches the diversity of perspectives but also enhances a culture of excellence and innovation within these pivotal medical specialties.

References

Ritika Manik, Gelareh Sadigh, Diversity and inclusion in radiology: a necessity for improving the field, *British Journal of Radiology*, Volume 94, Issue 1126, 1 October 2021, 20210407, https://doi.org/10.1259/bjr.20210407

Images/Tables

TABLE 1. Data Regarding Citizenship and Medical School Site

Numbers/ (%)	Citizenship	First Citizenship	Medical School Location
DR PD (191)	Available data (115)	Available data (117)	Available data (188)
US	114 (99.1%)	98 (83.8%)	170 (90.4%)
Non-US	1 (0.9%)	19 (16.2%)	18 (9.6%)
NR PD (94)	Available data (68)	Available data (71)	Available data (90)
US	61 (89.7%)	40 (56.3%)	70 (77.8%)
Non-US	7 (10.3%)	31 (43.7%)	20 (22.2%)
Chair of DR (192)	Available data (121)	Available data (116)	Available data (186)
US	120 (99.2%)	83 (71.5%)	160 (86.0%)
Non-US	1 (0.8%)	33 (28.5%)	26 (14.0%)
NR Chief (91)	Available data (67)	Available data (69)	Available data (85)
US	63 (94.0%)	41 (59.4%)	66 (77.6%)
Non-US	4 (6.0%)	28 (40.6%)	19 (22.4%)
TOTAL (568)*	371 (65.3%)	373 (65.7%)	549 (96.6%)

There were 46 people who had multiple roles in their departments, including six IMGs and 40 AMGs

TABLE 2. Median H indices of AMGs and IMGs

H index differences		
AMGs	10 [7,12]	p-value = 0.021
IMGs	14 [11,20]	

TABLE 3. Median H Index Differences Between IMG and AMG for Each Leadership Group Separately

H Index	AMG	IMG	p-value
DR PD	5 [4,7]	7 [5,16]	0.387
NR PD	8 [7,12]	11.5 [8,14]	0.160
DR Chair	15 [12,20]	19 [16,50]	0.243
NR Chief	20 [16,28]	21 [20,29]	0.818

1070

Evaluating PSR and rCBV as Markers of Radiation Necrosis: Impact of Gadolinium Preload vs. No Preload Contrast.

Edgar Zamora MD, Scott Faro MD, Ajit Karambelkar MD, Joga R Chaganti PhD
Thomas Jefferson Hospital, Philadelphia, PA, USA

Abstract Category

Adult Brain

Purpose

Gadolinium preload has become a standard practice in dynamic susceptibility contrast enhanced perfusion imaging, offering a streamlined technique to measure neoangiogenesis and blood volume in the postoperative environment. However, this approach has also highlighted issues related to the measurement of capillary permeability, which may be more sensitive in detecting local recurrence.

We retrospectively analyzed the impact of gadolinium preload on percentage of signal recovery (PSR) and correlated PSR with relative cerebral blood volume (rCBV) to evaluate its influence on the sensitivity and specificity of PSR in identifying tumor recurrence compared to rCBV.

Materials & Methods

Thiry subjects, confirmed as having radiation necrosis either through biopsy or serial follow-up studies, were included in this retrospective analysis. Each patient underwent a minimum of three MRI studies, spaced at intervals of three months or more. DSC perfusion imaging was performed according to ASFNR guidelines, using a flip angle of 80°, with gadolinium preload administered as per protocol. Out of these 10 subjects underwent perfusion imaging without gadolinium preload.

MR perfusion data was analyzed using Olea software, which incorporated standard image processing steps, including motion correction, co-registration, spatial smoothing, calculation of pre- and post-bolus baseline intensities, signal-to-concentration conversion, leakage correction, and CBV estimation.

Targeted ROIs were independently placed by two senior neuroradiologists using baseline data. PSR and rCBV values were measured as previously described.

Results

The study included 24 male and 6 female subjects, with a mean age of 45 years. In the preload group, tumor locations included parietal (7), frontal (6), temporal (4), and basal ganglionic regions (3). In the no-preload group, tumors were located in the frontoparietal and temporal regions. The mean rCBV was 2.1 ml/100 g, and the mean PSR was 70% in 12 out of 20 subjects of preload group. In 8 subjects, the mean rCBV of 2.4 ml/100 g and the mean PSR was 60 %. In no preload group of 8 subjects, the mean rCBV of 2.4 ml/100 g and mean of PSR of 90% to 92%.

Conclusion

PSR is a highly sensitive marker for radiation necrosis when no gadolinium preload is used. In the group with gadolinium preload, PSR sensitivity decreases, necessitating the application of correction measures to address this limitation.

References

Malik DG, Rath TJ, Urcuyo Acevedo JC, Canoll PD, Swanson KR, Boxerman JL, Quarles CC, Schmainda KM, Burns TC, Hu LS. Advanced MRI Protocols to Discriminate Glioma From Treatment Effects: State of the Art and Future Directions. Front Radiol. 2022 Apr 15;2:809373. doi: 10.3389/fradi.2022.809373. PMID: 37492687; PMCID: PMC10365126

1075

Spinal Vascular Malformation in Hereditary Hemorrhagic Telangiectasia

Mahi Shah, Vedmanvitha Ketireddy, Doris D.M. Lin MD, PhD
Johns Hopkins University, Baltimore, MD, USA

Abstract Category

Spine

Purpose

Perimedullary arteriovenous fistula (AVF) is the most common spinal vascular malformation (VM) in patients with Hereditary Hemorrhagic Telangiectasia (HHT), but the occurrence is rare (<1%) and screening spinal MRI is not part of recommended guidelines[1]. Screening MRI in both children and adults (particularly pregnant women) is hence not consistently performed in the general practice among different academic centers. The aim of this study was to examine

the frequency and characteristics of spinal VM in HHT patients evaluated with spinal MRI and/or spinal MRA, stratified by age, clinical indication and presenting symptoms.

Materials & Methods

Patients with HHT presenting with spine MR evaluation between Jul 2002 and Feb 2024 at Johns Hopkins Hospital were searched from the Radiology database. Clinical diagnosis, indication for exam and findings of spinal VM were analyzed by classification into 3 age groups: A) 1-21 years, B) 22-45 years and C) >45 years.

Results

179 MR records of 98 patients were obtained from initial data search, yielding a total of 73 patients (age range 1-96 years) after excluding those without the diagnosis of HHT (based on Curaçao criteria[2] and/or genetic testing). In group A (n=18), 2/18 (7 and 2 years of age, both male) were found to have spinal AVF and both presented symptoms (Figure 1); none of the other 16 asymptomatic patients had spinal vascular abnormalities (P=0.0065, Fisher exact test). In group B (n=22), 15/22 were referred during pregnancy or planning pregnancy, 5/22 as part of HHT screening, 2/22 for back pain; none was found to have spinal vascular abnormalities. Finally in group C (age 46-96 years, n=33), the majority (22/33, 67%) were examined because of back or neck pain, sciatica, paresthesia, radiculopathy including 3 following trauma, no VM was found except in one. In a single asymptomatic female because of a small calcified spinal mass seen on screening chest CTA, further work-up including a subsequent catheter angiography demonstrated a small epidural AVF.

Conclusion

This single center experience confirms the low frequency of spinal VM in HHT, predominantly occurring in young children presenting with symptoms. In the absence of symptoms, screening MRI frequently performed for adult women during or in anticipation of pregnancy has a low yield, supporting the current guideline that routine screening is not indicated.

References

1. Faughnan ME, Palda VA, Garcia-Tsao G, et al. International guidelines for the diagnosis and management of hereditary haemorrhagic telangiectasia. J Med Genet 2011; 48: 73–87.
2. Shovlin C.L. et al., Diagnostic criteria for hereditary hemorrhagic telangiectasia (Rendu-Osler-Weber syndrome) Am. J. Med. Genet. 91:66-67, 2000

Images/Tables

Figure 1. 7-year-old boy with constipation and intermittent severe pain. Sagittal T2-weighted MRI shows a perimedullary AVF with a venous varix resulting in mass effect, scalloping and compression of the thoracic spinal cord.

1098

Assessment of Intracranial Atherosclerotic Plaque Evolution, Utilizing Vessel Wall Imaging-Based Radiomics and Personalized CFD from Multiple Time Points

Nandor K Pinter MD, Sricharan Veeturi PhD, Benjamin Morrish MD, Nicholas Mecca, Tatsat R Patel PhD, Jason Davies MD PhD, Kenneth Snyder MD PhD, Elad levy MD PhD, Adnan Siddiqui MD PhD, Vincent Tutino PhD

University at Buffalo, Buffalo, NY, USA

Abstract Category

Functional/Advanced Imaging

Purpose

Intracranial atherosclerotic disease (ICAD) is a common cause of primary and secondary stroke. Understanding plaque evolution can help in risk stratification and in selecting proper therapies. We explored how radiomics and hemodynamic features correlate with plaque progression over time.

Materials & Methods

Patients with ICAD and history of cerebral ischemia were included. Time-of-flight MRA, high-resolution vessel wall imaging (proton density-weighted, PD, and contrast-enhanced T1-weighted, T1CE) and phase-contrast MR-based volumetric flow (NOVA) were collected at multiple time points. MRA was used to segment lumen and perform Computational Fluid Dynamics (CFD). Flow rates from NOVA were used as boundary conditions in CFD. Plaques were segmented manually on PD images from each time point. The PD and T1CE scans were co-registered. Radiomics features (RFs) were extracted from the first time point from both image types. Plaques were compared between consecutive time points and classified as progressing, stable or regressing, based on volume change. Plaques smaller than 4 mm^3 were excluded. Demographics, clinical history of stroke and recurrent stroke, risk factors and medication history were registered. Univariate analysis was done to determine which features were different between the three groups of plaques. We also built logistic regression models to identify growing plaques with radiomics only and radiomics and hemodynamics combined.

Results

78 plaques from 26 patients were analyzed (mean age=70.9±9.3, F=11). Plaque distribution was as follows: 39 regression (decreased in volume), 18 stable, 21 progression (increased in volume). Mean follow-up time of MRI was 11.8 months. Mean plaque size at baseline was 24.23mm^3. Average growth in the progression group was 30.87mm^3. Patient demographics or clinical data points were not significantly different between the groups, but dual antiplatelet therapy was more frequent in the regression group. 49 RFs were significantly different ($p<0.05$) between the progressing and other plaques (6 shape-based, 28 based on PD signal intensity and 15 based on CET1). CFD showed no significant difference in hemodynamics; however, wall shear stress (WSS) was lower and WSS divergence was higher adjacent to regressing plaques. Multivariate models showed an AUC of 0.77 (Radiomics only) and 0.81 (Radiomics and hemodynamics combined)

Conclusion

We found significant differences in radiomic features between progressing, stable and regressing plaques, suggesting that vessel wall imaging-based radiomics analysis might help to better understand plaque evolution. We found trends in hemodynamic quantities, however more detailed analysis and larger sample size is required to find meaningful correlations.

References

Chung JW, Cha J, Lee MJ, et al. Intensive Statin Treatment in Acute Ischaemic Stroke Patients with Intracranial Atherosclerosis: a High-Resolution Magnetic Resonance Imaging study (STAMINA-MRI Study). J Neurol Neurosurg Psychiatry. 2020 Feb;91(2):204-211. doi: 10.1136/jnnp-2019-320893.

Lin X, Guo W, She D, et al. Follow-up assessment of atherosclerotic plaques in acute ischemic stroke patients using high-resolution vessel wall MR imaging. Neuroradiology. 2022 Dec;64(12):2257-2266. doi: 10.1007/s00234-022-03002-y.

Sun B, Wang L, Li X, et al. Intracranial Atherosclerotic Plaque Characteristics and Burden Associated With Recurrent Acute Stroke: A 3D Quantitative Vessel Wall MRI Study. Front Aging Neurosci. 2021 Jul 28;13:706544. doi: 10.3389/fnagi.2021.706544.

Images/Tables

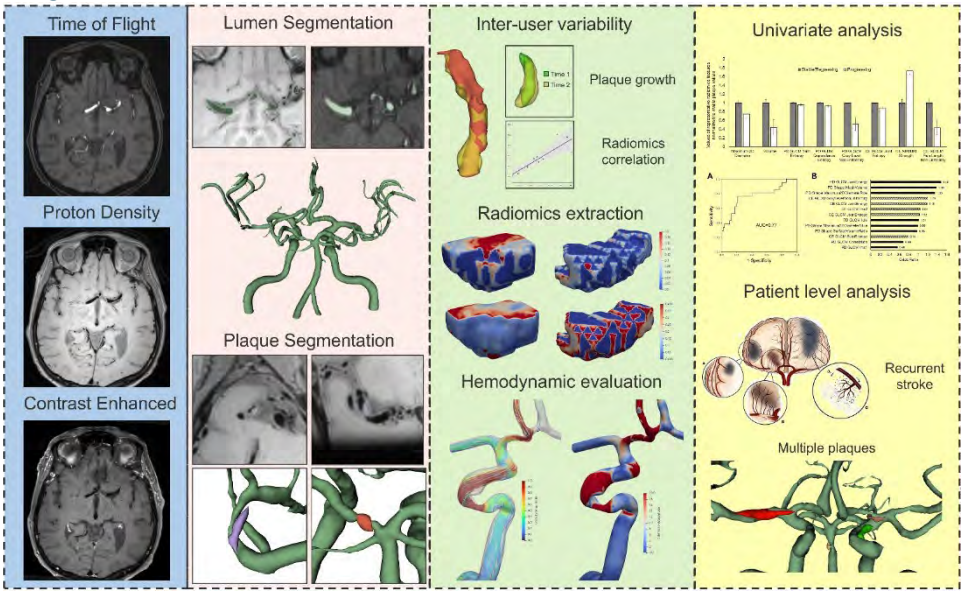

1127

Demographic, Clinical, and Imaging Characteristics of SOX2 Positivity Outside of T1 Contrast Enhancement in Glioblastoma at Autopsy

Samuel A Bobholz PhD, Aleksandra Winiarz, Benjamin Chao, Allison K Lowman, Savannah R Duenweg PhD, Biprojit Nath MS, Fitzgerald Kyereme, Jennifer Connelly MD, Kelly Mrachek MD, Elaine Tanhehco MD, Max Krucoff MD, Peter S LaViolette PhD

Medical College of Wisconsin, Milwaukee, WI, USA

Abstract Category

Adult Brain

Purpose

Sex-determining region Y-box 2 (SOX2) immunohistochemical staining has been used pathologically to identify pluripotent cells as a marker for tumor invasion[1,2]. This invasion is often observed even in areas where traditional tumor signatures such as hypercellularity are observed, indicating that SOX2 positivity may highlight the infiltrative edge of tumor growth. This study assessed the demographic and imaging correlates of SOX2 positivity using autopsy tissue samples aligned to conventional MRI as ground truth.

Materials & Methods

The cohort for this study consisted of 36 IDH wildtype glioblastoma patients (23 male, 13 female, mean age=61.9 years). Large format tissue samples (3-5 per patient) from areas within and beyond expected tumor were collected at autopsy for each patient using a previously described protocol to maximize structural integrity relative to the last MRI prior to death[3–5]. Collected samples were then stained for SOX2, digitized at 40X resolution, and segmented for cell density and SOX2% positivity via a color deconvolution based automated nuclei detection algorithm. The digitized samples were then aligned to the T2-weighted FLAIR image acquired closest to death using a nonlinear warping derived from manually defined control points, and the pre- and post-contrast-enhanced T1-weighted images (T1, T1C) and apparent diffusion coefficient (ADC) image were aligned to the FLAIR via SPM12[Click or tap here to enter text.]. Areas of contrast enhancement were manually annotated and excluded from all subsequent analyses. Mean SOX2% positivity was computed for the non-enhancing tumor regions and compared across age and sex as demographic factors. The voxelwise association between SOX2% positivity and cellularity was also computed and compared between patients who received standard therapy following surgery (n=31) to those who opted for no additional treatment aside from surgery (n=5) to assess the impact of treatment on the colocalization of hypercellularity and SOX2% positivity. Lastly, the mean standardized intensity from conventionally acquired MR images (pre-contrast T1, T1C, FLAIR, and ADC) were compared to mean SOX2% positivity to assess the ability for MRI to detect pluripotency.

Results

Males were found to have a higher SOX2+% than females (t=2.09, p=0.045), while no association with age was observed (r=0.146, p=0.397). Patients who received no additional treatment showed substantially higher associations between cellularity and SOX2+% than patients who had received additional treatments (t=2.90, p=0.006), with visual assessment showing more frequent SOX2% positivity occurring in areas of normal cell density. Only FLAIR intensity was found to be associated with SOX2% positivity amongst the imaging parameters (r=0.331, p=0.049).

Conclusion

These results indicate that SOX2 positive tumor extends well-beyond the contrast-enhancing margin and offers substantial new insights towards understanding GBM infiltration. The sex differences observed in this study align with work that suggests males tend to have worse prognoses, and the decoupling of cellularity with SOX2% positivity in treated patients suggests that more complicated tumor microenvironments develop in response to traditional therapies. While FLAIR intensity showed a significant association with SOX2% positivity, future research developing SOX2-specific radio-pathomic maps might be able to more precisely identify distant SOX2 positivity beyond the hyperintense margin.

References

1. Berezovsky AD, Poisson LM, Cherba D, et al. Sox2 promotes malignancy in glioblastoma by regulating plasticity and astrocytic differentiation. *Neoplasia (United States)*. 2014;16(3):193-206.e25. doi:10.1016/j.neo.2014.03.006

2. Bradshaw A, Wickremesekera A, Brasch HD, et al. Cancer Stem Cells in Glioblastoma Multiforme. *Front Surg*. 2016;3. doi:10.3389/fsurg.2016.00048

3. Bobholz SA, Lowman AK, Barrington A, et al. Radiomic Features of Multiparametric MRI Present Stable Associations With Analogous Histological Features in Patients With Brain Cancer. *Tomography*. 2020;6(2):160-169. doi:10.18383/j.tom.2019.00029

4. Bobholz SA, Lowman AK, Brehler M, et al. Radio-Pathomic Maps of Cell Density Identify Brain Tumor Invasion beyond Traditional MRI-Defined Margins. *AJNR Am J Neuroradiol*. 2022;43(5):682-688. doi:10.3174/ajnr.A7477
5. Bobholz SA, Lowman AK, Connelly JM, et al. Noninvasive Autopsy-Validated Tumor Probability Maps Identify Glioma Invasion Beyond Contrast Enhancement. *Neurosurgery*. 2024;95(3). https://journals.lww.com/neurosurgery/fulltext/2024/09000/noninvasive_autopsy_validated_tumor_probability.9.aspx

Images/Tables

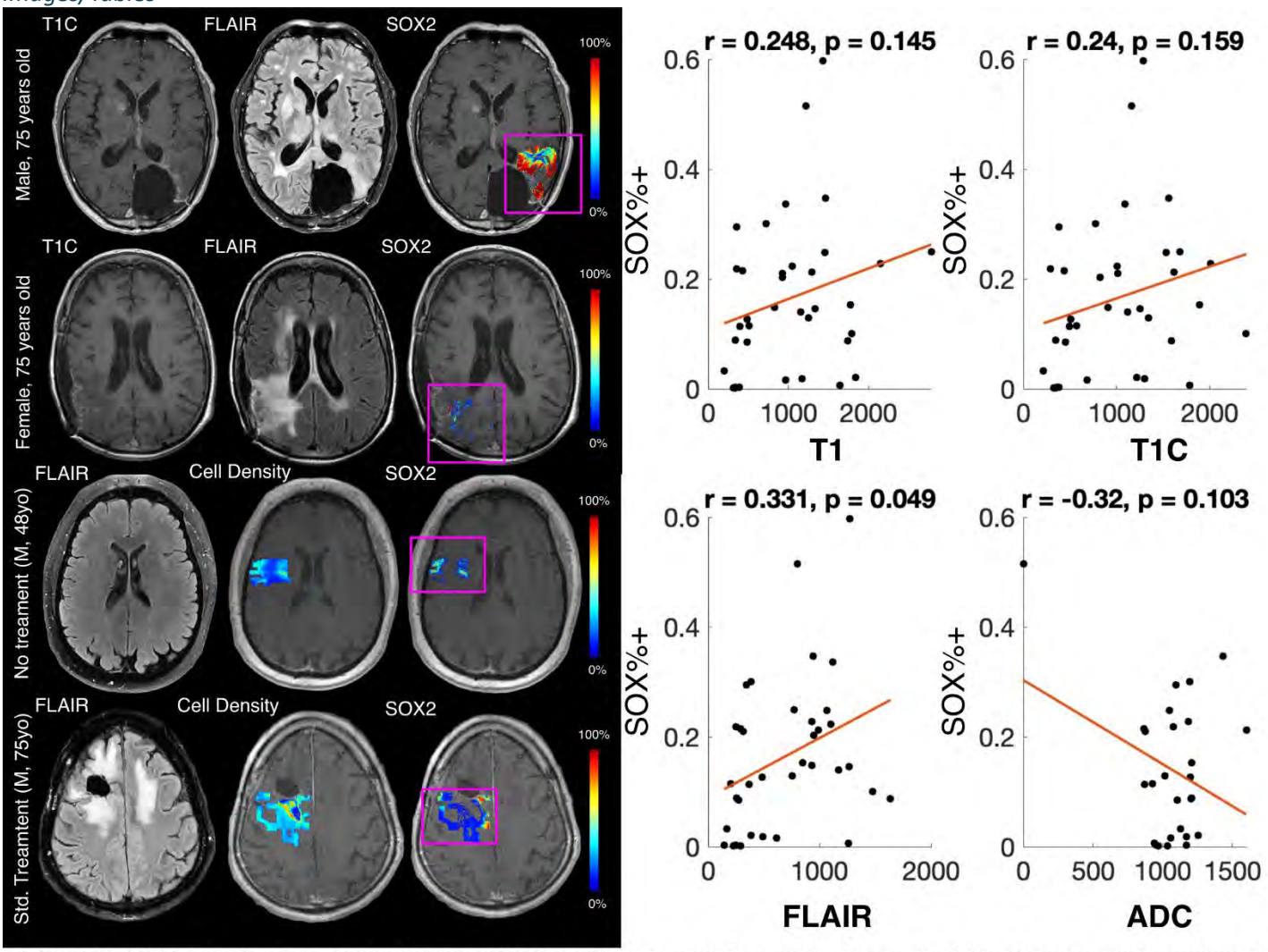

Figure 1: (left) Example cases demonstrating SOX2% positivity is more frequently observed outside of contrast enhancement in male patients, as well as that treated patients showing a decoupling of hypercellularity and SOX2% positivity compared to untreated patients. (right) Association between normalized MR intensity values and SOX2% positivity outside contrast enhancement.

1131

Cerebellar Cortical Dysplasias: Genetic or Secondary Etiology?

Edouard de Sousa MD, Riyad Hanafi MD
University Hospital Centre, Lille, Hauts-de-France, France

Abstract Category

Pediatrics

Purpose

Cerebellar cortical dysplasia (CCD) is an anomaly of cerebellar foliation caused by a neuronal migration disorder. Its genetic origin is well-established, but its potential secondary (acquired) etiology remains unclear and is debated in the literature.

Materials & Methods

In a cohort of 917 patients treated for cerebellar or neurodevelopmental disorders at Lille Hospital (France), we investigated isolated CCDs (without associated cerebral cortical malformation) on MRI to identify potential criteria for secondary CCDs. The main objective was to explore morphological differences between primary and secondary CCDs.

Results

We identified 61 cases of isolated CCD, of which 17 exhibited secondary features. We analyzed both local (gliosis, hemorrhage) and diffuse (dragonfly pattern, brainstem hypoplasia) abnormalities. We confirmed the presence of genetic variants previously associated with isolated CCDs in the literature (e.g., EBF3, LAMA1). Additionally, we identified 8 new genetic variants through Sanger sequencing that were associated with isolated CCDs.

Conclusion

This study highlights the morphological differences between primary and secondary isolated CCDs and suggests the involvement of new genetic variants in neuronal migration disorders.

References

(Gustavo Soto Ares was my research supervisor for my doctoral thesis, he will retire on january 2025 : his name will be on the e-poster but he won't be coming to the congress).

Journal Article

Soto-Ares G, Devisme L, Jorriot S, et al. Neuropathologic and MR imaging correlation in a neonatal case of cerebellar cortical dysplasia. AJNR Am J Neuroradiol. 2002 Aug;23(7):1101-4. PMID: 12169464.

Journal Article

Soto-Ares G. Analysis and classification of cerebellar malformations. AJNR Am J Neuroradiol. 2003 Jan;24(1):153; PMID: 12533349.

Journal Article

Riquet A, Quesque F, Soto Ares G et al. Differentiating Genetic Forms of Pontocerebellar Hypoplasia From Acquired Lesions Resembling Pontocerebellar Hypoplasia: Clinical, Neurodevelopmental, and Imaging Insight From 19 Extremely Premature Patients. J Child Neurol. 2023 Oct;38(10-12):622-630. www.doi.org/10.1177/08830738231201926.

Journal Article

Matéos M, Hacein-Bey L, Hanafi R et al. Advanced imaging in first episode psychosis: a systematic review. J Neuroradiol 2023. DOI: www.doi.org/10.1016/j.neurad.2023.04.001

Images/Tables

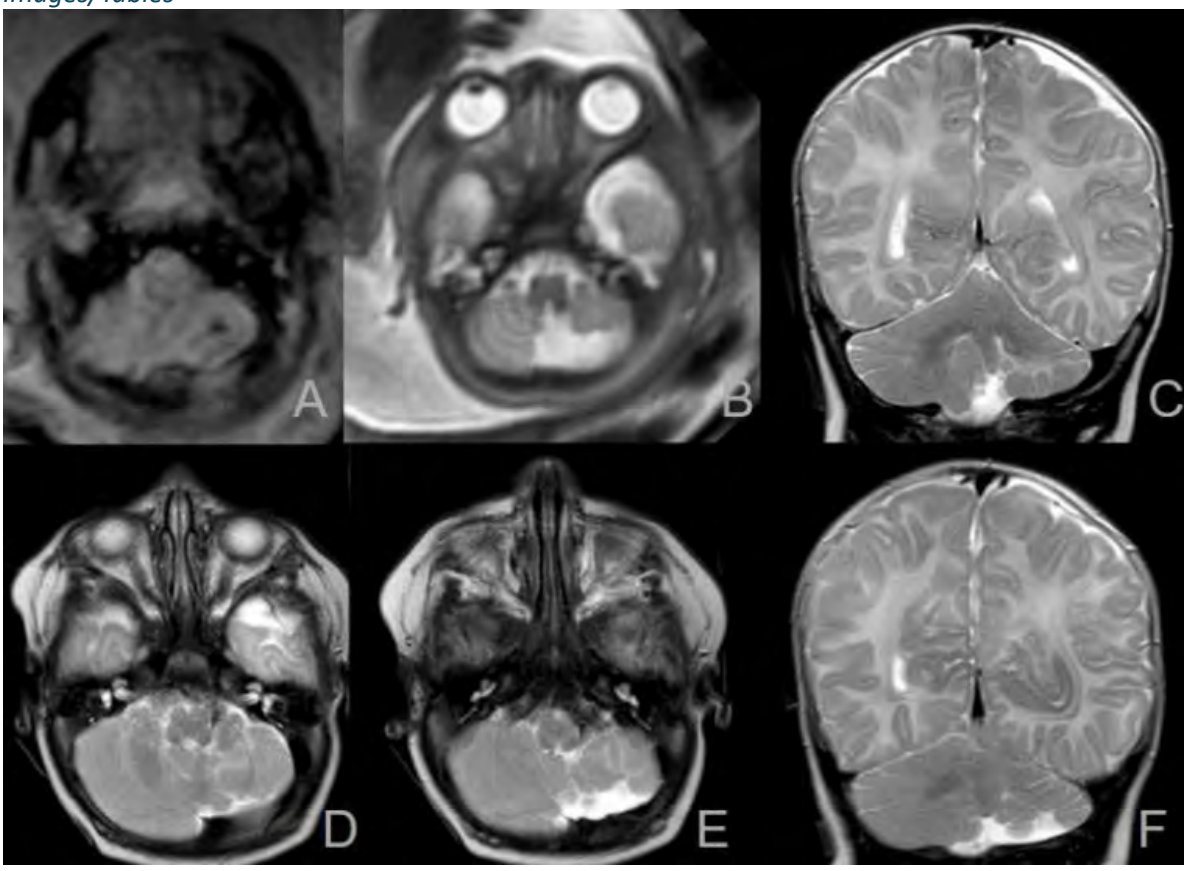

1132

Co-occurrence of Radiologic Findings and Optimal Imaging Approaches: A Network Analysis in Erdheim-Chester Disease from a Single Center

Fatemeh Dehghani Firouzabadi[1], Ali Sheikhy[2], Safa Samimi[2], Fahimul Huda[3], Aryan Zahergivar[2], Moozhan Nikpanah[2], Mojdeh Mirmomen[4], Faraz Farhadi[5], Mahshid Golagha[2], Fatemeh Homayounieh[2], Evrim Turkbay[2], Jhanavi Rao[2], Mark A. Ahlman[2], Corina Millo[2], Babak Sabouri[2], Ashkan A. Malayeri[2]

[1]San Francisco, California, USA. [2]National Institutes of Health, Bethesda, Maryland, USA. [3]Louisville, Kentucky, USA. [4]San Diego, California, USA. [5]Hanover, ew Hampshire, USA

Abstract Category

Adult Brain

Purpose

Consensus recommendations suggested imaging approach including FDG PET-CT imaging of brain and distal extremities, MRI of brain with gadolinium, and cardiac MRI in all newly diagnosed patients. (1) This study aims to investigate the co-occurrence of radiologic findings and determine the most effective imaging approaches in Erdheim-Chester Disease (ECD) using radiological findings.

Materials & Methods

A prospective analysis of radiological findings from a cohort of 40 biopsy-confirmed ECD patients was conducted. Various imaging modalities, including Chest and extremity CT, abdominal CT/MRI, and brain MRI, were utilized. Co-occurrence of radiologic findings across different anatomical sites was assessed using network analysis. Our evaluation of radiological findings comprised 10 organ involvements (including bone, pulmonary, CNS, uropathy, nephropathy, cardiac, vascular, orbit, hepatobiliary, and spleen), based on radiological findings. A team of expert radiologists, comprising 5 abdominal, 2 neuro, 1 thoracic, 2 clinical neuro and body fellows, and 2 nuclear medicine specialists, reviewed MRI/CT/PET-CT/Bone Scan studies. Discrepancies were resolved either by a third reader or by achieving consensus between two radiologists.

Results

Chest CT scans detected suspicious involvement/lesion in at least one anatomical site in 97.5% of ECD cases. Extremity CT scans achieved a 90% detection rate, while abdominal CT/MRI demonstrated an 85% efficacy. Combined use of imaging modalities, either both Chest CT with extremity CT or both Chest CT with Brain MRI or both Abdomen MRI/CT with extremity CT, and both Abdomen MRI/CT with extremity CT, achieved a comprehensive 100% detection rate. Co-occurrence analysis revealed a strong association between pulmonary, CNS, and bone involvement, while eye and hepatobiliary involvements showed the least rate of co-occurrence. (fig1) Statistically significant concurrence was observed between nephropathy, uropathy, cardiac, and vascular involvement in ECD network, with weak significant concurrence found between vascular, cardiac, and uropathy with orbital involvement.

Conclusion

Combining imaging modalities enhances detection rates, with combination of only 2 modalities offering complementary benefits. Co-occurrence analysis highlights patterns of involvement, particularly between pulmonary, CNS, and bone sites, informing clinical management strategies. This study represents the largest single-center investigation of ECD patients, encompassing a comprehensive assessment of radiological findings to understand the co-occurrence of radiologic findings and selecting optimal imaging approaches which can improve diagnostic accuracy and treatment planning in ECD.

References

1. Goyal G, Heaney ML, Collin M, Cohen-Aubart F, Vaglio A, Durham BH, et al. Erdheim-Chester disease: consensus recommendations for evaluation, diagnosis, and treatment in the molecular era. Blood, The Journal of the American Society of Hematology. 2020;135(22):1929-45.

Images/Tables

Fig 1. Co-occurrence analysis assessing the association between 10 organ involvement.

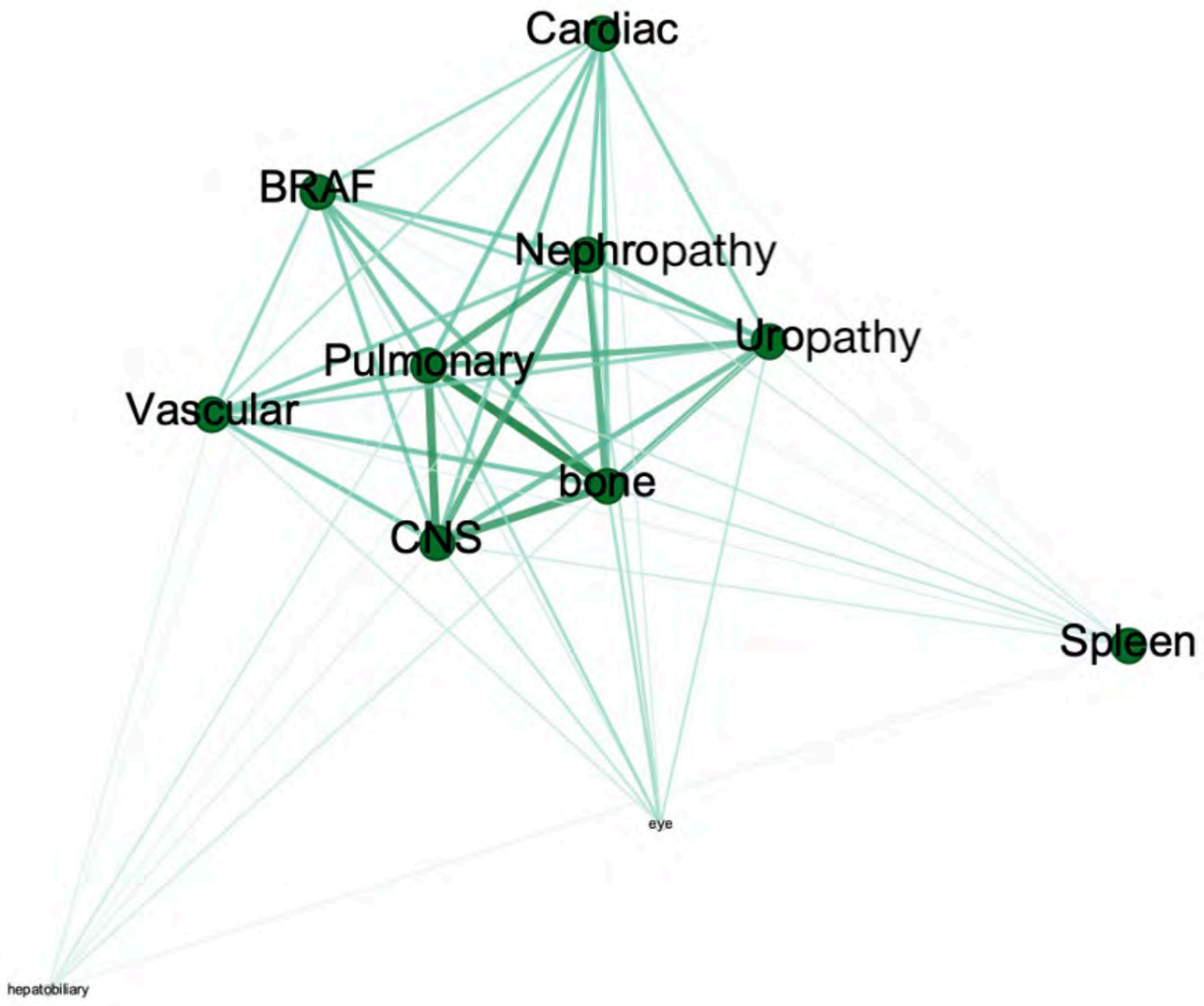

1134

Value of CT Neck Angiography in the Assessment of Blunt Cerebrovascular Injury in Blunt Cervical Trauma, Assaults, and Strangulation

Dr. Islam Ahmed Hassan Ahmed MBBS[1], Niousha Parsa MS3[2], Hala Mahdi MS2[2], Dr. Eduardo Portela De Oliveira MD[1]
[1]The Ottawa Hospital, Ottawa, ON, Canada. [2]University of Ottawa, Ottawa, ON, Canada

Abstract Category

Head & Neck

Purpose

The objective of this research is to investigate the value and clinical utility of neck CTA and the Expanded Denver Criteria in cases of blunt cervical trauma, assaults, and strangulation.

Materials & Methods

We retrospectively included 344 cases of patients who underwent CT angiography (CTA) following blunt cervical trauma, assaults, or strangulation between January 2013 and June 2023. Data were gathered from trauma reports and electronic

health records, focusing on demographics, trauma mechanisms, and CTA findings. This analysis aimed to assess the diagnostic yield of CTA and its clinical implications for identifying blunt cerebrovascular injury (BCVI) in these scenarios.

Results

Among the 344 cases analyzed, 38 patients (11%) were diagnosed with blunt cerebrovascular injury (BCVI), primarily graded as grade I according to the Biffl classification (55%). Grade 2 injuries accounted for 16% of BCVIs, while grades 3 and 4 accounted for 21% and 8%, respectively. Injuries most frequently involved the vertebral arteries (71%), followed by the internal carotid arteries (36.8%). Notably, 21% of BCVI cases did not meet the Expanded Denver Criteria (EDC), yet CTA successfully identified significant injuries. Motor vehicle crashes (MVC) were the predominant mechanism of injury (68%) and accounted for the majority of BCVI cases, while high-impact falls were also a significant contributor (29%). No BCVI cases were identified in the 29 patients with assault or strangulation mechanisms (8.4% of total cases).

Conclusion

The findings suggest that MVCs and high-impact falls are associated with a high BCVI detection rate, even in cases not meeting the EDC. This data supports revisiting CTA protocols to include high-risk trauma mechanisms independently of EDC adherence, potentially optimizing BCVI detection in MVC and high-impact fall cases. Given the absence of BCVI detection in our limited cohort of assault and strangulation cases, this finding aligns with the current literature suggesting a low yield of CTA in these scenarios. Further validation across additional trauma centers with larger cohorts is warranted.

References

1.Harper, P. R., Jacobson, L. E., Sheff, Z., Williams, J. M., & Rodgers, R. B. (2022). Routine CTA screening identifies blunt cerebrovascular injuries missed by clinical risk factors. Trauma Surgery and Acute Care Open, 7(1). https://doi.org/10.1136/tsaco-2022-000924

2.Fietz, D. (2021). Non-fatal strangulation and the gold coast forensic medicine clinical and legal experience. Pathology, 53. https://doi.org/10.1016/j.pathol.2021.05.035

3.Black, J. A., Abraham, P. J., Abraham, M. N., Cox, D. B., Griffin, R. L., Holcomb, J. B., Hu, P. J., Kerby, J. D., Liptrap, E. J., Thaci, B., Harrigan, M. R., & Jansen, J. O. (2021). Universal screening for blunt cerebrovascular injury. Journal of Trauma and Acute Care Surgery, 90(2). https://doi.org/10.1097/TA.0000000000003010

4. Wynn, M. S., Kesler, K. K., Bertroche, E., Pugely, A. J., & Igram, C. (2021). Patient specific predictive factors of vertebral artery injury following blunt cervical spine trauma. Clinical Neurology and Neurosurgery, 210. https://doi.org/10.1016/j.clineuro.2021.106988

5. Schellenberg, M., Inaba, K., Warriner, Z., Alfson, D., Roman, J., van Velsen, V., Lam, L., & Demetriades, D. (2019). Near hangings: Epidemiology, injuries, and investigations. Journal of Trauma and Acute Care Surgery, 86(3). https://doi.org/10.1097/TA.0000000000002134

1136

Association between BRAFV600E Mutation, Disease Severity, and Germ Line Layer Involvement in Erdheim-Chester Disease by Using Radiological Findings from a Unique ECD Population

Fatemeh Dehghani Firouzabadi[1], Ali Sheikhy[2], Safa Samimi[2], Fahimul Huda[3], Aryan Zahergivar[2], Moozhan Nikpanah[4], Mojdeh Mirmomen[5], Faraz Farhadi[6], Mahshid Golagha[2], Fatemeh Homayounieh[2], Evrim Turkbay[2], Jhanavi Rao[2], Mark A. Ahlman[2], Corina Millo[2], Babak Saboury[2], Ashkan A. Malayeri[2]

[1]Department of radiology, San Francisco, California, USA. [2]National Institutes of Health, Bethesda, Maryland, USA. [3]Louisville, Kentucky, USA. [4]Department of radiology, Birmingham, Alabama, USA. [5]Department of radiology, San Diego, California, USA. [6]Hanover, New Hampshire, USA

Abstract Category

Adult Brain

Purpose

This study evaluates the relationship between $BRAF^{V600E}$ mutation, disease severity, and germ line layer involvement in Erdheim-Chester Disease (ECD) using radiological findings.

Materials & Methods

A prospective analysis of radiological findings from a cohort of 40 biopsy-confirmed ECD patients were conducted. These patients had available imaging data along with $BRAF^{V600E}$ mutation status. Our evaluation of radiological findings comprised 10 organ involvements (including bone, pulmonary, CNS, uropathy, nephropathy, cardiac, vascular, orbit, hepatobiliary, and spleen)(table 1) and germ line layer involvement (Mesoderm, Endoderm, Ectoderm), based on

radiological findings. A team of expert radiologists, comprising 5 body, 2 neuro, 1 thoracic, 2 clinical fellows, and 2 nuclear medicine specialists, reviewed MRI/CT/PET-CT/Bone Scan studies. Discrepancies were resolved either by a third reader or by achieving consensus between two radiologists.

Results

A significant association was found between $BRAF^{V600E}$ mutation and disease severity based on organ involvement. Bone and pulmonary regions exhibited the highest frequency of involvement, regardless of the presence of $BRAF^{V600E}$mutation (95% and 92% respectively). Positive associations were found between $BRAF^{V600E}$ mutation and cardiac (OR=4.55, p=0.027) and vascular (OR=5.60, p=0.013) involvement. ECD patients showed full involvement in Mesoderm (100%), 93% in Endoderm, and 75% in Ectoderm using radiological findings. However, no significant correlation existed between germ line layer involvement and $BRAF^{V600E}$ mutation.

Conclusion

BRAF mutation is associated with disease severity in ECD, particularly in cases with more organ involvement. Bone and pulmonary regions are consistently affected, while cardiac and vascular involvement are associated with $BRAF^{V600E}$mutation. ECD patients showed full involvement in Mesoderm while no direct correlation was found with $BRAF^{V600E}$mutation with any specific germ line layer.This study represents the largest single-center investigation of ECD patients, encompassing a comprehensive assessment of radiological findings to elucidate the impact of the $BRAF^{V600E}$ mutation on disease severity, thereby facilitating risk stratification and treatment decision-making in ECD. Furthermore, the identification of $BRAF^{V600E}$ mutation status as a potential prognostic indicator highlights the multifaceted nature of ECD, underscoring the imperative for targeted therapeutic approaches and additional molecular research.

References

1. Goyal G, Heaney ML, Collin M, Cohen-Aubart F, Vaglio A, Durham BH, et al. Erdheim-Chester disease: consensus recommendations for evaluation, diagnosis, and treatment in the molecular era. Blood, The Journal of the American Society of Hematology. 2020;135(22):1929-45.

Images/Tables

Association between $BRAF^{V600E}$ mutation and Organ involvement

	OR (95% CI)	P- value
Bone	1.11 (0.06, 19.09)	0.942
Orbital	1.87 (0.45, 7.82)	0.388
CNS	0.5 (0.08, 3.10)	0.456
Uropathy	1.45 (0.40, 5.26)	0.568
Nephropathy	3.5 (0.75, 16.28)	0.110
Pulmonary	2.35 (0.19, 28.26)	0.499
Cardiac	4.55 (1.18, 17.52)	0.027
Vascular	5.60 (1.43, 21.95)	0.013
Hepatobiliary	0.39 (0.06, 2.45)	0.318
Spleen	0.625 (0.12, 3.24)	0.575

* Logistic regression model

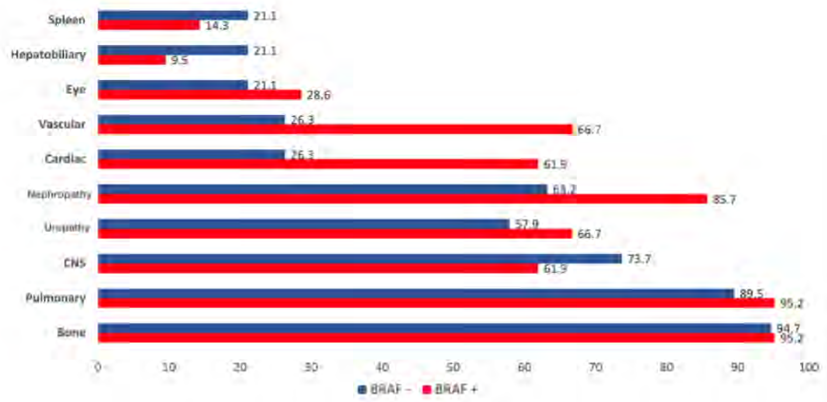

1145

Resting-state functional MRI: a non-invasive presurgical tool to lateralize temporal lobe epileptic focus

Sidney KRYSTAL MD PhD[1], Leila MAZZOLO MD[2], Lotfi HACEIN-BEY MD PhD[3], Jean-Pierre PRUVO MD PhD[4]
[1]Hôpiital-Fondation A. de Rothschild, Paris, France, France. [2]Hôpital-Fondation A. de Rothschild, Paris, France, France. [3]UC Davis, Sacramento, CA, USA. [4]CHU Lille, Lille, France, France

Abstract Category

Functional/Advanced Imaging

Purpose

Hippocampal sclerosis (HS) is a common pharmacoresistant epilepsy condition, where a leading cause of surgical failure is poor delineation and lateralization of the Epileptogenic Zone (EZ). The objective of this study was to assess the reliability and reproducibility of resting-state functional MRI (rs-fMRI) to lateralize the EZ in a cohort of adult patients with pharmacoresistant temporal lobe epilepsy associated with HS.

Materials & Methods

29 adults with HS diagnosed on MRI who underwent a rs-fMRI sequence in a single epilepsy surgery center between 2012 and 2019 were retrospectively included. For each patient, 120 rs-components were obtained using independent component analysis. Two radiologists blinded to standard MRI and electroclinical data classified them into noisy, physiological and epileptogenic networks, based on spatial and frequency features, to lateralize EZ. This rs-lateralization was compared to gold standard, determined on electro-clinical, morphological imaging, and, when available, post-surgery data.

Results

Of the 23 patients for whom the gold standard determined with certainty the EZ side, agreement was good with a κ score of 0.74 (95% CI: 0,56-0,92) between rs-fMRI and gold standard. False lateralization occurred for one patient (4.3%). Interobserver agreement rate was high, with a K score of 0.84 (95% CI: 0,68; 1,00). Contribution of rs-fMRI in cases of discrepancies between gold standard EZ assessment and rs-fMRI was also valuable.

Conclusion

rs-fMRI is a non-invasive modality reliable and reproducible for localizing EZ in adults suffering from HS, including cases with discordant presurgical investigations. This modality could increase the number of surgery candidates and avoid invasive acts.

References

1. Blümcke I, Thom M, Wiestler OD. Ammon's horn sclerosis: a maldevelopmental disorder associated with temporal lobe epilepsy. Brain Pathol. 2002 Apr;12(2):199-211.
2. Bernhardt BC, Hong S, Bernasconi A, Bernasconi N. Imaging structural and functional brain networks in temporal lobe epilepsy. Front Hum Neurosci. 2013 Oct 1;7:624.
3. Boerwinkle VL, Mohanty D, Foldes ST, Guffey D, Minard CG, Vedantam A, et al. Correlating Resting-State Functional Magnetic Resonance Imaging Connectivity by Independent Component Analysis-Based Epileptogenic Zones with Intracranial Electroencephalogram Localized Seizure Onset Zones and Surgical Outcomes in Prospective Pediatric Intractable Epilepsy Study. Brain Connect. 2017 Sep;7(7):424–42.
4. Boerwinkle VL, Cediel EG, Mirea L, Williams K, Kerrigan JF, Lam S, et al. Network-targeted approach and postoperative resting-state functional magnetic resonance imaging are associated with seizure outcome. Ann Neurol. 2019 Sep;86(3):344–56.

Images/Tables

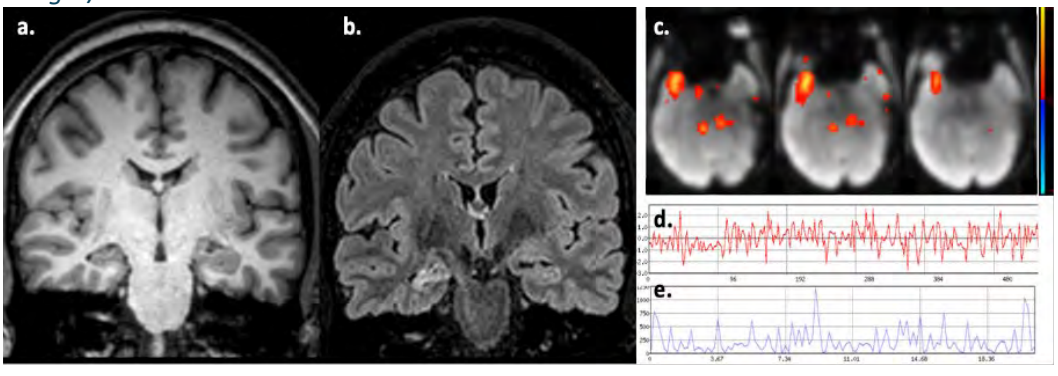

1156

Deep Learning in FCD Detection: Comparative Analysis of MNI and MELD Models in a UCSF Epilepsy Cohort

Lohith G Kini MD, PhD[1], Pierre Nedelec MS[1], Peter N Hadar MD, MSTR[2], Ankit N Khambhati PhD[1], Andreas M Rauschecker MD, PhD[1]

[1]University of California, San Francisco, San Francisco, CA, USA. [2]Massachusetts General Hospital, Boston, MA, USA

Abstract Category

AI/Informatics

Purpose

Focal cortical dysplasia (FCD) is a common cause of drug-resistant epilepsy[1], but it remains challenging to detect on structural MRI. Recent deep learning algorithms[2], such as the MNI deep learning method[3] and the MELD surface-based model[4], have shown promise in detecting FCD lesions across multi-center datasets. However, their performance needs further validation and comparison in diverse patient cohorts. This study aims to validate these models on a cohort of publicly available FCD patients[5] and a subset from UCSF, while also evaluating specificity using healthy controls.

Materials & Methods

We applied the MNI deep learning and MELD surface-based algorithms to 3D FLAIR and 3D T1-weighted MPRAGE images from a cohort of 20 patients with histologically confirmed FCD: 10 from UCSF (8 MRI-positive, 2 MRI-negative) and 10 from publicly available datasets. The same pre-operative imaging session from epilepsy patients was used for both models. Receiver Operating Characteristic (ROC) analysis was then used to evaluate the models' sensitivity and specificity. Additionally, the performance of the models was tested on 10 subjects from UCSF with normal for age MRIs . The control cohort helped assess the specificity of the models in detecting non-lesional regions. The models' saliency maps were also examined for interpretability.

Results

In the UCSF cohort, the sensitivity of the MNI method was 85% for MRI-positive FCD (7/8 cases detected), and 50% for MRI-negative FCD (1/2 cases detected). The MELD method demonstrated a 75% sensitivity for MRI-positive cases and 50% for MRI-negative cases. Both algorithms showed 90% specificity in healthy controls, with minimal false positives. On the publicly available dataset, both models demonstrated good generalizability, detecting MRI-positive FCD lesions with sensitivities ranging from 75% to 85%.

Conclusion

The MNI deep learning and MELD surface-based models showed strong performance in detecting MRI-positive FCD with high sensitivity and specificity in both UCSF and publicly available cohorts. However, the models' sensitivity for MRI-negative FCD remains a challenge, with values ranging from 50% to 60%, which was lower than published studies reporting 59-67% in MRI negative patients for the MELD[6] model and 83-85% for MNI model[3]. Future work will include a larger cohort of 96 patients with additional data from intracranial EEG and network biomarkers to determine if these can improve the detection of MRI-negative FCD. Additionally, data harmonization to correct for intra-site differences may reproduce the higher accuracy reported in previous published studies. Overall, this will help enhance the diagnostic accuracy of radiologists and inform treatment strategies for epilepsy patients.

References

1. 1. French JA. Refractory epilepsy: clinical overview. *Epilepsia*. 2007;48 Suppl 1:3-7. doi:10.1111/j.1528-1167.2007.00992.x
2. 2. Rauschecker AM, Gleason TJ, Nedelec P, et al. Interinstitutional Portability of a Deep Learning Brain MRI Lesion Segmentation Algorithm. *Radiol Artif Intell*. 2021;4(1). doi:10.1148/RYAI.2021200152
3. 3. Gill RS, Lee HM, Caldairou B, et al. Multicenter Validation of a Deep Learning Detection Algorithm for Focal Cortical Dysplasia. *Neurology*. 2021;97(16):E1571-E1582. doi:10.1212/WNL.0000000000012698
4. 4. Spitzer H, Ripart M, Fawaz A, et al. Robust and Generalisable Segmentation of Subtle Epilepsy-Causing Lesions: A Graph Convolutional Approach. *Lecture Notes in Computer Science (including subseries Lecture Notes in Artificial Intelligence and Lecture Notes in Bioinformatics)*. 2023;14227 LNCS:420-428. doi:10.1007/978-3-031-43993-3_41
5. 5. Schuch F, Walger L, Schmitz M, et al. An open presurgery MRI dataset of people with epilepsy and focal cortical dysplasia type II. *Scientific Data 2023 10:1*. 2023;10(1):1-7. doi:10.1038/s41597-023-02386-7

6. 6. Spitzer H, Ripart M, Whitaker K, et al. Interpretable surface-based detection of focal cortical dysplasias: a Multi-centre Epilepsy Lesion Detection study. *Brain*. 2022;145(11):3859-3871. doi:10.1093/BRAIN/AWAC224

Images/Tables

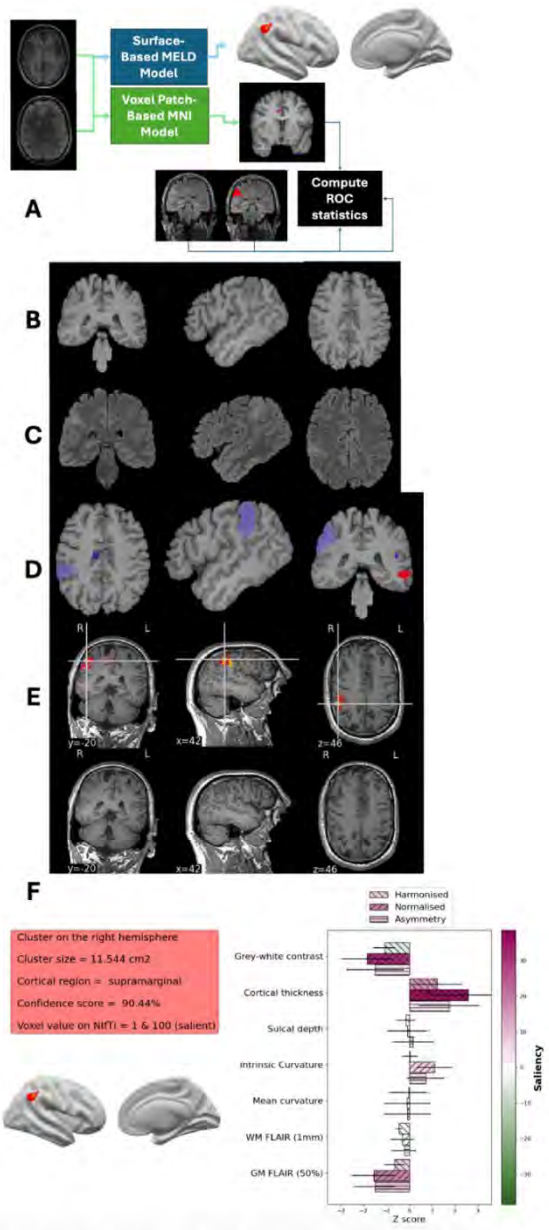

Figure Caption: Processing pipeline and sample results on a MRI+ case of FCD. **A**: A pipeline workflow for processing T1 and FLAIR MRI images through two parallel pipelines. The first pathway uses a surface-based MELD model, while the second employs a deep learning model with MNI registration. Each pathway calculates ROC statistics by comparing outputs with either expertly labeled FCD images or post-resection imaging to confirm lesion location. **B** and **C**: T1 and FLAIR MRI axial, sagittal, and coronal views of a patient with a known FCD lesion in the right frontoparietal lobe. **D**: Sample output from the deep learning MNI model, displaying some false positive clusters in FCD segmentation. **E**: Sample output for the same patient using the surface-based MELD model, showing highly sensitive and specific segmentation results with accurate lesion localization. **F:** Sample report with feature saliency output for the same patient using the surface-based MELD model demonstrating important interpretable features used to identify probable lesion clusters.

1161

Resting-State Functional MRI Metrics in IBS: Evaluating a Multi-Modal Approach to IBS Therapy

Andrew D Sam BS[1], George Zabrecky DC, MD[2], Daniel Monti MD, MBA[2], Nancy Wintering MSW, LCSW, CCRP[2], Feroze B Mohamed PhD[2], Andrew B Newberg MD[2]

[1]Sidney Kimmel Medical College, Philadelphia, PA, USA. [2]Thomas Jefferson University, Philadelphia, PA, USA

Abstract Category

Functional/Advanced Imaging

Purpose

This study employs resting-state functional magnetic resonance imaging (rs-fMRI) to measure voxel-based indices in individuals with irritable bowel syndrome (IBS) to evaluate the effectiveness of multi-modal nutrition and diet therapy.

Materials & Methods

21 participants with IBS received combined treatment, including Mediterranean diet, nutritional counseling, probiotics, fiber supplement, and nutrient supplement (glutamine, aloe, deglycerized licorice). Anatomical SAG T1 MPRAGE and resting-state BOLD scans using EPI sequence (parameters in table 1) were obtained for all participants before and after 3 months of treatment using a 3T Siemens Biograph mMR Positron Emission Tomography-MR scanner with 32-channel head coil. During rs-fMRI, participants were instructed to close their eyes, keep their heads still, and rest quietly without thinking about anything.

Data were preprocessed using Data Processing & Analysis for Resting-State Brain Imaging based on Statistical Parametric Mapping running on MATLAB R2024a. The first 10 volumes were discarded to account for magnet equilibration, and the remaining volumes received slice timing and head motion correction using six rigid body motion parameters. T1 images were co-registered to the mean of realigned EPI images and resting-state data were normalized to the EPI template in Montreal Neurological Institute space with resampling voxel size of 3 mm x 3 mm x 3 mm. Head motion was regressed out using Friston 24-parameter model and temporal band-pass of 0.01-0.08 Hz was applied to reduce respiratory and cardiac noise.

Five indices were calculated for each scan: amplitude of low frequency fluctuation (ALFF), degree centrality, fractional amplitude of low frequency fluctuation (fALFF), regional homogeneity (ReHo), and voxel-mirrored homotopic connectivity (VMHC), and the statistics analysis module in DPABI-V8.2 toolkit was used for analysis. Paired t-tests were performed to compare participants before and after treatment across all indices and resulting statistical maps were corrected for multiple comparisons to a significance level of $p < 0.05$ using generalized random forests correction. Clusters showing significant group differences are available in table 2. Significant brain regions were labelled in accordance with the Automated Anatomical Labeling (AAL3) atlas.

Results

Table 2 shows clusters showing significant group differences from participants before and after treatment in ALFF, binarized and weighted degree centrality, fALFF, ReHo, and VMHC. Clusters are named by the brain region with peak intensity (T score), and cluster size, coordinates of peak intensity, and peak intensity value are shown. Significant difference ($p<0.05$) was seen in the cerebellum, post-central gyrus, calcarine sulcus, frontal, temporal, parietal, and occipital lobes.

Conclusion

Comparison of key rs-fMRI metrics in IBS participants before and after treatment reveals changes in functional activity throughout the brain. Of note, changes in activity were observed in the frontal lobe and the postcentral gyrus, which have been shown to be involved in responses to nociceptive somatosensory stimuli and visceral pain in IBS, respectively.[1,2] Moreover, when compared to healthy individuals, the multimodal treatment protocol was found to partially reverse changes in the frontal lobe and postcentral gyrus associated with IBS. Future research is needed to fully assess the impacts of multimodal diet and nutritional therapy, but these early results suggest its potential to impact connectivity in individuals with IBS.

References

1. Zhang X, Li L, Huang G, et al. A multisensory fMRI investigation of nociceptive-preferential cortical regions and responses. *Front Neurosci* 2021;15:635733. Doi: doi.org/10.3389/fnins.2021.635733

2. Nan J, Yang W, Meng P, et al. Changes of the postcentral cortex in irritable bowel syndrome patients. *Brain Imaging and Behavior* 2020;14:1566-1576. Doi: doi.org/10.1007/s11682-019-00087-7

Images/Tables

Table 1

SAG T1 MPRAGE		rs-BOLD	
Repetition Time	1.6 s	Repetition Time	2.0 s
Echo Time	2.46 ms	Echo Time	30 ms
Field of View	250 mm x 250 mm	Field of View	23.6 cm
Matrix	512 x 512	Voxel Size	3 mm^3 x 3 mm^3 x 4 mm^3
Voxel Size	0.49 x 0.49	Number of Volumes	180
Number of Slices	176	Number of Slices	34
Slice Thickness	1 mm	Slice Thickness	4 mm

Table 2

Brain Region of Peak Coordinate	Cluster Size (Voxels)	Peak MNI Coordinate (x y z)	T Value
ALFF			
Cerebellum_Crus1_R	6582	39 -57 -36	-5.56
Parietal_Inf_R	2241	57 -48 45	6.28
Postcentral_L	2010	-54 -24 54	5.19

Brain Region of Peak Coordinate	Cluster Size (Voxels)	Peak MNI Coordinate (x y z)	T Value
Degree Centrality Binarized			
Cerebellum_Crus2_L	3925	-9 -87 -36	-5.03
Frontal_Sup_2_L	1287	-12 36 51	6.64
Parietal_Inf_R	1064	54 -54 48	5.26
Temporal_Sup_L	646	-48 -3 -15	-5.78
Calcarine_R	464	27 -60 6	4.52

Brain Region of Peak Coordinate	Cluster Size (Voxels)	Peak MNI Coordinate (x y z)	T Value
Degree Centrality Weighted			
Cerebellum_Crus2_L	3808	-9 -87 -36	-5.13
Frontal_Sup_2_L	1216	-12 36 51	5.97
Parietal_Inf_R	1010	54 -54 48	5.23
Temporal_Sup_L	782	-48 -3 -15	-5.82

Brain Region of Peak Coordinate	Cluster Size (Voxels)	Peak MNI Coordinate (x y z)	T Value
fALFF			
Occipital_Sup_R	10294	27 -63 39	3.24
Cerebellum_9_R	3633	9 -48 -39	-3.38

Brain Region of Peak Coordinate	Cluster Size (Voxels)	Peak MNI Coordinate (x y z)	T Value
ReHo			
Temporal_Sup_R	5057	54 0 -6	-4.92
Parietal_Inf_L	1947	-48 -54 48	7.18
Postcentral_R	1513	51 -27 60	6.72

Brain Region of Peak Coordinate	Cluster Size (Voxels)	Peak MNI Coordinate (x y z)	T Value
VMHC			
Postcentral_R	4336	39 -36 66	6.47
Cerebellum_8_R	1554	30 -66 -48	-4.03

1166

Subventricular Zone and MGMT Methylation Prediction in Glioblastomas

Kanwar Singh[1], Chandan Ganesh Yogananda PhD[2], Matthew Lee MD[1], Rajan Jain[1]

[1]NYU Grossman School of Medicine, New York, NY, USA. [2]UT Southwestern Medical Center, Dallas, TX, USA

Abstract Category

Adult Brain

Purpose

O6-methylguanine-DNA methyltransferase (MGMT) promoter status is an important biomarker for glioblastoma (GBM) diagnosis & therapy. Recently, the subventricular zone (SVZ) has been identified as a potential origin for GBMs due to its neural stem cells that may harbor the initial tumor-driving mutations.[1] This study sought to use an MRI-based machine learning (ML) method to assess the predictive value of the SVZ for MGMT promoter status.

Materials & Methods

Multi contrast MRI and genomic data from 194 patients diagnosed at our institution with IDH-wildtype glioblastomas and confirmed MGMT status were retrospectively reviewed. After excluding cases with insufficient imaging, 157 patients were included. Preoperative MRIs (T2, T2-FLAIR, pre- and post-contrast T1) were preprocessed and segmented using the FeTS tool.[2]

The SRI brain atlas was used to create an ROI for the SVZ. Multi-contrast MRI, FeTS tumor segmentations and the SVZ ROI were used to calculate containment scores for tumor-SVZ overlap. The containment score quantifies the spatial overlap of the tumor region within SVZ and vice-versa. Cases with scores above 0.1 (at least 10% overlap) were selected. We used pyradiomics for feature extraction from the corresponding MRIs, BORUTA for feature selection & SMOTE to address class imbalances. These features were used to train a Random Forest (RF) classifier to predict MGMT status.[3,4] The data was split into 80% training and 20% testing sets. Stratified k-fold cross-validation (CV) was applied to the training set for reliability and the CV models were used to test the testing set. Average test accuracy across folds was reported.

Results

107 cases were MGMT-unmethylated with a mean containment score of 0.125 (range, 0 - 0.567), and 50 were MGMT-methylated with a mean containment score of 0.137 (range, 0 - 0.508). 71 subjects had a containment score >0.1. In the validation phase, the mean CV accuracy was 58.53%. The CV models, when tested on the held-out test set, achieved a mean accuracy of 48%.

Conclusion

This study explored the potential of the subventricular zone (SVZ) as an ROI to predict MGMT status in GBM patients; however, it did not establish a definitive correlation. Despite employing advanced imaging segmentation and a classical ML model, the results demonstrated moderate predictive accuracy, with variability across folds. Even though the SVZ is a critical area of interest, its utility in predicting MGMT remains inconclusive.

References

1. Lee JH, Lee JE, Kahng JY, et al. Human glioblastoma arises from subventricular zone cells with low-level driver mutations. *Nature* 2018;560:243–7.
2. Pati S, Baid U, Edwards B, et al. Federated learning enables big data for rare cancer boundary detection. *Nat Commun* 2022;13:7346.
3. Kursa MB, Rudnicki WR. Feature Selection with the Boruta Package. *J Stat Softw* 2010;36:1–13.
4. Chawla N V, Bowyer KW, Hall LO, et al. *SMOTE: Synthetic Minority Over-sampling Technique*.; 2002.

Images/Tables

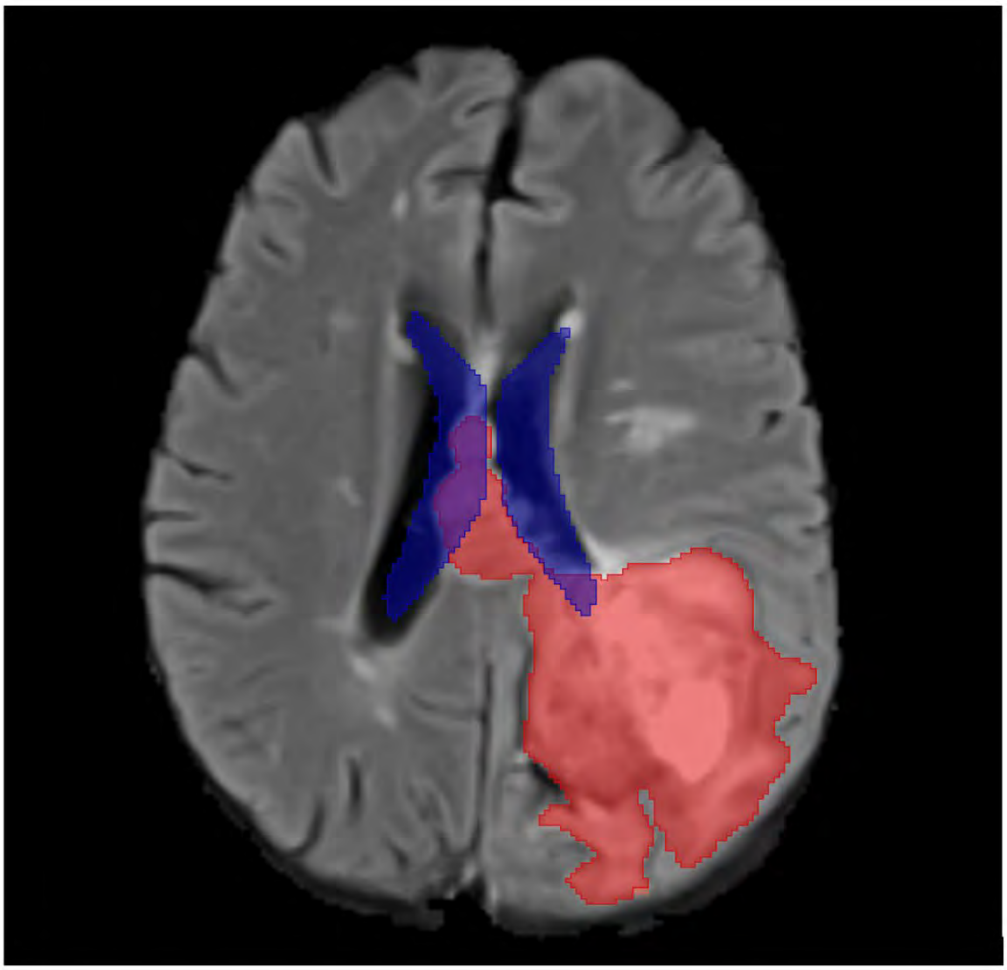

Figure 1: T2 FLAIR image with glioblastoma segmentation (Red) and Ventricles (Blue).

1171

Novel In Vitro Model for the Performance Assessment of Non-DMSO-based Liquid Embolics in NeuroInterventional Treatment

Tracy Nguyen BS[1], Ichiro Yuki MD[1], Kousaku Ohkawa PhD[2], Rebecca Back BS[1], Beatrice Malvar BS[1], Jordan Xu MD[1], Hemdeep Kaur MS[1], Frank P.K. Hsu MD PhD[1], Chloe M Jin BA[1], Shuichi Suzuki MD PhD[1]
[1]UC Irvine Medical Center, Orange, CA, USA. [2]Institute of Fiberengineering at Shinshu University, Ueda, Nagano, Japan

Abstract Category

Interventional

Purpose

This study introduces a novel in vitro model for evaluating the performance of emerging non-DMSO-based, non-adhesive liquid embolic agents, intended as alternatives to conventional DMSO-dependent agents. These new embolics often composed of water-soluble, non-adhesive formulations or utilize shear-thinning mechanisms, eliminating the need for toxic organic solvents while maintaining radiopacity under fluoroscopy. Despite these advantages, non-DMSO-based embolics face challenges, such as higher injection force due to increased viscosity. Precise control over coagulation speed and distal penetration is also necessary to tailor these embolics for specific clinical applications. In this study, varying concentrations of pAES, a prototype water-soluble embolic agent, were used as a reference, with the Onyx Embolic System® as a control, to assess the model's capacity to evaluate embolic performance, injection force, and radiopacity.

Materials & Methods

A porous vascular model commonly used for hands-on Onyx training with neuro-interventionalists was utilized in this study. The model, constructed from porous polyurethane and heat-shrink tubing, simulates a single-feeder, single-drainer AVM. It was integrated into a closed-circuit pump system circulating artificial plasma with regulated blood pressure through circuit resistance, closely mimicking physiological conditions. High-resolution imaging and fluoroscopy were used to observe each material’s embolization behavior, allowing for evaluation of its visibility under direct and fluoroscopic views. pAES was tested in its undiluted form (100%) and diluted forms (80% and 60%) using an iodinated contrast medium (iohexol), with Onyx 18 serving as the control. Each embolic was loaded into a Medalion® 1cc syringe and hand-injected via an Excelcior SL10® microcatheter (ID 0.0165). Injections were performed at a rate of 0.6 mL/min and terminated upon achieving complete occlusion, observing 30 mm reflux, or reaching a total injection volume of 1 mL. Parameters assessed included radiopacity (grayscale intensity), distal penetration (mm) within the AVM model, and injection resistance (N).

Results

Eight injections were conducted in total, with two injections performed per material, and averages calculated. AES at 100% and 80% concentrations, as well as Onyx 18, achieved full occlusion and reflux within the AVM model, while AES 60% achieved only partial occlusion without reflux. Distal penetration values were 13.2 mm for Onyx 18, 50.8 mm for AES 100%, 59.9 mm for AES 80%, and 44.9 mm for AES 60%, showing superior distal penetration with AES. Injection resistance was lowest for Onyx 18 (11.6 N) and increased with AES concentration, with measurements of 19.9 N for AES 60%, 33.4 N for AES 80%, and 40.9 N for AES 100%. Fluoroscopic visibility (inverted grayscale) scored 156 for Onyx 18, while AES 100% and 80% scored 134 and 120, respectively.

Conclusion

This in vitro model effectively evaluates non-DMSO-based liquid embolics by providing essential performance insights relative to conventional embolics, such as Onyx, especially in terms of injection resistance, distal penetration, and radiopacity. The model’s ability to assess and compare these parameters supports the optimization of new embolic agents for diverse clinical applications, facilitating their refinement for enhanced clinical performance.

References

Brassel F, Meila D (2015) Evolution of Embolic Agents in Interventional Neuroradiology. Clin Neuroradiol 25 Suppl 2:333-339.

1172

Quantitative Susceptibility Mapping for Microbleed Detection in Patients Undergoing Anti-Amyloid Therapy Eligibility MRIs

Nima Omid-Fard MD[1], Jeremy N Ford MD[1], Saurabh Rohatgi MD[1], Benjamin M Kozak MD[1], Esteban C Cadavid MD[1], Hana Farzaneh MD[1], Odette G Chagui[1], Maryam Vejdani-Jahromi MD, PhD[1], Harry R Griffin MD[1], Shenghua Zhu MD, PhD[1], Jarrel CY Seah MBBS[1], Yi Wang PhD[2], Javier M Romero MD[1]

[1]MGH, Boston, MA, USA. [2]Cornell, Ithaca, NY, USA

Abstract Category

Adult Brain

Purpose

The detection of microbleeds is a major component of the Boston 2.0 criteria, with large diagnostic implications for missing even a single lobar microhemorrhage or focus of cortical superficial siderosis.[1] Similarly, accurate detection is important in ARIA assessment to suspend or continue therapy.[2] Although T2* GRE remains the standard sequence for microbleed detection in the setting of anti-amyloid treatment eligibility and dose-adjustment, it is less sensitive compared to SWI.[2] Quantitative Susceptibility Mapping (QSM), in which voxel intensity is linearly proportional to the underlying tissue susceptibility,[3] may provide complementary tissue contrast to enhance microbleed detection; however, this has not been demonstrated in patients undergoing eligibility MRIs for anti-amyloid therapies.

Materials & Methods

204 consecutive brain MRIs screening for microhemorrhages were analyzed. We selected only those with at least one microhemorrhage seen on any T2*-weighted imaging, yielding 35 studies, 30 of which had QSM. Microbleed counts had been determined by six different raters who had previously demonstrated intraclass correlation coefficients of 0.764 for GRE and 0.951 with SWI. The difference between SWI and QSM+SWI detection of microbleeds was assessed using Wilcoxon matched-pairs signed rank test and Bland-Altman analysis.

Results

Using SWI, a total of 125 microbleeds were detected (mean 3.57 per patient), compared to 140 microbleeds detected using QSM+SWI (mean 4.0). The Wilcoxon test showed a significant difference between groups (P = 0.0039), and Bland-Altman analysis showed a slight positive bias of 0.4286, favoring increased microbleed detection in the QSM+SWI group.

Conclusion

QSM with SWI may be more sensitive for detecting microbleeds compared to SWI alone, with a small positive bias. Further study with larger and longitudinal samples are needed to establish the relationship between QSM-evident microbleeds and ARIA risk.

References

1. Charidimou A, Boulouis G, Frosch MP, et al. The Boston Criteria v2.0 for cerebral amyloid angiopathy: A multicentre MRI-neuropathology diagnostic accuracy study. *Lancet Neurol*. 2022;21(8):714. doi:10.1016/S1474-4422(22)00208-3
2. Cogswell PM, Barakos JA, Barkhof F, et al. Amyloid-Related Imaging Abnormalities with Emerging Alzheimer Disease Therapeutics: Detection and Reporting Recommendations for Clinical Practice. *Am J Neuroradiol*. 2022;43(9):E19-E35. doi:10.3174/ajnr.A7586
3. Harada T, Kudo K, Fujima N, et al. Quantitative Susceptibility Mapping: Basic Methods and Clinical Applications. *RadioGraphics*. 2022;42(4):1161-1176. doi:10.1148/rg.210054

Images/Tables

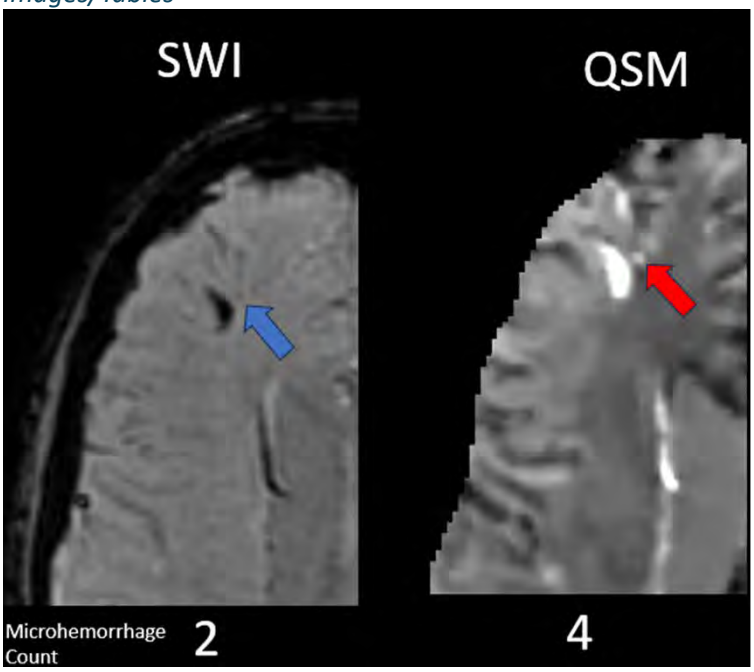

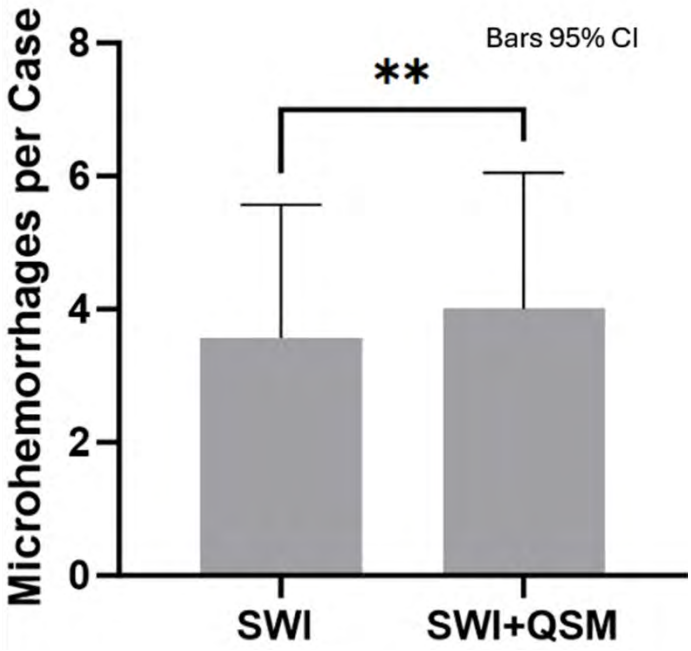

1184

Targeted Blood Brain barrier Opening Enhances Delivery of Sonodynamic Therapy Agent.

Deepshikha Bhardwaj Ph.D[1], Samuel Achilefu Ph.D[2], Walter Akers Ph.D[2], Nisha Gamadia[2], Bhavya R Shah MD, Ph.D[3]
[1]UT Southwestern Medical Center, Transcranial Focused Ultrasound lab, Neuro-Radiology and Neurointervention Section, Department Of Radiology, Dallas, Texas, USA. [2]UT Southwestern Medical Center, Department Of Biomedical Engineering, Dallas, Texas, USA. [3]UT Southwestern Medical Center, Transcranial Focused Ultrasound lab, Neuro-Radiology and Neurointervention Section, Department Of Radiology, Department of Neurological Surgery, Dallas, Texas, USA

Abstract Category

Functional/Advanced Imaging

Purpose

Despite the development of novel therapies, the prognosis of patients diagnosed with Glioblastoma is poor. Photodynamic therapy uses light but cannot reach deep tumors. Sonodynamic Therapy (SDT) uses ultrasound energy and can target tumors in deep brain regions across an intact skull. There are active clinical trials studying SDT in combination with 5-ALA, but these approaches are limited by an inability of the 5-ALA to penetrate the brain and be specific enough for targeted SDT of brain tumors. We have developed a novel approach, Focused ultrasound Initiated Glioma Homing Therapy (FIGHT) therapy, as a novel strategy for improving the penetration of SDT agents into the brain.

Materials & Methods

After tail vein cannulation Lipid microspheres (microbubbles) were instilled through the catheter. Focused Ultrasound (FUS) sonications targeting the right hippocampus was performed with a 1.57 MHz transducer. After confirming BBB with post-gadolinium T1W MRI, 60nM of a novel SDT agent, LS301, was injected through the tail vein. The mice were then imaged by fluorescence molecular tomography (in vivo) and Pearl imager (2D, ex vivo).

Results

Both in vivo and ex vivo imaging confirmed LS301 levels to peak at 4 hours post injection after FUS BBB opening. The contralateral side served as a control and demonstrated reduced LS301 delivery.

Conclusion

FUS-mediated BBB opening improves accumulation of LS301's distribution in targeted regions of the mouse brain.

References

Sheng KW, Marc AS, Stuart LM et al. MR-guided Focused Ultrasound Facilitates Sonodynamic Therapy with 5-Aminolevulinic Acid in a Rat Glioma Model. Sci Rep 2019; 18:9, 10465. doi: 10.1038/s41598-019-46832-2

Images/Tables

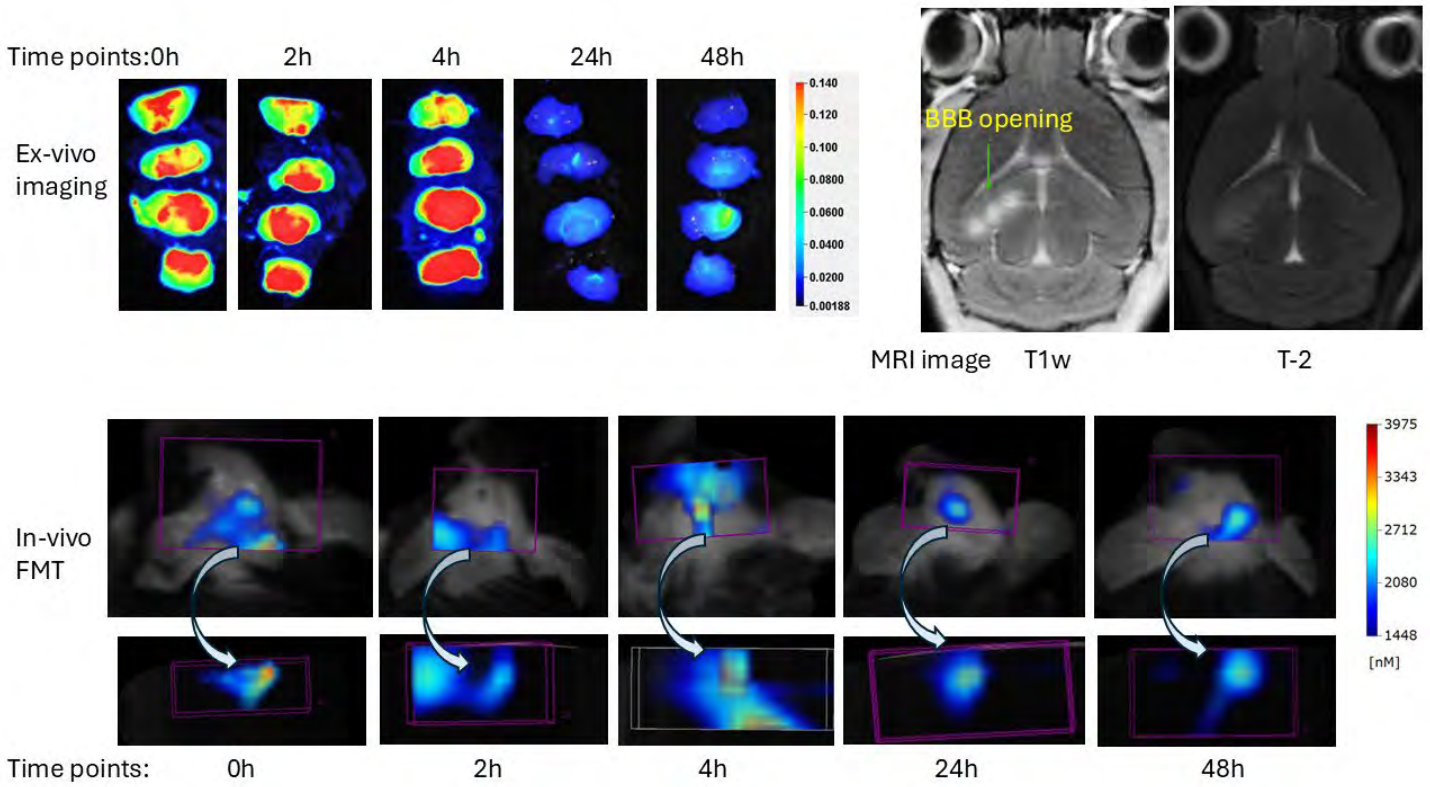

1201

Study of 18F-Fluciclovine PET/CT for Assessment of Glioblastoma Tumor Volume and Radiation Response

Samir A. Dagher MD[1], Rania M.M. Mohamed MD[1], Shehbaz Ansari[2], Jason Johnson[3], Lesley Flynt[1], Ho-Ling Liu PhD[1], Ahmed Msherghi MD[1], Sahar Alizada MD[1], Ceylan Altintas Taslicay MD[1], Richard Dagher MD[1], Max Wintermark MD[1], Dawid Schellingerhout[1], Jeffrey Weinberg[1], Sherise Ferguson[1], Maria Gule-Monroe[1]

[1]The University of Texas MD Anderson Cancer Center, Houston, TX, USA. [2]RUSH University Medical Center, Chicago, IL, USA. [3]Yale New Haven Hospital, New Haven, CT, USA

Abstract Category

Functional/Advanced Imaging

Purpose

Recent studies have supported the incorporation of 18F-Fluciclovine PET/CT during diagnosis, treatment planning and monitoring of high-grade gliomas.[1–4] However, the relationship between glioblastoma tumor volumes on conventional MRI and F18-Fluciclovine PET/CT at key time points from diagnosis throughout treatment remains unclear. This study compares these volumes at the preoperative, pre-radiation, and post-radiation stages and evaluates their change throughout disease course.

Materials & Methods

This prospective study conducted between September 2019 and October 2021 included adult patients with suspected or biopsy-confirmed glioblastoma, IDH-wildtype who were candidates for surgical resection followed by a six-week course of chemoradiation. Participants underwent 18F-Fluciclovine PET/CT paired with standard-of-care MRI within 14 days prior to surgery, within 7 days prior to radiotherapy, then 1 and 6 months after completing radiotherapy. The amino acid hypermetabolic volume (AHV) was defined as having a tumor-to-background ratio≥1.5 and segmented using the PETEdge+ tool of MIMv7.2. The T2-FLAIR and contrast-enhancing T1 volumes (FLAIRV and T1CV) were manually segmented. Volumes were compared with the Friedman test with post-hoc Bonferroni-adjusted comparisons at diagnosis and before radiotherapy. Changes in volumes with surgery and radiotherapy were computed and stratified by extent of resection (EOR) of contrast-enhancing tumor as assessed by a board-certified neuroradiologist.[5] An exploratory

Kaplan-Meier analysis stratified by postoperative pre-radiotherapy residual AHV was conducted, and median overall survival were compared with the Breslow test.

Results

8 participants (5 males; median age=63 [IQR 54–66] years; median preoperative KPS=90) were enrolled. 4 participants underwent complete or near-total resection (CR/NTR), while 4 underwent subtotal resection (STR). Volumes on 18F-Fluciclovine PET/CT and MRI differed at diagnosis (p=.002); post-hoc pairwise comparison revealed the median AHV=27.21mL (IQR 20.09–38.52) was twice as high as median T1CV=13.32mL (IQR 6.35–23.39) but did not differ from median FLAIRV=28.14mL (IQR 25.16–44.12) (adjusted p=.031 and .952, respectively). Volumes on 18F-Fluciclovine PET/CT and MRI similarly differed prior to radiotherapy (p=.011); median AHV=25.21mL (9.16–42.05) was around 3 times higher than median T1CV=6.89mL (0–14.03) but did not differ from median T2-FLAIR volume=26.78mL (10.72–39.90) (adjusted p=.028 and 1.00, respectively). Participants who underwent CR/NTR had a median decrease in AHV=49.5%(IQR 28.3–50.7%); those with STR had a median increase in AHV=50.2%(IQR 24.3–72.5). These ranges fall short of the reported EOR ranges,[5] suggesting significantly more non-enhancing residual tumor than expected on T1C. A nonsignificant trend towards improved survival was observed in participants with postoperative residual AHV≤26mL (median OS=383 versus 1,246 days, p=.239). Participants who initially underwent CR/NTR had a median decrease in AHV=34.9%(IQR 25–44.8) then AHV=77.7%(IQR 65.1–90.2) at 1 and 6 months after completing radiotherapy in the absence contrast-enhancing tumor. Those with STR had a median decrease in AHV=18.9%(-27.0–19.1) one month post-radiotherapy compared to their postoperative pre-radiotherapy residual volume.

Conclusion

Glioblastoma volumes on 18F-Fluciclovine PET/CT are consistently larger and slower to decrease throughout radiotherapy and surgery compared to contrast-enhancing volumes on conventional MRI. Treatment planning in conjunction with 18F-Fluciclovine PET/CT might improve treatment outcomes in this population.

References

1. Parent EE, Benayoun M, Ibeanu I, et al. [18F]Fluciclovine PET discrimination between high- and low-grade gliomas. *EJNMMI Res* 2018;8:67.
2. Nabavizadeh A, Bagley SJ, Doot RK, et al. Distinguishing Progression from Pseudoprogression in Glioblastoma Using 18F-Fluciclovine PET. *J Nucl Med* 2023;64:852–8.
3. Karlberg A, Berntsen EM, Johansen H, et al. 18F-FACBC PET/MRI in Diagnostic Assessment and Neurosurgery of Gliomas. *Clin Nucl Med* 2019;44:550.
4. Fatania K, Frood R, Tyyger M, et al. Exploratory Analysis of Serial 18F-fluciclovine PET-CT and Multiparametric MRI during Chemoradiation for Glioblastoma. *Cancers* 2022;14:3485.
5. Karschnia P, Vogelbaum MA, van den Bent M, et al. Evidence-based recommendations on categories for extent of resection in diffuse glioma. *Eur J Cancer* 2021;149:23–33.

Figure

74-year-old female participant with glioblastoma, MGMT promoter methylated, centered in the right frontal centrum semiovale and abutting the ipsilateral corticospinal tract. Karnofsky Performance Score at diagnosis was 90. The participant underwent near-total resection of the contrast-enhancing tumor followed by concurrent chemoradiation (total dose of 40.05 Gy) and subsequent cycles of temozolomide. The participant underwent 18F-Fluciclovine PET/CT at 4 timepoints during her disease course. The contralateral normal brain depicted in light blue is used as a threshold for delineating the AHV represented in magenta. Axial fusion scans (top row) show a decreased AHV from 19.0 mL preoperatively, to 9.16 mL pre-radiation, to 5.06 and 1.74 mL at one and six months after radiotherapy, respectively. A similar trend can be appreciated on conventional MRI (middle and bottom rows). It is worth noting that contrast-enhancing volume is consistently lower than AHV. The participant passed away 1,246 days after diagnosis.

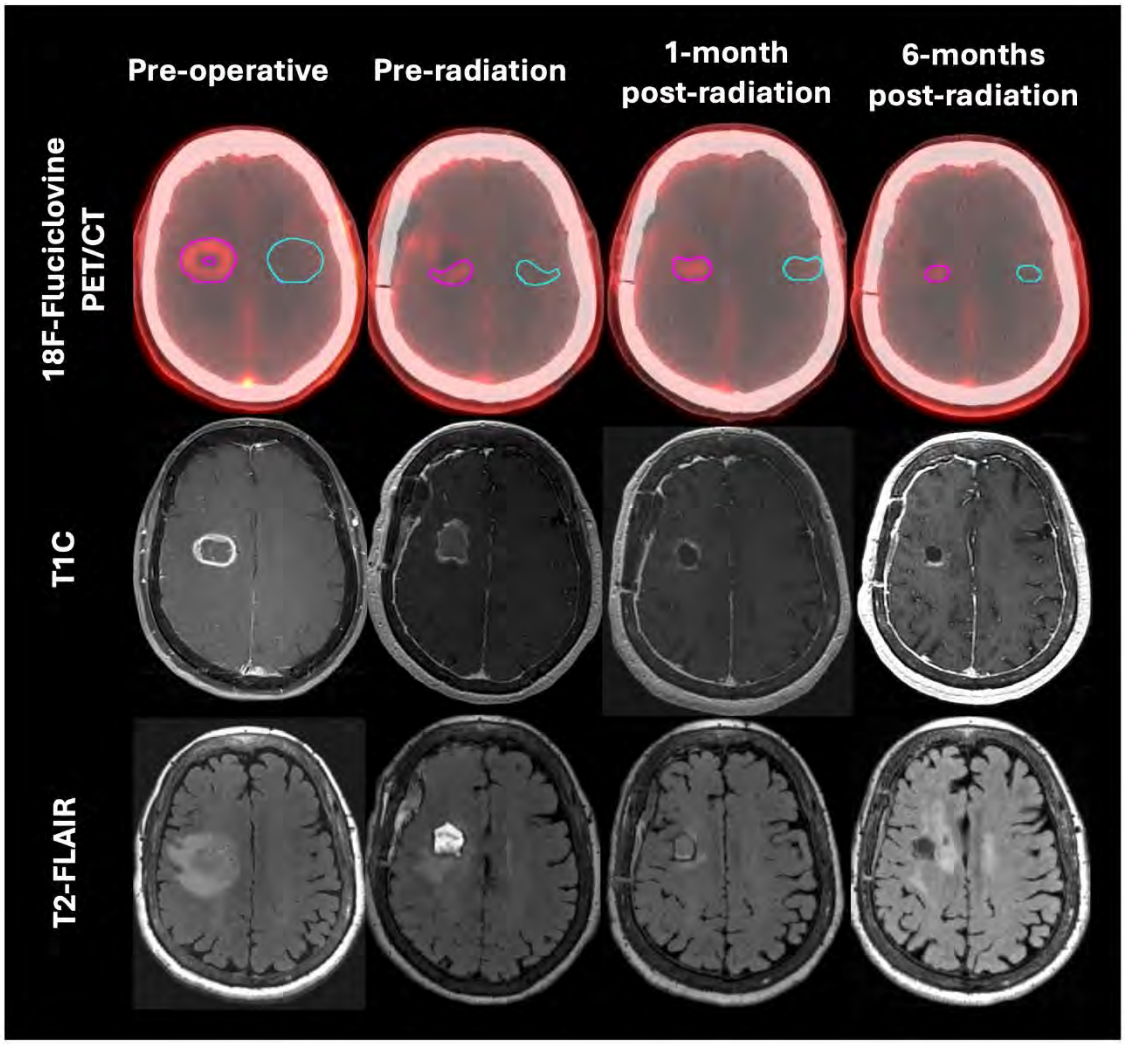

1219

Evaluating the Efficacy of the MRI Entire Spine Protocol in the Emergency Setting among Age Groups

Krishna Subbiah[1], Evan Jacobs[1], Andrew Owens[1], Sherif Zineldine[1], Daniel Gridley MD[2]
[1]Creighton University School of Medicine, Phoenix, AZ, USA. [2]Valleywise Medical Health Center, Phoenix, AZ, USA

Abstract Category

Spine

Purpose

The purpose of this study is to evaluate the likelihood of identifying actionable findings stratified by patient age on MRI entire spine scans conducted in the emergency department. Total spine MRI is often ordered when there is concern for spinal cord compression, spinal cord injury, or in the setting where the clinical neurological examination cannot localize the level of concern. By examining MRI findings and categorizing impressions based on actionable outcomes across various patient age groups, this study aims to provide insights that may guide indications for ordering MRI entire spine examinations in the acute care setting.

Materials & Methods

This is a retrospective analysis of clinical data for patients from 2018 through 2023 who received the entire spine MRI protocol (T1, T2, and STIR sagittal sequences) at Valleywise Hospital Systems in the acute care setting. Selected patients were categorized in the following age groups for further analysis: 44 years and below, 45 to 64 years, and 65 years and above. The primary endpoint of this study is to assess the likelihood of finding positive, actionable findings when a complete spine MRI protocol is used in the acute care setting for patients across varying age demographics.

Results

After exclusion of non-diagnostic studies, 656 patients were included in the study. In total, 42.2% of all patients had significant acute radiological findings. For patients older than 65, 72.3% of studies resulted in acute findings. Among the 45-64 year old cohort, 47.3% of studies resulted in acute findings. For those under 44, 26.3% of studies resulted in acute findings. Based on this patient population, increased age is correlated with increased chance of being positive for acute actionable findings on imaging ($P < 0.001$).

Conclusion

Entire spine MRI protocols play an important role in the acute care setting especially when suspected pathology is related to the spinal cord, nerve roots, or intervertebral discs. This study demonstrates that the likelihood of identifying positive, actionable findings significantly increases with patient age, underscoring the importance of age-based considerations in imaging decisions.

References

Huang CW, Chu Y, Klumpp M, et al. Major radiologic and clinical outcomes of total spine MRI performed in the emergency department at a major academic medical center. AJNR Am J Neuroradiol 2020;41(6):1120-1125 10.3174/ajnr.A6578

Morris M, Destian S, Chu Y, Klumpp M, Zohrabian VM. Investigation of whole spine MRI in the emergency department at two large tertiary care academic medical centers in the United States. Curr Probl Diagn Radiol 2021;50(5):637-645 10.1067/j.cpradiol.2020.07.005

Bozzo A, Marcoux J, Radhakrishna M, et al. The role of magnetic resonance imaging in the management of acute spinal cord injury. J Neurotrauma 2011;28(8):1401-1411 10.1089/neu.2009.1236

1221

Diagnostic Performance of ASL-MRI and FDG-PET in Frontotemporal Dementia: A Systematic Review and Meta-Analysis

Richard Dagher MD[1], Parisa Arjmand MD[2], Burak B Ozkara MD[1], Mahla Radmard MD[3], Mona Gad MD[4], Ali Sheikhy MD[5], Samir A Dagher MD[1], Ceylan Altintas Taslicay MD[1], Sahar Alizada MD[1], Ahmed Msherghi MD[1], Max Wintermark[1], Licia P Luna[3]
[1]The University of Texas MD Anderson Cancer Center, Houston, TX, USA. [2]University Hospitals Cleveland Medical Center/Case Western Reserve University, Cleveland, OH, USA. [3]Johns Hopkins University School of Medicine, Baltimore, MD, USA. [4]Radiology Department, Mansoura University Faculty of Medicine, Mansoura, Dakahlia, Egypt. [5]National Institutes of Health, Bethesda, MD, USA

Abstract Category
Functional/Advanced Imaging
Purpose
While the diagnosis of frontotemporal dementia (FTD) is based mostly on clinical features, [18F]-FDG PET has been investigated as a potential imaging golden standard in ambiguous cases, with arterial spin labeling (ASL) MRI gaining recent interest. The purpose of this study is to conduct a systematic review and meta-analysis on the diagnostic performance of ASL MRI in FTD patients and compare it to that of [18F]-FDG PET.
Materials & Methods
A systematic search of PubMed, Scopus and EMBASE was conducted until March 13, 2024. Inclusion criteria were: original articles, patients with FTD and/or its variants, use of ASL MR perfusion imaging with or without [18F]-FDG PET, presence of sufficient diagnostic performance data. Exclusion criteria were: meeting abstracts, comments, summaries, protocols, letters and guidelines, longitudinal studies, overlapping cohorts. The quality of eligible studies was assessed using the Quality Assessment of Diagnostic Accuracy Studies-2. Pooled sensitivity, specificity, and diagnostic odds ratio (DOR) for [18F]-FDG PET and ASL MRI were calculated, and a summary receiver operating characteristic curve was plotted.
Results
Seven eligible studies were identified, which included a total of 102 FTD patients. Aside from some of the studies showing at worst an unclear risk of bias in patient selection, index test, flow and timing, all studies showed low risk of bias and applicability concerns in all categories. Data from 4 studies was included in our meta-analysis for ASL MRI and 3 studies for [18F]-FDG PET. Pooled sensitivity, specificity and DOR were 0.70 (95% CI: 0.59-0.79), 0.81 (95% CI: 0.71-0.88) and 8.00 (95% CI: 3.74-17.13) for ASL MRI, and 0.88 (95% CI: 0.71-0.96), 0.89 (95% CI: 0.43-0.99) and 47.18 (95% CI: 10.77-206.75) for [18F]-FDG PET.
Conclusion
While ASL MRI performed worse than [18F]-FDG PET in the diagnosis of FTD, it exhibited a decent diagnostic performance to justify its further investigation as a quicker and more convenient alternative.
References
Abe K, Fukushima K, Katsuura T, et al. Can arterial spin labeling perfusion image diagnose dementia -Comparison with single photon emission computed tomographic image-. Journal of the Neurological Sciences 2017;381:312.
Binnewijzend M, Kuijer J, Van der Flier W, et al. IC-P-062: The role of ASL-measured cerebral blood flow in the differential diagnosis of Alzheimer's disease, frontotemporal dementia and dementia with Lewy bodies. Alzheimer's & Dementia 2013;9:P38–P38.
Verfaillie SCJ, Adriaanse SM, Binnewijzend MAA, et al. Cerebral perfusion and glucose metabolism in Alzheimer's disease and frontotemporal dementia: two sides of the same coin? Eur Radiol 2015;25:3050–9.
Marterstock DC, Knott MFX, Hoelter P, et al. Pulsed Arterial Spin Labeling and Segmented Brain Volumetry in the Diagnostic Evaluation of Frontotemporal Dementia, Alzheimer's Disease and Mild Cognitive Impairment. Tomography 2022;8:229–44.

Images/Tables

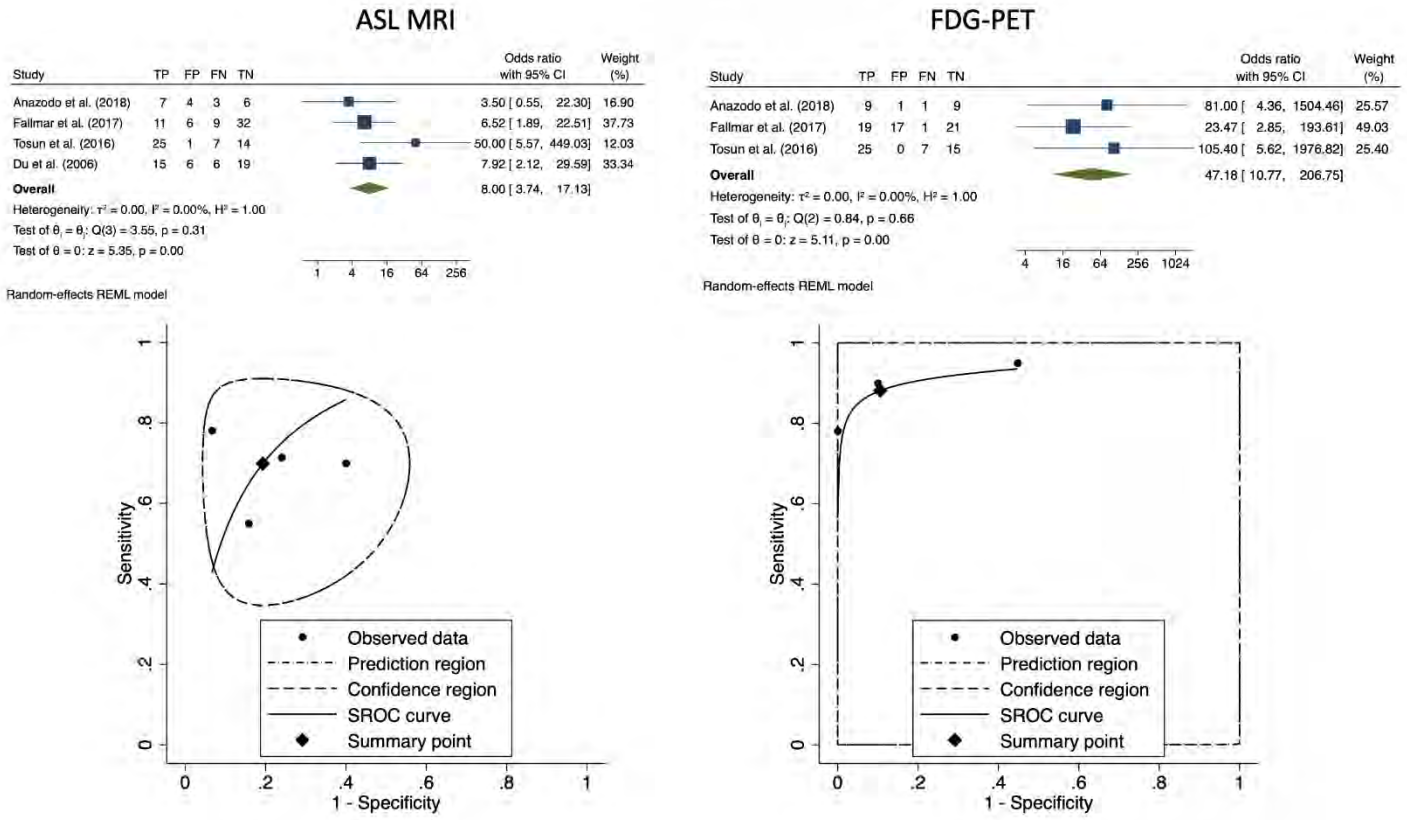

1227

Comparative Analysis of Voxel Volumes Across MRI Sequence Types in Pediatric High-Grade Gliomas: Insights from Neuroimaging Data

Andrew J Goulian MPH

California Northstate University- College of Medicine, Elk Grove, CA, USA

Abstract Category

Pediatrics

Purpose

High-grade gliomas (HGGs) are aggressive, life-threatening brain tumors in pediatric patients. Accurate imaging is essential for diagnosis, treatment planning, and monitoring progression. While MRI is the primary modality for assessing pediatric HGGs, the variation in voxel volumes across different MRI sequences (T1, T1-Post, T2, T2-FLAIR) remains poorly understood. These sequences are crucial for evaluating tumor size, location, and surrounding tissue, yet the differences in voxel volumes across them have not been fully explored. This study aims to compare voxel volumes across T1, T1-Post, T2, and T2-FLAIR sequences in pediatric HGG patients to identify the most reliable sequence for consistent and clinically relevant voxel measurements. The findings could inform future imaging protocols, enhancing tumor assessment and clinical decision-making in pediatric HGG management.

Materials & Methods

This retrospective study used MRI data from the DFCI-BCH-BWH-Peds-HGG collection available through The Cancer Imaging Archive (TCIA). The dataset includes imaging from 61 pediatric patients diagnosed with high-grade gliomas, with MRI scans obtained using T1-weighted pre- and post-contrast, T2-weighted, and FLAIR sequences. Image preprocessing steps such as skull stripping, alignment, and voxel size normalization were applied to ensure consistency in voxel volume calculations across all sequences. Voxel volumes were calculated for each MRI sequence type, focusing on the tumor region. A one-way ANOVA was conducted to assess the statistical differences in voxel volumes across the four sequence types. Tukey's Honest Significant Difference (HSD) post-hoc test was performed to explore pairwise comparisons between the sequence types. Statistical significance was set at $p<0.05$.

Results

A total of 61 pediatric patients with high-grade gliomas were included in the analysis. One-way ANOVA revealed significant differences in voxel volumes across MRI sequence types ($F(3,73) = 5.232$, $p < 0.01$). Post-hoc testing indicated that T2-FLAIR had significantly larger voxel volumes compared to T1-Post (mean difference = 1.39 mm^3, $p < 0.01$). No significant differences were found between T1-Pre, T2, and T1-Post sequences. The mean voxel volume for T2-FLAIR was 2.66 mm^3, while T1-Post had the smallest mean voxel volume at 2.92 mm^3. These findings suggest that T2-FLAIR may provide superior resolution in analyzing pediatric high-grade gliomas, offering enhanced voxel volume measurements compared to other MRI sequences.

Conclusion

Our study demonstrates that T2-FLAIR MRI sequences provide significantly larger voxel volumes compared to other commonly used sequences (T1-Pre, T2, T1-Post) in pediatric high-grade gliomas. These results suggest that T2-FLAIR may offer superior resolution for evaluating tumor characteristics and for assessing tumor volume in neuroimaging analysis. However, further studies are needed to confirm these findings and evaluate their clinical relevance, particularly in optimizing the diagnostic and monitoring process in pediatric brain tumor care. By identifying specific MRI sequences with more reliable voxel volumes, clinicians may be able to improve the precision of neuroimaging and better tailor treatment strategies for pediatric patients with high-grade gliomas. The use of T2-FLAIR may ultimately enhance both the accuracy of tumor assessments and the monitoring of tumor progression.

References

Chen, X., Cui, Y., & Zou, L. Treatment advances in high-grade gliomas. Front Oncol 14, 1287725 (2024). https://doi.org/10.3389/fonc.2024.1287725.

Chen, J., et al. Review on neuroimaging in pediatric-type diffuse low-grade gliomas. Front Pediatr 11, 1149646 (2023). https://doi.org/10.3389/fped.2023.1149646.

Ailion, A.S., Hortman, K. & King, T.Z. Childhood Brain Tumors: a Systematic Review of the Structural Neuroimaging Literature. Neuropsychol Rev 27, 220–244 (2017). https://doi.org/10.1007/s11065-017-9352-6.

Images/Tables

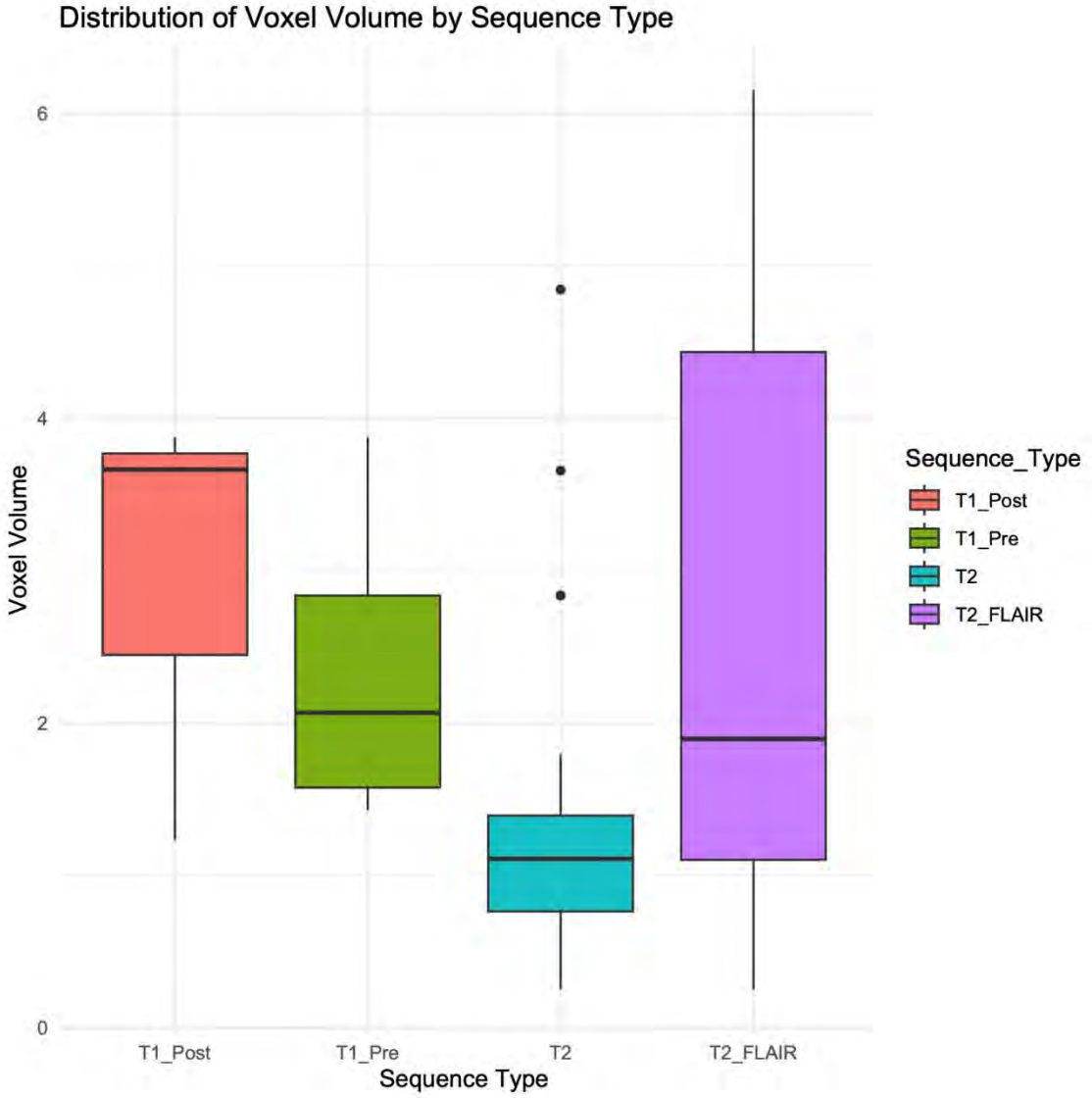

1233

Neuroimaging Manifestations of Baraitser-Winter Cerebrofrontofacial Syndrome

Khalid Al-Dasuqi MD[1], Sedat Kandemirli MD[2], Bulent Aslan MD[3], Cesar Alves MD[4]

[1]Sidra Medical Center, Doha, NA, Qatar. [2]Duke University, Durham, NC, USA. [3]Beth Israel Deaconess Medical Center, Boston, MA, USA. [4]Boston Children's Hospital, Boston, MA, USA

Abstract Category

Pediatrics

Purpose

Baraitser-Winter syndrome (BWS) is a rare autosomal dominant developmental disorder caused by genetic alterations in the ACTB and ACTG1 genes. The syndrome is characterized by distinct craniofacial dysmorphisms, intellectual disability, epilepsy, and various structural brain abnormalities. Patients also invariably present with cardiac defects and urogenital abnormalities. While the clinical features have been well-reported in BWS (Velroes et al 2014), the neuroimaging manifestations of BWS remain under-characterized due to the rarity of the condition. This study aims to provide further insights into the characteristic neuroimaging features of this syndrome.

Materials & Methods

Retrospective review of brain MRIs for nine patients with confirmed BWS diagnosis was independently performed by two pediatric neuroradiologists. All patients had genetic confirmation except for one whose clinical presentation was deemed highly consistent with BWS

Results

The median age at the time of imaging was 4 years. Genetic testing performed in 8 out of 9 patients revealed likely pathogenic variants in the ACTB (6/8) and ACTG1 (2/8) genes. All patients had craniofacial dysmorphisms as has been previously reported in BWS. Cardiac and urogenital abnormalities were observed in one-third of patients in this cohort. Imaging review of the brain MRIs revealed cortical migration abnormalities in nearly all (8/9) patients ranging from subtle dysgyria to severe lissencephaly with subcortical band heterotopia and most frequently manifesting as diffuse dysgyria-pachygria. Two-thirds of patients had some degree of corpus callosal dysgenesis. Thinning and indistinction of the lamina terminalis was also seen in 6/9 patients, and interhypothalamic adhesions were observed in 5/9 cases. Incomplete hippocampal rotation and olfactory bulb hypoplasia/aplasia were seen in 7/9 cases. Five patients had unusually prominent perivascular spaces in the periventricular and juxtacortical white matter of the cerebral hemispheres. More than half of cases had some degree of C1 posterior arch hypoplasia.

Conclusion

Baraitser-Winter syndrome presents a distinct neuroimaging pattern, including cortical malformations, callosal dysgenesis and other midline abnormalities. These findings can assist in early radiological diagnosis and guide clinical management.

References

Verloes, A., Di Donato, N., Masliah-Planchon, J. et al. Baraitser–Winter cerebrofrontofacial syndrome: delineation of the spectrum in 42 cases. Eur J Hum Genet 23, 292–301 (2015). https://doi.org/10.1038/ejhg.2014.95

1241

Assessing the Diagnostic Performance of Automated Pituitary Gland Volume Measurement for Idiopathic Central Precocious Puberty

HaYoun Kim MD,PhD, In Kyu Yu MD,PhD
Eulji University Hospital, Daejeon, daejeon, Korea, Republic of

Abstract Category

Pediatrics

Purpose

It has been known that the pituitary gland volume (PV) in idiopathic central precocious puberty (IPP) is significantly higher than in healthy children. However, most PV measurements rely on manual quantitative methods, which are time-consuming and labor-intensive. This study aims to automatically measure the PV of patients with IPP using artificial intelligence to accurately quantify the correlation between IPP and PV, and to improve the efficiency of diagnosing IPP.

Materials & Methods

From July 2016 to February 2024, 226 patients diagnosed with IPP and underwent brain MR were included (117 males and 109 females, median age, 8 years; interquartile range, 7–9years). A control group of 52 patients who underwent brain MR imaging without symptoms of precocious puberty was also included (37 males and 15 females, median age, 8 years; interquartile range, 8–9 years). Measurement variability was examined between manual and automatic measurements (n=57). The pituitary gland volume was measured using 1-3 mm thickness T1 sagittal images from non-enhanced brain MR imaging, analyzed with the MA-net artificial intelligence learning method. Physical characteristics (height, weight, and age) were correlated with PV, and the difference in PV between the IPP group and the control group was evaluated.

Results

The intraclass correlation coefficient was 0.993 for agreement between manual and automatic measurement. Confounding bias was reduced by PSM. PV was positively correlated with age and body weight in the IPP group (17.4%, P =0.009, and 14.0%, P =.037). The median values of PV were 432mm^3 in the IPP group and 380mm^3 in the control group, showing a significant difference of 52mm^3 (P <0.05).

Conclusion

The PV in the IPP group was significantly higher than in the control group. Automatically measuring PV along with assessing hormone levels could enable a faster and more straightforward diagnosis of the IPP.

References

1. Wu S, Yang Y, Wang Y, et al. Diagnostic value of pituitary volume in girls with precocious puberty. *BMC Pediatr* 2020;20:425

2. Xu YQ, Li GM, Li Y. Advanced bone age as an indicator facilitates the diagnosis of precocious puberty. *J Pediatr (Rio J)* 2018;94:69-75
3. Hongyang Jiang ZS, Xiaoming Luo MW, Mei Wang,, Qi Feng JC, Chunmiao Lin,, et al. Noninvasive radiomics-based method for evaluating idiopathic central precocious puberty in girls. *Journal of International Medical Research* 2021;492(2):1-11
4. Sharafuddin MJ, Luisiri A, Garibaldi LR, et al. MR imaging diagnosis of central precocious puberty: importance of changes in the shape and size of the pituitary gland. *AJR Am J Roentgenol* 1994;162:1167-1173
5. Peper JS, Brouwer RM, van Leeuwen M, et al. HPG-axis hormones during puberty: a study on the association with hypothalamic and pituitary volumes. *Psychoneuroendocrinology* 2010;35:133-140
6. Tien RD, Kucharczyk J, Bessette J, et al. MR imaging of the pituitary gland in infants and children: changes in size, shape, and MR signal with growth and development. *AJR Am J Roentgenol* 1992;158:1151-1154
7. Myung Soon Kim JSP, Ki Joon Sung. MR measurement of Normal Pituitary Gland Height on Midsagittal Section: Age and Sex Differentiation. Journal of Korean Radiological Society 1992;28(4):523-526
8. Litjens G, Kooi T, Bejnordi BE, et al. A survey on deep learning in medical image analysis. *Med Image Anal* 2017;42:60-88
9. Greenspan. H VGB, Summers. R. M. Challenges and opportunities in medical image analysis using deep learning. *Annual Review of Biomedical Engineering* 2016;18:221-248
10. Rubin. C BC. Manual vs. automated segmentation methods in medical imaging. *Journal of Digital Imaging* 2012;25(4):545-552
11. He. L ZX, Ren. S, Sun. J. Deep residual learning for image recognition. *In Proceedings of the IEEE Conference on Computer Vision and Pattern Recognition* 2016:770-778
12. Fan. T WG, Li. Y, Wang. H. MA-Net: A Multi-Scale Attention Network for Liver and Tumor Segmentation. *IEEE Access* 2020;8:179656-179665
13. Qubvel. *Segmentation models pytorch*. GitHub repository. Retrieved https://github.com/qubvel-org/segmentation_models.pytorch; 2023
14. Muneuchi J, Nagatomo Y, Okada S, et al. Increased Pituitary Volumes in Children after Fontan Operation: Congestion in the Other Portal Circulation. *J Pediatr* 2018;193:249-251
15. Sari S, Sari E, Akgun V, et al. Measures of pituitary gland and stalk: from neonate to adolescence. *J Pediatr Endocrinol Metab* 2014;27:1071-1076
16. Fink AM, Vidmar S, Kumbla S, et al. Age-related pituitary volumes in prepubertal children with normal endocrine function: volumetric magnetic resonance data. *J Clin Endocrinol Metab* 2005;90:3274-3278
17. Han X, Xiu J, Huang Z, et al. Three-dimensional magnetic resonance volumetry of the pituitary gland is effective in detecting short stature in children. *Exp Ther Med* 2014;8:551-556
18. Fehrenbach U, Jadan A, Auer TA, et al. Obesity and pituitary gland volume - a correlation study using three-dimensional magnetic resonance imaging. *Neuroradiol J* 2020;33:400-409
19. Berntsen EM, Haukedal MD, Haberg AK. Normative data for pituitary size and volume in the general population between 50 and 66 years. *Pituitary* 2021;24:737-745
20. Pratiksha Yadav SS, Surbhi Chauhan, Saumya Harit. MRI Evaluation of Size and Shape of Normal Pituitary Gland: Age and Sex Related Changes. *Journal of Clinical and Diagnostic Research* 2017;11:01-04
21. Deepti Naik, Prashanth Reddy D., M. G. Srinath, et al. Pituitary Gland Assessment by MR Volumetry in the Normal Indian Adolescent Population. International Journal of Medical Imaging 2015;3(6):105-109
22. Ertekin T, Acer N, Turgut AT, et al. Comparison of three methods for the estimation of the pituitary gland volume using magnetic resonance imaging: a stereological study. Pituitary 2011;14:31-38
23. İlknur Okur Akşan AS. The assessment of the pituitary volume in normal prepubertal children with three-dimensional MRI. *Cukurova Medical Journal* 2021;46(3):912-919